WILEY-VCH

Edited by
Reiner Salzer and Heinz W. Siesler

Infrared and Raman Spectroscopic Imaging

Second, Completely Revised and Updated Edition

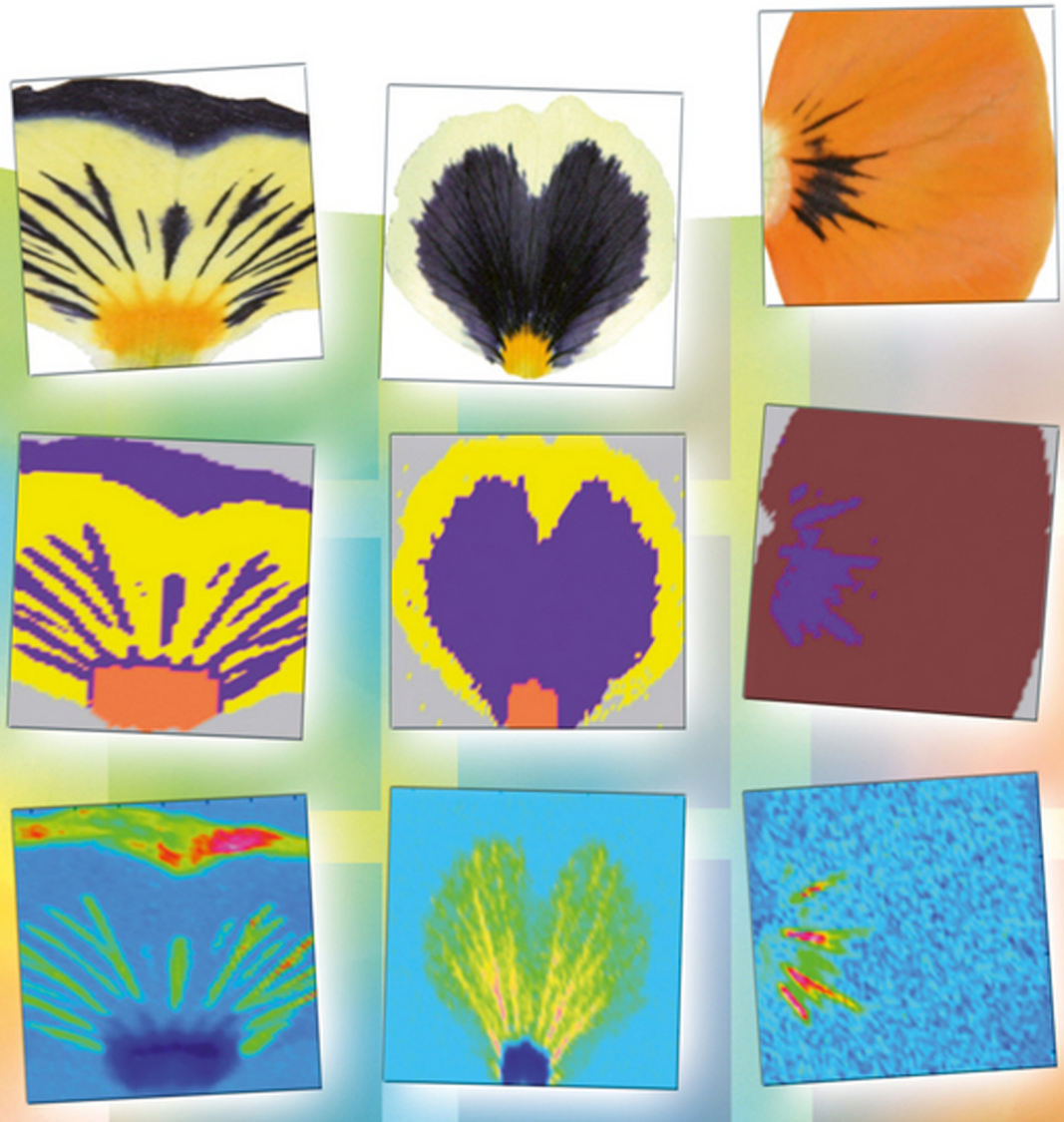

Edited by
Reiner Salzer and
Heinz W. Siesler

Infrared and Raman Spectroscopic Imaging

Related Titles

Gauglitz, G., Moore, D. S. (eds.)

Handbook of Spectroscopy
Second, Completely Revised and Enlarged Edition

2014
ISBN: 978-3-527-32150-6

Leahy, M. J. (ed.)

Microcirculation Imaging

2012
ISBN: 978-3-527-32894-9

Schlücker, S. (ed.)

Surface Enhanced Raman Spectroscopy
Analytical, Biophysical and Life Science Applications

2011
ISBN: 978-3-527-32567-2

Zerbe, O., Jurt, S.

Applied NMR Spectroscopy for Chemists and Life Scientists

2014
ISBN (Hardcover): 978-3-527-32775-1
ISBN (Softcover): 978-3-527-32774-4

Edited by Reiner Salzer and Heinz W. Siesler

Infrared and Raman Spectroscopic Imaging

Second, Completely Revised and Updated Edition

WILEY-VCH
Verlag GmbH & Co. KGaA

The Editors

Prof. Reiner Salzer
Bioanalytische Chemie
Technische Universität Dresden
Helmholtzstr 10
01062 Dresden
Germany

Prof. Heinz W. Siesler
Universität Duisburg-Essen
Inst. f. Physikalische Chemie
Schützenbahn 70
45117 Essen
Germany

All books published by **Wiley-VCH** are carefully produced. Nevertheless, authors, editors, and publisher do not warrant the information contained in these books, including this book, to be free of errors. Readers are advised to keep in mind that statements, data, illustrations, procedural details or other items may inadvertently be inaccurate.

Library of Congress Card No.: applied for

British Library Cataloguing-in-Publication Data
A catalogue record for this book is available from the British Library.

Bibliographic information published by the Deutsche Nationalbibliothek
The Deutsche Nationalbibliothek lists this publication in the Deutsche Nationalbibliografie; detailed bibliographic data are available on the Internet at <http://dnb.d-nb.de>.

© 2014 Wiley-VCH Verlag & Co. KGaA, Boschstr. 12, 69469 Weinheim, Germany

All rights reserved (including those of translation into other languages). No part of this book may be reproduced in any form – by photoprinting, microfilm, or any other means – nor transmitted or translated into a machine language without written permission from the publishers. Registered names, trademarks, etc. used in this book, even when not specifically marked as such, are not to be considered unprotected by law.

Print ISBN: 978-3-527-33652-4
ePDF ISBN: 978-3-527-67816-7
ePub ISBN: 978-3-527-67815-0
Mobi ISBN: 978-3-527-67814-3
oBook ISBN: 978-3-527-67813-6

Cover-Design Adam Design, Weinheim Germany
Typesetting Laserwords Private Limited, Chennai, India
Printing and Binding Markono Print Media Pte Ltd., Singapore

Printed on acid-free paper

Contents

Preface *XVII*
List of Contributors *XIX*

Part I Basic Methodology *1*

1 Infrared and Raman Instrumentation for Mapping and Imaging *3*
Peter R. Griffiths and Ellen V. Miseo
1.1 Introduction to Mapping and Imaging *3*
1.2 Mid-Infrared Microspectroscopy and Mapping *4*
1.2.1 Diffraction-Limited Microscopy *4*
1.2.2 Microscopes and Sampling Techniques *6*
1.2.3 Detectors for Mid-Infrared Microspectroscopy *9*
1.2.4 Sources for Mid-Infrared Microspectroscopy *11*
1.2.5 Spatial Resolution *14*
1.2.6 Transmission Microspectroscopy *18*
1.2.7 Attenuated Total Reflection Microspectroscopy *19*
1.3 Raman Microspectroscopy and Mapping *20*
1.3.1 Introduction to Raman Microspectroscopy *20*
1.3.2 CCD Detectors *24*
1.3.3 Spatial Resolution *26*
1.3.4 Tip-Enhanced Raman Spectroscopy *29*
1.4 Near-Infrared Hyperspectral Imaging *30*
1.5 Raman Hyperspectral Imaging *35*
1.6 Mid-Infrared Hyperspectral Imaging *37*
1.6.1 Spectrometers Based on 2D Array Detectors *37*
1.6.2 Spectrometers Based on Hybrid Linear Array Detectors *43*
1.6.3 Sampling *45*
1.7 Mapping with Pulsed Terahertz Radiation *48*
1.8 Summary *52*
Acknowledgments *54*
References *54*

2 Chemometric Tools for Image Analysis *57*
Anna de Juan, Sara Piqueras, Marcel Maeder, Thomas Hancewicz, Ludovic Duponchel, and Romà Tauler
2.1 Introduction *57*
2.2 Hyperspectral Images: The Measurement *58*
2.2.1 The Data Set and the Underlying Model *58*
2.3 Image Preprocessing *60*
2.3.1 Signal Preprocessing *61*
2.3.1.1 De-noising *61*
2.3.1.2 Baseline Correction *61*
2.3.1.3 Detection and Suppression of Anomalous Pixels or Anomalous Spectral Readings *63*
2.3.2 Data Pretreatments *63*
2.3.3 Image Compression *64*
2.4 Exploratory Image Analysis *65*
2.4.1 Classical Image Representations: Limitations *65*
2.4.2 Multivariate Image Analysis (MIA) and Principal Component Analysis (PCA) *66*
2.5 Quantitative Image Information: Multivariate Image Regression (MIR) *70*
2.6 Image Segmentation *73*
2.6.1 Unsupervised and Supervised Segmentation Methods *74*
2.6.2 Hard and Fuzzy Segmentation Approaches *78*
2.6.3 Including Spatial Information in Image Segmentation *79*
2.7 Image Resolution *80*
2.7.1 The Image Resolution Concept *80*
2.7.2 Spatial and Spectral Exploration *81*
2.7.3 The Resolution Process: Initial Estimates and Constraints *86*
2.7.4 Image Multiset Analysis *91*
2.7.5 Resolution Postprocessing: Compound Identification, Quantitative Analysis, and Superresolution *95*
2.7.5.1 Compound Identification *98*
2.7.5.2 Quantitative Analysis *100*
2.7.5.3 Superresolution *104*
2.8 Future Trends *106*
References *106*

Part II Biomedical Applications *111*

3 Vibrational Spectroscopic Imaging of Soft Tissue *113*
Christoph Krafft and Jürgen Popp
3.1 Introduction *113*
3.1.1 Epithelium *114*
3.1.2 Connective Tissue and Extracellular Matrix *115*
3.1.3 Muscle Tissue *116*

3.1.4 Nervous Tissue *117*
3.2 Preparation of Soft Tissue for Vibrational Spectroscopic Imaging *118*
3.2.1 General Preparation Strategies *118*
3.2.2 Vibrational Spectra of Reference Material *120*
3.2.3 Preparation for FT-IR Imaging *121*
3.2.4 Preparation for Raman Imaging *123*
3.3 Applications to Soft Tissue *125*
3.3.1 Colon Tissue *125*
3.3.2 Brain Tissue and Brain Tumors *130*
3.3.2.1 Mouse Brains *130*
3.3.2.2 Primary Brain Tumors *132*
3.3.2.3 Secondary Brain Tumors *134*
3.3.2.4 Cellular Resolution *137*
3.3.3 Cervix Uteri and Squamous Cell Carcinoma *139*
3.3.4 Atherosclerosis *143*
3.4 Conclusions *145*
References *147*

4 Vibrational Spectroscopic Analysis of Hard Tissues *153*
Sonja Gamsjaeger, Richard Mendelsohn, Klaus Klaushofer, and Eleftherios P. Paschalis
4.1 Introduction *153*
4.1.1 Hard Tissue Composition and Organization *153*
4.1.2 Elements of Hard Tissues, Detectable by Vibrational Spectroscopy *153*
4.2 Importance of Tissue Age versus Specimen Age *155*
4.2.1 Biologically Important Questions That May Be Answered by This Type of Analysis *155*
4.3 FT-IR Spectroscopy *156*
4.3.1 Specimen Preparation and Typical FT-IR Spectrum *156*
4.3.2 Examples from Published Literature *158*
4.4 Raman Spectroscopy *160*
4.4.1 Instrumental Choices, Specimen Preparation, and Typical Raman Spectra *160*
4.4.2 Bone: Typical Raman Bands and Parameters *161*
4.4.3 Examples from Published Literature *163*
4.5 Clinical Applications of Raman Spectroscopy *165*
References *166*

5 Medical Applications of Infrared Spectral Imaging of Individual Cells *181*
Max Diem, Jennifer Schubert, Miloš Miljković, Kostas Papamarkakis, Antonella I. Mazur, Ellen Marcsisin, Jennifer Fore, Benjamin Bird, Kathleen Lenau, Douglas Townsend, Nora Laver, and Max Almond

5.1 Introduction *181*
5.2 Methods *183*
5.2.1 Cell Collection and Culturing Methods *183*
5.2.1.1 Exfoliated Cells *183*
5.2.1.2 Cultured Cells *183*
5.2.2 Sample Preparation *184*
5.2.2.1 Sample Substrates *184*
5.2.2.2 Sample Fixation *184*
5.2.2.3 Sample Deposition *184*
5.2.3 Data Acquisition *185*
5.2.3.1 Infrared Instrumentation *185*
5.2.3.2 PapMap Methodology *185*
5.2.4 Methods of Data Analysis *188*
5.2.4.1 Correction for R-Mie Effects and Data Preprocessing *188*
5.2.4.2 Principal Component Analysis (PCA) *190*
5.2.4.3 Diagnostic Algorithms *190*
5.3 Results and Discussion *191*
5.3.1 General Aspects of SCP *191*
5.3.2 Fixation Studies *194*
5.3.2.1 Fixation Studies of Exfoliated Cells *195*
5.3.2.2 Fixation Effects of Cultured Cells *198*
5.3.3 Spectral Cytopathology: Distinction of Cell Types and Disease in Human Urine-Borne Cells and Oral, Cervical, and Esophageal Cells *200*
5.3.3.1 SCP of Urine-Borne Cells *200*
5.3.3.2 SCP of Oral Mucosa Cells *202*
5.3.3.3 SCP of the Cervical Mucosa *210*
5.3.3.4 SCP of Esophageal Cells *212*
5.3.4 SCP of Live Cells in Aqueous Environment *216*
5.4 Future Potential of SCP/Conclusions *218*
Acknowledgment *219*
References *220*

Part III Agriculture, Plants, and Food *225*

6 Infrared and Raman Spectroscopic Mapping and Imaging of Plant Materials *227*
Hartwig Schulz, Andrea Krähmer, Annette Naumann, and Gennadi Gudi
6.1 Introduction, Background, and Perspective *227*
6.2 Application of Mapping and Imaging to Horticultural Crops *229*
6.2.1 Carotenoids *229*
6.2.2 Polyacetylenes *232*
6.2.3 Flavonoids *234*
6.2.4 Essential Oils *236*
6.2.5 Tissue Constituents *241*

6.2.6 Environmental Interactions and Processing *242*
6.3 Application of Mapping and Imaging to Agricultural Crops *244*
6.3.1 Tissue-Specific Functional-Group Analysis *245*
6.3.2 Cell Wall Microstructure *246*
6.3.2.1 Carbohydrates and the Endosperm *246*
6.3.2.2 Protein Secondary Structure *250*
6.3.2.3 Lignin and Cellulose *250*
6.3.3 Environmental Impact and Processing *251*
6.3.4 Uptake and Fate of Environmental Contaminants/Crop Protection Products *253*
6.4 Mapping and Imaging of Wild Plants and Trees *254*
6.4.1 Mapping and Imaging of Trees *256*
6.4.1.1 IR Mapping and Imaging of Trees *256*
6.4.1.2 Raman Mapping and Imaging of Trees *258*
6.4.2 Mapping and Imaging of *Arabidopsis thaliana* *261*
6.4.2.1 IR Mapping and Imaging *261*
6.4.2.2 Raman Mapping and Imaging *262*
6.4.3 Mapping and Imaging of Wild Plants *262*
6.5 Application of Mapping and Imaging to Algae *264*
6.5.1 Taxonomic Differentiation and Classification of Algae *265*
6.5.2 Cell Wall Composition and Compound Distribution *266*
6.5.3 Environmental Influences on Algae Metabolism *268*
6.5.4 Chemometrical and Instrumental Developments *271*
6.5.4.1 Raman Techniques *271*
6.5.4.2 IR Techniques *272*
6.6 Interaction Between Plant Tissue and Plant Pathogens *273*
6.6.1 Bacterial Plant Pathogens *274*
6.6.2 Fungal Plant Pathogens *275*
6.6.3 Fungal Degradation of Plant Material *279*
6.6.4 Interaction with Nonwoody Plants *282*
References *282*

7 NIR Hyperspectral Imaging for Food and Agricultural Products *295*
Véronique Bellon-Maurel and Nathalie Gorretta
7.1 Introduction *295*
7.1.1 A Brief History of NIR Spectral Imagers *295*
7.1.2 When is NIR Hyperspectral Imaging Used for Food and Agricultural Products? *297*
7.2 HSI as a "Super" NIR Analyzer *298*
7.2.1 Assessment and Quantification of Physicochemical or Sensory Properties of Food and Agricultural Products *298*
7.2.2 Chemical Mapping *300*
7.2.2.1 Fruit *300*
7.2.2.2 Wood *301*
7.2.2.3 Fish *301*

7.2.2.4 Meat *303*
7.2.2.5 Laboratory Batch Cultures *304*
7.2.2.6 Kernels *305*
7.2.2.7 Other Applications: Process Monitoring *305*
7.2.2.8 Conclusion: Some Pitfalls of HSI When Used for Chemical Mapping *306*
7.2.3 Analysis of the Physical Properties of the Food/Agricultural Items *308*
7.3 NIR HS Imager as a "Super" Vision System *310*
7.3.1 Why HS Imaging May Replace RGB Cameras for Sorting or Mixture Characterization *310*
7.3.1.1 The Failure of RGB Systems in Food Quality Control *310*
7.3.1.2 How Did Online NIR Imaging Emerge? *311*
7.3.2 External Contamination (Foreign Bodies, Adulteration) *312*
7.3.2.1 Foreign Bodies *313*
7.3.2.2 Adulteration and Nonconformities *315*
7.3.2.3 Surface Contaminations *315*
7.3.3 Surface and Subsurface Defects *317*
7.3.3.1 Human-Detectable Defects *318*
7.3.3.2 Potential Defects: Chilling Injuries, Potential Greening Area *320*
7.3.4 Detection of Internal Defects by Candling *320*
7.3.4.1 Internal Foreign Bodies *321*
7.3.4.2 Internal Tissue Defects *322*
7.3.5 Classification of Biological Objects *323*
7.3.5.1 Inspecting Small Objects *323*
7.3.5.2 ROI in Multicompartment Products *324*
7.3.6 Conclusion *325*
7.4 Conclusion *326*
7.4.1 When is NIR Imaging Worth Using in Online Settings? *326*
7.4.1.1 Software *327*
7.4.1.2 Hardware *327*
References *328*

Part IV Polymers and Pharmaceuticals *339*

8 FT-IR and NIR Spectroscopic Imaging: Principles, Practical Aspects, and Applications in Material and Pharmaceutical Science *341*
Elke Grotheer, Christian Vogel, Olga Kolomiets, Uwe Hoffmann, Miriam Unger, and Heinz W. Siesler
8.1 Introduction *341*
8.2 Instrumentation for NIR and FT-IR Imaging *343*
8.2.1 NIR Imaging in Diffuse Reflection *343*
8.2.2 NIR Imaging in Transmission *345*
8.2.3 FT-IR Imaging *345*
8.2.3.1 Micro FT-IR Imaging *346*

8.2.3.2 Macro FT-IR Imaging *347*
8.2.3.3 Measurement of an FT-IR Image *348*
8.2.3.4 Possible Artifacts Encountered in FT-IR/ATR Imaging *349*
8.2.3.5 Spatial Resolution of FT-IR Imaging Measurements *354*
8.3 Applications of FT-IR and FT-NIR Imaging for Polymer Characterization *361*
8.3.1 Investigation of Phase Separation in Biopolymer Blends *361*
8.3.2 Imaging Anisotropic Materials with Polarized Radiation *364*
8.3.2.1 Blends of PHB and PLA *364*
8.3.2.2 Stress-Induced Phase Transformation in Poly(vinylidene Fluoride) *368*
8.3.3 Applications of FT-NIR Imaging for Diffusion Studies *370*
8.3.3.1 Experimental *372*
8.3.3.2 Results and Discussion *373*
8.3.4 Conclusions *378*
8.4 NIR Imaging Spectroscopy for Quality Control of Pharmaceutical Drug Formulations *378*
8.4.1 Quantitative Determination of Active Ingredients in a Pharmaceutical Drug Formulation *379*
8.4.2 Spatial Distribution of the Active Ingredients in a Pharmaceutical Drug Formulation *381*
8.4.3 Conclusions *386*
8.5 FT-IR Spectroscopic Imaging of Inorganic Materials *387*
8.5.1 Introduction *387*
8.5.2 Experimental *388*
8.5.3 Determination of P-Fertilizer–Soil Reactions *388*
8.5.4 Determination of Mineral Phases in Soils *392*
8.5.5 Conclusion *393*
References *394*

9 FT-IR Imaging in ATR and Transmission Modes: Practical Considerations and Emerging Applications *397*
Jennifer Andrew Dougan, K. L. Andrew Chan, and Sergei G. Kazarian
9.1 FT-IR Imaging: Introduction *397*
9.1.1 ATR FT-IR Imaging *398*
9.1.2 Transmission FT-IR Imaging *400*
9.2 FT-IR Imaging: Technical Considerations *401*
9.2.1 Transmission FT-IR Imaging: Mapping Versus FPA *401*
9.2.2 ATR FT-IR Imaging: Mapping Versus FPA *401*
9.2.3 ATR FT-IR Imaging: Field of View *402*
9.2.3.1 Overview of ATR FT-IR Imaging Approaches: Micro (Ge), Macro (Diamond, Si), Expanded FOV (ZnSe), Variable Angle *402*
9.2.3.2 Micro-ATR FT-IR Imaging *403*
9.2.3.3 Diamond ATR FT-IR Imaging *404*
9.2.3.4 Expanded FOV (ZnSe) *406*

9.2.4 ATR FT-IR Imaging: Depth of Penetration *407*
9.2.5 ATR FT-IR Imaging: Quantitation *408*
9.3 Practical Applications *410*
9.3.1 Materials Characterization of Polymer Interfaces and Blends *410*
9.3.1.1 Investigating a Polymer: Carbon Fiber Interface *410*
9.3.1.2 Polystyrene: Polyethylene Blend – Imaging the Effect of a Compatibilizer *411*
9.3.1.3 Hydrogels *412*
9.3.2 Pharmaceuticals: Studying Tablets, Dissolution, Drug Diffusion, and Biopharmaceuticals *413*
9.3.2.1 Imaging of Compacted Tablets *413*
9.3.2.2 ATR FT-IR Imaging of Tablet Dissolution *415*
9.3.2.3 ATR FT-IR Imaging of Drug Diffusion Across Tissue Sections: Biomedical Applications *419*
9.3.2.4 Biopharmaceuticals Development: Optimizing Protein Crystallization *421*
9.3.3 Forensics Applications *424*
9.3.3.1 Imaging of Counterfeit Tablets *424*
9.3.3.2 Detection of Trace Materials and Chemical Fingerprinting *425*
9.3.4 Imaging of Live Cells *427*
9.3.4.1 ATR FT-IR Imaging of Live Cells *427*
9.3.4.2 Transmission Mode FT-IR Imaging of Live Cells in Microfluidic Devices *427*
9.3.5 High-Throughput Studies with ATR FT-IR Imaging *430*
9.3.5.1 Transmission Mode High-Throughput Imaging *432*
9.3.5.2 Imaging and Microfluidics *433*
9.4 Conclusion and Outlook *436*
Acknowledgment *437*
References *438*

10 Terahertz Imaging of Drug Products *445*
Michel Ulmschneider
10.1 Introduction *445*
10.2 Low Wavenumber Region in the Infrared Spectrum *446*
10.2.1 Far-Infrared Spectroscopy *446*
10.2.2 THz Spectroscopy *448*
10.3 THz-TDS Technology and Applications *448*
10.3.1 THz Pulse Generation and Detection *448*
10.3.1.1 Emission *448*
10.3.1.2 Reception *449*
10.3.1.3 Sampling *450*
10.3.2 Current Applications of THz Spectroscopy *450*
10.3.3 Concise Description of THz Imaging *451*
10.4 THz Imaging in the Pharmaceutical Industry *452*
10.4.1 Introduction *452*

10.4.2 Imaging of Solid Dosage Forms *453*
10.4.3 Investigating Pharmaceutical Samples by Means of THz Imaging *455*
10.4.4 Experimental Setup to Measure Solid Dosage Forms *458*
10.4.5 Typical Applications to Solid Dosage Forms *460*
10.4.6 Discussion *468*
10.5 Going Forward *470*
10.6 Competition versus Cost: A Challenge for the Future *471*
10.7 Conclusion *472*
Acknowledgments *472*
References *473*

Part V Imaging Beyond the Diffraction Limit *477*

11 Spectroscopic Imaging of Biological Samples Using Near-Field Methods *479*
Lucas Langelüddecke, Tanja Deckert-Gaudig, and Volker Deckert
11.1 Tip-Enhanced Raman Scattering (TERS) *479*
11.1.1 From SERS to TERS *479*
11.1.2 Investigation of Nonbiological Samples with TERS *480*
11.1.3 Technical Considerations of TERS *481*
11.1.3.1 Application *481*
11.2 Detection of Biomolecules *483*
11.2.1 Differentiation/Identification of Single Biomolecules *484*
11.2.1.1 Amino Acids *484*
11.2.1.2 DNA/RNA Nucleobases and Derivatives *487*
11.2.2 Detection of Structural/Chemical Changes on a Molecular Level *491*
11.3 Biopolymers *494*
11.3.1 DNA/RNA Strands *495*
11.3.2 Proteins and Fibrils *496*
11.4 Membranes, Viruses, and Bacteria *500*
11.5 Conclusion *505*
References *505*

12 Infrared Mapping below the Diffraction Limit *513*
Peter R. Griffiths and Ellen V. Miseo
12.1 Introduction and Description of Early Work *513*
12.1.1 Near-Field Microscopy with Small Apertures *513*
12.1.2 Scanning Photothermal Microscopy and Microspectroscopy *515*
12.1.3 First Description of AFM/FT-IR *518*
12.2 Near-Field Microscopy by Elastic Scattering from a Tip *519*
12.3 Combination of AFM and Photothermal FT-IR Spectroscopy *529*
References *538*

Part VI Developments in Methodology *541*

13 Subsurface Raman Spectroscopy in Turbid Media *543*
Pavel Matousek
13.1 Introduction *543*
13.2 Techniques for Deep Noninvasive Raman Spectroscopy *544*
13.2.1 Spatially Offset Raman Spectroscopy (SORS) *544*
13.2.2 Inverse SORS *547*
13.2.3 Transmission Raman Spectroscopy *548*
13.2.4 Raman Tomography *549*
13.2.5 SESORS *549*
13.3 Examples of Application Areas *550*
13.3.1 Probing of Bones through Skin for Disease Diagnosis *550*
13.3.2 Chemical Identification of Calcifications in Breast Cancer Lesions *554*
13.3.2.1 Cancer Margins *554*
13.3.2.2 Glucose Detection *555*
13.3.3 Probing of Pharmaceutical Tablets and Capsules in Quality Control *556*
13.3.4 Forensic and Security Applications *556*
13.4 Conclusions *558*
References *558*

14 Nonlinear Vibrational Spectroscopic Microscopy of Cells and Tissue *561*
Roberta Galli and Gerald Steiner
14.1 Introduction *561*
14.2 Principles of Nonlinear Optical Imaging *562*
14.2.1 Important Processes for Nonlinear Optical Imaging *562*
14.2.2 Coherent Anti-Stokes Raman Scattering *563*
14.2.3 CARS Microscopy *567*
14.3 Instrumentation for Multimodal Nonlinear Microscopy *568*
14.3.1 Laser Sources *568*
14.3.2 Optics *570*
14.3.3 Scanning Microscope *571*
14.4 Applications *572*
14.4.1 Identification of Tumor Tissue *572*
14.4.2 Brain Structures and Brain Tumors *574*
14.4.3 Normal and Injured Spinal Cord *576*
References *580*

15 Widefield FT-IR 2D and 3D Imaging at the Microscale Using Synchrotron Radiation *585*
Eric C. Mattson, Miriam Unger, Julia Sedlmair, Michael Nasse, Ebrahim Aboualizadeh, Zahrasadat Alavi, and Carol J. Hirschmugl
15.1 Introduction *585*
15.1.1 Synchrotron IR Radiation Sources *585*
15.1.2 Synchrotron-Based Infrared Raster-Scanned (IR SR) Spectromicroscopy *586*
15.1.3 Synchrotron-Based Infrared Widefield Spectromicroscopy *586*
15.1.4 Synchrotron-Based Infrared Spectromicrotomography *588*
15.2 Optical Evaluation *588*
15.2.1 Microscopy Optics and Diffraction-Limited Resolution *588*
15.2.2 Experimental and Simulated Point Spread Functions *589*
15.3 Mathematical Evaluation of Hyperspectral Cubes *590*
15.3.1 Hyperspectral Deconvolution *590*
15.3.2 3D Spectromicrotomographic Reconstruction *593*
15.4 Widefield versus Raster Scanning Geometries *595*
15.4.1 Effects of Numerical Aperture, Spatial Oversampling, and Deconvolution on Spatial Resolution *595*
15.4.2 Signal-to-Noise Ratio Comparisons *597*
15.4.3 Time–Area Trade-Off *598*
15.4.4 New Directions: Spectromicrotomography *600*
15.5 Examples *600*
15.5.1 General Applications *600*
15.5.1.1 Nanocellulose *600*
15.5.1.2 Matisse *603*
15.5.2 Influence of Deconvolution *604*
15.5.2.1 Labeled Cells *604*
15.5.2.2 Layered Polymers–Transmission and Reflection *604*
15.5.3 Time-Dependent Infrared Imaging *609*
15.5.3.1 Algal Biochemistry: Diatom Response to Changes in Carbon Dixide Supply *609*
15.5.3.2 Surface Chemistry: NH_3 Adsorption on Reduced Graphene Oxide *611*
15.5.4 Infrared Spectromicrotomography *611*
15.5.4.1 Human Hair *611*
15.5.4.2 Populus–Cell Walls of Wood *613*
15.6 Conclusions *615*
References *616*

Index *619*

Preface

Five years after the completion of the first edition of this book, Wiley-VCH approached us with the request to prepare a second edition. On the one hand, this was certainly a consequence of the successful marketing of this book but, on the other hand, we accepted this challenge because since the publication of the first edition numerous new instrumental developments and improvements as well as a significant expansion of the imaging technique have taken place. Thus, for example, the combination of IR imaging with atomic force microscopy (AFM) enhanced the achievable lateral resolution by an order of magnitude down to a few hundred nanometers and thereby launched a multiplicity of new applications in material science. Furthermore, Raman and IR spectroscopic imaging studies have become key technologies for the life sciences and today contribute tremendously to a better and more detailed understanding of numerous biological and medical research topics.

In order to cover these novel developments, the chapters of the previous edition have not only been updated but new chapters have been added. For this purpose, the topical structure of the new edition had to be extended and is now subdivided into four parts. In Part 1, the fundamentals of the instrumentation for infrared and Raman imaging and mapping and an overview on the chemometric tools for image analysis are treated in two introductory chapters. Part 2 comprises Chapters 3–10 and describes a wide variety of applications ranging from biomedical via food, agriculture, and plants to polymers and pharmaceuticals. In Part 3, Chapters 11 and 12 describe imaging techniques operating beyond the diffraction limit, and finally Part 4 (Chapters 13–15) covers special methodical developments and their utility in specific fields.

We would like to thank the authors of the previous edition for the willingness to contribute again the latest achievements in their field of research and gratefully acknowledge the spontaneous agreement of the new authors to add their expertise to the new edition. We are fully aware that without the effort, commitments, and sacrifices of these authors, the timely publication of this volume would not have been possible. We

would also like to acknowledge the superb job and professional support by Wiley-VCH in the final composition and edition of the book. Last but not least, our greatest debt of gratitude goes to our families for their patience and understanding.

Dresden and Essen
January 2014

Reiner Salzer and
Heinz W. Siesler

List of Contributors

Ebrahim Aboualizadeh
University of
Wisconsin-Milwaukee
Department of Physics
Milwaukee, WI 53211
USA

Zahrasadat Alavi
University of Wisconsin-
Milwaukee
Department of Physics
Milwaukee, WI 53211
USA

Max Almond
Gloucestershire Hospitals NHS
Foundation Trust
Department of Esophagogastric
Surgery
Great Western Road
Gloucester, GL13NN
UK

Véronique Bellon-Maurel
IRSTEA – Montpellier Supagro
UMR ITAP, Information –
Technologies – Environmental
Analysis – Agricultural
Processes
BP 50 95, Montpellier Cedex 1,
34033
France

Benjamin Bird
Northeastern University
Laboratory for Spectral
Diagnosis (LSpD)
Department of Chemistry and
Chemical Biology
360 Huntington Ave
Boston, MA 02115
USA

K. L. Andrew Chan
Department of Chemical
Engineering
Imperial College London
London, SW7 2AZ
United Kingdom

Volker Deckert
Institute of Physical Chemistry
and Abbe Center of Photonics
University of Jena
Helmholtzweg 4
07743 Jena
Germany

and

Leibniz Institute of Photonic
Technology – IPHT
Albert-Einstein-Str. 9
07745 Jena
Germany

Tanja Deckert-Gaudig
Leibniz Institute of Photonic Technology – IPHT
Nanoscopy department
Albert-Einstein-Str. 9
07745 Jena
Germany

Max Diem
Northeastern University
Laboratory for Spectral Diagnosis (LSpD)
Department of Chemistry and Chemical Biology
360 Huntington Ave
Boston, MA 02115
USA

Jennifer A. Dougan
Department of Chemical Engineering
Imperial College London
London, SW7 2AZ
United Kingdom

Ludovic Duponchel
Université Lille 1. Sciences et Technologies de Lille (USTL)
Laboratoire de Spectrochimie Infrarouge et Raman (LASIR CNRS UMR 8516)
Bâtiment C5
Villeneuve d'Ascq, 59655
France

Jennifer Fore
Northeastern University
Laboratory for Spectral Diagnosis (LSpD)
Department of Chemistry and Chemical Biology
360 Huntington Ave
Boston, MA 02115
USA

Roberta Galli
Dresden University of Technology
Carl Gustav Carus Faculty of Medicine
Clinical Sensoring and Monitoring
Fetscher Str. 74
01307 Dresden
Germany

Sonja Gamsjaeger
Hanusch Hospital
1st Medical Department, Ludwig Boltzmann Institute of Osteology at the Hanusch Hospital of WGKK and AUVA Trauma Centre Meidling
Heinrich Collin Str. 30
A-1140, Vienna
Austria

Nathalie Gorretta
IRSTEA – Montpellier Supagro
UMR ITAP
Information – Technologies – Environmental Analysis – Agricultural Processes
BP 50 95, Montpellier Cedex 1
34033
France

Peter R. Griffiths
Griffiths Consulting LLC
4150 Edgehill Drive
Ogden, UT 84403
USA

Elke Grotheer
Beiersdorf AG
Research & Development
Unnastraße 48
D 20253 Hamburg
Germany

Gennadi Gudi
Julius Kühn-Institute
Federal Research Centre for
Cultivated Plants
Institute for Ecological
Chemistry
Plant Analysis and Stored
Product Protection
Königin-Luise-Strasse 19
14195 Berlin
Germany

Thomas Hancewicz
Unilever Research &
Development
Trumbull. 40 Merrit Blvd.
Trumbull, CT 06611
USA

Carol J. Hirschmugl
University of Wisconsin-
Milwaukee
Department of Physics
Milwaukee, WI 53211
USA

and

US Forest Service
Forest Products Laboratory
One Gifford Pinchot Drive
adison, WI 53726
USA

Uwe Hoffmann
NIR-Tools
Katernberger Straße 107
D 45327 Essen
Germany

Anna de Juan
Universitat de Barcelona
Department of Analytical
Chemistry
Chemometrics group
Diagonal 645
Barcelona, 08028
Spain

Sergei G. Kazarian
Department of Chemical
Engineering
Imperial College London
London SW7 2AZ
United Kingdom

Klaus Klaushofer
Hanusch Hospital
1st Medical Department, Ludwig
Boltzmann Institute of Osteology
at the Hanusch Hospital of
WGKK and AUVA Trauma
Centre Meidling
Heinrich Collin Str. 30
Vienna, A-1140
Austria

Olga Kolomiets
MS S.P.R.L.,
206/9 Avenue van Overbeke
BE 1083 Ganshoren
Belgium

Christoph Krafft
Institute of Photonic Technology
07745 Jena
Germany

Andrea Krähmer
Julius Kühn-Institute
Federal Research Centre for
Cultivated Plants
Institute for Ecological
Chemistry
Plant Analysis and Stored
Product Protection
Königin-Luise-Strasse 19
14195 Berlin
Germany

Lucas Langelüddecke
Institute of Physical Chemistry
and Abbe Center of Photonics
Nanospectroscopy department
University of Jena
Helmholtzweg 4
07743 Jena
Germany

Nora Laver
Tufts Medical Center
Department of Pathology
Boston, MA
USA

Kathleen Lenau
Northeastern University
Department of Chemistry and
Chemical Biology
Laboratory for Spectral
Diagnosis (LSpD)
360 Huntington Ave
Boston, MA 02115
USA

Marcel Maeder
The University of Newcastle
Department of Chemistry
Callaghan NSW, 2308
Australia

Ellen Marcsisin
Northeastern University
Department of Chemistry and
Chemical Biology
Laboratory for Spectral
Diagnosis (LSpD)
360 Huntington Ave
Boston, MA 02115
USA

Eric C. Mattson
University of
Wisconsin-Milwaukee
Department of Physics
Milwaukee, WI 53211
USA

Pavel Matousek
STFC Rutherford Appleton
Laboratory
Central Laser Facility
Research Complex at Harwell
Harwell Oxford, OX11 0QX
UK

Antonella I. Mazur
Northeastern University
Department of Chemistry and
Chemical Biology
Laboratory for Spectral
Diagnosis (LSpD)
360 Huntington Ave
Boston, MA 02115
USA

Miloš Miljković
Northeastern University
Department of Chemistry and
Chemical Biology
Laboratory for Spectral
Diagnosis (LSpD)
360 Huntington Ave
Boston, MA 02115
USA

Ellen V. Miseo
Analytical Answers, Inc.
4 Arrow Drive, Woburn
MA 01801
USA

Richard Mendelsohn
Rutgers University
Department of Chemistry
Newark College
New Jersey, 07102 Newark
USA

Annette Naumann
Julius Kühn-Institute
Federal Research Centre for
Cultivated Plants
Institute for Ecological
Chemistry
Plant Analysis and Stored
Product Protection
Königin-Luise-Strasse 19
14195 Berlin
Germany

Michael Nasse
University of
Wisconsin-Milwaukee
Department of Physics
Milwaukee, WI 53211
USA

and

Laboratory for Applications of
Synchrotron Radiation
Karlsruhe Institute of
Technology
Karlsruhe
Germany

Kostas Papamarkakis
Northeastern University
Department of Chemistry and
Chemical Biology
Laboratory for Spectral
Diagnosis (LSpD)
360 Huntington Ave
Boston, MA 02115
USA

Eleftherios P. Paschalis
Hanusch Hospital
1st Medical Department, Ludwig
Boltzmann Institute of Osteology
at the Hanusch Hospital of
WGKK and AUVA Trauma
Centre Meidling
Heinrich Collin Str. 30
A-1140 Vienna
Austria

Sara Piqueras
Universitat de Barcelona
Department of Analytical
Chemistry, Chemometrics
group, Diagonal 645
Barcelona, 08028
Spain

and

IDAEA-CSIC
Jordi Girona 18
Barcelona, 08034
Spain

Jürgen Popp
Institute of Physical Chemistry
and Abbe Center of Photonics
University Jena
Helmholtzweg 4 Jena, 07743
Germany

and

University Jena
Institute of Physical Chemistry
and Abbe Center of Photonics
07743 Jena
Germany

Jennifer Schubert
Northeastern University
Department of Chemistry and
Chemical Biology
Laboratory for Spectral
Diagnosis (LSpD)
360 Huntington Ave
Boston, MA 02115
USA

Hartwig Schulz
Julius Kühn-Institute
Federal Research Centre for
Cultivated Plants
Institute for Ecological
Chemistry
Plant Analysis and Stored
Product Protection
Königin-Luise-Strasse 19
14195 Berlin
Germany

and

Julius Kühn-Institute
Federal Research Centre for
Cultivated Plants
Institute for Ecological
Chemistry
Plant Analysis and Stored
Product Protection
Erwin-Baur-Strasse 27
06484 Quedlinburg
Germany

Julia Sedlmair
US Forest Service
Forest Products Laboratory
One Gifford Pinchot Drive
Madison, WI 53726
USA

Heinz W. Siesler
University of Duisburg-Essen
Department of Physical
Chemistry
Schuetzenbahn 70
D 45117 Essen
Germany

Gerald Steiner
Dresden University of
Technology
Carl Gustav Carus Faculty of
Medicine
Clinical Sensoring and
Monitoring
Fetscher Str. 74
01307 Dresden
Germany

Romá Tauler
IDAEA-CSIC
Jordi Girona 18
Barcelona, 08034
Spain

Douglas Townsend
Northeastern University
Department of Chemistry and
Chemical Biology
Laboratory for Spectral
Diagnosis (LSpD)
360 Huntington Ave
Boston, MA 02115
USA

Michel Ulmschneider
Pharmaceutical Quality Control
F. Hoffmann - La Roche AG
4070 Basel
Switzerland

Miriam Unger
CETICS Healthcare
Technologies GmbH
Schelztorstraße 54-56 73728
Esslingen am Neckar
Germany

Christian Vogel
BAM Federal Institute for
Materials Research and Testing
Unter den Eichen 87
D 12205 Berlin
Germany

Part I
Basic Methodology

Infrared and Raman Spectroscopic Imaging, Second Edition. Edited by Reiner Salzer, Heinz W. Siesler.
© 2014 Wiley-VCH Verlag GmbH & Co. KGaA. Published 2014 by Wiley-VCH Verlag GmbH & Co. KGaA.

1
Infrared and Raman Instrumentation for Mapping and Imaging

Peter R. Griffiths and Ellen V. Miseo

1.1
Introduction to Mapping and Imaging

The analysis of localized regions of samples by vibrational microspectroscopy can be accomplished in two ways, *mapping* or *imaging.* Mapping involves the sequential measurement of the spectrum of each adjacent region of a sample by moving each region of the sample into the beam after recording the spectrum. The measurement is repeated until the entire region of interest has been covered. Imaging, on the other hand, is like taking a digital picture and requires an image of the sample to be focused onto an array detector. The intensity of the radiation passing through each region of the sample is measured simultaneously at each pixel.

Mapping experiments in which the sample is moved in both x and y dimensions should not be properly called imaging, since the spectra have not been acquired by an array detector. However, the spectra that are obtained can be treated in exactly the same way as if these spectra had been acquired with an array detector. Commercially available hybrid mapping/imaging instruments have also been described in which a linear array of, say, 32 detectors is used to acquire a line map after which the sample is moved and the process is repeated.

In *hyperspectral imaging,* the images at more than 10 wavelength regions are recorded simultaneously with a two-dimensional array detector. Vibrational hyperspectral imaging can be accomplished through the measurement of either the mid-infrared, near-infrared (NIR), or Raman spectrum. The measurement of each type of spectrum is accomplished in different ways, although the instruments that have been developed for the measurement of NIR and Raman spectra are more closely related than that of mid-infrared hyperspectral imaging spectrometers. In NIR and Raman instruments, the signal at a given wavelength is recorded at each pixel. In NIR imaging instruments, the radiation from the source is usually focused on the sample and then passed through a monochromator or narrow bandpass filter, for example, a liquid crystal tunable filter (LCTF), before being focused on the array detector. The image from one wavelength region is measured at all pixels simultaneously. The wavelength region is then changed (usually, but not necessarily, to an adjacent spectral region) and the intensity at

Infrared and Raman Spectroscopic Imaging, Second Edition. Edited by Reiner Salzer, Heinz W. Siesler.
© 2014 Wiley-VCH Verlag GmbH & Co. KGaA. Published 2014 by Wiley-VCH Verlag GmbH & Co. KGaA.

each pixel is measured again. This process is repeated until all wavelengths of interest in the spectrum have been measured.

An analogous approach is used for Raman imaging, except that the monochromator must be located after the sample. The signal from all pixels for a given wavelength setting is acquired rapidly in NIR imaging instruments, where the signal-to-noise ratio (SNR) is usually high. The SNR for Raman imaging is much lower, so that a much longer integration time is needed. Thus, Raman imaging can be quite slow unless only a few wavelength regions are measured. In both NIR and Raman imaging spectrometers, the bandpass of the monochromator or filter determines the spectral resolution. Sometimes only a short spectral range or a few wavelength regions may be sufficient to classify samples that are composed of just a few components. On the other hand, for complex or previously uncharacterized samples, it is often necessary to measure data over the entire spectral range.

In mid-IR imaging instruments, it is more common to couple the array to an interferometer, so that interferograms from different spatial regions of the sample are recorded at each detector element. Subsequent Fourier transformation yields the desired hyperspectral data set. All types of systems are described in this chapter.

The end result of either spectroscopic mapping or hyperspectral imaging is an array of spectra (sometimes called a *hyperspectral cube* or *hypercube*) from which the identifying characteristics of inhomogeneous samples can be obtained. For Raman imaging, the sample does not have to be of constant thickness; however, ideally the sample should be as flat as possible. Conversely, when mid-IR or NIR transmission spectra are to be measured, the thickness of the sample should be as uniform as possible. In this case, it is sometimes possible to synthesize an image that shows the concentration of a certain component by simply plotting the absorbance at a certain wavelength of a band that is isolated from all others in the spectrum. If this approach proves to be feasible, the image may be plotted either as a gray scale, with white representing the absence of the component and dark gray representing its greatest concentration, or – more commonly – through the use of color. Many applications of imaging spectroscopy will be described throughout this book. In this chapter, the design of the instruments used to acquire these data is described.

1.2 Mid-Infrared Microspectroscopy and Mapping

1.2.1 Diffraction-Limited Microscopy

The diffraction pattern resulting from a circular aperture that is uniformly illuminated with monochromatic light has a bright region in the center, known as the *Airy disk*, which together with the series of concentric bright rings around this disk is called the *Airy pattern*. The beam half-angle θ' at which the first minimum

occurs, measured from the direction of incoming light, is given by

$$\sin\theta' = \frac{1.22\lambda}{nd} \tag{1.1}$$

where λ is the wavelength of the light and d is the diameter of the aperture. Similarly, if the half-angle of the beam at the sample is θ and n is the refractive index of the medium in which the sample is immersed, the diameter of the sample under observation, x, is given by

$$x = \frac{1.22\lambda}{n\sin\theta} \tag{1.2}$$

The product of the refractive index n and sin θ is known as the *numerical aperture* (*NA*).

The Rayleigh criterion for barely resolving two objects is that the center of the Airy disk for the first object occurs at the first minimum of the Airy disk of the second object. Figure 1.1 shows the calculated signal from two point sources separated by 0.5λ, 1.0λ, and 1.5λ. It can be seen that the spots are not able to be distinguished when the separation is equal to 0.5λ, are just distinguishable when the separation is equal to λ, and are well separated when the spots are separated by 1.5λ.

For most transmission spectroscopic measurements made with a microscope, the sample is in contact with air and so n is usually approximately equal to 1. Since for most microscopes $\theta \sim 40°$, NA is usually close to 0.6 (sin $40° = 0.64$). Thus, the spatial resolution is approximately equal to λ. (We note here that the Abbe resolution is often defined as $\lambda/2$, but this performance is only accomplished for coherent illumination.) For mid-infrared measurements at the highest spatial resolution, it is customary to set the microscope aperture to give the diffraction-limited resolution at 1000 cm^{-1} ($\lambda = 10\,\mu m$) so that the resolution at longer wavelengths is set by the value at 1000 cm^{-1} (about 10 μm). Better resolution is achieved in attenuated total reflection (ATR), especially when the internal reflection element (IRE) is silicon ($n = 3.4$) or germanium ($n = 4.0$), but achieving optical spatial resolution better than about 3 μm is essentially impossible for diffraction-limited mid-infrared measurements.

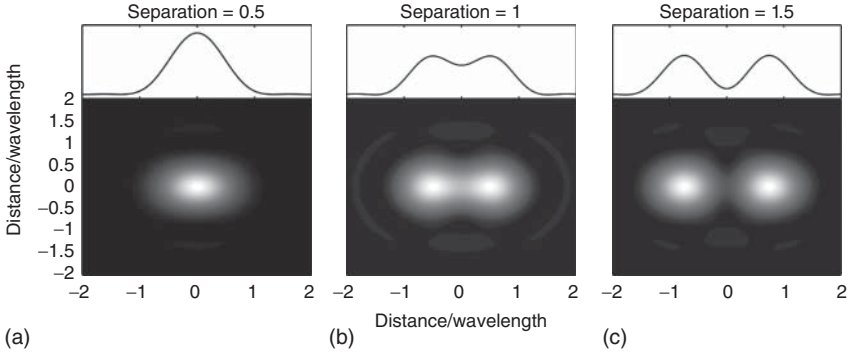

Figure 1.1 Calculated images of two point sources separated by (a) 0.5λ, (b) 1.0λ, and (c) 1.5λ. (Courtesy of Pike Technologies, Inc.)

1.2.2
Microscopes and Sampling Techniques

Although some noble efforts at fabricating a microscope for infrared spectrometry using a prism monochromator were made in the 1940s and 1950s [1–6] and PerkinElmer actually advertised a microscope that could be installed in one of their prism spectrometers [7], the performance of these early instruments was marginal and the use of infrared microscopes never caught on commercially until the late 1980s. Until that time, the mid-infrared spectra of minute samples were measured by mounting the sample behind a pinhole of the appropriate dimensions so that only the region of the sample of interest was irradiated. The sample was then held at the focus of a simple beam condenser that fit in the sample compartment of the spectrometer. As the size of the region of interest decreased, locating the sample so that the region of interest corresponded to the position of the pinhole became increasingly difficult. The situation was dramatically improved when a standard reflecting microscope was interfaced with a Fourier transform infrared (FT-IR) spectrometer. In this case, the previous function of the pinhole was replaced by a remote aperture at a conjugate focus of the sample. A simplified schematic of a typical infrared microscope is shown in Figure 1.2.

The microscope shown in Figure 1.2 is designed to operate in either the transmission mode or the reflection mode. In the transmission mode, the beam from the interferometer is passed onto a toroidal coupling optic and therefrom to the

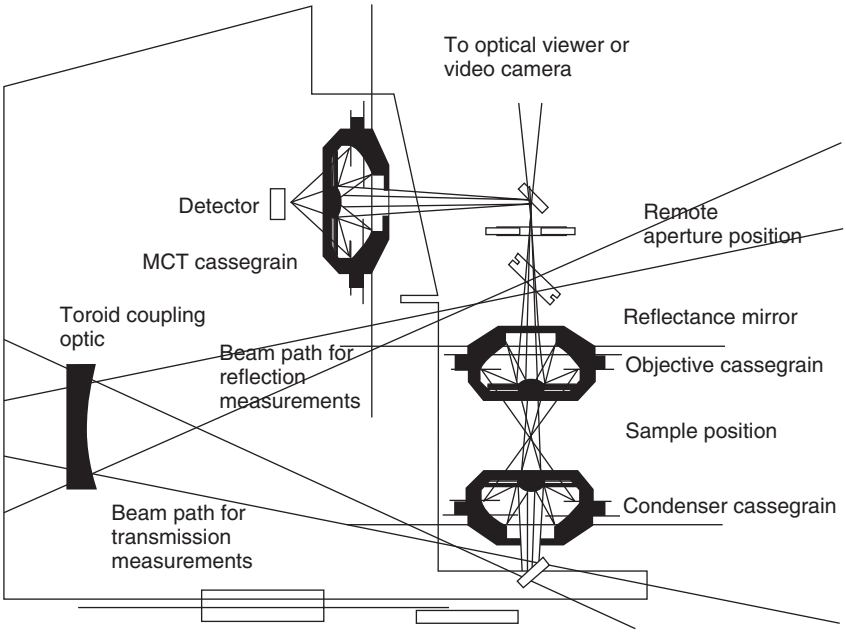

Figure 1.2 Simplified schematic of a typical microscope interfaced with an FT-IR spectrometer. (Courtesy of PerkinElmer Inc.)

Cassegrain condenser. The condenser focuses the beam into a small spot where the sample is mounted. The radiation that is transmitted through the sample is collected by a Cassegrain objective and refocused at a remote adjustable aperture. The part of beam that passes through the aperture is imaged onto an optical viewer or, more frequently today, a video camera, so that the visible image of the sample can be viewed. The sample is usually mounted on an *x, y, z* stage. The height of the sample is adjusted with the *z*-control to ensure that the position of the sample is coincident with the beam focus. The *x* and *y* controls are then used to adjust the location of the sample so that the region of interest is at the center of the beam. The jaws of the aperture are then adjusted so that only the region of interest is seen at the viewer. The aperture is often rectangular and can be rotated through 180° to allow the region of interest to be isolated. After the conditions have been optimized, a 45° mirror is slid into position so the light that is transmitted through the remote aperture is collected by the third Cassegrain and focused onto the detector, which measures the spectrum of the desired region of the sample.

We note here that the condensing mirrors go by two names: some call it a *Cassegrain* while others call it a *Schwarzschild* objective. Both objectives comprise a convex and concave mirror, with a hole in the latter for the light to travel through. The key feature of the Schwarzschild design is the concentricity, or near-concentricity, of the two mirrors; there is no requirement of concentricity whereas this is not the case for Cassegrain objectives. Thus, all Schwarzschild objectives are Cassegrain objectives but the reverse is not the case. The Schwarzschild objective has been used in almost all FT-IR microscopes, and is still used to this day as it has excellent imaging characteristics over a surprisingly wide field of view (FOV), a fact that arises from the mirror concentricity. The first commercial FT-IR microscope, the Digilab UMA-150, used this design because the designers were aware that the 1953 PerkinElmer microscope for dispersive spectrometers used such a Schwarzschild objective.

When the microscope shown in Figure 1.2 is used in the external reflection mode, the same Cassegrain is used as both a condenser and an objective. In the external reflection mode, the angle at which the toroidal coupling optic is held is switched so that the beam is passed to the top of the objective via a small deflection mirror. The size and location of this mirror are such that half the beam enters the Cassegrain. The beam is demagnified by the primary and secondary mirrors and focused on the sample, which is at the same location as for transmission measurements. The reflected beam is then reconfigured by the secondary and primary mirrors, the optical properties of which are such that the beam misses the small deflection mirror and passes to the remote aperture. Even if a perfect mirror is held at the sample focus, it can be seen that, in comparison to a transmission measurement, only half the signal can be measured when the microscope is used in its reflection mode.

Three types of external reflection spectra can be measured with the microscope optics in the reflection mode shown in Figure 1.2. In the first (which is of increasing popularity for mid-infrared spectroscopy), *transflection spectroscopy,* a sample

of thickness between 5 and 10 μm is deposited on a reflective substrate. In measurements of this type, the beam passes through the sample, is reflected from the substrate and passes back through the sample before it reemerges from the surface of the sample, and then passes to the detector. This type of measurement has occasionally been used for tissue samples and has proved quite beneficial when the sample is deposited on a "low-e glass" (low emissivity glass) slide (Kevley Technologies, Chesterland, OH), which is a glass slide that has been coated with an Ag/SnO_2 layer. The coating is thin enough to be transparent to visible light, but is highly reflective in the mid-infrared region. Thus, any tissue sample on these slides can be inspected by visual microscopy, and the transflection spectrum can be measured subsequently [8].

Transflection spectra have the disadvantage that radiation reflected from the front surface of the sample will also reach the detector and give rise to a distortion of the pure transflection spectrum. Merklin and Griffiths [9] showed that the contribution by front-surface reflection can be eliminated by measuring the spectrum at Brewster's angle using p-polarized radiation, that is, radiation polarized such that its electric vector is parallel to the plane of incidence. Brewster's angle for tissue samples is about 50°, which is slightly higher than the angle of incidence of most infrared microscopes, but the distortion introduced by front-surface reflection will be reduced significantly. It should be noted, however, that the use of a polarizer will reduce the SNR of the spectrum by a factor of between 2 and 3, thus this approach may not be beneficial if very small samples, such as single cells, are being investigated.

The other two types of external reflection microspectroscopy are less well suited to the characterization of tissue samples. In the first type, which is variously called *specular reflection*, *front-surface reflection*, or *Kramers–Kronig reflection*, the reflectance spectra of thick, nonscattering, bulk samples are measured and converted to the wavenumber-dependent optical constants, that is, the refractive index $n(\tilde{\nu})$ and the absorption index $k(\tilde{\nu})$ by the Kramers–Kronig transform, as discussed by Griffiths and de Haseth [10]. As the requirement for thick nonscattering samples is essentially never met for tissue samples, this type of measurement is never used in medical diagnosis but has occasionally been used for the study of polymer blends.

The other type of measurement that can be made with the microscope in its reflection mode is *diffuse reflection* (DR) spectroscopy. There are very few applications of mid-infrared microspectroscopy of neat samples because for mid-infrared DR spectrometry, samples should be diluted to a concentration of 0.5–5% with a nonabsorbing diluent, such as KBr powder, to preclude band saturation and severe distortion by reflection from the front surface of the particles. However, this mode has substantial application for NIR measurements, where sample dilution is not needed. Because absorption of NIR radiation by most samples is rather weak, they must be either at least 1 mm thick or mounted on a reflective or diffusing substrate, such as a ceramic or Teflon® disk. In the latter case, the spectrum is caused by a combination of DR, transflection, and front-surface reflection (with hopefully DR being the dominant process.)

1.2.3
Detectors for Mid-Infrared Microspectroscopy

Essentially all mid-infrared spectra are measured today by FT-IR spectrometers for which the optical path difference (opd) of the interferometers is varied rapidly and continuously. Most standard laboratory FT-IR spectrometers are equipped with a 1×1 or $2 \times 2\,mm^2$ pyroelectric (either deuterated triglycine sulfate (DTGS) or deuterated L-alanine-doped triglycine sulfate (DLATGS) detector operating at or slightly below ambient temperature. However, the sensitivity of pyroelectric detectors is too low to allow them to be used to measure the relatively weak signals encountered after the beam has been passed through smaller microscope apertures than that of 100 μm. Instead, the more sensitive liquid nitrogen-cooled mercury cadmium telluride (MCT) detector is usually used. For standard FT-IR spectrometers, these detectors operate in the photoconductive (PC) mode, that is, when infrared radiation is incident on them, photons promote electrons from the valence band to the conduction band and the increase in conductivity is a measure of the photon flux.

The properties of MCT detectors depend on their composition, that is, their Hg : Cd ratio. "Narrow-band" MCT detectors are typically about 50 times more sensitive than DTGS but do not respond to radiation below ~750 cm^{-1}. The cutoff can be extended to lower wavenumber but at the expense of sensitivity. Thus, "mid-band" MCT detectors have a cutoff of about 600 cm^{-1}, but their sensitivity is about half that of the narrow-band detector. "Wide-band" detectors cut off at ~450 cm^{-1} but are even less sensitive. Fortunately, few spectra of organic samples contain useful bands much below 700 cm^{-1}, so FT-IR microscopes are almost invariably equipped with narrow-band MCT detectors. It should be noted that the response of narrow-band MCT detectors is nonlinear with radiation flux so that when large spatial regions are to be examined, the effect of this nonlinearity may become evident as a baseline offset [11].

The *noise equivalent power* (*NEP*) of an infrared detector is a measure of the noise generated by the detector and is given by

$$\mathrm{NEP} = \frac{\sqrt{A_D}}{D^*} \tag{1.3}$$

where A_D is the area of the detector element and D^* is the specific detectivity of the detector (which is typically a constant for a given wavelength, detector composition, and temperature). The greater the NEP, the lower is the sensitivity of the detector. Most detectors are specified in terms of their D^* rather than their NEP. The D^* of a narrow-band MCT detector is close to the value given by the background limit for infrared photons and can only be improved significantly by operating at lower temperature.

From Equation 1.1, it can be seen that the area of any detector used for infrared microspectroscopy should be as small as possible. Provided that all the radiation that passes through the sample is focused on the detector, the use of a 0.25 mm detector gives an SNR that is four times greater than if a

1 mm detector were to be used for the characterization of microsamples. For mid-infrared microspectroscopy, the detector is usually a narrow-band MCT PC detector of 250 μm × 250 μm size, although some vendors do provide options for 100 μm × 100 μm or even 50 μm × 50 μm sized elements. Since identical objectives are usually used to focus the beam onto the sample and the detector (see, e.g., Figure 1.1), there is 1× magnification and the *largest* sample that can be measured with a 250 μm detector is 250 μm × 250 μm; however, this is rarely a significant limitation in mid-infrared microspectroscopy when samples *smaller* than 250 μm are usually of interest.

The SNR of an FT-IR spectrum (i.e., the reciprocal of the noise of a 100% line measured in transmittance) is given by the following equation [12]:

$$\mathrm{SNR} = \frac{U_\nu(T)\Theta\Delta\tilde{\nu}D^* t^{-\frac{1}{2}}\xi}{A_{\mathrm{D}}{}^{\frac{1}{2}}} \tag{1.4}$$

where $U_\nu(T)$ is the spectral energy density of the source radiation (W sr^{-1} cm^2 cm^{-1}), Θ is the optical throughput or *étendue* (cm^2 sr), $\Delta\tilde{\nu}$ is the resolution at which the spectrum is measured (cm^{-1}), t is the measurement time (s), D^* is the specific detectivity of the detector (cm Hz$^{1/2}$ W^{-1}), ξ is the efficiency of the optics, and A_{D} is the detector area (cm^2). Microscopes are designed to have high optical efficiency ξ and a large solid angle at the objective. The spectral resolution $\Delta\tilde{\nu}$ is determined by the nature of the sample and the information required by the operator. It is always true that the noise level is lower when the spectrum is measured at low resolution but useful spectroscopic information may be lost if the spectrum comprises narrow bands. If the spectrum comprises relatively broad bands, however, there is no point in measuring the spectrum at high resolution.

Mapping performed with a spatial resolution close to the diffraction limit can be very time consuming. For spectra measured when using sample apertures approaching the diffraction limit (<10 μm), even a 30 s collection may result in a spectrum with a rather poor SNR and may need an increased signal averaging. It may be noted that if the measurement of each spectrum takes 30 s and a 64 × 64 map is required at 10 μm spatial resolution, it would take over 34 h to acquire all the spectra required for the image!

At this point, it may be asked if certain parameters can be changed to decrease the measurement time to allow maps to be acquired in reasonable times. Since the size of the remote aperture for most applications is smaller than 250 μm, it is valid to suggest that even smaller detectors should be installed in FT-IR microscopes so that the SNR is optimized for samples that are 50 μm or smaller in dimension. The answer is a very practical one: it is simply very difficult to keep the beam aligned with the tighter tolerance required for the beam to be focused accurately on a detector that is smaller than 250 μm. As described later, the situation is different when array detectors with very small pixels are used for hyperspectral imaging.

The measurement time t is largely determined by the goal of the experiment. If only a few regions of the sample are of interest, several minutes can be used for each measurement. If the sample is to be mapped, however, hundreds of spectra

are often needed and the time for each should be significantly less than a minute if the measurement is to be completed in a reasonable time.

1.2.4 Sources for Mid-Infrared Microspectroscopy

One parameter in Equation 1.2 has not yet been discussed, namely the spectral energy density, $U_\nu(T)$. The only parameter that can lead to a significantly improved SNR is the spectral energy density of the source radiation, $U_\nu(T)$. In general, the operators of laboratory FT-IR spectrometers have little control over the source installed in their instruments. Most instruments are equipped with an incandescent silicon carbide source, such as a Globar®, operating at about 1400 K. The emission characteristics of mid-infrared sources are usually similar to those of a blackbody, so that it is possible to increase the spectral energy density with an increase in the temperature of the source. However, increasing the temperature of a Globar often leads to cracking and the rapid degradation of the electrical contacts at the end of the rod. One material that has been reported to be operable to over 1950 K is molybdenum silicide. Another source that can be taken up to a temperature close to 2000 K is a homogeneous material with the chemical formula $Mo_x\ W_{1-x}\ Si_2$, which is commercially available under the name Kanthal Super 1900. The molybdenum and tungsten atoms are isomorphous in this chemical formula, and can thus replace each other in the same structure. However, a detailed comparison of any of these materials with a Globar with respect to infrared microspectroscopy has never been reported to the best knowledge of these authors.

Provided that samples can be removed from the laboratory, there are two alternative sources of infrared radiation that are far better than incandescent sources for mid-infrared microspectroscopy, namely the *synchrotron* and the *free electron laser* (FEL) [13]. A synchrotron is a particular type of cyclic particle accelerator, or cyclotron, in which the particles are electrons. A magnetic field is used to bend the path of the electrons, and an electric field is used to accelerate them. Both fields are carefully synchronized with the traveling beam of electrons. By increasing the two fields appropriately as the particles gain energy, their path can be controlled as they are accelerated. This allows the particles to be contained within a large narrow ring with some straight sections between the bending magnets and some bent sections within the magnets giving the ring the shape of a round-cornered polygon. This shape also allows (and, in fact, requires) the use of multiple magnets to bend the particle beam. The strength of the transverse magnetic field is varied periodically by arranging magnets with alternating poles along the beam path. This array of magnets is sometimes called an *undulator*, or *wiggler*, because it forces the electrons in the beam to assume a sinusoidal path. The acceleration of the electrons along this path results in the release of a photon.

In a typical cyclotron, the maximum radius is quite limited as the particles start at the center and spiral outward; thus, the entire path must be a self-supporting disk-shaped evacuated chamber. Since the radius is limited, the power of the

device becomes limited by the strength of the magnetic field. Synchrotrons overcome this limitation through the use of a narrow beam pipe that can be surrounded by much smaller and more tightly focused magnets. The ability of this device to accelerate particles is limited by the fact that the particles must be charged to be accelerated at all, but all charged particles under acceleration emit photons, thereby losing energy. The limiting beam energy is reached when the energy lost to the lateral acceleration required to maintain the beam path in a circle equals the energy added to each cycle. More powerful accelerators are built using larger radius paths and more numerous, powerful cavities to accelerate the particle beam between corners. Recent advances in the instrumentation for mid-infrared microspectroscopy using a synchrotron source are discussed in more detail in Chapter 15.

An FEL shares the same optical property as a conventional laser, that is, the emission of a beam of coherent electromagnetic radiation that can reach high power. However, FELs use some very different operating principles than a conventional laser to form the beam. Unlike conventional lasers that rely on bound atomic or molecular states, FELs use a relativistic electron beam as the lasing medium, which gives them the widest frequency range of any laser type, and make many of them widely tunable, currently ranging in wavelength from microwaves to soft X-rays. In certain respects, the FEL is similar to a synchrotron. To create an FEL, a beam of electrons is accelerated to relativistic speeds. As in the operation of a synchrotron, the beam passes through a periodic, transverse magnetic field. However, in an FEL, the undulator is placed in an optical cavity or a resonator that reflects the emitted light back and forth. The electrons become tightly bunched because of interactions with a light beam that is also passing through the undulator. The light either may be introduced from an external "seed" laser or, more frequently, is the radiation that has been generated from a previous bunch of electrons that is reflected from mirrors that form an optical cavity outside the undulator.

Viewed relativistically in the rest frame of the electron, the magnetic field can be treated as if it were a virtual photon. The collision of the electron with this virtual photon creates an actual photon by Compton scattering. Mirrors capture the released photons to generate a resonant gain. The wavelength can be tuned over a wide range by adjusting either the energy of the electrons or the field strength. Since the energy of the emitted photons is governed by the speed of the electron beam and magnetic field strength, an FEL can be tuned. Furthermore, because the resonance is specific for light of a given wavelength, the power of the beam is significantly greater than that of a synchrotron, for which broadband radiation is emitted.

What makes this device a laser is that the electron motion is in phase with the field of the light already emitted, so that the fields add coherently. As the intensity of the emitted light depends on the square of the field, the light output is increased. In the rest frame moving along the undulator, any radiation will still move with the speed of light and pass over the electrons, allowing their motion to become synchronized. The phase of the emitted light is introduced from the outside. Depending on the position along the undulator, the oscillation of the

electrons is in-phase or out-of-phase with the radiation introduced from the outside. The light tries to either accelerate or decelerate these electrons. It thereby gains or loses kinetic energy, so it moves faster or slower along the undulator. This oscillatory motion causes the electrons to form bunches. When the photons are synchronized with the field, coherent radiation is emitted.

Steiner *et al.* [14] have reported the measurement of maps of octadecanephosphonic acid (OPA) molecules deposited on a microstructured aluminum oxide/gold surface using an FEL source that was modulated by a rapid-scanning interferometer. The beam was then passed through a wire-grid polarizer and a photoelastic modulator so that the polarization was switched at a rate of 75 kHz. The beam was then passed through a pinhole and focused onto the sample with a Cassegrain objective at an incidence angle of about 60° such that the diameter of the Airy disk was about 15 μm. Light that was polarized such that the electric vector was parallel to the surface was absorbed by the surface species, whereas light that was polarized such that the electric vector was perpendicular to the surface was not absorbed. The beam was collected by a second Cassegrain and then refocused at the detector. As the detector signal is passed into a lock-in amplifier referenced to the polarization modulation frequency, the interferogram was caused only by the surface species [15]. The sample was moved in a raster fashion in order to generate the map. The spectroscopic map revealed that OPA is attached on the aluminum oxide surface and not to gold. The attached molecules form a highly ordered film. A lower degree of ordering was found for phosphonic acid adsorbed on gold. Under normal conditions, the operators of the FEL need 10–20 min to change the wavelength of the FEL. Thus, it required at least a day to measure the image at just three wavelengths.

From a spectroscopic standpoint, the main difference between a synchrotron and an FEL is that a synchrotron emits broadband radiation while the FEL emits monochromatic radiation with several orders of magnitude of higher brilliance than a synchrotron. Thus, radiation from a synchrotron can be expanded and passed into an FT-IR spectrometer, for which the interferometer and all the subsequent optics are no different from those in a conventional FT-IR spectrometer (or microspectrometer). When an FEL is used for spectroscopy, the monochromatic radiation that is generated can be modulated in any appropriate manner (e.g., by a tuning fork chopper) before being passed onto the sample and detector. In principle, FELs can be used for imaging by passing monochromatic radiation onto a focal-plane array (FPA) detector and measuring the signal from each pixel (see below), although such experiments have not yet be reported. The laser would then be tuned to the next wavelength of interest, and this process would be repeated for as many wavelengths as are needed to characterize the sample.

The synchrotron has an equivalent blackbody temperature of 10 000 K [16]. The effective diameter of the beam from a synchrotron is typically about 100 μm and light is emitted into a narrow range of angles, making this an almost perfect radiation source for mid-infrared microspectroscopy. Not all synchtrotrons are equipped with infrared beam lines, but as the importance of the results that are being obtained continues to increase, this situation is changing. Beam time on

most synchrotrons is highly prized and potential users often have to write a short proposal to be granted beam time. However, since FT-IR microscopes with a synchrotron source allow spectra with diffraction-limited spatial resolution and high SNR to be measured in a few seconds, many spectroscopists are starting to use the combination of synchrotron source, FT-IR spectrometer, and either a single-element detector or an array detector [17–20].

1.2.5 Spatial Resolution

Today, FT-IR microscopes are designed to allow spectra of physically small samples, or regions of small samples, to be measured as quickly and easily as possible. On most microscopes, a video image of the sample is displayed on the monitor screen immediately adjacent to the sample, allowing the position of the sample and the jaws of the aperture to be optimized prior to the measurement of the spectrum. A motorized sample stage allows mapping to be readily accomplished.

As noted above, the best spatial resolution of a microscope is ultimately determined by diffraction of the radiation. Thus, the spatial resolution is limited by the radius r of the Airy disk for the longest wavelength in the spectrum and hence depends on n, the refractive index of the medium in which the optics are immersed, for example, 1.0 for air and up to 1.56 for oils. Oil immersion is almost never used for infrared microspectroscopy because of absorption by the oil but has occasionally been used to improve the spatial resolution in Raman microspectroscopy. Immersion oils have been shown to be essential in order to obtain good depth resolution with confocal Raman microscopy [21]. Of greater importance from a practical standpoint for infrared microspectroscopy is the improvement in spatial resolution that is achieved in an attenuated total reflection (ATR) measurement with a hemispherical IRE, especially when the IRE is fabricated from germanium ($n = 4.0$) or silicon ($n = 3.4$.)

Although it was stated that the spatial resolution of a microscope is ultimately limited by diffraction, all modes of chemical imaging employ detector elements of finite size. When the image of the detector element (or pixel for measurements made with an array detector, see below) at the sample plane becomes the limiting aperture, it can often become the limiting factor determining the ultimate spatial resolution before wavelength-limited diffraction effects become apparent. As the wavelengths of radiation across the mid-infrared spectrum typically range from 2.5 to about 14 μm, if the pixel size at the sample plane (which is a function of native detector pixel size and overall system magnification) is larger than the wavelength being used to measure it, then the system is said to be "pixel-size limited." Conversely, if the wavelength of light being used to measure the sample is smaller than the pixel size at the sample plane, the system is said to be "diffraction limited." This is an important, yet often misunderstood, concept. For example, the use of higher magnification objectives, such as 36×, results in very small images at the sample plane. However, this does not necessarily result in improved spatial resolution,

as these systems are often already diffraction limited. For some imaging systems that incorporate FPA detectors, a pixel size of 1.1 μm has been reported when a 36× objective is used, but this is a "waste of pixels" as the pixel size is significantly smaller than the wavelengths of light in the mid-infrared, that is, the resolution is already diffraction limited. In the example of the 36× objective providing a 1.1 μm pixel size, this spatial resolution could only really be achieved at 9000 cm^{-1}, well beyond the high wavenumber cutoff of the FPA.

Several types of microscopes are commercially available for mid-infrared microspectroscopy; they differ in how the sample is apertured and how the light is transferred within the microscope. The first has the simple design concept shown in Figure 1.2, such that the beam from the interferometer is focused at the sample; thus, the sample is at an image of either the source or the Jacquinot stop (for higher resolution FT-IR spectrometers). The beam is then refocused at the remote aperture and then again onto the detector. In the alternative design, the beam from the interferometer is passed through two apertures, one before and one after the sample, as shown schematically in Figure 1.3. This approach, which was originally called *redundant aperturing* and is now more frequently known as *dual aperturing*, gives slightly higher spatial resolution near the diffraction limit than the single-aperture design, as shown theoretically in Figure 1.4. The second aperture serves much the same purpose as the pinhole in a confocal microscope

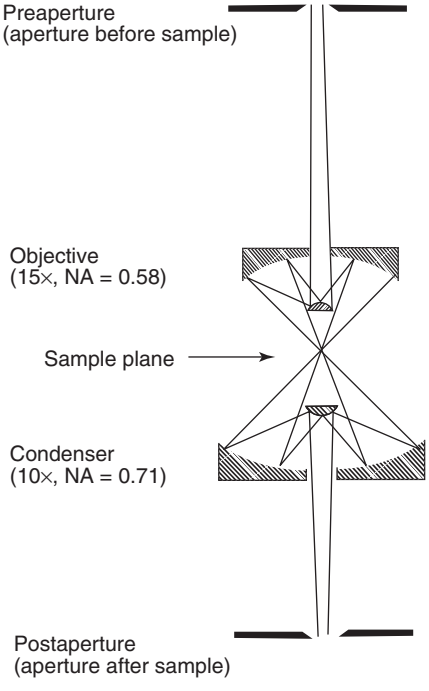

Figure 1.3 Dual-aperture microscope similar to the optics of an IRPlan microscope. (Reproduced with permission from Ref. [22]. Copyright 1991, Society for Applied Spectroscopy.)

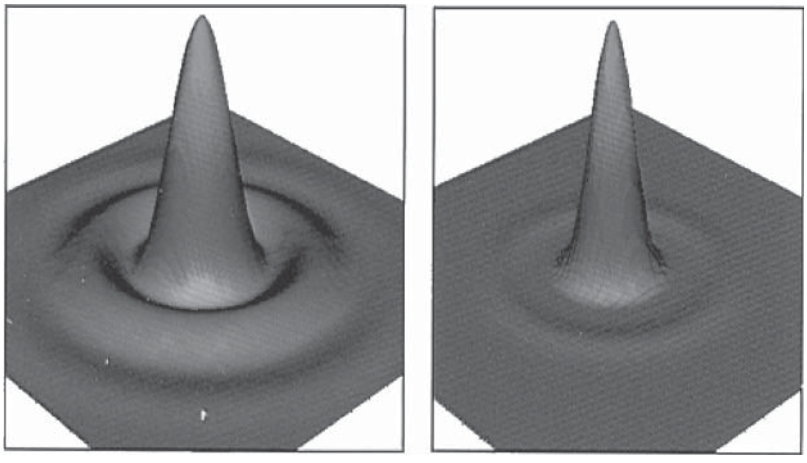

Figure 1.4 (a) Energy profile showing the diffracted radiation outside the area defined by a single aperture. (b) Corresponding profile obtained with masks located before and after the sample. (Reproduced from Ref. [10]. Copyright 2007, John Wiley & Sons.)

(see below). The performance for dual remote apertures and a single aperture located before the sample is comparable, as shown in Figure 1.4. However, it should be noted that the dual-aperture design has the limitation that less energy reaches the detector than with the single-aperture design, so that the SNR for a given spatial resolution is decreased (Figure 1.5).

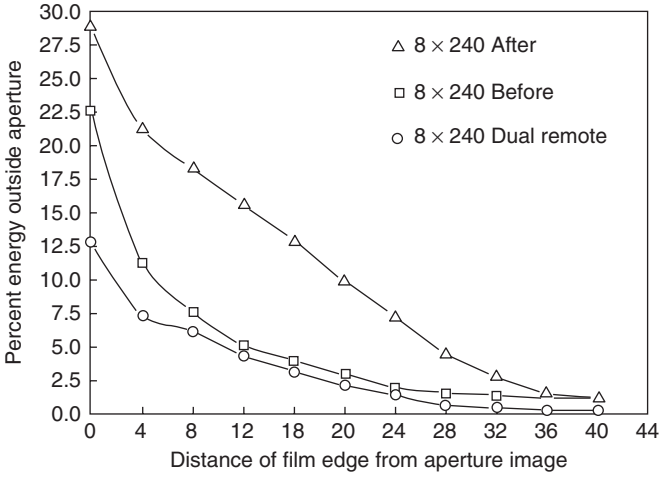

Figure 1.5 Percent of stray energy outside the area defined by an 8 μm × 240 μm rectangular aperture for various imaging modes. (Reproduced with permission from Ref. [22]. Copyright 1991, Society for Applied Spectroscopy.)

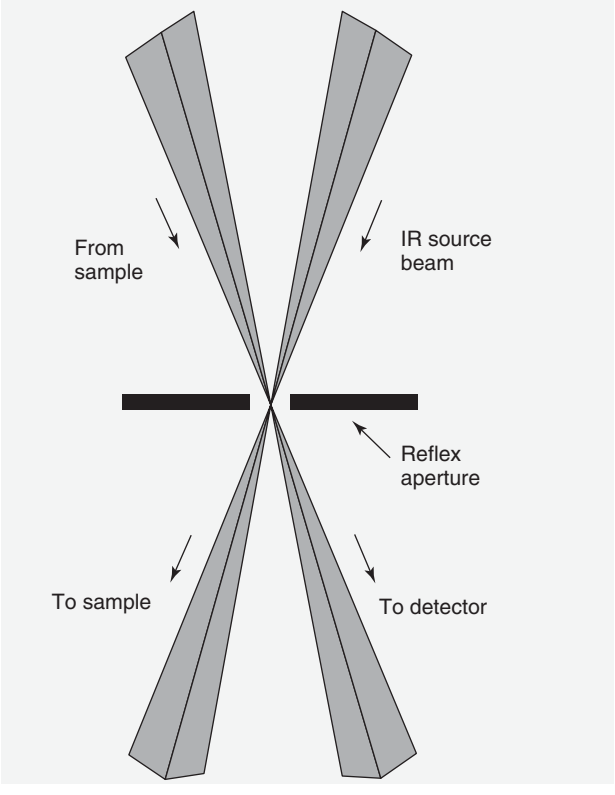

Figure 1.6 Dual confocal aperturing achieved with a single physical aperture. (Reproduced from Ref. [10]. Copyright 2007, John Wiley & Sons.)

It was found that keeping the apertures of a dual-aperture microscope in alignment over a long period of use was not an easy task, especially when high spatial resolution is desired and the apertures must be very small. Thermo-Fisher devised a clever scheme to get around the latter problem by using the same aperture twice, in the way shown in Figure 1.6.[1)] The dual-aperture concept is similar to that of a confocal microscope (see below, Section 1.3.1). Both the dual-aperture design and confocal microscopes preclude imaging measurements; however, in order to image a sample, all regions of the sample that are of interest must be completely illuminated by the source radiation and the detector pixels serve the purpose of the remote aperture that would normally be located after the sample. The dual-aperture system is ideally suited to mapping measurements with diffraction-limited spatial resolution, in

1) Nicolet Corporation made its first FT-IR spectrometer in 1971 and became the market leader shortly afterwards. In 1995, Thermo Electron Corporation purchased Nicolet. In 2006, Thermo Electron purchased Fisher Scientific and the corporation is now known as *Thermo-Fisher*.

which case a source of very high brightness such as a synchrotron would be beneficial.

1.2.6 Transmission Microspectroscopy

Occasionally, transmission spectra of small inhomogeneous samples show the presence of artifacts. For example, the effect of scattering may cause symmetrical bands to lose their symmetry. Instead of having the symmetric shape of the absorption index spectrum, the stronger bands start to take on appearance of the refractive index spectrum. (This phenomenon is sometimes called the *Christiansen effect* [23].) Romeo *et al.* [24, 25] observed a second effect caused by light scattering while measuring the infrared spectrum of whole cells by FT-IR microspectroscopy. They demonstrated that light scattering by the nucleus introduces a broad undulating spectral feature into the baseline of the spectrum, which they attributed to Mie-type scattering by the cell nucleus. Dielectric spheres are known to scatter electromagnetic radiation if the wavelength of the light is comparable to the size of the dielectric sphere. The theory of this scattering process was first described theoretically by Mie [26] and has been nicely summarized by Romeo *et al.* [24, 25].

Davis *et al.* [27–29] have recently published a comprehensive framework for the infrared microscopic analysis of both homogeneous and heterogeneous materials. This framework validated by experimental data can be used to explain distortions in microspectroscopic data and, as shown in the cited work, to recover the spectra. Mie theory assumes a spherical scattering particle in the field of a plane electromagnetic wave. The scattering cross section Q_{sca} of a dielectric sphere interacting with a plane electromagnetic wave is given by a series expansion of the size parameter ρ and complicated expressions in the half-integer order Bessel (Ricatti–Bessel) functions of the first kind and their complex equivalents (Hankel functions). The size parameter ρ is defined by

$$\rho = \frac{2\pi r m_o}{\lambda} \tag{1.5}$$

where r is the radius of the sphere, λ the wavelength of the light, and m_o the ratio of refractive indices between the sphere and the surroundings. The Bessel functions account for the undulating wavelength dependence of Mie scattering.

The angular dependence of Mie scattering is given by series expansions in the Legendre polynomials and their derivatives with respect to the scattering angle. Although the exact solution of this problem is rather complex, Diem's group also used an approximate formula, which was first reported by Walstra [30]:

$$Q_{sca} = 2 - \left(\frac{4}{\rho}\right)\sin\rho + \left(\frac{4}{\rho^2}\right)(1 - \cos\rho) \tag{1.6}$$

where ρ is the size factor defined earlier. This approximation reproduces the rigorous calculation within 1% and matches the spectra remarkably well. Using the approximate calculations, Romeo *et al.* were able to model the Mie scattering

background satisfactorily and correct the distorted spectra by subtracting the modeled Mie background.

1.2.7 Attenuated Total Reflection Microspectroscopy

It can be seen from Equations 1.3 and 1.4 that the spatial resolution of infrared microspectroscopy can be improved by immersing the sample in a medium of high refractive index. This is exactly what is done in ATR spectroscopy using a single-reflection hemispherical IRE. For example, if a germanium ($n = 4.0$) hemispherical IRE is used, not only do you get an increase in the NA because of the increased refractive index of Ge, but also the outer ray angle of incidence (which defines NA) is increased, as the light is refracted inward. The difference between the focusing that occurs with a triangular prism and a hemispherical IRE is seen in Figure 1.7a,b.

The first ATR accessory to make use of a single-reflection IRE with approximately hemispherical geometry was the Split Pea (Harrick Scientific), the usual image size of which is about 250 μm when used with a germanium IRE. Although germanium has the highest refractive index of infrared transparent materials (and therefore gives the greatest demagnification), it has the great disadvantage that it is opaque to visible light. As a result, sample alignment in some of the earlier devices was quite tricky. Since the introduction of the Split Pea, a number of analogous accessories have been introduced for ATR microspectroscopy, including several that have been explicitly designed to replace the objective in a standard infrared microscope. The Bruker Optics Hyperion, the optics of which are shown in Figure 1.8, is just one example of a microscope designed for FT-IR microspectroscopy and analogous systems are available from a number of different vendors. Several manufacturers have designed accessories where

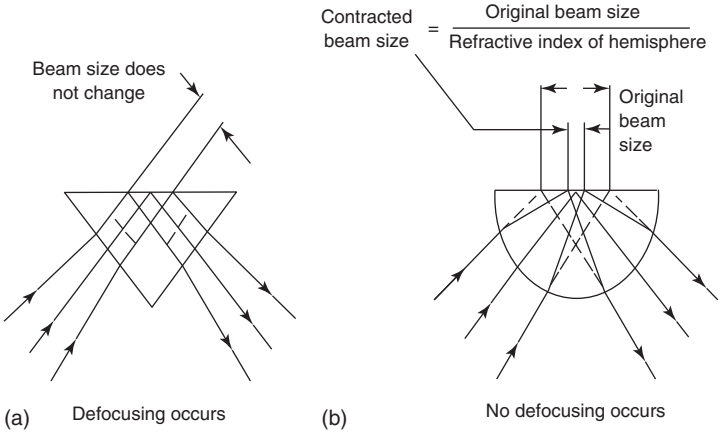

Figure 1.7 Beam focusing through (a) prismatic and (b) hemispherical internal reflection element.

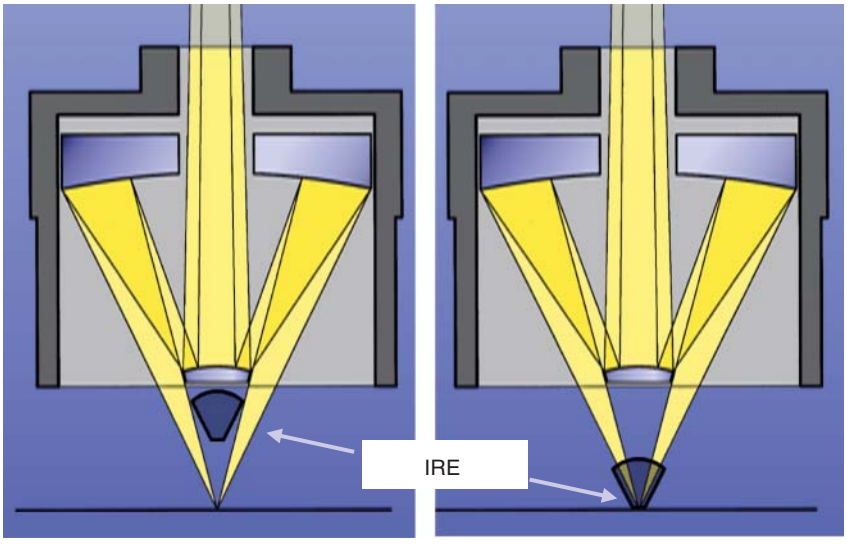

Figure 1.8 Optical schematic of the Bruker Optics ATR objective used in the (a) alignment mode and (b) spectral acquisition mode. (Courtesy of Bruker Optics.)

the sample can be aligned without being in contact with the IRE. Once the appropriate region has been selected, the IRE is moved into place. With the Bruker Hyperion, the tip of the IRE is 100 μm in linear dimension to achieve high spatial resolution. It is equipped with an electronic pressure sensor to ensure good contact with the sample, which is particularly important for mapping by ATR microscopy. The IRE is spring loaded to avoid damage, and there are five different pressure steps to allow optimal contact for hard and soft samples.

Similar to germanium, silicon also has a fairly high refractive index ($n = 3.4$). Silicon is rarely used for the fabrication of large IREs, for which the optical path may be several centimeters, because the presence of trace impurities leads to excessive absorption of the radiation below about 1200 cm^{-1}. With the very short path through the IRE installed in a microscope objective, however, this is no longer a problem. Thus, either silicon or germanium can be used productively as the IRE in an ATR objective.

1.3
Raman Microspectroscopy and Mapping

1.3.1
Introduction to Raman Microspectroscopy

In principle, Raman microspectroscopy is attractive because the practical diffraction limit is on the order of the excitation wavelength, which is about 10×

smaller for Raman spectroscopy with a visible laser than that for mid-infrared spectroscopy. It is therefore possible to focus visible or NIR laser light to much smaller spot sizes (~1 μm or less) than that may be examined by mid-infrared radiation. Until the mid-1980s, however, Raman spectrometry was a relatively unpopular, time-consuming technique for the characterization of both macro- and microsamples for the following reasons:

- The intensities of strong bands in Raman spectra are usually at least 10^8 times weaker than the intensity of the incident monochromatic beam.
- When photomultiplier tubes (PMTs) were used for the detection of Raman spectra, high-power gas lasers, such as Ar^+, were required to yield enough photons for the measurement of Raman spectra in less than 1 h; the power supplies for the early versions of these lasers generated so much heat that they often required water cooling.
- Inefficient double, and occasionally triple, monochromators were required to eliminate stray light from the Rayleigh line.
- No multiplex or multichannel technique was available for the measurement of Raman spectra, so instruments were based on scanning monochromators with a single PMT detector.
- Many "real-world" samples fluoresce when illuminated with visible light, especially green light from a frequency-doubled neodymium-doped yttrium aluminum garnet (Nd:YAG) laser at 532 nm or from an argon ion laser at 488 or 514.5 nm.

Even though nothing can be done to make the Raman cross section of vibrational bands any greater without the application of such techniques as resonance Raman spectroscopy or surface-enhanced Raman scattering (SERS), several important technological developments led to the design of today's truly powerful Raman spectrometers. These included (in no particular historical order) the development of the following:

- highly efficient notch filters that eliminate the Rayleigh line and transmit both the Stokes- and anti-Stokes Raman bands or edge filters that transmit only the Stokes Raman bands and block all shorter wavelength radiation, eliminating the need for the second or third monochromator;
- small, efficient single monochromators based on concave holographic gratings, transmission holographic gratings, or standard Czerny–Turner monochromators in combination with a notch filter;
- "scientific" charge-coupled device (CCD) array detectors with quantum efficiencies close to 100% and, more recently, electron-multiplied CCDs (see Section 1.3.2);
- diode lasers emitting at 785 and 840 nm, which minimize fluorescence and are still compatible with silicon-based CCD detectors over much of the Raman spectrum;
- diode-pumped Nd:YAG lasers emitting at 1064 nm: with a laser operating at this long wavelength, fluorescence from the sample is often minimized and sometimes eliminated;

- the frequency-doubled Nd:YAG laser emitting at 532 nm that requires far less power than an Ar^+ laser;
- efficient fiber-optic probes.

Fourier transform (FT) Raman spectrometry, which was needed because the Raman spectrum generated 1064 nm radiation, is at too long wavelength for polychromators equipped with silicon-based CCD detectors. The first report of the design and testing of an FT-Raman spectrometer was by Hirschfeld and Chase in 1986 [31], and these instruments became commercially available the following year. NIR laser excitation is needed because many compounds fluoresce when illuminated with visible light leading to excess photon shot noise. With most FT-Raman spectrometers, the sample is illuminated with a 1064 nm radiation from a Nd:YAG laser, and the Rayleigh and Raman-scattered light is modulated by a two-beam interferometer. After removal of the Rayleigh-scattered radiation by a notch or edge filter, the Raman interferogram is detected with either an indium gallium arsenide (InGaAs) or germanium detector. Within another year, however, multichannel Raman spectrometers based on a polychromator and a CCD array detector were also brought onto the market. These instruments were compatible with essentially any laser that led to the generation of a Raman spectrum at shorter wavelength than the 1100 nm cutoff of silicon-based CCD detectors. CCD-Raman spectrometers with longer wavelength lasers and InGaAs array detectors are commercially available, but these instruments rarely have the sensitivity to be used in conjunction with a microscope.

The development of CCD-Raman spectrometers revolutionized Raman spectroscopy. Within the space of about 5 years, about 10 Raman spectrometers based on multichannel technologies were introduced commercially. Several of the CCD-Raman spectrometers were either designed for or could be readily modified for microspectroscopy. Although FT-Raman microspectrometers have been reported (e.g., [22]), they have not proved very popular for three reasons: safety, sample heating, and sensitivity. In practice, therefore, CCD-Raman spectrometers have proved to be far more successful for Raman microspectroscopy than FT-Raman spectrometers and most instruments are based on this concept.

Raman microspectroscopy is not a new concept. In 1966, Delhaye and Migeon [32] showed that a laser beam could be tightly focused at a sample, and that Raman-scattered light could be collected and transferred to a spectrometer with minimal loss. Their calculations showed that the increased irradiance more than compensated for the decrease in the size of the irradiated volume. The first Raman microscope was reported by Delhaye and Dhamelincourt in 1975 [33]. An instrument based on these principles (the MOLE™) was introduced by Jobin-Yvon at about the same time; however, the optical scheme used for imaging, which employed global illumination, was inefficient and it was not until the advent of CCD-Raman spectrometers that the advantages of Raman microscopy became apparent.

Arguably the most important advantage of many microscopes used for Raman microspectroscopy is the fact that they have a confocal design. In a typical confocal design, see Figure 1.9, the laser beam is focused on a small aperture (to clean

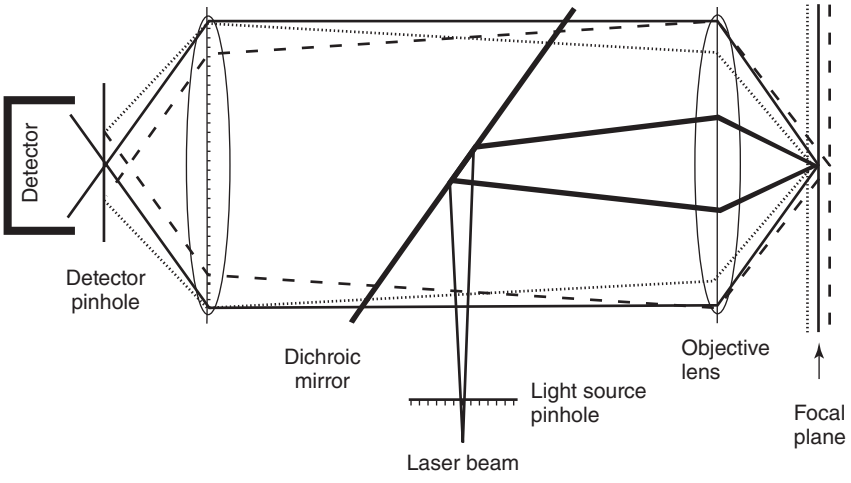

Figure 1.9 Schematic representation of the optics of a confocal microscope.

up the beam profile and present a diffraction-limited source) and then refocused by an objective lens with a large NA onto a small (ideally diffraction-limited) focal volume within the sample. A mixture of the Raman- and Rayleigh-scattered light from the illuminated spot is then collected by the objective lens. The high NA of these optics allows the light to be collected over a solid angle of almost a full hemisphere. An objective with a NA of 0.95 collects about 70% of the radiation emitted over 2π steradians. A dichroic beamsplitter (typically a notch filter or an edge filter) reflects the radiation from the Rayleigh line and transmits the Stokes-shifted Raman-scattered radiation at longer wavelength. After passing through a pinhole, the Raman-scattered light is passed into the monochromator and the intensity at each wavelength is measured. The small spot enables the image to be transferred to the spectrometer though the narrow (typically about 100 μm) entrance slit with minimal loss in energy. Today, most Raman microspectrometers employ confocal optics, which give the capability to produce blur-free images of thick samples at various depths. It may be noted, however, that spherical aberration limits sampling with diffraction-limited resolution at depths much greater than 10 μm.

As seen in Figure 1.9, the detector pinhole obstructs the so-called out-of-focus (or out-of-plane) light, especially light from adjacent spatial regions and fluorescent emission not originating from the focal plane of the objective lens. Light rays from below the focal plane come to a focus before reaching the detector pinhole, and then expand out so that most of the rays are physically blocked from reaching the detector by the pinhole. In the same way, light from above the focal plane is focused behind the detector pinhole, so that most of this light is also vignetted by the pinhole and is not detected. However, all the light from the illuminated focus (solid lines) is imaged at the pinhole and passed to the detector. The detected light originating from an illuminated volume element within the specimen is then focused on the entrance slit of a polychromator and the spectrum is measured

with a CCD detector. Since the out-of-focus rays from above and below the focal plane are largely removed, sharper images are measured than can be acquired from conventional (nonconfocal) microscopy techniques. Mapping is accomplished by moving the sample by small amounts after each spectrum has been recorded.

Several modes of operation are available in state-of-the-art confocal Raman microspectroscopy, including the measurement of samples with a spatial resolution of less than 1 μm, depth profiling, and line mapping. LaPlant and Ben-Amotz have given a detailed description of the design and construction of a confocal Raman microspectrometer [34] and a number of instruments are available commercially.

Several companies market Raman spectrometers with confocal optical configurations. The WITec alpha300 R confocal Raman microscope differs from other confocal Raman microspectrometers in that it has been designed especially for fast microspectroscopy. The data acquisition time for entire spectra can be less than 1 ms, which allows Raman mapping of over 10 000 spectra in less than a minute when the Raman signal is adequate. These data sets can already be evaluated during data acquisition by using filters. For example, the integrated intensities of certain bands of interest may be calculated or the position or full width at half maximum of the bands may be evaluated. Band fitting to Gaussian or Lorenzian shapes, as well as various other fitting algorithms, can also be applied to the data set. Using these filters, several 3D data sets that can be displayed as images are created from the 4D hyperspectral data.

The WITec alpha300 R confocal Raman microscope can be upgraded to perform atomic force microscopy, tip-enhanced Raman spectrometry, and near-field scanning optical microscopy, and is arguably the most versatile instrument for Raman microspectroscopy available today, although the competition is rapidly closing the gap.

1.3.2 CCD Detectors

The quantum efficiency of contemporary array detectors can be remarkably high – greater than 90% in the case of back-illuminated CCDs. The two main sources of noise for CCD cameras are as follows:

- dark current, which is largely caused by thermal emission and is usually reduced to a negligibly low level by thermoelectrically cooling the detector below -60 °C, and
- readout noise, which is the number of electrons introduced per pixel into the final signal upon the readout of the device and is caused by both the lack of repeatability of the conversion from an analog signal to a digital number and the introduction of spurious electrons into the camera electronics, leading to unwanted random fluctuations in the output. Readout noise, which is usually given in terms of electrons, is dependent on the readout rate; typical values are

from 5–10 electrons for a 50 kHz readout rate to ~30 electrons for a 2.5 MHz readout rate.

The combination of these two random effects produces an uncertainty in the final output value for each pixel. In the output of the CCD image, readout noise is added into every pixel every time the array is read out. This means that a CCD with a readout noise of 30 electrons will, on average, contain 30 extra electrons of charge in each pixel upon readout. As a consequence, CCDs with high readout noise (more than 80–100 electrons) are not very good to use if a sequence of short exposure frames is co-added instead of using one long exposure. However, for modern scientific CCDs, readout noise values are very low, in the range of 10 electrons per pixel per read or less. Ideally, the limiting noise source in any Raman spectrometer should be photon shot noise. Because photons follow Poisson statistics, for a given signal the uncertainty is the square root of the signals in electrons. In this case, the SNR of many Raman spectra can be remarkably high, even though the signal is so low. For example, even if only 100 photons are detected (converted to electrons), the SNR is still 10 provided that the only noise source is photon shot noise.

For Raman mapping measurements, the readout time per pixel must be very short. For example, if an image consisting of 128 pixels/line and 128 lines is acquired with an integration time of 1 s/pixel, the total acquisition time is just a little over 4.5 h. Reducing the readout time to 100 ms/pixel decreases the measurement time to 27 min. A further 10-fold increase in the readout rate decreases the acquisition time to less than 3 min. The latter situation would allow hundreds of images to be acquired per day instead of just one or two. Unfortunately, this condition is not readily achievable in practice because the faster is the readout time of the detector electronics, the noisier is the readout amplifier.

Hollricher and Ibach [35] have described how the SNR of Raman spectra can be increased through the use of an electron multiplying charge-coupled device (EMCCD). This device is a normal CCD with an additional readout register that is driven with a significantly higher clock voltage than a normal CCD readout register. The effect of the high clock voltage is to affect an electron multiplication through impact ionization. In practice, the gain may be increased by a factor of up to 1000 in this way, so that the photon shot noise is always much greater than the readout noise. The SNR of Raman bands does not increase linearly with the gain and is actually reduced at high gain; typically the optimal SNR achieved through the use of an EMCCD is about five times greater than if the same spectrum had been measured with a conventional CCD array. The improved SNR allows superb images to be obtained from Raman mapping experiments in a remarkably short time. For example, a 200×200 pixel color-coded image of a 7.1 nm layer of poly(methyl methacrylate) (PMMA) contaminated with 4.2 nm fibers acquired with a WITec alpha300 R confocal Raman microscope is shown in Figure 1.10. The integration time was 7 ms per spectrum for a total acquisition time of less than 6 min.

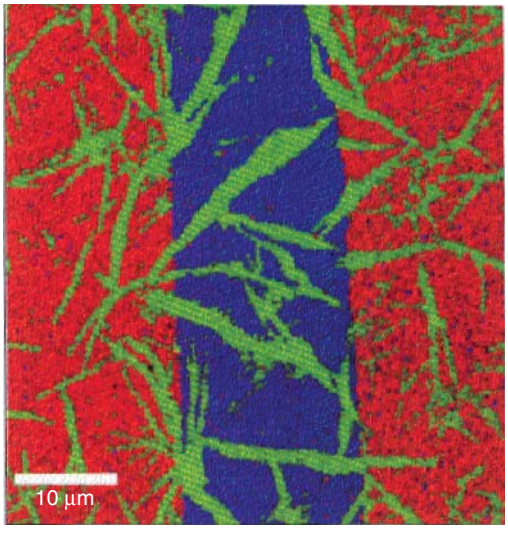

Figure 1.10 Color-coded confocal Raman map of a 7.1 nm thick PMMA layer (red) and a 4.2 nm contaminant layer (green) on glass (blue). The map was computed from 200 × 200 spectra, with an integration time of 7 ms per spectrum, for a total acquisition time of 5.4 min. (Reproduced with permission from Ref. [35] Spectroscopy Supplement, June, 2007. Copyright 2007, Avanstar Publications.)

Another source of "noise" in spectra measured using a CCD is caused by the pixel-to-pixel variation in the quantum efficiency of neighboring pixels. This variation can be corrected by illuminating the detector array with a uniform light source and measuring the signal from each pixel. Once the relative response of each pixel has been determined, a correction known as a *flat field correction* can be applied.

Despite all the efforts to minimize the noise in Raman spectra measured in the short times needed for mapping measurements, it is rare that the spectroscopist would not be more satisfied if the SNR were higher. Cai *et al.* [36] reported a more powerful way of reducing the noise in Raman spectra with less band broadening than Savitzky–Golay [37] smoothing. In their approach, multiresolution wavelet transformation and block thresholding were used to both suppress the background caused by fluorescence and reduce the noise without a significant loss in spectral resolution.

1.3.3 Spatial Resolution

For diffraction-limited microscopy, it may be thought that the image should be focused on the CCD such that the Airy disk fills one pixel. However, Adar *et al.* [38] demonstrated that image quality can be improved significantly if the sample step is much smaller than the spatial resolution of the measurement. For example,

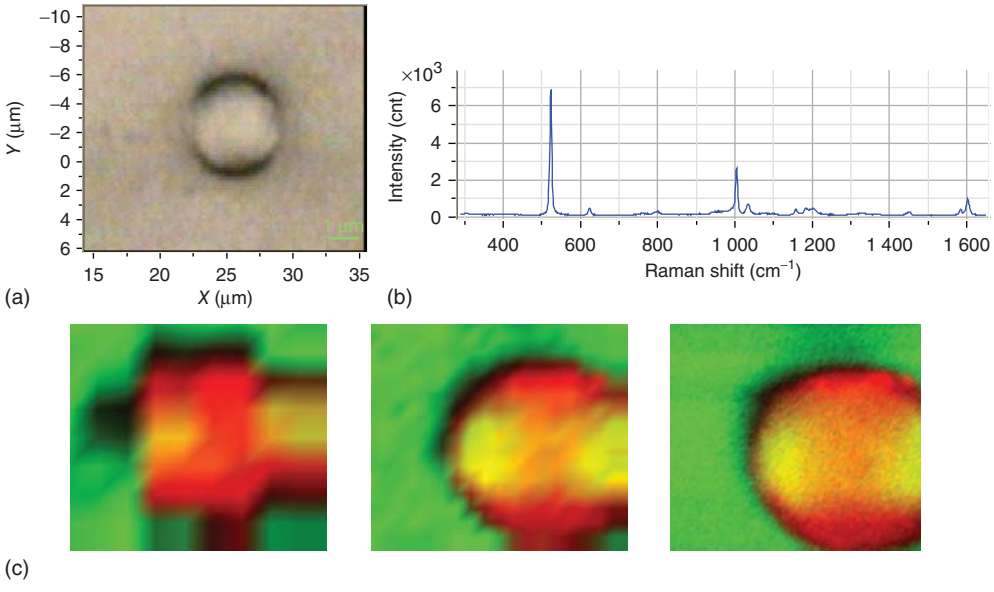

Figure 1.11 (a) Visual image of a 1 μm diameter polystyrene bead. (c) Raman image of this bead, recorded with a 100× (NA = 0.95) infinity-corrected microscope objective at increments of 1.0, 0.5, and 0.1 μm/step. (b) Raman spectrum measured from the center of one of these beads. (Reproduced with permission from Ref. [38]. Copyright 2006, Avanstar Publications.)

Figure 1.11 shows the Raman map of an 8 μm polystyrene bead on a silicon substrate recorded with a 100× objective with steps of 1.0, 0.5, and 0.1 μm. The visual image recorded through a standard optical microscope is shown for comparison. Clearly, reconstructing the image from data taken with steps smaller than the resolution given by the Rayleigh criterion gives a higher quality Raman image.

The strength of the objective is also important, as it controls the NA. Figure 1.12A shows Raman maps of five 5.18 μm polystyrene spheres recorded with 100×, 50×, and 20× objectives, with the increment between data points being 0.2 μm and Figure 1.12B shows the line profiles across the two beads at the top right of these images.

Information can also be collected from different focal planes by raising or lowering the microscope stage. The computer can generate a 3D picture of a specimen by assembling a stack of these 2D images from successive focal planes. Some care is needed in the interpretation of the results obtained by depth profiling with a confocal Raman microscope, however. For example, Everall [39] has shown that when using metallurgical objectives, which are typically supplied as standard with confocal Raman microscopes, the focus is both much deeper than might be first thought and blurred because of spherical aberration, as shown in Figure 1.13. Even in the absence of spherical aberration, Everall showed that bands originating from sample regions far above and below the optimum focal plane can still contribute significantly to the spectrum [40]. He demonstrated this by investigating

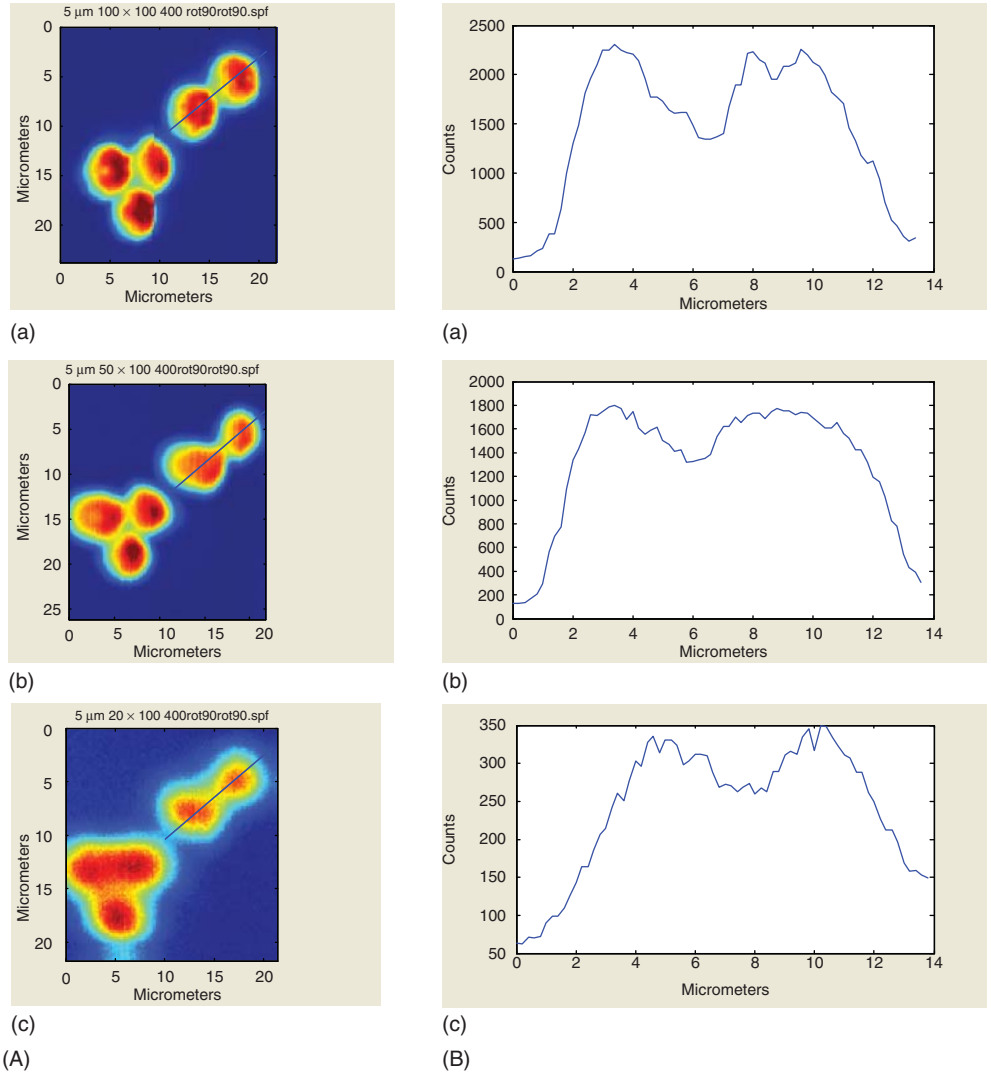

Figure 1.12 (A) Raman maps of 5.18 μm diameter polystyrene beads recorded with 100×, 50×, and 20× objectives. Increments between data points were 0.2 μm for all three images. (B) Line profiles of the two beads at the upper right. (Reproduced with permission from Ref. [38]. Copyright 2006, Avanstar Publications.)

the Raman spectra of a 20 μm thick layer of polyethylene (PE) over a 100 μm sheet of poly(ethylene terephthalate), PET. The spectra measured at different depths, including locating the focus 10 μm above the sample, are shown in Figure 1.14. It is clear that signals from the PET contribute significantly to the spectrum even when focused in or well above the PE. Everall demonstrated a similar effect when he scanned laterally across the same sample. These results were found because

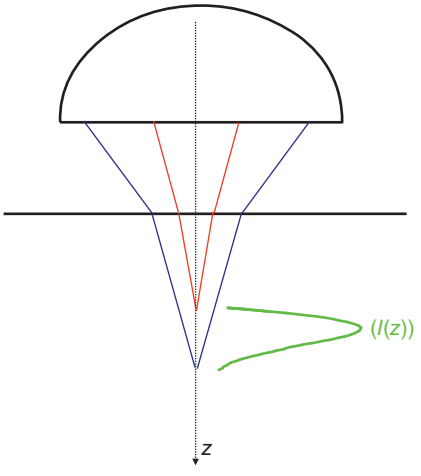

Figure 1.13 Schematic diagram showing how the effect of refraction leads to an increase in the depth of field for Raman microscopy. (Figure courtesy of Dr. Neil Everall, Measurement Science Group, Intertek Corporation.)

for every point within the entire illuminated volume of a transparent sample (not just the beam waist), there are some rays that can reach the detector. When all of these paths are added together, there can be a significant signal originating from those parts of the sample that are out of focus. This effect is particularly noticeable when the sample present in the "out-of-focus" region is a stronger Raman scatterer than the sample in the "in-focus" region. Macdonald and Vaughn have developed a simple mathematical model to quantify the contribution of "out of focus" regions of the sample [40].

1.3.4 Tip-Enhanced Raman Spectroscopy

Using the techniques discussed in the earlier sections of this chapter, it can be seen that the spatial resolution achievable by infrared or Raman microspectroscopy is governed by the diffraction limit shown in Equation 1.3. It is possible to improve on the diffraction limit in mid-infrared microspectroscopy using the techniques we describe in Chapter 12 of this book. There is also a technique, known as *tip-enhanced Raman spectroscopy* (*TERS*), whereby the spatial resolution of Raman spectroscopy can be reduced significantly below the diffraction limit [41]. TERS is a hybrid system that combines the nanometer resolution afforded by scanning probe microscopy (e.g., atomic force microscopy) with the molecular specificity of SERS. It is well known that the Raman spectrum of species with a few nanometers of roughened silver or gold surfaces is enhanced by at least four orders of magnitude. The primary enhancement in SERS arises from the electric field of the radiation being greatly increased because of resonance between the wavelength

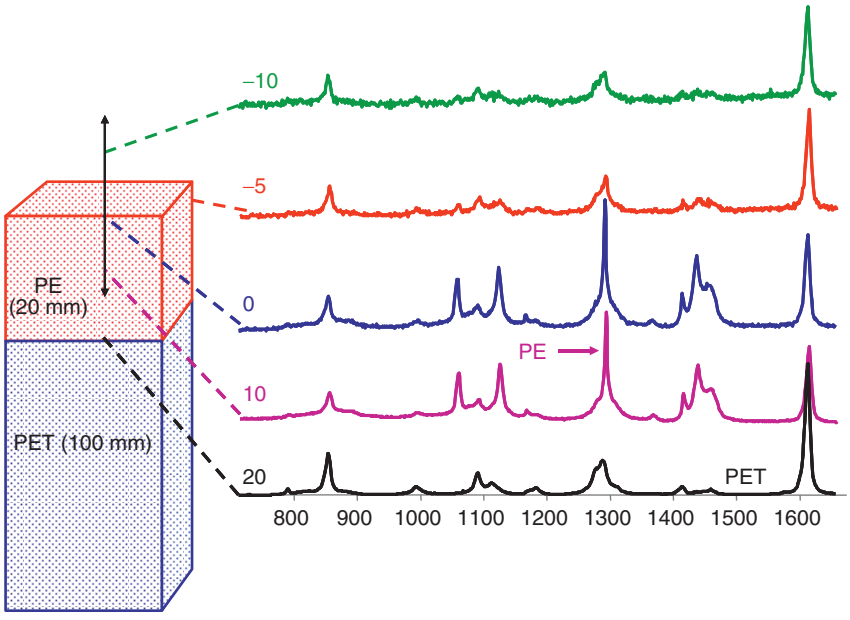

Figure 1.14 Spectra measured by raising the level of a polymer laminate sample consisting of a 100 μm layer of poly(ethylene terephthalate) under a 20 μm layer of poly(ethylene). The strongest bands in the Raman spectra of PE and PET are marked with arrows. (Figure courtesy of Dr. Neil Everall, Measurement Science Group, Intertek Corporation.)

of the illumination laser and the nearby Raman signals and the wavelengths of the surface plasmon resonance of the metal nanostructures.

It has been shown that localized plasmon polaritons in the region of sharp metal tips act in an analogous fashion, giving rise to TERS. In the usual mode of operation, TERS employs a sharp metal tip, which is illuminated from the outside to create a localized light source [42]. Alternatively, silver nanoparticles have been deposited on silica or titania surfaces and a silicon tip is used [43, 44]. TERS is rapidly becoming an important technique for microspectroscopy and is described in some detail in Chapter 11 of this book.

1.4 Near-Infrared Hyperspectral Imaging

Following the above introduction to the types of microscopes used for single-point sampling and sample mapping, the instrumentation used for hyperspectral imaging by vibrational spectrometry will now be described. NIR imaging spectrometers will be introduced first, as these are the simplest instruments in their design. Raman imaging spectrometers will then be discussed, as they bear considerable similarity to that of their NIR counterparts. The instrumentation for mid-infrared

imaging will be covered subsequently, as the principle of these instruments is somewhat different from that of NIR and Raman imaging systems. Finally, terahertz imaging that is based on a completely different principle from any of the other types of imaging instruments will be introduced.

Perhaps the simplest type of instrument for NIR hyperspectral imaging spectrometer is the one originally developed by Spectral Dimensions, Inc. (Olney, MD, USA, now Malvern Instruments). In this instrument, the radiation from a broadband source of NIR radiation (a simple tungsten or quartz–tungsten–halogen lamp) is passed through a LCTF so that a narrow region of the NIR spectrum is isolated. A typical LCTF is constructed from an interwoven stack of Lyot stages (linear polarizers and liquid–crystal variable retarders mounted on birefringent quartz crystals), usually mounted in a temperature-controlled housing. Varying the voltage applied to the liquid crystals shifts the passband in less than 1 ms without any mechanical motion or vibration of the optics. Thus, the filter can be tuned to an almost infinite number of times since there is no wear and tear.

The operation of an LCTF may be understood by considering a simplified Lyot filter stack, in which $(N+1)$ polarizers are separated by N layers of liquid crystals sandwiched between birefringent crystals. The optical retardation, R (nm), introduced by birefringent crystals is dependent on the thickness of the crystal, d (nm), and the difference between the refractive index of the ordinary ray, n_o, and the extraordinary ray, n_e, at the wavelength of interest:

$$R = d(n_e - n_o) \tag{1.7}$$

The velocities of the extraordinary and ordinary rays differ, and they emerge from the stack with a phase delay, Γ radians, that is dependent on the wavelength λ of the radiation:

$$\Gamma = \frac{2\pi R}{\lambda} \tag{1.8}$$

The transmittance of the crystal T is given by

$$T = 0.5\cos^2\left(\frac{\Gamma}{2}\right) \tag{1.9}$$

In a typical Lyot filter, crystals are often selected so that transmission has its maximum value at the wavelength determined by the thickest crystal retarder, with other stages in the filter serving to block the transmission of unwanted wavelengths. The spectral region passed by the LCTF is dependent on the choice of polarizer, optical coating, and the liquid crystal characteristics (nematic, cholesteric, smectic, etc.). In practice, a Lyot LCTF may have as many as 11 polarizers and 10 liquid crystalline layers and is sometimes equipped with an internal microprocessor to tune all of the stages.

Wavelength scanning in NIR hyperspectral imaging spectrometers has also been accomplished with both a scanning monochromator and an acousto-optic tunable filter (AOTF). AOTFs are electro-optical devices that function as electronically tunable filters. They rely on a birefringent crystal, the optical properties of which vary upon interaction of the crystal with an acoustic wave. The resulting

compression and rarefaction of the crystal give the properties of a diffraction grating. Changes in the acoustic frequency alter the grating constant, enabling the wavelength to be tuned very rapidly. Switching time is limited only by the acoustic transit time across the crystal and is rarely greater than 50 μs. AOTFs designed for operation in the NIR region typically consist of an optically anisotropic tellurium dioxide crystal to which a piezoelectric transducer is bonded. In response to the application of an oscillating radio frequency electrical signal, the transducer generates a high-frequency acoustic wave that propagates into the crystal. The alternating ultrasonic acoustic wave induces a periodic redistribution of the refractive index through the crystal, which then acts as a transmission diffraction grating. Changing the frequency of the transducer signal applied to the crystal alters the period of the refractive index variation and, therefore, the angle through which the radiation is diffracted, and hence the wavelength band that reaches the detector. The design parameters that affect resolution include the dispersion constant of the crystalline material (related to degree of birefringence), the incidence angle, and the acousto-optic interaction length. The relative intensity of the diffracted beam is determined by the amplitude (power) of the signal applied to the crystal and by the widths of the entrance and exit slits of the monochromator.

One of the more important parameters governing which of these wavelength selection devices to use is their bandpass, that is, the full-width at half-height (FWHH) of their transmittance window. The typical bandpass of an NIR LCTF is 5 nm. As the FWHH of most bands in the NIR spectrum is greater than 10 nm, a bandpass of 5 nm is more than adequate for NIR hyperspectral imaging. The LCTF has a far higher ètendue than a monochromator operated at 5 nm resolution, although when the size of the sample being examined is very small, as it is in any microscopic measurement, the potential throughput advantage is rarely met in practice.

The bandpass of a typical AOTF ranges from several nanometers to tens of nanometers for the visible and NIR spectral regions. This resolution is suitable for fluorescence spectroscopy where bands are very broad, and is just adequate for Raman hyperspectral imaging, albeit with lower resolution than may be achieved with a monochromator. A NIR spectrometer based on an AOTF has also been sold commercially. However, the transmission of these devices for NIR hyperspectral imaging is somewhat poorer than that of LCTFs and they degrade the image quality slightly more than LCTFs. The optical efficiency of monochromators for NIR hyperspectral imaging is poorer than that of both LCTFs and AOTFs. Thus, despite the fact that the FWHH of the passband of a monochromator can be made much narrower than that of LCTFs and AOTFs, the highest performance for NIR microspectroscopy is usually found when wavelength selection is accomplished through the use of one of these devices (usually an LCTF) rather than a monochromator.

The NIR hyperspectral imaging spectrometers marketed by Malvern Instruments are equipped with a Stirling-engine-cooled indium antimonide (InSb) FPA detector with 320 pixels in one dimension and 256 pixels in the other (total 81 920

pixels) that operates in the range 1200–2450 nm. Wavelength tuning is by an LCTF with which the entire spectral range can be covered in 2 min. Alternatively, as described above, if the signal from just a few wavelengths is all that needs to be measured, the LCTF allows rapid switching between a few selected wavelengths and the measurement is over in a few seconds. A short-wavelength alternative instrument is also available that is equipped with an InGaAs FPA detector that operates in the range from 950 to 1720 nm.

As this instrument is designed for NIR operation, it is possible to use a microscope with refractive optics. In the case of the Malvern Instruments system, a refractive objective that has 1× magnification is used. With this lens, the sample is imaged directly onto the FPA detector. This objective can be easily removed and objectives with higher (micro mode) or lower (macro mode) magnification can be easily installed. Initial alignment of the sample is performed manually, but if a series of samples is to be measured, a programmable sample stage enables the sequential analysis of multiple samples.

It is probably true to say that instruments for NIR hyperspectral imaging are more versatile and rugged than corresponding instruments that measure mid-infrared and Raman spectra. However, they have two disadvantages. The first disadvantage is that the absorptivities of the overtone and combination bands in the NIR spectrum are far weaker than those of corresponding fundamentals from which they are derived. For measurements in the transmission mode, the ideal sample thickness is one that yields a low-noise spectrum with bands that are strong enough to allow rapid identification or quantification. For *mid-infrared* spectrometry, this thickness is about 10 μm. As the center wavelength of mid-infrared spectra is about 5 μm, the sample thickness is approximately equal to the smallest dimension in the x–y plane that can be observed, that is, the diffraction limit when the NA is approximately equal to 0.6. For conventional NIR spectrometry (1200–2450 nm), on the other hand, the absorptivities of the stronger bands are in an order of magnitude less than the stronger fundamentals from which they are derived and so the sample thickness should be at least 100 μm. However, the diffraction-limited spatial resolution for NIR measurements is less than 3 μm if optics with an NA of 0.6 are used. Thus, even though the ultimate spatial resolution is *in principle* determined by the optics of the spectrometer, in practice this resolution is never achievable because the thickness of the sample means that the diameter of the beam waist at the top or bottom surface of the sample is larger than the diffraction-limited spatial resolution.

For short-wavelength NIR spectra (950–1720 nm), where the absorption bands are caused by transitions to the third or fourth vibrational states of C–H, N–H, and O–H stretching modes, along with weak combination bands, the situation is even worse because bands are so weak that the sample thickness must be increased to about 500 μm, even though the diffraction limit is less than 2 μm. It is at least, in part, for this reason that NIR hyperspectral imaging is rarely used for measurements with very high spatial resolution. Thus, for example, the standard

objective of the Malvern Instruments imaging spectrometer is a refractive lens with 1× magnification and low NA.

The second disadvantage of NIR hyperspectral imaging is more subtle as it is only evident for measurements of powders. Perhaps the most common application of NIR hyperspectral imaging is in the characterization of intact pharmaceutical tablets by DR spectrometry. These measurements have a significant limitation in terms of their spatial resolution caused by the effect of light scattering. Photon time-of-flight measurements [45–51] have shown that photons in diffuse transmission and reflection measurements emerge from compacted powdered samples (such as pharmaceutical tablets) in a time that is much greater than would be expected if no scattering took place. In analogous measurements made by mid-infrared DR spectrometry, Averett and Griffiths [52] estimated that the average path traveled by mid-infrared photons through very weakly absorbing samples is at least 100 particles, strongly implying that photons do not emerge from the same point into which they enter the sample. The greater the particle size, the more strongly a given particle will absorb at a given wavelength. Similarly, the greater is the scattering coefficient, the fewer particles are encountered by photons in a DR measurement and the better is the spatial resolution. For scattering samples, this effect clearly has a highly deleterious effect on spatial resolution. In DR measurements, photons are extensively scattered on entering the sample, passing through several particles (often much more than 10) before reemerging from the top surface.

The effect of scattering on spatial resolution in DR/NIR imaging was discussed by Hudak *et al.* [53] who measured the DR spectrum of polystyrene powder and then placed a clear polystyrene window of known thickness over the sample and remeasured the spectrum. From the increase in the intensity of the polystyrene bands, they were able to show that the effective path length though the powder was 1 mm (±~50%). The more intense the band they measured, the shorter the path length that they calculated (although these authors did not recognize the fact that the path length varied inversely with the absorptivity). They then devised a way of correlating the effective path length with the sampling volume using a random walk model to estimate the volume sampled by a typical photon (called by these authors a *voxel*). They calculated that the average path length, that is, the sampling radius from which 68% (one standard deviation) of the measured intensity imaged onto a single detector pixel originates, was between 30 and 50 μm. It is this distance, which is well over an order of magnitude greater than the diffraction limit, that determines the spatial resolution of NIR imaging measurements made in the DR mode. Since the spatial resolution of NIR hyperspectral imaging measurements of scattering samples, such as pharmaceutical tablets, is far larger than the diffraction limit, it is clear that NIR DR imaging is best used to characterize samples with a particle size that is far larger than the diffraction limit.

An alternative approach for NIR hyperspectral imaging to the one described earlier is to use a Fourier transform near-infrared (FT-NIR) spectrometer. Since the design of FT-NIR microspectrometer is more similar to that of instruments

for mid-infrared hyperspectral imaging than that of the dispersive instruments described earlier, their description will be dealt with in Section 1.6.

1.5 Raman Hyperspectral Imaging

Both Raman mapping and imaging involve the use of CCD array detectors. In mapping, the spectrum of a point of the sample is dispersed across the detector and the sample is moved after each spectrum has been measured. In Raman imaging, on the other hand, the image of the sample at a single wavelength is focused on the detector and the wavelength is changed after each measurement. Raman imaging methods can be broadly classified as line imaging or wide-field source illumination approaches [54]. In the line approach, a cylindrical lens or a Powell lens is employed to distribute the laser beam in one direction across the sample. The Powell lens is a combination of a cylindrical lens and a prism. It may be visualized as a prism with a small radius at one edge, which operates as a cylindrical lens with a radius of curvature decreasing from center to edge. The effect is a monotonic decrease in beam divergence from center to edge, so that the generated line has a nearly uniform intensity along its length [55]. The laser line dimension is oriented parallel to the direction of the entrance slit of a polychromator so that the spectrum is dispersed in the short direction of the CCD. This approach reduces the duration of the experiment by $\sqrt{n}$, where n is the number of image pixels, assuming that the laser power per pixel is kept constant. The spatial resolution parallel to the laser line is the convolution of the microscope magnification by the pixel size, whereas in the perpendicular direction it is equal to the width of the laser line convolved by the scanning precision of the instrument. As a result, the resolution in one dimension is frequently greater than in the second direction.

In wide-field or global imaging, the entire sample field-of-view is illuminated by defocusing the laser. The scattered radiation is usually first passed through a notch filter or a long-pass filter to remove the Rayleigh-scattered radiation and then through a device that blocks all but one wavelength region. This device may be a monochromator, a dichroic filter, an AOTF, or a LCTF, with the LCTF being generally favored. The wide-field approach is generally favored over line-scan imaging when high-fidelity images at a limited number of wavenumbers are desired. In wide-field imaging, the spatial resolution is determined by the convolution of diffraction, the CCD pixel size, and the microscope magnification at the focal plane of the CCD.

Surprisingly, global laser illumination leads to sample heating degradation at much lower laser intensities than point illumination because of inefficiency in conducting heat away from a surface sheet rather than a point. For steady-state measurements at a given total laser power (in watts), the optical damage threshold for a given material scales as the square root of the illuminated area (rather than linearly with the area). Thus, the laser intensity ($W\,m^{-2}$) required to damage a sample is higher for a point illumination than for line illumination, which is in

turn higher than for area illumination. There is still an advantage in distributing power over a wider area; it is just that this so-called power distribution advantage is not as great as was previously assumed [56].

As noted in Section 1.3, *confocal* microscope designs have been used in several Raman microspectrometers that allow sample mapping by moving the sample between the measurement of each spectrum. However, confocal microscopy cannot be used for wide-field Raman imaging as the entire region of the sample of interest must be illuminated and clearly the "light source pinhole" in confocal microscopes does not allow this. For hyperspectral Raman imaging, the high image quality attained by the use of confocal optics and mapping is sacrificed somewhat for data acquisition speed. However, this approach is only fast if an image is to be acquired at a single wavelength – for the acquisition of full spectra, it can be very slow.

One of the first Raman imaging spectrometers manufactured was designed and fabricated by Levin's group at the U.S. National Institutes of Health (NIH) [57]. The wavelengths for this instrument were controlled by a TeO_2 AOTF. This instrument produced high-fidelity, large-format images with a theoretical spatial resolution of about 1 μm. However, because of dispersion by the TeO_2 crystal, the finite spectral bandwidth of the AOTF resulted in a slight smearing of the output image along one axis. This degradation, which is given by the internal beam spread in the crystal, $\Delta\theta_{di}$, can be estimated from the approximate relationship reported by Suhre *et al.* [58]:

$$\frac{\Delta\theta_{di}}{\Delta\lambda} = \left(\frac{\Delta n}{n_0\lambda_0}\right)(\sin 4\theta_1 + \sin 2\theta_1)^{\frac{1}{2}} \tag{1.10}$$

where $\Delta\lambda$ is the passband (2 nm), λ_0 is the center wavelength (700 nm), Δn is the difference in refractive index of TeO_2 for the ordinary and extraordinary rays at λ_0 (0.138), n_0 is the refractive index of TeO_2 for the ordinary ray (2.177), and θ_1 is the angle between the incident beam and the optical axis of the crystal (22.5°); the values for the AOTF used by Goldstein *et al.* are given in parentheses. These values give an external beam spread, $\Delta\theta_{di}$, of 0.13 mrad (0.0037°). This value may be compared with that of the diffracted beam spread of 0.19 mrad caused by the 7 mm square aperture presented to the AOTF entrance pupil. In total, these values would lead one to predict that the image resolution along one axis would be degraded by about a factor of 2.5 on passage through the AOTF. For each AOTF passband frequency, the image on the CCD will be shifted slightly because of dispersion by the crystal, and software correction is needed if the visual and Raman images are to be correlated.

In the instrument described by Goldstein *et al.* [57], the 647.1 nm beam from a krypton ion laser was delivered to the sample by an infinity-corrected microscope objective using an epi-illumination scheme in which light from the rear housing is passed down a horizontal shaft, after which it is reflected down through the objective to the sample. The 180° backscattered light is returned to the objective and then to the spectrometer. Wavelength selection was accomplished by an AOTF that could provide either random or continuous wavelength selection.

The epi-illumination scheme preserves the linear polarization of the incident laser beam. Because the AOTF is polarization sensitive, a half-wave plate is used to rotate the plane of polarization by 180° in order to preserve the AOTF output. The collimated output from the AOTF was first imaged by a tube lens and then by a projection lens onto a liquid-nitrogen-cooled silicon CCD array. One or, occasionally, two holographic notch filters were placed in front of the detector to eliminate stray radiation from the Rayleigh line. These filters transmitted between 75% and 80% of the Raman emission beyond 75 cm^{-1} of the Rayleigh line.

To minimize data acquisition time, the overall magnification of this system was made as small as possible, consistent with the spatial resolution desired. Since the image is sampled by the discrete pixels of the CCD camera, the Nyquist sampling criterion must be obeyed to avoid the generation of artifacts. There is an explicit relationship describing how the number of counts per pixel depends on the optical design. We know from Equation (1.2) that the radius of the Airy disk r is equal to $0.61\lambda/\mathrm{NA}$ (since $x = 2r$). If the size of the CCD pixel is p, then the Nyquist sampling criterion requires that the overall magnification M satisfies the condition that $Mr > 2p$. Goldstein *et al.* designed their system such that $Mr = 2.3p$, in other words, the smallest resolvable feature was sampled by at least two pixels [57]. This rule of thumb is equally applicable to imaging spectrometers where the spatial resolution of the measurement should be spread over at least two pixels. A similar system explicitly designed for *in vivo* tissue diagnostics has been described by Vo-Dinh *et al.* [59].

ChemImage, Corp., markets a Raman imaging spectrometer that shares some of the features of the NIH instrument reported by Goldstein *et al.* but nonetheless has some significant differences. First and foremost, wavelength selection is accomplished through the use of an LCTF rather than an AOTF. The spectral bandpass of this instrument is 9 cm^{-1}, and it has the capability of being tuned at finer increments. It is claimed that a *spectral resolving power* of more than 0.1 cm^{-1} has been consistently achieved. This term probably refers to the accuracy to which the center wavenumber of the LCTF bandpass may be set, as the FWHH of the passband of an LCTF is never as small as 0.1 cm^{-1}. The Raman microscope sold by Renishaw, Inc., may also be used in the imaging mode by holding the monochromator at a certain wavelength for each time increment. However, the Renishaw instruments are mainly used in the Raman microscopy and mapping modes.

1.6 Mid-Infrared Hyperspectral Imaging

1.6.1 Spectrometers Based on 2D Array Detectors

The first true mid-infrared imaging microspectrometer was reported by Levin's group at NIH and Marcott's group at Procter and Gamble [60]. They used a

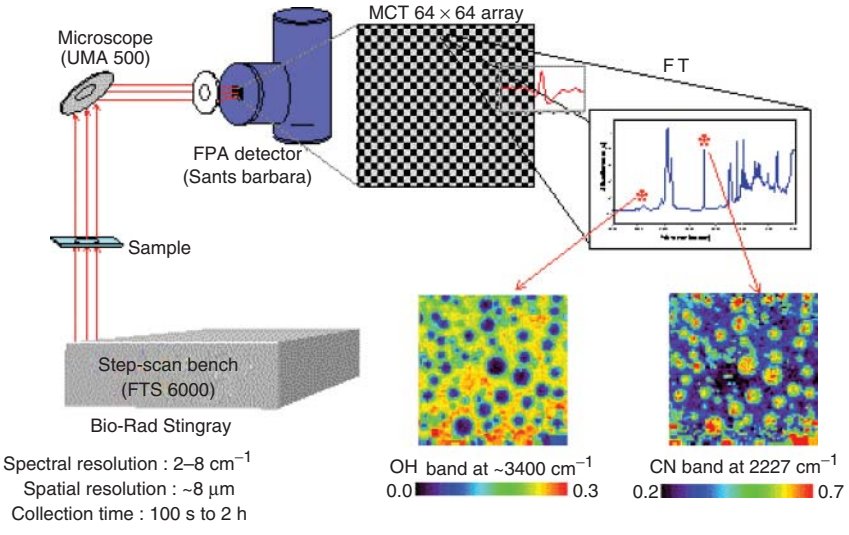

Figure 1.15 Schematic diagram of the Bio-Rad Stingray hyperspectral imaging spectrometer. (Courtesy of Agilent Corporation.)

Bio-Rad (now Agilent[2]) FTS 6000 step-scan FT-IR spectrometer equipped with a UMA-500 microscope. In their earliest instrument, the single-element detector mounted in the microscope was replaced by an indium antimonide (InSb) FPA detector with 64×64 elements imaging an average spatial area of $500\,\mu m \times 500\,\mu m$. A CaF_2 lens was used to focus the sample area onto the FPA detector. As InSb has a cutoff of $1800\,cm^{-1}$, the fingerprint region of the mid-infrared spectrum could not be measured with this instrument.

A short time later, Levin's group modified their system to operate with a mid-IR MCT FPA detector. Unlike most MCT detectors used in FT-IR spectrometers, which operate in the PC mode, the pixels of MCT FPA detectors operate in the photovoltaic (PV) mode. As noted in Section 1.2.2, the cutoff wavenumber of narrow-band MCT PC detectors is at about $750\,cm^{-1}$. The PV detector elements used in MCT FPA detectors have the same high sensitivity as narrow-band MCT PC detectors but the cutoff wavenumber is higher at about $850\,cm^{-1}$.

The first commercial instrument employing the concepts developed by the Levin group was designed by Bio-Rad and marketed as the *Stingray* in 1995.

2) Like several other corporations in the field, the company now doing business as Varian has undergone several name changes. It was first known as Digilab, Inc. Founded in 1969, Digilab developed the first FT-IR spectrometer of the modern era, that is, the first with HeNe laser referencing, the use of a pyroelectric (TGS) detector, and the first under minicomputer control. Digilab was purchased by Bio-Rad in 1978. In 2001, Bio-Rad sold the company to a group of private investors, who renamed the company Digilab LLC. The group sold Digilab to Varian in 2004 and was later acquired by Agilent. During each of these manifestations, this organization made many of the innovations that have led to the remarkable popularity of FT-IR spectroscopy today. In this chapter, the name of the company will be given as it was when the work was reported.

This instrument is shown schematically in Figure 1.15. To maintain the image quality, a ZnSe lens was used to focus the sample image onto an MCT FPA detector rather than the Cassegrain system used in most microscopes. The instrument was equipped with a germanium long-pass filter to block visible and short-wave NIR radiation and hence to prevent detector pixel saturation and improve the SNR. A lightly sanded KRS-5 plate placed in the beam path before the condenser further improved the spatial homogeneity in the camera field-of-view and prevented the detector elements in the center of the array from saturating.

These first attempts of the mid-1990s at true mid-IR FPA imaging using a 2D MCT FPA detector were based on the detectors mounted in military heat-seeking missiles, and the spectrometers that resulted are now termed *first-generation* instruments. As the detectors used in the first-generation instruments were not designed specifically for spectroscopic imaging, they had a number of limitations. One such limitation was the tendency for pixels to "delaminate," whereby the pixels would separate from its substrate. As these first-generation detectors were designed essentially for "one use" military applications, they could not cope with the thermal stresses of repeated heating-cooling cycles from liquid nitrogen cooling.

Another major limitation arose at that time from the need to employ a step-scan interferometer. This necessity came from the relatively slow readout rates of these first-generation FPAs, which were of the order of only a few hundred Hertz. The readout rate (or *frame rate*) of an FPA detector determines the type of interferometer that must be used for FT-IR imaging, as the FPA cannot be triggered (for data transfer) any faster than its maximum readout (frame rate) speed. Since the first-generation FPAs were only capable of frame rates in the hundreds of Hertz and rapid-scanning interferometers required a faster frame rate, the use of step-scan interferometers, where the movable mirror of the interferometer could be held a given opd for several seconds, was mandated.

In 1999, Snively *et al.* [61] described the first report of the use of a rapid-scan interferometer in conjunction with a small first-generation FPA for spectroscopic imaging. In an attempt to design a mid-IR chemical imaging system designed specifically for spectroscopic applications, Digilab, together with the FPA supplier, developed and marketed the first commercial mid-infrared "rapid-scan" imaging systems in 2001, with the launch of the "second-generation" FPA, designed specifically for spectroscopic chemical imaging. These second-generation FPAs had frame rates at an order of magnitude faster than their first-generation analogs, which meant that the standard laboratory-type rapid-scanning FT-IR spectrometer could now be used for chemical imaging, significantly increasing the affordability and reducing the complexity of the system, and leading to an increase in the use and application of mid-infrared imaging spectrometers.

In addition to pioneering the developments in FPA detectors designed specifically for fast mid-infrared hyperspectral imaging, Digilab redesigned their microscope to launch the first microscope designed specifically to cater for the unique requirements of FPA-based imaging. Such improvements included a wider and

more uniform illumination FOV of up to 700 μm × 700 μm, removing the need for any diffusers, removal of refractive focusing optics, and the introduction of optical zoom capabilities to change the pixel size at the sample plane from 5.5 to 11 μm (with a corresponding increase in FOV).

The arrays used on the current generation instruments are "windowable," meaning that the area used for detection by the array can be changed. In these windowable arrays, as the window gets smaller the frame readout rate increases from several kHz for the smallest 16 × 16 windows to rates of just over 1 kHz for the largest commercially available array used in commercial instruments.

Using this windowing capability, the array can be set to a smaller dimension and the data were collected faster. Using this approach, Coutts–Lendon and Koenig [62] were able to visualize the impact of molecular weight on the dissolution behavior of a drug in aqueous systems. The overall timescale of the experiment was ~15 min with a time resolution of 15 s, providing a large enough number of data points to examine the impact of molecular weight in the system. Another characteristic of these arrays is that they are normally equipped with a Ge window that limits the spectral range from 900 to 5000 cm^{-1}. This window limits the flux on the array from NIR and visible radiation, thus allowing for longer integration times. When the window on the dewar is changed to KBr, these systems can be used in the NIR [63]. When working in this range, the visible and longer-wave infrared must be minimized. Mid-infrared radiation is attenuated by the beam splitter in the instrument and optical filters are used to remove the visible light.

The data is captured from the array in a similar manner to single-point detection. The response at each frame (all the pixels) is triggered by the interferometer as a function of opd. At each trigger, the pixel responses are readout in "snapshot" mode (i.e., all pixels are readout simultaneously), processed, and transferred to the data system to provide an interferogram data point for each pixel in the array at each opd. The triggering rate must be less than the maximum frame rate of the FPA so that all the data are collected

For a 64 × 64 FPA, the maximum frame rate is 3.77 kHz. Because of the discrete speed settings available on most commercial FT-IR spectrometers, for a spectral range of 7900 cm^{-1} (the Nyquist wavenumber for a HeNe laser-referenced system with an undersampling ratio of 2), the fastest scan speed that can currently be used to collect data from a 64 × 64 FPA is 2.5 kHz. The use of an undersampling ratio of 2 allows for data to be collected without any aliasing into the mid-IR spectral region (<4000 cm^{-1}). For a complete description of the concept of undersampling an interferogram, see Griffiths and de Haseth [64].

The interferometer speed can be increased up to 5 kHz, by further undersampling the interferogram. An undersampling ratio of 4 (where the FPA is triggered for data readout at every fourth He–Ne laser zero-crossing, that is, every second wavelength of the HeNe interferogram) provides for a Nyquist wavenumber of 3950 cm^{-1}. However, to prevent spectral artifacts caused by aliasing from appearing in the spectrum, a low-pass filter must be mounted in the optical path to prevent radiation with wavenumbers above 3950 cm^{-1} from reaching the FPA detector. These filters have benefits and drawbacks that should be considered before

use. They give the benefit of limiting detector saturation by preventing light from outside the spectral region of interest from reaching the detector, allowing longer integration times for increased SNR. However, they also reduce the intensity of the radiation in the spectral region of interest. Furthermore, in a reflection geometry experiment, there will be a double pass through the filter lowering the energy hitting the FPA.

For measurements made in this way, the FPA is still being triggered at 2.5 kHz, but now at every fourth zero-crossing. The net effect is that the interferometer speed can be increased twofold while still allowing the entire frame to be collected. At 2.5 kHz, the time available to record a frame is 0.40 ms, with typical integration times of 0.01 – 0.05 ms for high-throughput systems. In such measurements, it is clear that the FPA is typically integrating for only a fraction of the full available frame period. An unanticipated benefit of this property is that experiments with a relatively low optical throughput become more efficient.

Since the introduction of the FPA camera that is used today in various commercial instruments, there have been major changes in the array technology. Unfortunately, these changes have not been incorporated into next-generation laboratory-based imaging systems. Some of the changes that have been made include smaller pixel sizes, larger format cameras, and faster frame rates. As pointed out by Bhargava [65], all these features would benefit the spectroscopist.

The major stumbling block to the commercial use of these arrays on FT-IR instruments is their expense and US government regulations, especially the International Traffic in Arms Regulations (ITAR). These regulations govern the import and export of materials defined as defense articles, services, and technical data. The arrays that are or could be used for mid-infrared imaging are listed on the US Military Critical Technologies List (MCTL). The ITAR and the listing on the MCTL preclude sale to certain countries and require extensive paperwork for export to any other country. This constraint in itself limits sales and destroys the driver that any instrument company would have to invest in new technology and has effectively stalled the development of instruments incorporating array detectors.

By analogy with Equation 1.2, Sniveley and Koenig showed that the SNR on the baseline of spectra measured with an imaging FT-IR spectrometer is given by

$$\mathrm{SNR} = \frac{0.12\pi A\{1 - \sqrt{1 - (\mathrm{NA})^2}\}U_{\tilde{\nu}}(T)\Delta\tilde{\nu}D^*\sqrt{t}}{A_{\mathrm{D}}^{\frac{1}{2}}} \tag{1.11}$$

where NA is the numerical aperture and A is the area of the sample imaged onto the pixel. All the other parameters have the same meaning as in Equation 1.4 [66]. The factor of 0.12 is analogous to the efficiency term in Equation 1.4. Sniveley and Koenig used this equation to compare the performance of FT-IR imaging and single-detector microspectrometers and found that, for measurements near the diffraction limit, the performance of imaging spectrometers should be higher than that of standard FT-IR microspectrometers if it is assumed that the D^* of the detectors and the area of the sample imaged onto the pixel are the same in both

types of instruments. (In practice, the D^* of PV MCT detectors is slightly higher than that of PC detectors for signals modulated at frequencies greater than 1 kHz, but the difference is small.) The biggest advantage of the imaging spectrometers is in the A_D term for array detectors. Most FT-IR microscopes are equipped with 250 μm detectors, whereas the pixel size in most FPAs is 40 μm, which leads to an advantage in $\sqrt{A_D}$ by a factor of ~6 for the imaging spectrometer for measurements at close to the diffraction limit of spatial resolution.

However, the benefit in SNR of an imaging system over a single-point system when near the diffraction limit is much greater than a factor of 6. The probable reason for the significantly greater performance of the imaging spectrometers is that Equation 1.11 fails to account for the sample aperture (and its resulting degradation in étendue) when a spectrometer is operated at near the diffraction limit. Because they do not require an aperture, each entire pixel is fully illuminated in imaging systems. Consider the case of a measurement made at near the diffraction limit with a 10 μm. For a spectrometer with a single-element 250 μm detector, only 0.16% of its surface is illuminated, with the remaining 99.84% contributing only noise. When this factor is taken into account, together with the 2.5-fold improvement predicted by Equation 1.11, imaging spectrometry performed near the diffraction limit provides for SNR benefits of many orders of magnitude!

In the original design of all imaging systems, an assumption was made that the magnifications available should be those used in single-point analysis. This was the approach used by Bruker, Digilab, and PerkinElmer. As the systems were used, it became obvious that high spatial resolution was not necessary in all instances. In some cases, there were reasons for less resolution but a wider FOV since not all inhomogeneities were very small in size. The optical zoom feature mentioned above allows refractive optics to be inserted into the beam path in order to demagnify the image of the sample on the detector by a factor of two. In this way, the effective pixel size on the sample is doubled from 5.5 to 11 μm, which allows the use of very small (16 × 16) cameras. When a motorized stage is incorporated, an image can be stitched together to mimic the full image available from a 128 × 128 camera.

Other strategies have also been developed to allow for true imaging with less spatial resolution. One is the development of a 4× refractive objective. This objective provides a 1.2 mm × 1.2 mm FOV with an approximate 20 μm per pixel spatial resolution. Coupled with the optical zoom capability, larger size samples can be examined without resorting to an external compartment.

Although chemical imaging is typically performed with a microscope, it need not be limited to microscopes and samples in the micro domain. In 1998, Digilab released the "Large Sampling (LS) accessory," which consisted of an external sample compartment unit in which the FPA detector could be mounted and transferred as required between the microscope and the LS accessory. In the original design, the LS accessory could be mounted either directly off the FT-IR spectrometer or off the microscope via "pass through" optics, which allow the IR beam to bypass the internal optics of the microscope. In the current design, it is mounted on the side opposite the microscope. Under this configuration, the

overall magnification is 1 : 1, so that the pixel size at the sample plane matches that of the native FPA pixel size at 40 μm × 40 μm. Therefore, with a 128 × 128 FPA, sample areas of up to 5.1 mm × 5.1 mm can be imaged at once.

1.6.2 Spectrometers Based on Hybrid Linear Array Detectors

An alternative approach to hyperspectral imaging that is a hybrid of imaging and mapping was introduced in 2001 by PerkinElmer as the *Spectrum Spotlight.* This instrument is an imaging FT-IR spectrometer that incorporates a linear array of 16 narrow-band MCT PC detectors interfaced with a relatively inexpensive rapid-scanning interferometer. Though this detector is commonly (and perhaps for the sake of simplicity) often referred to as a 1 × 16 linear array detector, the pixels are in fact arranged in a 2 × 8 format. As the cutoff for the narrow-band MCT PC detectors used in this spectrometer is about 720 cm^{-1}, the spectral range of this instrument is at least 130 cm^{-1} wider than that of the PV-MCT FPA detectors that are incorporated in most other hyperspectral imaging FT-IR spectrometers. The signals from each of the 16 detectors in the linear array are digitized simultaneously with separate ADCs. The sample is mounted on a computer-controlled stage that can be rapidly repositioned to allow the spectra from an adjacent region to be measured once the spectral data from a given stage position have been acquired. The spectra are then quilted together to produce the image. This process is repeated until the entire spatial region of interest has been covered. In addition to this linear detector array, a single 100 μm medium-band MCT detector is mounted in the same dewar that allows individual spectra to be acquired over a wider spectral range than the spectra measured with the array. A similar instrument is now available from ThermoFisher Corporation that consists of a 28 pixel linear array arranged in a 2 × 14 pixel format. Other vendors have recently adopted this technology because of the lack of regulatory hurdles. It is interesting to note that these detectors are not impacted by the export control regulations that are described earlier. This is the most likely reason that this instrumentation approach has grown at the expense of the faster, higher resolution monolithic devices.

Much confusion exists as to the advantages and disadvantages of linear array versus FPA-based imaging systems, and detailed analysis and comparison is beyond the scope of this chapter. However, Bhargava and Levin proposed a useful metric to aid in comparing the performance of two imaging systems that can be conveniently applied to the comparison of a linear array system against an FPA imaging system [67]. The figure of merit defined is the pixels per minute "pixpm" and compares the performance of two imaging systems relative to each other for a specified SNR at defined spectral and spatial resolutions. The ratio of the pixpm values of two instruments is given by

$$R_{21} = \frac{n_2}{n_1}\left(\frac{t_1}{t_2}\right)\left(\frac{\mathrm{SNR}_2}{\mathrm{SNR}_1}\right)^2 \tag{1.12}$$

Table 1.1 Comparison of imaging spectrometers with a 64 × 64 pixel FPA and a 16-pixel linear array.

	System 2 ($i = 2$)	**System 1 ($i = 1$)**
Detector	64 × 64 FPA (5.5 μm projected pixel size)	6.25 μm projected pixel size
n_i (number of pixels collected for a 700 × 700 sample area)	16 384 (four tiles)	12 544 (784 line scans)
t_i	5 min (32 scans co-added)	150 min (16 scans co-added)
SNR	200	200

where R_{21} is the ratio of the pixpm of system 2 to system 1, n_i is the number of pixels collected over the defined sample measurement area, t_i is the time required to collect image (of either one scan or to achieve the required SNR), and the SNR_i is the average SNR achieved over the sample measurement area. Hence, the relative performance is linearly related to the time and number of pixels collected and to the square of the SNR.

Let us assume the sample area to be measured is moderate in size, say 700 μm × 700 μm, and is to be collected at high spatial resolution and 4 cm^{-1} spectral resolution at an SNR of 200. Based on manufacturers' typical specifications, if all other parameters are kept equal, we have the data as shown in Table 1.1.

Thus, from Table 1.1, it can be concluded that the FPA imaging system is 30 times faster, under the specified conditions, despite requiring twice as many scans (32 vs 16). This result can be rationalized by considering the massive multichannel advantage of a 64 × 64 FPA (4096 detectors) over a 16-element linear array. There are 256 times as many detectors collecting data simultaneously for the FPA compared to that of the linear array. To cover the same 700 μm × 700 μm area, the 64 × 64 FPA, with its 5.5 μm pixel size requires a four-tile mosaic, whereas the 16-element linear array in its high spatial resolution mode of 6.25 μm requires 784 separate line scans. Thus, even though the time at which a given interferogram can be acquired with the linear array is faster than when an FPA is used, the FPA-based spectrometer required a total of 128 (4 × 32) scans, the instrument that incorporated the linear array required 12 544 (16 × 784) scans. The acquisition of almost a hundred times more scans has resulted in a significantly slower overall time of collection when the linear array is used. The smaller pixel size of the FPA system (5.5 μm) compared to that of the linear array (6.25 μm) results in more pixels being collected for the same sample measurement area, which according to Equation 1.12 further increases the advantage of the FPA-based instrument.

The differences between FPAs and linear arrays are not always of this magnitude, but they are usually in favor of the FPA-based imaging system. In fact, when employing even larger FPAs, such as the 128 × 128 FPA, the differences are even larger. Linear array systems are, however, generally at their most efficient when

operated at relatively low spatial and spectral resolutions (say 25 μm and 16 cm^{-1}, respectively) and with only a few co-added scans, where the synchronization of interferometer step and stage travel is most accurately achieved.

1.6.3 Sampling

Imaging can be accomplished using any of the approaches used in mid-infrared mapping, namely, transmission, external reflection, and attenuated total reflection. In some instruments, the microscope objective can be changed to permit operation at high or low magnification. The key to any imaging measurement is that the sample should be accurately located at a beam focus so that it can be exactly reimaged on the array detector. The first applications of mid-infrared imaging were performed in the transmission mode, with a few examples of reflection spectroscopy. Imaging by ATR took longer to be reported, even though ATR imaging is by no means a new concept. For example, in his 1967 book *Internal Reflection Spectroscopy*, Harrick showed the visible ATR image of a fingerprint recorded photographically [68].

Digilab received a patent on ATR imaging in 2000 [69]; Sommer *et al.* [70] used an ATR accessory with a germanium IRE mounted in the external beam of a *Stingray* spectrometer/microscope. They demonstrated a spatial resolution of about 8 μm in the fingerprint region and claimed to have shown that the 4× magnification factor associated with the germanium IRE was realized. However, a 4× reduction of the diffraction limit for a microscope with an NA of 0.6 should have meant that the spatial resolution was improved to 2.5 μm, and this was not explicitly demonstrated. Later Chan and Kazarian [71] reported a detailed study of ATR imaging using a patterned film of PMMA on a silicon substrate; the visible image shows circles of the polymer 4 μm in diameter with a separation of 2 μm (see Figure 1.16). Micro-ATR imaging with a diamond IRE ($n = 2.4$) showed that the PMMA circles were resolved when the spectrum was integrated between 1753 and 1672 cm^{-1} (average wavelength, $\lambda_{ave} = 5.8$ μm), but the image tended to wash out at longer wavelength as the diffraction limit was exceeded, as shown in Figure 1.17.

A detailed investigation into the resolution of ATR imaging instruments was presented by Everall [72], who first calculated the edge profile by convolving the image at 1600 cm^{-1} of the interface between the two polymers with the Airy disk, taking into account the 10 μm size of the pixels in the MCT FPA detector. He then measured the ATR image 1600 cm^{-1} of a laminate of acrylonitrile butadiene-styrene (ABS) polymer in the region of the interface using a *Stingray* imaging spectrometer equipped with a diamond ATR element. The fit was remarkably accurate, as shown in Figure 1.18.

Everall also demonstrated the problems of quantitative ATR imaging when trying to measure the image of a sample containing hard spheres with a diameter equal to or smaller than the depth of penetration [72]. He showed that shallow penetration combined with the finite spatial resolution of an imaging

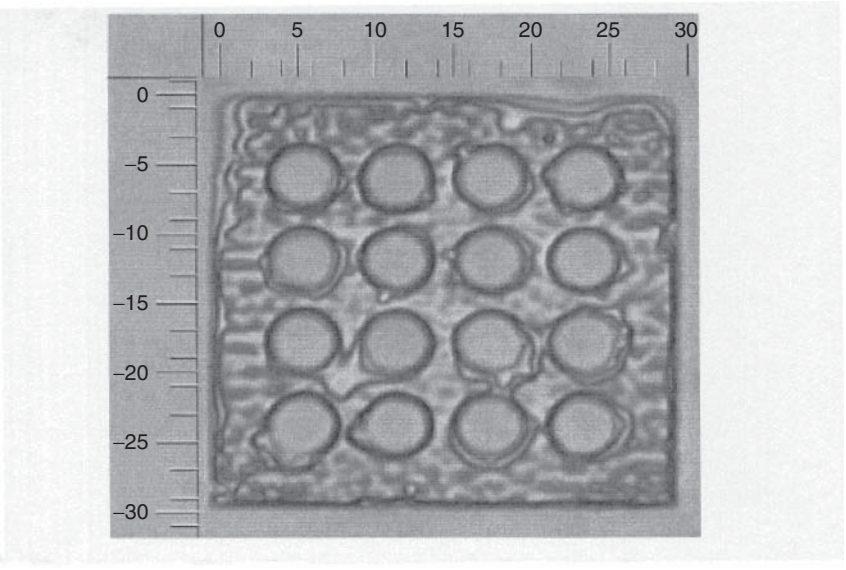

Figure 1.16 Visible image of the patterned PMMA film on a silicon wafer, captured with a 100× objective. The scales on the image are in micrometers. (Reproduced from Ref. [71]. Copyright 2003, Society for Applied Spectroscopy.)

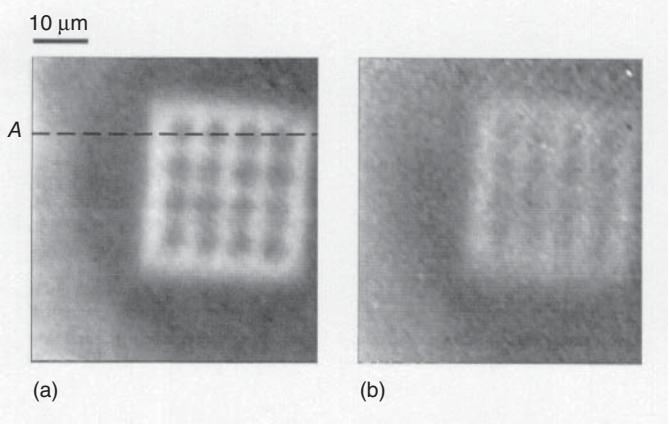

Figure 1.17 Micro-ATR images of the PMMA film on a silicon wafer obtained by integrating (a) 1753 and 1672 cm^{-1} ($\lambda_{ave} = 5.8\,\mu m$) and (b) 1179 and 1090 cm^{-1} ($\lambda_{ave} = 8.8\,\mu m$). (Reproduced from Ref. [71]. Copyright 2003, Society for Applied Spectroscopy.)

spectrometer makes ATR insensitive to hard spherical particles with domain sizes in the range 10–150 μm. For large spheres, the shallow penetration depth underestimates the diameter, whereas for small spheres, the finite spatial resolution overestimates the diameter because of blurring, causing the apparent size insensitivity of the technique for spheres. His conclusions are equally valid for

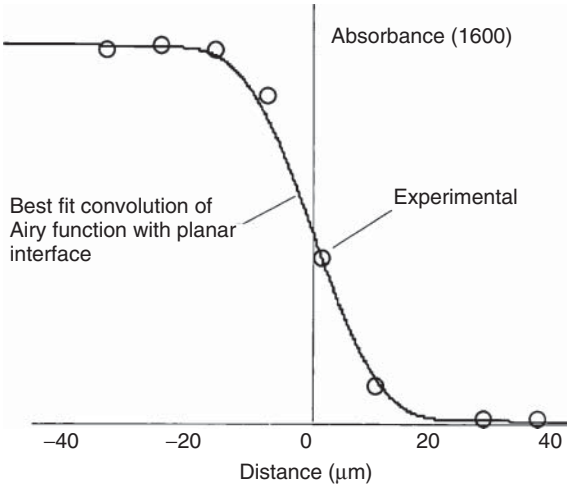

Figure 1.18 Calculated and experimental variation of the1600 cm^{-1} band of polyurethane as a function of distance from the interface of a polyurethane–ABS laminate. (Figure courtesy of Dr. Neil Everall, Measurement Science Group, Intertek Corporation.)

other irregular inclusions, while flat or platey domains should yield more accurate results. Everall further showed that compression of soft particles increases their apparent size, albeit in a noncontrolled fashion. He stressed that ATR imaging is nonetheless a valuable technique for assessing variations in the surface composition of polymer samples. He suggested that by sectioning the samples, a more accurate picture of the near-surface composition could be obtained.

Everall's group also measured the images of polystyrene spheres of several diameters using the 1450 cm^{-1} (6.9 μm) band of polystyrene [73]. He found that transmission spectroscopy gave far better estimates of the sphere diameter than ATR imaging. The error in estimating the sphere diameter was about +10% when the diameter was 50 μm or more, whereas with ATR imaging the estimated particle diameter was considerably less than the actual diameter. When the diameter of the spheres was 10 μm or less, their apparent diameter as measured by transmission imaging was a little worse than the diffraction limit (typically about 20 μm).

To capitalize on the capability of the Agilent LS accessory, the design of the Specac "Golden Gate" single-reflection diamond accessory was modified so that it could be used in the imaging mode. Using patented optics [74], this accessory could achieve ~6.5 μm per pixel spatial resolution and could accommodate up to a 64 × 64 pixel array detector. This version of the Golden Gate optics differs from the standard version by its image-preserving optical design, which is necessary if the spatial relationships of the image are to be preserved while being propagated through the IRE. The FOV with this accessory can be as large as 640 μm × 640 μm when used with a 64 × 64 FPA detector.

Another image preserving ATR accessory that has been used in conjunction with "macro imaging" is the Harrick FastIR 75, which consists of a simple inverted

ZnSe prism such as the one shown in Figure 1.7a. Since the IRE is fabricated from ZnSe rather than diamond, this accessory is less robust, but does offer the advantage of having a considerably larger FOV. A similar accessory is made and has been used to characterize heterogeneous materials by varying the crystal and angle of incidence by Pike Technologies (Madison, WI, USA). These accessories open up a whole new avenue of research, as now one can combine the already proven and well-established benefits of ATR accessories such as limited or no sample preparation, with the information-rich content afforded by FPA chemical imaging.

In another Digilab patent [75], a "side port" adaptor directs the beam that would otherwise enter the objective (in reflection mode) via a 45° flat mirror toward the front of the instrument into an objective now facing outward. In such a configuration, the sample size is no longer limited by the working distance of the objective (typically ~24 mm). Thus, large samples may be placed in front of the outward-facing objective for measurement. In such a configuration, only the external reflection or ATR modes of sampling are possible. This measurement mode makes it conceivably possible for large objects such as complete vehicle bumper bars to be stood on the floor and held in contact with the micro-ATR accessory on the outward-facing side port objective.

In summary, ATR imaging has a number of advantages over transmission or external reflection imaging for studying surfaces that do not have spherical or irregular inclusions, not the least of which is the absence of artifacts caused by Mie scattering. Sample preparation is much easier and the diffraction-limited spatial resolution that can be obtained is less than that could be obtained by transmission imaging by a factor equal to the refractive index of the IRE. However, because the depth of penetration is low, the peak absorbance of even quite strong bands can be rather weak, especially if a germanium or silicon IRE is used. It should also be remembered that strong bands in ATR spectra, especially those measured using IREs with a high refractive index, can be significantly shifted with respect to the same band measured in transmission mode. Finally, as noted above, if the samples contain spherical or irregular particles, they may not be adequately interrogated by the evanescent wave, making the particles appear smaller than they actually are. In an interesting example of "what goes around, comes around," Kazarian's [76] group published hyperspectral imaging data of human fingerprints in which trace quantities of drugs of abuse could be detected in a few of the spectra. The science of imaging has certainly come a long way since Harrick's original ATR photograph of a fingerprint.

1.7 Mapping with Pulsed Terahertz Radiation

Vibrational spectroscopy covers the spectral region from about 0.75 μm (~13 500 cm^{-1}) to 1000 μm (10 cm^{-1}). To this point, we have covered the NIR (0.75 – 2.5 μm or ~13 500 – 4000 cm^{-1}) and mid-infrared (2.5 – 25 μm or 4000 – 400 cm^{-1}) regions. The final region is the far-infrared (25 – 1000 μm or

400 – 10 cm^{-1}) region that is discussed in this section. Many different types of transitions are seen in the far-infrared region of the spectrum. They include intramolecular stretching modes involving heavy atoms, skeletal bending modes involving the entire molecules, torsional modes, ring-puckering vibrations of small-ring molecules, intermolecular vibrations of hydrogen – bonded molecules, and charge-transfer complexes and lattice bands (or phonon modes) [77]. Until only a few years ago, far-infrared spectra were difficult to measure and were rarely used for chemical analysis. This state of affairs was a result of the fact that the radiative energy emitted by sources of continuous far-infrared radiation, such as a Globar or high-pressure mercury lamp, is far lower than the corresponding energy emitted by mid-infrared sources. The measurement of far-infrared spectra using such sources is slow, even with a Fourier transform spectrometer.

In 2003, a completely new way of generating far-infrared radiation was developed so that far-infrared spectra can be measured faster and at higher sensitivity than before [78, 79]. As a result, there has been a renewed interest in this spectral region. To distinguish the "old way" of measuring far-infrared spectra from this "new way," this new technology has been called *terahertz spectroscopy* since the wavenumber region from 1.2 to 130 cm^{-1} corresponds to the frequency region from 0.05 to 4 THz (1 THz = 1×10^{12} Hz.).

The source for terahertz spectroscopy is an ultrashort-pulsed laser (usually Ti:Sapphire) that emits a stream of pulses of NIR radiation at ~80 MHz, with each pulse lasting about 70 fs. The laser pulses are focused on a PC switch, sometimes known as an *Auston switch*, which is a small semiconductor crystal (often GaAs) on which two planar metal electrodes support a large electric field across its surface [80]. The design of these metal electrodes is that of an antenna. The pulses of NIR radiation cause electron – hole pairs to be generated at the surface of the semiconductor, thereby changing the conductance and effectively closing the switch. With a carefully designed antenna, the electron – hole pairs are accelerated by a DC electric field applied across the device, leading to a rapid change in the current density. The changing dipole produces a terahertz transient in the antenna that is radiated into free space. The resulting effect is the emission of short bursts of broadband coherent terahertz radiation with each laser pulse. The radiation with long wavelength that is generated by this technique can then be collected using a silicon lens.

A small fraction of the NIR laser pulse is also used in the detection process. This radiation is focused onto a second semiconductor device where, once again, electron – hole pairs are generated at the surface. On this device, however, the electric field that is created by the coincident pulses of terahertz radiation induces a measurable photocurrent. The femtosecond laser pulse effectively acts as an optical gate, which is only open for the lifetime of the electron – hole pairs in the semiconductor (<200 fs). By sweeping the time delay between the arrival of the femtosecond laser pulse and the terahertz pulse, a waveform comprising the terahertz signal as a function of time can be constructed (see Figure 1.19). The Fourier transform of this signal yields the single-beam spectrum, as shown in Figure 1.20.

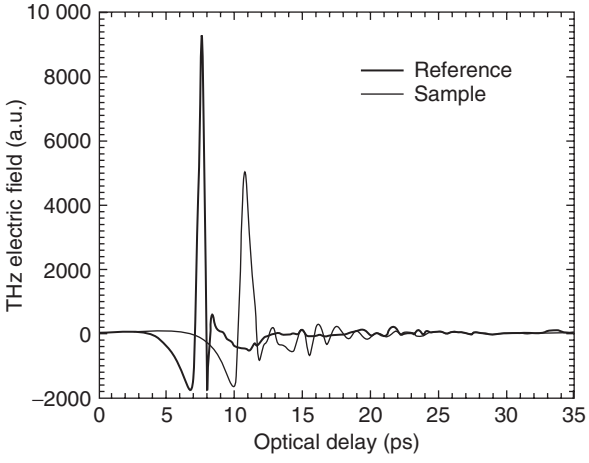

Figure 1.19 The terahertz electric field recorded as a function of time for the background(centerburst of interferogram to the left) and when the beam passes through a 4-mm thick silicon sample (centerburst of interferogram to the right).(Reproduced with permission from Ref. [78]. Copyright 2004, John Wiley and Sons, Ltd.)

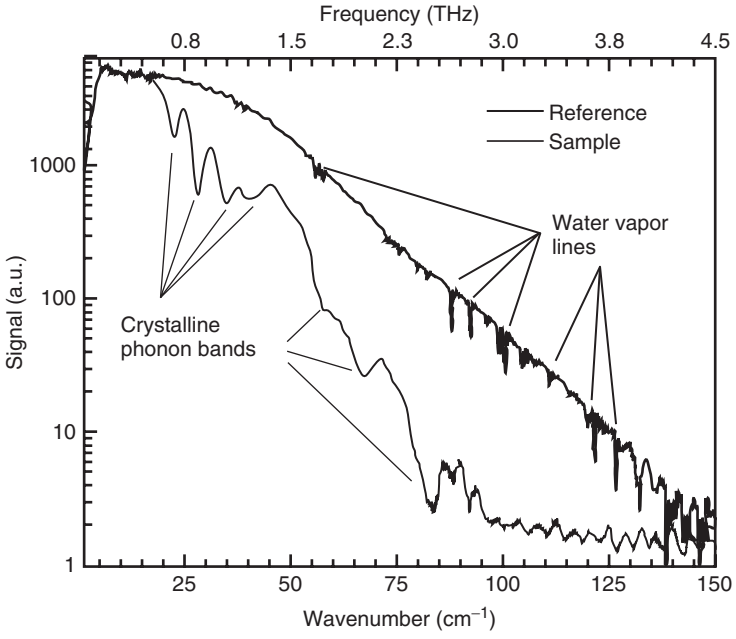

Figure 1.20 Fourier transforms of the two time domain waveforms shown in Figure 1.19. The signal is plotted on a logarithmic scale to show the dynamic range of the instrument. Pure rotation lines of water vapor are seen on the background spectrum (above). The sample spectrum (below) is that of crystalline silicon. (Reproduced with permission from Ref. [78]. Copyright 2004, John Wiley and Sons, Ltd.)

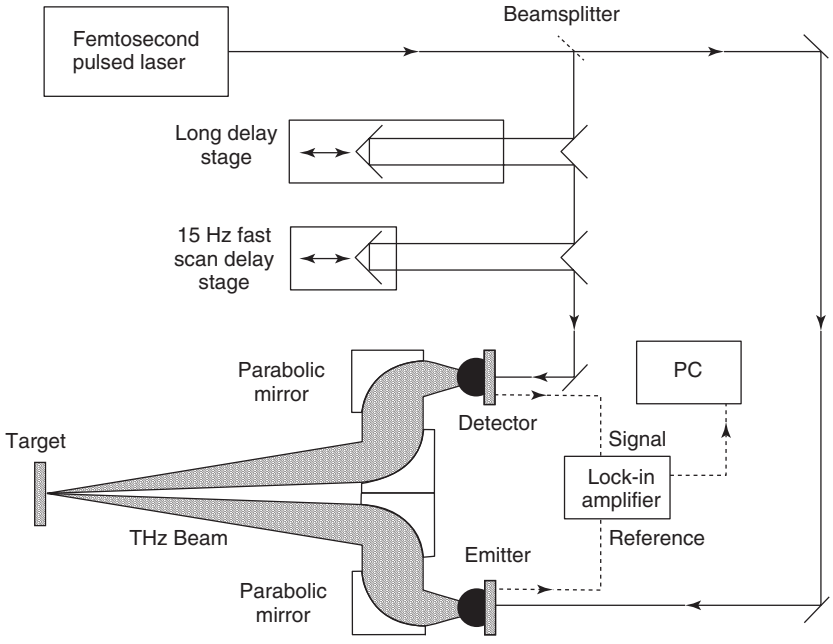

Figure 1.21 Schematic of a terahertz spectrometer. (Reproduced from Ref. [81]. Copyright 2004, John Wiley and Sons, Ltd.)

An instrument that is based on this principle, manufactured by TeraView Ltd. (Cambridge, UK), is shown in Figure 1.21 [81]. This spectrometer generates pulsed broadband terahertz radiation in the range 0.05–4 THz (1.4–130 cm^{-1}). Measurements made using this instrument can be recorded in two modes: a rapid-scan mode where the optical time delay is generated by mirrors that move rapidly and continuously and for which the maximum resolution is 1 cm^{-1} and a step-scan mode where the time delay is generated by a cube-corner retroreflector, the position of which is controlled by a stepper motor, where the maximum resolution is 0.1 cm^{-1}. The rapid-scanning delay line allows both the delay position and the output of the lock-in amplifier to be digitized and re-interpolated to obtain the terahertz field as a function of optical delay in real time.

Terahertz radiation has the great advantage that, because the wavelengths are so long, scattering is minimized. Thus, it is often possible to measure a terahertz transmission spectrum through a pharmaceutical tablet or cardboard packaging material. However, the absorption spectrum of water contains a very strong broadband centered at 5.6 THz (17.9 cm^{-1}), which has been assigned to the resonant stretching of the hydrogen bond between the water molecules, although one of the authors of this chapter (PRG) believes that mode should be observed at a considerably higher frequency and the 5.6 THz band is more likely to be due to a bending or torsional mode of the hydrogen bond. In any event, the high absorption of water in the terahertz region makes it possible to accomplish whole body imaging [82] to observe the contrast between muscle and adipose

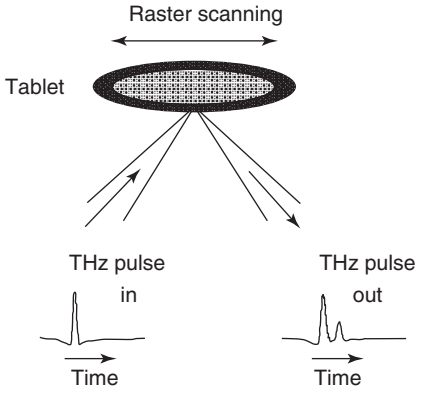

Figure 1.22 Schematic diagram of the experimental arrangement to examine the coating of a pharmaceutical tablet. (Reproduced from Ref. [85]. Copyright 2005, John Wiley & Sons, Ltd.)

tissue [83] and between tumor and normal tissue [84]. In an important related development, devices that measure images using millimeter-wave technology can now be found in most American airports.

The spatial resolution in the x and y dimensions are determined by the diffraction limit (see Equation 1.3). As λ is between ~70 and 700 μm, the resolution in these directions is far worse than for near- or mid-infrared microspectroscopy. On the other hand, significantly better resolution in the z-direction may be obtained, since the terahertz pulse duration of less than 200 fs produces an axial resolution of 30 μm. The 3D structure of the coating of pharmaceutical tablets has been studied by Fitzgerald *et al.* [85]. When the instrument is operated in the reflection mode, a reflected terahertz signal occurs whenever there is a change in boundary conditions, that is, the refractive index of two adjacent layers changes. This results in multiple pulses being returned to the detector, as shown schematically in Figure 1.22. Measurements of this type can be made in two ways. One mode allows for a rapid single-point measurement of the coating thickness. Alternatively, multipoint measurements can be made by rastering the sample to allow false color maps of the uniformity of different layers to be produced.

An example of the time domain waveforms at several points on ibuprofen tablets from two different manufacturers is shown in Figure 1.23. The lower trace is for a tablet that has a single coating, whereas the upper trace is for a tablet with multiple coatings. Knowing the refractive index of each layer, its thickness can be calculated.

1.8 Summary

Powerful instruments for mapping and hyperspectral imaging in the near-, mid-, and far-infrared regions and by Raman spectroscopy are now commercially

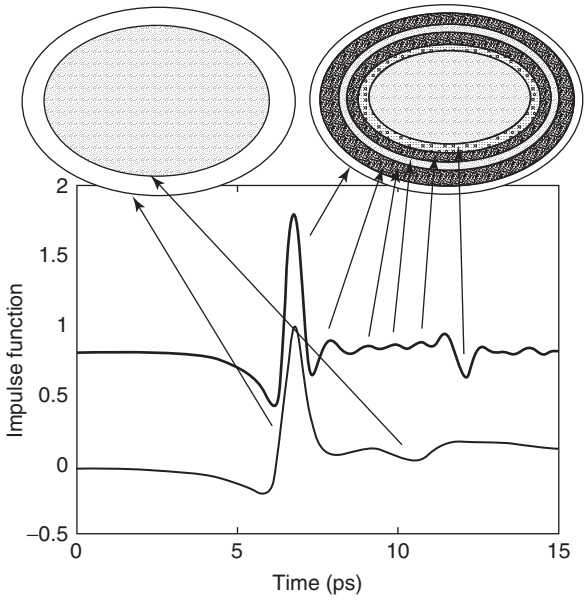

Figure 1.23 Example of depth profiling by terahertz spectroscopy. Pulses arise from interfaces between the coating layers, as illustrated by the schematic drawings of the tablets. The lower trace is for the sample on the left and the upper trace for the sample on the right. (Reproduced from Ref. [85]. Copyright 2005, John Wiley & Sons, Ltd.)

available. Though instruments for imaging were initially expensive, frequently costing more than US$200 000, the price tag is dropping. For example, with the advent of rapid-scanning FPA imaging systems, the cost of mid-infrared imaging spectrometers now starts from <US$150 000. Mapping measurements, where spectra of single points on the sample are measured sequentially and the position of the sample is changed after each measurement, are made on less expensive instruments than imaging spectrometers, but measurements are far more time consuming and spectra measured with high spatial resolution typically have decreased SNR. The hybrid linear array mapping approach, though being much faster than single-point mapping and with increased SNR and spatial resolution, is still several times less efficient in terms of speed (time), SNR, and spatial resolution than contemporary rapid-scanning FPA-based chemical imaging systems. With NIR instruments, a similar comparison cannot be made, as most imaging measurements are made by changing the wavelength with an LCTF and mapping NIR microspectrometers are rarely encountered. The situation is less definitive with Raman spectrometry, as mapping instruments are both sensitive and fast, especially with the development of EMCCDs. In summary, it can certainly be said that hyperspectral imaging spectrometers are revolutionizing the way in which vibrational spectroscopy is used, especially with respect to the analysis of pharmaceutical products and for medical diagnosis.

Acknowledgments

PRG would like to thank the Alexander von Humboldt Foundation for a senior research fellowship; most of the corresponding chapter for the first edition was written while he was working in the Laboratory of Professor Reiner Salzer at the Technical University of Dresden. He owes a debt of gratitude to several people who read through this chapter in the first edition of this book and made many useful suggestions. They include Fran Adar (Horiba Jobin-Yvon), Bruce Chase (then with du Pont), Neil Everall (then with ICI), Louise Ho (then with Cambridge University), Mustafa Kansiz (Agilent), and Bob Messerschmidt (then with Aspectrics Corp.). We would also like to thank Ann Marie Woysl at Pike Technologies for providing Figure 1.1 of this chapter.

References

1. Burch, C.R. (1947) *Proc. Phys. Soc. London*, **59**, 41–48.
2. Barer, R., Cole, A.R.H., and Thompson, H.W. (1949) *Nature (London)*, **163**, 198–201.
3. Gore, R.C. (1949) *Science*, **110**, 710–711.
4. Blout, E.R., Bird, G.R., and Grey, D.S. (1950) *J. Opt. Soc. Am.*, **40**, 304–313.
5. Wood, D.L. (1959) *Rev. Sci. Instrum.*, **21**, 764–766.
6. Norris, K.P. (1954) *J. Sci. Instrum.*, **31**, 284–287.
7. Perkin-Elmer Instrument News, vol. 4, p. 4 (1951)
8. Rafferty, D.W. and Virnelson, R.C. (1997) *Spectroscopy*, **12** (5), 42–44.
9. Merklin, G.T. and Griffiths, P.R. (1997) *J. Chem. Phys. B*, **101**, 7408–7413.
10. Griffiths, P.R. and de Haseth, J.A. (2007) *Fourier Transform Infrared Spectrometry*, 2nd edn, Wiley-Interscience, Hoboken, NJ, pp. 277–281.
11. Griffiths, P.R. and de Haseth, J.A. (2007) *Fourier Transform Infrared Spectrometry*, 2nd edn, Wiley-Interscience, Hoboken, NJ, pp. 188–189.
12. Griffiths, P.R. and de Haseth, J.A. (2007) *Fourier Transform Infrared Spectrometry*, 2nd edn, Wiley-Interscience, Hoboken, NJ, pp. 161–168.
13. Williams, G.P. (2002) in *Handbook of Vibrational Spectroscopy*, vol. 1 (eds J.M. Chalmers and P.R. Griffiths), John Wiley & Sons, Ltd, Chichester, pp. 341–348.
14. Steiner, G., Sablinskas, V., Kitsche, M., and Salzer, R. (2006) *Anal. Chem.*, **78**, 2487–2493.
15. Griffiths, P.R. and de Haseth, J.A. (2007) *Fourier Transform Infrared Spectrometry*, 2nd edn, Wiley-Interscience, Hoboken, NJ, pp. 282–292.
16. Dumas, P. and Tobin, M.J. (2003) *Spectrosc. Eur.*, **15** (6), 17–23.
17. Levenson, E., Lerch, P., and Martin, M.C. (2006) *Infrared Phys. Technol.*, **49**, 45–52.
18. Miller, L.M. and Smith, R.J. (2005) *Vib. Spectrosc.*, **38**, 237–240.
19. Miller, L.M. and Dumas, P. (2006) *Biochim. Biophys. Acta*, **1758**, 846–857.
20. Dumas, P., Jamin, N., Teillaud, J.L., Miller, L.M., and Beccard, B. (2004) *Faraday Discuss.*, **126**, 289–302; discussion 303–311.
21. Everall, N., Lapham, J., Adar, F., Whitley, A., Lee, E., and Mamedov, S. (2007) *Appl. Spectrosc.*, **61**, 251–259.
22. Sommer, A.J. and Katon, J.E. (1991) *Appl. Spectrosc.*, **45**, 1633–1640.
23. Smith, A.L. (1958) *Appl. Spectrosc.*, **12**, 153–159.
24. Romeo, M.J., Mohlenhoff, B., and Diem, M. (2006) *Vib. Spectrosc.*, **42**, 9–14.
25. Romeo, M.J., Boydston-White, S., Matthäus, C., Miljković, M., Bird, B., Chernenko, T., Lasch, P., and Diem, M. (2008) Infrared and Raman microspectroscopic studies of individual human cells, in *Vibrational Spectroscopy for Medical Diagnosis* (eds M. Diem, P.R.

Griffiths, and J.M. Chalmers), John Wiley & Sons, Ltd, Chichester.
26. Mie, G. (1908) *Ann. Phys. (Leipzig)*, **25**, 377–452.
27. Davis, B.J., Carney, P.S., and Bhargava, R. (2010) *Anal. Chem.*, **82**, 3474–3486.
28. Davis, B.J., Carney, P.S., and Bhargava, R. (2010) *Anal. Chem.*, **82**, 3487–3499.
29. Davis, B.J., Carney, P.S., and Bhargava, R. (2011) *Anal. Chem.*, **83**, 525–532.
30. Walstra, P. (1964) *Br. J. Appl. Phys*, **15**, 1545–1552.
31. Hirschfeld, T. and Chase, B. (1986) *Appl. Spectrosc.*, **40**, 133–137.
32. Delhaye, M. and Migeon, M. (1996) *Contes Rendues Acad. Sci. Paris*, **262**, 702–705, 1513-1516.
33. Delhaye, M. and Dhamelincourt, P. (1975) *J. Raman Spectrosc.*, **3**, 33–43.
34. LaPlant, F. and Ben-Amotz, D. (1995) *Rev. Sci. Instrum.*, **66**, 3537–3544.
35. Hollricher, O. and Ibach, W. (2007) *Spectroscopy*, **2007**, 38–43.
36. Cai, T.T., Zhang, D., and Ben-Amotz, D. (2001) *Appl. Spectrosc.*, **55**, 1124–1130.
37. Savitzky, A. and Golay, M.C.E. (1964) *Anal. Chem.*, **36**, 1627–1639.
38. Adar, F., Lee, E., Mamedov, S., and Whitley, A. (2006) *Spectrosc. Suppl.: Raman*, **2006**, 38–43.
39. Everall, N.J. (2007) Paper 1820-5 at Pittcon 2007, Chicago, Illionois, February 28, 2007.
40. Macdonald, A.M. and Vaughan, A.S. (2007) *J. Raman Spectrosc.*, **38**, 584–592.
41. Pettinger, B. (2006) *Top. Appl. Phys.*, **103**, 217–240.
42. Zhang, W., Yeo, B.S., Schmid, T., and Zenobi, R. (2007) *J. Phys. Chem. C*, **111**, 1733–1738.
43. Yeo, B.S., Zhang, W., Vannier, C., and Zenobi, R. (2006) *Appl. Spectrosc.*, **60**, 1142–1147.
44. Yeo, B.S., Schmid, T., Zhang, W., and Zenobi, R. (2007) *Anal. Bioanal. Chem.*, **387**, 2655–2662.
45. Abrahamsson, C., Johansson, J., Andersson-Engels, S., Svanberg, S., and Folestad, S. (2005) *Anal. Chem.*, **77**, 1055–105.
46. Abrahamsson, C., Lowgren, A., Stromdahl, B., Svensson, T., Andersson-Engels, S., Johansson, J., and Folestad, S. (2005) *Appl. Spectrosc.*, **59**, 1381–1387.
47. Chauchard, F., Roger, J.M., Bellon-Maurel, V., Abrahamsson, C., Andersson-Engels, S., and Svanberg, S. (2005) *Appl. Spectrosc.*, **59**, 1229–1235.
48. Johansson, J., Folestad, S., Josefson, M., Sparen, A., Abrahamsson, C., Andersson-Engels, S., and Svanberg, S. (2002) *Appl. Spectrosc.*, **56**, 725–731.
49. Tsuchikawa, S. and Tsutsumi, S. (2000) *Appl. Spectrosc.*, **56**, 869–876.
50. Delphy, D.T., Cope, M., van der Zee, P., Arridge, S., Wray, S., and Wyatt, J. (1988) *Phys. Med. Biol.*, **33**, 1433–1442.
51. Long, W. and Burns, D. (1997) *Anal. Chim. Acta*, **348**, 553–563.
52. Averett, L.A. and Griffiths, P.R. (2008) *Appl. Spectrosc.*, **62**, 377–382.
53. Hudak, S.J., Haber, K., Sando, G., Kidder, L.H., and Lewis, E.N. (2007) *NIR News*, **18** (6), 68.
54. Treado, P.J. and Nelson, M.P. (2001) in *Handbook of Vibrational Spectroscopy*, vol. 2 (eds J.M. Chalmers and P.R. Griffiths), John Wiley & Sons, Ltd, Chichester, pp. 1429–1459.
55. Christensen, K.A. and Morris, M.D. (1998) *Appl. Spectrosc.*, **52**, 1145–1148.
56. Zhang, D., Hanna, J.D., Jiang, Y., and Ben-Amotz, D. (2001) *Appl. Spectrosc.*, **55**, 61–65.
57. Goldstein, S.R., Kidder, L.H., Herne, T.M., Levin, I.W., and Lewis, E.N. (1996) *J. Microsc.*, **184**, 35–45.
58. Suhre, D.R., Gottlieb, M., Taylor, L.H., and Melamed, N.T. (1992) *Opt. Eng.*, **31**, 2118–2123.
59. Vo-Dinh, T., Stokes, D.L., Wabuyele, M.B., Martin, M.E., Soon, J.M., Jafannathan, R., Michaud, E., Lee, R.J., and Pan, X. (2004) *IEEE Eng. Med. Biol. Mag.*, **2004**, 40–49.
60. Lewis, E.N., Treado, P.J., Reeder, R.C., Story, G.M., Dowrey, A.E., Marcott, C., and Levin, I.W. (1995) *Anal. Chem.*, **67**, 3377–3381.
61. Snively, C.M., Katzenberger, S., Oskarsdottir, G., and Lauterbach, J. (1999) *Opt. Lett.*, **24**, 1841–1843.
62. Coutts-Lendon, C. and Koenig, J.L. (2005) *Appl. Spectrosc.*, **58**, 976–985.
63. Miseo, E.V. and Leonardi, J. (2008) *Spectroscopy*, **2008**, 19–20.

64. Griffiths, P.R. and de Haseth, J.A. (2007) *Fourier Transform Infrared Spectrometry*, 2nd edn, Wiley-Interscience, Hoboken, NJ, pp. 63–64.
65. Bhargava, R. (2012) *Appl. Spectrosc.*, **66**, 1091–1120.
66. Snively, C.M. and Koenig, J.L. (1999) *Appl. Spectrosc.*, **53**, 170–177.
67. Bhargava, R. and Levin, I.W. (2005) in *Spectrochemical Analysis using Infrared Multichannel Detectors*, Chapter 1 (eds R. Bhargava and I.W. Levin), Blackwell Publishing Ltd, Oxford, pp. 1–24.
68. Harrick, N.J. (1967) *Internal Reflection Spectroscopy*, John Wiley & Sons, Inc., New York.
69. Burka, E.M. and Curbelo, R. (2000) *Imaging ATR spectrometer* US Patent 61,41,100 A.
70. Sommer, A.J., Tisinger, L.G., Marcott, C., and Story, G.M. (2001) *Appl. Spectrosc.*, **55**, 252–256.
71. Chan, L.A. and Kazarian, S.G. (2003) *Appl. Spectrosc.*, **53**, 381–389.
72. Everall, N.J. (2007) *Spectrometer Apparatus* Presentation on ATR Imaging at a Meeting of the Infrared and Raman Discussion Group, Sheffield, April, 2007.
73. Everall, N.J., Preistnall, I.M., Clarke, F., Jayes, L., Poulter, G., Coombs, D., and George, M.W. (2009) *Appl. Spectrosc.*, **63**, 313–320.
74. Thomson, G. and Poulter, G. (2004) *Imaging ATR spectrometer* US Patent 61,41,100 A.
75. Davis, J.R. (2003) *Infrared microscope adapter for viewing at an angle* US Patent 61,41,100 A.
76. Ricci, C., Bleay, S., and Kazarian, S.G. (2007) *Anal. Chem.*, **79**, 5771–5776.
77. Griffiths, P.R. (2001) in *Handbook of Vibrational Spectroscopy*, vol. 1 (eds J.M. Chalmers and P.R. Griffiths), John Wiley & Sons, Ltd, Chichester, pp. 229–239.
78. Taday, P.F. and Newnham, D.A. (2004) *Spectrosc. Eur.*, **16** (5), 20–24.
79. Pickwell, E. and Wallace, V.P. (2006) *J. Phys. D Appl. Phys.*, **39**, R301–R310.
80. Auston, D.H., Cheung, K.P., Valdmanis, J.A., and Kleinman, D.A. (1984) *Phys. Rev. Lett.*, **53**, 1555–1558.
81. Baker, C., Tribe, W.R., Cole, B.E., and Kemp, M.C. (2005) in *Optics and Photonics for Counterterrorism and Crime Fighting, Proceeding of the Socity Photo-Optical Instrumantion Engineering*, vol. 5616 (eds T.P. Donaldson and C. Lewis), SPIE, Bellingham, WA, pp. 61–68.
82. Siegel, P.H. (2004) *IEEE Trans. Microw. Theory Tech.*, **52**, 1538–1547.
83. Fitzgerald, A.J., Berry, E., Zinv'ev, N.N., Homer-Vanniasinkam, S., Miles, R.E., and Smith, M.A. (2003) *J. Biol. Phys.*, **129**, 123–128.
84. Pickwell, E., Fitzgerald, A.J., Cole, B.E., Pye, R.J., Ha, T., Pepper, M., and Wallace, V.P. (2005) *J. Biomed. Opt.*, **10**, 064021.
85. Fitzgerald, A.J., Cole, B.E., and Taday, P.F. (2005) *J. Pharm. Sci.*, **94**, 177–183.

2
Chemometric Tools for Image Analysis

Anna de Juan, Sara Piqueras, Marcel Maeder, Thomas Hancewicz, Ludovic Duponchel, and Romà Tauler

2.1
Introduction

Hyperspectral images are measurements with a high quality and quantity of information. The spectral output from an image provides a massive data set, and there is a clear need to find tools to handle this measurement to extract interpretable knowledge. Before the analysis of an image is attempted, two main questions should be answered: what are the chemical and mathematical properties of the measurement and what is the objective of the analysis. The answer to the first question will delimit the families of methods that can be potentially used and will help in the design of new algorithms that may take into account the specificities linked to the image nature. Setting the objective of the analysis will point to the specific algorithm to be used taking into account the input information available and the desired outcome.

The use of chemometric tools in image analysis is crucial to take advantage of the full measurement, as opposed to classical approaches, where only a partial visualization or interpretation of the raw data is obtained. Image analysis is a field in constant development in chemometrics, where some solid knowledge has been already built and new working possibilities are still under study. The first works were devoted to the exploration of the spectral and spatial information contained in an image (known under the general denomination of multivariate image analysis, MIA) and to the assignment of the pixels of an image to different groups according to the similarity of their spectral features (image segmentation). On these areas, there are excellent reference works and tutorials published [1–4] and improvements to the existing methodologies are continuously appearing. Afterwards, the extension of regression or calibration methods to relate the information of the image to external properties, such as concentrations, was put in practice. As in classical spectroscopy, this area is particularly relevant in near infrared (NIR) images of food or pharmaceutical products. Multivariate resolution (or unmixing) methods are among the most recent tools incorporated to the field of image analysis, and they have proven to be most adapted to the nature

Infrared and Raman Spectroscopic Imaging, Second Edition. Edited by Reiner Salzer, Heinz W. Siesler.
© 2014 Wiley-VCH Verlag GmbH & Co. KGaA. Published 2014 by Wiley-VCH Verlag GmbH & Co. KGaA.

of this measurement. Indeed, resolution methods are meant to provide the pure spectra and distribution maps of the image constituents from the sole raw image measurement.

The diversity of existing and in-progress methodologies for image analysis is enormous and cannot be treated exhaustively in a single chapter. Instead, we have selected focusing on the general description of the hyperspectral measurement and on the most relevant families of image analysis methods, combining the basics of the methods with recent trends in theoretical and practical developments. We also put the accent on aspects and methodologies, such as resolution (unmixing) methods, that may have been less commented in the available literature and that we think can be of particular interest because of the nature of IR and Raman images, the fine spectral features of which provide excellent structural information and the possibility to differentiate the image constituents based on their distinct spectral fingerprints. Because of this reason, linked to the nature of the measurement, and to the still smaller amount of literature about image resolution, a large part of the chapter will be devoted to this field.

2.2 Hyperspectral Images: The Measurement

Hyperspectral images are a particular kind of measurement that contains spatial and chemical/spectroscopic information about a sample. The sample is physically preserved and compartmented into small surface or volume areas (called *pixels* or *voxels*, respectively), on which spectra are recorded. Information on the chemical composition of the sample analyzed can be extracted from spectral features and the consequent association with functional groups or the matching with a spectra library. Information on the constituent distribution is obtained from the pixel-to-pixel spectral variation.

It is important, therefore, taking into account the spectral and spatial information contained in an image because this duality conforms the singularity of this kind of measurement as opposed to other bulk sample spectroscopic signals. Data analysis tools should take this spatial/spectral character into account if the maximum information is to be extracted from the raw measurement.

2.2.1 The Data Set and the Underlying Model

Hyperspectral images are often displayed as cubes where two dimensions are the pixel coordinates (x and y) and the third dimension is the spectral coordinate. When we deal with a multilayer image, we should imagine a hypercube with three spatial directions (the x-, y-, and z-voxel coordinates) and the spectral direction.

This visualization is very faithful to the nature of the measurement, but it is also important to think about the underlying chemical (mathematical) model of the

measurement. Only knowing the model, we will be able to select the data tools that adapt best to it. Association of the visual 3D or 4D representation of monolayer or multilayer images with equally dimensioned mathematical representations would force us to look for chemometric tools that were handling tensors or higher-order data sets. However, the mathematical description of the variation of an image data set is much simpler and goes back to use data tables that represent adequately the underlying chemical model of any spectroscopic measurement, that is, the Beer–Lambert law.

Thus, it is well known that the spectrum of any pixel is represented by the concentration-weighted sum of the contributions of the pure spectra of the image constituents. These concentration weights vary from pixel to pixel, depending on the pixel composition, but the pure spectra of the constituents are the same along the whole image. These chemical ideas can be mathematically expressed by a bilinear model. First, we should unfold the image cube into a data table that contains the spectra of all pixels as rows one under the other (see Figure 2.1). This data table contains the raw image measurement and can be expressed as the product of a matrix of pure spectra by the concentration weights of these pure components in each pixel. In matrix form, the expression reminds clearly the

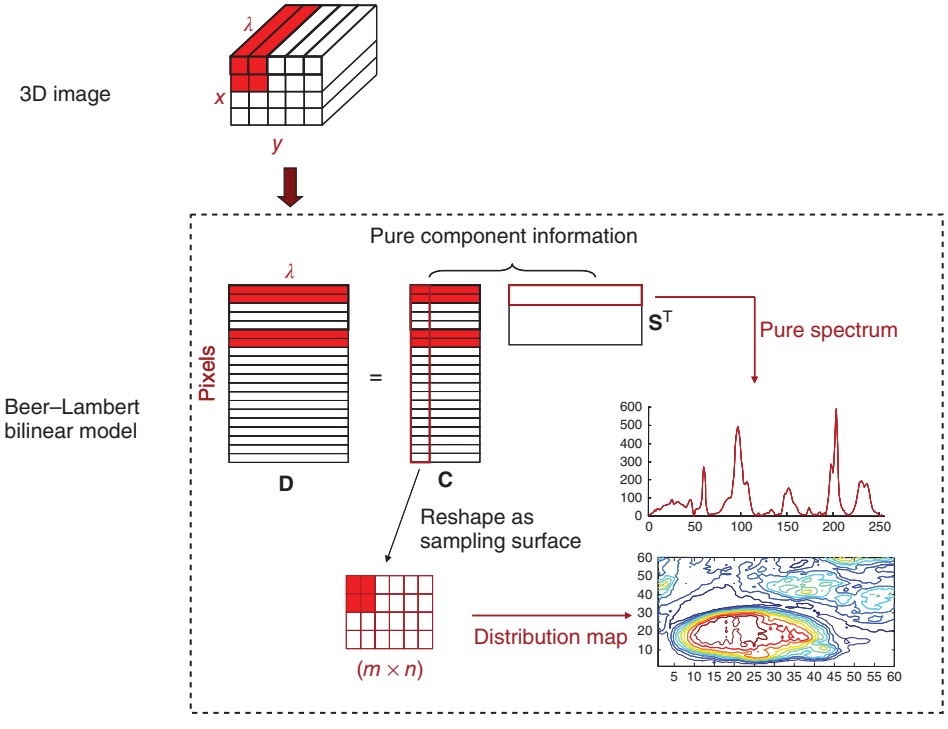

Figure 2.1 Underlying Beer–Lambert law model of hyperspectral images.

Beer–Lambert law.

$$\mathbf{D} = \mathbf{C}\mathbf{S}^{\mathbf{T}} + \mathbf{E} \tag{2.1}$$

The rows of matrix $\mathbf{S}^{\mathbf{T}}$ contain the pure spectra of the image constituents as rows and the rows of matrix **C**, the concentration values of these constituents in every pixel. Since we work with real measurements, **E** contains the experimental error because of signal variation not associated with chemical information. Taking a row of the **C** matrix, information on the chemical composition of the related pixel can be obtained, whereas taking a column, the pixel-to-pixel variation of the concentration of a particular image constituent can be seen. Folding back each **C** column to recover the original 2D or 3D image configuration, the distribution map of each particular image constituent is obtained.

There are important consequences linked to the image bilinear model. The positive points are linked to the simplicity of the mathematical model. There are many well-known chemometric tools that work decomposing the raw data into bilinear models and that, therefore, can be potentially suitable for image analysis. The negative part is the decrease in the image dimensionality, that is, from the original 2D or 3D spatial dimensions into a single pixel direction, which implies that the concept of pixel neighborhood is lost and we should find additional ways of incorporating this spatial information into the classical bilinear analysis tools.

There is a wealth of methods and algorithms that can be used to deal with images. As will be seen in the following sections, the selection will be mainly influenced by the goal of the analysis. We may just want to explore the image and can be more interested in the spatial or the spectral information; we may try to segment the image into groups of similar pixels; we may try to establish a quantitative model between the image measurement and some external information; or we may try to recover the underlying model of maps and spectra of the pure constituents out of the raw measurement. We should select the right tool for the right purpose and take advantage of the new developments and adaptation of existing chemometric tools to the particular features of an image data set to obtain as much information as we can from the complex raw measurement.

2.3 Image Preprocessing

Hyperspectral images contain a lot of information, but the quality of the raw measurements is often affected by noise or by instrumental variations that hinder extracting relevant knowledge. This is the reason why a good preprocessing can significantly improve the results obtained from any image data analysis tool. Typical problems encountered in image measurements are high noise level, presence of intense and irregularly shaped baseline contributions, or anomalous pixel spectra (dead pixels or outliers) that may influence the results of the image analyzed. Additional data pretreatments or image compression may be necessary depending on the data analysis to be carried out.

2.3.1 Signal Preprocessing

2.3.1.1 De-noising

There are many methods designed to de-noise spectroscopic data sets, and all those can be applied to the pixel spectra in hyperspectral images [5, 6]. Some methods rely on classical smoothing procedures (by averaging or fitting neighboring spectral channels to a polynomial function, such as the Savitzky–Golay approach [7]) or on mathematical signal filtering (Fourier transform filters or wavelet-based filters [8, 9]). Recent works preferentially use wavelet-based filtering in hyperspectral imaging because of the adaptability to the nature of the spectral features and the fact of being a localized filter [10]. Some adaptations of wavelet filter approaches do not act only on the raw spectra as independent entities but also take into consideration the spatial structure of the image [11]. When applying any of these methodologies, we should be sure that we do not remove relevant features of the data set together with the noise. Other methods, such as principal component analysis, PCA, decompose the original data set into a bilinear model of latent variables [5, 12]. The first few latent variables relate to chemical variation and the rest to noise. Reproducing the data set taking only the model with the relevant components is also a good way of de-noising (see Figure 2.2a, raw spectra, and Figure 2.2b to appreciate the de-noising effect of PCA on the spectra of a Raman emulsion image, more detailed information on the PCA method can be found in Section 2.4).

2.3.1.2 Baseline Correction

This is a common preprocessing step in image analysis that works better if performed after image de-noising. Doing it this way, the baseline is better defined and can, as a consequence, be better subtracted or corrected. Typical baseline correction, based on linear models or on more complex mathematical functions, can be performed [6, 13]. Other strategies, such as working with derivative spectra instead of the raw spectra or using classical multiplicative scatter correction (MSC), help to suppress or to balance instrumental variations, such as offsets or linear baselines, unrelated to the chemical composition of the image [14].

However, Raman and infrared images are often affected by intense and irregularly shaped baselines. This complex behavior is often attributed to fluorescence contributions in Raman hyperspectral images or to other phenomena, such as the Mie scattering [15], commonly found in biological IR images. For these situations, more sophisticated baseline correction methods that can handle complex baselines changing from pixel to pixel have appeared.

Thus, variations of the classical MSC method, such as extended multiplicative scatter correction (EMSC), have appeared to handle nonlinear baselines that may be better expressed by polynomial functions [16]. Recently, modifications of the EMSC algorithm, especially adapted to handle the Mie scattering effects caused by biological images, have also been implemented [17].

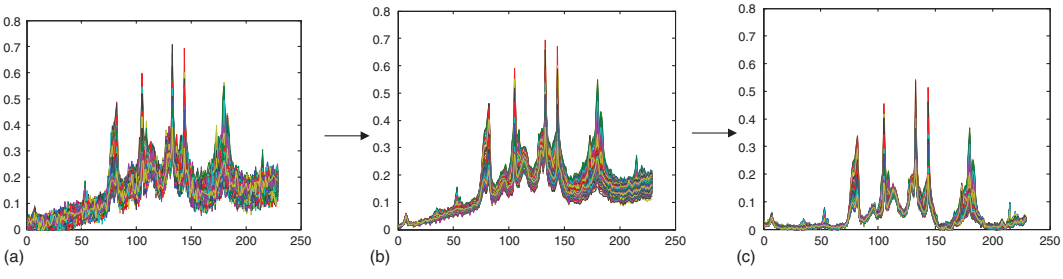

Figure 2.2 (a) Raw spectra of a Raman emulsion layer image; (b) spectra after de-noising by principal component analysis (PCA); and (c) spectra after de-noising and baseline correction by asymmetric least squares.

Asymmetric least squares (AsLSs), proposed originally by Eilers, is perhaps the best representative of this new family of baseline correction methodologies [18]. AsLS is based on a recursive local fitting of the whole spectrum with a baseline obtained by using a Whittaker smoother. In each new iterative cycle, the spectral channels that provided positive residuals in the previous iteration, that is, those channels where there is an absorption band, are downweighted in the baseline fitting operation. After a small number of fitting cycles, no more variation occurs and the fitted baseline obtained is used to correct the spectrum. Two parameters are tuned according to the shape of the baseline: one linked to the smoothness (λ) of the fit and the other to the penalty imposed to the points giving positive residuals in the fit (p). This type of correction was particularly designed to correct baselines smoother and with a significantly lower frequency than the useful signal, as it happens with fluorescent contributions and Mie scattering when compared with the related Raman and IR spectral features, respectively [19, 20]. To appreciate the baseline correction effect by AsLS on the de-noised emulsion data, see Figure 2.2c.

2.3.1.3 Detection and Suppression of Anomalous Pixels or Anomalous Spectral Readings

Because of diverse instrumental artifacts, some of the pixels may show unexpected spectral readings, for example, spikes, or present completely abnormal spectra (*dead* pixels) [21]. The presence of these very different measurements can distort the results obtained from image analysis, and they should be detected and eliminated/corrected. An easy way to detect unexpectedly high or low results may be done by using thresholding methodologies that can point out spectral readings (or complete spectra) that are well below or above than a representative reference value (spectrum). Median values for spectral readings or median spectra taken from region of interest (ROI) in the image can be used as references for this detection. Mean values are not recommended because they can be significantly modified by the influence of abnormal measurements [21]. Anomalous readings, for example, spikes, can be replaced by interpolated values obtained taking the readings of normal neighboring spectral channels for this purpose. Likewise, dead pixels can be replaced by interpolated spectra taking as reference the normal neighboring pixels around them [22].

2.3.2 Data Pretreatments

Once the signal preprocessing is accomplished, additional pretreatments can be carried out to enhance certain properties of the image data set. Note that signal treatment has always to be done. Data pretreatment depends on the goal of the analysis and it may even be avoided in some cases. Thus, the spectra in an image can be subject to any data pretreatment used in traditional spectroscopic data sets, and the choice will depend on the spectral structure and the goal of the data analysis. To give some examples, derivatives can be carried out to stress subtle

differences in spectral features among spectra. Spectra normalization may be an option when the focus is on comparing the shapes of the pixel spectra independently from their global intensity, for example, for pixel classification purposes. Centering or scaling of spectral channels can be options in quantitative regression methods. In contrast, keeping the original spectra intensity may be relevant in resolution methods. The reader may consult the reference literature to know more about the effect of the main data set pretreatments on the data analysis results [1, 5, 6, 13, 21, 23, 24]. Unfortunately, there is no golden rule that can uniquely address toward the optimal pretreatment. The choice will depend on the nature of the measurement analyzed, on where and how the relevant information is located in the signal, and on the final objective of the analysis [25, 26].

2.3.3 Image Compression

Very often, raw images are too huge to permit reasonable computation times to be analyzed or, some of them, to be even loaded in standard computers. Depending on the size of the image and on the computation intensiveness of the data analysis tool selected, the original image should be compressed. Compression can be performed on the spectral and/or on the spatial dimension. The simplest compression is binning the image as much as needed to reach the desired data set size. Binning means adding the readings in an interval of neighboring spectral channels to form a single measurement (spectral binning) or doing likewise adding the spectra of neighboring pixels (binning in the pixel direction) to obtain a single spectrum. Which direction (spatial/spectral) should be binned will depend on the resolution of the image and on which kind of information is preferred. The binned image will enclose the information in all spectral channels or pixels but will suffer a loss of spatial or spectral resolution. Many images, however, can be reduced in this way without losing relevant information. Compressed representations of the image keeping all the information in the spectral channels can be obtained by other methods, such as PCA. In this case, the original spectral channels are replaced by a small number of variables (principal components), which are linear combinations of the original ones and express very efficiently the image information [1]. Other kind of scores, based on bilinear decompositions, such as those coming from independent component analysis (ICA) or multivariate curve resolution (MCR) [19] can be used for this purpose.

Other compressed image representations do not work with the total amount of information on the image, but with a selection of pixels or spectral channels according to different criteria. This is the case when feature selection is performed in the spectral direction or if the analysis is done on a representative pixel subset. There are many methodologies available for this purpose. Some rely on the straight selection of the purest pixels or the purest spectral channels, such as SIMPLISMA [27–29], whereas others are based on more exhaustive search strategies, such as genetic algorithms [30–32]. Selection can also be done on spectral channels previously transformed, as in wavelet-transformed data, where only significant

wavelet coefficients will be used for later analyses [8, 10, 33, 34]. Representative pixel subsets can also be obtained by using sampling methodologies, taking into account the same strategies followed in chemical sampling [1] or looking for image regions with low complexity, that is, low compound overlap [35]. If the compression performed does keep the relevant information on the original image, no matter which methodology used, the quality of the image analysis will not suffer.

2.4 Exploratory Image Analysis

Exploratory image analysis in both spatial and spectral directions provides a first insight into the most relevant spectral features or into particularities linked to the component distribution and should be the starting point of any other kind of study based on image data analysis.

2.4.1 Classical Image Representations: Limitations

Basic image exploration is usually oriented to obtain visual plots of easy interpretation with a minimum or null computation effort. Usual classical representations of hyperspectral images are maps derived from a single spectral channel or from an integrated spectral band, meant to be compound specific, and global intensity plots, aiming at providing a general view of all information contained in an image. However, these representations result in an incomplete and, often, biased information about the raw measurement.

Thus, a distribution map of a constituent derived from the representation of a slice of the image associated with a particularly relevant wavenumber not only discards all other spectral channels carrying useful information, but implies that the selected wavenumber has selective information for that particular component. This last assumption is only reliable when all the constituents of the image (and their pure spectra) are perfectly known and the spectral features are fine enough to refer to a single compound. When a particular component does not have any selective wavenumber, a map derived using a single spectral channel with mixed information will be, at the most, an approximation of the real situation. In addition, images from natural or complex samples may contain unknown components and, then, assuming the presence of selective spectral channels without any solid evidence could provide wrong distribution maps.

Global intensity plots are obtained by adding up the readings of all spectral channels in a pixel spectrum. In this way, each pixel is represented by a single number related to the total spectral intensity measured. These plots allow the representation of some spatial features in the image, but do not tell any information about the chemical composition of the image because all the spectral information is collapsed into a single numerical value. At most, they provide a first approximation into the physical characteristics of the image. Figure 2.3 shows the global intensity

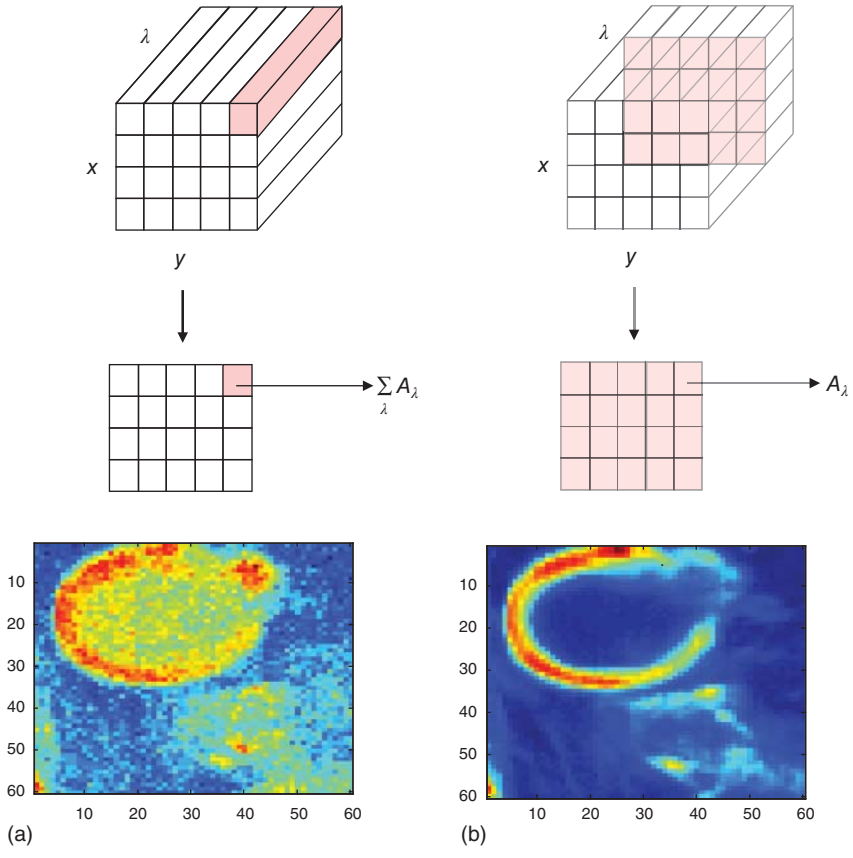

Figure 2.3 Classical visualizations of a Raman emulsion layer hyperspectral image. (a) Global intensity plot and (b) distribution map derived from a single wavenumber.

plot and a distribution map based on a single spectral channel for a monolayer emulsion image.

2.4.2
Multivariate Image Analysis (MIA) and Principal Component Analysis (PCA)

In contrast to classical approaches, MIA uses all the information contained in the original image in the spatial and in the spectral direction and provides simple ways of visualizing the image preserving the relevant original information [1, 36–39]. When chemometrics started to be used for the study of hyperspectral images, the expression MIA was generally associated with PCA, although nowadays many other methodologies would fit into this general denomination. The early and widespread use of PCA to analyze images is easily understandable looking at the inner properties of this methodology. PCA is a chemometric method that decomposes a data table into a bilinear model of latent variables, the so-called

principal components, according to the expression:

$$\mathbf{D} = \mathbf{TP}^{\mathbf{T}} + \mathbf{E}$$

where $\mathbf{T}$ are the scores and $\mathbf{P}^{\mathbf{T}}$ the loadings. $\mathbf{E}$ accounts for the experimental error. Principal components are linear combinations of all the original variables in the image, and they are calculated so that they express the maximum variance contained in the data set in a decreasing order of importance with null correlation among them [5, 12, 23]. In the context of image analysis, this means that even though an image can have hundreds or thousands of spectral channels, the relevant information in all these channels is contained in a very small number of principal components. This is due to the redundant information among spectral channels in the original image. Therefore, although a number of principal components equal to the number of spectral channels are calculated, only the first few components describe spectral variations linked to the chemical composition of the image and the rest account for noise-related signal contributions.

It is worth noting the identical form of the PCA model and the Beer–Lambert law in matrix form, $\mathbf{D} = \mathbf{CS}^{\mathbf{T}} + \mathbf{E}$. The chemical model of an image only needs as many pure spectra as image constituents to reproduce any pixel spectrum. Therefore, it is not surprising that the number of principal components needed to describe an image data set be equal to the number of chemical constituents of the image. Indeed, the rows in the loadings matrix ($\mathbf{P}^{\mathbf{T}}$) could be interpreted as abstract pure spectra, and the columns in the scores matrix ($\mathbf{T}$) can also be folded back to form abstract distribution maps (as happened with the stretched concentration profiles in $\mathbf{C}$ in Figure 2.1). It is illustrative comparing the real pure spectra and distribution maps of an image with the analogous loadings and scores representations, respectively.

Figure 2.4 shows the comparison of the results obtained from the PCA and the real chemical models for a Raman emulsion image [40]. The emulsion image is formed by four constituents related to the drop phase, the interphase, an additive, and the off-drop phase. The two models (real and PCA) resemble each other when looking at general trends, for example, the "score maps" resemble the real distribution maps, although the information seem to be more mixed, and the most salient spectral features in the real spectra can also be found in the different "loading spectra" (see circled bands in Figure 2.4). However, there are relevant differences that should be taken into account. When comparing the pure spectra and the loadings, the first striking difference is the lack of chemical meaning of the loadings, with negative bands (below the dashed line), inexistent in the original Raman spectra. Likewise, we find negative values in the score distribution maps (color scale not shown), unacceptable for real concentrations. This stems from the fact that principal components are calculated to keep null correlation among them, that is, the different "loadings spectra" are completely uncorrelated. However, real spectra of constituents often do not obey this condition. This is the reason why a principal component should never be straightforwardly associated with a real chemical compound because the mathematical properties and chemical meaning of both of them are essentially different.

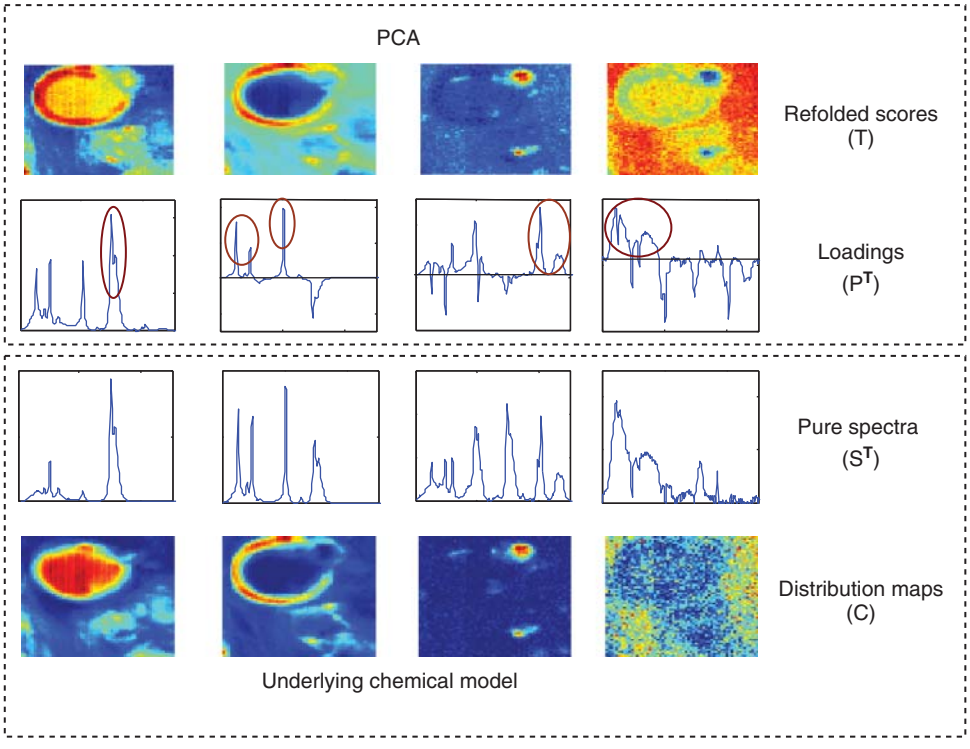

Figure 2.4 PCA model and real chemical Beer–Lambert model for a Raman emulsion image.

Nevertheless, performing PCA on an image data set is always useful because, often, the *a priori* information available is very scarce. Looking at the loading plots, high absolute values will mark relevant spectral features for the image description. The score distribution maps will also give insight into which zones of the image are most related to the features detected in the related loadings. It is worth stressing that PCA allows for a drastic decrease in dimensionality of the original image data preserving all the relevant information, enclosed in the abstract principal components. In contrast with classical approaches, where few spectral channels are chosen for visualization and the information in the rest of channels is discarded, PCA represents the information of all wavenumbers in the different PC combinations. So, image scores and loadings are an excellent first approach to visualize an image in a space of small dimensions without losing the richness of information of the original measurement.

It is interesting to look in a complementary way to the PCA-compressed representation of an image. In a PCA model, a pixel is no longer represented by a full spectrum, but by a small number of score values that provide information related to its chemical composition. Thus, pixels of similar composition in an image are expected to have similar score values. This idea has been used for image

segmentation purposes by using the score values instead of the full pixel spectrum as an input information for the suitable segmentation algorithms. A simple visual way to detect pixel clusters without the need of further calculation is through the observation of scatter plots of pixel scores. In these 2D plots, two principal components are the axes and each pixel is represented by a dot located according to the related score coordinates. Different scatter plots can be produced using different combination pairs of principal components. In scatter plots, similar pixels cluster together in the displayed PC space. MIA software often allows for the creation of "pixel masks," enclosing pixel clusters in scatter plots that are afterwards located spatially in the original image [41]. These masks can be created by visual inspection of the score plots, enclosing groups of close pixels or be automated with the help of auxiliary chemometric tools [42]. Figure 2.5 shows this procedure on the emulsion example. In this figure, the scatter score plot of PC3 versus PC2 is displayed (each pixel is a dot in this plot, see Figure 2.5A-b). Figure 2.5B shows how the different masks in this scatter plot (drawn by visual inspection and marked in

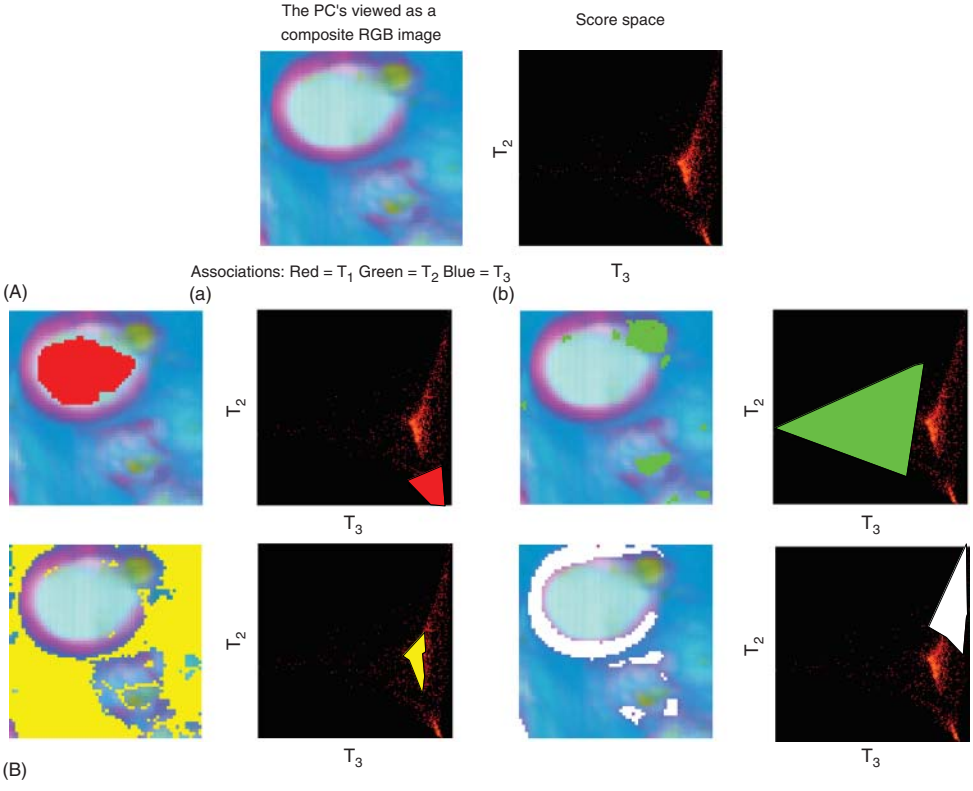

Figure 2.5 (A) a: RGB plot of the score images related to PC1, PC2, and PC3; b: scatter score plot of PC3 versus PC2. (B) Pixel masks in scatter score plot and location of mask pixels in the Raman monolayer emulsion image.

different colors) group pixels with similar score values, which belong to the different image constituents in the sample (drop, additive, interphase, and off-drop phase). The plots at the left of the masked score plots display the pixels masked on the original 2D spatial image representation.

In the approach presented, the shape of the pixel spectra is the driving force to detect structures or similarities among pixels. Recent improvements of MIA software incorporate explicit information on the spatial coordinates of the pixels to help out in the whole interpretation of the image information.

Similar to PCA, other methods exist that represent the image raw data in a space of smaller dimensionality trying to keep all the relevant information. Some of them also rely on a bilinear decomposition and do a projection of the image in a small space according to mathematical criteria, such as statistical independence in ICA [43]. Again, it should be reminded that the straightforward association of independent components (or other components obtained using mathematical criteria) with real compounds is dangerous unless the real spectra of the compounds obey the same mathematical conditions used for the bilinear decomposition [44]. This being said, ICA results may have the same exploratory value as PCA results and, at times, having the complementary image descriptions of diverse data analysis methods, may help to get a clearer picture of the image analyzed.

2.5 Quantitative Image Information: Multivariate Image Regression (MIR)

Although the main value of images is providing information on the chemical composition of the sample and the compound distribution, there are possibilities to use them for quantitative purposes if reference information is available. The methodologies in this field have been often known under the name of multivariate image regression (MIR), although the denomination MIR extends, in a more general way, to the relationship that may be established between an image and any related property to be predicted or also among images [45–50]. MIR includes multivariate calibration methods used in spectroscopic data sets that have been adapted to the work with images [5, 6, 23]. As in other chemical data examples, the most commonly used algorithm is partial least squares (PLS) [51]. PLS works building an inverse calibration model, $\mathbf{Y} = \mathbf{XB}$ between a matrix of spectra ($\mathbf{X}$) and a matrix with the properties to be predicted ($\mathbf{Y}$), that is, concentration values in quantitative analysis, or any other kind of properties, for example, sensory properties in food samples. Instead of working with the original variables in matrices $\mathbf{X}$ and $\mathbf{Y}$, PLS encloses the information of these original variables in a small number of latent variables calculated so that they capture the maximum covariance between $\mathbf{X}$ and $\mathbf{Y}$. The same cautions used in building a PLS model for classical spectroscopic data, for example, selection of number of latent variables and internal and external validation, should be taken into account when the method is used with image data sets [5, 6, 23].

The main difference between using calibration methods for classical spectroscopic data sets and images is that, in the first case, there is a reference concentration (or property) value per spectrum, whereas for images, the single concentration value relates to thousands of pixel spectra. In addition, the reference concentration value refers to the bulk sample and, within an image, there may be pixel-to-pixel variations of concentration for a particular compound. Therefore, strategies should be found that keep the validity of the relationship between the bulk concentration value and the spectral information in the image. It should be also taken into account that, because of instrumental reasons, the relationship between the spectrum intensity and the concentration may vary from pixel to pixel. Some works recommend specific kinds of image preprocessing to account for these nonchemical differences [52].

The ideal situation to use calibration methods in images would be having reference concentration information for each pixel. In this instance, each individual pixel spectrum could be used to build the calibration model. This is, however, very uncommon. The usual situation is having one sample bulk concentration value per image, and this is the scenario that will be considered from now on. In this context, the specificities linked to the use of multivariate calibration in image data sets are linked to the strategy used to build the calibration model and to the information obtained in the prediction step.

For the establishment of the calibration model, the available information is a set of calibration images and its related concentration values. Due to the pixel-to-pixel heterogeneity, a model built selecting a pixel spectrum per image would be neither representative nor reliable. A good approach to seek for representativeness is proposed by Geladi [21] and consists of taking the median spectrum obtained from a ROI in the image as the representative spectrum of the image. The ROI should be large and contains many pixels to provide a median spectrum that is representative of the bulk concentration of the sample. The median spectrum is not a real measured spectrum and is constructed taking the median value of all spectral readings at each of the spectral channels measured. Median instead of mean spectra is preferred to avoid the influence of extreme spectral readings (from anomalous pixels or spectral channels) in the spectrum used to build the calibration model. Median spectra obtained from replicate images taken from the same sample can be used to be related to the same concentration value (see Figure 2.6 for the scheme followed in the establishment of the calibration model).

Once the calibration model is obtained, the validation is performed by applying the calibration model (the **B** matrix) to median spectra obtained from a set of validation images, for which the reference concentration value is known. As in any other calibration procedure, the predictions obtained can be used to evaluate the accuracy and the precision of the bulk concentration estimates by examining the bias and the root mean square error in prediction (RMSEP).

$$\text{Bias} = \sum_i (y_i \widehat{y}) \text{RMSEP} = \sqrt{\frac{\sum_i (c_i - \widehat{c}_i)^2}{\text{ns}}}$$

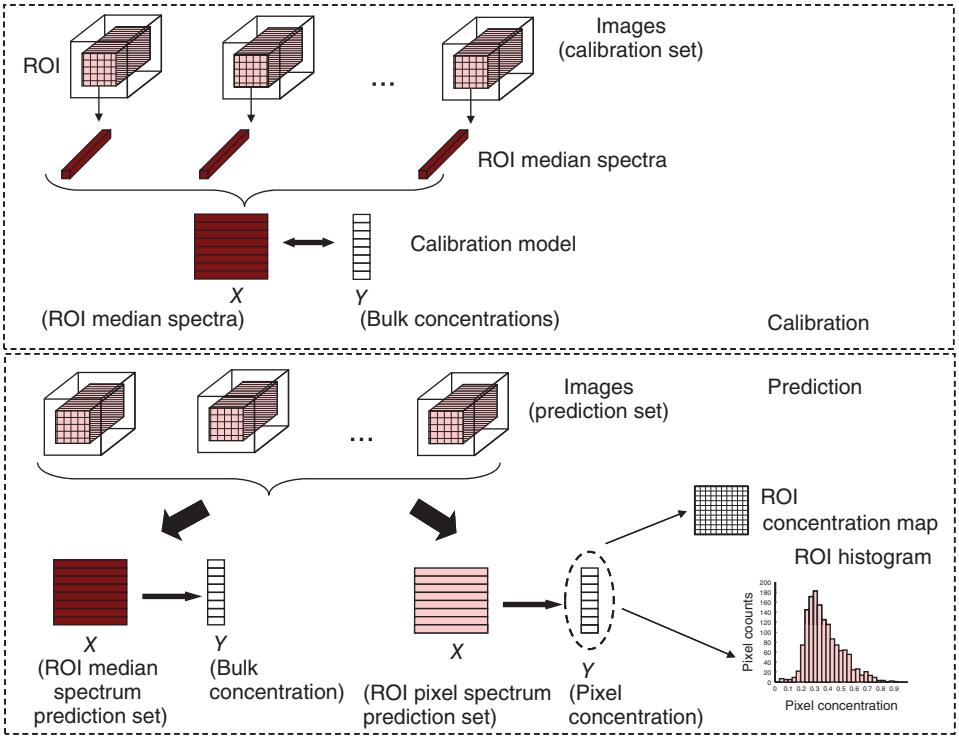

Figure 2.6 Strategies of calibration and prediction in multivariate image regression.

where y_i is the real reference concentration value for the ith sample, $\hat{y}_i$ is the predicted concentration by the calibration model, and ns is the number of samples. Once the model is validated, it can be used to predict bulk concentration values in unknown images.

So far, what has been presented does not differ much from the calibration models obtained with classical spectroscopic data sets. However, the information obtained increases considerably if we take into account the real nature of the image and we use all the available information, that is, all the ROI pixel spectra, in the prediction step. When this is done, we obtain as many predicted concentration values as pixels in the image. The pixel concentration values obtained can be used in a straightforward way to display a distribution map of real concentrations, keeping the original spatial structure of the image (see Figure 2.6). This allows obtaining concentration information in a local context and shows also the homogeneity of compound distribution along the scanned image.

For statistical purposes, a histogram representation may be preferred, where the x-axis shows the concentration predicted values and the y-axis shows the pixel counts [21]. This histogram may provide information on the characteristics of the sample and on the quality of the calibration model. As for sample characteristics, the homogeneity of compound distribution is represented by the width of

the distribution obtained (the narrower, the more homogeneous the sample) and the presence of outlying pixels can be detected at the most extreme values of the histogram. The quality of the calibration model can be assessed in different ways, e.g., a shift between the central value of the histogram and the reference concentration value of the calibration sample can detect the presence of a bias because of a bad selection of the number of components to be included in the model, to the use of insufficiently representative image ROIs, or to other reasons. The width of the histogram is also an indicative of the precision of the calibration model. Although the heterogeneity of the scanned sample will always be the main factor to define the width of the histogram, it can be interesting to see whether the application of data pretreatments oriented to reduce instrumental variations of the measurements can also result in a decrease in histogram width. Recently, statistical diagnostics have been proposed that look for the right balance between the histogram width and the shift between the center of the histogram and the reference concentration values to select the right number of components in the calibration model.

It is relevant to stress that calibration using hyperspectral images can provide results comparable to those given by spectrometer data when median spectra are used to predict bulk sample concentrations [53]. Moreover, when all pixel spectra are included in the prediction step, images provide much more detailed information about the complexity of the sample, showing aspects related to purity and heterogeneity that would never be known from a single spectroscopic measurement per sample. These are crucial aspects in pharmaceutical formulations, where heterogeneity is assessed from a constitutional and distributional point of view [54, 55]. IR is often used at local pixel level in product control to detect distribution of compounds in food products, for example, fat and moisture ([53, 56, 57]). Although PLS-based MIR is the basic tool to obtain quantitative information related to images, other regression algorithms based on nonlinear models have been used when the relationships to be established may be more complex (e.g., sensometric/physical properties or minor constituents to be predicted with images) [58]. It is also worth mentioning that methods belonging to other data analysis families, such as resolution methods, can also provide quantitative information (see Section 2.7.5.2)

2.6 Image Segmentation

One of the goals of image analysis is finding groups of similar pixels in an image, that is, pixels with similar spectra and, therefore, similar composition and chemical or biological properties [4]. This operation is denominated image segmentation and can be used for different purposes, for example, to separate zones in biomedical samples that may be later assigned to certain pathologies [59], to detect defects in food products and automatically sort them in a production line [60] or, simply, to get an insight into the variation of chemical composition along the surface

scanned [61]. There are many tools aimed at performing image segmentation. The main differences among them are linked to the *a priori* knowledge used in the segmentation process (unsupervised and supervised methods) and to the definition of class membership for a particular pixel (hard and fuzzy segmentation schemes).

Although the aim of image segmentation is easily defined as finding groups of pixels with similar spectra, segmentation methods can work with other kinds of starting information that also reflect the characteristics of the original pixels. Given the large size of image data sets, using compressed representations of pixel spectra significantly decreases the computation time required for the segmentation task. As mentioned in earlier sections, these compressed representations of pixel information can be based on feature selection, for example, using only some spectral channels or significant coefficients of transformed data, such as wavelet coefficients. However, many times it is preferred to start with data reductions that use all the relevant information in the original data set, such as PCA [62], ICA [63] scores, or analogous compressed representations coming from resolution methods [19].

Originally, the chemometric tools for image segmentation were conceived to analyze classical spectroscopic data and, therefore, they compare the spectral shape of the different pixels, as if they were completely independent from each other (as it happens when spectra come from different samples). Recently, some of these methodologies have been adapted to incorporate the spatial information linked to pixel neighborhood, and this has resulted in a better clustering performance for image data sets [34, 64].

2.6.1 Unsupervised and Supervised Segmentation Methods

These two families of methodologies can be distinguished according to the previous knowledge about the pixel classes used in the segmentation process. Unsupervised methods do not rely on any *a priori* knowledge and take the whole unknown image to look for the presence and spatial location of pixel clusters or classes, whereas supervised methods use previous knowledge on the pixel classes that need to be defined, that is, class models are generated with well-identified pixels and these models are afterwards applied for class assignment of unknown pixels [5, 6, 65, 66].

Unsupervised methods assign pixels to the same cluster when their spectra (or other pixel-related information) are similar enough. Pixel similarity can be assessed with many different parameters depending on the algorithm at hand. As has been seen in the exploratory image analysis section, PCA is a good unsupervised segmentation method when we use the information in the scores' scatter plot for this purpose (see Figure 2.5). In this case, the clusters are defined from visual inspection of the scatter plots, creating masks that enclose pixels that group together in the PC space [1, 41]. A good point in the use of PCA for clustering is that the complementary information in the loading plots allows for an easy detection of spectral features linked to the different groups detected.

Other classical unsupervised cluster analysis methods rely on using mathematical indicators, such as distances, to quantify the similarity among pixel spectra. Thus, each pixel can be viewed as a point in the space of original wavenumbers or on other spaces, for example, PC space. The coordinates of a pixel can be the spectral readings at the different wavenumbers (in the original image space) or the scores (in the PC space). Similar pixels should be close in the reference space and, therefore, distance measurements, such as Euclidean distance ($\wp$), can be used to assess this proximity.

$$\wp(x_i, x_j) = \sqrt{\sum_{l=1}^{d} (x_{il}, x_{jl})^2}$$

where x_i and x_j are the spectra of two pixels and d is the total number of variables (wavenumbers, scores or else) defining the pixel coordinates. Distances with other mathematical definitions can be used for the same purpose. Distances can be calculated among pairs of pixels or between a pixel and the centroid (central point) of a cluster or between cluster centroids depending on the clustering criterion of the method used [4, 65, 66]. The main distinction in *modus operandi* among unsupervised clustering methods based on distance measures is between agglomerative methods, which work providing nested tree structures showing all possible clustering schemes from individual pixel groups until a single complete image group, and partition methods, which optimize a single clustering scheme with a predetermined number of clusters. There are methods using other concepts, such as density-based functions, which are not described in this section but the details can be found in the literature [1, 67, 68].

In unsupervised image segmentation, agglomerative clustering methods tend to be less used because the computationally intensive task linked to the size of an image data set and the massive tree-structured output obtained [69–71]. Sometimes, modifications of these algorithms focusing on relevant tree sections are used instead [72]. Partition methods are preferred because they work optimizing a single clustering scheme with a preselected number of clusters [65, 66] and, therefore, the computation time is drastically decreased and the interpretability is straightforward. Partition methods start generally with an initial set of centroid pixels, and the rest of pixels assemble around the closest centroid. Iterative cycles are carried out modifying the centroids every time to reach a major degree of compactness in the clusters or to improve a different optimization criterion, for example, minimizing the within-cluster variance and maximizing the between cluster variance.

Partition methods are fast and flexible because they do not nest clusters, that is, clustering schemes with five and six groups can be completely different. However, the selection of the number of clusters is not easy and, often, different results can be obtained depending on the starting point (centroids) of the clustering process. A good selection of the centroids is crucial to ensure good results and stable clustering schemes. Nowadays, K-means is among the preferred partition clustering methodologies. This iterative method starts with a set of preselected centroids and

groups all the pixels around the closest one; after this step, the centroids are recalculated and the clustering process is repeated until convergence is achieved [73].

Figure 2.7 shows the results of a partition clustering method on a kidney calculus image by k-means method. On the left, segmentation schemes obtained by

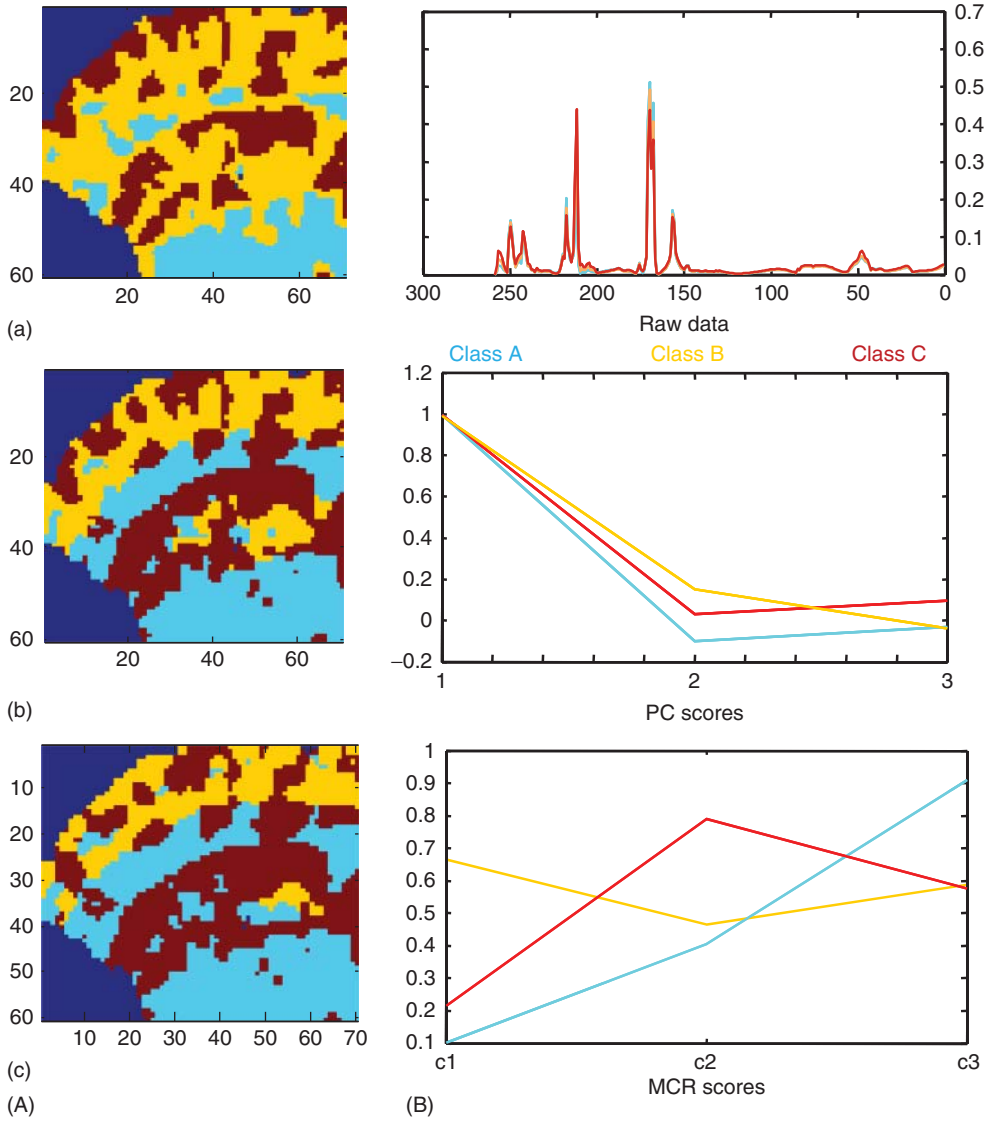

Figure 2.7 Results of image segmentation by k-means method (hard clustering approach) for a Raman kidney calculus. (A) segmentation schemes; (B) class centroids. Results obtained using (a) raw pixel spectra, (b) PCA scores, and (c) MCR scores. (Reprinted from Ref. [19]. Elsevier.)

using different kinds of pixel information, that is, raw spectra (Figure 2.7a), PCA scores (Figure 2.7b), and MCR scores (Figure 2.7c) [19]. Using compressed representations of the pixel information, similar segmentation schemes are obtained. Calculating the centroid information (spectrum, PC or MCR scores), information on the structural nature of the clusters is obtained [19].

Supervised segmentation methods work defining the different pixel classes beforehand with a series of well-identified pixels. Each different class is described by a model and these models are used to assign unknown pixels to the predefined classes. Reference pixels in and out of the classes can be selected by applying class membership masks in the image score scatter plots [74, 75], for instance, or by using results from unsupervised segmentation methods.

Self-interactive modeling of class analogy (SIMCA) [76–78] and partial least squares discriminant analysis (PLS-DA) [79–81] are among the linear algorithms most used of this family. SIMCA is a PCA-based method that works for one class problems and detects whether pixels are in or out of the selected class. A first step is carried out defining the PCA space and boundaries associated with a certain class, for example, some kind of weed in a cultivar, and then, new pixels are projected onto the model to detect whether they can be associated with the modeled class (weed pixels in this case) or not [82]. Although SIMCA is a single class method, as many SIMCA models as classes can be built for multiclass problems. PLS-DA is a method that works building PLS classification models by relating reference pixel spectra (**X**) with class membership information (**Y**). The class membership information is coded in a binary way, assigning a value of "1" to a pixel in the class and a value of "0" to a pixel out of the class. Once the discrimination model is built, it can be used to predict class membership values for unknown pixels. Since the **Y** predicted values for unknown pixels will hardly ever be one or zero, threshold values between 0 and 1 are established that mark the membership of a pixel to a class. If the predicted class membership value is above the threshold, the pixel is in the class; if below, it is out of the class [81, 83]. PLS-DA can be used to model a single class at a time or to deal with multiclass problems with a single PLS2-DA model.

Supervised methods are very often integrated in the software of hyperspectral acquisition systems, and once the classification model is built for a particular problem, this model acts automatically in new acquired images and allows for *in situ* analysis (e.g., in portable imaging devices to distinguish acceptable fruits or not [84]) or for online control for pushbroom imaging systems (e.g., in sorting production lines for food or other materials [60, 85]).

So far, most of the unsupervised and supervised algorithms mentioned are based on linear methods, which are the most generally used in segmentation problems. However, other works have been reported addressing more complex segmentation problems in remote sensing or biomedical areas that require the use of segmentation approaches based on nonlinear methodologies, such as support vector machines, artificial neural networks, and others [72, 86].

Although supervised and unsupervised methods have been well-separated families, there have appeared hybrid approaches combining both unsupervised and

supervised classifiers for image segmentation purposes and, often, the information from unsupervised methodologies is the first step in supervised segmentation approaches [87].

2.6.2 Hard and Fuzzy Segmentation Approaches

This distinction refers to the concept of class membership used in the segmentation method. In hard clustering methods, a pixel belongs to a single class, whereas in fuzzy clustering schemes, a pixel can have different probabilities to belong to several classes, that is, it has a fractional degree of membership for all clusters [4, 88, 89]. In hard clustering schemes, clusters are perfectly separated, whereas in fuzzy clustering, cluster overlap is allowed. The fractional degree of membership of the pixel to a cluster will be inversely related to the distance that separates the pixel from that particular cluster (higher degree if the pixel is closer and lower degree if it is further away).

Several factors can be considered to decide which segmentation modality is more suitable. On the one hand, hard clustering schemes provide a clear definition of the image groups, which may be more desirable when a clear segmentation scheme is needed, for example, when defining whether a food product keeps some quality requirements or not [85]. However, in images where interfacing zones among classes may exist, for example, in remote sensing images, where interfacing zones among land sectors are present [90], or when a crisp definition of classes is not possible, for example, when classes refer to different evolving disease states in a biological tissue [91], a fuzzy segmentation approach may be more appropriate to describe the real nature of the image. The more relaxed definition of class membership of fuzzy schemes accounts for these situations.

There are many unsupervised fuzzy segmentation algorithms, which define the fuzziness and degree of class membership in different ways. However, the fuzzy C-means (which could be described as the fuzzy version of K-means) is likely the most used in image segmentation [92]. Commonly used supervised segmentation methods, such as SIMCA or PLS-DA, allow also for fractional class membership assignment. Although modeling of classes and prediction of unknown pixels happen always in the same way, the class membership assignment is done *a posteriori*. Thus, in a multiclass context, an unknown pixel can be predicted as belonging to more than one class. In this case, two options are possible: (a) the pixel is assigned to the class for which the assignment is more likely, for example, predicted value closer to 1 in PLS-DA. Doing it this way, a hard segmentation scheme is finally achieved, or (b) the pixel is assigned to several classes, modifying the degree of membership according to the likelihood to belong to each particular class, for example, looking at the closeness to 1 in PLS-DA for the predicted values in the different classes. This second approach will provide a fuzzy segmentation scheme for the same kind of problem.

As in the earlier section, there are many works in which hard and fuzzy segmentation schemes are provided for a common problem since both furnish complementary information [92–95].

2.6.3 Including Spatial Information in Image Segmentation

Originally, chemometric tools for image segmentation were conceived to analyze classical spectroscopic data, where each spectrum belonged to a particular sample and it was completely independent from the rest. Pixel spectra in an image do not fulfill this condition because there is an evident correlation among the spectral shape of neighboring pixels in most of the images. Therefore, adapting segmentation tools to image specificities must necessarily go in the direction of including and actively using the spatial information contained in this kind of measurements [4, 64].

Using this information will be much more valuable in situations where the sample surface analyzed is strongly spatially structured. Two areas in which this is clearly the case are remote sensing images and biological images. In these scenarios, land sections or biological elements are very well defined spatially, and it is not meaningful obtaining classes with scattered pixels in the space. As a consequence, favoring classes that are spatially compact and hindering the inclusion of far pixels in a class is part of the problem-oriented algorithm adaptation. However, one should not ignore that there are also images in which these spatial constraints should not be applied, for example, pharmaceutical formulations, in which homogeneous powder mixtures may (should) have pixels with similar composition throughout the sample.

There are many recent efforts oriented to incorporate the spatial information linked to pixel neighborhood in image segmentation approaches, and this can be done as a pre-, in-, or postprocessing step in the used algorithm [34, 64, 96].

A straightforward way to take into account the pixel neighborhood concept is incorporating the spatial distance among pixels as an additional criterion in the clustering schemes. Thus, similarity measures based on spectral distances, such as $\wp$, can be weighted incorporating pixel neighboring information, for example, Euclidean distance can be redefined as

$$\widetilde{\wp}(x_i, \varpi_j) = \wp(x_i, \varpi_j) \cdot w(x_i, \partial_i, \varpi_j)$$

or

$$\widetilde{\wp}(x_i, \varpi_j) = \wp(x_i, \varpi_j) + w(x_i, \partial_i, \varpi_j)$$

where the term $w(x_i, \partial_i, \varpi_j)$ is the weight accounting for the neighborhood information between a pixel and a cluster, which can be defined in different ways. ∂_i is the symbol of the term that accounts for the neighborhood concept. When the pixel is close to a group, the weight term becomes small and so the considered

distance for clustering, $\widetilde{\wp}(x_i, \varpi_j)$. This strategy favors the incorporation of neighboring pixels into a group in the detriment of distant pixels, with larger weight terms [64].

Other ways to incorporate the spatial information in an image imply designing hybrid segmentation methodologies that combine classical segmentation algorithms for spectroscopic data, devoted only to compare pixel spectral information, with methodologies coming from the classical image analysis field, in which due to the lack of spectral information in gray or red–green–blue (RGB) images, the spatial information was the driving force [97].

The incorporation of information also has specificities according to the application areas. In remote sensing analysis, watershed algorithms [86], methods including topological information [98], and GIS-related functions [99] are options to enclose the spatial information, whereas other approaches based on preserving the edge of clusters are used in biomedical areas [100].

There are many general benefits derived from including the spatial information in the segmentation approaches. First, distant outlying pixels are not incorporated in clusters, the noise effect is minimized, and the general clustering scheme is smoothened. Another relevant improvement concerns the differentiation of spatially distant clusters that may be defined by similar spectral features. Adding spatial information, distances between far pixels are enhanced and cluster merging is hindered. Inclusion of spatial information has been found also useful in supervised segmentation methods, which do not use the concept of distance. The ways of incorporating spatial information are very algorithm dependent and application area dependent, but this option is a clear asset to improve the general performance of image segmentation methods [34, 101].

2.7 Image Resolution

2.7.1 The Image Resolution Concept

The resolution of hyperspectral images is focused on recovering the component-based underlying spectroscopic model out of the raw recorded image. Thus, the goal is extracting the spatial (distribution map) and chemical (pure spectrum) information about each particular image constituent out of the sole information in the raw measurement [102–104]. In this chapter, the denomination resolution analysis is adopted because it is the general name for chemometric methods, providing a chemically meaningful (Beer–Lambert-like) bilinear model out of a raw mixed data set. These methods were applied since long in many different areas (process analysis, analytical and environmental data tables, etc.) before being introduced in hyperspectral image analysis [105, 106]. However, in the context of image analysis, it is relevant to say that the resolution concept is also defined

by other terms, such as linear unmixing or endmember analysis, which are more common expressions in remote sensing and some biomedical areas [107, 108].

The common goal to all resolution algorithms is decomposing the original raw image into the Beer–Lambert bilinear model, $\mathbf{D} = \mathbf{C}\mathbf{S}^{\mathbf{T}} + \mathbf{E}$, where $\mathbf{D}$ is the raw image, $\mathbf{S}^{\mathbf{T}}$ is the matrix of pure spectra, and $\mathbf{C}$ are the stretched concentration profiles. To do so, as shown in the introductory part of this chapter (see Figure 2.1), the original 2D or 3D image should be unfolded into a data table with the spectra of all pixels one under the other. The spatial structure of the image is recovered after the resolution process by folding back the stretched concentration profiles into the higher dimensional spatial ordering.

Nowadays, resolution can be applied to a single image or to a multiset structure formed by several images. Image multisets may contain a set of images related to each other and collected with the same platform, for example, a multilayer image coming from a single sample or a series of images collected monitoring a process, or may be formed by images acquired on the same sample using different spectroscopic platforms. Working with multiset structures, the bilinear model is kept and the final results have less uncertainty.

The following sections will address relevant aspects associated with the resolution of images, introducing the tools and related information that we can gather before, during, and after the resolution process.

2.7.2 Spatial and Spectral Exploration

Resolution methods do not need *a priori* knowledge to perform the bilinear decomposition of the image but, when such information is available, it can be included to obtain more accurate and chemically meaningful results. Exploring an image implies paying attention to the spectral and spatial aspects of the measurement, and if this task is oriented to a later resolution of the image, it is not surprising that the methods presented in this section seek to find the most unmixed information in the hyperspectral measurement. Therefore, exploratory analysis acting on the spectral direction will be mainly oriented to find the "purest" (most dissimilar) pixel spectra in the measured image, whereas methods more devoted to screen the spatial dimension will look for the complexity (compound overlap) of the different pixel areas trying to find out selective zones, if existing, or zones with low compound overlap.

A big family of resolution-oriented exploratory methods is focused on finding the purest variables in a data set. In an image context, this means finding either purest spectral channels or purest pixels in the raw hyperspectral image [29, 109]. The rows related to purest pixels will give good approximations of the pure spectra of the constituents in an image, whereas the columns linked to purest spectral channels will allow building approximate distribution maps.

There are many algorithms that work using different mathematical criteria to look for the most dissimilar variables in a data set [110]. As an example, SIMPLISMA is one of the pioneering methodologies used for this purpose and, as

stated before, can find either the purest pixels or the purest spectral channels in an image [27]. To find the purest pixels, a purity index, p_i, is calculated per each pixel spectrum as

$$p_i = \frac{s_i}{m_i + f_i}$$

where s_i is the standard deviation of the elements in the pixel spectrum, m_i is the mean, and f_i is an offset factor that accounts for the noise percentage in the data. The inclusion of this noise offset prevents the selection of background or noise pixels. The first spectrum selected is the one with highest purity. Then, the rest of the spectra are normalized and a purity index is recalculated for each of them, as $p'_i = w_i p_i$, where w_i is a weighting factor that takes into consideration the dissimilarity of the pixel under analysis with the purest pixel previously selected (the more dissimilar the spectrum, the larger the weight). The second pixel selected will be the one with largest recalculated purity, p'_i. The sequence of purity recalculation (according to new weights based on the dissimilarity with all previously selected pixels) and new pixel selection will continue until a number of pixel spectra equal to the number of image constituents has been obtained. No previous knowledge on the number of image constituents is needed since the process can be stopped when the last purest spectrum selected is very similar in shape to a previously selected spectrum. Working in the pixel direction, the purest spectra of the image are obtained [28, 29]. Likewise, the selection could be done to find the purest spectral channels and, as a consequence, the purest distribution maps could be derived.

Figure 2.8 shows an example of SIMPLISMA applied in the pixel and in the spectral direction to an emulsion image with four compounds (a drop, an interphase, an additive, and an off-drop constituent). In Figure 2.8, a–d are the purest pixels selected in the image and provide the plotted spectra on the right. Labels 1–4 are the purest spectral channels that, once refolded, give the distribution maps at the bottom of the figure.

The pixels selected (a–d) are located in zones associated with the four constituents described and, therefore, their spectra will be very close, when not identical, to the real pure spectra sought. However, spectral channels 1–3 produce reasonable distribution maps for the drop, interphase, and additive constituents, and channel 4 fails in giving a good map for the off-drop phase. Channel 4, although being the most representative for the off-drop phase, has signal contributions from the rest of components and, therefore, produces an unacceptable map for this component.

The results obtained with SIMPLISMA in this example illustrate a relevant fact that should be considered when applying any method based on purest variable selection on images. Purest spectra or maps obtained with these exploratory methods give a very good first insight into the characteristics of the compounds in the image analyzed, but cannot be generally associated with spectra and maps of pure constituents in the sample because the presence of selective pixels or spectral channels in the measurement for each particular constituent cannot be

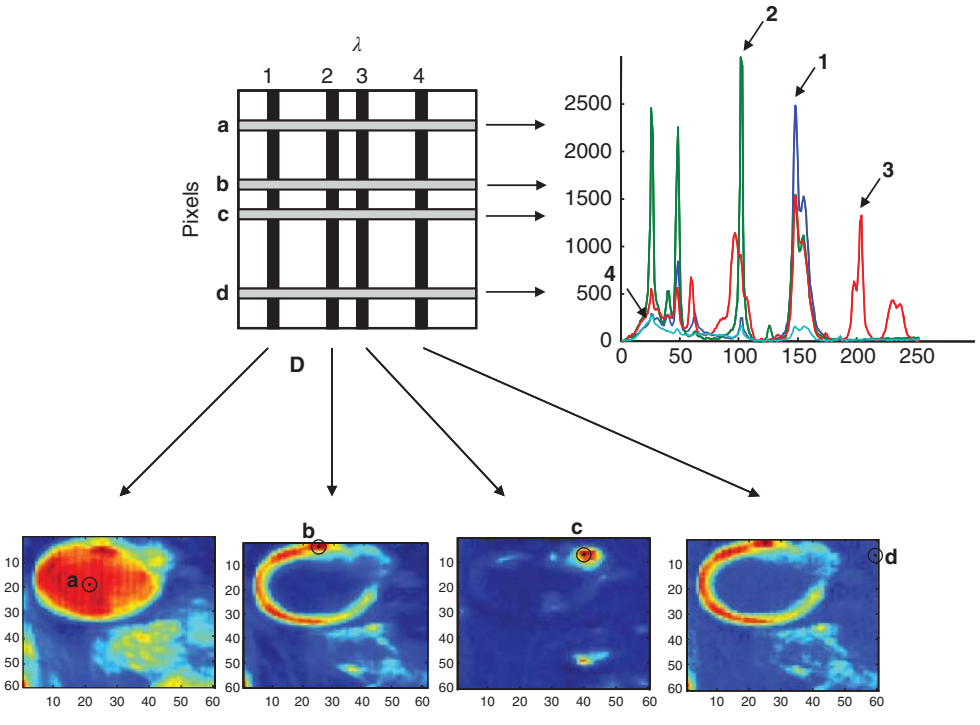

Figure 2.8 SIMPLISMA analysis on Raman emulsion image. Representation of the spectra of the purest pixels (right plot) and the distribution map related to the purest spectral channels (bottom plot). Letters and numbers in both plots mark the location of purest pixels and purest spectral channels, respectively,

ensured. However, these sets of purest profiles (specially, spectra) are an excellent initial guess in resolution methods that work performing an iterative search of the true $\mathbf{C}$ and $\mathbf{S}^{\mathbf{T}}$ profiles.

Linked to the importance of the presence of selective pixels or spectral channels, exploring the variation of the degree of compound overlap along the surface/volume scanned, is another possibility to obtain information for future resolution purposes. As we have seen in earlier section, PCA on the whole image provides information on the total number of constituents of the data set. This information comes from a global image analysis and does not mean that all constituents are present in all pixels. To result in local information, PCA analyses are performed on small areas of the data set (a pixel and its surrounding neighbors in the two or three spatial dimensions) until all the image is PCA scanned.

Fixed-size image window-evolving factor analysis (FSIW-EFA) is an evolution of the local rank algorithm fixed size moving window-EFA [111], particularly designed for the study of the local pixel complexity in images [112]. To do so, two main ideas are taken into account: the need to divide the image into small areas to get local information and the need to preserve the 2D or 3D spatial

image structure, by analyzing contiguous small areas, taking one pixel plus all its surrounding neighbors.

FSIW-EFA performs local PCA in the whole image by moving small windows around each individual pixel area until the entire image has been scanned. Displaying the obtained singular value plots and setting a threshold to separate significant singular values from noise, local rank maps can be derived that represent the degree of compound overlap in each pixel area (see Figure 2.9).

FSIW-EFA works with image windows formed by a particular pixel and all its neighbors in the two or three spatial dimensions of the image (see Figure 2.9a). The number of pixels in the window should be the smallest possible to preserve the spatial resolution of the image, but should equal or exceed the total number of compounds in the image to allow for rank values, representing all possible situations of compound overlap in the image. The singular values obtained in these local analyses are displayed together in singular value plots where the spatial structure of the image is preserved (see Figure 2.9b). In these plots, large values represent significant contributions to the signal related to the presence of chemical constituents, whereas small values describe the experimental noise.

Local rank maps are derived from the singular value plots by displaying the number of significant singular values in each pixel area. A threshold value or a threshold band is set to mark the limit between significant and noise-related singular values (see original reference for more details about threshold selection [112]). Depending on the threshold selection and on the information sought, we can distinguish between complete local rank maps (in Figure 2.9c) and partial local rank maps (in Figure 2.9d). Complete local rank maps display how many singular values are above a preset threshold value for each pixel in the image, that is, they show how many compounds overlap in each pixel. Complete local rank maps give a good indication on which zones of the image have a lower or higher composition complexity. As expected for the emulsion example, zones with higher local rank values appear in interphase zones of the drop and in other potential zones of compound overlap.

Partial local rank maps are constructed using a threshold band to separate significant from nonsignificant singular values. The use of a threshold band, as wide as needed, is meant to account for the threshold dependency on the estimation of the pixel local rank. For some pixels, the local rank will stay invariant in the highest and lowest boundaries of the threshold band, whereas for some others, different rank values will be obtained when the lowest or the highest boundary of the threshold band are taken as a reference. Pixels that preserve an invariant rank along the threshold band offer robust local rank information, whereas pixels that do not, have less reliable local rank estimates. Partial local rank maps only display the pixels with a "robust" local rank estimation. Although this representation has some "void" pixels, it is the adequate representation to ensure the reliable detection of selective pixels or pixels with low complexity for resolution purposes.

As with its parent algorithm, the local character of the PCA analyses performed by FSIW-EFA is particularly suitable in the detection of minor compounds in the image (impurities) that could pass unnoticed in a global PCA analysis. This aspect

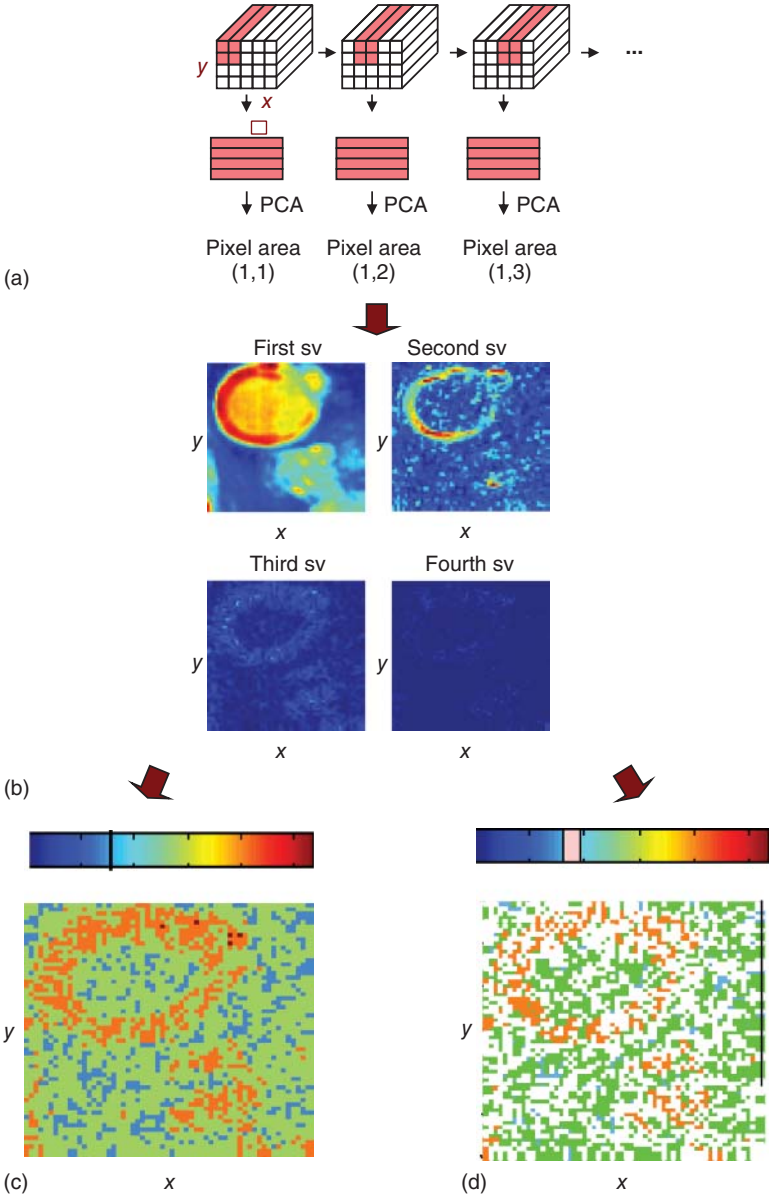

Figure 2.9 FSIW-EFA *modus operandi* (monolayer Raman emulsion image). (a) Construction of pixel windows; (b) singular value plots of local PCA analyses; (c) complete local rank map and (d) partial local rank map.

has been particularly useful for the analysis of impurities in images of pharmaceutical formulations. For this kind of samples, FSIW-EFA also provided relevant information on the pill heterogeneity [102].

FSIW-EFA can also be used in multilayer images, taking into account the 3D neighborhood of the voxels to build the small windows to be PCA scanned [112]. In this context, a number of local rank maps equal to the number of layers in the image are obtained. It is important to note that the information in the local rank map of a particular layer has been obtained taking into consideration the pixels of that layer and those in the neighboring layers in the depth direction.

Both the results of purest variable selection methods and of FSIW-EFA can be used as the starting information to do resolution-oriented image compression. When resolution is the main goal, the information to be kept should be representative and as unmixed as possible. The perfect and maximum compression would consist of taking a selective spectral channel or a selective pixel per image constituent. This would be the smallest amount of representative information needed to resolve the image. This ideal situation is hardly ever found in practice, but approximations based on this idea can be proposed. Thus, compression in the spectral direction can be performed taking the spectral channels selected with pure variable approaches and small bands around them. These channels are selective or, if not, they are the purest ones in the image and contain the best available information per each image constituent. Likewise, the purest selection could be carried out in the pixel direction, keeping the purest pixels and their closest neighbors in two or three spatial directions. Another option to select the simplest pixels would be based on the local rank information provided by FSIW-EFA. In this case, the pixels with lowest rank could be selected as the compressed subset to perform the resolution analysis as long as the total rank of the selected subset was equal to the rank of the entire image. When the compressed image keeps all relevant information, correct resolution is possible. In this case, only one of the two directions is directly recovered by resolution analysis (the uncompressed one). The profiles related to the compressed mode are recovered with a single nonnegative least squares approach, taking the full image matrix and the resolved complete mode in the bilinear decomposition [35].

2.7.3 The Resolution Process: Initial Estimates and Constraints

Resolution of data sets into their underlying bilinear models can be performed with algorithms based on very diverse backgrounds [113–115]. In the chemometrics field, most noniterative algorithms were conceived for data sets with a sequential evolution of concentration profiles, for example, processes, and relied essentially on this specific mathematical structure of the data set [113]. Image data sets lack this structure because the pixel-to-pixel variation of composition seldom follows a smooth evolution along the whole image and, if existing, would be artificially truncated because the pixel data table does not preserve the spatial structure of the original measurement. This is the reason why the best

algorithms for resolution of images are those whose performance is not affected by the lack of pattern in the concentration direction. Since image resolution cannot benefit from the combination of subspaces with specific mathematical properties, the capability to introduce external chemical information about the properties of spectra and pixel composition during the resolution process becomes relevant.

The use of information (usually coded under the form of constraints) in image resolution is a common trend in iterative resolution algorithms and in many unmixing methods born in the remote sensing field [116]. Explained in a very simplified way, many remote sensing methodologies, such as vertex component analysis (VCA), [117] and iterative constrained endmembers (ICE) [108], perform the unmixing task finding the smallest simplex that can enclose all pixels in the hyperspectral image space subject to the constraints of nonnegativity in concentrations and closure (e.g., sum of all constituents should amount to a constant value). The vertices of the simplex are the endmembers (pure spectra) sought. Instead, iterative resolution algorithms in chemometrics often work optimizing in a constrained least squares sense the matrices $\mathbf{C}$ and/or $\mathbf{S}^{\mathbf{T}}$ from the bilinear model $\mathbf{D} = \mathbf{C}\mathbf{S}^{\mathbf{T}}$, and the constraints used are related to diverse mathematical and chemical properties of the maps or spectra to be recovered. Whenever sufficient selectivity-related information exists, any of the algorithms above can work with similar efficiency [118]. When this is not the case, there may be differences in the final solutions obtained and the quality of the solution will depend on the amount and quality of the information introduced in the data analysis.

Describing all image resolution algorithms would be an enormous task that would certainly exceed the scope of this chapter. The world of remote sensing unmixing methods is vast and has been described elsewhere [92, 116]. Considering the application areas toward which this book is oriented, we prefer to refer the reader to more specialized remote sensing literature for additional information, although we will make some comments when parallel concepts among remote sensing unmixing and resolution methods from the chemometrics area are required.

Within the chemometrics field, there has been significant progress in iterative resolution methods since the last decade and, quite likely, the most widely used algorithm nowadays is multivariate curve resolution-alternating least squares (MCR-ALS) [114, 119–121], which is described in detail in this section. The main assets of this algorithm when applied to hyperspectral image analysis are the possibility to introduce very diverse information (constraints) during the optimization process and the capacity to work with single or multiset image structures.

MCR-ALS is an iterative algorithm that performs the decomposition of the data matrix $\mathbf{D}$ into the bilinear model $\mathbf{D} = \mathbf{C}\mathbf{S}^{\mathbf{T}}$ by means of a constrained alternating least squares optimization of the matrices $\mathbf{C}$ and $\mathbf{S}^{\mathbf{T}}$. The sequence of application of the algorithm involves three main steps:

1) Determination of the number of compounds in the raw image, **D**.
2) Generation of initial estimates (e.g., $\mathbf{S}^{\mathbf{T}}$-type matrix).
3) Constrained alternating least squares optimization of **C** and $\mathbf{S}^{\mathbf{T}}$ until convergence is achieved.

The number of image constituents can be known beforehand or be determined by PCA on the whole image. The alternating optimization should always start using the original measurement, **D**, and an initial guess of either the **C** or the $\mathbf{S}^{\mathbf{T}}$ matrices. Typically, in images, the initial estimate is a matrix $\mathbf{S}^{\mathbf{T}}$, formed by pixel spectra picked up from the image according to previous knowledge (from pixels in areas of interest) or from the result of chemometric tools for purest pixel selection, such as SIMPLISMA [27]. Spectral initial estimates are more common because some of the image constituents (and, consequently, their spectra) may be known or, when this is not the case, it is generally more probable finding selective pixels and, as a consequence, good spectral estimates than selective spectral channels.

The alternating least squares procedure involves the operations $\mathbf{C} = \mathbf{DS}(\mathbf{S}^{\mathbf{T}}\mathbf{S})^{-1}$ and $\mathbf{S}^{\mathbf{T}} = (\mathbf{C}^{\mathbf{T}}\mathbf{C})^{-1}\mathbf{C}^{\mathbf{T}}\mathbf{D}$, respectively. The end of the iterative process is reached when the reproduction of the original image from the product of the resolved concentration profiles and spectra has enough quality, and there is no significant variation among the results of consecutive cycles. The quality in the data reproduction can be estimated through the lack of fit expressed as

$$\text{Lack of fit (\%)} = 100 \times \sqrt{\frac{\sum (d_{ij}^{*} - d_{ij})^{2}}{\sum d_{ij}^{2}}}$$

where d_{ij} is an element on the image data table and d_{ij}^{*} is the reproduced element by the MCR-ALS model. Different criteria can be adopted to mark the end of the optimization process, for example, the comparison between consecutive cycles of the percentage of data fit variation or the dissimilarity of the concentration profiles and spectra recovered. Alternatively, the iterative process can also be stopped when a preselected number of cycles have been reached.

The way to incorporate previous knowledge about the images in MCR-ALS is through the use of constraints. Constraints can be defined as chemical or mathematical properties that the concentration profiles or spectra should fulfill [114, 115, 119]. During the iterative process, the calculated concentration profiles and spectra are modified so that they obey the preselected conditions. The application of constraints is optional and flexible and takes into account the natural characteristics of the data set. Thus, concentration profiles and spectra can obey different constraints, and within the **C** or $\mathbf{S}^{\mathbf{T}}$ matrices, constraints can be applied profile-wise or even element-wise. Constraints play a double role in resolution methods. On the one hand, they ensure the chemical meaning of the recovered distribution maps and spectra and, on the other hand, they greatly decrease the ambiguity in the resolved profiles.

The concept of ambiguity in curve resolution is linked to the fact that a range of $\mathbf{CS}^{\mathbf{T}}$ products can reproduce the original data set with the same optimal fit,

that is, many sets of concentration profiles and spectra can be potentially valid to describe the data. In mathematical notation, we can write the bilinear model as

$$\mathbf{D} = \mathbf{C}\mathbf{S}^{\mathbf{T}}$$

or, in an equivalent form, as

$$\mathbf{D} = \mathbf{C}\mathbf{T}\mathbf{T}^{-1}\mathbf{S}^{\mathbf{T}} = \mathbf{C}'\mathbf{S}^{\mathbf{T}'}$$

where $\mathbf{C}' = \mathbf{C}\mathbf{T}$ and $\mathbf{S}^{\mathbf{T}'} = \mathbf{T}^{-1}\mathbf{S}^{\mathbf{T}}$ and we could have infinite $\mathbf{T}$ matrices (solutions). The way to decrease the range of feasible solutions in the resolution results is by limiting the possible solutions to those that fulfill the preset constraints. Thus, the more the efficient constraints are, the more accurate are the resolution results.

In image analysis, nonnegativity is the most commonly used constraint. Indeed, the contribution to the signal (concentration) of any constituent is always positive and the raw IR or Raman measurement as well. As a consequence, elements in both $\mathbf{C}$ and $\mathbf{S}^{\mathbf{T}}$ profiles are, by nature, positive [28, 117, 102–104, 122, 123].

There is a wide range of literature about constraints in curve resolution methods, but few apply to images, because of the mentioned lack of pattern in the concentration direction of this kind of data sets. Instead, other kinds of information are used. A fairly intuitive possibility is including the knowledge of the identity (and pure spectrum) of certain image constituents. When this is the case, these spectral shapes are fixed in the $\mathbf{S}^{\mathbf{T}}$ matrix during the iterative resolution process. Doing so, the possible combinations for spectral shapes of unknown constituents decrease and the quality of the distribution map recovered for the known component improves [19].

So far, there are not many constraints specifically designed for image resolution. Some attempts have involved the introduction of information coming from cluster analysis in the modeling of the concentration profiles [124] and the use of a smoothing constraint on a local basis for the concentration of each pixel and the immediate neighbors [125]; others include the use of the angle among resolved profiles or contrast enhancement to find the sought solutions [126, 127]. However, particular attention should be paid to the adaptation of the so-called local rank constraints for image analysis [128]. These constraints, which include the well-known condition of selectivity and, in general, set the absence of one or more components in certain pixels (in the $\mathbf{C}$ profiles), have been used since long in resolution and are among the most efficient to help in the accurate definition of concentration profiles and spectra, decreasing or suppressing completely the rotational ambiguity [114, 119].

Long ago, Manne proposed two theorems that clearly stated when the true unique solution ($\mathbf{C}$ and $\mathbf{S}^{\mathbf{T}}$ profiles) of a resolution problem can be recovered based on the natural local rank conditions of the data set [129]. Although these conditions were originally meant for structured processes, they can be easily reformulated for hyperspectral image data analysis as follows:

a) The *distribution map* of a certain constituent can be recovered when its overlapping constituents are present in *pixels where this constituent is absent*.

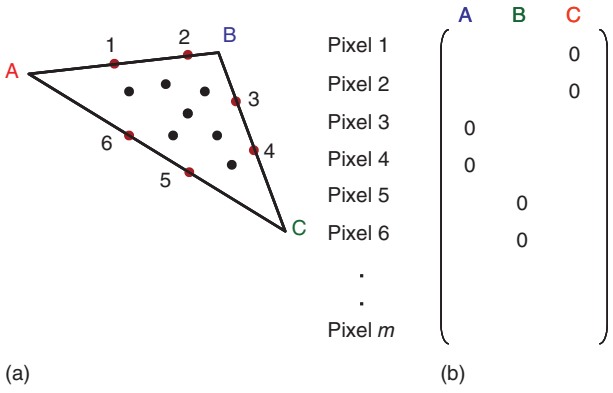

Figure 2.10 Graphical representation of necessary conditions for unique resolution of images. (a) As presence of pixels in the simplex sides in remote sensing unmixing methods, and (b) as the absence of each constituent in some pixels in a matrix setting local rank constraints in resolution methods.

b) The *spectrum* of a constituent can be recovered if *its pixels are not always overlapping with another constituent*.

which comes down to say that correct and unique solutions can be recovered if each image constituent is absent in some pixels. It is interesting to note that this condition is also formulated for linear unmixing methods in remote sensing in a different way (Figure 2.10):

a) To recover the endmembers of an image, there should be, at least, two pixels, in each of the sides of the image simplex (every simplex side lacks, at least, one image constituent).

Note that the condition of absence of all constituents in some pixels is much less strict than requiring selectivity for all compounds in the image, a misstatement often used when referring to the necessary information for image resolution/unmixing methods.

In image analysis, local rank constraints set the absence of certain image constituents in a pixel. The extreme and most useful local rank constraint is selectivity. When a pixel is selective, that is, only a particular image constituent is present, the pure spectrum for this constituent can be straightforwardly derived. Likewise, when a spectral channel is selective, the distribution map of the related component can be directly obtained. Selectivity is introduced by forcing the absent constituents to present null or extremely low concentration values or spectral readings in the selective pixels in $\mathbf{C}$ or in the selective spectral channels in $\mathbf{S}^{\mathbf{T}}$, respectively. Milder local rank constraints can be set when the rank of a pixel is lower than the total by setting only some of the image constituents to be absent.

The introduction of local rank constraints in image analysis requires finding out the number and identity of the missing components in the pixels to be constrained. Therefore, only pixels with a robust rank estimation and clear constituent identification will be constrained.

To set local rank constraints, the local rank information obtained from FSIW-EFA will be combined with reference spectral information [128] (see Figure 2.11). Potential pixels to be constrained will be those in the local rank map because they have a robust estimation of the rank and, therefore, of the number of missing components in the pixel. However, FSIW-EFA information is insufficient to identify the absent components in the constrained pixels. For identification purposes, the local rank information (Figure 2.11a) should be combined with reference spectral information (Figure 2.11b). The ideal reference would be the pure spectra of the constituents but, in most images, not all of them are known. For image components with no pure spectrum available, approximations of their pure spectrum can come from purest variable selection methods or, better, be the result of a simpler MCR-ALS analysis where only nonnegativity constraints have been applied.

Knowing the rank found for a particular pixel in an image, the way to identify the absent components is calculating the correlation coefficient between the raw pixel spectrum and each one of the reference spectra for the different image constituents. The constituents with the lowest correlation coefficient with the pixel spectrum will likely be the constituents missing in the pixel. This procedure is done individually for each of the pixels that can be potentially constrained. To prevent misidentifications, a second check is done that takes into consideration the natural correlation among the reference spectra of the image constituents. Thus, the absence of a particular constituent in a pixel will not be confirmed unless the correlation coefficient between the pixel spectrum and the reference spectrum of that constituent is equal or lower than the highest correlation coefficient that can be found for the reference spectrum of this constituent with the rest of reference spectra. Local rank constraints will be finally encoded into a "mask" matrix, sized as **C** (no. of pixels × no. of components), that will be used to introduce the local rank constraints in the resolution process (in Figure 2.11d). This constraint can be applied keeping null values in the concentration elements of the missing components in the constrained pixels (equality constraint) but, in practice, better results are obtained if these missing components are set to have a concentration value equal or smaller than a very small predefined value.

The consequences of introducing local rank information are a better definition of the distribution maps and pure spectra of the components and a decrease in the ambiguity linked to the resolution results [128].

2.7.4 Image Multiset Analysis

Image multiset analysis deals with data sets that contain several images together. Image multisets can be formed by images collected on one sample (or a set of related samples) using the same spectroscopic platform or on the same sample using different spectroscopic platforms. In some instances, it seems very natural to work with multiset structures, especially when a set of images is collected on the same sample, such as sets of image layers at different sample depths, or in process monitoring (where images can be acquired as a function of time or

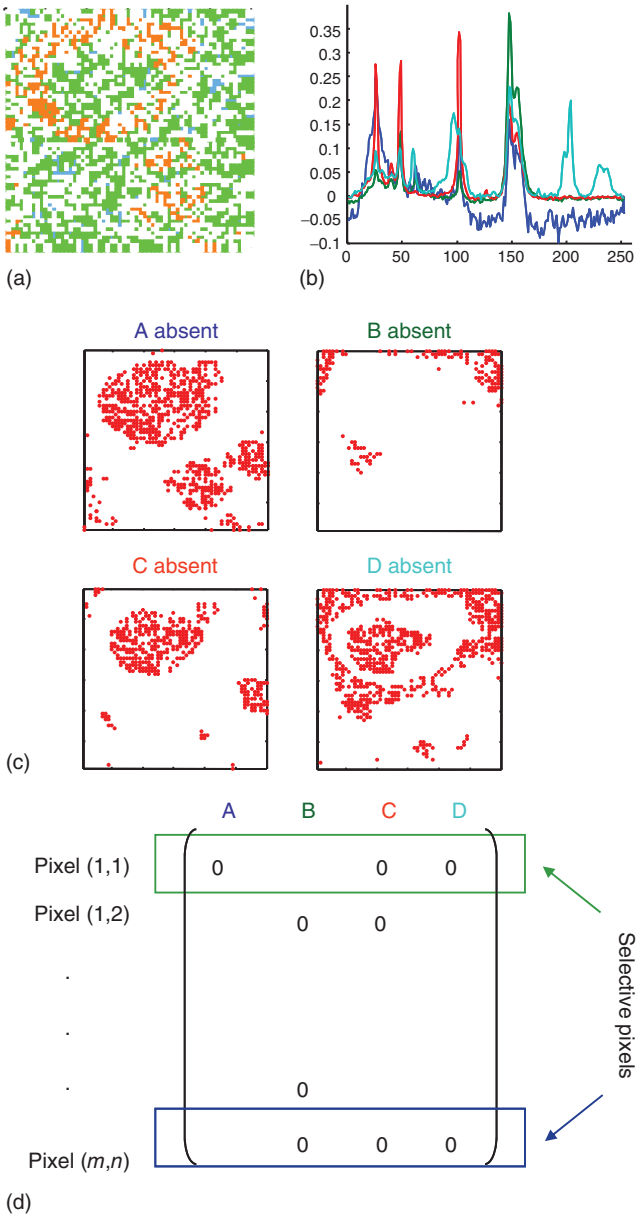

Figure 2.11 Procedure followed to incorporate local rank constraints in resolution (monolayer emulsion example). (a) Partial local rank map; (b) reference spectral information (from SIMPLISMA); (c) pixel masks for absence of constituents in image; and (d) transfer of information in (c) to a local rank information matrix.

temperature) or when the same sample is exposed to different spectroscopic platforms. Working with image multisets also offers advantages in many other scenarios, as long as the images are somehow related or some constituents are present in common [102, 106].

In resolution analysis, image multisets are formed by appending the unfolded matrix representation of the images to give as a result a multiset structure or augmented data matrix (see Figure 2.12). An image multiset can be a column-wise augmented data matrix, formed by images collected with the same platform (i.e., the common mode is the spectral) or a row-wise augmented matrix, built with images collected on the same sample with different platforms (i.e., the common mode is the pixel direction). Since multiset structures are formed by appended data matrices, for column-wise augmentation the images combined do not need to share the same regular set structure, that is, images with different number of pixels and spatial geometry can be combined as long as they have a common spectral mode. Image multisets preserve also the bilinear model shown in the resolution of a single image. Now, the pixel spectra of all images are organized in a data table **D**, where a set (or submatrix) belongs to a particular image. The decomposition $\mathbf{D} = \mathbf{CS}^{\mathbf{T}}$ provides a single matrix $\mathbf{S}^{\mathbf{T}}$ of pure spectra, valid for all the images analyzed, and a matrix **C**, formed by as many submatrices as

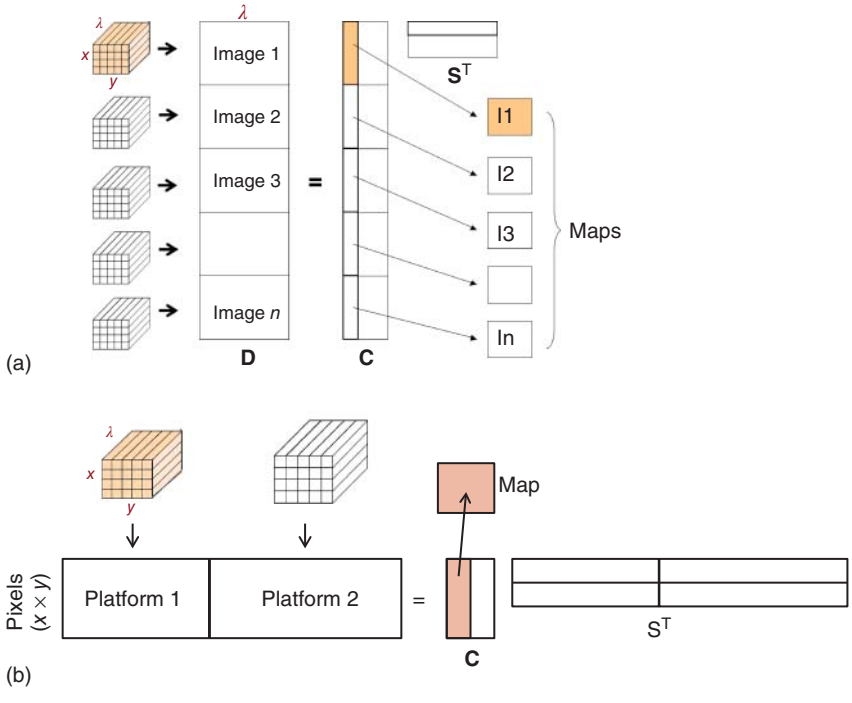

Figure 2.12 Image multisets and related bilinear model. (a) Multiset with common spectral mode (column-wise augmented), and (b) multiset with common pixel mode (row-wise augmented).

images in the data set, if the multiset has the spectral mode in common. The profiles in each of the **C** submatrices can be refolded conveniently to recover the related constituent distribution maps of each image. When the pixel direction is the common mode, a single matrix **C** and a matrix $\mathbf{S}^{\mathbf{T}}$, formed by as many submatrices as spectroscopic platforms used, are obtained.

When multiset structures come from images collected by different spectroscopic platforms, a preprocessing step may be required in which images are spatially matched with each other (i.e., different pixel sizes should be balanced and translation/rotation/scaling transformations should be done if required). Although image spatial matching is a solved problem when images come from the same technique and have a clear structure with common landmarks, that is, in remote sensing, it is less straightforward matching chemical images obtained with different techniques because the signal intensity pattern varies among techniques and morphological sample patterns are less clear. There is ongoing work to solve this multitechnique image matching bottleneck and allow the work with multitechnique image multiset structures.

When images are collected with the same spectroscopic system, building a multiset structure is straightforward and there is a gradual increase in the use of this kind of data sets to solve very varied scenarios. There are some important issues linked to resolution analysis applied to multisets with common spectral mode. First, the fact of obtaining a single $\mathbf{S}^{\mathbf{T}}$ matrix for all images ensures the spectral consistency of the final solution, that is, the fact that the same image constituent has always associated the same pure spectrum in all analyzed images. The other relevant advantage comes from the complementary information in the different images, which always helps to the global improvement of the resolution results [102, 120]. The benefits of image multiset analysis are most pronounced when differences in concentration level of constituents or in compound overlap are encountered among images. In these situations, minor constituents in an image are more easily resolved when analyzed with an image where these compounds are present in a major proportion and, likewise, images with a high compound overlap are better resolved when analyzed with images with less overlapping information.

The *modus operandi* of MCR-ALS for image multiset analysis is essentially identical to the analysis of a single image, with the added value that the concentration submatrices linked to different images can be constrained in different ways if needed. There is a multiset-conceived constraint, denominated correspondence of species, which encodes the presence/absence of certain constituents in the images that form the multiset. This constraint has a close connection with the local rank information mentioned earlier in this section, being the only difference that the information of presence/absence of constituents affects full images instead of a limited set of pixels. The effect of presence/absence of constituents in images in the quality of resolution results is the same as that provided by local rank constraints in single image analysis with the advantage that, often, one can actively participate in the design of a multiset structure, and selective (or simpler) information can be included with images collected particularly with this purpose, helping to resolve the more complex images of interest.

Two examples will illustrate the advantages of multiset analysis in terms of the relevance of spectral consistency (and, therefore, definition of compounds) and on the advantages of using hyperspectral imaging toward classical spectroscopy in the modeling of complex processes (transformations).

The first example is the analysis of a Raman multilayer emulsion image, where the multiset is formed by the images collected on the different layers of the emulsion image. Figure 2.13a shows the resolution results of the individual image analysis of emulsion layers, with the obtained distribution maps, and stresses the large differences among the resolved pure spectra for the top and the bottom layers. Figure 2.13b shows the distribution maps and the single set of pure spectra obtained by multiset analysis of all emulsion layers.

In the multiset analysis, spectral consistency and, therefore, compound identity are ensured because of the architecture of the multiset (with a single $\mathbf{S}^{\mathbf{T}}$ matrix), and distribution maps are better defined. The deficient quality of the results obtained by individual single image analysis in this example is due to two different factors: (a) not all sample constituents are sufficiently represented in all emulsion layers and (b) the quality of the Raman signal (signal-to-noise ratio) decreases as depth increases. These problems are solved with multiset analysis because of the complementary composition information from the different images and the better signal-to-noise ratio of top emulsion layers that influence the quality of the overall multiset structure results.

The second example is a thermal-dependent polymorphic transformation monitored by Raman imaging [130]. The multiset is formed by images acquired at different temperatures on the same sample. Figure 2.14 shows (a) the distribution maps and (b) the pure spectra of the polymorphic forms involved in the process. Global thermal process profiles are obtained by plotting the average value of the distribution maps as a function of the temperature for the three forms (see Figure 2.14c). Note that, in this case, the two initial polymorphic forms evolve thermally in the same way, but they can be distinguished because the polymorphs have a different spatial distribution on the sample surface. This kind of distinction would have never been possible in classical process monitoring where only one spectrum per temperature would have been registered; only a single starting form would have been detected with a spectral signature equal to a mixture of the two initial polymorphs. Note that pure Raman spectra are not temperature dependent in the working thermal range.

2.7.5
Resolution Postprocessing: Compound Identification, Quantitative Analysis, and Superresolution

Image resolution provides intrinsically relevant information on the identity and spatial distribution of sample constituents through the resolved pure spectra and distribution maps, respectively. However, these two sets of profiles are also the seeding information for interesting postprocessing approaches.

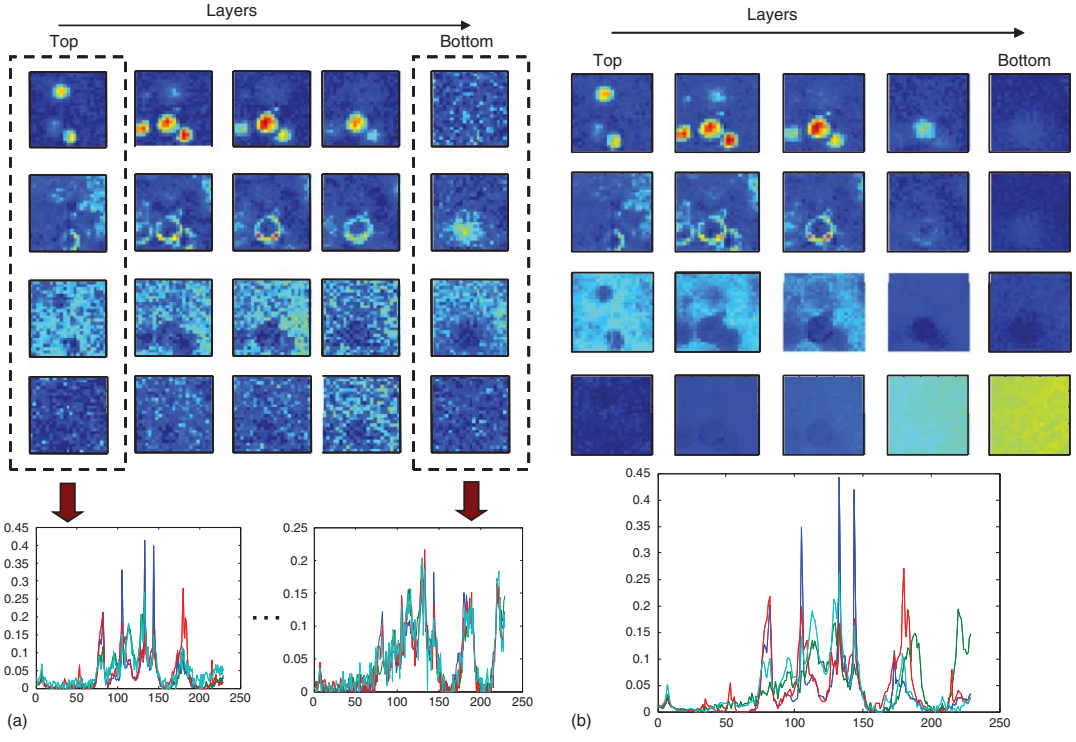

Figure 2.13 Resolution analysis of a multilayer emulsion image. (a) Distribution maps of emulsion layers and resolved pure spectra from top and bottom layers obtained by individual layered resolution and (b) pure spectra and distribution maps coming from image multiset analysis.

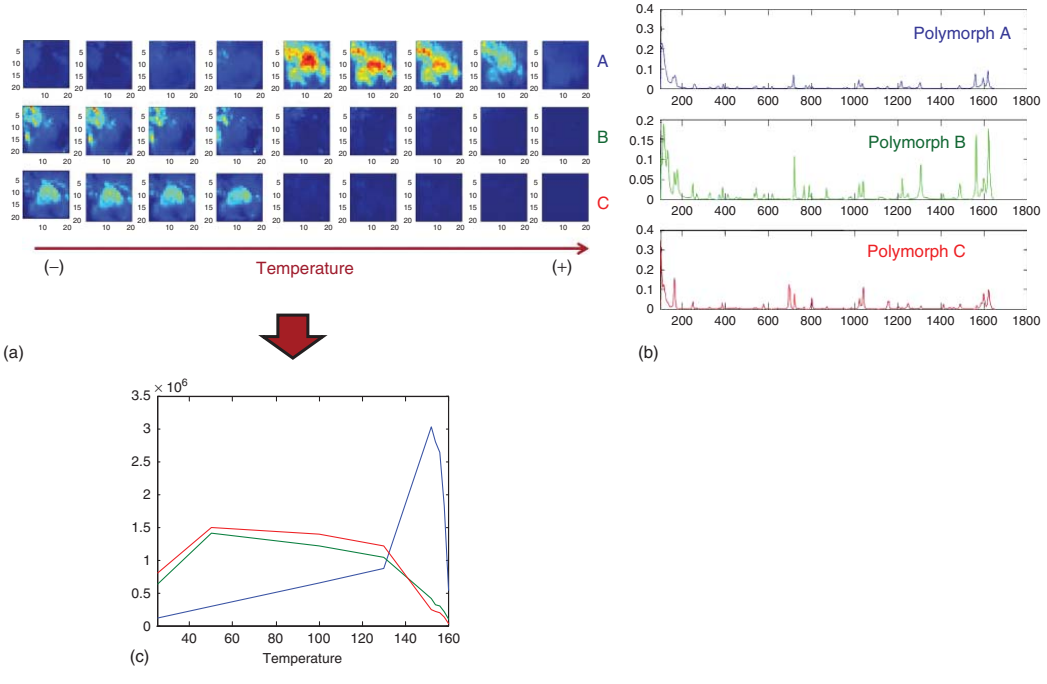

Figure 2.14 Resolution results of a thermal-dependent polymorphic transformation monitored by Raman imaging. (a) Distribution maps, (b) pure spectra, and (c) thermal process profiles.

2.7.5.1 Compound Identification

Resolution of images can be performed even if no knowledge of the image constituents is available. When partial information on the identity of constituents exists, it can be incorporated in the resolution process by forcing the pure spectrum of a certain constituent to keep a known shape. A different case is formed by certain families of images, for example, biomedical images, for which spectra library with the most commonly found constituents may be available. Libraries of spectra are often large, and there is a need for screening methodologies to identify candidates that may be present in a measured image. There are methodologies designed to perform this task without the need of a previous resolution of the image, such as target factor analysis [131, 132]. However, the information obtained by this and other screening methods is only the presence or absence of a potential constituent in the image. It is not possible, then, to know whether unidentified compounds, not included in the library, may also exist. Therefore, distribution maps cannot be directly derived using only the accepted library spectra.

A good alternative to perform this screening can be carried out as a postprocessing step in image resolution. To illustrate this possibility, we present an example of a kidney calculus image. Figure 2.15a shows the resolution of this image into three image constituents, with their related pure spectra and distribution maps. A library of Raman spectra is available with the spectra of the most common inorganic compounds present in this kind of biomedical samples [133].

If the image raw data met the local rank conditions for resolutions and the resolution results lacked ambiguity, the resolved spectra would be identical to some library spectra but, even if this is not the case, the resolved profiles are close to the true profiles. Despite the degree of ambiguity in the resolution results, the matrix $\mathbf{S}^{\mathbf{T}}$ allows for a good reproduction of the spectral variation in the raw image data set, using either the real pure spectra of the constituents or good approximate linear combinations of them. From a geometrical point of view, this means that the resolved spectra in matrix $\mathbf{S}^{\mathbf{T}}$ span the spectral space of the image and the library spectra related to image constituents should belong to this space. Therefore, the screening is performed by projecting the spectrum of the potential library candidate onto the space defined by $\mathbf{S}^{\mathbf{T}}$ (see Figure 2.15b for a schematic view of the projection process). To perform this projection, a transformation vector, $\mathbf{r_i}$, is calculated that relates the library spectrum to be checked, $\mathbf{t_i}$, to the space $\mathbf{S}^{\mathbf{T}}$ as follows:

$$\mathbf{t_i} = \mathbf{S}\mathbf{r_i}$$
$$\mathbf{r_i} = (\mathbf{S}^{\mathbf{T}}\mathbf{S})^{-1}\mathbf{S}^{\mathbf{T}}\mathbf{t_i}$$

Afterwards, the projection of the library spectrum onto $\mathbf{S}^{\mathbf{T}}$ is obtained as

$$\mathbf{t_o} = \mathbf{S}\mathbf{r_i}$$

When the library spectrum, $\mathbf{t_i}$, and its projection onto the $\mathbf{S}^{\mathbf{T}}$ space, $\mathbf{t_o}$, are identical or very similar, the candidate is a constituent present in the image. When the distance among them, e_i, is large (the original spectrum is far away from the $\mathbf{S}^{\mathbf{T}}$ space), the potential candidate is absent. Figure 2.15b shows the plot of e_i for all

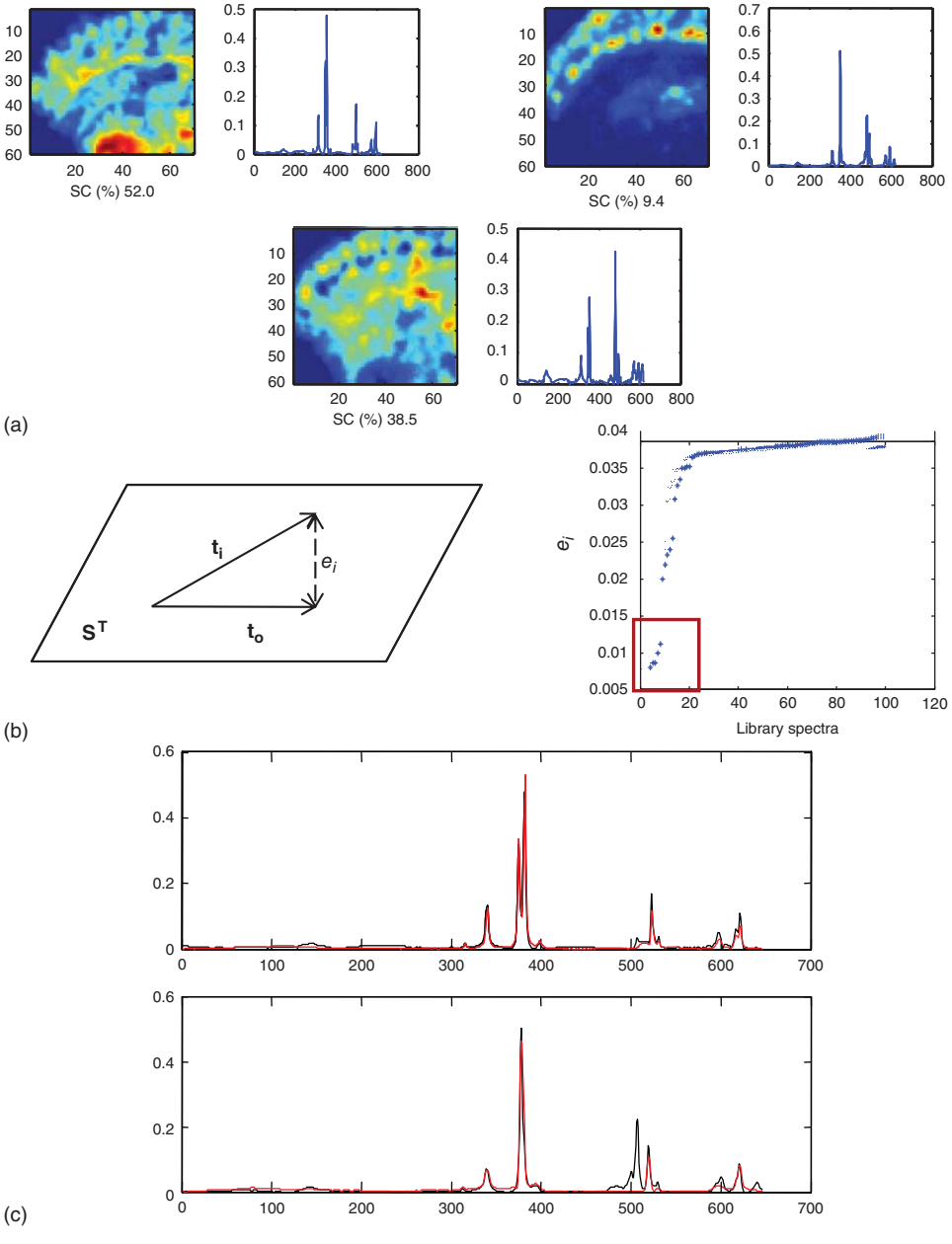

Figure 2.15 (a) Resolution results for a kidney calculus, distribution maps, and related pure spectra; (b) image constituent screening by projection of library spectra, $\mathbf{t}_i$, onto resolved spectra space, $\mathbf{S}^T$; and (c) clear straightforward identification of two of the accepted candidates as calculi constituents (black spectra, resolved spectra from MCR-ALS; red spectra, library spectra).

the library spectra of the calculus example. As can be seen, five library candidates show e_i values significantly lower than the rest of spectra and can be potential constituents of the analyzed sample. From these results, two constituents were unambiguously identified as whewellite and weddellite because of the excellent agreement with two of the pure spectra obtained during the resolution process (see the clear overlap between the library spectra, in red, and the resolved spectra, in black, in Figure 2.15c). As a second step (not shown), these library spectra were fixed in a new resolution analysis and the identification of the third image constituent (dahllite) could be carried out.

In general, there are certain advantages of this resolution postprocessing identification step over the classical TFA process. Basically, the library spectra accepted from the projection approach can pass through a second identification check by visual comparison with the resolved spectra in $\mathbf{S^T}$ and by calculation of the correlation coefficient. In difference with TFA, which defines the image space through abstract score profiles, the pure spectra in $\mathbf{S^T}$ are chemically meaningful and we can make a straight association between accepted candidates/resolved spectra. In addition, the resolution provides complete information about the image (distribution maps and pure spectra) and, in case that components out of the library were also present in the image, their pure spectra and distribution maps would also be obtained. As could be seen in the calculus example, after a first identification step, the library spectra of the confirmed components can be fixed in a new resolution process to improve the results and to help in the modeling (or eventual identification) of unknown components.

2.7.5.2 Quantitative Analysis

Although the main goal of hyperspectral image resolution is providing the identification and location of components in a sample surface through the pure spectra and related distribution maps, there exists also the possibility to obtain quantitative information. At this point, we should distinguish between within-image quantitation, which aims at providing information on the relative presence of the different compounds in an image, and the standard absolute quantitative information that can be extracted when we work in a multiset analysis context (see Figure 2.16).

The within-image quantitation is more correctly described as the signal contribution of a certain constituent to the overall signal. The relative signal contribution over the global image signal can be expressed by $\mathbf{sc_i}$ (%) defined as

$$\mathbf{sc_i}(\%) = 100 \times \frac{\sum \mathbf{c_i s_i^T}}{\sum \mathbf{CS^T}}$$

where the numerator $\mathbf{c_i s_i^T}$ is the signal of a pure constituent, defined by the product of the dyad of the concentration profile and the related pure spectrum, and the denominator the global raw image signal. Figure 2.15a contains the signal

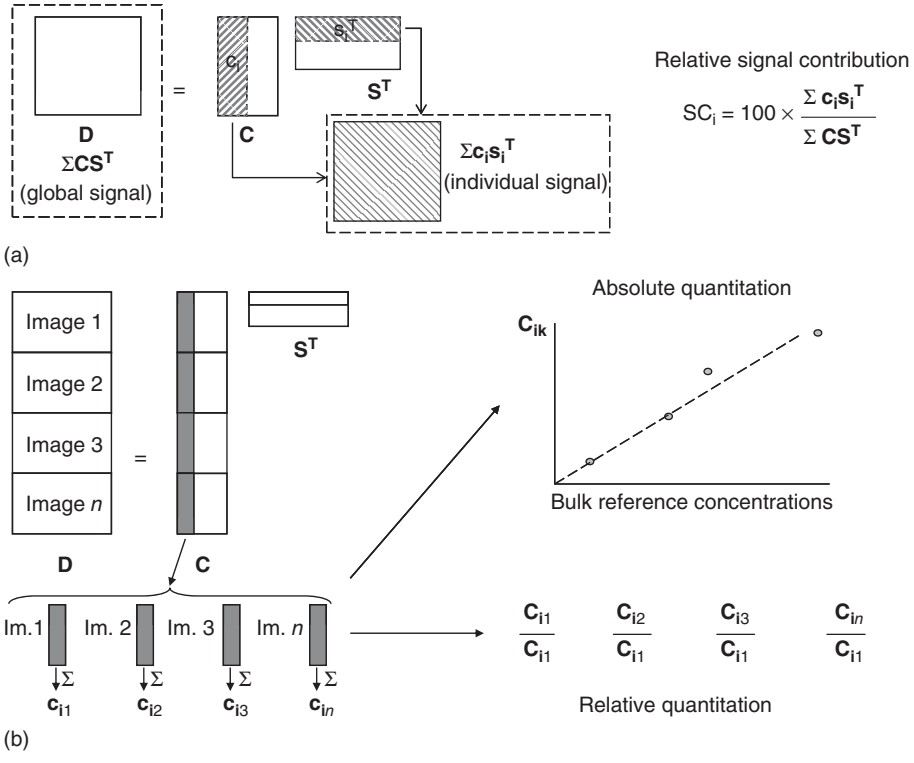

Figure 2.16 (a) Scheme followed to obtain within-image "quantitative" information (percent of signal contribution); (b) scheme followed to obtain between-image quantitative information in image analysis.

contributions of each kidney calculus constituent in the collected image. It is relevant to note that the signal contribution value cannot be straightforwardly associated with compound concentration because of the different absorptivity or Raman intensity of the different compounds in the image.

Absolute quantitative information is a concept linked to multiset image analysis and requires, as calibration methods do, the presence of a set of standard images with known composition and a set of unknown images, the concentration of which wants to be predicted.

In a resolution context, where the information of each constituent is clearly separated in a specific concentration profile and related pure spectrum, the quantitation is done separately for each compound. Thus, the calibration/prediction process starts building a univariate calibration model for a particular compound, regressing the average value of the distribution maps (concentration profiles) of the calibration images against the reference concentration values. Once this calibration line is built, it can be used to predict concentration values on unknown images from the average values of the distribution maps obtained for these unknown images (see Figure 2.16b). In cases where some resolved

compounds were unexpected or lack reference concentration information, we can always obtain relative quantitative information by comparing the ratio of the average values obtained in the related distribution maps.

Several aspects are worth to be commented on (a) the representativeness of the average concentration value used in the calibration/prediction step, (b) the configuration of the multiset used for quantitative information, and (c) the ability to do predictions at a global level and at a pixel level.

Representativeness of average concentration values is always an issue when using images for quantitative analysis. Several aspects can be easily taken into account: (a) background pixels should be cropped when the average concentration value has to be calculated, (b) median concentration values may be used instead of mean values when anomalous pixels or very heterogeneous samples are analyzed. However, when high heterogeneity is observed in the distribution maps, one should be sure that the image is large enough to obtain a representative concentration value and this may be not so simple in some instances.

The configuration of the multiset used for the analysis may also affect the quality of the final results. Two aspects should be taken into account: the kind of information introduced in the multiset, that is, the composition of the calibration images used and the architecture of the multisets used for the calibration/validation steps.

With respect to the calibration images, we should be using images that reflect the concentration range we expect to find in unknown images (as with any calibration method) but, specific for resolution analysis, they should have whenever possible a composition that allows meeting the conditions for a correct resolution of the data, that is, we need calibration images to be designed so that all constituents to be determined are absent in some of these images [129]. Pure standard images are a good option but, when this is not possible, mixture standards lacking some constituents are a good alternative and mimic better the properties of the unknown samples [134].

There are also different possibilities regarding the multisets used for calibration and validation (see Figure 2.17). Essentially, there are three options: (1) The entire set of standard images is analyzed within the same multiset in a single resolution analysis. The distribution maps (concentration profiles) of each image are split in two halves and the average value of one half is used for calibration and the average of the other half is used for validation. (2) All raw standard images are split in two halves before resolution. Multiset resolution analysis is performed on one half and the calibration models are built. The concentration profiles related to the other half of the images are obtained by a single nonnegative least squares step using the $\mathbf{S}^{\mathbf{T}}$ matrix obtained from the previous resolution analysis and the related average values are used for validation purposes. (3) The set of standard matrices is divided into a set of calibration images and a set of validation images. Resolution analysis is done on the image calibration set and calibration lines are built. The concentration profiles related to validation images are obtained by a single nonnegative, least squares step using the $\mathbf{S}^{\mathbf{T}}$ matrix obtained from the previous resolution analysis, and the related average values are used for validation purposes. As long as calibration images are representative, the three strategies provide very similar results and

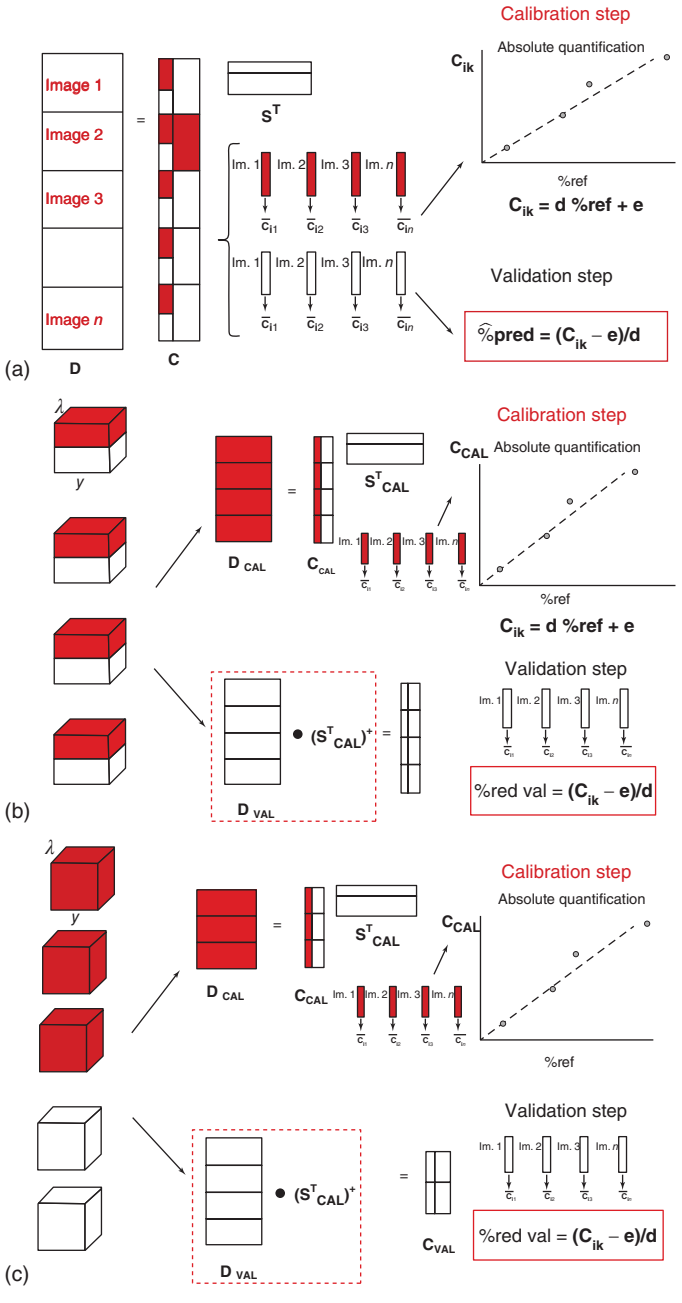

Figure 2.17 Schemes of calibration/validation strategies for quantitative analysis using MCR-ALS information. (a) Strategy 1, (b) strategy 2, and (c) strategy 3, as described in main text. (Reprinted from Ref. [134].)

the related figures of merit, as proven on a study of determination of compounds in pharmaceutical mixtures by NIR image analysis [134].

Quantitative analysis can also be used for quantitative prediction at a pixel level. Similar to what is shown in Figure 2.6, the univariate calibration lines built per each compound can also be used to predict real pixel concentration values based on the resolved concentration values obtained by resolution analysis. As mentioned in Section 2.5, the distribution maps with real concentration values can be used later on for heterogeneity studies or other purposes.

Although figures of merit tend to be similar or slightly worse than the figures obtained with classical calibration methods, the advantages of using resolution for quantitative analysis toward classical calibration methods are that the quantitative information goes together with structural information (pure spectra) for the compounds of interest determined and a complete description of the samples analyzed is obtained, since additional information for interfering/unknown compounds in the sample is also retrieved through the resolved pure spectra and distribution maps.

2.7.5.3 **Superresolution**

Although image acquisition systems improve their spatial resolution, there are instrumental limits related to this parameter. Superresolution strategies are mathematical procedures devoted to obtain spatial descriptions of the sample surface that go beyond the limits of the instrumental spatial resolution [135, 136].

Superresolution algorithms started working with gray images and were based on the fact that several images of low spatial resolution shifted from each other with a motion step smaller than the pixel size could be recombined to obtain a single superresolved image with a pixel size equal to the motion step used [137]. The mathematical principle behind superresolution is that a low-resolution image can be obtained as the result of shifting, blurring, and decimating a high-resolution image [137]. Based on this fact, a back transform taking a series of low-resolution images with sufficient complementary information as the starting information allows reconstructing an image with high spatial resolution.

The natural expansion of the superresolution concept to hyperspectral images would imply applying the algorithm to each of the spectral channels registered with the consequent complexity and computation time, and the outcome would only be a raw superresolved image that would need further analysis. Therefore, working with compressed hyperspectral image representations is a clear need.

Multiset image analysis offers the perfect framework to obtain compressed meaningful representations of the set of shifted low spatial resolution images, which can be afterwards combined for superresolution purposes. First, the set of low spatial resolution images shifted adequately from each other should be organized to form a multiset (see Figure 2.12a). MCR-ALS is afterwards applied and the results obtained are a single matrix of pure spectra and a set of low spatial resolution distribution maps per each of the image constituents. This procedure has a double advantage: (a) on the one hand, spectral (compound identity) consistency is ensured in the sets of distribution maps resolved because

of the single $\mathbf{S}^{\mathbf{T}}$ matrix obtained in multiset analysis; (b) on the other hand, the compressed image representations provided by the sets of resolved distribution maps are noise filtered and contain compound-specific information instead of the mixed information in the raw images acquired. Once multiset analysis has been performed, the superresolution algorithm is applied to each set of distribution maps and a single superresolved map is obtained per each image constituent. In this way, superresolution is applied as many times as image constituents instead of hundred or thousand times, as number of spectral channels present in the raw image.

Figure 2.18 shows the sequence followed on the study of a single HeLa cell by IR synchrotron imaging using the combination of multiset analysis with superresolution postprocessing [20]. To solve this problem, 36 low spatial resolution images with pixel size 3.5 μm and an image size of ($x \times y \times \nu : 15 \times 7 \times 436$) were acquired. Each of these images was shifted from the closest one by a motion step of 0.6 μm in the x- or y-direction. Shifts in the x- and y-direction with respect to the original image went from 1 to 6 times 0.6 μm. After resolution of the multiset formed by the 36 images, three contributions were modeled with clear spectral signatures. By application of the superresolution postprocessing to the three sets of low spatial

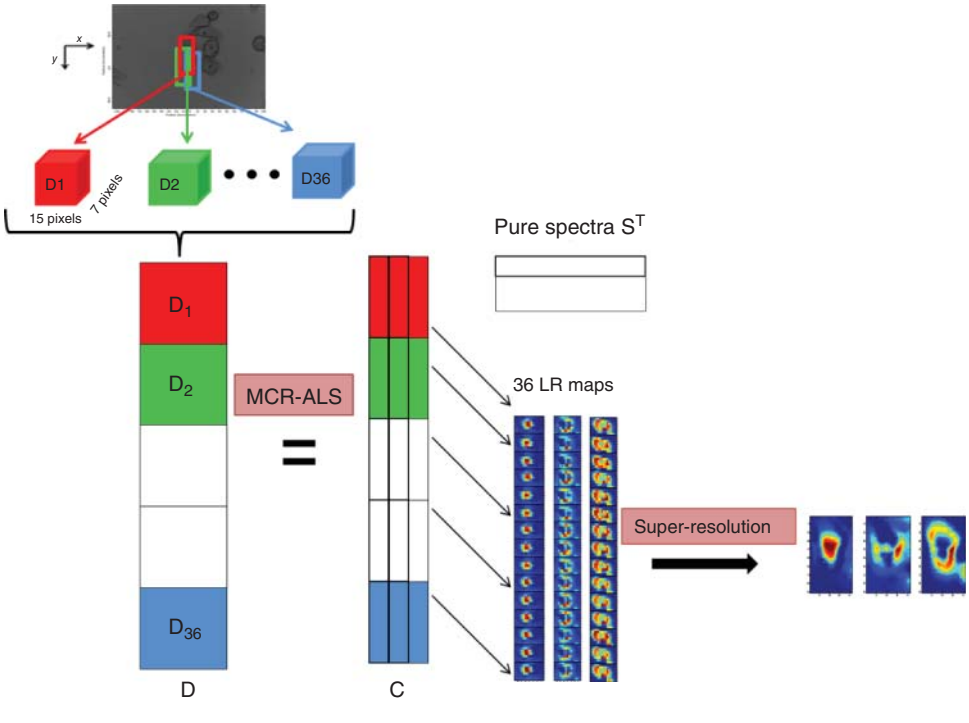

Figure 2.18 Graphical scheme of the combination of image multiset analysis and superresolution postprocessing. (Reprinted from Ref. [20].)

resolution maps, three superresolved distribution maps with a pixel size of 0.6 μm (equal to the motion step among images) were finally obtained.

As a general conclusion, the strategy combining multiset image analysis and superresolution postprocessing simultaneously saves computation time and, above all, provides unmixed, spatially detailed, constituent-specific interpretable information on the sample analyzed.

2.8 Future Trends

Although the progress in the area of hyperspectral image analysis is very fast and it is difficult to predict what may happen in the future, there are directions that can be envisioned. There is increasing use and incorporation of multivariate algorithms in image acquisition systems in laboratories and for routine online control of products, especially in food or pharmaceutical industries [85, 93]. The flexibility and diversity of instrumentation also provide more typologies of images that will need to be combined. Matching these images from different origins and designing algorithms based on multiset or multiblock analysis are still areas that need to be further developed [138, 139]. Likewise, specific modifications of existing algorithms taking into account the spatial information of the instrumental measurement or characteristics of the sample linked to morphology, biological, or environmental attributes should still be explored.

References

1. Geladi, P. and Grahn, H. (1996) *Multivariate Image Analysis in Chemistry and Related Areas: Chemometric Image Analysis*, John Wiley & Sons, Ltd, Chichester.
2. Grahn, H.F. and Geladi, P. (2007) *Techniques and Applications of Hyperspectral Image Analysis*, John Wiley & Sons, Ltd, Chichester.
3. Krooshof, P.W.T., Geert, J., Postma, G.J., Melssen, W.J., and Buydens, L.M.C. (2009) in *Evaluation of Spectroscopic Images, in Biomedical Imaging: Principles and Applications* (ed. R. Salzer), John Wiley & Sons, Ltd, Chichester, pp. 1–29.
4. Tran, T.N., Wehrens, R., and Buydens, L.M.C. (2005) *Chemom. Intell. Lab. Syst.*, **77**, 3–17.
5. Massart, D.L., Vandeginste, B.G.M., Buydens, L.M.C., de Jong, S., Lewi, P.J., and Smeyers-Verbeke, J. (1997) *Handbook of Chemometrics and Qualimetrics*, Data Handling in Science and Technology, vol. 20, Elsevier.
6. Naes, T., Isaksson, T., Fearn, T., and Davies, T. (2002) *Multivariate Calibration and Classification*, NIR Publications, Chichester.
7. Savitzky, A. and Golay, M. (1964) *Anal. Chem.*, **36**, 1627–1639.
8. Walczak, B. (ed.) (2000) *Wavelets in Chemistry*, Elsevier, Amsterdam.
9. Ehrentreich, F. and Summchen, L. (2001) *Anal. Chem.*, **73**, 4364–4373.
10. Singh, C.B., Choudhary, R., Jayas, D.S., and Paliwal, J. (2010) *Food Bioprocess Technol.*, **3**, 2–12.
11. Vogt, F., Banerji, S., and Booksh, K. (2004) *J. Chemom.*, **18**, 350–362.
12. Wold, S. (1975) in *Perspectives in Probability and Statistics* (ed J. Garni), Academic Press, London, pp. 117–142.

13. Eriksson, L., Johansson, E., Kettaneh-Wold, N., and Wold, S. (2001) *Multi- and Megavariate Data Analysis*, Umetrics, Umeå.
14. Geladi, P., MacDougall, D., and Martens, H. (1985) *Appl. Spectrosc.*, **39**, 491–500.
15. Romeo, M., Mohlenhoff, B., and Diem, M. (2006) *Vib. Spectrosc.*, **42**, 9–14.
16. Afseth, N.K. and Kohler, A. (2012) *Chemom. Intell. Lab. Syst.*, **117**, 92–99.
17. Kohler, A., Sulé-Suso, J., Sockalingum, G.D., Tobin, M., Bahrami, F., Yang, Y., Pijanka, J., Dumas, P., Cotte, M., van Pittius, D.G., Parkes, G., and Martens, H. (2008) *Appl. Spectrosc.*, **62**, 259–266.
18. Eilers, P. (2004) *Anal. Chem.*, **76**, 404–411.
19. Piqueras, S., Duponchel, L., Tauler, R., and de Juan, A. (2011) *Anal. Chim. Acta*, **705**, 182–192.
20. Piqueras, S., Duponchel, L., Offroy, M., Jamme, F., Tauler, R., and de Juan, A. (2013) *Anal. Chem.*, **85**, 6303–6311.
21. Burger, J. and Geladi, P. (2006) *J. Chemom.*, **20**, 106–119.
22. López-Alonso, J.M. and Alda, J. (2002) *Opt. Eng.*, **41**, 2152–2157.
23. Lasch, P. (2012) *Chemom. Intell. Lab. Syst.*, **117**, 100–114.
24. Esquerre, C., Gowen, A.A., Burger, J., Downey, G., and O'Donnell, C.P. (2012) *Chemom. Intell. Lab. Syst.*, **117**, 129–137.
25. Vidal, M. and Amigo, J.M. (2012) *Chemom. Intell. Lab. Syst.*, **117**, 138–148.
26. Burger, J. and Geladi, P. (2007) *J. Near Infrared Spectrosc.*, **15**, 29–37.
27. Windig, W. and Guilment, J. (1991) *Anal. Chem.*, **63**, 1425–1432.
28. Gallagher, N.B., Shaver, J.M., Martin, E.B., Morris, J., Wise, B.M., and Windig, W. (2004) *Chemom. Intell. Lab. Syst.*, **73**, 105–117.
29. Windig, W., Markel, S., and Thompson, P.M. (2007) in *Techniques and Applications of Hyperspectral Image Analysis* (eds H.F. Grahn and P. Geladi), John Wiley & Sons, Ltd, Chichester, pp. 69–87.
30. Leardi, R. (ed) (2003) Nature-inspired methods in chemometrics: genetic algorithms and artificial neural networks, in *Data Handling in Science and Technology*, vol. 23, Elsevier, Amsterdam.
31. Chtioui, Y., Bertrand, D., and Barba, D. (1998) *J. Sci. Food Agric.*, **76**, 77–86.
32. Wang, M., Zhou, X.B., King, R.W., and Wong, S.T.C. (2007) *BMC Bioinform.*, **8**, 1–12, Art. 32.
33. Ramos, P.M. and Ruisánchez, I. (2006) *Anal. Chim. Acta*, **558**, 274–282.
34. Jay Liu, J. and McGregor, J.F. (2007) *Chemom. Intell. Lab. Syst.*, **85**, 119–130.
35. de Juan, A., Maeder, M., Hancewicz, T., Duponchel, L., and Tauler, R. (2009) in *Infrared and Raman Spectroscopic Imaging* (eds R. Salzer and H.W. Siesler), Wiley-VCH Verlag GmbH, Weinheim, pp. 65–106.
36. Esbensen, K. and Geladi, P. (1989) *Chemom. Intell. Lab. Syst.*, **7**, 67–86.
37. Geladi, P., Wold, S., and Esbensen, K.H. (1986) *Anal. Chim. Acta*, **191**, 473–480.
38. Bharati, M.H. and MacGregor, J.F. (1998) *Ind. Eng. Chem. Res.*, **37**, 4715–4724.
39. Kohler, A., Bertrand, D., Martens, H., Hannesson, K., Kirschner, C., and Ofstad, R. (2007) *Anal. Bioanal. Chem.*, **389**, 1143–1153.
40. Andrew, J.J., Browne, M.A., Clark, I.E., Hancewicz, T.M., and Millichope, A.J. (1998) *Appl. Spectrosc.*, **52**, 797–807.
41. Dunn, K.G. MACC Multivariate Image Analysis (MACCMIA). Manual and Tutorial for Version 1.81. *http://macc.mcmaster.ca* (accessed 15 February 3014).
42. Liu, J.J., Bharati, M.H., Dunn, K.G., and MacGregor, J. (2005) *Chemom. Intell. Lab. Syst.*, **79**, 42–54.
43. de Edelenyi, F.S., Simonetti, A.W., Postma, G., Huo, R., and Buydens, L.M.C. (2005) *Anal. Chim. Acta*, **544**, 36–46.
44. Nascimento, J.M.P. and Bioucas-Dias, J.M. (2005) *IEEE Trans. Geosci. Remote Sens.*, **43**, 175–187.
45. Geladi, P. and Esbensen, K. (1991) *J. Chemom.*, **5**, 97–111.

46. Esbensen, K.H., Geladi, P.L., and Grahn, H.F. (1992) *Chemom. Intell. Lab. Syst.*, **14**, 357–374.
47. Lied, T.T., Geladi, P., and Esbensen, K.H. (2000) *J. Chemom.*, **14**, 585–598.
48. Lied, T.T. and Esbensen, K.H. (2001) *Chemom. Intell. Lab. Syst.*, **58**, 213–226.
49. Yu, H.L. and MacGregor, J.F. (2003) *Chemom. Intell. Lab. Syst.*, **67**, 125–144.
50. Bharati, M.H., MacGregor, J.F., and Champagne, M. (2004) *Tappi J.*, **3**, 8–14.
51. Wold, S., Martens, H., and Wold, H. (1983) *Lect. Notes Math.*, **973**, 286–293.
52. Burger, J. and Geladi, P. (2005) *J. Chemom.*, **19**, 355–363.
53. Burger, J. and Geladi, P. (2006) *Analyst*, **131**, 1152–1160.
54. Petersen, L., Minkkinen, P., and Esbensen, K. (2005) *Chemom. Intell. Lab. Syst.*, **43**, 175–187.
55. Rosas, J.G. and Blanco, M. (2012) *J. Pharm. Biomed. Anal.*, **70**, 680–690.
56. Weinstock, A.B., Janni, J., Hagen, L., and Wright, S. (2006) *Appl. Spectrosc.*, **60**, 9–16.
57. Xing, J., Symons, S., Hatcher, D., and Shahin, M. (2011) *Biosyst. Eng.*, **108**, 303–310.
58. Fernández Pierna, J.A., Vermeulen, P., Amand, O., Tossens, A., Dardenne, P., and Baeten, V. (2012) *Chemom. Intell. Lab. Syst.*, **117**, 233–239.
59. Wehrens, R., Simonetti, A.W., and Buydens, L.M.C. (2002) *J. Chemom.*, **16**, 274–282.
60. Vermeulen, P., Fernández Pierna, J.A., van Egmond, H.P., Dardenne, P., and Baeten, V. (2011) Online detection and quantification of ergot bodies in cereals using near infrared hyperspectral imaging. *Food Addit. Contam. Part A Chem. Anal. Control Exposure Risk Assess.*, **29**, 232–240.
61. Lin, W.Q., Jiang, J.H., Yang, H.F., Ozaki, Y., Shen, G.L., and Yu, R.Q. (2006) *Anal. Chem.*, **78**, 6003–6011.
62. Gowen, A.A., O'Donnell, C.P., Taghizadeh, M., Cullen, P.J., Frias, J.M., and Downey, G. (2008) *J. Chemom.*, **22**, 259–267.
63. Wang, J. and Chang, C.I. (2006) *IEEE Trans. Geosci. Remote Sens.*, **44**, 1586–1600.
64. Krooshof, P.W.T., Tran, T.N., Postma, G.J., Melsen, W.J., and Buydens, L.M.C. (2006) *TrAC, Trends Anal. Chem.*, **25**, 1067–1080.
65. Massart, D.L. and Kaufman, L. (1983) *The Interpretation of Analytical Chemical Data by the Use of Cluster Analysis*, John Wiley & Sons, Inc., New York.
66. Webb, A. (2002) *Statistical Pattern Recognition*, John Wiley & Sons, Ltd, Malvern.
67. Sander, J., Ester, M., Kriegel, H.P., and Xu, X.W. (1998) *Data Min. Knowl. Discovery*, **2**, 169–194.
68. Tran, T.N., Nguyen, T.T., Willemsz, T.A., van Kessel, G., Frijlink, H.W., Van Maarschalk, K., and van der Voort, K. (2012) *Anal. Chim. Acta*, **725**, 14–21.
69. Sneath, P.H.A. (1957) *J. Gen. Microbiol.*, **17**, 201–226.
70. Lance, G.N. and Williams, W.T. (1967) *Comput. J.*, **9**, 373.
71. Ward, J.H. (1963) *J. Am. Stat. Assoc.*, **58**, 236.
72. Gonçalves, M.L., Netto, M.L.A., Costa, J.A.F., and Zullo Junior, J. (2008) *Int. J. Remote Sens.*, **29**, 3171–3207.
73. Lloyd, S.P. (1982) *IEEE Trans. Info. Theor.*, **28**, 129–137.
74. Grahn, H., Szeverenyi, N., and Roggenbuck, M.W. (1989) *Chemom. Intell. Lab. Syst.*, **7**, 87–93.
75. (a) Geladi, P., Swerts, J., and Lindgren, F. (1994) *Chemom. Intell. Lab. Syst.*, **24**, 145–167. (b) Wold, S. (1976) *Pattern Recogn.*, **8**, 127–139.
76. Wold, S. (1976) *Pattern Recogn.*, **8**, 127–139.
77. Kohler, A., Skaga, A., Hjelme, G., and Skarpeid, H.J. (2002) *Comput. Electron. Agric.*, **36**, 3–16.
78. Krafft, C., Shapoval, L., Sobottka, S.B., Geiger, K.D., Schackert, G., and Salzer, R. (2006) *Biochim. Biophys. Acta Biomembr.*, **1758**, 883–891.
79. Barker, M. and Rayens, W. (2003) *J. Chemom.*, **17**, 166–173.
80. Wold, S., Albano, C., Dunn, W.J. III, Edlund, U., Esbensen, K., Geladi, P., Hellberg, S., Johansson, E.,

Lindberg, W., and Sjostrom, M. (1984) in *Chemometrics, Mathematics and Statistics in Chemistry* (ed B.R. Kowalski), Reidel Publishing Company, Dordrecht, pp. 17–95.

81. Chevallier, S., Bertrand, D., Kohler, A.P., and Courcoux, P. (2006) *J. Chemom.*, **20**, 221–229.
82. Borregaard, T., Nielsen, H., Norgaard, L., and Have, H. (2000) *J. Agric. Eng. Res.*, **75**, 389–400.
83. Ahlinder, L., Ekstrand-Hammarström, B., Geladi, P., and Österlund, L. (2013) *Biophys. J.*, **105**, 310.
84. Guzmán, E., Baeten, V., Fernández-Pierna, J.A., and García-Mesa, J.A. (2012) *Talanta*, **93**, 94–98.
85. Dale, L.M., Thewis, A., Boudry, C., Rotar, I., Dardenne, P., Baeten, V., and Fernández-Pierna, J.A. (2013) *Appl. Spectrosc. Rev.*, **48**, 142.
86. Tarabalka, Y., Chanussot, J., and Benediktsson, J.A. (2010) *Pattern Recogn.*, **43**, 2367–2379.
87. Noordam, J.C., van den Broek, W.H.A.M., Geladi, P., and Buydens, L.M.C. (2005) *Chemom. Intell. Lab. Syst.*, **75**, 115–126.
88. Bezdek, J.C. (1981) *Pattern Recognition With Fuzzy Objective Function Algorithms*, Plenum Press, New York.
89. Teppola, P., Mujunen, S.P., and Minkkinen, P. (1999) *Chemom. Intell. Lab. Syst.*, **45**, 23–38.
90. Schowengerdt, R.A. (2007) *Remote Sensing: Models and Methods for Image Processing. Models and Methods for Image Processing*, Academic Press.
91. Steller, W., Einenkel, J., Horn, L.C., Braumann, U.D., Binder, H., Salzer, R., and Krafft, C. (2006) *Anal. Bioanal. Chem.*, **384**, 145–154.
92. Krafft, C., Diderhoshan, M.A., Recknagel, P., Miljkovic, M., Bauer, M., and Popp, J. (2011) *Vib. Spectrosc.*, **55**, 90–100.
93. Amigo, J.M., Cruz, J., Bautista, M., Maspoch, S., Coello, J., and Blanco, M. (2008) *TrAC, Trends Anal. Chem.*, **27**, 696.
94. Mansfield, J.R., Sowa, M.G., Majzels, C., Collins, C., Cloutis, E., and Mantsch, H.H. (1999) *Vibr. Spectrosc.*, **19**, 33.
95. Martha, T.R., Kerle, N., van Westen, C.J., Jetten, V., and Kumar, K.V. (2011) *IEEE Trans. Geosci. Remote Sens.*, **49**, 4928–4943.
96. Trede, D., Schiffler, S., Becker, M., Wirtz, S., Steinhorst, K., Strehlow, J., Aichler, M., Kobarg, J.H., Oetjen, J., Dyatlov, A., Heldmann, S., Walch, A., Thiele, H., Maass, P., and Alexandrov, T. (2012) *Anal. Chem.*, **84**, 6079–6087.
97. Goretta, N., Roger, J.M., Christophe, F., Bellon-Maurel, V., Rabatel, G., and Lelong, C. (2009) *Traitement Signal*, **26**, 161–174.
98. Gorretta, N., Rabatel, G., Fiorio, C., Lelong, C., and Roger, J.M. (2012) *Chemom. Intell. Lab. Syst.*, **117**, 183–188.
99. Fan, F.L., Wang, Y.P., and Wang, Z.S. (2008) *Environ. Monit. Assess.*, **137**, 127–147.
100. Alexandrov, T. and Kobarg, J.H. (2011) *Bioinformatics*, **27**, i230–i238.
101. Bharati, M.H., Liu, J.J., and MacGregor, J.F. (2004) *Chemom. Intell. Lab. Syst.*, **72**, 57–71.
102. de Juan, A., Tauler, R., Dyson, R., Marcolli, C., Rault, M., and Maeder, M. (2004) *TrAC, Trends Anal. Chem.*, **23**, 70–79.
103. Wang, J.H., Hopke, P.K., Hancewicz, T.M., and Zhang, S.L.L. (2003) *Anal. Chim. Acta*, **476**, 93–109.
104. Duponchel, L., Elmi-Rayaleh, W., Ruckebusch, C., and Huvenne, J.P. (2003) *J. Chem. Info. Comput. Sci.*, **43**, 2057–2067.
105. de Juan, A. and Tauler, R. (2003) *Anal. Chim. Acta*, **500**, 195–210.
106. de Juan, A. and Tauler, R. (2006) *Crit. Rev. Anal. Chem.*, **36**, 163–176.
107. Nascimento, J.M. and Bioucas-Dias, J.M. (2005) *IEEE Trans. Geosci. Remote Sens.*, **43**, 898–910.
108. Berman, M., Phatak, A., Lagerstrom, R., and Wood, B.R. (2009) *J. Chemom.*, **23**, 101–116.
109. Berman, M., Miiveri, H., Lagerstrom, R., Ernst, A., Dunne, R., and Huntington, J.F. (2004) *IEEE Trans. Geosci. Remote Sens.*, **42**, 2085–2095.
110. Windig, W. (2009) in *Comprehensive Chemometrics*, vol. 2 (eds S. Brown,

R. Tauler, and R. Walczak), Elsevier, Oxford, pp. 275–307.
111. Keller, H.R. and Massart, D.L. (1991) *Anal. Chim. Acta*, **246**, 379.
112. de Juan, A., Maeder, M., Hancewicz, T., and Tauler, R. (2005) *Chemom. Intell. Lab. Syst.*, **77**, 64–74.
113. Liang, Y. (2009) in *Comprehensive Chemometrics* (eds S. Brown, R. Tauler, and R. Walczak), Elsevier, Oxford, pp. 309–324.
114. de Juan, A., Rutan, S.C., and Tauler, R. (2009) in *Comprehensive Chemometrics* (eds S. Brown, R. Tauler, and R. Walczak), Elsevier, Oxford, pp. 325–344.
115. Tauler, R., Maeder, M., and de Juan, A. (2009) in *Comprehensive Chemometrics* (eds S. Brown, R. Tauler, and R. Walczak), Elsevier, Oxford, pp. 473–505.
116. Bioucas-Dias, J.M., Plaza, A., Dobigeon, N., Parente, M., Du, Q., Gader, P., and Chanussot, J. (2012) *IEEE J. Sel. Top. Appl. Earth Obs. Remote Sens.*, **5**, 354–379.
117. Budevska, B.O., Sum, S.T., and Jones, T.J. (2003) *Appl. Spectrosc.*, **57**, 124–131.
118. Zhang, X. and Tauler, R. (2013) *Anal. Chim. Acta*, **762**, 25–38.
119. Tauler, R., Smilde, A.K., and Kowalski, B.R. (1995) *J. Chemom.*, **9**, 31–58.
120. Tauler, R. (1995) *Chemom. Intell. Lab. Syst.*, **30**, 133–146.
121. Jaumot, J., Gargallo, R., de Juan, A., and Tauler, R. (2005) *Chemom. Intell. Lab. Syst.*, **76**, 101–110.
122. Wentzell, P.D., Karakach, T.K., Roy, S., Martínez, M.J., Allen, C.P., and Werner-Washburne, M. (2006) *BMC Bioinform.*, **7**, 343, Art. 343.
123. Zhang, L., Henson, M.J., and Sekulic, S.S. (2005) *Anal. Chim. Acta*, **545**, 262–278.
124. Hancewicz, T.M. and Wang, J.H. (2005) *Chemom. Intell. Lab. Syst.*, **77**, 18–31.
125. Hancewicz, T.M., Wang, J.-H., Pudney, P.D.A., and Zhang, S.L. (2004) Multivariate image resolution for spectroscopic image analysis. 228th ACS National Meeting, Philadelphia, PA, August 22, 2004, Paper #15
126. Windig, W. and Keenan, M.R. (2011) *Appl. Spectrosc.*, **65**, 349–357.
127. Windig, W., Shaver, J.M., Keenan, M.R., and Wise, B.M. (2012) *Chemom. Intell. Lab. Syst.*, **117**, 159–168.
128. de Juan, A., Maeder, M., Hancewicz, T., and Tauler, R. (2008) *J. Chemom.*, **22**, 291–298.
129. Manne, R. (1995) *Chemom. Intell. Lab. Syst.*, **27**, 89.
130. S. Piqueras, L. Duponchel, R. Tauler, A. de Juan (2014) *Anal. Chim. Acta*, **819**, 15–25.
131. Malinowski, E.R. (2002) *Factor Analysis in Chemistry*, 3rd edn, John Wiley & Sons, Inc., New York.
132. McCue, M. and Malinowski, E.R. (1981) *Anal. Chim. Acta: Comput. Technol. Optim.*, **5**, 125–136.
133. Dao, N.Q. and Daudon, M. (1997) *Infrared and Raman Spectra of Calculi*, Elsevier, Paris.
134. Piqueras, S., Burger, J., Tauler, R., and de Juan, A. (2012) *Chemom. Intell. Lab. Syst.*, **117**, 169–182.
135. Offroy, M., Roggo, Y., Milanfar, P., and Duponchel, L. (2010) *Anal. Chim. Acta*, **674**, 220–226.
136. Offroy, M., Roggo, Y., and Duponchel, L. (2012) *Chemom. Intell. Lab. Syst.*, **117**, 183–188.
137. Duponchel, L., Milanfar, P., Ruckebusch, C., and Huvenne, J.P. (2008) *Anal. Chim. Acta*, **607**, 168–175.
138. Allouche, F., Hanafi, M., Jamme, F., Robert, P., Guillon, F., and Devaux, M.F. (2012) *Chemom. Intell. Lab. Syst.*, **113**, 43–51.
139. Allouche, F., Hanafi, M., Jamme, F., Robert, P., Barron, C., Guillon, F., and Devaux, M.F. (2012) *Chemom. Intell. Lab. Syst.*, **117**, 200–212.

Part II
Biomedical Applications

Infrared and Raman Spectroscopic Imaging, Second Edition. Edited by Reiner Salzer, Heinz W. Siesler.
© 2014 Wiley-VCH Verlag GmbH & Co. KGaA. Published 2014 by Wiley-VCH Verlag GmbH & Co. KGaA.

3
Vibrational Spectroscopic Imaging of Soft Tissue

Christoph Krafft and Jürgen Popp

3.1
Introduction

In general, biological tissue is a collection of cells, which also includes its extracellular matrix (ECM). Cells within a particular tissue perform a similar function within an organism. In principle, all compartments of a multicellular organism, for example, organs, structures, and other contents of animals, can be assigned to a tissue class or are produced by a tissue type. The study of tissue is known as *histology* or – in connection with disease – histopathology. The classical tools for studying tissue include fixing, embedding in a wax block, cutting tissue sections, mounting on slides, staining, and inspecting them by optical microscopy. Developments in electron microscopy, fluorescence microscopy, and molecular biology significantly increased the knowledge about the structure and function of tissues in the last couple of decades. With these tools, tissues can be examined in health and disease, enabling considerable refinement of clinical diagnosis. However, all methods require substantial preparation procedures, labeling molecules, and experts for interpretation. Problems of label-based techniques may occur because of the limited accessibility of the labels to the target, their insufficient binding specificity, and their low stability.

After sensitive and rapid Fourier transform infrared (FT-IR) and Raman spectrometers have been developed, vibrational spectroscopy appeared as a complementary tool to assess tissues and their pathological changes. Generally, more bands are observed in vibrational spectra of tissues than in other optical spectra because numerous vibrations of biomolecules can be probed simultaneously giving a fingerprint-like signature. Therefore, more potential information about the biochemistry, composition, and molecular structure of the underlying sample may be collected without external labels, with minimal preparation and without damaging the samples. Early studies in the literature were based on single spectra with low lateral resolution. As the inherent inhomogeneity of tissue could not be fully considered, a correlation between the histology and the vibrational spectra were only achieved for homogenous regions of interest. Major improvements resulted from the combination of vibrational spectroscopy with spatial information, which

Infrared and Raman Spectroscopic Imaging, Second Edition. Edited by Reiner Salzer, Heinz W. Siesler.
© 2014 Wiley-VCH Verlag GmbH & Co. KGaA. Published 2014 by Wiley-VCH Verlag GmbH & Co. KGaA.

opens wide perspectives in biomedical imaging applications. After coupling to microscopy, these powerful imaging techniques enable to characterize soft tissue with diffraction-limited lateral resolution. Spectroscopic near-field imaging can even resolve details below the diffraction limit as described in Chapters 11 and 12 of this book. Nonlinear spectroscopic modalities can achieve image acquisition with video time frame rates as described in Chapter 14. Vibrational spectroscopic images can be analyzed by automatic procedures, enabling high throughput and high reproducibility. As the information is usually distributed over a wide spectral range and the spectral variances between the tissue types and pathological states are partly small, multivariate algorithms are more appropriate than univariate algorithms for analysis. False color images produced by segmentation and classification of vibrational spectroscopic images are directly comparable to outcomes of standard histopathological staining protocols and can be interpreted also by nonspectroscopists. Furthermore, these methods offer the possibility for optical biopsies under *in vivo* situations using fiber optic probes.

There are four basic types of soft tissues in all vertebrates including the human body and in most invertebrates with some exceptions (e.g., fungi). They are called *epithelium*, *connective tissue*, *muscle tissue*, and *nervous tissue*. Vegetable fibers and tissues are introduced in Chapter 6 of this book. This chapter focuses on applications of Raman and FT-IR imaging to soft tissues. Section 3.2 deals with the fundamental aspects of preparation of soft tissues for vibrational spectroscopic imaging. Instrumental considerations and data treatment are not discussed. Section 3.3 deals with (i) colon tissue, which contains epithelium, connective tissue, muscle tissue, and nerve cells; (ii) brain tissue, which represents nervous tissue; (iii) cervical tissue, which constitutes an example for carcinoma originating from epithelium; and (iv) atherosclerosis in which an artery wall thickens as a result of the accumulation of fatty materials such as cholesterol and triglyceride. In addition to the chapter in the first edition of this book, data from the nonlinear-variant coherent anti-Stokes Raman scattering (CARS) are included for comparison. Furthermore, new approaches in sample preparation and data processing are described. The literature has been updated although this contribution does not intend to give a comprehensive overview of the field. A tutorial was published on Raman and CARS microspectroscopy for biomedical applications [1]; recent reviews were reported on fiber optic probes for Raman and CARS spectroscopy [2], Raman spectroscopy for deep noninvasive medical diagnosis [3], and disease recognition by infrared (IR) and Raman spectroscopy [4]. The following are some general features of the four basic tissue types.

3.1.1 Epithelium

Epithelium is the biological and medical collective term for cover and glandular tissues. It is composed of layers of cells that line the outside and the inside surfaces of organs. The outermost layer of the skin is composed of stratified squamous epithelial cells. Other epithelial cells line the inner layers of the respiratory,

the gastrointestinal, the reproductive, and the urinary tracts, and make up the exocrine and endocrine glands. Functions of epithelial cells include secretion, absorption, protection, transcellular transport, sensation detection, and selective permeability. Endothelium – the inner lining of blood and lymph vessels – is a specialized form of epithelium.

Epithelial cells are classified by shape, stratification, and specialization. The shape is subdivided into squamous, cuboidal, columnar, and transitional. Squamous cells are flat cells with an irregular flattened shape. A one-celled layer of simple squamous epithelium forms the alveoli of the respiratory membrane and the endothelium and is a minimal barrier to diffusion. Other places where squamous cells can be found include the filtration tubules of the kidneys and the major cavities of the body. These cells are relatively metabolically inactive and are associated with the diffusion of water, electrolytes, and other substances. Cuboidal cells have a shape similar to a cube, meaning its width is of the same size as its height. Columnar cells are longer than they are wide. The small intestine is a tubular organ lined with simple columnar epithelium that is made up of a single layer of cells. Unicellular glands are scattered throughout this type of tissue and secrete mucus. Translational epithelium is found in organs that can stretch such as the urothelium that lines the bladder and ureter of mammals.

The superficial layer is used to classify the stratification into simple, which consists of a single layer of cells, and stratified, which consists of more than one layer of cells. Stratified epithelium is usually composed of three layers. Cell division takes place in the basal cell layer (layer 1). Cells migrate and differentiate in the intermediate cell layer (layer 2) until they reach the superficial cell layer (layer 3). Specializations include keratinized and ciliated cells. Keratinized epithelium, which contains the cytoskeletal protein keratin and provides a tough impermeable barrier, occurs mainly in the skin. Ciliated cells have apical plasma membrane extensions composed of microtubules capable of beating rhythmically to move mucus or other substances through a duct. Cilia are common in the respiratory system.

The epithelium covers the surface of organs and is exposed to the environment and is in contact to a broad range of potentially aggressive or harmful chemical and physical conditions, which can induce a deregulation of cell division in the basal cell layer. Therefore, carcinomas of the epithelium are among the most common forms of cancer. FT-IR and Raman imaging studies were reported for many abundant carcinomas including of breast [5], prostate [6], colon [7], lung [8], bladder [9], endometrium/cervix uteri [10], stomach [11], skin [12], oral cavity [13], and esophagus [14].

3.1.2 Connective Tissue and Extracellular Matrix

Connective tissue is a group of tissue types, which significantly differ in form and function from each other, but share common features in development and structural organization. It is involved in the structure and support of an organism; fills

interspaces with ECM; and generates in the broadest sense further specialized tissues such as blood, cartilage, and bone, which are usually considered connective tissue. However, because these specialized connective tissues differ so substantially from the other tissues in this class, the phrase "connective tissue proper" is commonly used to exclude those three. Connective tissue proper is classified into the following four groups. (1) Areolar or loose connective tissue holds organs and epithelia in place. It is separated from the epithelium by the basal membrane. It contains a variety of proteinaceous fibers, including collagen and elastin, and is also important in inflammation. (2) Adipose tissue contains adipocytes, which are used for cushioning, thermal insulation, lubrication, and energy storage as fat. (3) Dense or fibrous connective tissue forms ligaments and tendons. Its densely packed collagen fibers have great tensile strength. (4) Reticular connective tissue is a network of reticular fibers made of fine collagen, Type III. These fibers form a soft skeleton to support the lymphoid organs such as lymph nodes, bone marrow, and spleen.

The ECM is defined as the collection of macromolecules outside the plasma membrane of cells in tissues and organs. ECM is the main feature of connective tissue although it is also found in epithelium, muscle, and nervous tissues. Its functions include shape forming of tissues and organs, water storage, elasticity, stability, and signal transduction. Its dominant components are various proteins, glycoproteins, and polysaccharides. The largest group of proteins is the collagen family, which consists of 28 known members. They are involved in the formation of various fibers. Carbohydrates are another large group, in particular long-chain polysaccharides called *glycosaminoglycans*. Except for hyaluronic acid, they associate with proteins forming proteoglycans.

Connective tissues have often been reported in Raman and FT-IR images adjacent to epithelium or carcinomas. Articular cartilage [15], ECM damage [16], and sarcoma, which is a neoplastic process originating within connective tissue [17], were studied by Raman spectroscopy. Applications of vibrational spectroscopic imaging to bone, which belongs to supportive connective tissue and is considered as hard tissue, are described in Chapter 4 of this book.

3.1.3
Muscle Tissue

Muscle is the contractile tissue of the body. Its function is to produce force and cause motion, either locomotion or movement within internal organs. Muscles are organized into fibers, which are mainly composed of muscle cells. Within these cells are myofibrils. They contain sarcomeres, which are composed of the filament-forming proteins actin, myosin, and titin. Muscle tissue is further separated into three distinct categories. (1) A skeletal muscle or a "voluntary muscle" is anchored to bone and is used to affect skeletal movement such as locomotion and in maintaining posture. Although this postural control is generally maintained as a subconscious reflex, the muscles responsible react to conscious control such as nonpostural muscles. An average male is made up of 40–50% of skeletal

muscle and an average female is made up of 30–40%. Skeletal muscle is further subdivided into Type I, slow oxidative fibers; Type IIa, fast oxidative glycolytic fibers; and Type IIx, fast glycolytic fibers. They differ in composition, enzyme activity, contractile speed, and color. (2) A smooth muscle or an "involuntary muscle" is found within the wall of organs and structures such as the esophagus, stomach, intestines, bronchi, uterus, urethra, bladder, and blood vessels. Unlike skeletal muscle, smooth muscle is not under conscious control. (3) A cardiac muscle is a specialized kind of muscle found only within the heart. It is also considered as an "involuntary muscle."

In the context of muscle tissue, FT-IR and Raman imaging studies have been applied more often to smooth muscle than skeletal muscle. FT-IR and Raman imaging studies of blood vessels were applied to obtain both chemical and spatial information about atherosclerosis [18]. Raman images of bronchial tissue that contains cartilage and epithelium as well as smooth muscle were reported [8]. Other FT-IR and Raman imaging studies on esophagus, intestines, and uterus concentrated rather on the epithelium than on smooth muscle because carcinomas arise in epithelial tissue.

3.1.4 Nervous Tissue

Nervous tissues are composed of nerve cells (neurons) and glial cells. These cells form the central nervous system (CNS) and the peripheral nervous system (PNS). The CNS consists of the brain and spinal cord. The PNS consists of all other nerves that do not lie within the CNS. The PNS transmits sensory stimuli to the CNS and information to muscles, glands, and sensory organs. The CNS is responsible for the assessment of stimuli and the subsequent reaction, the development of thoughts and emotions, and the formation and storage of memories. The CNS can be subdivided into gray matter and white matter. Gray matter is composed of unmyelinated neurons (neural cell bodies) as opposed to white matter, which is composed of myelinated neurons (axons). Myelin is an electrically insulating phospholipid layer that surrounds the axons of many neurons. These neurons are connected to a complex network that processes and transmits cellular signals. Glial cells in the human brain are smaller and more abundant than neurons. They are classified according to their structure and function into astrocytes, oligodendrocytes, microglia, ependymal cells, radial glia, Schwann cells, and satellite cells. The main functions of glial cells are to surround neurons and hold them in place, to supply nutrients and oxygen to neurons, to insulate one neuron from another, and to destroy pathogens and remove dead neurons. Glial cells retain the ability to undergo mitosis in adulthood while neurons cannot. This view is based on the general deficiency of the mature nervous system in replacing neurons after an insult or injury, while very often there is a profound proliferation of glia, called *gliosis*, near or at the stage of damage. However, there is also recent evidence for neural stem cells in few regions of the mature nervous system that can generate new neurons. The CNS is enveloped by the meninges. The meninges are a system of connective

tissues that consist of the dura mater, the arachnoid mater, and the pia mater. The arachnoid and pia mater are sometimes together called the *leptomeninges*. The primary function of the meninges is to protect the CNS.

The application of FT-IR microspectroscopy was reviewed to analyze CNS tissues and neurodegenerative diseases such Alzheimer's disease, Parkinson's disease, multiple sclerosis, transmissible spongiform encephalopathies, and brain tumors [19]. Brain tumors can be divided into primary brain tumors, which originate from brain cells, and secondary brain tumors, also called *brain metastases*, which originate from tumors outside the brain. As neurons largely lost the ability to divide, most primary brain tumors are derived from glial cells. The broad field of neuro-oncological applications of FT-IR and Raman imaging studies includes primary brain tumors [20], tumors of the meninges called *meningeomas* [21], *secondary brain tumors* [22], and a *murine brain tumor model* [23].

3.2 Preparation of Soft Tissue for Vibrational Spectroscopic Imaging

3.2.1 General Preparation Strategies

Due to the high sensitivity of vibrational spectroscopy, accurate sample preparation procedures are essential in order to obtain reproducible results and to transfer the results from one laboratory to another. Major advantages of both IR and Raman spectroscopic studies are that they are nondestructive and require minimal or no preparation that make them also attractive for *in vivo* applications. However, depending on the experimental configuration and the origin of the tissue, samples often have to be processed before image acquisition in order to fulfill the specific requirements of the spectroscopic method. Standardized preparation procedures have not been defined yet. The effects of *ex vivo* handling procedures (drying, freezing, thawing, and formalin fixation) on mammalian tissue [24], the effects of fixation on human bronchial tissue [25], and the efficacy of dewaxing agents on cervical tissue [26] were described for Raman spectroscopy. Effects of light exposures on oxidation of unsaturated fatty acids in biological tissue were described for IR spectroscopy [27]. Some general considerations are given next.

To date, much of the work on vibrational spectroscopic imaging of soft tissues had been carried out on *ex vivo* specimens that were either snap frozen at the time of collection or fixed using formalin or transferred to optimal cutting temperature (OCT) medium or embedded in paraffin. Due to the time lapse between tissue excision and spectroscopic examination, such preservations are performed by many groups in order to maintain the biochemical state of the specimens. Fixation by formaldehyde solution (formalin) preserves tissue by preventing autolysis and stabilizing tissue structure. Formaldehyde reacts with the amino groups of amino acids and promotes coagulation, not precipitation of proteins. Paraffin and OCT serve as support media. Subsequently, thin tissue sections are cut

using a microtome in case of paraffin-embedded tissue or a cryotome in case of snap-frozen tissue. Fixation of thin tissue sections by air drying also works surprisingly well. After the water content has been vaporized in a dry atmosphere, the proteins are precipitated to form an insoluble mass that is resistant to degradation. Spectral data collected from samples that have been fixed in this manner reveal no apparent spectral changes when compared directly to those that have been formalin-fixed [28].

Staining reagents such as hematoxylin for the cell nuclei and eosin for the cytoplasm give additional spectral contributions. Therefore, unstained tissue sections are usually prepared for FT-IR and Raman spectroscopic studies, although there are also different opinions. In a study of hematoxylin and eosin (H&E)-stained breast tissue sections by FT-IR spectroscopy in the attenuated total reflection (ATR) mode (see Chapter 9), spectral contributions of the staining reagents were found to be negligibly small [29]. Due to the nondestructivity of the methods, tissue sections can be stained by H&E or by more specific stains after data acquisition, thus allowing visual imaging and pathological examination. For a pre-assessment and selection of regions of interest before vibrational spectroscopic image acquisition, a parallel section can be prepared on standard glass slides, stained, and inspected.

The process of paraffin embedding requires fixation and sample dehydration before embedding and removal of the support medium by organic solvents after sectioning. Tissues are dehydrated by dipping in a graded series of ethanol/water mixtures and then by bathing in xylene or benzene. A danger of this process is that the conformation of proteins and structure of cells might be distorted, and the chemical composition of the sample is altered, for example, hydrophobic constituents, such as tissue lipids, will be partly dissolved by solvent treatment as well. One should be aware that each processing step may change the chemical or molecular properties of the sample. However, these changes induced by the processing procedures may not be a cause for concern as long as one protocol is strictly adopted throughout a study.

Two new approaches were reported in the literature. First, FT-IR imaging was applied directly on formalin-fixed paraffin-embedded samples of nonmelanoma skin cancers [12]. Chemometric and multivariate statistical analyses were developed to generate an automated IR-based histology without any chemical dewaxing. Second, to avoid denaturation of biomolecules in dried tissue section due to dehydration, samples were stored on dried ice and transferred into aqueous buffer during Raman image acquisition [30]. These specimens were found to contain cell nuclei with enhanced spectral contributions of nucleic acids, lipids, and cholesterol, which did not form microcrystals. Analysis of such nondried specimens by vibrational spectroscopy provides a closer model to *in vivo* applications and offers complementary information for histopathological inspection because lipids that are washed out during standard protocols can be assessed as well. The amount and composition of lipids are important diagnostic features in atherosclerotic plaques and brain tumors.

3.2.2
Vibrational Spectra of Reference Material

The vibrational spectra of reference material are introduced in Figure 3.1, which belong to the main components of soft tissue. The IR spectrum (trace A) and Raman spectrum (F) of the all-beta protein concanavalin A are shown in Figure 3.1. IR bands due to the peptide backbone with β-sheet secondary structures are found at 3284 (amide A), 1636 (amide I), 1531 (amide II), and 1235 cm^{-1} (amide III). Bands at 1403 (COO^-) and 2963, 2874, 1455 cm^{-1} (CH_3) are assigned to amino acid side chains. These bands are located in the Raman spectrum at similar positions at 1398 and 1449 cm^{-1}. The Raman amide I band is centered at 1672 cm^{-1}, the amide III band at 1238 cm^{-1}, and the weak amide II band is not observed. Instead, other Raman bands of amino acids are identified at 759 and 1555 cm^{-1} for Trp; 621, 1003, 1031, and 1208 cm^{-1} for Phe; 643, 829, and 853 cm^{-1} for Tyr; and 1126, 1317, and 1340 cm^{-1} (CH_2/CH_3) for aliphatic amino acids. The IR spectrum (B) and Raman spectrum (G) of the all alpha protein bovine serum albumin show a number of differences. The amide bands

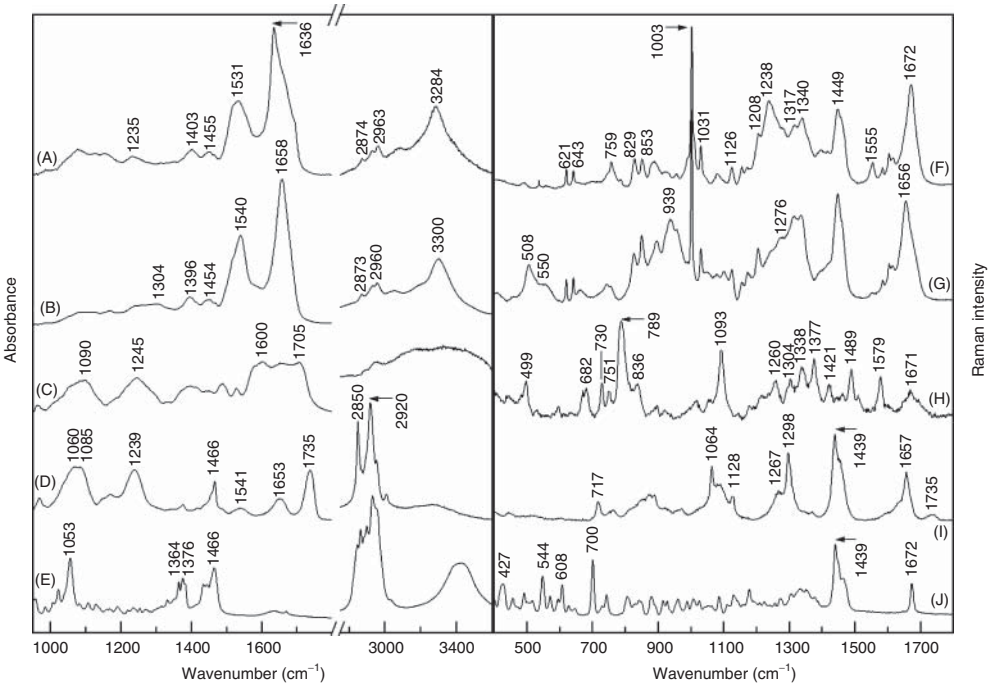

Figure 3.1 IR spectra from 950 to 1800 and from 2750 to 3600 cm^{-1} (A–E) and Raman spectra from 400 to 1800 cm^{-1} (F–J) of the protein concanavalin A (A, F), the protein bovine serum albumin (B, G), DNA from calf thymus (C, H), a lipid extract (D, I), and cholesterol (E, J). The wavenumber scale of the IR spectra in the interval 2750–3600 cm^{-1} is twofold compressed.

are shifted because of the predominant α-helical secondary structures to 1304, 1540, 1658, and 3300 cm^{-1} (B) and to 1276 and 1656 cm^{-1} (F). Additional Raman bands are found at 939 cm^{-1} because of C–C vibrations of α-helices and at 508 and 550 cm^{-1} because of S–S vibrations of disulfide bridges. Other intensity differences are caused by changes in primary and tertiary structures. The most intense bands in the IR spectrum of DNA (C) correspond to vibrations of the nucleotides in the interval 1600–1705 cm^{-1} and to antisymmetric and symmetric vibrations of the phosphodioxy groups of the backbone at 1245 and 1090 cm^{-1}, respectively. The Raman spectrum of DNA (H) provides more information related to nucleotides thymine (751, 1377, 1671 cm^{-1}), cytosine (789, 1260 cm^{-1}), adenine (730, 1304, 1338 cm^{-1}), and guanine (499, 682, 1489, 1579 cm^{-1}). Further bands are assigned to the phosphodiester group (836 cm^{-1}), phosphodioxy group (1093 cm^{-1}), and CH_2 group (1421 cm^{-1}) of the backbone.

The IR spectrum (D) of a brain lipid extract (Fluka No. 53282, Taufkirchen, Germany) in Figure 3.1 contains bands of phosphate groups of phospholipids (1085, 1239 cm^{-1}), ceramide groups of glycolipids (1541, 1653 cm^{-1}), C=O groups (1735 cm^{-1}), C–C groups (1060 cm^{-1}), and CH_2 groups (1466, 2850, 2920 cm^{-1}). The corresponding bands in the Raman spectrum (I) are at 1064 (C–C), 1085 (PO_2), 1439 (CH_2), and 1735 cm^{-1} (C=O). Additional Raman bands are assigned to the choline groups of hydrophilic lipid head groups (717 cm^{-1}) and to C=C groups in unsaturated fatty acid side chains (1267, 1657 cm^{-1}). There are numerous bands of the aromatic system of cholesterol with the most intense IR bands at 1053, 1364, 1376, and 1466 cm^{-1} (E) and the most intense Raman bands at 427, 544, 608, 700, 1439, and 1672 cm^{-1} (J). More comprehensive band assignments of biomolecules have been published in the *Handbook of Vibrational Spectroscopy* [31] and by De Gelder *et al*. [32]. Altogether, the spectra demonstrate that they provide a sensitive fingerprint for each molecule and that IR and Raman spectra complement each other to some extent.

3.2.3
Preparation for FT-IR Imaging

If FT-IR images are collected in a transmission mode, samples have to be sufficiently thin and the substrates have to be transparent to the wavelength range of the probing radiation in the mid-IR range from 400 to 4000 cm^{-1}. In order to fulfill these conditions, tissue sections of typically 5–20 µm thickness are mounted on substrates made from materials such as CaF_2, BaF_2, or ZnSe. In particular, CaF_2 is a material with excellent spectral properties for FT-IR imaging of soft tissue. In contrast to BaF_2, CaF_2 is nearly insoluble in water and thus allows post-staining of the sections by H&E. In contrast to ZnSe, the refractive index of CaF_2 is relatively low, so that the extend of optical fringing and chromatic aberrations introduced by the window material are reduced [33]. Disadvantages of CaF_2 are the high price (~50€ per slide) and decreasing transmission toward zero for wavenumbers below 1000 cm^{-1}. Glass slides coated with a thin metal layer are also used as less expensive substrates (~2$ per slide) for thin tissue sections (e.g., MirrIR slides by Kevley,

Chesterland, OH, USA). Visible light penetrates these slides, allowing the tissue to be visually examined by light microscopy. IR radiation is reflected by these slides allowing IR spectroscopy in reflection–absorption mode. However, the IR spectra collected from these samples are often affected by dispersion artifacts [34]. Within the last 5 years, two independent algorithms were developed to correct these artifacts [35, 36]. The computation of first algorithm is time consuming by iterative fitting around an external reference spectrum, whereas the second algorithm can be easily adapted to larger FT-IR images and it uses an internal spectrum for correction. Another problem of FT-IR spectroscopy in reflection–absorption is an electric field standing wave effect that cannot be corrected yet [37]. Therefore, slides with reflective metal coating should be used with caution for FT-IR spectroscopy.

Thin tissue sections rapidly dry under ambient conditions, which improve the penetration of IR radiation in tissue because water strongly absorbs IR radiation. Evaporation of water induces molecular changes in tissue constituents such as proteins, lipids, and nucleic acids. Proteins may denature, lipids may crystallize (see Section 3.2.4), and nucleic acids may undergo a change from the natural B-conformation. FT-IR images can also be collected from nontransparent samples in backscattered geometry using the ATR mode (see Chapter 9). Here, samples are in contact to an ATR crystal made from IR-transparent material of high refractive index. When IR radiation hits the ATR crystal at a proper angle of incidence, the radiation undergoes total internal reflection. Inside the ATR crystal a standing wave of radiation is established, called an evanescent wave, that penetrates a little beyond the surface. A sample that is in contact with the crystal can interact with the evanescent wave and absorb IR radiation resulting in an IR spectrum. As penetration of IR radiation is restricted to few micrometers (typically on the order of 0.5–3.5 μm), it is important to establish a close contact between the sample and the ATR crystal, which is sometimes difficult for hydrated tissue and might be destructive for tissue sections.

The IR spectra (A–C) in Figure 3.2 demonstrate the effect of treating tissue sections with polar and nonpolar solvents. The IR spectrum (A) was obtained from a dried tissue section of a glioblastoma multiforme (GBM) brain tumor. In contrast to the spectra in Figure 3.1, it is evident that this tissue is mainly composed of proteins and lipids. IR spectrum (B) was acquired from a consecutive tissue section that was treated for 10 min with a drop of toluene. The overlay of the normalized spectra indicates that lipid-associated bands at 1740, 2852, and 2925 cm^{-1} decrease. IR spectrum (C) was acquired from a consecutive tissue section that was treated for 10 min with a drop of water. The overlay of the normalized spectra indicates that lipid-associated bands near 1070, 1230, 1740, 2852, and 2925 cm^{-1} increase. In summary, the relative intensity ratios of lipid-to-protein bands increase in the order (C)>(A)>(B). This is consistent with a removal of lipids by toluene and with a removal of proteins by water. Furthermore, the shapes of the amide bands change that is consistent with secondary structure changes in proteins.

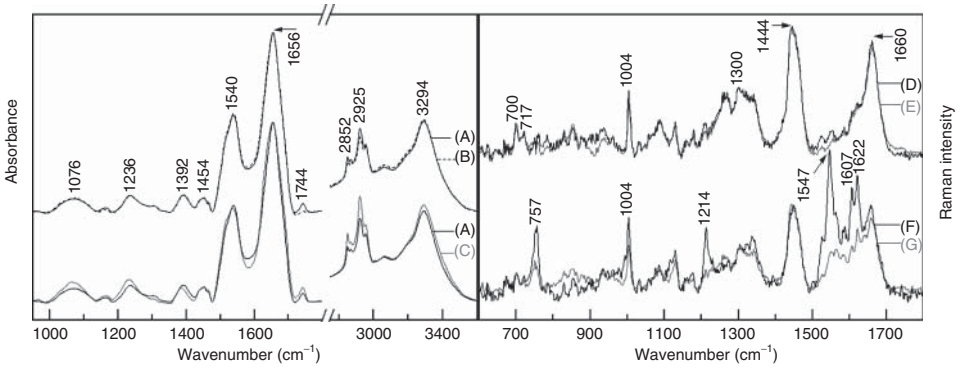

Figure 3.2 IR spectra from 950 to 1800 and from 2750 to 3600 cm^{-1} (A–C) and Raman spectra from 400 to 1800 cm^{-1} (D–G) of brain tissue. Untreated tissue section (A), tissue section after treatment with toluol (B), and tissue section after treatment with water (C). Native tumor tissue 1 h (D) and 10 h (E) after surgery. Native tumor tissue with hemorrhage 1 h (F) and 10 h (G) after surgery. The wavenumber scale of the IR spectra in the interval 2750–3600 cm^{-1} is twofold compressed.

3.2.4
Preparation for Raman Imaging

Raman images of tissues are usually collected in a backscattering geometry using near infrared (NIR) radiation excitation between 700 and 850 nm. Then, most Stokes-shifted Raman bands are below 1100 nm, which enables their sensitive detection by silicon-based NIR-optimized charge-coupled device (CCD) cameras. In the visible wavelength range (400–700 nm), most tissues show high absorbance mainly because of hemoglobin, which limits the penetration of the incident and scattered photons. Furthermore, strong autofluorescence is usually excited using visible lasers, which masks the inherently weak Raman signals. Alternatively, it is possible to use UV light at wavelengths below 270 nm to circumvent the fluorescence interference problem. Due to absorption of UV light by nucleotides and aromatic amino acids, their Raman signals are enhanced by a resonance effect. However, tissue penetration depth is only in the order of micrometers and one has to be careful with tissue damages when using UV light. The autofluorescence background can also be suppressed by shifted subtracted Raman spectroscopy [38], shifted excitation Raman difference spectroscopy [39], multi-excitation Raman spectroscopy [40], and modulated wavelength excitation Raman spectroscopy [41]. The principle of these approaches is that the broad fluorescence emission does not significantly vary upon multiple wavelength excitation in contrast to the Raman signatures with narrow Raman bands. In the context of tissue, modulated wavelength excitation Raman spectroscopy has been demonstrated to suppress ambient light and also system transfer function including etaloning effects [42].

Thin sections are mounted on substrates with low background signals. Upon 785 nm excitation, CaF_2 or BaF_2 slides have a particularly low background and they allow also collecting FT-IR images. Tissue can also be studied in its native state under *in vivo* conditions by Raman spectroscopy as water contributes only marginally to the Raman signals. Light penetration depends on factors such as excitation wavelength, excitation intensity, sample composition, and optical geometry. Using low magnification objectives in combination with fiber optic probes or with microscopes, radiation might penetrate several hundreds of micrometers. Chapter 13 of this book describes how to collect spectral information from deeper layers. Using confocal microscopes with high magnification/high numerical aperture objectives, diffraction-limited lateral resolution can be achieved below 1 µm and the depth of view is reduced to a few micrometers. As the laser needs to be accurately focused to optimally excite and collect the Raman signals, a fixed focus can only be applied for flat samples. For uneven samples, the focus has to be adjusted before each measurement. Autofocus routines can be used for adjustment during Raman image acquisition in the mapping mode.

The Raman spectra (D–G) in Figure 3.2 demonstrate the effects of aging for a native specimen of a GBM brain tumor. Spectra (D, F) represent two mean spectra of a Raman image, which was acquired from the specimen just 1 h after surgery. Main spectral contributions of proteins are identified at 1004, 1450, and 1660 cm^{-1}; of lipids at 717, 1300, and 1440 cm^{-1}; and of cholesterol at 700 and 1440 cm^{-1}. Additional bands at 757, 1214, 1547, 1607, and 1622 cm^{-1} in spectrum (F) are assigned to hemoglobin of red blood cells [43]. These bands are enhanced by a resonance effect because the heme group partly absorbs the excitation radiation. The Raman spectra (E, G) represent two mean spectra of a Raman image, which was acquired from the same specimen 10 h after surgery. Overlay of Raman spectra (D) and (E) indicates that both spectra corresponding to tumor tissue are almost identical. However, overlay of Raman spectra (F) and (G) indicates differences in tumor tissue with high blood cell content. The total and relative intensity changes point to a degradation and deoxygenation of the heme group. Further changes were observed after freezing and thawing. Details have been published [44]. Upon drying of brain tissue sections, crystallization of hydrophobic components and denaturation of biomolecules are induced. The Raman spectra of these crystals indicated that they contain almost pure cholesterol or cholesterol ester [45, 46]. This artifact can only be avoided if nondried tissue sections are studied as shown previously for brain tissue [30, 47]. In the latter studies, tissue sections were immersed in buffer and the Raman spectra were acquired using a water immersion objective. Hyperspectral unmixing of Raman images of such tissue sections resolved the inhomogeneous distribution of lipids, cholesterol, cholesterol ester, and other constituents without drying effects. In summary, effects of aging, freezing, subsequent thawing, and drying have to be considered before results are transferred to spectra recorded under *in vivo* situations.

3.3 Applications to Soft Tissue

3.3.1 Colon Tissue

Colon tissue was selected as a model for the comparative analysis of soft tissue by FT-IR and Raman imaging studies at low and high lateral resolution because it contains all four major tissue types such as muscle tissue, connective tissue, epithelium, and nerve cells [48]. Another study compared CARS images at 2850, 1660, 1450, and 1000 cm^{-1} and Raman images from colon tissue sections [49].

The vibrational spectroscopic fingerprints of normal tissues and their distribution in control samples were determined. The compilation of such data is important before the methods can be applied to pathological colon tissue such as colorectal adenocarcinoma, which is the third most common form of cancer and the second leading cause of death among cancers in the Western world. Colorectal adenocarcinomas originate from epithelial cells and are able to infiltrate the subjacent layers of colon and rectum. A colon specimen was obtained with written parental consent from the colostomy site of a neonate with an anorectal malformation. The studied sample represents a fraction of normal colon tissue. A tissue section of 20 µm thickness was prepared by a cryotome at temperatures between −18 and −22 °C. Figure 3.3 displays the photomicrograph of an unstained thin section of colon tissue (b), an FT-IR image (a), and a Raman image (c). The photomicrograph (e) shows a ganglion in the boxed area in (b) at a 15-fold magnification. The FT-IR and Raman microscopic images of this area are included in (d) and (f), respectively.

The images were acquired by an FT-IR imaging system, which was coupled to a 64 × 64 focal plane array (FPA) detector (Bruker Optik GmbH, Ettlingen, Germany). The field of view in the macro chamber IMAC® (Bruker) without magnification using a 4 × 4 mm^2 FPA detector was 4 × 4 mm^2. Because the size of the tissue section exceeded the field of view, three individual images were recorded and combined in Figure 3.3a. The field of view in the IR microscope Hyperion (Bruker) with 15× magnification using a 2.5 × 2.5 mm^2 FPA detector was reduced to 170 × 170 μm^2. A mosaic of 3 × 3 images was recorded and combined in Figure 3.3d. Although each pixel corresponds to an area of just 2.6 × 2.6 μm^2, the actual lateral resolution is limited by diffraction to 10 µm at 1500 cm^{-1} [50].

The Raman images were acquired by a Raman system, which consists of a 785 nm diode laser, a microscope, a notch filter, a spectrograph with a reflective grating, and a CCD detector (Renishaw, Wotton-under-Edge, UK). Using a motorized sample stage, the spectra were sequentially registered from a predefined grid. The grating was moved during acquisition in order to access an extended spectral range from 600 to 1800 cm^{-1}. The Raman image in Figure 3.3c contained 79 × 79 spectra at a step size of 62 µm. The step size was selected in order to compare the data with the FT-IR image, where each pixel corresponds

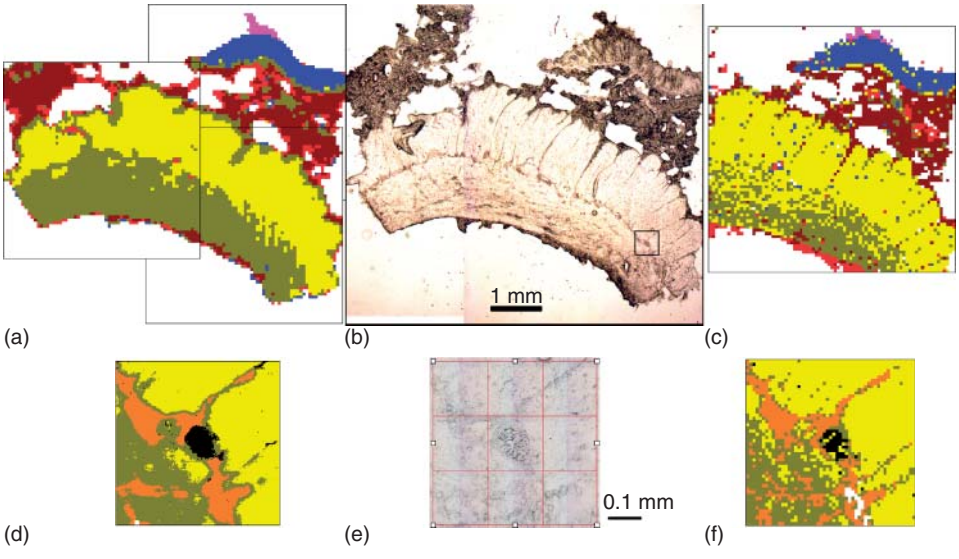

Figure 3.3 FT-IR images (a, d), photomicrographs (b, e), and Raman images (c, f) of a colon tissue section. The region of interest with a ganglion in the center (e) is indicated in (b) by a box. The color code represents the segmentation of spectra by cluster analysis: mucus (magenta), mucosa (blue), submucosa (red, brown), circular muscle (yellow), longitudinal muscle (olive), fibrous septa (orange), and ganglion (black). Further details are presented in the text.

to an area of $62 \times 62\,\mu m^2$. The laser of ~25 mW intensity was focused onto the sample by a 50×/NA 0.75 objective to a rectangular spot of $\sim 2 \times 7\,\mu m$. The Raman image (f) contained 53×52 spectra at a step size of 10 µm.

A widely used multivariate method to segment vibrational spectroscopic images is cluster analysis. After preprocessing procedures, the spectra are grouped according to their similarity. The group or cluster memberships are color coded for representation. Here, preprocessing encompassed removal of low intensity spectra, subtraction of background, baseline and offset, and normalization. These procedures separate variances because of physical effects such as elastic light scattering and sample thickness from the chemical information. The algorithm k-means cluster analysis grouped the spectra into a predefined number of groups using an Euclidean distance metric. Removed spectra appear as white regions in the vibrational spectroscopic images. Further details have been published [48].

The resulting clusters in Figure 3.3a,c,d,f correspond to the gross architectural division of the colon tissue. The mucosa (blue) is the innermost, highly specialized layer of the gastrointestinal tract that is responsible for absorption and secretion, which are important processes in digestion. Some mucus (magenta) that is secreted by epithelial glands is found at the top part. A thin layer of muscle tissue (olive/yellow), called *muscularis mucusae*, is located between mucosa and submucosa (red/brown). The submucosa consists of a dense irregular layer of connective

tissue. Below the submucosa, a circular muscle layer (yellow) and a longitudinal muscle layer (olive) are identified. Serosa (red/brown), which belongs to the connective tissue class, is found at the bottom. Nerves and ganglia are the neurons of the enteric nervous system that controls the gastrointestinal tract. Ganglia are often connected with each other to form a complex system known as *plexus*. A ganglion (black) of the myenteric plexus between the longitudinal and circular muscle layers and fibrous septa (orange), which surrounds the ganglion, are resolved at higher magnification.

The cluster-averaged spectra of the six classes in Figure 3.4 reveal information about the underlying spectral properties. Calculating averages offers the advantages that pixel-to-pixel variations are reduced and the signal-to-noise ratios (SNRs) are improved. This was particularly important for Raman spectra, which had typical SNR of 34 under the applied experimental conditions. The SNR of single spectra could be increased by longer exposure times, which however would also increase the total acquisition time. As the current exposure times were already as long as 27 h (Figure 3.3f) and 62 h (Figure 3.3c), a further increase is impracticable. This low SNR might contribute to the noisy appearance in the

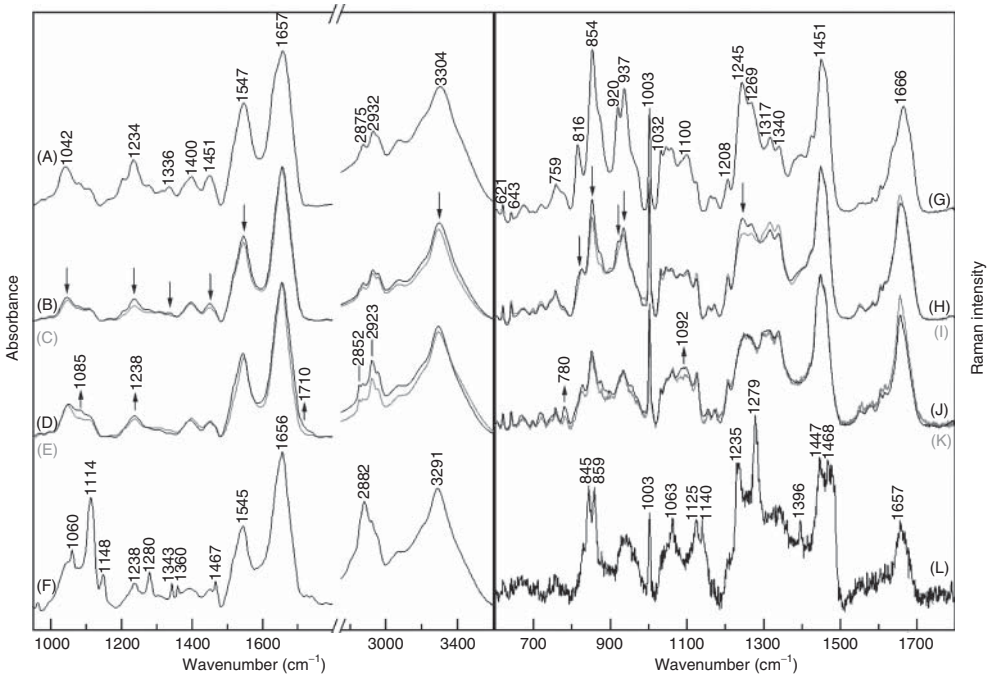

Figure 3.4 IR spectra from 950 to 1800 cm^{-1} and from 2750 to 3600 cm^{-1} (A–F) and Raman spectra from 400 to 1800 cm^{-1} (G–L) represent the clusters of the images in Figure 3.3: submucosa (A, G), longitudinal (B, H) and circular (C, I) muscle layers, ganglion (D, J), mucosa (E, K), and mucus (F, L). The wavenumber scale of the IR spectra in the interval 2750–3600 cm^{-1} is twofold compressed.

cluster assignments of the Raman images in Figure 3.3. As a consequence of the small clusters and low signal intensities for the ganglion (black) and for mucus (magenta), the averaged spectra (K) and (L) have lower SNR than spectra (G, H, I). Data acquisition by FT-IR imaging is much faster yielding higher quality spectra. Typical acquisition times were between 1 and 5 min per FT-IR image, which consisted of 4096 individual spectra with SNR between 500 (Figure 3.3a) and 1000 (Figure 3.3d). In spite of these differences, the cluster segmentations of the FT-IR and Raman images coincide well.

The IR spectra in Figure 3.4 are normalized to equal intensities of the amide I band near 1657 cm^{-1} and the Raman spectra to equal intensities of the CH_2/CH_3 bands near 1451 cm^{-1}. Compared with the previous spectra of reference material in Figure 3.1 and of brain tumors in Figure 3.2, the IR and Raman spectra of submucosa contain additional spectral contributions, most evident at 1042, 1234, 1336, 1451, and 1547 cm^{-1} (A) and at 759, 816, 854, 920, 937, and 1245 cm^{-1} (G). These bands are assigned to collagen, which is a major component in connective tissue. Collagen has an unusual amino acid composition with high content of hydroxyproline, proline, and glycine and a special coiled-coil triple-helical secondary structure. The reduced intensities of collagen-associated bands constitute the main difference between submucosa (A, G) and muscle tissue and between longitudinal muscle layer (B, H) and circular muscle layer (C, I). Smooth muscle tissue often must be stretched, so elasticity is an important attribute. Therefore, smooth muscle cells secrete a complex ECM including collagen. The detection of the relatively small decrease of collagen bands in circular versus longitudinal muscle requires spectra of high SNR, which is the case for the IR spectra, but which is not the case for the Raman spectra before averaging as stated above. This result is consistent with some overlap between the yellow and the olive clusters in the Raman images of Figure 3.3c,f. The collagen-associated bands further decrease in the Raman spectra of mucosa (J) and of the ganglion (K). More intense Raman bands at 780 and 1092 cm^{-1} point to higher DNA content in mucosa. This observation is confirmed by more intense IR bands at 1085, 1238, and 1710 cm^{-1} in spectrum (D) than in (E) that are assigned to DNA phosphate groups and to carbonyl groups of nucleotides, respectively. More intense IR bands at 2852 and 2923 cm^{-1} compared with IR spectra (A – D) indicate that more intense lipid bands also contribute to the bands near 1051, 1085, and 1238 cm^{-1}. Due to the overlap of spectral contributions from lipids, DNA, and collagen in the interval 1000 – 1300 cm^{-1}, it is difficult to obtain this information from the IR spectra alone. Raman spectra provided complementary information about DNA and collagen contents. The IR (F) and Raman (L) spectra of mucus are markedly different from the previous spectra. Additional IR bands are found at 1060, 1114, 1148, 1238, 1280, 1343, 1360, 1467, and 2882 cm^{-1}, and additional Raman bands are found at 845, 859, 1063, 1125, 1140, 1235, 1279, 1396, and 1468 cm^{-1}. The spectral signatures are consistent with carbohydrates and peptides. The main constituent of mucus is mucin, which is known to consist of highly glycosylated peptides. Furthermore, some bands point to poly(ethylene glycol) 4000, which was administered before surgery to flush the gastrointestinal tract.

This example demonstrates that FT-IR and Raman imaging studies are able to distinguish different tissue types in unstained tissue sections. Lower lateral resolution in the 60 µm range gave an overview over an extended area. Higher lateral resolution in the 10 µm range identified a single ganglion. As the diffraction-limited resolution of Raman imaging is below 1 µm, it was recently shown that even subcellular features could be resolved in ganglia [48]. The underlying spectra reveal detailed information about the chemical composition. The high DNA content in mucosa indicates a high metabolic activity. Together with the fact that the mucosa is the outermost layer of the colon and therefore it is exposed to various, potentially carcinogenic substances, this explains why the carcinogenesis most often occurs from the mucosa and the epithelial layer. The combined use of both modalities offers advantages over the individual application of Raman and FT-IR imaging.

As a consequence of the several orders of magnitude-enhanced signal intensities, the CARS detection scheme can be coupled to laser scanning microscopes that enable acquisition times of a few seconds per image or less. CARS and Raman microscopy have been applied as complementary techniques to study colon tissue sections [49]. Raman images were registered at 785 nm excitation and 0.5 µm step size using the confocal Raman microscopy CRM 300 (WITec, Ulm, Germany). The in-house built CARS microscope consisted of the pump laser at 532 nm, a Ti-sapphire laser generating 100 fs pulses at 76 MHz, two optical parametric oscillators, a laser scanning microscope, and optics to synchronize the laser pulses in space and time [51]. Variations within a specimen could be visualized in chemical images of CARS and Raman images by plotting band intensities at selected wavenumbers. Figure 3.5a,d plots both the Raman band at 1440 cm^{-1} and the CARS signal at 2850 cm^{-1}, respectively, representing predominantly the distribution of lipids. A small gap is similarly resolved in both images. Figure 3.5b and

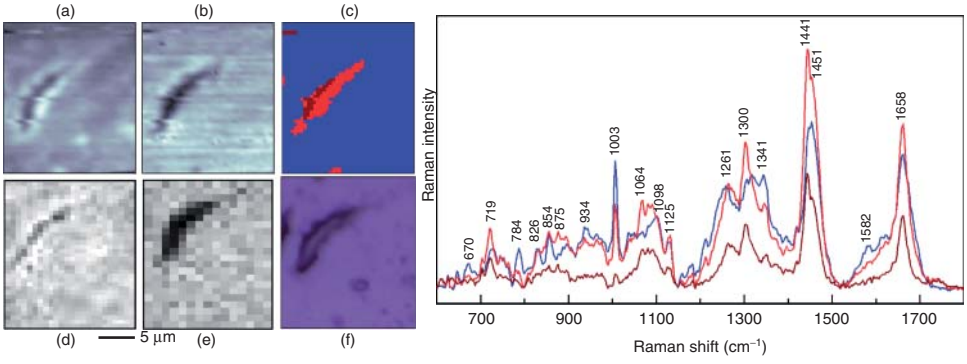

Figure 3.5 Chemical images of lipids (a, d) and proteins (b, e) in a colon tissue section obtained by plotting the Raman band near 1440 (a) and 1000 cm^{-1} (b) and the CARS signal at 2850 (d) and 1000 cm^{-1} (e). For comparison, the cluster membership of the Raman image (c) and the photomicrograph (f) are included. Mean cluster spectra represent tissue (blue), strong lipid intensities (red), and weak lipid intensities (brown).

E plots the Raman band and CARS signal at 1000 cm^{-1} that are assigned predominantly to proteins. A wider gap is similarly resolved here. Cluster analysis of the Raman image identifies three main groups of spectra that are displayed in Figure 3.5. The spectrum of the tissue (blue cluster) contains spectral contributions of proteins and nucleic acids, whereas lipid bands are weak. The intensities of lipid bands increase and the intensities of proteins and nucleic acids decrease in the spectra of the gaps. It can be concluded that the gap is filled with lipids of different density. The result of the underlying chemical composition can only be obtained by multivariate analysis of hyperspectral Raman data such as k-means cluster analysis. Similar observations were also made for brain tissue as described in the later section.

3.3.2 Brain Tissue and Brain Tumors

Brain tissue was selected for the comparative analysis of dried, thin tissue sections by FT-IR imaging and nondried, native tissue by Raman imaging. Further experiments were performed using CARS microscopy because brain tissue contains high lipid content, and lipids provide a high contrast in CARS images. Potential applications are the histopathological assessment of tissue sections to determine the tumor type, tumor grade, or the primary tumor of brain metastases, and the intraoperative delineation of the tumor margins, which is particularly important in neurosurgery in order to maximize tumor removal with minimal neurological damage. Due to the large number of FT-IR images, classification models have been trained that could identify several nonpathological and pathological tissue types based on their IR spectroscopic fingerprint. Recently, a large number of Raman images have also been collected, which give similar classification results. Furthermore, the high spatial resolution in Raman and CARS images enabled to identify cellular details that also correlated with histopathological findings. Raman images of whole mouse brains and murine brain tumors under *in vivo* conditions were also collected using a fiber optic probe.

3.3.2.1 Mouse Brains

An important step in the development of new diagnostic tools is their application in animal models. Figure 3.6 displays the FT-IR image (a) and photomicrograph of an unstained thin section of murine brain (b), and the Raman image of the consecutive native tissue sample (c). The box indicates the approximate region of interest which was analyzed by Raman imaging. The color code represents the score plot of a principal component analysis (PCA), which constitutes another widely used multivariate method to analyze vibrational spectroscopic images. PCA calculates the eigenvalues (scores) and eigenvectors (loadings) of the data matrix. The first principal components explain most of the variance within the data sets, whereas the higher principal components are dominated by noise. The PCA was performed in the high wavenumber range from 2800 to 3000 cm^{-1} which has previously been suggested to distinguish morphological structures in brain tissue

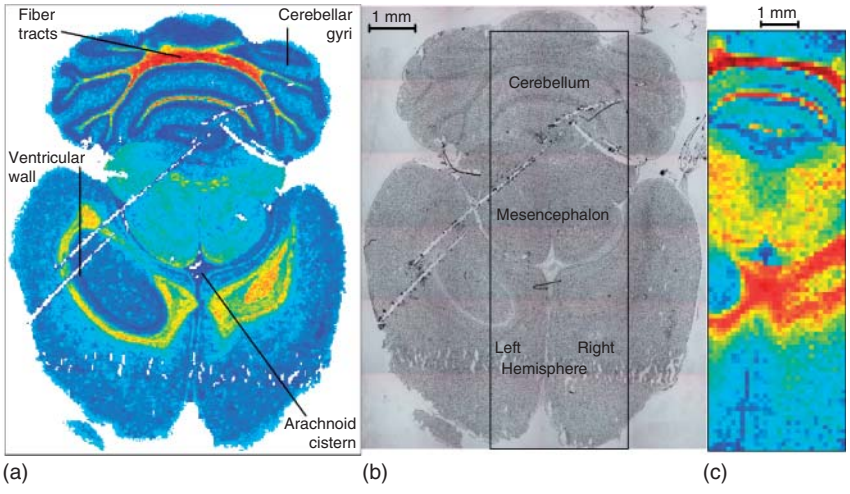

Figure 3.6 FT-IR image (a), photomicrograph (b), and Raman image (c) of a mouse brain tissue section. The approximate position of the Raman image is indicated in (b) by a box. The color codes represent the second principal component scores.

[52]. The FT-IR image visualizes fiber tracts and cerebellar gyri in the cerebellum at the top, the mesencephalon in the middle part, the arachnoid cistern below the mesencephalon, and the ventricular wall within a ventricle of the left hemisphere. Distortion of the soft pristine brain tissue after transfer to the sample compartment was small, so the Raman image coincides remarkably well with the FT-IR image. Larger structures such as the fiber tracts, the mesencephalon, the arachnoid cistern, and the ventricle of the left hemisphere are also identified. Finer structures such as the cerebellar gyri and the ventricular wall are not resolved, probably because the Raman map was recorded at a larger step size.

The FT-IR image was acquired by a different FT-IR imaging system than described in Section 3.3.1. The applied system Spotlight 300 (Perkin Elmer, Waltham MA, USA, cf. Chapter 1) was equipped with a small array of 16 detector elements, which were rapidly scanned over a predefined grid of 310×398 pixels. Each pixel corresponds to an area of $25 \times 25\ \mu m^2$, which enabled to resolve smaller details in the FT-IR image (Figure 3.6a) than in the Raman image (Figure 3.6c).

The Raman image was acquired by a Raman system, which consists of a 785 nm diode laser, a fiber optic probe (Inphotonics, Norwood, MA, USA), a notch filter, a spectrograph with a transmissive holographic grating, and a CCD detector (Kaiser Optical Systems, Ann Arbor, MI, USA). The specimen was placed onto a motorized stage, the laser radiation was focused by the probe to a spot of 60 µm, the scattered light was collected by the probe, and spectra were sequentially registered from a 30×91 grid at a step size of 120 µm. The grating covered the entire spectral region from 200 to 3550 cm^{-1} without moving upon each exposure of the CCD. During data acquisition, the specimen was covered by a CaF_2 window and sealed in a compartment in order to prevent the sample from drying.

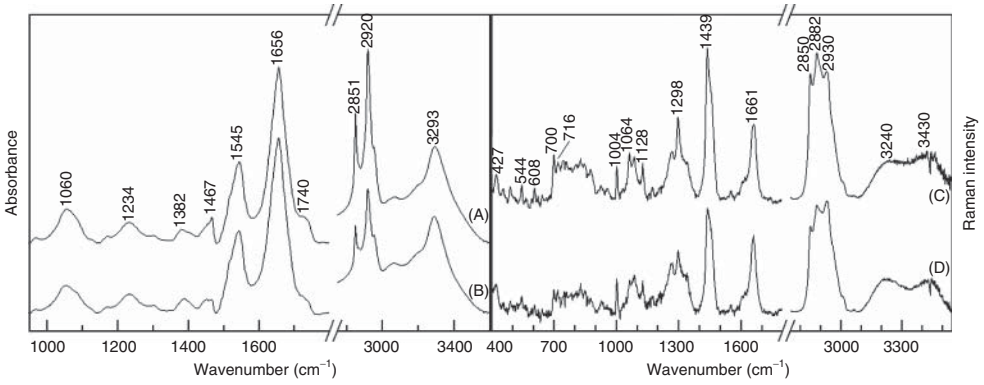

Figure 3.7 IR spectra from 950 to 1800 and from 2750 to 3600 cm^{-1} (A, B) of a mouse brain tissue section. Raman spectra from 400 to 1800 and from 2750 to 3550 cm^{-1} (C, D) of native mouse brain tissue. The wavenumber scale of the IR spectra in the interval 2750–3600 cm^{-1} is twofold compressed.

The IR and Raman spectra in Figure 3.7 were extracted from the images in Figure 3.6. They represent the fiber tracts (traces A, C) and the mesencephalon (B, D). The spectra contain more intense spectral contributions of lipids and cholesterol relative to the protein bands than the spectra of brain tumors in Figure 3.2. This is evident from the IR bands at 1060, 1234, 1382, 1467, 1740, 2851, and 2920 cm^{-1} and from the Raman bands at 427, 544, 608, 700, 716, 1064, 1298, 1439, 2850, 2882, and 2930 cm^{-1}. The Raman bands above 3100 cm^{-1} are assigned to water. Spectral contributions of proteins do not change significantly in IR spectra (A, B) and Raman spectra (C, D). More details of vibrational spectroscopic imaging of mouse brains and the detection of metastases from malignant melanomas in mouse brains have recently been published [53]. The fiber optic Raman imaging approach was already transferred to living mice [23]. Brain metastases were induced by injection of tumor cells in the carotid artery. After a few weeks, a cranial window was inserted on the skull and Raman images were collected that delineated the tumor.

3.3.2.2 **Primary Brain Tumors**

Normal human brain tissue is composed of 68–80% water, 10–11% proteins, and 5–15% lipids with higher lipid (15%) and lower water (68%) content in white matter and lower lipid (5%) and higher water (80%) content in gray matter [54]. Most other tissues such as muscle tissue (4%), liver (3.1%), and lung (2.9%) contain less amounts of lipids. The high lipid content is a consequence of the fact that neurons and nerve cells are surrounded by a sheath of lipids. If tissue of lower lipid content is found within the brain, it might point to a different tissue type such as dura mater, leptomeninges, hemorrhage, or brain tumors. Dura mater and leptomeninges form the layers of the brain encapsulating meninges, and both have skin-like properties and high spectral contributions of collagen [21, 44, 46]. Another property of most brain cells, which distinguish them from proliferating

and dedifferentiated tumor cells, is that they are postmitotic that means they do no undergo cell division and all cells are in the same stage of maturation. Brain tissue is a very soft tissue because of its high water content, which even increases in patients with intracranial neoplasms and cerebrovascular pathologies up to 90% [55].

Tumors that begin in brain tissue are known as *primary brain tumors*. They are classified by the cell types from which they originate. Astrocytic gliomas are the most frequent primary brain tumors which originate from astrocytes, a special class of glial cells. Their malignancies are divided according to the World Health Organization (WHO) into grades I and II, which are benign tumors, and grades III and IV, which are malignant tumors with a rapid and infiltrative growth pattern and a strong tendency to form metastases [56]. After more than 100 FT-IR images of human brain tissue and gliomas were acquired, a supervised classification model was trained that distinguished into six classes: (1) normal tissue of regular cell density; (2–4) tissues of low, intermediate, and highly increased cell density; (5) hemorrhage; and (6) other tissues. The low, intermediate, and highly increased cell density was found to correlate with the tumors astrocytoma grade II, astrocytoma grade III, and GBM grade IV, respectively. The model was based on the algorithm linear discriminant analysis (LDA), which uses three band ratios as molecular descriptors. The key information is the ratio of the lipid band at $2850\,cm^{-1}$ and the protein band at $1655\,cm^{-1}$, which decreases with increasing malignancy. It has been reported that the model can assign single spectra, FT-IR images that were recorded with a single channel detector in the sequential mode, and FT-IR images that were recorded with an FPA multichannel detector [57]. The class assignments are color coded to visualize the results. The selection of training data and the classification results were validated by a histopathological inspection of consecutive H&E-stained tissue sections. In a retrospective study, multiple brain tissue specimens from one patient were obtained under neuronavigation surveillance [58]. The LDA classification of FT-IR images was able to distinguish the central part of the tumor with high cell densities from the peripheral region with regular, low, and intermediate cell densities. This success enables to apply FT-IR imaging as a complementary, *ex vivo* tool to monitor the progress of tumor extirpation. An example is shown in Figure 3.8 for 10 tissue sections on CaF_2 slides obtained from a brain tumor patient with a multifocal GBM. FT-IR images were acquired by an FT-IR imaging system, which was coupled to a 64×64 FPA detector (Bruker Optik GmbH, Ettlingen, Germany). The field of view in the macro chamber IMAC (Bruker Optik GmbH, Ettlingen, Germany) was $4 \times 4\,mm^2$ per image. The color-coded FT-IR images demonstrate the inhomogeneous nature of the tumor. The diagnosis of a GBM is unambiguously confirmed by FT-IR image (c) which is dominated by most malignant tissue of high cell density (red). FT-IR images (d, h, i, j) also contain extended regions of high (red) and intermediate (orange) cell densities, whereas FT-IR images (a, b, e, f, g) indicate mainly regular (green) and low cell densities (blue), which are consistent low malignancies and low number of tumor cells, respectively. It is important to note in the context of gliomas that astrocytoma grades II and III are used as descriptive terms

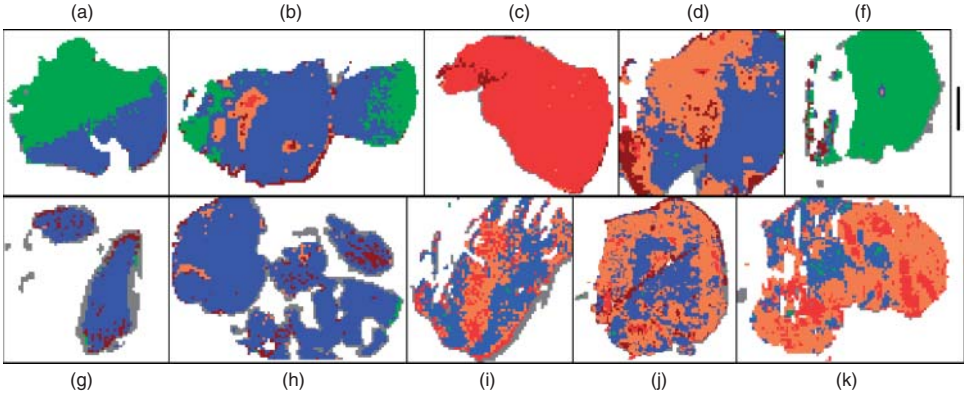

Figure 3.8 FT-IR images of 10 brain tissue sections obtained from a brain tumor patient with a multifocal glioblastoma multiforme. The color code represents the classification by an LDA model into six classes: regular (green), low increased (blue), intermediate (orange) and high (red) cell density, hemorrhage (brown), and other tissues (gray). The red and orange classes are characteristic of malignant brain tumors of the glioma type. Bar = 1 mm.

delineating the cellularity and morphological appearance of tumor areas in analogy to the morphological parameters used for WHO grading. However, they are not identical with the respective WHO classification. In a tumor that contains areas of obvious malignancy (Figure 3.8c), areas of low cellularity with only few tumor cells do not represent a benign tumor astrocytoma grade II. Despite the morphologically benign appearance, these tumor cells may retain their malignant potential. This fact explains the strong tendency of GBMs to recur within a short period. Cure of GBMs is unlikely unless the tumor is eradicated completely, which also involves other approaches such as immunotherapy or vector-mediated gene therapy as adjuncts to surgery.

The concept to use soft reference information has been applied to Raman spectroscopic grading of astrocytoma [59]. This approach considers the fact that the tumors form a histopathologic continuum, may progress from low malignancy to high malignancy, may encompass mixed tumor grades, and consequently are difficult to describe to hard, crisp classifiers. Predictive soft logistic regression models achieved about 85%, 67%, and 84% sensitivities and specificity for normal, low, and high grades, respectively.

3.3.2.3 Secondary Brain Tumors

Metastasis is the spread of cancer. Cancer that begins in other parts of the body may spread to the brain and cause secondary brain tumors, also called *brain metastases*. Brain metastases occur in about 15–40% of all cancer patients [60]. In up to 15% of all cases, the primary tumor of brain metastases remains unknown despite thorough investigation by standard screening techniques. The failure to detect the primary tumor is usually due to its small size and lack of symptoms, and constitutes the main problem to select an organ-specific therapy.

Lung cancer (LC), which is known to cause thoracic symptoms in a fairly late stage of tumor development, is the most frequent site for brain metastases. Other frequent primary tumors are colorectal cancer (CC), breast cancer (BC), renal cell carcinoma (RCC), prostate cancer, and malignant melanoma. The concept to apply vibrational spectroscopy to identify the primary tumor is that metastatic tumor cells contain molecular information of the primary tumor, and vibrational spectra provide a molecular fingerprint of the tissue type, which may enable its assignment by a supervised classification model. Classification models were introduced to distinguish white and gray matters of normal brain tissue and brain metastases of RCC, LC, BC, and CC using FT-IR images [61, 62]. The first model was based on the LDA algorithm. In comparison with the three molecular descriptors for the classification of gliomas, the number of band ratios was increased to eight because the differences between the tissue types were smaller. The second model was based on the algorithm soft-independent modeling of class analogies (SIMCA). Here, the classes are defined by a set of principal components of training data. After performing a PCA of test data, they are projected into the multidimensional data space of the training data and assigned to the class with the closest distance. Because 10 PCs in the interval $950-1800\,cm^{-1}$ were able to describe more variances, the SIMCA model tend to give better classification rates of three control specimens and 17 tumor specimens than the LDA model.

Figure 3.9 compares the color-coded classification results by the SIMCA and LDA models for five specimens. Four tissue sections were prepared on CaF_2 substrates from different brain metastases. A normal brain specimen was obtained from an autopsy. FT-IR images were acquired by an FT-IR imaging system, which was coupled to a 64×64 FPA detector (Bruker Optik GmbH,

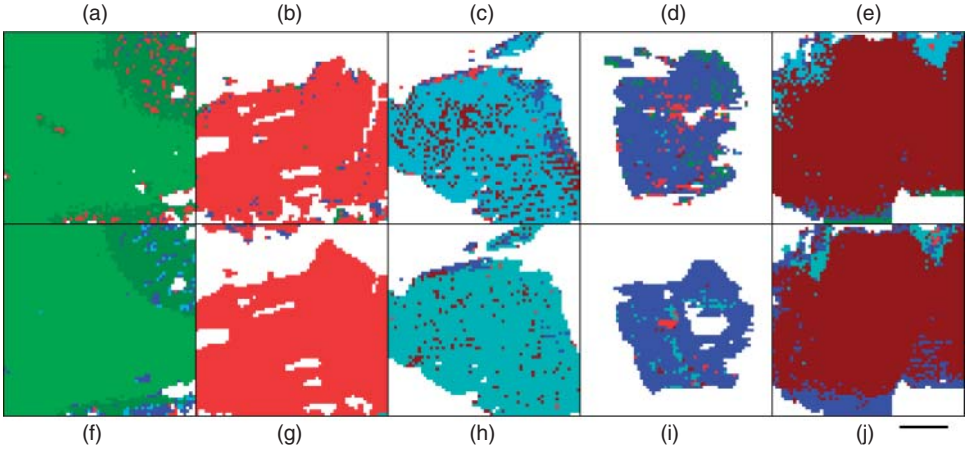

Figure 3.9 FT-IR images of brain tissue sections obtained from an autopsy (a, f) and four brain metastasis patients (b–e and g–j). The color codes represent the classification by an LDA model (a–e) and a SIMCA model (f–j) into six classes: white matter (green), gray matter (dark green), brain metastases of renal cell carcinoma (red), of colon cancer (cyan), of lung cancer (blue), and of breast cancer (brown). Bar = 1 mm.

Ettlingen, Germany). The field of view in the macro chamber IMAC (Bruker Optik GmbH, Ettlingen, Germany) was $4 \times 4\,mm^2$. The resolution of 62 µm per pixel was sufficient to identify the molecular information of the main tissue classes. The SIMCA model assigned 94.1% of spectra from the normal sample in Figure 3.9a and the LDA model assigned 95.4% spectra in Figure 3.9f to white and gray matters. Incorrect assignments were observed mainly in gray matter. A total of 99.0% and 95.7% of spectra from the RCC brain metastasis were assigned to RCC in Figure 3.9b,g by the SIMCA and LDA models, respectively. A typical molecular property of renal cells is the expression and accumulation of glycogen. The high correct classification rates are based on the detection of glycogen throughout the FT-IR image of the brain metastasis. As glycogen is not present in significant amounts in normal brain tissue and in the other brain metastases, this molecular marker is an indicative of RCC. The molecular markers are less pronounced for the other brain metastases. Nevertheless, the majority of spectra are always assigned to the correct primary tumor: 74.3% to CC (c), 86.3% to LC (d), 82.7% to BC (e), 90.2% to CC (h), 90.8% to LC (i), and 80.4% to BC (j). In addition to model deficiencies, classification rates below 100% can have several reasons. First, a fraction of normal tissue might be present. Second, a tissue type that was not included in the model might exist. Third, the images might be affected by noise or physical effects that change the spectral profile. In particular, incorrect classifications were observed at the tissue margins in Figure 3.9e,j. Here, the spectra have low intensities and SNRs. Furthermore, dispersion artifacts usually have maximum intensity in IR spectra near tissue margins. The classification models can be optimized by more training data, more tissue classes, or other algorithms such as artificial neural networks or support vector machines (SVM).

The SVM approach was recently realized to determine the primary tumor of brain metastases from bladder cancer, LC, BC, colon cancer, prostate cancer, and RCC using Raman [63] and FT-IR [22] images. Here, hierarchical classification schemes were applied that distinguish cancer from noncancer (normal brain, necrosis, remaining tissue) in the first level and identify the primary tumor in the second level using the cancer spectra as input. SVM is a large margin classifier where support vectors define hyperplanes to separate classes. In contrast to LDA, SVM is also able to separate nonlinear class boundaries. Direct comparison of the accuracy rates of LDA, SIMCA, and SVM is difficult because different samples, instrumentation, and classification schemes were used. The overall biochemical features in all reports coincide well. Figure 3.10 compares Raman (b, c) and FT-IR (d, e) results for the first and second classification levels. As indicated in the first color scheme, the tissue section of a brain metastasis contains necrosis and carcinoma (b, d). Cracks, holes, and the margin are assigned to the remaining group. Normal brain tissue is not detected. According to the second color scheme, the majority of Raman and IR carcinoma spectra are correctly assigned to the primary tumor lung carcinoma (c, e). An H&E-stained tissue section confirms the findings of solid tumor in the right portion and necrosis with scattered tumor cells in the left portion (a). The specimen was also investigated by CARS microscopy.

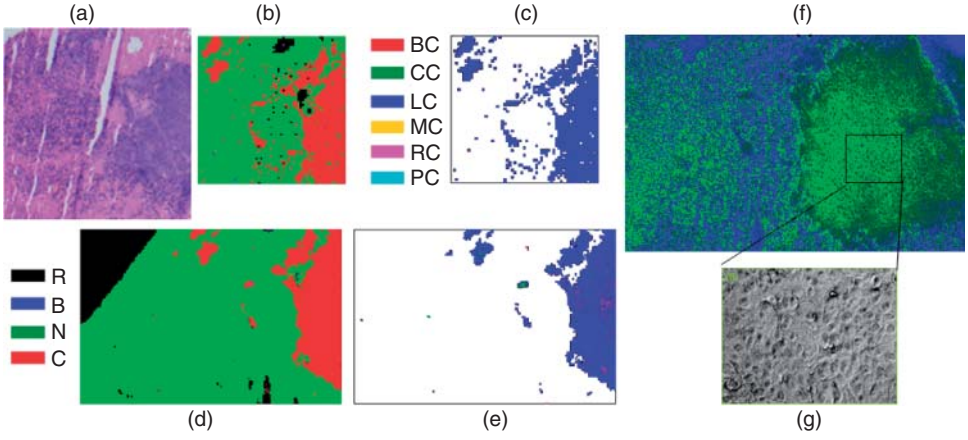

Figure 3.10 Photomicrograph of H&E-stained tissue section (a), Raman image (b, c), FT-IR image (d, e), and CARS image (f, g) of brain metastasis from lung cancer. The four color codes indicate first-level SVM classification in (b, d), and the six color codes indicate the second-level SVM classification in (c, e).

The region of interest was larger than in FT-IR and Raman images. The color code indicates the intensity of the CARS signal at 2850 cm^{-1} (f). The tumor margin is clearly resolved that corresponds to the first classification level. However, a differential diagnosis cannot be obtained. The magnified area demonstrates that the CARS image provides cellular details such as the cell nuclei. The prospects of such cellular resolution will be described in the later section.

3.3.2.4 **Cellular Resolution**

Single-band CARS microscopy is one of the fastest implementation of nonlinear vibrational imaging, allowing for video rate image acquisition times. CARS imaging within the C–H stretching region was shown to enable detection of single cells and nuclei as demonstrated in Figure 3.10g. This label-free morphological contrast allows for histopathologic grading of tissue. Relevant information such as nucleus-to-cytoplasm ratio, cell density, nucleus size, and shape is extracted from CARS images by innovative image processing procedures [64]. A complication constitutes the fact that cell nuclei give negative contrast in CARS images (see Figure 3.10g). In this contribution [64], CARS image contrast within the CH stretching region was interpreted by direct comparison with Raman imaging.

Three progresses contribute to cellular resolution in Raman imaging. First, Raman microscopic images are collected at a small step size of less than 2 µm using high magnification objectives. Second, the Raman images are analyzed by bilinear hyperspectral unmixing algorithms that extract endmember signatures and concentration plots. Third, tissue sections are studied in aqueous buffer using water immersion objectives. This preparation prevents specimens from drying and avoids denaturation of biomolecules and crystallization of hydrophobic constituents such as cholesterol. High spatial resolution and cluster analysis are

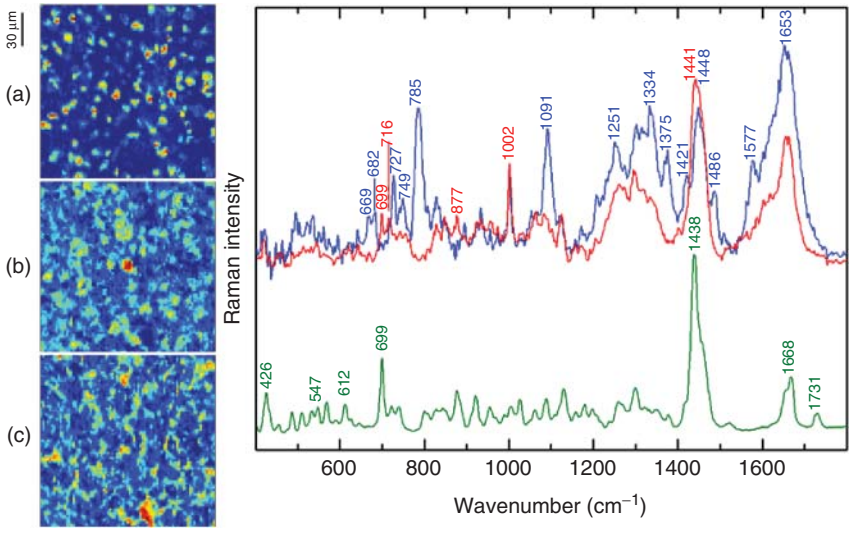

Figure 3.11 Spectral unmixing by vertex component analysis of a Raman image of nondried, brain tumor tissue section immersed in aqueous buffer. Concentration plots and endmember signatures are assigned to nucleic acids in cell nuclei (a, blue trace), proteins (b, red trace), and lipids (c, green trace).

not sufficient and appropriate to give cellular resolution as shown in Figure 3.5 and in reference [65].

Figure 3.11 gives an example of hyperspectral unmixing for a Raman image of brain tissue. Analogous to PCA, vertex component analysis (VCA) or N-FINDR calculates weights or concentrations and vectors or endmembers to describe spectral variations within a data set. The constraints differ for each algorithm. In VCA, the endmembers represent the most dissimilar spectra with nonnegative intensities and the concentrations are also nonnegative. Details have been published [66, 67]. The endmembers can often be assigned to chemical components. In Figure 3.11, the blue spectrum is dominated by spectral contributions of DNA as compared with Figure 3.1, the red spectrum by spectral contributions of proteins, and the green spectrum by cholesterol. The plots of the concentrations display the distribution of constituents. The DNA bands were found to be more intense in Raman spectra of nonhydrated tissue sections [30, 47] than the spectra of dried tissue sections [20]. Chemical parameters such as DNA content and lipid content were found to correlate with morphological parameters such as cell nuclei number and nucleus-to-cytoplasm ratio. As these parameters change with the malignancy of primary brain tumors, they offer potential as diagnostic marker for the tumor grade. It is interesting to note that the morphology can rapidly be assessed by nonlinear microscopy, whereas the biochemistry requires more time-consuming experimental tools, namely Raman and FT-IR microscopy.

3.3.3
Cervix Uteri and Squamous Cell Carcinoma

Beside colon, tissue of cervix uteri is presented as another application of FT-IR imaging to epithelial and connective tissues. In addition, the tissue section also encompassed dysplasia and carcinoma. *Dysplasia* is a term used in pathology to refer to an abnormality in maturation of cells within a tissue. It is often indicative for an early neoplastic process. Furthermore, this section deals with the problem that FT-IR imaging is a high throughput technique, which can acquire images from several extended regions with microscopic resolution in a relative short time. The large amount of data constitutes a challenge for analysis. A processing procedure for data reduction will be introduced.

One field of research that received substantial attention in the last decade was the application of FT-IR and Raman spectroscopic studies to gynecological screening for cervical dysplasia and malignancies (review in [68]). It is estimated that screening programs and follow-up intervention have reduced the incidence of cervical cancer by about 80% [69]. The current accepted technique for diagnosing exfoliated cells is the Papanicolaou (Pap) smear test where cells are collected from the cervical transformation zone and stained with the Pap stain. Despite its success, cytological screening by the Pap smear test has limitations, the most important being high numbers of false-negative results. Therefore, since the pioneering work by Wong and coworkers [70] in the early 1990s, the main objective has been to improve the diagnostic accuracy of the Pap smear by FT-IR spectroscopy of exfoliated cervical cells. Focus of the Raman spectroscopic research on cervical tissue was *in vivo* assessment of squamous dysplasia by fiber optic probes [71]. Cervical tissue sections have been studied by FT-IR imaging [72]. Multiple adenocarcinoma tissue sections from a cervical biopsy were used as a model system to demonstrate the generation of 3D FT-IR images [73].

Although cervical samples were usually obtained by cone biopsy from patients diagnosed by cytology with high-grade cervical dysplasia or carcinoma, the specimen in [72] originated from a patient with a cervical carcinoma who underwent a radical hysterectomy. A tissue section of the specimen was mounted on a CaF_2 slide and studied by FT-IR microscopic imaging in a transmission mode. The FT-IR imaging system was coupled to a microscope, which was equipped with a 64×64 FPA detector (Bruker Optik GmbH, Ettlingen, Germany). The field of view using 15× magnification was $270 \times 270\,\mu m^2$ per image, and each pixel corresponded to an area of $4.2 \times 4.2\,\mu m^2$. Altogether 122 FT-IR images totaling to 499 712 IR spectra were recorded from seven areas, which represented cervical stroma, squamous epithelium, dysplasia, and carcinoma. A dedicated strategy to segment this large data set of ~3 GB by cluster analysis was developed, which was able to identify the main tissue types. The goal was to perform a hierarchical cluster analysis (HCA) over the entire set of spectra to fully characterize the range of spectral variations through all areas. HCA on each individual area would give a different clustering result because some tissue

types are not present in all FT-IR images. It has been reported that HCA is the superior clustering algorithm for segmentation of FT-IR images compared with fuzzy C-means (FCM) and k-means cluster analyses [74]. Disadvantages of HCA are that it is difficult to visualize the relation of a large number of spectra in the resulting dendrogram and that it requires long computation times to calculate the distance matrix ($n \times n$) for large wavenumber intervals and high number of spectra (n). Therefore, a cluster analysis using the FCM algorithm was applied as a preprocessing procedure to group the spectra in less than 100 clusters so that each tissue type is represented by at least one cluster. The advantage of FCM cluster analysis is that it can handle large data sets in relatively short computation times. This first cluster analysis reduces the number of spectra to a better manageable size for subsequent HCA and improves the SNR because each group is the average over a certain set of IR spectra. The application to the current data set was further optimized by parallel computing using several processors. The sequential cluster analysis approach combines the advantages of FCM and HCA to enlarge the tissue area to be characterized at once by FT-IR imaging.

Two examples of such an analysis are shown in Figure 3.12. Photomicrographs of H&E-stained tissue sections are compared with FT-IR microscopic images of consecutive, unstained tissue sections. The deviations between each pair of tissue

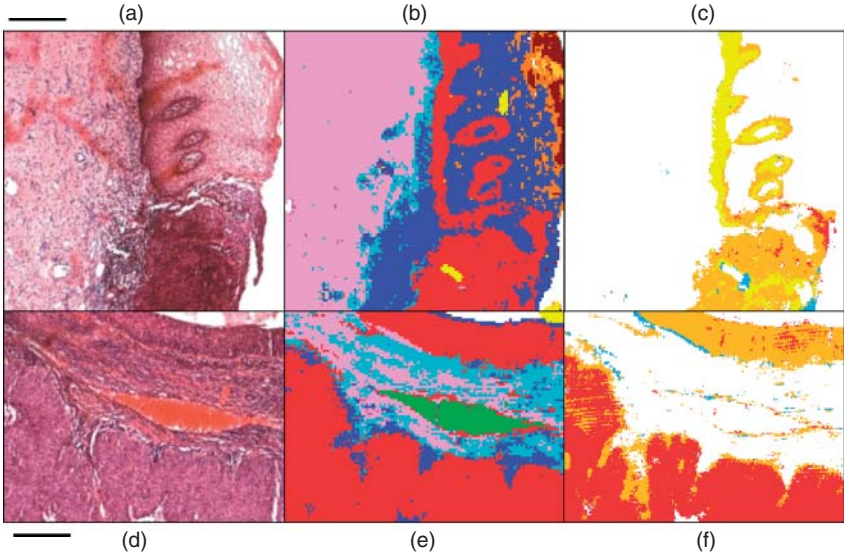

Figure 3.12 Photomicrographs of H&E-stained tissue sections (a, d) and FT-IR microscopic images (b, c, e, f) of consecutive, unstained tissue sections obtained from a patient with squamous cell cervical carcinoma. Transition zone from normal epithelium to a dysplastic lesion (a–c) and carcinoma surrounded by cervical stroma containing blood vessels and inflammatory response (d–f). Color codes represent the segmentation of two sequential cluster analyses. Bar = 200 µm.

sections are small. FT-IR image (b) is a mosaic of 4×4 individual images, which is composed of 256×256 spectra. FT-IR image (e) is a mosaic of 4×3 individual images, which is composed on 256×192 spectra. The color codes represent the results of the sequential cluster analyses. In Figure 3.12b,e, the sequential cluster analyses were performed for all spectra in the spectral region from 950 to 1480 cm^{-1}. At the interface between stroma (pink) and the basal cell layer (red), a thin zone of mild inflammatory response (cyan) is visible (Figure 3.12b). Intermediate (light and dark orange) and superficial (brown) layers of epithelium are found at the right. The zone of severe inflammatory response (blue) broadens toward the dysplastic lesion (red) in the lower part. The red coloring indicates that this initial approach cannot yet distinguish the basal cell layer and the dysplastic lesion. Similarly, the dysplastic lesion in the top part of Figure 3.12e overlaps with the carcinoma in the lower part (both red). A blood vessel (green) in the middle part is surrounded by stroma (pink) and inflammatory infiltration (cyan, blue). A small fraction of mucus (yellow) is observed in the top right part. In order to separate the overlapping tissue types, the red cluster was subjected to a second cluster analysis in the interval 1420 – 1480 cm^{-1}. Figure 3.12c shows that the normal basal cell layer (yellow) can now be distinguished from dysplasia (orange). Figure 3.12f shows that dysplasia (orange) can be distinguished from carcinoma (red). The blue cluster represents spectra of different tissue types. Overall, the distinction of normal basal cell layer from dysplasia and squamous cell carcinoma was much more difficult than distinction of the different tissue types such as cervical stroma or upper layers of the epithelium. The reason for the difficulties could be that normal and neoplastic basal cells go to the same cell cycle stages at approximately the same rate. The key difference is that neoplastic cells do not regulate this process, which is a hallmark of cancer [75]. As a consequence, the cytoplasm consists of similar composition and the nucleus-to-cytoplasm ratio is similar, which is also indicated by the darker H&E staining patterns of the respective tissue regions in Figure 3.12a,d.

The cluster-averaged IR spectra of the main cervical tissue types are shown in Figure 3.13. The spectral variations in the amide I and II bands were small. Therefore, the spectral interval 1480 – 1800 cm^{-1} did not improve the cluster segmentation and was omitted. Bands at 1026, 1080, and 1151 cm^{-1} in spectra (A – D) indicate a gradual increase in the glycogen level from the parabasal to the intermediate and to the superficial layers of the epithelium. The increase is consistent with an accumulation of glycogen on maturation of epithelial cells. Bands at 1232, 1336, 1448, and 1538 cm^{-1} are more intense in the IR spectrum of cervical stroma (E) than in the other IR spectra. These bands were found earlier (see Figure 3.4, trace A) as an indicative for collagen, which is typical for connective tissue. The spectra of inflammatory response (F, G) are similar to the spectra of stroma, which suggests that this inflammation pertains to stroma. The main difference is a band near 1069 cm^{-1}, which gradually increase with the grade of inflammation. Spectral contributions near 1069 cm^{-1} are assigned to polymorphonuclear leukocytes (PMNs). The presence of PMNs in a cervical sample has been reported to be consistent with inflammatory

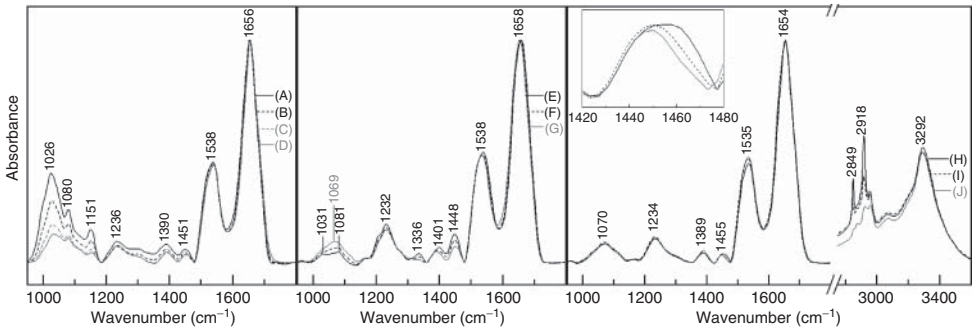

Figure 3.13 IR spectra from 950 to 1800 (A–J) and from 2750 to 3600 cm^{-1} (H–J) of a cervix uteri tissue section: superficial (A), intermediate (B, C), and parabasal (D) cell layers of epithelium, cervical stroma (E), mild (F) and severe (G) inflammatory response, basal cell layer (H), dysplasia (I), and carcinoma (J). Spectra are normalized and baseline corrected for comparison. The wavenumber scale of the IR spectra in the interval 2750–3600 cm^{-1} is twofold compressed.

conditions [76]. The IR spectra of the basal cell layer (H), dysplasia (I), and carcinoma (J) are very similar, which explains the observed overlap in one cluster in Figure 3.12b,e. The basal cell layer is the germ line for the epithelium. Upon cell division, basal cells generate cells, which migrate to the surface and mature. Cancer cells originate from these progenitor cells, which makes the similarity plausible. The most significant spectral change in the interval 950–1480 cm^{-1} is the shift of the band at 1455 cm^{-1} toward 1448 cm^{-1} with a concomitant intensity decrease as a function of malignancy (inset of Figure 3.13). A cluster analysis was able to differentiate these three tissue types using the spectral variances in the interval 1420–1480 cm^{-1} as shown in Figure 3.12c,f. The bands in this interval are assigned to CH_2/CH_3 deformation vibrations. The CH_2/CH_3 stretching vibrations in the interval 2800–3000 cm^{-1} confirm the intensity decrease. The bands at 2849 and 2918 cm^{-1} are assigned to side chains of fatty acids. They have maximum intensity for the basal cell layer, medium intensity for dysplasia, and minimum intensity for carcinoma. A decrease in these bands with increasing malignancy was also observed in brain tumors (see Section 3.3.2). In view of the minimal spectral differences in the interval 950–1300 cm^{-1} in spectra (H, I, J) where bands due to the polar head groups of lipids are located, the pronounced differences of the CH_2 vibrations are unexpected. The work has utilized formalin-fixed, paraffin-embedded tissue because of its availability and relevance in the pathology laboratory. Fixation of the tissue specimen with formalin cross-links proteins. During the following course of tissue dehydration with solvents (e.g., ethanol), paraffin embedding, and deparaffinization of tissue sections with solvents (e.g., xylol), the unfixed fatty acids, lipids, and their polar head groups are expected to be washed out. Spectral contributions due to incomplete removal of the paraffin-sectioning medium could be excluded because of the histopathologically confirmed correlation between the intensity of the CH_2 vibrations and the malignancy. Further

experiments are required to study the effects of fixation, dehydration, and deparaffinization on cervical tissue in more detail.

3.3.4 Atherosclerosis

Atherosclerotic cardiovascular diseases are one of the most common causes of death in the western hemisphere and usually a consequence of unhealthy lifestyle and aging. The progression of this chronic disease is complex and not yet fully understood. Due to aging and oxidative stress, arterial membranes become susceptible to permeation and deposition of various lipids circulating through the bloodstream, as well as crystalline calcium compounds, usually in the form of calcium apatite. This process is followed by a migration of monocytes, a type of white blood cells that differentiate into macrophages, which are responsible for lipid incorporation. These cells cannot process the contained lipids and will rupture after they reached their ultimate size. The subsequent cell death and cellular debris contribute to the arterial swelling. Continuous swelling can lead to the rupture of these plaques, with often fatal consequences such as heart attack or stroke. The inner arterial plaque composition can vary with the influence of various risk factors, for instance hypertonia, hyperlipidemia, insulin resistance, smoking, or adipositas. To correlate the composition of plaque depositions with certain disease patterns and vulnerability, long-term studies of plaque biopsies may offer potential inside for diagnostic strategies and applications. Angiography has long been the focus of human diagnostic techniques to detect areas of severe narrowing of blood vessels, but not the underlying atherosclerosis disease. An anatomical detection of the underlying atherosclerosis disease can be achieved by coronary calcium scoring by computed tomography (CT), carotid intimal media thickness measurement by ultrasound, intravascular ultrasound, and intravascular optical coherence tomography. The individual plaque components triglycerides, cholesterol, cholesterol ester, crystalline calcium and proteoglycans [77, 78], and lipid concentrations [79] can be identified by Raman spectroscopy. A classification model was presented to identify atherosclerosis in human coronary arteries [80]. Furthermore, Raman experiments were reported in arteries under *ex vivo* [81] and *in vivo* conditions using fiber optic probes [82–84], and fiber optic Raman spectroscopy was combined with intrinsic fluorescence and diffuse reflectance spectroscopy to detect vulnerable plaque sites [85].

The following examples describe a series of experiments on an atherosclerotic plaque model on rabbits that were treated with a cholesterol-enriched diet. Raman, FT-IR, and CARS microscopy on tissue sections and correlation with histopathology are important before application to the diagnosis based on fiber optic measurements. Figure 3.14 shows photomicrographs of elastic van Gieson stained and consecutive unstained aortic cross sections of rabbit artery. The intima (I) is thickened, which is an indicative of atherosclerotic plaques. At physiological conditions, the intima would not be visible at this magnification as it would be merely composed of an endothelial cell layer and few underlying

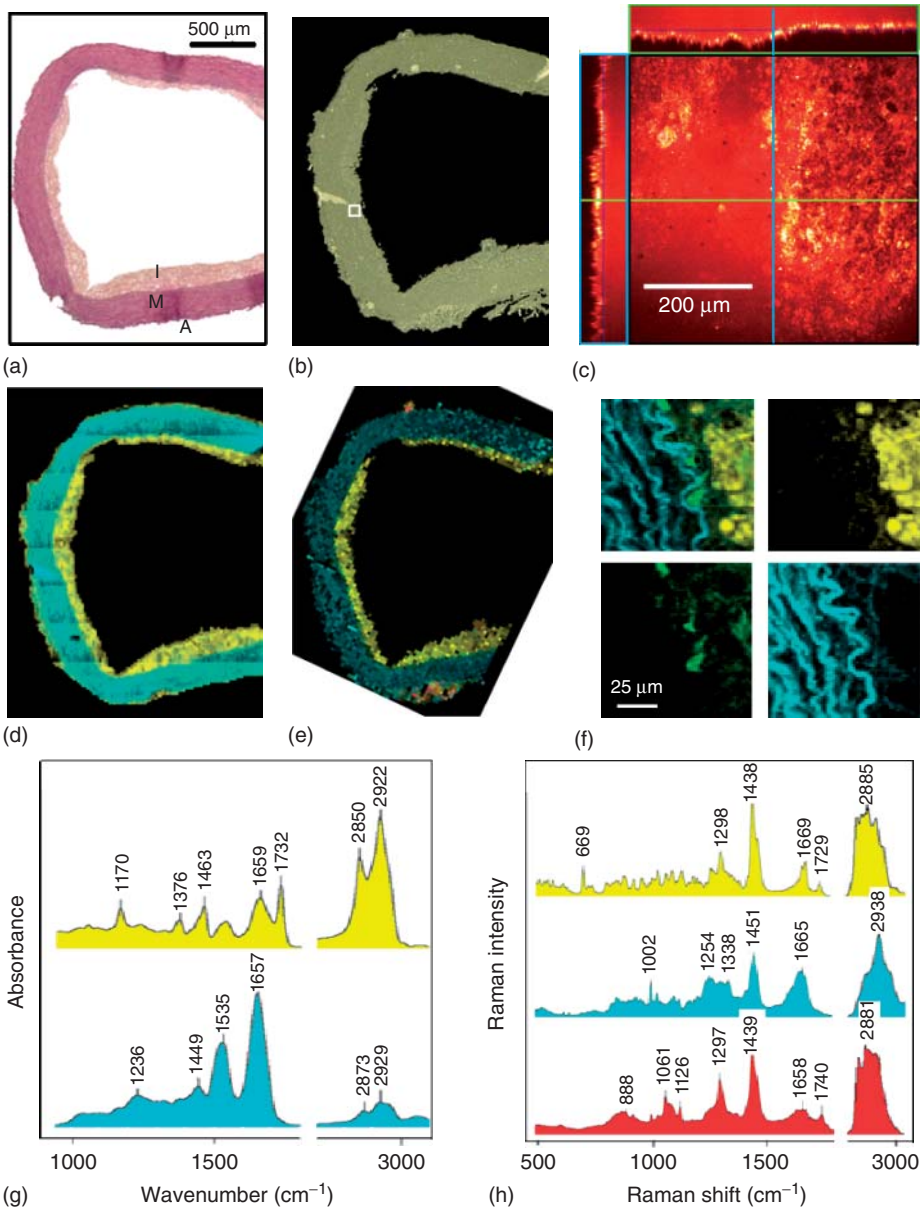

Figure 3.14 Photomicrographs of elastica van Gieson stained (a) and unstained (b) cross sections of rabbit artery. CARS image of intima with depth profiles along the green and blue lines (c). FT-IR (d) and Raman (e) images of the unstained tissue section shown in (b). Raman image of the region of interest shown as white box in (b). IR spectra (g) and Raman spectra (h) obtained from spectral unmixing by the VCA algorithm. The color code of the spectral profiles (g, h) and images (d, e) are identical: cholesterol ester (yellow), protein (cyan), and triglyceride (red).

smooth muscle cells. The artery wall that consists of proteins of the ECM and smooth muscle cells is called *media (M)* and the outer portion *adventitia (A)*. The contrast in the unstained tissue section does not allow to distinguish these tissues. A CARS image at 2850 cm^{-1} was collected from the intima and enables to visualize plaque deposits. CARS microscopy offers an inherent confocality because the signal is generated only in a small volume. This property is demonstrated by depth profiles along the blue and green lines that gave signals up to 50 μm tissue depth. The plaque deposits are just a few micrometers thick at these locations. The fibrillar structures, distribution of lipids, and smoothness of the surface were different for intima of control arteries as studied in CARS images at 2930 cm^{-1} [83].

The FT-IR image was composed of a mosaic of individual $350 \times 350\ \mu m^2$ images. The spectral unmixing algorithm VCA identified two main components (see Section 3.3.2.4). The concentrations of the components' lipid depositions and proteins are color-coded yellow and cyan, respectively, and are plotted in Figure 3.14d. The IR spectra of the components are shown in Figure 3.14g. The intima-media and the lipid–protein ratio were quantified for five specimens, and the IR-based results agreed well with the histopathological determination as reported in [18].

The Raman image was collected from the same sample at a step size of 20 μm for comparison with the FT-IR image. Here, the spectral unmixing algorithm identified three main components. Beside proteins (cyan), the lipid fraction was further discriminated into cholesterol ester (yellow) and triglycerides (red) – with the latter assigned predominantly to adventitial adipocytes in perivascular tissue at the top and bottom. The concentrations of the components are presented in Figure 3.14e, the Raman spectra in 3.14 h.

Another Raman image was collected from a smaller region of interest ($100 \times 100\ \mu m^2$) at a step size of 1 μm. The VCA algorithm resolves another component of the lipid fraction, that is, cholesterol (green). The Raman spectrum of cholesterol is distinguished from the spectrum of cholesterol ester by the lack of fatty acids and ester bands (see also Figure 3.1, trace J). The distribution of each component and an overlay of all components are shown in Figure 3.14f. The results suggest that the cholesterol largely colocalize with cholesterol ester except for aggregates in the center. Altogether, Raman imaging offers better spectral resolution than FT-IR imaging, which is evident from the identification of additional components, and better lateral resolution, which is evident from the identification of morphological details such as the arrangement of internal elastic lamina delimiting intima from media and separating the lipid-rich region from the media in Figure 3.14f.

3.4 Conclusions

The examples, references, and an early review [86] demonstrated that more FT-IR than Raman imaging studies of soft tissue were reported. This is mainly due to

the highly developed instrumentation for FT-IR imaging, which is able to acquire high-quality images within minutes. The rapid acquisition of FT-IR images can complement histopathology as a tool to assess tissue sections. FT-IR-based classification models have been developed for prostate tissue [87], primary [58], and secondary brain tumors [61] to name a few. The latter models allow an on-site analysis of cryostat sections accompanying neurosurgery which are performed to confirm initial diagnoses and to determine tumor margins. Size and location of tumors are usually determined by CT or magnetic resonance imaging (MRI) before surgery. This preoperative information is transferred during surgery by a neuronavigation system. However, the accuracy is limited because the margins may deviate from the preoperative locations due to intraoperative brain shift or edema.

Acquisition of Raman images is usually more time consuming and the SNR is inferior. Nevertheless, Raman imaging offers advantages in terms of (i) studying nondried, native tissue, (ii) the maximal, diffraction-limited lateral resolution is higher, (iii) the spectral range can easily be extended to lower wavenumbers, (iv) the technique can be coupled to fiber optic probes, and (v) enhancement effects can be utilized. For example, the resonance Raman effect was used for rapid and sensitive detection of carotenoids in skin [88] and retina [89] and melanin in brain metastases of malignant melanomas [23]. So far, almost all Raman images have been recorded using the sequential point-mapping mode. In order to improve sample throughput in the future, faster and more sensitive Raman systems have to be developed utilizing also new sampling techniques such as line mapping or global imaging. An alternative is nonlinear Raman modalities such as CARS and stimulated Raman scattering (SRS) that can be coupled to rapid laser scanning microscopes and enable rapid image acquisition of extended regions, however, usually only at selected bands.

Complete assessment of an extended, inhomogeneous soft tissue sample exceeding $1\,cm^2$ by vibrational microspectroscopic imaging with lateral resolutions below $10\,\mu m$ requires accumulation of more than 1 000 000 spectra. Recently, an FT-IR image of colon tissue section ($1.65 \times 1.5\,cm^2$) was analyzed that encompassed almost eight million spectra and took 2 days of registration with 128×128 FPA detector [7]. On the one hand, this is time consuming using the currently available instruments – even FT-IR imaging systems – and, on the other hand, the resulting large data set is difficult to analyze or classify using the currently available computer equipment. Therefore, Raman and FT-IR microscopic imaging as a screening tool seems to be limited to smaller samples or smaller sampling areas so far.

Although in its early stages, one can be optimistic that vibrational spectroscopic imaging has the potential to be fully accepted as a diagnostic tool for soft tissues with sufficient sensitivity and specificity for rapid and nondestructive *in vitro*, *ex vivo*, and *in vivo* analyses.

References

1. Krafft, C., Dietzek, B., Schmitt, M., and Popp, J. (2012) Raman and coherent anti-Stokes Raman scattering microspectroscopy for biomedical applications. *J. Biomed. Opt.*, **17**, 040801.
2. Latka, I., Dochow, S., Krafft, C., Dietzek, B., and Popp, J. (2013) Fiber optic probes for linear and nonlinear Raman applications: current trend and future development. *Laser Photonics Rev.*, **2** (7), 698–731.
3. Matousek, P. and Stone, N. (2013) Recent advances in the development of Raman spectroscopy for deep non-invasive medical diagnosis. *J. Biophotonics*, **6**, 7–19.
4. Krafft, C., Steiner, G., Beleites, C., and Salzer, R. (2009) Disease recognition by infrared and Raman spectroscopy. *J. Biophotonics*, **2**, 13–28.
5. Haka, A.S., Volynskaya, Z., Gardecki, J.A., Nazemi, J., Shenk, R., Wang, N., Dasari, R.R., Fitzmaurice, M., and Feld, M.S. (2009) Diagnosing breast cancer using Raman spectroscopy: prospective analysis. *J. Biomed. Opt.*, **14**, 054023.
6. Baker, M.J., Gazi, E., Brown, M.D., Shanks, J.H., Clarke, N.W., and Gardner, P. (2009) Investigating FTIR based histopathology for the diagnosis of prostate cancer. *J. Biophotonics*, **2**, 104–113.
7. Kallenbach-Thieltges, A., Grosseruschkamp, F., Mosig, A., Diem, M., Tannapfel, A., and Gerwert, K. (2013) Immunohistochemistry, histopathology and infrared spectral histopathology of colon cancer tissue sections. *J. Biophotonics*, **6**, 88–100.
8. Koljenovic, S., Bakker Schut, T.C., van Meerbeek, J.P., Maat, A.P., Burgers, S.A., Zondervan, P.E., Kros, J.M., and Puppels, G.J. (2004) Raman microspectroscopic mapping studies of human bronchial tissue. *J. Biomed. Opt.*, **9**, 1187–1197.
9. de Jong, B.W., Schut, T.C., Maquelin, K., van der Kwast, T., Bangma, C.H., Kok, D.J., and Puppels, G.J. (2006) Discrimination between nontumor bladder tissue and tumor by Raman spectroscopy. *Anal. Chem.*, **78**, 7761–7769.
10. Tan, K.M., Herrington, C.S., and Brown, C.T.A. (2011) Discimination of normal from pre-malignant cervical tissue by Raman mapping of de-paraffinized histological tissue sections. *J. Biophotonics*, **4**, 40–48.
11. Teh, S.K., Zheng, W., Ho, K.Y., Teh, M., Yeoh, K.G., and Huang, Z. (2010) Near-infrared Raman spectroscopy for early diagnosis and typing of adenocarcinoma in the stomach. *Br. J. Surg.*, **97**, 550–557.
12. Ly, E., Piot, O., Durlach, A., Bernard, P., and Manfait, M. (2009) Differential diagnosis of cutaneous carcinomas by infrared spectral micro-imaging combined with pattern recognition. *Analyst*, **134**, 1208–1214.
13. Cals, F.L.J., Schut, T.C.B., Koljenovic, S., Puppels, G.J., and de Jong, R.J.B. (2013) Method development: Raman spectroscopy-based histopathology of oral mucosa. *J. Raman Spectrosc.*, **44**, 963–972.
14. Almond, L.M., Hutchings, J., Shepherd, N., Barr, H., Stone, N., and Kendall, C. (2011) Raman spectroscopy: a potential tool for early objective diagnosis of neoplasia in the oesophagus. *J. Biophotonics*, **4**, 685–695.
15. Bonifacio, A., Beleites, C., Vittur, F., Marsich, E., Semeraro, S., Paoletti, S., and Sergo, V. (2010) Chemical imaging of articular cartilage sections with Raman mapping, employing uni- and multi-variate methods for data analysis. *Analyst*, **135**, 3193–3204.
16. Votteler, M., Carvajal Berrio, D.A., Pudlas, M., Walles, H., Stock, U.A., and Schenke-Layland, K. (2012) Raman spectroscopy for the non-contact and non-destructive monitoring of collagen damage within tissues. *J. Biophotonics*, **5**, 47–56.

17. Huang, Z.W., Lui, H., McLean, D.I., Korbelik, M., and Zeng, H.S. (2005) Raman spectroscopy in combination with background near-infrared autofluorescence enhances the in vivo assessment of malignant tissues. *Photochem. Photobiol.*, **81**, 1219–1226.
18. Lattermann, A., Matthaus, C., Bergner, N., Beleites, C., Romeike, B.F., Krafft, C., Brehm, B.R., and Popp, J. (2013) Characterization of atherosclerotic plaque depositions by Raman and FTIR imaging. *J. Biophotonics*, **6**, 110–121.
19. Caine, S., Heraud, P., Tobin, M.J., McNaughton, D., and Bernard, C.C.A. (2012) The application of Fourier transform infrared microspectroscopy for the study of diseased central nervous system tissue. *Neuroimage*, **59**, 3624–3640.
20. Krafft, C., Belay, B., Bergner, N., Romeike, B.F., Reichart, R., Kalff, R., and Popp, J. (2012) Advances in optical biopsy – correlation of malignancy and cell density of primary brain tumors using Raman microspectroscopic imaging. *Analyst*, **137**, 5533–5537.
21. Koljenovic, S., Bakker Schut, T.C., Vincent, A., Kros, J.M., and Puppels, G.J. (2005) Detection of meningeoma in dura mater by Raman spectroscopy. *Anal. Chem.*, **77**, 7958–7965.
22. Bergner, N., Romeike, B.F., Reichart, R., Kalff, R., Krafft, C., and Popp, J. (2013) Tumor margin identification and prediction of the primary tumor from brain metastases using FTIR imaging and support vector machines. *Analyst*, **138**, 3983–3990.
23. Kirsch, M., Schackert, G., Salzer, R., and Krafft, C. (2010) Raman spectroscopic imaging for in vivo detection of cerebral brain metastases. *Anal. Bioanal. Chem.*, **398**, 1707–1713.
24. Shim, M.G. and Wilson, B.C. (1996) The effects of ex vivo handling procedures on the near-infrared Raman spectra of normal mammalian tissues. *Photochem. Photobiol.*, **63**, 662–671.
25. Huang, Z.W., McWilliams, A., Lam, S., English, J., McLean, D.I., Lui, H., and Zeng, H. (2003) Effect of formalin fixation on the near-infrared Raman spectroscopy of normal and cancerous human bronchial tissues. *Int. J. Oncol.*, **23**, 649–655.
26. Faolain, E.O., Hunter, M.B., Byrne, J.M., Kelehan, P., Lambkin, H.A., Byrne, H.J., and Lyng, F.M. (2005) Raman spectroscopic evaluation of efficacy of current paraffin wax section dewaxing agents. *J. Histochem. Cytochem.*, **53**, 121–129.
27. Stitt, D.M., Kastyak-Ibrahim, M.Z., Liao, C.R., Morrison, J., Albensi, B.C., and Gough, K.M. (2012) Tissue acquisition and storage associated oxidation considerations for FTIR microspectroscopic imaging of polyunsaturated fatty acids. *Vib. Spectrosc.*, **60**, 16–22.
28. Romeo, M., Mohlenhoff, B., and Diem, M. (2006) Infrared micro-spectroscopy of human cells: causes for the spectral variance of oral mucosa (buccal) cells. *Vib. Spectrosc.*, **42**, 9–14.
29. Dukor, R.K., Liebman, M.N., and Johnson, B.L. (1998) A new, nondestructive method for analysis of clinical samples with FT-IR microspectroscopy. Breast cancer tissue as an example. *Cell. Mol. Biol.*, **44**, 211–217.
30. Bergner, N., Krafft, C., Geiger, K.D., Kirsch, M., Schackert, G., and Popp, J. (2012) Unsupervised unmixing of Raman microspectroscopic images for morphological analysis of non-dried brain tumor specimens. *Anal. Bioanal. Chem.*, **403**, 719–725.
31. Chalmers, J.M. and Griffiths, P.R. (2002) *Handbook of Vibrational Spectroscopy*, John Wiley & Sons, Ltd, Chichester.
32. De Gelder, J., De Gussem, K., Vandenabeele, P., and Moens, L. (2007) Reference database of Raman spectra of biological molecules. *J. Raman Spectrosc.*, **38**, 1133–1147.
33. Carr, G.L. (2001) Resolution limits for infrared microspectroscopy explored with synchrotron radiation. *Rev. Sci. Instrum.*, **72**, 1613–1619.
34. Romeo, M. and Diem, M. (2005) Correction of dispersive line shape artifact observed in diffuse reflection infrared spectroscopy and absorption/reflection (transflection) infrared micro-spectroscopy. *Vib. Spectrosc.*, **38**, 129–132.
35. Bassan, P., Sachdeva, A., Kohler, A., Hughes, C., Henderson, A., Boyle,

J., Shanks, J.H., Brown, M., Clarke, N.W., and Gardner, P. (2012) FTIR microscopy of biological cells and tissue: data analysis using resonant Mie scattering (RMieS) EMSC algorithm. *Analyst*, **137**, 1370–1377.

36. Bird, B., Miljkovic, M., and Diem, M. (2010) Two step resonant Mie scattering correction of infrared micro-spectral data: human lymph node tissue. *J. Biophotonics*, **3**, 597–608.
37. Bassan, P., Lee, J., Sachdeva, A., Pissardini, J., Dorling, K.M., Fletcher, J.S., Henderson, A., and Gardner, P. (2013) The inherent problem of transflection-mode infrared spectroscopic microscopy and the ramifications for biomedical single point and imaging applications. *Analyst*, **138**, 144–157.
38. Bell, S.E.J., Bourguignon, E.S.O., and Dennis, A. (1998) Analysis of luminescent samples using subtracted shifted Raman spectroscopy. *Analyst*, **123**, 1729–1734.
39. Maiwald, M., Schmidt, H., Sumpf, B., Erbert, G., Kronfeldt, H.-D., and Traenkle, G. (2009) Microsystem 671 nm light source for shifted excitation Raman difference spectroscopy. *Appl. Opt.*, **48**, 2789–2792.
40. McCain, S.T., Willett, R.M., and Brady, D.J. (2008) Multi-excitation Raman spectroscopy technique for fluorescence rejection. *Opt. Express*, **16**, 10975–10991.
41. De Luca, A.C., Mazilu, M., Riches, A., Herrington, C.S., and Dholakia, K. (2010) Online fluorescence suppression in modulated Raman spectroscopy. *Anal. Chem.*, **82**, 738–745.
42. Dochow, S., Bergner, N., Matthäus, C., Praveen, B.B., Ashok, P.C., Mazilu, M., Krafft, C., Dholakia, K., and Popp, J. (2012) Etaloning, fluorescence and ambient light suppression by wavelength modulated Raman spectroscopy. *Biomed. Spectrosc. Imaging*, **1**, 383–389.
43. Wood, B.R. and McNaughton, D. (2006) Resonance Raman spectroscopy in malaria research. *Expert Rev. Proteomics*, **3**, 525–544.
44. Krafft, C., Sobottka, S.B., Schackert, G., and Salzer, R. (2005) Near infrared Raman spectroscopic mapping of native brain tissue and intracranial tumors. *Analyst*, **130**, 1070–1077.
45. Koljenovic, S., Choo-Smith, L.P., Bakker Schut, T.C., Kros, J.M., van den Bergh, H., and Puppels, G.J. (2002) Discriminating vital tumor from necrotic tissue in human glioblastoma tissue samples by Raman spectroscopy. *Lab. Invest.*, **82**, 1265–1277.
46. Krafft, C., Sobottka, S.B., Schackert, G., and Salzer, R. (2006) Raman and infrared spectroscopic mapping of human primary intracranial tumors: a comparative study. *J. Raman Spectrosc.*, **37**, 367–375.
47. Bergner, N., Medyukhina, A., Geiger, K.D., Kirsch, M., Schackert, G., Krafft, C., and Popp, J. (2013) Hyperspectral unmixing of Raman micro-images for assessment of morphological and chemical parameters in non-dried brain tumor specimens. *Anal. Bioanal. Chem.*, **47** (405), 8719–8728.
48. Krafft, C., Codrich, D., Pelizzo, G., and Sergo, V. (2008) Raman and FTIR microscopic imaging of colon tissue: a comparative study. *J. Biophotonics*, **1**, 154–169.
49. Krafft, C., Ramoji, A., Bielecki, C., Vogler, N., Meyer, T., Akimov, D., Rösch, P., Schmitt, M., Dietzek, B., Petersen, I., Stallmach, A., and Popp, J. (2009) A comparative Raman and CARS imaging study of colon tissue. *J. Biophotonics*, **2**, 303–312.
50. Lasch, P. and Naumann, D. (2006) Spatial resolution in infrared micro spectroscopic imaging of tissues. *Biochim. Biophys. Acta, Biomembr.*, **1758**, 814–829.
51. Meyer, T., Akimov, D., Tarcea, N., Chatzipapadopoulos, S., Muschiolik, G., Kobow, J., Schmitt, M., and Popp, J. (2008) Three-dimensional molecular mapping of a multiple emulsion by means of CARS microscopy. *J. Phys. Chem. B*, **112**, 1420–1426.
52. Koljenovic, S., Bakker Schut, T.C., Wolthuis, R., de Jong, B., Santos, L.F., Caspers, J.M., Kros, J.M., and Puppels, G.J. (2005) Tissue characterization using high wave number Raman spectroscopy. *J. Biomed. Opt.*, **10**, 031116.

53. Krafft, C., Kirsch, M., Beleites, C., Schackert, G., and Salzer, R. (2007) Methodology for fiber-optic Raman mapping and FT-IR imaging of metastases in mouse brains. *Anal. Bioanal. Chem.*, **389**, 1133–1142.
54. Agranoff, R.W. and Hajra, A.K. (1994) in *Basic Neurochemistry*, 5th edn (eds G.J. Siegel, R.W. Agranoff, P.B. Albers, and P.B. Molinoff), Raven Press, New York, pp. 97–116.
55. Yates, A.J., Thompson, D.K., Boesel, C.P., Albrightson, C., and Hart, R.W. (1979) Lipid-composition of human neural tumors. *J. Lipid Res.*, **20**, 428–436.
56. Louis, D.N., Ohgaki, H., Wiestler, O.D., Cavenee, W.K., Burger, P.C., Jouvet, A., Scheithauer, B.W., and Kleihues, P. (2007) The 2007 WHO classification of tumours of the central nervous system. *Acta Neuropathol.*, **114**, 97–109.
57. Krafft, C., Thummler, K., Sobottka, S.B., Schackert, G., and Salzer, R. (2006) Classification of malignant gliomas by infrared spectroscopy and linear discriminant analysis. *Biopolymers*, **82**, 301–305.
58. Sobottka, S.B., Geiger, K.D., Salzer, R., Schackert, G., and Krafft, C. (2009) Suitability of infrared spectroscopic imaging as an intraoperative tool in cerebral glioma surgery. *Anal. Bioanal. Chem.*, **393**, 187–195.
59. Beleites, C., Geiger, K., Kirsch, M., Sobottka, S.B., Schackert, G., and Salzer, R. (2011) Raman spectroscopic grading of astrocytoma tissues: using soft reference information. *Anal. Bioanal. Chem.*, **400**, 2801–2816.
60. Polyzoidis, K.S., Miliaras, G., and Pavlidis, N. (2005) Brain metastasis of unknown primary: a diagnostic and therapeutic dilemma. *Cancer Treat. Rev.*, **31**, 247–255.
61. Krafft, C., Shapoval, L., Sobottka, S.B., Geiger, K.D., Schackert, G., and Salzer, R. (2006) Identification of primary tumors of brain metastases by SIMCA classification of IR spectroscopic images. *Biochim. Biophys. Acta*, **1758**, 883–891.
62. Krafft, C., Shapoval, L., Sobottka, S.B., Schackert, G., and Salzer, R. (2006) Identification of primary tumors of brain metastases by infrared spectroscopic imaging and linear discriminant analysis. *Technol. Cancer Res. Treat.*, **5**, 291–298.
63. Bergner, N., Bocklitz, T., Romeike, B.F.M., Reichart, R., Kalff, R., Krafft, C., and Popp, J. (2012) Identification of primary brain tumors of brain metastases by Raman imaging and support vector machines. *Chemom. Intell. Lab. Syst.*, **117**, 224–232.
64. Meyer, T., Bergner, N., Medyukhina, A., Dietzek, B., Krafft, C., Romeike, B.F., Reichart, R., Kalff, R., and Popp, J. (2012) Interpreting CARS images of tissue within the C-H-stretching region. *J. Biophotonics*, **5**, 729–733.
65. Krafft, C., Alipour Didehroshan, M., Recknagel, P., Miljkovic, M., Bauer, M., and Popp, J. (2011) Crisp and soft algorithms visualizes cell nuclei in Raman images of liver tissue sections. *Vib. Spectrosc.*, **55**, 90–100.
66. Hedegaard, M., Matthäus, C., Hassing, S., Krafft, C., Diem, M., and Popp, J. (2011) Spectral unmixing and clustering algorithms for assessment of single cells by Raman microscopic imaging. *Theor. Chem. Acc.*, **130**, 1249–1260.
67. Miljkovic, M., Chernenko, T., Romeo, M.J., Bird, B., Matthaus, C., and Diem, M. (2010) Label-free imaging of human cells: algorithms for image reconstruction of Raman hyperspectral datasets. *Analyst*, **135**, 2002–2013.
68. McNaughton, D., Bambery, K.R., and Wood, B.R. (2008) in *Vibrational Spectroscopy for Medical Diagnosis* (eds M. Diem, J.M. Chalmers, and P.R. Griffiths), John Wiley & Sons, Ltd, Chichester, pp. 187–202.
69. Roden, R. and Wu, T.C. (2006) How will HPV vaccines affect cervical cancer? *Nat. Rev. Cancer*, **6**, 753–763.
70. Wong, P.T., Wong, R.K., Caputo, T.A., Godwin, T.A., and Rigas, B. (1991) Infrared spectroscopy of exfoliated human cervical cells: evidence of extensive structural changes during carcinogenesis. *Proc. Natl. Acad. Sci. U.S.A.*, **88**, 10988–10992.
71. Utzinger, U., Heintzelmann, D.L., Mahadevan-Jansen, A., Malpica, A., Follen, M., and Richards-Kortum, R. (2001) Near-infrared Raman spectroscopy for in vivo detection of

cervical precancers. *Appl. Spectrosc.*, **55**, 955–959.
72. Steller, W., Einenkel, J., Horn, L.C., Braumann, U.D., Binder, H., Salzer, R., and Krafft, C. (2006) Delimitation of squamous cell cervical carcinoma using infrared microspectroscopic imaging. *Anal. Bioanal. Chem.*, **384**, 145–154.
73. Wood, B.R., Bambery, K.R., Evans, C.J., Quinn, M.A., and McNaughton, D. (2006) A three-dimensional multivariate image processing technique for the analysis of FTIR spectroscopic images of multiple tissue sections. *BMC Med. Imaging*, **6**, 12.
74. Lasch, P., Haensch, W., Naumann, D., and Diem, M. (2004) Imaging of colorectal adenocarcinoma using FT-IR microspectroscopy and cluster analysis. *Biochim. Biophys. Acta*, **1688**, 176–186.
75. Hanahan, D. and Weinberg, R.A. (2000) The hallmarks of cancer. *Cell*, **100**, 57–70.
76. Chiriboga, L., Xie, P., Vigorita, V., Zarou, D., Zakim, D., and Diem, M. (1998) Infrared spectroscopy of human tissue II: a comparative study of spectra of biopsies of squamous epithelium and of exfoliated cervical cells. *Biospectroscopy*, **4**, 55–59.
77. Romer, T.J., Brennan, J.F. III, Puppels, G.J., Zwinderman, A.H., van Duinen, S.G., van der Laarse, A., van der Steen, A.F., Bom, N.A., and Bruschke, A.V. (2000) Intravascular ultrasound combined with Raman spectroscopy to localize and quantify cholesterol and calcium salts in atherosclerotic coronary arteries. *Arterioscler. Thromb. Vasc. Biol.*, **20**, 478–483.
78. Römer, T.J., Brennan, J.F., Schut, T.C., Wolthuis, R., van den Hoogen, R.C., Emeis, J.J., Van der Laarse, A., Bruschke, A.V., and Puppels, G.J. (1998) Raman spectroscopy for quantifying cholesterol in intact coronary artery wall. *Atherosclerosis*, **141**, 117–124.
79. Nazemi, J.H. and Brennan, J.F. III, (2009) Lipid concentrations in human coronary artery determined with high wavenumber Raman shifted light. *J. Biomed. Opt.*, **14**, 034009.
80. Peres, M.B., Silveira, L. Jr., Zangaro, R.A., Tavares Pacheco, M.T., and Pasqualucci, C.A. (2011) Classification model based on Raman spectra of selected morphological and biochemical tissue constituents for identification of atherosclerosis in human coronary arteries. *Lasers Med. Sci.*, **26**, 645–655.
81. van de Poll, S.W., Kastelijn, K., Bakker Schut, T.C., Strijder, C., Pasterkamp, G., Puppels, G.J., and van der Laarse, A. (2003) On-line detection of cholesterol and calcification by catheter based Raman spectroscopy in human atherosclerotic plaque ex vivo. *Heart*, **89**, 1078–1082.
82. Buschman, H.P., Marple, E.T., Wach, M.L., Bennet, B., Bakker Schut, T.C., Bruining, H.A., Bruschke, A.V., van der Laarse, A., and Puppels, G.J. (2000) In vivo determination of the molecular composition of artery wall by intravascular Raman spectroscopy. *Anal. Chem.*, **72**, 3771–3775.
83. Matthäus, C., Dochow, S., Bergner, G., Lattermann, A., Romeike, B., Marple, E., Krafft, C., Dietzek, B., Brehm, B., and Popp, J. (2012) In vivo characterization of atherosclerotic plaque depositions by Raman-probe spectroscopy and in vitro CARS microscopic imaging on a rabbit model. *Anal. Chem.*, **84**, 7845–7851.
84. Motz, J.T., Fitzmaurice, M., Miller, A., Gandhi, S.J., Haka, A.S., Galindo, L.H., Dasari, R.R., Kramer, J.R., and Feld, M.S. (2006) In vivo Raman spectral pathology of human atherosclerosis and vulnerable plaque. *J. Biomed. Opt.*, **11**, 021003.
85. Scepanovic, O.R., Fitzmaurice, M., Miller, A., Kong, C.-R., Volynskaya, Z., Dasari, R.R., Kramer, J.R., and Feld, M.S. (2011) Multimodal spectroscopy detects features of vulnerable atherosclerotic plaque. *J. Biomed. Opt.*, **16**, 011009.
86. Krafft, C. and Sergo, V. (2006) Biomedical applications of Raman and infrared spectroscopy to diagnose tissues. *Spectroscopy*, **20**, 195–218.
87. Fernandez, D.C., Bhargava, R., Hewitt, S.M., and Levin, I.W. (2005) Infrared spectroscopic imaging for histopathologic recognition. *Nat. Biotechnol.*, **23**, 469–474.
88. Hata, T.R., Scholz, T.A., Ermakov, I.V., McClane, R.W., Khachik, F., Gellermann,

W., and Pershing, L.K. (2000) Non-invasive Raman spectroscopic detection of carotenoids in human skin. *J. Invest. Dermatol.*, **115**, 441–448.

89. Bernstein, P.S., Zhao, D.Y., Sharifzadeh, M., Ermakov, I.V., and Gellermann, W. (2004) Resonance Raman measurement of macular carotenoids in the living human eye. *Arch. Biochem. Biophys.*, **430**, 163–169.

4
Vibrational Spectroscopic Analysis of Hard Tissues

Sonja Gamsjaeger , Richard Mendelsohn, Klaus Klaushofer, and Eleftherios P. Paschalis

4.1
Introduction

4.1.1
Hard Tissue Composition and Organization

Biological hard tissues such as bone and dentin are composite materials with a hierarchical structure. They consist mainly of mineral (usually poorly crystalline hydroxyapatite, or in cases such as tooth enamel, highly crystalline hydroxyapatite) and an organic matrix (collagen and noncollagenous moieties such as proteoglycans, lipids, and noncollagenous proteins). The organic matrix is impregnated by mineral crystallites in a very precise manner (usually within collagen hole-zones), and as such, normal biological hard tissues manifest a high degree of organization [1].

4.1.2
Elements of Hard Tissues, Detectable by Vibrational Spectroscopy

Vibrational spectroscopy provides information on the functional groups present in the mineral and organic matrix components of hard tissues, as well as their "molecular neighborhood" [2, 3]. The mineralized tissue components and properties that can be easily determined through both Fourier transform infrared (FT-IR) or Raman spectroscopic analysis and their biological significance are as follows:

- *Mineral content*: The mineral of biological minerals such as bone and dentin is nonstoichiometric, poorly crystalline apatite. Apatite's formula is $Ca_{10}(PO_4)_6(OH)_2$, but in biological tissues there are crystal lattice substitutions such as Na^+, K^+, Mg^{2+} for Ca^{2-}; ${CO_3}^{2-}$ for either OH^- or ${PO_4}^{3-}$; ${HPO_4}^{2-}$ for ${PO_4}^{3-}$; as well as crystal lattice vacancies. On the other hand, the mineral phase of enamel is highly crystalline. From a biomechanical standpoint, the mineral component is responsible for the plastic properties of the tissues [4, 5]. The mineral content is usually estimated by the integrated area of the

Infrared and Raman Spectroscopic Imaging, Second Edition. Edited by Reiner Salzer, Heinz W. Siesler.
© 2014 Wiley-VCH Verlag GmbH & Co. KGaA. Published 2014 by Wiley-VCH Verlag GmbH & Co. KGaA.

ν_3 or ν_4 PO_4^{3-} band in FT-IR, or the ν_1, ν_2, ν_3, or ν_4 PO_4^{3-} bands in Raman analysis [2, 3].

- *Mineral maturity/crystallinity*: Since vibrational spectroscopy provides information on the chemical makeup of the biological mineral crystallites, the mineral maturity is measured; since changes in crystallite chemistry are responsible for changes in their size and shape, crystallinity is also measured by extrapolation. This parameter is usually estimated by resolution of the ν_1,ν_3 PO_4^{3-} FT-IR band to its underlying constituents through techniques such as second derivative spectroscopy or deconvolution that enhance spectral resolution and quantification of their relative contribution based on curve fitting [3, 6, 7]. In the case of Raman analysis, the mineral maturity/crystallinity is estimated by the full width at half height (FWHH) of the ν_1 PO_4^{3-} band, which is inversely related to this mineral characteristic, or by monitoring the wavenumber at the band maximum of the ν_1 PO_4^{3-} [2, 8].
- *Acidic phosphate content*: In biological apatites, acidic phosphate is one of the major crystal lattice substitutions, thus in part responsible for the mineral maturity/crystallinity as well as the solubility of the crystallites. In FT-IR analysis, the acidic phosphate content is determined usually through resolution of the ν_1, ν_3 PO_4^{3-} band to its underlying components through either second derivative spectroscopy or deconvolution methods, and quantification of their contribution through curve fitting [7, 9].
- *Carbonate content*: It is a major biological mineral apatite crystal substitution, contributing to the crystallite shape (depending on the type of substitution), solubility, and mineral maturity/crystallinity. In FT-IR analysis, its content is usually estimated by the integrated area of the band ~890 cm^{-1}, and the substitution type through resolution of it to its three underlying components followed by curve fitting routines. In Raman spectra, the A and B types of carbonate Raman bands are presented at 1103 and 1070 cm^{-1} [2, 10].
- *Organic matrix content*: The organic matrix of biological hard tissues such as bone and dentin consists of collagen and noncollagenous proteins, and is responsible for the elastic properties of the tissues from a biomechanical point of view [4, 5]. The main constituent is type I collagen [11]. Its content may be determined through integration of any of the amide bands (amide I, II, and III in FT-IR, and amide I or III in Raman) [2, 3]. Vibrational spectroscopic techniques such as FT-IR and Raman are one of the two techniques (the other being ash weight measurements) that can directly measure simultaneously both the mineral and the organic matrix contents of the tissue investigated. Since the mechanical properties of mineralized tissues depend on both the mineral and organic matrix components, accounting for both offers a big advantage over other techniques such as bone mineral density determined by either dual X-ray absorptiometry or micro-CT (computed tomography).
- *Proteoglycan content*: Proteoglycans are part of the organic matrix and are important determinants of tissue homeostasis. *In vitro* [12], *in situ* [13, 14], and *in vivo* [15–17] experiments have shown them to be negative modulators of mineralization, responsible for maintaining osteocyte lacunae and canaliculi

free of mineral [18, 19], and to modulate remodeling [15, 20, 21]. When dealing with mineralized tissues, their content may be easily determined by Raman analysis through integration of the 1365–1390 cm^{-1} band, characteristic of glycosaminoglycan chains [22, 23]. Unfortunately, in FT-IR, the bands used for proteoglycan determination in soft tissues are greatly overlapped by the mineral spectral signal and the amide III, making Raman the technique of choice to address questions pertaining to proteoglycans.

- *Lipid content*: In biological hard tissues, lipids have been reported to be mineral nucleators [24–26]. As is the case with proteoglycans, their content is rather easily established in Raman spectra through the integrated area of the characteristic band at ~1298 cm^{-1} [27].
- *Enzymatic collagen cross-links*: The most distinct feature of type I collagen in mineralized tissues is its cross-linking chemistry and molecular packing structure, which is responsible for various mechanical properties such as tensile strength and viscoelasticity [11]. At present, seven major collagen cross-links have been established as naturally occurring intermolecular cross-links. They are (1) dehydrodihydroxylysinonorleucine (deH-DHLNL), (2) dehydrohydroxylysinonorleucine (deH-HLNL), (3) dehydrohistidinohydroxymerodesmosine (deH-HHMD), (4) pyridinoline (Pyr), (5) deoxypyridinoline (d-Pyr; lysyl analog of Pyr), (6) pyrrole, and (7) histidinohydroxylysinonorleucine (HHL). The first three are $NaBH_4$ reducible while the rest are nonreducible compounds. The importance of collagen intermolecular cross-links to the mechanical performance of bone is very apparent in the pyridoxine-deficient chick animal model [28] as well as in lathyrism [29, 30]. Vibrational spectroscopic analysis (both FT-IR and Raman) is able to indirectly, through the perturbation these bonds exert on the vibrations of the carbonyl groups in the collagen molecule, determine two types of collagen cross-links to date, namely pyridinoline and divalent [31].
- *Mineral crystallite and collagen orientation/organization*: The mineral crystallites are intimately associated with the organic matrix (mainly type I collagen), and the resulting composite material is highly organized. Vibrational spectroscopic analysis is capable of providing information on hard tissue orientation/organization by either inserting a polarizer in the path of the FT-IR beam [32] or using selected Raman bands as the Raman beam is inherently polarized [33–35].

4.2
Importance of Tissue Age versus Specimen Age

4.2.1
Biologically Important Questions That May Be Answered by This Type of Analysis

The aforementioned mineralized tissue properties are not time invariant but rather demonstrate changing values as a function of subject age, tissue age,

and disease. One major confounding factor in determining these properties is their dependence on tissue age within the same subject as a result of various biological processes. For example, in normal humans, cortical bone constitutes ~80% of the human skeletal mass and trabecular bone constitutes ~20%. Bone surfaces may be inactive, undergoing formation or resorption. These processes occur throughout life in both cortical and trabecular bones. Bone remodeling is a surface phenomenon, and in humans it occurs on periosteal, endosteal, Haversian canal, and trabecular surfaces. The rate of cortical bone remodeling, which may be as high as 50% per year in the mid-shaft of the femur during the first 2 years of life, eventually declines to a rate of 2–5% per year in the elderly. Rates of remodeling in trabecular bone are proportionately higher throughout life and may normally be 5–10 times higher than cortical bone remodeling rates in the adult. This information is critical when evaluating bone properties at the microscopic level, thus tissue age should be considered as well. Both FT-IR and Raman spectroscopies can circumvent this problem, since modern apparatus used for either measurement can readily be altered to have microscopes attached so that distinct microanatomical areas may be analyzed and compared. Other additions such as fluorescent lamps may be appended to identify and analyze areas based on the presence of fluorescent double labels (a routine method in histology/histomorphometry), allowing the analysis of specific, well-defined tissue ages.

More recently, Raman instruments have been combined with atomic force microscopes, allowing the determination of molecular and biomechanical properties at the same micron or even sub-micron tissue region. Such a strategy may provide insight as to whether changes are solely due to biological mechanisms or whether other factors such as physical chemical mechanisms contribute to these changes. Moreover, since the frequently monitored hard tissue properties have a range of values in the normal case, it is feasible to determine whether changes in disease are outside this range, or the kinetics of maturation processes are altered, or a combination of the two is responsible for the observed changes. In addition, both FT-IR and Raman techniques are capable of providing simultaneous information on the amount and the quality of the mineral and organic matrix constituents of biological hard tissues, providing important and otherwise unattainable information of biological and physical chemical mechanisms in health and disease.

4.3 FT-IR Spectroscopy

4.3.1 Specimen Preparation and Typical FT-IR Spectrum

Historically, hard tissues were analyzed by FT-IR as homogenized powders in KBr or other infrared transparent material pellets of known sample concentrations.

With the advent of FT-IR microspectroscopic and imaging techniques, the most common specimen preparation routine is tissue fixation in alcohol (as other fixatives such as formaldehyde may interfere with the spectral signature of the organic matrix), embedding in a plastic medium such as polymethyl methacrylate (PMMA) (a preferable medium as it has minimal interference with spectra of hard tissues compared to other embedding media) [36], and acquisition of thin sections (0.5–5 μm depending on the tissue under investigation) for analysis in transmittance. The fact that thin tissue sections instead of homogenates may be analyzed enables the monitoring of the various parameters as a function of tissue age or microanatomical location. Direct correlation with outcomes of other analytical methods such as histology/histomorphometry or electron microscopy, among others, may be readily acquired [3, 37–40]. Recently, a method was described for FT-IR microspectroscopic analysis in the reflection mode [41], which potentially eliminates the need for embedding and sectioning of the tissue, although it should be kept in mind that the vast majority of at least human specimens suitable for FT-IR analysis are already embedded because of clinical requirements.

A typical FT-IR spectrum of human bone from an iliac crest biopsy of a 42-year-old healthy female subject is shown in Figure 4.1 with the bands of interest appropriately labeled, while in Figure 4.2 typical outcomes of FT-IR imaging in the area of trabecular bone from an iliac crest biopsy of the same subject are shown. Depending on the microanatomical location from which the spectra are acquired,

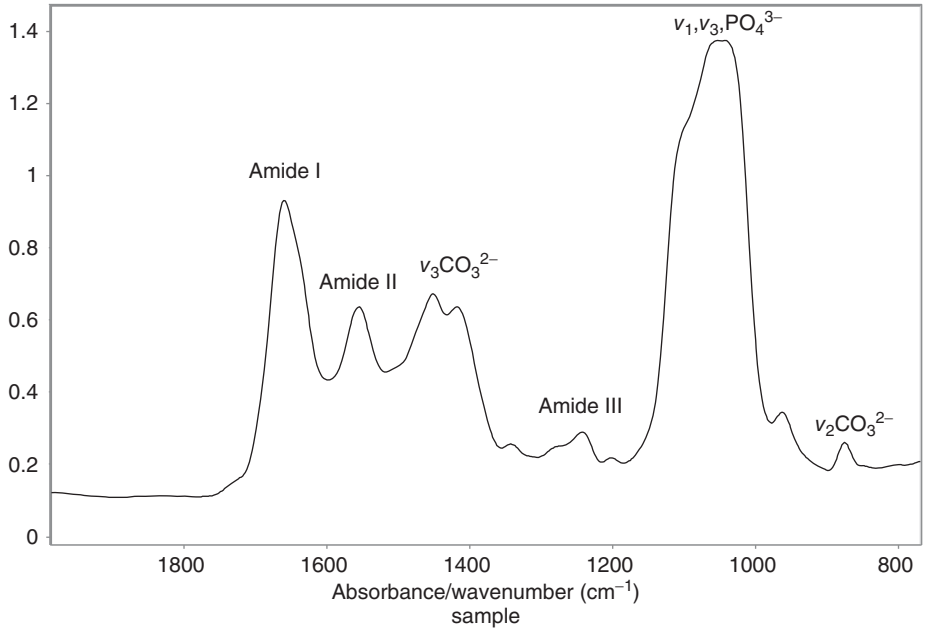

Figure 4.1 Typical FT-IR spectrum of bone from an iliac crest biopsy with all the relevant bands appropriately labeled.

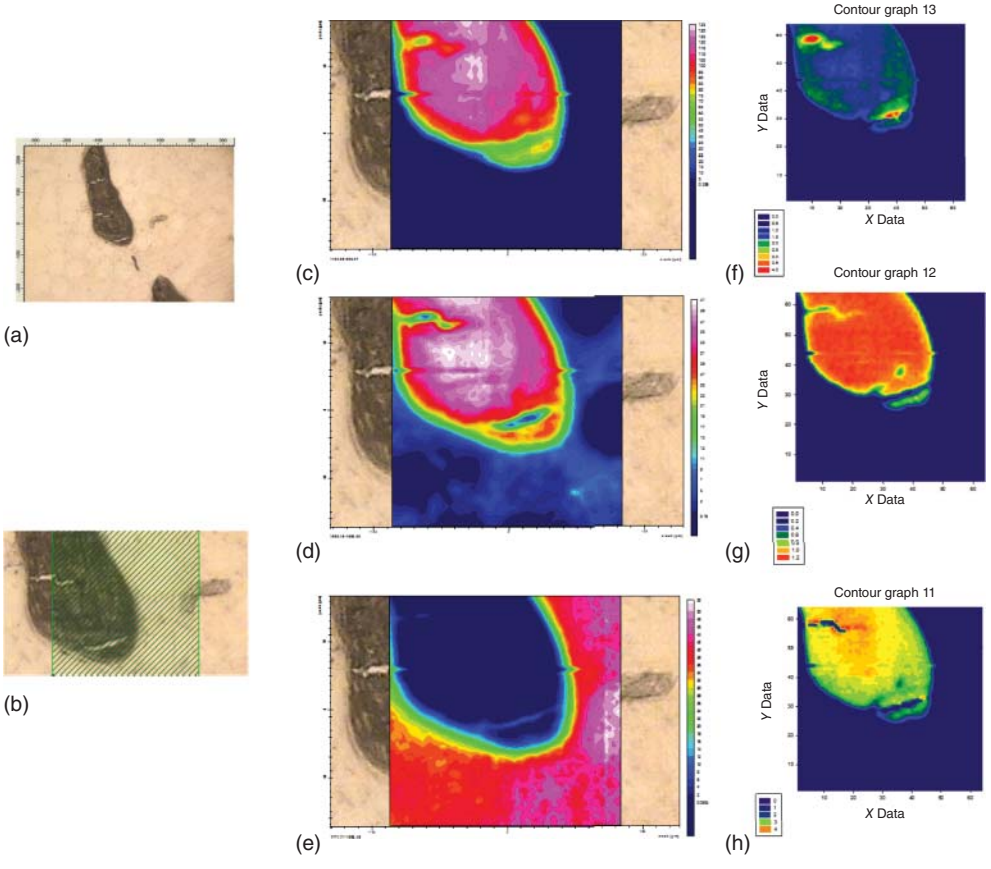

Figure 4.2 (a) A picture taken through the 4× objective in the trabecular bone of an iliac crest biopsy; (b) same trabecula through the 15× objective with the area of analysis shaded; (c) spatial distribution of the mineral component content; (d) spatial distribution of the organic matrix content; (e) spatial distribution of the PMMA (embedding medium) content; (f) calculated spatial distribution of the mineral/matrix ratio; (g) calculated spatial distribution of the mineral maturity/crystallinity; and (h) calculated spatial distribution of the pyridinoline/divalent collagen cross-link ratio.

PMMA spectral interference may be present, in which case the spectra should be processed appropriately as published elsewhere, so as to eliminate the embedding medium spectral contribution [36, 38, 39, 42, 43].

4.3.2 Examples from Published Literature

FT-IR analysis has been extensively applied to the analysis of the mineral and organic matrix components of teeth and bones in animal models and human specimens.

Results of such analysis of enamel (the outermost layer of teeth) has contributed to the understanding of its chemical makeup (composite of crystalline apatite mineral and organic matrix consisting of proteins such as amelogenins) [44–52], especially the precise composition of the mineral phase, including considerations such as type and extent of carbonate substitution in the apatitic crystal lattice (influencing the shape and the solubility of the mineral crystallites). Moreover, FT-IR analysis has contributed to the understanding of factors that influence enamel hardness [53, 54] as well as tooth shade [55]. Moreover, it has been used to evaluate the effect on enamel properties of various dental procedures such as bleaching, etching [56–66], and adhesives [58–60, 65, 67]. In addition, such analysis has aided in defining the mechanism of caries formation and management/prevention [51, 63, 68–74], and the evaluation of the effect of commonly used fluoride for either caries prevention or enamel regeneration [56, 68, 69, 73, 75]. It has also assisted in understanding the role of ameloblasts [44, 76–78], how genes and organic moieties such as matrix metalloproteinases regulate the biomineralization process [76, 78, 79], the study of dental plaque and oral biofilms [63, 67], and compositional changes in disease [80, 81].

Similarly, FT-IR analysis has aided in the determination of the composition of dentin [82]; its pathogenesis and repair [83]; changes in its structure due to irradiation or heating [84–87]; the effect of dental bleaching on its structure and composition [61, 66, 88–90]; the role of proteoglycans in dentin mineralization [91]; the effect of dental primers, conditioners, bonding agents, and resins [60, 87, 92–133]; understanding the mechanism of caries formation and repair [83, 130, 134–143]; the role of dentinal tubules and their response to various dental procedures [80, 90, 136, 139, 144–156], as well as the structure and composition of reactionary dentin [145].

Although FT-IR analysis has proven to be a useful tool in the study of dental hard tissues, its most important contribution to date may be seen in the bone-related literature. The advent of FT-IR microspectroscopic and imaging instruments allows the acquisition of large amounts of data in a short time period, and efficient software for multivariate analysis performs the various analyses as a function of anatomical location and tissue age. This enables the correlation of the spectroscopic outcomes with the outcomes obtained through other analyses such as histology/histomorphometry, nanoindentation, and electron microscopy [3, 39, 43]. The FT-IR-determined outcomes are of particular importance since it is widely accepted nowadays that bone strength depends on both the amount of the mineral and organic matrix components and the quality. Bone quality is a multifactorial entity encompassing the structural (as determined by μCT analysis) and material properties of bone [1]. The outcomes of FT-IR analysis are related to the bone material properties. Moreover, FT-IR uniquely allows the description of collagen cross-links in a spatially resolved manner [31]. Finally, in addition to the amount and quality of mineral, FT-IR analysis directly and simultaneously measures the amount and quality of the organic matrix component of bone unlike routinely used in the clinical setting such as dual x-ray absorptiometry (DXA).

FT-IR analysis to date has aided in understanding bone composition and quality in health [7, 157–161] as well as changes due to either tissue age [7, 157, 158, 161], subject aging [162, 163], disease [3, 30, 37–39, 43, 164–175–180], or in response to therapies due to disease [170, 173, 181–193]. We emphasize that even in cases that the widely clinically used bone strength surrogate of bone mineral density failed to correlate with fracture incidence or bone strength determined by biomechanical tests, FT-IR derived parameters such as mineral maturity/crystallinity and especially collagen cross-links have consistently revealed correlations [30, 164, 171, 175, 193].

4.4 Raman Spectroscopy

4.4.1 Instrumental Choices, Specimen Preparation, and Typical Raman Spectra

Raman microspectroscopy is a nondestructive vibrational spectroscopic technique that measures both the mineral and the organic matrix components of hard tissues with high spatial resolution (0.6–1 μm) that depends on the laser wavelength and the numerical aperture (NA) of the objective, while the depth of penetration is a function of the NA of the objective lens, the refractive index of the immersion medium (n), and the wavelength of the light (λ) [194]. The selection of the laser is critical not only for the lateral resolution but also for any broad fluorescence background influencing prominent Raman bands [195]. The most commonly used solid-state laser emits at 785 nm, but the Raman scattering is about five times less intense than a 532 nm excitation source. Other common laser lines emit at 1064 and 633 nm. Raman spectroscopy with a deep-ultraviolet excitation (244 nm) was used to study human cortical bone, as this approach avoids the fluorescence background usually associated with visible and near-infrared excitation [196].

Raman spectroscopy can analyze native (without prior fixation and embedding procedures) hard tissue, although for clinical reasons most of the available hard tissues for analysis have been already fixed and plastic embedded. Yeni *et al.* [197] have reported on the effect of ethanol and glycerol as fixatives as well as a variety of embedding media. Both fixation and embedding processes altered the spectral signature of bone tissue to an extent that the parameters derived from spectra were significantly different from freshly hydrated bone tissue [197–199]. Nevertheless, methods to account for the tissue processing interference with the obtained spectra have been described [197].

Another important criterion for Raman microspectroscopic analysis is the selection of the areas to be analyzed, as this offers the possibility to directly correlate the spectroscopically determined outcomes with results from other techniques such as histology/histomorphometry [200]. In addition, most of the samples from clinical or animal studies are in most cases labeled with

fluorochromes (tetracycline, alizarin, or calcein), according to a standard protocol. In tissue samples, forming areas (new mature bone) can be seen through a fluorescence microscope, and with the high lateral resolution of Raman microscopy (50× objective) measurements can be obtained in the osteoid, between the two fluorescence labels and in older (more mature) bone [171, 188, 201, 202].

4.4.2
Bone: Typical Raman Bands and Parameters

A typical Raman spectra obtained from an iliac crest biopsy of a 42-year-old healthy female subject at microanatomical locations of different tissue age (as determined by fluorescence labels) are shown in Figure 4.3 with all the bands of interest appropriately labeled. Figure 4.4 shows typical Raman imaging outcomes in the area of trabecular and osteonal (cortical) bones in the same biopsy, while Figure 4.5 shows Raman imaging outcomes from the analysis of the bone–cartilage interface in a tissue block from the knee of a 57-year-old healthy male necropsy specimen. Information concerning the mineral component may be derived from the phosphate and carbonate vibrational modes. The ν_1 phosphate stretching vibration at 960 cm^{-1} is the strongest marker for bone mineral. The ν_2 and ν_4 phosphate-bending vibrations are visible at 430 and 580 cm^{-1} while the ν_3 stretching mode appears at 1045 cm^{-1} [2]. Type A and type B carbonate bands may be detected at 1103 and 1071 cm^{-1}, respectively, and at 756 cm^{-1} for type B carbonate [10, 203–205]. In Raman spectroscopic analysis, band shifts are of

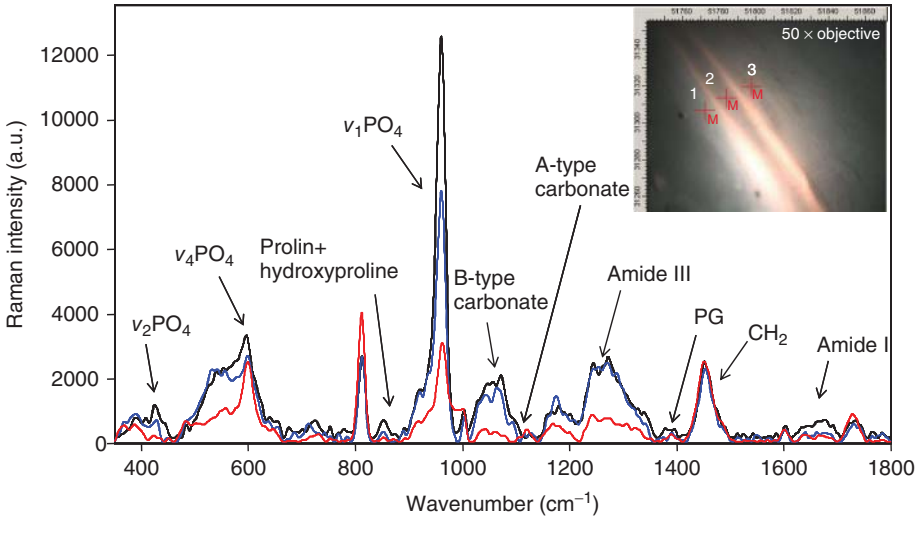

Figure 4.3 Raman spectra obtained in different tissue age mineralized bone from a tracecula; red position 1 youngest, blue position 2 middle, black position 3 older; 785 nm laser, 100 mW, 5 s/10 co-additions, with the peaks of interest labeled.

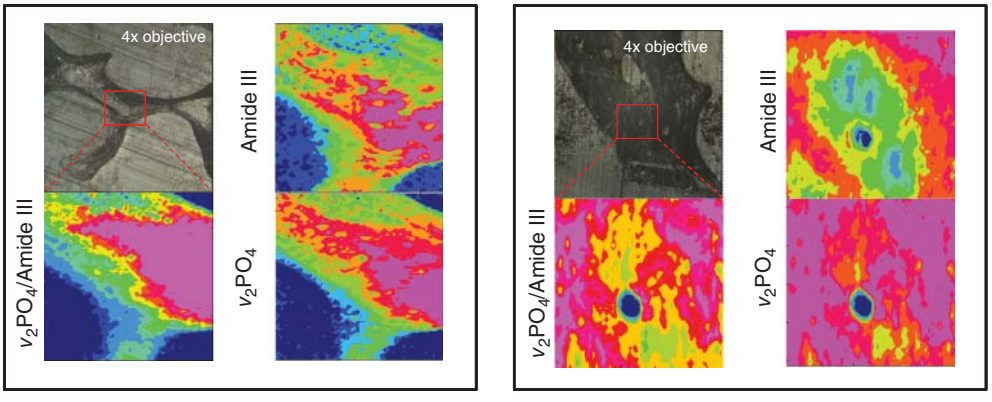

Figure 4.4 Raman image from a human trabecula (a) obtained through the 20× objective, step size 5 µm; 785 nm laser, 100 mW, 1 s/3 co-additions, showing the spatial distribution of the mineral and the organic matrix content as well as the calculated mineral/matrix ratio. Similar images in (b) describe the same parameters in the osteonal (cortical) bone in the same iliac crest biopsy.

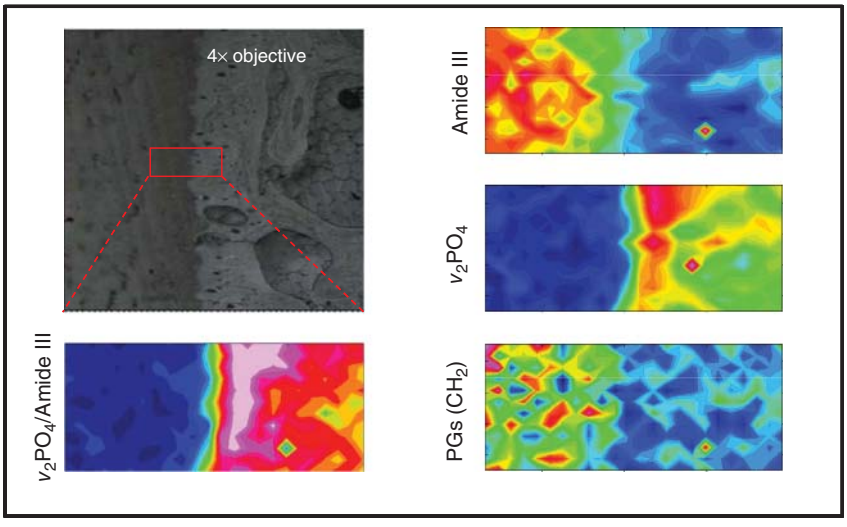

Figure 4.5 Raman image from a human cartilage–bone interface (knee joint) obtained through the 20× objective, step size 5 µm; 785 nm laser, 100 mW, 1 s/2 co-additions. The spatial distributions of the mineral, organic matrix, and proteoglycan content as well as the calculated mineral/matrix ratio are shown.

particular interest, as they reveal information concerning chemical changes of the mineral component [8]. For example, in carbonated apatites (the major mineral phase in most biologically relevant hard tissues) the ν_1 mode of phosphate at 960 cm^{-1} for hydroxyapatite is shifted to lower wavenumbers [10], whereas the ν_1 phosphate mode of the Raman spectra of bones treated with fluoride is shifted from 961 to 964 cm^{-1} [206]. In addition, the FWHH of the ν_1 PO_4 band around 960 cm^{-1} has been shown to be inversely related to mineral maturity/crystallinity [2, 207].

As noted earlier, hard tissues are composite materials consisting of mineral and organic matrix. In Raman spectroscopic analysis, the organic matrix is identified by methylene side chains (CH_2 at 1450 cm^{-1}), amide III (~1200–1300 cm^{-1}), amide I (~1620–1700 cm^{-1}), phenylalanine (1002 cm^{-1}) or the combined proline (921 and 855 cm^{-1}), and hydroxyproline (876 cm^{-1}) bands [2, 27, 208–210]. The main band representative of collagen is the amide I region from ~1620 to 1700 cm^{-1}, although it does encompass information from noncollagenous proteins, lipids, and proteoglycans (e.g., proteins with α-helix domains do contribute at ~1645–1654 and at 1670 cm^{-1}) [23, 27, 208, 211, 212]. Lipids are identified by the CH vibrations at 1296 (CH_2 twisting), 1440, and at 1465 cm^{-1} (CH_2 scissoring) [27].

Unlike FT-IR, the mineral/matrix ratio in Raman spectra may be expressed based on different bands, such as the ν_1PO_4/amide I ratio, ν_2PO_4/amide III ratio, or the ν_1PO_4/combined proline and hydroxyproline (851 + 873 + 917 cm^{-1}) ratio [2, 210, 213]. The choice of parameters is dependent on the embedding material, instrumentation and the band sensitivity to orientation [33–35]. Other parameters that are commonly reported are the carbonate-to-mineral ratio from the B-type carbonate at 1071 cm^{-1} and either the ν_1 or ν_2 phosphate bands [2, 210]. This ratio is indicative of the age (maturation status) of mineral crystals in biological hard tissues [214]. The relative proteoglycan content may also be deduced, expressed usually as the ratio of the proteoglycan to the amide III bands [188, 201]. For proteoglycan determination, the band around 1060 cm^{-1} is used [215–217], which has been associated with sulfates because of the symmetric stretching vibration of the OSO_3 group [22]. On the other hand, type I collagen (the major constituent of the organic matrix in most biological hard tissues) also gives rise to a band in the area at 1060 cm^{-1} [208], and type B carbonated apatites also express a strong band around 1070 cm^{-1}. For this reason, it is better to use another Raman band for the identification of proteoglycans, ~1375–1377 cm^{-1}, which is due to the CH_3 symmetric deformation of the glycosaminoglycan groups present in proteoglycans [22, 23] although lipid chain modes may interfere with this measurement.

4.4.3 Examples from Published Literature

In dental hard tissues (enamel, dentin), Raman spectroscopic analysis has aided in the establishment of their composition [10], the effect of lactic acid on their

structure showing that the modifications because of the acidic attack essentially concern the mineral phosphate group, and that changes in intensity of the PO_4 band are linked to the type of dentin, to its anatomical location, and to the age of the subject [218–220]. Raman analysis has also been used in the investigation of dental-related disease such as osteoradionecrosis (ORN) of the mandibular bone, a serious complication that may occur after radiation therapy [221]. The mechanical properties of both dentin and enamel have been investigated through a combinatorial instrumental approach combining atomic force microscopy (AFM) with Raman spectroscopy [222–224]. Raman analysis has also proven useful in understanding compositional changes in dental hard tissues because of irradiation by Nd:YAG, Er:YAG, and CO_2 lasers [225–227]; the pathogenesis, prevention, and treatment of carious and noncarious lesions [228–231]; the effect of hydrogen peroxide bleaching strips on tooth surface color, surface microhardness, surface and subsurface ultrastructure, and microchemical composition [232–234]; and the effects of commonly used dental materials in preventive or operative dentistry on dentin permeability and remineralization [235]. Finally, due to its superb spatial resolution, Raman microspectroscopic analysis is particularly well suited for investigations of the dentin–enamel junction (DEJ), an interface that plays an important role in preventing crack propagation from enamel into dentin [236, 237].

In bone-related research, Raman spectroscopic and microspectroscopic analyses have proven useful in understanding biomineralization mechanisms both in cell cultures [238–242] and in intact bone from animal models and humans [214]. The approach has also described the evolution of the mineral phase of bone during specimen aging, by revealing the presence of other transient calcium phosphate phases (in addition to the poorly crystalline hydroxyapatite) at the very early stages (from a specimen age point of view) of bone formation [243]. As mentioned earlier, the bone mineral characteristics change because of both specimen and tissue age, and Raman microspectroscopic analysis has been used to monitor these characteristics as a function of both types of ages in an animal model [33]. The impact of gender on bone mineral properties was investigated in a mouse model of osteogenesis imperfecta (OI) in female and male tibia. The male mice had inherently more bone compared to that of genotype-matched female counterparts with a corresponding increase in bone biomechanical strength. The primary influence of gender was structure/geometry in bone growth and mechanical properties, whereas the mineral/matrix composition and hydroxyproline content of bone were influenced primarily by the OI collagen mutation [244]. Raman spectroscopic analysis has been used in the study of bones from animal models with the goal of understanding compositional and structural changes in disease, and also to determine the main contribution to overall bone strength [245–260]. Analyzing human specimens by Raman spectroscopy, it was shown in human femoral cortical bone that the quantity and microstructural organization of bone rather than the mean chemical composition of the tissue change with age [261]. Yerramshetty *et al.* [262, 263] analyzed mid-diaphyseal portions of human femora from male (age range, 52–85 years) and showed an

increase in the compositional and physicochemical homogeneity of male femoral cortex as well as associations between mineral crystallinity and the mechanical properties of human cortical bone. Raman spectroscopic outcomes have been extensively correlated with results of biomechanical (including nanoindentation) tests in the same bones, offering important clues about the relationship between bone material properties and bone strength [264–274], and considerations such as microdamage [275, 276], as well as the intimate interaction between mineral particles and collagen fibers [222].

Recently, Raman microspectroscopic analysis has been the analytical tool of choice to determine human bone compositional and structural changes in health and disease, as a function of aging, and in response to various therapies, due to its superb spatial resolution and its combination with other techniques such as nanoindentation, quantitative backscattered electron imaging, FT-IR, and histology/histomorphometry [163, 171, 186, 188, 201, 202, 262, 274, 277–281].

Raman spectroscopic analysis is inherently sensitive to molecular orientation distribution, and as such has been used to discriminate between compositional and structural/orientational changes in mineralized tissues [2, 33–35, 210, 282–285]. Raman spectral imaging has been utilized [34] to demonstrate the orientation of mineral and collagen components in osteonal lamellae from a healthy human female. Polarized Raman spectroscopy was used to analyze bones from an animal model of OI, showing that mineral crystallites are not as well aligned in the affected animals as that of gender and age-matched controls [284]. Nevertheless, caution should be exercised when attempting to quantify these organizational changes as bands such as the phosphate and amides are composite ones consisting of underlying features specific to certain molecular environments with differing sensitivity to polarization. Morris *et al.* have convincingly shown that one has to be aware of systematic errors from elastic scattering in bone tissue that can be reduced by the use of a high NA objective to minimize depolarization [284]. In tissues with higher turbidity and an anisotropy factor of >0.9, an oil- or water-immersion objective might be required to limit depth of field, but such objectives themselves partially depolarize Raman scatter because of their high collection angles. Corrections for this effect are complicated. Moreover, the mathematical description of orientation effects in Raman spectra has been derived for single fibers, not for extended arrays of fibers that are found in bone. Finally in human bone, the thickness of the lamellae is about 2–9 μm and the confounding effects of multiple lamellae would be diminished, but multiple scattering can still occur [284].

4.5 Clinical Applications of Raman Spectroscopy

Outcomes of FT-IR and Raman spectroscopic analyses are complementary and each technique has its advantages. For example, FT-IR has superior signal-to-noise ratio while Raman has superior lateral spatial resolution and minimal sample

preparation requirements. Although both are very powerful analytical tools, the question lingers whether they can be routinely applied in clinical settings. Both can analyze biopsied tissue, but obtaining biopsies for general diagnostic purposes is becoming less frequent. FT-IR techniques, whether in transmission or in reflection, do require excised tissue. On the other hand, recent reports open the possibility of the Raman analysis to be used in the clinical setting [286]. Efforts have been undertaken toward using Raman analysis of fingernails as a surrogate for bone strength [287–289]. Even more exciting is the progress reported in analyses employing of spatially offset Raman spectroscopy (SORS, see Chapter 13 of this book), allowing the subsurface probing of specific tissues through different overlying tissues such as assessment of bone quality through skin [290–306]. Esmonde-White *et al.* [216] have described Raman spectroscopy for arthroscopy of joint tissues using a custom-built fiber-optic probe. Differentiation of healthy and damaged tissue or examination of subsurface tissue, such as subchondral bone, is a challenge in arthroscopy because visual inspection may not provide sufficient contrast. Discrimination of healthy versus damaged tissue may be improved by incorporating point spectroscopy or hyperspectral imaging into arthroscopy where the contrast is based on the molecular structure or chemical composition.

References

1. Fratzl, P. *et al.* (2004) Structure and mechanical quality of the collagen–mineral nano-composite in bone. *J. Mater. Chem.*, **14**, 2115–2123.
2. Morris, M.D. and Mandair, G.S. (2011) Raman assessment of bone quality. *Clin. Orthop. Relat. Res.*, **469** (8), 2160–2169.
3. Paschalis, E.P., Mendelsohn, R., and Boskey, A.L. (2011) Infrared assessment of bone quality: a review. *Clin. Orthop. Relat. Res.*, **469** (8), 2170–2178.
4. Burstein, A.H. and Wright, T.W. (1994) in *Fundamentals of Orthopaedic Biomechanics* (ed. W.M.I. Passano), Williams & Wilkins, Baltimore, MD, pp. 133–170.
5. Burstein, A.H. *et al.* (1975) Contribution of collagen and mineral to the elastic-plastic properties of bone. *J. Bone Joint Surg.*, **57A**, 956–961.
6. Gadaleta, S.J. *et al.* (1996) Fourier transform infrared spectroscopy of the solution-mediated conversion of amorphous calcium phosphate to hydroxyapatite: new correlations between X-ray diffraction and infrared data. *Calcif. Tissue Int.*, **58** (1), 9–16.
7. Paschalis, E.P. *et al.* (1997) FTIR microspectroscopic analysis of normal human cortical and trabecular bone. *Calcif. Tissue Int.*, **61** (6), 480–486.
8. Kazanci, M. *et al.* (2006) Complementary information on in vitro conversion of amorphous (precursor) calcium phosphate to hydroxyapatite from Raman microspectroscopy and wide-angle X-ray scattering. *Calcif. Tissue Int.*, **79** (5), 354–359.
9. Spevak, L. *et al.* (2013) Fourier transform infrared spectroscopic imaging parameters describing acid phosphate substitution in biologic hydroxyapatite. *Calcif. Tissue Int.*, **92** (5), 418–428.
10. Penel, G. *et al.* (1998) MicroRaman spectral study of the PO4 and CO3 vibrational modes in synthetic and biological apatites. *Calcif. Tissue Int.*, **63** (6), 475–481.
11. Yamauchi, M. (1996) in *Calcium and Phosphorus in Health and Disease* (eds J.J.B. Anderson and S.C. Garner), CRC Press, New York, pp. 127–141.
12. Boskey, A.L. *et al.* (1997) Effects of bone CS-proteoglycans, DS-decorin, and DS-biglycan on hydroxyapatite

formation in a gelatin gel. *Calcif. Tissue Int.*, **61** (4), 298–305.
13. Mochida, Y. *et al.* (2003) Decorin modulates matrix mineralization in vitro. *Biochem. Biophys. Res. Commun.*, **305** (1), 6–9.
14. Mochida, Y. *et al.* (2009) Decorin modulates collagen matrix assembly and mineralization. *Matrix Biol.*, **28** (1), 44–52.
15. Nielsen, K.L. *et al.* (2003) Biglycan deficiency interferes with ovariectomy-induced bone loss. *J. Bone Miner. Res.*, **18** (12), 2152–2158.
16. Bi, Y. *et al.* (2006) Biglycan deficiency increases osteoclast differentiation and activity due to defective osteoblasts. *Bone*, **38** (6), 778–786.
17. Xu, T. *et al.* (1998) Targeted disruption of the biglycan gene leads to an osteoporosis-like phenotype in mice. *Nat. Genet.*, **20** (1), 78–82.
18. Sauren, Y.M. *et al.* (1992) An electron microscopic study on the presence of proteoglycans in the mineralized matrix of rat and human compact lamellar bone. *Anat. Rec.*, **232** (1), 36–44.
19. Thompson, W.R. *et al.* (2011) Perlecan/Hspg2 deficiency alters the pericellular space of the lacunocanalicular system surrounding osteocytic processes in cortical bone. *J. Bone Miner. Res.*, **26** (3), 618–629.
20. Gualeni, B. *et al.* (2013) Alteration of proteoglycan sulfation affects bone growth and remodeling. *Bone*, **54** (1), 83–91.
21. Ohtsuki, T. *et al.* (1995) Immunohistochemical identification of proteoglycan form of macrophage colony-stimulating factor on bone surface. *Calcif. Tissue Int.*, **57** (3), 213–217.
22. Bansil, R., Yannas, I.V., and Stanley, H.E. (1978) Raman spectroscopy: a structural probe of glycosaminoglycans. *Biochim. Biophys. Acta*, **541** (4), 535–542.
23. Ellis, R., Green, E., and Winlove, C. (2009) Structural analysis of glycosaminoglycans and proteoglycans by means of raman microspectrometry. *Connect. Tissue Res.*, **50**, 29–36.
24. Boskey, A.L. and Reddi, A.H. (1983) Changes in lipids during matrix: induced endochondral bone formation. *Calcif. Tissue Int.*, **35** (4-5), 549–554.
25. Goldberg, M. and Boskey, A.L. (1996) Lipids and biomineralizations. *Prog. Histochem. Cytochem.*, **31** (2), 1–187.
26. Raggio, C.L., Boyan, B.D., and Boskey, A.L. (1986) In vivo hydroxyapatite formation induced by lipids. *J. Bone Miner. Res.*, **1** (5), 409–415.
27. Penel, G. *et al.* (2005) Composition of bone and apatitic biomaterials as revealed by intravital Raman microspectroscopy. *Bone*, **36** (5), 893–901.
28. Masse, P.G. *et al.* (1996) Pyridoxine deficiency affects biomechanical properties of chick tibial bone. *Bone*, **18** (6), 567–574.
29. Oxlund, H., *et al.*, Reduced concentrations of collagen cross-links are associated with reduced strength of bone. *Bone*, 1995. **17**(4, Suppl.): 365S-371S.
30. Paschalis, E.P. *et al.* (2011) Lathyrism-induced alterations in collagen cross-links influence the mechanical properties of bone material without affecting the mineral. *Bone*, **49**, 1232–1241.
31. Paschalis, E.P. *et al.* (2001) Spectroscopic characterization of collagen cross-links in bone. *J. Bone Miner. Res.*, **16** (10), 1821–1828.
32. Gadaleta, S.J. *et al.* (1996) Polarized FT-IR microscopy of calcified turkey leg tendon. *Connect. Tissue Res.*, **34** (3), 203–211.
33. Gamsjaeger, S. *et al.* (2010) Cortical bone composition and orientation as a function of animal and tissue age in mice by Raman spectroscopy. *Bone*, **47**, 392–399.
34. Kazanci, M. *et al.* (2006) Bone osteonal tissues by Raman spectral mapping: orientation-composition. *J. Struct. Biol.*, **156** (3), 489–496.
35. Kazanci, M. *et al.* (2007) Raman imaging of two orthogonal planes within cortical bone. *Bone*, **41** (3), 456–461.
36. Aparicio, S. *et al.* (2002) Optimal methods for processing mineralized tissues for Fourier transform infrared microspectroscopy. *Calcif. Tissue Int.*, **70** (5), 422–429.

37. Boskey, A. and Mendelsohn, R. (2005) Infrared analysis of bone in health and disease. *J. Biomed. Opt.*, **10** (3), 031102.
38. Mendelsohn, R., Paschalis, E.P., and Boskey, A.L. (1999) Infrared spectroscopy, microscopy, and microscopic imaging of mineralizing tissues: spectra-structure correlations from human iliac crest biopsies. *J. Biomed. Opt.*, **4** (1), 14–21.
39. Paschalis, E.P. (2009) Fourier transform infrared analysis and bone. *Osteoporos. Int.*, **20** (6), 1043–1047.
40. Boskey, A.L. (2006) Assessment of bone mineral and matrix using backscatter electron imaging and FTIR imaging. *Curr. Osteoporos. Rep.*, **4** (2), 71–75.
41. Acerbo, A.S. *et al.* (2012) Imaging the material properties of bone specimens using reflection-based infrared microspectroscopy. *Anal. Chem.*, **84** (8), 3607–3613.
42. Marcott, C. *et al.* (1998) Infrared microspectroscopic imaging of biomineralized tissues using a mercury-cadmium-telluride focal-plane array detector. *Cell Mol. Biol. (Noisy-le-grand)*, **44** (1), 109–115.
43. Paschalis, E.P. (2012) Fourier transform infrared imaging of bone. *Methods Mol. Biol.*, **816**, 517–525.
44. Aoba, T. and Moreno, E.C. (1990) Changes in the nature and composition of enamel mineral during porcine amelogenesis. *Calcif. Tissue Int.*, **47** (6), 356–364.
45. Beniash, E. *et al.* (2009) Transient amorphous calcium phosphate in forming enamel. *J. Struct. Biol.*, **166** (2), 133–143.
46. Bonar, L.C. *et al.* (1991) Structural and composition studies on the mineral of newly formed dental enamel: a chemical, x-ray diffraction, and 31P and proton nuclear magnetic resonance study. *J. Bone Miner. Res.*, **6** (11), 1167–1176.
47. Miake, Y. *et al.* (1993) Epitaxial overgrowth of apatite crystals on the thin-ribbon precursor at early stages of porcine enamel mineralization. *Calcif. Tissue Int.*, **53** (4), 249–256.
48. Rey, C. *et al.* (1991) A resolution-enhanced Fourier transform infrared spectroscopic study of the environment of the CO3(2-) ion in the mineral phase of enamel during its formation and maturation. *Calcif. Tissue Int.*, **49** (4), 259–268.
49. Rey, C. *et al.* (1990) Resolution-enhanced Fourier transform infrared spectroscopy study of the environment of phosphate ions in the early deposits of a solid phase of calcium-phosphate in bone and enamel, and their evolution with age. I: Investigations in the upsilon 4 PO4 domain. *Calcif. Tissue Int.*, **46** (6), 384–394.
50. Rey, C. *et al.* (1991) Resolution-enhanced Fourier transform infrared spectroscopy study of the environment of phosphate ion in the early deposits of a solid phase of calcium phosphate in bone and enamel and their evolution with age: 2. Investigations in the nu3PO4 domain. *Calcif. Tissue Int.*, **49** (6), 383–388.
51. Sonju Clasen, A.B. and Ruyter, I.E. (1997) Quantitative determination of type A and type B carbonate in human deciduous and permanent enamel by means of Fourier transform infrared spectrometry. *Adv. Dent. Res.*, **11** (4), 523–527.
52. Sowa, M.G. and Mantsch, H.H. (1994) FT-IR photoacoustic depth profiling spectroscopy of enamel. *Calcif. Tissue Int.*, **54** (6), 481–485.
53. Bajaj, D. *et al.* (2008) A comparison of fatigue crack growth in human enamel and hydroxyapatite. *Biomaterials*, **29** (36), 4847–4854.
54. Eimar, H. *et al.* (2012) Regulation of enamel hardness by its crystallographic dimensions. *Acta Biomater.*, **8** (9), 3400–3410.
55. Eimar, H. *et al.* (2011) The role of enamel crystallography on tooth shade. *J. Dent.*, **39** (Suppl. 3), e3–e10.
56. Chen, L. *et al.* (2013) Regeneration of biomimetic hydroxyapatite on etched human enamel by anionic PAMAM template in vitro. *Arch. Oral Biol.*, **58** (8), 975–980.
57. Cimilli, H. and Pameijer, C.H. (2001) Effect of carbamide peroxide bleaching

agents on the physical properties and chemical composition of enamel. *Am. J. Dent.*, **14** (2), 63–66.
58. Eliades, T., Katsavrias, E., and Eliades, G. (2002) Moisture-insensitive adhesives: reactivity with water and bond strength to wet and saliva-contaminated enamel. *Eur. J. Orthod.*, **24** (1), 35–42.
59. Fu, B. *et al.* (2005) Interfacial interaction of tartaric acid with hydroxyapatite and enamel. *J. Mater. Sci. Mater. Med.*, **16** (9), 827–831.
60. Kanehira, M. *et al.* (2006) Relationship between degree of polymerization and enamel bonding strength with self-etching adhesives. *J. Adhes. Dent.*, **8** (4), 211–216.
61. Severcan, F. *et al.* (2008) Effects of in-office and at-home bleaching on human enamel and dentin: an in vitro application of Fourier transform infrared study. *Appl. Spectrosc.*, **62** (11), 1274–1279.
62. Sun, L. *et al.* (2011) Surface alteration of human tooth enamel subjected to acidic and neutral 30% hydrogen peroxide. *J. Dent.*, **39** (10), 686–692.
63. Taube, F. *et al.* (2010) Morphological and chemical characterization of tooth enamel exposed to alkaline agents. *J. Dent.*, **38** (1), 72–81.
64. Taubee, F. *et al.* (2010) Scanning electron microscopic and X-ray micro analysis on tooth enamel exposed to alkaline agents. *Swed. Dent. J.*, **34** (3), 129–137.
65. Torres-Rodriguez, C. *et al.* (2012) Selective removal of mineral and organic components of bovine enamel by phosphoric acid. *J. Adhes. Dent.*, **14** (4), 329–334.
66. Zimmerman, B. *et al.* (2010) Alteration of dentin-enamel mechanical properties due to dental whitening treatments. *J. Mech. Behav. Biomed. Mater.*, **3** (4), 339–346.
67. Landa, A.S., van der Mei, H.C., and Busscher, H.J. (1997) Detachment of linking film bacteria from enamel surfaces by oral rinses and penetration of sodium lauryl sulphate through an artificial oral biofilm. *Adv. Dent. Res.*, **11** (4), 528–538.
68. Fan, Y. *et al.* (2011) Amelogenin-assisted ex vivo remineralization of human enamel: effects of supersaturation degree and fluoride concentration. *Acta Biomater.*, **7** (5), 2293–2302.
69. Fan, Y., Sun, Z., and Moradian-Oldak, J. (2009) Effect of fluoride on the morphology of calcium phosphate crystals grown on acid-etched human enamel. *Caries Res.*, **43** (2), 132–136.
70. Fried, D. *et al.* (2006) Dissolution studies of bovine dental enamel surfaces modified by high-speed scanning ablation with a lambda = 9.3-microm TEA CO(2) laser. *Lasers Surg. Med.*, **38** (9), 837–845.
71. Harris, D.M. *et al.* (2002) Selective ablation of surface enamel caries with a pulsed Nd:YAG dental laser. *Lasers Surg. Med.*, **30** (5), 342–350.
72. Huang, S. *et al.* (2011) Remineralization potential of nano-hydroxyapatite on initial enamel lesions: an in vitro study. *Caries Res.*, **45** (5), 460–468.
73. Langhorst, S.E., O'Donnell, J.N., and Skrtic, D. (2009) In vitro remineralization of enamel by polymeric amorphous calcium phosphate composite: quantitative microradiographic study. *Dent. Mater.*, **25** (7), 884–891.
74. Staninec, M. *et al.* (2003) Influence of an optically thick water layer on the bond-strength of composite resin to dental enamel after IR laser ablation. *Lasers Surg. Med.*, **33** (4), 264–269.
75. Fan, Y., Sun, Z., and Moradian-Oldak, J. (2009) Controlled remineralization of enamel in the presence of amelogenin and fluoride. *Biomaterials*, **30** (4), 478–483.
76. Cheng, Z.J. *et al.* (2009) Disturbed enamel biomineralization in col1-caPPR mouse incisor. *Calcif. Tissue Int.*, **84** (6), 494–501.
77. Porto, I.M. *et al.* (2009) Enamel mineralization in the absence of maturation stage ameloblasts. *Arch. Oral Biol.*, **54** (4), 313–321.
78. Tye, C.E. *et al.* (2009) DPPI may activate KLK4 during enamel formation. *J. Dent. Res.*, **88** (4), 323–327.
79. Bartlett, J.D. *et al.* (2004) Decreased mineral content in MMP-20 null mouse

enamel is prominent during the maturation stage. *J. Dent. Res.*, **83** (12), 909–913.

80. Guven, G. *et al.* (2008) Mucopolysaccharidosis type I (Hurler syndrome): oral and radiographic findings and ultrastructural/chemical features of enamel and dentin. *Oral Surg. Oral Med. Oral Pathol. Oral Radiol. Endod.*, **105** (1), 72–78.
81. Rohanizadeh, R. *et al.* (1998) Ultrastructural organization and microanalysis studies of deciduous enamel crystallites in regional odontodysplasia (RO). *J. Oral Pathol. Med.*, **27** (10), 501–507.
82. Verdelis, K. *et al.* (2003) Spectroscopic imaging of mineral maturation in bovine dentin. *J. Dent. Res.*, **82** (9), 697–702.
83. About, I. and Mitsiadis, T.A. (2001) Molecular aspects of tooth pathogenesis and repair: in vivo and in vitro models. *Adv. Dent. Res.*, **15**, 59–62.
84. Bachmann, L. *et al.* (2005) Changes in chemical composition and collagen structure of dentine tissue after erbium laser irradiation. *Spectrochim. Acta A Mol. Biomol. Spectrosc.*, **61** (11-12), 2634–2639.
85. Eugenio, S. *et al.* (2005) Characterisation of dentin surfaces processed with KrF excimer laser radiation. *Biomaterials*, **26** (33), 6780–6787.
86. Hayashi, M. *et al.* (2012) Effects of heating on the mechanical and chemical properties of human dentin. *Dent. Mater.*, **28** (4), 385–391.
87. Ritts, A.C. *et al.* (2010) Dentin surface treatment using a non-thermal argon plasma brush for interfacial bonding improvement in composite restoration. *Eur. J. Oral Sci.*, **118** (5), 510–516.
88. Jiang, T. *et al.* (2007) Effects of hydrogen peroxide on human dentin structure. *J. Dent. Res.*, **86** (11), 1040–1045.
89. Sato, C. *et al.* (2013) Tooth bleaching increases dentinal protease activity. *J. Dent. Res.*, **92** (2), 187–192.
90. Ubaldini, A.L. *et al.* (2013) Hydrogen peroxide diffusion dynamics in dental tissues. *J. Dent. Res.*, **92** (7), 661–665.
91. Haruyama, N. *et al.* (2009) Genetic evidence for key roles of decorin and biglycan in dentin mineralization. *Matrix Biol.*, **28** (3), 129–136.
92. Abo, T. *et al.* (2006) Short- and long-term in vitro study of the bonding of eight commercial adhesives to normal and deproteinized dentin. *Acta Odontol. Scand.*, **64** (4), 237–243.
93. Argolo, S. *et al.* (2012) Effect of increased dwell times for solvent evaporation on the bond strength and degree of conversion of an ethanol-based adhesive system. *Acta Odontol. Latinoam.*, **25** (1), 109–114.
94. Atai, M. *et al.* (2009) PMMA-grafted nanoclay as novel filler for dental adhesives. *Dent. Mater.*, **25** (3), 339–347.
95. Bae, J.H. *et al.* (2005) Adhesive layer properties as a determinant of dentin bond strength. *J. Biomed. Mater. Res. B Appl. Biomater.*, **74** (2), 822–828.
96. Bayle, M.A., Gregoire, G., and Sharrock, P. (2007) The role of acrylophosphonic acid monomers in the formation of hybrid layers based on self-etch adhesives. *J. Dent.*, **35** (4), 302–308.
97. Bayle, M.A. *et al.* (2008) Acrylophosphonic acid reactivity with calcium ions and biological apatite. *Dent. Mater.*, **24** (3), 386–391.
98. Botta, S.B. *et al.* (2012) Effect of dental tissue conditioners and matrix metalloproteinase inhibitors on type I collagen microstructure analyzed by Fourier transform infrared spectroscopy. *J. Biomed. Mater. Res. B Appl. Biomater.*, **100** (4), 1009–1016.
99. Cekic-Nagas, I. *et al.* (2008) Influence of polymerization mode on degree of conversion and micropush-out bond strength of resin core systems using different adhesive systems. *Dent. Mater. J.*, **27** (3), 376–385.
100. Cunha, L.G. *et al.* (2009) Degree of conversion and contraction stress development of a resin composite irradiated using halogen and LED at two C-factor levels. *Oper. Dent.*, **34** (1), 24–31.
101. Eliades, G., Vougiouklakis, G., and Palaghias, G. (1999) Effect of dentin primers on the morphology, molecular composition and collagen conformation

of acid-demineralized dentin in situ. *Dent. Mater.*, **15** (5), 310–317.

102. Eliades, G., Vougiouklakis, G., and Palaghias, G. (2001) Heterogeneous distribution of single-bottle adhesive monomers in the resin-dentin interdiffusion zone. *Dent. Mater.*, **17** (4), 277–283.

103. Faria-e-Silva, A.L. *et al.* (2010) Degree of conversion of etch-and-rinse and self-etch adhesives light-cured using QTH or LED. *Oper. Dent.*, **35** (6), 649–654.

104. Feng, L., Carvalho, R., and Suh, B.I. (2009) Insufficient cure under the condition of high irradiance and short irradiation time. *Dent. Mater.*, **25** (3), 283–289.

105. Ferreira, S.Q. *et al.* (2011) Improvement of exposure times: effects on adhesive properties and resin-dentin bond strengths of etch-and-rinse adhesives. *J. Adhes. Dent.*, **13** (3), 235–241.

106. Franz, A. *et al.* (2009) Cytotoxic effects of dental bonding substances as a function of degree of conversion. *Dent. Mater.*, **25** (2), 232–239.

107. Gaintantzopoulou, M., Rahiotis, C., and Eliades, G. (2008) Molecular characterization of one-step self-etching adhesives placed on dentin and inert substrate. *J. Adhes. Dent.*, **10** (2), 83–93.

108. Giannini, M. *et al.* (2008) Effects of the solvent evaporation technique on the degree of conversion of one-bottle adhesive systems. *Oper. Dent.*, **33** (2), 149–154.

109. Gu, L.S. *et al.* (2010) Changes in stiffness of resin-infiltrated demineralized dentin after remineralization by a bottom-up biomimetic approach. *Acta Biomater.*, **6** (4), 1453–1461.

110. Ikemura, K. *et al.* (2003) Bonding mechanism and ultrastructural interfacial analysis of a single-step adhesive to dentin. *Dent. Mater.*, **19** (8), 707–715.

111. Imazato, S. *et al.* (2003) Antibacterial activity and bonding characteristics of an adhesive resin containing antibacterial monomer MDPB. *Dent. Mater.*, **19** (4), 313–319.

112. Imazato, S. *et al.* (1997) Incorporation of antibacterial monomer MDPB into dentin primer. *J. Dent. Res.*, **76** (3), 768–772.

113. Ito, S. *et al.* (2010) Water sorption/solubility of self-etching dentin bonding agents. *Dent. Mater.*, **26** (7), 617–626.

114. Jacobsen, T. and Soderholm, K.J. (1995) Some effects of water on dentin bonding. *Dent. Mater.*, **11** (2), 132–136.

115. Jose, P. *et al.* (2011) Degree of conversion of two dentin bonding agents with and without a desensitizing agent using fourier transform infrared spectroscopy: an in vitro study. *J. Conserv. Dent.*, **14** (3), 302–305.

116. Kakaboura, A.I., Eliades, G.C., and Palaghias, G. (1996) Laboratory evaluation of three visible light-cured resinous liners. *J. Dent.*, **24** (3), 223–231.

117. Kim, J.S. *et al.* (2006) Effect of light-cure time of adhesive resin on the thickness of the oxygen-inhibited layer and the microtensile bond strength to dentin. *J. Biomed. Mater. Res. B Appl. Biomater.*, **78** (1), 115–123.

118. Lee, S.Y., Greener, E.H., and Mueller, H.J. (1995) Effect of food and oral simulating fluids on structure of adhesive composite systems. *J. Dent.*, **23** (1), 27–35.

119. Loguercio, A.D. *et al.* (2009) Effect of solvent removal on adhesive properties of simplified etch-and-rinse systems and on bond strengths to dry and wet dentin. *J. Adhes. Dent.*, **11** (3), 213–219.

120. Loguercio, A.D. *et al.* (2011) Adhesive temperature: effects on adhesive properties and resin-dentin bond strength. *Oper. Dent.*, **36** (3), 293–303.

121. Malacarne-Zanon, J. *et al.* (2009) Effects of ethanol addition on the water sorption/solubility and percent conversion of comonomers in model dental adhesives. *Dent. Mater.*, **25** (10), 1275–1284.

122. Moshaverinia, A. *et al.* (2011) Surface properties and bond strength measurements of N-vinylcaprolactam (NVC)-containing glass-ionomer cements. *J. Prosthet. Dent.*, **105** (3), 185–193.

123. Mountouris, G., Silikas, N., and Eliades, G. (2004) Effect of sodium hypochlorite treatment on the molecular composition and morphology of human coronal dentin. *J. Adhes. Dent.*, **6** (3), 175–182.

124. Oook, S. *et al.* (2004) Influence of polymerization mode of dual-polymerized resin direct core foundation systems on bond strengths to bovine dentin. *J. Prosthet. Dent.*, **92** (3), 239–244.

125. Ouyang, X. *et al.* (2011) Synthesis and characterization of triethylene glycol dimethacrylate nanocapsules used in a self-healing bonding resin. *J. Dent.*, **39** (12), 825–833.

126. Papadogiannis, D. *et al.* (2009) Setting characteristics and cavity adaptation of low-shrinking resin composites. *Dent. Mater.*, **25** (12), 1509–1516.

127. Sadek, F.T. *et al.* (2008) Early and 24-hour bond strength and degree of conversion of etch-and-rinse and self-etch adhesives. *Am. J. Dent.*, **21** (1), 30–34.

128. Solhi, L. *et al.* (2012) A novel dentin bonding system containing poly(methacrylic acid) grafted nanoclay: synthesis, characterization and properties. *Dent. Mater.*, **28** (10), 1041–1050.

129. Solhi, L. *et al.* (2012) Poly(acrylic acid) grafted montmorillonite as novel fillers for dental adhesives: synthesis, characterization and properties of the adhesive. *Dent. Mater.*, **28** (4), 369–377.

130. Spencer, P. *et al.* (2005) Physicochemical interactions at the dentin/adhesive interface using FTIR chemical imaging. *J. Biomed. Opt.*, **10** (3), 031104.

131. Tassery, H. *et al.* (2001) In vitro assessment of polymerization procedures in Class II restorations: sealing, FTIR, and microhardness evaluations. *J. Adhes. Dent.*, **3** (3), 247–255.

132. Yamada, M., Miyazaki, M., and Moore, B.K. (2004) Influence of interchanging adhesive resins and self-etching primers on the mechanical properties of adhesive resins. *Oper. Dent.*, **29** (5), 532–537.

133. Yesilyurt, C. *et al.* (2008) Bond strengths of two conventional glass-ionomer cements to irradiated and non-irradiated dentin. *Dent. Mater. J.*, **27** (5), 695–701.

134. Arvidsson, A. *et al.* (2002) Chemical and topographical analyses of dentine surfaces after Carisolv treatment. *J. Dent.*, **30** (2-3), 67–75.

135. Chu, C.H. *et al.* (2012) Effects of silver diamine fluoride on dentine carious lesions induced by Streptococcus mutans and Actinomyces naeslundii biofilms. *Int. J. Paediatr. Dent.*, **22** (1), 2–10.

136. Gu, H. *et al.* (2013) Experimental antibacterial and mineralizing calcium phosphate-based treatment for dentin surfaces. *J. Biomater. Appl.*, **27** (7), 783–790.

137. Kawasaki, K. *et al.* (2000) Relationship between mineral distributions in dentine lesions and subsequent remineralization in vitro. *Caries Res.*, **34** (5), 395–403.

138. Mei, M.L. *et al.* (2013) Antibacterial effects of silver diamine fluoride on multi-species cariogenic biofilm on caries. *Ann. Clin. Microbiol. Antimicrob.*, **12**, 4.

139. Mixson, J.M. *et al.* (1995) Surface morphology and chemical characterization of abrasion/erosion lesions. *Am. J. Dent.*, **8** (1), 5–9.

140. Rahiotis, C. and Vougiouklakis, G. (2007) Effect of a CPP-ACP agent on the demineralization and remineralization of dentine in vitro. *J. Dent.*, **35** (8), 695–698.

141. Shinohara, M.S. *et al.* (2009) Fluoride-containing adhesive: durability on dentin bonding. *Dent. Mater.*, **25** (11), 1383–1391.

142. Wang, Y., Yao, X., and Parthasarathy, R. (2009) Characterization of interfacial chemistry of adhesive/dentin bond using FTIR chemical imaging with univariate and multivariate data processing. *J. Biomed. Mater. Res. A*, **91** (1), 251–262.

143. Zhang, X. *et al.* (2012) Remineralization of partially demineralized dentine substrate based on a biomimetic strategy. *J. Mater. Sci. Mater. Med.*, **23** (3), 733–742.

144. Advincula, M.C. *et al.* (2009) Polypeptide-catalyzed silica for dental applications. *J. Biomed. Mater. Res. B Appl. Biomater.*, **88** (2), 321–331.
145. Charadram, N. *et al.* (2013) Structural analysis of reactionary dentin formed in response to polymicrobial invasion. *J. Struct. Biol.*, **181** (3), 207–222.
146. Eliades, G., Palaghias, G., and Vougiouklakis, G. (1997) Effect of acidic conditioners on dentin morphology, molecular composition and collagen conformation in situ. *Dent. Mater.*, **13** (1), 24–33.
147. Kishen, A. and Vedantam, S. (2007) Hydromechanics in dentine: role of dentinal tubules and hydrostatic pressure on mechanical stress-strain distribution. *Dent. Mater.*, **23** (10), 1296–1306.
148. Magne, D. *et al.* (2002) Fourier transform infrared microspectroscopic investigation of the organic and mineral constituents of peritubular dentin: a horse study. *Calcif. Tissue Int.*, **71** (2), 179–185.
149. Pascon, F.M. *et al.* (2012) Morphological and chemical changes in dentin after using endodontic agents: fourier transform Raman spectroscopy, energy-dispersive x-ray fluorescence spectrometry, and scanning electron microscopy study. *J. Biomed. Opt.*, **17** (7), 075008.
150. Qin, C., Xu, J., and Zhang, Y. (2006) Spectroscopic investigation of the function of aqueous 2-hydroxyethylmethacrylate/glutaraldehyde solution as a dentin desensitizer. *Eur. J. Oral Sci.*, **114** (4), 354–359.
151. Suge, T. *et al.* (1995) Effects of fluoride on the calcium phosphate precipitation method for dentinal tubule occlusion. *J. Dent. Res.*, **74** (4), 1079–1085.
152. Verdelis, K. *et al.* (1999) Effect of chelating agents on the molecular composition and extent of decalcification at cervical, middle and apical root dentin locations. *Endod. Dent. Traumatol.*, **15** (4), 164–170.
153. Wang, Z. *et al.* (2011) The dentine remineralization activity of a desensitizing bioactive glass-containing toothpaste: an in vitro study. *Aust. Dent. J.*, **56** (4), 372–381.
154. Wang, Z. *et al.* (2011) Dentine remineralization induced by two bioactive glasses developed for air abrasion purposes. *J. Dent.*, **39** (11), 746–756.
155. Wang, Z. *et al.* (2012) Nerve-targeted desensitizing toothpastes occlude dentin tubules and induce mineral precipitation. *Am. J. Dent.*, **25** (1), 26–30.
156. Zhou, Y.Z. *et al.* (2012) Polydopamine-induced tooth remineralization. *ACS Appl. Mater. Interfaces*, **4** (12), 6901–6910.
157. Paschalis, E.P. *et al.* (2003) Distribution of collagen cross-links in normal human trabecular bone. *J. Bone Miner. Res.*, **18** (11), 1942–1946.
158. Isaksson, H. *et al.* (2010) Collagen and mineral deposition in rabbit cortical bone during maturation and growth: effects on tissue properties. *J. Orthop. Res.*, **28** (12), 1626–1633.
159. Miller, L.M. *et al.* (2001) In situ analysis of mineral content and crystallinity in bone using infrared micro-spectroscopy of the nu(4) PO(4)(3-) vibration. *Biochim. Biophys. Acta*, **1527** (1-2), 11–19.
160. Ou-Yang, H. *et al.* (2001) Infrared microscopic imaging of bone: spatial distribution of CO3(2-). *J. Bone Miner. Res.*, **16** (5), 893–900.
161. Paschalis, E.P. *et al.* (1996) FTIR microspectroscopic analysis of human osteonal bone. *Calcif. Tissue Int.*, **59** (6), 480–487.
162. Boskey, A.L. and Coleman, R. (2010) Aging and bone. *J. Dent. Res.*, **89** (12), 1333–1348.
163. Gamsjaeger, S. *et al.* (2014) Transmenopausal changes in trabecular bone quality. *J. Bone Miner. Res.*, **29** (3), 608–617.
164. Blank, R.D. *et al.* (2003) Spectroscopically determined collagen Pyr/deH-DHLNL cross-link ratio and crystallinity indices differ markedly in recombinant congenic mice with divergent calculated bone tissue strength. *Connect. Tissue Res.*, **44** (3-4), 134–142.

165. Blouin, S. *et al.* (2009) Bone matrix quality and plasma homocysteine levels. *Bone*, **44** (5), 959–964.

166. Boskey, A. (2003) Mineral changes in osteopetrosis. *Crit. Rev. Eukaryot. Gene Expr.*, **13** (2-4), 109–116.

167. Boskey, A.L. (1990) Bone mineral and matrix. Are they altered in osteoporosis? *Orthop. Clin. North Am.*, **21** (1), 19–29.

168. Boskey, A.L. *et al.* (2005) Comparison of mineral quality and quantity in iliac crest biopsies from high- and low-turnover osteoporosis: an FT-IR microspectroscopic investigation. *Osteoporos. Int.*, **16** (12), 2031–2038.

169. Faibish, D., Ott, S.M., and Boskey, A.L. (2006) Mineral changes in osteoporosis: a review. *Clin. Orthop. Relat. Res.*, **443**, 28–38.

170. Gadeleta, S.J. *et al.* (2000) A physical, chemical, and mechanical study of lumbar vertebrae from normal, ovariectomized, and nandrolone decanoate-treated cynomolgus monkeys (Macaca fascicularis). *Bone*, **27** (4), 541–550.

171. Misof, B.M. *et al.* (2012) Bone material properties in premenopausal women with idiopathic osteoporosis. *J. Bone Miner. Res.*, **27** (12), 2551–2561.

172. Paschalis, E.P. *et al.* (1997) FTIR microspectroscopic analysis of human iliac crest biopsies from untreated osteoporotic bone. *Calcif. Tissue Int.*, **61** (6), 487–492.

173. Paschalis, E.P. *et al.* (2003) Bone mineral and collagen quality in humeri of ovariectomized cynomolgus monkeys given rhPTH(1-34) for 18 months. *J. Bone Miner. Res.*, **18** (4), 769–775.

174. Paschalis, E.P. *et al.* (1996) Fourier transform infrared microspectroscopic analysis identifies alterations in mineral properties in bones from mice transgenic for type X collagen. *Bone*, **19** (2), 151–156.

175. Paschalis, E.P. *et al.* (2004) Bone fragility and collagen cross-links. *J. Bone Miner. Res.*, **19** (12), 2000–2004.

176. Zoehrer, R. *et al.* (2008) Bone quality determined by Fourier transform infrared imaging analysis in mild primary hyperparathyroidism. *J. Clin. Endocrinol. Metab.*, **93** (9), 3484–3489.

177. Cassella, J.P. *et al.* (2000) A fourier transform infrared spectroscopic and solid-state NMR study of bone mineral in osteogenesis imperfecta. *J. Bone Miner. Metab.*, **18** (5), 291–296.

178. Camacho, N.P., Landis, W.J., and Boskey, A.L. (1996) Mineral changes in a mouse model of osteogenesis imperfecta detected by Fourier transform infrared microscopy. *Connect. Tissue Res.*, **35** (1-4), 259–265.

179. Bogan, R. *et al.* (2013) A mouse model for human osteogenesis imperfecta type VI. *J. Bone Miner. Res.*, **28** (7), 1531–1536.

180. Satomura, K. *et al.* (2007) Osteopetrosis complicated by osteomyelitis of the mandible: a case report including characterization of the osteopetrotic bone. *Int. J. Oral Maxillofac. Surg.*, **36** (1), 86–93.

181. Bargman, R. *et al.* (2012) Comparable outcomes in fracture reduction and bone properties with RANKL inhibition and alendronate treatment in a mouse model of osteogenesis imperfecta. *Osteoporos. Int.*, **23** (3), 1141–1150.

182. Calton, E.F., Macleay, J., and Boskey, A.L. (2011) Fourier transform infrared imaging analysis of cancellous bone in alendronate- and raloxifene-treated osteopenic sheep. *Cells Tissues Organs*, **194** (2-4), 302–306.

183. Boskey, A.L., Spevak, L., and Weinstein, R.S. (2009) Spectroscopic markers of bone quality in alendronate-treated postmenopausal women. *Osteoporos. Int.*, **20** (5), 793–800.

184. McCarthy, E.A. *et al.* (2002) Alendronate treatment for infants with osteogenesis imperfecta: demonstration of efficacy in a mouse model. *Pediatr. Res.*, **52** (5), 660–670.

185. Durchschlag, E. *et al.* (2006) Bone material properties in trabecular bone from human iliac crest biopsies after 3- and 5-year treatment with risedronate. *J. Bone Miner. Res.*, **21** (10), 1581–1590.

186. Gamsjaeger, S. *et al.* (2011) Effects of one year daily teriparatide treatment on trabecular bone material properties in

postmenopausal osteoporotic women previously treated with alendronate or risedronate. *Bone*, **49** (6), 1160–1165.

187. Geoffroy, V. *et al.* (2011) Effects of risedronate in Runx2 overexpressing mice, an animal model for evaluation of treatment effects on bone quality and fractures. *Calcif. Tissue Int.*, **88** (6), 464–475.

188. Hofstetter, B. *et al.* (2012) Effects of alendronate and risedronate on bone material properties in actively forming trabecular bone surfaces. *J. Bone Miner. Res.*, **27** (5), 995–1003.

189. Li, C. *et al.* (2010) Strontium is incorporated into mineral crystals only in newly formed bone during strontium ranelate treatment. *J. Bone Miner. Res.*, **25** (5), 968–975.

190. Monier-Faugere, M.C. *et al.* (1999) Intermittent and continuous administration of the bisphosphonate ibandronate in ovariohysterectomized beagle dogs: effects on bone morphometry and mineral properties. *J. Bone Miner. Res.*, **14** (10), 1768–1778.

191. Ouyang, H. *et al.* (2004) Fourier transform infrared microscopic imaging: effects of estrogen and estrogen deficiency on fracture healing in rat femurs. *Appl. Spectrosc.*, **58** (1), 1–9.

192. Paschalis, E.P. *et al.* (2003) Effect of hormone replacement therapy on bone quality in early postmenopausal women. *J. Bone Miner. Res.*, **18** (6), 955–959.

193. Paschalis, E.P. *et al.* (2005) Bone mineral and collagen quality in iliac crest biopsies of patients given teriparatide: new results from the fracture prevention trial. *J. Clin. Endocrinol. Metab.*, **90** (8), 4644–4649.

194. Juang, C., Finzi, L., and Bustamante, C. (1998) Design and application of a computer-controlled confocal scanning differential polarization microscope. *Rev. Sci. Instrum.*, **59**, 2399–2408.

195. Golcuk, K. *et al.* (2006) Is photobleaching necessary for Raman imaging of bone tissue using a green laser? *Biochim. Biophys. Acta*, **1758** (7), 868–873.

196. Ager, J.W. III, *et al.* (2006) On the increasing fragility of human teeth with age: a deep-UV resonance Raman study. *J. Bone Miner. Res.*, **21** (12), 1879–1887.

197. Yeni, Y.N. *et al.* (2006) Effect of fixation and embedding on Raman spectroscopic analysis of bone tissue. *Calcif. Tissue Int.*, **78** (6), 363–371.

198. Finlay, J.B. and Hardie, W.R. (1994) Anisotropic contraction of cortical bone caused by dehydration of samples of the bovine femur in vitro. *Proc. Inst. Mech. Engl.*, **208**, 27–32.

199. McElderry, J.D., Kole, M.R., and Morris, M.D. (2011) Repeated freeze-thawing of bone tissue affects Raman bone quality measurements. *J. Biomed. Opt.*, **16** (7), 071407.

200. Morris, M.D. *et al.* (2004) Compatibility of staining protocols for bone tissue with Raman imaging. *Calcif. Tissue Int.*, **74**, 86–94.

201. Gamsjaeger, S. *et al.* (2013) Effects of 3 years treatment with once-yearly zoledronic acid on the kinetics of bone matrix maturation in osteoporotic patients. *Osteoporos. Int.*, **24** (1), 339–347.

202. Gamsjaeger, S. *et al.* (2011) Bone material properties in actively bone-forming trabeculae in postmenopausal women with osteoporosis after three years of treatment with once-yearly Zoledronic acid. *J. Bone Miner. Res.*, **26** (1), 12–18.

203. Awonusi, A., Morris, M.D., and Tecklenburg, M.M. (2007) Carbonate assignment and calibration in the Raman spectrum of apatite. *Calcif. Tissue Int.*, **81** (1), 46–52.

204. Nishino, M. *et al.* (1981) The laser-Raman spectroscopic studies on human-enamel and precipitated carbonate-containing apatites. *J. Dent. Res.*, **60**, 751–755.

205. Willamson, B.E. (1982) Low-temperature laser Raman spectroscopy of synthetic carbonated apatites and dental enamel. *Aust. J. Chem.*, **35**, 715–727.

206. Freeman, J.J. *et al.* (2001) Raman spectroscopic detection of changes in bioapatite in mouse femora as a function of age and in vitro fluoride treatment. *Calcif. Tissue Int.*, **68** (3), 156–162.

207. de Mul, F. *et al.* (1988) Calculation of the Raman line broadening on carbonation in synthetic hydroxyapatite. *J. Raman Spectrosc.*, **19**, 13–21.

208. Frushour, B.G. and Koenig, J.L. (1975) Raman scattering of collagen, gelatin, and elastin. *Biopolymers*, **14**, 379–391.

209. Bandekar, J. (1992) Amide modes and protein conformation. *Biochim. Biophys. Acta*, **1120** (2), 123–143.

210. Gamsjäger, S., Paschalis, E., and Fratzl, P. (2009) in *Raman Spectroscopy for Soft Matter Applications* (ed. M. Amer), John Wiley & Sons, Inc., Hoboken, NJ, pp. 227–269.

211. Tsuboi, M. *et al.* (2000) Intensity of the polarized Raman band at 1340-1345 cm-1 as an indicator of protein alpha-helix orientation: application to Pf1 filamentous virus. *Biochemistry*, **39** (10), 2677–2684.

212. Tsuboi, M. *et al.* (2005) Structural details of the thermophilic filamentous bacteriophage PH75 determined by polarized Raman microspectroscopy. *Biochemistry*, **44** (12), 4861–4869.

213. Kohn, D.H. *et al.* (2009) Exercise alters mineral and matrix composition in the absence of adding new bone. *Cells Tissues Organs*, **189** (1-4), 33–37.

214. Tarnowski, C.P., Ignelzi, M.A. Jr., and Morris, M.D. (2002) Mineralization of developing mouse calvaria as revealed by Raman microspectroscopy. *J. Bone Miner. Res.*, **17** (6), 1118–1126.

215. Mainreck, N. *et al.* (2011) Rapid characterization of glycosaminoglycans using a combined approach by infrared and Raman microspectroscopies. *J. Pharm. Sci.*, **100** (2), 441–450.

216. Esmonde-White, K.A. *et al.* (2011) Fiber-optic Raman spectroscopy of joint tissues. *Analyst*, **136** (8), 1675–1685.

217. Bonifacio, A. *et al.* (2010) Chemical imaging of articular cartilage sections with Raman mapping, employing uni- and multi-variate methods for data analysis. *Analyst*, **135** (12), 3193–3204.

218. Tramini, P. *et al.* (2000) A Raman spectroscopic investigation of dentin and enamel structures modified by lactic acid. *Caries Res.*, **34** (3), 233–240.

219. Tramini, P. *et al.* (2001) A method of age estimation using Raman microspectrometry imaging of the human dentin. *Forensic Sci. Int.*, **118** (1), 1–9.

220. Ho, S.P. *et al.* (2009) Structure, chemical composition and mechanical properties of human and rat cementum and its interface with root dentin. *Acta Biomater.*, **5** (2), 707–718.

221. Lakshmi, R.J. *et al.* (2003) Osteoradionecrosis (ORN) of the mandible: a laser Raman spectroscopic study. *Appl. Spectrosc.*, **57** (9), 1100–1116.

222. Balooch, M. *et al.* (2001) Local mechanical and optical properties of normal and transparent root dentin. *J. Mater. Sci. Mater. Med.*, **12** (6), 507–514.

223. He, L.H. and Swain, M.V. (2009) Enamel--a functionally graded natural coating. *J. Dent.*, **37** (8), 596–603.

224. Pelin, I.M. *et al.* (2012) Adhesion forces between AFM tips and superficial dentin surfaces. *J. Colloid Interface Sci.*, **376** (1), 262–268.

225. Soares, L.E. *et al.* (2006) Molecular analysis of Er:YAG laser irradiation on dentin. *Braz. Dent. J.*, **17** (1), 15–19.

226. Soares, L.E. *et al.* (2009) Effects of Er:YAG laser irradiation and manipulation treatments on dentin components, part 1: Fourier transform-Raman study. *J. Biomed. Opt.*, **14** (2), 024001.

227. Yamada, M.K. *et al.* (2004) Three-dimensional topographic scanning electron microscope and Raman spectroscopic analyses of the irradiation effect on teeth by Nd:YAG, Er: YAG, and CO(2) lasers. *J. Biomed. Mater. Res. B Appl. Biomater.*, **71** (1), 7–15.

228. Sakoolnamarka, R. *et al.* (2005) Raman spectroscopic study of noncarious cervical lesions. *Odontology*, **93** (1), 35–40.

229. Wang, Y., Spencer, P., and Walker, M.P. (2007) Chemical profile of adhesive/caries-affected dentin interfaces using Raman microspectroscopy. *J. Biomed. Mater. Res. A*, **81** (2), 279–286.

230. Pai, V.S. *et al.* (2009) Chemical analysis of dentin surfaces after Carisolv

treatment. *J. Conserv. Dent.*, **12** (3), 118–122.

231. Karan, K. *et al.* (2012) Chemical characterization of etched dentin in non-carious cervical lesions. *J. Adhes. Dent.*, **14** (4), 315–322.

232. Duschner, H. *et al.* (2006) Effects of hydrogen peroxide bleaching strips on tooth surface color, surface microhardness, surface and subsurface ultrastructure, and microchemical (Raman spectroscopic) composition. *J. Clin. Dent.*, **17** (3), 72–78.

233. Gotz, H. *et al.* (2007) Effects of elevated hydrogen peroxide 'strip' bleaching on surface and subsurface enamel including subsurface histomorphology, micro-chemical composition and fluorescence changes. *J. Dent.*, **35** (6), 457–466.

234. Gotz, H. *et al.* (2007) Physical, morphological, and micro-Raman chemical studies on bleaching strip effects on enamel, coronal dentin, and root dentin. *J. Clin. Dent.*, **18** (4), 112–119.

235. Sauro, S., Thompson, I., and Watson, T.F. (2011) Effects of common dental materials used in preventive or operative dentistry on dentin permeability and remineralization. *Oper. Dent.*, **36** (2), 222–230.

236. Xu, C. *et al.* (2009) Chemical/molecular structure of the dentin-enamel junction is dependent on the intratooth location. *Calcif. Tissue Int.*, **84** (3), 221–228.

237. Schulze, K.A. *et al.* (2004) Micro-Raman spectroscopic investigation of dental calcified tissues. *J. Biomed. Mater. Res. A*, **69** (2), 286–293.

238. Rousseau, M. *et al.* (2008) Low molecular weight molecules of oyster nacre induce mineralization of the MC3T3-E1 cells. *J. Biomed. Mater. Res. A*, **85** (2), 487–497.

239. Wang, C. *et al.* (2009) Confocal laser Raman microspectroscopy of biomineralization foci in UMR 106 osteoblastic cultures reveals temporally synchronized protein changes preceding and accompanying mineral crystal deposition. *J. Biol. Chem.*, **284** (11), 7100–7113.

240. Evans, N.D. *et al.* (2012) Gene-expression analysis reveals that embryonic stem cells cultured under osteogenic conditions produce mineral non-specifically compared to marrow stromal cells or osteoblasts. *Eur. Cell. Mater.*, **24**, 211–223.

241. McManus, L.L. *et al.* (2012) Assessment of an osteoblast-like cell line as a model for human primary osteoblasts using Raman spectroscopy. *Analyst*, **137** (7), 1559–1569.

242. Gajjeraman, S. *et al.* (2007) Matrix macromolecules in hard tissues control the nucleation and hierarchical assembly of hydroxyapatite. *J. Biol. Chem.*, **282** (2), 1193–1204.

243. Crane, N.J. *et al.* (2006) Raman spectroscopic evidence for octacalcium phosphate and other transient mineral species deposited during intramembranous mineralization. *Bone*, **39** (3), 434–442.

244. Yao, X. *et al.* (2013) Gender-dependence of bone structure and properties in adult osteogenesis imperfecta murine model. *Ann. Biomed. Eng.*, **41** (6), 1139–1149.

245. Balooch, G. *et al.* (2005) TGF-beta regulates the mechanical properties and composition of bone matrix. *Proc. Natl. Acad. Sci. U.S.A.*, **102** (52), 18813–18818.

246. van Apeldoorn, A.A. *et al.* (2005) Parallel high-resolution confocal Raman SEM analysis of inorganic and organic bone matrix constituents. *J. R. Soc. Interface*, **2** (2), 39–45.

247. Dehring, K.A. *et al.* (2006) Identifying chemical changes in subchondral bone taken from murine knee joints using Raman spectroscopy. *Appl. Spectrosc.*, **60** (10), 1134–1141.

248. Uthgenannt, B.A. *et al.* (2007) Skeletal self-repair: stress fracture healing by rapid formation and densification of woven bone. *J. Bone Miner. Res.*, **22** (10), 1548–1556.

249. Yang, Q. and Wang, Y.L. (2007) Raman spectra of fossil dinosaurs from different regions. *Guang Pu Xue Yu Guang Pu Fen Xi*, **27** (12), 2468–2471.

250. Goodyear, S.R. *et al.* (2009) A comparison of cortical and trabecular bone from C57 Black 6 mice using Raman spectroscopy. *Bone*, **44** (5), 899–907.

251. Kavukcuoglu, N.B., Patterson-Buckendahl, P., and Mann, A.B. (2009) Effect of osteocalcin deficiency on the nanomechanics and chemistry of mouse bones. *J. Mech. Behav. Biomed. Mater.*, **2** (4), 348–354.

252. Juillard, A. *et al.* (2010) Molecular interactions between zoledronic acid and bone: an in vitro Raman microspectroscopic study. *Bone*, **47** (5), 895–904.

253. Shen, J. *et al.* (2010) A longitudinal Raman microspectroscopic study of osteoporosis induced by spinal cord injury. *Osteoporos. Int.*, **21** (1), 81–87.

254. da Silva, F.F. *et al.* (2011) Effects of different swimming exercise intensities on bone tissue composition in mice: a Raman spectroscopy study. *Photomed. Laser Surg.*, **29** (4), 217–225.

255. Iwasaki, Y. *et al.* (2011) Changes in chemical composition of cortical bone associated with bone fragility in rat model with chronic kidney disease. *Bone*, **48** (6), 1260–1267.

256. Maher, J.R. *et al.* (2011) Raman spectroscopy detects deterioration in biomechanical properties of bone in a glucocorticoid-treated mouse model of rheumatoid arthritis. *J. Biomed. Opt.*, **16** (8), 087012.

257. McLaughlin, G. and Lednev, I.K. (2011) Potential application of Raman spectroscopy for determining burial duration of skeletal remains. *Anal. Bioanal. Chem.*, **401** (8), 2511–2518.

258. Zhong, W.J. *et al.* (2011) Periostin-like-factor-induced bone formation within orthopedic maxillary expansion. *Orthod. Craniofac. Res.*, **14** (4), 198–205.

259. de Souza, R.A. *et al.* (2012) Influence of creatine supplementation on bone quality in the ovariectomized rat model: an FT-Raman spectroscopy study. *Lasers Med. Sci.*, **27** (2), 487–495.

260. Takahata, M. *et al.* (2012) Mechanisms of bone fragility in a mouse model of glucocorticoid-treated rheumatoid arthritis: implications for insufficiency fracture risk. *Arthritis Rheum.*, **64** (11), 3649–3659.

261. Akkus, O. *et al.* (2003) Aging of microstructural compartments in human compact bone. *J. Bone Miner. Res.*, **18** (6), 1012–1019.

262. Yerramshetty, J.S. and Akkus, O. (2008) The associations between mineral crystallinity and the mechanical properties of human cortical bone. *Bone*, **42** (3), 476–482.

263. Yerramshetty, J.S., Lind, C., and Akkus, O. (2006) The compositional and physicochemical homogeneity of male femoral cortex increases after the sixth decade. *Bone*, **39** (6), 1236–1243.

264. Donnelly, E. *et al.* (2010) Effects of tissue age on bone tissue material composition and nanomechanical properties in the rat cortex. *J. Biomed. Mater. Res. A*, **92** (3), 1048–1056.

265. Donnelly, E. *et al.* (2010) Contribution of mineral to bone structural behavior and tissue mechanical properties. *Calcif. Tissue Int.*, **87** (5), 450–460.

266. Pathak, S. *et al.* (2012) Assessment of lamellar level properties in mouse bone utilizing a novel spherical nanoindentation data analysis method. *J. Mech. Behav. Biomed. Mater.*, **13**, 102–117.

267. Burket, J.C. *et al.* (2013) Variations in nanomechanical properties and tissue composition within trabeculae from an ovine model of osteoporosis and treatment. *Bone*, **52** (1), 326–336.

268. Carden, A. *et al.* (2003) Ultrastructural changes accompanying the mechanical deformation of bone tissue: a Raman imaging study. *Calcif. Tissue Int.*, **72** (2), 166–175.

269. Morris, M.D. *et al.* (2004) Bone tissue ultrastructural response to elastic deformation probed by Raman spectroscopy. *Faraday Discuss.*, **126**, 159–168; discussion 169–183.

270. de Carmejane, O. *et al.* (2005) Bone chemical structure response to mechanical stress studied by high pressure Raman spectroscopy. *Calcif. Tissue Int.*, **76** (3), 207–213.

271. Pezzotti, G. (2005) Raman piezospectroscopic analysis of natural and synthetic biomaterials. *Anal. Bioanal. Chem.*, **381** (3), 577–590.

272. Dooley, K.A. *et al.* (2009) Stress mapping of undamaged, strained, and failed regions of bone using Raman

spectroscopy. *J. Biomed. Opt.*, **14** (4), 044018.

273. Bi, X. *et al.* (2011) Raman and mechanical properties correlate at whole bone- and tissue-levels in a genetic mouse model. *J. Biomech.*, **44** (2), 297–303.

274. Carretta, R. *et al.* (2013) Within subject heterogeneity in tissue-level post-yield mechanical and material properties in human trabecular bone. *J. Mech. Behav. Biomed. Mater.*, **24**, 64–73.

275. Wasserman, N., Yerramshetty, J., and Akkus, O. (2005) Microcracks colocalize within highly mineralized regions of cortical bone tissue. *Eur. J. Morphol.*, **42** (1-2), 43–51.

276. Sahar, N.D., Hong, S.I., and Kohn, D.H. (2005) Micro- and nano-structural analyses of damage in bone. *Micron*, **36** (7-8), 617–629.

277. Buchwald, T. *et al.* (2012) Identifying compositional and structural changes in spongy and subchondral bone from the hip joints of patients with osteoarthritis using Raman spectroscopy. *J. Biomed. Opt.*, **17** (1), 017007.

278. Kozielski, M. *et al.* (2011) Determination of composition and structure of spongy bone tissue in human head of femur by Raman spectral mapping. *J. Mater. Sci. Mater. Med.*, **22** (7), 1653–1661.

279. McCreadie, B.R. *et al.* (2006) Bone tissue compositional differences in women with and without osteoporotic fracture. *Bone*, **39** (6), 1190–1195.

280. Olejnik, C. *et al.* (2011) Compatibility of fluorochrome labeling protocol with Raman spectroscopy to study bone formation. *Bull. Group Int. Rech. Sci. Stomatol. Odontol.*, **50** (2), 34–36.

281. Olejnik, C. *et al.* (2011) Molecular interaction between bisphosphonates and human bone: a preliminary study on osteonecrosis sequesters of the jaw. *Bull. Group Int. Rech. Sci. Stomatol. Odontol.*, **50** (1), 52–53.

282. Gevorkian, B.Z., Arnotskaia, N.E., and Fedorova, E.N. (1984) Study of bone tissue structure using polarized Raman spectra. *Biofizika*, **29** (6), 1046–1052.

283. Nyman, J.S. *et al.* (2011) Measuring differences in compositional properties of bone tissue by confocal Raman spectroscopy. *Calcif. Tissue Int.*, **89** (2), 111–122.

284. Raghavan, M., Sahar, N.D., Wilson, R.H., Mycek, M.A., Pleshko, N., Kohn, D.H., Morris, M.D. (2010) Quantitative polarized Raman spectroscopy in highly turbid bone tissue. *J. Biomed. Opt.*, **15** (3), 037001. doi: 10.1117/1.3426310

285. Bonifacio, A. and Sergo, V. (2010) Effects of sample orientation in Raman microspectroscopy of collagen fibers and their impact on the interpretation of the amide III band. *Vib. Spectrosc.*, **53**, 314–317.

286. Choo-Smith, L.P. *et al.* (2002) Medical applications of Raman spectroscopy: from proof of principle to clinical implementation. *Biopolymers*, **67** (1), 1–9.

287. Pillay, I. *et al.* (2005) The use of fingernails as a means of assessing bone health: a pilot study. *J. Womens Health (Larchmt)*, **14** (4), 339–344.

288. Moran, P. *et al.* (2007) Preliminary work on the development of a novel detection method for osteoporosis. *J. Mater. Sci. Mater. Med.*, **18** (6), 969–974.

289. Towler, M.R. *et al.* (2007) Raman spectroscopy of the human nail: a potential tool for evaluating bone health? *J. Mater. Sci. Mater. Med.*, **18** (5), 759–763.

290. Draper, E.R. *et al.* (2005) Novel assessment of bone using time-resolved transcutaneous Raman spectroscopy. *J. Bone Miner. Res.*, **20** (11), 1968–1972.

291. Matousek, P. *et al.* (2005) Subsurface probing in diffusely scattering media using spatially offset Raman spectroscopy. *Appl. Spectrosc.*, **59** (4), 393–400.

292. Matousek, P. *et al.* (2006) Noninvasive Raman spectroscopy of human tissue in vivo. *Appl. Spectrosc.*, **60** (7), 758–763.

293. Schulmerich, M.V. *et al.* (2006) Transcutaneous fiber optic Raman spectroscopy of bone using annular illumination and a circular array of collection fibers. *J. Biomed. Opt.*, **11** (6), 060502.

294. Matousek, P. (2007) Deep non-invasive Raman spectroscopy of living tissue

and powders. *Chem. Soc. Rev.*, **36** (8), 1292–1304.

295. Schulmerich, M.V. *et al.* (2008) Optical clearing in transcutaneous Raman spectroscopy of murine cortical bone tissue. *J. Biomed. Opt.*, **13** (2), 021108.

296. Schulmerich, M.V. *et al.* (2008) Noninvasive Raman tomographic imaging of canine bone tissue. *J. Biomed. Opt.*, **13** (2), 020506.

297. Schulmerich, M.V. *et al.* (2009) Transcutaneous Raman spectroscopy of murine bone in vivo. *Appl. Spectrosc.*, **63** (3), 286–295.

298. Okagbare, P.I. *et al.* (2010) Development of non-invasive Raman spectroscopy for in vivo evaluation of bone graft osseointegration in a rat model. *Analyst*, **135** (12), 3142–3146.

299. Buckley, K. and Matousek, P. (2011) Non-invasive analysis of turbid samples using deep Raman spectroscopy. *Analyst*, **136** (15), 3039–3050.

300. Demers, J.L. *et al.* (2012) Multichannel diffuse optical Raman tomography for bone characterization in vivo: a phantom study. *Biomed. Opt. Express*, **3** (9), 2299–2305.

301. Okagbare, P.I. *et al.* (2012) Noninvasive Raman spectroscopy of rat tibiae: approach to in vivo assessment of bone quality. *J. Biomed. Opt.*, **17** (9), 90502–90501.

302. Okagbare, P.I. and Morris, M.D. (2012) Polymer-capped fiber-optic Raman probe for non-invasive Raman spectroscopy. *Analyst*, **137** (1), 77–81.

303. Praveen, B.B. *et al.* (2012) Fluorescence suppression using wavelength modulated Raman spectroscopy in fiber-probe-based tissue analysis. *J. Biomed. Opt.*, **17** (7), 077006.

304. Xie, H.N. *et al.* (2012) Tracking bisphosphonates through a 20 mm thick porcine tissue by using surface-enhanced spatially offset Raman spectroscopy. *Angew. Chem. Int. Ed.*, **51** (34), 8509–8511.

305. Peterson, J.R. *et al.* (2013) Early detection of burn induced heterotopic ossification using transcutaneous Raman spectroscopy. *Bone*, **54** (1), 28–34.

306. Matousek, P. and Stone, N. (2013) Recent advances in the development of Raman spectroscopy for deep non-invasive medical diagnosis. *J. Biophotonics*, **6** (1), 7–19.

5
Medical Applications of Infrared Spectral Imaging of Individual Cells

Max Diem, Jennifer Schubert, Miloš Miljković, Kostas Papamarkakis, Antonella I. Mazur, Ellen Marcsisin, Jennifer Fore, Benjamin Bird, Kathleen Lenau, Douglas Townsend, Nora Laver, and Max Almond

5.1
Introduction

A chapter entitled "Infrared and Raman Spectroscopy and Spectral Imaging of Individual Cells" was published in 2009 in the first edition of this volume [1]. In the ensuing 4 years, enormous progress was achieved in the field of vibrational spectroscopy of individual cells; in fact, so much progress that in this revised chapter, only infrared (IR) results from the authors' laboratory, the Laboratory of Spectral Diagnosis (LSpD), will be presented. For the Raman results from the LSpD, the reader is referred to the original literature [2–8].

The most significant changes since the writing of the last version of this chapter occurred in the technology of data acquisition, data processing, and overall understanding of the medical implications of the spectral results. The first of these changes, in the data acquisition methodology, has allowed hundreds of thousands of individual cell spectra to be collected, compared to only a few hundreds of spectra previously. Thus, different levels of statistical significance were achieved in the recent studies.

Second, the overall understanding of confounding effects that have plagued IR microspectroscopy of individual cells, namely the distortion of observed absorptive line shapes [9], received an enormous boost by several papers from the groups of Gardner in Manchester, UK [10], and Bhargava at the University of Illinois [11, 12]. These distortions, to be discussed in more detail in Section 5.2.4.1, are partially due to the morphology of the cells [13] and the limitations inherent in the design of modern IR microspectrometers [11, 12]. Since then, several methods have been developed [14–16] to correct these effects by data processing procedures. Consequently, high quality, highly reliable spectra of human cells and tissue can now be obtained. The understanding of the confounding effects has also eliminated many misinterpretations of spectral patterns that were caused by morphological changes in the sample; in particular, the often discussed changes in cellular spectra upon fixation were found to be mostly due

Infrared and Raman Spectroscopic Imaging, Second Edition. Edited by Reiner Salzer, Heinz W. Siesler.
© 2014 Wiley-VCH Verlag GmbH & Co. KGaA. Published 2014 by Wiley-VCH Verlag GmbH & Co. KGaA.

to changes in sample morphology, rather than chemical changes due to fixation [17, 18].

Finally, the sheer number of cellular spectra, collected for various diseases and disease stages under well-defined conditions and protocols, allows for some medical conclusions about the sensitivity of the spectral methodology, namely spectral cytopathology (SCP). This term was coined for the combination of IR microspectral data acquisition and multivariate analysis of the observed cellular spectra. Careful correlation between results from SCP and results from classical cytology has revealed that SCP, in general, can detect disease earlier than standard cytology. In fact, most of the SCP results reported in this chapter were carried out on "morphologically normal" cells, that is, from cells that were harvested from patients with disease, but that still exhibited normal morphology. These cells already show spectral abnormalities that can be related to the spectra of cells that were diagnosed as cancerous cells. Thus, SCP was shown to present spectral patterns that can aide in the earliest detection of cellular abnormalities.

Finally, the realization that spectra of cells do exhibit a natural variance, due to a number of factors such as metabolic activity, stage in the cell cycle, and so on, has necessitated a statistical approach to the interpretation of SCP data. Since spectra of cells may be noisy – due to the small amount of sample in a typical cell ($\sim 10^{-8}$ g) – multivariate methods of data analysis should be employed on the spectral data sets to help differentiate uncorrelated changes (noise) with variance associated with the desired (or suspected) cause of change. The availability of increased computational power to carry out these analyses was among the most important developments to propel SCP toward the commercial realm.

In addition, visible images of the cells must be available to allow correlation of the spectral changes to either confounding morphological causes, contamination, or the actual desired changes in cellular events (disease). The results presented here differ in the scientific philosophy from that normally seen in the field of "Spectroscopy of Biological Molecules" in that the spectra of cells and tissue pixels are more complicated (they are a superposition of component spectra of unknown abundance), and they are no longer static, but subject to changes that are normally ignored in spectroscopy (morphology, metabolic activity, disease). Thus, those spectroscopists who are accustomed to spectral reproducibility and constancy are forewarned herewith that the remainder of the discussion later will challenge these concepts, but will demonstrate that vibrational spectroscopy of biological systems such as cells and tissue can be interpreted, and valuable diagnostic information can be deduced from spectral results.

As mentioned earlier, this review article will concentrate mostly on SCP results from the authors' laboratory since the LSpD has contributed to this field more than that of the other fields in spectral diagnostics. Also, the size of the data sets in terms of patient numbers (>200 each for oral and cervical cytology) exceeds by far any other data sets investigated by other groups.

5.2
Methods

5.2.1
Cell Collection and Culturing Methods

5.2.1.1 Exfoliated Cells

Oral cells exfoliated by LSpD personnel as part of an oral cancer screening program at Northeastern University (NEU), under a local Institutional Review Board (IRB) authorization, as well as all cervical cells and oral cells from clinical patients at Tufts Medical Center (TMC) in Boston, were treated in the same manner. The cells were exfoliated via cytobrushes, which were immersed into SurePath® fixative immediately after exfoliation. This fixation medium consists of 24% aqueous solution of ethanol and 1% each of methanol and isopropyl alcohol. SurePath fixation was shown to change cellular spectra minimally, even after prolonged exposure of the cells (1 month) to the fixative, and that spectral changes due to disease are much larger than those produced by fixation protocols and exposure to fixatives [17, 18]. The SurePath fixation protocol was adapted at the LSpD since it was the method of choice at TMC, from where all clinical oral and all cervical samples were derived. A comparison of formalin- and SurePath-fixed cells showed minimal differences [17]. A discussion of fixation methodology and the spectral changes because of fixation will be discussed in detail later. Urine-borne cells were obtained by filtration of fresh urine from laboratory volunteers. Esophageal cells were exfoliated endoscopically by one of us [M.A.] under a local ethics board approval using an endoscope-based exfoliation brush.

After repeated wash and centrifugation cycles, cells were spin-deposited via cytocentrifugation onto "low-e" slides (see later). Uniform, sparse samples of cells, which adhere to the substrate very strongly, could be produced this way.

5.2.1.2 Cultured Cells

Most cells grown in the authors' laboratory were purchased from ATCC (Manassas, VA, USA) and cultured in 75 cm^3 culture flasks (Corning, Lowell, MA) using minimum essential Eagle's medium (ATCC, Manassas, VA, USA) supplemented with 10%, by volume, fetal bovine serum (FBS, ATCC). Cultured flasks were incubated at 37 °C and kept in an atmosphere of 5% CO_2. Cells were cultured until confluent and removed from the flasks using trypsin-EDTA (ATCC). Cells were then reseeded onto the windows of choice, "low-e" slides (see later) or CaF_2 disks for IR measurements, immersed in fresh culture medium supplemented with 10% FBS, and placed back into incubation for approximately 12 h. Cells were fixed with SurePath solution (see earlier) prior to IR data acquisition. The effects of this fixation protocol will be discussed in Section 5.3.2

5.2.2 Sample Preparation

5.2.2.1 Sample Substrates

Except for some of the fixation studies (for which Raman data were also acquired) and for studies in aqueous media (see later), all sample preparations used reflection-coated glass slides as sample substrates. Raman data are prone to show some glass signatures when these slides are used; consequently, some studies that relied on a combination of Raman and IR data were carried out on CaF_2 disks. Similarly, CaF_2 was used as a substrate for IR studies of live cells, as prolonged exposure to water damaged the reflective slides.

The reflection-coated glass slides used in this study are commercially available from Kevley Technologies (Chesterland, OH, USA) and are also known as *low-e* (for low emissivity) or MirrIR slides. They are manufactured from silver-coated glass with a thin SnO_2 overcoating, and are nearly completely transmissive in the visible spectral range and nearly completely reflective in the IR spectral range. These slides, which are relatively inexpensive, can therefore be used for both visual cytopathology and SCP. This is extremely important for the correlation of spectral and cytological results. Furthermore, the large number of slides required for some of the studies reported here makes the use of any other substrates presently available fiscally impossible.

Recently, a potential source of artifacts was pointed out [19] due to a standing electromagnetic wave that forms on all reflective surfaces. The amplitude of this wave depends strongly on the wavelength of the incident radiation and confounds the observed intensities. However, we have shown [16] that the errors for thin flat cells are relatively small, and can be further reduced by data preprocessing methods.

5.2.2.2 Sample Fixation

As indicated earlier, all samples were fixed in SurePath solution. The effects of this fixation protocol will be discussed in Section 5.3.2.

5.2.2.3 Sample Deposition

All exfoliated cells were spin-deposited onto the low-e slides using a cytocentrifuge (Thermo Shandon, Waltham, MA, USA). To this end, the washed and fixed cells were resuspended in buffer solution, and about 1 ml of cell suspension was added to a cytology funnel that was clamped onto a low-e slide. This assembly was inserted into the rotor of the cytocentrifuge. Under the influence of the centrifugal force, the liquid was pressed through a 5 mm diameter hole of the funnel, and the cells were attached to the slide, while the liquid was wicked away by a layer of paper between the slide and the funnel assembly. The final number of cells on the substrate can be controlled by the volume of cell suspension and the centrifugation time. Uniform, sparse monolayers of cells could be produced by this method.

5.2.3 Data Acquisition

5.2.3.1 Infrared Instrumentation

All IR spectroscopic results presented in this article were acquired microscopically via one of three imaging IR microspectrometers (Spectrum One/Spotlight 400, PerkinElmer Corporation, Shelton, CT, USA) at the LSpD, henceforth referred to as the *PE400*. IR spectra of cells were collected in transflection (reflection–absorption) mode from samples mounted on "low-e" slides (see Section 5.2.2.1) at a spectral resolution of $4\,cm^{-1}$. All IR data represented in this review were collected in imaging mode at 6.25 μm pixel size using the 16-element photoconductive HgCdTe focal plane detector, operating at liquid nitrogen temperature. The spatial resolution of the PE400 was established using the military resolution targets, and was about twice the diffraction limit at $1600\,cm^{-1}$, about 12 μm. For the sake of simplicity, one may assume that the voxel size interrogated by the instrument is about $10 \times 10 \times 5\,\mu m^3$ (in the x, y, and z directions, respectively) in the mid-IR, where the z-direction is not so much determined by the diffraction limit but determined by the maximum thickness of a cell. The pixel size used in these studies allows the detection of spectral differences of items as small as a cellular nucleus. Since the goal of SCP is the detection and diagnosis of individual cancer cells, it is advantageous to operate the spectrometers at a pixel resolution of about the size of a cellular nucleus. In the past, four to eight interferograms were co-added for each pixel; however, after the implementation of the noise-adjusted principal component reconstruction (see later), only one or two interferograms are co-added. Background spectra for all 16 detector elements were collected using 128 co-added interferograms to reduce the noise contributions of the background as much as possible.

Under these conditions, acquisition of a complete (about $700–4000\,cm^{-1}$) Fourier transform infrared (FT-IR) spectrum for one pixel requires 5–10 ms using the PE400. Fourier transform was carried out with Norton–Beer apodization and one-level zero-filling. Raw spectra were stored as 800 point intensity vectors with $2\,cm^{-1}$ data spacing from 800 to $4000\,cm^{-1}$ in native PE400 imaging format (.fsm files).

5.2.3.2 PapMap Methodology

At the time of writing the original chapter on IR and Raman spectroscopy of cells in 2009 [1], all data acquisition was carried out in a "point-and-shoot" mode, in which a cell was centered in the field of view of the IR microspectrometer. Subsequently, an aperture was used to block areas of the field of view not occupied by the cell, and a spectrum of the cell was acquired within a few seconds. Since a microscope slide contains hundreds or thousands of individual cells, this process was automated using the instrument manufacturer's software to visually select positions, aperture sizes, and orientations of hundreds of cells; store these parameters; and, subsequently, have the microspectrometer acquired data at each of the stored

cell positions. Although this method was quite successful in preliminary studies [1, 20], the process was tedious and time consuming, and may have omitted cells on the slide that were not recognized as such, since at the time of data acquisition the cells are unstained, and their recognition is difficult. Acquisition of 200 cells took about 4 h.

In 2008, another approach was implemented and subsequently submitted for patent protection. In this approach, the entire surface of the sample spot produced by the cytocentrifuge (about 5 mm in diameter) is imaged at a pixel size smaller than the diffraction limit, regardless of whether the surface is occupied by a cell or not, producing a large spectral data set of the entire sample area. Subsequently, the spectra of individual cells are reconstituted from pixel spectra of areas identified to belong to one cell. This approach was referred to as the *PapMap method* [21].

For cytological applications, a $4\,\text{mm} \times 4\,\text{mm}$ area of the 5 mm diameter sample spot was scanned at a pixel size of 6.25 µm on edge, resulting in a data set of $(4000/6.25)^2 = 409\,600$ individual spectra and occupying about 2.5 GB. The PapMap algorithm determines which pixel spectra belong to a cell by constructing a binary mask that establishes contiguous areas belonging to one cell. Figure 5.1a depicts the visual image stored by the PE400 before IR spectral data acquisition, and Figure 5.1c shows the corresponding binary mask. Contiguous white regions in this image are assumed to belong to one or a few overlapping cells. These contiguous regions will be henceforth referred to as *raw cells*.

The following step refines the binary mask by removing clumps of overlapping or partially overlapping cells, and debris such as broken cells, cellular nuclei, or bacteria. This is accomplished by defining lower and upper bounds on the number of pixels associated with a cell (see Section 5.2.4.1). Any "raw cell" regions falling outside these ranges will be eliminated.

Next, spectra of individual cells will be calculated by averaging all pixel spectra in a given "raw cell," which are further subjected to two constraints: band location and intensity. These constraints are necessary since the pixels from the edge of cells

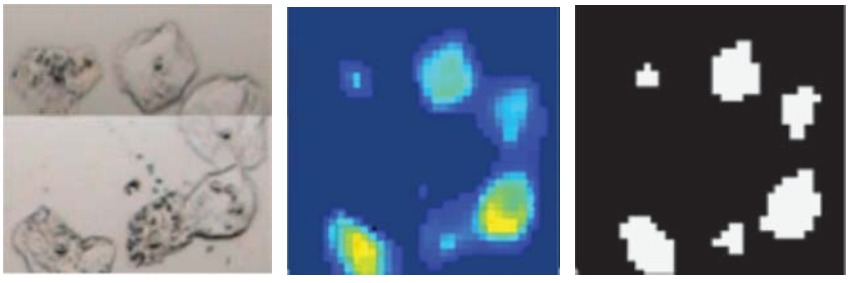

Figure 5.1 (a) Visible image of unstained squamous cells taken during IR data acquisition. (b) Raw IR intensity map of pixel spectra from (a). (c) Binary mask constructed from raw pixel intensities.

are often very weak and, therefore, exhibit a poor signal-to-noise (S/N) ratio. By adding these spectra to the final spectra of the cell may degrade the signal quality of the final cellular spectrum. The second constraint is to reduce the "edge effect," a distortion of the absorptive line by dispersive components; this is now commonly referred to as the *resonance Mie ("R-Mie") effect* [13]. This subject will be discussed in more detail in Section 5.2.4.1.

To reduce the R-Mie contributions, the following procedure is applied. In each of the contiguous "raw cell" regions, the pixel with the highest amide I intensity is determined. These pixels are shown in Figure 5.1b by the brightest (yellow) hues. These pixels are assumed to originate from the nucleus of the cell, which always has the highest amide I intensity. The nuclear amide I intensities are higher than those of the cytoplasm primarily owing to two reasons: first, the nucleus is thicker than the cytoplasm (by a factor of about 3–5) for dried cells. Second, the abundance of nuclear proteins is very high. Thus, pixels from the nucleus often have absorbance values of 0.2–0.5 optical density (OD), whereas pixels from the cytoplasm typically have absorbance values of 0.02 OD. We further assume that the pixel of the nucleus, generally from the interior of a cell, is relatively free of the "edge effects." This spectrum must pass stringent conditions before it can be used as a "seed spectrum" to reconstruct the cellular spectrum: the intensity maximum must occur between 1630 and 1670 cm^{-1}, and must be above an intensity threshold typical for nuclear spectra. Starting from this "seed spectrum," all spectra in the contiguous area of the "raw cell" are co-added to the seed spectrum if their amide I intensity is above a certain percentage of the amide I intensity of the seed spectrum, and if their amide I frequency is within a shift of 4 cm^{-1} of the amide I frequency of the seed spectrum. If the pixel within the contiguous area does not fulfill these criteria, then it will be excluded from the co-addition procedure. A comparison between a cellular spectrum constructed by co-adding individual pixel spectra from a single cell and a cellular spectrum obtained using single-point data acquisition demonstrated [21] that the co-addition process described earlier results in a spectrum that is identical to the single-point cellular spectrum. The loss of S/N ratio in any given pixel, caused by sampling at an aperture that is smaller than a cell, is recovered by the co-addition process.

A further improvement of this procedure was implemented in 2011. This implementation uses the spectra of areas not occupied by cells to establish the noise characteristics of the instrument during data acquisition. Using a procedure known as *noise-adjusted principal component analysis* (*NA-PCA*), pixel spectra from areas occupied by cells can be corrected for instrument noise, thus reducing the noise components of the spectra by an order of magnitude [16, 22, 23]. This approach allowed for a much quicker data acquisition, co-adding only two interferograms for each pixel spectrum. This breakthrough approach makes up for the extra time spent scanning areas not occupied by cells by using this information for noise reduction.

5.2.4 Methods of Data Analysis

5.2.4.1 Correction for R-Mie Effects and Data Preprocessing

The origin of the distortion of observed absorption features in IR microspectroscopy has been discussed in a number of ground-breaking papers [13, 24] and will not be reiterated here. May it suffice here to state that these effects are due to the morphology of the sample; in particular, spherical particles exhibit these effects particularly strongly. However, as demonstrated theoretically by Bhargava and coworkers [11, 12], any sample with strong gradients of the refractive index (for example, a straight edge of a particle boundary) will exhibit these effects as well. At present, there exist several computational approaches to correct these phenomena, based on either an iterative numerical process [14], a step-wise approximation method [15], or a phase-correction approach that was suggested as early as 2005 [9, 16, 24]. All these approaches are approximate in nature and some require extraordinarily long computation times. An *ab initio* approach to circumvent this problem has been proposed by R. Bhargava (private communication, 2011); but until this approach is implemented in IR microspectrometers, the approximate methods need to be employed. Recently, Dazzi *et al*. [25] demonstrated that the use of an integration sphere for data acquisition can eliminate the problem, but this approach is not suitable for simultaneous detection of multiple pixels of data, using an array detector.

The aforementioned computational procedures have been demonstrated to reduce the spectral distortions to acceptable levels. This was established by comparison of "uncontaminated" spectra, collected from samples with low morphological heterogeneity, with spectra that were originally strongly contaminated and processed via the correction algorithms [9].

All data preprocessing was carried out by software written in-house in 64-bit MATLAB (The Mathworks, Natick, MA, USA) for the automatic analysis of an entire data set at one time. The sequence of data processing steps for each of the 409,600 spectra data set is summarized later. A more detailed discussion of all steps involved can be found in the literature [16].

1) *Conversion of transmittance spectra to absorbance units*. This step was required since the PE400 stores spectra in the mapping file as raw transmission spectral vectors. The spectral vector corresponding to a given 6.25 μm × 6.25 μm pixel will be henceforth referred to as *pixel spectrum*.
2) *Construction of a noise data set from areas not occupied by cells*. This step was accomplished using a simple integrated amide I intensity criterion to define areas of the substrate not occupied by cells.
3) *Construction of a signal data set from areas occupied by cells*. These areas were selected by several criteria, including integrated intensity at the amide I band, integration over the entire spectrum, and defining minimum and maximum ranges for the amide I band position.
4) *NA-PCA* [23] *to increase the S/N ratio of each cellular pixel spectrum*. NA-PCA is based on constructing separate signal and noise correlation

matrices, using the same equations according to which the correlation matrix is constructed in standard principal component analysis, PCA (see Section 5.2.4.2). Subsequently, the pixel spectra were reconstructed from the first 30 eigenvectors of the noise-normalized signal correlation matrix; the noise normalization scales the eigenvectors such that they are no longer arranged in order of decreasing variance, but in order of increasing noise. The ensuing reconstructed spectra exhibit reduced noise without the loss of spectral fidelity.

5) *Reduction of water vapor contributions in cellular pixel spectra*. This was accomplished using a multiplicative signal correction (MSC) algorithm first described by Bruun *et al*. [26]. This procedure reduces residual water vapor signals by over an order of magnitude. This step was found to be advantageous in spite of the fact that the PE400 instruments were continuously purged with −40 °C dew point dry air.
6) *Construction of a binary mask to delineate areas occupied by cells from those of the blank substrate*. This step is the centerpiece of the PapMap^{P} procedure, as discussed earlier. This step defines contiguous areas of the substrate occupied by individual cells. These areas must contain a number of pixel spectra that is set between a lower and an upper limit that are dependent on the cell type investigated. For squamous epithelial cells, for example, the lower limit may be set to 9, which implies that only areas larger than 3×3 pixels, or about $20\,\mu m \times 20\,\mu m$, are considered cells; any objects smaller than this limit are considered cell fragments, lymphocytes, or clumps of bacteria. The upper limit may be set at 100 pixel spectra, corresponding to about $60\,\mu m \times 60\,\mu m$, which is the size of a large squamous cell. This limit eliminates clusters or clumps of overlapping cells, which confound the analysis.
7) *Conversion to second derivatives and expansion of spectra to 1800–778 cm^{-1}*. All spectra contained in the areas of the binary mask and associated with cellular spectra were subsequently expanded in the fingerprint spectral range (1800–778 cm^{-1}), and were converted to second derivative spectra using a Savitsky–Golay sliding window algorithm [27]. The low wavenumber limit was selected to obtain spectral vectors whose lengths are an integral power of 2 for the ensuing Fourier processing. Second derivative spectra are used for all analyses since second derivatives enhance spectral resolution and reduce the dependence on absolute intensities. This point is extremely important since the intensities of bands can be distorted by the electric field standing wave effects [19] discussed in Section 5.2.2.1.
8) *Correction of scattering effects in cellular pixel spectra indicated by the binary mask*. Resonant-Mie-induced scattering effects, discussed earlier, that can mix the real (dispersive) and imaginary (absorptive) line shapes of a vibrational transition, and thereby creating shifts in band position and intensity distortions in the observed spectra, are corrected by a phase-correction algorithm [28] between the real and imaginary components obtained by finite Hilbert transform (truncated reverse fast Fourier transform, FFT) [29].

9) *Computation of cellular spectra from individual pixel spectra for each cell identified in the binary mask*. The spectra within "occupied" areas in the binary mask were co-added to create a cellular spectrum. This co-addition is subject to a number of criteria aimed at eliminating weak and noisy spectra from the edge of a cell, which may also be the most contaminated by residual scattering effects.
10) *Elimination of spectra due to noncellular materials in the sample*. At this point, all cell spectra were compared with spectra expected of a given cell type to eliminate artifacts due to contamination by, for example, a nylon bristle of the cytobrush or other materials.
11) *Export spectra of individual cells, cell coordinates, and name tags to patient-based data structure*. Each region of the binary mask identified as a cellular spectrum was tagged with a numerical cell name, its size, and coordinates and stored in a MATLAB database.

The acquisition of a 4 mm × 4 mm sampling area required about 3 h, whereas the processing of each data set required about 3 min, typically yielding between 500 and 1000 high-quality IR absorption spectra of individual cells.

5.2.4.2 Principal Component Analysis (PCA)

Data analysis was carried out by unsupervised and supervised multivariate methods. PCA [30], an unsupervised method, was initially used to determine if systematic variations were present in cellular spectra. PCA was discussed in detail in the first edition of this chapter [1] and was carried out using the PLS (partial least squares) Toolbox 402 (Eigenvector Research, Wenatchee, WA) in MATLAB. Spectral vectors in the 1800–900 cm^{-1} range were used after vector normalization.

PCA results are displayed as 2D or 3D "scores plots," in which each symbol represents one cell spectrum. The axes in these scores plots are the contributions (scores) of each cellular spectrum along the principal components indicated. Clustering of spectra indicates that significant variations exist in the data sets.

5.2.4.3 Diagnostic Algorithms

If PCA plots show significant spectral differences between spectral classes, it is likely that a supervised algorithm can be trained to analyze or diagnose unknown data. Supervised algorithms, such as artificial neural networks (ANNs) [30] have been used to diagnose spectra from test data sets with high accuracy. To this end, the entire data set was divided into a training and a test data set, each one comprising equal number of the two spectral classes to be discriminated (e.g., normal and diseased). A number of randomly selected spectra from two classes were used to train the ANN. Fifty (intensity) features were selected from the 451 data points[1)] in each spectral vector via entropy-based feature selection, using the "rankfeature"

1) The number of data points in each spectral vector is determined by the difference between the high and the low wavenumber limits of the spectra divided by the data point spacing, that is, $(1/2[1800 - 900]+1)$.

function in MATLAB. The MATLAB "feedforward" ANN function was utilized for ANN construction, employing the 50 inputs ("features") discussed earlier, one hidden layer with two nodes, and one output neuron (abnormal/normal). The ANN obtained in this manner was tested with a data set consisting of a matching number of spectra from the two classes. This process was repeated for different random selection of spectra from the test and training sets.

5.3 Results and Discussion

5.3.1 General Aspects of SCP

One of the early goals of researchers involved in SCP was the development of methods to aid in the diagnosis of cervical cell smears used for screening for cervical cancer (the so-called Papanicolaou test or "Pap" test for short) [31, 32]. The reason for selecting this subject was the well-documented high rate of false-positive and false-negative readings of these samples by cytologists and cytotechnicians. Interestingly, one should not take the low sensitivity and specificity[2)] of the Pap test as a failure of the method; quite contrary, no single test has reduced the incidence of and morbidity from a given cancer as much as the Pap test. Yet, for a single reading of a classical "smear," the overall accuracy (average of sensitivity and specificity) was less than 70%. Improvements were achieved by producing better samples: rather than smearing the exfoliated cells on a microscope slide, followed by staining, liquid-based methods were devised [33] that produced sparse monolayers of cells, which, after staining, provided a much clearer picture of individual cells. A small section of such a stained sample is shown in Figure 5.2.

This figure, reproduced from [34] shows about 50 cervical squamous cells from a small section of a liquid-based sample that stain either pale blue or pale pink; in addition, this sample contains bacteria (1), polymorphonuclear leukocytes (PMNs, 2), cellular debris such as naked nuclei, and one "abnormal" cell (3), indicated by an enlarged nucleus. The difficulty in classical (visual) cytopathology is the detection of a few percent of abnormal cells in a sample that may contain 1000–10 000 cells. Furthermore, an enlarged nucleus *per se* (a larger nucleus/cytoplasm (N/C) ratio) is also observed for cells from the lower layers of the cervical epithelium; thus further criteria, such as the morphology of the nuclear membrane, need to be invoked for a reliable discrimination of normal from abnormal cells. The level of abnormality also needs to be graded; for cervical cytology, the grades in order of increasing severity include reactive, low-grade dysplasia (low-grade squamous intraepithelial lesion, LSIL), high-grade dysplasia

2) The terms sensitivity and specificity are used in this chapter in the clinical sense, where sensitivity refers to the ratio of true diagnoses divided by the total number of true-negative plus false-negative diagnoses, and specificity refers to the ratio of true-negative diagnoses divided by the true-negative plus false-positive diagnoses.

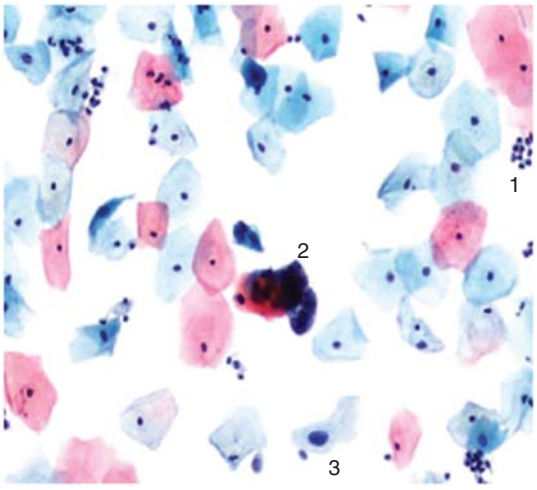

Figure 5.2 Microscopic image of a cervical cell preparation. See text for details. (From Ref. [34].)

(high grade squamous intraepithelial lesion, HSIL), carcinoma-in-site (CIS) and invasive cancer.

Given the complexity of the problem, it was no surprise that cervical cancer screening was selected as a target for early spectral diagnostics. When first attempts at this goal were made in the early 1990s, IR microspectroscopy had not progressed to a level that permitted acquisition of spectra of individual cells in reasonable times; thus, cell pellets of unknown composition in terms of the cell types contained in the pellet were used as samples, and the measurements were carried out macroscopically. To allow direct assessment of individual cells and to convince the value of the spectral method to the cytologists, the authors' laboratory switched to single cell-based SCP in 2002. Although much more time consuming than the pellet-based approach, the single cell method permits a direct comparison of spectral results with visual inspection of a cell, and thus, is of much higher inherent value to a cytologist. To this end, the sample is stained and cover-slipped after IR data acquisition, and cells can be located on the substrate by their stored positions. Early results showed promise: the distinction between squamous cells from the distal urethra from urothelial (bladder) cells by spectral methods proved to be straightforward [20], and the classification of superficial and intermediate cells from cervical epithelium and effects of hormonal influences could be established quite readily [35]. The hormonal effects were originally sought to help classify samples from premenopausal and menopausal women, but needed to be expanded to include menstrual status since the level of hormones influences the maturation of cervical cells. This was first established for canine cervical cells [36] but was found to hold for human cervical cells as well. In order to facilitate the detection and diagnosis of cervical disease, to be discussed later, only women using oral contraceptives were used,

since they keep the hormonal level constant, and thereby eliminate one variable in the process of establishing SCP as a possible diagnostic method [35]. Results of the cervical work will be presented later in this section.

Concurrent with the efforts on cervical cells, development of a screening test for oral cancer was initiated at the LSpD. Oral mucosa, like cervical mucosa, consists of stratified squamous epithelium, but due to digestive enzymes in the saliva, it does not exhibit large spectral contributions because of glycogen, which mask a large part of the low-frequency spectrum ($1000-1200\,cm^{-1}$). The original results for the oral mucosa were extremely intriguing and largely form the basis of our present understanding of spectral cytology. Before presenting these results, a short introduction of stratified squamous tissue will be presented, followed by cursor interpretation of a typical vibrational spectrum of a cell.

Stratified squamous epithelial tissue is a frequently found epithelium in the human body (nasopharyngeal and oral cavities, esophagus, urethra, vagina, cervix, and others). It is a multilayered structure consisting of a layer of actively dividing basal cells anchored to the basement membrane, beneath which one finds connective tissue (stroma). The daughter cells created by the division of the basal cells form the parabasal layer and mature and migrate to the surface layer. In this process, their morphology and chemical composition change drastically. Although the basal cells are roughly cuboidal in shape, about 20 μm on edge, with a large nucleus and very little cytoplasm, the mature stratified (flat) cells may measure up to 60 μm on edge and exhibit very small pyknotic nuclei. They also accumulate glycogen for energy storage (except for the oral mucosal cells, see earlier); since they are fully differentiated, their chemical composition reflects a reduction of certain compounds in the cytoplasm. Using high spatial resolution of synchrotron radiation FT-IR imaging and enzymatic digestion studies, it was observed that the nuclear DNA is virtually unobservable in pyknotic cells [37] but contributes to the observed spectra in rapidly dividing cells, for example, cancer cells and lymphocytes.

A typical IR spectrum of human cells is shown in the traces in Figure 5.3a. The $1500-1700\,cm^{-1}$ region of the spectrum of a cell is dominated by the protein amide I and amide II bands; both these peaks split into sub-bands in the second derivative spectra and are known to be in exciton-like coupled states of mainly C=O and O=C–N stretching coordinates, respectively [38]. Certain proteins, in particular the proteins of connective tissue (collagen), have sufficiently different IR spectra to allow detection of their spectral signatures with the naked eye. A high-frequency band, at about $1740\,cm^{-1}$, is due to the ester linking of phospholipids [39]. The antisymmetric and symmetric P–O stretching vibrations of the phosphodiester moiety,

$$-O-PO_2^--O-$$

are observed at about 1235 and $1090\,cm^{-1}$ in DNA, RNA, and phospholipids. The C=O stretching bands of nonhydrogen-bonded nucleotides are observed mostly as high-frequency shoulders of the amide I peak.

The amide III vibration occurs superimposed on the antisymmetric phosphodiester stretching vibration. Carbohydrates show strong bands owing to C–O–H

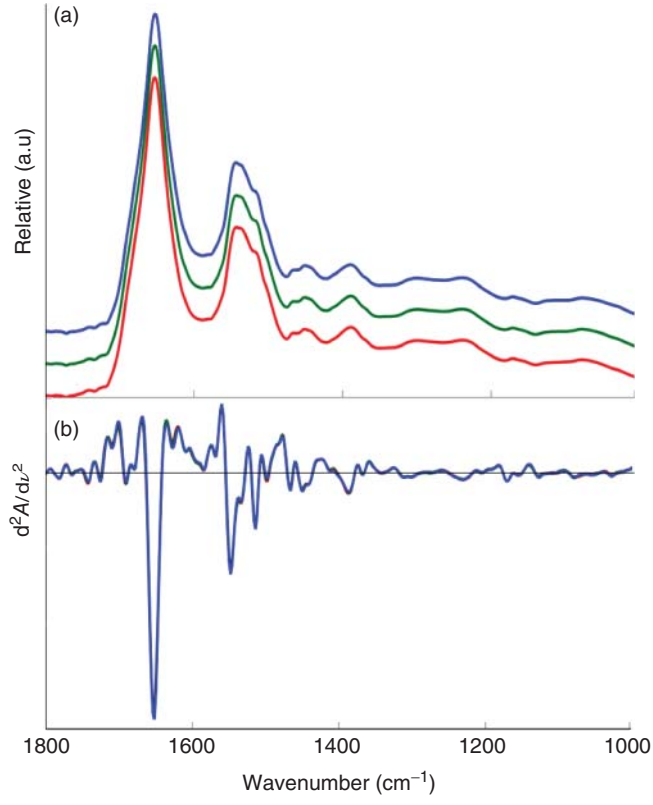

Figure 5.3 (a) Mean absorption spectra of about 45 dried oral mucosa cells after 1 day (red), 1 week (green), and 1 month (blue). (b) Superposition of the second derivatives of the three traces shown in (a).

deformation and C–O stretching coordinates between 1000 and 1200 cm^{-1} (see Figure 5.7). One of the most abundant cellular carbohydrates is glycogen, which shows three strong bands at 1151, 1078, and 1028 cm^{-1}. Carbohydrate bands are also observed in glycoproteins, particularly in mucus.

5.3.2 Fixation Studies

In contrast to classical cytopathology, where sample fixation and staining methods have been documented for nearly a century [40], effects of fixation and storage of cells for SCP are still largely unknown and have been the subject of numerous (largely unjustified and negative) comments from referees and reviewers. To answer these comments once and forever, the following study was undertaken to ascertain that fixation procedures induce only very minute changes in the observed IR spectra.

Here, results of a study are reported that compare the effects of fixation methods commonplace in cytology: fixation by buffered formalin solution or by a commercial mixture of alcohols (the SurePath method). These two fixation methods are compared with rapid drying (desiccation) of the cellular samples followed by immediate spectral data acquisition. All fixation methods aim to preserve cells by rendering them insensitive to spontaneous or bacteria-caused degradation. Rapid drying accomplishes this by dehydrating and precipitating the proteins, making them chemically less reactive. Alcohol-based fixation, such as the SurePath method, will kill bacteria, in addition to dehydrating the biochemical components. Excessive treatment with ethanol, however, will dissolve some of the membrane phospholipids and, therefore, cause spectral changes to a cell. Formalin fixation actually cross-links proteins in a well-understood mode of action, and renders the resulting protein mass even less prone to degradation and bacterial digestion.

Oral mucosa (buccal) cells, harvested from the inside of the cheek, as well as cultured HeLa cells were used in this study in order to establish changes in spectral patterns between fixed and dried cells, as a function of fixation and storage time. Large spectral changes reported in the past [41] were most likely due to morphological differences in cells that can lead to scattering effects and changes in band shapes and frequencies. We demonstrate that the three methods of sample preparation (buffered formalin solution, SurePath alcohol mixture, and rapid desiccation) produce small but reproducible spectral changes, and that cells left for prolonged times in fixative solutions exhibit slight spectral changes. This knowledge will define the best procedures for future applications of SCP.

5.3.2.1 Fixation Studies of Exfoliated Cells

Time Evolution of Unfixed Cells First, the stability of unfixed (desiccated) cells over a time period of up to 1 month will be presented [17, 42]. Figure 5.3a displays the mean absorbance spectra of unfixed cells recorded at 24 h, 1 week, and 4 weeks after sample preparation. The number of individual cellular spectra averaged at each of the three different time points was 47 ± 2. At times in-between data acquisition, the sample was stored in a desiccator.

Inspection of the mean spectra in Figure 5.3a shows no noticeable spectral differences between the three time points. The correlation coefficient between them was 0.99. This indicates that there are no gross biochemical changes within 4 weeks of preparing an unfixed cell sample. Figure 5.3b shows an overlay of the mean second derivative spectra of the data shown in Figure 5.3a. In general, second derivative spectra are more sensitive toward the detection of small spectral changes since unresolved shoulders in the original absorbance spectra may appear as individual bands.

Since these second derivative spectra are nearly superimposable, one concludes that the average biochemical composition of dried cell samples is invariant over a period of 1 month, if the cells are stored in a dry and clean environment. In order to ascertain whether or not individual cells exhibit systematic spectral changes

that are too small to be perceived by visual inspection of the spectra, all individual second derivative spectra in the entire data set of unfixed cells were subject to PCA. The resulting PCA plot showed some dependence on water vapor components for the 4-week data (presumably due to residual outgassing of the sample) but only with a very minor shift in the protein amide I position [17].

Comparison of fixed and dried cells In this section, spectra of unfixed (dried) cells at 24 h, and cells that were fixed for 24 h in SurePath or phosphate-buffered formalin solutions and subsequently dried, are compared. In Figure 5.4, the red traces show the mean second derivative spectra for cells subject to the three different protocols after 24 h. Similarly, the green and blue traces represent the mean spectra for the three fixation protocols at 1 and 4 weeks, respectively.

These mean second derivative spectra for all fixation protocols are very similar and dispel the notion that fixation methods cause strong changes in spectral patterns, as reported previously [41]. The similarity of the spectra may come as a surprise, given the fact that the different sample treatments do slightly change the chemical composition. In the past, we have shown that fixation in pure ethanol changes the phospholipid spectral features of cultured cells [43]; however, these previous experiments were carried out using 100% ethanol and cultured cells (fibroblasts) that showed relatively large phospholipid features at about 1740 cm^{-1}. These phospholipid signals are very weak or absent in exfoliated oral mucosa cells.

In principle, one should expect to see the effects of protein cross-linking because of formaldehyde fixation, but given the low number of cross-links formed, it is plausible that the spectral changes are beyond the detection limit, when inspecting the mean spectra by eye. A slight spectral change, not apparent in the absorbance spectra but apparent in the second derivative spectra, is a small shoulder on the low-frequency side of the amide I band (see arrow in Figure 5.4) that is most pronounced in the SurePath-fixed samples. This indicates a small, fixation-induced protein conformational change that occurs immediately upon SurePath fixation, but is not observed in the formalin fixed or unfixed samples.

However, as previously observed for the unfixed cells, PCA was able to distinguish very small spectral changes and revealed individual clusters for each fixation methods [17]. The loading vectors (not shown) indicate that there is a slight shift of the amide I band for the formalin-fixed samples when compared to that of the unfixed and SurePath-fixed samples. These changes are discussed in more detail in the original literature [17]. When the spectral measurements were repeated after 1 week or 1 month, no further spectral differences could be detected. Thus, even prolonged exposure of samples to the fixatives did not produce any effects on the cellular spectra.

More important than the small changes observed using PCA is a discussion about the absolute magnitude of these changes as compared to spectral changes due to disease. This aspect is addressed in Figure 5.5, which depicts a PCA scores plot of the normal cells, at 24 h fixation with clinical samples of oral disease,

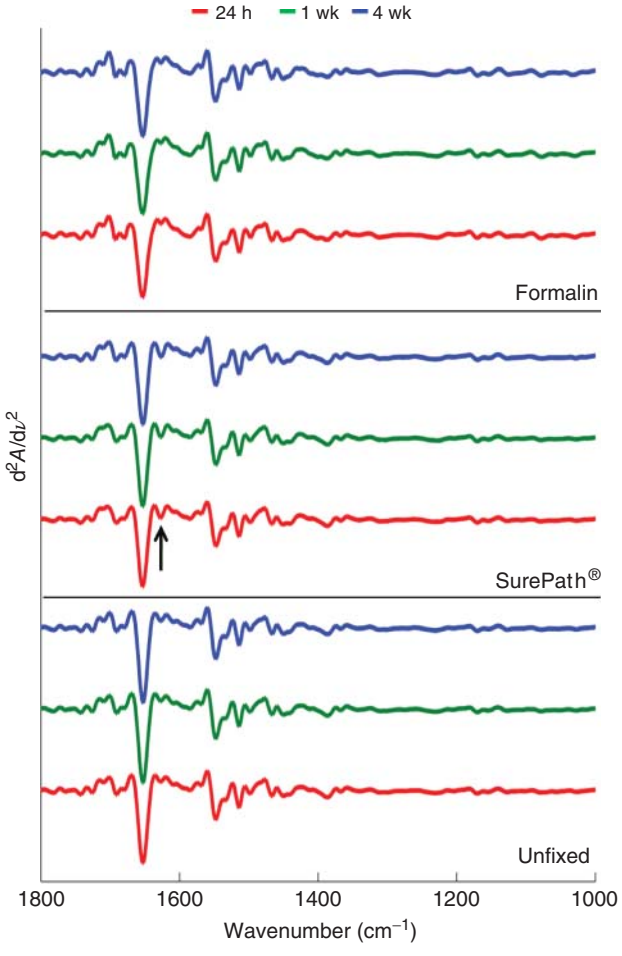

Figure 5.4 Mean second derivative spectra of cells fixed by three different methods, as a function of fixation exposure.

namely hyperplasia and mild dysplasia, at the same time point. We have shown previously [44] that the spectra from abnormal, but not cancerous, cells occupy a region in PCA space in-between the normal and cancerous cell spectra. Figure 5.5 demonstrates that the variations influenced by the fixation methods are much smaller than those caused by hyperplasic and "atypical" diagnoses.

In classical cytopathology, dried unfixed cells are rarely used, since cell morphology is believed to change over a period of 1 month and the uptake of immunohistochemical stains is poor. However, the photomicrographs of representative unstained cells revealed virtually no morphological changes at 24 h, 1 week, and 4 weeks after fixation [17]. These images were from unstained cells and may not have revealed all the details a cytologist is expected to discern for stained and

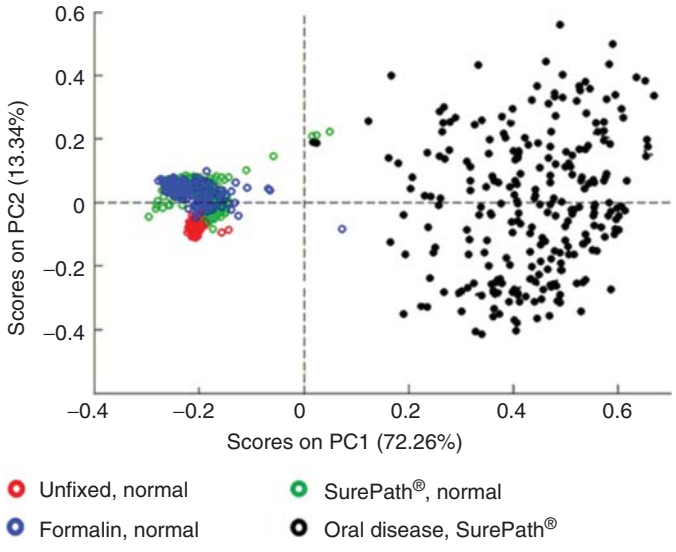

Figure 5.5 PCA scores plot of normal exfoliated buccal cells, fixed by the three methods discussed in the text, and abnormal buccal cells fixed by SurePath solution.

cover-slipped cells. However, these images dispel the notion that there are major cellular morphological and spectral changes with time for unfixed cells.

5.3.2.2 Fixation Effects of Cultured Cells

All exfoliated cell samples were spin-deposited on the sample substrates, whereas cultured cells were grown directly onto the CaF_2 slides. Since the low-e slides used in the previous study were found to be incompatible with long exposure to cell culture media, CaF_2 slides were used in this study. Cultured cells appear much more delicate in morphology – they exhibited the typical pseudo-pod morphology of cultured cells. Thus, we surmised that cultured cells may exhibit more pronounced fixation effects. To study effects of fixation on cultured cells, similar time-dependent and fixation-dependent experiments were carried out for cultured HeLa cells, a cancerous cervical cell line. Figure 5.6 shows spectra of unfixed HeLa cells for a time course study similar to the one reported in Figure 5.3. The spectral changes (results not shown) for different fixation protocols (desiccation, formalin, and SurePath fixation) and their time evolution parallel to those observed for cultured cells, see Figure 5.4, with an additional shoulder on the low-frequency side of the amide I band appearing in the SurePath-fixed cells [18].

Two major observations can be made at this point. First, the spectral traces are still invariant with time, thus dispelling the notion that the cultured cells with their more delicate morphology are chemically less stable than exfoliated cells, and the SurePath fixation appears to produce a small additional band in the protein region in both exfoliated and cultured cells. The origin of this band is not known,

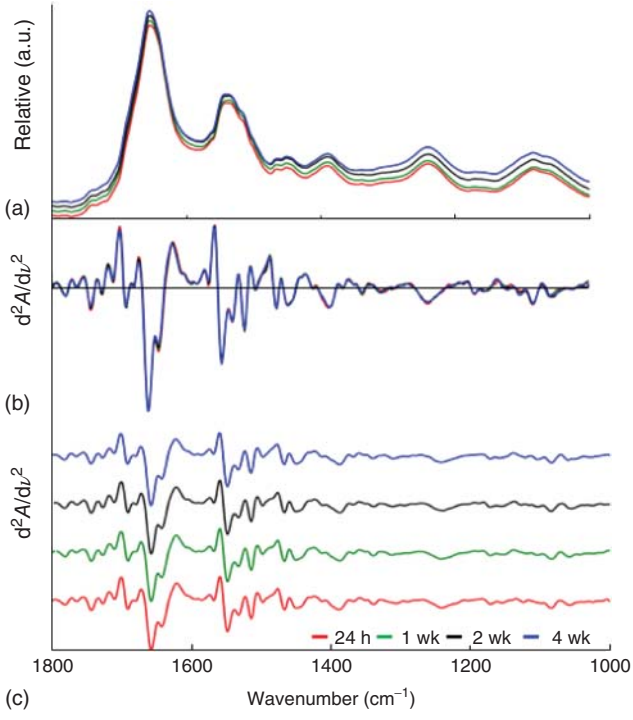

Figure 5.6 (a) Mean absorbance spectra of about desiccated 70 HeLa cells at 1 day (red), 1 week (green), 2 weeks (black), and 4 weeks (blue). (b) Superposition of second derivatives of traces shown in (a). (c) Stack plot of same traces.

but the results suggest that for a given fixation protocol, reliable spectra can be collected. The exposure time to the fixative does not seem to affect the spectral results.

Second, significant spectral changes between the cultured HeLa and the exfoliated buccal cells (see Figures 5.3 and 5.6) exist. The spectral changes reproduce the original work on individual cells by Lasch *et al*. [45], in which exfoliated buccal and cultured giant sarcoma and fibroblast cells were compared. The spectral changes are most pronounced in the DNA/RNA spectral regions, where all actively growing and dividing (cultured) cells show more pronounced signals than the terminally differentiated buccal cells that exhibit a pyknotic nucleus. The spectral differences are particularly pronounced in the second derivative traces. One should refrain from interpreting these spectral differences in terms of "cancer versus not cancer," since these differences are likely due to the metabolic activity of the terminally differentiated cells, on the one hand, and actively growing cells, on the other.

In addition, the cultured HeLa cells display a strong additional protein band in the second derivative spectra at about 1645 cm^{-1} that is totally absent in the second derivative spectra of the buccal cells. In the original studies [45], the S/N

ratio of the spectra was insufficient to utilize second derivatives; thus, it is not clear whether or not this band was contained in the spectra of the fibroblasts and giant sarcoma cells. In the underivatized absorption spectra, the presence of this band can barely be discerned as a broadening of the amide I band. Interestingly, this band at about 1645 cm^{-1} was prominently observed in the spectral patterns of "abnormal" oral mucosa cells [44]. This study, to be discussed in Section 5.3.3.2, demonstrated that morphologically normal cells from patients with oral cancer or precancer (which are referred to as *abnormal cells*) could be separated by PCA from the spectra of truly normal cells. Since oral and cervical cancer and precancer are often linked to infection with an oncogenic virus (see later), this band was tentatively linked to the presence of proteins due to viral infection.

5.3.3
Spectral Cytopathology: Distinction of Cell Types and Disease in Human Urine-Borne Cells and Oral, Cervical, and Esophageal Cells

In this section, the efforts carried out at the LSpD toward establishing SCP as a viable method for detecting the onset of disease in exfoliated cells will be summarized. These efforts originally were concentrated on detecting bladder disorders from cells collected from urine and for the diagnosis of cervical dysplasia, but later shifted toward an overall understanding of the spectral differences between normal and abnormal cells, and the diagnosis of disease in organs in which there is no good screening method at this time. While the earlier studies demonstrated the potential for SCP, they also pointed toward inadequate methodology at the time. Here, the results are presented in order in which the experimental work was carried out.

5.3.3.1 SCP of Urine-Borne Cells

The first application of SCP that shall be discussed is urine cytology, in which epithelial cells contained in urine were analyzed [20]. The original goal of this study was the development of a method that automatically distinguished cells from the distal urethra, and urothelial cells from the lining of the bladder. The latter cells may show abnormal spectral patterns in cases of bladder cancer; however, urine cytology is not carried out routinely in the United States, although urine samples are collected frequently, and while bladder cancer was the fifth most common cancer in males, and the eighth most common cancer in females in 2005. Presumably, routine urine cytological screening is not being carried out at this time because of the overall low accuracy of cytology and the lack of cytological laboratories to perform the extra screening.

Normal human urine contains both squamous cells from the urethra and urothelial cells from the lining of the bladder. This former type may be further subdivided into glycogen-containing and glycogen-free squamous cells. In this study, we established that IR spectral methods, followed by multivariate data analysis, can distinguish these cell types. Acquisition of the urine-borne cells

was still accomplished in the "point-and-shoot" method as described in Section 5.2.3.2), that is, before the implementation of the PapMap methodology.

Figure 5.7D displays photomicrographs captured from the three main types of epithelial cell identified in urine sediments after Pap staining [46]. It is known that voided urine collected from healthy individuals for conventional urinalysis contains very small numbers of transitional (urothelial) epithelial cells [47]. Our spectroscopic studies confirmed this observation.

Spectra recorded from urothelial cells display much higher absorbance intensities in the amide I band than squamous cells. We hypothesized that this observed intensity difference for urothelial cells is caused by an increase in cell thickness of the cells and larger nuclear size. Normalization (cf. Figure 5.7A) removes the dependence of the spectral amplitude on the cell thickness. Comparison of the spectral traces in Figure 5.7A,B reveals extraordinary reproducibility of the spectra of the squamous cells (except for the glycogen features), and very different spectral signatures for the urothelial cells that have very different physiological functions and chemical composition. This difference is most pronounced in the protein amide I and amide II spectral regions (1750 – 1500 cm^{-1}), highlighting a significant change in the protein composition of these cell types.

Figure 5.7C presents results obtained from PCA of the entire spectral data set that comprised both squamous and urothelial epithelial cells. As can be seen

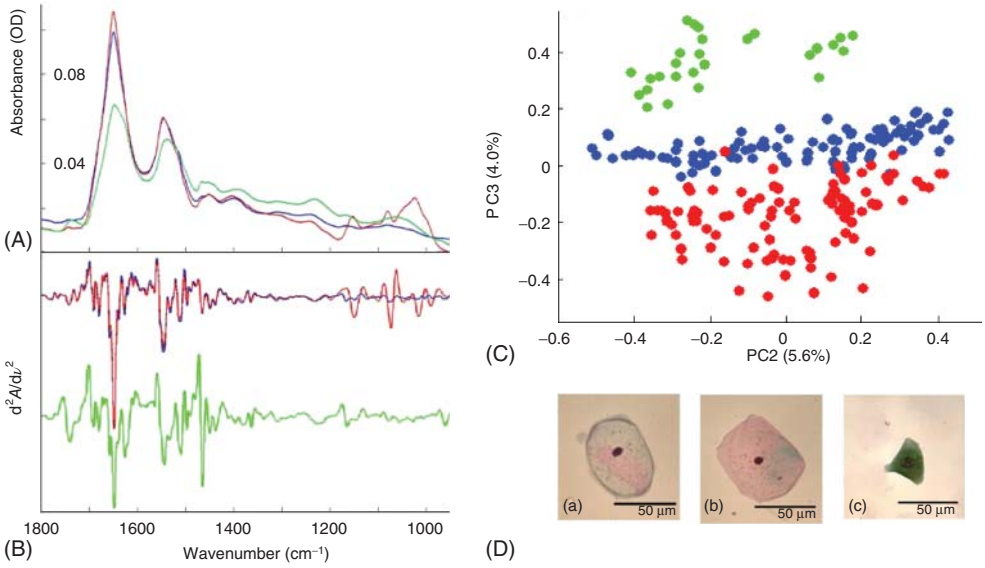

Figure 5.7 (A) Vector-normalized absorbance spectra of glycogen-rich (red) and glycogen-free (blue) squamous cells and urothelial (green) cells. (B) Corresponding second derivative traces. Notice the similarity of the red and blue traces, except in the glycogen spectra region. (C) PCA scores plot of cells collected from urine. Same color scheme as in (A) and (B). (D) Photomicrographs of (a) glycogen-rich and (b) glycogen-free squamous cells and (c) urothelial cells.

in the diagram, the main types of normal epithelial cells identified in the urine sediments divide into three clusters. The green cluster, representative of urothelial cells, displays a distinct separation from the squamous cells and indicates a substantial spectral difference among these cells. Furthermore, the glycogen-rich (red) and glycogen-free (blue) squamous cells are also clearly differentiated. A more detailed discussion of these results can be found in the original literature [20]. This study still applied the "point-and-shoot" data acquisition strategy. Since unstained urothelial cells were extremely difficult to detect, many of these may have been missed during data acquisition, thus requiring the change in data acquisition toward the PapMap strategy. With the low number of urothelial cells in the database, it proved impossible to detect any significant spectral changes because of the presence of bladder cancer.

5.3.3.2 SCP of Oral Mucosa Cells

Cells of the oral mucosa presented an easy target for establishing SCP as a diagnostic test for disease due to the easy availability of these cells. In addition, the medical collaborator (N.L.) at TMC in Boston has experienced a steady flow of patients from far-eastern origin in which oral cancer is quite prevalent. In fact, TMC offers these population groups free screening for oral cancer once a year.

Like many cancers of the squamous mucosa, oral cancers are rather asymptomatic and, although slow growing, present a serious diagnostic problem since they are often not detected until they have reached advanced stages. Widespread cytological screening (similar to that of the cervical Pap test, see Sections 5.3.1 and 5.3.3.3) is not being carried out at this time, presumably due to the low accuracy of classical cytology and the lack of cytologists to carry the extra work load. However, such screening could improve disease detection and prognosis in high-risk populations, such as heavy smokers or tobacco-chewing groups. Furthermore, the prevalence of viral diseases in the oral cavity (*human papillomavirus* (*HPV*), *Herpes simplex*, Epstein–Barr) has increased the prevalence of oral cancers and precancers and has added new impetus for the development of methods to detect this disease early.

For the initial studies of oral mucosa cells, normal cytological samples were harvested from laboratory volunteers, whereas clinical samples were collected at TMC, as described in Section 5.2.1.1, and immediately inserted into a vial filled with SurePath fixative. Data acquisition was carried out via the PapMap approach as discussed in Section 5.2.3.2; thus, for the first time, thousands of cellular spectra were available for statistical analysis. This large number of cells allowed several ancillary studies, for example, the immediate effects of smoking and over-the-counter medication on the spectra of oral cells, as well as the dependence of spectral characteristics on the site of cell collection. It was found that cells from the top of the tongue, the mouth floor, and the inside of the cheeks had slightly different spectral characteristics, which could be attributed to some different expression of proteins in these cells. Cells from the tongue, for example, had slightly different

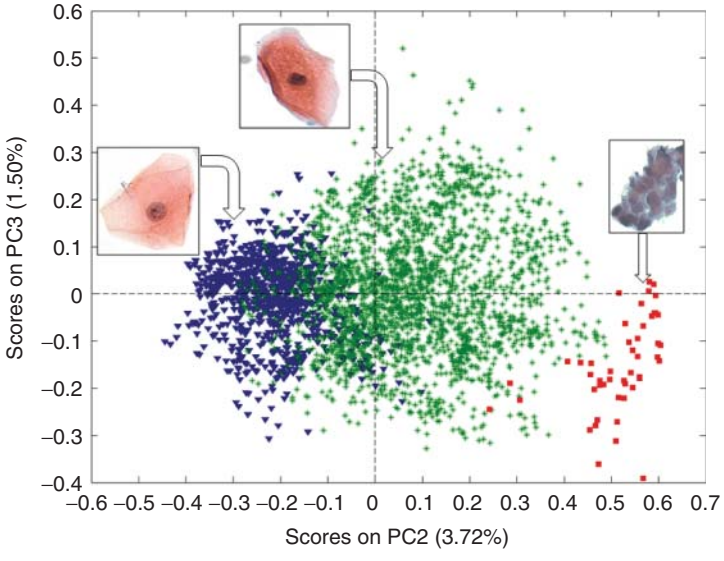

Figure 5.8 PCA scores plot of spectra from oral mucosa cells. Blue triangles: cells from normal volunteers; green crosses: morphologically normal cells from patients with oral disease; and red squares: cells harvested from a cancerous lesion.

spectral traces in the protein region because of higher abundance of keratin [44, 48].

In Figure 5.8, first results of a comparison between stages of oral disease of cells from the tongue are presented. Since the spectral characteristics of cells are slightly different for different sites of the oral cavity, a comparison of the stages of disease was made only for cells from similar collection sites. Figure 5.8 shows a PCA scores plot of squamous cells from six normal volunteers (blue triangles), squamous cells with normal morphology from patients with oral disease (green crosses), and frank cancer cells from one patient diagnosed with oral cancer (red squares). Photomicrographs of typical cell morphology are included in Figure 5.8. It is not surprising that the spectra of normal and cancerous cells are quite different; however, the difference in spectral characteristics between normal squamous cells from presumed healthy volunteers and those of squamous cells with normal morphology from patients with disease was somewhat surprising, but followed a finding that had been reported before for cervical cells [49]. The results in this earlier work implied that morphologically normal cells from abnormal samples exhibit abnormal spectra that represented a progression from normal to cancerous cells. However, the sample set reported then was too small to reach any detailed conclusions.

Figure 5.9 shows mean second derivative spectra from the normal (blue), morphologically normal cells from areas adjacent to the cancerous lesion (green), and cancerous (red) cells. There is a progression of spectral features that indicates increasing contributions from a spectral signature that is associated

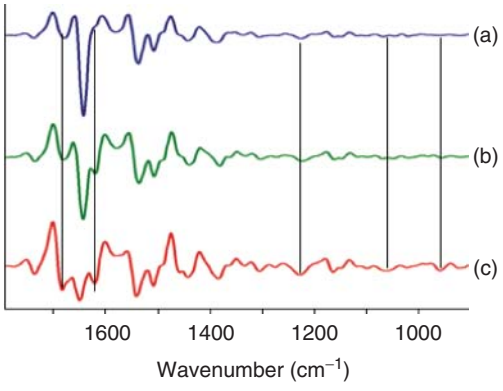

Figure 5.9 Mean second derivative spectra from (a) normal, (b) morphologically normal cells from abnormal samples, and (c) cancerous cells from the tongue.

with malignancy (see vertical lines in Figure 5.9). Some of these signals are associated with DNA, while the low-frequency shoulder on the amide I band at about 1645 cm^{-1} coincides with the band observed for HeLa cells (see Figure 5.6). This study also included, for the first time, the spectral changes induced by a common viral infection (*H. simplex* virus). A terminally infected cell showed a spectral signature completely different than that of a normal cell [44].

Encouraged by these results and the availability of a small NIH grant to study the detection of epithelial cancers, a preclinical trial was initiated at NEU to screen the oral mucosa for possible viral infection and to link spectral changes with patient data. Oral mucosa cells from 93 campus volunteers were collected from three different sites in the oral cavity: the cheeks, the mouth floor under the tongue, and the upper surface of the tongue, resulting in about 280 cytological samples (cf. Table 5.1). These samples were augmented by 29 clinical samples from TMC for which the collection site and the medical diagnoses were known. Altogether, these samples comprise a data set of about a quarter million cellular spectra that was referred to as the *preclinical trial*, and is, at present, the largest spectroscopic cytology effort. In order to facilitate accurate and rapid data acquisition and handling, a barcode system was introduced that identified the completed volunteer data sheets (see later) as well all slides produced for all

Table 5.1 Partial statistics of participants in oral screening preclinical trial.

Gender	Race	Smoker	Age
46 F	4 African Americans	74 nonsmokers	Mean: 29.6
4 NA	12 Asian	4 NA	Maximum: 72
43 M	5 NA	15 smokers	Minimum: 19
	11 others		
	61 Caucasian		

participants and the different collection sites. As pointed out in the previous discussion, the spectra collected for oral mucosa cells depend on a number of conditions, including the anatomical region of data collection, oral dysplasia or neoplasia, tobacco, alcohol, over-the-counter and prescription medication, and the presence of viral infections by *H. simplex* or *HPV*. All this information ("patient metadata") including age, gender, and ethnicity was collected via a questionnaire filled out by the volunteer just prior to sample collection. The study was carried out under an IRB at NEU and conformed to all regulations pertaining to patient privacy.

The earlier results on the differences between cells from the cheeks, the mouth floor, and the tongue were further validated with an increase in the number of normal volunteers in this study. Of the 93 volunteers in the data set, 19 samples were deemed "normal" for cheek, 20 for mouth floor, and 17 for tongue, with the different numbers because of the cellularity of samples and the concomitant ability to prepare a sample from the contents of the swab. "Normal" samples, in this context, were defined as samples collected from volunteers who indicated no use of tobacco or medications, no recent or active cold sores, no history of mononucleosis or abnormal oral infections, and no HPV vaccination. The entire data set from these volunteers comprise 13 651 cell spectra. Based on the number of cells in the smallest data set, 3500 spectra were selected randomly from each data set for the PCA analysis.

Figure 5.10 illustrates PCA results for the distinction of the three anatomical regions. In this figure, blue represents spectra of cells from the cheek, red from the mouth floor, and green from the tongue. In comparison to previous results, the separation between the three classes was not quite as crisp, although the mean cluster spectra reported here are virtually identical to those of the prior study, albeit with a slightly better S/N ratio because of the increased number of spectra. The increased overlap of the different classes may be due to the fact that new and unexpected variances were introduced in the present study. However, the dependence of spectral characteristics on anatomical regions should only be taken as a baseline step for the clinical studies to be discussed next and are aimed at reducing variance because of the region of sample collection for these more important studies.

The main motivation of this preclinical trial was to develop a prescreening tool for oral disease. To this end, clinical samples, that is, samples with diagnosed oral disease, were compared with normal samples for which patient information (metadata) was available. As mentioned before, the cellular samples prepared from the clinical specimens contained mostly cells with normal morphology, and the SCP-based distinction between normal and clinical samples was based on small changes occurring in the abnormal cells before they were manifested as morphological changes.

The results of these analyses are shown in Figure 5.11. Figure 5.11a is based on the analysis of cheek cells for which 3 clinical samples and 20 normal samples were available. Figure 5.11b shows results for the mouth floor (4 clinical and 19 normal samples) and Figure 5.11c shows results of the analysis of tongue cells (22 clinical

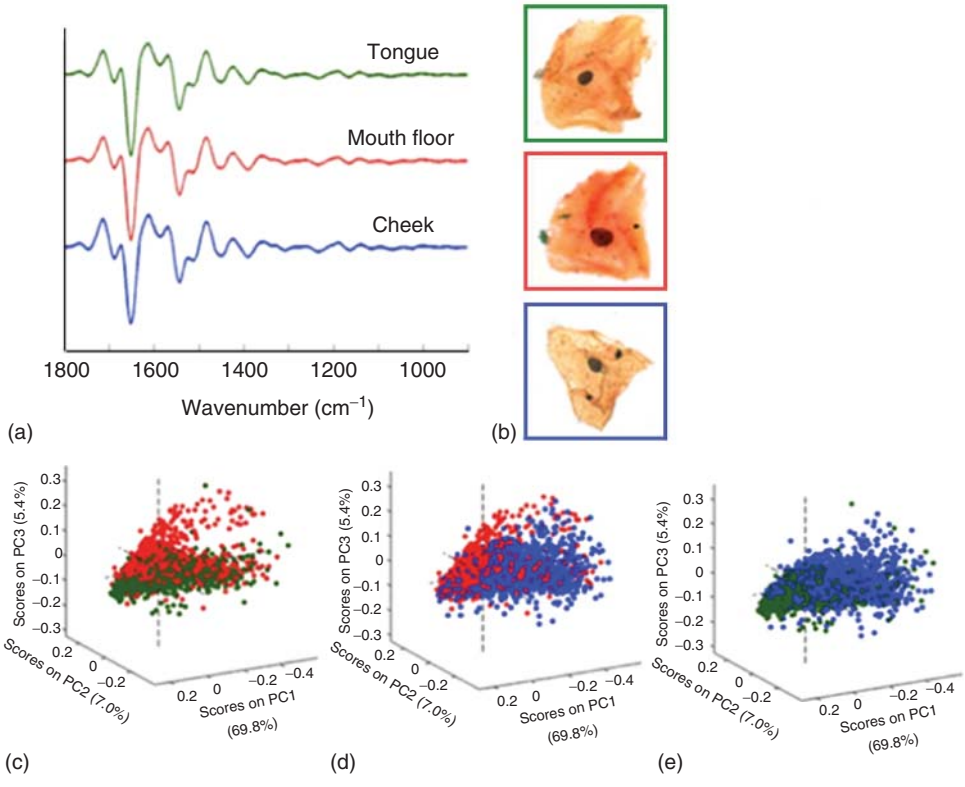

Figure 5.10 (a) Mean second derivative infrared spectra for different anatomical regions of the oral cavity. (b) Visual images of squamous cells from different regions. (c–e) Scores plot of two of the three cell types shown (c) mouth floor versus tongue, (d) cheek versus mouth floor, and (e) tongue versus cheek.

samples, 17 normal samples). In order not to bias the data analysis, each of the PCA input data sets was equalized in size: for the analysis of mouth floor cells, 507 spectra from each of the two classes were utilized, for cheek cells 639 spectra, and for tongue cells 3909 spectra from each class were utilized. The spectra were randomly selected from the entire data set of each class.

Each of the scores plots in Figure 5.11 reproduced results from previous reports [44, 49, 50] where biochemical changes are observed from the majority of morphological normal-looking cells from clinical samples. These results indicate the ability of SCP to monitor changes induced by disease from a much larger number of "diagnostic" cells than that are available for classical cytopathology. In all three panels, the main differentiation between normal and clinical cells occurs along PC1; thus, Figure 5.11d displays the three PC1 traces for the tongue, cheek, and mouth floor disease cases. PC1 is an indicative of the largest change between the normal and abnormal cells, and accounts for 65–80% of the variance between the classes. However, the amplitude of PC1, which may be considered the major

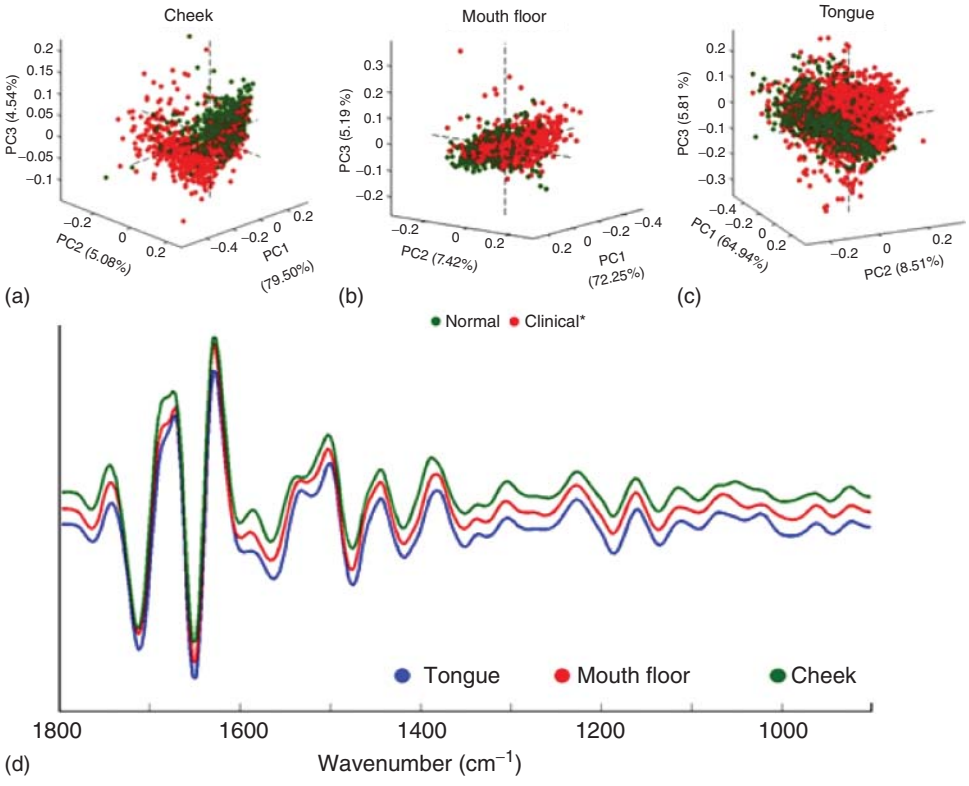

Figure 5.11 Scores plot for distinction of clinical versus normal cell samples from (a) the cheek, (b) the mouth floor, and (c) the tongue. (d) Plot of PC1 along which normal and clinical cells are distinguished for the three distinct anatomical regions of the oral cavity. The traces are offset for clarity.

difference between the mean second derivative spectra [48], only amounts to about 0.2% of the total spectral amplitude.

The spectral traces in Figure 5.11d are difficult to interpret since they indicate the major changes in the second derivative spectra of the different classes. However, the similarity of the 3 first principal components is interesting because it indicates that there is a common disease-induced change occurring among the three cell types, which is not surprising since the cells are most likely subject to the same chemical changes upon the onset of disease. The chemical changes expressed by PC1 could be due to an immune response, different protein expression due to a viral infection [51], or any of a number of other causes. The largest differences occur within the amide I and amide II bands, indicating that protein changes seem to be dominant, although there are significant changes between the normal and diseased cells, in all three sites and in the $1100-1200\,cm^{-1}$ region. Figure 5.11 gives a good indication that there exist consistent and interpretable changes between the spectra of normal and clinical

samples. Such a change, therefore, can be used as a diagnostic indicator for oral disease.

Such a diagnosis is obtained best using supervised or trained algorithms. A number of such predictive algorithms exist, some very similar to that of the principles of PCA (i.e. soft independent modeling of class analogy, SIMCA), linear discriminant analysis (LDA) to more complicated classifiers such as support vector machines (SVMs), which are based on separating spectral classes by complicated, multidimensional separation planes [30]. At the LSpD, ANNs have been used [52–54] for supervised prediction of class memberships.

Thus, an ANN was created with data from tongue cancer since this data set offered the largest patient number. The aim of this ANN was to determine whether or not the small biochemical changes induced by disease allowed a supervised algorithm to distinguish these classes of spectra. Such algorithms will ultimately be used as a screening diagnostic tool in the future. Table 5.2 shows the results for the ANN trained with 600 spectra (300 randomly selected spectra from normal and 300 spectra from clinical samples) and tested on 800 spectra from tongue cells (400 from normal cells and 400 from clinically abnormal samples). The results from this trained algorithm summarized in Table 5.2 are, obviously, excellent and offer a glimpse into the sensitivity and specificity that can be achieved with the spectral methods. The overall accuracy is comparable to the results obtained in spectral histopathology (SHP) for the distinction of certain lung cancers [54]. In particular, we wish to emphasize that these results were obtained from cells that were morphologically normal, that is, from cells that make up the vast majority in exfoliated cell samples. In the past, Schubert [35] has shown that the few diagnostic cells with abnormal morphology show spectral signatures indistinguishable from the majority of (morphologically normal looking) cells of an abnormal sample. The observations reported here reemphasize the fact that biochemical compositional changes occur before morphological changes, thus offering the possibility of developing spectral screening methods of high

Table 5.2 Sensitivity, specificity, and accuracy of the ANN trained to distinguish normal and clinical samples of tongue cancer.

		Classical cytopathology: Positive	Classical cytopathology: Negative
Spectral cytopathology	Positive	384 (48.0%)	23 (2.9%)
	Negative	16 (2.0%)	377 (47.1%)

Sensitivity	Specificity	Accuracy
96.0%	94.3%	95.1%

sensitivity, since the majority of cells in an abnormal sample presents "diagnostic" spectra.

The data set obtained during this preclinical trial was scrutinized for other correlations between spectral characteristics and personal metadata. In particular, any spectral changes due to the use of medication, previous vaccination (Gardasil), and history of disease that may affect the spectra of oral mucosal cells (mononucleosis, *H. simplex* infection, smoking, etc.) were being sought. However, in spite of the fact that this was the largest patient number data set for SCP collected to date, it was found that the number of participants was still too small to data-mine for correlations between spectra and patient metadata. However, one correlation could be achieved, namely the effects of oral contraceptives on oral mucosa cells of the mouth floor. In the past, we [1] and others [55] have reported that cervical squamous cells show spectral differences depending on hormonal levels that cause maturation of the cervical cells. Thus, in order to carry out the early studies on cervical screening, only women using oral contraceptives were included (see Section 5.3.3.3, since their hormonal levels are kept at a constant level. Interestingly, we found small differences in spectral characteristics of the oral mucosa for women using oral contraceptives, as demonstrated by the scores plot in Figure 5.12. It is established [56] that oral mucosa cells express estrogen receptors; thus, it is not unlikely that oral mucosa cells show a response to oral contraceptives similar to that observed for cervical cells, in which the full maturation of cells depends on estrogen levels. This was first demonstrated via SCP for canine cervical cells and later confirmed for human cells as well (see Section 5.3.3.3). However, this result further demonstrates that massive amounts of patient metadata need to be collected and analyzed to establish a new, highly sensitive method such as SCP to ascertain that the desired outcome is not influenced by confounding effects.

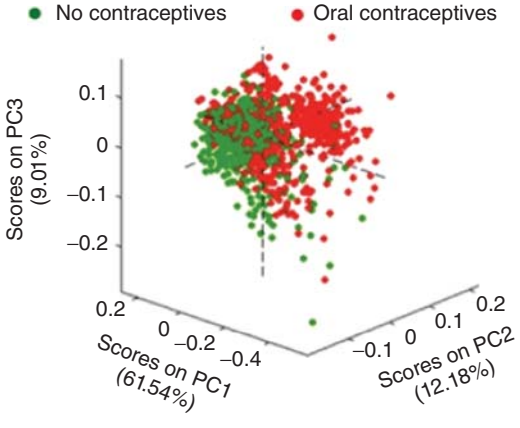

Figure 5.12 PCA scores plot of the effect of oral contraceptives on cellular spectra from the mouth floor.

5.3.3.3 SCP of the Cervical Mucosa

In cervical cytology, which was the original goal of many research efforts in SCP, completely analogous results were observed, namely that the majority of cells from abnormal samples showed spectral abnormality, although they exhibited normal morphology. These results mirror the earlier findings by Cohenford *et al*. [49, 57] but took into account additional confounding factors, as indicated earlier: the cells are subject to hormone-mediated maturation processes that include, for example, the accumulation of glycogen in the final stage of maturation. Since the glycogen absorption bands mask a large part of the low-frequency ($1000-1200\,cm^{-1}$) spectrum, valuable information in the nucleic acid phosphate stretching region (about 1090 and $1235\,cm^{-1}$) is rendered inaccessible. Thus, the studies reported below were from subjects using oral contraceptives that prevent complete maturation of the squamous cervical epithelium and, therewith, reduce the glycogen abundance. The changes in maturation patterns of cervical cells in response to menopause could be demonstrated nicely using SCP [1].

Figure 5.13 shows the results of PCA analysis of cells exfoliated from normal patients and patients diagnosed with LSIL/HSIL [50]. Here, the results of the oral cytology are reproduced in that most of the cells from patients with dysplasia exhibit spectral abnormalities, although the cell morphology is normal (see cell images in Figure 5.13). Even more surprising is the fact that the cells from a patient with a prior diagnosis of HSIL, and subsequent treatment, still exhibit abnormal spectral patterns and cluster with the abnormal spectra.

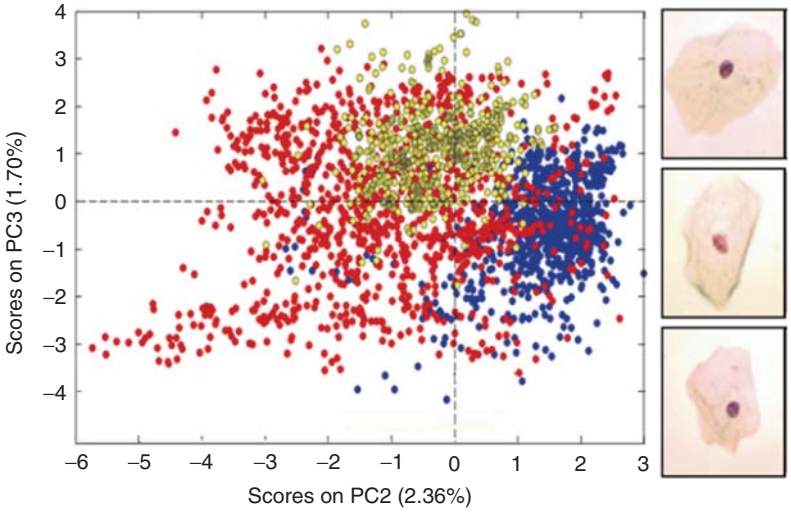

Figure 5.13 PCA scores plot of cervical cells from normal patients (blue), and patients with LSIL/HSIL (red) and a history of HSIL (gold). Images of morphologically normal cells used in this study are shown on the right. (From Ref. [35])

To demonstrate the validity of the assumption that the "abnormal" spectra observed for morphologically normal cells was not an artifact due to hitherto unknown confounding effects, a few morphologically abnormal cells were identified in the samples from patients diagnosed with LSIL. These few cells, immersed in a large excess of cells with normal morphology, are the ones on which an "abnormal" cytology diagnosis is based. The particular location of these abnormal cells in the PCA scores plot was identified and found to be surrounded by morphologically normal cells, but with abnormal spectra. This observation demonstrates beyond doubt that in a sample of LSIL/HSIL, the cells with normal morphology already exhibit the same spectral patterns as the cells that are morphologically abnormal. The implications of this observation are quite far reaching in that detection of abnormality is not restricted to the few cells in a cervical exfoliate that exhibit abnormal morphology. Rather, SCP detects abnormal spectral signatures that are exhibited by most cells, even if they still have normal morphology (Figure 5.14).

The fact that the abnormality persists after treatment led us to explore the possibility that the spectral changes (and, therewith, the "malignancy associated changes" [58] or "field cancerization" [59]) are actually due to viral infection. In part, this thought was provoked by results from a patient with an acute *H. simplex* infection of the oral cavity. In this case, most of the cells showed spectral abnormality, not only those that were so grotesquely deformed by the viral infection that they could be visually diagnosed by a cytologist [44]. Since

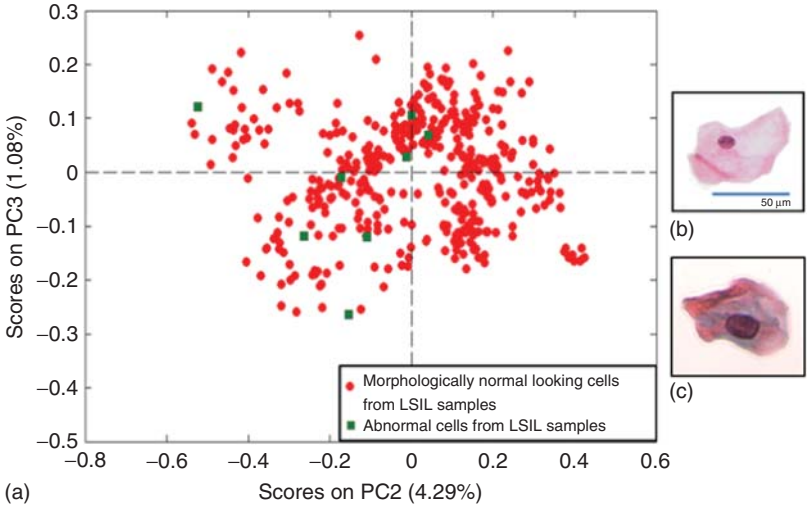

Figure 5.14 (a) PCA scores plot of a few cells with abnormal morphology (green squares) within the PCA cluster of morphologically normal cells (red) from an LSIL sample. (b) Morphologically normal cell in a sample diagnosed with LSIL. (c) Cell with abnormal morphology in a sample diagnosed with LSIL. (From Ref. [35])

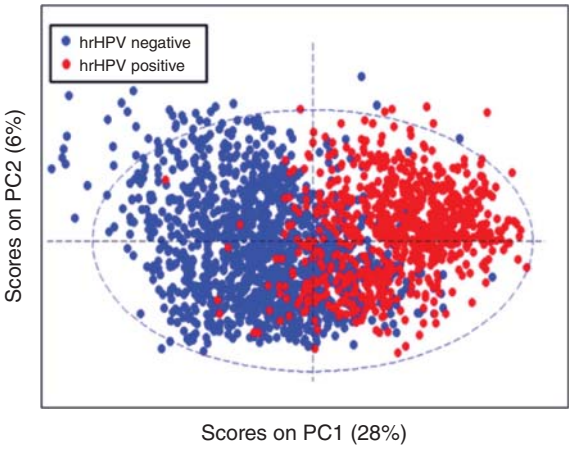

Figure 5.15 PCA scores plot for 10 samples of hrHPV positive and hrHPV negative samples of cervical cells. (From Ref. [35])

statistically over 95% of all cervical dysplasia occur along with (and likely are caused by) infection with the HPV, the possibility exists that SPC detects the infection by HPV in cervical cytology [60]. Similarly, oral dysplasia could be caused by the Epstein–Barr or HPV as well.

In order to explore the sensitivity of SCP toward viral infections, a study was undertaken in which 48 samples were tested for high-risk human papillomavirus infection (hrHPV) via the Digene Hybrid Capture test (Qiagen, Valencia, CA). For a subset of 10 samples, shown in Figure 5.15, the results looked extremely promising, with good spectral separation of HPV-positive and HPV-negative samples. When applied to the entire sample set, good sensitivity of 88% was achieved, yet the specificity was below 50%. This implies that SCP was quite good at detecting the hrHPV strain when it was present (as determined by the Digene test), but not sufficiently accurate to discriminate against the low risk human papillomavirus (lrHPV) infection that is epidemic in the population of women between 20 and 25 years of age, with infection rates of about 30%, or about the same as the infection rate with hrHPV [61]. Thus, it is quite likely that the samples that tested negative for hrHPV by the Digene test had lrHPV infection, which the spectral methods were not able to differentiate.

5.3.3.4 SCP of Esophageal Cells

The diagnosis of esophageal disease by spectral methods has a long history. In fact, very early studies by Puppels and coworkers [62] and later by Stone and coworkers [63–65] have demonstrated that *in vivo* and *ex vivo* Raman spectroscopy may present a valuable alternative to the presently available diagnostic methods, to be discussed later.

Diagnosis of esophageal disease is of utmost importance, since adenocarcinoma of the esophagus is a nearly incurable disease. Early stages include

a benign (metaplastic) precursor known as *Barrett's esophagus*, in which the transformation zone between the mostly squamous cells of the esophagus and the columnar cells of the lining of the stomach moves up into the esophagus. Dysplasia may develop in the columnar cells, leading to the possibility of a transition to adenocarcinoma of the esophagus. The early stages of disease, in particular of Barrett's esophagus, are associated with chronic inflammation caused by prolong acid reflux conditions. Presently, early stages of disease are diagnosed by endoscopic examination of the lower esophagus. White light endoscopy can sometimes detect the presence of metaplasia, but this method is quite unreliable. Fluorescence endoscopy, particularly using extraneous labels, offers somewhat better discrimination, but the most reliable classical method has been the collection of dozens of punch biopsies, at different depth in the transformation zone and at typically eight angular positions at every depth. The number of biopsies to be analyzed microscopically by a pathologist represents an enormous workload; furthermore, the positive diagnosis of Barrett's esophagus requires the finding of colonic goblet cells that may occur in very low numbers in a biopsy.

Raman endoscopy has offered a new approach to the diagnosis of Barrett's esophagus, since it can detect the differences between normal squamous and columnar epithelium, as well as dysplasia and cancer. However, even endoscopic Raman measurements are still carried out in a point-by-point measurement mode, and the changes of missing a malignant or premalignant lesion during Raman endoscopy persists. Thus, a cytology-based approach is reported here based on the SCP methodology described earlier, and using cell exfoliation techniques by an endoscopic brush. The rationale for this approach is as follows. Raman endoscopy offers a point-by-point instantaneous diagnosis of the disease stage, whereas a cytology approach represents an integrating sampling technique since large portions of the esophageal surface can be sampled in one brushing.

Similar to that of the problems encountered with the cells from the urethra and the bladder, the columnar and squamous cells from the esophagus are quite variable in size. The squamous cells typically occupy an area as large as 4000 μm^2 (about 60 μm on edge), whereas typical columnar cells may occupy an area as small as 400 μm^2 (about 20 μm on edge). This is shown in Figure 5.16. It would have been nearly impossible to visually detect the small, unstained cells if data were to be collected using the "point-and-shoot" SCP approach discussed earlier; however, the PapMap method allowed many of the small cells to be captured and analyzed. To this end, the area defining a "raw cell" (see Section 5.2.3.2) was widened to between 10 and 100 pixels, corresponding to areas of 400 – 4000 μm^2. After staining, the small "raw cell areas" could be associated with individual columnar cells, as shown in Figure 5.16. Subsequent classical cytology identified some of them to be, indeed, dysplastic.

At present, there are about 4800 esophageal cell spectra in the data set. Obviously, this data set is still much smaller than the data sets reported earlier

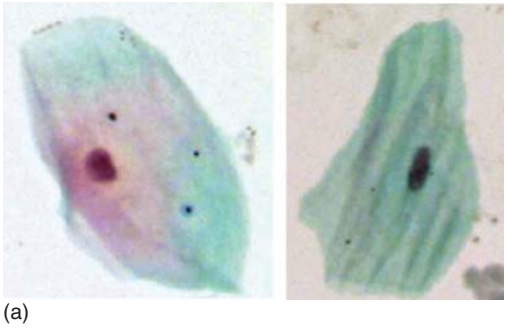

(a)

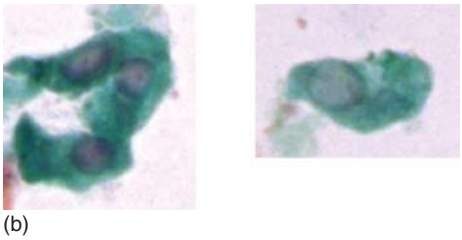

(b)

Figure 5.16 (a) Squamous cells from the esophagus; (b) glandular cells from the esophagus (Pap stain).

for cervical and oral cells. However, the results follow similar patterns described earlier.

Of the 4800 cells, about 2340 cells are from 10 normal patients, about 1720 cell spectra are from 8 patients diagnosed with Barrett's disease, and about 750 cell spectra are from two patients with Barrett's disease/possible dysplasia, for an average of about 240 cells per patient. Mean second derivative spectra for the three groups (normal, Barrett's and Barrett's/possible dysplasia) are shown in Figure 5.17. The small spectral differences observed between the three traces are most likely significant, since they are based on a large number of individual cell spectra.

As expected, SCP can distinguish squamous from columnar cells of the esophagus quite readily. This is shown by the scores plot (Figure 5.17b), in which the green cell spectra are reasonably well separated from the blue and red clusters. This separation may be partially due to the fact that in normal patients a much higher percentage of squamous cells are harvested, and that the distinction of cell types is mostly due to the size difference between squamous and columnar cells. Cell size-based distinction of cells has been reported before [36], and it was argued that different nucleus-to-cytoplasm ratios of large and small cells most likely are responsible for the spectral discrimination. In the situation of the urinary tract cells discussed earlier, an enormous difference in biochemical composition between the squamous and the urothelial cells was observed; clearly, this is not the case here, as demonstrated by the similarity of the mean second derivative spectra (Figure 5.17a) of the three cell types.

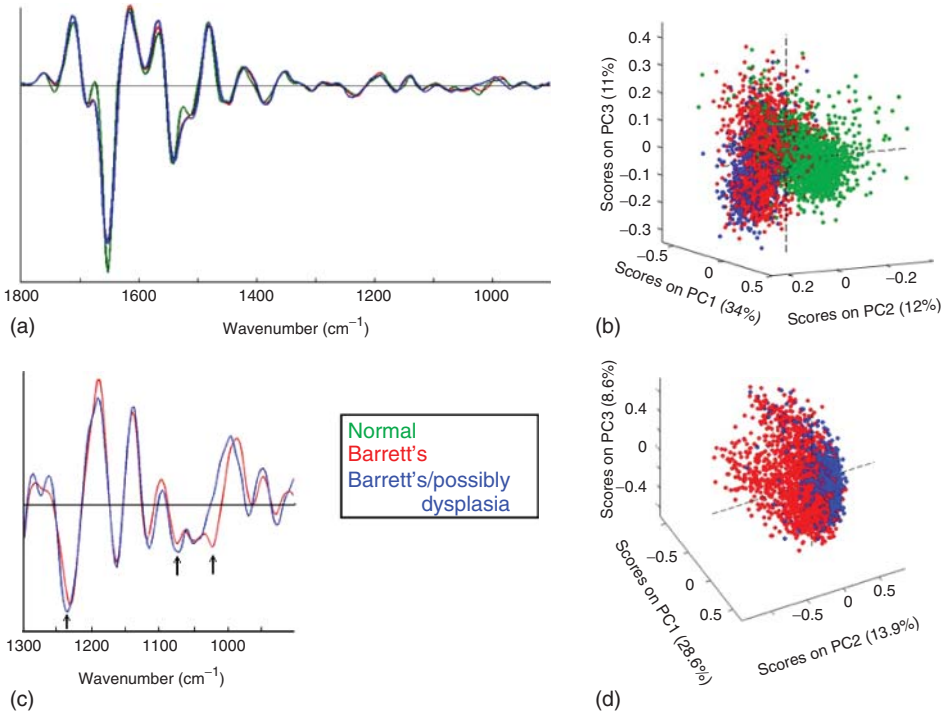

Figure 5.17 SCP results for cells exfoliated from the esophagus. (a) Second derivative spectra of normal cells from the esophagus (green), cells from patient diagnosed with Barrett's disease (red) and Barrett's patients with possible dysplasia (blue). (b) PCA scores plot of the same three cell types as (a). (c) Expanded second derivatives of Barrett's cells and Barrett's cells with possible dysplasia. (d) Scores plot of the two cell types in (c).

However, a close inspection of these mean spectra also reveals several small spectral changes between the Barrett's and the Barrett's/dysplasia cell spectra. To emphasize these differences, the low-frequency spectral region is shown in Figure 5.17c for just these two cell types. The blue spectrum in Figure 5.17c shows slightly enhanced nucleic acid (DNA) features at about 1235 and 1090 cm^{-1} (see arrows); furthermore, a band at about 1020 cm^{-1} is missing in the blue spectrum. This latter band is generally assigned to C–O stretching and C–O–H deformation coordinates in carbohydrates, either in glycogen or in glycoproteins. The absence of carbohydrate spectral features in dysplastic cells was documented earlier in cervical cells [66]; alternatively, the spectral changes in this region could be due to reduced mucus secretion of the dysplastic cells.

Figure 5.17d demonstrates that PCA can achieve some separation of these spectra, and an ANN trained to diagnose and differentiate these cell types achieved good accuracy. However, it is clear that more dysplastic cells are needed to confirm the spectral findings: of the samples labeled "Barrett's/possibly dysplasia," only two

cells were found cytologically to be attributed to dysplasia. Here, the promise of SCP discussed earlier, namely the ability to diagnose disease before morphological changes occur, would add a new dimension to the distinction of early stages of esophageal disease.

5.3.4 SCP of Live Cells in Aqueous Environment

From a viewpoint of pharmacological and drug interaction studies, SCP of live cells in an aqueous environment would be highly desirable. This goal is difficult to achieve since cells can only be kept alive in an aqueous environment, which poses a very serious problem for IR data acquisition. This is due to the fact that water possesses one of the largest IR transition dipole moments, producing very strong water absorption features which, in turn, make the observation of IR spectra in aqueous medium extremely difficult. Furthermore, extensive hydrogen bonding in liquid water results in broadbands in the IR spectrum, masking wide spectral regions. However, a number of publications from the authors' laboratory [67, 68] established that IR transmission and transflection measurements can be carried out microscopically in aqueous media, and that cells can be kept alive for at least 24 h, but likely much longer, in suitable cell chambers.

To this end, a flow-through cell chamber was designed and constructed that utilized a CaF_2 window into which about 10 µm deep trough had been ion-etched, and a CaF_2 top window with two small holes for the flow of cell culture medium [69]. Human cells were cultured directly onto the etched window; after a suitable culture time, the chamber was assembled and mounted in a thermostated aluminum block. Cell culture medium was gravity fed from an IV-bag through the cell chamber. This flow system allowed the medium to be changed dynamically; for example, the cell culture medium could be substituted with pure buffer, starving the cells. Alternatively, a drug could be added to the medium flow to follow the drug-induced spectral changes in the cells. Software was developed to correct absorbed spectra for small, but unavoidable liquid water, contributions to the cell spectra. These contaminations occur because a spectrum measured through a cell contains less of a water contribution than the background spectrum collected through pure water (or medium); thus, the spectra of cells were overcompensated for by the water background and needed a correction step. As before, second derivative spectra were used for data analysis that improved the situation enormously.

Although the high water background absorption degraded the S/N ratio of the measurement, the use of the PapMap method, including NA-PCA (see Sections 5.2.3.2 and 5.2.4.1, respectively), allowed for the collection of excellent spectra of live cells and the effects of chemicals perturbing these cells. Furthermore, we could demonstrate that cells could be kept alive for at least 24 h, and that starvation of the cells by changing the medium to a buffer solution caused cell death in a relatively short time [68, 69].

In the course of these studies, a peculiar advantage of collecting cellular spectra in an aqueous environment was found. In the literature, most often only the disadvantages arising from water interferences are discussed, which include the need for short path lengths, the problem of maintaining constant path lengths between sample and background measurement, and the difficulties of compensating for the water contribution between sample and background spots. However, all these difficulties are accompanied by an enormous advantage of working in an aqueous environment: the absence of dispersive band shape contributions, resulting from "resonance Mie" scattering [13] and other effects that depend strongly on gradients of the reflective index, which are often observed in the IR spectra of cells and tissues. A significant advantage to live cell work in aqueous media is the absence of these effects. This can be attributed to the fact that the difference in refractive index between an individual hydrated cell and water is so small that scattering effects were not detected in the data presented here.

In two recent publications, we showed that cells cultured directly into the CaF_2 live cell chamber did not exhibit any spectral nor morphological changes when kept in an environment suitable for cell survival, namely 37 °C and fresh cell culture medium. When the flow of cell culture medium was stopped and the medium was replaced with pure buffer solution, morphological and spectral changes were observed [69]. Thus, we concluded that the cells in the presence of cell culture medium were alive, although cell division was never observed. This may have been due to the fact that the thin space in which the cells were confined did not permit the morphological changes that precede mitosis.

Furthermore, we demonstrated that SCP is capable of differentiating live HeLa cells exposed to chemotherapeutical agents from untreated cells. Figure 5.18 shows the scores plot of live cells treated with an anticancer drug, cyclophosphamide monohydrate, and an untreated control group of cells. Cyclophosphamide monohydrate is an alkylating agent that acts on DNA at the seventh position of nitrogen in guanine bases [70–72] and interrupts cell function by causing inter- and intrastrand cross-links as well as other DNA

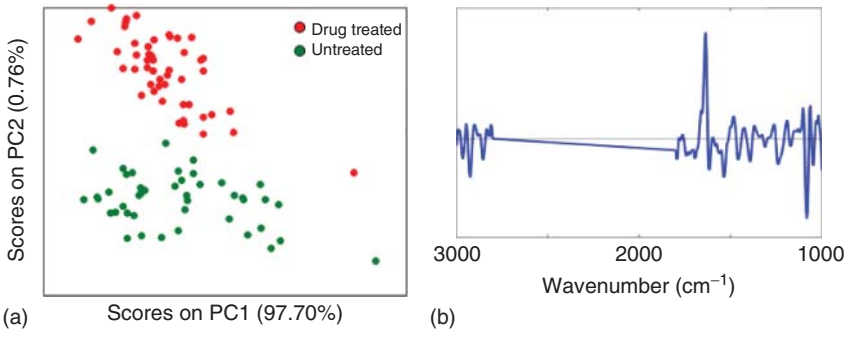

Figure 5.18 (a) Scores plot of untreated cells, and cells treated with cyclophosphamide monohydrate. (b) Loading vector PC2 along which the PCA data are split. (from Ref. [68]).

mutations [70–74]. It is a common chemotherapeutic in the treatment of various cancers [73, 74].

The cell spectra were collected via the PapMap image approach coupled to NA-PCA image reconstruction as described earlier. To assure that the changes detected were a result of the drug acting on the cells and not a result of the detection of the drug in the surrounding culture medium, cells were only exposed to the drug during the incubation period. In the live cell sample chamber, cells were subjected to flow of normal culture medium. Thus, the observed changes reported here reflect overall changes occurring within the cells, not the drug itself.

Figure 5.18 demonstrates crisp separation along PC2 of the drug treated and the untreated cells. A plot of PC2 demonstrates that most of the spectral variation between the untreated and drug exposed cells occurs in the protein and low wavenumber regions. Specifically, there is a monosignate positive band in the loading vector at about 1635 cm^{-1}; a monosignate band generally indicates the occurrence of a new spectral feature (band shifts in the PC vectors are indicated by bisignate bands). The band position coincides with amide I signatures observed previously because of necrosis and apoptosis [75] and could be an early indication of cell death upon drug treatment. The low-frequency negative bands in the loading vector at 1090 and 1240 cm^{-1} are typically associated with the PO_2^- symmetric and antisymmetric stretching vibrations of DNA/RNA. Such changes could be directly due to drug-induced modifications of the DNA structure or spectral changes in DNA/RNA features due to cell death.

5.4 Future Potential of SCP/Conclusions

Aside from the fixation studies, which were carried out for both exfoliated and cultured cells, the majority of the work presented in the sections above has dealt with exfoliated cells; that is, it reported a truly new form of cytology, namely SCP. To the best of our knowledge, work on exfoliated cells at the cell-by-cell level is now being carried out exclusively at the LSpD, and the size of the data sets at the LSpD far exceeds all previously collected data sets combined [35, 44]. At the time of writing this summary, it appears that the SCP has matured to a level that allows for detection of cellular abnormalities, such as dysplasia, cancer, and viral infection in exfoliated cells and, thus, is poised to be applied to areas where classical cytology has very poor performance, in many cases below 50% accuracy.

The reason that the progress in SCP has been somewhat slower than that in other areas of spectral diagnostics is the fact that the correlation between classical cytopathology and SCP is difficult. In SCP, one has to rely on luck that within an ensemble of cells scrutinized by SCP there is a diagnosable, abnormal cell. After a few thousands of cells from dysplastic patients, however, it will become very likely that some cells are found that display abnormal spectra and can, indeed, be

diagnosed. Such a case is shown in Figure 5.14 where the spectrum of a clearly dysplastic cell clusters with spectra of spectra from morphologically normal cells from abnormal samples [35].

For cultured cells, the efforts and research directions are more diversified and represent a number of other research groups as well as the LSpD. These efforts have demonstrated that IR microspectroscopy can detect the stages of a cells division cycle [53], the effect of drug treatment on cells [69, 76, 77], the degree of aggressiveness [78], μRNA expression [79], cancer activation of fibroblasts [80], and a few others. In general, the results of these studies demonstrate that carefully carried out FT-IR studies can reveal an extraordinary amount of information on the complex biochemical changes that occur when cells undergo natural or induced processes. A few general rules seem to apply for carefully planned and executed studies. The raw spectra, whether monitoring drug treatment or any other of the changes listed earlier, exhibit no or barely visible spectral changes, and multivariate methods of analysis need to be employed to visualize spectral variations. A typical example is the study by the Brussels group [76], which demonstrated elegantly that the spectra of untreated cells, and those treated with drugs are virtually identical to the naked eye, but that statistical (or, in this case, 2D) analysis of these data sets reveals changes that can be interpreted biochemically. Some of the spectral changes, for example, due to drug interactions are smaller than the changes due to cancerous disease; thus, the authors believe that the spectroscopy of cells can reveal much more subtle details. For bacterial cells, for example, IR spectroscopy, coupled to the analysis by neural networks, could predict the mode of action of newly discovered drugs [81].

In this review, aspects of IR spectroscopy for medical diagnostics have been presented. There are major differences between this new field and classical spectroscopy of biomolecules due to the size and complexity of the systems, but it is important to point out that this work is based on, and relies on, decades of research in biospectroscopy. Yet there are two major differences between "classical" biospectroscopy and the medical applications: first, there is a heavy reliance on mathematical methods for data analysis, since multivariate methods of analysis are highly suitable for extracting small, correlated spectral differences that are often smaller than and are buried in uncorrelated spectral variations. Second, and even more important, is the fact that for medical applications, conclusions can never be based on single measurements, since the variability of the sample is enormous, both on a patient-to-patient and on a cell-to-cell level. Thus, the authors hope that this research not only advances the field of medical diagnostics by spectral methods but also helps to usher in new ways to look and process spectral data.

Acknowledgment

Partial support of this research by grants CA 090346 and CA 153148 from the National Institutes of Health during the past 5 years is gratefully acknowledged.

References

1. Diem, M. *et al.* (2009) in *Infrared and Raman Spectroscopic Imaging* (eds R. Salzer and H.W. Siesler), Wiley-VCH Verlag GmbH, Weinheim, pp. 173–202.
2. Matthäus, C. *et al.* (2007) Label-free detection of mitochondrial distribution in cells by nonresonant Raman micro-spectroscopy. *Biophys. J.*, **93**, 668–673.
3. Matthäus, C. *et al.* (2008) New ways of imaging uptake and intracellular fate of liposomal drug carrier systems inside individual cells, based on Raman microscopy. *Mol. Pharm.*, **5** (2), 287–293.
4. Chernenko, T. *et al.* (2009) Label-free imaging of intracellular delivery and degradation patterns of polymeric nanoparticle systems. *ACS Nano*, **3**, 3552–3558.
5. Matthäus, C. *et al.* (2011) in *Confocal Raman Imaging* (eds O. Hollricher and T. Dieing), Springer-Verlag, Heidelberg, pp. 137–162.
6. Zuser, E. *et al.* (2010) Confocal Raman Microspectral Imaging (CRMI) of murine stem cell colonies. *Analyst*, **136**, 3030–3033.
7. Cherchi, C. *et al.* (2011) Impact of nano titanium dioxide exposure on cellular structure of anabaena varabilis and evidence of internalization. *Environ. Toxicol. Chem.*, **30** (4), 861–869.
8. Chernenko, T. *et al.* (2012) Raman microscopy for noninvasive imaging of pharmaceutical nanocarriers: intercellular distribution of cationic liposomes of different composition. *Mol. Pharm.*, **9**, 930–936.
9. Miljković, M., Bird, B., and Diem, M. (2012) Dispersive line shape effects in infrared spectroscopy. *Analyst*, **137**, 3954–3964.
10. Bassan, P. *et al.* (2009) Reflection contributions to the dispersion artefact in FTIR spectra of single biological cells. *Analyst*, **134**, 1171–1175.
11. Davis, B.J., Carney, P.S., and Bhargava, R. (2010) Theory of midinfrared absorption microspectroscopy: I. Homogeneous samples. *Anal. Chem.*, **82**, 3474–3486.
12. Davis, B.J., Carney, P.S., and Bhargava, R. (2010) Theory of mid-infrared absorption microspectroscopy: II. Heterogeneous samples. *Anal. Chem.*, **82**, 3487–3499.
13. Bassan, P. *et al.* (2009) Resonant Mie scattering in infrared spectroscopy of biological materials – understanding the 'dispersion artefact'. *Analyst*, **134**, 1586–1593.
14. Bassan, P. *et al.* (2010) Resonant Mie Scattering (RMieS) correction of infrared spectra from highly scattering biological samples. *Analyst*, **135**, 268–277.
15. Bird, B., Miljković, M., and Diem, M. (2010) Two step resonant Mie scattering correction of infrared micro-spectral data: human lymph node tissue. *J. Biophotonics*, **3** (8-9), 597–608.
16. Miljković, M. *et al.* (2013) Spectral cytopathology: new aspects of data collection, manipulation and confounding effects. *Analyst*, **138**, 3975–3982.
17. Mazur, A.I. *et al.* (2012) Evaluating different fixation protocols for spectral cytopathology, part 1. *Anal. Chem.*, **84**, 1259–1266.
18. Mazur, A.I. *et al.* (2012) Evaluating different fixation protocols for spectral cytopathology, part 2. *Anal. Chem.*, **84**, 8265–8271.
19. Bassan, P. *et al.* (2013) The inherent problem of transflection-mode infrared spectroscopic microscopy and the ramifications for biomedical single point and imaging applications. *Analyst*, **138**, 144–157.
20. Bird, B. *et al.* (2008) Cytology by infrared micro-spectroscopy: automatic distinction of cell types in urinary cytology. *Vib. Spectrosc.*, **48** (1), 101–106.
21. Schubert, J.M. *et al.* (2010) Single point vs. mapping approach for spectral cytopathology (SCP). *Biophotonics*, **3** (8-9), 588–596.
22. Marcsisin, E. *et al.* (2012) Noise adjusted principal component reconstruction to optimize infrared microspectroscopy of individual live cells. *Analyst*, **136**, 2958–2964.
23. Reddy, R.K. and Bhargava, R. (2010) Accurate histopathology from low

signal-to-noise ratio spectroscopic imaging data. *Analyst*, **135**, 2818–2825.
24. Romeo, M.J. and Diem, M. (2005) Correction of dispersive line shape artifact observed in diffuse reflection infrared spectroscopy and absorption/reflection (transflection) infrared micro-spectroscopy. *Vib. Spectrosc.*, **38** (1-2), 129–132.
25. Dazzi, A., Deniset-Besseau, A., and Lasch, P. (2013) Minimising contributions from scattering in infrared spectra by means of an integrating sphere. *Analyst*, **138**, 4191–4201.
26. Bruun, S.W. *et al.* (2006) Correcting attenuated total reflection-Fourier transform infrared spectra for water vapor and carbon dioxide. *Appl. Spectrosc.*, **60** (9), 1029–1039.
27. Savitzky, A. and Golay, M.J.E. (1964) Smoothing and differentiation of data by simplified least-squares procedures. *Anal. Chem.*, **36** (8), 1627–1639.
28. Griffiths, P.R. and De Haseth, J.A. (1986) in *Fourier Transform Infrared Spectrometry*, Chemical Analysis, vol. 83 (eds P.J. Elving and J.D. Winnefordner), John Wiley & Sons, Inc., New York.
29. Bertie, J.E. and Zhang, S. (1992) Infrared intensities of liquids. IX. The Kramers-Kronig transform, and its approximation by the finite Hilbert transform via fast Fourier transforms. *Can. J. Chem.*, **70**, 520–531.
30. Adams, M.J. (2004) in *Chemometrics in Analytical Spectroscopy*, RSC Analytical Spectroscopy Monographs, 2nd edn (ed N.W. Barnett), Royal Society of Chemistry, Cambridge.
31. Papanicolaou, G.N. and Traunt, H.F. (1941) Smear diagnosis of carcinoma of the cervix. *Am. J. Obstet. Gynecol.*, **42** (2), 193–206.
32. Papanicolaou, G.N. (1948) *The Epithelium of Women's Reproductive Organs*, The Commonwealth Fund, New York.
33. van Driel-Kulker, A.M.J. *et al.* (1980) A preparation technique for exfoliated and aspired cells allowing different staining procedures. *Anal. Quant. Cytol.*, **2** (4), 243–246.
34. Diem, M. *et al.* (2012) Applications of infrared and Raman micro-spectroscopy of cells in medical diagnostics: present status and future promises. *Spectrosc. – Biomed. Appl.*, **27** (5-6), 463–496.
35. Schubert, J.M. (2011) Spectral cytology of human oral and cervical samples, in *Chemistry and Chemical Biology*, Northeastern University, Boston, MA.
36. Romeo, M.J. *et al.* (2006) Infrared micro-spectroscopic studies of epithelial cells. *Biochim. Biophys. Acta*, **1758** (7), 915–922.
37. Lasch, P., Pacifico, A., and Diem, M. (2002) Spatially resolved IR microspectroscopy of single cells. *Biopolymers*, **67** (4-5), 335–338.
38. Brauner, J.W., Flach, C.R., and Mendelsohn, R. (2005) A quantitative reconstruction of the amide I contour in the IR spectra of globular proteins: from structure to spectrum. *J. Am. Chem. Soc.*, **127**, 100–109.
39. Diem, M., Griffiths, P.R., and Chalmers, J.M. (2008) in *Vibrational Spectroscopy for Medical Diagnosis* (eds M. Diem, P.R. Griffiths, and J.M. Chalmers), John Wiley & Sons, Ltd, Chichester.
40. Demay, R.M. (2005) *The Pap Test*, American Society for Clinical Pathology Press, Chicago, IL.
41. O'Faolain, E. *et al.* (2005) A study examining the effects of tissue processing on human tissue sections using vibrational spectroscopy. *Vib. Spectrosc.*, **38**, 121–127.
42. Mazur, A.I. (2013) Spectral pathology: automated classification of cytological and histological specimens utilizing infrared micro-spectroscopy, in *Chemistry & Chemical Biology*, Northeastern University, Boston, MA.
43. Pacifico, A. *et al.* (2003) Infrared spectroscopy of cultured cells. II. Spectra of exponentially growing, serum-deprived and confluent cells. *Vib. Spectrosc.*, **32**, 107–115.
44. Papamarkakis, K. *et al.* (2010) Cytopathology by optical methods: spectral cytopathology of the oral mucosa. *Lab. Invest.*, **90**, 589–598.
45. Lasch, P. *et al.* (2002) FT-IR spectroscopic investigations of single cells on the subcellular level. *Vib. Spectrosc.*, **28** (1), 147–157.

46. Papanicolaou, G.N. and Marshal, V.F. (1945) Urine sediment smears: a diagnostic procedure in cancers of urinary tract. *Science*, **101**, 519–520.
47. Brunzel, N.A. (1994) *Fundamentals of Urine and Body Fluid Analysis*, W. B. Saunders, Philidelphia, PA.
48. Diem, M. *et al.* (2009) The infrared spectral signatures of disease: extracting the distinguishing spectral features between normal and diseased states. *Appl. Spectrosc.*, **63** (11), 307A–318A.
49. Cohenford, M. and Rigas, B. (1998) Cytologically normal cells from neoplastic cervical samples display extensive structural abnormalities on IR spectroscopy: implications for tumor biology. *Proc. Natl. Acad. Sci. U.S.A.*, **95**, 15327–15332.
50. Schubert, J.M. *et al.* (2010) Spectral cytopathology of cervical samples: detecting cellular abnormalities in cytologically normal cells. *Lab. Invest.*, **90**, 1068–1077.
51. Diem, M. *et al.* (2012) Detection of viral infection in epithelial cells by infrared spectral cytopathology, in *Handbook of Biophotonics*, Photonics for Health Care, vol. 2 (eds J. Popp *et al.*), Wiley-VCH Verlag GmbH.
52. Lasch, P. *et al.* (2007) Artificial neural networks as supervised techniques for FT-IR microspectroscopic imaging. *J. Chemom.*, **20** (5), 209–220.
53. Boydston-White, S., Romeo, M.J., Chernenko, T., Regina, A., Miljkovic, M., and Diem, M. (2006) Cell-cycle-dependent variations in FTIR microspectra of single proliferating HeLa cells: principal component and artificial neural network analysis. *Biochim. Biophys. Acta*, **1758** (7), 908–914.
54. Bird, B. *et al.* (2012) Infrared Spectral Histopathology (SHP): a novel diagnostic tool for the accurate classification of lung cancers. *Lab. Invest.*, **92**, 1358–1373.
55. Romeo, M.J., Wood, B.R., and McNaughton, D. (2002) Observing the cyclical changes in cervical epithelium using infrared microspectroscopy. *Vib. Spectrosc.*, **28** (1), 167–175.
56. Leimola-Virtanen, R. *et al.* (2000) Expression of estrogen receptors (ER) in oral mucosa and salivary glands. *Maturitas*, **36** (2), 131–137.
57. Cohenford, M. *et al.* (1997) Infrared spectroscopy of normal and abnormal cervical smears: evaluation by principal component analysis. *Gynecol. Oncol.*, **66**, 59–65.
58. Ogden, G.R., Cowpe, J.G., and Green, M.W. (1990) The effect of distant malignancy upon quantitative cytologic assessment of normal oral mucosa. *Cancer*, **65**, 477–480.
59. van Oijen, M.G.C.T. and Slootweg, P.J. (2000) Oral field cancerization: carcinogen-induced independent events or micrometastatic deposits? *Cancer Epidemiol. Biomarkers Prev.*, **9**, 249–256.
60. zur Hausen, H. (2006) *Infections Causing Human Cancer*, Wiley-VCH Verlag GmbH, Weinheim.
61. Centers for Disease Control and Prevention (2007) Prevalence of High-Risk and Low-Risk Strains of HPV (2003-2004).
62. Bakker Schut, T.C., Van Dekken, H., Tilanus, H.W., Bruining, H.A., and Puppels, G.J. (1997) in *Spectroscopy of Biological Molecules: Modern Trends* (eds P. Carmona, R. Navarro, and A. Hernanz), Kluwer Academic Publishers, Dordercht, pp. 455–456.
63. Kendall, C. *et al.* (2010) Evaluation of Raman probe for oesophageal cancer diagnostics. *Analyst*, **135**, 3038–3041.
64. Barr, H., Kendall, C., and Stone, N. (2004) The light solution for Barrett's esophagus: photodiagnosis and photodynamic therapy for columnar-lined esophagus. *Photodiagnosis Photodyn. Ther.*, **1** (1), 75–84.
65. Barr, H., Kendall, C., and Stone, N. (2008) Raman spectroscopy as a potential tool for early diagnosis of malignancies in esophageal and bladder tissues, in *Vibrational Spectroscopy for Medical Diagnosis* (eds M. Diem, P.R. Griffiths, and J.M. Chalmers), John Wiley & Sons, Ltd, Chichester.
66. Chiriboga, L. *et al.* (1997) Infrared spectroscopy of human tissue. III. Spectral differences between squamous and columnar tissue and cells from the human cervix. *Biospectroscopy*, **3**, 253–257.

67. Miljković, M. *et al.* (2004) Infrared microspectroscopy of individual human cervical cancer (HeLa) cells suspended in growth medium. *Biopolymers*, **74** (1-2), 172–175.
68. Marcsisin, E.J. (2011) Infrared spectroscopy to monitor drug response of individual live cells, in *Department of Chemistry*, Northeastern University, Boston, MA.
69. Marcsisin, E.J. *et al.* (2010) Infrared microspectroscopy of live cells in aqueous media. *Analyst*, **135**, 3227–3232.
70. Ralhan, R. and Kaur, J. (2007) Alkylating agents and cancer therapy. *Expert Opin. Ther. Patents*, **9** (17), 1061–1075.
71. Malayappan, B. *et al.* (2010) Quantitative high-performance liquid chromatography-electrospray ionization tandem mass spectrometry analysis of bis-N7-guanine DNA-DNA cross-links in white blood cells of cancer patients receiving cyclophosphamide therapy. *Anal. Chem.*, **82** (9), 3650–3658.
72. Wang, J., Prorok, G., and Vaughan, W.P. (1992) Cytotoxicity, DNA cross-linking, and DNA single-strand breaks induced by cyclophophamide in a rat leukemia in vivo. *Cancer Chemother. Pharmacol.*, **31**, 381–386.
73. Souliotis, V.L., Dimopoulos, M.A., and Sfikakis, P.P. (2003) Gene-specific formation and repair of DNA monoadducts and interstrand cross-links after therapeutic exposure to nitrogen mustards. *Clin. Cancer Res.*, **9** (12), 4465–4474.
74. Hemminki, K. (1985) Binding of metabolites of cyclophosphamide to DNA in a rat liver microsomal system and in vivo in mice. *Cancer Res.*, **45** (9), 4237–4243.
75. Jamin, N. *et al.* (2003) Chemical heterogeneity in cell death: combined synchrotron IR and fluorescence microscopy studies of single apoptotic and necrotic cells. *Biopolymers (Biospectroscopy)*, **72**, 366–373.
76. Gaspar, R. *et al.* (2011) Time dependence of cellular chemical changes induced in prostate PC-3 cancer cells by two structurally related cardenolides monitored by Fourier transform infrared (FT-IR) spectroscopy. *Appl. Spectrosc.*, **65** (6), 584–594.
77. Flower, K.R. *et al.* (2011) Synchrotron FTIR analysis of drug treated ovarian A2780 cells: an ability to differentiate cell response to different drugs? *Analyst*, **136**, 498–507.
78. Gazi, E. *et al.* (2006) A correlation of FTIR spectra derived from prostate cancer tissue with gleason grade, psa and tumour stage. *Eur. Urol.*, **50**, 750–761.
79. Ozek, N.S. *et al.* (2010) Characterization of microRNA-125b expression in MCF7 breast cancer cells by ATR-FTIR spectroscopy. *Analyst*, **135**, 3094–3102.
80. Holton, S.E., Walsh, M.J., and Bhargava, R. (2011) Subcellular localization of early biochemical transformations in cancer-activated fibroblasts using infrared spectroscopic imaging. *Analyst*, **136**, 2953–2958.
81. Schiffer, G. *et al.* (2002) Application of FTIR spectroscopy in antibacterial drug research, in *Workshop on FTIR Spectroscopy in Microbiological and Medical Diagnostic*, Robert Koch Institute, Berlin.

Part III
Agriculture, Plants, and Food

Infrared and Raman Spectroscopic Imaging, Second Edition. Edited by Reiner Salzer, Heinz W. Siesler.
© 2014 Wiley-VCH Verlag GmbH & Co. KGaA. Published 2014 by Wiley-VCH Verlag GmbH & Co. KGaA.

6
Infrared and Raman Spectroscopic Mapping and Imaging of Plant Materials

Hartwig Schulz, Andrea Krähmer, Annette Naumann, and Gennadi Gudi

6.1
Introduction, Background, and Perspective

There is a growing interest in botany, agricultural research, and industry to obtain a more comprehensive understanding of the chemical composition of various plant tissues in the authentic state. Numerous sensitive hyphenated analytical techniques such as gas chromatography-mass spectrometry (GC-MS) or liquid chromatography-mass spectrometry (LC-MS) exist to identify the plant metabolite profiles in the headspace, solvent extract, or distillate; however, this approach does not provide any information concerning the local quantity and structural arrangement of the individual substances in the analyzed sample. Furthermore, all chromatographic techniques include an individual sample pretreatment, which may cause a partial destruction or discrimination of individual plant substances.

Therefore, during the past 30 years, numerous vibrational spectroscopic methods (near infrared, NIR; infrared, IR; and Raman spectroscopy) have been introduced as very efficient alternatives, which are widely used today to determine fats, proteins, and carbohydrates and also numerous secondary plant substances occurring in agricultural products. For authentication purposes, the mentioned spectroscopic techniques can provide the valuable data in a few minutes, allowing the discrimination of different agrofood samples. Also new developments of IR and Raman microscopes have considerably extended the field of application. These sophisticated techniques allow to perform point-by-point measurements (mapping) or to acquire simultaneously spectra (imaging) from a small sample area.

Raman and IR macrospectroscopy and microspectroscopy combined with mapping or imaging techniques offer the special advantage to measure whole plant organs such as seeds, fruits, leaves, flowers, or stems nondestructively and also permit analysis of plant cell architecture and changes in biochemistry at the cellular level. Especially the introduction of the FT-Raman spectroscopy technique with excitation in the NIR range (1064 nm) enabled to develop numerous applications on fresh (living) green plant material by eliminating the problem

Infrared and Raman Spectroscopic Imaging, Second Edition. Edited by Reiner Salzer, Heinz W. Siesler.
© 2014 Wiley-VCH Verlag GmbH & Co. KGaA. Published 2014 by Wiley-VCH Verlag GmbH & Co. KGaA.

of fluorescence and photochemical degradation, which normally occurs when UV – Vis lasers are applied.

IR spectroscopy methods have been extensively used for authentication and quantification purposes in the field of food and agricultural research. Usually mid-IR spectra obtained from plant samples are very complex because each functional group in a molecule contributes more or less to the complete spectral output. Therefore, band assignments may be sometimes difficult due to the fact that overlapping and mixing of various vibrational modes occur.

Applications of IR imaging spectroscopy are more or less limited to dry plant material because of the strong absorptions of water. Nevertheless, this technique provides important information regarding the occurrence of major cell substances such as lignin, cellulose, and various polysaccharides. Furthermore, changes induced by biotic (e.g., pathogens) and abiotic stressors (e.g., salinity, desiccation, inorganic, and organic contaminants) on plant structure could be successfully characterized. Today, Fourier transform infrared (FT-IR) microscopes are equipped with multielement detectors, which allow analyzing tissue sections within a few minutes. Usually a complete IR spectrum is acquired at each image point and the distribution of main plant components (lipids, proteins, and polysaccharides) can be identified very easily. The ability to produce spatially localized images revealing the molecular structure, distribution, and relative amount of various components with respect to plant anatomy and possible influences because of environmental stress factors has made this technique very attractive for researchers working in the field of plant sciences. Nevertheless, in most cases, it is necessary to prepare microtome sections of the plant material (usually with a thickness of 5 – 10 µm) to prevent total absorption of the emitted IR radiation. Only a few applications have been described to measure nondestructively the surface of plant samples in reflection using the attenuated total reflectance (ATR)-IR imaging technique (e.g., to identify the occurrence and distribution of waxes or pesticide residues) since the reflection intensities of the analytes are usually low.

It can be assumed that especially chemical imaging based on IR spectroscopy will become an important technique in the near future. Similar to that of NMR spectroscopy/imaging, this technique will be presumably used more and more also by nonspectroscopists if efficient pattern recognition methods will be adapted to simplify the application of this sophisticated technique. Furthermore, it can be supposed that existing limitations to apply Raman spectroscopy in plant analysis with regard to sensitivity and spatial resolution will be partly removed in the future. Promising techniques such as surface-enhanced Raman scattering (SERS) and surface-enhanced Raman resonance spectroscopy (SERRS) show that principally a significant enhancement of the Raman scattering is possible (by a factor of up to 10^7). Also coherent anti-Stokes Raman scattering (CARS) microscopy as a label-free imaging technique becomes increasingly important for studies of biological samples (see Chapter 15 of this book).

6.2
Application of Mapping and Imaging to Horticultural Crops

6.2.1
Carotenoids

Most applications of Raman spectroscopy in the field of horticultural crops are related to carotenoids and have been directly performed on the fresh plant tissue. Although these secondary plant substances occur as minor components at the milligram per kilogram level, a very sensitive detection is obtained by resonance Raman spectroscopy in the visible region, when the excitation wavelength coincides with an electronic transition of the analyzed carotenoid [1, 2]. Also FT-Raman spectroscopy using a Nd:YAG laser (excitation at 1064 nm) provides strong carotenoid bands owing to the known pre-resonance enhancement, and thus disturbing fluorescence effects are reduced to a minimum.

Main carotenoid signals occur in the wavenumber ranges between 1550–1500 and 1170–1150 cm^{-1}, which are related to in-phase C=C and C–C stretching vibrations of the polyene chain. In addition, in-plane rocking modes of CH_3 groups attached to the polyene chain occur as bands of medium intensity in the range 1020–1000 cm^{-1} [3, 4]. It has been observed that with increasing number of conjugated C=C groups in the carotenoid chain, the wavenumber positions of the carotenoid signals decrease significantly. Therefore, in principle, the distribution of different carotenoids can be determined simultaneously, if Raman mapping is based on the characteristic C=C stretching vibrations for 7-, 8-, 9-, and 11-conjugated systems [4–6].

Roots of different carrot cultivars (cv. Beta III, cv. High Carotene Mass (HCM), cv. Purple Haze, cv. Bolero, cv. Regulus Imperial, cv. Panitat Special) have been screened for their individual carotenoid distribution using the strong β-carotene signal at 1520 cm^{-1} for integration [7]. Although orange- and purple-colored cultivars present a symmetric β-carotene band at 1520 cm^{-1}, for yellow roots the corresponding carotenoid signals were shifted and much broader. This is related to the complex composition resulting from the presence of other carotenoids in the tissue, for instance lutein or α-carotene [4]. In all analyzed roots, the β-carotene distribution was heterogeneous across the root section, independent of the individual genotype. Generally, highest concentration was found in the secondary phloem, whereas periderm/pericyclic parenchyma and the tissue along the vascular cambium contained comparatively low amounts of carotenoids (Figure 6.1). The authors report that especially cultivars HCM and Beta III accumulated high content of β-carotene in the secondary xylem (Figure 6.2a). Raman maps with a spatial resolution of 100 µm clearly demonstrate the presence of characteristic carotenoid rays (Figure 6.2b). Further increase in the resolution to 25 µm revealed that the carotene-rich rays are clearly separated by parenchyma of lower carotene content (Figure 6.2c,d). The level of carotenoids in the essential oil ducts, appearing as blue spots in the Raman map, was found to be below the detection limit. In yellow carrot roots, mainly lutein in addition to low amounts

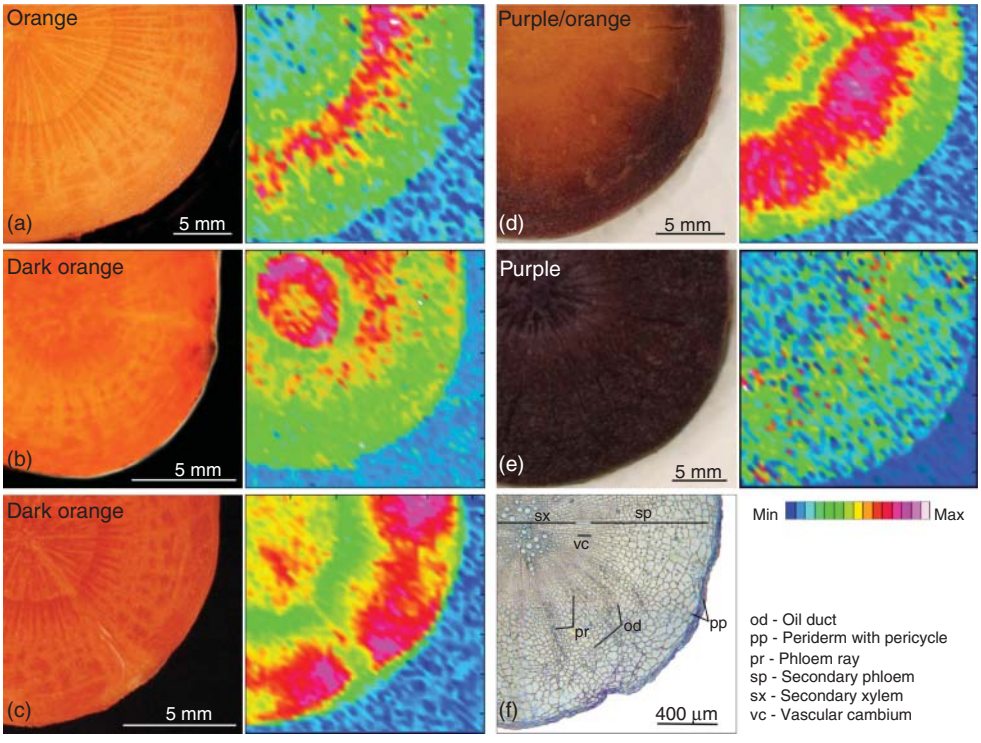

Figure 6.1 Visual images of a quarter of transversely cut carrot roots and their Raman maps colored according to the band intensity in the range 1523–1517 cm^{-1} related to β-carotene contents: (a) orange, Bolero F_1; (b) dark orange, Beta III; (c) dark orange, HCM; (d) purple orange, Purple Haze F_1; and (e) purple line, Bejo 01-0102. Mapping increment of 250 µm (a, b), 400 µm (c), 500 µm (d), and 300 µm (e). Microscopic section of carrot root at early secondary growth stained with toluidine blue (f). (Reproduced with permission from Ref. [7]. © Springer.)

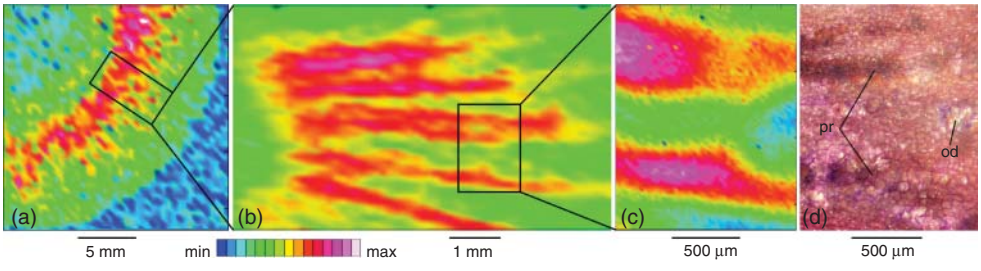

Figure 6.2 Raman maps obtained from a section of orange Bolero F_1 root with mapping increment of 500 µm (a), 100 µm (b), and 25 µm (c), respectively. The maps are colored according to the band intensity in the range 1523–1517 cm^{-1} related to the β-carotene content in the carrot root. (d) Microscopic image of the same fragment as in map (c) stained with toluidine blue; od – oil duct, pr – phloem rays. (Reproduced with permission from Ref. [7]. © Springer.)

of α-carotene was detected. Using FT-Raman microspectroscopy, Baranska *et al.* even obtained carotenoid signals from single carotenoid crystals in the natural environment without destroying the carotene–protein complexes in the root tissue [8]. For this purpose, they prepared microscopic slides with monolayer cells taken from the carrot root secondary phloem. The authors stress that Raman spectroscopy offers the special advantage to get direct insight into carotenogenesis in living tissue and allows studying carotenoid sequestration even at microscopic dimensions.

FT-Raman mapping was also applied for *in situ* studies of the ornamental plant species *Pelargonium* × *hortorum* to illustrate the heterogeneous distribution of the individual carotenoids in the leaves [6]. A hyperspectral macroscale Raman imaging method was developed to measure the distribution of lycopene in cross sections of cut tomatoes as a maturity parameter during the fruit ripening process [9]. The presented Raman technique also allows extracting subsurface Raman chemical information. In order to reduce the fluorescence background to a minimum, a modified polynomial curve-fitting method was applied to all Raman spectra. Then, the fitted baseline at each hyperspectral pixel was subtracted from the original spectrum to generate a corrected spectrum with very low background noise [9].

A detailed review highlighting the potential of Raman microscopy and Raman imaging in plant research was published by Gierlinger and Schwanninger [10]. The authors stress the advantages of pre-resonance intensity enhancement effect accompanying the FT-Raman measurements allowing to detect carotenoids even in trace amounts with simultaneous elimination of background fluorescence of the plant sample. These special advantages of FT-Raman spectroscopy applied to 2D Raman mappings enabled to illustrate the distribution of individual plant carotenoids independently from each other in the same sample [4]. Furthermore, the high potential of FT-Raman microspectroscopy to obtain detailed information about microstructure and chemical composition of fennel fruits, chamomile inflorescence, and curcuma roots was demonstrated [11].

Recently, nonlinear CARS has been applied to image carotenoids in fresh and thermally treated plant tissues [12]. The authors quantified sizes, shapes, densities, and location of different intracellular carotenoid bodies in orange-fleshed sweet potatoes (OFSPs), carrot roots, and mango fruits. The distribution of starch granules and β-carotene bodies in the plant matrix are presented as 3D visual information as well as in quantitative terms. Although the OFSP presented heterogeneous rod-shaped bodies with high carotenoid density (indicated by higher CARS signals), the lipid droplets in mango fruits appeared as homogeneous low-density aggregates of round shape. It is assumed that nonlinear microscopy in future will become very useful within plant biology and food sciences to get a more detailed insight into the structure of provitamin A carotenoids and its relation to bioavailability.

The ornamental plant *Euonymus fortunei* (cv. Canadale Gold) is a chlorophyll mutant showing light green or yellow-colored edges on their leaf blades. In order to determine the carotenoid distribution, Raman maps

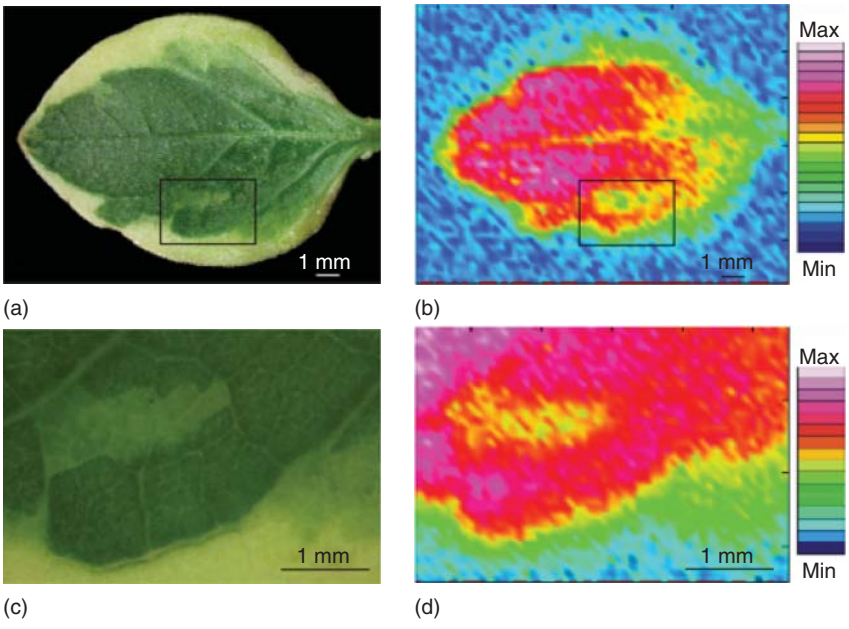

Figure 6.3 Picture of an *Euonymus fortunei* leaf (cv. Canadale Gold) (a), microscopic image of the defined area (b), and corresponding Raman maps colored according to the intensity of the carotenoid band at 1525 cm^{-1} (c and d). (Reproduced with permission from Ref. [4]. © Wiley.)

were established by integration of the intensive carotenoid signal at 1525 cm^{-1} (Figure 6.3) [4].

Due to its healthy properties and pleasant smell, tea prepared from green or fermented rooibos (*Aspalathus linearis*) is of increasing interest for the nutraceutical and cosmetic industries [13]. Therefore, attempts have been made to determine the content of aspalathin, which represents the most important flavonoid in the leaves of rooibos by FT-Raman spectroscopy [14]. Using the key band of aspalathin at 784 cm^{-1} (aromatic C–H out-of-plane deformation mode) for Raman mapping studies, it could clearly be seen that this active principle is distributed more or less heterogeneously in the sample; however, highest concentration was observed in the inner part of the leaves. In addition to aspalathin, the signals at 1607 cm^{-1} and 1525 cm^{-1} were also integrated to illustrate the distribution of lignin and carotenoids, respectively.

6.2.2 Polyacetylenes

In addition to carotenoids, –C≡C– stretching modes of plant polyacetylenes also present strong and polarized Raman bands in the wavenumber range between 2300 and 2100 cm^{-1}. Falcarinol and falcarindiol, the most bioactive

polyacetylenes in carrot roots, show intensive bands at 2258 and 2252 cm^{-1}, respectively [15, 16]. Using micro-Raman mapping, it could be proved that polyacetylenes are mainly located in the outer section of the carrot roots. Therefore, the authors assume that polyacetylenes occur in vascular bundles in young secondary phloem as well as in pericycle oil channels in the vicinity of the periderm [15]. The authors found a very good correlation between accumulation of polyacetylenes and an increased concentration of carotenes in the plant tissue although polyacetylenes and carotenoids occur at different areas in the investigated plant material. The Raman maps presented for the distribution of polyacetylenes and carotenoids in orange-colored carrot root show clearly that polyacetylenes are concentrated in the pericyclic parenchyma and the phloem part close to the secondary cambium, but even there they are not distributed uniformly [16].

Wild carrot species (*Daucus carota* ssp. *maritimus*, *D. carota* ssp. *gummifer*, *D. carota* ssp. *commutatus*) were also investigated regarding the accumulation of polyacetylenes. Raman spectra prove that mainly falcarindiol is present in the individual wild species. Recently, differences in the Raman spectra of two wild carrot species have been described in more detail (*D. carota* ssp. *gummifer*, *D. carota* ssp. *maximus*) [17]. Furthermore, Raman mapping clearly presented the different distribution of polyacetylenes in wild and orange carrots. It could be shown that the whole phloem tissue was rich in polyacetylenes, but the maxima were also observed near the pericyclic parenchyma. An analogous distribution of polyacetylenes was found in roots of other carrot wild species.

In recent studies, Roman *et al.* showed that the distribution of polyacetylenes within the phloem tissue is not uniform and areas with high amounts of these compounds may also occur occasionally [17]. In addition, the authors could not find higher concentration of polyacetylenes close to the periderm. Significant amounts of falcarindiol detected in wild carrot species are related to their resistance to some plant diseases such as root knot nematodes. Raman mapping was also used to assess the distribution of lignin and polysaccharide substances in carrot tissues. Based on the results obtained, the individual accumulation of starch and cell wall components such as lignin, pectin, and cellulose could be successfully demonstrated.

In roots of American ginseng (*Panax quinquefolium*), detectable amounts of falcarinol and its epoxy derivative (panaxydol) have been detected [18]. A strong polyacetylene signal occurs clearly separated from other signals at 2237 cm^{-1} when the spectra are taken *in situ* from fresh roots. Measurements of dried roots show a significant shift of this signal to 2258 cm^{-1}, which corresponds very well with the spectral response of pure falcarinol (2258 cm^{-1}) and panaxydol (2260 cm^{-1}). The Raman maps obtained from horizontal root sections illustrate that the content of both polyacetylenes decreases with an increase in root size, which is in accordance with formerly performed HPLC (high-performance liquid chromatography) studies. Furthermore, the mapping results demonstrate that the detected polyacetylenes are stored in special channels, which are mainly located in the outer parts of the root [18].

Several other plant species (e.g., *Coreopsis grandiflora*, *Chrysanthemum leucanthemum*, *Centaurea cyanus*, *Centaurea ruthenica*) containing different polyacetylenes in various organs have also been analyzed so far [19]. The same authors performed Raman mapping of apache beggarticks flowers (*Bidens ferulifera*). Other species of the genus *Bidens* are widely used in Chinese medicine, such as *Bidens pilosa* and *Bidens campylotheca*, and have been therefore extensively studied by HPLC [20, 21].

In addition to the occurrence in carrots, polyacetylenes were also found in numerous other plant species from the Apiaceae family. Recently, parsnip (*Pastinaca sativa*), celeriac (*Apium graveolens* var. *rapaceum*), and parsley (*Petroselinum crispum*) have been investigated aiming to show the distribution of the individual polyacetylene substances in the roots [22]. The Raman spectra obtained from various areas of the parsnip roots showed distinct signals in the region of 2270–2180 cm^{-1}, and it was found that the spectral profiles and band positions depend significantly on the localization within the root.

According to former HPLC studies, which detected falcarinol, falcarindiol, 8-*O*-methylfalcarindiol, panaxydiol, falcarinone, and falcarinolone in celeriac roots, Raman spectra were measured at different areas of the root presenting more or less the same pattern and a band maximum at about 2252 cm^{-1}. Therefore, the authors assume that falcarindiol dominates in celeriac root, whereas the other polyacetylenes occur only in lower amounts. Raman mapping was also performed to study the polyacetylene distribution within the whole transversely cut root. As to be seen in Figure 6.4, polyacetylenes are accumulated only in a few small areas occasionally localized close to the peel [22].

6.2.3 Flavonoids

In recent years, several attempts have been made to get Raman data from different plant flavonoids [23–25]. Resonance Raman spectra of six common anthocyanidins and some of their glycosylated derivatives from acidic aqueous solutions were measured, and the authors detected a strong resonance Raman signal for anthocyanidin-3-glycoside close to 540 cm^{-1}. In the vacuoles of wine berries (*Vitis vinifera*), resonance Raman spectroscopy was also successfully applied to detect comparatively low amounts of the pigment malvidin-3-glucoside [23].

Several flavones, widely distributed in the plant kingdom, were measured as pure substances in order to study their vibrational frequencies, and detailed structural studies were performed of quercetin [26].

Also Raman mapping combined with cluster analysis was successfully applied to discriminate flavonoids, anthocyanins, and carotenoids occurring in differently colored flower petals of various pansy cultivars (*Viola* × *wittrockiana*) [27]. Extracts of the viola petals were separated by thin-layer chromatography (TLC) in order to get the Raman data of the individual pure substances. Applying hierarchical cluster analysis (HCA) of the spectra taken from the flower petals and from the pure TLC extracts, flavonols, anthocyanins, and carotenoids could

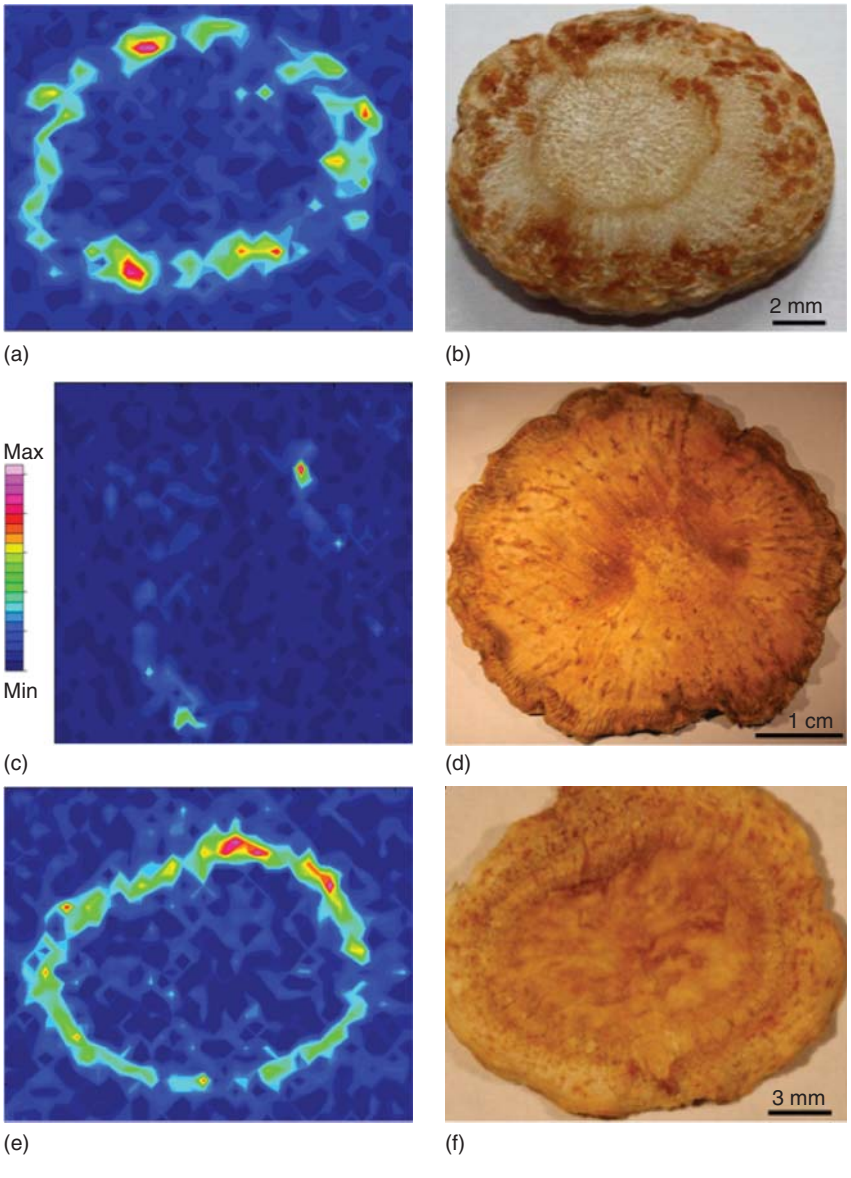

Figure 6.4 Raman maps and related images obtained from transversely root sections of parsnip (a, b), celeriac (c, d), and parley (e, f). Maps are colored according to the individual band intensities in the wavenumber ranges 2280–2160 cm^{-1} (parsnip) and 2280–2200 cm^{-1} (celeriac and parsley). (Reproduced with permission from Ref. [22]. © American Chemical Society.)

be successfully discriminated. A clear correlation between the visual appearance and the Raman mapping images could be achieved (Figure 6.5).

In addition, HCA (based on the spectral data sets) was applied to investigate how far *in situ* discrimination of flavonols against anthocyanins and carotenoids can be successfully performed. The following spectral marker regions for the individual pigments were used: 1172 – 1140 cm^{-1} for carotenoids, 1272 – 1225 cm^{-1} for keracyanin-like anthocyanins, and 1588 – 1550 cm^{-1} for flavonol glycosides. The authors mention that principally also other pigment markers may be used for Raman mapping, as long as a clear separation of the spectral response obtained from various pigments in flower petals is possible [27].

6.2.4 Essential Oils

Several studies were performed to determine the content and composition of essential oils and solvent extracts isolated from various medicinal and aromatic plant species applying IR and Raman spectroscopic methods [28 – 30]. In most cases, characteristic key bands that can be used as markers for chemotaxonomic discrimination of different plant species or chemotypes are found [31 – 34]. Raman spectra of several commercial oils obtained from anise (*Pimpinella anisum*), fennel (*Foeniculum vulgare*), cumin (*Cuminum cyminum*), dill (*Anethum graveolens*), caraway (*Carvum carvi*), coriander (*Coriandrum sativum*), carrot (*D. carota*), lavender (*Lavandula angustifolia*), spike lavender (*Lavandula spicata*), and gentian species (*Gentiana lutea* and *Gentiana punctata*) were also measured, and the results were compared with spectra of pure standards in order to analyze their chemical composition [35, 36]. In addition to discrimination of different chemotypes and quantification, several *in situ* mapping experiments of horticultural plant species have also been successfully performed. For example, it was possible for the first time to use Raman maps obtained for transverse and longitudinal sections of fennel fruits to show the distribution of essential oil and fatty acids directly in a single fruit [11]. In a similar approach, the distribution of essential oil substances in fennel fruits was measured on the cellular level [37]. As a result of these studies, the authors found essential oil substances predominantly in the pericarp, whereas the endosperm region of the analyzed fennel fruits presented mainly Raman bands because of fatty oil components (wavenumber region between 1632 and 1666 cm^{-1}, Figure 6.6a,b) [37]. Figure 6.6c clearly illustrates the morphologic structure of single cells of the plant tissue because of the decreased fluorescence of the corresponding cell walls (1580 – 1690 cm^{-1} for lignin, blue region). In another study, Strehle *et al.* described measurements on the endosperm region of anise fruits (*P. anisum*) and identified essential oil droplets in the wavenumber region between 1573 and 1618 cm^{-1} according to the marker band of anethole at 1604 cm^{-1} being the main component of anise oil (Figure 6.7) [36]. In this context, the authors point out that during sample pretreatment the excretory cells of the anise fruits were cut with a microtome and consequently the essential oil leaked out from the schizogenic excretory canals

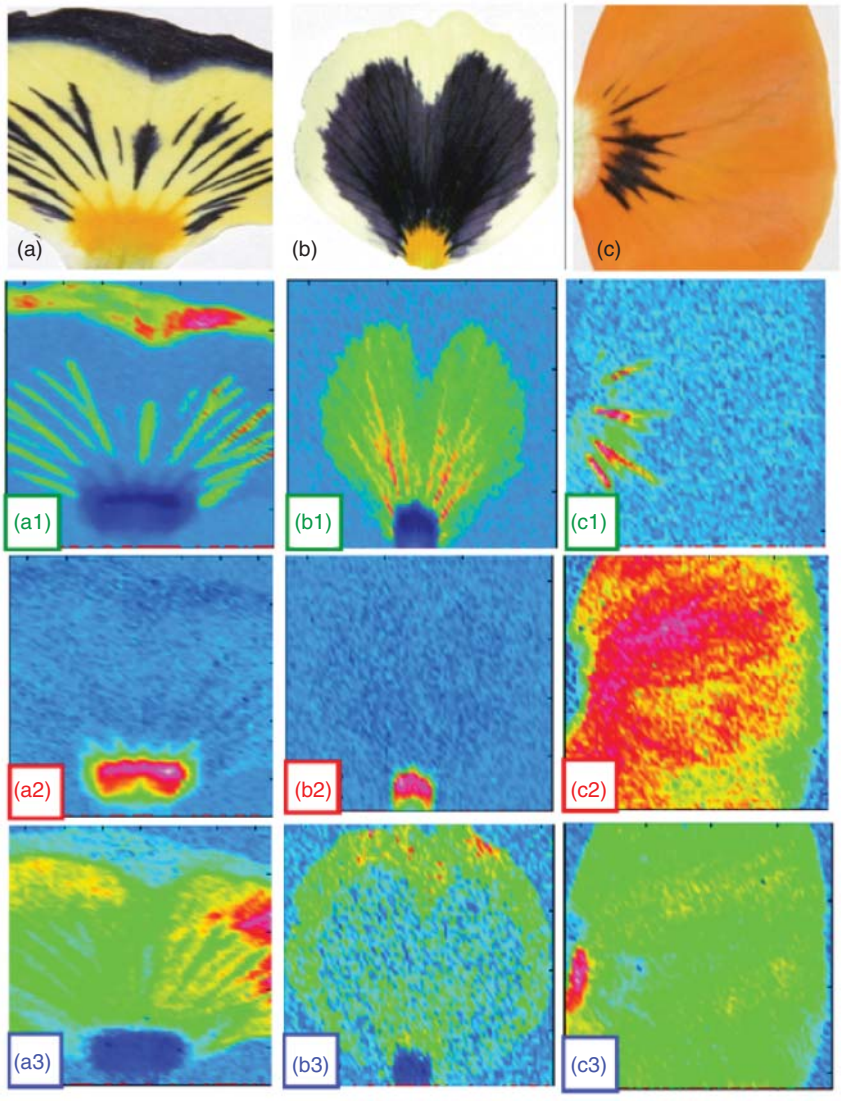

Figure 6.5 The first row shows the visual images (a, b, and c) of petals of *Viola* × *wittrockiana*, whereas the second row presents the resulting chemical images obtained by hierarchical cluster analysis (HCA) of the wavenumber range of 1700–1000 cm^{-1}. The chemical images in the lower three rows show the patterns resulting from the integrated spectral intensity: in a1, b1, and c1 for the anthocyanin marker (integration range 1272–1225 cm^{-1}); in a2, b2, and c2 for the carotenoid marker (integration range 1172–1140 cm^{-1}); in a3, b3, and c3 for flavonol glycoside marker (integration range 1588–1550 cm^{-1}). The color scale correlates with the magnitude of the integrated intensity and is a signature of the relative concentration. (Reproduced with permission from Ref. [27]. © John Wiley & Sons, Ltd.)

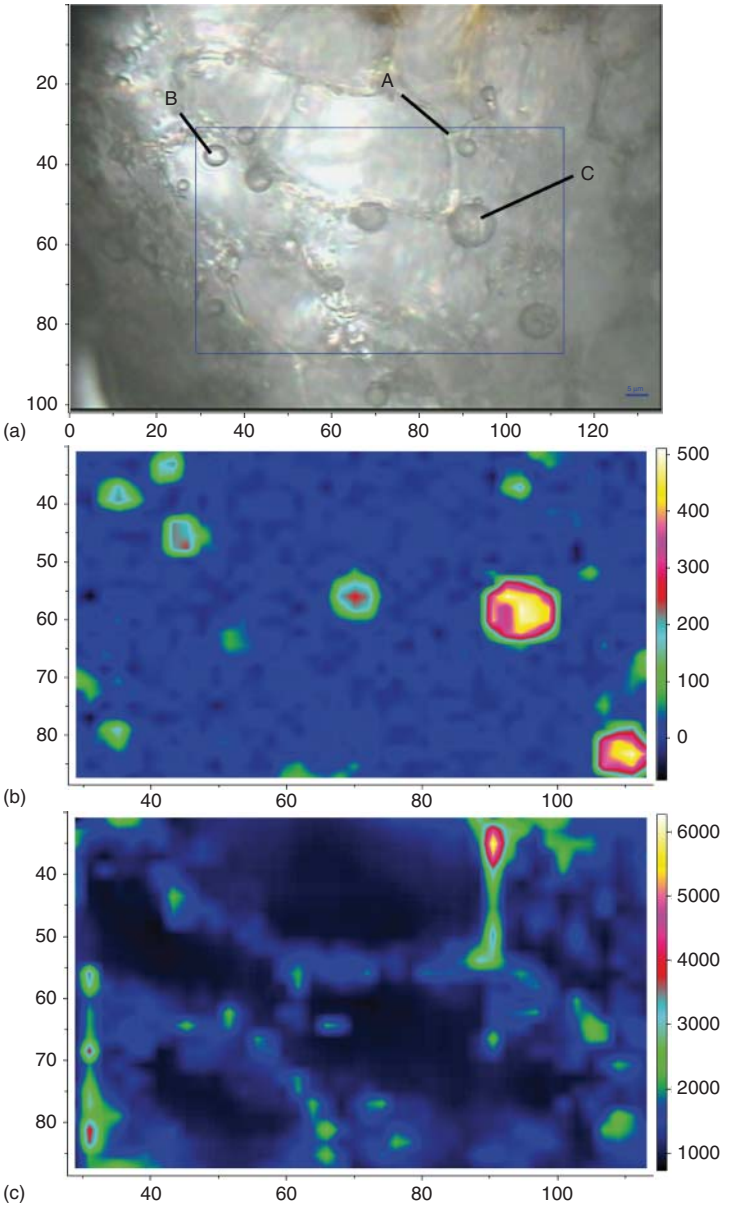

Figure 6.6 Raman mapping in the pericarp region of a fennel seed. (a) Microscopic image of the scanned region. (b) False color plot representing the intensity distribution of 1635–1666 cm^{-1}. A baseline correction was performed. (c) False color plot representing the intensity distribution of 1580–1690 cm^{-1}. No baseline correction was performed. (Reproduced with permission from Ref. [37]. © Wiley Periodicals, Inc.)

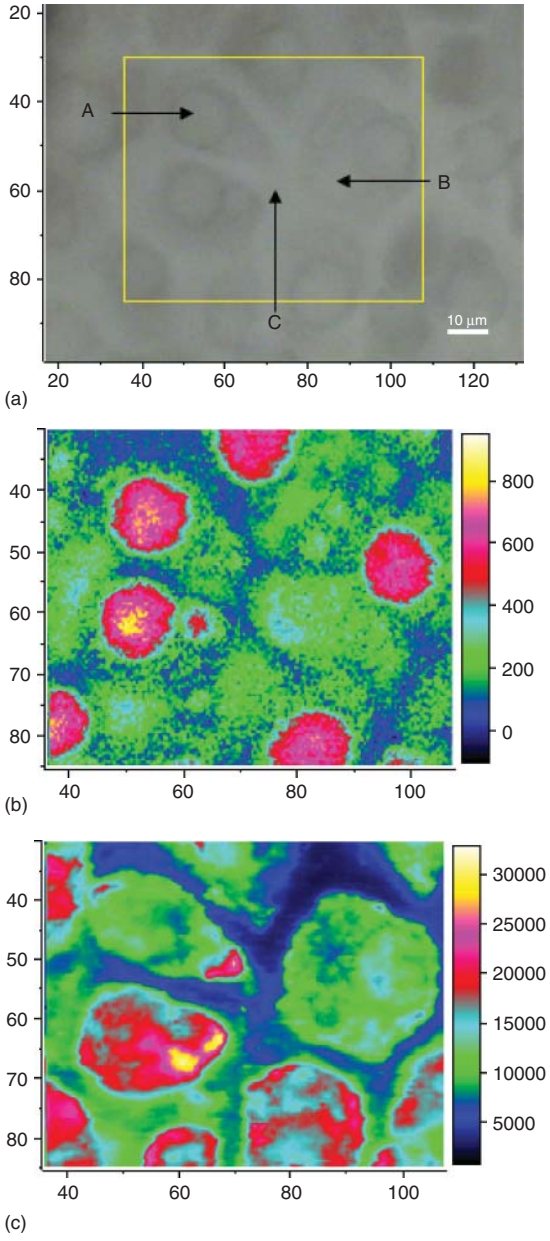

Figure 6.7 (a) Micro-Raman maps of the endosperm region of anise fruit. Microscopic image of the scanned region, (b) false color plot presenting the distribution of components detected in the wavenumber range between 1573 and 1618 cm^{-1}, (c) false color plot of the same wavenumber range without baseline correction. (Reproduced with permission from Ref. [36]. © American Chemical Society.)

in the pericarp region. As the essential oil substances are highly soluble in fatty oils (which occur in the endosperm region), they accumulated after a few hours when the micro-Raman mapping experiments were performed.

It is known that the essential oil of chamomile (*Chamomilla recutita*) contains mainly chamazulene, α-bisabolol, bisabololoxides A and B, as well as *cis*- and *trans*-spiroethers. Especially spiroethers belonging to the group of polyacetylenes cause very strong Raman signals in the range between 2250 and 2150 cm^{-1}. Integration of these signals demonstrates that spiroethers are accumulated in the middle part of the receptacle (Figure 6.8). Contrary to this, carotenoids presenting characteristic signals at 1525, 1156, and 1004 cm^{-1} are located at the top of the flower head [11].

FT-Raman spectroscopy could be also successfully applied to investigate the occurrence of curcumin, the valuable dyeing component of curcuma root (*Curcuma longa*) with widespread use in the Asian cuisine. Most intense bands of curcumin occur at 1630 and 1601 cm^{-1}, which are assigned to the benzene ring,

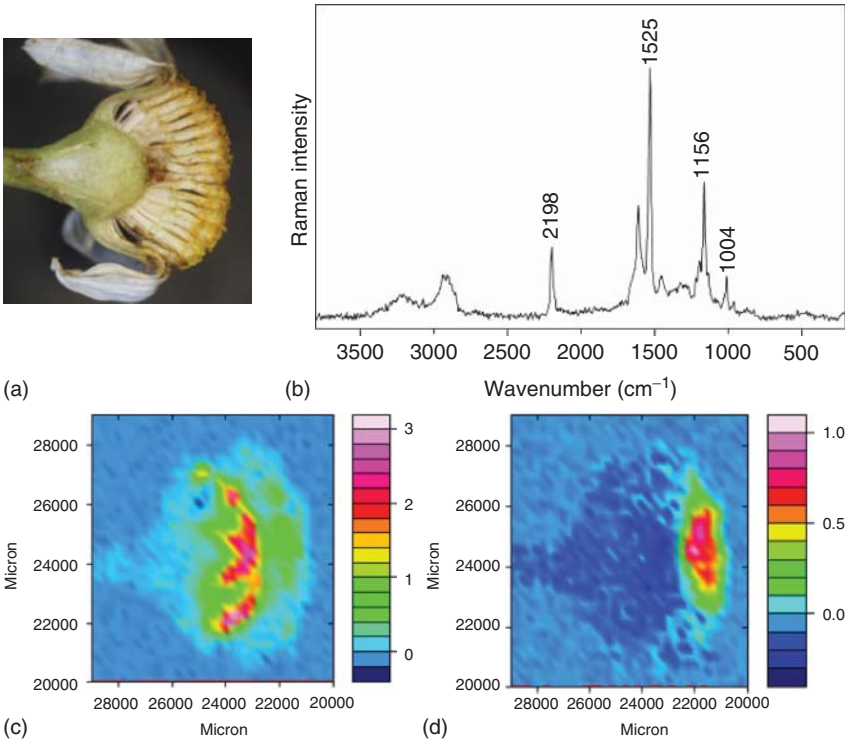

Figure 6.8 Light-optical microscopic image of chamomile inflorescence (a), FT-Raman spectrum obtained from the receptacle (b) Raman mapping showing the distribution of polyacetylenes (c) and carotenoids (d). The relative concentration of polyacetylenes was determined according to the intensity of the acetylene band at 2198 cm^{-1}, whereas carotenoids were identified based on the signal at 1525 cm^{-1}. (Reproduced with permission from Ref. [11]. © Royal Society of Chemistry.)

whereas signals at 1185 and 965 cm^{-1} are due to COC and COH vibrations. In order to screen the curcumin distribution in a sprouting curcuma root, Raman maps were calculated using the signals at 1630 and 1601 cm^{-1} for integration. Highest concentration of the dye was found in the core of the root whereas the outer layers contained only slight amount of curcumin [11].

Attempts were also made to investigate the essential oil in *Eucalyptus globulus* and *Eucalyptus cinerea* [38]. The spectra directly obtained from the oil droplets of the eucalyptus leaves show a strong marker band at 652 cm^{-1} because of the ring deformation vibrational mode of 1,8-cineole. Based on this Raman signal, the distribution of the essential oil over the eucalyptus leaf could be determined. Using the same spectral data set, a Raman image based on the carotenoid signal at 1525 cm^{-1} was integrated. This Raman map proves that carotenoids occur mainly outside the essential oil cavities.

A new approach to image the leaves of the tree *Eucalyptus botryoides* with a focal plane array (FPA) IR detector was described [39]. Contrary to conventional IR mapping, requiring 8 h to image an area of 350 μm^2, FPA imaging was already finished after 2 min. However, a slightly lower spatial resolution and a reduced signal-to-noise ratio were observed compared to the point-to-point IR mapping technique. Based on the individual marker bands, the images for protein and lignin were calculated showing the distribution of these substances in the leaf tissue [39].

Studies performed by Schulz *et al.* [40] to identify the pungent principle as well as the most important aroma substances of pepper oil provide characteristic Raman signals, which can be used for quality control purposes and also for mapping studies of intact peppercorns. Most of the well-resolved Raman signals detected in the spectra of green, white, and black peppercorns were assigned to the alkaloid component piperine, which is known to be the main pungent principle in pepper. Integration of the specific piperine key bands in the wavenumber ranging between 1580 and 1635 cm^{-1} (aromatic and aliphatic $-C{=}C-$ as well as $>N-C{=}O$ stretching vibrations) allows to localize the distribution of the alkaloid in whole pepper berries. The authors observed that the pungent principle is distributed more or less in the whole perisperm of the green pepper fruit, whereas the endosperm contains significantly lower amounts of piperine. In the black peppercorn, the alkaloid is mainly found beneath the skin of the dried fruit [40].

6.2.5
Tissue Constituents

In addition to applications in the area of systematic fingerprinting and quantification of valuable plant substances, FT-IR microspectroscopy has become a powerful tool for monitoring cell wall constituents such as pectins, proteins, aromatic phenols, cellulose, and hemicellulose [41].

A hyperspectral imaging system was developed by Nicolaï *et al.* to identify a pit lesion on apples. A partial least squares (PLS) calibration model was constructed to discriminate between pixels of unaffected and bitter pit lesions [42]. The obtained calibration model was successfully validated on different apples. The

system was able to identify bitter pit lesions, even when they were not visible, but could not discriminate between bitter pit lesion and corky tissue.

In strawberry achene, vascular bundles, and cortical cell walls, different chemical substances were identified and localized by means of FT-IR spectroscopy [43]. In this context, sections of frozen strawberries were cut in a cryostat and subsequently analyzed by the use of FT-IR microspectroscopy. The measurements prove that lignin represents an important component of achene and vascular bundles, whereas the cortical cell walls contain mainly pectin and cellulose in the middle lamella, and protein as deposits in the outer layer.

Morphological and molecular patterns of St. John's wort (*Hypericum perforatum*) were studied using FT-IR imaging [44]. For tissue preparation, the paraffin-embedded samples were sliced with a microtome into 5 µm sections, mounted on 1 mm thick CaF_2 slides, deparaffinized with octane, and dried at room temperature. The obtained FT-IR imaging results demonstrate clearly that the distribution of lipids, phospholipids, proteins, carbohydrates, nucleic acids, and cellulose in the caulis of St. John's wort can be successfully analyzed. The imaging results illustrate that the epidermis and sclerenchyma tissues produce comparatively high amounts of nucleic acids, whereas xylem and protoxylem tissues produce predominantly lignin.

6.2.6 Environmental Interactions and Processing

Transmission IR microspectroscopy was successfully applied to study the infection of potato tubers by *Erwinia carotovora* ssp. *carotovora* (a widespread bacterium causing soft rot in potato tubers) in aerobic and anaerobic conditions [45]. This sophisticated technique generally permits the study of localized changes occurring in cell wall composition and structure. According to present knowledge, the bacteria degrade the starch granules resulting in a significant decrease of polysaccharide C–O stretching vibrations in the region 1150–980 cm^{-1}. Furthermore, a slight increase in protein bands was seen that may be due to cell wall hydrolyses secreted by the pathogenic bacteria [45].

ATR-IR spectroscopy was used for *in situ* analysis of naturally occurring carotenoids in tomato fruits and tomato products [5]. Most important pigments of red tomato fruits are lycopene and β-carotene, which are 11- and 9-conjugated carotenes, respectively.

In order to characterize influences of sublethal sunscald injury, Raman mapping was performed at the same tomato fruit [6]. The affected area of the fruit was measured and the bands at 1510 cm^{-1} (lycopene) and 1524 cm^{-1} (β-carotene) were integrated.

As can be seen in Figure 6.9, highest lycopene concentration is found only in the nonaffected tissue (red area in the maps), whereas the necrotic tissue shows more or less no presence of both carotenoids (blue area in the maps). Surprisingly, β-carotene is accumulated in the shape of a ring located around the discolored spot of the sublethal sunscald.

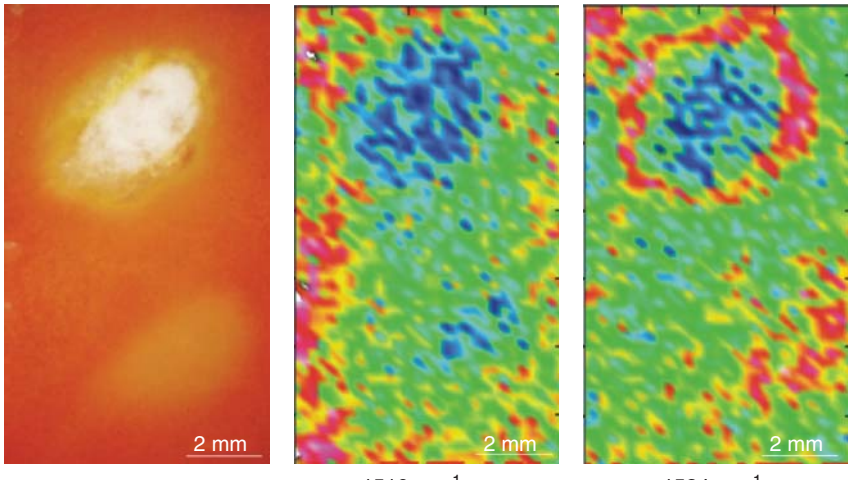

Figure 6.9 Visual image of a sunscald injury in tomato fruit (a) and Raman maps integrated at 1510 cm^{-1} (b) and 1524 cm^{-1} (c) related to lycopene and β-carotene, respectively. (Reproduced with permission from Ref. [6]. © Springer.)

A similar study was performed aiming to characterize biochemical changes in parsley leaves when infected by the fungus *Septoria petroselini* [6]. Applying the same Raman mapping technique, a gradual decrease in the carotenoid content toward the center of the necrotic tissue was seen. Again a significant increase in carotenoids was observed around the lesion.

Furthermore, micro-Raman mapping of a diseased leaf of sugar beet (*Beta vulgaris*) showed clearly a local carotenoid decline at infection site [6].

Another research group analyzed the cuticles isolated from tomato leaves by FT-IR spectroscopy to determine its chemical composition (cellulose, pectin, fatty acids, phenolics, and waxes) [46]. Because the cuticle serves as the first barrier against pest infections, it is of major interest to get a better understanding of the molecular structure of this biological polymer.

In this context, the structure of tomato cell walls comprising two independent but coexisting networks (cellulose/hemicellulose and pectin) was also characterized by FT-IR microspectroscopy [47].

Microspectroscopy using the light from a synchrotron, which is two to three orders of magnitude brighter than conventional IR light sources, provided valuable chemical information on the composition of the root zone of mung beans [48]. The IR studies show that roots of mung bean plants, exposed to low and sufficient phosphorus supply, can be clearly discriminated. Nutrient-sufficient plants showed very strong absorbance features at 1627, 1399, and 1269 cm^{-1} and weaker signals at 1003 and 775 cm^{-1}. In contrast to this, low-phosphorus supplied mung beans presented stronger aliphatic bands in the wavenumber range between 2950 and 2850 cm^{-1} and showed an isolated absorbance band at 1729 cm^{-1}.

Onion bulbs (*Allium cepa*) were used as a model to perform detailed studies of the parenchyma cell walls by using IR microspectroscopy. Most absorption bands were found in the region between 2000 and 900 cm^{-1}. At ~1740 cm^{-1} carboxylic ester groups were detected, amide-stretching bands of protein occur at 1650 and 1550 cm^{-1}, carboxylic acid groups related to pectin absorb at 1610 cm^{-1}, phenolics are observed at 1600 and 1500 cm^{-1}, and carbohydrate bands are seen between 1200 and 900 cm^{-1} [49]. The authors demonstrated that FT-IR microspectroscopy could be successfully applied to detect large conformational changes in pectic polymers because of the enzymatic removal from the cell walls or because of drying. A decrease in the proportion of unesterified pectin between maximal cell division and maximal cell elongation was found in every cell wall.

It was demonstrated that micro-Raman spectroscopy in combination with several chemometric methods allows to distinguish between the two sources of natural indigo occurring in *Indigofera tinctoria* and *Isatis tinctoria* [50]. The band positions correspond with the detailed interpretation that was already provided earlier by Tatsch and Schrader [51]. Further studies were focused on fast and reliable quantification of indigo in dyer's knotweed (*Polygonum tinctorium*) applying Raman and ATR-IR spectroscopic studies [52]. The most intense Raman signal of indigo bands, observed near 1571 cm^{-1}, is assigned to stretching vibration of the conjugated system of C=C, C=O, and N–H groups. If the blue indigo is reduced to the yellow *leuco* indigo, characteristic spectral shifts were observed [52]. Raman mapping of *P. tinctorium* was performed in order to follow the enzymatically controlled process of indigo formation upon leaf drying. The individual Raman maps, calculated by integration of the marker band near 1570 cm^{-1}, correspond very well with the visual images presenting increasing amounts of blue indigo (especially in the damaged areas of the fresh leaves) during the drying process [53].

A few spectroscopic studies were performed to develop alternative analytical options for efficient quality control of devil's claw roots (*Harpagophytum procumbens*) [54, 55]. The main medicinal value (anti-inflammatory and analgetic properties) is attributed to the iridoid substance harpagoside, occurring in the secondary roots of the plant indigenous to South Africa. Applying FT-Raman spectroscopy, harpagoside could be identified and quantified in the root tissue as well as in related phytopharmaceutical products such as ethanolic extracts or tablets [54]. Integration over the strongest harpagoside signals (1656–1618 cm^{-1}) showed a heterogeneous distribution of the active principle with highest concentration in the outer part of the secondary root (Figure 6.10). Contrary to this, maps of devil's claw tablets presented nearly the same harpagoside distribution over the whole sample.

6.3 Application of Mapping and Imaging to Agricultural Crops

Since the introduction of vibrational microspectroscopic methods into the applied sciences in the early 1990s, agricultural crops stood under intensive investigation.

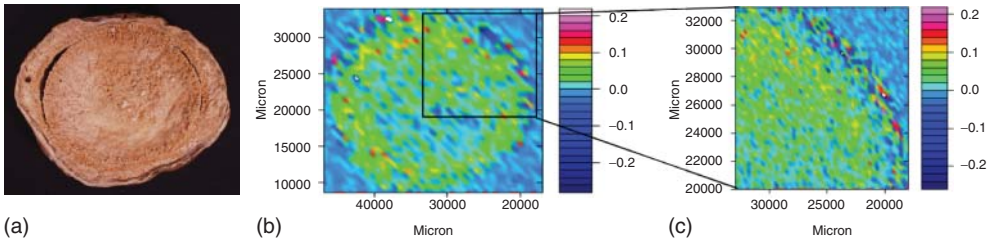

Figure 6.10 Microscopic image of freeze-dried devil's claw root (a) and corresponding micro-Raman mapping measured with an increment of 750 µm (b) and a more detailed map with increments of 300 µm (c). (Reproduced with permission from Ref. [54]. © Wiley Periodicals, Inc.)

Wheat and maize are the two plants in between all agricultural crops, which are most intensively studied by FT-IR and FT-Raman mapping and imaging.

In addition to the analysis of plant tissue in cross sections of stems and seeds and the assignment of chemical components identified by distinct functional groups in the spectra, much work was done on the structural analysis of tissue-related compounds, especially proteins, starch, cellulose, and lignin. Investigations of the secondary structure of proteins, the branching level and monomeric composition of carbohydrates, or the ratio of lignin and cellulose in plant skeletal structures were performed under the focus of breeding progress, plant development, environmental impact, and processing of the crops.

In recent years, an increasing number of investigation deals with the uptake and disposition of environmental contaminants (pollutants, crop protection products) and the following metabolic reactions of the plant.

6.3.1
Tissue-Specific Functional-Group Analysis

First insights into tissue structure and chemical composition relationship analyzed by FT-IR mapping were presented by Reffner in his fundamental work on maize kernels in 1990 [56]. Based on characteristic marker bands in the IR spectra, he was able to assign lipids ($\nu(CH_2)$ at 2920 cm^{-1}, $\nu(C{=}O)$ at 1735 cm^{-1}), proteins ($\nu(NH)$ 3330–3180 cm^{-1}, amide I/II/III at 1650/1520/1290 cm^{-1}), and carbohydrates ($\nu(COC)$ at 1100–1025 cm^{-1}) to the pericarb, aleurone, sub-aleurone endosperm, and endosperm tissue in the cryosections of maize seeds. Three years later, a brief description of wheat seed sections according to the chemical composition identified by FT-IR microspectroscopic mapping followed by Wetzel and Reffner [57]. These findings allowed a qualitative chemical description of different anatomical seed compartments and estimation of their relative quantitative composition.

This band assignment was extended by the results of further FT-IR and FT-Raman studies, which investigated the molecular composition of maize primary cell walls. McCann and coworkers identified the IR signals of differently branched

carbohydrates by neural network analysis and hence could observe a change in the degree of branching during coleoptile development [58]. Another approach of Sené *et al.* shows the perspectives of FT-IR and FT-Raman analyses on taxonomic classification of plant cell walls based on spectral fingerprinting of pectins, proteins, aromatic phenolics, cellulose, and hemicellulose [59].

With the introduction of FPA detection, the analysis of plant material reached a new quality of resolution accompanied by rapid simultaneous recording of a defined sample area instead of single-point measurement. Marcott *et al.* showed the different chemical composition of the germ tissue in wheat seeds. As presented in Figure 6.11, the primary root cells show high content of carbohydrates and proteins (Figure 6.11a,b), whereas the epidermis of the primary root is mainly composed of lipids (Figure 6.11c) compared to the coleorhizae with the highest lipid content and also the greatest spectral variability, indicating a large variety of cell types in this tissue (Figure 6.11d) [60].

Within the grains, also studies on the chemical microstructure of plant tissue and protein secondary structure were performed for barley (*Hordeum vulgare*) and sorghum (*Sorghum bicolor*) [61–63]. By synchrotron radiation infrared microspectroscopy (SR-IMS) mapping, Yu and coworkers investigated the grain tissue of barley and sorghum concerning the main structural components: proteins, lipids, lignin, starch, and cellulose. In accordance with wheat and maize, the same tissue structures (pericarb, seed coat, aleurone, endosperm) could be differentiated based on distinct spectral features. To reduce the influence of sample inhomogeneities, Yu *et al.* discussed the advantages of biological component ratio mapping compared to distribution maps for individual components based on single absorption bands [62]. In a subsequent work on maize, the same group discusses the benefit of multivariate analysis instead of unique band integration especially for signal overlapping in the fingerprint region [64, 65].

6.3.2 Cell Wall Microstructure

6.3.2.1 Carbohydrates and the Endosperm

The mechanical properties of cell walls are determined by the underlying chemical and molecular structures. It has been found that wheat grain hardness is related to the endosperm tissue cohesion, which again is genetically determined [66].

A lot of research on the starchy endosperm of wheat was done by the group around Toole and Mills. Investigating the branching structure of arabinoxylan (AX) in endosperm cell walls by evaluating the COH bending modes at 1075 and 1042 cm^{-1}, they identified the degree of water extractable AX as possible tool for the discrimination of soft and hard wheat cultivars [66]. Subsequent studies showed that the architecture of the endosperm cell wall is already determined at 14 days after anthesis. In addition, the composition alters dynamically from highly to less branched AX during grain filling [67, 68].

Based on these results, 50 different wheat cultivars and later other economically important grains such as spelt, rye, or barley were evaluated concerning the

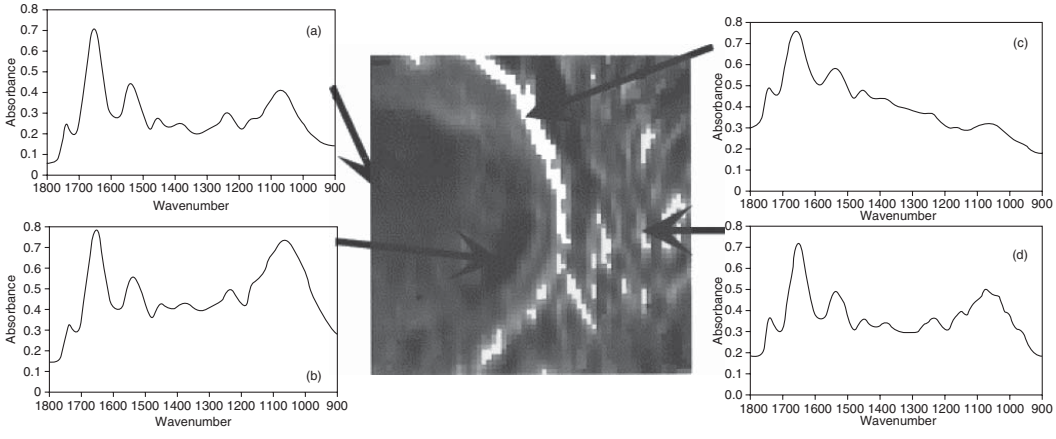

Figure 6.11 IR image taken from inside the germ of an 8 μm thick cross section of a wheat kernel. The lightest pixels represent regions of highest absolute absorbance at 1736 cm^{-1}. IR spectra a, b, c, and d represent the average of about 50–200 pixels from near a region indicated by the corresponding arrow. (Reproduced with permission from Ref. [60]. © Elsevier.)

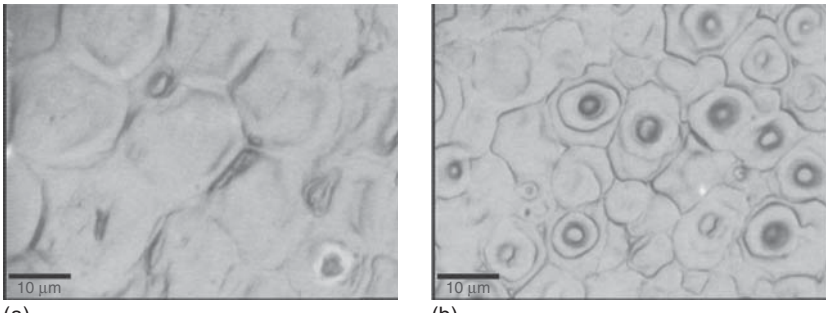

Figure 6.12 Light micrographs of unstained sections from the inner endosperm area of wild type (a) and *ae* mutant maize kernel (b). Scale bars = 10 µm. (Reproduced with permission from Ref. [71]. © Wiley-VCH Verlag GmbH & Co. KGaA.)

ratio of water extractable AX to total AX content [69, 70]. These studies clearly present the correlation of the endosperm cell wall composition and the genetic relationship of the investigated cereals.

The Raman spectroscopic work of Wellner *et al.* focuses on another important biopolymer, the starch [71]. The confocal Raman microspectroscopic study compares the size, distribution, and structure (branching level) of the starch granules found in wild type and *ae* mutant maize [71].

Figure 6.12 shows the light micrographs of unstained sections from the inner endosperm area of wild type (Figure 6.12a) and *ae* mutant (Figure 6.12b) maize kernels, whereas Figure 6.13 presents the corresponding Raman maps.

The Raman band ratios assigned in Figure 6.13 represent the type and degree of branching in the starch polymeric structure: 952 cm^{-1} is assigned to the linear $\alpha(1\rightarrow4)$ D-glucose linkage in the amylose chain (c and d) and 942 cm^{-1} to the $\alpha(1\rightarrow6)$ linkage. The band at 865 cm^{-1} is used as a marker for the crystalline structure of the starch granules (for whole granules, e and f), whereas the band at 486 cm^{-1} is used for describing the crystalline structure inside the granules (g and h). All maps are normalized against the 942 cm^{-1} band as an internal standard for the starch content [71].

As can be seen, the wild-type endosperm is characterized by a generally more uniform size of the starch granules and a homogeneous distribution within indicated by the area maps for proteins in the endosperm cell walls (Figure 6.13a,b). On the other hand, the *ae* mutant shows a higher diversity in shape and size of the granules. Furthermore, the ratio of the signals at 952 and 942 cm^{-1}, representing the ratio of linear-to-branched residues within the starch molecules, indicates a higher $\alpha(1\rightarrow4)$-linkage and a more linear character of the starch molecules in the *ae* mutant compared to the wild type (Figure 6.13c,d).

Figure 6.13 shows the patterns of crystallinity of the starch between different granules (e and f) and within single granules (g and h). Generally, for the wild type, a much higher homogeneity is observed both between and within the granules,

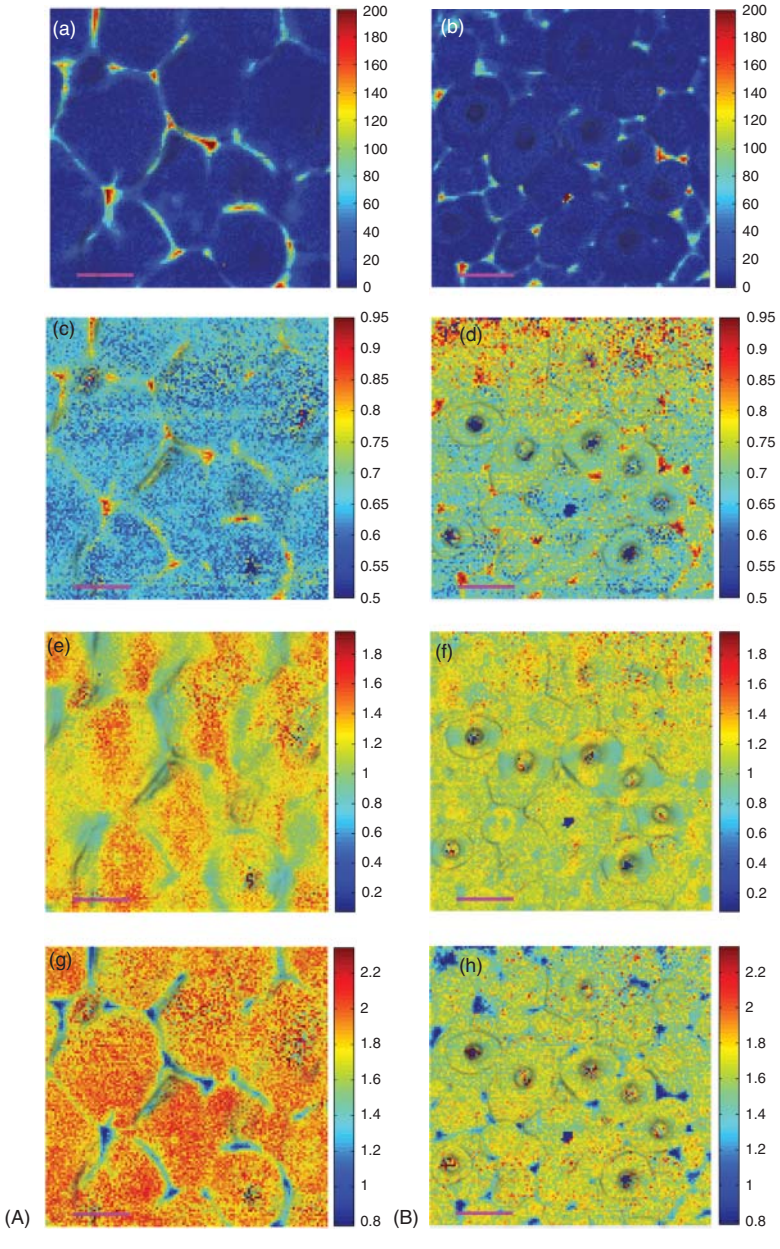

Figure 6.13 Raman maps of the selected inner endosperm region for wild type (A) and *ae* mutant maize (B). The maps are overlaid on the visible images. Scale bars = 10 μm. Area of protein amide I band (1655 cm^{-1}) in wild type (a) and *ae* maize (b); map of the 952/942 cm^{-1} band ratio for the wild type (c) and *ae* maize (d); map of the 865/942 cm^{-1} band ratio for the wild type (e) and *ae* maize (f); and map of the 486/942 cm^{-1} band ratio for the wild type (g) and *ae* maize (h). (Reproduced with permission from Ref. [71]. © Wiley-VCH Verlag GmbH & Co. KGaA.)

whereas for the *ae* mutant, the level of crystallinity seems to be much lower with a random orientation of the crystalline structures.

6.3.2.2 Protein Secondary Structure

In addition to various studies on protein composition and distribution within the plant tissue [72], the influence of protein secondary structure on global crop attributes, such as nutritive values, baking quality, or digestive behavior, achieved increasing interest.

The secondary structure of endosperm protein as either α-helix or β-sheet is generally identified by the line shape and position of the amide I (α-helix $\sim 1650\,cm^{-1}$, β-sheet $\sim 1630\,cm^{-1}$) or amide II band coupled with band modeling processes.

In 1998, Wolkers *et al.* [73] identified changes in the protein secondary structure in association with desiccation tolerance of developing maize embryos by SR-IMS. The same technique was used by Yu *et al.* for comparison of the protein secondary structure of various grains with those of feathers. Feathers contain more than 80% of β-folded protein, whereas grain is mainly composed of α-helix structured protein that is located in higher concentrations only in the endosperm [63, 74].

Wetzel and coworkers used SR-IMS to discriminate different wheat cultivars based on their protein secondary structure. The ratio of α-helix to β-sheet was determined to range from 1.4 to 2.2 for hard and 1.0 for soft wheat cultivars, respectively [75, 76]. Studying the protein content and composition during grain development pointed out an increase in α-helix protein during ripening.

By combination of FT-IR hyperspectral imaging and multivariate curve resolution (MCR) analysis, Budevska *et al.* [77] could identify two separate corn storage proteins, the so-called zeins in maize seed sections. By univariate analysis, these proteins could not be separated from the entire protein complex caused by superimposition of the corresponding amide I signals around $1656\,cm^{-1}$.

6.3.2.3 Lignin and Cellulose

Lignin and cellulose, both highly polymerized biomolecules incorporated in plant cell walls, mainly achieve protective and stabilizing functions. Hence, the properties of the individual tissue are determined by the content and composition of cellulose and lignin. Both compounds can be easily distinguished based on characteristic C=C stretch vibration bands for aromatic structures around 1600 and $1510\,cm^{-1}$ in lignin compared to that of various signals for the stretch vibration of the C–O bonds in cellulose appearing in the range $1400–1000\,cm^{-1}$.

Dokken *et al.* [78] analyzed the increasing degree of lignification in maize and sunflower roots with a growing distance from the root tip by SR-IMS. Applying principle component analysis (PCA), they could clearly distinguish sunflower and maize root epidermis from different root tip distances. Both sunflower and maize can be clearly distinguished based on the content of hydrocinnamic acid ($1635\,cm^{-1}$) in the lignified tissue.

Under the aspect of bioenergy feedstock, Sun *et al.* investigated the lignin and cellulose distribution in corn stover and eucalyptus by hyperspectral Raman imaging. In addition to the analysis of cellulose and lignin distributions in various tissue/cell types, this work is also focused on quantitative comparison of the tissue composition. As shown for corn stover stems, the cellulose content in sclerenchyma cells and tracheids is five times higher than in the parenchyma cells [79].

Zeng *et al.* followed the same approach when comparing wild type and lignin downregulated alfalfa mutants by CARS. With a lateral resolution of around 350 nm, the distribution and relative quantity of lignin were analyzed in native plant cell walls. The strongest decrease of lignin in the mutants compared to the wild type was observed for the cell corners and the compound middle lamella [80].

Based on the degree of lignification in the glume, wheat varieties can be divided into "soft" and "tough" cultivars. The lignin–cellulose ratio of the glume has great impact of the threshing quality as far as low lignin content allows efficient separation of undamaged kernels from husk and straw. Therefore, breeding programs focus on cultivars with soft glume. By FT-IR imaging, the lignin-to-cellulose ratio was determined to be between 1.18 and 1.57 for species with tough glume and between 0.21 and 0.51 in case of soft ones [81]. These findings enable the breeding industry to rapidly evaluate the degree of lignin expression and to distinguish between soft and tough cultivars.

Another important role of lignin and cellulose in the reaction of plant organism to external influences or in consequence of plant development is described by Schreiber *et al.* They investigated the mechanism of contraction of the proximal root in red clover (*Trifolium pratense*) and revealed by confocal Raman mapping that the wood fibers in the root of *T. pratense* have similar microstructural and chemical characteristics like tension wood fibers in angiosperm trees. The analysis showed that the cell wall is composed of a lignified layer (S-layer) and an attached G-layer of cellulose, with high swelling capacity by large water uptake. Together with the microfibril angle of the S-layer, swelling of the G-layer will result in a longitudinal contraction of the fiber observed as root shortening of up to 30% [82].

6.3.3 Environmental Impact and Processing

Vibrational microspectroscopic techniques turned out as a promising tool for breeding control, offering the opportunity of nondestructive analysis of plant material.

The group of Wetzel [83] investigated the process of preharvest germination in intact wheat kernels by near-infrared spectroscopy (NIRS) and mid-infrared spectroscopy (MIRS) FPA imaging. Smail *et al.* [84] could differentiate sprouted and unsprouted wheat kernels based on the developing embryo already 6 h after germination by nondestructive NIRS imaging. A subsequent study by MIR

microspectroscopy determines these differences to a predominance of embryo-related proteins going along with a reduced lipid population in the scutellum [85]. These results were used in a following screening approach of different wheat cultivars for possible premature germination resistance finding. By FPA-NIRS analyses, at least one hard wheat cultivar with higher sprouting resistance could be identified [86]. Figure 6.14 shows the corresponding FT-NIRS images for two wheat varieties with different sensitivity for sprouting. The variety "Betty" (left) showed evidence of early germination already after 6 h of exposure to moisture, indicated by the circles, whereas the cultivar "KS 2174" showed no evidence of sprouting until 24 h (right).

Due to an increased demand for natural fibers, flax undergoes a certain renaissance in agriculture resulting in several vibrational microspectroscopic studies on *Linum usitatissimum.* The group of Himmelsbach *et al.* [87, 88] investigated the chemical composition of flax stem sections with special regard to the cellulose fibers both by FT-IR and FT-Raman spectroscopic studies. It is shown that the flax fibers are mainly composed by cellulose and hemicelluloses, whereas pectins and noncellulosic polysaccharides are found in parenchyma tissue. Based on these findings, in a later work Himmelsbach *et al.* [89] developed a successful approach for enzymatic retting of flax stems using FT-IR mapping for quality control and process optimization.

The optimization of processing by the help of microspectroscopic techniques was also the motivation for Yan and coworkers to investigate the chemical composition of cotton seed coat (CSC) by FT-IR mapping. They wanted to improve the biodegradation of CSC fragments in the process of bioscouring of cotton by identifying enzymes necessary for a successful degradation of this material. By locally resolved analysis of the chemical structure of epidermis, outer pigment layer, palisade layer, and inner pigment layer, they found cutin, waxes, pectins, hemicelluloses, and lignins as undesired contaminants indicating a multienzyme complex as promising for quantitative degradation of CSC [90].

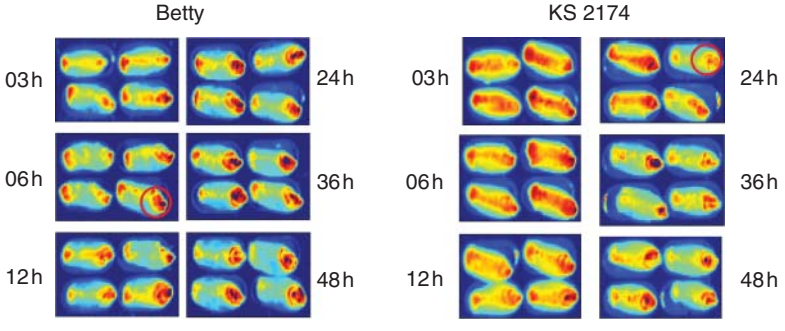

Figure 6.14 Images of two quartets of kernels from hard wheat varieties, Betty and KS 2174, assembled in columns according to the time of exposure of each group of kernels to moist condition that enables sprouting. Left column (top to bottom) 3, 6, and 12 h; right column 24, 36, and 48 h. (Reproduced with permission from Ref. [84]. © Elsevier.)

6.3.4 Uptake and Fate of Environmental Contaminants/Crop Protection Products

The high potential of nondestructive microspectroscopic methods is represented by the increasing number of recent publications, dealing with the uptake and metabolism of environmental contaminants and crop protection products.

Dokken *et al.* could visualize the benzotriazole (BT) uptake and possible lignin incorporation by synchrotron FT-IR mapping of hydroponically grown sunflower root tips. Mapped sections of secondary roots show characteristic aromatic bands of BT, and distribution maps indicate an increased concentration mainly in the xylem gone along with an alteration in the protein production and arrangement [91].

Applying hyperspectral ATR-IR imaging, Budevska investigated the deposition of a commercial insecticide on young cotton leaves with special regard to the quality of the resulting images [92]. It was shown that multivariate approaches can both avoid false-positive or false-negative detection and improve the signal-to-noise ratio. In addition, a quantitative model obtained by target PLS analysis of multiple hyperspectral images with known and unknown concentrations of the analyte is presented [92].

The perspectives of nanotechnology and nanomaterials, for example, carbon nanotubes (CNTs) in modern agriculture and soil remediation led to an increased interest in analyzing possible uptake and plant metabolic reactions.

Miralles *et al.* investigated the uptake of CNT and included impurities in wheat and alfalfa grown on contaminated agar or hydroponic cultures and observed enhanced root elongation in alfalfa and earlier wheat germination. A possible CNT uptake was analyzed by Raman microspectroscopy [93]. CNTs can be clearly identified by Raman spectroscopy based on characteristic signals at 1350 cm^{-1} (D band) and 1585 cm^{-1} (G-Band), respectively. Raman mapping showed adsorbed CNT on the root surface but apparently no uptake into the tissue. Nevertheless, the appearance of signals from not CNT-related functional groups (e.g., carboxylic acid, isothiocyanates) indicates chemical interaction with plant cell walls [93].

An Australian group focused on the quantitative estimation of possible uptake and distribution patterns of ^{14}C-radiolabeled multiwalled CNTs by Raman spectroscopic investigation. Only less than 0.005‰ was taken up by roots of wheat and rapeseed [94]. In agreement with the previous study, Larue *et al.* only found higher intensities on the most peripheral area of the leaf.

Another very recent work on stimulated Raman scattering (SRS) microscopy investigates the distribution of plant epicuticular waxes and the deposition of several agrochemicals on the leaf surface of maize and cotton [95]. Mansfield *et al.* used the region of symmetric and antisymmetric stretch vibration of C–H bonds to distinguish the wax layer (2840 cm^{-1}) from the cell walls (2930 cm^{-1}) in maize and cotton leaves and localized lignin in the leaf vein by its C=C stretching mode around 1600 cm^{-1}. Both crop plants can be clearly distinguished based on their ratio of pectin to cellulose in the cell wall, which indicates higher

content of cellulose in cotton compared with that of pectin-dominated maize cell wall.

For consideration of a possible agrochemical metabolism, azoxystrobin and chlorothalonil as well as deuterated glyphosate were applied to the leaf surface of maize. The characteristic Raman bands of the nitrile groups (C≡N) in azoxystrobin and chlorothalonil around 2225 and 2234 cm^{-1}, respectively, proved to be suitable for the differentiation even of a mixture of both. In case of D_2-glyphosate, where no nitrile group is present in the molecule, the identification is obtained due to the significant Raman signals of the deuterated group between 2150 and 2250 cm^{-1} as shown in Figure 6.15a,b and d. The recrystallization of the agrochemical on the leaf surface is indicated by the distribution maps presented in Figure 6.15c,e [95].

6.4 Mapping and Imaging of Wild Plants and Trees

A multitude of mapping and imaging studies were performed in trees, and here the focus was laid especially on wood [96]. Application of mapping and imaging to wild plants was mainly concentrated on *Arabidopsis thaliana*, used as a model plant with a sequenced genome and many available genetically modified genotypes [91]. Few other wild plants were examined so far, and examples were given at the end of this chapter.

Mapping and imaging techniques in this context are particularly helpful to elucidate the relationship between function and molecular composition of cell walls. Traditional wet chemical analyses cannot solve this problem because the complex ultrafine structure of the cell wall – essential for special cell wall functions – is destroyed during the extraction procedure of the cell wall polymers. Extraction also changes the chemical composition of the cell wall since it requires the breaking of chemical bonds. Advantageously, microspectroscopic mapping and imaging enable the visualization of the chemical composition *in situ*. IR and Raman microspectroscopic studies provide important insights into the overall compositional changes of single fibers and different tissue types. For the investigation of individual cell wall layers, the better spatial resolution of Raman microspectroscopy (maximally 0.3 µm) is necessary.

Consisting mainly of dead plant cells, wood exhibits experimental advantages for mapping and imaging compared to living plant tissue. The structure of wood is stable, and sectioning with a sliding microtome at room temperature with section thickness of 6–20 µm usually gives good results. In plants with high water content, the turgor contributes to the stability of structure. Cutting destroys the cells, and the turgor, therefore, usually cryosectioning is applied to obtain good quality sections with undisturbed cell structure. In addition, the chemical composition of wood sections is comparatively stable and does not significantly change after cutting. Contrarily, in living tissue, solutes might be redistributed due to the sectioning procedure, and the original distribution may be disturbed or volatile

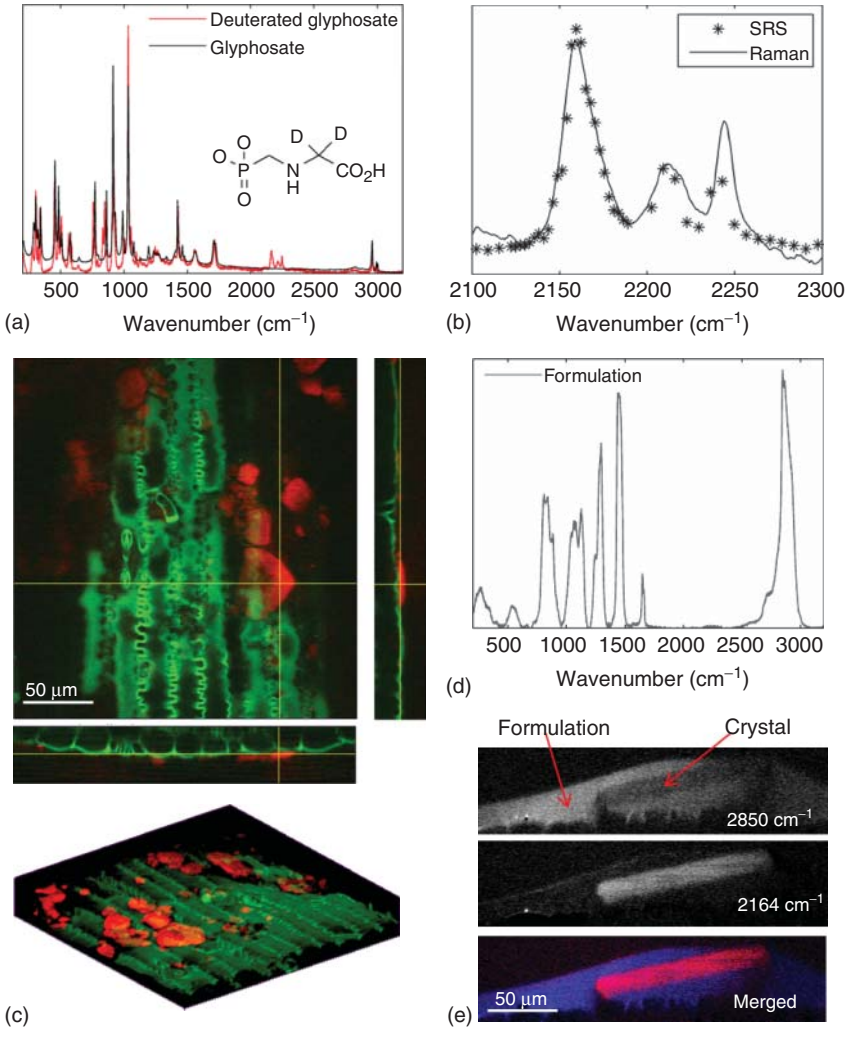

Figure 6.15 Deuterated glyphosate application with formulation onto maize leaves. (a) Spontaneous Raman spectrum of deuterated and nondeuterated glyphosate showing the bands generated in the silent region by deuteration (inset shows the hydrogen atoms within the molecule which have been replaced with deuterium). (b) Stimulated Raman spectra of the C–D bands in the deuterated glyphosate. (c) Deuterated gylphosate crystals on a maize leaf (red, glyphosate; green, cell walls). (d) Spontaneous Raman spectrum of glyphosate formulation showing a very strong band at 2850 cm^{-1} corresponding to CH vibrations in aliphatic chains. (e) Imaging deuterated glyphosate (2164 cm^{-1}) and formulation (2850 cm^{-1}) applied to leaves in the merged image blue = 2850 cm^{-1} and red = 2164 cm^{-1}. (Reproduced with permission from Ref. [95]. © American Chemical Society.)

substances such as essential oils might evaporate and be lost prior to measurement. Also embedding, in order to preserve the cell structure, comprises the risk of chemical redistributions and changes and therefore should be avoided.

6.4.1 Mapping and Imaging of Trees

6.4.1.1 IR Mapping and Imaging of Trees

To illustrate the potential of IR microspectroscopy in combination with a FPA detector, the lignin distribution in cross sections of beech (*Fagus sylvatica* L.) and poplar (*Populus* × *canescens*) wood was analyzed by calculating chemical images of the lignin-specific band (Figure 6.16) [97, 98]. Even the thin poplar cell walls of about 2 µm thickness could be resolved. Computation of the guaiacyl–syringyl lignin ratio showed high values for some parts of vessel cell walls.

The chemical image associated with syringyl lignin in longitudinal poplar sections suggested a higher lignin content in the outer bark than in the inner bark and a lower content in the cambium between the inner bark and the xylem [99, 100]. The crystallinity index of cellulose, which effects physical, mechanical, and chemical properties of cell walls, can be examined spatially resolved [100–102].

The fibers encircling the vessels in *Populus tremula* show a chemotype with higher lignin content compared to fibers in fiber-rich regions [103]. In addition, an increased lignin content was found in the narrow band of parenchyma cells at the annual ring [103]. This probably reflects the thick primary cell wall and the additional wall layer described for this cell type.

Synchrotron IR imaging of cross sections of *Populus trichocarpa* stems revealed the distribution of aromatic compounds, fatty oils and waxes, acyl esters, proteins, lignin, and polysaccharides [104]. Acyl esters showed a close spatial distribution with cell wall polysaccharides.

Genetic modification of the lignin biosynthesis by downregulation of the cinnamoyl-coenzyme A reductase in poplar (*P. tremula* × *Populus alba*) decreased the lignin content and increased breakdown or remodeling of noncellulosic cell wall polymers as supported by FT-IR analysis [105].

In combination with polarization modulation, synchrotron IR microspectroscopy of single spruce fibers (*Picea abies* L.) provided information on hydrogen bonding, orientation, and accessibility of structural units to heavy water and dimethylacetamide applied in a custom-built microfluidic cuvette [106]. A tabulated overview about the assignments of hydrogen bonds and their orientation is also provided by the authors.

As already mentioned in Section 6.2.4, the macromolecular composition of transverse leaf sections of *E. botryoides* was investigated by Heraud *et al.* [39] comparing synchrotron mapping and FPA imaging. Both methods produced similar IR images, which resolved chemical differences at the single cell level and differentiated all tissue types in the leaves. Despite the slightly lower spatial resolution and a reduced signal-to-noise ratio, in terms of data acquisition time,

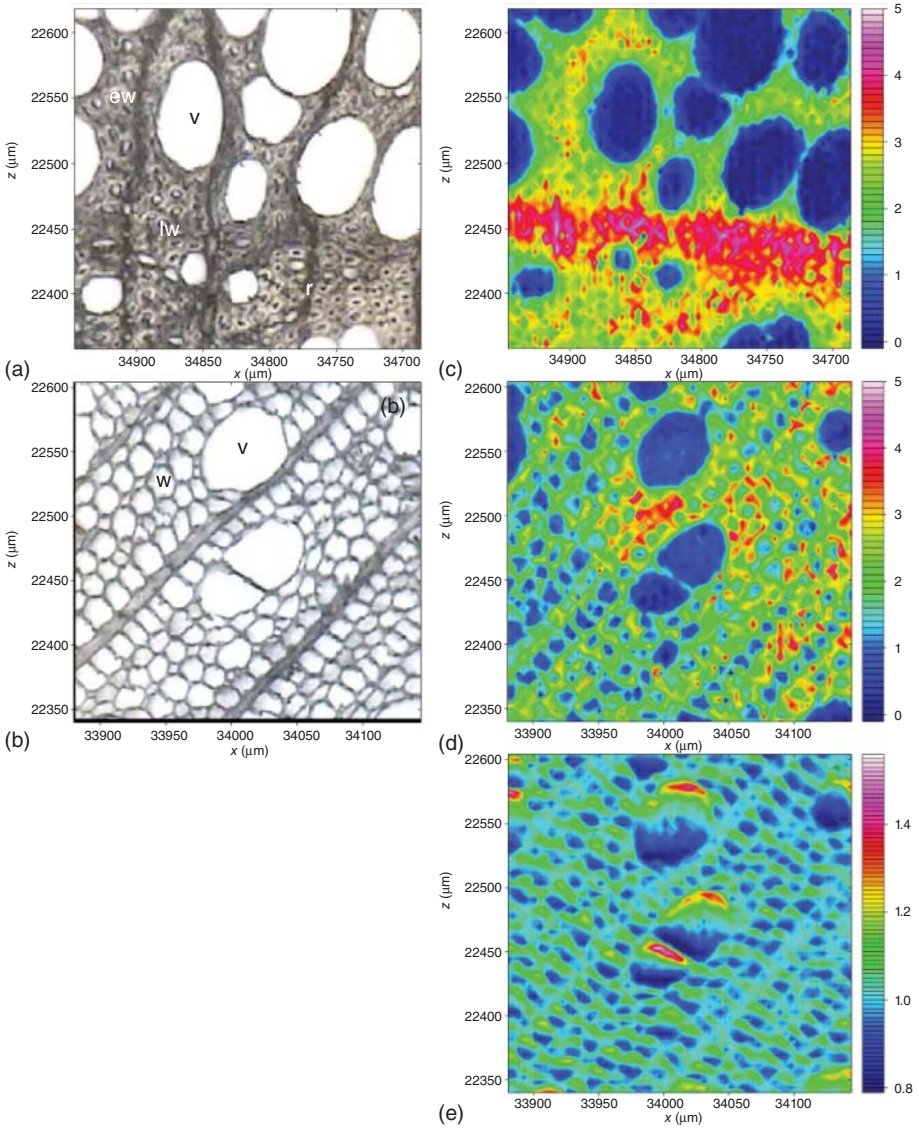

Figure 6.16 Light microscopic view of beech (a) and poplar (b) wood cross sections with vessels (v), wood fibers (w) in the late (l) or early (e) wood and xylem rays (r). The corresponding FPA images for beech (c) and poplar (d) are integrated in the range 1530–1490 cm^{-1}. The distribution of the ratio at 1508/1320 cm^{-1}, tentatively assignable to the guaiacyl–syringyl lignin ratio, is shown in (e). The color scale represents increasing lignin content from blue (low) to pink (high). (Reproduced with permission from Ref. [97]. © Springer.)

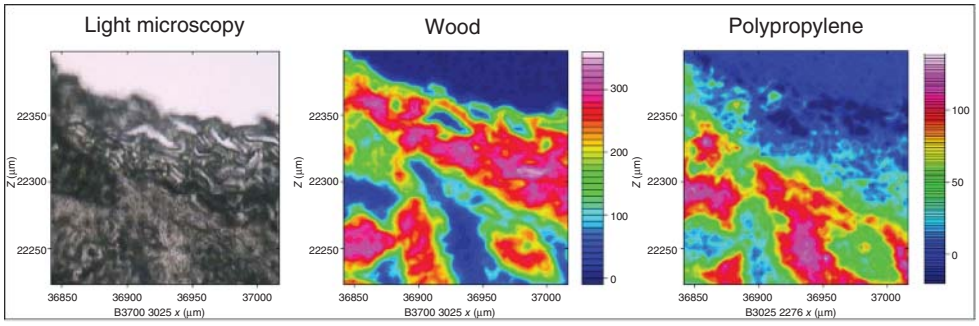

Figure 6.17 Light microscopic and FT-IR images of wood–plastic composite section with integration of FT-IR regions specific for wood (3700–3025 cm^{-1}) and polypropylene (3025–2276 cm^{-1}). (Reproduced with permission from Ref. [107]. © Elsevier.)

expense and ease of use, FPA imaging offers a convenient, laboratory-based approach to microscopic chemical imaging of leaves.

It has been found that IR imaging enables visualizing the distribution of not only wood compounds but also wood particles in the polymer matrix within wood–plastic composites (Figure 6.17) [107]. The interaction at the interphase between wood and polymers, glue, or paint is often critical for product performance and can be investigated accurately using IR spectroscopy [99].

6.4.1.2 Raman Mapping and Imaging of Trees

During the last years, various wood species have been investigated by Raman mapping with the aim to image the macromolecular composition of cell wall layers at high spatial resolution.

Applying polarized Raman spectroscopy, Gierlinger and Schwanninger [10, 108] visualized the lignin and cellulose distribution of poplar (Figure 6.18). Moreover, using orientation-sensitive Raman bands, they elucidated the orientation of the cellulose molecules and the phenyl ring of lignin with respect to the wood fiber axis.

In tension wood (reaction wood in angiosperms), the imaging technique enabled even the differentiation of a lignin layer thinner than 5 µm toward the lumen of the cellulosic gelatinous layer. Also the gelatinous layer of tension wood in maple (*Acer* spp.), beech (*F. sylvatica*), and oak (*Quercus robur*) contained aromatic, lignin-like compounds; however, the first two species exhibited only a very low amount [109]. In reaction wood of the tropical species *Laetia procera*, two 1 µm thick layers of cellulose with a high angle with respect to the fiber axis were detected [110]. In spruce (*P. abies*), the dependence between cellulose and laser orientation direction was successfully used to establish models for predicting the microfibril angles in normal, opposite, and compression wood [111]. Glucomannan and xylan appeared to have a parallel orientation with regard to the orientation of cellulose in spruce and, in all probability, an almost parallel orientation with regard to the fiber axis [112].

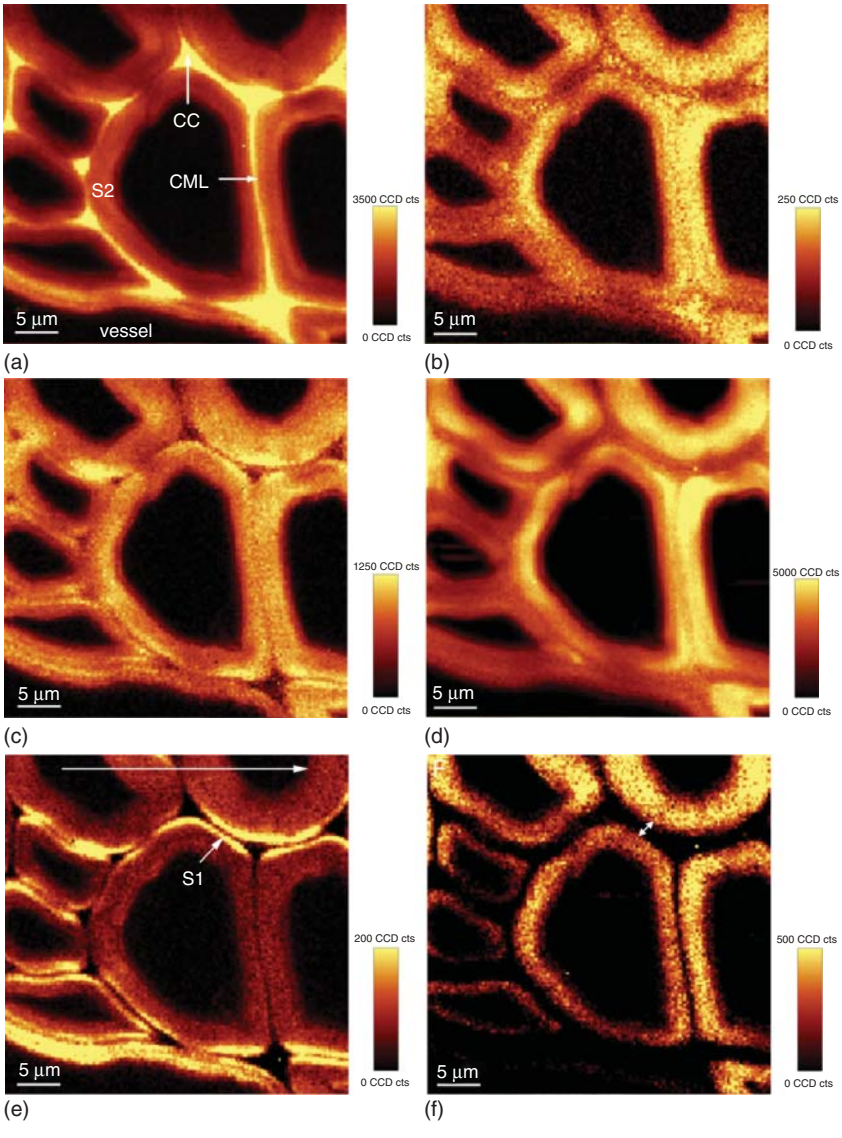

Figure 6.18 (a–f) Raman images (40 µm × 40 µm) of a cross section of poplar wood calculated by integrating from 1540 to 1760 cm^{-1} (a, lignin), 352 to 401 cm^{-1} (b, cellulose), 1178 to 1001 cm^{-1} (c, cellulose), 2769 to 3043 cm^{-1} (d, cellulose) and very restricted wavenumber ranges to accentuate the orientation-sensitive cellulose band at 1097 cm^{-1} (1114 to 1079 cm^{-1}, e) and 2898 cm^{-1} (2931 to 2819 cm^{-1}, f). The big arrow in (e) indicates the direction of laser polarization. (Reproduced with permission from Ref. [10]. © IOS Press.)

Also imaging of the distribution of coniferyl aldehyde and coniferyl alcohol, phenylpropanes and two of the many substructures in lignin, was feasable by Raman microspectroscopy. In *Picea marina,* the distribution of coniferyl aldehyde and coniferyl alcohol was similar to the lignin distribution and no enrichment in particular cell wall layers was detected [113]. Using coniferyl aldehyde/lignin and coniferyl alcohol/lignin ratios instead of a band range, a clear distinction in the distribution of coniferyl aldehydes and coniferyl alcohols in cell wall layers was observed between pine (*Pinus sylvestris*) and spruce (*P. abies*) [114]. Compositional heterogeneity of lignin and cellulose was additionally imaged in wood cell walls of *F. sylvatica* and in combination with coniferyl alcohol and aldehyde as well in *Cornus alba* using confocal Raman microspectroscopy [115, 116].

To overcome the problem of high spectral overlap of lignin, cellulose, and hemicelluloses, Perera *et al.* [117] used k-means clustering in order to reconstruct cell wall images of poplar (*P. trichocarpa*) with cluster identities (Figure 6.19). Here, 10 average spectra represent each of the 10 clusters (Figure 6.20). With the help of estimated pure component spectra of lignin and carbohydrates, the relative distribution in the cell wall image was calculated.

A detailed protocol for imaging of plant cell walls by Raman imaging is summarized in Gierlinger *et al.* [118].

Crystallinity of cellulose could be determined spatially resolved based on the experimental work described by Agarwal *et al.* [119].

As an appraoch to improve the efficiency of wood saccharification, transgenic reduction of lignin is promising. The lignification of wild type and lignin-reduced transgenic *P. trichocarpa* stem wood was compared using confocal

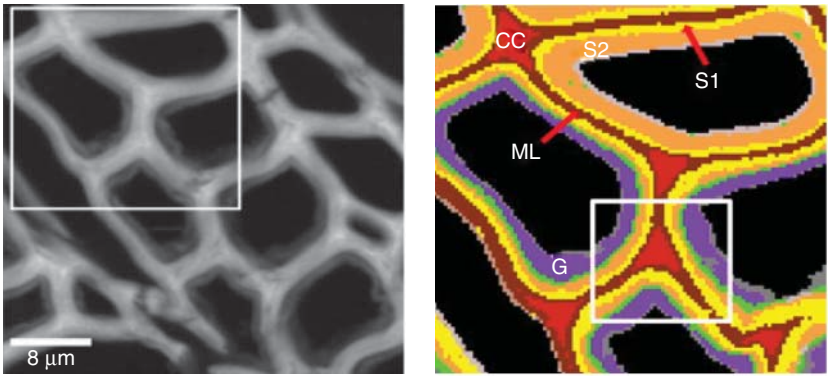

(a) (b)

Figure 6.19 Confocal Raman image of xylem cells of wild type *P. trichocarpa*: (a) CH intensity image (WITec 1.94 software) and (b) reconstructed image of the marked rectangle in (a) with 10 clusters. Colors in (b) are arbitrary and provide visual contrast of the clusters. Most significant layers of the cell wall are indicated (CC, cell corner; ML, middle lamella; S1–S1 layer; S2–S2 layer; G–G layer). (Reproduced with permission from Ref. [117]. © Elsevier.)

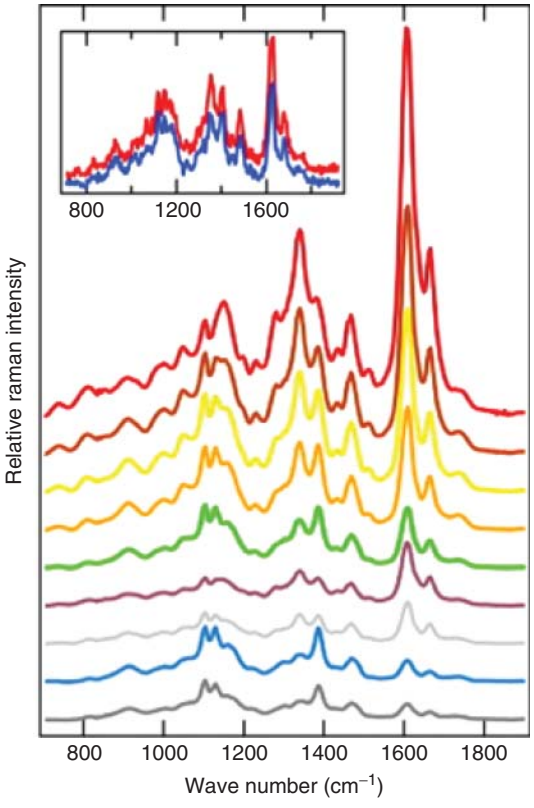

Figure 6.20 Average cluster spectra obtained from *P. trichocarpa* (lumen excluded). Spectra were vertically offset for clarity. Colors of the spectra correspond to different cell wall layers with the same color in Figure 6.19. Inset: Two representative original Raman spectra of the cell wall with significant noise contribution. (Reproduced with permission from Ref. [117]. © Elsevier.)

Raman microspectroscopy [120]. Transgenic reduction of lignin was particularly pronounced in the S2 cell wall layer (thickest sublayer of secondary cell wall, according to Gierlinger and Schwanninger) [108] of fibers. Further examples of the use of genetically modified genotypes will be given in the following chapter especially related to *Arabidopsis.*

6.4.2
Mapping and Imaging of *Arabidopsis thaliana*

6.4.2.1 IR Mapping and Imaging

Since the genome sequence of *A. thaliana* became available in 2000, a multitude of studies made use of this model plant in order to combine functional genomics and spectroscopic analysis, especially to elucidate the complex biosynthetic pathways involved in the buildup of the cell wall. Numerous mutants were designed

with deficiencies in cellulose, pectin, lignin, cutin, and other cell wall polysaccharides. In their pioneering work, McCann and coworkers and later also Höfte and coworkers explored the potential of IR microspectroscopy to identify and classify such mutants and the effects of chemical treatments [121–127]. Dokken *et al.* gave an overview on the use of IR microspectroscopy for the characterization of wild type and genetically as well as chemically modified genotypes [128].

IR imaging is especially suited for cell-specific chemotyping. In combination with multivariate imaging (orthogonal projections to latent structures, OPLS), separation of fibers and vessels was successful and the related spectral features were revealed [103]. Comparison of an *Arabidopsis* wild type with a mutant deficient in xylan biosynthesis demonstrated the importance of the *fra8* gene for xylan biosynthesis in both lignified and nonlignified fibers of the secondary xylem of the *Arabidopsis* hypocotyl [103]. A two-class model, established to separate vessels and fibers in the outer lignified xylem, resulted in numerous unclassified pixels in the inner nonlignified xylem and the epidermis. Thus, cell wall chemotypes unknown to a model can be localized.

Fast mapping with a single element detector enabled the simultaneous assessment of cutin and cell wall polysaccharides in whole *Arabidopsis* petals [129]. The petals show a characteristic zoning with high amount of aliphatic compounds and esters in the lamina and of polysaccharides in the stalk of the petals (Figure 6.21). Mutants in cutin deposition showed not only reduced intensities assigned to esters and aliphatic compounds compared to that of the wild type, but also changes in other compound classes.

To examine the impact of invertase and sucrose synthase on the entry of carbon into the metabolism and thus plant growth and cell wall development, the cellulose distribution of sucrose synthase-deficient mutants was imaged [130]. FT-IR imaging of stem sections revealed no differences between the wild type and mutants at IR regions dominated by cellulose. Average spectra of wild types and mutants – irrespective of whether representing cortex, phloem, xylem, and interfascicular tissue – resembled each other to a high degree in the carbohydrate region.

6.4.2.2 Raman Mapping and Imaging

As already mentioned earlier, the high autofluorescence of green plant samples disturbs Raman imaging by obscuring Raman bands. To overcome this problem, Schmidt *et al.* [131] used senescent plants produced by not watering the plants for 3 weeks . This procedure enabled imaging of lignin and carbohydrates in stem sections of *Arabisopsis thaliana*. The authors demonstrate that a chemometric approach can make hemicelluloses and pectin accessible.

6.4.3 Mapping and Imaging of Wild Plants

Among higher terrestrial plants, horsetail species (*Equisetum* spp.) are well known as *strong accumulators of silicon*. In addition to X-ray element mapping,

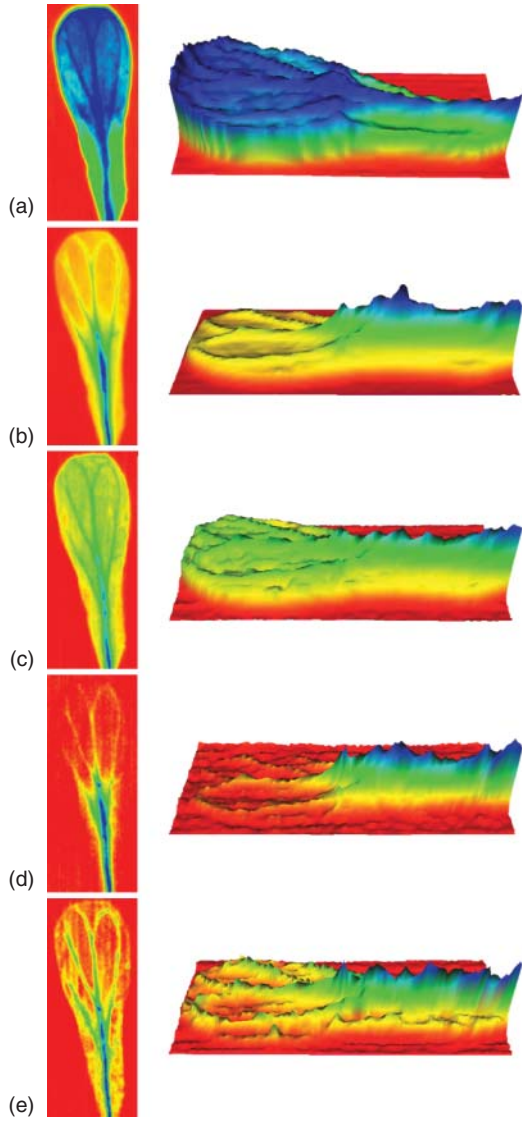

Figure 6.21 FT-IR imaging: absorbance maps obtained on the basis of the second derivative of spectra for esters of fatty acids at 1734 cm^{-1} (a), amides at 1656 cm^{-1} (b), unidentified pattern 1 (UNP1; potentially cellulose) at 1106 cm^{-1} (c), UNP2 (potentially hemicellulose) at 1454 cm^{-1} (d), and UNP3 (potentially lignin) at 1508 cm^{-1} (e). More negative intensities (high concentration) are indicated in dark blue; the zero level is indicated in red. (Reproduced with permission from Ref. [129]. © John Wiley & Sons Ltd.)

Raman microspectroscopy has been successfully applied to study the distribution and nanostructure of silica in the internodes of *Equisetum hyemale* [132]. The authors identified the predominant silification pattern as a thin layer on the entire outer epidermis with the highest density in particular knob regions containing up to 33 wt% of pure hydrated amorphous silica. To image the distribution of silica and free silanol groups, signals in the regions of 245–570 cm^{-1} (in plane Si–O–Si vibrations) and 937–993 cm^{-1} (surface and internal Si–OH stretching) were integrated. In the epidermal layer and hypodermal sterome, no silanol groups were found [133]. The silica was therefore supposed to be closely associated with polysaccharides (cellulose, hemicelluloses, pectin).

Applying resonance Raman (RR) spectroscopy with excitation in the UV range, the walls of xylem cells from the rhizome of the fern *Dennstaedtia cicutaria* were analyzed [134]. In order to avoid any thermal damages of the plant tissue, the laser energy was reduced to 0.04 mW and measuring time was limited to 1–2 s. Up to 90 UV-RR spectra were acquired along the individual single cell wall segments resulting in a much higher signal-to-noise ratio when compared to single-point spectra.

6.5 Application of Mapping and Imaging to Algae

The term *algae* summarizes a great variety of more than 10 000 life forms with very diverse morphological structures and cell composition but unique in their dependency of moisture and light. The great variability of these species is responsible for their high ability of adaption to various environmental conditions for which reason algae may not only occur in marine and sweet water biotopes but also under aerial conditions on trees and stones (*Trentepohlia aurea*) [135], in terrestrial habitats like forest soil (*Fritschiella tuberosa*) [136], or even on snowfields in the mountains (*Chlamydomonas nivalis*) [137].

Going along with high morphological diversity (cell size ranges from single micrometer up to several hundred micrometers) and environmental situations in the natural habitat, the experimental setup for algae analysis by vibrational spectroscopy has to be adapted to the scientific point of interest in each case.

The introduction of microspectrosopy by coupling IR and Raman spectroscopic studies with confocal microscopes directed the research focus away from the chemical analysis of macroscopic assemblies (biofilms, whole algae communities) or extracts [138, 139] to the point of studies on single individuals [140, 141] and even to the (sub)cellular level of individual cells [142, 143]. The introduction of mapping and imaging techniques enlarged the scientific view to distributional analysis in addition to the classical qualitative and quantitative determination.

6.5.1
Taxonomic Differentiation and Classification of Algae

In their review from 2009, Murdock and Wetzel give a comprehensive summary of IR microspectroscopic research on algae since its early beginning in 1993 [144].

In addition to few reports about red algae, dinoflagellates, or euglenoids, the most experimental work investigates one of the three groups of algae uniting the majority of identified species: green algae, diatoms, and cyanobacteria. Even if the latter belong to the *prokaryote*s, cyanobacteria are often subsumed to the group of algae because of their ability to practice photosynthesis and their possible role as progenitor of the chloroplasts.

As far as these three groups of algae differ significantly in their composition due to immense structural and chemical variation, they can be clearly distinguished by their unique IR spectral features as shown by Murdock and Wetzel [144].

The spectra given in Figure 6.22 show highest variation in the fingerprint region, which is characterized by strong carbohydrate absorptions in the range 1200 – 900 cm^{-1} for green algae (top), a prominent siloxane signal between 1100 and 1060 cm^{-1} in diatoms (center), and intensive lipid and amide bands for the cyanobacteria (bottom) around 1740 and 1650/1540 cm^{-1}, respectively.

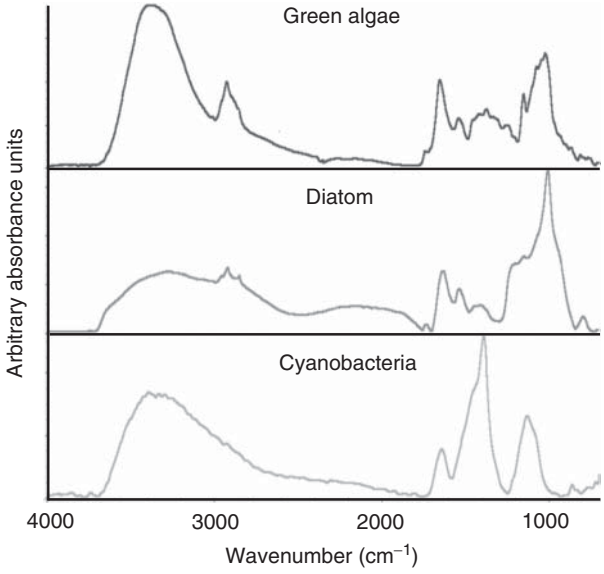

Figure 6.22 Typical spectra for three dominant algal groups: green algae, diatoms, and cyanobacteria. Distinct differences include abundant carbohydrates (1200 – 900 cm^{-1}) in green algae and a prominent silica band (~1060 cm^{-1}) in diatoms. Spectra of cyanobacteria are similar to those of green algae but often have more distinct protein bands and lack cellulose, particularly in cell walls. (Reproduced with permission from Ref. [144]. © Taylor & Francis.)

These differences in the macromolecular patterns are related to variations in the cell wall composition (cellulose, pectin, silica, peptidoglycan), energy storage molecules (starch, lipids, glycogen), or pigments (carotenoids, chlorophylls, xanthophylls).

Due to the high variation in the chemical composition, one of the main scientific aims is to investigate species discrimination and classification by FT-IR spectroscopy [141, 145–147]. As far as environmental conditions and nutrient availability strongly influence the chemical composition in the cells and hence the observed bands and intensities in the resulting spectra, not only different genera but even individuals of the same species with different spatial origin can be distinguished [148].

6.5.2 Cell Wall Composition and Compound Distribution

In addition to the taxonomic approach, investigating the distribution of bioactive macromolecules within the organism as well as construction and changes of algal cell wall is essential for a better understanding of environmental adaption and species-specific responses to nutritional conditions.

With introduction of FPA detection, the technical device for a fast and simultaneous recording of IR spectra over a defined sample area and a better detection limit was given. In addition, the development of Raman methods such as CARS, SERS, and SRS could overcome basic problems such as low Raman scattering of cross sections and high sample fluorescence and, hence, opened it for the application in algae analysis.

In a recent study, Kammer *et al.* [149] have identified a not yet known inorganic constituent in the honeycomb-like silicon cell wall structure of the diatom *Stephanopyxir turris* by Raman mapping and FT-IR imaging. As shown in Figure 6.23, the prominent band at 970 cm^{-1} characterizes the silicon-containing structures [149].

Although cell wall compounds of algae and their chemical structures are mostly known to date, their interaction and spatial arrangement inside the cell wall architecture still remains challenging.

Investigating the cell wall polymer structure and arrangement in green seaweed *Codium fragile* by synchrotron FT-IR, Estevez and coworkers found a gradient of (1-4)-β-D-mannan from the boundaries toward the center of mucron cell walls by increasing carbohydrate band intensities at 1151, 1092, 1061, and 1032 cm^{-1}, respectively [150].

The Raman spectroscopic study of Collins *et al.* [151] focuses on the distribution analysis of astaxanthin (ATX), β-carotene, and chlorophyll within cells of *Haematococcus pluvialis* by MCR. Kaczor and colleagues investigated single cells of the same species both *in situ* and *in vivo* by FT-Raman mapping. It was shown that the cells accumulate ATX under stress conditions up to 4% of dry weight, and the distribution of ATX changes according to the algal life cycle. The results also indicate that the molecular structure of ATX in the cell differs from that of

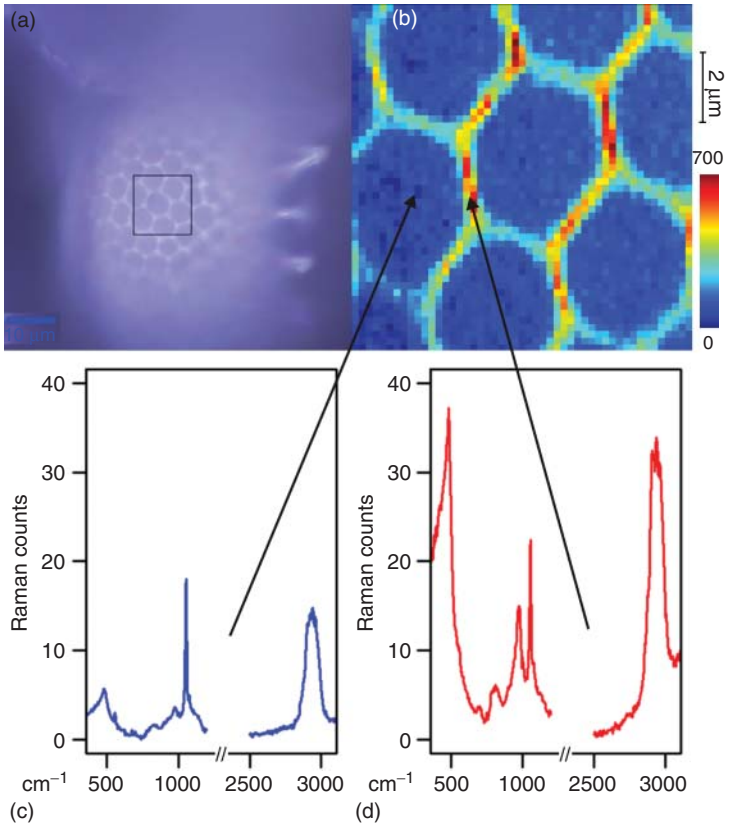

Figure 6.23 Photomicrograph of *S. turris* (a). The Raman map was taken from the boxed region with 488 nm excitation wavelength and 200 nm step size (b) and shows the intensity distribution of the band at 970 cm^{-1}, that is, the silica distribution. Representative spectra for the bottom layer region (c) and the highly silicified honeycomb-like structures (d) are also shown. (Reproduced with permission from Ref. [149]. © Springer.)

synthetic standard possibly because of the chemical surrounding in the cell [152]. Figure 6.24 presents such a *H. pluvialis* cell after collapsing of the cytoplasm (last stage of life cycle) and the resulting inhomogeneous ATX distribution.

Another Raman study visualized the gradient of carotenoids in the diffusion boundary layer around the cells of the brown alga *Fucus vesiculosus* and green alga *Ulva* sp. [153].

The investigation of the lateral distribution of fucoxanthin on the algal surface resulted in the surprising detection of a release of nonpolar carotenoids into the polar aqueous surrounding with estimated concentrations decreasing from 4 mM directly on the algal surface down to 0.09 mM at the distance of 150 µm to the alga.

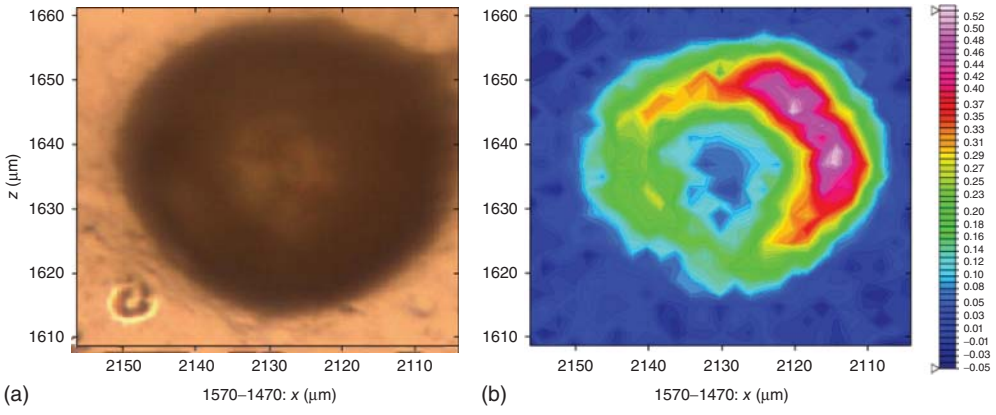

Figure 6.24 Visual image focused inside of the *Haematococcus pluvialis* cell with the collapsed cytoplasm (a, magnification 40×) and distribution of ATX in the same cell obtained by integration of the marker band at 1520 cm^{-1} (b, color code defined in the scale). The map was obtained by measuring 729 points (the distance between points on the *x* and *z* axes equals 2.0 μm). (Reproduced with permission from Ref. [152]. © Royal Society of Chemistry.)

Using CARS, Dementjev and coworkers visualized the ring shape distribution of carotenoids in the two considered diatoms *Nostoc commune* and *Nostoc* sp. and the green alga *Chlorella* sp. [142].

6.5.3
Environmental Influences on Algae Metabolism

Algae possess a high ability of adaption to changing environmental conditions and diminishment of aquatic pollution. Hence, understanding of the related metabolic processes is necessary for utilization of this capability.

In the past, ecological, environmental, nutritional, and fossil questions regarding algae were investigated by "single spectrum" IR or Raman spectroscopy. For example, the macromolecular profile of algae species under nutrient stress (e.g., limited supply of N or P) was investigated [154, 155]. Further studies also deal with the *in vivo* lipid profiling of oil-producing microalgae concerning the degree of unsaturation and transition temperature for possible application as algal biodiesel [156].

With the introduction of imaging techniques, the investigation of algal metabolic processes reached a new kind of quality, insofar as changes in the qualitative and quantitative composition could now be spatialized to distinct areas in the cell or cell wall [157].

Hirschmugl *et al.* could observe changes in the overall protein and lipid content in reaction to changing nutrient supply only on an overall level, whereas Heraud and coworkers and later Patel *et al.* could assign changing lipid and protein concentrations in *Micrasterias hardyi* in reaction to nutrient deficiency or the

influence of polluting pharmaceutical ingredients to distinct cell components such as chloroplasts, nucleus, or lipid storage areas [143, 158]. In addition, by using IR transparent flow-through cells, Heraud *et al.* and Patel *et al.* were able to *measure in vivo* cells of *M. hardyi* [143, 158].

Figure 6.25 nicely presents the lipid and protein distributions in untreated cells of *M. hardyi* with high accumulations of both compound classes in the center of the cells.

In contrast, the images shown in Figure 6.26 reveal a dramatic decrease of proteins in the cell center after exposition to various active pharmaceutical ingredients (APIs) such as propranolol (Ai), metoprolol (Bi), and mefenamic acid (Ci) based on changes of the amide I band at 1625 cm^{-1}.

The lipid levels determined by the stretch vibrations at 2946 cm^{-1} differ only slightly in cells treated with mefenamic acid and metoprolol (Figure 6.26 Bii and

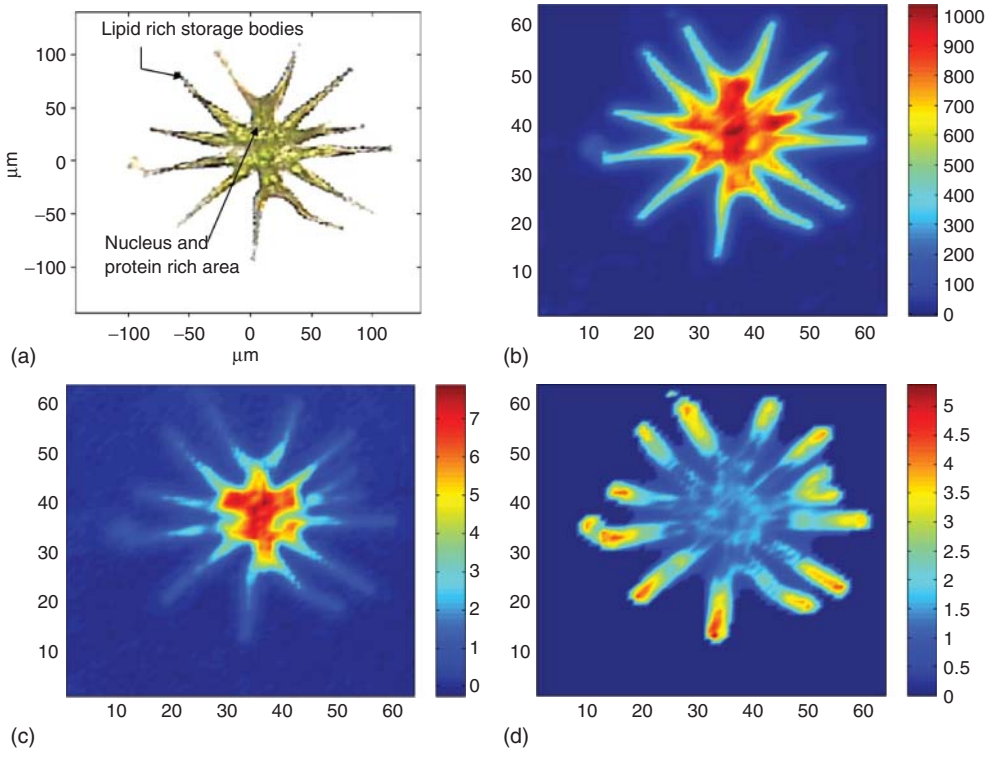

Figure 6.25 (a) Photomicrograph image of *M. hardyi*. FT-IR images of *M. hardyi* are based on the results of (b) the total IR signal absorbed by the sample and the surrounding area, (c) the integration under the amide I band (cm^{-1}), (d) the ratio of the lipid:protein (cm^{-1}) bands. The rainbow map represents the intensity of the IR signal absorbed, red showing high and blue showing low. The FT-IR image was collected using a 64 × 64 FPA detector, generating 4096 spectra giving a spatial resolution of ~4 µm (while we of course recognize that this is effectively diffraction limited at 10 µm). (Reproduced with permission from Ref. [158]. © Royal Society of Chemistry.)

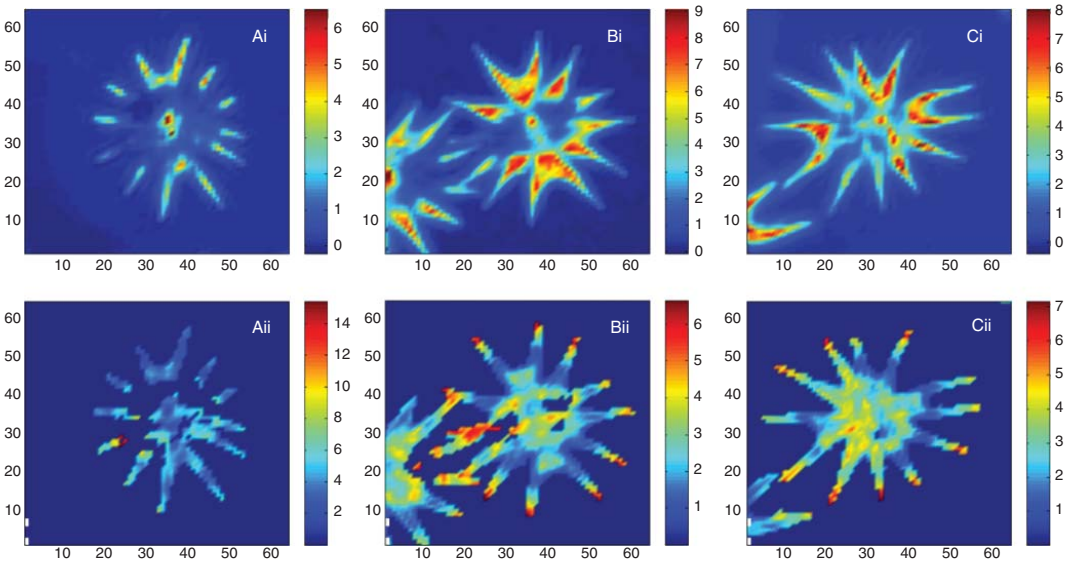

Figure 6.26 FT-IR images of *M. hardyi* showing changes in protein (i) and lipid (ii) levels after treatment with (A) propranolol, (B) mefenamic acid, and (C) metoprolol at concentrations of 0.002, 0.01, and 0.01 mM, respectively. Images were taken using a 64 × 64 FPA detector, generating 4096 spectra giving a spatial resolution of ~4 μm. (Reproduced with permission from Ref. [158]. © Royal Society of Chemistry.)

Cii, respectively), whereas only propranolol caused a considerable loss of lipids in the cells (Figure 6.26 Aii).

Murdock and coworker [159] studied the nitrogen uptake and incorporation in the benthic macro alga *Cladophora glomerata* collected in natural assemblage by application of ^{15}N labeled $K^{15}NO_3$ serving as nitrogen source. This interesting approach allows tracking the temporal nutrient uptake in the IR spectra on filament, cellular, and subcellular levels by observation of the shifting amide II band due to incorporation of ^{15}N into the proteins (^{14}N amide II at 1545 cm^{-1}shifting to ^{15}N amide II band at 1535 cm^{-1}) [159].

In a later study, Murdock *et al.* investigated difference in the nutrient distribution in single cell diatoms *Achnanthes affinis* and colonial diatoms *Fragilaria virescens*, as well as changes in the relative chemical composition over time under reduced nutrient supply [160].

With relation to a possible use for biofuel production, Huang and coworkers analyzed different growth conditions for enhancing the lipid production of *Chlorella sorokiniana* and *Neuchloris oleabundans.* By confocal Raman mapping of single cells, they found that nitrogen starvation leads to production of triglycerides in the algal cells [161].

6.5.4
Chemometrical and Instrumental Developments

In addition to their interesting biological findings, the following publications are predominantly discussed under the focus of spectral quality enhancement by chemometrical and technical developments.

6.5.4.1 Raman Techniques

Introducing a new multivariate method based on targeted orthogonal partial least squares (T-OPLS) analysis, Abbas *et al.* could display even small changes of carotenoid distribution within algae cells of *Dunailella* (*Chlamydomonadales*) and *Phaeodactylum* (diatoms) [162].

This method offers the evaluation of spectra showing strong background noise and only low spectral variation and the prediction of the relative carotenoid concentration by using only a single reference spectrum. In addition, this reference compound does not need to be structurally identical to the target compound, as demonstrated for the predicted versus measured target spectrum for carotenoids [162].

In a later work combining the T-OPLS approach with SERS, the successful detection of 1,1,3,3-tetrabromo-2-2-heptanone (THB), an antibacterial substance of the red alga *Bonnemaisonia hamifera*, at the concentration levels around some tens of femtograms per square micrometers is presented [163].

By the use of gold colloids (60 nm particle size) covered with a monolayer of 4-mercaptobenzonitrile serving as an internal standard for normalization of variations in the SERS effect, Abbas and coworkers could accurately calculate the distribution of THB over cell surfaces and close vicinity [163].

Another approach for the quantitative determination of bioactive compounds such as lipids, pigments, and proteins in *Botrycoccus braunii* microalgae cultures was based on SRS as an alternative to CARS microspectroscopy and allowed a straightforward image interpretation, as long as nonresonant background problems are avoided [164]. The authors compared biomass production within single cells under different lighting conditions: continuous illumination and a 12 h light–dark cycle. It was shown that continuous illumination leads to an increased concentration of all components, mostly for pigments (95%) followed by lipids (68%) and proteins (56%).

Oh and coworkers [165] successfully designed a special Raman approach based on statistic filters and PLS in data processing for a real-time assessment of glucose content on microalgae.

6.5.4.2 IR Techniques

Tan *et al.* [166] present the potential of a new chemometric method (band target entropy minimization combined with multilinear regression, BTEM-MLR) for estimating the concentration maps of four significant components associated with cellular water, α-helical proteins, lipids, and spectral aberration in FPA images [166].

Species, such as the considered *Nanochloropsis* sp., causing Mie-type scattering due to its nominal cell size of about 5 µm result in distorted FT-IR spectra [167]. By application of an RMieS-EMSC algorithm (extended multiplicative signal correction modified by resonant Mie-scattering correction) created by Gardner and coworkers, Tan *et al.* avoid influences of Mie-type scattering [166, 168].

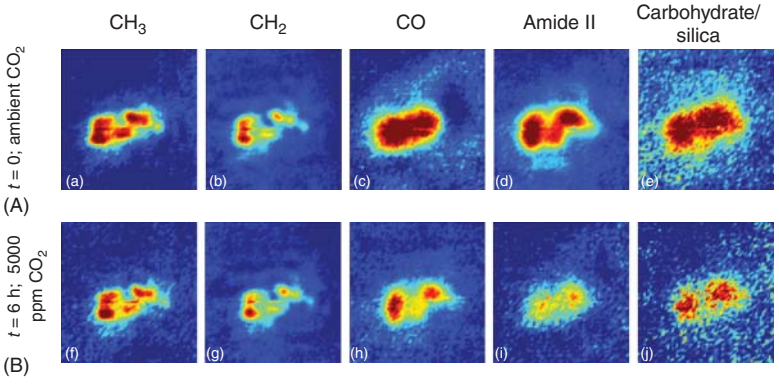

Figure 6.27 Chemical images of *Thallassosira weissflogii* taken at time $t = 0$ (A) when the cells had been acclimated to ambient CO_2 conditions, and after 6 h (B) exposure to 5000 ppm CO_2 conditions in a flow cell, maintained at 20 °C and with full light conditions during the entire 6 h. The images from left to right correspond to the integrated intensities under the bands from 2936 to 2902 cm^{-1} (CH_3 stretches, a and f), 2862–2831 cm^{-1} (CH_2 stretches, b and g), 1700–1760 cm^{-1} (CO stretch commonly associated with phospholipid, c and h), 1500–1545 cm^{-1} (amide II, d and i) and the 900–1200 cm^{-1} (overlapping carbohydrate and silica bands, e and j). (Reproduced with permission from Ref. [170]. © Elsevier.)

A recent development called IRENI (IR ENviromental Imaging) uses a multiple beam synchrotron radiation source coupled with FPA detection for achieving highest spatial resolution [169].

An example of successful application of IRENI for high spectrally and spatially resolved *in vivo* express measurements (below 1 min per image) on algae cells of *Thallasossira weissflogii* is presented by Nasse *et al.* [170]. Figure 6.27 shows the macromolecular distribution within the diatom cell at ambient (Figure 6.27A) and increased (Figure 6.27B) carbon dioxide atmosphere [170].

6.6 Interaction Between Plant Tissue and Plant Pathogens

The big advantages of vibrational microspectroscopic methods become clearly apparent when studying plant–pathogen interactions.

The large variety of possible sample applications (transmission of thin sample slides, reflection mode of thicker sections by Raman, MIRS, and NIRS with several millimeters of penetration depths) allows the direct analysis of infected plant tissue without any previous steps of isolation or cleanup, as demonstrated on the following plant fungal disease.

As shown for leaves of pear (*Pyrus communis*) infected with *Gymnosporangium fuscum* (pear rust), the degradation of leaf tissue damaged by the pathogen and changes in the metabolite profile of the necrotic tissue can be visualized by Raman mapping (results from Schulz *et al.*, unpublished data). Figure 6.28 shows the visual image of an infected side of a pear leaf (Figure 6.28a) and the resulting cluster image (hierarchical clustering, Figure 6.28b). Figure 6.28c presents the corresponding spectra characteristic for each class indicating that the level of phenolic compounds (marker bands at 1620–1600 cm^{-1}) is increased at the infection site with a simultaneous decline of carotenoids (marker bands at 1526, 1158, and 1005 cm^{-1}). The presence of an enrichment of phenolics can be easily explained by the production of suberin, a lignin analog acting as plant-generated wound closure.

Interaction between plant tissue and plant pathogens involves at least two partners. The use of vibrational spectroscopy was frequently mainly focused on the degradation of plant material, especially in wood. The pathogen, however, often received minor or no attention. In many cases, the pathogen is attempted to be removed from the plant material prior to spectroscopy, for example, when assessing the mass loss of wood blocks due to fungal decay according to the European Norm DIN EN 113/A1:2004-04 [171]. Spectroscopic methods are suitable to monitor the composition of plant tissue as well as of plant pathogens. In order to elucidate the complex interaction between plant tissue and plant pathogen, a more holistic spectroscopic view on both interaction partners should contribute to a better understanding. This requires an interdisciplinary approach combining expertise on plants and microorganisms.

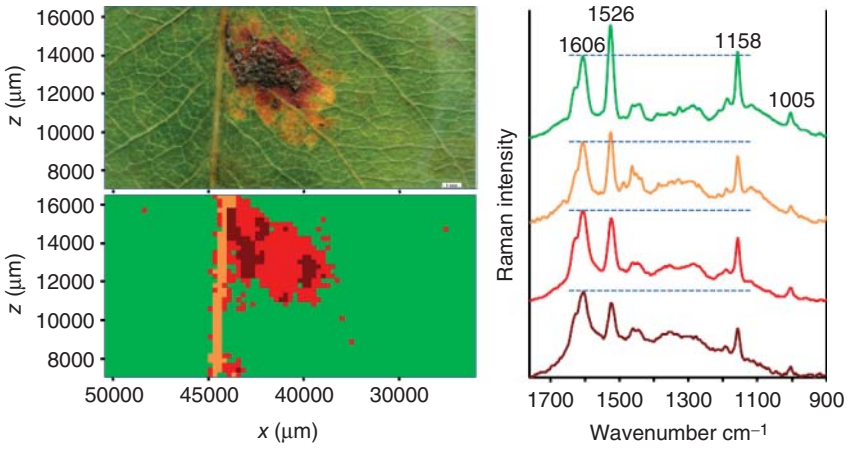

Figure 6.28 Visual image of a pear leaf infected by the pear rust *Gymnosporangium fuscum* (a), the corresponding cluster image created by hierarchical cluster analysis (b), and averaged spectra of each cluster (c). Spectra are color coded according to the clustered image in (b).

6.6.1 Bacterial Plant Pathogens

FT-IR spectroscopy has been successfully applied for the classification of bacterial species and strains since decades but mostly restricted to single-point measurements [172–174]. There are two actual reviews summarizing nicely vibrational spectroscopic contributions in bacterial analysis. The review of Alvarez-Ordóñez gives a brief overview about the diverse fields of application for FT-IR spectroscopy, mostly compositional studies for classification and identification of foodborne pathogens and the detection of bacterial membranes under changing environmental conditions [172]. In contrast, the work of Li *et al.* [173] explains the analytical options for bacteria analysis given by the various Raman techniques, allowing the detection of single cells with resolutions in the nanometer range.

Even if a lot of economically relevant plant diseases are caused by bacteria (*Erwinia amylorova*, *Xanthomonas*), vibrational spectroscopic imaging and mapping techniques were apparently not applied yet for studying their interactions with the host plant. Nevertheless, there are few reports presenting the promising utilization of these nondestructive methods for the analysis of biofilm activity in *Escherichia coli* or for the characterization of mycobacteria, gram-negative bacteria, and co-cultures of both by coupled atomic force microscopy (AFM) and Raman spectroscopy [175, 176]. Figure 6.29 shows an appropriate Raman map of co-colonized *Mycobacterium* spp. MCS and *Pseudomonas putida* analyzed and discriminated by coupled AFM and Raman spectroscopy.

Bacterial degradation of waterlogged archeological wood and foundation piles under low-oxygen conditions resulted in increased lignin content [177]. This

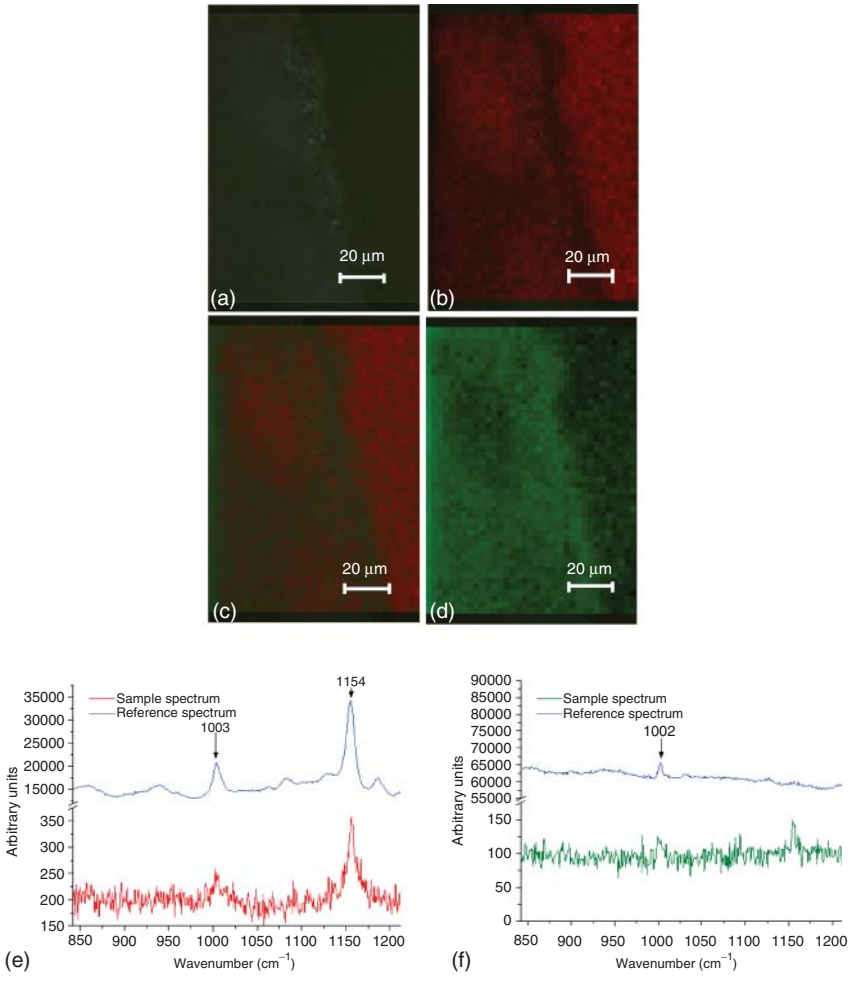

Figure 6.29 Raman mapping on the agar surface containing both *Mycobacterium* sp. MCS and *P. putida* KT2440. Bright field image (a); Raman mapping (b) on the agar surface containing both *Mycobacterium* sp. MCS (c) and *P. putida* KT2440 (d); direct classical least square (DCLS) spectral data fit to a spectrum of *Mycobacterium* sp. MCS (e) (blue curve); DCLS spectral data fit to a spectrum of *P. putida* KT2440 (f) (blue curve). (Reproduced with permission from Ref. [176]. © Springer.)

ATR-IR spectroscopic analysis demonstrates the specific potential for a closer investigation by microspectroscopic imaging.

6.6.2 Fungal Plant Pathogens

Also unicellular fungal cells (yeasts) and spores could be distinguished in the same manner [178, 179]. However, the taxonomic discrimination of fungal

mycelia – the important growth form of the vast majority of fungi – is technically more difficult and requires essential methodological changes. Colonies of unicellular individuals can be transferred on an IR transmissive sample holder in a homogeneous film, which contains many individual cells and therefore is a representative subsample of the whole colony.

Contrarily, mycelium germinates from a single spore or piece of mycelium. The mycelium culture reaches several centimeters of diameter after a few days, but is still only one individual consisting of many branching and intermingling hyphae. The composition of these hyphae can vary considerably, for example, age has a distinct impact. It is complicated or even impossible to prepare a homogeneous film from these hyphae and the representativeness of the subsample for one or more whole individuals is questionable. Preparing powder from mycelium grown on solid agar plates and measuring ATR-IR spectra resulted in reproducible spectra. By grouping the spectra according to their spectral similarity using cluster analysis, 99% of the 233 spectra belonging to 26 fungal strains of 24 species were successfully classified on the species level [180]. The high potential of this method to discriminate mycelium of fungal strains grown in pure culture under standardized growth conditions was thus demonstrated. A high-throughput protocol for the identification of trouble-shooting fungi in the food industry was developed by Shapaval *et al.* [181].

Although classification of microorganisms in pure culture is already challenging, investigating interactions between plant tissue and plant pathogens adds further complexity. In this case, the chemical compositions of the plant as well as the pathogen have to be detected within the complex and variable matrix of the other interaction partner. Moreover, both partners change their chemical compositions during their interaction. The plant composition is changed, for example, due to microbial decay and resistance reactions. The fungus produces degrading enzymes (protein) and converts plant material into new fungal material.

Microspectroscopic techniques provide the opportunity to analyze infected material spatially resolved. Applying FT-IR microspectroscopy, mycelia of two fungal species were successfully discriminated within beech wood sections and chemical differences of the mycelia grown on top and within vessels of the wood blocks were revealed (Figure 6.30) [182].

FT-IR microspectroscopy enabled the visualization of fungal mycelium within a beech wood section. Cluster analysis of FT-IR spectra from an FPA data set resulted in three classes of spectra, which correlated very well with the distribution of fungal mycelium, wood, and air in the vessels visible in the light microscopic image (Figure 6.31) [182].

Although accumulations of mycelium in the vessels are detectable, the detection of single hyphae, usually of a diameter between 2 and 10 µm, is close to the resolution limit of FT-IR imaging at about 5 µm. Especially challenging is the detection of hyphae embedded in a complex matrix such as wood, particularly at early (incipient) infection stages, where the relative amount of hyphae compared to wood is very small. Single FPA pixels measuring fungal mycelium and wood within the 4×4 or $6.25 \times 6.25\ \mu m^2$ area (depending on producer) would record spectra with

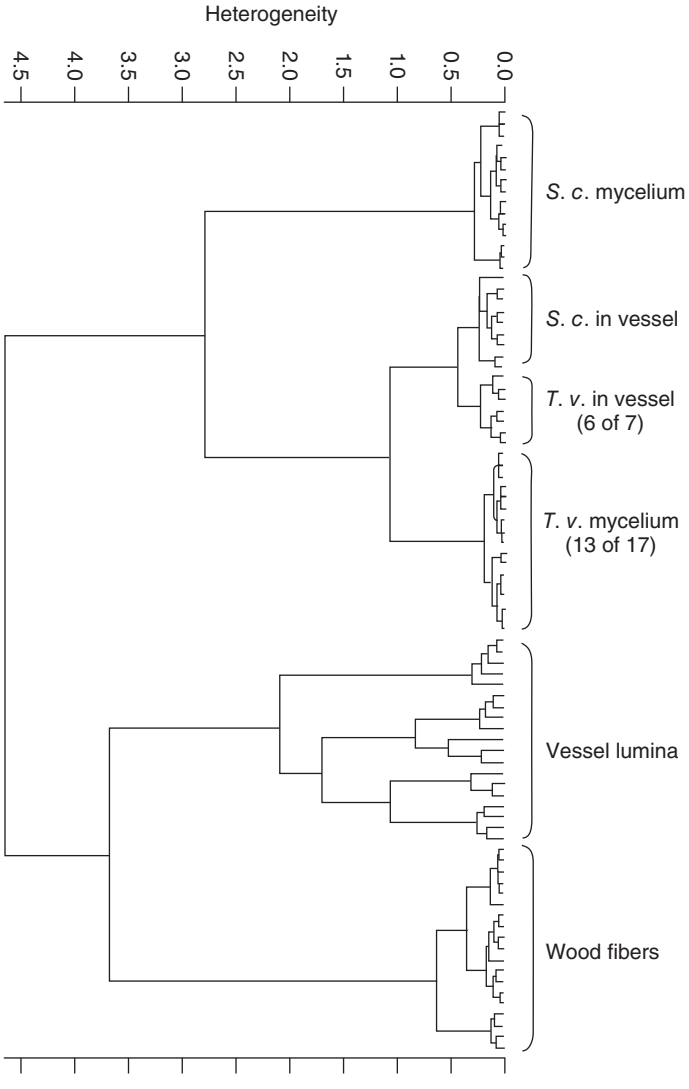

Figure 6.30 Cluster analysis of vector-normalized spectra obtained from beech wood fibers (wood), mycelium of *Schizophyllum commune* (*S. c.*), and *Trametes versicolor* (*T. v.*) growing on the wood surface and in vessel lumina (*S. c.* in vessel, *T. v.* in vessel), and vessel lumina without mycelium (vessel lumina). (Reproduced with permission from Ref. [182]. © Elsevier.)

contributions of each material according to its relative content. Synchrotron FT-IR (sFT-IR) mapping achieves a better spatial resolution (about 3 μm) and of better signal-to-noise ratio due to the brighter source [183]. In pure single hyphae, sFT-IR microspectroscopy and FPA imaging enabled the visualization of the spatial distribution of protein and mannitol (Figure 6.32) [184].

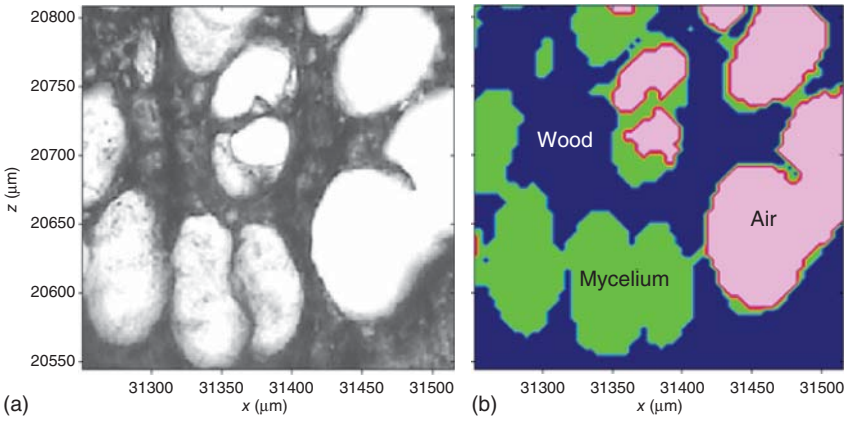

Figure 6.31 Light microscopic image of fungal mycelium in a beech wood section (a) and cluster analysis of FT-IR spectra from a focal plane array (FPA) data set in the range 1188–922 cm^{-1} (b). (Adapted with permission from Ref. [182]. © Elsevier.)

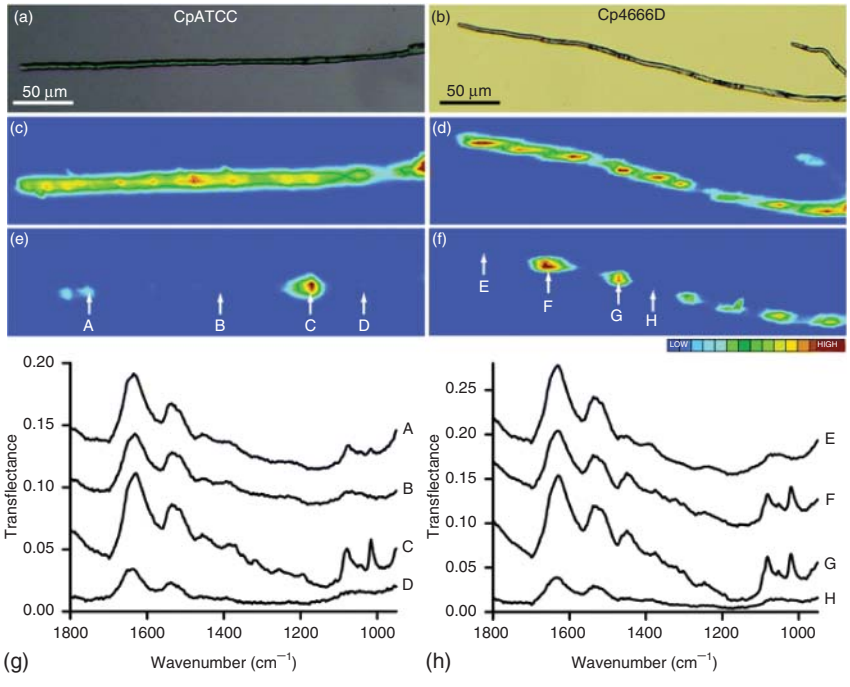

Figure 6.32 Photographs of hyphae from two isolates of *Curvularia protuberata* (a) CpATCC and (b) Cp4666D. FPA images were processed to show (c and d) protein distribution and (e and f) mannitol distribution. (g, h) FT-IR–FPA spectra extracted from images at points A–D and E–H. (Reproduced with permission from Ref. [184]. © Royal Society of Chemistry.)

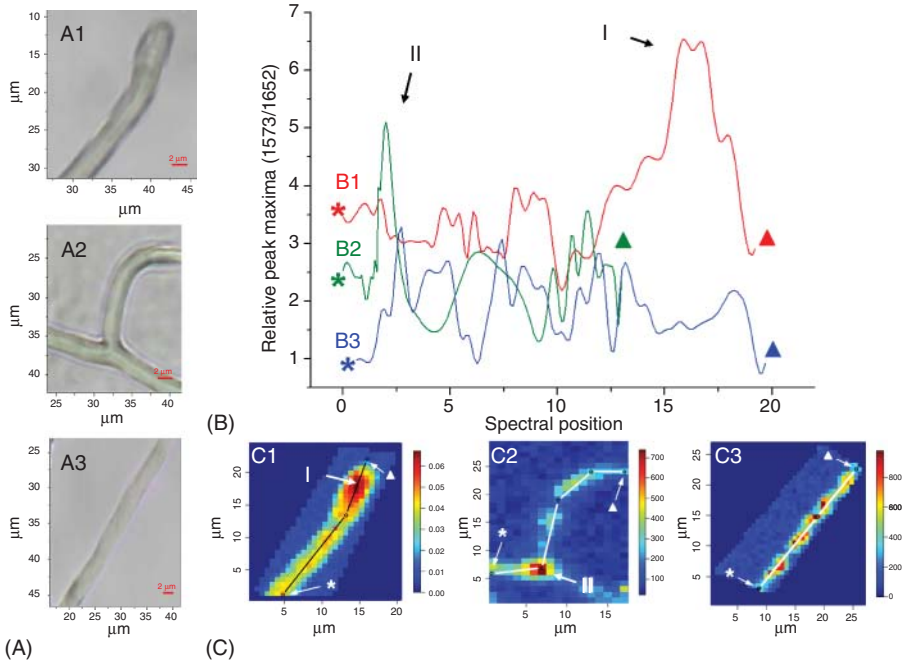

Figure 6.33 (A) Microscopic pictures of a hyphal tip (A1), branching region (A2), and the fully grown hypha (A3). False color plots of the absolute intensity of the cytochrome marker band (1573 cm^{-1}) within the mapped regions of the hyphal tip cell (B1), the branching region (B2), and the central compartment (B3). The normalized cytochrome content is determined by the 1573–1652 cm^{-1} ratio along the white line – beginning from the star and ending at the triangle (see B1–B3). The calculated intensity ratios are depicted as graphs C1, C2, and C3. The two cytochrome maxima I and II are highlighted in the graphs C1 and C2, respectively. Maximum I is located within the apical region of the hyphal tip cell (I in C1 and B1), whereas maximum II correlates with the branching spot of B2. (Reproduced with permission from Ref. [185]. © Royal Society of Chemistry.)

Raman mapping enables even better spatial resolution below 1 µm. Figure 6.33 illustrates the quantification of the relative cytochrome content at different hyphal compartments [185].

Raman spectra of spores from different *Lactarius* species show a high degree of similarity and few, small spectral differences. Comparison with reference substances indicated high lipid content, especially oleate, as well as polysaccharides, chitin, and amylopectin [186].

6.6.3
Fungal Degradation of Plant Material

Especially in trees and construction wood, fungal degradation poses a serious safety risk due to collapse. Often invisible from the outside, mechanical strength

is dangerously reduced quite early during fungal decay. The underlying chemical changes are so small that they are difficult to trace with the methods of traditional wet chemistry. Spectroscopic and microspectroscopic methods have proved to be a valuable tool to detect early (incipient) decay and contribute essentially to understand fungal wood decay [187]. Numerous studies with various wood and fungal species are summarized in the previously mentioned review.

Wood consists mainly of a highly ordered structure built of cellulose, hemicelluloses, and lignin. Only some higher fungi have the ability to degrade this durable material. Their degradation mechanisms differ considerably. White rot fungi degrade foremost lignin and leave the cellulose fibers [188, 189]. Brown rot fungi metabolize mainly cellulose fibers with the brownish lignin leftover [189, 190]. Soft rot fungi infect wood in damp environments and form cavities around their hyphae degrading lignin and cellulose [189]. Boundaries between these decay types are not always clear cut, transitions are possible [189].

Vibrational spectroscopic methods analyzing homogenized powdered wood samples (KBr disks in transmission, ATR spectroscopy) contributed greatly to elucidate fungal degradation of wood on the larger scale since decades [191, 192]. Detection and understanding of the highly variable fungal degradation within the chemically variable wood profit essentially from the higher spatial resolution accessible by mapping and imaging.

Fackler *et al.* [188, 190] applied FT-IR imaging to brown- and white-rot degraded wood. PCA-based multivariate image analysis enabled localizing incipient brown rot in spruce wood sections with a spatial pixel resolution of $6.25\,\mu m \times 6.25\,\mu m$. Using a partial least squares discriminant analysis (PLS-DA), a model capable of detecting early decay at the same resolution in spruce wood sections was built (Figure 6.34) [187]. Fackler *et al.* [188, 190] found a significant reduction of glycosidic linkages within polysaccharides ($1160\,cm^{-1}$) in relation to carbohydrate ring structures in brown- and white-rot degraded wood. These findings were highly indicative for incipient brown rot and early white rot [187].

The enzymatic degradation of poplar-wood cross sections was investigated by Gierlinger *et al.* using FT-IR microspectroscopy in a custom-built fluidic cell [193]. Cross sections of poplar wood were treated with the multicomponent enzyme Onozuka RS with cellulase activity and other cell wall degrading activities. This approach enables analysis of biological samples in the wet state and aims at uniform accessibility of the enzyme to different cell wall layers of the wood cells. The fast, selective hydrolysis of the cellulose-rich gelatinous (G) layer was demonstrated and thus the G-layer identified as interesting for the production of bioethanol.

Interaction of fungi and bacteria in wood degradation was studied by Weißhaupt *et al.* [194] using FT-IR spectroscopy. Decomposition of wood blocks by the fungus *Hypholoma fasciculare* was similar without bacteria and in co-culture with bacteria. In conclusion, the bacteria coexisting with *H. fasciculare* rather competed for the same nitrogen sources than supported fungal nitrogen supply by diazotrophic activity.

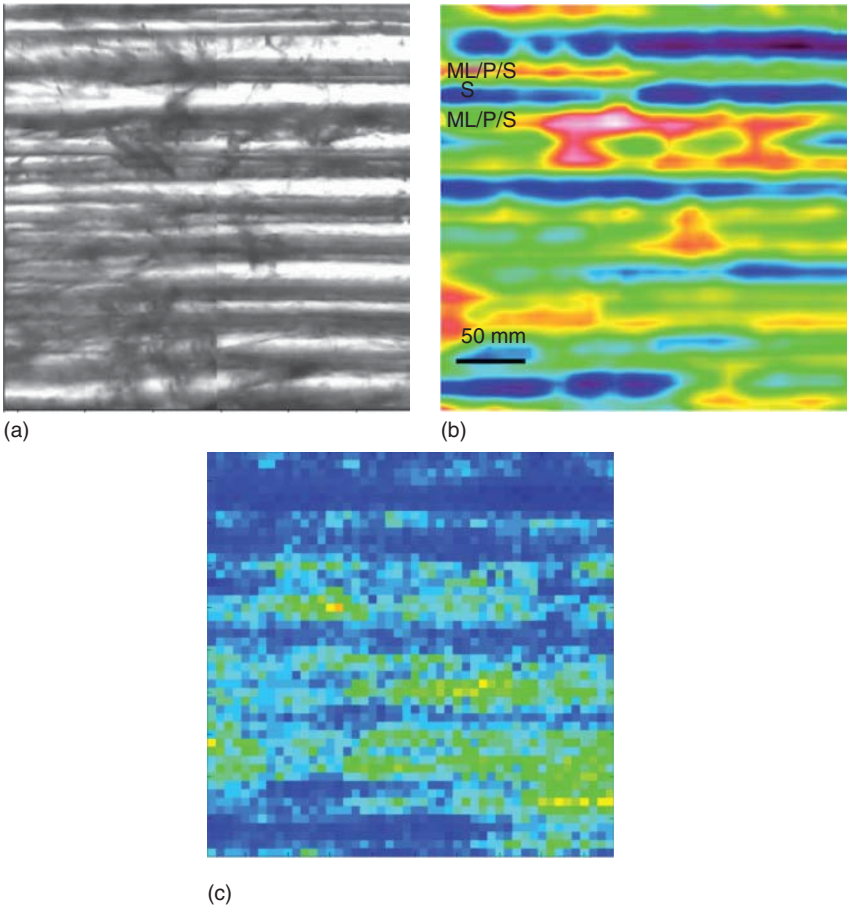

Figure 6.34 Localization of early brown-rot degradation within a radial thin section of spruce wood with FT-IR imaging microspectroscopy: (a) Charge-coupled device (CCD) camera image of 10 tracheids of a degraded spruce wood section from a sample degraded by the brown-rot fungus *G. trabeum* for 4 weeks. (b) FT-IR pseudocolor spectral absorbance image. Zones of high total absorbance (red) show a high contribution of middle lamella (ML) and primary cell walls (P) and outer layers of secondary cell walls S1, named as ML/P/S. Those with low total absorbance (blue) can be assigned to regions with a high contribution of secondary cell walls S2 and pits, named as S. (c) Example of a partial least squares discriminant analysis image gained through multivariate image analysis – degraded pixels are plotted yellow to light green and are found in ML/P/S regions of the section in 6.25 µm pixel resolution. (Reproduced with permission from Ref. [187]. © Springer.)

To elucidate the chemical basis of host resistance against Dutch elm disease, FT-IR microspectroscopy (single-point measurements) was performed [195]. Spectra of resistant elm seedlings showed increased formation of lignin and suberin after inoculation with the pathogenic fungus *Opiostoma novo-ulmi*.

6.6.4 Interaction with Nonwoody Plants

Erukhimovitch *et al.* [196] examined the potential of FT-IR microspectroscopy (single-point measurement) for easy and rapid detection and identification of fungal pathogens directly from the surface of infected potatoes, as a representative model for *in vivo* rapid detection of plant fungal pathogens. The results obtained in this study provide unique, consistent, and significant spectral biomarkers for the infected region with different fungal pathogens. Using these biomarkers, it was possible to discriminate between the different examined fungi.

The detection of the fungus *Fusarium graminearum* on maize by ATR-IR spectroscopy as an indicator for the presence of deoxynivalenol is described in Kos *et al.* [197].

An indirect description of a plant pathogen interaction is described by Lu and coworkers for the reaction of the human pathogen *Campylobacter jejuni* on sulfur-containing components of garlic (*Allium sativum*) [198]. Single-cell mapping by Raman spectroscopy could clearly show the absorption of organosulfur compounds from garlic concentrate supporting previous findings, assuming a free penetration of these compounds through the pathogen cell membrane.

References

1. Ozaki, Y., Cho, R., Ikegaya, K., Muraishi, S., and Kawauchi, K. (1992) Potential of near-infrared Fourier-transform Raman-spectroscopy in food analysis. *Appl. Spectrosc.*, **46** (10), 1503–1507.
2. Withnall, R., Chowdhry, B.Z., Silver, J., Edwards, H.G.M., and de Oliveira, L.F.C. (2003) Raman spectra of carotenoids in natural products. *Spectrochim. Acta, Part A*, **59** (10), 2207–2212.
3. Rimai, L., Heyde, M.E., and Gill, D. (1973) Vibrational spectra of some carotenoids and related linear polyenes – Raman spectroscopic study. *J. Am. Chem. Soc.*, **95** (14), 4493–4501.
4. Schulz, H., Baranska, M., and Baranski, R. (2005) Potential of NIR-FT-Raman spectroscopy in natural carotenoid analysis. *Biopolymers*, **77** (4), 212–221.
5. Baranska, M., Schütze, W., and Schulz, H. (2006) Determination of lycopene and β-carotene content in tomato fruits and related products: Comparison of FT-Raman, ATR-IR, and NIR spectroscopy. *Anal. Chem.*, **78** (24), 8456–8461.
6. Baranski, R., Baranska, M., and Schulz, H. (2005) Changes in carotenoid content and distribution in living plant tissue can be observed and mapped in situ using NIR-FT-Raman spectroscopy. *Planta*, **222** (3), 448–457.
7. Baranska, M., Baranski, R., Schulz, H., and Nothnagel, T. (2006) Tissue-specific accumulation of carotenoids in carrot roots. *Planta*, **224** (5), 1028–1037.
8. Baranska, M., Baranski, R., Grzebelus, E., and Roman, M. (2011) *In situ* detection of a single carotenoid crystal in a plant cell using Raman microspectroscopy. *Vib. Spectrosc.*, **56** (2), 166–169.
9. Qin, J.W., Chao, K.L., and Kim, M.S. (2011) Investigation of Raman chemical imaging for detection of lycopene changes in tomatoes during postharvest ripening. *J. Food Eng.*, **107** (3-4), 277–288.
10. Gierlinger, N. and Schwanninger, M. (2007) The potential of Raman microscopy and Raman imaging in plant research. *Spectrosc. Int. J.*, **21** (2), 69–89.

11. Baranska, M., Schulz, H., Rösch, P., Strehle, M.A., and Popp, J. (2004) Identification of secondary metabolites in medicinal and spice plants by NIR-FT-Raman microspectroscopic mapping. *Analyst*, **129** (10), 926–930.
12. Brackmann, C., Bengtsson, A., Alminger, M.L., Svanberg, U., and Enejder, A. (2010) Visualization of β-carotene and starch granules in plant cells using CARS and SHG microscopy. *J. Raman Spectrosc.*, **42** (4), 586–592.
13. Schulz, H., Joubert, E., and Schütze, W. (2003) Quantification of quality parameters for reliable evaluation of green rooibos (*Aspalathus linearis*). *Eur. Food Res. Technol.*, **216** (6), 539–543.
14. Baranska, M., Schulz, H., Joubert, E., and Manley, M. (2006) *In situ* flavonoid analysis by FT-Raman spectroscopy: identification, distribution, and quantification of aspalathin in green rooibos (*Aspalathus linearis*). *Anal. Chem.*, **78** (22), 7716–7721.
15. Baranska, M., Schulz, H., Baranski, R., Nothnagel, T., and Christensen, L.P. (2005) *In situ* simultaneous analysis of polyacetylenes, carotenoids and polysaccharides in carrot roots. *J. Agric. Food Chem.*, **53** (17), 6565–6571.
16. Baranska, M. and Schulz, H. (2005) Spatial tissue distribution of polyacetylenes in carrot root. *Analyst*, **130** (6), 855–859.
17. Roman, M., Dobrowolski, J.C., Baranska, M., and Baranski, R. (2011) Spectroscopic studies on bioactive polyacetylenes and other plant components in wild carrot root. *J. Nat. Prod.*, **74** (8), 1757–1763.
18. Baranska, M., Schulz, H., and Christensen, L.P. (2006) Structural changes of polyacetylenes in American ginseng root can be observed *in situ* by using Raman spectroscopy. *J. Agric. Food Chem.*, **54** (10), 3629–3635.
19. Schrader, B., Schulz, H., Baranska, M., Andreev, G.N., Lehner, C., and Sawatzki, J. (2005) Non-destructive Raman analyses – polyacetylenes in plants. *Spectrochim. Acta, Part A*, **61** (7), 1395–1401.
20. Alvarez, L., Marquina, S., Villarreal, M.L., Alonso, D., Aranda, E., and Delgado, G. (1996) Bioactive polyacetylenes from *Bidens pilosa*. *Planta Med.*, **62** (4), 355–357.
21. Redl, K., Breu, W., Davis, B., and Bauer, R. (1994) Antiinflammatory active polyacetylenes from *Bidens campylotheca*. *Planta Med.*, **60** (1), 58–62.
22. Roman, M., Baranski, R., and Baranska, M. (2011) Nondestructive Raman analysis of polyacetylenes in *Apiaceae* vegetables. *J. Agric. Food Chem.*, **59** (14), 7647–7653.
23. Merlin, J.C., Statoua, A., and Brouillard, R. (1985) Investigation of the *in vivo* organization of anthocyanins using resonance Raman microspectrometry. *Phytochemistry*, **24** (7), 1575–1581.
24. Merlin, J.C., Cornard, J.P., Stastoua, A., Saidiidrissi, M., Lautie, M.F., and Brouillard, R. (1994) Vibrational analysis of hydroxyflavylium derivatives by IR, Fourier transform Raman and resonance Raman spectroscopies. *Spectrochim. Acta, Part A*, **50** (4), 703–712.
25. Merlin, J.C., Statoua, A., Cornard, J.P., Saidiidrissi, M., and Brouillard, R. (1994) Resonance Raman-spectroscopic studies of anthocyanins and anthocyanidins in aqueous-solutions. *Phytochemistry*, **35** (1), 227–232.
26. Vrielynck, L., Cornard, J.P., Merlin, J.C., and Lautie, M.F. (1994) Semiempirical and vibrational studies of flavone and some deuterated analogs. *Spectrochim. Acta, Part A*, **50** (13), 2177–2188.
27. Gamsjaeger, S., Baranska, M., Schulz, H., Heiselmayer, P., and Musso, M. (2011) Discrimination of carotenoid and flavonoid content in petals of pansy cultivars (*Viola* x *wittrockiana*) by FT-Raman spectroscopy. *J. Raman Spectrosc.*, **42** (6), 1240–1247.
28. Schulz, H., Schrader, B., Quilitzsch, R., Pfeffer, S., and Krüger, H. (2003) Rapid classification of basil chemotypes by various vibrational spectroscopy methods. *J. Agric. Food Chem.*, **51** (9), 2475–2481.
29. Schulz, H., Ozkan, G., Baranska, M., Krüger, H., and Ozcan, M. (2005) Characterisation of essential oil plants from Turkey by IR and Raman spectroscopy. *Vib. Spectrosc.*, **39** (2), 249–256.

30. Schulz, H. and Baranska, M. (2007) Identification and quantification of valuable plant substances by IR and Raman spectroscopy. *Vib. Spectrosc.*, **43** (1), 13–25.
31. Baranska, M., Schulz, H., Krüger, H., and Quilitzsch, R. (2005) Chemotaxonomy of aromatic plants of the genus *Origanum* via vibrational spectroscopy. *Anal. Bioanal. Chem.*, **381** (6), 1241–1247.
32. Daferera, D.J., Tarantilis, P.A., and Polissiou, M.G. (2002) Characterization of essential oils from *Lamiaceae* species by Fourier transform Raman spectroscopy. *J. Agric. Food Chem.*, **50** (20), 5503–5507.
33. Schulz, H., Schrader, B., Quilitzsch, R., and Steuer, B. (2002) Quantitative analysis of various citrus oils by ATR/FT-IR and NIR-FT Raman Spectroscopy. *Appl. Spectrosc.*, **56** (1), 117–124.
34. Schulz, H., Baranska, M., Belz, H.H., Rösch, P., Strehle, M.A., and Popp, J. (2004) Chemotaxonomic characterisation of essential oil plants by vibrational spectroscopy measurements. *Vib. Spectrosc.*, **35** (1-2), 81–86.
35. Andreev, G.N., Schrader, B., Schulz, H., Fuchs, R., Popov, S., and Handjieva, N. (2001) Non-destructive NIR-FT-Raman analyses in practice. Part 1. Analyses of plants and historic textiles. *Fresenius J. Anal. Chem.*, **371** (7), 1009–1017.
36. Strehle, K.R., Rösch, P., Berg, D., Schulz, H., and Popp, J. (2006) Quality control of commercially available essential oils by means of Raman spectroscopy. *J. Agric. Food Chem.*, **54** (19), 7020–7026.
37. Strehle, M.A., Rösch, P., Baranska, M., Schulz, H., and Popp, J. (2005) On the way to a quality control of the essential oil of fennel by means of Raman spectroscopy. *Biopolymers*, **77** (1), 44–52.
38. Baranska, M., Schulz, H., Reitzenstein, S., Uhlemann, U., Strehle, M.A., Krüger, H., Quilitzsch, R., Foley, W., and Popp, J. (2005) Vibrational spectroscopic studies to acquire a quality control method of Eucalyptus essential oils. *Biopolymers*, **78** (5), 237–248.
39. Heraud, P., Caine, S., Sanson, G., Gleadow, R., Wood, B.R., and McNaughton, D. (2007) Focal plane array infrared imaging: a new way to analyse leaf tissue. *New Phytol.*, **173** (1), 216–225.
40. Schulz, H., Baranska, M., Quilitzsch, R., Schütze, W., and Losing, G. (2005) Characterization of peppercorn, pepper oil, and pepper oleoresin by vibrational spectroscopy methods. *J. Agric. Food Chem.*, **53** (9), 3358–3363.
41. Kacurakova, M. and Wilson, R.H. (2001) Developments in mid-infrared FT-IR spectroscopy of selected carbohydrates. *Carbohydr. Polym.*, **44** (4), 291–303.
42. Nicolai, B.M., Lotze, E., Peirs, A., Scheerlinck, N., and Theron, K.I. (2006) Non-destructive measurement of bitter pit in apple fruit using NIR hyperspectral imaging. *Postharvest Biol. Technol.*, **40** (1), 1–6.
43. Suutarinen, J., Anakainen, L., and Autio, K. (1998) Comparison of light microscopy and spatially resolved Fourier transform infrared (FT-IR) microscopy in the examination of cell wall components of strawberries. *Food Sci. Technol. -Leb.*, **31** (7-8), 595–601.
44. Huck-Pezzei, V.A., Pallua, J.D., Pezzei, C., Bittner, L.K., Schoenbichler, S.A., Abel, G., Popp, M., Bonn, G.K., and Huck, C.W. (2012) Fourier transform infrared imaging analysis in discrimination studies of St. John's wort (*Hypericum perforatum*). *Anal. Bioanal. Chem.*, **404** (6-7), 1771–1778.
45. Stewart, D. (1996) Fourier transform infrared microspectroscopy of plant tissues. *Appl. Spectrosc.*, **50** (3), 357–365.
46. Luque, P., Heredia, A., Ramirez, F.J., and Bukovac, M.J. (1993) Characterization of NO_2 bound to the plant cuticle by FT-IR spectroscopy. *Z. Naturforsch. C*, **48** (7-8), 666–668.
47. Wells, B., McCann, M.C., Shedletzky, E., Delmer, D., and Roberts, K. (1994) Structural features of cell walls from tomato cells adapted to grow on the herbicide 2,6-dichlorobenzonitrile. *J. Microsc. (Oxford)*, **173**, 155–164.
48. Raab, T.K. and Martin, M.C. (2001) Visualizing rhizosphere chemistry of

legumes with mid-infrared synchrotron radiation. *Planta*, **213** (6), 881–887.

49. McCann, M.C., Hammouri, M., Wilson, R., Belton, P., and Roberts, K. (1992) Fourier-transform infrared microspectroscopy is a new way to look at plant-cell walls. *Plant Physiol.*, **100** (4), 1940–1947.
50. Vandenabeele, P. and Moens, L. (2003) Micro-Raman spectroscopy of natural and synthetic indigo samples. *Analyst*, **128** (2), 187–193.
51. Tatsch, E. and Schrader, B. (1995) Near-infrared Fourier transform Raman spectroscopy of indigoids. *J. Raman Spectrosc.*, **26** (6), 467–473.
52. Fiedler, A., Baranska, M., and Schulz, H. (2011) FT-Raman spectroscopy – a rapid and reliable quantification protocol for the determination of natural indigo dye in *Polygonum tinctorium*. *J. Raman Spectrosc.*, **42** (3), 551–557.
53. Baran, A., Fiedler, A., Schulz, H., and Baranska, M. (2010) *In situ* Raman and IR spectroscopic analysis of indigo dye. *Anal. Methods*, **2** (9), 1372–1376.
54. Baranska, M., Schulz, H., Siuda, R., Strehle, M.A., Rösch, P., Popp, J., Joubert, E., and Manley, M. (2005) Quality control of *Harpagophytum procumbens* and its related phytopharmaceutical products by means of NIR-FT-Raman spectroscopy. *Biopolymers*, **77** (1), 1–8.
55. Joubert, E., Manley, M., Gray, B.R., and Schulz, H. (2005) Rapid measurement and evaluation of the effect of drying conditions on harpagoside content in *Harpagophytum procumbens* (devil's claw) root. *J. Agric. Food Chem.*, **53** (9), 3493–3502.
56. Reffner, J.A. (1990) Molecular microspectral mapping with the FT-IR microscope. *Inst. Phys. Conf. Ser.*, **98**, 559–569.
57. Wetzel, D.L. and Reffner, J.A. (1993) Using spatially resolved Fourier-transform infrared microbeam spectroscopy to examine the microstructure of wheat kernels. *Cereal Foods World*, **38** (1), 9–20.
58. Sene, C.F.B., McCann, M.C., Wilson, R.H., and Grinter, R. (1994) Fourier-transform Raman and Fourier-transform infrared-spectroscopy – an investigation of 5 higher-plant cell-walls and their components. *Plant Physiol.*, **106** (4), 1623–1631.
59. McCann, M.C., Defernez, M., Urbanowicz, B.R., Tewari, J.C., Langewisch, T., Olek, A., Wells, B., Wilson, R.H., and Carpita, N.C. (2007) Neural network analyses of infrared spectra for classifying cell wall architectures. *Plant Physiol.*, **143** (3), 1314–1326.
60. Marcott, C., Reeder, R.C., Sweat, J.A., Panzer, D.D., and Wetzel, D.L. (1999) FT-IR spectroscopic imaging microscopy of wheat kernels using a Mercury-Cadmium-Telluride focal-plane array detector. *Vib. Spectrosc.*, **19** (1), 123–129.
61. Yu, P.Q., McKinnon, J.J., Christensen, C.R., Christensen, D.A., Marinkovic, N.S., and Miller, L.M. (2003) Chemical imaging of microstructures of plant tissues within cellular dimension using synchrotron infrared microspectroscopy. *J. Agric. Food Chem.*, **51** (20), 6062–6067.
62. Yu, P.Q., McKinnon, J.J., Christensen, C.R., and Christensen, D.A. (2004) Using synchrotron transmission FTIR microspectroscopy as a rapid, direct and nondestructive analytical technique to reveal molecular microstructural-chemical features within tissue in grain barley. *J. Agric. Food Chem.*, **52** (6), 1484–1494.
63. Yu, P.Q., McKinnon, J.J., Christensen, C.R., and Christensen, D.A. (2004) Using synchrotron-based FTIR microspectroscopy to reveal chemical features of feather protein secondary structure: comparison with other feed protein sources. *J. Agric. Food Chem.*, **52** (24), 7353–7361.
64. Yu, P.Q. (2005) Application of cluster analysis (CLA) in feed chemical imaging to accurately reveal structural-chemical features of feeds and plants within cellular dimension. *J. Agric. Food Chem.*, **53** (8), 2872–2880.
65. Yu, P.Q., McKinnon, J.J., Christensen, C.R., and Christensen, D.A. (2004) Imaging molecular chemistry of pioneer

corn. *J. Agric. Food Chem.*, **52** (24), 7345–7352.

66. Barron, C., Parker, M.L., Mills, E.N.C., Rouau, X., and Wilson, R.H. (2005) FTIR imaging of wheat endosperm cell walls *in situ* reveals compositional and architectural heterogeneity related to grain hardness. *Planta*, **220** (5), 667–677.
67. Toole, G.A., Wilson, R.H., Parker, M.L., Wellner, N.K., Wheeler, T.R., Shewry, P.R., and Mills, E.N.C. (2007) The effect of environment on endosperm cell-wall development in *Triticum aestivum* during grain filling: an infrared spectroscopic imaging study. *Planta*, **225** (6), 1393–1403.
68. Toole, G.A., Barron, C., Le Gall, G., Colquhoun, I.J., Shewry, P.R., and Mills, E.N.C. (2009) Remodelling of arabinoxylan in wheat (*Triticum aestivum*) endosperm cell walls during grain filling. *Planta*, **229** (3), 667–680.
69. Toole, G., Gall, G., Colquhoun, I., Drea, S., Opanowicz, M., Bedo, Z., Shewry, P., and Mills, E. (2012) Spectroscopic analysis of diversity in the spatial distribution of arabinoxylan structures in endosperm cell walls of cereal species in the HEALTHGRAIN diversity collection. *J. Cereal Sci.*, **56** (2), 134–141.
70. Toole, G.A., Le Gall, G., Colquhoun, I.J., Johnson, P., Bedo, Z., Saulnier, L., Shewry, P.R., and Mills, E.N.C. (2011) Spectroscopic analysis of diversity of arabinoxylan structures in endosperm cell walls of wheat cultivars (*Triticum aestivum*) in the HEALTHGRAIN diversity collection. *J. Agric. Food Chem.*, **59** (13), 7075–7082.
71. Wellner, N., Georget, D.M.R., Parker, M.L., and Morris, V.J. (2011) In situ Raman microscopy of starch granule structures in wild type and *ae* mutant maize kernels. *Starch-Stärke*, **63** (3), 128–138.
72. Piot, O., Autran, J.C., and Manfait, M. (2000) Spatial distribution of protein and phenolic constituents in wheat grain as probed by confocal raman microspectroscopy. *J. Cereal Sci.*, **32** (1), 57–71.
73. Wolkers, W.F., Bochicchio, A., Selvaggi, G., and Hoekstra, F.A. (1998) Fourier transform infrared microspectroscopy detects changes in protein secondary structure associated with desiccation tolerance in developing maize embryos. *Plant Physiol.*, **116** (3), 1169–1177.
74. Yu, P.Q. (2011) Microprobing the molecular spatial distribution and structural architecture of feed-type sorghum seed tissue (*Sorghum Bicolor* L.) using the synchrotron radiation infrared microspectroscopy technique. *J. Synchrotron Radiat.*, **18**, 790–801.
75. Wetzel, D.L., Srivarin, P., and Finney, J.R. (2003) Revealing protein infrared spectral detail in a heterogeneous matrix dominated by starch. *Vib. Spectrosc.*, **31** (1), 109–114.
76. Bonwell, E.S., Fisher, T.L., Fritz, A.K., and Wetzel, D.L. (2008) Determination of endosperm protein secondary structure in hard wheat breeding lines using synchrotron infrared microspectroscopy. *Vib. Spectrosc.*, **48** (1), 76–81.
77. Budevska, B.O., Sum, S.T., and Jones, T.J. (2003) Application of multivariate curve resolution for analysis of FT-IR microspectroscopic images of *in situ* plant tissue. *Appl. Spectrosc.*, **57** (2), 124–131.
78. Dokken, K.M. and Davis, L.C. (2007) Infrared imaging of sunflower and maize root anatomy. *J. Agric. Food Chem.*, **55** (26), 10517–10530.
79. Sun, L., Simmons, B.A., and Singh, S. (2011) Understanding tissue specific compositions of bioenergy feedstocks through hyperspectral Raman imaging. *Biotechnol. Bioeng.*, **108** (2), 286–295.
80. Zeng, Y.N., Saar, B.G., Friedrich, M.G., Chen, F., Liu, Y.S., Dixon, R.A., Himmel, M.E., Xie, X.S., and Ding, S.Y. (2010) Imaging lignin-downregulated alfalfa using coherent anti-stokes Raman scattering microscopy. *Bioenergy Res.*, **3** (3), 272–277.
81. Brewer, L.R. and Wetzel, D.L. (2010) Phenotypic expression in wheat revealed using FT-IR microspectroscopy. *Vib. Spectrosc.*, **52** (1), 93–96.
82. Schreiber, N., Gierlinger, N., Puetz, N., Fratzl, P., Neinhuis, C., and Burgert, I. (2010) G-fibres in storage roots of *Trifolium pratense* (Fabaceae): tensile

stress generators for contraction. *Plant J.*, **61** (5), 854–861.

83. Wetzel, D.L. (2012) Mid-IR and near-IR chemical imaging: complementary for biological materials. *Vib. Spectrosc.*, **60**, 29–33.

84. Smail, V.W., Fritz, A.K., and Wetzel, D.L. (2006) Chemical imaging of intact seeds with NIR focal plane array assists plant breeding. *Vib. Spectrosc.*, **42** (2), 215–221.

85. Koc, H. and Wetzel, D.L. (2007) Imaging local chemical microstructure of germinated wheat with synchrotron infrared microspectroscopy. *Spectroscopy*, **22** (10), 24–32.

86. Koc, H., Smail, V.W., and Wetzel, D.L. (2008) Reliability of InGaAs focal plane array imaging of wheat germination at early stages. *J. Cereal Sci.*, **48** (2), 394–400.

87. Himmelsbach, D.S., Khalili, S., and Akin, D.E. (1998) FT-IR microspectroscopic imaging of flax (*Linum usitatissimum* L.) stems. *Cell. Mol. Biol.*, **44** (1), 99–108.

88. Himmelsbach, D.S., Khahili, S., and Akin, D.E. (1999) Near-infrared-Fourier-transform-Raman microspectroscopic imaging of flax stems. *Vib. Spectrosc.*, **19** (2), 361–367.

89. Himmelsbach, D.S., Khalili, S., and Akin, D.E. (2002) The use of FT-IR microspectroscopic mapping to study the effects of enzymatic retting of flax (*Linum usitatissimum* L.) stems. *J. Sci. Food Agric.*, **82** (7), 685–696.

90. Yan, H.J., Hua, Z.Z., Qian, G.S., Wang, M., Du, G.C., and Chen, J. (2009) Analysis of the chemical composition of cotton seed coat by Fourier-transform infrared (FT-IR) microspectroscopy. *Cellulose*, **16** (6), 1099–1107.

91. Dokken, K.M., Davis, L.C., Erickson, L.E., Castro-Diaz, S., and Marinkovic, N.S. (2005) Synchrotron Fourier transform infrared micro spectroscopy: a new tool to monitor the fate of organic contaminants in plants. *Microchem. J.*, **81** (1), 86–91.

92. Budevska, B.O. (2009) Application of target partial least squares for analysis of Fourier transform infrared-attenuated total reflection hyperspectral images for characterization of the distribution of crop protection products on the leaf surface. *Appl. Spectrosc.*, **63** (9), 992–999.

93. Miralles, P., Johnson, E., Church, T.L., and Harris, A.T. (2012) Multiwalled carbon nanotubes in alfalfa and wheat: toxicology and uptake. *J. R. Soc. Interface*, **9** (77), 3514–3527.

94. Larue, C., Pinault, M., Czarny, B., Georgin, D., Jaillard, D., Bendiab, N., Mayne-L'Hermite, M., Taran, F., Dive, V., and Carriere, M. (2012) Quantitative evaluation of multi-walled carbon nanotube uptake in wheat and rapeseed. *J. Hazard. Mater.*, **227**, 155–163.

95. Mansfield, J.C., Littlejohn, G.R., Seymour, M.P., Lind, R.J., Perfect, S., and Moger, J. (2013) Label-free chemically specific imaging in planta with stimulated Raman scattering microscopy. *Anal. Chem.*, **85** (10), 5055–5063.

96. Fackler, K. and Thygesen, L.G. (2013) Microspectroscopy as applied to the study of wood molecular structure. *Wood Sci. Technol.*, **47** (1), 203–222.

97. Naumann, A. and Polle, A. (2006) FTIR imaging as a new tool for cell wall analysis of wood. *N. Z. J. For. Sci.*, **36** (1), 54–59.

98. Naumann, A., Peddireddi, S., Kües, U., and Polle, A. (2007) in *Wood Production, Wood Technology and Biotechnological Impacts* (ed U. Kües), Universitätsverlag Göttingen, Göttingen, pp. 179–196.

99. Labbe, N., Rials, T.G., and Kelley, S.S. (2008) in *Characterization of the Cellulosic Cell Wall* (eds D.D. Stokke and L.H. Groom), Blackwell Publishing Professional, Oxford, Ames, IA, pp. 110–122.

100. Labbe, N., Rials, T.G., Kelley, S.S., Cheng, Z.M., Kim, J.Y., and Li, Y. (2005) FT-IR imaging and pyrolysis-molecular beam mass spectrometry: new tools to investigate wood tissues. *Wood Sci. Technol.*, **39** (1), 61–76.

101. Kataoka, Y. and Kondo, T. (1996) Changing cellulose crystalline structure in forming wood cell walls. *Macromolecules*, **29** (19), 6356–6358.

102. Kataoka, Y. and Kondo, T. (1998) FT-IR microscopic analysis of changing cellulose crystalline structure during wood cell wall formation. *Macromolecules*, **31** (3), 760–764.

103. Gorzsas, A., Stenlund, H., Persson, P., Trygg, J., and Sundberg, B. (2011) Cell-specific chemotyping and multivariate imaging by combined FT-IR microspectroscopy and orthogonal projections to latent structures (OPLS) analysis reveals the chemical landscape of secondary xylem. *Plant J.*, **66** (5), 903–914.

104. Gou, J.Y., Park, S., Yu, X.H., Miller, L.M., and Liu, C.J. (2008) Compositional characterization and imaging of "wall-bound" acylesters of *Populus trichocarpa* reveal differential accumulation of acyl molecules in normal and reactive woods. *Planta*, **229** (1), 15–24.

105. Leple, J.C., Dauwe, R., Morreel, K., Storme, V., Lapierre, C., Pollet, B., Naumann, A., Kang, K.Y., Kim, H., Ruel, K., Lefebvre, A., Joseleau, J.P., Grima-Pettenati, J., De Rycke, R., Andersson-Gunneras, S., Erban, A., Fehrle, I., Petit-Conil, M., Kopka, J., Polle, A., Messens, E., Sundberg, B., Mansfield, S.D., Ralph, J., Pilate, G., and Boerjan, W. (2007) Downregulation of cinnamoyl-coenzyme A reductase in poplar: multiple-level phenotyping reveals effects on cell wall polymer metabolism and structure. *Plant Cell*, **19** (11), 3669–3691.

106. Schmidt, M., Gierlinger, N., Schade, U., Rogge, T., and Grunze, M. (2006) Polarized infrared microspectroscopy of single spruce fibers: hydrogen bonding in wood polymers. *Biopolymers*, **83** (5), 546–555.

107. Naumann, A., Stephan, I., and Noll, M. (2012) Material resistance of weathered wood-plastic composites against fungal decay. *Int. Biodeterior. Biodegrad.*, **75**, 28–35.

108. Gierlinger, N. and Schwanninger, M. (2006) Chemical imaging of poplar wood cell walls by confocal Raman microscopy. *Plant Physiol.*, **140** (4), 1246–1254.

109. Lehringer, C., Gierlinger, N., and Koch, G. (2008) Topochemical investigation on tension wood fibres of *Acer* spp., *Fagus sylvatica* L. and *Quercus robur* L. *Holzforschung*, **62** (3), 255–263.

110. Gierlinger, N. (2010) in *Confocal Raman Microscopy* (eds T. Dieing, O. Hollricher, and J. Toporski), Springer-Verlag, Berlin, Heidelberg, pp. 225–236.

111. Gierlinger, N., Luss, S., König, C., Konnerth, J., Eder, M., and Fratzl, P. (2010) Cellulose microfibril orientation of *Picea abies* and its variability at the micron-level determined by Raman imaging. *J. Exp. Bot.*, **61** (2), 587–595.

112. Stevanic, J.S. and Salme, L. (2009) Orientation of the wood polymers in the cell wall of spruce wood fibres. *Holzforschung*, **63** (5), 497–503.

113. Agarwal, U.P. (2006) Raman imaging to investigate ultrastructure and composition of plant cell walls: distribution of lignin and cellulose in black spruce wood (*Picea mariana*). *Planta*, **224** (5), 1141–1153.

114. Hanninen, T., Kontturi, E., and Vuorinen, T. (2011) Distribution of lignin and its coniferyl alcohol and coniferyl aldehyde groups in *Picea abies* and *Pinus sylvestris* as observed by Raman imaging. *Phytochemistry*, **72** (14-15), 1889–1895.

115. Ma, J.F., Ji, Z., Zhou, X., Zhang, Z.H., and Xu, F. (2013) Transmission electron microscopy, fluorescence microscopy, and confocal Raman microscopic analysis of ultrastructural and compositional heterogeneity of *Cornus alba* L. Wood cell wall. *Microsc. Microanal.*, **19** (1), 243–253.

116. Röder, T., Koch, G., and Sixta, H. (2004) Application of confocal Raman spectroscopy for the topochemical distribution of lignin and cellulose in plant cell walls of beech wood (*Fagus sylvatica* L.) compared to UV microspectrophotometry. *Holzforschung*, **58** (5), 480–482.

117. Perera, P.N., Schmidt, M., Schuck, P.J., and Adams, P.D. (2011) Blind image analysis for the compositional and structural characterization of plant cell walls. *Anal. Chim. Acta*, **702** (2), 172–177.

118. Gierlinger, N., Keplinger, T., and Harrington, M. (2012) Imaging of plant cell walls by confocal Raman

microscopy. *Nat. Protoc.*, **7** (9), 1694–1708.

119. Agarwal, U.P., Reiner, R.R., and Ralph, S.A. (2013) Estimation of cellulose crystallinity of lignocelluloses using near-IR FT-Raman spectroscopy and comparison of the Raman and Segal-WAXS methods. *J. Agric. Food Chem.*, **61** (1), 103–113.

120. Schmidt, M., Schwartzberg, A.M., Perera, P.N., Weber-Bargioni, A., Carroll, A., Sarkar, P., Bosneaga, E., Urban, J.J., Song, J., Balakshin, M.Y., Capanema, E.A., Auer, M., Adams, P.D., Chiang, V.L., and Schuck, P.J. (2009) Label-free in situ imaging of lignification in the cell wall of low lignin transgenic *Populus trichocarpa*. *Planta*, **230** (3), 589–597.

121. McCann, M.C., Chen, L., Roberts, K., Kemsley, E.K., Sene, C., Carpita, N.C., Stacey, N.J., and Wilson, R.H. (1997) Infrared microspectroscopy: sampling heterogeneity in plant cell wall composition and architecture. *Physiol. Plant.*, **100** (3), 729–738.

122. Chen, L.M., Carpita, N.C., Reiter, W.D., Wilson, R.H., Jeffries, C., and McCann, M.C. (1998) A rapid method to screen for cell-wall mutants using discriminant analysis of Fourier transform infrared spectra. *Plant J.*, **16** (3), 385–392.

123. McCann, M.C., Bush, M., Milioni, D., Sado, P., Stacey, N.J., Catchpole, G., Defernez, M., Carpita, N.C., Höfte, H., Ulvskov, P., Wilson, R.H., and Roberts, K. (2001) Approaches to understanding the functional architecture of the plant cell wall. *Phytochemistry*, **57** (6), 811–821.

124. Robert, S., Mouille, G., and Höfte, H. (2004) The mechanism and regulation of cellulose synthesis in primary walls: lessons from cellulose-deficient *Arabidopsis* mutants. *Cellulose*, **11** (3-4), 351–364.

125. Mouille, G., Robin, S., Lecomte, M., Pagant, S., and Höfte, H. (2003) Classification and identification of *Arabidopsis* cell wall mutants using Fourier-transform infrared (FT-IR) microspectroscopy. *Plant J.*, **35** (3), 393–404.

126. Robin, S., Lecomte, M., Höfte, H., and Mouille, G. (2003) A procedure for the clustering of cell wall mutants in the model plant *Arabidopsis* based on Fourier-transform infrared (FT-IR) spectroscopy. *J. Appl. Stat.*, **30** (6), 669–681.

127. Ha, M.A., MacKinnon, I.M., Sturcova, A., Apperley, D.C., McCann, M.C., Turner, S.R., and Jarvis, M.C. (2002) Structure of cellulose-deficient secondary cell walls from the irx3 mutant of *Arabidopsis thaliana*. *Phytochemistry*, **61** (1), 7–14.

128. Dokken, K.M., Davis, L.C., and Marinkovic, N.S. (2005) Use of infrared microspectroscopy in plant growth and development. *Appl. Spectrosc. Rev.*, **40** (4), 301–326.

129. Mazurek, S., Mucciolo, A., Humbel, B.M., and Nawrath, C. (2013) Transmission Fourier transform infrared microspectroscopy allows simultaneous assessment of cutin and cell-wall polysaccharides of *Arabidopsis* petals. *Plant J.*, **74** (5), 880–891.

130. Barratt, D., Derbyshire, P., Findlay, K., Pike, M., Wellner, N., Lunn, J., Feil, R., Simpson, C., Maule, A., and Smith, A. (2009) Normal growth of *Arabidopsis* requires cytosolic invertase but not sucrose synthase. *Proc. Natl. Acad. Sci. U.S.A.*, **106** (31), 13124–13129.

131. Schmidt, M., Schwartzberg, A.M., Carroll, A., Chaibang, A., Adams, P.D., and Schuck, P. (2010) Raman imaging of cell wall polymers in *Arabidopsis thaliana*. *Biochem. Biophys. Res. Commun.*, **395** (4), 521–523.

132. Sapei, L., Gierlinger, N., Hartmann, J., Noske, R., Strauch, P., and Paris, O. (2007) Structural and analytical studies of silica accumulations in *Equisetum hyemale*. *Anal. Bioanal. Chem.*, **389** (4), 1249–1257.

133. Gierlinger, N., Sapei, L., and Paris, O. (2008) Insights into the chemical composition of *Equisetum hyemale* by high resolution Raman imaging. *Planta*, **227** (5), 969–980.

134. Czaja, A.D., Kudryavtsev, A.B., and Schopf, J.W. (2006) New method for the microscopic, nondestructive acquisition of ultraviolet resonance Raman spectra

from plant cell walls. *Appl. Spectrosc.*, **60** (4), 352–355.

135. Howland, L.J. (1929) The moisture relations of terrestrial algae. IV. Periodic observations of *Trentepohlia aurea*, Martius. *Ann. Bot. (London)*, **43** (169), 173–202.

136. Iyengar, M. (1932) *Fritschiella*, a new terrestrial member of the Chaetophoraceae. *New Phytol.*, **31** (5), 329–335.

137. Fogg, G.E. (1967) Observations on snow algae of South Orkney Islands. *Philos. Trans. R. Soc. London, Ser. B*, **252** (777), 279–287.

138. Craigie, J.S., Correa, J.A., and Gordon, M.E. (1992) Cuticles from *Chondrus crispus* (Rhodophyta). *J. Phycol.*, **28** (6), 777–786.

139. Derenne, S., Largeau, C., Berkaloff, C., Rousseau, B., Wilhelm, C., and Hatcher, P.G. (1992) Nonhydrolyzable macromolecular constituents from outer walls of *Chlorella fusca* and *Nanochlorum eucaryotum*. *Phytochemistry*, **31** (6), 1923–1929.

140. Fournet, I., Gall, E.A., Deslandes, E., Huvenne, J.P., Sombret, B., and Floch, J.Y. (1997) *In situ* measurements of cell wall components in the red alga *Solieria chordalis* (Solieriaceae, Rhodophyta) by FTIR microspectrometry. *Bot. Mar.*, **40** (1), 45–48.

141. Sigee, D.C., Dean, A., Levado, E., and Tobin, M.J. (2002) Fourier-transform infrared spectroscopy of *Pediastrum duplex*: characterization of a micropopulation isolated from a eutrophic lake. *Eur. J. Phycol.*, **37** (1), 19–26.

142. Dementjev, A. and Kostkeviciene, J. (2013) Applying the method of Coherent Anti-stokes Raman microscopy for imaging of carotenoids in microalgae and cyanobacteria. *J. Raman Spectrosc.*, **44** (7), 973–979.

143. Heraud, P., Wood, B.R., Tobin, M.J., Beardall, J., and McNaughton, D. (2005) Mapping of nutrient-induced biochemical changes in living algal cells using synchrotron infrared microspectroscopy. *FEMS Microbiol. Lett.*, **249** (2), 219–225.

144. Murdock, J.N. and Wetzel, D.L. (2009) FT-IR microspectroscopy enhances biological and ecological analysis of algae. *Appl. Spectrosc. Rev.*, **44** (4), 335–361.

145. Dean, A., Martin, M., and Sigee, D. (2007) Resolution of codominant phytoplankton species in a eutrophic lake using synchrotron-based Fourier transform infrared spectroscopy. *Phycologia*, **46** (2), 151–159.

146. Kansiz, M., Heraud, P., Wood, B., Burden, F., Beardall, J., and McNaughton, D. (1999) Fourier transform infrared microspectroscopy and chemometrics as a tool for the discrimination of cyanobacterial strains. *Phytochemistry*, **52** (3), 407–417.

147. Vardy, S. and Uwins, P. (2002) Fourier transform infrared microspectroscopy as a tool to differentiate *Nitzschia closterium* and *Nitzschia longissima*. *Appl. Spectrosc.*, **56** (12), 1545–1548.

148. Dean, A.P. and Sigee, D.C. (2006) Molecular heterogeneity in *Aphanizomenon flos-aquae* and *Anabaena flos-aquae* (Cyanophyta): a synchrotron-based Fourier-transform infrared study of lake micropopulations. *Eur. J. Phycol.*, **41** (2), 201–212.

149. Kammer, M., Hedrich, R., Ehrlich, H., Popp, J., Brunner, E., and Krafft, C. (2010) Spatially resolved determination of the structure and composition of diatom cell walls by Raman and FTIR imaging. *Anal. Bioanal. Chem.*, **398** (1), 509–517.

150. Estevez, J.M., Fernandez, P.V., Kasulin, L., Dupree, P., and Estevez, J.M. (2009) Chemical and *in situ* characterization of macromolecular components of the cell walls from the green seaweed *Codium fragile*. *Glycobiology*, **19** (3), 212–228.

151. Collins, A.M., Jones, H.D.T., Han, D.X., Hu, Q., Beechem, T.E., and Timlin, J.A. (2011) Carotenoid distribution in living cells of *Haematococcus pluvialis* (Chlorophyceae). *PLoS One*, **6** (9), e24302.

152. Kaczor, A., Turnau, K., and Baranska, M. (2011) *In situ* Raman imaging of astaxanthin in a single microalgal cell. *Analyst*, **136** (6), 1109–1112.

153. Grosser, K., Zedler, L., Schmitt, M., Dietzek, B., Popp, J., and Pohnert, G.

(2012) Disruption-free imaging by Raman spectroscopy reveals a chemical sphere with antifouling metabolites around macroalgae. *Biofouling*, **28** (7), 687–696.

154. Sigee, D.C., Bahrami, F., Estrada, B., Webster, R.E., and Dean, A.P. (2007) The influence of phosphorus availability on carbon allocation and P quota in *Scenedesmus subspicatus*: a synchrotron-based FTIR analysis. *Phycologia*, **46** (5), 583–592.

155. Stehfest, K., Toepel, J., and Wilhelm, C. (2005) The application of micro-FTIR spectroscopy to analyze nutrient stress-related changes in biomass composition of phytoplankton algae. *Plant Physiol. Biochem.*, **43** (7), 717–726.

156. Wu, H., Volponi, J.V., Oliver, A.E., Parikh, A.N., Simmons, B.A., and Singh, S. (2011) *In vivo* lipidomics using single-cell Raman spectroscopy. *Proc. Natl. Acad. Sci. U.S.A.*, **108** (9), 3809–3814.

157. Hirschmugl, C.J., Bayarri, Z.E., Bunta, M., Holt, J.B., and Giordano, M. (2006) Analysis of the nutritional status of algae by Fourier transform infrared chemical imaging. *Infrared Phys. Technol.*, **49** (1-2), 57–63.

158. Patel, S.A., Currie, F., Thakker, N., and Goodacre, R. (2008) Spatial metabolic fingerprinting using FT-IR spectroscopy: investigating abiotic stresses on *Micrasterias hardyi*. *Analyst*, **133** (12), 1707–1713.

159. Murdock, J.N., Dodds, W.K., and Wetzel, D.L. (2008) Subcellular localized chemical imaging of benthic algal nutritional content via HgCdTe array FT-IR. *Vib. Spectrosc.*, **48** (2), 179–188.

160. Murdock, J.N., Dodds, W.K., Reffner, J.A., and Wetzel, D.L. (2010) Measuring cellular-scale nutrient distribution in algal biofilms with synchrotron confocal infrared microspectroscopy. *Spectroscopy*, **25** (10), 32–41.

161. Huang, Y.Y., Beal, C.M., Cai, W.W., Ruoff, R.S., and Terentjev, E.M. (2010) Micro-Raman spectroscopy of algae: composition analysis and fluorescence background behavior. *Biotechnol. Bioeng.*, **105** (5), 889–898.

162. Abbas, A., Josefson, M., and Abrahamsson, K. (2011) Characterization and mapping of carotenoids in the algae *Dunaliella* and *Phaeodactylum* using Raman and target orthogonal partial least squares. *Chemom. Intell. Lab. Syst.*, **107** (1), 174–177.

163. Abbas, A., Josefson, M., Nylund, G.M., Pavia, H., and Abrahamsson, K. (2012) Chemical images of marine bio-active compounds by surface enhanced Raman spectroscopy and transposed orthogonal partial least squares (T-OPLS). *Anal. Chim. Acta*, **737**, 37–44.

164. Fu, D., Lu, F.K., Zhang, X., Freudiger, C., Pernik, D.R., Holtom, G., and Xie, X.S. (2012) Quantitative chemical imaging with multiplex stimulated Raman scattering microscopy. *J. Am. Chem. Soc.*, **134** (8), 3623–3626.

165. Oh, S.K., Yoo, S.J., Jeong, D.H., and Lee, J.M. (2013) Real-time estimation of glucose concentration in algae cultivation system using Raman spectroscopy. *Bioresour. Technol.*, **142**, 131–137.

166. Tan, S.T., Balasubramanian, R.K., Das, P., Obbard, J.P., and Chew, W. (2013) Application of mid-infrared chemical imaging and multivariate chemometrics analyses to characterise a population of microalgae cells. *Bioresour. Technol.*, **134**, 316–323.

167. Mohlenhoff, B., Romeo, M., Diem, M., and Wood, B.R. (2005) Mie-type scattering and non-beer-lambert absorption behavior of human cells in infrared microspectroscopy. *Biophys. J.*, **88** (5), 3635–3640.

168. Bassan, P., Kohler, A., Martens, H., Lee, J., Byrne, H.J., Dumas, P., Gazi, E., Brown, M., Clarke, N., and Gardner, P. (2010) Resonant Mie Scattering (RMieS) correction of infrared spectra from highly scattering biological samples. *Analyst*, **135** (2), 268–277.

169. Hirschmugl, C.J. and Gough, K.M. (2012) Fourier transform infrared spectrochemical imaging: review of design and applications with a focal plane array and multiple beam synchrotron radiation source. *Appl. Spectrosc.*, **66** (5), 475–491.

170. Nasse, M.J., Bellehumeur, B., Ratti, S., Olivieri, C., Buschke, D., Squirrell, J.,

Eliceiri, K., Ogle, B., Patterson, C.S., Giordano, M., and Hirschmugl, C.J. (2012) Opportunities for multiple-beam synchrotron-based mid-infrared imaging at IRENI. *Vib. Spectrosc.*, **60**, 10–15.

171. Deutsches Institut für Normung (2004) DIN EN 113/A1:2004-04. *Wood Preservatives – Test Method for Determining the Protective Effectiveness Against Wood Destroying Basidiomycetes – Determination of the Toxic Values. Normenausschuss Materialprüfung (NMP) im DIN*, Beuth Verlag, Berlin.
172. Alvarez-Ordóñez, A., Mouwen, D.J.M., López, M., and Prieto, M. (2011) Fourier transform infrared spectroscopy as a tool to characterize molecular composition and stress response in foodborne pathogenic bacteria. *J. Microbiol. Methods*, **84** (3), 369–378.
173. Li, M., Xu, J., Romero-Gonzalez, M., Banwart, S.A., and Huang, W.E. (2012) Single cell Raman spectroscopy for cell sorting and imaging. *Curr. Opin. Biotechnol.*, **23** (1), 56–63.
174. Naumann, D., Helm, D., and Labischinski, H. (1991) Microbiological characterizations by FT-IR spectroscopy. *Nature*, **351** (6321), 81–82.
175. Holman, H.Y., Miles, R., Hao, Z., Wozei, E., Anderson, L., and Yang, H. (2009) Real-time chemical imaging of bacterial activity in biofilms using open-channel microfluidics and synchrotron FTIR spectromicroscopy. *Anal. Chem.*, **81** (20), 8564–8570.
176. Tang, M., McEwen, G., Wu, Y., Miller, C., and Zhou, A. (2013) Characterization and analysis of mycobacteria and Gram-negative bacteria and co-culture mixtures by Raman microspectroscopy, FTIR, and atomic force microscopy. *Anal. Bioanal. Chem.*, **405** (5), 1577–1591.
177. Gelbrich, J., Mai, C., and Militz, H. (2008) Chemical changes in wood degraded by bacteria. *Int. Biodeterior. Biodegrad.*, **61** (1), 24–32.
178. Fischer, G., Braun, S., Thissen, R., and Dott, W. (2006) FT-IR spectroscopy as a tool for rapid identification and intra-species characterization of airborne filamentous fungi. *J. Microbiol. Methods*, **64** (1), 63–77.
179. Wenning, M., Seiler, H., and Scherer, S. (2002) Fourier-transform infrared microspectroscopy, a novel and rapid tool for identification of yeasts. *Appl. Environ. Microbiol.*, **68** (10), 4717–4721.
180. Naumann, A. (2009) A novel procedure for strain classification of fungal mycelium by cluster and artificial neural network analysis of Fourier transform infrared (FTIR) spectra. *Analyst*, **134** (6), 1215–1223.
181. Shapaval, V., Moretro, T., Suso, H.P., Asli, A.W., Schmitt, J., Lillehaug, D., Martens, H., Böcker, U., and Kohler, A. (2010) A high-throughput microcultivation protocol for FTIR spectroscopic characterization and identification of fungi. *J. Biophotonics*, **3** (8-9), 512–521.
182. Naumann, A., Navarro-Gonzalez, M., Peddireddi, S., Kües, U., and Polle, A. (2005) Fourier transform infrared microscopy and imaging: detection of fungi in wood. *Fungal Genet. Biol.*, **42** (10), 829–835.
183. Kaminskyj, S., Jilkine, K., Szeghalmi, A., and Gough, K. (2008) High spatial resolution analysis of fungal cell biochemistry - bridging the analytical gap using synchrotron FTIR spectromicroscopy. *FEMS Microbiol. Lett.*, **284** (1), 1–8.
184. Isenor, M., Kaminskyj, S.G.W., Rodriguez, R.J., Redman, R.S., and Gough, K.M. (2010) Characterization of mannitol in *Curvularia protuberata* hyphae by FTIR and Raman spectromicroscopy. *Analyst*, **135** (12), 3249–3254.
185. Walter, A., Erdmann, S., Bocklitz, T., Jung, E.M., Vogler, N., Akimov, D., Dietzek, B., Rösch, P., Kothe, E., and Popp, J. (2010) Analysis of the cytochrome distribution via linear and nonlinear Raman spectroscopy. *Analyst*, **135** (5), 908–917.
186. De Gussem, K., Vandenabeele, P., Verbeken, A., and Moens, L. (2005) Raman spectroscopic study of *Lactarius spores* (Russulales, Fungi). *Spectrochim. Acta, Part A*, **61** (13-14), 2896–2908.
187. Fackler, K. and Schwanninger, M. (2012) How spectroscopy and microspectroscopy of degraded wood

contribute to understand fungal wood decay. *Appl. Microbiol. Biotechnol.*, **96** (3), 587–599.

188. Fackler, K., Stevanic, J.S., Ters, T., Hinterstoisser, B., Schwanninger, M., and Salmen, L. (2011) FT-IR imaging microscopy to localise and characterise simultaneous and selective white-rot decay within spruce wood cells. *Holzforschung*, **65** (3), 411–420.

189. Schwarze, F. (2007) Wood decay under the microscope. *Fungal Biol. Rev.*, **21** (4), 133–170.

190. Fackler, K., Stevanic, J.S., Ters, T., Hinterstoisser, B., Schwanninger, M., and Salmen, L. (2010) Localisation and characterisation of incipient brown-rot decay within spruce wood cell walls using FT-IR imaging microscopy. *Enzyme Microb. Technol.*, **47** (6), 257–267.

191. Pandey, K.K. and Pitman, A.J. (2003) FTIR studies of the changes in wood chemistry following decay by brown-rot and white-rot fungi. *Int. Biodeterior. Biodegrad.*, **52** (3), 151–160.

192. Takahashi, M. and Nishimoto, K. (1967) Studies on the mechanism of wood decay (2). Changes in infrared spectra of Buna and Sugi wood as decay proceeds. *Wood Res.*, **42**, 1–12.

193. Gierlinger, N., Goswami, L., Schmidt, M., Burgert, I., Coutand, C., Rogge, T., and Schwanninger, M. (2008) *In situ* FT-IR microscopic study on enzymatic treatment of poplar wood cross-sections. *Biomacromolecules*, **9** (8), 2194–2201.

194. Weisshaupt, P., Naumann, A., Pritzkow, W., and Noll, M. (2013) Nitrogen uptake of *Hypholoma fasciculare* and coexisting bacteria. *Mycol. Prog.*, **12** (2), 283–290.

195. Martin, J.A., Solla, A., Woodward, S., and Gil, L. (2005) Fourier transform-infrared spectroscopy as a new method for evaluating host resistance in the Dutch elm disease complex. *Tree Physiol.*, **25** (10), 1331–1338.

196. Erukhimovitch, V., Tsror, L., Hazanovsky, M., and Huleihel, M. (2010) Direct identification of potato's fungal phyto-pathogens by Fourier-transform infrared (FTIR) microscopy. *Spectrosc. Int. J.*, **24** (6), 609–619.

197. Kos, G., Lohninger, H., and Krska, R. (2002) Fourier transform mid-infrared spectroscopy with attenuated total reflection (FT-IR/ATR) as a tool for the detection of *Fusarium* fungi on maize. *Vib. Spectrosc.*, **29** (1-2), 115–119.

198. Lu, X.N., Rasco, B.A., Jabal, J.M.F., Aston, D.E., Lin, M.S., and Konkel, M.E. (2011) Investigating antibacterial effects of garlic (*Allium sativum*) concentrate and garlic-derived organosulfur compounds on *Campylobacter jejuni* by using Fourier transform infrared spectroscopy, Raman spectroscopy, and electron microscopy. *Appl. Environ. Microbiol.*, **77** (15), 5257–5269.

7
NIR Hyperspectral Imaging for Food and Agricultural Products

Véronique Bellon-Maurel and Nathalie Gorretta

7.1
Introduction

7.1.1
A Brief History of NIR Spectral Imagers

Imaging in the near infrared (NIR) spectral range was first developed for remote sensing applications in the 1970s. Interest in NIR imaging of food products was first shown in the late 1990s by pioneers building their own systems, which were usually equipped with multispectral cameras [1, 2]. These practices were really generalized at the beginning of the twenty-first century. They were driven by the availability of reliable NIR imaging systems for both online and laboratory purposes. Indeed, the Finnish PGP, that is, Prism–Grating–Prism, which provided a low-cost NIR imager system, was first introduced during this period [3]. Figure 7.1 represents the results of a thorough bibliometric study carried out by our team on hyperspectral imaging (HSI)/multispectral imaging for food and agricultural products. Around 300 journal-published papers have been inventoried to date (250 at the end of 2012), with around 30% of them, that is, 73, published during 2012 alone!

Another indicator of the vitality of this scientific topic is the number of reviews that has flourished over the last years: no less than 23 reviews have been published since 2007! Most deal with hyperspectral (HS) techniques for food and agrofood quality and safety inspection [4–18] and, except for Kim *et al*. [14], who focus on shortwave NIR and visible, they generally include not only NIR HS vision but also visible, Raman, and fluorescence imaging. Others focus on one type of commodity, such as fruit [19–21], meat [6], hams [22], wine wastes [23], or one specific issue such as fecal and microbial contamination [24].

NIR imaging experiments create 3D images: two dimensions provide spatial information and one dimension provides spectral information. If the third dimension is restricted to a limited number of wavelength bands (typically between 3 and 10), a multispectral image is created; when the whole spectrum is scanned,

Infrared and Raman Spectroscopic Imaging, Second Edition. Edited by Reiner Salzer, Heinz W. Siesler.
© 2014 Wiley-VCH Verlag GmbH & Co. KGaA. Published 2014 by Wiley-VCH Verlag GmbH & Co. KGaA.

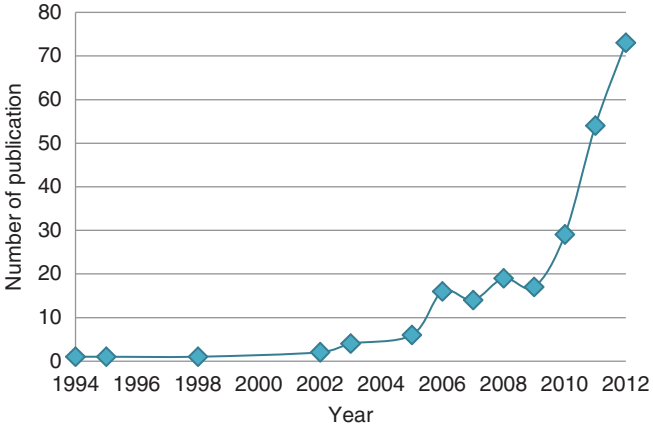

Figure 7.1 The take-off of publications concerned with NIR hyperspectral and multispectral imagers applied to food and agricultural products.

the image created is termed *hyperspectral*, which will be abbreviated as HS in the following sections (Figure 7.2).

Optimizing the acquisition of this kind of image has been a major challenge in the last 25 years. Two techniques have emerged, which are now the standards. The first one consists of consecutively recording the images at each wavelength, that is, band-by-band, using a filter wheel – for multispectral imaging only – or a tuneable filter, generally an acousto-optic tuneable filter (AOTF) or a liquid crystal tuneable filter (LCTF) for HSI. The main advantage of these whole image single-band approaches is that the spatial resolution is very good and the entire image is

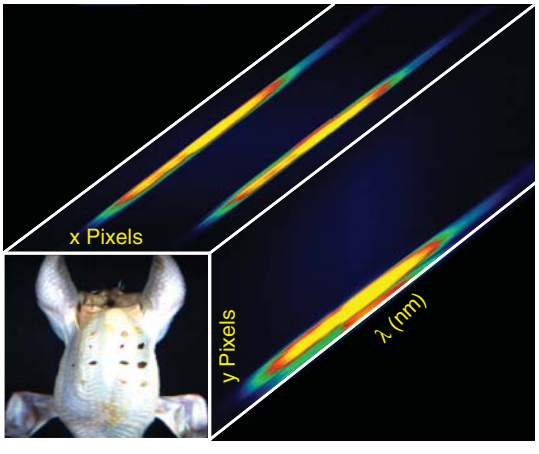

Figure 7.2 Hyperspectral image of poultry; the third dimension provides the spectral information. (Courtesy of B. Park.)

acquired instantly, thereby minimizing the number of artifacts on the image. The downside is that inconsistencies may appear when the wavelength is changed, and the optical device or the sample is not stabilized.

The second approach used to create NIR images involves acquiring one line of a sample at a time, by projecting the spectral axis on the second dimension of the imaging array (cf. Chapter 1 of this book). By sweeping the sample line-by-line, it is possible to reconstruct the overall HSI of the sample. This technology, which is widely used in remote sensing, is generally chosen for online cameras because the displacement of the sample on the conveyor belt is compatible with the need for the relative repositioning of the sample below the array; the image is thereby acquired as the sample proceeds in front of the camera. The appearance in the late 1990s of PGP components, which were designed for the 400–900 nm range, boosted the development of line-by-line imagers. Such components are now also available in the 900–1700 nm range, and prototypes have been introduced for the 1000–2450 nm range [25]. Today, Fabry–Perot microinterferential filters coupled to the matrix detector are available at reasonable prices. The detectors are cameras usually based on a silicon array for the short wavelength range (400–1000 nm) or InGaAs, InSb, or mercury cadmium telluride (MCT) arrays for longer wavelengths.

7.1.2 When is NIR Hyperspectral Imaging Used for Food and Agricultural Products?

NIR imaging is increasingly used in food analysis. As shown in the reviews cited in Section 7.1.1, applications range from online quality monitoring to the spatially resolved evaluation of structural and biochemical compositions of various products. The breadth of applications exploits both the broad wavelength range that is attributed to the NIR spectrometry and the facility with which applications can be developed, thanks to the simplicity of sampling. There are no strict rules governing where instrumentation may be most beneficial, that is, in the laboratory, at line or online, but, online, there has been a general move toward the use of short-wavelength range instruments, while in the laboratory imaging systems accessing the longer wavelength range is more commonly used. There are many reasons for these preferences; the most important factors are probably related to cost and the type of information that is needed. This has led to two main types of NIR HS imager usages:

- As a powerful extension of NIR spectrometry dedicated to analyzing product composition or properties. HSI accesses the same chemical information as NIR spectrometry, but uses a spatially resolved multispectral parallel approach. HSI laboratory devices are generally aimed at developing knowledge on product composition or for routine quality control. These uses take advantage of the two most powerful features of NIR HSI: (i) its ability to map chemical components and (ii) the possibility of high-throughput analysis like screening. In addition,

NIR imaging enables acquisition with a small pixel size and can therefore considerably reduce detection limits regarding mixture analysis when compared to those of traditional NIR spectrometry. These features open very interesting avenues for the detection of contaminants and small biochemical changes, especially those associated with genetically modified organisms (GMOs).

- As a powerful extension of vision and image analysis systems, when classical red/green/blue (RGB) vision systems fail. This is particularly the case for inline vision systems, which have been designed to detect foreign bodies or products with anomalous areas (defects, etc.). In the following chapters, we will describe these different applications and examples, illustrating today's state-of the art technologies and methodologies.

7.2 HSI as a "Super" NIR Analyzer

In this case, HSI can be seen as an analytical technique that represents a powerful extension of NIR spectrometry: it provides access to the same kind of information as NIR, that is, chemical and physical information, and also offers the spatial advantages of imaging, thus facilitating higher precision levels or mapping. These applications include the following:

- Assessment and quantification of physicochemical or sensory properties of food and agricultural products
- Chemical mapping
- Analysis of the physical properties of the food/agricultural items.

7.2.1 Assessment and Quantification of Physicochemical or Sensory Properties of Food and Agricultural Products

In many cases, HSI may replace NIR spectrometers to compute concentrations of various compounds or to estimate quality parameters of agricultural and food products. HSI can be used to assess properties as diverse as oil content, moisture, flour yield, softness, sucrose solvent retention capacity, and alpha-amylase activity in grains [26–28]; sugar content and maturity of fruits like apple or banana [29–31]; drip loss, water-holding capacity, color, pH, and sensory properties of meat [32–39]; analysis of mixtures to detect the presence of substances such as, in forages [40], or the concentration of $n-3$ polyunsaturated fatty acids in designer eggs [41].

However, after reviewing the numerous studies found in the literature, it became apparent that many researchers did not take full advantage of the spatial properties of HSI, some of them only using HSI as a "mere spectrometer."

This is the case when spectral images are processed by averaging the spectra on the whole sample in order to generate one spectrum per sample [30–32]. This

data processing technique does not take full advantage of the spatial properties of imaging, and it is possible that a simple spectrometric measurement would yield better results. Very few researchers compared performances of HSI and NIR spectrometry. Mora *et al*. [42], who studied the density and moisture of wood disks, is one of the few teams who attempted a comparison. They concluded that NIR spectrometry was superior to imaging as this technique provided much less noisy spectra. Kimiya *et al*. [43], working on fish fillets, obtained very similar results with both NIR and HSI, but considered that HSI could be improved by targeting specific areas of the fillet (i.e., thin parts of the fillet), whereas automatic NIR spectrometry could not.

In most examples, however, the spatial advantage of HSI is properly exploited in the spectral analysis, thus enabling researchers to target certain areas (region of interest or ROI) and to exclude other areas. The most telling examples concern meat chop or meat slice characterization. For instance, teams of Teagasc and University College Dublin systematically define the ROI as the whole lean part, or the eye-loin, thus excluding fat areas [33–35, 38]. They then generally average the spectra over the whole ROI. In one case, in addition to spectral averaging, textural features were extracted from gray-level co-occurrence matrix (GLCM), but they showed rather low correlations with tenderness [37]. Other researchers working on meat [36, 39] design smaller circular ROIs in these lean regions. For apples, Garrido-Novell *et al*. [29] defined the ROI – on which spectra were averaged – as the apple surface excluding the specular reflection area. For grain, the advantage of focusing the analysis on dedicated locations has been exploited by Delwiche *et al*. [27] and Xing *et al*. [28]. Delwiche *et al*. [27] attempted to estimate three quality properties (flour yield, softness equivalent, and sucrose solvent retention capacity), based on reflectance images (1000–1700 nm) of nontouching kernels. They defined five 9×9 pixels' ROIs along the main axis of the grain to study spectral properties. Five morphological properties (area, elliptical eccentricity, major and minor axis lengths, and ellipsoidal volume) and four spectral properties, that is, texture properties (contrast, correlation, energy, and homogeneity), were calculated from gray-level co-occurrence matrices (GLCM) of principal component scores 1–3 images. The combination of morphological and spectral properties produced better models than either property group alone. Xing *et al*. [44] was one of the few teams to compare HSI with NIR spectrometry (Fourier transform-near infrared, FT-NIR) performance, when trying to predict alpha-amylase activity in wheat kernels. They have chosen to focus on the germ as the alpha-amylase activity is known to be mainly distributed in this region of the kernel. Therefore, only the spectra from the germ regions were utilized in order to minimize the influence of other major components of wheat kernel, that is, protein, on analysis and to increase the sensitivity of the signal. The spectra from the pixels (around 200 pixels) within the segmented germ region were averaged. Models built from the short-wavelength infrared (SWIR) HSI system performed as well as the FT-NIR data in terms of R^2 and root mean square error (RMSE) values: the measured alpha-amylase activities were estimated with the highest R^2 values of 0.88 and 0.82 with SWIR HSI and FT-NIR, respectively.

In line with these authors' approaches, we recommend not to average spectra over the whole sample but to take advantage of the spatial display of spectra in order to reinforce the spectral analysis. Attributes, as simple as the variance spectrum of the sample, or more complex ones similar to those extracted from a mapping process or from textural analysis such as the GLCM, should be systematically tested as additional variables to decide whether it is preferable to use HSI instead of NIR spectrometry.

7.2.2 Chemical Mapping

When dealing with homogeneous products or product streams (liquid, slurry), NIR spectrometric devices are often sufficient to give a good estimate of chemical content. But with heterogeneous products or solid product streams (streams of particles), imaging is necessary in order to avoid averaging over regions of different concentrations. The mapping of chemical gradients at a macroscopic scale is usually performed on fruit, wood, and fish products, and at a smaller scale with cereal kernels.

7.2.2.1 Fruit

In this sector, one of the very first experiments was carried out in 1998 by Hart *et al*. [45], who mapped the soluble solid content (SSC) of kiwi fruit. An NIR HSI spanning the spectral range 650–1100 nm was used on the section of a cut kiwi fruit. The crucial reference data issue was solved as follows: SSC of plugs cut from thin slices of fruit were measured and related to the spectra collected on the same areas from which the plugs were taken. A prediction error of 1.2 Brix (over a 4.7–14.1 Brix range) was obtained. Later, Tsuta *et al*. [46] built a 16-bit charge-coupled device (CCD) camera system using band-pass filters at 846, 874, 902, and 930 nm to map the sugar content of half-cut melons. Cores measuring 25 mm in diameter were analyzed to calibrate the system. Long *et al*. [47] developed a low-cost multispectral system with an 8-bit CCD camera and five filters at 830, 850, 870, 905, and 930 nm for the same purpose. They concluded that it was necessary to average on 23×23 pixel blocks to obtain satisfactory prediction rates ($R^2 = 0.98$ and standard error of cross-validation = 1.1 Brix), and that a 10-bit camera was required to increase the signal-to-noise ratio (SNR).

In relation to maturity issues, Peirs *et al*. [48] presented an application in which NIR HSI was used to eliminate the handling of toxic products, that is, iodine, as practiced in apple grading. This approach involves measuring the regression of starch in half-cut apples to determine their maturity stage. Normally the apple is stained with an iodine solution – which turns black in the presence of starch – and then analyzed using an RGB or black and white camera. Using an NIR HS camera eliminates the need for the staining step and can be used to image the continuous gradient of starch content and thus replace the binary (starch/non starch) response. To get a reasonably good evaluation of starch/nonstarch areas, a threshold is applied to the first principal score image. The authors suggest that

a multispectral camera be used to perform this mapping, which would both decrease the price of the device and speed up the measurement time.

7.2.2.2 **Wood**

Wood is the other vegetal commodity in which NIR HSI has received huge interest. The most sought-after application here is compression wood mapping. Compression wood represents a major problem as it provokes distortion of sawn wood. Therefore, the mapping of compression wood on timber sections would be very useful for both timber grading and research purposes in order to better understand the factors leading to compression wood. Compression wood has a chemical composition that is different from that of normal wood as the lignin content is higher. Several studies on this topic are reported based on either HS or multispectral NIR imaging systems. The first method (in 1941!) [49] developed for detecting compression wood was based on candling wood slices in the visible range: compression wood is opaque whereas normal wood is translucent in visible light. But this method had some drawbacks, and methods based on NIR imaging have subsequently been developed. For instance, Nyström and Hagman [50] used a commercially available scanning system (IVP, Sweden) combined with a PGP spectrograph to create a real-time NIR imager. Whole wood planks were scanned in reflectance in the 400–710 nm range. The reference method for determining compression wood was scanning electron microscopy (SEM) coupled with human judgment. This system was evaluated on 4 m long planks of Norway Spruce, conveyed at 0.3 m s^{-1} with a resolution of 2 mm in the feeding direction. Principal component analysis (PCA) and partial least squares regression (PLS) were carried out on pixels, and real-time classification was correct in 11 out of 14 cases.

Noordam *et al*. [51] used a multispectral imager made up of a PbS camera and a filter wheel (680, 740, 800, 840, 1010, 1110 nm) to view two wooden disks of pine and spruce wood (Figure 7.3). Based on PCA performed on single pixels, they were able to map three regions: bark wood, compression wood, and normal wood.

More recently, several researchers got involved in mapping wood compression or other wood properties: Duncker and Spiecker [52] and Meder and Meglenb [53] studied wood compression, respectively, in Norway spruce and pine Fernandes *et al*. [54] measured intragrowth ring wood density in pine, whereas Thumm *et al*. [55] mapped biochemical components such as lignin, glucose, and galactose in *Pinus radiata*, based on calibrations previously built in NIR spectroscopy.

7.2.2.3 **Fish**

Among animal products, fish offers the best example of chemical mapping, with online devices now commercially available. Several researchers have addressed this issue, for instance, for mapping water characteristics in fish flesh, such as moisture distribution [56] and water-holding capacity indices [57] in salmon, or water content in salted cod [58]. In addition to water, color – an important quality criterion – is another property that could be mapped, for example, for salmon. Although color can be determined by visible imaging, when the aim is to develop an industrial system, measuring it using long-wave NIR imaging (900–1700 nm)

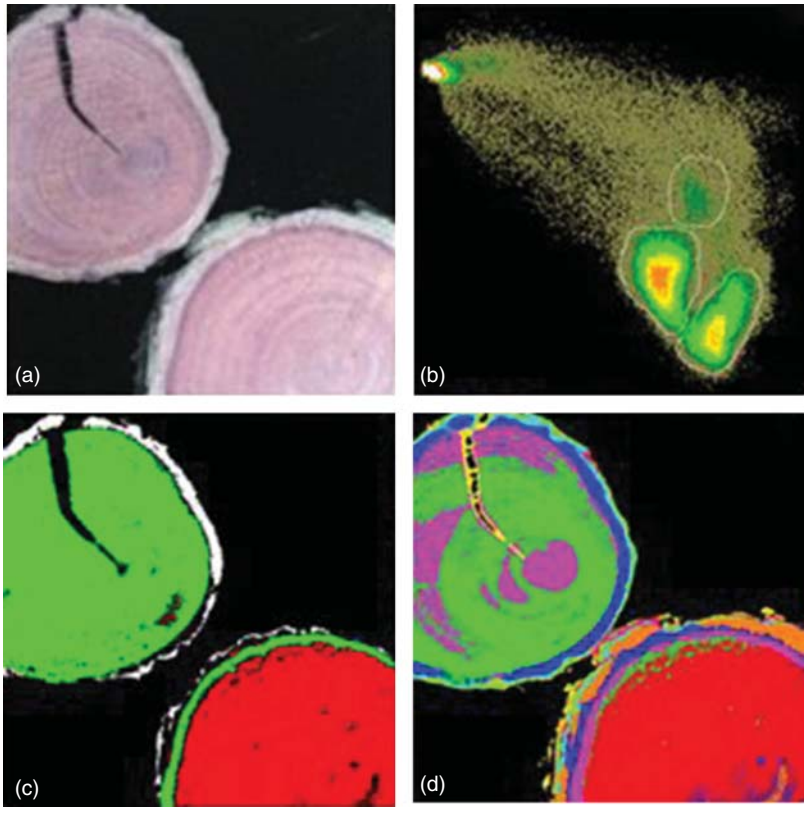

Figure 7.3 A multispectral wood image: the pseudocolor image (a), score plot (b), multivariate image analysis (MIA) combined score image (c), and the feedback multivariate model selection (FEMOS) nine-class segmented image (d). (Adapted from with permission elsevier Ref. [51].)

could be very relevant as this range is also suitable for other chemical purposes such as moisture and fat analysis. Based on this principle, Wu *et al*. [59] succeeded in evaluating L, a^*, and b^* values of salmon flesh by using only a set of wavelengths (<7) in this range. Finally, NIR imaging (400 – 1000 nm) has proved to be useful for locating the different parts of a fish fillet as each of them have different commercial values [60]; this knowledge is crucial because it determines fillet flaw severity: flaws are judged to be more severe when they are located in the fillet parts of highest value, for example, the loin. A combination of two bands (525 and 715 nm) enabled them to find the centerline of the fish fillet, which is needed to identify the part of the fillet belonging to the loin, belly flap, center cut, and tail.

Based on some of these studies, commercial systems have been designed for the fish industry, especially for measuring water content, fat, and color. The first commercially available system was developed in the early 2000s, and was the fruit of the collaboration between SPECMOD, that is, the Centre for Biospectroscopy and

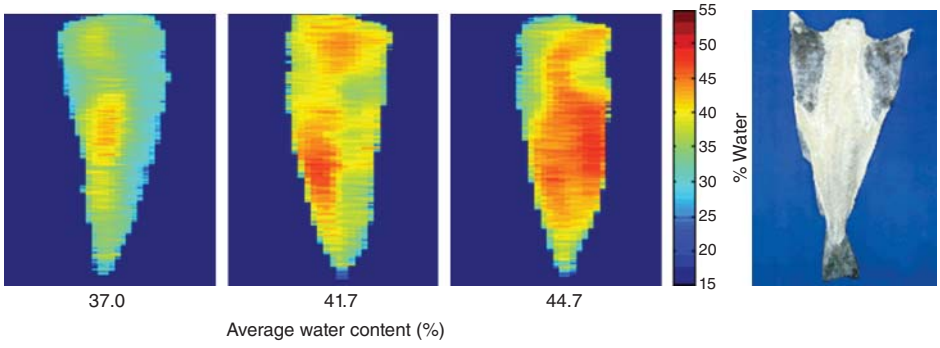

Figure 7.4 Prediction of water contents in dried and salted cod. An image of a dried and salted cod for comparison to the right. (Adapted from SPECMOD, Aas, Norway.)

Data Modelling (Aas, Norway), together with Sintef ICT, and the Norwegian company Qvision AS (Oslo, Norway). This industrial online vis–NIR spectroscopic imaging scanner was used for mapping (i) water content in salted cod [58] and (ii) fat and pigment contents in salmon fillet (Figure 7.4) [61].

This system works in the transflectance mode, with a penetration depth of around 20–25 mm. The capacity of the system is about 60 fillets per second. The same company developed another application designed to evaluate the amount of edible meat in live crabs; a correlation as high as 0.96 has been attained [62]. Since 2008, most of the development work in Qvision AS has been focused on assessing meat quality.

7.2.2.4 **Meat**

As in the case of fish, meat pieces are very likely to be mapped with regard to the concentration of various components such as water, proteins, fat in, respectively, beef [63] and lamb meat [64] water, protein in cooked hams [65] and water, fat and salt in dry-cured hams [66].

As outlined by ElMasry *et al*. [63], one particular issue to be addressed is marbling, that is, the presence of intramuscular fat distributed as a mesh. Intramuscular fat is part of the fat content of the meat slice and should therefore be correlated with fat content. However, intermuscular fat has distinct morphological and spectral features that differentiate it from the lean portions, whereas intramuscular fat pixels exhibit reflectance values very close to that produced by the lean pixels in several spectral regions, which make their segmentation a very tricky task. On beef meat, ElMasry *et al*. [63] found satisfactory models (R^2 equal to 0.89, 0.84, and 0.86, respectively, for water, fat, and protein) and also succeeded in identifying 8, 7, and 10 feature wavelengths, respectively, for water, fat, and protein content prediction, thus enabling them to map these three constituents (Figure 7.5). On pork, Qiao *et al*. [67] also tackled the marbling issue using a 400–1000 nm imager, although using a different approach. These authors carried out a PCA on all the pixels of the image, which successfully distinguished between lean and intramuscular fat. After pixels were segmented into two classes, a textural analysis was

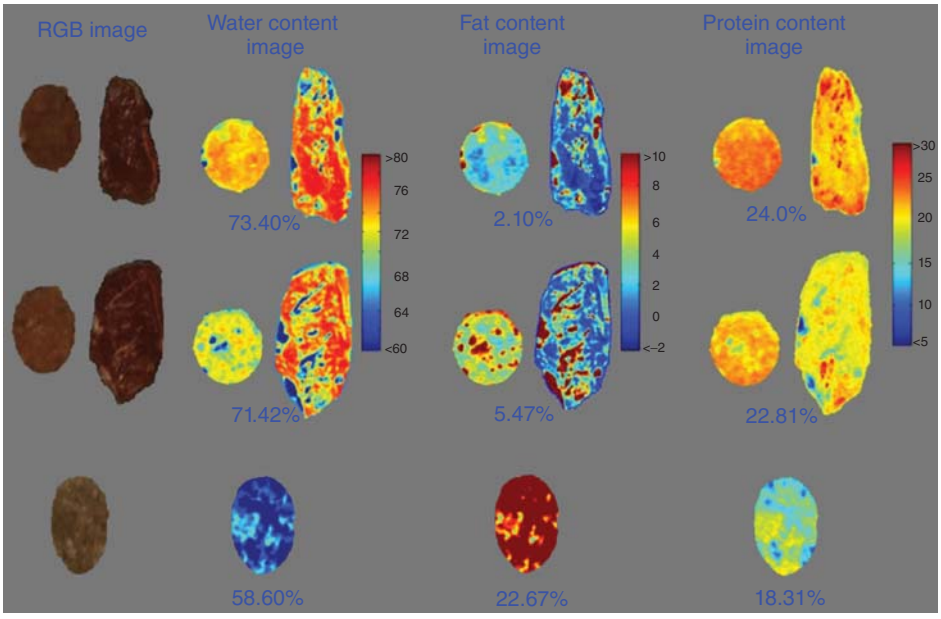

Figure 7.5 Chemical images of water, fat, and protein contents resulting from two different samples (first and second rows) and from fat trimmings of beef samples (third row). In the color bar used in the visualization, the blue values correspond to low content and red values correspond to high constituent content. (Adapted from Ref. [63].)

carried out (GLCM) and the indexes were related to a marbling score established by experts.

HSI may lead to more specific chemical analysis in meat products. Since both the fat content and fatty acid composition are important in evaluating the quality of beef, Kobayashi *et al*. [68, 69] proposed to map not only fat but also fat components such as unsaturated fatty acids and oleic acids using a custom-made NIR imager using three rotating filters in the 1300–2200 nm range. The three filter instruments performed well as a classical HSI.

7.2.2.5 Laboratory Batch Cultures

Several microbiology tests performed in laboratories are based on the culture of microorganisms on either agar plates or various media (soil, compost, etc.), which is then followed by visual observations. Although traditional culture-based direct-planting methods are still the "gold standard" for presumptive-positive pathogen screening, visual analysis of these agar media by highly skilled technicians is very difficult as microorganisms with similar morphological characteristics can grow simultaneously. Laboratories are demanding rapid methods to detect and identify microorganisms. Yoon *et al*. [70–73] proposed to use HSI to directly classify various pathogens in agar media. After focusing on the detection of Campylobacter in foods of animal origin [70], Yoon's team addressed the difficult issue of identifying

common forms of *Escherichia coli* bacteria (Shiga-toxin producing *Escherichia coli*, STEC type). With an HSI system in 368–1024 nm range, Yoon *et al*. [70] were able to classify the six most common STEC serogroups on pure spot plates. But the model suffered from insufficient sampling of data over many different colony populations (inadequate generalization power). Later on, Yoon's team proposed more efficient models and investigated the effects of preprocessing and the size of ROI on the classification results [72–74]. Similarly, Yao *et al*. [75] cultivated fungi, specific to corn and wheat on agar plates, and classified the strains using HSI.

Working on a more complex medium, that is, compost, Serranti's team used HS mapping to study the quality of composts in term of maturity and amount of contaminants [76] and carried out real-time monitoring of an anaerobic digestion process [23]. In this study, an SWIR HSI system (1000–1700 nm) allowed them to demonstrate the correlation between standard chemical parameters typically measured related of specific biomass (pH, chemical oxygen demand (COD), volatile solids, nitrate (NO^{3-}) and phosphate (PO^{3-}), and spectral features of digestate samples.

Similar approaches can also be carried out on soils. Indeed, they could serve to analyze the small-scale variability of soil properties in order to understand soil microbial functioning and, consequently, its potential vulnerability to disturbances such as temperature increase [77]. Very recently, this issue has been addressed by Gobrecht *et al*. [78] using a vis–NIR HSI system (400–1000 nm). Here, the spatial and temporal microvariability of soil respiration was successfully estimated (Figure 7.6).

7.2.2.6 **Kernels**

Small objects, such as grains, also present an opportunity for constituent mapping, although specific magnifying setups may be necessary. Kernels are so small that they can be viewed by either reflectance or transmittance. HSI has a twin advantage as it offers high throughput for individual kernel analysis (several kernels can be analyzed on the same image) instead of bulk analysis and provides representative maps at high resolution. Both advantages are of prime interest as they improve the sensitivity and the detection limits of NIR. This may be of particular interest when low-level components are being looked for, for instance, for plant breeders. We came across applications as diverse as the mapping of oil/oleic acids in corn [79], the identification of pregerminated barley at an early stage (~12 h after pregermination) [80], the mapping of the floury/vitreous endosperm of maize [81], or the tracking of moisture diffusion in conditioned wheat kernels [82]. In this last example, it is interesting to note that the authors attempted to distinguish between bound and free (conditioning) water in the wheat kernels using D_2O instead of H_2O during conditioning, but with little success because of the low sensitivity of NIR spectroscopy when detecting D_2O.

7.2.2.7 **Other Applications: Process Monitoring**

HSI is useful for mapping the physicochemical changes in products during a process and can be used, therefore, to monitor the process itself. Unlike in the above

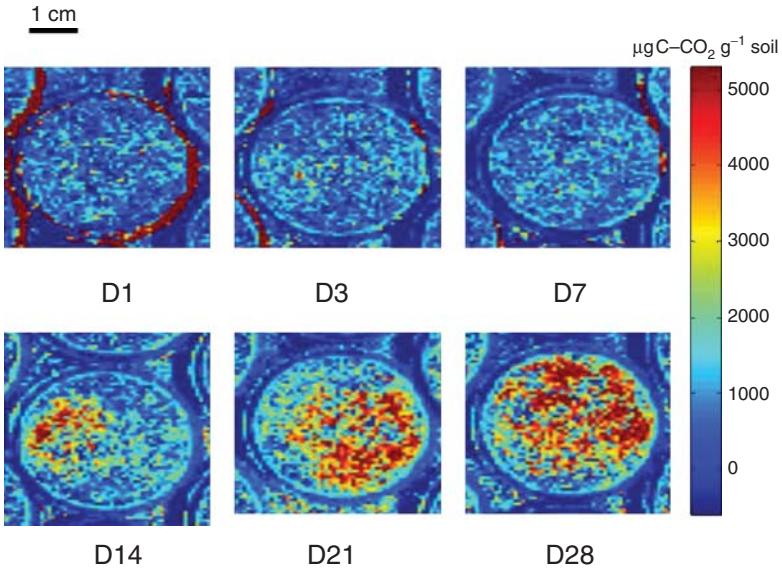

Figure 7.6 Prediction of respiration of a soil sample (µg $C–CO_2$ g^{-1}) over time (day 1 to day 28) obtained by PLS modelization. Samples were built by putting 30 g soil amended with 0.04 mg straw g^{-1} soil at the bottom of pots, covered by seven different 1 cm thick mixes of soil and straw and was then incubated at 28°C for 28 days. In the color bar used in the visualization, the blue values correspond to low respiration and red values correspond to high respiration. (Adapted from Ref. [78].)

mentioned example of grain hydration process [82], Wu *et al*. [83] mapped the moisture distribution in individual prawns during prawn dehydration. Nguyen *et al*. [84] combined HSI (400–1000 nm) and texture analysis to detect the "cooking front" of boiling potatoes. Modeling changes in the "cooking front" over time enabled them to predict the optimal boiling time.

7.2.2.8 Conclusion: Some Pitfalls of HSI When Used for Chemical Mapping

The first pitfall, which is specific to grain, is that the images are very sensitive to grain topography. This issue is not encountered with bigger objects such as meat slices, fish fillets, or wood disks as these objects are generally flat and observed in reflectance. This is not the case for grain as evidenced by several authors. Nansen *et al*. [85] tried to distinguish between a wild-type and mutant-inbred maize lines, using HSI (in reflectance mode) on both whole and ground samples. They concluded that optimal discrimination is obtained for ground samples and not for whole kernels and attributed this failure to the topography of the kernel: "as within a single kernel, most of the variability is attributed to the three-dimensional shape of kernels, which determines the projection angle, and causes a low level of spectral repeatability." Manley *et al*. [86] specifically studied this topic with single whole kernels of three cereals (barley, wheat, and sorghum) possessing varying

degrees of topographic complexity. The greatest source of variation for spectra for all three grain types proved to be kernel curvature, despite spectral preprocessing with standard normal variate (SNV) transformation.

The second pitfall of HSI-based mapping of physicochemical properties can be illustrated using the several previously mentioned examples. Indeed, unlike for mixture analysis of solid particle (pharmaceutical tablets, bulk kernels, etc.), analysis of biological objects poses the problem of what reference values to be given to each pixel. When mixtures of particles are dealt with, it is easy to make a spectrum of each component before the mixing and therefore to build up calibrations using these spectra. When bulk biological samples are studied, this procedure is no longer possible. Four strategies are generally used to address this issue. First, in some rare cases, it is possible to map the reference value at high resolutions when the property under study can be imaged by another high-resolution mapping technology. In wood, this is illustrated by a density measurement, which was mapped using an X-ray microdensitometer [54]. When pixel size is 79 nm, the resolution for the X-ray microdensitometer is 100 μm. To a lesser extent, that is, for a larger reference area, this strategy has been used by Meder and Meglenb [53], who determined reference wood compression severity with a 6 mm diameter NIR probe. To map reference values at high resolution, Raman imaging could provide an alternative [87]. The second strategy is based on measuring the reference on a subsample of the object to be mapped. For instance, Wu and Sun [57] and He *et al*. [56] chose to subsample small cubes (1.5 in. × 1.5 in. × 1 in.) of flesh in order to perform water content analysis and to relate these data to the pixels of the extracted cube. In the third strategy, it is assumed that the intrasample variation of the property is smaller than the intersample variation. Therefore, each sample as a whole (i.e., a wood disk, a bunch of kernels) undergoes a reference measurement (i.e., the wood bulk density or moisture content, the grain moisture content), and all the pixels of each individual sample are given the same value. Here are some examples: Mora *et al*. [42] chose this strategy for wood disk analysis and Manley *et al*. [82] for tracking water diffusion in wheat grains. All three strategies were based on a supervised learning process, whereas the latter relies on unsupervised classification and expert knowledge on the possible classes. Here, the spectra of all the pixels of all the samples are submitted to a PCA in order to group the pixels into clusters. By mapping the clusters on the original samples, the expert is able to label each of them. Each new pixel spectrum will be assigned to one of these clusters. This last strategy combining unsupervised/supervised analysis has been used, for instance, by Qiao *et al*. [67] who had to process "tricky" images of marbled pork slices, by Noordam *et al*. [51] who termed it FEMOS (feedback multivariate model selection) or by Manley *et al*. [81], who studied maize grains and surprisingly found a third class of endosperm when studying floury and vitreous endosperms. These last authors suspected that this new class, which appeared as an intermediary on the score plots, was the result of a superposition of floury and vitreous layers in the kernel.

7.2.3 Analysis of the Physical Properties of the Food/Agricultural Items

Due to good diffusion performance in scattering media, NIR is better at providing information about scattering properties across media than the visible range. NIR HSI is therefore used to measure scattered light profiles and to correlate them to scattering properties. As the NIR range also provides chemical information, one can kill two birds with one stone, that is, measure both the absorption and scattering coefficients of the absorbing medium.

Since 2003, Lu's team [88] applied NIR HSI to measure the scattering properties of solids such as fruits. Scattering properties relate to quality traits, such as firmness, which in turn are linked to the structure of fruit tissues. Firstly, a very straightforward method is used to process the reflectance image of apples and to extract three spectra for each fruit: the maximum reflectance spectrum (close to the incident point), the mean reflectance spectrum, and the standard deviation spectrum. Then, these spectra are fed into a neural network to predict both firmness and SSC. The standard error of prediction (SEP) ranges were between 6 and 7.3 $N\,cm^{-1}$ for firmness and between 0.72 and 0.81 Brix for SSC. Later on, a more accurate method was developed by Lu's team to analyze reflectance images. At each wavelength, the reflectance profile is modeled by a Lorentzian function, using two parameters a and b. This gives rise to two spectra – for a and b, respectively – which are then used to predict firmness. In peaches, 10–11 wavelengths were required to obtain a good prediction, $R = 0.77$ and 0.58, for two varieties [89] whereas, in apples, the best predictions of fruit firmness ($R^2 = 0.894$ and the SEP of 6.14 N) and of SSC (with $R = 0.883$ and SEP = 0.73%) were obtained with 21 and 23 wavelengths, respectively [90]. Later on, Qin and Lu also employed this HS system, called *optical property analyzer* (OPA), as a spatially resolved spectroscopy (SRS) system to measure the absorption and reduced scattering coefficients of fruits and vegetables [91]. This equipment when coupled to Monte Carlo simulations and diffusion theory was suitable for providing relevant information about the maximum depth penetration of vis–NIR light in Golden Delicious apples. Light penetration depths in "Golden Delicious" apples, defined as the depths at which the incident light was reduced by 99%, were in the range of 0.43–8.67 cm over the 500–1000 nm spectral range, with a majority of the samples (approximately 68%) in the range of 0.81–4.48 cm [92]. Apple ripening and the associated physiological changes have also been successfully monitored by the OPA [93]. Recently, the same team exploited differences in reduced scattering coefficient to detect pickling cucumbers damaged by a mechanical stress [94]. Spectra of the absorption and reduced scattering coefficients for pickling cucumbers were extracted from the spatially resolved scattering profiles using an inverse algorithm from a diffusion theory model for the spectral range 700–1000 nm. Within 1 h after mechanical damage was inflicted, changes in the absorption and reduced scattering coefficients for the cucumbers were observed to minimal. One day after mechanical damage, the absorption coefficient for the cucumbers increased significantly (from 5% to 10%)

for the 700–920 nm wavelengths, whereas the reduced scattering coefficient decreased significantly (−10%) for the 700–1000 nm wavelengths suggesting that effective defect detection can be achieved by enhancing scattering characteristic measurement in the optical evaluation of pickling cucumbers.

Huang and Lu [95] adopted Lu's team [91] approaches for measuring the mealiness of apples [extraction of the average reflectance for each diffusion profile, correction for object size and lighting effects, and construction of a prediction model using a partial least squares discriminant analysis (PLS-DA)]. However, the first results were disappointing for an early detection of mealiness levels. More recently, the same authors [96] proposed to use a Local Linear Embedding algorithm (LLE) associated with PLS and support vector machine (SVM) classifiers to address the same issue. The LLE algorithm was directly used to extract the spectral features of the diffusion profiles (dimension reduction), and these features were then used to build models. The classification results were encouraging with 80 and 82% of good classification obtained using LLE coupled with PLS-DA and SVM, respectively. With the aid of an artificial neural network, ElMasry *et al*. [97] tackled apple mealiness because of chilling injuries. They were able to identify five optimal wavelengths (717, 751, 875, 960, and 980 nm) to detect firmness alterations. An average classification rate of 98% between normal and injured fruits was obtained. However, the HSI was used as a mere spectrometer, as all the spectra of each apple were averaged into a single spectrum.

As in the case of fruit, the qualitative properties of meat have been studied using HSI as a tool to capture HS scattering images and to evaluate scattering properties. The qualitative features of meat such as meat tenderness [98–100] or early assessment of meat deterioration [101, 102] have been estimated. In all these studies, distributions of Lorentz using two or three parameters were chosen to fit the diffusion profiles. It is worth noting Wu's approach [100], which was based on the selection of relevant wavelengths using a stepwise approach, prior to a linear regression. This allowed them to correctly estimate the tenderness and color of beef pieces using a multispectral tool that could be easily implemented online.

Finally, HSI is also useful as an SRS system to be used on liquid samples. Qin and Lu used an NIR HSI to determine the optical properties of turbid liquid foods. They first used this technique in 2006 on liquid phantoms [103] and then in 2007 on real food liquids [104]. The system used (16-bit camera coupled to an ImSpector spectrograph) was developed by USDA/ARS, Michigan, and covered the 530–900 nm range. The absorption coefficient μ_a and reduced coefficient of scattering μ'_s were calculated for model liquids, milk, and fruit juices, using the Farrel's model, which is a simplification of the radiation transfer equation (Boltzmann equation). Coefficients μ_a and μ'_s were found by simulation and by data assimilation using 38 wavelengths with a 10 nm increment in the 530–900 nm range images. In this first study, absorption coefficients were not used to predict chemical values, but milk fat content was deduced from μ'_s coefficient at 600 nm.

In conclusion, thanks to its spatial dimension, HSI can replace setups such as SRS, as they can provide the same type of data, that is, transflectance intensity obtained at various distances from the point source, but at higher resolutions (SRS

generally have a limited number of measurement points). As the NIR community tackling food product issues gains a better understanding of scattering and absorption coefficients, we should observe the emergence of more HSI applications in this field.

7.3 NIR HS Imager as a "Super" Vision System

HSI is considered a "magical" technology by certain practitioners who seek to sort food/agricultural products into various categories, and who ordinarily use color cameras or visual analysis, to perform this arduous task. This work is generally carried out online to detect foreign bodies or abnormal products; but it can also play a useful role in the routine control laboratory when mixtures are being analyzed. In this section, we will explain why HSI is so much in demand for food quality control and we will show the possibilities and limitations of this technology when used for different applications, which are as follows:

- Detection of foreign bodies in a food product flow.
- Detection of surface or subsurface defects by reflectance (bruises, disease, etc.).
- Detection of internal defects (pits, cracks, etc.) by candling.
- Classification of food/agricultural products in quality classes.

7.3.1 Why HS Imaging May Replace RGB Cameras for Sorting or Mixture Characterization

7.3.1.1 The Failure of RGB Systems in Food Quality Control

In the food industry, numerous online controls are still based on human vision observations, especially for detecting and eliminating bad-looking products or foreign bodies. This generates many problems: human operators may fail to notice defective items, the work itself is tedious and line speed is dependent on the number of operators in charge of monitoring. Although visual sorting can be an arduous task for humans, cameras can perform the task easily and image analysis can provide very accurate results: for instance, machine vision sorting with regard to size (diameter, length, etc.) or shape (roundness) has provided much better performance levels than those obtained by human vision. Vision systems, therefore, have been the source of high expectations in the food industry for many years.

However, in spite of all their obvious advantages, vision systems are still not widely exploited in the food industry. Indeed, the problems related to food products, that is, biological products that have been submitted to various processing operations, stem from the wide variety of states they can be found (liquid, solid, fragmented, etc.), shape, color, chemical composition and so on. The same commodity can vary drastically depending on origin, or between the beginning and the end of the season.

When technically – and economically – feasible, appropriate artificial vision systems have been developed for the food industry based on classical RGB video cameras. However, far too often, RGB vision systems fail to detect defects or contaminants. There are two main reasons for this poor performance.

The first reason is that the colors of the objects to be discriminated are too similar; the three color components (RGB or hue intensity saturation coordinates) are not discriminative enough to detect the differences between the object of interest and the surrounding objects. This problem is amplified by the high color variability associated with biological products: the variance of the colorimetric components inside an object may be greater than the variance between this object and the objects to be removed. In this case, the solution is to look for other pieces of information, either in the visible spectrum or in the NIR spectrum. The NIR spectrum provides information about the chemical composition and the internal physical structure, which can be used to distinguish same-color objects of different compositions.

The second reason for the failure of RGB systems is the complexity of the scenes to be analyzed. Except for flat products (meat slices, fish, biscuits, etc.), the third dimension of food products can be relatively unusual, with concave areas leading to shadowing and color changes. This is typically the case of the calyx cavity in fruits, which is generally "seen" as a defect by classical RGB vision systems. The same misclassification problems due to concavities occur for chicken carcasses. However, NIR imaging can be used to reduce the effects of shadowing and of depth of field.

7.3.1.2 How Did Online NIR Imaging Emerge?

The main driver behind the introduction of NIR wavelength vision systems for online sorting has undoubtedly been the performance cul-de-sac reached with standard RGB camera-based applications. In the late 1980s, IRSTEA (previously Cemagref, Montpellier, France) built a vision system in which three CCD cameras could be equipped with three different filters for finding bruised apples. When equipped with only a red, a green, and an NIR filter, this system successfully differentiated the stem-end/calyx and bruises on apples [1]. The hypothesis was that an NIR image could help detect an object with water content or an internal structure different from its surrounding structures. Based on this hypothesis, other applications were developed. For instance, in the 1990s, an NIR imager was developed to detect stone fragments on peach halves for canning companies.

In canning plants, peaches are pitted automatically and stones can be broken by the blade. A sorting step is necessary to remove the remaining stone fragments. RGB cameras were totally inefficient at this task. This task is carried out manually and is very tedious. As the water content of the stone significantly differs from that of the flesh, IRSTEA proposed to use a very rough NIR imaging system based on the water absorption band. The flesh with a high content of water absorbs NIR radiation, whereas the stone fragments do not and are therefore have a different light color in the image (Figure 7.7). The IRSTEA device used a linear InGaAs array (Model G8160-256S, module C8161, Hamamatsu, Japan). Custom

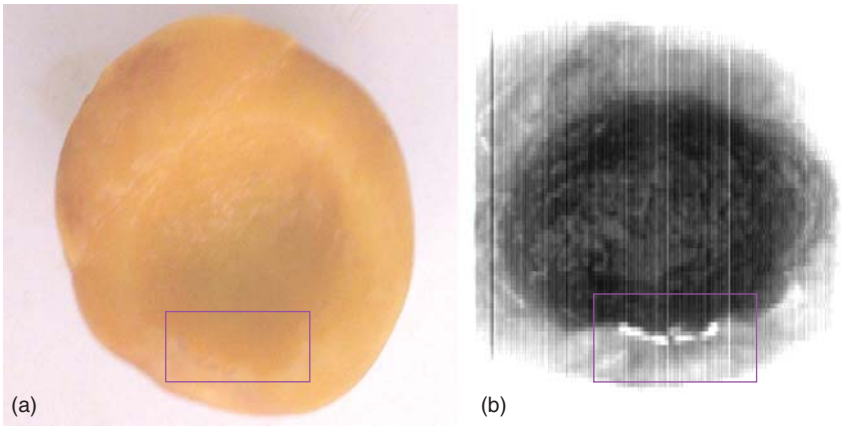

Figure 7.7 Detection of stone fragments in peach halves (canning industry): (a) the visual image of the peach half and (b) the NIR image of the same peach; stone pieces are inside the purple rectangle (white spots in the NIR image). (Adapted from Gorretta – IRSTEA, Christophe Guizard, Irstea, France)

image analysis software was developed to automatically detect the white spots of a minimal area.

The same very rough one-band InGaAs camera system was also used in the ASTEQ project [105] to detect bruises on bicolor Jonagold apples (Figure 7.8). Bruises change the internal structure of the flesh: cells are destroyed and cytoplasm invades the intercellular space. These modifications lead to a change in scattering and absorption coefficients, thereby creating black spots.

In addition to differences in scattering, NIR lighting/imaging can also be used to take advantage of more subtle chemical differences between objects. In this case, more sophisticated systems based on multispectral or HSI are required.

In the following sections, we will describe several examples of NIR imaging use in the food industry. Examples are categorized according to the industrial issues they address.

7.3.2 External Contamination (Foreign Bodies, Adulteration)

The main quality concern in the food industry is undoubtedly safety. Safety entails keeping food free from contamination and preventing food-borne diseases. Food-borne diseases must be prevented by ensuring that processing is correctly carried out to avoid further microbial development (e.g., time–temperature profiles must be maintained during thermal treatment and cans or jars must be hermetically sealed). Food contamination includes macroscopic physical contamination (foreign bodies) and microscopic contamination by foreign bodies, microbes, or hazardous chemicals (e.g., pesticide residues). External contamination excludes all contaminants embedded in the product, and only concerns those that adhere

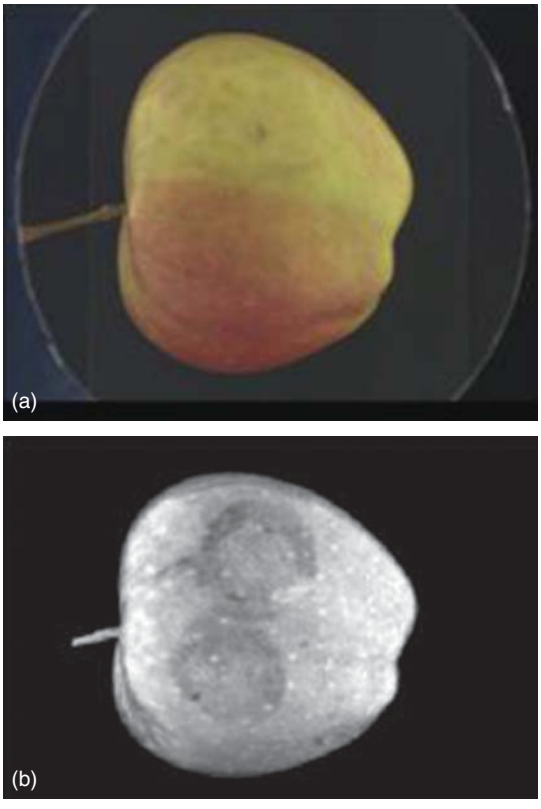

Figure 7.8 Detection of bruises on a Jonagold apple: (a) color image and (b) NIR image at 1200 nm revealing two bruises. (Adapted from Christophe Guizard, Irstea, France.)

to the surface of the object (e.g., feces contamination on chicken) or are mixed with the stream of product of interest (e.g., straw in wheat samples) as foreign bodies.

7.3.2.1 **Foreign Bodies**

Foreign bodies may be either intrinsic, such as bone in an animal food product or stems/leaves in a vegetable food product, or extrinsic, such as metal, glass, or insects. Foreign bodies may have a color similar to that of the commodity, but can be distinguished by their chemical composition and internal structure; in such cases, NIR imaging will be more efficient than RGB imaging at foreign body detection.

When the objects to be differentiated are very different in chemical composition, a small number of wavelengths are sufficient. For instance, HSI was evaluated for discriminating potato tubers from clods in the field and under varying humidity conditions [106]. The objective was to select optimal wavelengths to implement

a multispectral tool for discrimination in the field. Two optimal wavelengths (480 and 752 nm) were sufficient to yield a 97% discrimination of tubers and clods in different humidity conditions.

But more sophisticated imaging systems based on multispectral imaging have recently been proposed for this purpose. For example, TOMRA Sorting Solutions Group (previously BEST in Heverlee, Belgium) has proposed sorters equipped with up to 12 lasers that simultaneously analyze the products on one or both sides (some of which are in the NIR range). This sorting of foreign bodies and unwholesome products concerns numerous food product, for example, dried fruits such as raisins, apricots, cranberries, prunes; vegetables and particularly fresh cut commodities such as *whole head* or *mixed* salads; *baby leaves*; grains; beans; and tobacco leaves.

In these systems, laser lines are projected consecutively onto the stream of objects, and NIR multispectral images are created using CCD cameras (Figure 7.9). The objects are sorted based on scattering and absorbance differences.

Detecting fragments of insects – which for instance have been ground by the process – is difficult because of the size of the targeted particles. In the United States, relevant legislation tolerates a maximum of 75 insect fragments per 50 g of finished product, while in Canada, no more than 20 fragments in three 50 g test samples are allowed. Bhuvaneswari *et al.* [107] addressed this issue in the case of semolina. The authors used a 900–1700 nm imager on differently contaminated samples of semolina; a PLS model using 15 latent variables achieved a good level of correlation between the reference value and the rate of insect fragments predicted ($R^2 = 0.99$). The high number of latent variables is partly explained by the wide variety of insect fragments.

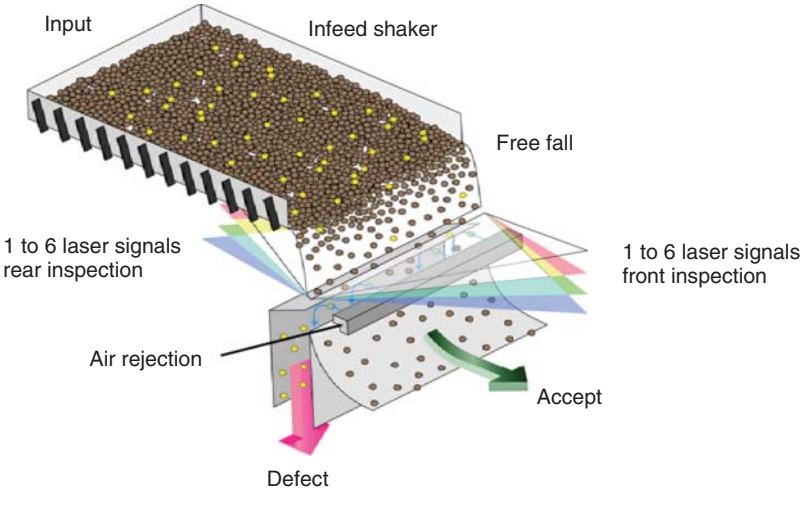

Figure 7.9 Sorting of small fruit using laser lighting and CCD cameras used to create multispectral images. (Illustration courtesy of BEST.)

Fernandez-Pierna *et al.* [108] have proposed a novel approach for the detection of various undesirable particles (straw, seeds from other crops, weed seeds, insects, stones, fragments of plastic, wood and painting, animal feces, etc.) in grain dedicated to feed. Based on a large spectral range (900–2400 nm) requiring two types of cameras, they built discrimination models for different impurities using a quadratic SVM classifier applied to principal components. A dichotomous classification tree was then performed using five groups of impurities (i.e., animal contaminants, cereals, botanical impurities, cellulose waste, and other contaminants). Each sample was analyzed, pixel by pixel, by the discrimination tree from the easiest to detect contaminant (animal contaminant) to the most difficult contaminant (cellulose). This approach allowed them to obtain a classification rate of over 95% for all lots tested.

7.3.2.2 Adulteration and Nonconformities

The detection of food nonconformities and adulteration is another important challenge that HSI can tackle, thanks to its spatial resolution feature.

For instance, Kamruzzaman *et al.* [109] focused their efforts on the detection and visualization of adulteration of minced lamb by pork. They used a HS camera operating in the range 890–1750 nm (ImSpector N17E, Spectral Imaging Ltd., Finland), coupled with a CCD camera (Xeva 992 Xenics Infrared Solutions, Belgium) with a 0.578 mm spatial resolution. The average pixel spectrum of the whole sample – background excluded – was computed. The PLSR model-based prediction showed strong correlation (R^2 cross-validation equal to 0.99) with adulteration levels that varied from 0 to 40%. Four major wavelengths (940, 1067, 1144, and 1217 nm) were selected to build a multivariate linear model (MLR) and yielded a good performance prediction (R^2 cross-validation equal to 0.98). However, despite the good performance of HSI in this particular application, one can speculate about its relevance as it is used as a mere spectrometer (the pixel spectra are averaged) on this homogeneous sample (minced meat).

7.3.2.3 Surface Contaminations

Surface contaminants are generally fungi, or alternatively liquids and slurries splashing on the food products. These contaminants generate spots on food surfaces. These two types of surface contamination have been the subject of numerous studies. They are slightly different: feces-related contamination is only the addition of a foreign substance, whereas fungi may induce biochemical changes in the infected products – which in certain cases are detectable.

Feces Contamination Feces contamination leads to food-borne diseases such as *E. coli*, which has been the subject of thorough investigation in apple production, on the one hand, and in poultry, on the other.

The FDA (Food and Drugs Administration) recommends removing feces-contaminated apples from the flow of apples in the packaging station to prevent cross-contamination in the washing pool. Researchers in the USDA Agricultural Research Service in Beltsville/MD have therefore being working on an NIR imager

to detect cattle manure on apples. The studies were carried out with prototyped line-by-line imaging system, named the ISL (Instrumentation and Sensing Laboratory) imager, comprising a PGP spectrograph imager (Specim, Oulu, Finland) in the 350–950 nm range [110]. The aim was to use a HS system to identify optimal spectral bands to be used in a multispectral detection scheme. First, the 450–850 nm spectral range was selected for its high SNR [111]. PCA was carried out and showed that the most suitable wavelength bands were the longest bands, thus indicating that it would be worthwhile to examine wavelengths above 850 nm. In a second study [112], the investigated range was extended to 950 nm and the sensitivity to contaminant concentration evaluated. Average spectra were calculated in three types of ROI: for uncontaminated, slightly contaminated, and significantly contaminated apples. Whatever the apple variety or the skin color, average reflectance intensities decreased from uncontaminated to significantly contaminated apples. The team concluded that the 675–950 nm spectral range was the most suitable for developing a variety-stable calibration. In order to transfer it online, the potential of a low-cost, dual-band system based on the 725 nm/811 nm band ratio was investigated. However, this system proved to be unsuccessful at detecting thin litter contamination on apples. Other spectral techniques such as fluorescence imaging were also investigated to overcome this problem.

Poultry provides another example of food product contaminated by litter, but the contamination detection task is even more complex than with apples. The complexity is related to different factors: the odd shape of poultry carcasses featuring several concave-shaded areas (under the wings and the leg folds), skin color heterogeneity due to the relative transparency of chicken skin, and by the wide range of potential food safety hazards associated with chickens.

In Beltsville, there was a series of studies performed using the ISL HSI to differentiate wholesome carcasses from unwholesome carcasses including cadaver and those with disease such as septicemia and tumors. The team first used a 650–900 nm system [110], and later a prototype of a specially designed three-wavelength camera [113].

The Athens HS system was similar to the one used at Beltsville/MD; it was made up of an ImSpector PGP spectrograph and a CCD camera. It worked in the 400–900 nm range, with a nominal resolution of 2.5 nm. The aim was to define the specifications for a multispectral system based on few wavelengths for a future online setup designed to detect ceca, duodenum, and colon feces on wholesome skin. In a first study [114], four wavelengths of interest were extracted from the analysis of the loadings: 434, 517, 565, and 628 nm. In the following study, image analysis was dedicated to these four spectral planes. Shadows are removed using ratio images. The best performances were obtained with 565 nm/517 nm ratio images (Figure 7.10): not only were all the contaminants revealed, including those hidden in wing shadows, but blood clots, which are not contaminants, were also detected and correctly classified as "wholesome." A later study [115] confirmed that the two-band ratio 565 nm/517 nm was the best suited to the task; the prediction accuracy of surface contaminants was 96.2% and the number of false positives

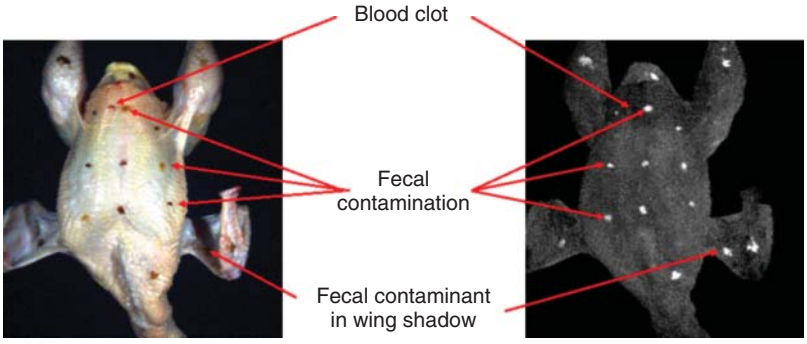

Figure 7.10 Performance of a multispectral machine vision to detect fecal contamination on poultry carcasses: (a) RGB image, (b) 565 nm/517 nm image ratio. Fecal contaminants are clearly highlighted in the 565 nm/517 nm image ratio. (Adapted from Bosoon Park, ARS USDA, USA.)

was the lowest. A line speed of 140 birds viewed per minute is what the industry is aiming at.

Fungi The presence of mold is a very important concern for the grain industry, because of its potential sanitary consequences. For instance, Fusarium head blight (also called *scab*) produces mycotoxins (deoxynivalenol, DON) that become concentrated in (but are not limited to) the infected kernel. The FDA specifies that the DON content of finished wheat products destined for human consumption should not exceed 1 ppm. Moreover, the monetary value of wheat may be reduced by 40% (or even more) even if only 5% of the kernels are infected. The potential of NIR HSI for the detection of wheat kernels infected by fungi has been evaluated by several authors [116–120]. For instance, Singh *et al.* [117, 121, 118] used HSI to detect wheat kernels infected by various fungi (*Penicillium* spp., *Aspergillus glaucus*, *Aspergillus niger*); Delwiche *et al.* [119] used NIR HSI to differentiate healthy grains from grains affected by black dot (speckle). With a shortwave imager (400–1000 nm), Jin *et al.* [120] attempted to identify toxigenic from nontoxigenic strains of *Aspergillus flavus* fungus, which is a difficult task due to the great genetic similarity between the strains. Relevant wavebands were selected using a genetic algorithm and submitted to an SVM classifier which achieved satisfactory classification rates of 85% for toxigenic pixels and 74% for nontoxigenic pixels.

7.3.3
Surface and Subsurface Defects

Although contamination is related to the addition of materials that are very different from the surface under investigation, other defects can be generated by changes in the surface or subsurface optical properties of the product. In this aspect, RGB cameras are generally efficient when the change occurs on a

homogeneous surface, and is sufficiently contrasted with the background color. In all other cases, HS (and multispectral) imaging represents the only alternative for defect detection. HSI is most relevant for detecting two types of defects that RGB cameras have difficulty in identifying:

- Actual defects: the defects that would be recognized by a thorough human inspection, such as bruises and bitter pit; these are generally characterized by a change in not only spectral absorption but also light scattering because of water exchanges.
- Potential defects: the "defects" that are not yet detectable by the human eye but which will turn into actual defects during processing; the spectral changes are small and are not accompanied by light scattering changes. These defects often relate to chilling injuries or to latent greening. In addition, HSI is used to differentiate between defects and shaded areas such as calyx/stem ends.

7.3.3.1 Human-Detectable Defects

"Actual defects" such as bruises or bitter pit generate scattering coefficient changes because of water movements in the tissues. These types of defect (bruise, bitter pit, necrosis) are relatively easy to detect, and several research groups having successfully tackled the problem.

Bruises The presence of mechanical damage (e.g., bruises) not only affects the appearance of the apples but also accelerates spoilage [122]. Therefore, early detection of these defects is needed to maintain batch quality, which is essential for the fruit and vegetable sectors of the economy. Indeed, Xing's team [123, 122] tackled bruise detection on apples using a custom-built HS imager based on an ImSpector V10 imaging spectrograph (Specim, Finland) in the 400–1000 nm range. Their first study [124] performed on Jonagold apples developed a procedure based on principal component scores for distinguishing sound apples from bruised apples and for identifying the stem-end calyx from the bruised regions. Here, only six wavelengths (571, 608, 671, 709, 798, and 867 nm) were deemed necessary for successful discrimination (the classification levels obtained were as high as 85% for nonbruised apples, 77% for bruised apples, and 98% for the stem-end/calyx group). In the second study [122], Xing *et al*. investigated the same issue on Golden delicious apples using both PCA and PLS-DA. Both the PCA algorithm and PLS model used four wavelengths (558, 678, 728, and 882 nm) for discrimination. Regarding classification accuracy, the algorithm based on PCA provided similar results to those obtained using PLS-DA (93 and 100%, respectively, for sound apples, and 86% and 82%, respectively, for bruised apples). However, according to the results obtained in this study, PLS-DA does not perform as well as PCA score images for the identification of stem-end/calyx. In another study, Xing *et al.* dealt with the issue of stem-end/calyx discrimination from defects [125]. Based on PCA of HSI, four and six effective wavebands were chosen to detect bruises on Golden delicious and Jonagold apples, respectively. These wavelength were also used to recognize the stem-end/calyx from the cheek surface using the principal score images and analysis of contour features.

In 2008, ElMasry *et al.* [126] investigated the use of HSI system for the early detection of bruises (<12 h) using different background colors on McIntosh apples (green, red, and greenish red). According to the author's arguments, previous studies were conducted to detect bruises after 24 h and on varieties with only one uniform background. HSIs acquisition was realized using a spectrograph (ImSpector, V10E, PCO, Germany) coupled with a CCD camera on the 400–1000 nm spectral band. The PLS method and stepwise discrimination analysis made it possible to define several optimal wavelengths, that is, 750, 820, and 960 nm to form multispectral images. A multispectral adaptive thresholding method was then used to segment bruise areas at different time intervals after bruising.

Recently, Baranowski *et al.* [127] examined the applicability of a HSI in visible and near infrared (VNIR) (400–1000 nm) and SWIR (1000–2500 nm) wavelength ranges for classification of apple bruising with respect to the time after damage to five selected cultivars. Several combinations of preprocessing procedures and classifiers were evaluated in order to distinguish time after bruise occurrence within the 2-week period after bruising. The best classification results (up to 94%) were obtained using a linear logistic regression (LLR) model based on 40 relevant wavelengths selected using a correlation-based features selection (CFS) algorithm.

Bruises were also investigated on other commodities such as pickled cucumbers [128], mushrooms [129, 130], strawberries [131], and kiwifruits [132]. In the study presented by Gaston *et al.* [130], HSI in the shortwave NIR spectral range was used in order to predict the appearance of bruises on mushrooms by measuring their enzymatic activity.

Other Types of Skin Damage In vegetables, common forms of skin damage are due to insect attacks, wind scarring, thrip-related scarring, scale infestation, canker spot, copper burn, phytotoxicity, or decay. Li *et al.* [133], Qin *et al.* [134], and Zhao *et al.* [135] investigated the use of a HSI system to detect common defect on oranges and citrus skin. Li *et al.* [133] used a combination of six wavelengths (determined by PCA) in the VNIR regions (400–1000 nm) to discriminate these defects. However, the stem-ends were easily confused with defective areas. After investigation, the use of a two-band ratio (875 nm/691 nm) image could be used to effectively differentiate stem-ends from defects. Ultimately, accuracy rates of up to 91% were achieved but the algorithm was not able to discriminate the different kinds of defects. The School of Agriculture in University College of Dublin carried out extensive studies on mushroom quality inspection disease detection [136, 137]. Diezma *et al.* [138] focused on the monitoring of quality deterioration in ready-to-use leafy spinach during storage. Lorente *et al.* [21, 139, 140] investigated the use of HSI in the 400–1000 nm range to classify decay of mandarins with a success rate of 89%. They used images of mandarins with pixels labeled in five classes (two types of sound skin, two types of decay, and one for scars). They compared a feature selection method using the area under the receiver operating characteristic (ROC) curve with other common feature selection techniques,

in order to select an optimal set of wavelengths that could be used to effectively detect decay. Singh *et al.* [141, 142] and Kaliramesh *et al.* [143] investigated the use of an HSI system for the detection of insect damage in wheat kernels and mung beans, respectively. For this last topic, three relevant wavelengths in the 900–1700 nm spectral range were determined using a PCA to detect bruchid infestation in mung beans. Six statistical features (maximum, minimum, mean, median, standard deviation, and variance) and 10 histogram features from images at the significant wavelengths were extracted and given as input to nonparametric statistical classifiers. Average classification accuracy rates of more than 85% and 82% were obtained for uninfested and infested mung bean kernels, respectively, using statistical classifiers.

Dealing with animal products, Chao's team [144–146] investigated broiler wholesomeness (skin tumors detection, diseases, etc.) using a HS-multispectral line-scan imager.

7.3.3.2 Potential Defects: Chilling Injuries, Potential Greening Area

"Potential" defects are defects too slight to be detected by the naked eye, which may host chemical, and therefore spectral, changes. These defects include chilling injuries and potential greening areas.

Chilling injuries are difficult to detect because the symptoms develop after the product has been placed in a warmer environment. On citrus fruit, Menesatti *et al.* [147] used a 400–970 nm HS camera (ImSpector v10 and Teli CCD camera) in reflectance mode to detect chilling injuries 14 days before they were revealed visually; the detection was based on reflectance levels and reflectance ratios (610/680, 610/750, and 680/750 nm). When studying cucumbers, Cheng [148] showed that cucumbers with severe and moderate chilling injuries had greater absorbance rates than wholesome fruit, above 700 nm. With the ISL imager (450–950 nm), a performance rate of about 90% was achieved, along with good noise robustness. In French fries, Noordam *et al.* [149] were able to detect latent greening defects that were invisible to the human eye or to an RGB camera by using a 430–900 nm HS camera consisting of a spectrograph (ImSpectorV9; Specim) combined with a monochrome camera (model PMI 1400EC; QImaging, Burnaby, Canada) and a SVM classifier.

7.3.4 Detection of Internal Defects by Candling

HSI of internal defects is based on a transmittance measurement, that is, object candling using an infrared source followed by the analysis of the resulting image. NIR radiation is more suitable than the visible method for candling because it is much less scattered than visible radiation. In biological samples, the reduced scattering coefficient μ_s' decreases constantly from the visible range to the NIR range, as can been seen in Figure 7.11. Absorption has a lower influence because absorption coefficients are around 10 times (in slightly scattering media such as cartilage, as shown in Figure 7.11) to 100 times lower (in highly scattering media

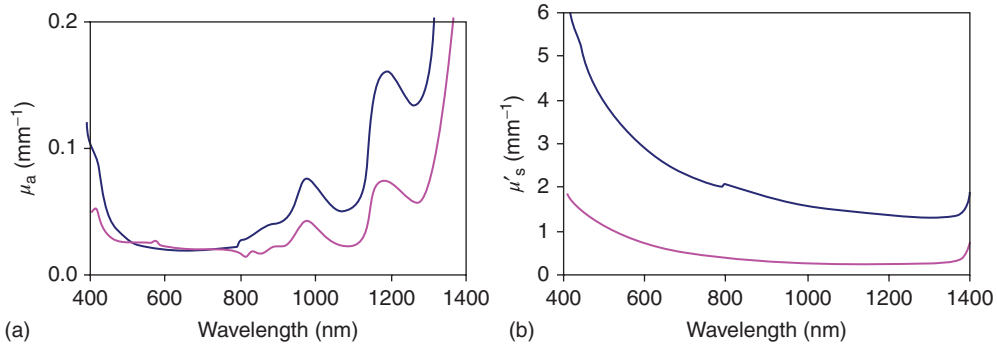

Figure 7.11 Absorption μ_a (a) and reduced scattering μ_s' coefficients (b) of aural (pink) and nasal septal (blue) cartilage samples as a function of the wavelength. (Adapted from TE Miller, Center for Biomedical Engineering, Univ Austin, TX, USA.)

such as apples as shown in Qin and Lu [104] or Chauchard *et al.* [150] than scattering coefficients. Therefore, transmittance is much greater in the NIR than in the visible range.

7.3.4.1 Internal Foreign Bodies

Internal foreign bodies, that is, foreign bodies embedded in the food material, are a nightmare for food plant quality monitoring. Detection systems are generally based on X-ray, the absorbance of which depends on the atomic number and concentration of the material [151]. But very often, X-rays are not sensitive to intrinsic foreign bodies such as stem, pits, skin, or pieces or hair, because the tissues are not significantly different in their atomic number.

Detection of remaining pits in unpitted cherries [152] is an example of embedded foreign body detection. Qin and Lu used the same camera as in the feces detection on apple study and fruit, which were illuminated in transmission with a quartz halogen lamp irradiating through a 13 mm diameter hole. The correctly unpitted cherries gave brighter images than the cherries containing a residual pit. The best spectral range for separating the two classes of objects ranked from 692 to 856 nm. Fruit size and defects had a great influence on the classification performance, whereas fruit orientation, color, and postbruising treatments had negligible effects. Last but not least, the detection carried out based on an ROI of the NIR image was twice as good as the one carried out on a single NIR spectrum, leading to an average error of 3%.

HSI has also been used in transmittance mode to detect fruits and vegetables infected by insects. For instance, Lu and Ariana [153] combined HS reflectance in the visible range (450–740 nm) and transmittance in the NIR range (740–1000 nm), which were acquired simultaneously to discriminate normal (infestation-free) pickling cucumbers from fruitfly infested specimens in three size classes (mean diameters of 16.8, 22.1, and 27.6 mm, respectively). The spectra were averaged on the whole pickling cucumber, then corrected from size effects and finally analyzed using PLS-DA. Transmittance (740–1000 nm) yielded better

classification results than reflectance for both normal (between 91% and 97%) and infested (between 84% and 90%) cucumbers, with overall transmittance accuracies ranging between 88% and 93% (depending on the size class). When the reflectance and transmittance data were combined, no improvements in the classification results were observed compared to those obtained in the transmittance mode alone. These results suggest that transmittance in NIR offered advantages over reflectance in detecting pest infestation in cucumbers. The authors suggest different approaches to improve the detection performance by (i) not averaging the pixel values on the whole pickling cucumber, but on areas of interest, and (ii) by working on fresh pickling cucumbers instead of vinegar-brined pickling cucumbers, which are less suited to transmittance studies.

7.3.4.2 Internal Tissue Defects

Although less crucial than embedded foreign materials, internal defects are still very important from a commercial point of view because of consumer reaction to undetectable internal defects. Internal defects must have a large impact on the NIR signal to be detectable. This means that only large defects, which generate a significant change of the scattering coefficient will be detected. This is generally the case for defects leading to internal holes, such as mechanical damage in cucumbers or apples.

Mechanical damage inflicted to cucumbers results in carpel separation and hollow centers. As the transmittance signal is very low, it is not possible to detect such disturbances with standard spectroscopy. HSI, thanks to its spatial resolution feature, can successfully perform this damage detection task. It minimizes the risk of confusion between the relevant signal – emanating from the unwholesome region – and that produced by the wholesome region, therefore increasing sensitivity. At Michigan State University Ariana *et al.* [128] used a transmission vis–NIR HSI developed at USDA/ARS (450–950 nm) to detect internal defects in cucumbers. The setup comprises an imaging spectrograph (ImSpector, Specim, Finland) and a backlighted CCD camera; a 150 W halogen light candled the cucumber with dual-fiber optic light lines. Three images were recorded for each cucumber by rotating it on its main axis and taking images 120° apart. The cucumbers were imaged before and after (2 h and 1, 2, 3, and 6 days) mechanical injuries were applied. Both the average spectrum along the longitudinal line and standard deviation spectrum (of the pixels along that line) were recorded. As expected, transmission was greater for defective cucumbers with hollow hearts than for normal cucumbers. Also, the defective cucumbers showed a greater standard deviation of transmittance levels because the defect was not homogeneous along the longitudinal axis. Finally, a single-band image (at 800 nm) was found to be sufficient for this application and yielded a classification rate of around 90%. Further work on pickling cucumbers showed predictability of internal defects reaching 99% based on a HSI method using the spectral range 700–1000 nm [154, 155]. Based on these results, the authors further developed a waveband HSI, which will be easier to implement online [156]. The highest classification accuracies (94.7 and 82.9%) were achieved using the optimal

four-waveband sets of 745, 805, 965, and 985 nm at 20 nm spectral resolution for cucumbers and of 745, 765, 885, and 965 nm at 40 nm spectral resolution for whole pickles, respectively.

No other works related to the detection of deeply embedded defects such as vitreous melons, brown-hearted pears, or frost-damaged citrus has been found. These defects would be well worth investigating as they are only currently detectable with nuclear magnetic resonance (NMR) and occasionally by X-ray-based analysis.

7.3.5 Classification of Biological Objects

Various authors have used HSI for classifying biological objects in different categories. The aim here is to use image analysis to identify the ROI, that is, the target when chemical analysis has to be carried out.

7.3.5.1 Inspecting Small Objects

This is typically the case for the analysis of small objects such as kernels or small fruits. HSI can be used for the simultaneous analysis of tens of kernels, either individually, when the kernels are spread onto the sampling plate – whereas a spectrometer would require the kernels to be scanned individually – or in bulk. In kernel classification, HSI has been applied to classify vitreous wheat kernels [157, 158] or maize [159]; to identify cultivars of wheat [160–163] or maize [164]; to check the viability of barley, wheat, and sorghum grains [165]; to assess the germinative capacity of barley during storage [166]; or more generally to evaluate the general quality of cereal grains by differentiating oat and groat, for instance, as carried out by Serranti *et al*. [167]. The latter team investigated the use of a SWIR HS system (1000–1700 nm) to identify three durum wheat kernels (vitreous, yellow berry, and fusarium-damaged) in a batch (mixed kernels). In this study, the NIR HS data were processed using PCA for explorative purposes, PLS-DA for classification, and interval partial least squares discriminant analysis (iPLS-DA) for the selection of a reduced set of effective wavelength intervals. The results obtained demonstrated good classification for both entire and selected interval wavelength ranges.

Regarding small fruits, Rodríguez-Pulido *et al.* [168] imaged grape seeds, the composition of which changed with maturation, Baiano *et al.* [169] found correlation between spectra averaged over a grape grain and titrable acid, pH, and sugar content, but not sensory properties. Leiva-Valenzuela *et al.* [170] adopted the same approach with blueberries and were able to predict firmness and SSC, whereas Taghizadeh *et al.* [171] showed that a 400–1000 nm system was superior to an RGB camera to predict the L value, as a quality index, of mushroom caps. In these different examples, the authors averaged the spectra collected for each grain/kernel.

As examples of more "exotic" applications, let us cite Zhao *et al.* [172] who attempted to classify five grades of green tea with HIS, or Vermaak *et al.* [173]

who used HSI to identify toxic seeds of *Illicium anisatum* (Japanese star anise) in batches of *Illicium verum* (Chinese star anise). This last study is original as the authors combined spectral information and morphology to discriminate between both species.

As a conclusion, authors working with bulk samples usually adopt one of two well-known strategies. They can either simply count the percentage of pixels related to the different classes and therefore give an assessment of the quality of the sample; as in Wetzel *et al.* [174], who used a chemical imaging system (Matrix NIR, Spectral dimensions/Malvern, Columbia, MD, USA) to monitor the amounts of wheat endosperm and nonendosperm particles in a flour milling process. This work was performed to assess the operational efficiency of the milling process. Alternatively, they can use texture analysis to improve the classification performance. For instance, Choudhary *et al.* [160] applied wavelet texture analysis to classify eight Western Canadian wheat classes of bulk sample images (960–1700 nm) and Zhang *et al.* [164] computed four textural variables (i.e., contrast, homogeneity, energy, and correlation) on the images of three optimal wavelengths (523, 579, and 863 nm) selected by implementing PCA directly on each image. Other authors preferred to display the kernels on a sample plate and to analyze them individually, with some of them averaging on the single kernel [157, 161], while others worked pixel by pixel [159, 165, 167] to provide maps and classify the kernel according to the number of pixel allocated to each category.

7.3.5.2 ROI in Multicompartment Products

Complex objects such as meat slices are made up of several parts or may have mixed composition compartments, when confronted with this detection challenge an ROI may be chosen to focus spectral analysis on one specific part or compartment.

Applications of HSI to meat products are designed to identify muscle origin from either different species [175] or the same species [176], in order to predict standard quality parameters such as PSE (pale, soft, exudative), PFN (pale, firm, non-exudative), RFN (red, firm, non-exudative), RSE (red, soft, exudative), and DFD (dark, firm, dry) in pork [177], to classify fresh pork meat in four quality classes [178] or to distinguish cooked turkey ham with regard to quality categories [179]. Generally, the image is exploited to average pixel spectra over particular ROI such as the lean part [175, 179], or the loin-eye area [177]. For instance, in pork quality studies [39, 177], spectral analyses were concentrated on the loin-eye area: the loin-eye ROI is segmented from fat and the background, and then spectra from this ROI are averaged for each sample. After a PCA, the wavelengths with the highest weight are selected and fed into a neural network, and four quality classes are obtained [177]. Classification with regard to quality yielded a rate of 87% using this method. Barbin *et al.* [180] identified three pork qualities by comparing the average spectrum of both the lean and fat areas on pork slices.

Other important properties that need to be evaluated for meat and fish products are freshness and the detection of frozen-thawed pieces. Over the last 15 years,

NIR has proven to be efficient at evaluating meat/fish freshness [181, 182], and to date approximately 20 papers have been published on this subject. It is therefore not surprising that HSI should be tested for the same purpose. Salmon is a favorite fish species for such studies [43, 183, 184]. However, results have been disappointing because (i) generally, the visible range proved to be sufficient to assess for freshness because most spectral variations are due to oxidation of the heme pigments such as hemoglobin (Hb) and myoglobin (Mb) and (ii) that the use of NIR imaging instead of NIR spectroscopy generally proved to be unnecssary, except in Kimiya *et al.* [43] whose results show that better predictions for freshness of frozen-thawed tissues were obtained in the thinner parts of the fillets, and that tail-end localized analysis offered better performances. Two studies, however, are more original and merit to be described in more detail. In the same shortwave NIR range (380–1000 nm), Zhu *et al.* [185] were able to achieve a 97% discrimination rate between fresh and frozen-thawed halibut fillets by coupling texture features (obtained from the GLCM) with reflectance average spectra from an ROI at the center of the image. Barbin *et al.* [186] worked in the 900–1700 nm NIR range to distinguish frozen-thawed parts from fresh longissimus muscles of pork. They were able to identify particularly suitable wavebands, as a 100% discrimination result was achieved. Waveband alteration detected during the thawing process had three main causes (i) proteins undergoing relaxation and proteolysis, (ii) free water molecules, self-associating with, and interacting with, other components such as proteins and fatty acids through hydrogen bonding, and (iii) relaxation of meat lipids originating during thawing progression.

7.3.6 Conclusion

HS NIR imagers have many online applications that cover a wide range of detection and identification issues: detection of foreign bodies of contaminants (either exogenous or endogenous, or internal or external), identification for sorting purposes, localized spectral analysis in a given ROI, chemical mapping, and so on.

As the objects move during analysis, HSIs are easily created line by line. But due to the high-throughput speeds of the processing/packaging lines, huge amounts of data must be collected and processed; consequently, companies generally strive to reduce the quantity of information and often switch from HSI to multispectral imaging through either software wavelength selection using the HS system or hardware modification geared toward multispectral imaging systems.

Up to now, online applications have mainly relied on the very NIR, infrared, and visible ranges (400–1000 nm) with systems made up of PGP spectrographs and CCD cameras of various dynamic ranges (from 10 to 16 bits). Nevertheless, an increasing number of applications are based on NIR longer wavelengths, that is, NIR wavelengths in the 900–1700 nm range, which became more widely available and cost-effective toward the end of the 2000s. Such a spectral range can be used to tackle problems requiring the increased chemical specificity that is now available, thanks to access to lower order overtone bands and combination bands.

7.4 Conclusion

HSI solutions for food quality and safety control have made giant strides in the last 10 years. Accordingly, the number of applications described in the scientific literature has rocketed during the same period. Let us sum up the reasons for this and point out the expectations in research:

7.4.1 When is NIR Imaging Worth Using in Online Settings?

As mentioned earlier, the first advantage is that online NIR imaging is able to discriminate *same-color objects of different chemical composition*. This is possibly the NIR HSI property that mostly exploited in online settings to sort objects of diverse chemical composition.

The second advantage offered by NIR HSI is that it can provide *transmission images* of commodities because of smaller absorption and diffusion coefficients in the NIR range (e.g., in apples [92]). With visible light, transmission is only possible through small and low absorbing tissues. With NIR light, transmission can be carried out on thicker samples, such as entire fruit. Therefore, internal defects can be detected, provided that they are large enough.

The third property of NIR imaging is its ability to *map areas of varying chemical components in one sample*. This property is largely used in laboratory studies, especially in the pharmaceutical industry, but examples are also found in the food industry, sometimes online.

The fourth property of NIR imaging is that, even if used in reflection it *reveals much more information on the internal structure of products than visible light*. This is mainly due to the fact that the diffusion coefficient is lower in NIR, and that the light is not altered by pigments at the surface of commodities. This is used for determining the physical traits of the sample or for revealing beneath-skin defects.

Finally, appropriate combination of molecular chemical information (NIR) and morphological measurements that can be made in the macroscopic image (e.g., shape, optical texture, size) can facilitate the analysis of complex biological objects. This is particularly relevant when objects composed of different color-same compartments are being dealt with (e.g., meat slice) or when the product to be analyzed is made of heterogeneous pieces within a bulk, such as animal feed.

All these properties have been exploited by researchers, and now by industry, to create new quality control tools for the food sector. In the following, we will describe several examples of NIR imaging use in the food industry. Examples are categorized according to the industrial issues they address.

However, are the potentialities of HSI fully exploited? Has the exponential growth in publications led to genuine innovation and real advances in HSI equipment and methodologies? What are the most viable avenues for further research and inventions?

When sifting through these papers, it became apparent that this huge HSI-related scientific production has been mainly driven by easier access to cost-effective HSI equipment now present in many laboratories. Therefore, several researchers in explorative work are using HSI to analyze food products, as once was done with NIR spectrometers.

It was however surprising to learn that in some cases, the imaging system is used as a mere spectrometer focused on single objects. Several examples are described in Section 7.3.5; let us cite, for instance, Kamruzzaman *et al.* [176] for the discrimination of muscle of pork, beef, and lamb, or Foca *et al.* [187] in an application used to distinguish fat from lean pork. In this case, we wonder whether a NIR spectrometer would not be a better option, but, regretably, comparisons were not systematically carried out. As shown in other examples from Section 7.3.5, the use of HSI is justified when authors use the spatial advantage offered by HSI, that is, focus on specific ROIs – such as the lean part [175, 179] or the loin-eye area [177] – in which these teams averaged the pixel spectra. This allowed them to significantly reduce spectral "contamination" by pixels that do not represent the same tissues, and this approach provided much better spectral precision. Rare authors go even further and use processing tools.

7.4.1.1 **Software**

If we consider the 300 or more papers read before writing this chapter, very few evidenced applications that really take advantage of spatial information. Some used textural information [27, 178, 188] or shape characteristics of the objects [122, 173] to perform classification. In addition, very few researchers explored the possibility of developing software capable of managing two complex issues associated with HSI use, that is, to simultaneously manage and exploit spectral and spatial dimensions. Bernard *et al.* [189], Fauvel *et al.* [190], Gorretta *et al.* [191], and Tarabalka *et al.* [192–194] are some of the few authors who wrote software designed to more closely integrate spectral and spatial information. Unfortunately, these efforts are far too rare despite the fact that this work could undoubtedly improve classification results.

7.4.1.2 **Hardware**

The future will also see the emergence of new HSIs based on micro-optics (Fabry Perot filters) that are compatible with complementary metal oxide semiconductor (CMOS) cameras, such as those now offered by the IMEC company (www.imec.be). The rapid growth of smart mobile phones today has also stimulated the development of mobile phone applications that can be used for the quality control of food products in controlled conditions or in field using ambient illumination: applications using smart mobile phones and classical RGB camera are now available to roughly evaluate food product quality, using the visible range (e.g., FruitChecker, color detector). In addition, the German Fraunhofer Institute is developing a smartphone equipped with a miniature NIR–infrared spectrometer for fruit quality assessment. The coupling of both technologies for developing low-cost mobile NIR imaging for food and agricultural products is desirable.

Miniaturization of HSIs is also the subject of advanced research as shown by the patent filed by Majumdar *et al.* [195], which describes a spectroscopic device that can be used to acquire single-frame spatial, spectral, and polarization information of an object. One can also hope that the substantial progress made in sensor miniaturization will lead to the design of smart phones equipped with HSIs.

References

1. Bellon, V., Rabatel, G., and Guizard, C. (1992) Automatic sorting of fruit: sensors for the future. *Food Control*, **3** (1), 49–54.
2. Park, B., Chen, Y.-R., and Huffman, R.W. (1995) *Integration of Visible/NIR Spectroscopy and Multispectral Imaging for Poultry Carcass Inspection*, Society of Photo-Optical Instrumentation Engineers, Boston, MA.
3. Aikio, M. (2001) *Hyperspectral Prism-Grating-Prism Imaging Spectrograph*, vol. 4, VTT Publications, pp. 4–114.
4. Boldrini, B. *et al.* (2012) Hyperspectral imaging: a review of best practice, performance and pitfalls for in-line and on-line applications. *J. Near Infrared Spectrosc.*, **20** (5), 483–508.
5. Dale, L.M. *et al.* (2013) Hyperspectral imaging applications in agriculture and agro-food product quality and safety control: a review. *Appl. Spectrosc. Rev.*, **48** (2), 142–159.
6. ElMasry, G. *et al.* (2012) Principles and applications of hyperspectral imaging in quality evaluation of agro-food products: a review. *Crit. Rev. Food Sci. Nutr.*, **52** (11), 999–1023.
7. Feng, Y.Z. and Sun, D.W. (2012) Application of hyperspectral imaging in food safety inspection and control: a review. *Crit. Rev. Food Sci. Nutr.*, **52** (11), 1039–1058.
8. Gowen, A.A. *et al.* (2007) Hyperspectral imaging – an emerging process analytical tool for food quality and safety control. *Trends Food Sci. Technol.*, **18** (12), 590–598.
9. Lu, R. and Park, B. (2008) Hyperspectral and multispectral imaging for food quality and safety. *Sens. Instrum. Food Qual. Saf.*, **2** (3), 131–132.
10. Mollazade, K. *et al.* (2012) Principles and applications of light backscattering imaging in quality evaluation of agro-food products: a review. *Food Bioprocess Technol.*, **5** (5), 1465–1485.
11. Qin, J. *et al.* (2013) Hyperspectral and multispectral imaging for evaluating food safety and quality. *J. Food Eng.*, **118** (2), 157–171.
12. Wu, D. and Sun, D.-W. (2013) Advanced applications of hyperspectral imaging technology for food quality and safety analysis and assessment: a review – Part II: applications. *Innovative Food Sci. Emerg. Technol.*, **19**, 15–28.
13. Wu, D. and Sun, D.W. (2013) Advanced applications of hyperspectral imaging technology for food quality and safety analysis and assessment: a review – Part I: fundamentals. *Innovative Food Sci. Emerg. Technol.*, **19**, 1–14.
14. Kim, M.S. *et al.* (2011) Visible to SWIR hyperspectral imaging for produce safety and quality evaluation. *Sens. Instrum. Food Qual. Saf.*, **5** (5), 155–164.
15. Gomes, J.F.S. and Leta, F.R. (2012) Applications of computer vision techniques in the agriculture and food industry: a review. *Eur. Food Res. Technol.*, **235** (6), 989–1000.
16. Vijayarekha, K. (2012) Machine vision application for food quality: a review. *Res. J. Appl. Sci., Eng. Technol.*, **4** (24), 5453–5458.
17. Manleya, M. and Downeyb, G. (2012) Guest editorial: enhancing near infrared spectroscopy with an added spatial dimension. *J. Near Infrared Spectrosc.*, **20** (5), v–viii.

18. Wang, N. *et al.* (2007) Spectral imaging techniques for food quality evaluation. *Stewart Postharvest Rev.*, **3** (1), 1–8.
19. Cubero, S. *et al.* (2011) Advances in machine vision applications for automatic inspection and quality evaluation of fruits and vegetables. *Food Bioprocess Technol.*, **4** (4), 487–504.
20. Hong, T. *et al.* (2007) Review of hyperspectral image technology for non-destructive inspection of fruit quality. *Nongye Gongcheng Xuebao* (*Trans. Chin. Soc. Agric. Eng.*), **23** (11), 280–285.
21. Lorente, D. *et al.* (2012) Recent advances and applications of hyperspectral imaging for fruit and vegetable quality assessment. *Food Bioprocess Technol.*, **5** (4), 1121–1142.
22. Valous, N.A., Mendoza, F., and Sun, D.-W. (2010) Emerging non-contact imaging, spectroscopic and colorimetric technologies for quality evaluation and control of hams: a review. *Trends Food Sci. Technol.*, **21** (1), 26–43.
23. Serranti, S., Fabbri, A., and Bonifazi, G. (2012) Hyperspectral imaging techniques applied to the monitoring of wine waste anaerobic digestion process. *Opt. Eng.*, **51** (11), 111708.
24. Teena, M. *et al.* (2013) Potential of machine vision techniques for detecting fecal and microbial contamination of food products: a review. *Food Bioprocess Technol.*, **6** (7), 1621–1624.
25. Hyvärinen, T. *et al*. (2007) High speed NIR Chemical imaging. NIR 2007, The 13th International Conference on Near Infrared Spectroscopy (13th ICNIRS) 2007, Umeå, Sweden, June 17–21, 2007.
26. Cogdill, R.P., Hurburgh, C.R., and Rippke, G.R. (2004) Single-kernel maize analysis by near-infrared hyperspectral imaging. *Trans. ASAE*, **47** (1), 311–320.
27. Delwiche, S.R., Souza, E.J., and Kim, M.S. (2013) Limitations of single kernel near-infrared hyperspectral imaging of soft wheat for milling quality. *Biosyst. Eng.*, **115** (3), 260–273.
28. Xing, J. *et al.* (2011) Comparison of short-wavelength infrared (SWIR) hyperspectral imaging system with an FT-NIR spectrophotometer for predicting alpha-amylase activities in individual Canadian Western Red Spring (CWRS) wheat kernels. *Biosyst. Eng.*, **108** (4), 303–310.
29. Garrido-Novell, C. *et al.* (2012) Grading and color evolution of apples using RGB and hyperspectral imaging vision cameras. *J. Food Eng.*, **113** (2), 281–288.
30. Rajkumar, P. *et al.* (2012) Studies on banana fruit quality and maturity stages using hyperspectral imaging. *J. Food Eng.*, **108** (1), 194–200.
31. Zhao, J. *et al.* (2009) Nondestructive measurement of sugar content of apple using hyperspectral imaging technique. *Maejo Int. J. Sci. Technol.*, **3** (1), 130–142.
32. Barbin, D.F. *et al.* (2013) Nondestructive determination of chemical composition in intact and minced pork using near-infrared hyperspectral imaging. *Food Chem.*, **138** (2-3), 1162–1171.
33. Barbin, D.F. *et al.* (2012) Predicting quality and sensory attributes of pork using near-infrared hyperspectral imaging. *Anal. Chim. Acta*, **719**, 30–42.
34. Elmasry, G., Sun, D.W., and Allen, P. (2012) Near-infrared hyperspectral imaging for predicting colour, pH and tenderness of fresh beef. *J. Food Eng.*, **110** (1), 127–140.
35. ElMasry, G., Sun, D.-W., and Allen, P. (2011) Non-destructive determination of water-holding capacity in fresh beef by using NIR hyperspectral imaging. *Food Res. Int.*, **44** (9), 2624–2633.
36. Iqbal, A., Sun, D.-W., and Allen, P. (2013) Prediction of moisture, color and pH in cooked, pre-sliced turkey hams by NIR hyperspectral imaging system. *J. Food Eng.*, **117** (1), 42–51.
37. Kamruzzaman, M. *et al.* (2013) Non-destructive assessment of instrumental and sensory tenderness of lamb meat using NIR hyperspectral imaging. *Food Chem.* **141** (1), 389–396.
38. Kamruzzaman, M. *et al.* (2012) Prediction of some quality attributes of lamb meat using near-infrared hyperspectral imaging and multivariate analysis. *Anal. Chim. Acta*, **714**, 57–67.

39. Qiao, J. *et al.* (2007) Prediction of drip-loss, pH, and color for pork using a hyperspectral imaging technique. *Meat Sci.*, **76** (1), 1–8.
40. Dale, L.M. *et al.* (2012) Research on crude protein and digestibility of Arnica montana L. using conventional NIR spectrometry and hyperspectral imaging NIR. *J. Food Agric. Environ.*, **10** (1), 391–396.
41. Abdel-Nour, N. and Ngadi, M. (2011) Detection of omega-3 fatty acid in designer eggs using hyperspectral imaging. *Int. J. Food Sci. Nutr.*, **62** (4), 418–422.
42. Mora, C.R. *et al.* (2011) Determination of basic density and moisture content of loblolly pine wood disks using a near infrared hyperspectral imaging system. *J. Near Infrared Spectrosc.*, **19** (5), 401–409.
43. Kimiya, T., Sivertsen, A.H., and Heia, K. (2013) VIS/NIR spectroscopy for non-destructive freshness assessment of Atlantic salmon (Salmo salar L.) fillets. *J. Food Eng.*, **116** (3), 758–764.
44. Xing, J. *et al.* (2009) Using a Short Wavelength Infrared (SWIR) hyperspectral imaging system to predict alpha amylase activity in individual Canadian western wheat kernels. *Sens. Instrum. Food Qual. Saf.*, (3), 211–218.
45. Hart, D.A. *et al.* (1998) Measuring soluble solids distribution in kiwifruit using near-infrared imaging spectroscopy. *Postharvest Biol. Technol.*, **14** (3), 271–281.
46. Tsuta, M., Sugiyama, J., and Sagara, Y. (2002) Near-infrared imaging spectroscopy based on sugar absorption band for melons. *J. Agric. Food Chem.*, **50** (1), 48–52.
47. Long, R.L., Walsh, K.B., and Greensill, C.V. (2005) Sugar "imaging" of fruit using a low cost charge-coupled device camera. *J. Near Infrared Spectrosc.*, **13** (4), 177–186.
48. Peirs, A. *et al.* (2003) Starch index determination of apple fruit by means of a hyperspectral near infrared reflectance imaging system. *J. Near Infrared Spectrosc.*, **11** (5), 379–389.
49. Pillow, M. (1941) A new method for detecting compression wood. *J. For.*, **39**, 385–387.
50. Nyström, J. and Hagman, O. (1999) Real-time spectral classification of compression wood in Picea abies. *J. Wood Sci.*, **45** (1), 30–37.
51. Noordam, J.C. *et al.* (2005) A new procedure for the modelling and representation of classes in multivariate images. *Chemom. Intell. Lab. Syst.*, **75** (2), 115–126.
52. Duncker, P. and Spiecker, H. (2009) Detection and classification of Norway spruce compression wood in reflected light by means of hyperspectral image analysis. *IAWA J.*, **30** (1), 59–70.
53. Meder, R. and Meglenb, R.R. (2012) Near infrared spectroscopic and hyperspectral imaging of compression wood in Pinus radiata D. Don. *J. Near Infrared Spectrosc.*, **20** (5), 583–589.
54. Fernandes, A. *et al.* (2013) Comparison between neural networks and partial least squares for intra-growth ring wood density measurement with hyperspectral imaging. *Comput. Electron. Agric.*, **94**, 71–81.
55. Thumm, A. *et al.* (2010) Near infrared hyperspectral imaging applied to mapping chemical composition in wood samples. *J. Near Infrared Spectrosc.*, **18** (6), 507–515.
56. He, H.-J., Wu, D., and Sun, D.-W. (2013) Non-destructive and rapid analysis of moisture distribution in farmed Atlantic salmon (Salmo salar) fillets using visible and near-infrared hyperspectral imaging. *Innovative Food Sci. Emerg. Technol.*, **18**, 237–245.
57. Wu, D. and Sun, D.W. (2013) Application of visible and near infrared hyperspectral imaging for non-invasively measuring distribution of water-holding capacity in salmon flesh. *Talanta*, **116**, 266–276.
58. Wold, J.F. *et al.* (2006) Non-contact transflectance near infrared imaging for representative on-line sampling of dried salted coalfish (bacalao). *J. Near Infrared Spectrosc.*, **14** (1), 59–66.
59. Wu, D., Sun, D.W., and He, Y. (2012) Application of long-wave near infrared hyperspectral imaging for measurement

of color distribution in salmon fillet. *Innovative Food Sci. Emerg. Technol.*, **16**, 361–372.

60. Sivertsen, A.H. *et al.* (2009) Ridge detection with application to automatic fish fillet inspection. *J. Food Eng.*, **90** (3), 317–324.
61. Segtnan, V.H. (2007) Handling heterogeneity in online NIR food analysis. Invited lecture. NIR 2007, The 13th International Conference on Near Infrared Spectroscopy (13th ICNIRS) 2007, Umeå, Sweden, June 17–21, 2007.
62. Wold, J.P., Kermit, M., and Woll, A. (2010) Rapid nondestructive determination of edible meat content in crabs (Cancer pagurus) by near-infrared imaging spectroscopy. *Appl. Spectrosc.*, **64** (7), 691–699.
63. ElMasry, G., Sun, D.W., and Allen, P. (2013) Chemical-free assessment and mapping of major constituents in beef using hyperspectral imaging. *J. Food Eng.*, **117** (2), 235–246.
64. Kamruzzaman, M. *et al.* (2012) Non-destructive prediction and visualization of chemical composition in lamb meat using NIR hyperspectral imaging and multivariate regression. *Innovative Food Sci. Emerg. Technol.*, **16**, 218–226.
65. Talens, P. *et al.* (2013) Prediction of water and protein contents and quality classification of Spanish cooked ham using NIR hyperspectral imaging. *J. Food Eng.*, **117** (3), 272–280.
66. Gou, P. *et al.* (2013) Feasibility of NIR interactance hyperspectral imaging for on-line measurement of crude composition in vacuum packed dry-cured ham slices. *Meat Sci.*, **95** (2), 250–255.
67. Qiao, J. *et al.* (2007) Pork quality and marbling level assessment using a hyperspectral imaging system. *J. Food Eng.*, **83** (1), 10–16.
68. Kobayashi, K.I. *et al.* (2010) Near infrared spectroscopy and hyperspectral imaging for prediction and visualisation of fat and fatty acid content in intact raw beef cuts. *J. Near Infrared Spectrosc.*, **18** (5), 301–315.
69. Kobayashi, K.I. *et al.* (2012) Visualisation of fat and fatty acid distribution in beef using a set of filters based on near infrared spectroscopy. *J. Near Infrared Spectrosc.*, **20** (5), 509–519.
70. Yoon, S.C. *et al.* (2010) Detection of Campylobacter colonies using hyperspectral imaging. *Sens. Instrum. Food Qual. Saf.*, **4** (1), 35–49.
71. Yoon, S.C. *et al.* (2012) Hyperspectral imaging for detection of non-O157 Shiga-toxin producing Escherichia coli (STEC) serogroups on spread plates of mixed cultures. *Journal of Near Infrared Spectroscopy.*, **21** (2), 81–95.
72. Yoon, S.C. *et al.* (2013) Differentiation of big-six non-O157 Shiga-toxin producing Escherichia coli (STEC) on spread plates of mixed cultures using hyperspectral imaging. *J. Food Meas. Charact.*, **7** (2), 47–59.
73. Yoon, S.C. *et al.* (2013) Hyperspectral imaging for differentiating colonies of non-O157 Shiga-toxin producing Escherichia coli (STEC) serogroups on spread plates of pure cultures. *J. Near Infrared Spectrosc.*, **21** (2), 81–95.
74. Windham, W.R. *et al.* (2012) The effect of regions of interest and spectral pre-processing on the detection of non-0157 Shiga-toxin producing Escherichia coli serogroups on agar media by hyperspectral imaging. *J. Near Infrared Spectrosc.*, **20** (5), 547–558.
75. Yao, H. *et al.* (2008) Differentiation of toxigenic fungi using hyperspectral imagery. *Sens. Instrum. Food Qual. Saf.*, **2** (3), 215–224.
76. Dall'Ara, A., Bonoli, A., and Serranti, S. (2012) An innovative procedure to characterize properties from tailored composts. *Environ. Eng. Manage. J.*, **11** (10), 1825–1832.
77. Fromin, N. *et al.* (2012) Spatial variability of the functional stability of microbial respiration process: a microcosm study using tropical forest soil. *J. Soils Sediments*, **12**, 1030–1039.
78. Gobrecht, A. *et al*. (2013) Potential of proximal hyperspectral imaging to estimate the spatial and temporal variability of micro-heterogeneity of soil respiration. 16th International Conference on Near Infrared Spectroscopy, La grande Motte, France.

79. André Weinstock, B. *et al.* (2006) Prediction of oil and oleic acid concentrations in individual corn (Zea mays L.) kernels using near-infrared reflectance hyperspectral imaging and multivariate analysis. *Appl. Spectrosc.*, **60** (1), 9–16.
80. Arngren, M. *et al.* (2011) Analysis of pregerminated barley using hyperspectral image analysis. *J. Agric. Food Chem.*, **59** (21), 11385–11394.
81. Manley, M. *et al.* (2009) Near infrared hyperspectral imaging for the evaluation of endosperm texture in whole yellow maize (Zea maize L.) Kernels. *J. Agric. Food Chem.*, **57** (19), 8761–8769.
82. Manley, M., du Toit, G., and Geladi, P. (2011) Tracking diffusion of conditioning water in single wheat kernels of different hardnesses by near infrared hyperspectral imaging. *Anal. Chim. Acta*, **686** (1–2), 64–75.
83. Wu, D. *et al.* (2012) Rapid prediction of moisture content of dehydrated prawns using online hyperspectral imaging system. *Anal. Chim. Acta*, **726**, 57–66.
84. Nguyen Do Trong, N. *et al.* (2011) Prediction of optimal cooking time for boiled potatoes by hyperspectral imaging. *J. Food Eng.*, **105** (4), 617–624.
85. Nansen, C., Kolomiets, M., and Gao, X. (2008) Considerations regarding the use of hyperspectral imaging data in classifications of food products, exemplified by analysis of maize kernels. *J. Agric. Food Chem.*, **56** (9), 2933–2938.
86. Manley, M. *et al.* (2012) Influence of grain topography on near infrared hyperspectral images. *Talanta*, **89**, 223–230.
87. Gierlinger, N. and Schwanninger, M. (2007) The potential of Raman microscopy and Raman imaging in plant research. *Spectroscopy*, **21** (2), 69–89.
88. Lu, R. (2003) Imaging spectroscopy for assessing Internal quality of apple fruit. ASAE Annual International Meeting 2003, Las Vegas, NV.
89. Lu, R. and Peng, Y. (2006) Hyperspectral scattering for assessing peach fruit firmness. *Biosyst. Eng.*, **93** (2), 161–171.
90. Peng, Y. and Lu, R. (2008) Analysis of spatially resolved hyperspectral scattering images for assessing apple fruit firmness and soluble solids content. *Postharvest Biol. Technol.*, **48** (1), 52–62.
91. Qin, J. and Lu, R. (2008) Measurement of the optical properties of fruits and vegetables using spatially resolved hyperspectral diffuse reflectance imaging technique. *Postharvest Biol. Technol.*, **49** (3), 355–365.
92. Qin, J. and Lu, R. (2009) Monte Carlo simulation for quantification of light transport features in apples. *Comput. Electron. Agric.*, **68** (1), 44–51.
93. Cen, H. *et al.* (2013) Relationship of the optical absorption and scattering properties with mechanical and structural properties of apple tissue. *Postharvest Biol. Technol.*, **85**, 30–38.
94. Lu, R., Ariana, D.P., and Cen, H. (2011) Optical absorption and scattering properties of normal and defective pickling cucumbers for 700-1000 nm. *Sens. Instrum. Food Qual. Saf.*, **5** (2), 51–56.
95. Huang, M. and Lu, R. (2010) Optimal wavelength selection for hyperspectral scattering prediction of apple firmness and soluble solids content. *Trans. ASABE*, **53** (4), 1175–1182.
96. Huang, M. *et al.* (2012) Analysis of hyperspectral scattering images using locally linear embedding algorithm for apple mealiness classification. *Comput. Electron. Agric.*, **89**, 175–181.
97. ElMasry, G., Wang, N., and Vigneault, C. (2009) Detecting chilling injury in Red Delicious apple using hyperspectral imaging and neural networks. *Postharvest Biol. Technol.*, **52** (1), 1–8.
98. Cluff, K. *et al.* (2008) Optical scattering in beef steak to predict tenderness using hyperspectral imaging in the VIS-NIR region. *Sens. Instrum. Food Qual. Saf.*, **2** (3), 189–196.
99. Peng, Y. and Wu, J. (2008) Hyperspectral scattering profiles for prediction of beef tenderness. ASABE St. Joseph, Michigan, June 29–July 2, 2008.
100. Wu, J. *et al.* (2012) Prediction of beef quality attributes using VIS/NIR hyperspectral scattering imaging technique. *J. Food Eng.*, **109** (2), 267–273.

101. Peng, Y. *et al.* (2011) Potential prediction of the microbial spoilage of beef using spatially resolved hyperspectral scattering profiles. *J. Food Eng.*, **102** (2), 163–169.

102. Tao, F. *et al.* (2012) Simultaneous determination of tenderness and Escherichia coli contamination of pork using hyperspectral scattering technique. *Meat Sci.*, **90** (3), 851–857.

103. Qin, J. and Lu, R. (2006) Hyperspectral diffuse reflectance imaging for rapid, noncontact measurement of the optical properties of turbid materials. *Appl. Opt.*, **45** (32), 8366–8373.

104. Qin, J. and Lu, R. (2007) Measurement of the absorption and scattering properties of turbid liquid foods using hyperspectral imaging. *Appl. Spectrosc.*, **61** (4), 388–396.

105. Holm, F. (2003) Food quality sensors. SMEs n°4, FairFlow Europe 2003, INRA, Paris, France, p. 34.

106. Al-Mallahi, A., Kataoka, T., and Okamoto, H. (2008) Discrimination between potato tubers and clods by detecting the significant wavebands. *Biosyst. Eng.*, **100** (3), 329–337.

107. Bhuvaneswari, K. *et al.* (2011) Image analysis for detecting insect fragments in semolina. *J. Stored Prod. Res.*, **47** (1), 20–24.

108. Fernández Pierna, J.A. *et al.* (2012) NIR hyperspectral imaging spectroscopy and chemometrics for the detection of undesirable substances in food and feed. *Chemom. Intell. Lab. Syst.*, **117**, 233–239.

109. Kamruzzaman, M. *et al.* (2013) Fast detection and visualization of minced lamb meat adulteration using NIR hyperspectral imaging and multivariate image analysis. *Talanta*, **103**, 130–136.

110. Lu, R. and Chen, Y.-R. (1998) Hyperspectral imaging for safety inspection of food and agricultural products. SPIE Conference on Pathogen Detection and Remediation for Safe Eating.

111. Kim, M.S. *et al.* (2002) Multispectral detection of fecal contamination on apples based on hyperspectral imagery: part I. Application of visible and near-infrared reflectance imaging. *Trans. ASAE*, **45** (6), 2027–2037.

112. Liu, Y. *et al.* (2007) Development of simple algorithms for the detection of fecal contaminants on apples from visible/near infrared hyperspectral reflectance imaging. *J. Food Eng.*, **81** (2), 412–418.

113. Chao, K., Mehl, P.M., and Chen, Y.R. (2002) Use of hyper- and multi-spectral imaging for detection of chicken skin tumors. *Appl. Eng. Agric.*, **18** (1), 113–119.

114. Lawrence, K.C. *et al.* (2006) Partial least squares regression of hyperspectral images for contaminant detection on poultry carcasses. *J. Near Infrared Spectrosc.*, **14** (4), 223–230.

115. Park, B. *et al.* (2006) Performance of hyperspectral imaging system for poultry surface fecal contaminant detection. *J. Food Eng.*, **75** (3), 340–348.

116. Delwiche, S.R., Kim, M.S., and Dong, Y. (2011) Fusarium damage assessment in wheat kernels by Vis/NIR hyperspectral imaging. *Sens. Instrum. Food Qual. Saf.*, **5** (2), 63–71.

117. Singh, C.B. *et al.* (2007) Fungal detection in wheat using near-infrared hyperspectral imaging. *Trans. ASABE*, **50** (6), 2171–2176.

118. Zhang, H. *et al.* (2007) Classification of fungal infected wheat kernels using near-infrared reflectance hyperspectral imaging and support vector machine. *Trans. ASABE*, **50** (5), 1779–1785.

119. Delwiche, S.R., Yang, I.C., and Kim, M.S. (2009) Hyperspectral imaging for detection of black tip damage in wheat kernels. *Proc. SPIE, 7315, Sensing for Agriculture and Food Quality and Safety*, **73150K**, (April 27, 2009).

120. Jin, J. *et al.* (2009) Classification of toxigenic and atoxigenic strains of Aspergillus flavus with hyperspectral imaging. *Comput. Electron. Agric.*, **69** (2), 158–164.

121. Singh, C.B. *et al.* (2012) Fungal damage detection in wheat using short-wave near-infrared hyperspectral and digital colour imaging. *Int. J. Food Prop.*, **15** (1), 11–24.

122. Xing, J., Saeys, W., and De Baerdemaeker, J. (2007) Combination of chemometric tools and image processing for bruise detection on

apples. *Comput. Electron. Agric.*, **56** (1), 1–13.

123. Xing, J. and De Baerdemaeker, J. (2005) Bruise detection on 'Jonagold' apples using hyperspectral imaging. *Postharvest Biol. Technol.*, **37** (2), 152–162.

124. Xing, J. *et al.* (2005) Detecting bruises on 'Golden Delicious' apples using hyperspectral imaging with multiple wavebands. *Biosyst. Eng.*, **90** (1), 27–36.

125. Xing, J., Jancsók, P., and De Baerdemaeker, J. (2007) Stem-end/calyx identification on apples using contour analysis in multispectral images. *Biosyst. Eng.*, **96** (2), 231–237.

126. ElMasry, G. *et al.* (2008) Early detection of apple bruises on different background colors using hyperspectral imaging. *LWT Food Sci. Technol.*, **41** (2), 337–345.

127. Baranowski, P., Mazurek, W., and Pastuszka-Woźniak, J. (2013) Supervised classification of bruised apples with respect to the time after bruising on the basis of hyperspectral imaging data. *Postharvest Biol. Technol.*, **86**, 249–258.

128. Ariana, D.P., Lu, R., and Guyer, D.E. (2006) Near-infrared hyperspectral reflectance imaging for detection of bruises on pickling cucumbers. *Comput. Electron. Agric.*, **53** (1), 60–70.

129. Gowen, A.A. *et al.* (2008) Hyperspectral imaging combined with principal component analysis for bruise damage detection on white mushrooms (Agaricus bisporus). *J. Chemometr.*, **22** (3-4), 259–267.

130. Gaston, E. *et al.* (2010) Prediction of polyphenol oxidase activity using visible near-infrared hyperspectral imaging on mushroom (agaricus bisporus) caps. *J. Agric. Food Chem.*, **58** (10), 6226–6233.

131. Nagata, M., Tallada, J.G., and Kobayashi, T. (2006) Bruise detection using NIR hyperspectral imaging for strawberry (Fragaria × ananassa Duch.). *Environ. Control. Biol.*, **44** (2), 133–142.

132. Lü, Q. *et al.* (2011) Vis/NIR hyperspectral imaging for detection of hidden bruises on kiwifruits. *Czech J. Food Sci.*, **29** (6), 595–602.

133. Li, J., Rao, X., and Ying, Y. (2011) Detection of common defects on oranges using hyperspectral reflectance imaging. *Comput. Electron. Agric.*, **78** (1), 38–48.

134. Qin, J. *et al.* (2009) Detection of citrus canker using hyperspectral reflectance imaging with spectral information divergence. *J. Food Eng.*, **93** (2), 183–191.

135. Zhao, X. *et al.* (2010) Effect of fruit harvest time on citrus canker detection using hyperspectral reflectance imaging. *Sens. Instrum. Food Qual. Saf.*, **4** (3), 126–135.

136. Gaston, E. *et al.* (2010) Visible-near infrared hyperspectral imaging for the identification and discrimination of brown blotch disease on mushroom (Agaricus bisporus) caps. *J. Near Infrared Spectrosc.*, **18** (5), 341–353.

137. Taghizadeh, M., Gowen, A., and O'Donnell, C.P. (2011) Comparison of hyperspectral imaging with conventional RGB imaging for quality evaluation of Agaricus bisporus mushrooms. *Biosyst. Eng.*, **108** (2), 191–194.

138. Diezma, B. *et al.* (2013) Examination of the quality of spinach leaves using hyperspectral imaging. *Postharvest Biol. Technol.*, **85**, 8–17.

139. Lorente, D. *et al.* (2013) Selection of optimal wavelength features for decay detection in citrus fruit using the ROC curve and neural networks. *Food Bioprocess Technol.*, **6** (2), 530–541.

140. Lorente, D. *et al.* (2012) Comparison of ROC feature selection method for the detection of decay in citrus fruit using hyperspectral images. *Food Bioprocess Technol.*, **6** 3613–3619.

141. Singh, C.B. *et al.* (2010) Identification of insect-damaged wheat kernels using short-wave near-infrared hyperspectral and digital colour imaging. *Comput. Electron. Agric.*, **73** (2), 118–125.

142. Singh, C.B. *et al.* (2009) Detection of insect-damaged wheat kernels using near-infrared hyperspectral imaging. *J. Stored Prod. Res.*, **45** (3), 151–158.

143. Kaliramesh, S. *et al.* (2013) Detection of infestation by Callosobruchus maculatus in mung bean using near-infrared

hyperspectral imaging. *J. Stored Prod. Res.*, **52**, 107–111.

144. Chao, K., Mehl, P.M., and Chen, Y.R. (2012) Use of hyper- and multi-spectral imaging for detection of chicken skin tumors. *J. Agric. Saf. Health*, **18** (1), 113–119.

145. Chao, K. *et al.* (2007) Hyperspectral-multispectral line-scan imaging system for automated poultry carcass inspection applications for food safety. *Poult. Sci.*, **86** (11), 2450–2460.

146. Chao, K., Yang, C.C., and Kim, M.S. (2010) Spectral line-scan imaging system for high-speed non-destructive wholesomeness inspection of broilers. *Trends Food Sci. Technol.*, **21** (3), 129–137.

147. Menesatti, P., Urbani, G., and Lanza, G. (2005) Spectral imaging VIS-NIR system to forecast the chilling injury onset on citrus fruits. *Acta Hortic.*, **2**, 1347–1354.

148. Cheng, X. (2004) *Hyperspectral Imaging and Pattern Recognition Technologies for Real-Time Fruit Safety and Quality Inspection*, University of Maryland, College Park, MD, p. 130.

149. Noordam, J.C., Van Den Broek, W.H.A.M., and Buydens, L.M.C. (2005) Detection and classification of latent defects and diseases on raw French fries with multispectral imaging. *J. Sci. Food Agric.*, **85** (13), 2249–2259.

150. Chauchard, F. *et al.* (2005) Least-squares support vector machines modelization for time-resolved spectroscopy. *Appl. Opt.*, **44** (33), 7091–7097.

151. Wallin, P. and Haycock, P. (1998) *Foreign Body Prevention, Detection and Control – A Practical Approach*, Blackie Academic & Professional, London.

152. Qin, J. and Lu, R. (2005) Detection of pits in tart cherries by hyperspectral transmission imaging. *Trans. Am. Soc. Agric. Eng.*, **48** (5), 1963–1970.

153. Lu, R. and Ariana, D.P. (2013) Detection of fruit fly infestation in pickling cucumbers using a hyperspectral reflectance/transmittance imaging system. *Postharvest Biol. Technol.*, **81**, 44–50.

154. Ariana, D.P. and Lu, R. (2008) Quality evaluation of pickling cucumbers using hyperspectral reflectance and transmittance imaging: part I. Development of a prototype. *Sens. Instrum. Food Qual. Saf.*, **2** (3), 144–151.

155. Ariana, D.P. and Lu, R. (2008) Quality evaluation of pickling cucumbers using hyperspectral reflectance and transmittance imaging – Part II. Performance of a prototype. *Sens. Instrum. Food Qual. Saf.*, **2** (3), 152–160.

156. Ariana, D.P. and Lu, R. (2010) Hyperspectral waveband selection for internal defect detection of pickling cucumbers and whole pickles. *Comput. Electron. Agric.*, **74** (1), 137–144.

157. Gorretta, N. *et al.* (2006) Determining vitreousness of durum wheat kernels using near infrared hyperspectral imaging. *J. Near Infrared Spectrosc.*, **14** (4), 231–239.

158. Symons, S.J., Van Schepdael, L., and Dexter, J.E. (2003) Measurement of hard vitreous kernels in durum wheat by machine vision. *Cereal Chem.*, **80** (5), 511–517.

159. McGoverin, C.M. and Manley, M. (2012) Classification of maize kernel hardness using near infrared hyperspectral imaging. *J. Near Infrared Spectrosc.*, **20** (5), 529–535.

160. Choudhary, R. *et al.* (2009) Identification of wheat classes using wavelet features from near infrared hyperspectral images of bulk samples. *Biosyst. Eng.*, **102** (2), 115–127.

161. Zhu, D. *et al.* (2012) Identification of wheat cultivars based on the hyperspectral image of single seed. *J. Nanoelectron. Optoelectron.*, **7** (2), 167–172.

162. Mahesh, S. *et al.* (2011) Identification of wheat classes at different moisture levels using near-infrared hyperspectral images of bulk samples. *Sens. Instrum. Food Qual. Saf.*, **5** (1), 1–9.

163. Mahesh, S. *et al.* (2008) Feasibility of near-infrared hyperspectral imaging to differentiate Canadian wheat classes. *Biosyst. Eng.*, **101** (1), 50–57.

164. Zhang, X. *et al.* (2012) Application of hyperspectral imaging and chemometric calibrations for variety

discrimination of maize seeds. *Sensors (Switzerland)*, **12** (12), 17234–17246.
165. McGoverin, C.M. *et al.* (2011) Characterisation of non-viable whole barley, wheat and sorghum grains using near-infrared hyperspectral data and chemometrics. *Anal. Bioanal. Chem.*, **401** (7), 2283–2289.
166. Yin, X.S. *et al.* (2006) An investigation on the detection of potential loss of germinative capacity during storage of malting barley. *J. Am. Soc. Brew. Chem.*, **64** (2), 94–99.
167. Serranti, S. *et al.* (2013) Classification of oat and groat kernels using NIR hyperspectral imaging. *Talanta*, **103**, 276–284.
168. Rodríguez-Pulido, F.J. *et al.* (2013) Grape seed characterization by NIR hyperspectral imaging. *Postharvest Biol. Technol.*, **76**, 74–82.
169. Baiano, A. *et al.* (2012) Application of hyperspectral imaging for prediction of physico-chemical and sensory characteristics of table grapes. *Comput. Electron. Agric.*, **87**, 142–151.
170. Leiva-Valenzuela, G.A., Lu, R., and Aguilera, J.M. (2013) Prediction of firmness and soluble solids content of blueberries using hyperspectral reflectance imaging. *J. Food Eng.*, **115** (1), 91–98.
171. Taghizadeh, M. *et al.* (2010) Use of hyperspectral imaging for evaluation of the shelf-life of fresh white button mushrooms (Agaricus bisporus) stored in different packaging films. *Innovative Food Sci. Emerg. Technol.*, **11** (3), 423–431.
172. Zhao, J. *et al.* (2009) Automated tea quality classification by hyperspectral imaging. *Appl. Opt.*, **48** (19), 3557–3564.
173. Vermaak, I., Viljoen, A., and Lindström, S.W. (2013) Hyperspectral imaging in the quality control of herbal medicines – The case of neurotoxic Japanese star anise. *J. Pharm. Biomed. Anal.*, **75**, 207–213.
174. Wetzel, D.L., Posner, E.S., and Dogan, H. (2010) InSb focal plane array chemical imaging enables assessment of unit process efficiency for milling operation. *Appl. Spectrosc.*, **64** (12), 1320–1324.
175. Kamruzzaman, M. *et al.* (2012) Potential of hyperspectral imaging and pattern recognition for categorization and authentication of red meat. *Innovative Food Sci. Emerg. Technol.*, **16**, 316–325.
176. Kamruzzaman, M. *et al.* (2011) Application of NIR hyperspectral imaging for discrimination of lamb muscles. *J. Food Eng.*, **104** (3), 332–340.
177. Jun, Q. *et al.* (2007) Pork quality classification using a hyperspectral imaging system and neural network. *Int. J. Food Eng.*, **3** (1), 1–12.
178. Liu, L. *et al.* (2010) Categorization of pork quality using Gabor filter-based hyperspectral imaging technology. *J. Food Eng.*, **99** (3), 284–293.
179. ElMasry, G. *et al.* (2011) Quality classification of cooked, sliced turkey hams using NIR hyperspectral imaging system. *J. Food Eng.*, **103** (3), 333–344.
180. Barbin, D. *et al.* (2012) Near-infrared hyperspectral imaging for grading and classification of pork. *Meat Sci.*, **90** (1), 259–268.
181. Chen, Y.R., Huffman, R.W., and Park, B. (1996) Changes in the visible/near-infrared spectra of chicken carcasses in storage. *J. Food Process Eng.*, **19** (2), 121–134.
182. Zhang, H.Z. and Lee, T.C. (1997) Rapid near-infrared spectroscopic method for the determination of free fatty acid in fish and its application in fish quality assessment. *J. Agric. Food Chem.*, **45** (9), 3515–3521.
183. Ivorra, E. *et al.* (2013) Detection of expired vacuum-packed smoked salmon based on PLS-DA method using hyperspectral images. *J. Food Eng.*, **117** (3), 342–349.
184. Sone, I. *et al.* (2012) Classification of fresh Atlantic salmon (Salmo salar L.) fillets stored under different atmospheres by hyperspectral imaging. *J. Food Eng.*, **109** (3), 482–489.
185. Zhu, F. *et al.* (2013) Application of visible and near infrared hyperspectral imaging to differentiate between fresh and frozen-thawed fish fillets. *Food Bioprocess Technol.*, **6** 2931–2937.
186. Barbin, D.F., Sun, D.-W., and Su, C. (2013) NIR hyperspectral imaging as

non-destructive evaluation tool for the recognition of fresh and frozen–thawed porcine longissimus dorsi muscles. *Innovative Food Sci. Emerg. Technol.*, **18**, 226–236.

187. Foca, G. *et al.* (2013) Classification of pig fat samples from different subcutaneous layers by means of fast and non-destructive analytical techniques. *Food Res. Int.*, **52** (1), 185–197.

188. Zhang, J. *et al.* (2012) Using in-situ hyperspectral data for detecting and discriminating yellow rust disease from nutrient stresses. *Field Crop Res*, **134**, 165–174.

189. Bernard, K. *et al.* (2012) Spectral-spatial classification of hyperspectral data based on a stochastic minimum spanning forest approach. *IEEE Trans. Image Process.*, **21** (4), 2008–2021.

190. Fauvel, M. *et al.* (2013) Advances in spectral-spatial classification of hyperspectral images. *Proc. IEEE*, **101** (3), 652–675.

191. Gorretta, N. *et al.* (2012) An iterative hyperspectral image segmentation method using a cross analysis of spectral and spatial information. *Chemom. Intell. Lab. Syst.*, **117**, 213–223.

192. Tarabalka, Y. and Tilton, J.C. (2011) Spectral-spatial classification of hyperspectral images using hierarchical optimization. 3rd Workshop on Hyperspectral Image and Signal Processing: Evolution in Remote Sensing (Whispers 2011), Lisbon, Portugal.

193. Tarabalka, Y., Chanussot, J., and Benediktsson, J.A. (2010) Segmentation and classification of hyperspectral images using watershed transformation. *Pattern Recognit.*, **43** (7), 2367–2379.

194. Tarabalka, Y. and Tilton, J.C. (2012) Improved hierarchical optimization-based classification of hyperspectral images using shape analysis. 32nd IEEE International Geoscience and Remote Sensing Symposium (IGARSS), Munich, Germany.

195. Majumdar, Z.K., Steinhardt, A.O., and Fischer, J. (2011) *Mobile Phone Hyperspectral Imager with Single-Frame Spatial, Spectral and Polarization Information*, Booz, Allen & Hamilton, McLean VA.

Part IV
Polymers and Pharmaceuticals

Infrared and Raman Spectroscopic Imaging, Second Edition. Edited by Reiner Salzer, Heinz W. Siesler.
© 2014 Wiley-VCH Verlag GmbH & Co. KGaA. Published 2014 by Wiley-VCH Verlag GmbH & Co. KGaA.

8
FT-IR and NIR Spectroscopic Imaging: Principles, Practical Aspects, and Applications in Material and Pharmaceutical Science

Elke Grotheer, Christian Vogel, Olga Kolomiets, Uwe Hoffmann, Miriam Unger, and Heinz W. Siesler

8.1
Introduction

Both, Fourier-transform mid-infrared (FT-IR) and near-infrared (NIR) spectra of a multicomponent sample measured with a single-element detector can provide information on the identity of the different components in the investigated sample area, but it does not yield any information on their spatial separation. For many analytical problems, however, this is the crucial point of the investigation. In this aspect, the development of focal plane array (FPA) detectors [1, 2] for imaging measurements in the mid-IR and NIR has launched vibrational spectroscopy into a new era of analytical applications. Thus, several thousand spectra of laterally resolved sample positions can be measured simultaneously within a few minutes thereby providing "chemical images" of the investigated sample area. As a consequence, both FT-IR and NIR imaging techniques have over the last years proved powerful tools for a broad range of industrial and research applications. The experimental principles of operation, however, are partly different for the two imaging methods (see also Chapter 1). Although FT-IR imaging is mainly operated in transmission or in attenuated total reflection (ATR) as a macro or – in combination with a microscope – as a microtechnique, NIR imaging is widely applied in diffuse reflection in the macro mode and less frequently in the transmission mode. This can be explained in terms of the significantly higher absorptivities of the mid-IR absorption bands of fundamental vibrations compared to that of the NIR overtone and combination bands. The penetration depth of the ATR technique and the optimum sample thickness for mid-IR spectra lie in the range of a few microns, which corresponds approximately to the lateral resolution achievable by the FT-IR imaging technique. For NIR spectra, sample thicknesses up to several hundred micrometers may be required that are far beyond the theoretically feasible lateral resolution (in the micrometer range) for this wavelength region and the achievable penetration depth of the ATR technique. Consequently, the main focus of the two imaging techniques is in different fields of applications. Although FT-IR imaging is mainly applied to biomedical diagnostics and material

Infrared and Raman Spectroscopic Imaging, Second Edition. Edited by Reiner Salzer, Heinz W. Siesler.
© 2014 Wiley-VCH Verlag GmbH & Co. KGaA. Published 2014 by Wiley-VCH Verlag GmbH & Co. KGaA.

analysis, with few exceptions NIR imaging has been primarily used so far for the quality control of food or agricultural products and for the analysis of solid pharmaceutical drug formulations. Regarding material analysis, the present chapter will also cover the application of FT-IR imaging to the characterization of inorganic materials.

Selected research activities using an FPA detector for FT-IR imaging starting in the late 1990s in the group of Jack Koenig at Case Western Reserve University in Cleveland (USA) up to the last quarter of the first decade of the new century have been summarized in the analogous chapter of the previous edition of this book [3–19] and shall not be repeated here. The most important contributions beyond this period regarding FT-IR imaging have been documented in focal point articles of the *Journal of Applied Spectroscopy* [20–22] and a book by Sasic and Ozaki [23]. Specifically, Bhargava has contributed significantly toward the progress of this scientific discipline with the development of the fundamental theory and modeling of Raman and infrared chemical imaging (see also a recent Internet video presentation [24]).

With the advent of more economical, linear array-based, and large-format (320×256 pixels) FPA detectors, NIR hyperspectral imaging also developed to an important tool in selected industrial and research areas such as evaluation of food quality (see Chapter 7) or in pharmaceutical industry. Probably the delay of the implementation of NIR imaging relative to mid-IR and Raman imaging was also based on the (largely undeserved) reputation of inferior specificity of NIR compared to Raman and mid-IR spectroscopy. Based on the much simpler and more rugged instrumentation for NIR chemical imaging, its fast and nondestructive sampling and on the fact that in many cases a priori information on the investigated material is available (as, e.g., in pharmaceutical applications), the advantage of obtaining high fidelity, spatially resolved pictures of the chemistry of the sample has eventually accelerated the practical application of this imaging technique. It has to be pointed out, however, that compared to mid-IR and Raman imaging, the diffraction-limited spatial resolution in the NIR region (~2 μm) can in most applications not be exploited for two reasons:

- Due to the significantly lower (10- to 100-fold) absorptivities of overtone and combination bands compared to fundamental absorptions, the sample thickness for NIR transmission measurements has to be several hundred micrometers and
- In diffuse reflection measurements of particulate materials, scattering effects also lead to maximum pathlengths of several hundred micrometers of the photons within the sample (see later and Chapter 1).

Apart from food industry (Chapter 7), NIR chemical imaging has so far primarily been applied for qualitative and quantitative product characterizations in the pharmaceutical industry. The ability to visualize and assess the compositional heterogeneity and structure of the end products is extremely important for both the development and the manufacture of solid dosage forms [25]. NIR chemical images have been used to determine authenticity, content uniformity, particle

sizes and distribution of sample components, polymorph distributions, moisture content and location, contaminations, coating and layer thickness, and a host of other structural details [26–34].

8.2
Instrumentation for NIR and FT-IR Imaging

In what follows the instrumentation used for the application examples described in this chapter will be discussed in some detail. Specifically, the basic instrumental features of the imaging systems, different possible measurement modes, and the occurrence of instrument-related and sample-related artifacts and misinterpretations will be shortly outlined. Because NIR imaging instruments are simpler in design, they will be discussed first.

The application examples outlined in detail in this chapter refer to diffuse reflection NIR chemical imaging measurements of a pharmaceutical drug formulation and variable-temperature diffusion measurements of an organic liquid into a polymer. The main purpose of these investigations was to demonstrate that, on the one hand, from the imaging data qualitative and quantitative information regarding the homogeneity of the component distribution and the active ingredient content in the pharmaceutical formulation can be derived and that, on the other hand, important physical parameters of a polymer system become available from such measurements.

8.2.1
NIR Imaging in Diffuse Reflection

The NIR hyperspectral images presented later on in this chapter were recorded on a MatrixNIR system (Malvern (formerly Spectral Dimensions), Olney, MD, USA) with four quartz-halogen lamps as NIR sources, a liquid-crystal tunable filter (LCTF) as monochromator, and a thermoelectrically cooled 256 × 320 InGaAs FPA detector covering 118 channels (960–1662 nm or 10 417–6017 cm^{-1}) with a spectral resolution of 6 nm at 1600 nm (corresponding to 24 cm^{-1}). Figure 8.1a shows the instrument alongside an optical scheme of the system (Figure 8.1b). For high-throughput measurements, the instrument can also be adapted with a programmable sample carousel that enables the sequential analysis of multiple samples.

The quantitative determination of the active ingredients is only part of the quality control requirements for a solid pharmaceutical drug formulation. At least as important is the homogeneous distribution of the active ingredients in the formulation. In this respect, the inherent advantage of imaging measurements comes into play and provides the relevant information. Because the majority of the NIR spectroscopic imaging measurements are made in diffuse reflection, the pathlength of NIR radiation in the sample for such measurements has become a fundamental area of debate [34–40].

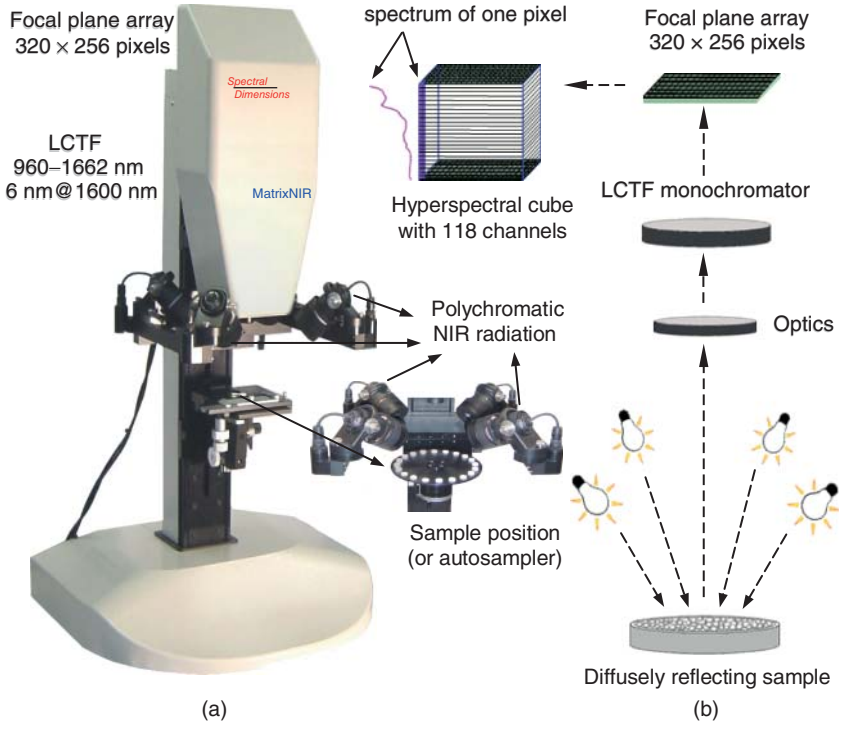

Figure 8.1 (a) The NIR imaging system and (b) the optical scheme of the instrument for diffuse reflection measurements of a powder sample.

The important issue with reference to the spatial resolution of imaging measurements is, on the one hand, the lateral extension of photons in the sample and, on the other hand, the maximum penetration depth of NIR radiation into the sample. The first question was addressed by Lewis *et al.* [41] whereby an effective pathlength of ~780 µm at 1660 nm (6024 cm^{-1}), resulting in a sampling volume of a sphere with a diameter of ~72 µm, was derived from theoretical calculations with a random walk model and transmission and diffuse reflection measurements of an aspirin (acetylsalicylic acid, ASA) tablet. Furthermore, it has been concluded that, depending on the wavelength, ~70% of the photons exiting the sample at any given point in a diffuse reflection measurement will have interacted with a spherical region of a diameter between 90 and 60 µm. The issue of maximum penetration depth has been addressed by Siesler *et al.* [42] by a somewhat different experimental approach. Poly(dimethylsiloxane) (PDMS) films (containing 25 wt% silica particles) were stacked with layers of different thickness (100–900 µm) of the specified drug formulation and the spectra of these different two-layered drug formulation/PDMS stacks were measured in diffuse reflection. The drug formulation used for these measurements had a composition of ASA: 18.10 wt%, ascorbic acid (ASC): 22.85 wt%, caffeine (CF): 19.05 wt%, and cellulose/starch (CE/ST 1 : 3 (wt)): 40 wt%.

PDMS has relatively sharp absorption bands in the NIR region that are not or only weakly superimposed by the broad absorption bands of the drug formulation. Thus, the polymer film can be used as a detection layer and the occurrence of signals in the PDMS-specific wavenumber regions are an indicative of the penetration of NIR radiation through the drug formulation layer into the polymer film. With this experimental set-up, the decrease in the PDMS-specific absorption bands could be monitored in different wavenumber regions as a function of increasing drug formulation layer thickness to an intensity value <5% of the corresponding pure PDMS diffuse reflection spectrum. These drug formulation layer thicknesses were taken as maximum penetration depth of the NIR radiation and the following values have been estimated for selected wavenumber regions: ~300 µm for the 4000–4500 cm^{-1} region, ~400 µm for the 5300–6000 cm^{-1} region, ~550 µm for the 7000–7500 cm^{-1} region, and ~650 µm at 8440 cm^{-1}. Despite the different experimental approach, these values are relatively consistent with previous estimates [34]. Thus, in view of the diffraction-limited spatial resolution <3 µm in the NIR region (see Chapter 1), the NIR imaging technique is best used for the characterization of scattering samples with a particle size that is far larger than the diffraction limit.

8.2.2 NIR Imaging in Transmission

If the limitations regarding sample thickness or penetration depth discussed earlier do not apply, NIR imaging transmission measurements may also provide valuable information. This will be demonstrated exemplarily with reference to monitoring the diffusion front of an organic liquid into a planar polymer film and the data derived thereof (Section 8.3.3).

For this purpose, the imaging measurements were performed with a PerkinElmer (Massachusetts, USA) imaging system, consisting of an FT-NIR spectrometer coupled to a microscope (Figure 8.2). This totally integrated instrument operates in the 2200–7600 cm^{-1} wavenumber range and incorporates a 16 × 1 element (400 µm × 25 µm) HgCdTe (MCT) array detector and a single-point, 100 µm × 100 µm MCT detector in the same Dewar. The symmetrically arranged objective and condenser provide an image magnification of 6× at 1 : 1 imaging and have a numerical aperture (NA) of 0.58. Specifically designed optics permit 1 : 1 or 4 : 1 imaging of the sampled area on the detector elements, resulting in 25 µm × 25 µm or 6.25 µm × 6.25 µm pixel sizes.

8.2.3 FT-IR Imaging

The Bruker FT-IR imaging system (Bruker Optik GmbH, Ettlingen, Germany) used for the investigations described in this chapter is shown in Figure 8.3. The system consists of an IFS66/S step-scan/rapid-scan FT-IR spectrometer (left), which

Figure 8.2 The PerkinElmer FT-NIR imaging system used for the investigations described in this chapter.

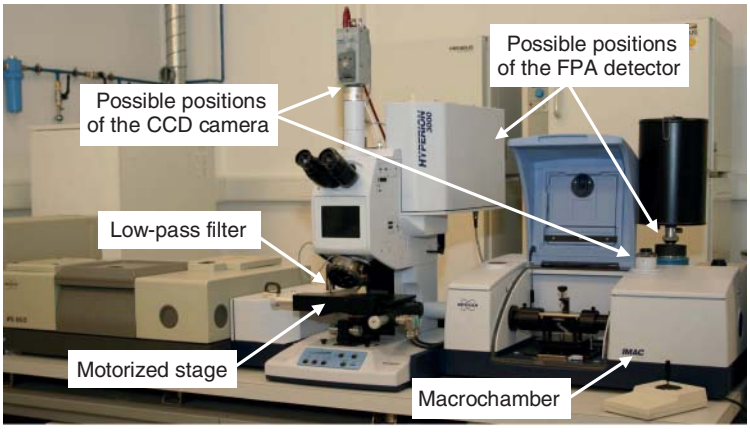

Figure 8.3 The Bruker FT-IR imaging system used for the investigations described in this chapter.

is connected to an IR microscope (Hyperion 3000) (center) and a macrochamber (IMAC®) for the investigation of larger imaging areas. Depending on the type of measurement, the FPA detector can be connected to either a microscope or a macrochamber. The low-pass filter between the FT-IR spectrometer and the microscope restricts the high-wavenumber range beyond 3850 cm^{-1} in order to avoid artifacts due to Fourier fold-over.

8.2.3.1 Micro FT-IR Imaging

For small samples or in order to achieve a higher spatial resolution, the microscope is used that is specially designed for FT-IR measurements. In this case, a motorized mirror in the microscope enables a change between single-point

Table 8.1 The objectives applied for the micro FT-IR imaging measurements and their corresponding instrumental parameters.

Objective	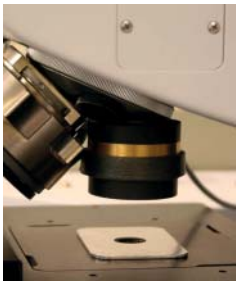	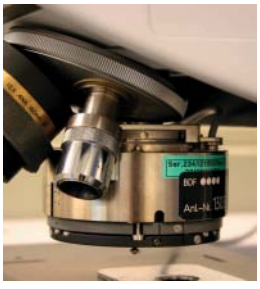
Type of measurement	Transmission/reflection	ATR (Ge crystal)
Magnification	15×	20×
Numerical aperture	0.4	0.6
Imaging area	260 µm× 260 µm	50 µm× 50 µm

measurements with a single-element detector and imaging measurements with the FPA detector. FT-IR images can be measured with different objectives in transmission, in reflection, or in the ATR mode. A computer-controlled motorized stage enables an exact positioning of the sample and a mapping with the single-element detector and also with the FPA detector. For transmission measurements, a well-aligned condenser focuses the IR radiation with maximum intensity on the sample. A live FPA image (see Section 8.2.3.3) is used to check the focus and facilitate the alignment.

For transmission and reflection measurements, a 15× objective with a NA of 0.4 and an imaging area or field of view (FOV) of 260 µm × 260 µm is used (see Table 8.1).

Micro ATR measurements in the reflection mode are performed with a special ATR objective with a Ge crystal. The tip has a diameter of 100 µm and is shaped slightly convex in order to ensure an optimal contact between the ATR crystal and the sample. It is a 20× objective with an NA of 0.6 and an FOV of 50 µm × 50 µm (see Table 8.1).

The ATR crystal can be moved to different positions, as shown in Figure 8.4; a schematic diagram shows the ATR objective in two different configurations. For the visual observation of the sample, the crystal is in the upper position (Figure 8.4a); in the measuring mode the ATR crystal is in contact with the sample (Figure 8.4b). Five different pressure stages (0.5 – 8 N) are available in order to optimize the contact between the crystal and the sample.

8.2.3.2 **Macro FT-IR Imaging**

If a larger FOV is required, the macrochamber IMAC is used instead of the microscope. It consists of an optical and a sample compartment and connections for

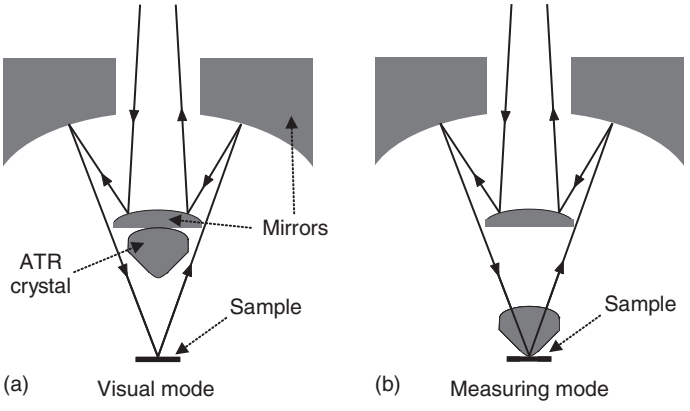

Figure 8.4 Schematic diagram showing the ATR objective in the two different measurement configurations. (a) Visual observation of the sample and (b) measuring mode with contact of the ATR crystal and the sample.

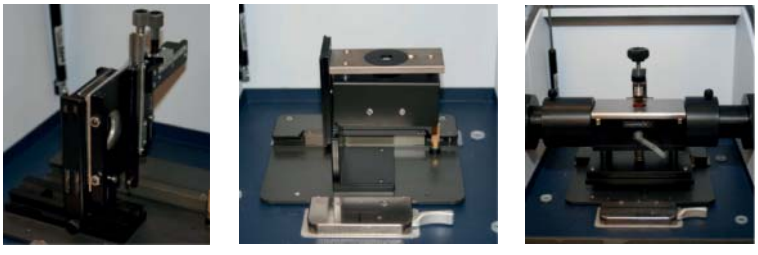

Figure 8.5 Available accessories for the imaging macrochamber. (a) Transmission (Bruker Optik GmbH, Ettlingen, Germany); (b) reflection (Pike Technologies, Madison, USA); and (c) ATR with a ZnSe crystal (Harrick Scientific Products Inc., New York, USA).

the FPA detector and the charge-coupled device (CCD) camera. There are several spectroscopic accessories that can be installed in the sample compartment.

The macrochamber enables measurements in transmission (with a manual x/y sample holder), in reflection, and in the ATR mode. Some of the different accessories available are shown in Figure 8.5.

The imaging area for transmission and reflection measurements is consistent with the detector size (3.9 mm × 3.9 mm). For ATR measurements, the imaging area is 3.9 mm × 5.5 mm because of the illumination geometry [43].

Usually, there is only one FPA detector available, and for macromeasurements the position of the FPA detector must be changed from the microscope to the macrochamber.

8.2.3.3 Measurement of an FT-IR Image

Although imaging measurements were operated in the step-scan mode with the first-generation FPA detectors, the new-generation FPA detectors are now

operating in the continuous rapid scan mode. Before the measurement, some parameters – such as the frame rate, offset, and gain – must be adjusted with the assistance of the live FPA image and the oscilloscope image. Both images indicate if some pixels have a very low intensity, and if the illumination of the imaging area is not perfect and, if necessary, an adjustment must be performed.

Because of delamination, each detector has a few so-called "bad" pixels, which can be seen very clearly in the live FPA image. Their intensity and the signal-to-noise ratio (SNR) differ from those of other pixels. New FPA detectors must not have more than 3% "bad pixels." Similar to that of conventional single-element MCT detectors, the detector pixels work at low temperature, which can be attained by cooling with liquid nitrogen. During cooling down, there is a thermal contraction of the detector pixels. Because the detector consists of layers of different materials (with different expansion coefficients), delamination can occur. However, the imaging software allows these "bad" pixels to be masked in order to avoid outliers in the IR image.

In order to minimize the number of cooling cycles guaranteed by the instrument manufacturers, special dewars with prolonged holding time up to about 50 h (at −196 °C) can be used (see black reservoir on the FPA detector in Figure 8.3).

Over many years, the common method to obtain an FT-IR image was to perform a point-by-point mapping with a microscope and a computer-controlled motorized stage. Despite automation, this mapping technique, however, was very time consuming, and due to the diffraction limit, aperture sizes of >15 – 20 µm were used thereby limiting the lateral resolution. With an infrared FPA detector, on the other hand, with 64 × 64 or 128 × 128 detector elements, 4096 or 16 384 spectra, respectively, from different locations of the sample can be measured simultaneously within a few minutes. In Figure 8.6, the mapping (b) and FPA imaging (c) technique are compared with reference to transmission measurements of a silicon oil in water emulsion. The development of color-coded images based on the intensities of specific absorption bands of the two components are schematically shown in Figure 8.6d,e, respectively.

8.2.3.4 Possible Artifacts Encountered in FT-IR/ATR Imaging

Observation of a Penetration Depth Gradient in FT-IR/ATR Spectroscopic Imaging Applications This phenomenon was described in detail in a previous publication [44] and will therefore only be discussed shortly. For test measurements to check the illumination uniformity of the ATR crystal of the FastIR™ accessory that was used in investigations with the macrochamber (Figure 8.5c), a homogeneous liquid sample (paraffin oil, Shell Deutschland Oil GmbH, Hamburg, Germany) was chosen because of its perfect contact with the ATR crystal. However, despite this perfect contact, the integrated absorbance values for a particular band were not found constant for the imaged area. Instead, an absorbance gradient in the Z-direction of the image (direction of the IR beam from the source to the detector) was observed in the image for the $\nu(CH/CH_2/CH_3)$ (3000 – 2800 cm^{-1}) and $\delta(CH_2)$ (1482 – 1425 cm^{-1}) absorption bands (Figure 8.7), which represent largely

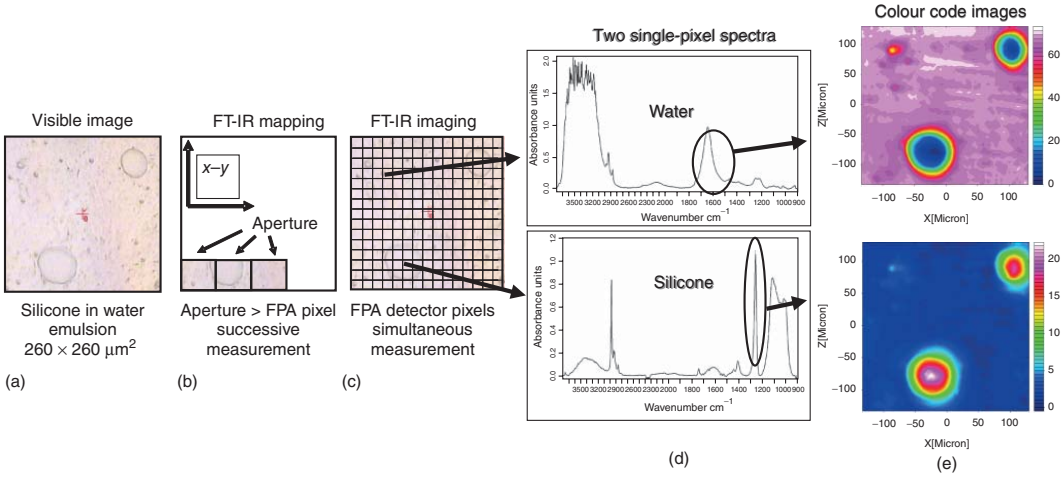

Figure 8.6 (a) Visible image of a silicone oil in water emulsion; (b) and (c) schematic comparison of the FT-IR mapping and FT-IR/FPA imaging techniques; (d) two single-pixel spectra; (e) color-coded images based on the water-specific (top) and silicone oil-specific (bottom) absorption bands.

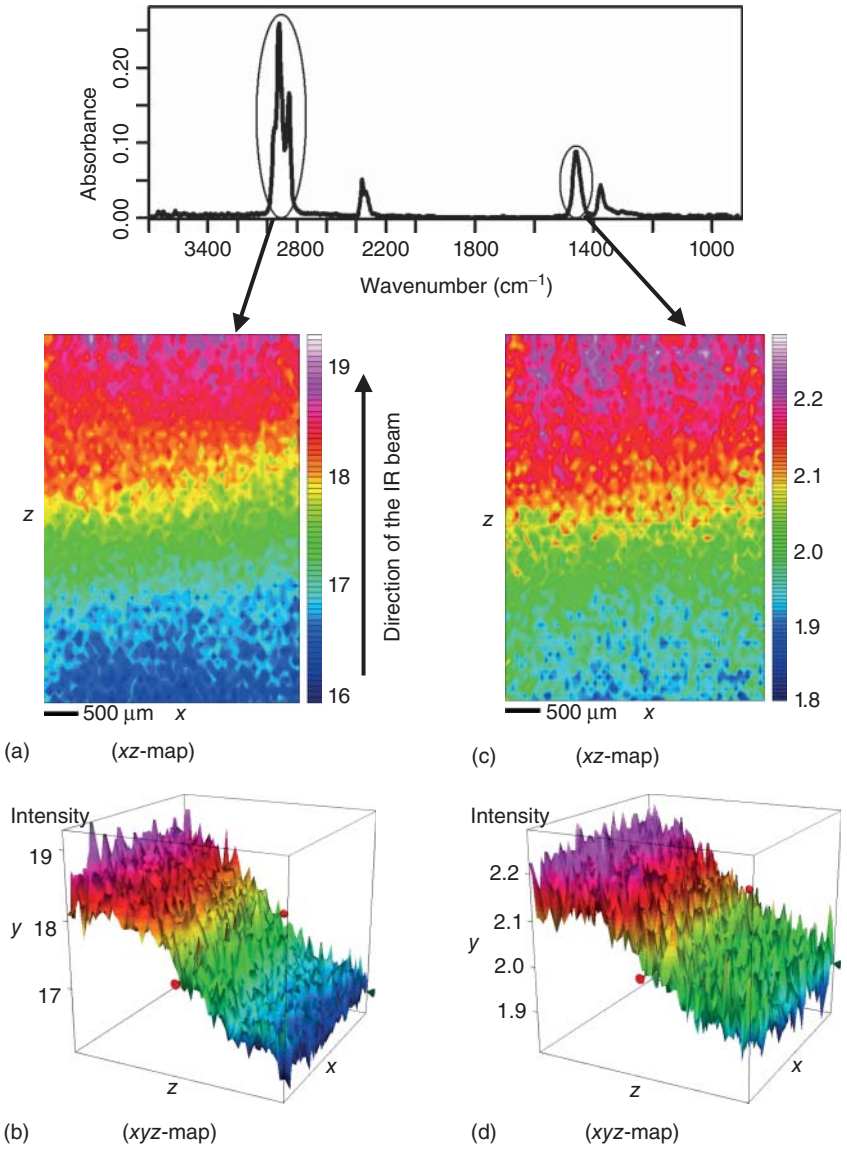

Figure 8.7 ATR FT-IR imaging results of paraffin oil for the $\nu(CH/CH_2/CH_3)$ absorption bands at 3000–2800 cm^{-1}: (a) 2D; (b) 3D and the $\delta(CH_2/CH_3)$ absorption bands at 1482–1425 cm^{-1}; (c) 2D; and (d) 3D. (Reproduced from Ref. [38] with permission. Copyright 2006 Society for Applied Spectroscopy.)

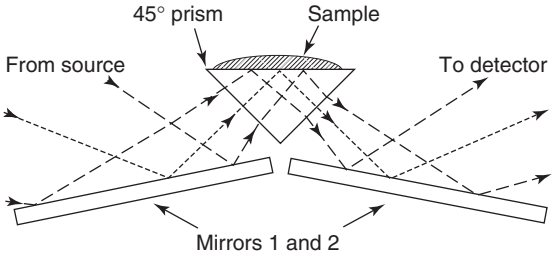

Figure 8.8 Schematic optical diagram of the ATR accessory FastIR™, demonstrating the different angles of incidence on the interface of the sample and the ATR reflection element. (Adapted from *http://www.harrricksci.com/accessories/H_fastir.cfm*.) The variably dashed rays have different angles of incidence, symbolizing the range from 45.6° to 44.3°. (Reproduced from Ref. [44] with permission. Copyright 2006 Society for Applied Spectroscopy.)

different penetration depths d_p of 0.64 and 1.28 µm [45, 46], respectively, for the nominal angle of incidence (45°) and refractive indices n(paraffin oil) = 1.4679 and n(ZnSe) = 2.4.

The explanation for the observed absorbance gradient is that the angle of incidence on the ZnSe reflection element is not exactly 45° for all IR rays, but varies between 45.6° and 44.3° (calculated by Bruker Optik GmbH by ray tracing technique) (Figure 8.8). This phenomenon is inherent to the construction of this accessory and cannot be eliminated by alignment. As a consequence, the penetration depth and the absorbance values increase in the Z-direction. As shown in Figure 8.7, the phenomenon is most pronounced in the central region of the imaged area. No gradient can be observed across the width of the infrared beam.

Generally, for a qualitative analysis of heterogeneous samples, the results will hardly be influenced by this phenomenon. For quantitative analysis, however, the effect had to be taken into account. By using another reflection element, for example, germanium with a higher refractive index (4.0 instead of 2.4 for ZnSe), the gradient would be much smaller (about one-third), because of the lower penetration depth under these experimental conditions.

Influence of Pressure on FT-IR/ATR Imaging Results This phenomenon is of more general occurrence due to the widespread pressure dependence of the conformation of polymers and solid, low-molecular-weight compounds. Thus, in FT-IR/ATR micro-imaging measurements with a germanium ATR objective (Figure 8.4), several polymer systems showed spectral differences in the area under observation although the investigated films were completely homogeneous.

Here, this artifact is exemplarily demonstrated for a poly(3-hydroxybutyrate-*co*-3-hydroxyhexanoate) (HHx = 12 mol%) film. Different image areas of 50 µm × 50 µm of the polymer film were measured with the pressure stages 1, 2, and 3 by accumulating 10 scans in the spectral range from 3800 to 900 cm^{-1} with a spectral resolution of 8 cm^{-1} (Figure 8.9).

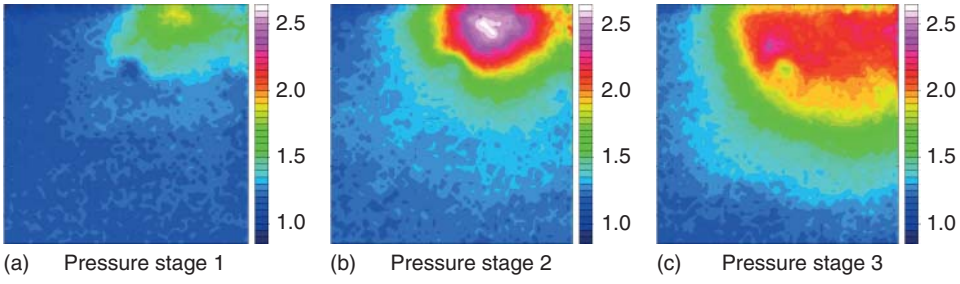

Figure 8.9 (a–c) IR images of a poly(3-hydroxybutyrate-*co*-3-hydroxyhexanoate) film measured by ATR FT-IR imaging (Ge ATR objective) with the pressure stages 1–3 (evaluation of the left wing of the ν(C=O) band; see Figures 8.10 and 8.11).

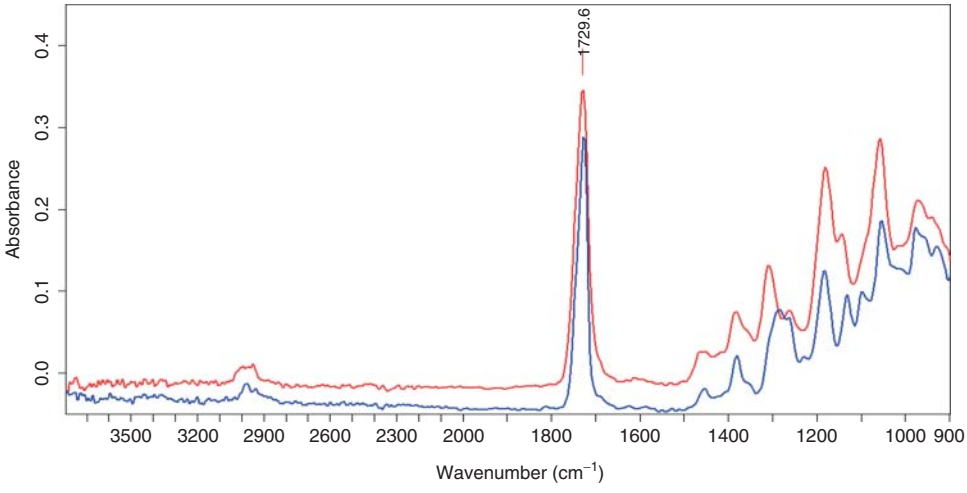

Figure 8.10 FT-IR/ATR imaging spectra of the poly(3-hydroxybutyrate-*co*-3-hydroxyhexanoate) film measured with pressure stage 3 of the Ge ATR objective: comparison of two spectra of the "red" (amorphous) and the "blue" (crystalline) regions.

The IR images of the analyzed sample areas were evaluated by the integration of the left wing of the ν(C=O) absorption band, which is characteristic of the weakly hydrogen-bonded amorphous regions of this biopolymer (see Figures 8.10 and 8.11). In order to compare the colors of the IR images at different pressure stages, a standardized color scale was used that included the range from the lowest to the highest integral absorbance of the three measurements.

Although the sample was a homogeneous copolymer film, inhomogeneities were detected in the IR images with an increase in pressure. Thus, the red areas in the upper corner of the IR images (Figure 8.9c) indicated a larger degree of amorphous content in the polymer film. However, this enrichment of amorphous regions is a consequence of the nonuniform contact pressure of the ATR crystal on the sample area and not due to the heterogeneity of the sample. Obviously, a higher pressure leads to the destruction of the crystalline regions and an

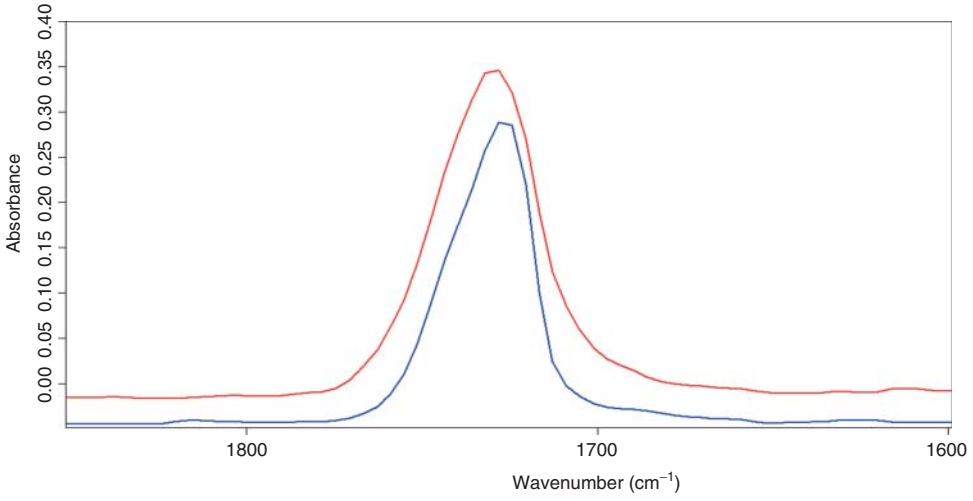

Figure 8.11 ν(C=O) absorption band of the FT-IR/ATR imaging spectra of a poly(3-hydroxybutyrate-*co*-3-hydroxyhexanoate) film measured with pressure stage 3 of the Ge ATR objective: comparison of two spectra of the "red" (amorphous) and the "blue" (crystalline) regions.

increase in the amorphous content in this pressure-sensitive biopolymer. The validity of this interpretation has been proved by repeated measurements of this copolymer film.

Figure 8.10 shows two spectra of the IR images measured with the pressure stage 3. The red spectrum corresponds to the red area in Figure 8.9 where the crystallinity has been reduced because of the higher contact pressure. The destruction of the crystallites is also accompanied by conformational changes of the polymer chains, because a comparison of the red and blue spectra clearly shows that there are also significant changes of the spectrum in the fingerprint region. For the accentuation of the changes in the ν(C=O) absorption region, an enlarged section of this wavenumber region is shown in Figure 8.11. Here, the higher intensity of the left wing of the ν(C=O) absorption band of the red spectrum can be seen more clearly than in the spectra of Figure 8.10.

Similar effects have also been observed for films of the pressure-sensitive polymers poly(vinylidene fluoride) (PVDF) and poly(tetrafluoroethylene). Thus, repeated measurements of the investigated polymer are recommended in order to confirm this phenomenon and to avoid misinterpretations. For samples without conformation and state-of-order sensitive absorption bands, this phenomenon is not relevant.

8.2.3.5 Spatial Resolution of FT-IR Imaging Measurements

For FT-IR imaging, a high spatial resolution is very important in order to visualize the distribution of different substances of a heterogeneous sample as precisely as possible. Theoretically, the lateral resolution is governed by the Rayleigh criterion

[47] (see also Section 1.2):

$$r = 0.61\frac{\lambda}{\mathrm{NA}} \tag{8.1}$$

where r is the distance between two measurement points, λ is the wavelength of the radiation, and NA is the numerical aperture defined as

$$\mathrm{NA} = n \sin\theta \tag{8.2}$$

with n the refractive index of the immersion medium between the objective and the sample (i.e., 1.0 for air, 4.0 for Ge in the case of ATR measurements), and θ is the half-angle of the maximum cone of light that can enter or exit the condenser or objective. Two objects are completely resolved if they are separated by $2r$, and barely resolved if they are separated by r. The largest NA that can generally be achieved for a Cassegrainian optic is ~0.6, so the diffraction-limited spatial resolution is approximately equal to the wavelength of the light when $n = 1.0$. Thus, the achievable lateral resolution is wavelength dependent and means that the higher the wavenumber (or the lower the wavelength) of the absorption band evaluated for the development of an image, the better the lateral resolution of this image. A summary of the achievable lateral resolutions by FT-IR imaging with a 64 × 64 FPA detector in the transmission or ATR mode for different sample areas is given in Figure 8.12. The distortion of the image dimension in the macro-ATR mode occurs because the radiation reflected from the internal reflection element is collected at an angle from the image plane [20].

As shown in Table 8.1, the size of the imaging area of a germanium (Ge) ATR objective is 50 µm × 50 µm. By using an FPA detector with 64 × 64 detector elements, an area of 0.78 µm × 0.78 µm can be allocated for each detector element. However, this does not mean that such a spatial resolution can be achieved because as shown earlier this parameter is not only limited by the pixel size and the magnification of the objective but also by the diffraction of the IR radiation (see Section 1.2).

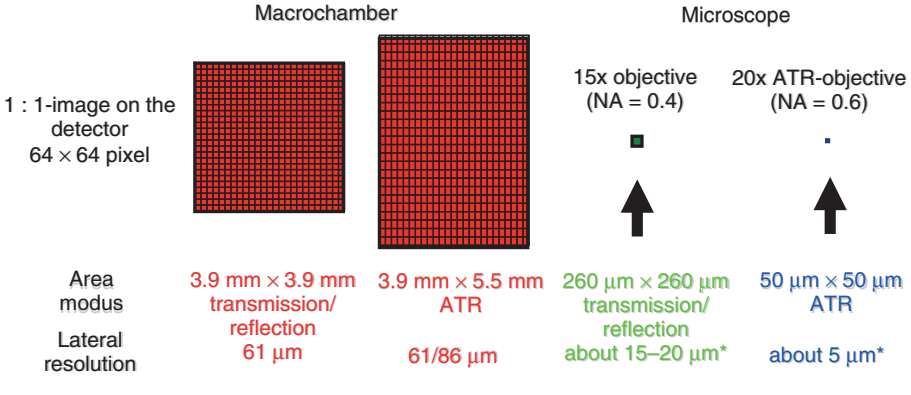

Figure 8.12 Image area and the corresponding achievable lateral resolution for different FT-IR imaging measurement modes with a 64 × 64 focal plane array detector (* wavelength dependent).

Chan and Kazarian [43] were able to achieve a spatial resolution of 3–4 μm with micro ATR FT-IR imaging measurements with a Ge ATR crystal. A report by Lasch and Naumann [48] described the lateral resolution of FT-IR imaging measurements in transmission, whereby numerous results from measurements of a resolution target USAF 1951 and tissue samples with different imaging systems from different manufacturers and with different objectives were compared.

Generally, the spatial resolution can be improved by evaluating absorption bands at high wavenumbers. Unfortunately, characteristic high-wavenumber absorption bands are not always available for the calculation of FT-IR images. However, by using a Ge ATR objective with a high NA, Sommer *et al.* and Chan and Kazarian [20, 43, 49] were able to optimize the spatial resolution by a factor in the range of the refractive index of the Ge crystal ($n = 4$).

The test systems In order to demonstrate the spatial resolution achieved in practical measurements, two test sample systems were investigated by FT-IR imaging measurements in the ATR mode and in transmission. The sizes of the imaging areas were 50 μm × 50 μm for the micro ATR FT-IR measurements (20× objective) and 260 μm × 260 μm for the micro FT-IR transmission measurements (15× objective).

The first system involved a polymer laminate of a polyethylene (PE) (25 μm) and polycarbonate (PC) (3 μm) films (both films from Bayer AG, Germany) will be discussed. A portion of PC film (~1 cm^2) was positioned on top of a 2 cm^2 PE film, and the two were sandwiched between two aluminum foils, heated to 150 °C in a drying oven for 1 h and then compressed (10 bar pressure). This sample was then imaged at the sharp borderline of the PE/PC laminate and the single PE layer in the ATR mode (50 μm × 50 μm) and in transmission (260 μm × 260 μm).

The second system involved a poly(ethylene terephthalate) (PET) film coated with a 3–4 nm aluminum layer. By using a semiconductor laser, grooves with a width and distance of 4.8 μm were written into the sample in the form of a grid (tesa AG, Hamburg, Germany), and FT-IR/ATR imaging measurements were performed within the area of the grid.

Evaluation and results The IR images of the analyzed sample areas were calculated by the integration of specific absorption bands (see Table 8.2). The integral absorbances were converted into a color code (see color scale beside the IR images). The visible image of Figure 8.13 showed a sharp separation line between the PC/PE polymer laminate and the single PE layer. This separation line can also

Table 8.2 Integration range for the image evaluation of the polymer samples.

Sample	Band assignment	Integration range (cm^{-1})
PC	ν(C=O)	1820–1740
PE	$\nu(CH_2)$	2960–2820
PET	ν(C=O)	1750–1695

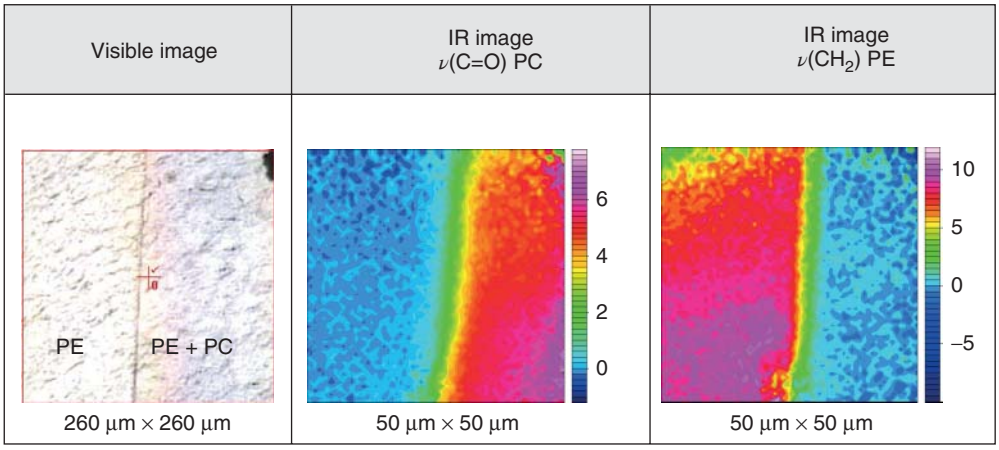

Figure 8.13 Visible image and FT-IR/ATR images of the borderline between PE and the PC/PE laminate (50 µm × 50 µm).

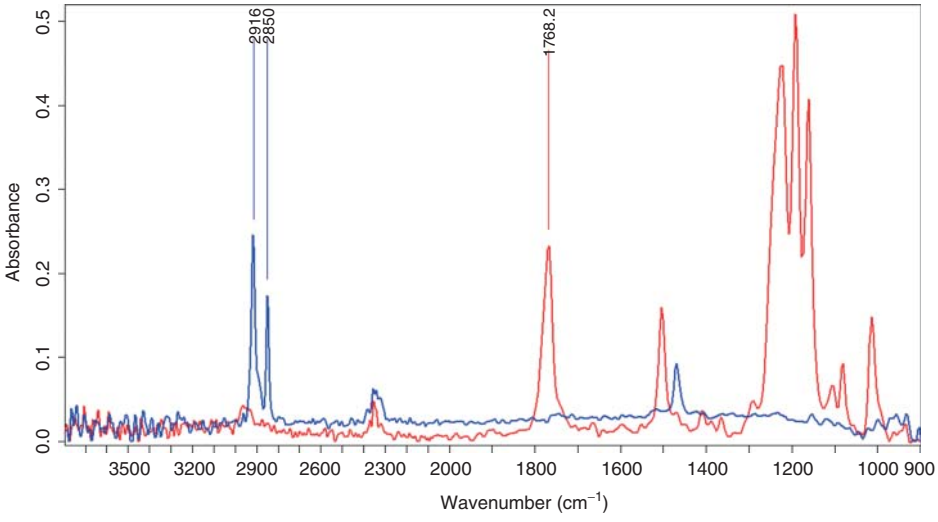

Figure 8.14 FT-IR/ATR spectra of the PE (blue) and PC (red) areas.

be seen in the IR images of Figure 8.13 for the evaluations of PC- and PE-specific absorption bands. The FT-IR/ATR spectra of the PE and PC areas are shown Figure 8.14.

Figures 8.15 and 8.16 show graphs of the integral absorbance of PE and PC (FT-IR/ATR imaging measurement) and of PC (FT-IR imaging measurement in transmission) versus pixel number of a row (64 pixel) perpendicular to the PE/PC borderline between the laminate (PE/PC) and the single layer (PE) (50 and 260 µm, respectively). The integral absorbances used for the calculation of the spatial resolution at 95% and 5% of the maximum integral absorbance (100%) are marked.

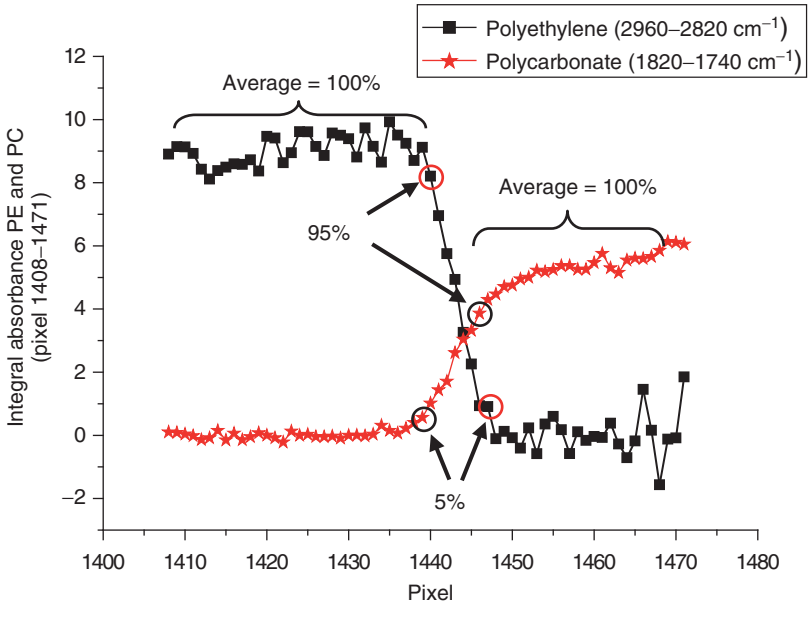

Figure 8.15 Graph of the integral absorbance of PE (black) and PC (red) (FT-IR/ATR imaging measurement) versus pixel number of a row (64 pixel) perpendicular to the PE/PC borderline (50 µm, 0.78 µm/pixel). The integral absorbances at 95% and 5% of the maximum integral absorbance (100%) used for the calculation of the spatial resolution are marked.

According to Sommer *et al.* [49], the spatial resolution is the distance between 95% and 5% of the maximum integral absorbance (100%). The maximum integral absorbance was determined by averaging the maximum integral absorbances on the left and right sides of the border line, respectively (see marks in the Figures 8.15 and 8.16). The pixels with 95% and 5% of the maximum integral absorbances were then determined, and the distance in micrometers was subsequently calculated from the number of pixels and the size of one pixel (ATR measurement: 50 µm/64 = 0.78 µm, transmission: 260 µm/64 = 4.06 µm). The results are summarized in Table 8.3. Thus, for the ATR measurement, a spatial resolution of about 6 µm was achieved at 2880 and 1728 cm^{-1}. For the measurement in transmission, a spatial resolution of 20 µm at 1728 cm^{-1} was derived.

Figure 8.17 shows the visible image of the laser-induced grid on the aluminum-metalized PET film (the dark lines indicate the PET) and the corresponding FT-IR/ATR image based on the PET-specific ν(C=O) band. Figure 8.18 shows FT-IR/ATR spectra of an exposed (irradiated) PET area (red) and of an aluminum-coated (nonirradiated) area (blue); this spectrum clearly shows the dispersion-shaped features of a reflection spectrum.

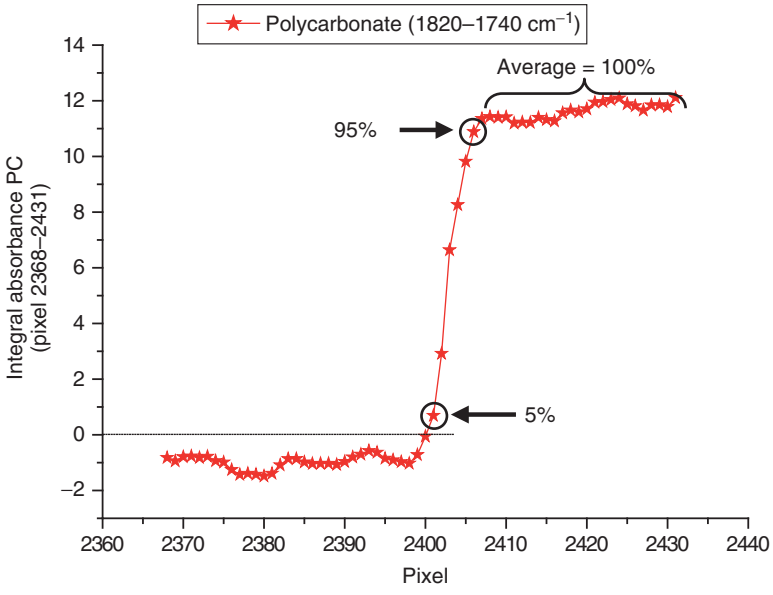

Figure 8.16 Graph of the integral absorbance of PC (FT-IR imaging measurement in transmission) versus pixel number of a row (64 pixel) perpendicular to the PE/PC borderline (260 µm, 4.06 µm/pixel). The integral absorbances at 95% and 5% of the maximum integral absorbance (100%) used for the calculation of the spatial resolution are marked.

Table 8.3 Results of the experimental determination of the spatial resolution for the polymer laminate (PE/PC) and the laser imprinted grid on an aluminum-metallized PET film.

	Wavenumber (cm^{-1})	Wavelength (µm)	Experimental (and theoretical) spatial resolution (µm)[a]	
			ATR	Transmission
PE	About 2880	3.5	5.5 (1.8)	—
PC	About 1768	5.7	6.3 (2.9)	20.3 (17.3)
PET	About 1716	5.8	4.0 (3.0)	—

a) Values in parentheses are the theoretical ($2r$) values.

Figure 8.19 shows the integral absorbance of the ν(C=O) band (PET) versus the pixels of a row perpendicular to the grid (50 µm). According to the method described earlier, a spatial resolution of ~4 µm could be derived with the 1716 cm^{-1} absorption band from this experiment.

The results for the experimental determination of spatial resolution for the polymer laminate (PE/PC) and the laser-imprinted grid on the aluminum-coated PET film are summarized in Table 8.3. Although a good agreement between the experimental and the theoretical ($2r$) values (in parentheses) was obtained for the

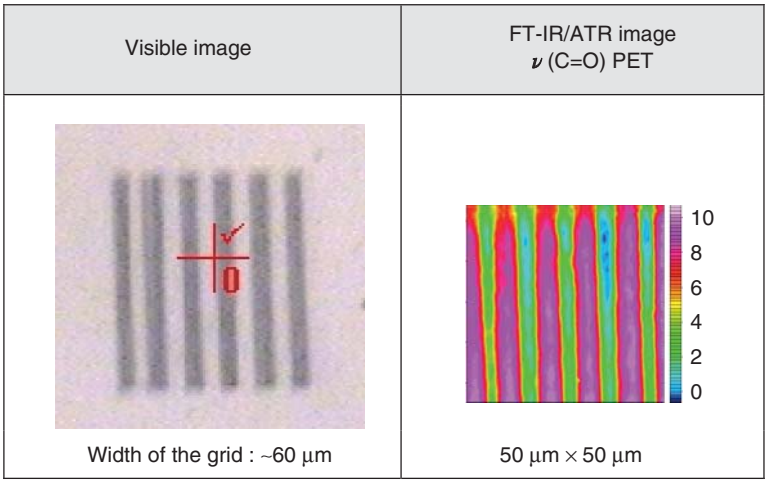

Figure 8.17 Visible image of a 60 µm wide grid written by a laser into an aluminum-metallized PET film (dark lines = PET) and the corresponding ν(C=O) FT-IR/ATR image.

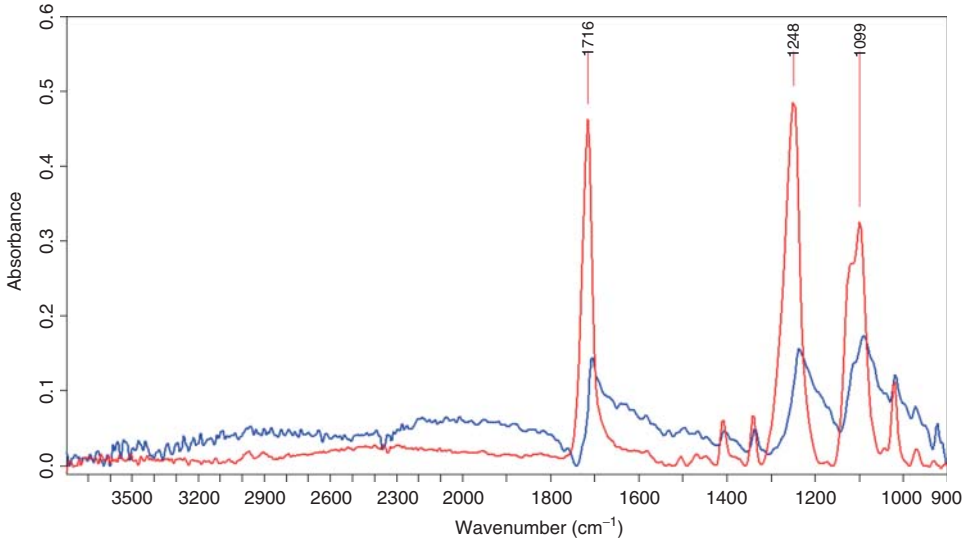

Figure 8.18 FT-IR/ATR spectra of an exposed (irradiated) PET area (red) and of an aluminum-coated (non-irradiated) layer (blue).

transmission measurement and the aluminum-coated PET film, relatively large deviations are observed for the FT-IR/ATR measurements and the theoretical values of the PE/PC laminate. This discrepancy can most likely be attributed to the thickness step along the borderline between the PC/PE dual layer and the PE monolayer film and the resulting nonoptimum contact of the polymer film in this area.

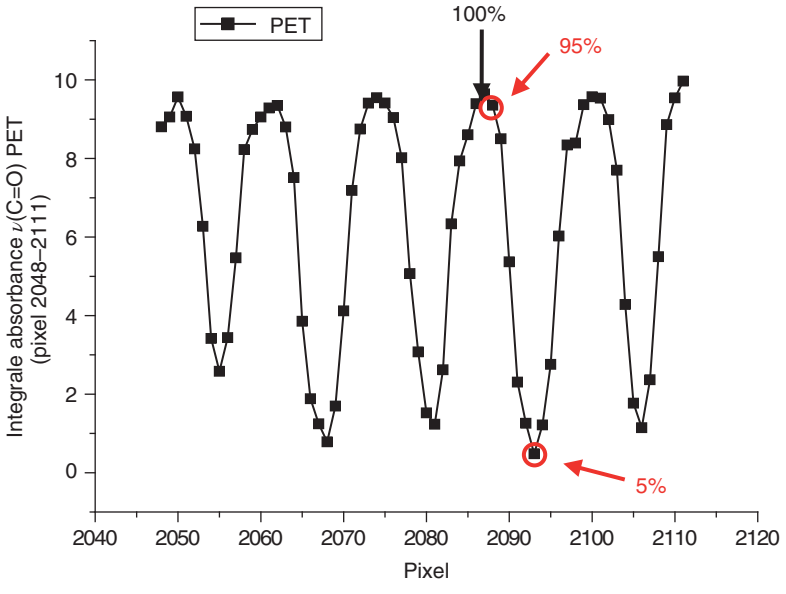

Figure 8.19 Graph of the integral absorbance of the ν(C=O) band (PET) versus the pixels of a row perpendicular to the grid (50 μm). The integral absorbances at 95% and 5% of the maximum integral absorbance (100%), which were used for the calculation of the spatial resolution are marked.

8.3
Applications of FT-IR and FT-NIR Imaging for Polymer Characterization

One area of material science where FT-IR and FT-NIR imaging studies have proved of extraordinary importance, in terms of scientific and practical aspects, is that of polymer analysis and polymer physics. In order to illustrate the broad range of applicability in these disciplines, we will now discuss some selected examples in detail, ranging from phase separation in biopolymer blends and the use of polarized radiation to produce anisotropy images of inhomogeneously deformed polymer films to the determination of the diffusion coefficients of butanol(OD) below and above the glass transition point of an aliphatic polyamide.

8.3.1
Investigation of Phase Separation in Biopolymer Blends

The blending of different polymers is a frequently used technique in industrial polymer production to optimize the material properties. The biodegradable polymer poly(3-hydroxybutyrate) (PHB) [50, 51], for example, which can be produced by bacteria from renewable resources, has the disadvantage of being stiff and brittle. The mechanical properties of PHB, however, can be readily enhanced by blending with another biopolymer, poly(lactic acid) (PLA) [52]. For the preparation of

the optimum blend, it has to be taken into account that the miscibility of different polymers depends on their concentration, the temperature, and their structural characteristics [53].

Polymer blends of PHB and PLA have previously been analyzed with miscellaneous methods by several other groups [54–56]. In the following, the use of transmission FT-IR imaging will be demonstrated as an alternative approach toward a better understanding of the chemical and physical properties of these materials.

The FT-IR transmission spectra of the individual blend components PHB and PLA and of a PHB/PLA (50 : 50 wt%) blend film are shown in Figure 8.20a,b, respectively. In Figure 8.20a, only a limited number of absorption bands are detectable, which are specific for the individual blend components PHB and PLA. For FT-IR imaging, primarily the nonoverlapped left and right wings of the intense ν(C=O) absorption bands in the blends (Figure 8.20b) can be used for the characterization of PLA (1755 cm^{-1}) and PHB (1724 cm^{-1}), respectively.

The visible images and the PHB- and PLA-specific FT-IR images of two polymer blends of PHB/PLA (50 : 50 and 30 : 70 wt%) are shown in Figure 8.21. The polymers were blended by dissolving the components in the appropriate weight ratio in chloroform p.a., and film samples with a thickness of 7–10 μm were prepared by solution casting on surface-roughened microscope slides (to avoid interference fringes in the transmission spectra) and subsequent evaporation of chloroform at 35 °C *in vacuo*. Areas (260 μm × 260 μm) of these polymer films were then analyzed in the transmission micro mode with the Bruker FT-IR imaging system (see Figure 8.3).

Figure 8.21a (left) shows the visual image of the PHB/PLA (50 : 50 wt%) blend with dark, circular-shaped islands embedded in a light matrix. For the preparation

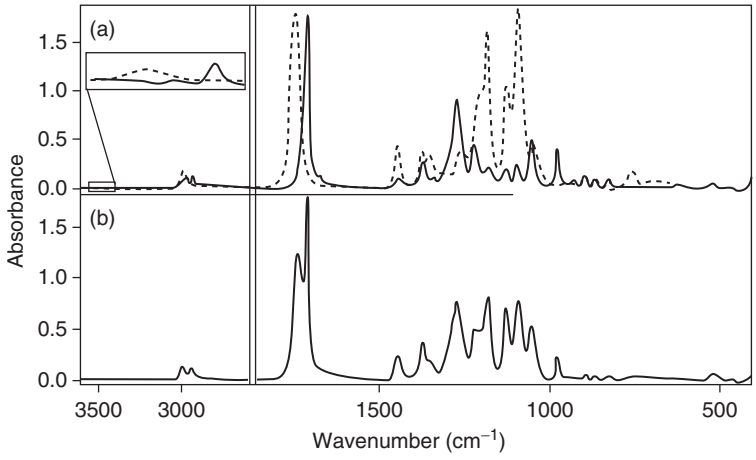

Figure 8.20 (a) FT-IR transmission spectra of a PHB (—) and a PLA (---) film (the inset shows the enlarged region of the 2 × ν(C=O) absorption bands of PLA and PHB); (b) FT-IR transmission spectrum of a PHB/PLA (50 : 50 wt%) blend film. (Reproduced with permission from Ref. [57]; © 2008, ACS Publications.)

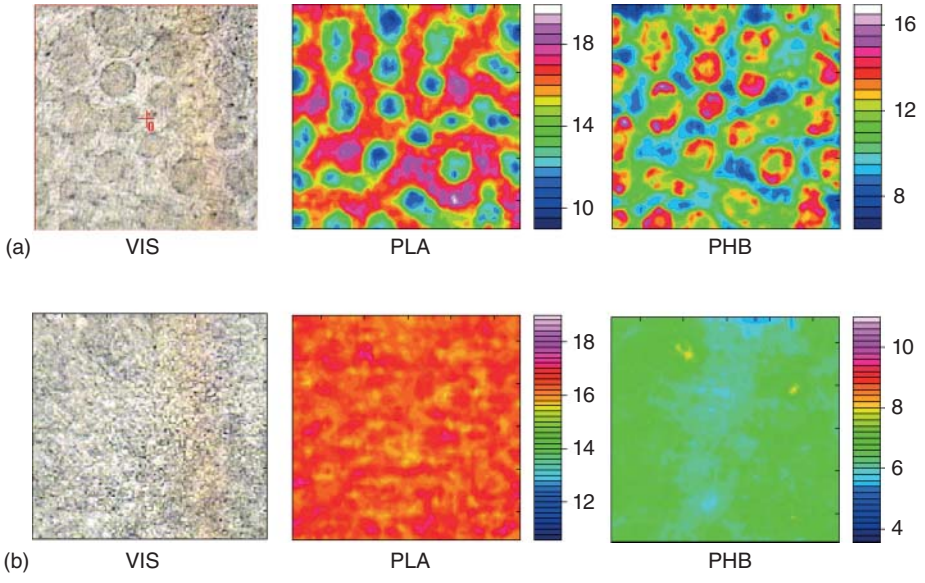

Figure 8.21 (a) Visual image (left), PLA-specific FT-IR image (center), and PHB-specific FT-IR image (right) of a PHB/PLA (50 : 50 wt%) blend; (b) visual image (left), PLA-specific FT-IR image (center) and PHB-specific FT-IR image (right) of a PHB/PLA (30 : 70 wt%) blend. (Reproduced with permission from Ref. [57]; ©2008, ACS Publications.)

of the FT-IR contour plots, the PHB- and PLA-specific absorption bands were integrated for all pixel spectra (PHB: 1720 – 1700 cm^{-1}; PLA: 1800 – 1770 cm^{-1}; baseline: 1880 – 1600 cm^{-1}). The FT-IR image based on the PHB-specific absorption band (Figure 8.21a, right) indicates a higher concentration of PHB in the islands (red-colored areas), which correlate with the darker areas in the visual image. On the other hand, the matrix has a higher concentration of PLA, which can be derived from the red-colored areas in the PLA-specific image (Figure 8.21a, center). In contrast, within the available lateral resolution at this wavelength range (~20 μm), phase separation could not be observed in the FT-IR images of the PHB/PLA (30 : 70 wt%) blend film nor in the visible image (Figure 8.21b).

For a detailed compositional analysis of the blend phases, different PHB/PLA blends ranging from (15 : 85 wt%) to (85 : 15 wt%) were analyzed by FT-IR imaging. To compare these blends in terms of phase homogeneity and composition, the peak maxima of the PHB ν(C=O) band at 1723 cm^{-1} and the PLA ν(C=O) band at 1759 cm^{-1}, respectively, were determined for the spectra with the highest absorption intensities for PLA and PHB. The PHB_{max}/PLA_{max} intensity ratios were then mapped versus the concentration of PLA (wt%) in Figure 8.22 for the different PHB/PLA blends. This graph clearly reflects that the polymer blends with 15, 30, 60, 70, and 85 wt% PLA exhibit only small differences in the PHB_{max}/PLA_{max} intensity ratios for the PHB-rich and PLA-rich areas. This observation indicates that these blends are homogeneous one-phase polymer systems. The blends with 40 and 50 wt% PLA, on the other hand, show significant

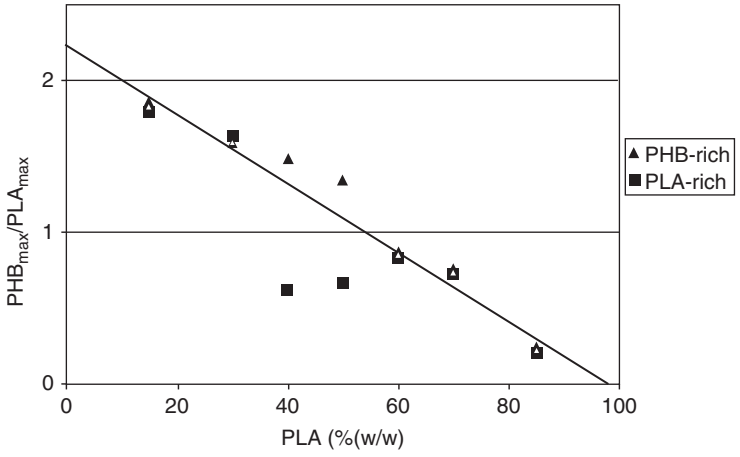

Figure 8.22 PHB_{max}/PLA_{max} ratio versus content of PLA for the PHB- and PLA-rich image areas of the different blend compositions (see text). (Reproduced with permission from Ref. [57]; © 2008, ACS Publications.)

differences in the PHB_{max}/PLA_{max} intensity ratios of their PHB-rich and PLA-rich phases. Thus, the FT-IR images provide the evidence that these blends are separated in two phases with different PHB/PLA compositions. These results were also confirmed with differential scanning calorimetry (DSC) measurements [57].

If a calibration line is drawn through the data points representing the miscible blends (15, 30, 60, 70, and 85 wt% PLA) in Figure 8.22, the compositions of the two phases in the phase-separated blends (40 and 50 wt% PLA) can be derived. In the PHB/PLA (50 : 50 wt%) blend, the PHB-rich phase has a concentration of 39 wt% PLA, and the PLA-rich phase contains 69 wt% PLA. For the PHB/PLA (60 : 40 wt%) blend, 33 and 71 wt% PLAs were calculated for the PHB-rich and PLA-rich phases, respectively.

8.3.2 Imaging Anisotropic Materials with Polarized Radiation

8.3.2.1 Blends of PHB and PLA

FT-IR imaging was also applied to analyze phase-separated PHB/PLA-blend films, which had previously been oriented by uniaxial mechanical elongation [58]. For this purpose, a selected area of the polymer film was measured with radiation polarized parallel and perpendicular, respectively, to the drawing direction of the film sample. From these data, the orientation functions of the PHB and PLA polymer chains were calculated and images representing the anisotropy of the phase-separated regions with respect to the two polymer components were then constructed. First reports on the use of polarized radiation in combination with FT-IR imaging have previously been reported by Chernev and Wilhelm [59] and Snively and Koenig [6].

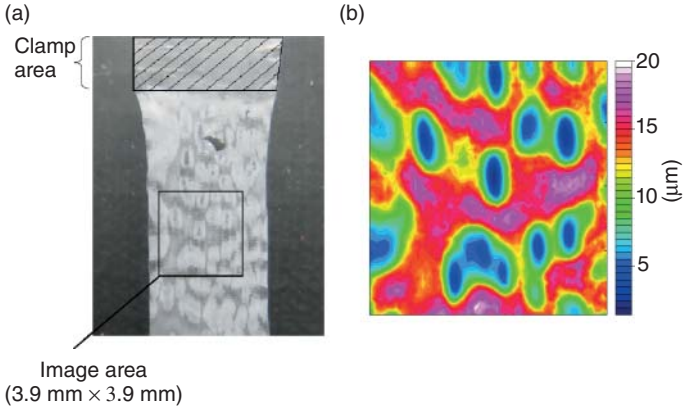

Figure 8.23 (a) Optical image and (b) FT-IR "thickness image" (3.9 mm × 3.9 mm) of the ν(C=O) $A_{0\ \mathrm{PHB+PLA}}$ (b) of the 50% stretched PHB/PLA (50 : 50 wt%) blend film.

The sample discussed here is a PHB/PLA blend (50 : 50 wt%) with an original thickness of 27 μm that was elongated to 50% strain in a miniaturized, computer-controlled stretching machine with a drawing rate of 10% strain per minute. During elongation, the white areas with a length of up to about 800 μm ("islands") (see Figure 8.23a) developed, and for the differentiation of the inhomogeneities, therefore an imaging area of 3.9 mm × 3.9 mm was used (black square). Based on the absorption intensities of a reference film with known thickness, an image of the ν(C=O) structural absorbance $A_{0\ \mathrm{PHB+PLA}}$ (see later) was calculated (Figure 8.23b), which represents the thickness variations of the analyzed film area. Thus, the white islands of the visible image (blue areas of the FT-IR image) are much thinner (thickness ~5 μm) compared to the darker matrix (red areas in the FT-IR image), which has a thickness of ~18 μm.

In polarization spectroscopy, frequently the structural absorbance A_0 is calculated from the band intensities measured with radiation-polarized perpendicular ($A_\perp$) and parallel ($A_\parallel$), respectively, by Equation 8.3:

$$A_0 = \frac{2A_\perp + A_\parallel}{3} \tag{8.3}$$

This intensity parameter eliminates the influence of anisotropy on the spectral data. In the present case, composition-specific images have been calculated (Figure 8.24a,b) with the structural absorbance ratios $A_{0\ \mathrm{PHB}}/A_{0\ \mathrm{PLA}}$ and $A_{0\ \mathrm{PLA}}/A_{0\ \mathrm{PHB}}$ to eliminate the significant sample thickness inhomogeneities in the stretched polymer (see Figure 8.23b). The ν(C=O) bands were evaluated with a baseline from 1880 to 1600 cm^{-1}, and the peak areas under the left wing (from 1779 to 1825 cm^{-1}) and under the right wing (from 1718 to 1691 cm^{-1}) were assumed to be characteristic for the PLA and PHB components, respectively. Figure 8.24a,b indicate that, here too, the islands are PHB-rich regions and the matrix has a higher PLA content.

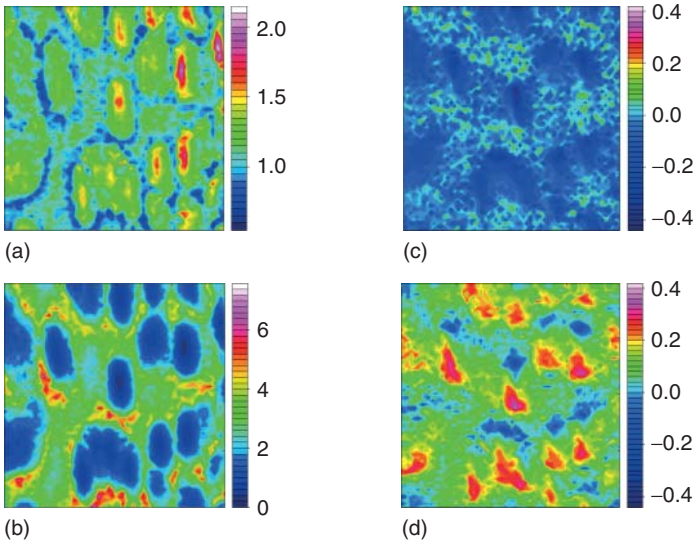

Figure 8.24 FT-IR images (3.9 mm × 3.9 mm) of A_{0PHB}/A_{0PLA} (a) and A_{0PLA}/A_{0PHB} (b) and the corresponding orientation function ($f_{\perp}$) images of PHB (c) and PLA (d) of the 50% stretched PHB/PLA (50 : 50 wt%) blend film (for optimum comparison the $f_{\perp}$ images (c) and (d) are shown with the same color scale). (Reproduced with permission from Ref. [58]; © 2008, ACS Publications.)

In order to monitor the changes in chain orientation as a consequence of the mechanical treatment, the ν(C=O) absorption bands of the PHB/PLA-blend films were evaluated to calculate the orientation function $f_{\perp}$ (assuming a perpendicular transition moment of the ν(C=O) absorption bands relative to the polymer chain direction) by

$$f_{\perp} = -2\frac{R-1}{R+2} \tag{8.4}$$

where $R = A_{||}/A_{\perp}$ is the dichroic ratio of the ν(C=O) absorption bands evaluated from the polarization spectra. For more detailed experimental and theoretical principles of FT-IR/FT-NIR polarization spectroscopy, the reader is referred to the relevant literature [60–63].

From the orientation function ($f_{\perp}$) images of the investigated sample area, a negative orientation ($f_{\perp} \approx -0.4$) can be derived for the PHB chains in the "islands" (Figure 8.24c), whereas the PLA orients positively in the same domains ($f_{\perp} \approx 0.3$) (Figure 8.24d). In the matrix, on the other hand, both PHB and PLA orient only very slightly positive ($f_{\perp}$ between 0 and 0.1) (Figure 8.24c,d). Thus, the two phases of the unstretched (50 : 50 wt%) PHB/PLA-blend film with uniform thickness respond completely different to the applied mechanical stress: the PHB-rich phase is oriented to higher degrees and lower thickness with opposite orientation of the two polymer components (PHB negative, PLA positive), whereas the PLA-rich phase undergoes only a small elongation with low thickness reduction and very low positive orientation for both polymer components.

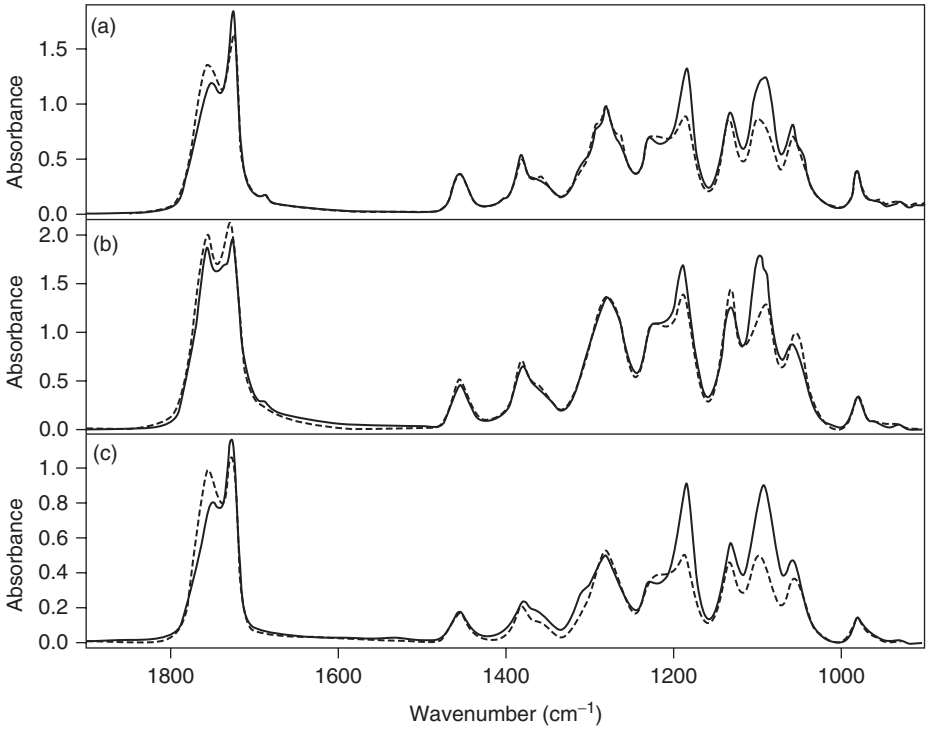

Figure 8.25 FT-IR polarization spectra ((—) parallel and (----) perpendicular to the strain direction) measured with a single-element detector of the whole area (a) and with one pixel in the matrix area (b) and "island" area (c) of the 50% elongated PHB/PLA (50/50 wt%) blend film. (Reproduced with permission from Ref. [58]; © 2008, ACS Publications.)

Figure 8.25a shows the FT-IR polarization spectra of the 3.9 mm × 3.9 mm area discussed earlier, however, measured with a single-element detector. Thus, a perpendicular dichroism (corresponding to a preferential orientation of the polymer chains in the drawing direction) is observed for the ν(C=O) absorption of PLA and a parallel dichroism (corresponding to a negative chain orientation) for the ν(C=O) absorption of the PHB component. This unusual orientation phenomenon of the PHB phase resembles the deformation mechanism of hard segments in polyurethanes and has been explained in detail in Ref. [57]. Figure 8.25b,c shows the FT-IR imaging polarization spectra of pixels located in the matrix and in an "island," respectively. In accordance with the discussion of Figures 8.24c,d, they reflect a slightly positive orientation for PHB and PLA in the matrix and an opposite orientation for the two polymer components (PHB negative, PLA positive) in the "islands." These figures clearly demonstrate that the polarization spectra recorded with a single-element detector cannot discriminate the different orientation mechanisms in the phase-separated, anisotropic structure of this polymer blend.

For a nonphase-separated blend of PHB/PLA, the visual image of the elongated polymer appears homogeneous and has a uniform thickness [58]. This observation is also reflected in the images derived from the PHB- and PLA-specific absorption bands. Furthermore, the orientation function $f_{\perp}$ of the PHB and PLA absorption bands is over the whole negative and positive areas, respectively.

8.3.2.2 Stress-Induced Phase Transformation in Poly(vinylidene Fluoride)

Another example for the use of polarized radiation in imaging studies is the analysis of PVDF films, which have been uniaxially elongated at different temperatures [64].

Depending on the thermal, mechanical, and electrical pretreatment, PVDF can exist in different modifications [65]. The crystal structure of the crumpled II(α) modification can be converted into the all-*trans* I(β) form by tensile stress below 140 °C (see Figure 8.26a). Figure 8.26b shows the stress–strain diagrams of PVDF films in the II(α) form, which have been elongated to 400% strain at 100 and 150 °C. The observed decrease in stress upon elevation of the experimental temperature to 150 °C demonstrates that the applied stress is too low to induce the conformational phase transition.

In order to monitor the transformation of the II(α) into the I(β) modification, the structural absorbance of the 975 cm^{-1} band ($\gamma_t(CH_2) + \nu_s(CF_2)$ vibration) $A_{0\,975}$ has been used, because this band is characteristic for the II(α)-form [66]. While the 975 cm^{-1} absorption band completely disappears in the film sample that has been elongated to 400% strain at 100 °C (Figure 8.27a), this II(α) phase-specific band is retained during elongation of a film at 150 °C (Figure 8.27b). The observed decrease in intensity is only a consequence of the significant film thickness reduction in the elongated sample.

The optical image of the film sample that had been elongated to 400% strain at 100 °C is shown in Figure 8.28a. The imaging area of 3.9 mm × 3.9 mm was selected at the border line of the clamp area (undeformed material) and at the

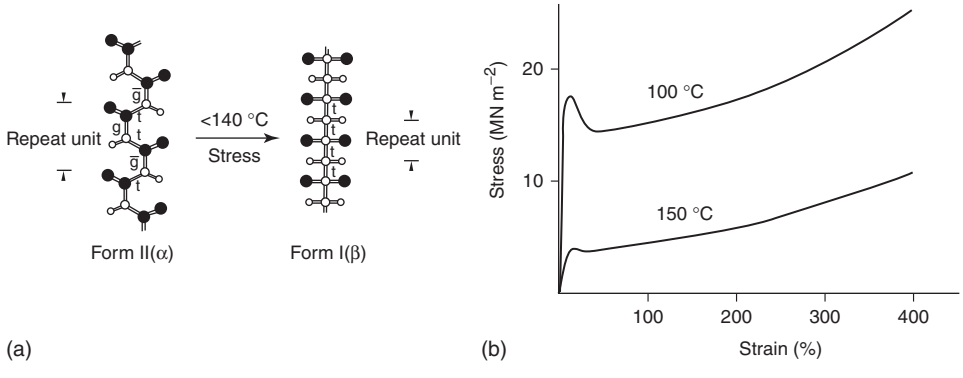

Figure 8.26 (a) Conformational changes occurring in the II(α)–I(β) transformation of PVDF; (b) stress–strain diagrams of PVDF films elongated to 400% strain at 100 and 150 °C. (Reproduced with permission from Ref. [64]; © 2008, Society for Applied Spectroscopy.)

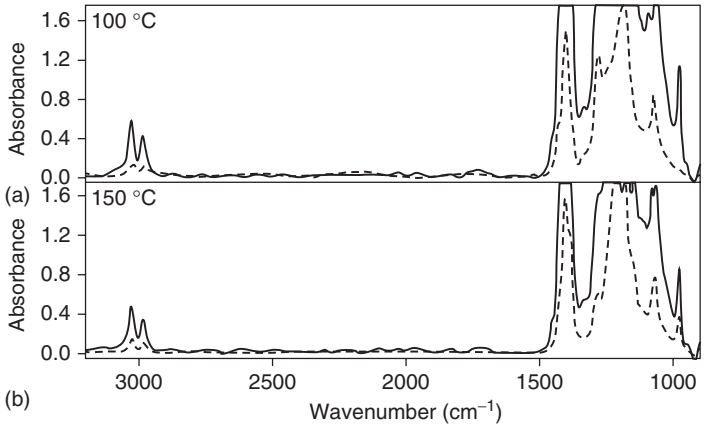

Figure 8.27 FT-IR imaging spectra measured in the clamp (—) and stretched (---) regions (a) and in the shoulder (—) and neck (---) regions (b) of PVDF samples elongated to 400% strain at 100 °C and to 100% strain at 150 °C, respectively. (Reproduced with permission from Ref. [64]; © 2008, Society for Applied Spectroscopy.)

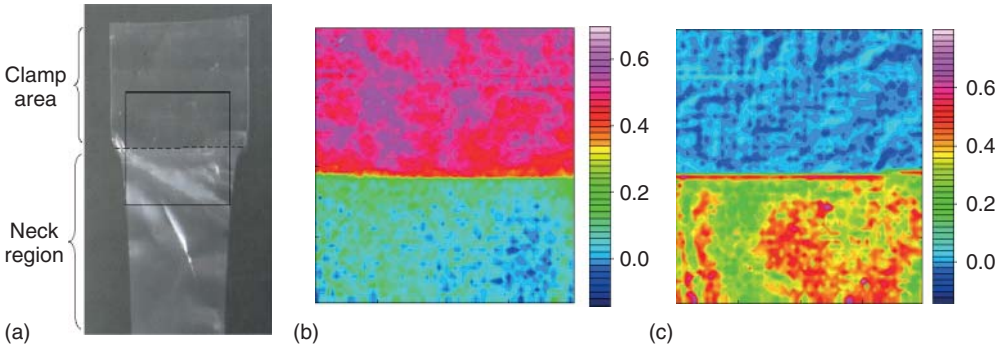

Figure 8.28 (a) Visual image; (b) $A_{0\ 975}/A_{0\ \nu(CH)}$ image; and (c) $f_{\perp}(\nu(CH))$ image recorded of a 3.9 mm × 3.9 mm area in the unstretched/stretched regions of a PVDF sample elongated to 400% strain at 100 °C. (Reproduced with permission from Ref. [64]; © 2008, Society for Applied Spectroscopy.)

neck region of the elongated part of the PVDF sample film (at elongations of 400% strain, the neck has extended over the whole sample between the clamps). The FT-IR image evaluated with the $A_{0\,975}/A_{0\,\nu(CH)}$ (integration $A_{0\,975}$: 996–961 cm^{-1}; $A_{0\,\nu(CH)}$: 3060–2940 cm^{-1}) band ratio is displayed in Figure 8.28b where the red and blue colors represent high and low values of this band ratio, respectively, corresponding to the extent of the stress-induced II(α) ⇒ I(β) transformation. The image shown in Figure 8.28c is based on the $f_{\perp}$ orientation function of the ν(CH) intensity (assuming a perpendicular transition moment). Although the undeformed clamp area appears homogeneous in both content of II(α) form (Figure 8.28b, top) and isotropy (orientation function $f_{\perp} \sim 0$) (Figure 8.28c, top),

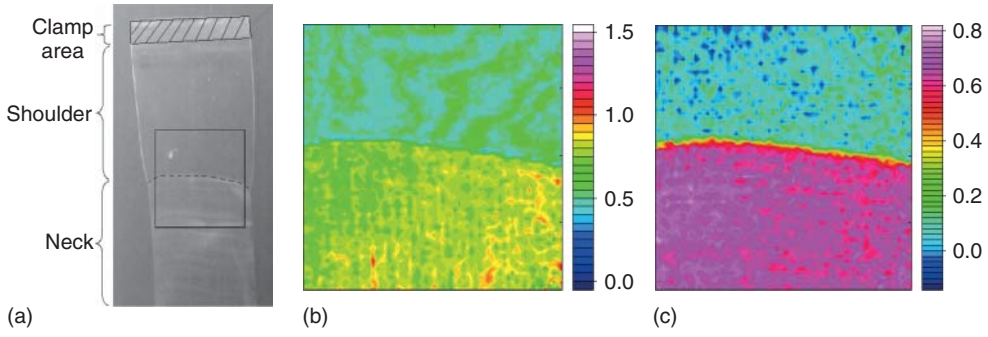

Figure 8.29 (a) Visual image; (b) $A_{0\ 975}/A_{0\ \nu(CH)}$ image; and (c) $f_{\perp}$ (975 cm^{-1}) image recorded of a 3.9 mm × 3.9 mm area in the shoulder/neck region of a PVDF sample elongated to 100% strain at 150 °C. (Reproduced with permission from Ref. [64]; © 2008, Society for Applied Spectroscopy.)

the neck region below the clamp area is quite inhomogeneous with reference to the extent of II(α) ⇒ I(β) transformation and anisotropy (variations of $f_{\perp}$ between 0.2 and 0.5). Thus, the imaging technique offers the possibility to visualize conformational as well as orientational inhomogeneities in this transition region.

The optical image of a PVDF film stretched to 100% strain at 150 °C is shown in Figure 8.29a. In contrast to the 400% elongated sample, here the shoulder–neck region has not extended over the whole sample region between the clamps, and three different sample regions are observable in the visual image (Figure 8.29a): the undeformed clamp area (top), the (only very slightly oriented) shoulder region (center), and the deformed neck region (bottom).

Because of the experimental temperature of 150 °C, no significant II(α) ⇒ I(β) transformation is expected during elongation in the neck region. This is confirmed by the $A_{0\ 975}/A_{0\ \nu(CH)}$ image (Figure 8.29b) at the shoulder–neck border line. The slight differences in the contour colors are mainly a consequence of the strong intensity decrease in the ν(CH) reference band. Contrary to the conformational similarity of the shoulder/neck regions (Figure 8.29b), a very strong difference could be detected in the anisotropy of these regions as represented by the orientation function ($f_{\perp}$) image obtained with the 975 cm^{-1} absorption band (Figure 8.29c). Values of $f_{\perp}$ between 0 and 0.2 were obtained for the shoulder region, whereas the neck region reflected $f_{\perp}$ values in the range 0.4–0.6.

8.3.3
Applications of FT-NIR Imaging for Diffusion Studies

The diffusion of small molecules into polymeric materials is important for many areas of application, for example, food packaging or protective clothing. Polyamides absorb small molecules such as water and alcohols, and this process is accompanied by a change of the melting and glass-transition temperatures [67] and also has a strong influence on their mechanical [68] and electrical [69]

properties. Thus, the measurement of the diffusion coefficient is crucial to both, a better understanding of the material transport mechanism and for the design of materials with optimized permeation properties. Several types of diffusion behavior have been identified [70]. Fickian (or case I) diffusion follows the second law of Fick [71]:

$$\frac{\partial c}{\partial t} = D\frac{\partial^2 c}{\partial x^2} \tag{8.5}$$

where c is the concentration of the diffusant, D is the diffusion coefficient, t is the time, and x is the distance along the diffusion direction. In general, Fickian diffusion is only observed in glassy systems when the diffusants are simple gases or solvents with small molecular diameters or partial solvents at very low temperatures and penetrant activities. At temperatures and penetrant activities where the polymer is swollen, transport is often controlled by a combination of polymer relaxation and Fickian diffusion mechanisms.

Case II transport occurs when the sorption is entirely controlled by stress-induced relaxations taking place at a sharp boundary separating an outer swollen shell, essentially at equilibrium penetrant concentration, from an unpenetrated glassy core. Ideally, this sharp boundary moves through the polymer at a constant velocity during case II transport. Supercase II transport occurs when the velocity of the case II sorption boundary is sufficiently slow so that a Fickian tail may develop ahead of the sorption discontinuity [70].

Numerous experimental techniques were applied to measure the diffusion coefficients of small molecules into a polymer by monitoring either the release from, uptake into, or permeation through the polymeric material. Gravimetric techniques [72–74] are the most frequently used methods. For polymers with labile hydrogen atoms in NH or OH functionalities, however, the H/D-isotope exchange (deuteration), in combination with NIR spectroscopy, has proved a convenient method to study the diffusion of D_2O and deuterated alcohols into polyamides [75]. Furthermore, Gupper and Kazarian [76] applied FT-IR imaging spectroscopy to study the kinetics of solvent diffusion of chloroform and solvent-induced crystallization in syndiotactic polystyrene. For these approaches, the calculation of the type of diffusion by Snively and Koenig [3, 4], which describes the position of the penetrant front versus time, can be applied:

$$d = At^{\alpha} \tag{8.6}$$

Here, d is the pathlength of the diffusion front (in the present investigations, the distance of the NH/ND exchange front to the polyamide 11 (PA11)/butanol(OD) interface), A is a proportionality factor, t is the time, and α is the diffusion exponent. This exponent α is characteristic of the diffusion process and can take on the values of 0.5 and 1.0 for the limiting cases of Fickian (case I) and case II diffusion, respectively [3, 4, 71].

In the presented study, FT-NIR spectroscopic imaging was utilized to monitor the penetration of butanol(OD) molecules into a PA11 film of several hundred micrometer thickness [77]. In a previous study [75], it was shown that the

rate of diffusion of different penetrants is controlled by their molecular structure and geometry. Furthermore, other factors such as polarity and hydrogen bonding interactions of the penetrating molecules also play an important role for the diffusion process. Thus, the stronger deuterium bonding between the D_2O molecules and deuterium bonds with amide groups of the polyamide chain leads to a much slower diffusion process compared to butanol(OD). For that reason, the diffusant butanol(OD) was used instead of D_2O, because it allows to monitor the diffusion in an experimentally manageable time frame. Because this isotope exchange is directly linked to the diffusion of butanol(OD) into the PA11, the FT-NIR imaging technique can be applied to follow the diffusion process as a function of time and monitor the lateral extension of the diffusion front. For this purpose, an area of ~300 µm × 210 µm across the butanol(OD)/PA11 interface was monitored. On the basis of the FT-NIR spectra measured in experiments at 25 and 50 °C, not only the type of diffusion but also the diffusion coefficient of butanol(OD) below and above the T_g of PA11 (46 °C), respectively, could be calculated [12, 77–79].

8.3.3.1 Experimental

The FT-NIR imaging measurements were performed with a PerkinElmer (Massachusetts, USA) imaging system consisting of a Spectrum One FT-NIR spectrometer coupled to a Spectrum Spotlight 300 NIR microscope (see Section 8.2.2). For the investigations described later, each image was measured in the transmission mode for an area of 300 µm × 210 µm with a pixel size of 6.25 µm × 6.25 µm and a spectral resolution of 16 cm^{-1} by co-adding eight scans for a spectrum. Thus, the measurement time for each image was about 5 min.

PA11 sheets with a thickness of 500 µm (Institut Francais du Petrole, Rueil Malmaison, France) and an area of 5 mm × 5 mm were sandwiched between two CaF_2 disks of different diameters (base plate, 25 mm; cover plate, 20 mm). In order to prepare a void-free stack of the CaF_2 windows and the PA11 film, the sandwich was heated to 250 °C on a heating plate and after melting of the PA11 film, the heating plate was switched off and the polymer was allowed to rapidly cool down to room temperature. Then, butanol(OD) was carefully dropped onto the CaF_2 base plate and allowed to penetrate into the free space between the CaF_2 windows under capillary action. When this process was finished, excess butanol(OD) was quickly removed, the CaF_2 windows were sealed with Vaseline to keep the butanol(OD) between the capillary space, and the time-dependent measurements were started. Based on the evaluation of the ν(NH) + amide II combination band at about 4875 cm^{-1}, this sample preparation provided a perfect boundary between the polymer and the butanol(OD) diffusant (see later). The experimental diffusion temperatures of 25 and 50 °C were chosen because from DSC measurements a T_g of 46 °C was determined for the PA11 film under investigation. Because the measurements were performed at different temperatures, a specifically designed sample holder for variable-temperature measurements had to be built that fits into the narrow available space of the microscope unit (Figure 8.2, left) and allows the experimental temperature control with a high THC-15 unit (Yokohama, Japan).

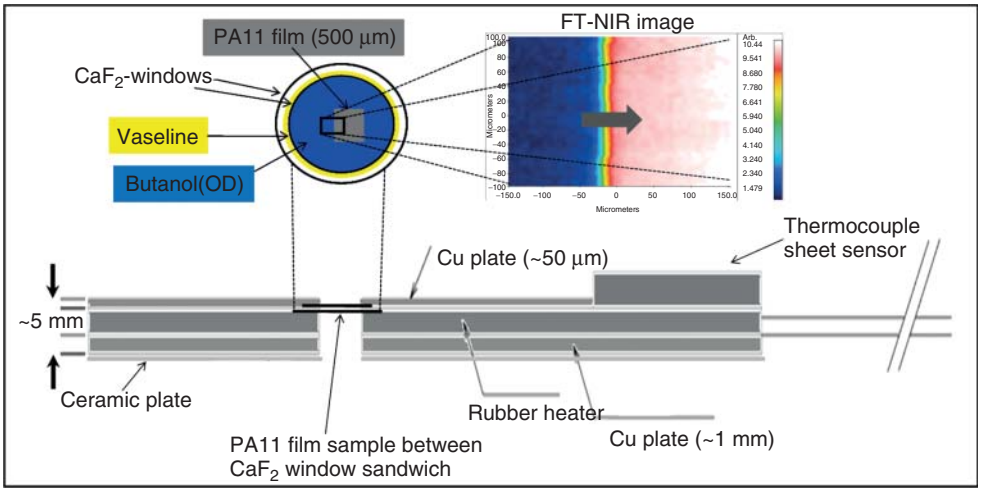

Figure 8.30 Sample holder for the temperature-controlled FT-NIR spectroscopic imaging measurements of the diffusion of butanol(OD) into a PA11 sheet. (Reproduced with permission from Ref. [77]; © 2011, Society for Applied Spectroscopy.)

A cross section of the variable-temperature sample holder including the sample presentation for the described experiment is shown in Figure 8.30.

8.3.3.2 Results and Discussion

In Figure 8.31, the ν(NH) + amide I and ν(NH) + amide II combination band doublet [80] in the FT-NIR spectra of the original PA11 film and after deuteration for 5 h 35 min at 50 °C are shown. From this figure, it becomes clear that the intensity reduction for the 4965 cm^{-1} band is much smaller than that for the 4875 cm^{-1} band. The reason is that with progressing deuteration, the 4965 cm^{-1} combination band is increasingly superimposed by an evolving $2 \times \nu$(ND) overtone. Therefore, the deuteration progress was evaluated as a function of time with the 4875 cm^{-1} band intensity. To prepare the FT-NIR contour plots, the ν(NH) + amide II absorption band was integrated in the 4935–4800 cm^{-1} region with a baseline from 5030 to 4800 cm^{-1}. Furthermore, a consistent color code of the FT-NIR images has been applied for the investigations at the different temperatures. Thus, the color assignment is based on the minimum and maximum absorbance values of the initial image at t_0.

In Figure 8.32, the 300 µm × 210 µm FT-NIR images of the ν(NH) + amide II combination band with the borderline between PA11 and butanol(OD) are shown for two different deuteration times at 25 °C (a,b) and 50 °C (c,d). On the left side (blue) the butanol(OD) and on the right side (light pink), the PA11 films are mapped. At the beginning ($t = 0$ min), no butanol(OD) has diffused into the polymer film. Thus, the PA11 part of the image is homogeneously lightly pink colored. After 10 h 15 min at 25 °C, the deuteration front has progressed into the PA11 area, and this leads to the decrease in the ν(NH) + amide II absorption

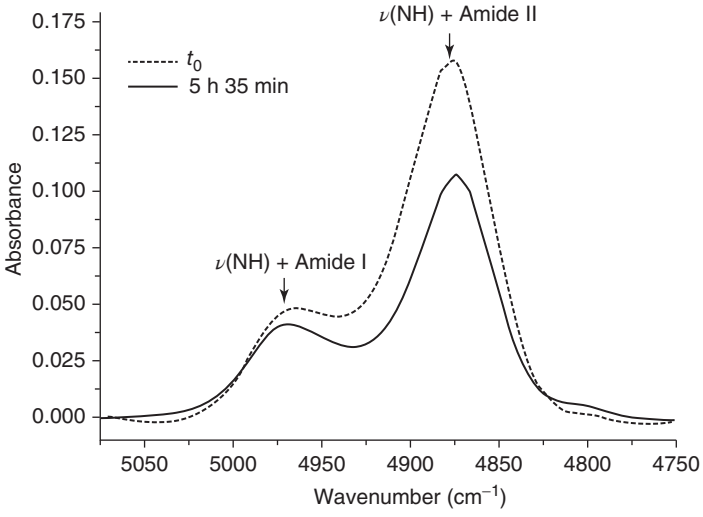

Figure 8.31 FT-NIR imaging spectra of PA 11 before (---) and after 5 h 35 min (—) deuteration with butanol(OD) at 50 °C. (Reproduced with permission from Ref. [77]; © 2011, Society for Applied Spectroscopy.)

band with an accompanying change to a yellow color (Figure 8.32b). In contrast to the deuteration progress at 25 °C, the front of the NH/ND exchange at 50 °C has reached approximately the same position already at about 1 h 45 min (Figure 8.32d). These results clearly indicate that significant differences of the diffusion rate below and above the glass transition temperature of PA11 occur.

For the calculation of the type of diffusion from FT-IR imaging data, Snively and Koenig [3, 4] used the logarithmic form of Equation 8.6, which allows to determine the diffusion exponent α from the slope of a plot of $\log d$ (d measured in micrometers) versus $\log t$ (t measured in seconds):

$$\log d = \log A + \alpha \cdot \log t \tag{8.7}$$

The diffusion front was evaluated by extracting spectra of pixels in eight neighboring rows extending perpendicular to the PA11/butanol(OD) borderline into the PA11 (Figure 8.32a, gray-shaded rectangle). The fluctuations of the integral absorbance of the ν(NH) + amide II band were compensated by the calculation of the mean spectrum corresponding to the eight neighboring pixels at the same distance. The position of the diffusion front with progressing time was defined as the distance from the PA11/butanol(OD) borderline at t_0 to the pixel position where the integrated ν(NH) + amide II band intensity has achieved its original value of the PA11/butanol(OD) borderline at t_0 (Figure 8.33a,b). Figure 8.34a shows the diagram of $\log d$ versus $\log t$ at 25 °C, from which a diffusion exponent α of 1.13 was derived, which can be interpreted in terms of a case II type diffusion. On the other hand, for the deuteration experiment at 50 °C, a diffusion exponent α of 0.64 was obtained (Figure 8.34b) and characterized in terms of a Fickian type of diffusion.

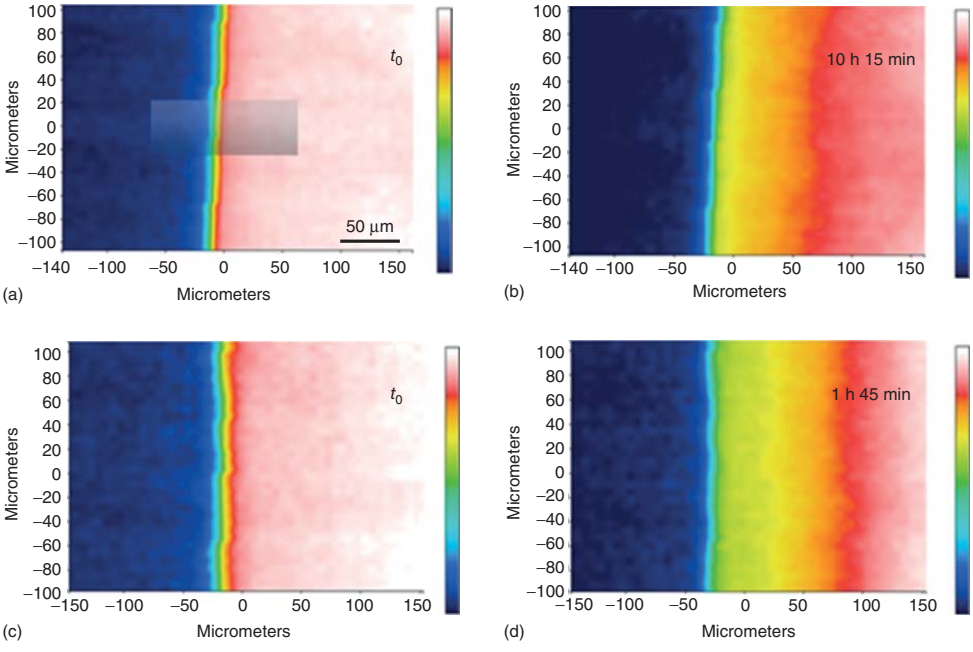

Figure 8.32 FT-NIR images based on the integrated ν(NH) + amide II absorbance for the deuteration times t_0 (a) and 10 h 15 min (b) at 25 °C and t_0 (c) and 1 h 45 min (d) at 50 °C. (Reproduced with permission from Ref. [77]; © 2011, Society for Applied Spectroscopy.)

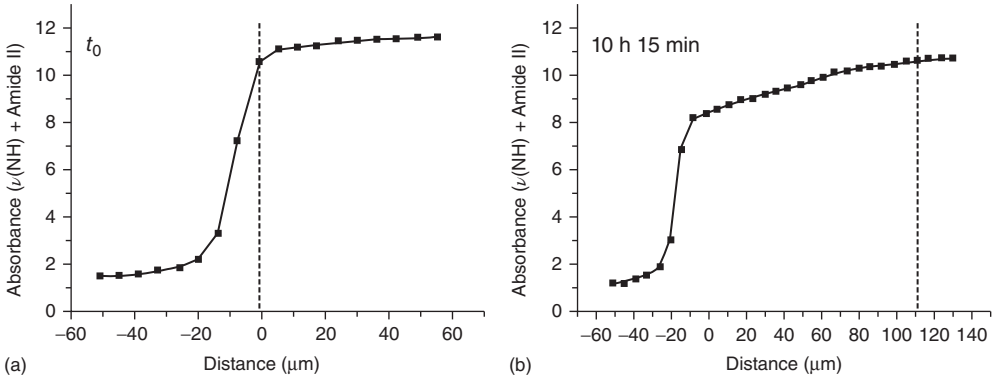

Figure 8.33 Determination of the diffusion front position for the 25 °C experiment at t_0 (a) and 10 h 15 min (b). The dashed lines indicate the butanol(OD)/PA11 interface at t_0 (a) and the diffusion front after 10 h 15 min (b). (Reproduced with permission from Ref. [77]; © 2011, Society for Applied Spectroscopy.)

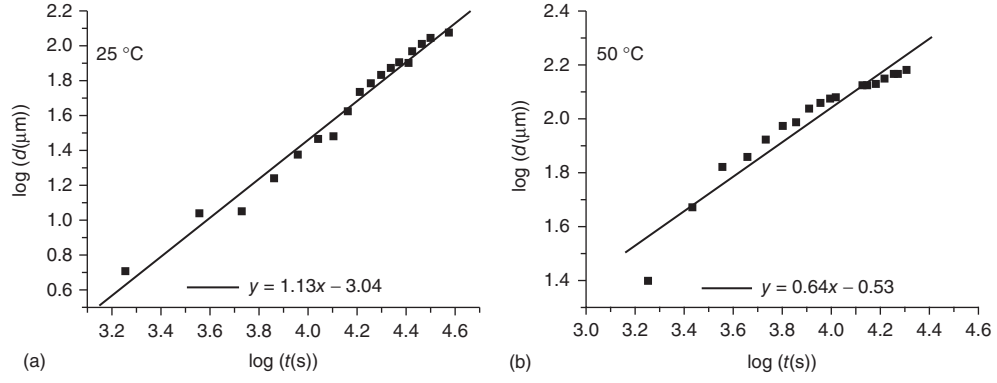

Figure 8.34 Plots of log d (d, distance in micrometer of the butanol(OD) diffusion front from the borderline PA11/butanol(OD) versus log t, where t is the deuteration time in seconds) for the experiments at 25 °C (a) and 50 °C (b). (Reproduced with permission from Ref. [77]; © 2011, Society for Applied Spectroscopy.)

In order to extract more information about the significant difference of diffusion rate below (25 °C) and above (50 °C) the glass transition temperature of PA11 and notwithstanding the different diffusion types, the diffusion coefficients were calculated based on Fickian diffusion according to the procedure of Rafferty and Koenig [12], also applied for imaging measurements. In a Fickian system, the position d of the penetrant front versus time can be described by the equation:

$$d = kt^{\frac{1}{2}} \tag{8.8}$$

where t is time and k is a proportionality constant that is related to the square root of the diffusion coefficient D (Equation 8.11). The average diffusion coefficient D can be calculated from the initial slope of the sorption curve of a gravimetrically

determined mass uptake [70, 71]. For this purpose, the values of M_t/M_{max} are plotted versus the square root of time according to Equation 8.9

$$\frac{M_t}{M_{max}} = \frac{4}{\sqrt{\pi}} \cdot \sqrt{\frac{Dt}{l^2}} \tag{8.9}$$

where M_t is the mass-uptake at time t, M_{max} is the mass-uptake at saturation, and l is the thickness of the film. For their FT-IR spectroscopic imaging measurements, Rafferty and Koenig [12] used the following equations:

$$d = \frac{4}{\sqrt{\pi}}\sqrt{Dt} \quad \text{with} \quad d = \frac{M_t}{M_{max}} \cdot l \tag{8.10}$$

After combination of Equation 8.8 with Equation 8.10, the following relation is obtained:

$$k = \frac{4}{\sqrt{\pi}}\sqrt{D} \tag{8.11}$$

Thus, the diffusion coefficient D can be calculated from the proportionality constant k by

$$D = \left(\frac{k\sqrt{\pi}}{4}\right)^2 = \frac{k^2\pi}{16} \tag{8.12}$$

In Figure 8.35, the distance d (in centimeters) of the NH/ND exchange front to the PA11/butanol(OD) borderline at t_0 is plotted versus the square root of time t (in seconds) for the investigations at 25 °C (Figure 8.35a) and 50 °C (Figure 8.35b). By linear regression, a proportionality constant k of 7.15×10^{-5} was derived and finally a diffusion coefficient of $1.00 \times 10^{-9}\,cm^2\,s^{-1}$ was calculated by (Equation 8.12) for the experiment at 25 °C. For the 50 °C diffusion experiment, a

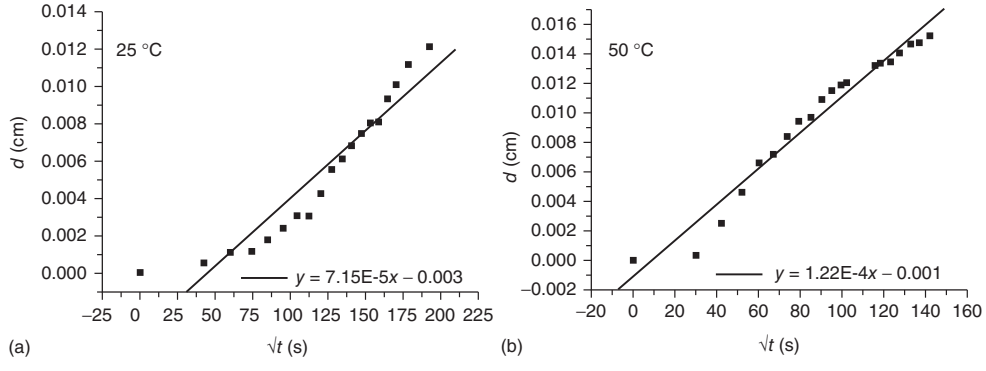

Figure 8.35 Plot of the distance d (in centimeters) of the butanol(OD) diffusion front from the borderline PA11/butanol(OD) versus the square root of the deuteration time t (in seconds) for the experiments at 25 °C (a) and 50 °C (b). (Reproduced with permission from Ref. [77]; © 2011, Society for Applied Spectroscopy.)

proportionality constant k of 1.22×10^{-4} was obtained and a diffusion coefficient of 2.92×10^{-9} cm^2 s^{-1} was determined. In summary, these results demonstrate that the rate of the diffusion process of butanol(OD) into a PA11 film strongly depends on the temperature. Thus, the diffusion coefficient above the glass transition temperature of PA11 (50 °C) is approximately three times larger than at the temperature below the T_g (25 °C).

8.3.4 Conclusions

The discussed examples demonstrate that FT-IR and FT-NIR spectroscopic imaging studies can be applied in a multiplicity of applications for the characterization of polymers. Thus, apart from the visualization of phase separation in polymer blends – including the quantitative determination of the blend components – FT-IR imaging can provide a thickness map of the investigated sample area. By the use of polarized radiation anisotropy, images based on orientation function values can be constructed. Last but not least, the potential of FT-NIR imaging for time-resolved investigations of diffusion phenomena at different temperatures was demonstrated. In conclusion, these examples show that a much more detailed picture on the chemical, physical, and orientational properties of polymers with reference to their lateral distribution can be obtained from imaging studies.

8.4 NIR Imaging Spectroscopy for Quality Control of Pharmaceutical Drug Formulations

Although NIR spectroscopic imaging was only introduced on a large scale following the initial development of FT-IR spectroscopic imaging, during the last few years it has achieved significant progress and proved extremely important in the field of agricultural and food (Chapter 7) and especially pharmaceutical quality control [31, 34]. Because most of these applications are performed in the diffuse reflection mode, the considerations on the effective pathlength of NIR radiation into solid materials [41] and previous work related to the penetration depth of NIR radiation [33, 35–40] have to be taken into account regarding the representative character of quantitative determinations by NIR imaging measurements.

In the application discussed in the following sections, the derivation of quantitative results from NIR spectroscopic imaging data of solid drug formulations will be reported. In order to assess the validity of the quantitative determination of solid drug formulations (powders, tablets) by NIR spectroscopic imaging, these results will be compared to the compositional analysis of the same sample set by conservative NIR spectroscopic diffuse reflection measurements with a single-element detector [42].

8.4.1 Quantitative Determination of Active Ingredients in a Pharmaceutical Drug Formulation

The solid drug formulations investigated consisted of mixtures in varying concentrations of the three crystalline, active ingredients ASA, ASC, and CF with the two amorphous excipients cellulose and starch in a fixed ratio and constant composition. A set of 48 samples was prepared by milling varying amounts of the active ingredients in the concentration range 13.77 – 26.04 wt% with equal amounts (40 wt%) of a 1 : 3 (wt) mixture of cellulose and starch for 5 min in a Retsch mill (type BMO, Retsch GmbH, Haan, Germany). From scanning electron microscopy, a final particle size of the mixtures after the milling procedure was determined between about 10 – 30 µm.

The NIR hyperspectral images were recorded on a MatrixNIR system (Malvern (formerly Spectral Dimensions), Olney, MD, USA) (see also Figure 8.1) with four quartz-halogen lamps as NIR sources, a LCTF as monochromator and a thermoelectrically cooled 256 × 320 InGaAs FPA detector in 118 channels (960 – 1662 nm or 10 417 – 6017 cm^{-1}) with a spectral resolution of 6 nm at 1600 nm (corresponding to 24 cm^{-1}). Each channel was scanned 10 times using a 64 ms integration time. The image FOV was 50 mm × 62 mm with ∼200 µm × 200 µm pixels and the total image acquisition time was around 5 min. For the imaging measurements, the powder drug formulations were presented in a circular sample holder (FOSS, Hillerod, Denmark) with an outer diameter of about 40 mm and a sample layer thickness of 3 mm. To eliminate the shadow effects of the sample holder, a region of interest (ROI) with a radius of 80 pixels (about 16 mm) was chosen, resulting in a sample pixel count of ∼20 000 points. All sample images were bracketed with sets of five images of Spectralon standard tiles with 2%, 25%, 50%, 75%, and 99% reflectance values (Labsphere Inc., North Sutton, NH, USA), and a second-order polynomial fit was used to create a transform function that translates instrument counts to percentage of reflectance. Finally, the reflectance data were transformed into $\log 1/R$ ("absorbance") spectra, and a multiplicative signal correction (MSC) was applied as data pretreatment. Euclidean distances to a mean spectrum were computed and then thresholded to eliminate outlier pixels from each hyperspectral image (any pixel >5 standard deviations was eliminated). This procedure typically left about 18 000 pixels with clean spectra for further data treatment.

From the total sample set (48 samples), 45 samples were used as calibration samples. The three samples not included in the calibration set were selected on the basis of a representative variation of their active ingredient concentrations and were finally used as "unknown test samples" to predict the content of their active ingredients. Partial least squares (PLS) models for each active ingredient were developed with the Unscrambler™ Software (version 9.6) (CAMO Software AS, Oslo, Norway) from the MSC-pretreated median spectra of all pixels of each of the 45 calibration sample images. Based on these calibration models, the predictions of the active ingredient content for each pixel of the imaging data of the

three test samples and their evaluation as histograms, contour plots, and RGB plots were performed with Matlab v. 7.0.4 software (see later).

The conventional single-element detector NIR spectra were measured on a Bruker Vector 22N FT-NIR spectrometer (Bruker Optik GmbH, Ettlingen, Germany) equipped with a tungsten-halogen light source, a quartz beam splitter, a thermoelectrically cooled InGaAs detector, and a light-fiber-coupled diffuse reflection probe. The data acquisition and manipulation were performed with the OPUS software (version 4.0.24) (Bruker Optik GmbH, Ettlingen, Germany). A home-made sample cell consisting of a cylindrical brass cup of 37 mm height and an internal diameter of 10.25 mm in the top 7 mm (to fit the probe head with a 10.0 mm external diameter) and a bore hole with an internal diameter of 4.0 mm for the residual 30 mm height (corresponding to the light-fiber bundle diameter of the probe head) was used. The interior of the sample cup was sand-blasted and subsequently gold-coated. For each measurement, the 30 mm/4 mm Ø volume of the sample cell was filled with the powder drug formulation, and the probe head was positioned on top of the sample in the 7 mm/10.25 mm Ø opening (Figure 8.36) [42]. Each sample was measured in duplicate (repacks) with a spectral resolution of 2 cm^{-1}, and 256 scans were accumulated. For the development of the calibration models, the mean spectra of the replicate measurements were used. To match the spectral resolution of these spectra to the imaging data (24 cm^{-1}), the spectral resolution was mathematically reduced with the OPUS software in two data sets with 16 and 32 cm^{-1}, respectively. The spectral range between 9050–7450, 7100–5570, and 5300–4000 cm^{-1} was selected for

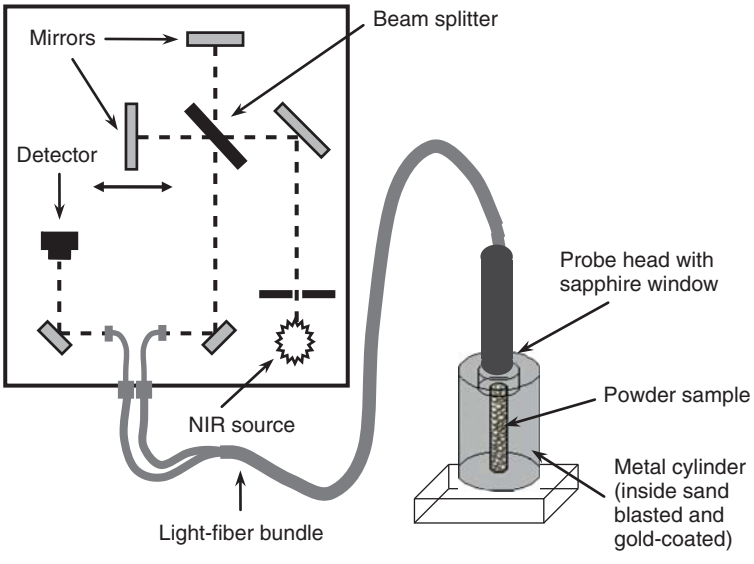

Figure 8.36 Schematic representation of the diffuse reflection measurements with a single-element detector FT-NIR spectrometer. (Reproduced with permission from Ref. [42]. © 2008 Society for Applied Spectroscopy.)

quantitative evaluation and an MSC was applied. The data pretreatment and the development of the PLS calibration models for each active ingredient (based on 45 of the 48 samples) was also performed with the Unscrambler Software for the data sets with 16 and 32 cm^{-1} spectral resolution.

In Figure 8.37a, the conservative NIR diffuse reflection spectra (reduced to 32 cm^{-1} spectral resolution) of the three test samples not contained in the calibration set are compared to typical single-pixel imaging spectra (Figure 8.37b). Apart from the limited wavenumber range of the imaging spectra, their SNR is much lower than the conservative diffuse reflection spectra. For the development of the PLS models for the quantitative evaluation of the content of active ingredients, the median spectra calculated from all pixels of each image of the 45 calibration samples have been used [81]. The improvement of SNR compared to the single-pixel spectra is demonstrated for the three test samples in Figure 8.37c. In Table 8.4, selected calibration/cross-validation parameters (correlation coefficient, random mean-square error of prediction (RMSEP), and number of factors) for the PLS models of the imaging median spectra of the 45 calibration samples are bracketed between the corresponding data for 32 and 16 cm^{-1} spectral resolution of the diffuse reflection measurements with the single-element detector for ASA, ASC, and CF. Despite the availability of a much smaller wavenumber region and the inferior SNR of the imaging median spectra (see Figure 8.37a,c), only slightly higher RMSEP values are obtained for the active ingredients. Based on these calibration models, the compositions of the three test samples (samples 22, 24, and 38) have then been predicted, on the one hand, from their conservative diffuse reflection single-element detector spectra (with 16 and 32 cm^{-1} spectral resolution) and, on the other hand, from their ROI single-pixel spectra. This last-mentioned prediction step has been performed by applying the $\mathbf{B}$ matrix of the inverse calibration model, $\mathbf{Y} = \mathbf{XB}$ (where $\mathbf{X}$ is the matrix of the 45 median imaging calibration spectra and $\mathbf{Y}$ is the reference concentration matrix) to the ROI single-pixel spectra of the three test samples. When this is done, as many predicted concentration values as pixels in the images of the three test samples have been obtained (see Chapter 2). The individual pixel concentration values have then been used to display a distribution map where the x-axis shows the concentration predicted values and the y-axis shows the pixel counts (with the central value of the histogram representing the predicted concentration; see Figure 8.38a). The predicted concentrations for the three active ingredients of the three unknown samples are shown in Table 8.5 and reflect the comparable prediction capability of the single-pixel imaging data with reference to the single-element detector measurements.

8.4.2 Spatial Distribution of the Active Ingredients in a Pharmaceutical Drug Formulation

The quantitative determination of the active ingredients is only part of the quality control requirements for a pharmaceutical drug formulation. At least as important is the homogeneous distribution of the active ingredients in the formulation. In

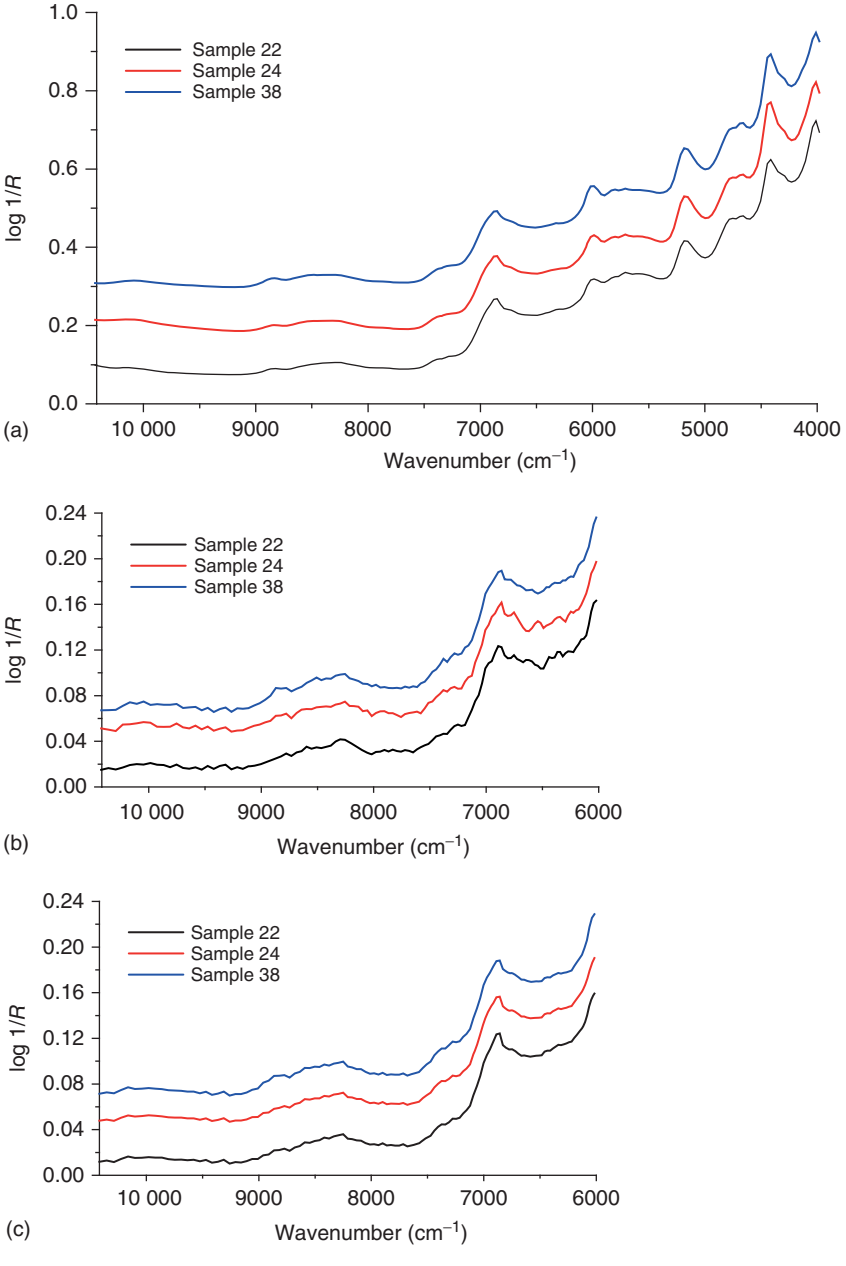

Figure 8.37 (a) NIR spectra of the three test samples measured in diffuse reflection with a single-element detector. (b) NIR single-pixel imaging spectra of the three test samples. (c) NIR median imaging spectra of the three test samples. (Reproduced with permission from Ref. [42]. © 2008 Society for Applied Spectroscopy.)

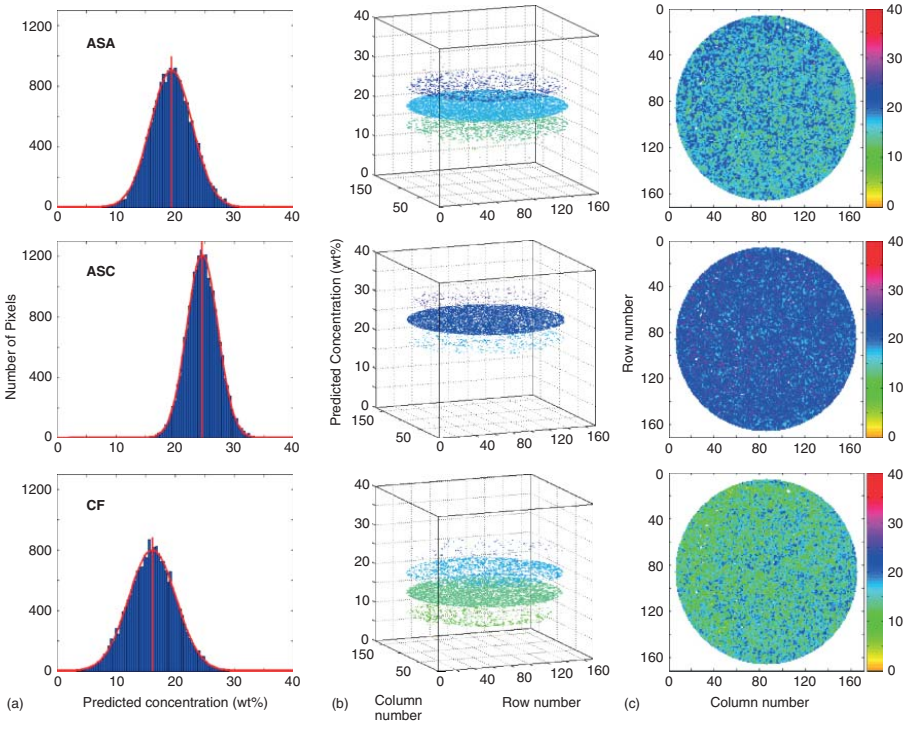

Figure 8.38 Typical imaging plots for test sample 22: (a) pixel count/pixel concentration histograms for the three active ingredients, (b) 3D contour plot in 5 wt% level intervals, and (c) 2D color image plot. (Reproduced with permission from Ref. [42]. Copyright 2008 Society for Applied Spectroscopy.)

Table 8.4 Calibration parameters of the PLS models for ASA, ASC, and CF for the two measurements techniques.

	RMSEP	Correlation coefficient	No. of factors
Single-element detector (16 cm^{-1})			
ASA	0.51	0.98	6
ASC	0.65	0.97	6
CF	0.51	0.99	2
Imaging median spectra (24 cm^{-1})			
ASA	0.71	0.96	4
ASC	0.65	0.97	2
CF	1.03	0.95	4
Single-element detector (32 cm^{-1})			
ASA	0.54	0.98	6
ASC	0.67	0.96	6
CF	0.52	0.99	2

this aspect, the inherent advantage of imaging measurements comes into play and provides the relevant information. As an example, in Figure 8.38, the width of the concentration distribution over all pixels and the lateral distribution of the three active ingredients over the imaged area of test sample 22 are shown in different representations:

- Histograms of the number of pixels versus concentration for the three active ingredients (Figure 8.38a). The bold vertical line represents the concentration predicted by the corresponding PLS model.
- 3D color contour plots of the concentration (in 5 wt% level intervals) (Figure 8.38b).
- 2D color image contour plots of the imaged sample area (representing the top view of the 3D color contour plots) (Figure 8.38c).

The histograms in Figure 8.38a demonstrate that CF has the lowest concentration uniformity over the imaged sample area compared to ASC and ASA (the same phenomenon has been detected for the test samples 24 and 38). This observation is in agreement with the larger particle size inhomogeneity of the original CF material (which was obviously not completely eliminated by milling) compared to ASC and ASA. Although the heterogeneity of the imaged sample will always be the dominating factor, the broader width of the CF histogram could also be partly indicative of the lower precision of the calibration model for this active ingredient (see also Table 8.5). Figure 8.38b,c represents the lateral distributions of the different concentration levels of the three active ingredients over the imaged sample area.

The lateral distribution of all three active ingredients may be represented in one RGB image. Figure 8.39a shows the RGB images for the three test samples 22, 24,

Table 8.5 Prediction results for the three test samples obtained from the diffuse reflection single-detector measurements (for 16 and 32 cm^{-1} spectral resolution) and the single-pixel imaging spectra.

	Sample 22		Sample 24		Sample 38	
	Reference	**Prediction**	**Reference**	**Prediction**	**Reference**	**Prediction**
NIR diffuse reflection single-element detector spectroscopy (spectral resolution 16 cm^{-1}, spectral calibration range: 9050–7450 cm^{-1}, 7100–5570 cm^{-1}, 5300–4000 cm^{-1})						
ASA	20.01	20.16	16.52	16.75	23.39	22.86
ASC	25.26	25.01	20.87	20.15	16.27	16.80
CF	14.73	15.05	22.61	22.57	20.34	20.28
NIR diffuse reflection imaging spectroscopy (spectral resolution 24 cm^{-1}, spectral calibration range: 10417–6017 cm^{-1})						
ASA	20.01	19.35	16.52	16.41	23.39	22.91
ASC	25.26	24.57	20.87	21.17	16.27	16.16
CF	14.73	16.13	22.61	22.69	20.34	20.51
NIR diffuse reflection single-element detector spectroscopy (spectral resolution 32 cm^{-1}, spectral calibration range: 9050–7450 cm^{-1}, 7100–5570 cm^{-1}, 5300–4000 cm^{-1})						
ASA	20.01	20.19	16.52	16.68	23.39	22.85
ASC	25.26	24.99	20.87	20.23	16.27	16.80
CF	14.73	15.05	22.61	22.56	20.34	20.31

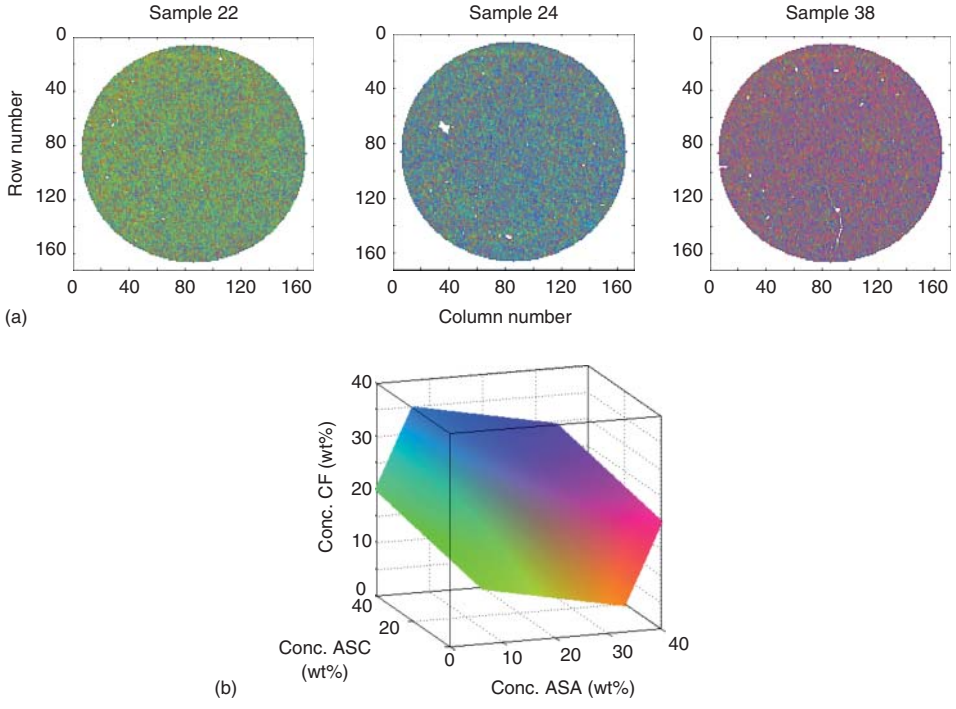

Figure 8.39 RGB (red, ASA; green, ASC; blue, CF) plots for the three test samples (a) and corresponding color scale (b). (Reproduced with permission from Ref. [42]. © 2008 Society for Applied Spectroscopy.)

and 38 based on the RGB scale included in Figure 8.39b (the white areas in the RGB images correspond to pixels whose spectra had been identified as outliers). On the one hand, the different compositions of the three "unknown" test formulations can be clearly visually discriminated by the tint of their RGB images and, on the other hand, the spatial distribution of the active ingredients becomes available from these data.

8.4.3 Conclusions

Notwithstanding the comparatively large penetration depth and effective pathlength of NIR radiation into particulate matter (see Section 8.2.1) and the limited wavenumber range and low SNR of NIR imaging spectra, this technique provides a powerful approach to combine quantitative investigations of multicomponent systems with the acquisition of information regarding the spatial distribution of the components in the investigated sample. Thus, PLS calibration models based on NIR imaging spectra yielded comparable results to calibration models of single-element detector diffuse reflection spectra for the prediction of the active ingredient content.

8.5
FT-IR Spectroscopic Imaging of Inorganic Materials

8.5.1
Introduction

In the following chapter, it will be demonstrated that imaging by vibrational spectroscopy is not only limited to a few applications in life science such as the determination of the mineral content in hard tissues [82] but can also be used to gain information about inorganic materials in industrial processes. Thus, the separation of organic and inorganic pollutants from sewage sludge, for example, has emerged as a possible process for phosphate fertilizer production, and the potential of mid-infrared imaging for an optimization of this process will be outlined later.

Phosphorus is an essential element for all forms of life. It is necessary for the metabolism process (ADP/ATP), an integral part of the DNA molecule, and the cell membrane. For this reason, phosphorus is termed a *macronutrient* and must be applied in agricultural crop production in the form of phosphorus fertilizers. In general, mineral phosphates from external sources (phosphate rock) are used for fertilizer production. With decreasing phosphate resources [83] and increasing phosphate rock prices, alternative sources of P-fertilizers such as sewage sludge become of increasing importance as a vital phosphate source.

In the 6th EU Framework Program (FP6) research project SUSAN (Sustainable and Safe Re-use of Municipal Sewage Sludge for Nutrient Recovery) [84] a two-step thermal process was developed, which transfers the important nutrient phosphorus contained in sewage sludge into a mineral phosphate fertilizer raw material with low heavy metals content. In the first step, sewage sludge is incinerated (mono-incineration) at 800–900 °C, destructing all organic matter including the organic pollutants. The resulting sewage sludge ashes (SSA) are rich in phosphorus (5–10% P) and other nutrients (calcium, magnesium, potassium, etc.) but still contain most of the heavy metals from the original sludge. In the second step, the SSA are thermochemically treated at ~1000 °C for about 30 min after mixing with a solid Cl-donor (e.g., $CaCl_2$, $MgCl_2$, NaCl, PVC (poly(vinyl chloride))) [85, 86] or with gaseous Cl_2 and HCl [87], respectively. Heavy metals can be effectively removed by the chloride pathway, and new bioavailable mineral phosphate phases are formed if sufficient Mg is present during thermochemical treatment or if a post-treatment with acid was carried out.

The plant availability of phosphates depends on their chemical form, hence analytical techniques to quickly determine the mineral phases are necessary. Hydrated forms (e.g., $Ca(H_2PO_4)_2 \cdot H_2O$ and $CaHPO_4 \cdot 2H_2O$) normally show better plant availability than non-hydrated phosphates (e.g., $Ca_5(PO_4)_3OH$). Previously, single beam mid- and far-infrared spectroscopy was successfully applied for the analysis of P-phases in SSA-based fertilizer [88]. Using spectroscopic imaging methods with a lateral resolution down to the diffraction limit of 5–10 µm for synchrotron radiation infrared microspectroscopy, almost pure mineral phases are detectable.

Thus, the identification of the chemical form of P-bearing mineral phases is much easier than with a single-beam spectrometer.

8.5.2 Experimental

Synchrotron infrared chemical images were collected with a Bruker Hyperion 2000 microscope (36× objective) coupled to a Bruker Vertex 80v spectrometer at the infrared microspectroscopy beamline of the Australian Synchrotron. The samples were mapped in transmission mode after compression between two diamond windows (spectral resolution 4 cm^{-1}; 64 scans were co-added per spectrum). An aperture of 5 µm × 5 µm and a step size of 5 µm were used for mapping. Infrared chemical images were constructed by color coding the integrated area of selected bands, which do not overlap with bands of other compounds, in the spectra (blue, low concentration; red/orange, high concentration). Four representative areas of ~80 µm × 60 µm were mapped for each sample. From the point with the highest intensity (red dot or area) of the infrared chemical images, a single spectrum was extracted and displayed next to the chemical image.

The SSA used in this work was sourced from an incineration plant in the Netherlands and originated from wastewater treatment plants (WWTPs) primarily using Fe salts for phosphate precipitation. Thermochemical treatments of SSA with calcium chloride ($CaCl_2 \cdot 2H_2O$; extra pure, Merck, Darmstadt, Germany) and magnesium chloride ($MgCl_2 \cdot 6H_2O$; crystalline, Merck, Darmstadt, Germany), respectively, were carried out in a rotary corundum furnace (Thermal Technology, RT1700, Bayreuth, Germany) for ~30 min at 950 °C (hereafter, the products of this treatment are referred to as SSA-Ca and SSA-Mg, respectively). SSA-Ca and SSA-Mg were also post-treated with 20% H_2SO_4 solution (+S) to form more plant-available phosphate phases. Furthermore, a commercial fertilizer, triple superphosphate (TSP, $Ca(H_2PO_4)_2 \cdot H_2O$) and different reference phosphates were used.

8.5.3 Determination of P-Fertilizer–Soil Reactions

The SSA-based fertilizers that were prepared with $CaCl_2$ or HCl, respectively, contain chlorapatite ($Ca_5(PO_4)_3Cl$) as the major P-phase, whereas thermochemical treatment with $MgCl_2$ results in formation of chlorapatite and trimagnesium phosphate ($Mg_3(PO_4)_2$). The plant availability of these fertilizers was tested in agricultural pot experiments with the result that the SSA-based fertilizers that contain trimagnesium phosphate consistently gave the highest grain yields.

Calcium and magnesium are in the same group of the periodic table, and the properties of their phosphates should not strongly diverge. Although there has been much research on calcium phosphates in the context of agriculture, there

has not been much research on magnesium phosphates in agricultural investigations. For the determination of the advantage of magnesium phosphates compared to calcium phosphates, P-fertilizer–soil reactions were analyzed. The chemical form of soil phosphorus has been analyzed by many different spectroscopic techniques (X-ray absorption near-edge structure (XANES), P-NMR, infrared, and Raman spectroscopy) in the past. All these methods have distinct advantages and disadvantages. The first infrared study in this area by Beaton *et al.* [89] used a dispersive infrared spectrometer to identify fertilizer–soil reactions of water-soluble P-fertilizers. XANES spectroscopy has a significant advantage in that it is unaffected by the host matrix (i.e., soil or other fertilizer components) but if there is more than one compound of an element in a sample, it is difficult to determine the chemical state.

The application of Raman microspectroscopy and synchrotron infrared microspectroscopy to visualize the P-fertilizer–soil reactions on a microscale [90] has the advantage that they have a lateral resolution down to the diffraction limit, allowing for the detection and characterization of small phosphate particles.

For the investigations, slightly alkaline soil (30 g) was mixed with 5 g of fertilizer and 10 g of water and stored in plastic boxes at 20 °C for 4–56 days. After different reaction times, parts of the samples were dried in a fume cupboard at 20 °C and analyzed by Raman and IR microspectroscopic studies, however, in what follows only the IR imaging data will be discussed in detail. For clarification of the P-fertilizer–soil reactions of SSA-based P-fertilizer, mixtures of reference phosphates with soil were also analyzed under the same experimental procedure.

In Figure 8.40, the visible image, infrared chemical images, extracted spectra, and reference spectra of soil + SSA-Mg + S after 28 days of wetting are displayed. The red-shaded areas in the extracted spectra show the bands for which the integrated absorption areas were used to construct each infrared chemical image. The fertilizer contains before wetting gypsum, quartz/aluminosilicates, magnesium pyrophosphate ($Mg_2P_2O_7$), and hydroxy/chlorapatite ($Ca_5(PO_4)_3OH/Cl$). After 28 days of wetting dimagnesium phosphate ($MgHPO_4{\cdot}3H_2O$), hydroxy/chlorapatite, $Ca/MgSO_4$, and quartz were detected. $Mg_2P_2O_7$ converted to the readily plant-available dimagnesium phosphate. Conversely, the calcium pyrophosphate of other samples did not show any reaction even after 56 days. Other researchers have also reported that calcium pyrophosphate does not hydrolyze in soil. Thus, $Mg_2P_2O_7$ is in contrast to $Ca_2P_2O_7$, a reactive pyrophosphate that forms plant-available P-phases.

Figure 8.41 shows the visible image, infrared chemical image, and related extracted spectrum of soil + TSP after 28 days of wetting. For comparison in Figure 8.41c, an infrared spectrum of pure TSP is displayed. After wetting, all monocalcium phosphate ($Ca(H_2PO_4)_2{\cdot}H_2O$) converted to dicalcium phosphate ($CaHPO_4{\cdot}2H_2O$). By X-ray diffraction analysis, other researchers also showed that dicalcium phosphate is the major product after a short period of wetting of TSP/monocalcium phosphate in soils. For clarification of the P-fertilizer–soil reactions of SSA-based fertilizer, the same experimental procedures but with mixtures of reference phosphates with soil were carried out. Figure 8.42

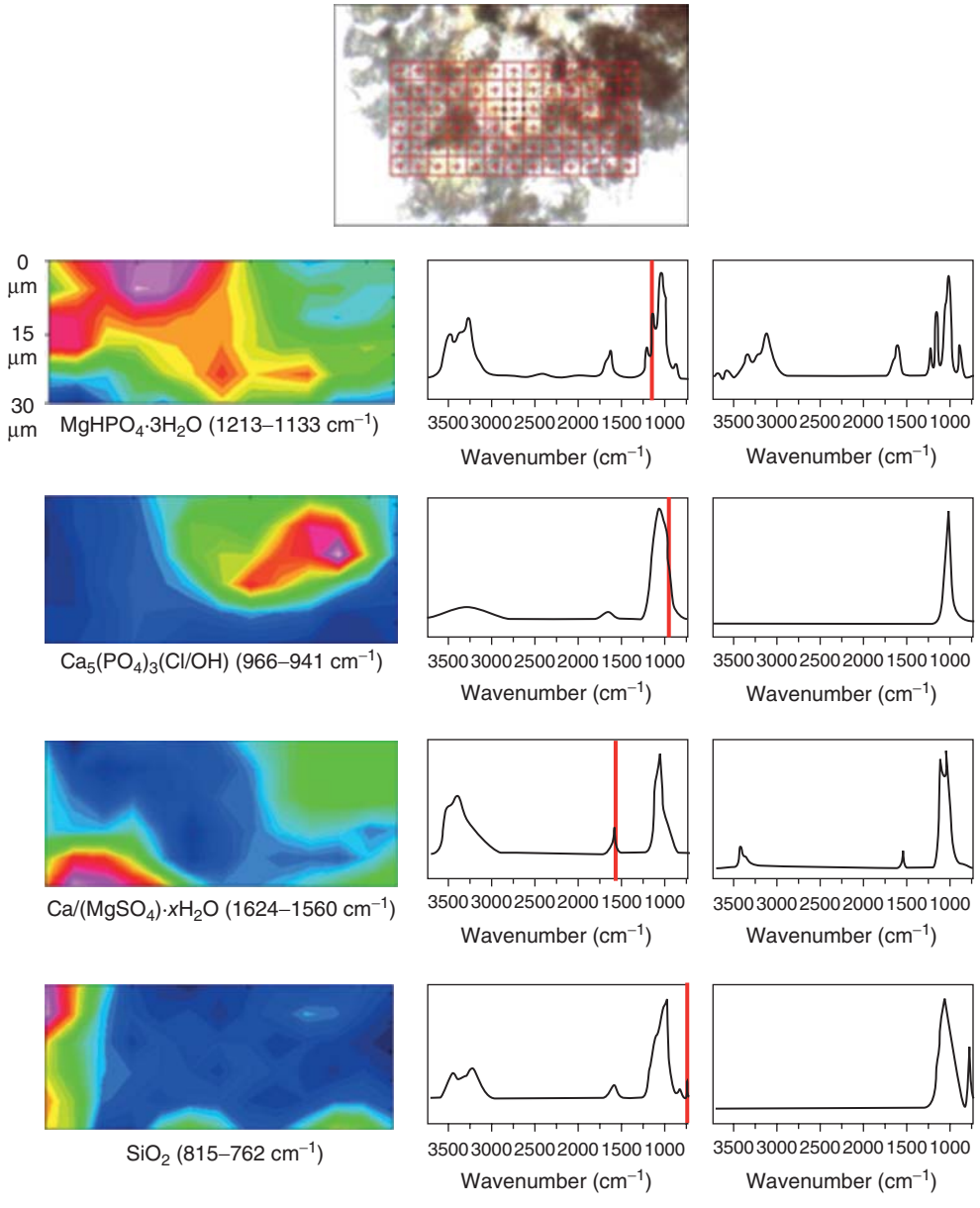

Figure 8.40 Visible image (top), infrared chemical images (left, 65 µm × 30 µm; blue, low concentration; red/orange, high concentration), and extracted spectra (center, integrated band areas are red shaded) for different compounds of soil + SSA-Mg + S after 28 days of wetting and related reference spectra (right). (Reproduced with permission from Ref. [90]. © 2013 Society for Applied Spectroscopy.)

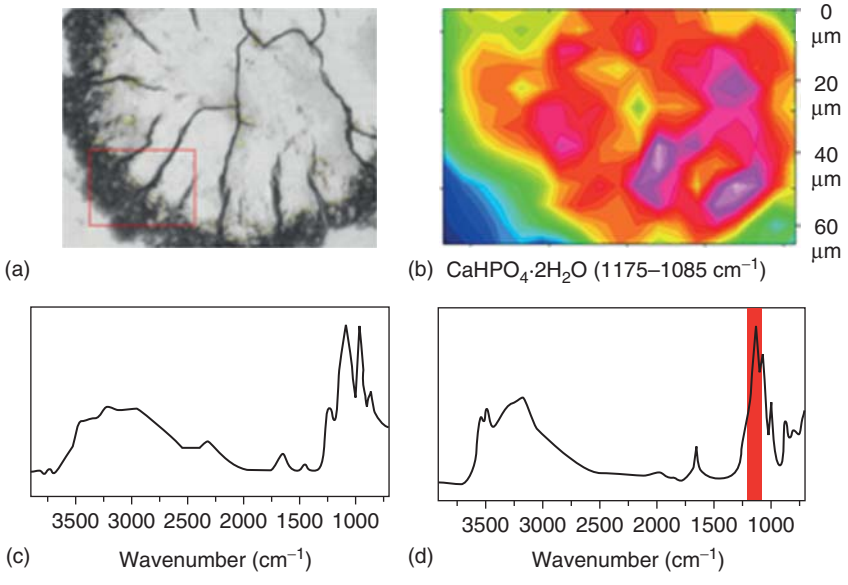

Figure 8.41 (a) Visible image; (b) infrared chemical image (95 µm × 65 µm; blue, low concentration; red/orange, high concentration); (c) infrared spectra of pure TSP; and (d) extracted spectrum of soil + TSP after 28 days of wetting (integrated band area is red shaded). (Reproduced with permission from Ref. [90]. © 2013 Society for Applied Spectroscopy.)

shows the reactions of the calcium and magnesium (pyro-)phosphates that were determined.

The calcium and magnesium phosphates react differently. As outlined earlier, calcium pyrophosphate did not react in soils, whereas magnesium pyrophosphate forms dimagnesium phosphate. The plant availability of the displayed phosphates in Figure 8.42 decreases from left to right. Monocalcium phosphate ($Ca(H_2PO_4)$) initially reacted to give dicalcium phosphate ($CaHPO_4$), and after a longer time

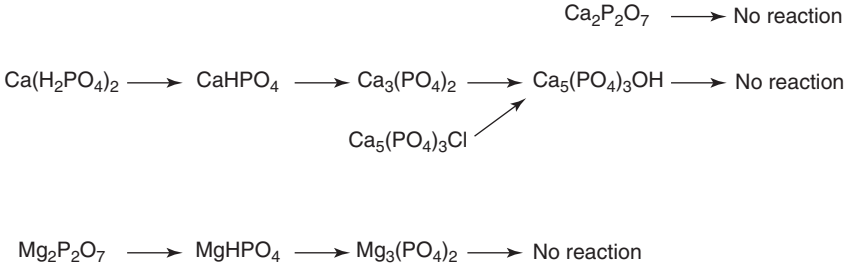

Figure 8.42 Schematic of determined reactions of calcium and magnesium (pyro-) phosphates on a slightly alkaline soil. (Reproduced with permission from Ref. [90]. © 2013 Society for Applied Spectroscopy.)

further reaction produced tricalcium phosphate ($Ca_3(PO_4)_2$) and finally the resultant hydroxyapatite ($Ca_5(PO_4)OH$), the phosphate with the lowest plant availability. Also chlorapatite ($Ca_5(PO_4)_3Cl$) reacted during wetting to produce hydroxyapatite in soils. Dimagnesium phosphate, however, only changes over time to trimagnesium phosphate because magnesium phosphates cannot form an apatite structure. Thus, the advantage of the magnesium phosphates is that the end product in soil is trimagnesium phosphate that still is plant available. Conversely, after a long period, all calcium orthophosphates convert to the non-plant-available hydroxyapatite.

8.5.4
Determination of Mineral Phases in Soils

In addition, we tried to detect P-phases in pure soil by Raman and synchrotron infrared microspectroscopic studies. Raman microspectroscopy measurements (with 413, 532, 633, and 785 nm lasers) of soils were impossible due to high fluorescence so the only information comes from synchrotron FT-IR microspectroscopy with its limited lateral resolution.

Figures 8.43 and 8.44 show the visible images, infrared chemical images, and extracted spectra of a sandy and an alluvial soil, respectively. In the sandy soil, two mineral phases were detected: quartz (SiO_2, dark area in visible image) and the aluminosilicate kaolinite ($Al_2Si_2O_5(OH)_4$, bright area in visible image).

The alluvial soil contains calcium carbonate ($CaCO_3$), quartz, and montmorillonite ($(Na,Ca)_{0.33}(Al,Mg)_2Si_4O_{10}(OH)_2$). In the extracted spectra of $CaCO_3$,

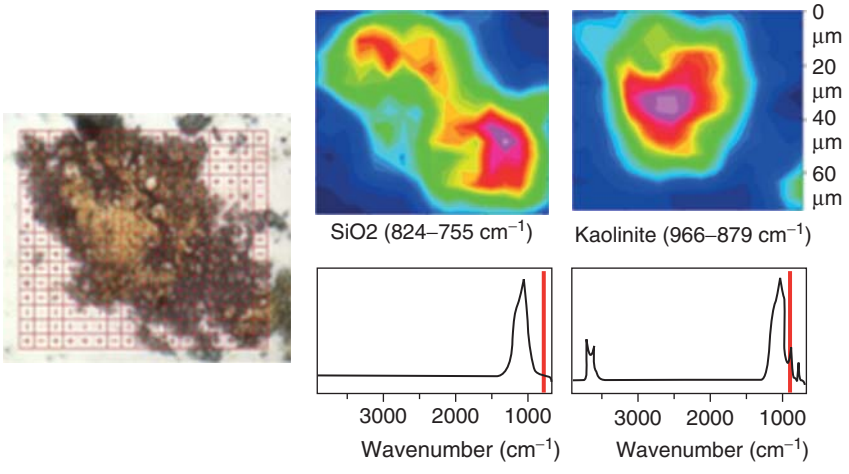

Figure 8.43 Visible image, infrared chemical images (85 µm × 75 µm; blue, low concentration; red/orange, high concentration), and extracted spectra for different compounds of a sandy soil (integrated band areas are red shaded). (Reproduced with permission from Ref. [90]. © 2013 Society for Applied Spectroscopy.)

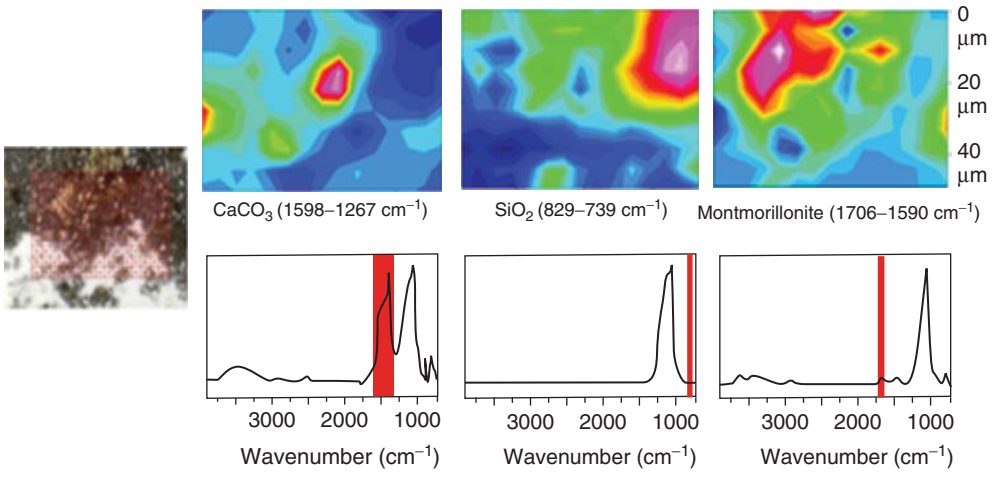

Figure 8.44 Visible image, infrared chemical images (75 µm × 50 µm; blue, low concentration; red/orange, high concentration), and extracted spectra for different compounds of an alluvial soil (integrated band areas are red shaded). (Reproduced with permission from Ref. [90]. © 2013 Society for Applied Spectroscopy.)

quartz and montmorillonite are also visible. Owing to the low mass fraction of phosphorus in the soil (<0.5%), no P-phases were detectable. The greater lateral resolution of Raman microspectroscopy would probably solve this problem but a 1064 nm or deep UV-based system of the type now becoming available would be required to overcome the fluorescent background. Furthermore, synchrotron scattering-scanning, near-field infrared spectroscopy with a lateral resolution of ~20 nm could be an option to determine P-phases in soils.

8.5.5 Conclusion

The differences in fertilizer–soil reactions of calcium and magnesium (pyro-) phosphates, respectively, were successfully determined by Raman and synchrotron infrared microspectroscopic studies. All calcium orthophosphates convert to hydroxyapatite in soil over time. On the other hand, magnesium orthophosphates react only as far as trimagnesium phosphate because of their inability to form an apatite structure. Thus, for the magnesium-based compound, phosphorus remains in a plant-available form. Also, the pyrophosphates of calcium and magnesium react very differently. Calcium pyrophosphate did not react in soil, whereas magnesium pyrophosphate quickly forms dimagnesium phosphate. Furthermore, mineral phases of soils were detectable by infrared microspectroscopy.

References

1. Lewis, E.N., Treado, P.J., Reeder, R.C., Story, G.M., Dowrey, A.E., Marcott, C., and Levin, I.W. (1995) *Anal. Chem.*, **67**, 3377–3381.
2. Challa, S.R., Wang, S.-Q., and Koenig, J.L. (1996) *Appl. Spectrosc.*, **50**, 1339–1344.
3. Snively, C.M. and Koenig, J.L. (1998) *Macromolecules*, **31**, 3753–3755.
4. Snively, C.M. and Koenig, J.L. (1999) *J. Polym. Sci., Part B: Polym. Phys.*, **37**, 2261–2268.
5. Bhargava, R., Wang, S.-Q., and Koenig, J.L. (1998) *Appl. Spectrosc.*, **52**, 323–328.
6. Snively, C.M. and Koenig, J.L. (1999) *J. Polym. Sci., Part B: Polym. Phys.*, **37**, 2353–2359.
7. Ribar, T., Bhargava, R., and Koenig, J.L. (2000) *Macromolecules*, **33**, 8842–8849.
8. Ribar, T. and Koenig, J.L. (2001) *Macromolecules*, **34**, 8340–8346.
9. Miller-Chou, B.A. and Koenig, J.L. (2002) *Macromolecules*, **35**, 440–444.
10. González-Benito, J. and Koenig, J.L. (2002) *Macromolecules*, **35**, 7361–7367.
11. Koenig, J. (2002) *Adv. Mater.*, **14**, 457–460.
12. Rafferty, D.W. and Koenig, J.L. (2003) *J. Controlled Release*, **83**, 29–39.
13. Bobiak, J.P. and Koenig, J.L. (2005) *J. Controlled Release*, **106**, 329–338.
14. Gupper, A., Wilhelm, P., Schmied, M., Kazarian, S.G., Chan, K.L.A., and Reuûner, J. (2002) *Appl. Spectrosc.*, **56**, 1515–1523.
15. Gupper, A., Wilhelm, P., Kothleitner, G., Eichhorn, K.-J., and Pompe, G. (2004) *Macromol. Symp.*, **205**, 171–180.
16. Li, G.L. and Koenig, J.L. (2002) *Appl. Spectrosc.*, **56**, 1390–1396.
17. Kazarian, S.G. and Chan, K.L.A. (2004) *Macromolecules*, **37**, 579–584.
18. Kaun, N., Vellekoop, M.J., and Lendl, B. (2006) *Appl. Spectrosc.*, **60**, 1273–1278.
19. Chan, K.L., Hammond, S.V., and Kazarian, S.G. (2003) *Anal. Chem.*, **75**, 2140–2146.
20. Kazarian, S.G. and Chan, K.L. (2010) *Appl. Spectrosc.*, **64**, 135A–152A.
21. Bhargava, R. (2012) *Appl. Spectrosc.*, **66**, 1091–1120.
22. Hirschmugl, C.J. and Gough, K.M. (2012) *Appl. Spectrosc.*, **66**, 475–491.
23. Sasic, S. and Ozaki, Y. (eds) (2010) *Raman, Infrared and Near-Infrared Chemical Imaging*, John Wiley & Sons, Inc., Hoboken, NJ.
24. Spectroscopy *http://bit.ly/182itQ9* (accessed 20 February 2014).
25. Clarke, F.C., Jamieson, M.J., Clark, D.A., Hammond, S.V., Jee, R.D., and Moffat, A.C. (2001) *Anal. Chem.*, **73**, 2213–2220.
26. Lewis, E.N., Carroll, J.E., and Clarke, F.C. (2001) *NIR News*, **12**, 16–18.
27. Lyon, R.C., Jefferson, E.H., Ellison, C.D., Buhse, L.F., Spener, J.A., Nasr, M.M., and Hussain, A.S. (2003) *Am. Pharm. Rev.*, **6**, 62–70.
28. Lyon, R.C., Lester, D.S., Lewis, E.N., Lee, E., Yu, L.X., Jefferson, E.H., and Hussain, A.S. (2002) *AAPS Pharm. Sci. Tech.*, **3**, 17.
29. Clarke, F.C. (2004) *Vib. Spectrosc.*, **34**, 25–35.
30. Clarke, F. and Hammond, S.V. (2003) *Eur. Pharm. Rev.*, **8**, 41–50.
31. Lewis, E.N., Schoppelrei, J.W., Lee, E., and Kidder, L.H. (2005) in *Process Analytical Technology* (ed K. Bakeev), Blackwell Publishing Ltd, Oxford, pp. 187–225.
32. Shah, R.B., Tawakkul, M.A., and Khan, M.A. (2007) *J. Pharm. Sci.*, **96**, 1356–1365.
33. Clarke, F.C., Hammond, S.V., Jee, R.D., and Moffat, A.C. (2002) *Appl. Spectrosc.*, **56**, 1475–1483.
34. Lewis, E.N., Kidder, L.H., Lee, E., and Haber, K.S. (2005) in *Spectrochemical Analysis Using Infrared Multichannel Detector* (eds R. Bhargava and I.W. Levin), Blackwell Publishing Ltd, Oxford, pp. 25–55.
35. Olinger, J.M. and Griffiths, P.R. (1992) in *Handbook of Near-Infrared Analysis* (eds D.A. Burns and E.W. Ciurczak), Marcel Dekker, New York, p. 28.
36. Berntsson, O., Danielsson, L.-G., and Folestad, S. (1998) *Anal. Chim. Acta*, **364**, 243–251.
37. Andersson, M., Josefson, M., Langkilde, F.W., and Wahlund, K.-G. (1999) *J. Pharm. Biomed. Anal.*, **20**, 27–37.

38. MacDonald, B.F. and Preeble, K.A. (1993) *J. Pharm. Biomed. Anal.*, **11**, 1077–1085.
39. Haanstra, W.G., Hansen, W., Huys, M.J.G., Kip, B.J., Palmen, P., Roulmen, J., Snieder, M., van der Weerdhof, T., Weidemann, S., and Wortel, V.a.L. (1998) *Appl. Spectrosc.*, **52**, 863–868.
40. Berntsson, O., Burger, T., Folestad, S., Danielsson, L.-G., Kuhn, J., and Fricke, J. (1999) *Anal. Chem.*, **71**, 617–623.
41. Hudak, S.J., Haber, K., Sando, G., Kidder, L.H., and Lewis, E.N. (2007) *NIR News*, **18**, 6–8.
42. Kolomiets, O., Hoffmann, U., Geladi, P., and Siesler, H.W. (2008) *Appl. Spectrosc.*, **62**, 42–50.
43. Chan, K.L.A. and Kazarian, S.G. (2003) *Appl. Spectrosc.*, **57**, 381–389.
44. Wessel, E., Heinsohn, G., Schmidt-Lewerkuehne, H., Wittern, K.-P., Rapp, C., and Siesler, H.W. (2006) *Appl. Spectrosc.*, **60**, 1488–1492.
45. Harrick, N.J. (1967) *Internal Reflection Spectroscopy*, John Wiley & Sons, Inc, New York, p. 327.
46. Mirabella, F.M. (1993) in *Practical Spectroscopy, 15: Internal Reflection Spectroscopy – Theory and Application* (ed E.G. Brame), Marcel Dekker, New York, p. 374.
47. Hecht, E. (2001) *Optik*, 3rd edn, Oldenburg Wissenschaftsverlag GmbH, Munich, p. 1040.
48. Lasch, P. and Naumann, D. (2006) *Biochim. Biophys. Acta*, **1758**, 814–829.
49. Sommer, A.J., Tisinger, L.G., Marcott, C., and Story, G.M. (2001) *Appl. Spectrosc.*, **55**, 252–256.
50. Hocking, P.J. and Marchessault, R.H. (1998) in *Biopolymers from Renewable Resources* (ed D.L. Kaplan), Springer-Verlag, Berlin, p. 220.
51. Doi, Y. and Steinbüchel, A. (2001) *Biopolymers, 3 b: Polyesters II – Properties and Chemical Synthesis*, Wiley-VCH Verlag GmbH, Weinheim, p. 480.
52. Auras, R., Harte, B., and Selke, S. (2004) *Macromol. Biosci.*, **4**, 835–864.
53. Coleman, M.M., Graf, J.F., and Painter, P.C. (1991) *Specific Interactions and the Miscibility of Polymer Blends*, Technomic Publishing Company, Lancaster, CA, p. 19.
54. Blümm, E. and Owen, A.J. (1995) *Polymer*, **36**, 4077–4081.
55. Park, J.W., Doi, Y., and Iwata, T. (2004) *Biomacromolecules*, **5**, 1557–1566.
56. Furukawa, T., Sato, H., Murakami, R., Zhang, J., Duan, Y.-X., Noda, I., Ochiai, S., and Ozaki, Y. (2005) *Macromolecules*, **38**, 6445–6454.
57. Vogel, C., Wessel, E., and Siesler, H.W. (2008) *Biomacromolecules*, **9**, 523–527.
58. Vogel, C., Wessel, E., and Siesler, H.W. (2008) *Macromolecules*, **41**, 2975–2977.
59. Chernev, B. and Wilhelm, P. (2006) *Monatsh. Chem.*, **137**, 963–967.
60. Siesler, H.W. (1984) *Advances in Polymer Science*, Springer-Verlag, Berlin, Heidelberg, pp. 1–77.
61. Siesler, H.W., Hoffmann, G.G., Kolomiets, O., Pfeifer, F., and Zahedi, M. (2007) in *Vibrational Spectroscopy of Polymers: Principles and Practice* (eds N.J. Everall, J.M. Chalmers, and P.R. Griffiths), John Wiley & Sons Ltd, Chichester, pp. 313–347.
62. Dechant, J. (1972) *Ultrarotspektroskopische Untersuchungen an Polymeren*, Akademie Verlag, Berlin, p. 516.
63. Siesler, H.W. (2012) in *Polymer Science: A Comprehensive Reference*, vol. 2 (eds K. Matyaszewski and M. Möller), Elsevier BV, Amsterdam, pp. 255–300.
64. Vogel, C., Wessel, E., and Siesler, H.W. (2008) *Appl. Spectrosc.*, **62**, 599–603.
65. Lando, J.B., Olf, H.G., and Peterlin, A. (1966) *J. Polym. Sci. A-1*, **4**, 941–951.
66. Enomoto, S., Kawai, Y., and Sugita, M. (1968) *J. Polym. Sci. A-2*, **6**, 861–869.
67. Batzer, H. and Kreibich, U. (1981) *Polym. Bull.*, **5**, 585–590.
68. Reimschuessel, H.K. (1978) *J. Polym. Sci. Polym. Chem. Ed.*, **16**, 1229–1236.
69. Kohan, M. (1973) *Nylon Plastics*, Wiley Interscience, New York.
70. Jacques, C.H.M., Hopfenberg, H.B., and Stannett, V. (1974) in *Permeability of Plastic Films and Coatings to Gases, Vapors and Liquids* (ed H.B. Hopfenberg), Plenum Press, New York, p. 73.
71. Crank, J. (1975) *The Mathematics of Diffusion*, 2nd edn, Oxford University Press, New York, p. 414.

72. Hopfenberg, H.B., Stannett, V., and Folk, G.M. (1975) *Polym. Eng. Sci.*, **15**, 261.
73. Hopfenberg, H.B., Stannett, V., and Jacques, C.H.M. (1975) *J. Appl. Polym. Sci.*, **19**, 2439.
74. Fieldson, G.T. and Barbari, T.A. (1993) *Polymer*, **34**, 1146.
75. Wu, P. and Siesler, H.W. (1999) *Macromol. Symp.*, **143**, 323–336.
76. Gupper, A. and Kazarian, S.G. (2005) *Macromolecules*, **38**, 2327.
77. Unger, M., Ozaki, Y., and Siesler, H.W. (2011) *Appl. Spectrosc.*, **65**, 1051–1055.
78. Wessel, E., Vogel, C., and Siesler, H.W. (2009) *Appl. Spectrosc.*, **63**, 1–5.
79. Mukai, U. (1995) *Macromolecules*, **28**, 4899.
80. Siesler, H.W. (2002) in *Near-Infrared Spectroscopy* (eds H.W. Siesler, Y. Ozaki, S. Kawata, and H.M. Heise), Wiley-VCH Verlag GmbH, Weinheim, p. 213.
81. Burger, J. and Geladi, P. (2006) *Analyst*, **131**, 1152–1160.
82. Morris, M.D., Schulmerich, M.V., Dooley, K.A., and Esmonde-White, K.A. (2009) in *Infrared and Raman Spectroscopic Imaging* (eds R. Salzer and H.W. Siesler), Wiley-VCH Verlag GmbH, Weinheim, p. 149.
83. Cordell, D., Drangert, J.-O., and White, S. (2009) *Global Environ. Change*, **19** (2), 292–305.
84. SUSAN *www.susan.bam.de* (accessed 27 May 2013).
85. Adam, C., Peplinski, B., Michaelis, M., Kley, G., and Simon, F.-G. (2009) *Waste Manag.*, **29**, 1122–1128.
86. Vogel, C., Exner, R.M., and Adam, C. (2013) *Environ. Sci. Technol.*, **47** (1), 563–567.
87. Vogel, C. and Adam, C. (2011) *Environ. Sci. Technol.*, **45** (17), 7445–7450.
88. Vogel, C., Kohl, A., and Adam, C. (2011) *Appl. Spectrosc.*, **65** (3), 265–271.
89. Beaton, J.D., Charlton, T.L., and Speer, R. (1963) *Nature*, **197**, 1329–1330.
90. Vogel, C., Adam, C., Sekine, R., Schiller, T., Lipiec, E., and McNaughton, D. (2013) *Appl. Spectrosc.*, **67** (10), 1165–1170.

9
FT-IR Imaging in ATR and Transmission Modes: Practical Considerations and Emerging Applications

Jennifer Andrew Dougan, K. L. Andrew Chan, and Sergei G. Kazarian

9.1
FT-IR Imaging: Introduction

Fourier transform infrared (FT-IR) spectroscopic imaging is a powerful chemical imaging technique. A range of approaches and applications of FT-IR imaging have been developed in both attenuated total reflection (ATR) and transmission modes for a broad range of materials and chemical systems. ATR and transmission approaches are often complementary – providing different advantages depending on the requirements of the system under study with respect to chemical composition, field of view (FOV), or spatial resolution, for instance.

FT-IR spectroscopic imaging is achieved by coupling an FT-IR spectrometer with a focal plane array (FPA) detector. Unlike single-element detectors, which provide an average signal from the illuminated sample area, FPA detectors allow the simultaneous detection of spatially resolved spectra across the whole imaged area as shown schematically in Figure 9.1. This powerful approach of coupling FT-IR spectroscopy with FPA detectors and thereby obtaining simultaneous, spatially resolved spectra allows systems to be studied as a function of spectral, spatial, and temporal domains. Since a full spectrum is recorded at each pixel, different chemical species and their relationship with one another can be revealed by studying the resulting images. Generally, the images are prepared by plotting the distribution of the integrated absorbance of a vibrational band of interest and assigning a false color to indicate its relative absorbance. Many images showing the distribution of different components in the sample can be generated from a single imaging measurement simply by post-measurement data analysis. Other parameters such as band position or width can be used to reveal chemical information about the system.

Single-element detectors or linear array detectors are capable of building chemical images through point-by-point mapping or raster scanning, respectively. Although this may be sufficient for some applications, the increased time required and the consecutive collection of spectra to build an image may not permit the study of dynamic systems nor is it particularly suitable for high-throughput studies.

Infrared and Raman Spectroscopic Imaging, Second Edition. Edited by Reiner Salzer, Heinz W. Siesler.
© 2014 Wiley-VCH Verlag GmbH & Co. KGaA. Published 2014 by Wiley-VCH Verlag GmbH & Co. KGaA.

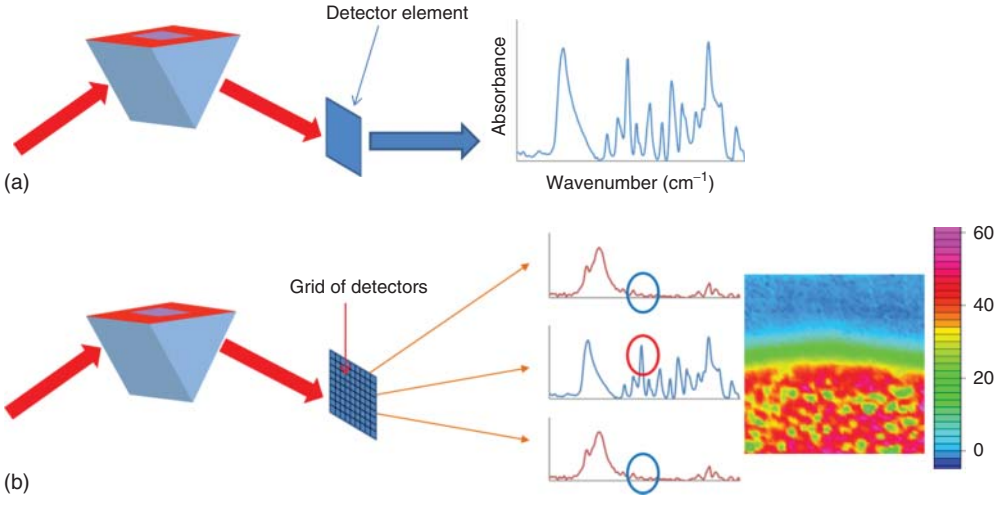

Figure 9.1 Schematic representations of (a) single-element FT-IR spectroscopy where a single average spectrum is obtained and (b) FPA-enabled FT-IR imaging where chemical images are generated by, for instance, false color plotting the integrated area under a band of interest.

In this chapter, we describe some general principles and applications of FT-IR imaging in ATR and transmission mode with a focus on technical considerations, new developments, and emerging applications.

9.1.1 ATR FT-IR Imaging

The ATR phenomenon can most easily be observed if a glass of water is held in the hand (Figure 9.2). When the skin or fingerprint makes contact with the glass, it can be observed through the surface of the water, while the rest of the light is

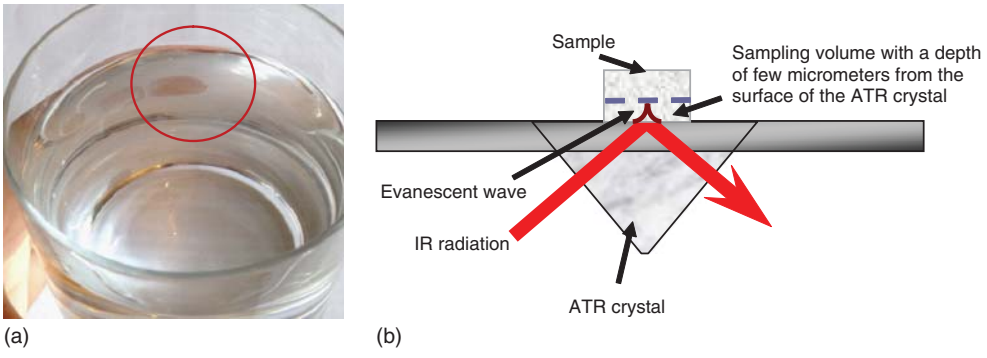

Figure 9.2 (a) Attenuated total reflection image of a fingerprint through a glass of water with visible light and (b) ATR process for infrared spectroscopy.

totally internally reflected. The area where the surface of the glass makes contact with the skin destroys the total reflection and forms an image of the fingerprint. An ATR image of a fingerprint was demonstrated by Harrick [1]. He obtained the ATR image by illuminating a prism with visible light while a finger pressed on the large surface and then focusing the light that was internally reflected off the prism onto a photo film. The same principle described by Harrick is applied with ATR FT-IR imaging. Instead, however, of shining visible light, and using a photo film to record the projected image, infrared (IR) light is shone through an interferometer, an IR transparent crystal, and onto an array of mercury cadmium telluride (MCT) detectors [2].

ATR FT-IR spectroscopy has been studied for many years. It relies on the attenuation of internally reflected IR light at the interface between a material of high refractive index (ATR crystal) and one of lower refractive index that absorbs frequencies of IR light (the sample) when the critical angle is exceeded. When coupled with an FPA detector, the data allow ATR FT-IR images to be generated.

The applicability of ATR FT-IR imaging ranges from micro-ATR imaging using a Ge microscope objective to the use of ATR accessories with focused or expanded optics without recourse to the microscope [3]. Thus, the range of areas in the samples that could be measured simultaneously using FPA detectors and a prism-shaped ATR crystal is from 500 μm × 700 μm to 1.6 cm × 2.1 cm (see Section 9.2.3 for further discussion). The measured area with macro-ATR imaging depends on the specific optics used in these ATR accessories and also on the size of the pixels in the array detector. Most of the currently used detectors have a pixel size of 40 μm × 40 μm or 60 μm × 60 μm.

One of the main advantages of FT-IR spectroscopic imaging in ATR mode is that it requires little or no sample preparation. Also, the small penetration of IR light into the sample when using the ATR mode allows images to be acquired when samples are in contact with highly absorbing material, such as aqueous solutions. Similar to any other technique, FT-IR imaging in the ATR mode has its limitations. In one of the first papers on the applications of ATR FT-IR imaging to a sample of a polymer blend (polyamide 6.6, poly(tetrafluoroethylene), and silicon oil), FT-IR imaging was carried out in transmission and ATR modes and the results were compared [4]. Furthermore, it was the first time that chemical images obtained by both FT-IR imaging and Raman microspectroscopy were compared for the same samples. The chemical images were also compared to the results of scanning electron microscopy with energy-dispersive X-ray spectrometry and microthermal imaging analysis. Remarkably the direct comparison between the four different imaging techniques resulted in excellent agreement between them. The agreement of the comparison between the FT-IR images obtained by transmission and ATR was helped by the fact that the thickness of the polymer film was 5 μm. However, one limitation of the micro- ATR FT-IR approach was highlighted in that study; because of the limited penetration of the evanescent wave into the sample, the images obtained by ATR FT-IR only reflect the composition of the surface layer of 1 – 3 μm depending on the type of ATR crystal, the angle of incidence, and the wavelength of light [4]. It was also noted that the small thickness of the probed

layer in ATR imaging could be advantageous. Imaging in transmission mode averages through the thickness of the sample, and microtoming of samples is usually required for thicknesses smaller than the domain size to ensure that imaging in transmission does not produce spurious images [5]. Other advantages and limitations of the two imaging approaches (transmission and ATR) in terms of spatial resolution, image FOV, and possible artifacts are discussed later in this chapter.

Micro-ATR imaging has the advantage of having excellent spatial resolution [6–8] while sample preparation is relatively simple (no need to microtome and polish). However, there is a general belief, since intimate contact between the sample and the crystal is required to obtain good quality ATR spectra, that there is always a need to apply pressure to samples. Although it is important to ensure homogeneous contact between the sample and the ATR crystal, such that any image generated is representative of the sample composition and not of the quality of the contact, there is often no need to apply pressure in order to achieve this. Examples include swelling pharmaceutical tablets [9], biomedical tissues, and live cells [10] when good reproducible contact is achieved between the sample and the surface of the ATR crystal without adding pressure. That said, some systems do benefit from the application of pressure, and in those cases, modern IR microscopes can use commercial or home-made pressure-monitoring devices to ensure that controlled and reproducible contact is achieved (see Chapter 1 of this book).

9.1.2 Transmission FT-IR Imaging

In transmission mode FT-IR spectroscopy, the IR light is passed through the sample and a spectrum is acquired as a measure of absorbance (or transmittance) of the sample as a function of wavenumber. In order to maintain adequate throughput of light, often the sample must be kept thin ~10 μm thick. Transmission FT-IR spectroscopy makes use of IR transparent windows on, or between, which the sample is mounted and the beam is passed through. Transmission mode FT-IR spectroscopy can be coupled with single-element detectors to provide an average spectrum from the sample or with FPA detectors to produce chemical images of the material through which the IR light passes. Transmission mode FT-IR benefits from a greater signal-to-noise ratio (SNR) than ATR [5] because the pathlength is not restricted to the depth of penetration of an evanescent wave. However, the fact that the IR beam passes through the sample does require that close attention is paid to the preparation of samples with highly absorbing species, such as water, such that the spectral features of interest are not obscured. Furthermore, any heterogeneity in sample thickness has the potential to produce misleading results with absorbance being a function of sample thickness across the area, and care should be taken to avoid this. Transmission mode FT-IR imaging can be carried out through a large sample compartment, or by use of an FT-IR microscope depending on the spatial resolution required. That said, the spatial resolution of transmission mode FT-IR imaging is lower than that of micro-ATR and only approaches that of micro-ATR when using a multibeam synchrotron source

coupled with a high magnification objective [11]. Nevertheless, in some cases, it is convenient to use transmission mode FT-IR imaging and the approach has made important contributions to the study of complex systems, particularly for biomedical and tissue imaging [12–19] and in many polymer applications [20–24].

9.2 FT-IR Imaging: Technical Considerations

9.2.1 Transmission FT-IR Imaging: Mapping Versus FPA

It is undoubtedly simpler to map transmission mode FT-IR measurements compared with that of ATR in order to generate images. Mapping allows an overall image to be built from the acquisition of single-element spectra that have been measured from contiguous locations. All that is required is a controlled sample stage, nevertheless the main disadvantage, rather than using an FPA detector for imaging, remains the inability to study dynamic systems and the overall increase in time required to physically move the sample during mapping and the long scanning time as a result of the low throughput of light through the small aperture. That said, transmission mode FT-IR mapping has been applied to study systems where the time domain is not critical.

9.2.2 ATR FT-IR Imaging: Mapping Versus FPA

Without using an FPA detector, it was, previously, difficult to obtain ATR FT-IR images. Using the mapping approach in ATR mode is complex as the sample is in contact with the ATR crystal throughout the measurement. As such, if the crystal remains in contact with the sample during translation from one measurement location to another, the sample could be deformed and the distribution of different components in the mixture could be altered. The increased risk of smearing the sample and/or its physical damage could reduce the reliability of using the ATR method for mapping in this way. Even if the crystal is detached from the sample when moving from one measuring point to another, the multiple contacts between the crystal and the sample may cause damage to the sample. In both cases, the time required to acquire a single map is extended by the need to relocate the sample on the crystal. Esaki *et al.* [25] developed an ATR crystal with a hexagonal shape that allows ATR mapping without the problems stated earlier. The crystal is translated with the sample attached while the size of the ATR map is limited only by the size of the crystal used (about 2 mm × 7 mm map). A specific ATR crystal is needed [26] for this type of measurement, which is currently not as widely available as the hemispherical ATR crystals. Lewis and Sommer [27] demonstrated ATR mapping with a hemispherical germanium crystal on photographic film laminate. The study involved mapping an image by translating the ATR crystal together with

the sample such that there is no smearing of the sample. Although this method eliminated the potential damage from the sample, it remains a relatively long process for mapping a relatively small area. Recently, the ATR mapping approach has also been developed by the use of a linear array detector instead of a single-element detector [28]. This approach speeds up the mapping process to a point that could rival the FPA approach [29]. This new development has a few advantages over the FPA detector such as more flexible imaging size (up to about 400 μm before significant optical aberration takes place) and a larger spectral range in the lower wavenumber spectral region (down to 700 cm^{-1}). However, spectra across the map are not all acquired at the same time, thus the method is not suitable for studying dynamic systems. The spatial resolution and depth of penetration of this approach are variable across the imaged area though it has been shown that a larger hemisphere can reduce this variation [29].

9.2.3 ATR FT-IR Imaging: Field of View

9.2.3.1 Overview of ATR FT-IR Imaging Approaches: Micro (Ge), Macro (Diamond, Si), Expanded FOV (ZnSe), Variable Angle

Using an FPA detector and a stationary ATR crystal, all spectral information across the whole imaging area is captured simultaneously [6]. The snapshot feature of this FPA FT-IR imaging approach enables the study of dynamic systems such as drug dissolution [20, 30], parallel analysis of many samples in a high-throughput manner [31–34], studies of biopolymers and biomedical systems [35–39], and diffusion processes *in situ* [40–43], and can be coupled with microfluidics devices [44, 45] to produce "chemical movies" [46]. Recent exciting applications of FT-IR imaging include micropatterning reactions [47]. Since there is no rastering with a fixed ATR crystal, the imaging area or the FOV is defined by the size of the FPA and the optics. Patterson *et al.* [29] have demonstrated that it is possible to combine the FPA imaging and mapping method using the translating ATR crystal to generate a large image by stitching together a map of images. We have also demonstrated the combined imaging and mapping in macro-ATR approach to capture a spatially resolved image of a whole fingerprint [48]. However, similar to other mapping methods, it is limited to the study of static systems. Another approach to obtain flexibility of imaging FOV, without sacrificing the ability to study dynamic systems, is to employ different optical arrangements or to use different sizes of detector. The FOV is defined by the number of pixels of the detector, the size of each pixel, and the optics used to project the light onto the detector. There is a range of different-sized FPA detectors that are commercially available from 32×32 to 256×256. Early FPA detectors had pixels of about 62 μm × 62 μm and were slower in performance than more recent FPA detectors that have pixels about 40 μm × 40 μm and are ~10 times faster. Since FPA detectors are relatively expensive, the choice of detector size is limited and switching between detectors requires alignment, it is preferable to obtain the desired flexibility in FOV by using different optical arrangements.

Considering a 64 × 64 FPA with a pixel size of about 40 μm and no magnification, the FOV of the image will be about 2.6 mm × 2.6 mm. In an IR microscope equipped with a 10× Ge ATR objective, the magnification will be 40× and hence the theoretical image size is 65 μm × 65 μm (measured image size of 50 μm × 50 μm using an old FPA with a 20× Ge ATR). Although the image size is relatively small, a high spatial resolution (4 μm) can be achieved. When assessing spatial resolution, it is important that a stringent test is used. Measuring the distance between 5% and 95% points on an absorbance profile obtained through a sharp interface between two materials with similar refractive indices [8] is preferable to using artificial resolution markers that use reflective and transparent features.

Although there is flexibility in the FOV using different objectives and FPA detectors, the range is rather small unless a rastering or mapping approach is adopted as discussed earlier. For imaging with a larger FOV using a stationary ATR crystal, it is advantageous to use a large sample compartment instead of the IR microscope. The large sample compartment allows different accessories to be used. Specifically, ATR accessories with an inverted prism can be used, which make measurements more convenient for many applications. The optical arrangement using an inverted prism is shown schematically in Figure 9.3b–d.

Using an inverted-prism diamond ATR accessory, it has been demonstrated that the FOV was about 500 μm × 700 μm (~5× magnification). For the inverted-prism ZnSe ATR accessory, which does not contain any lenses (e.g., Oil Analyzer, Specac, UK) [30], the FOV becomes about 2.6 mm × 3.6 mm. The change in the imaging aspect ratio is related to the geometry of the prism and the angle of incidence [8]. Other novel developments including a new diamond ATR accessory specifically designed for imaging applications, an inverted-prism ZnSe ATR accessory with expanding lenses [49], ATR imaging with variable angles of incidence ATR accessory [50] will be discussed later in this chapter. The different FOVs and spatial resolutions of different ATR accessories are summarized in Table 9.1 and further details are described later.

9.2.3.2 **Micro-ATR FT-IR Imaging**

The main advantage of micro-ATR imaging with the use of a microscope objective is the high spatial resolution of the images that can be achieved using this method. The high refractive index of the ATR crystal used for this type of ATR imaging (which is 4 for a Ge crystal) greatly increases the numerical aperture (NA) of the system, and hence it is possible to achieve a spatial resolution beyond the diffraction limit of light in air compared to transmission where the Ge crystal is not used [7, 51]. High spatial resolution FT-IR images up to the diffraction limit can also be obtained using a bright synchrotron source (cf. Chapter 15 of this book and [52]). However, images are obtained by rastering, and it is usually relatively slow and hence lacks the capability to study dynamic systems while spatial resolution is still limited by the diffraction of light traveling in air. The SNR of the spectra collected, on the other hand, is often better than those measured by FPA detectors and it can be a good complementary method. Measurements with the FPA detector in micro-ATR mode can be obtained within a few minutes of acquisition time, and

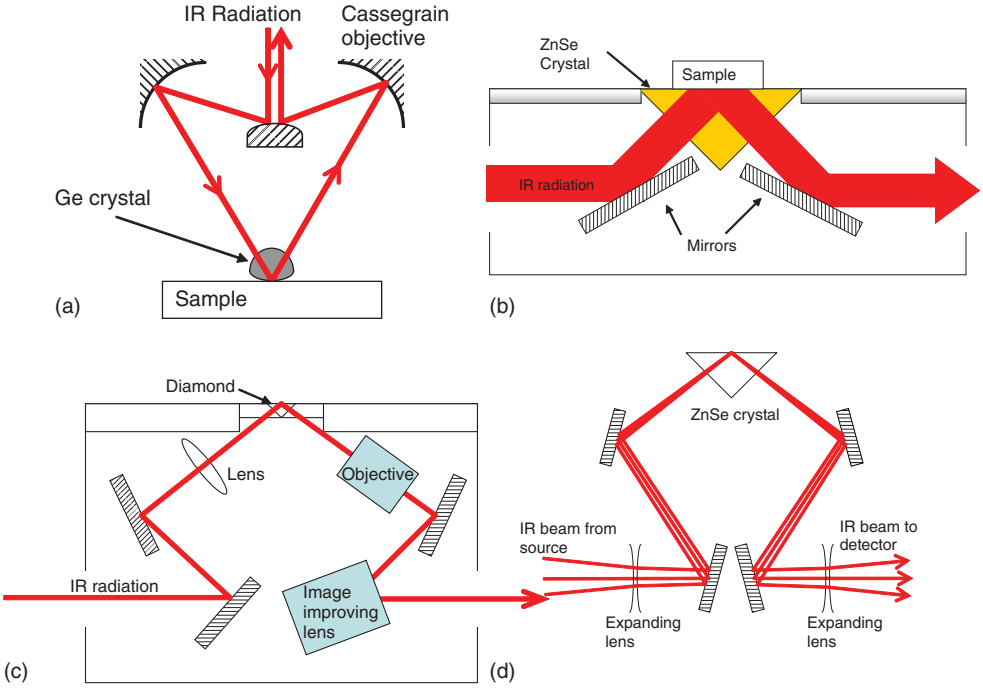

Figure 9.3 Schematic representations of optical setups for ATR FT-IR spectroscopy as typically used in imaging: (a) micro-ATR using a Ge crystal and microscope, (b) an inverted prism, ZnSe, ATR crystal, (c) an inverted prism diamond imaging accessory, and (d) a ZnSe expanded field of view setup. (Reproduced from [3] with the permission of the Society for Applied Spectroscopy [3].)

the achieved SNR is often sufficient for most applications. Micro-ATR imaging enables the measurements of small features which are otherwise not attainable. The high resolving power also enhanced the detection limits for heterogeneous materials [53]. It opens a range of new opportunities to study complex materials, polymer blends, and pharmaceutical tablets where the region of interest is often in the micrometer scale [4, 8, 35, 54–58]. The optical setup for micro-ATR spectroscopy is shown in Figure 9.3a.

9.2.3.3 Diamond ATR FT-IR Imaging

In ATR FT-IR spectroscopy, the crystal used to create the internal reflection has to be IR transparent in the spectral region of interest while the refractive index must be relatively high for the measurement of a wide range of materials. One such material that has been widely used is diamond. The high integrity of diamond has proven to be a valuable property as a high contact pressure between the sample and the crystal may be applied to improve the reproducibility of the spectrum without damaging the crystal [59, 60]. It also makes studies of polymer materials under a high-pressure environment *in situ* possible [61–63]. A diamond

Table 9.1 Parameters of various setups for ATR FT-IR imaging.

	Expanded field of view ATR (ZnSe)	Variable angle ATR accessory	Macro-ATR	Diamond ATR	Micro-ATR with 10× Ge objective
Field of view (mm × mm) [a]	15.4 × 21.5	~3.9 × 5.5	2.6 × 3.6	~0.5 × 0.7	0.064^2
Spatial resolution (μm, estimated)	500	150	60	15–20	4
Can be combined with a UV–vis detector	No	No	Yes	Yes	No
In situ compaction of samples	No	No	No	Yes	No
High-throughput applications (number of samples)	Yes (>100)	Yes (100)	Yes (50)[b]	Yes (10)[b]	No
Depth profiling	No	Yes	No	Yes	No

a) Calculated based on 40 μm^2 pixel size FPA detector.
b) Achieved using a microdroplet dispensing system.

ATR accessory that was not originally designed for imaging purposes has been shown to be applicable to the acquisition of FT-IR images [5, 8, 64]. Further development from this has led to the introduction of a new diamond ATR accessory, the Imaging Golden Gate™ (Specac, UK), which is designed specifically for imaging applications. The aspect ratio of the ATR images obtained using the original diamond ATR accessory had to be corrected by a factor of 1.4 owing to the geometry of the ATR crystal and the angle of incidence of the IR beam [8]. The new design of the accessory incorporated a pair of zinc selenide/germanium lenses and a new mirror configuration patented by Specac [65], which corrects optical aberrations and the aspect ratio of the images. A diamond ATR optical setup is shown schematically in Figure 9.3c.

New versus Old Diamond ATR Accessory ATR FT-IR images of poly(dimethyl siloxane) (PDMS) on a copper grid from the nonimaging diamond ATR accessory with the old FPA detector and from the new imaging diamond ATR accessory with the new FPA detector are shown in Figure 9.4. The images are generated based on the distribution of the absorbance of the spectral bands at 1150–950 cm^{-1}. The visible image of the copper grid used is shown in Figure 9.4c, and the distance between each square is about 63 μm. Chan and Kazarian [8] presented earlier a similar experiment with the same imaging system, but using poly(vinyl acetate) pressed onto the same copper grid. They had shown that the size of the chemical image captured is ~820 μm × 1140 μm. With the imaging diamond ATR accessory and the new FPA detector, it can be observed that there are about 9 squares in the x-direction and 8.4 squares in the y-direction; thus, the new imaged area is about

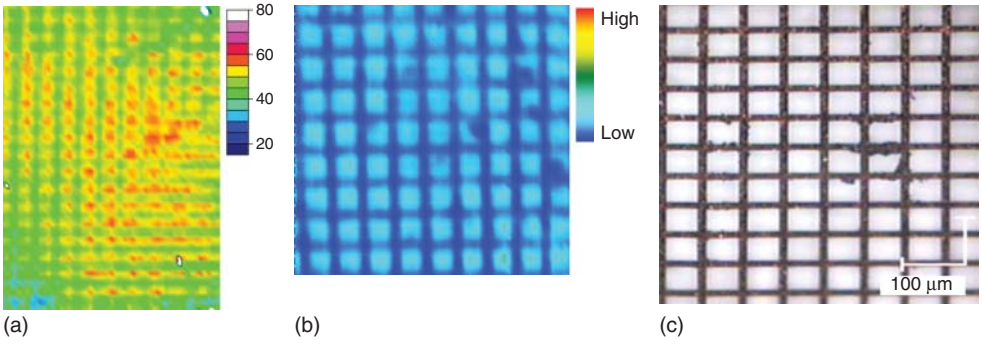

Figure 9.4 ATR FT-IR images of a copper grid with a thick film of PDMS pressed behind and measured using (a) the ordinary and (b) the new imaging diamond ATR accessory. (c) The white light image of the copper grid measured with a 5× objective.

570 µm × 530 µm. It also shows that the aspect ratio of the measured area has improved from 1 : 1.4 to 1 : 1.1. The new image of the copper grid not only showed a greater magnification but also appeared to be sharper and a better resemblance of the 5× optical image of the grid.

Note that the measured area is different from the specification given by the manufacturer of 650 µm × 650 µm. The aspect ratio and the magnification of the measured area are largely dependent on the alignment of the system. In a typical IR macroimaging system, the ATR accessory is placed in the large sample compartment and is able to adjust along the path of the IR beam. To get a well-focused image, the two most important parameters are the position of the objective lens in the ATR accessory and the image distance that can be taken as the path distance of the IR light from the objective lens to the FPA detector.

9.2.3.4 Expanded FOV (ZnSe)

For studies where a larger FOV would be advantageous, a large inverted ZnSe prism with a set of expanded optics can be used. The design of the optics utilises expanding lenses and slightly concaved surfaces of the ZnSe crystal (except the measurement surface) to increase the size of the FOV [49]. The area that can be measured in one single snapshot using this accessory is about 15.4 mm × 21.5 mm. A schematic diagram of this accessory is shown in Figure 9.3d. The large measuring area of this imaging method enables the simultaneous measurement of many samples. This accessory has been used to measure the spectrum of over a hundred samples in one single image acquisition and in a dissolution study of five different pharmaceutical formulations simultaneously [49]. However, with the expansion of the IR beam, the imaged pixel size will be increased together with a decrease in the NA of the system. The spatial resolution is significantly lower compared to the non-expanded ATR imaging method. This approach is not suitable for imaging samples with smaller features but would provide an overall distribution over a

larger area. Further discussion of this imaging method in high-throughput applications is included later in this chapter.

9.2.4
ATR FT-IR Imaging: Depth of Penetration

Depth profiling of materials using variable angle ATR spectroscopy is a well-established approach [66–69] based on the fact that the depth of penetration d_p is a function of the angle of incidence in an ATR measurement. The relationship between the d_p, the wavelength of light λ, the refractive indices of the ATR crystal and the sample, n_1 and n_2, and the angle of incidence θ is shown in Equation 9.1.

$$d_p = \frac{\lambda}{2\pi n_1 \left(\sin^2\theta - \left(\frac{n_2}{n_1} \right)^2 \right)^{0.5}} \tag{9.1}$$

However, the combination of variable angle of incidence ATR spectroscopy and the FPA detector provides the possibility of obtaining 3D images with chemical information [50]. This is made possible by the use of a macrosample chamber that has sufficient space for a variable angle ATR accessory and the associated alignment procedure. To demonstrate this imaging approach, a thin film of poly(vinyl pyrrolidone) (PVP) was cast on one half of the imaging FOV followed by pressing a thick PDMS film on top [50]. ATR FT-IR images at different angles of incidence were then captured. The result is shown in Figure 9.5 with the color scale normalized against the maximum PDMS absorbance observed in each image. The images in Figure 9.5 show how the thick PDMS film is distributed in the measured area. It is clear that when the thin film of PVP is not present, a strong PDMS absorbance can be observed (left-hand side of the image). At a 52° angle of incidence that corresponds to a depth of penetration, d_p, of about 1.3 μm, no PDMS can be observed on the side where the ATR crystal is covered by the thin film of PVP, which is shown by the zero absorbance of PDMS (represented as the dark blue on the color scale). At 45° ($d_p = 1.7$ μm), a small PDMS absorption (navy blue)

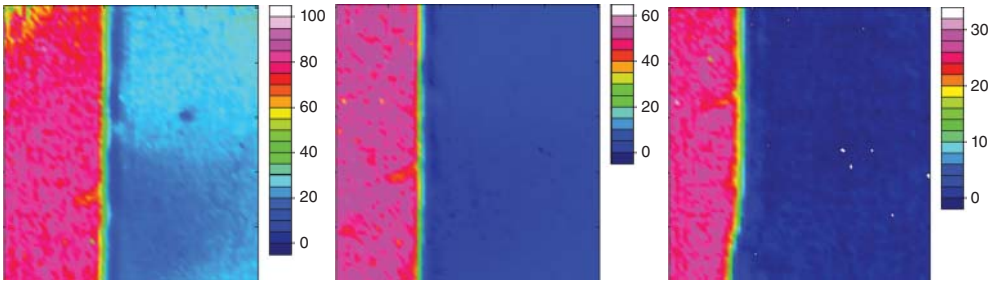

Figure 9.5 FT-IR images of a thin film of PVP covering half of the imaging area with a large piece of thick PDMS pressed on top.

can be seen through the PVP layer and the PDMS absorption becomes stronger (light blue) when the angle of incidence decreased by 41° ($d_p = 2.3\,\mu m$). This simple study demonstrated that information from different layers of the sample can be obtained by changing the angle of incidence while the lateral distribution is readily measured using the FPA detector. This can be applied to study heterogeneity in lateral and axial directions for the layers of samples adjacent to the surface of the ATR crystal. As the depth of penetration is not diffraction limited, imaging thin polymer films on the order of 300–100 nm thick has been achieved by varying the angle of incidence [70]. Care should be taken when measuring samples of high refractive index. "Anomalous dispersion" of the refractive index of samples can occur at wavelengths close to an absorbance band, causing distortion of band shapes or band shifts. These effects can be minimized in ATR measurements by employing a variable angle approach to increase the angle of incidence [71] or by using high refractive index ATR crystals, such as Ge instead of diamond [72].

Nevertheless, great potential exists in applications of variable angle of incidence ATR FT-IR imaging to heterogeneous materials, particularly to biomedical materials, for example, skin [50].

9.2.5
ATR FT-IR Imaging: Quantitation

As with single-element ATR and transmission mode FT-IR spectroscopy, ATR FT-IR imaging results can be analyzed quantitatively.

Quantitative analysis is possible as a result of the Beer–Lambert law; when the pathlength (l) of the sample is kept constant, the absorbance (A) at a wavenumber is proportional to the molar concentration (c) of the absorbing species (Equation 9.2), where ϵ is the molar absorptivity for an absorbing species at a given wavenumber (where ϵ is not known, the concentration can be obtained by reference with a calibration curve of the material). For transmission measurements, the pathlength is usually considered equal to the thickness of the sample. In ATR measurements, the effective pathlength d_e is used and can be calculated using Equation 9.3, where, again, n_1 and n_2 are the refractive indices of the ATR crystal and sample, respectively, θ is the angle of incidence, and λ is the wavelength of IR light in question. This equation holds true for nonpolarized light [50].

$$A = \epsilon l c \tag{9.2}$$

$$\frac{d_e}{\lambda} = \frac{\frac{n_2}{n_1}\cos\theta\left[3\sin^2\theta - 2\left(\frac{n_2}{n_1}\right)^2 + \left(\frac{n_2}{n_1}\right)^2\sin^2\theta\right]}{2\pi\left(1-\left(\frac{n_2}{n_1}\right)^2\right)\left[\left(1+\left(\frac{n_2}{n_1}\right)^2\right)\sin^2\theta - \left(\frac{n_2}{n_1}\right)^2\right]\left(\sin^2\theta - \left(\frac{n_2}{n_1}\right)^2\right)^{0.5}} \tag{9.3}$$

It is important to note that the measurement should operate at least a few degrees above the critical angle to avoid strong dispersion of the refractive index affecting the spectrum.

Some examples of quantitative analysis of ATR FT-IR imaging include the study of tablet dissolution in water where concentration profiles of hydroxypropylmethylcellulose (HPMC) and niacinamide at different stages of the dissolution process were used to understand the drug release mechanism [73]. It was demonstrated that concentration profiles of different components can be obtained utilizing the partial least squares method. With concentration profiles readily measurable, it is possible to obtain other quantities such as diffusion type, that is, Fickian versus non-Fickian mechanism of diffusion. The application of *in situ* ATR FT-IR spectroscopic imaging has been employed to investigate polymer interdiffusion of PVP and poly(ethylene glycol) (PEG) under high pressure CO_2 [74]. The diffusion mechanism of the system was described based on the spectroscopic imaging data, and it was found that CO_2 molecules dissolved in the polymeric system greatly enhanced the interdiffusion process.

It should be noted that an absorbance gradient was reported across an ATR FT-IR spectroscopic image when measuring homogeneous paraffin oil using a FastIR™ ATR accessory (see Chapter 8 in this book). The explanation for this phenomenon was that the angle of incidence (θ) was not uniform across the imaging plane [75]. Should the angle of incidence change across the imaging plane, the effective pathlength will be different, and hence the absorbance will not be the same even if the concentration of the sample is uniform. Therefore, alignment of the optics in the accessory is crucial in order to avoid the occurrence of this gradient effect. This was shown by performing similar experiments with a homogeneous sample, mineral oil (refractive index of ca 1.48), using both the ZnSe ATR accessory and the diamond ATR accessory (Supercritical Fluid Analyzer, Specac, UK). Both results show relatively homogeneous distribution of the integrated absorbance in the range $1480-1420\,cm^{-1}$ over the whole imaged area (Figure 9.6). For the ZnSe ATR accessory, the mean integrated absorbance is about 2.1 AU with a standard deviation of 0.09; for the diamond ATR accessory, the mean integrated absorbance is about 3.5 AU with a standard deviation of 0.26 AU. The difference in the mean integrated absorbance can be explained by the difference in the average angle of incidence between the two accessories. It has been reported previously that the angle of incidence is not necessarily the same as the specification given by the manufacturer [63]. Instead, it is very much dependent on the alignments of the spectrometer and the ATR accessory that may vary from system to system. These findings are important because they show that reliable quantitative imaging data are possible with the use of macro-ATR accessories and also point out that the choice of the accessory and its alignment are crucial for the reliability of quantitative data obtained with ATR FT-IR imaging.

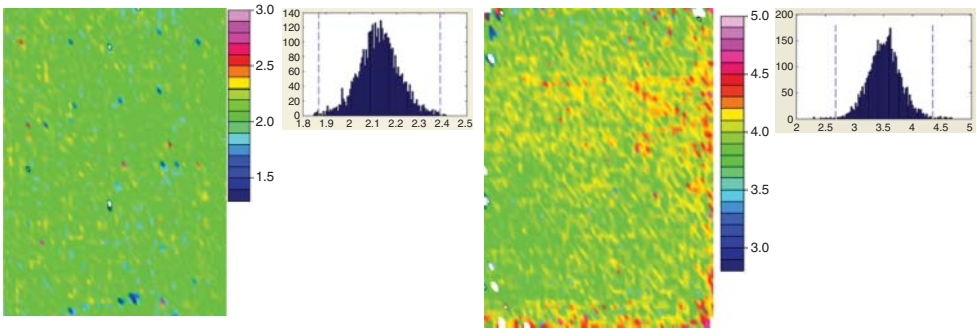

Figure 9.6 ATR FT-IR images of mineral oil measured with a ZnSe ATR accessory (left) and diamond ATR (right) showing the integrated absorbance at 1480–1420 cm^{-1} (left). The respective histograms show the number of detector pixels for different values of the integrated absorbance at the same range for the ATR FT-IR measurement.

9.3 Practical Applications

9.3.1 Materials Characterization of Polymer Interfaces and Blends

9.3.1.1 Investigating a Polymer: Carbon Fiber Interface

Understanding the interfacial properties in composite materials is key for their rational design and manufacturing. A composite product of micro-carbon fibers (5 µm diameter) embedded in a polymer matrix was manufactured for improved mechanical properties resulting from the synergy of the two materials. ATR FT-IR imaging was used to investigate the interfacial area between the micro-carbon fiber and polymer from cross sections (FT-IR microscope with Ge ATR crystal). As the carbon fiber absorbs all wavelengths in the mid-IR region (black body), the distribution of the micro-fibers in the polymer matrix could be observed (Figure 9.7). This was achieved by examining the changes in absorbance in the 3500–3000 cm^{-1} spectral region, where the polymer matrix does not produce spectral bands. The size of the micro-fiber shown in the micro-ATR FT-IR image is around 5 µm, which is very similar to the actual fiber size observed under a visible microscope demonstrating the power of the spatial resolution of the micro-ATR imaging technique. However, the real power of FT-IR imaging was revealed by extracting spectra from the polymer matrix area near the micro-fibers and comparing them to those from the bulk. The difference spectrum (not shown) revealed that the spectra extracted near the fibers have an extra band at 1011 cm^{-1}. An image generated by plotting the integrated absorbance of this band across the imaged area is shown in Figure 9.7b, displaying that the material in the polymer matrix that has this extra band appears to be distributed near the carbon fibers. The reason for this is due to the specific manufacturing process, and further details cannot be revealed as the sample

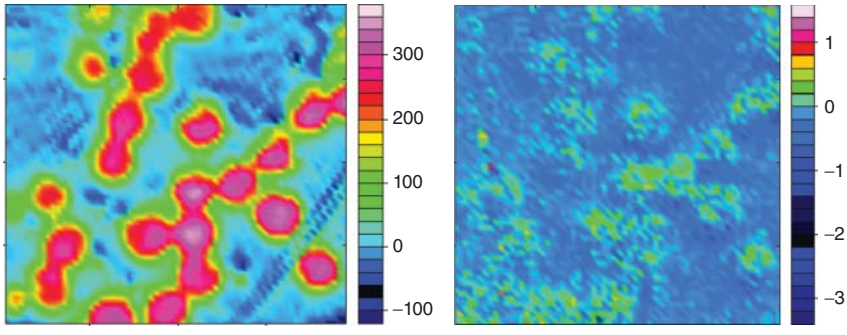

Figure 9.7 ATR FT-IR images of the polymer matrix showing the distribution of (a) carbon fiber and (b) distribution of the absorbance of the band at 1011 cm^{-1}. Image size is 50 μm × 50 μm.

is proprietary. Nevertheless, this is a useful example to highlight the spatially resolved chemically specific detail that can only be revealed with the use of high spatial resolution offered by micro-ATR FT-IR imaging. It should be noted that the interfacial area between the fiber and the polymer matrix is very small and thus diffraction of light, which is also present in ATR measurements, affects the quality of the image (Figure 9.7b). Nevertheless, the consistency of the polymer distribution with the distribution of fibers and the ability to extract its spectrum is an example of how imaging improves the understanding of novel composite materials.

9.3.1.2 Polystyrene: Polyethylene Blend – Imaging the Effect of a Compatibilizer

Mixing of polymers is an important process in the polymer industry; by combining the strength of different polymers through blending, new products with desirable physical properties can be produced [2]. FT-IR imaging with a micro-ATR objective has been used to study the effect of a compatibilizer on the mixing of two immiscible polymers, namely polystyrene (PS) and low-density polyethylene (LDPE). The compatibilizer used in this study is a triblock copolymer of polystyrene-*b*-poly(ethylene–butylene)-*b*-polystyrene (SEBS). The blends are prepared with a micro-extruder, which allows small amounts of the materials to be blended [2]. The two polymers are easily characterized by their specific absorption bands at 1492 and 1450 cm^{-1} for PS and the band at 1466 cm^{-1} for LDPE.

Two batches of PS and LDPE blend, one containing SEBS (5% (w/w)) and the other without SEBS were produced. FT-IR images of the compatibilized and uncompatibilized blends were generated, and the results, shown in Figure 9.8, demonstrate that the distribution of PS is complementary to that of PE indicating that good contact was established between the sample and the Ge ATR crystal. Without the addition of the compatibilizer, the blend exhibits large

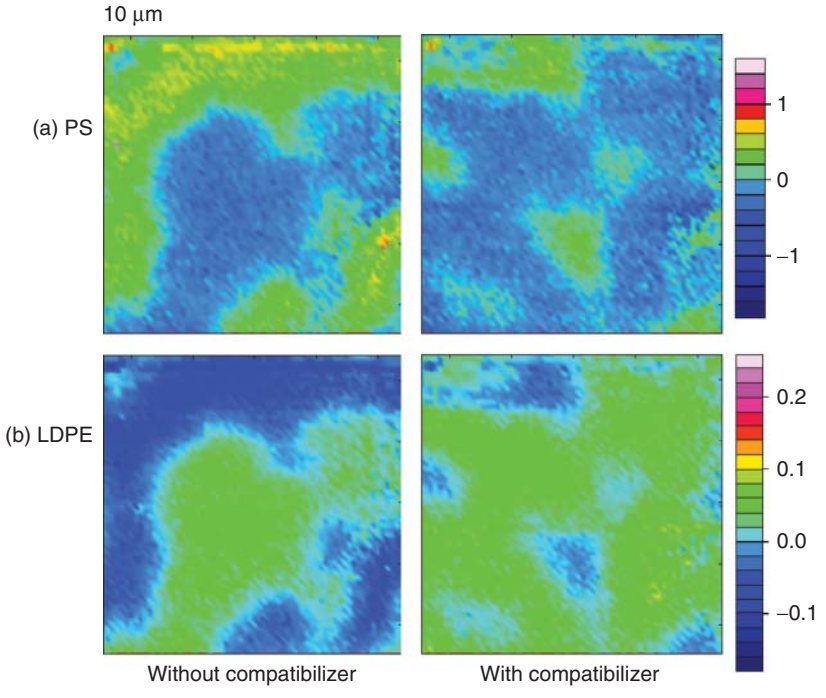

Figure 9.8 ATR FT-IR images showing the distribution of the absorbance of a band of (a) PE and (b) LDPE with and without compatibilizer.

segregation of LDPE and PS. However, the images of the blend with 5% (w/w) of added compatibilizer show a more disperse structure. PS domains of size about 5–15 μm are dispersed in the LDPE matrix. It is important to note that the small PS domains can only be revealed with sufficient spatial resolving power, and micro-ATR FT-IR imaging is most suitable for imaging this type of sample [2].

9.3.1.3 **Hydrogels**

Three-dimensional hydrogels are novel materials commonly developed as tissue- or bioengineering scaffolds that can be custom designed with physico-chemical properties for the application in question. This is a growing area of research and as with other material developments, studies to ascertain specific interactions are crucial for our understanding in order to advance their development. Recently ATR FT-IR imaging was used to study the fabrication of a chitosan/poly(ϵ-caprolactone) (PCL) hydrogel for tissue engineering purposes [76]. SEM analysis was used to identify the pore size and mechanical tests were carried out to ascertain the physical properties of the material, but it was the FT-IR results that provided information about molecular interaction. By examining the carbonyl region and amino bands derived from chitosan, the

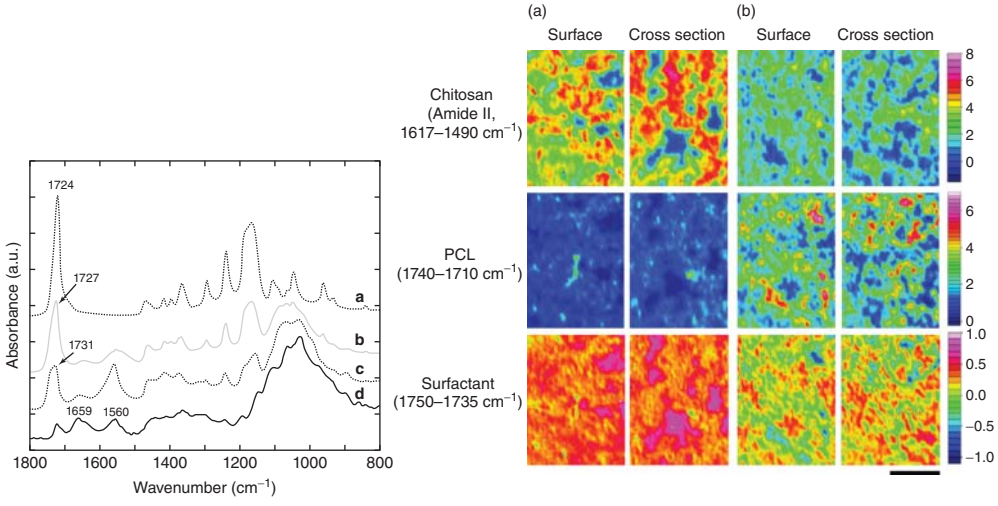

Figure 9.9 FT-IR plots: (a) pure PCL, (b) chitosan/PCL (50/50 (w/w)), (c) chitosan/PCL (75/25 (w/w)), and (d) pure chitosan. FT-IR images: (a) 25% PCL and (b) 50% PCL. Scale bar depicts 350 μm. (Reproduced from [76] with kind permission from Springer Science and Business Media.)

ATR spectral plots shown in Figure 9.9 indicated that the two materials had not chemically bonded to one another via amide bond formation, and were, instead, only physically mixed. ATR FT-IR imaging was carried out using a diamond accessory and revealed that the sample with lower weight percentage of PCL had a small but higher contribution from a surfactant, span-80, in the resulting product (images shown in Figure 9.9). This was consistent with SEM results showing a smaller pore size and, hence, higher surface area for this sample. It is clear from the images that the hydrogel prepared with the lower weight percentage of PCL produces images dominated by chitosan, whereas the hydrogel prepared with 50 : 50 wt% of PCL : chitosan is roughly equivalent to the two materials. The images also reveal that the chemical composition of the hydrogel surface is similar to that of the cross section, indicating that the mixing of the components is consistent throughout the material.

9.3.2 Pharmaceuticals: Studying Tablets, Dissolution, Drug Diffusion, and Biopharmaceuticals

9.3.2.1 Imaging of Compacted Tablets

The ATR FT-IR method is particularly suitable for the spectroscopic analysis of pharmaceutical tablets because of the minimal sample preparation required and the possibility to obtain quantitative chemical information from the sample. These

advantages are important for this sample type because it is difficult to microtome a tablet into a thickness that would be suitable for transmission studies (usually <10 μm), and the alternative diffuse-reflection technique is often difficult to calibrate for quantitative analysis. ATR FT-IR imaging has, therefore, become a very useful tool for studying the distribution of different components in compacted tablets [51, 73, 77–81].

The micro-ATR FT-IR imaging approach is readily applicable to study compacted tablets. The contact area of the ATR crystal is circular with a diameter in the region of 100 μm. This area is small enough to easily establish a homogeneous and intimate contact between the ATR crystal and the tablet. To prove this concept, a model tablet, composed of about 3 wt% caffeine in a matrix of starch : HPMC of 4 : 6, was compacted and imaged using the micro-ATR method and the result is shown in Figure 9.10.

The distribution of starch complements the distribution of HPMC, supporting the assumption that a good contact was formed between the ATR crystal and the tablet. The images reveal in great detail how different components are distributed in the tablet. For example, caffeine of particle size less than a few micrometers can be easily detected. However, the images may actually be misleading as to the amount of starch and HPMC that exist in the tablet due to the relatively small sampling volume used in this imaging measurement. Several images at different locations of the sample would be required to obtain results that are statistically significant if the determination of the amount of each component is the objective of the study. Alternatively, one can measure a larger area of the sample using different optical arrangements.

For imaging with a larger FOV, the shape of the tablet becomes an important issue. Industrially manufactured tablets often have curved surfaces to avoid chipping during the various stages of processing and transportation. This curvature of the tablet surface limits the size of the image that can be measured in one single measurement. Pressing the tablet with an applied pressure could achieve good contact over a larger surface area without having greatly altered the original distribution of different components. However, this will risk fracturing the

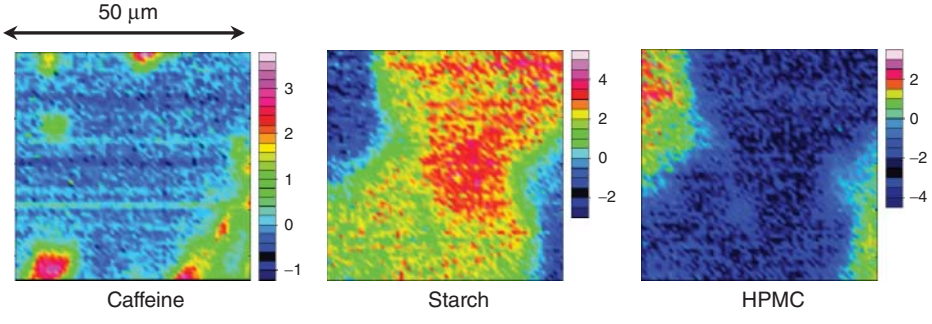

Figure 9.10 Micro-ATR FT-IR images of a tablet showing the distribution of caffeine, starch, and HPMC. Scale bar denotes 50 μm.

tablet during measurements. Also, many tablets are supplied with an outer coating which, due to the depth of penetration of ATR FT-IR spectroscopy, may obscure any information about the drug/excipient interaction that is under study. Another approach is to compact the tablet directly onto the measuring ATR crystal surface and perform the measurement *in situ*. This idea is schematically presented in Figure 9.11.

This approach enables the measurement of the compacted tablet during and after the process of compaction and can be used to evaluate the effect of pressure on the distribution of different components and the density of the tablet [80]. The *in situ* compaction study is only possible with hard ATR crystals due to the high compressive force during compaction. Diamond is the crystal of choice for this type of study, and the application of a diamond ATR accessory to obtain ATR FT-IR images of compacted tablets has been demonstrated [51]. ATR FT-IR images of a model pharmaceutical formulation containing about 56 wt% starch and 44 wt% caffeine were compacted and measured *in situ* on the diamond ATR accessory (Figure 9.12). The result shows that images with a larger FOV represent the actual composition of the tablet better.

9.3.2.2 ATR FT-IR Imaging of Tablet Dissolution

Understanding the mechanism of drug release is important for the safe and effective design of tablets and pharmaceutical formulations. ATR FT-IR spectroscopic

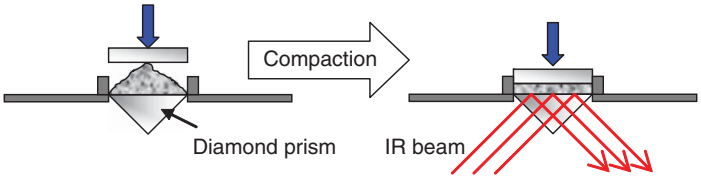

Figure 9.11 Schematic diagram showing the idea of *in situ* imaging of tablet compaction using a diamond ATR accessory.

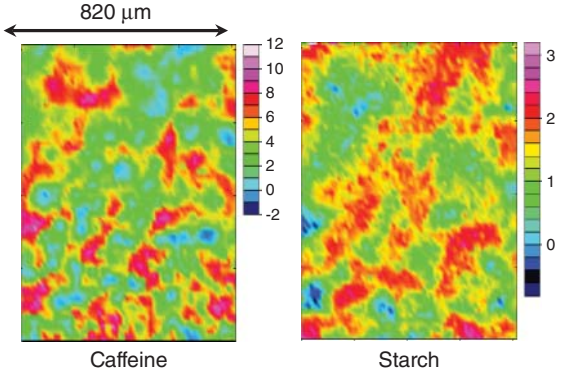

Figure 9.12 ATR FT-IR images of a tablet with two components compacted directly on the surface of the diamond crystal in the ATR accessory. Scale bar denotes 820 µm.

imaging has been shown to be a valuable asset in such studies and has allowed insight to be gained into many processes including drug polymorphism [30, 34, 82]; the effect of polymer swelling [9], pH (of the dissolution media) [79], the micro-environement [83], or the drug loading and sample preparation [73, 84] on drug release. The use of ATR FT-IR imaging to study tablet dissolution and drug release has been the subject of a recent review [85].

Apart from the ability to acquire thousands of IR spectra simultaneously within a matter of seconds, thus allowing dynamic systems to be studied for FT-IR imaging with the FPA detector [23, 30, 38], this type of study is made possible with the ATR approach allowing the study of samples in aqueous environments. It is challenging to perform the same experiments using the transmission approach because of the very strong absorption of water in the mid-IR region. Previous attempts in transmission mode required the use of deuterated water and a very thin spacer [86]. With the advantage of the ATR approach allowing quantitative analysis, the dissolution of pharmaceutical formulations including tablets in water can be studied [30]. This is achieved by visualizing the complex process of dissolution that leads to distribution and morphological changes of different components in the formulation as a function of space and time. A large FOV will be favorable for this kind of study, giving the opportunity to study the dissolved substance some distance away from the original tablet. However, a good spatial resolution is also desirable for the detection of small changes in the tablet or the formation of small crystallites [30, 82, 87]. This led to the application of both diamond and ZnSe ATR imaging to dissolution studies. These two approaches complement each other with different FOVs and spatial resolutions as summarized in Table 9.1. A schematic diagram for the dissolution setup is shown in Figure 9.13.

One important aspect for this type of dissolution approach is that a good contact between the crystal surface and the sample is needed not only for representative imaging of the tablet or pharmaceutical formulation but also to ensure that water penetrates the sample only from the side of the tablet. This is especially important when mathematical modeling of the dissolution process is compared to that of the experimental data. Using the diamond ATR approach, the tablet is pressed onto the diamond, and therefore leakage of water between the diamond surface and the tablet is not expected [88].

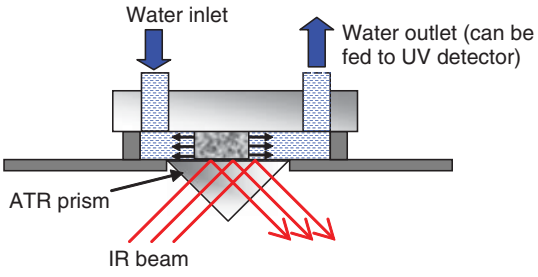

Figure 9.13 Schematic diagram of drug dissolution study using the ATR FT-IR imaging approach.

An innovative approach to study drug release using a specially designed dissolution cell fitted on a diamond ATR accessory that allowed that allowed controlled compaction of a tablet, and monitoring of the dissolution of the same tablet *in situ* has been demonstrated [77]. When a ZnSe crystal was used for the imaging with a larger FOV, the softness of the crystal would not allow a high pressure to be applied. For formulations that were produced by dissolving the drug in the molten polymer matrix, the formulation may be prepared directly on the ZnSe crystal surface, provided that the polymer matrix has a low melting point. This approach has been successfully applied to study the dissolution of PEG-based formulations [30, 84]. For matrices of a higher melting point such as HPMC, it was found that the swelling of polymer at the edge of the tablet upon contact with the water prevented the undesirable water ingress from the top or bottom of the tablet into the interfacial area with the ATR crystal [9]. An important feature of both the diamond and ZnSe ATR dissolution cells was the introduction of flow around the tablet in the cell in order to prevent saturation of the solution [73, 84]. An example to demonstrate the dissolution study of a model pharmaceutical formulation is shown in Figure 9.14. PEG was used as the model carrier matrix while nicotinamide was the model drug. The effect of different polymer molecular weights, PEG 35 000 and PEG 8000, on the drug release of 50% nicotinamide tablet was investigated using the ATR FT-IR method with the medium-sized ZnSe ATR accessory. The model drug is relatively highly water soluble and should be released once the polymer has dissolved. The drug release rate is therefore controlled by the polymer dissolution rate. The images show that the total drug release time was almost doubled when PEG 35 000 was used as the carrier compared to PEG 8000. When the polymer came into contact with water, the polymer swelled while the polymer chains remained entangled producing some impedance to drug dissolution into the surrounding water. As water accumulates in the polymer, the chains disentangle and the polymer dissolves. As the lower molecular weight PEG has a shorter polymer chain, it can be more easily disentangled and thus dissolve faster. With chemical and spatial information provided by ATR FT-IR spectroscopic imaging, complex processes that affect the overall drug release can be better understood. Other applications of the diamond ATR accessory include simultaneous imaging of tablet dissolution with optical photography and ATR imaging [89] and combined ATR imaging and X-ray microtomography of compacted pharmaceutical tablets [81].

It is notable that the approach described here is nondestructive, and as such, the effluent stream can be studied with an external UV–vis detector to simultaneously obtain results that are similar to industry standard dissolution tests such as the United States Pharmacopeia (USP). By combining ATR FT-IR imaging with inline UV–vis spectroscopy and optimizing computational simulations (results shown in Figure 9.15), it is possible to understand the physical properties of components of a drug-excipient matrix [90]. Nicotinamide formulations of 60% and 10% (w/w) in HPMC were prepared and studied by FT-IR imaging and UV–vis. By examining the images and UV–vis data obtained, the drug diffusion coefficient was calculated and found to be close to literature values.

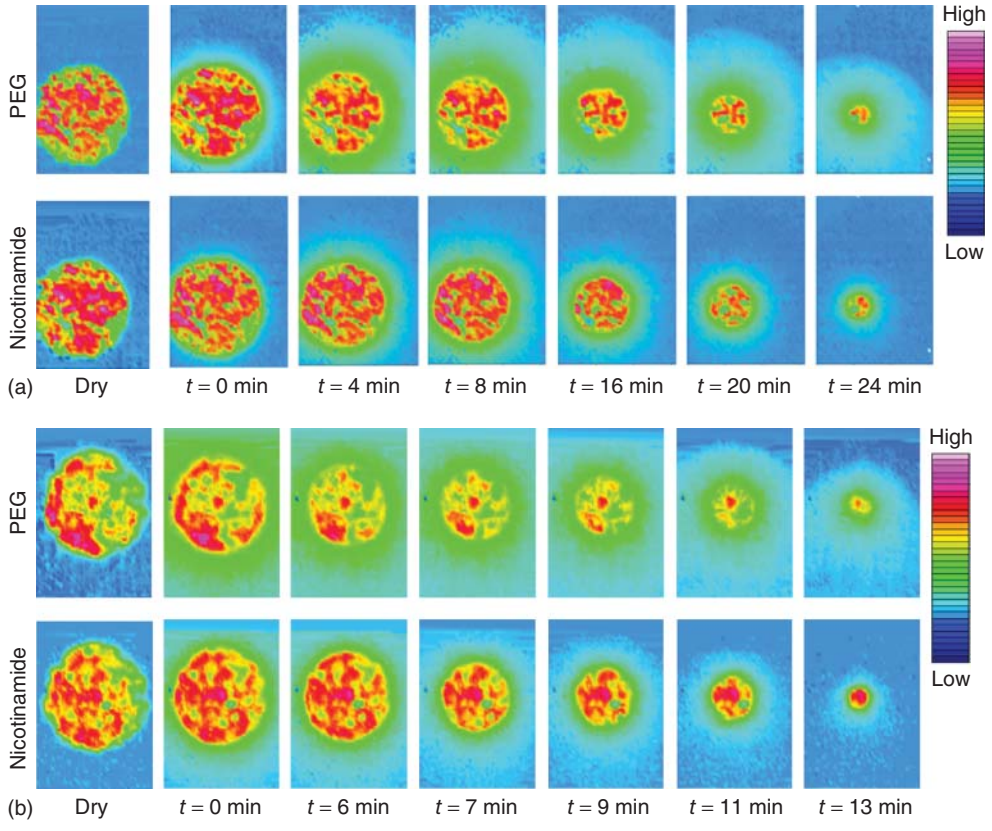

Figure 9.14 ATR FT-IR images showing distribution of PEG (top row) and nicotinamide (bottom row) through dissolution as a function of time for 50% nicotinamide tablet with (a) PEG 35 000 and (b) PEG 8000. Image size is about 1140 μm × 820 μm.

It was thus shown that FT-IR imaging offers benefits to the development and validation of models for drug release and physical properties by allowing a straightforward method to obtain component physical properties that are spatially resolved.

A further interesting example of the ATR FT-IR imaging approach to study drug dissolution was revealed by examining the behavior of ibuprofen during dissolution [30]. Dissolution and bioavailability are important parameters in drug formulation design and evaluation. Drugs tend to be more soluble in the amorphous, rather than crystalline, form, and the study of polymorphism is important to the pharmaceutical industry. In order to examine the behavior of ibuprofen dissolution, it was prepared in a PEG matrix in order for the drug to be molecularly dispersed. However, studying the dissolution process revealed that the ibuprofen, even though prepared as a molecularly dispersed solid, crystallized during dissolution (Figure 9.16). This occurs as the ibuprofen comes into contact with the aqueous solution as revealed by a band shift in the ν(C=O) region. This experiment

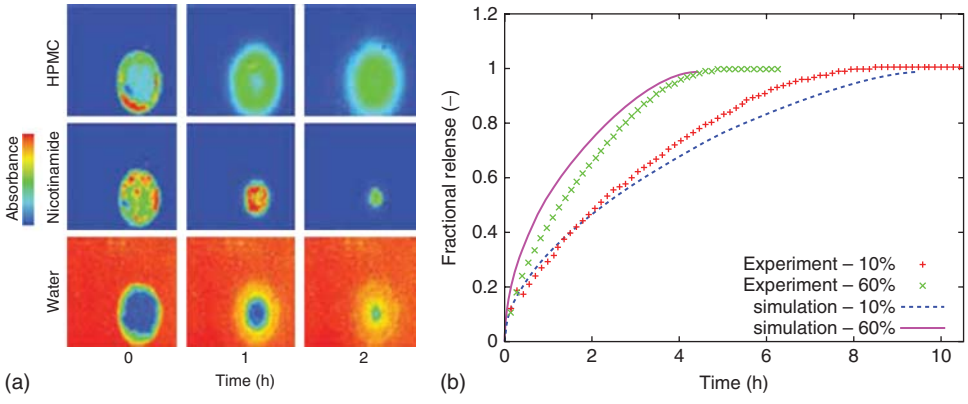

Figure 9.15 (a) ATR FT-IR images generated during nicotinamide release from HPMC (60 : 40 (w/w)) matrix during dissolution experiment and (b) corresponding experimental and simulated UV–vis results. (Adapted from [90] with permission from Elsevier (as per [85]).)

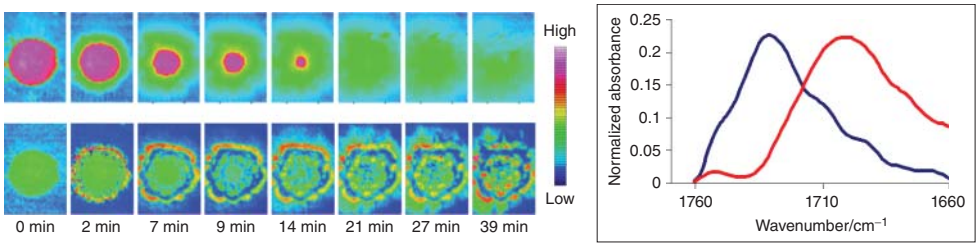

Figure 9.16 Images based on bands related to PEG 8000 and ibuprofen (top and bottom rows, respectively) as a function of time. Plot reveals spectral change in ν(C=O) region between molecularly dispersed (blue) and crystallized (red) ibuprofen. (Reprinted with permission from [30] Copyright 2013 American Chemical Society.)

clearly highlights the power of chemical imaging as applied to pharmaceutical formulation and dissolution studies. This led to the pH of the matrix microenvironment being shown, by ATR FT-IR imaging, to affect the crystallization process of ibuprofen during dissolution [83]. pH-sensitive hydrogels have also been prepared that prevented the formation of ibuprofen crystallites during dissolution [91].

9.3.2.3 ATR FT-IR Imaging of Drug Diffusion Across Tissue Sections: Biomedical Applications

An exciting extension of the ATR FT-IR imaging methodology in relation to pharmaceutical studies is the ability to study the diffusion of drugs through biomedically relevant materials. In a model system, sections of rabbit thoracic aorta were imaged as a function of time upon application of a drug [92]. Figure 9.17 shows the experimental setup for the study – a sample of rabbit thoracic aorta, S, was placed on a diamond ATR crystal, C, with a glass slide, G, applied on top with

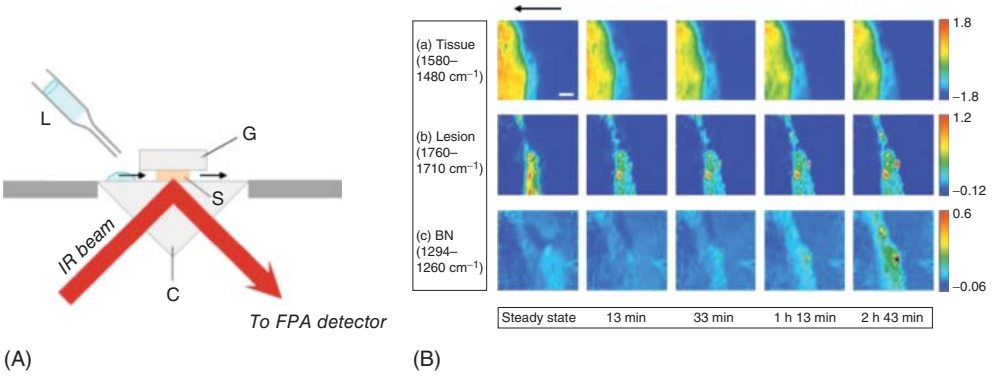

Figure 9.17 (A) The experimental setup for measuring drug diffusion through a tissue sample, where L is the liquid drug solution, C is the ATR FT-IR crystal, G is a glass slide applied with gentle pressure, S is the sample, the red arrow indicates the path of the IR beam while the black arrows indicate the direction of flow. (B) ATR FT-IR images obtained for the integrated absorbance of bands related to (a) tissue, (b) atherosclerotic lesion, and (c) benzyl nicotinate (BN). (Reproduced, with permission, from [92] © SPIE.)

gentle pressure to seal the sample compartment. The pressure, in this case, as with the tablet dissolution experiments was to ensure that ingress of the applied drug would only be possible from the epithelial side of the tissue section. The drug, in this case benzyl nicotinate (BN) in saturated Ringer's solution, L, was applied to the tissue section, and the system was imaged as a function of time. The results are shown in Figure 9.17B. Row "a" presents images generated by integrating the absorbance of the amide II band, a key component of proteins and an indicator for the presence of tissue. The images in row "b" were generated by integrating the absorbance of an ester band, highlighting the presence of atherosclerotic plaque. In row "c," the images were generated by integrating the absorbance of a band indicative of BN, the drug. The power of the chemical imaging approach reveals that not only does the BN diffuse through the tissue section, but that it accumulates in the region of the atherosclerotic plaque rather than the healthy tissue.

The methodology described has also been applied to study the diffusion of drugs across porcine [93] and human skin [94]. The human skin study was conducted *in vitro* with skin obtained from the abdomen of human cadavers. BN as an aqueous ethanolic solution, containing PEG, was applied to the skin sample. The results, shown in Figure 9.18, clearly show diffusion of BN across the *stratum corneum*. The top row of images were obtained before and the bottom row after diffusion across the tissue. By comparing these images with the images obtained before and after diffusion as a result of the amides and lipids of the tissue, it was possible to observe that the distribution of BN tended to match that of the underlying lipids, while the distribution of ethanol matched that of the amides and, hence, protein-rich areas. This is an excellent example that shows the spatial resolution of ATR FT-IR imaging, allowing information to be obtained about drug diffusion and distribution across human tissue.

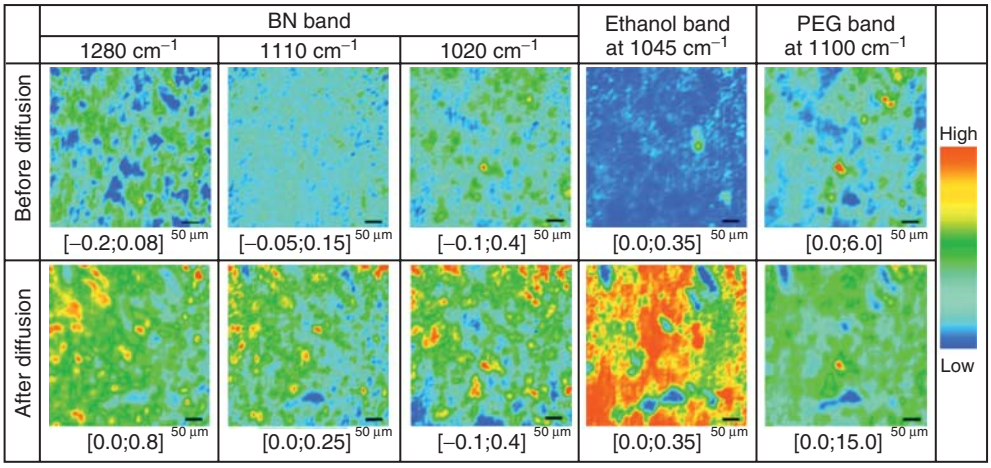

Figure 9.18 ATR FT-IR images relating to the components of the skin diffusion experiment where the top row of images were generated before diffusion and the bottom row of images were generated after diffusion. Bands relating to BN, ethanol, and PEG have been plotted. Note that the numbers in square brackets indicate the min–max values of the color bar. (Reproduced, with permission, from [94] © SPIE.)

An imaging study on the diffusion of DMSO-d_6 through porcine skin as a mimic for human skin has also been conducted in transmission mode [95]. In this case, the skin samples (both porcine and human) were formalin fixed, paraffin embedded, and microtomed (human) or frozen before being cryostat sectioned (porcine) to a thickness appropriate for transmission mode FT-IR spectroscopy (10 µm). FT-IR spectroscopy was used to confirm the chemical similarity of human and porcine skin, and thereafter transmission mode imaging was used to study the diffusion of the DMSO-d_6 through the porcine sample as a function of time.

9.3.2.4 Biopharmaceuticals Development: Optimizing Protein Crystallization

Microbatch Crystallization Biopharmaceuticals are a burgeoning field of the pharmaceutical industry and, with the drive behind synthetic biology, is set for further growth. X-ray diffraction is a key technique used to ascertain absolute protein structure in order to better understand function. The technique provides unparalleled resolution of protein structures; however, it requires high-quality protein crystals that can be time consuming and difficult to obtain. ATR FT-IR spectroscopy has been used to study protein structure and function with far more limited resolution. Nevertheless, there is a role for ATR FT-IR spectroscopy and imaging to play in protein crystallization optimization, an application that has been recently reviewed [96]. Owing to the complexity of obtaining high-quality protein crystal candidates for X-ray diffraction, it would be advantageous to screen crystallization conditions and crystals in a high-throughput manner

in order to better understand protein–surface interactions and crystallization procedures. One of the challenges in the protein crystal optimization process is to differentiate salt crystal from protein crystal. This is an important step to avoid time and energy being wasted in optimizing salt crystals rather than the target protein crystal. This has been achieved by use of ATR FT-IR imaging. In one example, proteins crystallized from an aqueous precipitant solution under a blanket of oil, commonly known as *microbatch crystallization*, were imaged by the ATR FT-IR approach. This was achieved by undertaking the crystallization procedure directly on the ATR crystal and studying the sample after 20 h. An image obtained is shown in Figure 9.19A where integration of the amide band clearly reveals the protein crystallites [97]. The imaging of microbatch crystallization can be extended to multiple samples being analyzed simultaneously, which allows a comprehensive study of response to crystallization conditions to be achieved (Figure 9.19B(a–d)). In that case, trypsin was studied under different crystallization conditions, having being deposited in aqueous solution, under oil, on a ZnSe ATR crystal.

Surface Modification for Protein Crystallization Silane surface modification chemistry is robust and well known. Since Si can be used for ATR FT-IR, it was possible

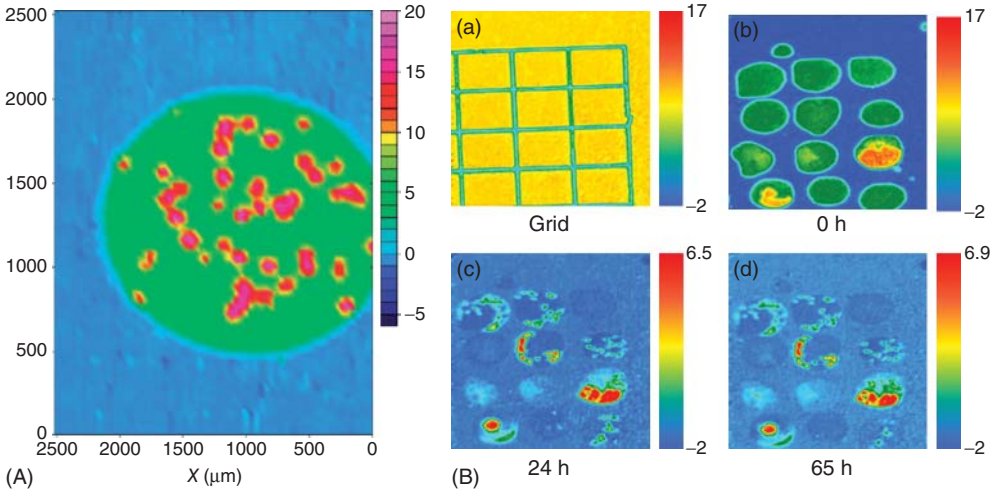

Figure 9.19 (A) ATR FT-IR image of accumulation of protein aggregates, 20 h after deposition with a crystallizing agent. The false color scale depicts the presence of protein bands, the image size is 2.56 mm × 3.6 mm. (B) Images of multisample batch crystallization where (a) shows the wax grid, (b) intensity based on water bending mode showing deposition location of aqueous protein solution, and (c,d) amide II band showing location of crystallized proteins within droplets after 24 and 65 h, respectively. ((A) Reproduced with permission from [97]. Copyright 2013 American Chemical Society. (B) Reproduced with permission from S. Glassford, PhD Thesis, Imperial College London, 2013.)

to exploit silane surface modification chemistry to study the crystallization of proteins across a gradient modified surface via ATR FT-IR imaging. A Si ATR crystal was modified with a gradient monolayer of octyltrichlorosilane (OTS) in order to study the differential crystallization of lysozyme – a commonly crystallizable protein [98]. The results show that with an increase in OTS coverage (and hence hydrophobicity) protein adsorption and crystallization increase (Figure 9.20). This result, coupled with the many functionalization options through silane chemistry, opens up the possibility of screening for adsorbate/crystallization favored conditions.

Hanging-drop Crystallization Another common protein crystallization technique is the "hanging-drop crystallization" method, where a drop of protein in precipitation solution is suspended above a reservoir until crystallization is realized. This protocol was mimicked in a recent study in which the protein/precipitant solution was suspended from a Ge ATR crystal [99]. The resulting images obtained allow discrimination between protein adsorbate and salt crystal formation (Figure 9.21). *In situ* micro-ATR FT-IR imaging of the protein crystallization

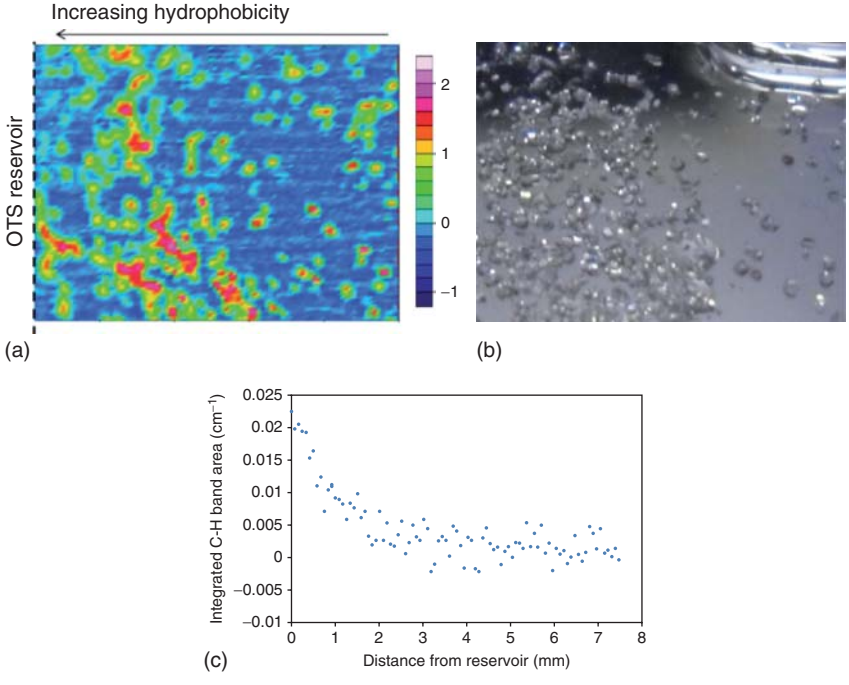

Figure 9.20 ATR FT-IR image of lysozyme crystals deposited on a gradient monolayer OTS surface on a silicon ATR crystal. The false color image (a) shows the abundance of protein compared with the white light image (b). Plot (c) shows the distribution of protein across the gradient surface. (Adapted with permission from [98]. Copyright 2013 American Chemical Society.)

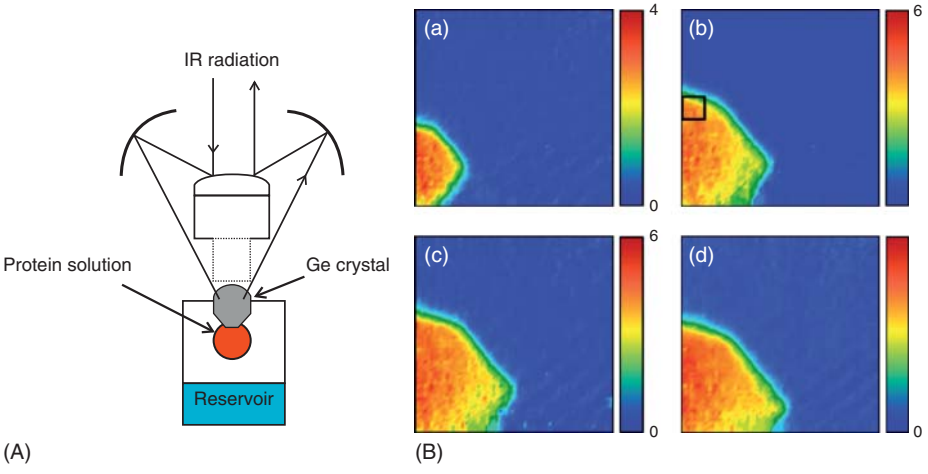

Figure 9.21 (A) Schematic representation of hanging-drop ATR FT-IR imaging. (B) Chemical images of lysozyme crystallization (based on amide II band) as a function of time. (Reprinted from [99]. Copyright 2013, with permission from Elsevier.)

is followed and offers an avenue for further exploration to aid researchers of protein crystallization.

9.3.3 Forensics Applications

9.3.3.1 Imaging of Counterfeit Tablets

Chemical imaging of pharmaceutical tablets is important not just for understanding and optimizing the production of specific pharmaceutical products, as described in Section 9.3.2, but also for the identification of counterfeit tablets. Counterfeit drugs and medicines present a threat to public health. The distribution of counterfeit artesunate antimalarial tablets is rather widespread in certain countries, and there is an urgent need to combat this phenomenon. It is not only important to identify genuine versus counterfeit materials, it would also be of benefit to understand the origin of the fake material. The chemical specificity of the FT-IR imaging approach and nondestructive nature of the ATR approach allows the investigation of these samples without the need to stain or dissolve them. To this end, the combined potential of ATR FT-IR imaging and desorption electrospray-ionization linear ion-trap mass spectrometry applied to counterfeit artesunate tablets was demonstrated [57]. The nondestructive approach of ATR FT-IR imaging was complemented by the high sensitivity of mass spectrometry in the analysis of counterfeit antimalarial tablets. Not only does FT-IR imaging contribute to understanding the chemical composition of tablets but also, as has been described earlier in this chapter, provides

insights into the spatial distribution and, by extension, may reveal the manufacturing processes used. This feature may be particularly useful for designating a batch of tablets as counterfeit or authentic. The advantages of micro-ATR imaging have been used to analyze localized areas of counterfeit tablets with a high spatial resolution to reveal the presence of unexpected and unwanted substances in counterfeit tablets [57]. In the most recent study, macro-ATR FT-IR imaging using a diamond accessory was combined with spatially offset Raman spectroscopy (see Chapter 13 of this book) to analyze both the bulk and surface compositions of counterfeit antimalarial tablets [100]. The depth-profiling power of this Raman technique was combined with the fast imaging capability of macro-ATR FT-IR imaging of relatively large areas. These investigations successfully combined the applications of ATR FT-IR imaging with mass spectrometry and Raman spectroscopy and demonstrated the potential of these methods for forensic investigations of fake medicine [57, 100].

9.3.3.2 Detection of Trace Materials and Chemical Fingerprinting

The detection of trace materials is of importance to forensic experts. For a homogeneous sample, the detection limit of a system is defined by the SNR of the measurement. As a rule of thumb, the SNR should not be <3 for the signal corresponding to a particular substance to be considered detected. For a heterogeneous system, the detection limit, apart from being a function of the SNR, is also determined by the sample volume that is being measured. Thus, a small sample volume would effectively improve the signal and hence the detection limits. This could be achieved by use of an aperture as illustrated schematically in Figure 9.22.

Although the signal is increased by decreasing the sampling volume, the statistical chance of detection is decreased. The reduced aperture also restricts the amount of light reaching the detector which increases the noise level in the measurement. Fast imaging methods without an aperture, such as using the FPA detector, give the opportunity to improve the detection limits for heterogeneous materials without a long measurement time since a full spectrum is produced at each point across the imaging area. A comparison of the detection limit between two FT-IR spectroscopic systems, one using a single-element detector and another using an FPA detector, has shown that the system using the FPA detector has a significantly better detection limit than the single-element detector system when applied to a heterogeneous sample [53]. Notably, the improvement in detection limit when comparing single-element detectors to array detectors

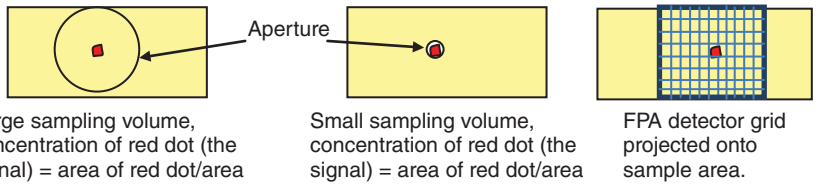

Figure 9.22 Schematic diagram demonstrating how the signal of the same sample may be enhanced by choosing a different sampling volume.

applies to all imaging methods (i.e. ATR, transmission, and transflection, see also Chapter 1 of this book). This feature is particularly important for the detection of trace materials in forensic investigations. The ease of sample preparation together with the power of FT-IR spectroscopy in material characterization makes the ATR FT-IR imaging method a potentially valuable tool in forensic studies [101, 102]. A clear example of the applicability of the approach was highlighted by the detection of small particle residues left on the surface of a finger. The surface of a finger was measured using the ATR FT-IR imaging method after handling some drug particles. A small drug particle, trapped between the ridges of the fingerprint, was imaged and identified by this method (Figure 9.23a,b). The size of the particle was estimated to be a few hundred micrometers and the spectrum extracted from the particle was identified as ibuprofen. The identification of cosmetics from lifted fingerprints has also been shown [103].

ATR FT-IR imaging was then combined with the tape-lifting method when particles were collected from different surfaces with adhesive tape [102]. Recent exciting examples of applications of ATR FT-IR imaging to samples of forensic interest include chemical imaging of latent fingerprint residues [104] rather than imaging of the surface of a finger as described earlier or imaging of developed fingermarks [105]. In this case, a fingerprint is lifted by use of a gelatin tape as is commonly used by scenes of crime officers and is imaged after deposition on an ATR crystal as shown in Figure 9.23c. FT-IR imaging in reflection has also been applied to image latent fingermarks [106]. Chemical images of the fingerprints provide valuable information to forensic scientists about possible chemical changes occurring in the fingerprint residues as a function of time [104]. Fingerprint residues left directly on the surface of the ATR crystal were analyzed with ATR FT-IR imaging as a function of temperature that is important in understanding the evolution of these residues at elevated temperatures. It was also shown to be possible to obtain spatially resolved images of a whole fingerprint by image

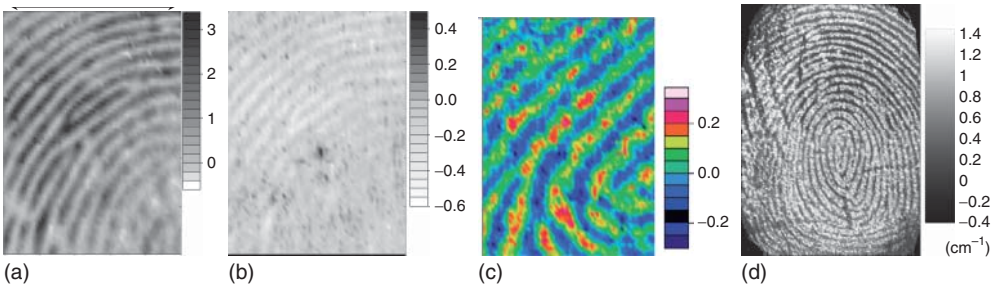

Figure 9.23 ATR FT-IR image of a finger directly on the ATR crystal surface where (a) and (b) represent the protein and ibuprofen distribution, respectively. Image (c) represents the lipid distribution from a fingerprint lifted from a door handle with BVDA gelatin gel-tape. (Reprinted with permission from [101]. Copyright 2013 American Chemical Society.) Image (d) represents the lipid distribution across a whole fingerprint deposited on an ATR crystal by mapping of images. (Reproduced from [48] with permission of the Society for Applied Spectroscopy.)

mapping the area [48]. This was achieved by translating the ATR crystal with the sample deposited on it with an accuracy of ±50 μm. The images were then stitched together with post-analysis software to provide the fully mapped image. In the case of fingerprint analysis, it was possible whether the fingerprint was deposited directly on the ATR crystal (Figure 9.23d) or by analyzing a fingerprint lifted from a banknote by gelatin tape.

9.3.4 Imaging of Live Cells

9.3.4.1 ATR FT-IR Imaging of Live Cells

The analysis of live cells is important in order to understand their behavior under different conditions and their response when exposed to varying environmental factors. Transmission mode measurements of live cells have been achieved by use of a powerful synchrotron IR source, thereby minimizing the problematic effect of intense water absorption in the aqueous environment [107–114]. An alternative method to avoid overexposure of the detector is to use the ATR approach, and this has been achieved for live cellular analysis. In the reported study, both diamond and Ge micro-ATR approaches were described [10]. The micro-ATR approach provides the best spatial resolution in order to study single cells, whereas the increased FOV with diamond ATR allows cell populations to be studied. The experimental approach is shown schematically in Figure 9.24. A small cell chamber was attached to a removable plate containing the Ge ATR crystal in which live cells were seeded. Inverting the chamber allowed the cells to be imaged by the ATR FT-IR approach. The cells adhered to the crystal and the medium remained in place by capillary action. The human cancer cells studied were readily imaged by this approach and their response to environmental stimuli – decreasing intracellular glycogen as a result of cell starvation – was observed.

Rather than culture directly onto an ATR crystal, it has been shown to be possible to approach fixed cells with a slide-on ATR accessory [116]. The advantage of this approach is that it has the potential to study cells by the ATR mode in many different environments and, indeed, an example was shown with fixed cells immersed in water having been imaged. Nevertheless, it remains an important step to apply this methodology to image live cells.

9.3.4.2 Transmission Mode FT-IR Imaging of Live Cells in Microfluidic Devices

Although live adherent cells can be studied upon incubation in medium at an ATR surface as shown, it would be an attractive option to combine the power of FT-IR imaging with microfluidics in order to study cells in controlled but changing environments. There are two potential approaches to this, one is to construct a microfluidics platform directly on top of an ATR crystal, and the other is to design a microfluidics system that is suitable for transmission mode measurements. The transmission mode remains an attractive option because of the potential for improved SNR. As with all transmission mode measurements involving aqueous systems, care must to be taken to ensure very

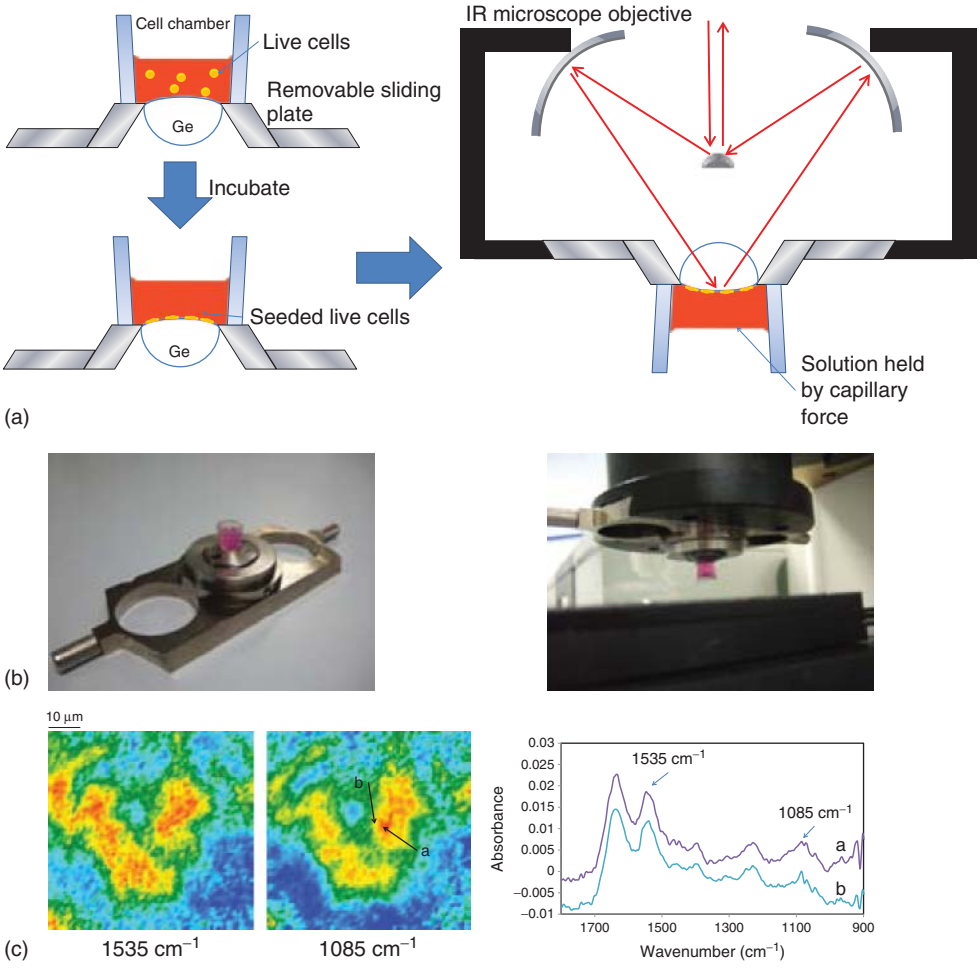

Figure 9.24 (a) Schematic representation of ATR imaging of live cells when seeded on Ge crystal, (b) white light image of an experimental set up, and (c) typical ATR FT-IR images and extracted spectra from the experiment. (Kazarian and Chan [115], 1940, Reproduced by permission of The Royal Society of Chemistry.)

small path lengths, ~10 μm, to avoid overexposure of the detector. The use of a synchrotron source for the measurement of live cells has proven to be a powerful method for cellular analysis (and is covered elsewhere in this edition). Nevertheless, there remain cases when access to a beamline facility is limited while standard transmission methods are available. In these cases, a liquid cell in which live cells incubate can be prepared from microdroplet printing of a fluidics device between two CaF_2 FT-IR windows and studied in transmission mode. Cells can be introduced to the device in cell culture medium and, once adhered, the top window can be added to seal the system. The desired thickness

is achieved by use of a spacer. The sample is then ready for FT-IR imaging analysis.

Care, however, should be taken when using thick IR windows for imaging applications. Although the liquid cell is commonly used in single-spectrum measurements, refraction of light at the IR windows of the liquid cell may have undesirable effects on the spatially resolved spectra in an imaging measurement [117–119]. For most FT-IR imaging measurements, IR light is often focused by optics onto the sample and collected by another set of optics before being directed to the detector. Light therefore approaches the surface of the liquid cell at an angle, and refraction occurs as a result of the difference in refractive index between the window of the liquid cell and air. The refraction is greater when the optics used have higher focusing power, for instance, in an IR microscope. The degree of refraction depends on the refractive index of the window. Since the refractive index of most materials used for the IR windows (e.g., CaF_2) is a function of wavenumber, chromatic dispersion of light occurs when the light enters and exits the window. As a result of this dispersion, IR light at different wavenumbers cannot be focused to the same point such that, when light of smaller wavenumber is in focus, the light with larger wavenumber will be out of focus and vice versa (shown schematically in Figure 9.25) [120]. Strategies to reduce the dispersion of light through a transmission cell include thin CaF_2 windows [119] or thin diamond windows [121]. Diamond is advantageous because of its relatively constant refractive index in the mid-IR region. Another method to completely eliminate the dispersion through the liquid cell using a window of ordinary thickness (~4 mm) has been recently introduced [120]. This method involves the use of a lens that creates a hemisphere above the sample when placed on the window to remove refraction such that the chromatic dispersion effect is eliminated when light passes through the transmission cell. The lens, made of the same materials as the window, was placed on the top side of the transmission cell window so that the IR light does not refract when it leaves the liquid cell, as shown in Figure 9.25. In the case of a microfluidics-based liquid cell for use in an FT-IR microscope for sample imaging, a hemispherical lens is created on both top and bottom of the device. The effect of the pseudosphere on correcting chromatic aberration and inducing a magnifying effect is shown in Figure 9.26. In the absence of the pseudosphere, when the sample is focused with white light, the lipid and amide bands of the cells seen by their distribution are diffuse across the sample area. These diffuse areas correspond, generally, to the location of the cell population but selecting specific areas would be challenging. In contrast, the images obtained when the pseudosphere was used are striking in the clarity with which the white light, lipid, and protein regions are coincident. Clearly, the potential impact on single cell studies is highlighted by these results, although care will need to be taken to ensure that any single cell work is conducted in regions where only a single cell is observed by white light.

In fact, this approach has been applied to image single cells trapped in droplets of Dulbecco's phosphate-buffered saline (DPBS) in oil with the potential to extend the methodology to study single cell dynamics as discussed in Section 9.3.5.2.

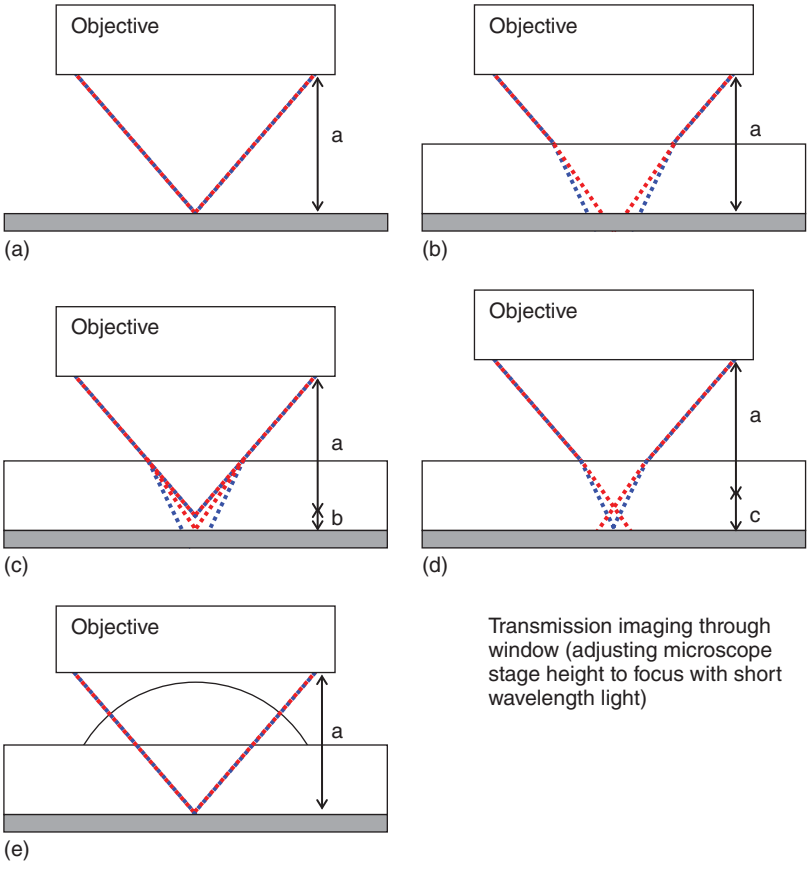

Figure 9.25 Schematic representation of the use of a lens to form a hemisphere and thereby eliminate chromatic aberration at thick infrared transparent windows. (Figure reproduced from Ref. [120] with permission from the American Chemical Society.)

9.3.5
High-Throughput Studies with ATR FT-IR Imaging

The possibility of applying chemical imaging in ATR mode to high-throughput analysis of pharmaceutical formulations has been demonstrated [34, 49, 122, 123]. It should be noted that the FT-IR mapping [124, 125] and also Raman spectroscopic mapping approaches also can be used in high-throughput applications. However, the use of mapping approaches means that sample measurements are not carried out simultaneously, a key advantage of the FT-IR imaging approach. FT-IR imaging of many solid samples in transmission may be challenging due to the need to prepare all samples with precise and small thickness (since thick samples may absorb too much IR light). Possible variations in the sample thickness and therefore pathlength would affect the quantitation of the analysis. ATR FT-IR

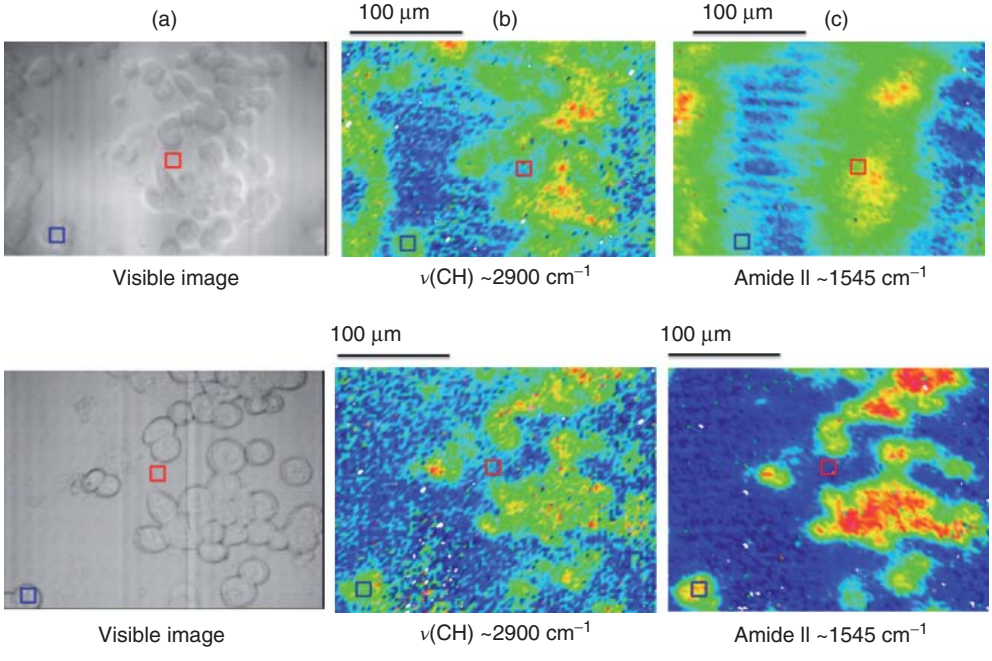

Figure 9.26 Row A presents results of transmission mode FT-IR images compared with white light image. Row B presents transmission mode FT-IR images when a pseudosphere is employed to correct chromatic aberration. (Adapted from [115] – Reproduced by permission of The Royal Society of Chemistry.)

imaging, however, is particularly amenable to high-throughput analysis due to the highly reproducible small pathlength, which is independent of sample preparation. High-throughput studies of the behavior of many different pharmaceutical formulations under different humidities are needed for the design of tablets for drug release and for finding ways to extend the shelf-life of pharmaceuticals.

This was successfully achieved using a drop-on-demand device by preparing arrays of microdrop samples directly on the surface of the ATR crystal. The development of the macro-ATR FT-IR imaging approach allowed us to study simultaneously more than 100 samples deposited on the surface of the ATR crystal under a controlled environment. Using this approach, it was possible to obtain "chemical snapshots" from a spatially defined array of many different polymer/drug formulations under identical conditions. This high-throughput approach informed us of the specific weight fraction of a drug, nifedipine, in a PEG matrix, which should not be exceeded during the formulation preparation in order to avoid crystallization of nifedipine [34]. This method provides a direct measurement of material properties for high-throughput formulation design and optimization. The simultaneous response (water sorption, crystallization, etc.) of the array of formulations to the environmental parameters was also studied. Expanding the methodology

further, a novel ATR accessory was designed and applied to obtain the IR spectra of more than 150 miniature samples simultaneously [49]. This approach could enable the measurement of up to 1024 samples. The introduction of this new accessory with an expanded FOV provided an opportunity to combine ATR FT-IR spectroscopic imaging with a multichannel grid that allowed simultaneous imaging of the dissolution of several different formulations. Different molecular weights of PEG, with or without the addition of ibuprofen, have been used as model pharmaceutical formulations, and chemical imaging of the simultaneous dissolution of five different formulations of PEG/ibuprofen was demonstrated. The use of a PDMS grid to serve as sample support plate has also been realized. Figure 9.27 shows one of the PDMS grids prepared that could be used for the imaging of many liquid samples simultaneously.

9.3.5.1 Transmission Mode High-Throughput Imaging

Despite the challenges of using FT-IR imaging in transmission for high-throughput analysis of pharmaceutical formulations, a novel approach that allowed macro FT-IR imaging in transmission of samples under a controlled environment has been demonstrated [123, 126]. This approach required construction of an optical accessory that enables the measurement of samples placed in a horizontal position in the macrochamber of the imaging system. The accessory expands the range of possible applications of macro FT-IR imaging studies. A combination of an accessory with a controlled humidity cell provided an opportunity to obtain chemical images of large areas of the samples under controlled humidity. The approach was applied to study the effect of humidity on the polymorphic transitions of a thin film of amorphous nifedipine [126]. It has been shown that exposure of the drug to the conditions of the experiment for 4 h resulted in the transition of the drug from the amorphous to the β-crystalline

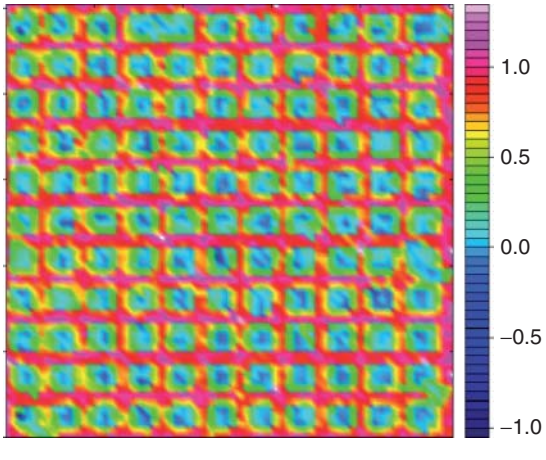

Figure 9.27 ATR FT-IR image of the grid made of PDMS containing the wells for 121 samples. The red lines show the walls of the PDMS grid.

form while further exposure for several hours resulted in the conversion from the β- to the α-form. It was also demonstrated, by monitoring *in situ* the crystallization of a series of different amorphous drugs simultaneously [123], that high-throughput FT-IR transmission imaging is possible using a 128×128 FPA detector. To avoid the problematic effect of varying sample thickness on the imaging results, the wavenumber position of characteristic vibrational bands was used to generate the chemical image rather than their integrated absorbance. Since the wavenumber corresponding to peak maxima of the ν(N–H) vibrational mode is sensitive to the formation of the various crystalline polymorphs of the studied drugs [123], changes in the band position indicated structural changes of the drug, which were not dependent on sample thickness. As such, this method could be applied in the transmission mode without challenging sample preparation.

9.3.5.2 Imaging and Microfluidics

Exciting opportunities for research exist with the combination of microfluidics devices with chemical imaging. This approach could serve as a new microfluidics platform with a powerful chemical imaging detection method [127]. Chemical and quantitative analyses of dynamic systems will certainly play an important role in the further development of microfluidics. The use of chemical imaging offered by ATR FT-IR imaging allows the simultaneous analysis of fluid composition as a function of spatial position for better understanding the dynamic properties of reactive systems. Chemical imaging will enhance the ability to utilize very small amounts of materials and fluids for new technologies because it is possible to obtain "chemical snapshots" from microarrays of samples or multichannel microsystems [49] for rapid process control and analysis. Separations using microfluidics are also set to benefit from *in situ* chemical imaging analysis with IR array detectors. This approach is also the first example of the application of spectroscopic imaging to microfluidics and may broaden its future use in miniaturized high-throughput devices [127].

To prove the principle of combining microfluidics with ATR FT-IR imaging, a device was prepared from PDMS onto a ZnSe ATR prism and enclosed with a thin layer of poly(methyl methacrylate), shown schematically in Figure 9.28A. To prove the efficacy of this approach, H_2O and D_2O were each introduced to the device at a flowrate of $50\,\mu l\,h^{-1}$ and imaged. Since hydrogen–deuterium exchange occurs upon mixing of H_2O and D_2O to form HDO, and since laminar flow is achieve and therefore mixing occurs by diffusion, it was possible to image HDO formation as a function of diffusion upon passage through the device (Figure 9.23b) [44].

Transmission mode FT-IR imaging of microfluidic devices remains attractive because it is important to be able to spectroscopically access the full flow of the system. Certain flow regimes, droplets in oil for instance, can produce results that are obscured by the ATR approach as the depth of penetration may not reach the aqueous droplet and could instead image only the carrier fluid, providing insufficient information about the desired system.

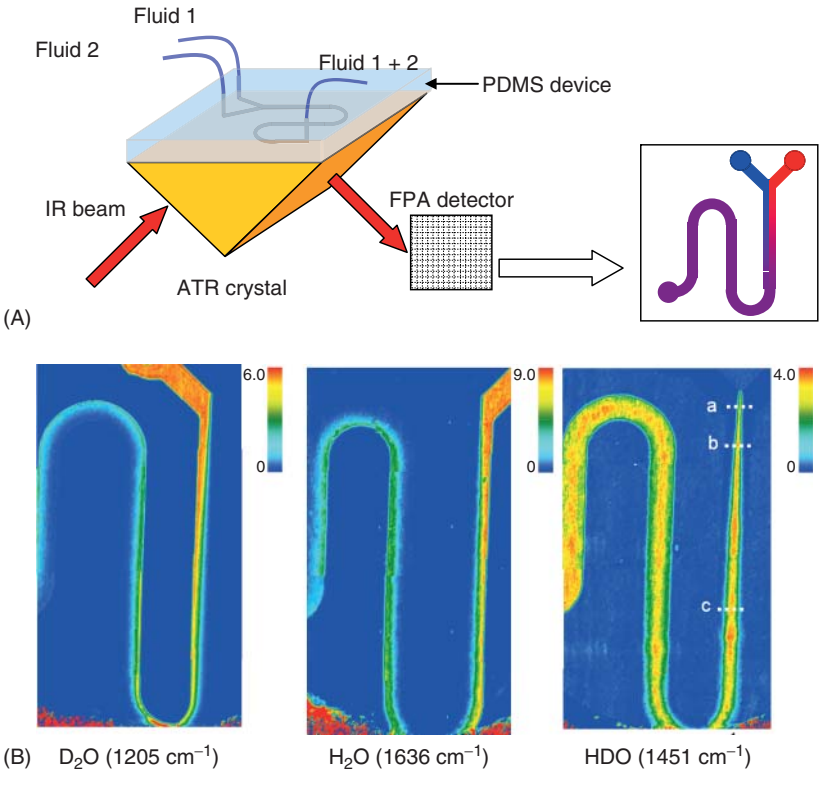

Figure 9.28 (A) Schematic representation of PDMS microfluidic device on ZnSe ATR prism and mixing setup. (B) ATR FT-IR images (a–c) show the abundance of D_2O, H_2O, and HDO, respectively. (Chan *et al.* [44] – Reproduced by permission of The Royal Society of Chemistry.)

As such an alternative method of preparing microfluidic devices for transmission FT-IR imaging was developed. Devices were built between IR transparent windows by a fast prototyping method [45]. To achieve this, paraffin wax droplets were deposited onto one of the IR transparent windows by a microdroplet printer, such that mild compression on top by a second window formed sealed channels as depicted in Figure 9.29A. The flow regime can be easily adjust between laminar and segmented flow [128]. To show this, two experiments were conducted – one with benzoic acid and sodium phosphate solution introduced via the plain T-junction setup, and the other where benzoic acid and sodium phosphate are introduced to one another via a nozzle junction that creates segmented flow (Figure 9.29B,C). The subsequent imaging analyses showed that a neutralization process could be visualized by this method, with concentration profiles readily extracted – this could have an impact on reaction modeling within microfluidic devices.

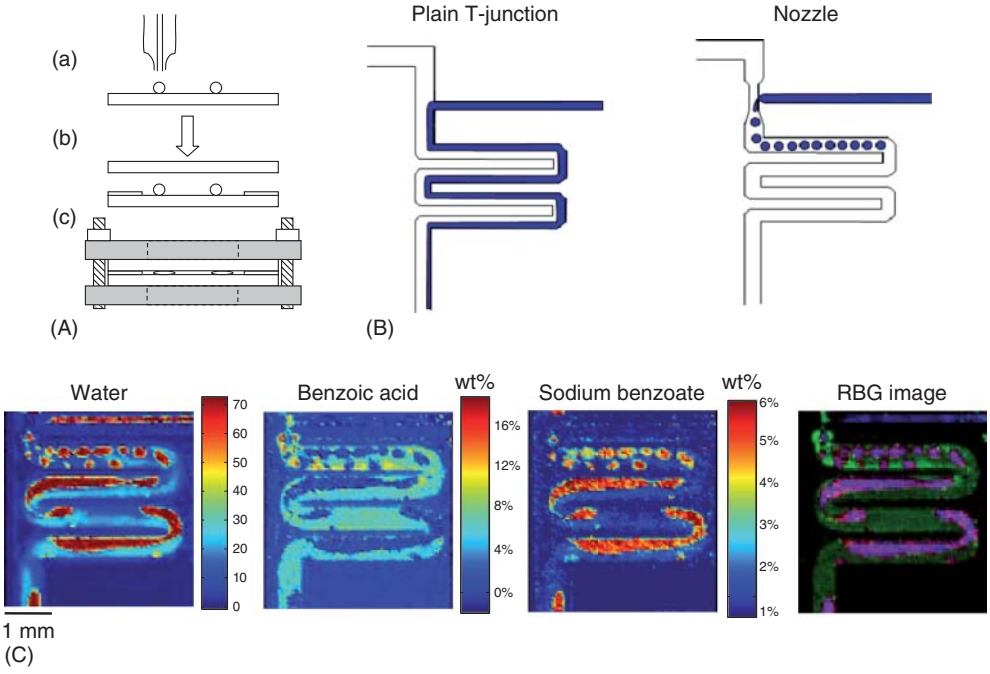

Figure 9.29 (A) Schematic representation of the microdrop deposition method used to prepare microfluidic devices sandwiched between IR transparent windows. (Chan and Kazarian [45] – Reproduced by permission of The Royal Society of Chemistry). (B) The flow regimes used. (C) An example of IR-imaged droplet flow is shown – the component that has been false color scaled is indicated above each image. (B and C reprinted with permission from [128]. Copyright 2013 American Chemical Society.)

The methodology has been extended beyond chemical photography and has allowed the generation of "chemical movies" [46]. In this case, water was introduced to oil flow at a rate such that droplets were formed. Fast imaging was achieved with an image acquisition time of 50 ms and temporal resolution of 120 ms. Streaming this process allows the droplet flow to be viewed as a chemical movie and is an exciting opportunity for investigating rapid dynamic systems.

A further extension of the droplet in oil flow regime was applied to study cells in a microfluidics system [115]. Cells in medium were introduced to a device prepared such that the flow of the oil and medium created droplets in flow. In this case, longer acquisition times were required than for the "chemical movies" described earlier. In fact, it is necessary to bring flow to a halt in order to image a cell in the droplet. A schematic illustration of the scheme is shown in Figure 9.30 along with images obtained by integrating the amide II band that is indicative of the presence of proteins. Clearly, the cells could not be visualized in the absence of the pseudosphere approach described in Section 9.3.4.2. However, the use of the pseudosphere does allow a single cell in a single droplet of medium in oil to be imaged within a microfluidics device. It is very exciting that this method

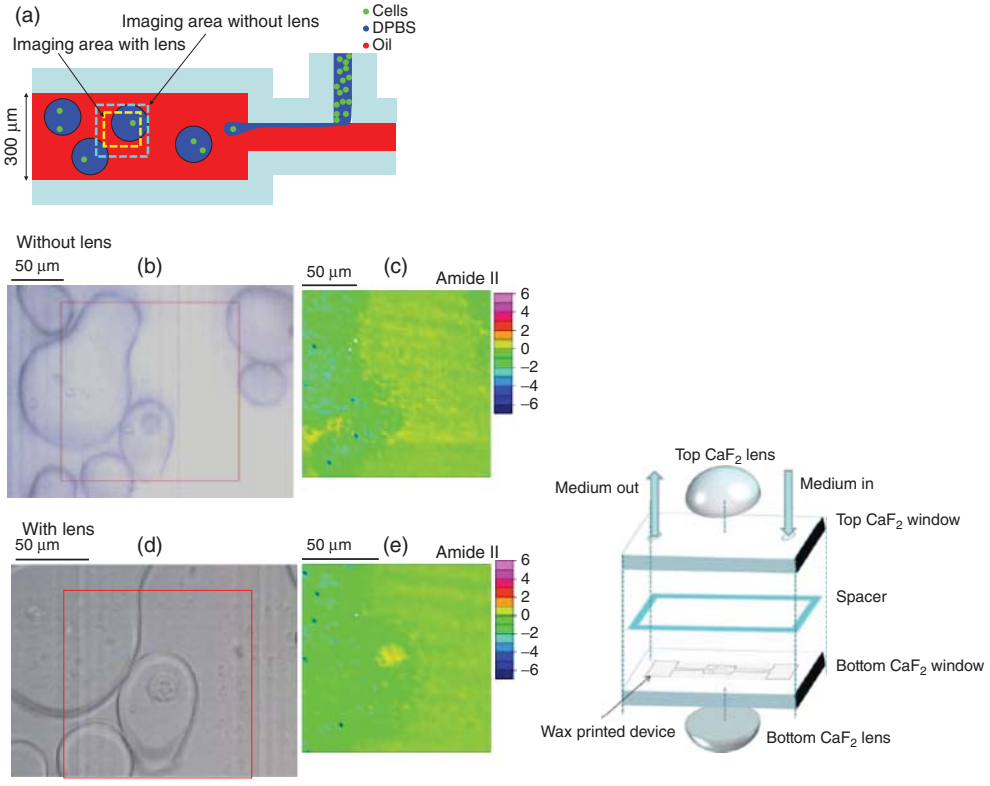

Figure 9.30 Representation of the microfluidic design to create aqueous droplets containing cells in oil flow. White light and FT-IR images obtained in transmission with and without the pseudosphere employed to correct chromatic aberration. Note that the FT-IR transmission images are plotted using the integrated absorbance of the amide II band, which is an indicative of proteins. This cannot be seen in the image generated without recourse to the pseudosphere. (Adapted from [115] – Reproduced by permission of The Royal Society of Chemistry.)

allows cells to be studied, temporally resolved, in a microenvironment where one could imagine studying their reaction to treatment over a period of time. As the analysis method is nondestructive, the cells could, in principle, be retained after the imaging experiment for further research.

9.4 Conclusion and Outlook

In this chapter, we have presented some of the recent developments and applications of ATR FT-IR imaging to pharmaceutical samples, materials development, and biomedical applications. The use of both micromode and macromode in ATR FT-IR imaging has been discussed as have relevant examples of transmission

mode imaging. Imaging in ATR mode is very versatile and allows different spatial resolution and fields of view to be exploited. It is important to remember that ATR imaging is a surface technique, providing information about the layer of the sample at the ATR crystal interface. The thickness of this layer ranges from a fraction of a micrometer to several micrometers. Chemical images can be obtained from layers of different thickness in this range using an accessory with variable angles of incidence. This allows one to combine chemical imaging with depth profiling, which is important for heterogeneous materials, for example, for biomedical materials. The spatial resolution in the *z*-direction, which is perpendicular to the plane of the imaged area, is not limited by diffraction but is determined by the depth of penetration that can be changed by varying the angle of incidence. One significant advantage of the small depth of penetration of ATR FT-IR spectroscopy is the ability to study materials, which are, by necessity, in close contact with high absorbing species. This has allowed the study of aqueous samples related to drug dissolution or the chemical imaging of live cells. As demonstrated in this chapter, the main advantage of chemical imaging using an FPA detector lies in the study of dynamic systems, such as diffusion, dissolution, or coupling with microfluidic devices. Significant potential exists in the application of FT-IR imaging and in particular ATR FT-IR imaging to high-throughput analysis of many samples. ATR FT-IR imaging under a controlled environment is beneficial for studying many samples as has been discussed here including pharmaceutical formulations, biopharmaceuticals, human tissue, and live cell analysis.

The enhanced spatial resolution of micro-ATR FT-IR imaging offers benefits to many areas of research ranging from polymeric materials to biomedical and forensic sciences. However, further improvements in spatial resolution using FT-IR imaging would be an important development of the technique. Recent reports using AFM to detect IR absorbance as a result of the photothermal effect offer an opportunity to further enhance resolution [129, 130] though it currently operates in a restricted wavelength range. Transmission mode imaging of live cells in microfluidics devices is an exciting field of study that could be improved by the development of brighter sources (such as quantum cascade lasers) or improved optics but in the meantime will be of interest to study cell fate. The further extension of ATR FT-IR 3D imaging on the nanoscale to pharmaceuticals or biomedical samples is an attractive opportunity that could increase our understanding of these complex systems. Surface-enhanced IR imaging is another area that may provide additional avenues for exploration.

Acknowledgment

SGK acknowledges the research funding from the European Research Council under the European Community's Seventh Framework Programme (FP7/2007-2013)/ERC advanced grant agreement no. [227950].

References

1. Harrick, N.J. (1976) *Internal Reflection Spectroscopy*, John Wiley & Sons, Inc., New York.
2. Kazarian, S.G. and Higgins, J.S. (2002) A closer look at polymers. *Chem. Ind.*, (10), 21–23.
3. Kazarian, S.G. and Chan, K.L.A. (2010) Micro- and macro-attenuated total reflection Fourier transform infrared spectroscopic imaging. *Appl. Spectrosc.*, **64** (5), 135A–152A.
4. Gupper, A. *et al.* (2002) Combined application of imaging methods fot the characterisation of a polymer blend. *Appl. Spectrosc.*, **56**, 1515–1523.
5. Kazarian, S.G. and Chan, K.L.A. (2006) Sampling approaches in Fourier transform infrared imaging applied to polymers. *Prog. Colloid Polym. Sci.*, **132** (206), 1–6.
6. Burka, E.M. and Curbelo, R. (2000) Imaging ATR spectrometer. US Patent 6141100.
7. Sommer, A.J. *et al.* (2001) Attenuated total internal reflection infrared mapping microspectroscopy using an imaging microscope. *Appl. Spectrosc.*, **55** (3), 252–256.
8. Chan, K.L.A. and Kazarian, S.G. (2003) New opportunities with micro and macro ATR-IR spectroscopic imaging: spatial resolution and sampling versatility. *Appl. Spectrosc.*, **57**, 381–389.
9. Van der Weerd, J. and Kazarian, S.G. (2004) Validation of macroscopic attenuated total reflection-Fourier transform infrared imaging to study dissolution of swelling pharmaceutical tablets. *Appl. Spectrosc.*, **58** (12), 1413–1419.
10. Kuimova, M.K., Chan, K.L.A., and Kazarian, S.G. (2009) Chemical imaging of live cancer cells in the natural aqueous environment. *Appl. Spectrosc.*, **63** (2), 164–171.
11. Nasse, M.J. *et al.* (2011) High-resolution Fourier-transform infrared chemical imaging with multiple synchrotron beams. *Nat. Methods*, **8** (5), 413–458.
12. Paschalis, E.P. *et al.* (2001) Spectroscopic characterization of collagen cross-links in bone. *J. Bone Miner. Res.*, **16** (10), 1821–1828.
13. Diem, M. *et al.* (2004) A decade of vibrational micro-spectroscopy of human cells and tissue (1994-2004). *Analyst*, **129** (10), 880–885.
14. Krafft, C. *et al.* (2006) Identification of primary tumors of brain metastases by SIMCA classification of IR spectroscopic images. *Biochim. Biophys. Acta, Biomembr.*, **1758** (7), 883–891.
15. Bhargava, R. (2007) Towards a practical Fourier transform infrared chemical imaging protocol for cancer histopathology. *Anal. Bioanal. Chem.*, **389** (4), 1155–1169.
16. Bird, B. *et al.* (2009) Detection of breast micro-metastases in axillary lymph nodes by infrared micro-spectral imaging. *Analyst*, **134** (6), 1067–1076.
17. Giorgini, E. *et al.* (2010) Effects of Lactobacillus rhamnosus on zebrafish oocyte maturation: an FTIR imaging and biochemical analysis. *Anal. Bioanal. Chem.*, **398** (7-8), 3063–3072.
18. Krafft, C. *et al.* (2007) Differentiation of individual human mesenchymal stem cells probed by FTIR microscopic imaging. *Analyst*, **132** (7), 647–653.
19. Bird, B. *et al.* (2011) Spectral detection of micro-metastases and individual metastatic cells in lymph node histology. *Technol. Cancer Res. Treat.*, **10** (2), 135–144.
20. Koenig, J. (2002) FTIR imaging of polymer dissolution. *Adv. Mater.*, **14**, 457–460.
21. Artyushkova, K. *et al.* (2001) Direct correlation of x-ray photoelectron spectroscopy and Fourier transform infrared spectra and images from poly(vinyl chloride)/poly(methyl methacrylate) polymer blends. *J. Vac. Sci. Technol., A*, **19**, 2791–2799.
22. Bhargava, R., Wang, S.-Q., and Koenig, J.L. (2003) FTIR microspectroscopy of polymeric systems. *Adv. Polym. Sci.*, **163**, 137–191.
23. Koenig, J.L. and Bobiak, J.P. (2007) Raman and infrared imaging of dynamic polymer systems. *Macromol. Mater. Eng.*, **292** (7), 801–816.

24. Miller-Chou, B.A. and Koenig, J.L. (2003) A review of polymer dissolution. *Prog. Polym. Sci.*, **28**, 1223–1270.
25. Esaki, Y., Nakai, K., and Araga, T. (1993) Development of attenuated total reflection prism for IR microscopy and some applications to local analysis. *Bunseki Kagaku*, **42** (3), 127–132.
26. Esaki, Y., Yokokawa, K., and Araga, T. (1993) Accessory and crystalline element for attenuated total reflection infrared spectroscopy. US Patent 5216244.
27. Lewis, L.L. and Sommer, A.J. (2000) Attenuated total internal reflection infrared mapping microspectroscopy of soft materials. *Appl. Spectrosc.*, **54** (2), 324–330.
28. Patterson, B.M. and Havrilla, G.J. (2006) Attenuated total internal reflection infrared microspectroscopic imaging using a large-radius germanium internal reflection element and a linear array detector. *Appl. Spectrosc.*, **60** (11), 1256–1266.
29. Patterson, B.M. *et al.* (2007) Infrared microspectroscopic imaging using a large radius germanium internal reflection element and a focal plane array detector. *Appl. Spectrosc.*, **61** (11), 1147–1152.
30. Kazarian, S.G. and Chan, K.L.A. (2003) "Chemical photography" of drug release. *Macromolecules*, **36**, 9866–9872.
31. Snively, C.M., Oskarsdottir, G., and Lauterbach, J. (2001) Chemically sensitive parallel analysis of combinatorial catalyst libraries. *Catal. Today*, **67** (4), 357–368.
32. Snively, C.M., Oskarsdottir, G., and Lauterbach, J. (2001) Parallel analysis of the reaction products from combinatorial catalysts libraries. *Angew. Chem. Int. Ed.*, **40**, 3028–3030.
33. Kubanek, P. *et al.* (2004) Imaging reflection IR spectroscopy as a tool to achieve higher integration for high-throughput experimentation in catalysis research. *J. Comb. Chem.*, **6** (3), 420–425.
34. Chan, K.L.A. and Kazarian, S.G. (2005) FTIR imaging for high-throughput analysis of pharmaceutical formulations. *J. Comb. Chem.*, **7**, 185–189.
35. Colley, C.S. *et al.* (2004) Spectroscopic imaging of arteries and atherosclerotic plaques. *Biopolymers*, **74** (4), 328–335.
36. Randle, W.L. *et al.* (2007) Integrated 3D expansion and osteogenic differentiation of murine embryonic stem cells. *Tissue Eng.*, **13**, 2957–2970.
37. Dehghani, F. *et al.* (2008) Effect of dense gas CO_2 on the coacervation of elastin. *Biomacromolecules*, **9** (4), 1100–1105.
38. Kazarian, S.G. and Chan, K.L.A. (2006) Applications of ATR-FTIR spectroscopic imaging to biomedical samples. *Biochim. Biophys. Acta, Biomembr.*, **1758** (7), 858–867.
39. Steiner, G. *et al.* (2007) Conformational changes during protein adsorption. FT-IR spectroscopic imaging of adsorbed fibrinogen layers. *Anal. Chem.*, **79** (4), 1311–1316.
40. Snively, C.M. and Koenig, J.L. (1999) Studying anomalous diffusion in a liquid crystal/polymer system using fast FTIR imaging. *J. Appl. Polym. Sci. B: Polym. Phys.*, **37**, 2261–2268.
41. Ribar, T., Bhargava, R., and Koenig, J.L. (2000) FT-IR imaging of polymer dissolution by solvent mixture. 1. Solvents. *Macromolecules*, **33**, 8842–8849.
42. Gupper, A. and Kazarian, S.G. (2005) Study of solvent diffusion and solvent-induced crystallization in syndiotactic polystyrene using FT-IR spectroscopy and imaging. *Macromolecules*, **38** (6), 2327–2332.
43. Gupper, A., Chan, K.L.A., and Kazarian, S.G. (2004) FT-IR imaging of solvent-induced crystallization in polymers. *Macromolecules*, **37** (17), 6498–6503.
44. Chan, K.L.A. *et al.* (2009) Chemical imaging of microfluidic flows using ATR-FTIR spectroscopy. *Lab Chip*, **9**, 2909–2913.
45. Chan, K.L.A. *et al.* (2010) Rapid prototyping of microfluidic devices for integrating with FT-IR spectroscopic imaging. *Lab Chip*, **10** (16), 2170–2174.

46. Chan, K.L.A. *et al.* (2011) Generation of chemical movies: FT-IR spectroscopic imaging of segmented flows. *Anal. Chem.*, **83** (9), 3606–3609.
47. Biswal, D. and Hilt, J.Z. (2006) Microscale analysis of patterning reactions via FTIR imaging: application to intelligent hydrogel systems. *Polymer*, **47** (21), 7355–7360.
48. Chan, K.L.A. and Kazarian, S.G. (2008) ATR-FTIR imaging of large areas using inverted prism crystals and combining imaging and mapping. *Appl. Spectrosc.*, **62** (10), 1095–1101.
49. Chan, K.L.A. and Kazarian, S.G. (2006) ATR-FTIR spectroscopic imaging with expanded field of view to study formulations and dissolution. *Lab Chip*, **6** (7), 864–870.
50. Chan, K.L.A. and Kazarian, S.G. (2007) Attenuated total reflection Fourier transform infrared imaging with variable angles of incidence: a three-dimensional profiling of heterogeneous materials. *Appl. Spectrosc.*, **61** (1), 48–54.
51. Chan, K.L.A., Hammond, S.V., and Kazarian, S.G. (2003) Applications of attenuated total reflection infrared spectroscopic imaging to pharmaceutical formulations. *Anal. Chem.*, **75** (9), 2140–2146.
52. Dumas, P. *et al.* (2004) Imaging capabilities of synchrotron infrared microspectroscopy. *Faraday Discuss.*, **126**, 289–302.
53. Chan, K.L.A. and Kazarian, S.G. (2006) Detection of trace materials with Fourier transform infrared spectroscopy using a multi-channel detector. *Analyst*, **131** (1), 126–131.
54. Kazarian, S.G. *et al.* (2004) Characterisation of bioactive and resorbable polylactide/Bioglasss composites by FTIR spectroscopic imaging. *Biomaterials*, **25**, 3931–3938.
55. Chan, K.L.A. *et al.* (2005) Fourier transform infrared imaging of human hair with a high spatial resolution without the use of a synchrotron. *Appl. Spectrosc.*, **59** (2), 149–155.
56. Ricci, C., Bloxham, S., and Kazarian, S.G. (2007) ATR-FTIR imaging of albumen photographic prints. *J. Cultur. Herit.*, **8** (4), 387–395.
57. Ricci, C. *et al.* (2007) Combined Fourier-transform infrared imaging and desorption electrospray-ionization linear ion-trap mass spectrometry for analysis of counterfeit antimalarial tablets. *Anal. Bioanal. Chem.*, **387** (2), 551–559.
58. Goodall, R.A. *et al.* (2008) Micro-attenuated total reflection spectral imaging in archaeology: application to maya paint and plaster wall decorations. *Appl. Spectrosc.*, **62** (1), 10–16.
59. Everall, N.J. and Bibby, A. (1997) Improvements in the use of attenuated total reflection Fourier transform infrared dichroism for measuring surface orientation in polymers. *Appl. Spectrosc.*, **51**, 1083–1091.
60. Kazarian, S.G., Brantley, N.H., and Eckert, C.A. (1999) Applications of vibrational spectroscopy to characterise poly(ethylene terephthalate) processed with supercritical CO_2. *Vib. Spectrosc.*, **19**, 277–283.
61. Kazarian, S.G. and Martirosyan, G.G. (2002) Spectroscopy of polymer/drug formulations processed with supercritical fluids: in situ ATR-IR and Raman study of impregnation of ibuprofen into PVP. *Int. J. Pharm.*, **232**, 81–90.
62. Kazarian, S.G. *et al.* (2001) The potential of ATR-IR spectroscopy in applications to supercritical fluids and liquefied gases. *Am. Lab.*, **33** (16), 44–49.
63. Flichy, N.M.B. *et al.* (2002) An ATR-IR study of poly(dimethylsiloxane) under high-pressure carbon dioxide: simultaneous measurement of sorption and swelling. *J. Phys. Chem. B*, **106**, 754–759.
64. Kazarian, S.G. and Chan, K.L.A. (2004) FTIR imaging of polymeric materials under high-pressure carbon dioxide. *Macromolecules*, **37**, 579–584.
65. Thomson, G. and Poulter, G. (2006) Spectrometer apparatus. US Patent 261274.
66. Ekgasit, S. and Ishida, H. (1997) New optical depth-profiling technique by

use of the multiple-frequency approach with single ATR FT-IR spectrum: theoretical development. *Appl. Spectrosc.*, **51** (10), 1488–1495.

67. Fina, L.J. and Gangchi, C. (1991) Quantitative depth profiling with Fourier transform infrared spectroscopy. *Vib. Spectrosc.*, **1**, 353–361.
68. Shick, R.A., Koenig, J.L., and Isihida, H. (1993) Theoretical development for depth profiling of stratified layers using variable-angle ATR. *Appl. Spectrosc.*, **47** (8), 1237–1244.
69. Kirov, K.R. and Assender, H.E. (2004) Quantitative ATR-IR analysis of anisotropic polymer films: extraction of optical constants. *Macromolecules*, **37**, 894–904.
70. Frosch, T. *et al.* (2010) Nondestructive three-dimensional analysis of layered polymer structures with chemical imaging. *Langmuir*, **26** (24), 19027–19032.
71. Tay, F.H. and Kazarian, S.G. (2009) Study of petroleum heat-exchanger deposits with ATR-FTIR spectroscopic imaging. *Energy Fuel*, **23** (8), 4059–4067.
72. Boulet-Audet, M. *et al.* (2010) Quantitative determination of band distortions in diamond attenuated total reflectance infrared spectra. *J. Phys. Chem. B*, **114** (24), 8255–8261.
73. Van der Weerd, J. and Kazarian, S.G. (2004) Combined approach of FTIR imaging and conventional dissolution tests applied to drug release. *J. Control. Release*, **98** (2), 295–305.
74. Fleming, O.S., Chan, K.L.A., and Kazarian, S.G. (2006) High-pressure CO_2-enhanced polymer interdiffusion and dissolution studied with in situ ATR-FTIR spectroscopic imaging. *Polymer*, **47** (13), 4649–4658.
75. Wessel, E. *et al.* (2006) Observation of a penetration depth gradient in attenuated total reflection Fourier transform infrared spectroscopic imaging applications. *Appl. Spectrosc.*, **60** (12), 1488–1492.
76. Zhong, X. *et al.* (2011) Fabrication of chitosan/poly(epsilon-caprolactone) composite hydrogels for tissue engineering applications. *J. Mater. Sci. - Mater. Med.*, **22** (2), 279–288.
77. Van der Weerd, J., Chan, K.L.A., and Kazarian, S.G. (2004) An innovative design of compaction cell for in situ FTIR imaging of tablet dissolution. *Vib. Spectrosc.*, **35**, 9–13.
78. Chan, K.L.A., Elkhider, N., and Kazarian, S.G. (2005) Spectroscopic imaging of compacted pharmaceutical tablets. *Chem. Eng. Res. Des.*, **83** (A11), 1303–1310.
79. Van der Weerd, J. and Kazarian, S.G. (2005) Release of poorly soluble drugs from HPMC tablets studied by FTIR imaging and flow-through dissolution tests. *J. Pharm. Sci.*, **94** (9), 2096–2109.
80. Elkhider, N., Chan, K.L.A., and Kazarian, S.G. (2007) Effect of moisture and pressure on tablet compaction studied with FTIR spectroscopic imaging. *J. Pharm. Sci.*, **95** (2), 351–360.
81. Wray, P. *et al.* (2008) Compaction of pharmaceutical tablets with different polymer matrices studied by FTIR imaging and X-ray microtomography. *J. Pharm. Sci.*, **97** (10), 4269–4277.
82. Chan, K.L.A. and Kazarian, S.G. (2004) FTIR spectroscopic imaging of dissolution of a solid dispersion of nifedipine in poly(ethylene glycol). *Mol. Pharm.*, **1**, 301–305.
83. Wray, P.S., Clarke, G.S., and Kazarian, S.G. (2011) Application of FTIR spectroscopic imaging to study the effects of modifying the pH microenvironment on the dissolution of ibuprofen from HPMC matrices. *J. Pharm. Sci.*, **100** (11), 4745–4755.
84. Kazarian, S.G. *et al.* (2005) Spectroscopic imaging applied to drug release. *Food Bioprod. Process.*, **83** (C2), 127–135.
85. Kazarian, S.G. and Ewing, A.V. (2013) Applications of Fourier transform infrared spectroscopic imaging to tablet dissolution and drug release. *Expert Opin. Drug Discovery*, **10**, 1207–1221.
86. Coutts-Lendon, C.A. *et al.* (2003) The use of FT-IR imaging as an analytical tool for the characterization of drug delivery systems. *J. Control. Release*, **93** (3), 223–248.
87. Chan, K.L.A. and Kazarian, S.G. (2004) FTIR spectroscopic imaging of dissolution of a solid dispersion of nifedipine

in poly(ethylene glycol). *Mol. Pharm.*, **1** (4), 331–335.
88. van der Weerd, J. and Kazarian, S.G. (2007) in *Techniques and Applications of Hyperspectral Image Analysis* (eds H.F. Grahn and P. Geladi), John Wiley & Sons, Ltd, Chichester, pp. 221–260.
89. Kazarian, S.G. and van der Weerd, J. (2008) Simultaneous FTIR spectroscopic imaging and visible photography to monitor tablet dissolution and drug release. *Pharm. Res.*, **25** (4), 853–860.
90. Kimber, J.A., Kazarian, S.G., and Stepanek, F. (2013) Formulation design space analysis for drug release from swelling polymer tablets. *Powder Technol.*, **236**, 179–187.
91. Velasco, D. *et al.* (2011) pH-sensitive polymer hydrogels derived from morpholine to prevent the crystallization of ibuprofen. *J. Control. Release*, **149** (2), 140–145.
92. Palombo, F. *et al.* (2009) Measurement of drug and macromolecule diffusion across atherosclerotic rabbit aorta ex vivo by attenuated total reflection-Fourier transform infrared imaging. *J. Biomed. Opt.*, **14** (4), 044008.
93. Boncheva, M., Tay, F.H., and Kazarian, S.G. (2008) Application of attenuated total reflection Fourier transform infrared imaging and tape-stripping to investigate the three-dimensional distribution of exogenous chemicals and the molecular organization in Stratum corneum. *J. Biomed. Opt.*, **13** (6), 064009.
94. Andanson, J.M., Hadgraft, J., and Kazarian, S.G. (2009) In situ permeation study of drug through the stratum corneum using attenuated total reflection Fourier transform infrared spectroscopic imaging. *J. Biomed. Opt.*, **14** (3), 034011.
95. Kong, R. and Bhargava, R. (2011) Characterization of porcine skin as a model for human skin studies using infrared spectroscopic imaging. *Analyst*, **136**, 2359–2366.
96. Glassford, S.E., Byrne, B., and Kazarian, S.G. (2013) Recent applications of ATR FTIR spectroscopy and imaging to proteins. *Biochim. Biophys. Acta, Proteins Proteomics*, **1834**, 2849–2858.
97. Chan, K.L.A. *et al.* (2009) Attenuated total reflection-FT-IR spectroscopic imaging of protein crystallization. *Anal. Chem.*, **81** (10), 3769–3775.
98. Glassford, S.E. *et al.* (2012) Chemical imaging of protein adsorption and crystallisation on a wettability gradient surface. *Langmuir*, **28**, 3174–3179.
99. Glassford, S.E. *et al.* (2012) Micro ATR FTIR imaging of hanging drop protein crystallisation. *Vib. Spectrosc.*, **63**, 492–498.
100. Ricci, C. *et al.* (2007) Characterization of genuine and fake artesunate antimalarial tablets using Fourier transform infrared imaging and spatially offset Raman spectroscopy through blister packs. *Anal. Bioanal. Chem.*, **389** (5), 1525–1532.
101. Ricci, C., Bleay, S., and Kazarian, S.G. (2007) Spectroscopic imaging of latent fingermarks collected with the aid of a gelatin tape. *Anal. Chem.*, **79** (15), 5771–5776.
102. Ricci, C., Chan, K.L.A., and Kazarian, S.G. (2006) Combining the tape-lift method and Fourier transform infrared spectroscopic imaging for forensic applications. *Appl. Spectrosc.*, **60** (9), 1013–1021.
103. Ricci, C. and Kazarian, S.G. (2010) Collection and detection of latent fingermarks contaminated with cosmetics on nonporous and porous surfaces. *Surf. Interface Anal.*, **42** (5), 386–392.
104. Ricci, C. *et al.* (2007) Chemical imaging of latent fingerprint residues. *Appl. Spectrosc.*, **61** (5), 514–522.
105. Tahtouh, M. *et al.* (2005) The detection and enhancement of latent fingermarks using infrared chemical imaging. *J. Forensic Sci.*, **50** (1), 64–72.
106. Crane, N.J. *et al.* (2007) Infrared spectroscopic imaging for noninvasive detection of latent fingerprints. *J. Forensic Sci.*, **52**, 48–53.
107. Holman, H.Y.N. *et al.* (2000) Synchrotron FTIR spectromicroscopy for assessment of stress responses of individual living human cells to low doses of environmental agents. *Abstr. Pap. Am. Chem. Soc.*, **219**, U101.
108. Holman, H.Y.N. *et al.* (2002) Synchrotron infrared spectromicroscopy

as a novel bioanalytical microprobe for individual living cells: cytotoxicity considerations. *J. Biomed. Opt.*, **7** (3), 417–424.

109. Holman, H.Y.N., Martin, M.C., and McKinney, W.R. (2003) Tracking chemical changes in a live cell: biomedical applications of SR-FTIR spectromicroscopy. *Spectrosc. Int. J.*, **17** (2-3), 139–159.

110. Goff, K.L. *et al.* (2009) *Wirms 2009: 5th International Workshop on Infrared Microscopy and Spectroscopy with Accelerator Based Sources. 2009*, American Institute of Physics, Melville, NY, pp. 54–56.

111. Holman, H.Y.N. *et al.* (2010) Synchrotron IR spectromicroscopy: chemistry of living cells. *Anal. Chem.*, **82** (21), 8757–8765.

112. Chen, L. *et al.* (2012) Synchrotron infrared measurements of protein phosphorylation in living single PC12 cells during neuronal differentiation. *Anal. Chem.*, **84** (9), 4118–4125.

113. Munro, K.L. *et al.* (2010) Synchrotron radiation infrared microspectroscopy of arsenic-induced changes to intracellular biomolecules in live leukemia cells. *Vib. Spectrosc.*, **53** (1), 39–44.

114. Whelan, D.R. *et al.* (2013) Synchrotron Fourier transform infrared (FTIR) analysis of single living cells progressing through the cell cycle. *Analyst*, **138** (14), 3891–3899.

115. Chan, K.L.A. and Kazarian, S.G. (2013) Aberration-free FTIR spectroscopic imaging of live cells in microfluidic devices. *Analyst*, **138**, 4040–4047.

116. Wroebel, T.P. *et al.* (2012) Attenuated total reflection Fourier transform infrared (ATR-FTIR) spectroscopy of a single endothelial cell. *Analyst*, **137**, 4135–4139.

117. Carr, G.L. (2001) Resolution limits for infrared microspectroscopy explored with synchrotron radiation. *Rev. Sci. Instrum.*, **72** (3), 1613–1619.

118. Wetzel, D.L. (2002) A new approach to the problem of dispersive windows in infrared microspectroscopy. *Vib. Spectrosc.*, **29** (1-2), 291–297.

119. Tobin, M.J. *et al.* (2010) FTIR spectroscopy of single live cells in aqueous media by synchrotron IR microscopy using microfabricated sample holders. *Vib. Spectrosc.*, **53** (1), 34–38.

120. Chan, K.L.A. and Kazarian, S.G. (2013) Correcting the effect of refraction and dispersion of light in FT-IR spectroscopic imaging in transmission through thick infrared windows. *Anal. Chem.*, **85** (2), 1029–1036.

121. Nasse, M.J. *et al.* (2009) Demountable liquid/flow cell for in vivo infrared microspectroscopy of biological specimens. *Appl. Spectrosc.*, **63** (10), 1181–1186.

122. Chan, K.L.A. and Kazarian, S.G. (2006) High throughput study of PEG/ibuprofen formulations under controlled environment using FTIR imaging. *J. Comb. Chem.*, **8**, 26–31.

123. Chan, K.L.A. *et al.* (2007) In situ high-throughput study of drug polymorphism under controlled temperature and humidity using FT-IR spectroscopic imaging. *Vib. Spectrosc.*, **43** (1), 221–226.

124. Fernandez, D.C. *et al.* (2005) Infrared spectroscopic imaging for histopathologic recognition. *Nat. Biotechnol.*, **23** (4), 469–474.

125. Bhargava, R. *et al.* (2006) High throughput assessment of cells and tissues: Bayesian classification of spectral metrics from infrared vibrational spectroscopic imaging data. *Biochim. Biophys. Acta*, **1758**, 830–845.

126. Chan, K.L.A. and Kazarian, S.G. (2006) Macro FTIR imaging in transmission under a controlled environment. *Vib. Spectrosc.*, **42** (1), 130–134.

127. Kazarian, S.G. (2007) Enhancing high-throughput technology and microfluidics with FTIR spectroscopic imaging. *Anal. Bioanal. Chem.*, **388** (3), 529–532.

128. Chan, K.L.A. and Kazarian, S.G. (2012) FT-IR spectroscopic imaging of reactions in multiphase flow in microfluidic channels. *Anal. Chem.*, **84** (9), 4052–4056.

129. Dazzi, A. *et al.* (2006) Subwavelength infrared spectromicroscopy using an AFM as a local absorption sensor. *Infrared Phys. Technol.*, **49** (1-2), 113–121.

130. Dazzi, A. *et al.* (2012) AFM-IR: combining atomic force microscopy and infrared spectroscopy for nanoscale chemical characterization. *Appl. Spectrosc.*, **66** (12), 1365–1384.

10
Terahertz Imaging of Drug Products

Michel Ulmschneider

10.1
Introduction

Chemical imaging demonstrated its usefulness in contributing to solve a variety of problems in the pharmaceutical industry. In particular, two-dimensional (2D) images were acquired of various pharmaceutical products, including solid drug formulations, powders, and packaging. Imaging was performed off-line and even online during process. In most cases, images were recorded in reflection mode based on optical spectra of a large collection of pixels at the sample surface. The introduction of three-dimensional (3D) imaging that enables details inside samples to be probed has ushered in a new era of sample inspection. The advantage is even greater if terahertz (THz) time-domain spectroscopy (TDS) is used to map inside solid dosage forms, for the measurement involved is nondestructive, comprising neither sample preparation nor operational limitations.

THz radiation falls in between mid-infrared (MIR) and microwave radiation in the electromagnetic spectrum. Its depth of penetration into samples is dependent on the material, but is typically of the order of several millimeters, that is, deeper than infrared (IR) radiation. THz radiation is nonionizing, noninvasive, sensitive to molecular structure, and probes intra- and intermolecular interactions. Unlike that of conventional 2D imaging with optical spectroscopy, where spectra reflected from the scanned surface elements are used to generate the 2D image, THz spectroscopy has the potential to reveal surface as well as subsurface information with high spatial resolution. THz imaging is based solely on interactions with matter that are a function of the refractive indices present. Thus, incident THz waves are reflected back by each layer inside the sample whenever there is a change in refractive index, without causing damage to either the structure or the components. THz radiation probes chemical properties as well and reflects back spectral content. Performing depth profiling by collecting pulses reflected from the sample surface and interior is similar to echo measurements. Spatial resolu-

Infrared and Raman Spectroscopic Imaging, Second Edition. Edited by Reiner Salzer, Heinz W. Siesler.
© 2014 Wiley-VCH Verlag GmbH & Co. KGaA. Published 2014 by Wiley-VCH Verlag GmbH & Co. KGaA.

tion is obtained in the z-direction during the $x-y$ raster mapping of the whole sample surface.

The current chapter will introduce the reader to the principles and techniques of THz-TDS as applied to spatially resolved imaging. A selection of examples where THz imaging was applied to solid drug formulations will be discussed thereafter. These applications illustrate how such an observation tool enables scientists to propose new ways of inspecting solid dosage forms. It also furthers the detailed understanding of more complex structures and improves the fine setting of process parameters.

10.2 Low Wavenumber Region in the Infrared Spectrum

10.2.1 Far-Infrared Spectroscopy

THz radiation has much in common with far-infrared (FIR) radiation, which domain is conventionally considered from the lower edge of the MIR range, at approximately 25 μm (400 cm^{-1}), to the microwave edge of the radiowave range, at 1 mm (10 cm^{-1}) [1]. This wavelength range spans frequencies from approximately 12 THz to 300 GHz. FIR and millimeter domains overlap between 1 and 0.5 mm, resulting in no clear separation. Based on this upper limit, low wavenumber infrared has also been termed the submillimeter range, below the millimeter microwaves. Figure 10.1 illustrates the electromagnetic spectrum of the region of interest with the corresponding vibrational and rotational modes. The range spanning from below 400 cm^{-1} and down to the microwave is where large-amplitude anharmonic vibrations take place. Absorption frequencies of any vibrational mode will appear in the FIR region of the spectrum either if the mass of at least one of the atoms involved in the vibration is high or if the force constant from the vibration is low. Because at the low wavenumber edge the FIR region includes millimeter range energies as well, in this respect the observed interactions with matter blend into microwave spectroscopy. Energy of THz photons lies in the range from a few tenth to a few tens of millielectronvolts, which is extremely weak compared to electronic transitions in atoms and molecules (~1 eV). In magnitude, THz energy can be assimilated to thermal energy at room temperature. The FIR domain covers the higher frequencies associated with pure molecular rotations in gas phase spectra. Interaction of FIR radiation with matter concerns metal–ligand skeletal bending, skeletal bending with more than two atoms, ring puckering, internal torsional modes about a single bond in small molecules, weak intermolecular hydrogen bond stretching, and torsion in liquids [2]. As FIR spectra include the lower bond vibration frequencies of molecules, mostly of the angle deformation and torsional types in condensed matter, spectroscopy in this region is applicable to the study of crystal changes [3], and is capable of sensing between conformers of small

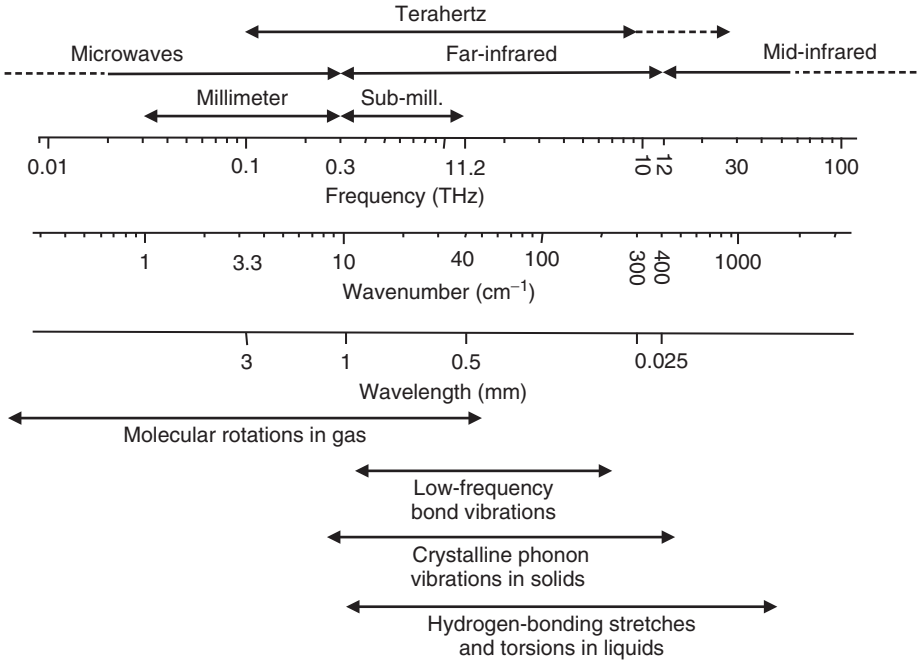

Figure 10.1 Low-wavenumber electromagnetic spectrum with the terahertz range of radiation to fall in between infrared and microwave domains. Spectra within the FIR/THz region probe intramolecular vibrations and intermolecular interactions.

molecules with few substituents. Moreover, FIR can be used to distinguish structurally similar active pharmaceutical ingredients (API) in mixtures with low detection limits. Finally, recording an FIR absorption spectrum produces a characteristic band pattern that identifies a great number of molecules and materials [4].

FIR spectroscopy used to merge technologies and devices that originated from the neighboring spectral domains. Sources, detectors, and instrument components were adapted in relation to the intended analytical task. Unlike in MIR spectroscopy, instruments for FIR spectroscopy no longer rely solely on interferometers. Above 10 THz, spectrometers can be designed identical to IR instruments and incorporate optical devices. At lower THz frequencies, optical components such as interferometers and gratings are less adapted, whereas millimeter wave emitters and waveguides become better to operate. Advances in optoelectronics have resulted in more sensitive instrumentation for FIR spectroscopy using novel radiation sources that produce bursts of FIR radiation. With the propagation of short-duration electromagnetic pulses inside samples, it was possible to determine the absorption spectra of the material and record the pulse dispersion as a function of time [5].

10.2.2
THz Spectroscopy

With the advent of ultrafast NIR lasers, the generation and detection of FIR spectra became principally associated with time-of-flight spectroscopy and optoelectronic devices such as Hertzian dipoles, for example. The use of *terahertz* proved preferable to that of FIR [6]. In the meantime, no standard definition of the THz range was established. The frequencies accessible by using ultrafast optoelectronics fall in between the high-frequency edge of the microwave range at 0.1 THz and the low-frequency edge of the IR range, that is, at 10 THz in the FIR range, extendable to 30 THz in the MIR (Figure 10.1). THz spectroscopy covers broadly millimeter, submillimeter, and FIR electromagnetic domains. Owing to this, properties of THz radiation are essentially those of FIR and partly microwave. THz radiation travels in a straight line and is nonionizing, with a depth of penetration that remains less than that of microwave radiation, however. Spectral patterns recognized by THz spectroscopy are common to those of FIR spectroscopy. A large variety of dielectric and dry materials with refractive indices between 1 and 2 are transparent to THz radiation. Dry air with a refractive index of 1 constitutes a media remarkably transparent to THz radiation. Relatively permeable to THz are low-density materials made of low-polarizable molecules, such as foams, fabrics, paper, cardboard, wood, and in particular most pharmaceutical excipients. On the contrary, ferroelectric and doped semiconductor materials feature refractive indices beyond 5 and are opaque to THz. Masonry, plastics, Plexiglas, and ceramics fall in between and are partially transparent. Electric conductors, humid materials, and polar liquids are highly absorbing THz radiations. In particular, water vapor features such a strong rotational spectrum with bands between 0.4 and 2.5 THz that any other signal is severely attenuated. As a result, ambient humidity may affect overall instrument performance if the vapor is not purged. At the far end of the scale, liquid water and metals completely stop THz radiation.

10.3
THz-TDS Technology and Applications

10.3.1
THz Pulse Generation and Detection

10.3.1.1 Emission

Commonly used THz-TDS is a technique in which samples are probed with ultrashort THz pulses [7]. Typically, THz pulses are generated by irradiating a photocommuter with a femtosecond laser. Photocommuters are electrical switches build in semiconductor material that is activated by the increase in electrical conductivity when the substrate is exposed to an electromagnetic field. The photon energy of the laser must be sufficient to overcome the bandgap of

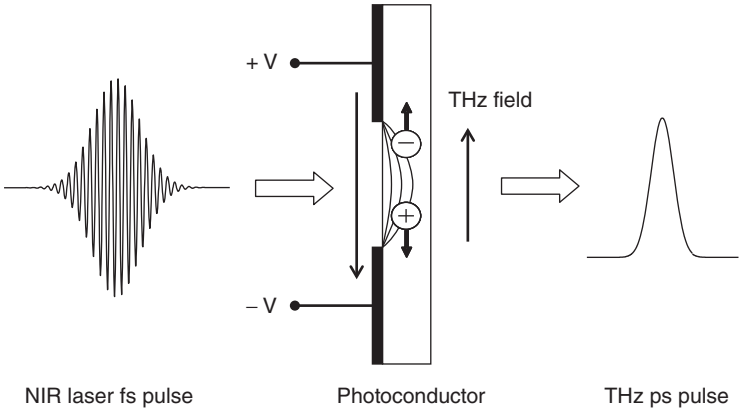

Figure 10.2 Signal conversion in a photoconductive semiconductor device. In presence of the pulsed incident, Ti:Sa laser carriers are created and accelerated by the applied voltage. This generates a transient current in the dipole antenna that in turn radiates a terahertz wave.

the semiconductor material and excite a large number of electrons across the gap: hence, irradiating a photocommuter with a laser generates an increase in the number of pairs of electron and hole. Such excitation process depicts the illumination in the NIR range of a gallium arsenide (GaAs) semiconductor substrate by a solid-state titanium ion-doped sapphire (Ti:Sa) laser. The latter has limited tunability between 700 and 1100 nm and emits pulses that will last for less than 10 fs, with energies in the range from sub-picojoules to a few tens of nanojoules. Because the GaAs substrate switches abruptly from being an insulator into being a conductor, a sudden electric current is generated across the semiconductor device. This transient current may persist for only a few hundred femtoseconds depending on the duration of the excitation laser pulse and the carrier lifespan in GaAs substrate [8]. For the construction of a THz emitter, two metallic electrodes typically with 5 μm separation gap are deposited at the surface of the substrate to constitute a Hertzian dipole antenna [9]. An electric field in the order of 300 kV cm^{-1} is generated inside the gap by applying a DC bias voltage (∼150 V) to the metallic electrodes. The biased Hertzian antenna is activated by the rapid rise of transient current and emits a pulse of broadband THz radiation (Figure 10.2). A single THz pulse will last for a few picoseconds only and cover frequencies in the range from approximately 0.1 to 10 THz with a mean power that can reach a few microwatts. Finally, a silicon lens system is used to shape the emitted pulse into a convenient THz radiation beam.

10.3.1.2 **Reception**

In conventional spectroscopy, detectors measure radiation intensity. This method is inappropriate for detecting pulsed radiation. Because THz electromagnetic fields affect electronic devices by inducing electronic transitions, it is the time evolution of the THz electric field that is measured instead. Hence, alternative

detection techniques that rely on semiconductor excitation dynamics have been adapted to THz detection. For that purpose, optoelectronic devices have been derived from the dipole-type scheme used for emission. In THz-TDS, the electric field of the pulse interacts in the dipole antenna with a much shorter laser pulse (e.g., 0.1 ps). This interaction produces a transient electric current that is proportional to the electromagnetic field of the THz pulse at the time the laser gates the detector on. The detection bandwidth of a photoconducting antenna can extend to 10 THz according to the duration of the gating laser pulses.

10.3.1.3 **Sampling**

No absolute reference of time exists, and a temporal reference frame is needed. For that purpose, the initial excitation pulse is split into two for use as gating and probe pulses. The relative time delay is adjusted with a translational stage that modifies the path length of the gating pulse. By repeating this procedure and varying the timing of the gating, the THz pulse is scanned as a function of time with an accuracy usually on the order of 0.1 fs. The captured THz waveform is the convolution of the sample response and the system response of the instrument, as well as signal perturbations. Deconvolution is applied to the measured waveform to extract the frequency spectrum from the time-domain data. Variations in amplitude and phase are function of refractive index, absorption coefficient, and thickness of the sample. As the time gap of the measurement is particularly narrow, noise is kept low and high signal-to-noise ratios can be obtained. Most significant distortions affecting waveforms observed are subsidiary oscillations in the antenna, time delays, material dispersive effects, liquid absorption, phase change, after-runners in the pulse, and reflections due to scattering effects. In general, noise intensity is insignificant compared to the fundamental reflections and can be minimized with various signal processing techniques. Scattering effects may affect observations in specific cases, as a void develops between layers inside the sample and initiates delamination, for example.

10.3.2
Current Applications of THz Spectroscopy

Advances in matters of optoelectronic devices and availability of reliable compact femtosecond lasers were key factors in the achievement of THz applications. Attainable objectives depend directly on the interaction of THz radiation with materials, that is, the differences in THz absorbance of components in a probed sample, and also that of the ambient surroundings. To form and record THz pictures of objects is in theory the most versatile application one can imagine, either in transmittance if the sample is sufficiently transparent, or in reflectance in the other case. The level of transparency of the imaged part will inform on degree of humidity, presence of metals, density, and so on. As already mentioned, surroundings such as dry air, clothing, wood, plastics, cardboard, paper, and masonry are virtually transparent to THz radiation. Thus, application of THz spectroscopy to

a large variety of situations is merely accomplished by remote and noninvasive measurements.

Exhaustive enumeration of applications from domains other than the pharmaceutical industry is beyond the scope of this chapter. A notable example was an *in situ* control of the thermal insulation on the external fuel tank of the space shuttle [10]. Noncontact THz spectroscopy was successfully applied to detect voids and delamination in the polyurethane foam prior to launch. In dentistry, THz imaging is an alternative to conventional radiography to monitor mineral density decay in the enamel and detect caries even at an early stage. In medical imaging, the risk of damaging human tissues with nonionizing THz is negligible unlike that of X-rays. THz radiation can penetrate several millimeters of tissue before being reflected back. It can be used to detect differences in water content, which is an indicative signal of diseased cells to map breast tumors, or detect the onset of skin cancer, for example. In defense and security matters, THz spectroscopy is capable of sensing trace amounts of explosive vapors and lethal gases remotely. So far, whole-body screening in THz-portal systems has been applied to detect weapons and explosives concealed underneath covering layers of fabrics or plastics [11]. In masonry, walls can be inspected with THz to visualize buried electric wires, cables, and switches. In manufacturing, THz sensing is employed for noncontact quality monitoring of goods directly through sealed plastic packaging [12]. The high contrast between plastics showing little absorptions and metals blocking THz radiation permits the inspection of integrated circuitry. In environmental chemistry and agriculture, pollutants having characteristic fingerprints can be detected remotely and identified. Prohibited drug substances can be detected and characterized. In addition, a variety of fundamental phenomena involving electrons have been studied in relation with picosecond THz pulses; these are capable of producing ultrafast switching in semiconductor components, of following carrier dynamics and transport, of monitoring chemical interactions, among others [13].

10.3.3
Concise Description of THz Imaging

The first images using THz radiation were generated in astronomy and date from the 1960s. Nonastronomy images were produced later [14]. In the mid-1990s, THz-TDS came into play and THz imaging gained improved interest with the development of systems available to industry. Meanwhile considerable progress was made and 3D images could be computed using THz radiation to map the internal structures of a variety of objects. THz imaging shares some similarities with that of X-ray micro-computed tomography (micro-CT), another promising imaging technique in the pharmaceutical industry. When X-rays interact with a sample, an exchange of energy takes place by fluorescence with the sample matrix components. The data are made of a high number of projection measurements. Subsequently, 2D cross-sectional slices of the sample are computed, and 3D topographic images of the internal structure of the object are reconstructed

by stacking up the 2D slices. The response of organic materials to X-rays is nonspecific and images are limited to density contrasts. For example, the detailed observation of soft materials embedded in hard materials is difficult. The ionizing and heating effects of X-rays may even damage the sample being measured. THz micro-CT is an imaging technique that relies on multiple projections similarly to X-ray tomography, but the preferred method of producing THz images is totally different, for it uses pulsed emission of THz waves to interact with the sample.

In THz time-domain imaging (THz-TDI) data acquisition is based solely on refractive index measurements [15]. THz imaging relies on multiple reflections that can be compared to that of multiple echo measurements. A single and ultrashort incident THz pulse impinges on a given point of the sample surface. Whenever there is a change in the refractive index at and below the probed surface point, a proportion of the incident pulse will be reflected back and collected. This results in a waveform with multiple peaks corresponding to each reflected pulse being modulated by the reflecting interfaces and absorbances in the probed materials. The collected data are an array of time-delayed and attenuated waveforms. Interfaces are characterized by variations in refractive indices, and the recorded time delay transcribes the location of interfaces inside the sample at the point of measurement. Given a depth of measurement that can reach a few millimeters, the inside of the sample can be probed. This procedure is repeated across the entire sample surface for a complete mapping [16]. Spatial resolution is limited by the pulse emission, whereas lateral resolution depends on the radiation wavelength [17]. Ideally high bandwidth pulses permit spatially resolved details less than 100 μm, with x and y resolutions down to approximately 40 μm [18].

10.4 THz Imaging in the Pharmaceutical Industry

10.4.1 Introduction

In NIR, MIR, and Raman spectroscopic studies, information is collected at or just below the sample surface and it is not possible to completely resolve this information spatially. Therefore, THz imaging is particularly well suited to the nondestructive surface and subsurface characterization of solid dosage forms that are not possible with conventional optical technique [19]. To date, THz pulsed imaging is limited to off-line measurements in the laboratory, while online or real-time imaging applications still require further development [20]. Current instruments are designed to fit a wide range of solid dosage forms, with dimensions varying from 5 mm to 20 mm, regardless of curvature and shape [21]. THz radiation does not require special sample preparation, dissection, cutting, or coating removal. To

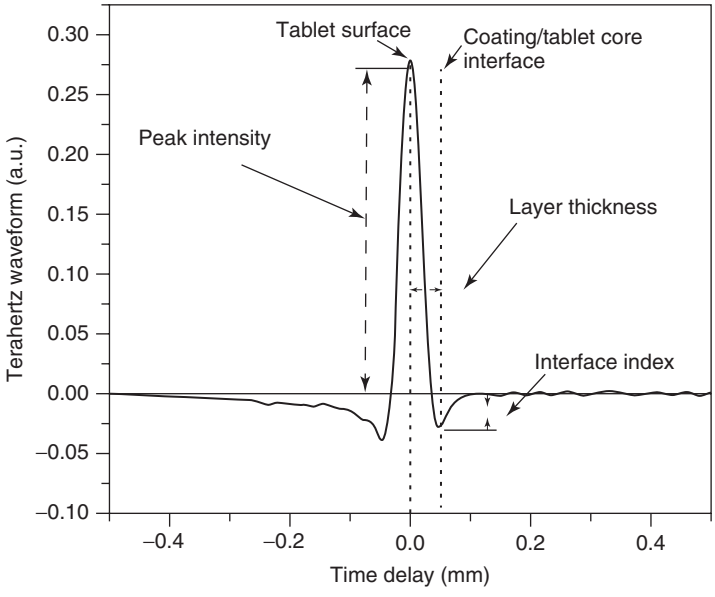

Figure 10.3 Typical terahertz time-domain waveform recorded at a single point on the surface of a coated tablet. The first reflection is due to the interface between air and the outer coating surface. The second peak corresponds to the interface between the inner coating layer and the tablet core. The scale is in millimeter, and the difference between the dotted lines marking both peaks corresponds to the layer thickness of the coating at that given point. The arrows indicate how peak intensity, layer thickness, and interface index are defined.

ensure consistent and reproducible measurement, strict positioning is required with regard to the impinging beam. Because there is no heat generation, ionization, or modification of physical or chemical characteristics, the sample remains intact and available for additional testing [22].

10.4.2 Imaging of Solid Dosage Forms

Figure 10.3 exhibits a typical THz time-domain waveform recorded at a single point of a coated tablet. The positive reflection peak at 0 mm arises due to the reflection of the THz pulse from the tablet surface. The negative peak at approximately 50 μm corresponds to a reflection assigned to the interface between the coating and tablet core. The interface index is defined as the peak height ratio of the reflection from the outer sample interface and the reference measurement from the metallic mirror. The coating thickness is determined as peak position difference between the surface reflection and the coat versus core interface. With more layers crossed by the THz waves, the successive back-reflected responses are delayed in time and the digitized spectrum features a series of positive and negative peaks for each change in index. This is illustrated by the

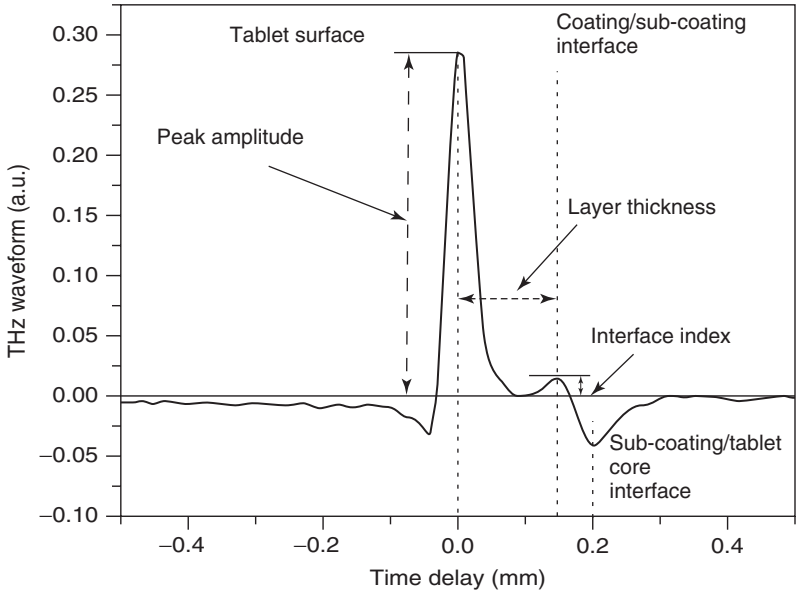

Figure 10.4 Terahertz time-domain waveform taken from a point on the surface of a double-coated tablet. The successive positive and negative peaks reflect each change in refractive index within the structure. The first peak is due to the reflection from the outer coating surface itself, the second and third peaks are reflections from the coating/subcoat and subcoat/core interfaces, respectively.

time-domain waveform taken from a pixel on the surface of a double-coated tablet in Figure 10.4. The first large peak is a reflection from the tablet surface. The smaller second and third peaks are THz reflections from the outer coat versus subcoat and the subcoat versus core interfaces, respectively. The time difference between these peaks corresponds to the thickness of each coating.

In chemical imaging, 2D $x-y$ projection is a common data visualization obtained by plotting the value of a given parameter at each scanned point (i.e., pixel) of the displayed surface. Interface index (Figure 10.5), coating thickness (Figure 10.6a), and refractive index can be mapped out in such representation [17, 18]. Using computer graphic tools, the value at each pixel of parameters of interest can be projected onto rotating 3D tablet models. Figure 10.6b depicts a typical 3D visualization of coating thickness. The B-scan is a cross-sectional representation obtained by plotting the mapped image data along one longitudinal axis, x or y, or azimuthally from the center of the sample surface (Figure 10.7). In B-scans, the surface curvature is computationally removed. This can be compared to that of ultrasonic representations and gives details of layered structures and variations in density inside the sample section (Figure 10.8). Amplitude values of thickness, refractive, and interface indices can be mapped on $x-y$ projections at any depth. A collection of such 2D maps with increasing depth can be used to track variations with continuous extension inside the tablet matrix (Figure 10.9).

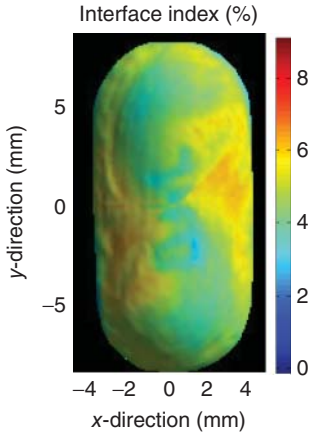

Figure 10.5 False color 2D map showing the interface index distribution across one tablet side. The image is obtained by plotting the relative value of the index at each probed point on the topographic model.

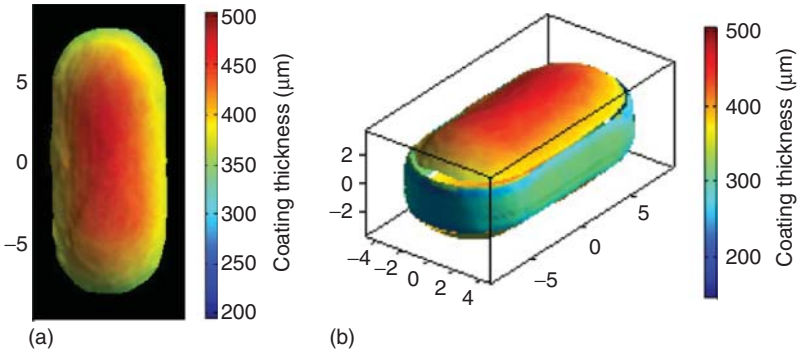

Figure 10.6 (a) 2D map showing the coating thickness distribution across one tablet side and (b) corresponding 3D representation displaying the thickness values on a 3D model of the tablet.

10.4.3
Investigating Pharmaceutical Samples by Means of THz Imaging

To further understanding of solid dosage forms, observations by any means need to penetrate beyond the outer surface of the sample. THz imaging can investigate the tablet coat and core simultaneously and visualize a wealth of details. Quality attributes of the surface and near-surface can be explored directly, such as coat integrity, uniformity of thickness and density [23], surface roughness [24], and variation of material homogeneity. Coating degradation can be visualized. For example, a porous structure in a coating can be detected because it triggers distortions in the reflected pulses, affecting the local refractive index [25]. More specifically, moisture and the presence of air gaps have an impact on signal processing, and solvent ingression can be tracked [26].

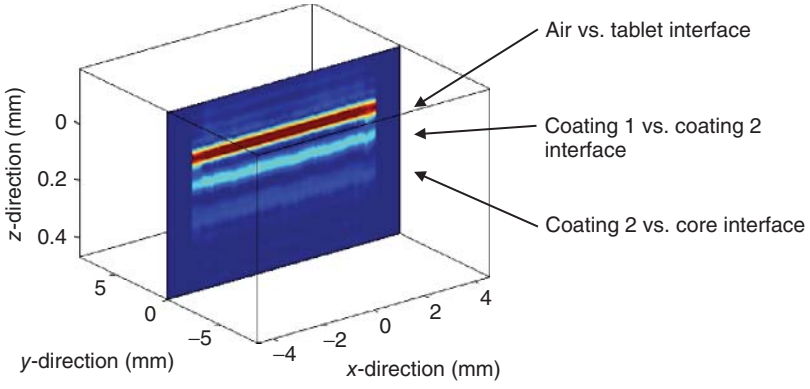

Figure 10.7 Cross section (B-scan) of a double-coated tablet where the slice cut is performed along one longitudinal axis and the surface curvature is computationally removed. Distances are measured from the center of the sample.

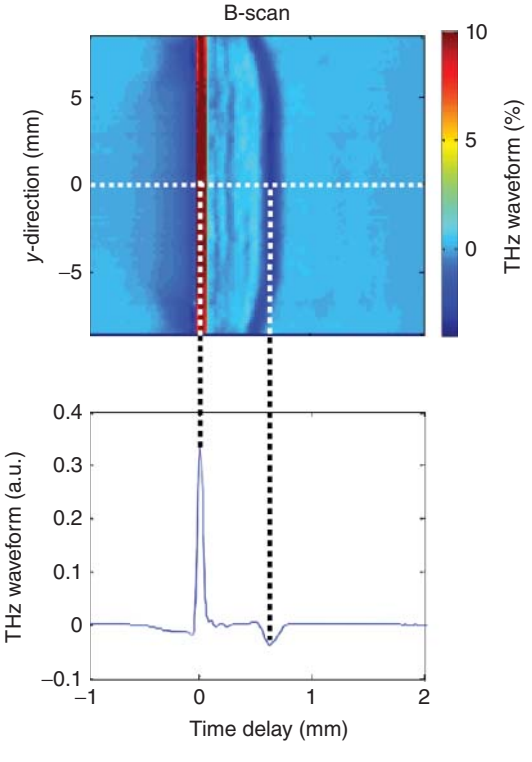

Figure 10.8 Cross section obtained by plotting the mapped data along the *y*-longitudinal axis. The dotted lines marking both peaks in the waveform correspond to the outer and inner layers of the tablet measured at the origin.

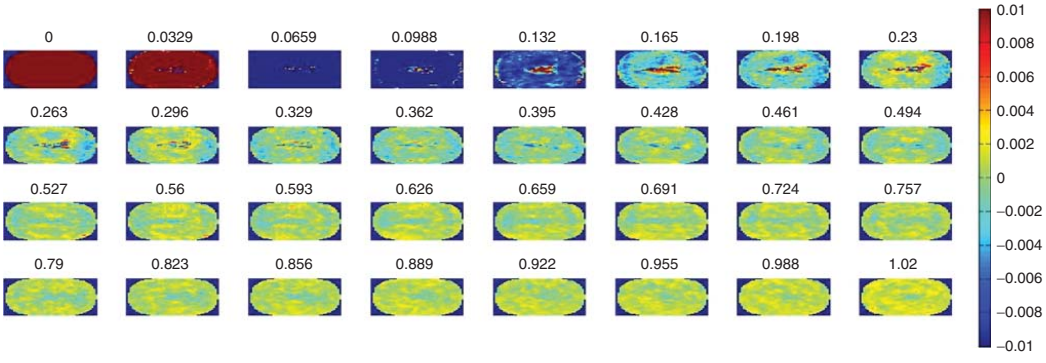

Figure 10.9 Series of refractive index maps spanning from the surface down to 1.02 mm at depths increase by approximately 330 μm. The series can be used to distinguish continuous features inside the tablet.

Slightly deeper inside the sample, the core–coat interface can be monitored, for example, for layer or multiple-layer uniformity, core–coat interaction, and uncontrolled sublayer structures [27]. THz imaging can be used to detect defects such as cracks, delamination, dislocations, buried layers, and air bubbles. By penetrating deeper below the sample surface, THz radiation probes the tablet matrix to evaluate the integrity of the tablet core itself, detect micro-cracks and density changes, and observe particle size variations or agglomeration that could affect the bioavailability of a drug. Another application of mapping is the visualization of heterogeneous domains indicative for dislocation patterns and core delamination. The 3D coverage of the matrix enables API versus excipient distribution to be visualized. And because the THz spectral region covers intermolecular bond vibrations affected by crystal changes, it can be used to detect polymorphism [28].

THz imaging can be employed to detect foreign particles if these are opaque to THz radiation, such as ceramic particles and metal splits. Kernels, film-coated tablets, or capsules originating from various manufacturing sites or suppliers can be compared easily, and differences between scale-up laboratories and production were evaluated [29]. For example, finished products can be compared with equivalents, such as generics, placebos, and counterfeits. THz imaging can be used to monitor stability testing under variable storage conditions. The speed and ease of mapping make this technique attractive for replacing wet dissolution testing in product development [30, 31]. As THz imaging provides significantly more detailed information on tablet core robustness and the propensity for defects, it is an informative tool for optimizing process parameters during tablet core manufacturing [32].

10.4.4 Experimental Setup to Measure Solid Dosage Forms

A commercially available THz-TDI system fitted with a six-axis tablet sampler was used in the experimental section of this chapter [33]. Figure 10.10 sketches a typical setup to perform time-domain imaging [34]. The instrument is capable of 3 mm maximum penetration depth and a spatial resolution of 100 μm at 3.0 THz, reduced to 300 μm at 1.0 THz. The minimum layer thickness measured reaches 50 μm with an accuracy of ±1 μm in optimal conditions. The system is designed to measure solid drug samples with diameters from 5 to 20 mm, regardless of curvature and shape. The maximum tablet weight accommodated by the sample holder is 10 g. Waveform digitizing takes 50 ms for a set of 512 data points; 10 min is necessary for measuring a circular 10 mm diameter tablet with a flat surface, increasing by 15 min for an 8 mm diameter tablet with a convex surface. The scan length, that is, penetration in air, can be adjusted according to the measured parameter and the required precision. For example, the length can be set to approximately 2.9 mm when uniformity, integrity, and density of the core are of main interest. This provides a penetration depth of approximately 1.9 mm into the tablet, taking into account the estimated refractive index of the whole sample. For studying the uniformity of coating layers or the quality of the interfaces

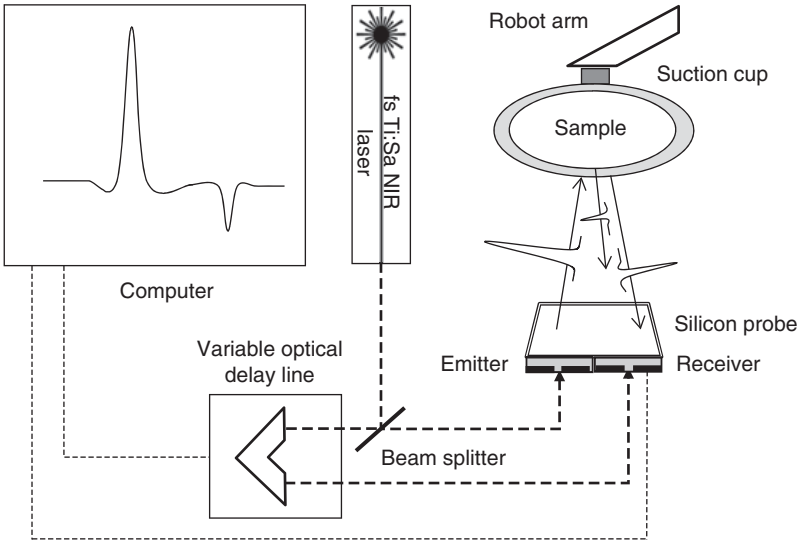

Figure 10.10 Schematic THz imaging set up to map solid dosage forms. The system comprises a robotic arm fitted with a suction cup to maintain the sample and present each surface point to the THz pulses. The fiber-fed silicon lens inside the measurement enclosure directs THz pulses toward the sample and focuses back-reflected signals.

between outer coating and core, the scan length is adjusted to provide highest spatial resolution. With 1 mm penetration in air, the sample is probed to a depth of approximately 0.65 mm.

In a typical operation mode, a reference signal is obtained from a perfect reflection on a mirror. The detector reading before the emitter generates the THz pulse is taken as the baseline signal. The fiber-fed THz probe mounted in the measurement enclosure is used to direct emitted pulses toward the sample and detect the reflected waves from within the sample. A suction cup holds the tablet to the robot arm that moves in relation to the THz beam to ensure that all parts of the tablet are analyzed. The NIR laser burst lasting 90 fs is produced and separated by a beam splitter into an excitation beam and a gating beam. The excitation beam impinges on the gated gallium arsenide (GaAs) semiconductor device, resulting in the optical excitation of the biased dipole antenna with the emission of a 500 fs THz pulse. The latter is collimated and focused onto the sample using a silicon lens system. Reflected and back-scattered pulses are collected and focused using the same silicon lens onto the photoconductive device for laser-gated detection. By sweeping the delay with a variable stage, the entire waveform is captured in about 50 ms. The zero is given by the first reflection produced at the interface between air and the tablet surface. Each response signal from the inner structure of the sample is compared to that of the initial reflection to compute the corresponding refractive index. The number of pixels measured depends on the scanned surface area, varying from a few hundred to thousands of pixels in 200 μm steps across the sample surface, for example.

Most pharmaceutical tablets have curved surfaces, and a precise model of the shape and curvature of the sample under investigation is a prerequisite for reliable measurement. The topography model is obtained prior to THz mapping with a visible laser gauge (e.g., 670 nm). The robot arm moves the tablet in front of the laser gauge to generate the model of the surface [16]. Topographic data and robot movements are stored for precise repetition of subsequent measurements and exact restitution of mapped image data. During mapping, the robot arm keeps the tablet at a constant focal position with regard to the probe. This standardized procedure is suited to any solid dosage form with shapes and surface curvatures that comply with the positioning prerequisites. Both the THz emitter and detector are embedded in the silicon lens system and the distance between lens and sample is less than 8 mm. As a consequence, the effect of water vapor absorption on the THz waveform can be minimized and no nitrogen purging or air evacuation is required, which simplifies the measurement procedure.

10.4.5 Typical Applications to Solid Dosage Forms

To date, nondestructive measurement of coated tablet samples is a straightforward application for THz imaging. Detailed structures of coatings and cores and their respective interfaces can be extracted directly from THz waveforms and used merely for finished product evaluation and process understanding. In the following practical examples, the focus was to resolve homogeneity issues of the coating across the entire surface of samples. Not only average coating thickness of the finished drug was critical, but local variations in coating and defects were spatially investigated. Suspected process failures or inadequacy of coating formulations were confirmed.

In a first example, THz-TDI was used to determine whether a coating process activated and amplified defects in coated tablets that were already present in the tablet core. The visible presence of micro-cracks in the center band of a specific sample was an initial indication. A number of features of the tablet can be seen in Figure 10.11a, which illustrates the peak intensity map at the center band around the tablet. The map shows nonuniform areas in the outer coating layer. The cross-section map (Figure 10.11b) confirms the presence of two cracks in the coating that correspond to structural failures penetrating deep inside the tablet core. These cracks are visible in the coating as well as at depth within the tablet core (Figure 10.11a). The implication was that once the tablet was coated, micro-cracks already present in the tablet core were exacerbated, leading to tablet failure. The shape of the THz waveform recorded at one of the defect locations shows marked distortion when compared to a nondefective location (Figure 10.11c and d). This defect modulated the back-reflection from the tablet surface, thus indicating a lower surface refractive index at this location. The cracks within the tablet core were responsible for the additional peak following reflection from the outer surface.

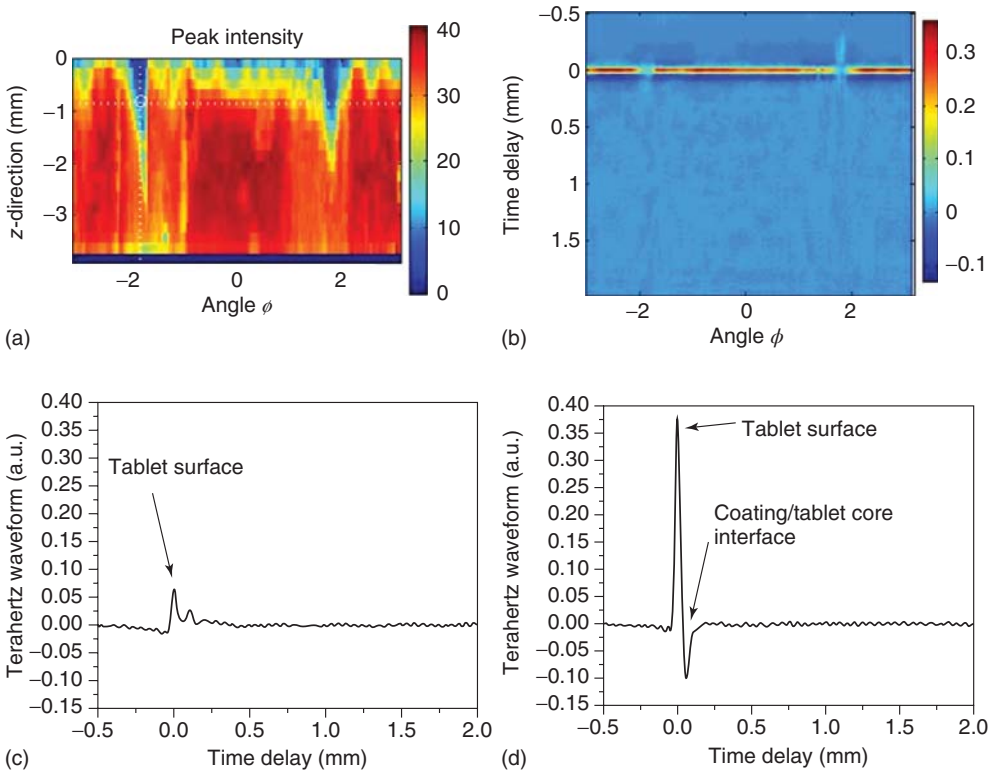

Figure 10.11 (a) Peak intensity map of the center band showing nonuniform areas in the outer layer that extend inside the core matrix; (b) cross section showing two cracks in the coating; (c) THz waveform of one cracked area showing distorted reflected peaks when compared to a waveform taken from a nondefect area (d).

In the next example, THz measurements of the tablet wall indicated abnormalities in the coat–core interaction, possibly due to changing particle size. Excessive variation was found in the coating thickness across the center band of a coated tablet (Figure 10.12a). The peak intensity map shows nonuniform distribution of center band intensities. Core features, on the other hand, showed no internal structural failure. Coating variations were attributed in this case to lateral damage. The cross-section map confirmed the differences in coating thickness (Figure 10.12b). The nonuniformities in the tablet wall indicated a potential change in coat–core interaction that could be due to particle size differences.

Depth profiling of a tablet core prior to coating indicated flaws that went on to affect bioavailability. Peak intensities of the sampled tablet core were projected in a 2D map (Figure 10.13a). The variations in peak intensity indicated damage at the core edges. The cross-section map that spans one of the defective edges (Figure 10.13b) illustrates this surface irregularity. Unlike that of the edge, the core

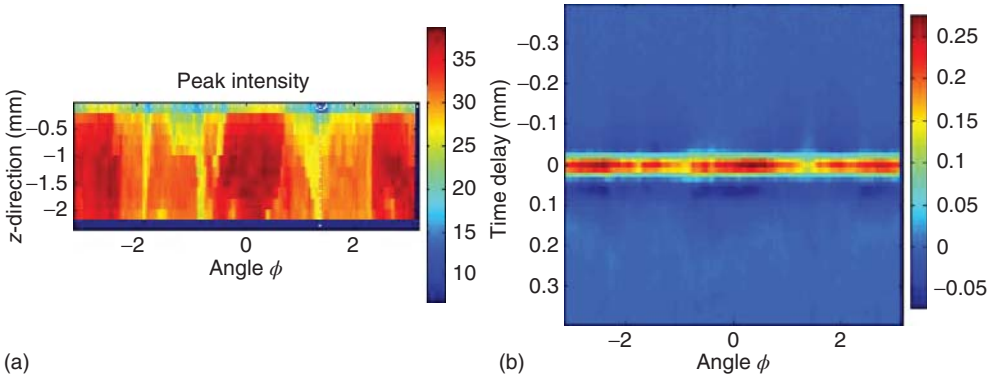

Figure 10.12 (a) Peak intensity map of a sample that features defects localized at the tablet surface and (b) corresponding cross-section map.

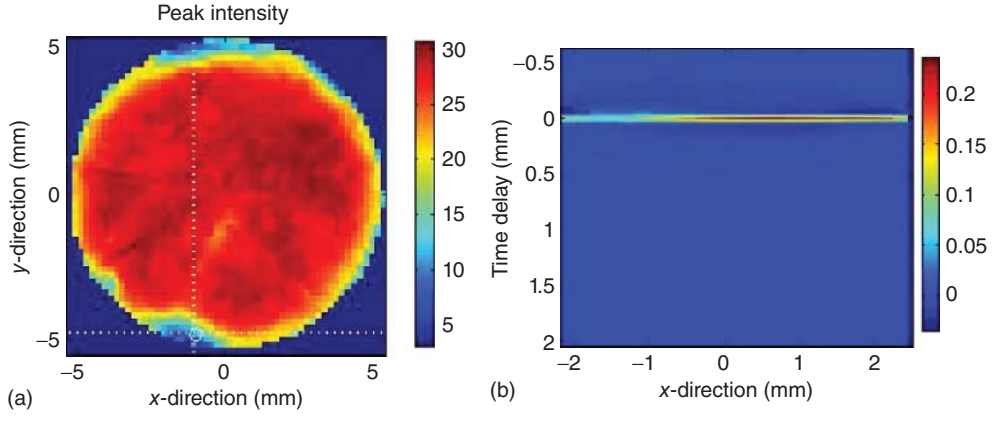

Figure 10.13 (a) Edge damages seen in the peak intensity map of a coated tablet and (b) corresponding cross section in the *x*-direction.

matrix features uniform intensity distribution. The defects shown occurred in the tablet core before coating. During coating the damaged edge affected coat–core interaction, resulting in subsequent poor bioavailability of the finished product.

Cross sections were plotted for two samples (tablets 1 and 2) of a solid drug product that differed in their dissolution behavior (Figure 10.14a and c). As coating is critical to the rate of drug release, abnormal variations in coating thickness were suspected in an initial hypothesis. In both B-scans, the high intensities of the red colored band correspond to the tablet coating. Tablet 1 features a series of additional interfaces deep inside the core parallel to the outer layer. The substructure is clearly observed in Figure 10.14a, whereas the second B-scan shows no analog substructure in tablet 2. In the corresponding THz waveforms (Figure 10.14b and d), these additional interfaces appear just after the coat–core interface as small oscillation ripples. The additional structure just below the coat–core interface of tablet

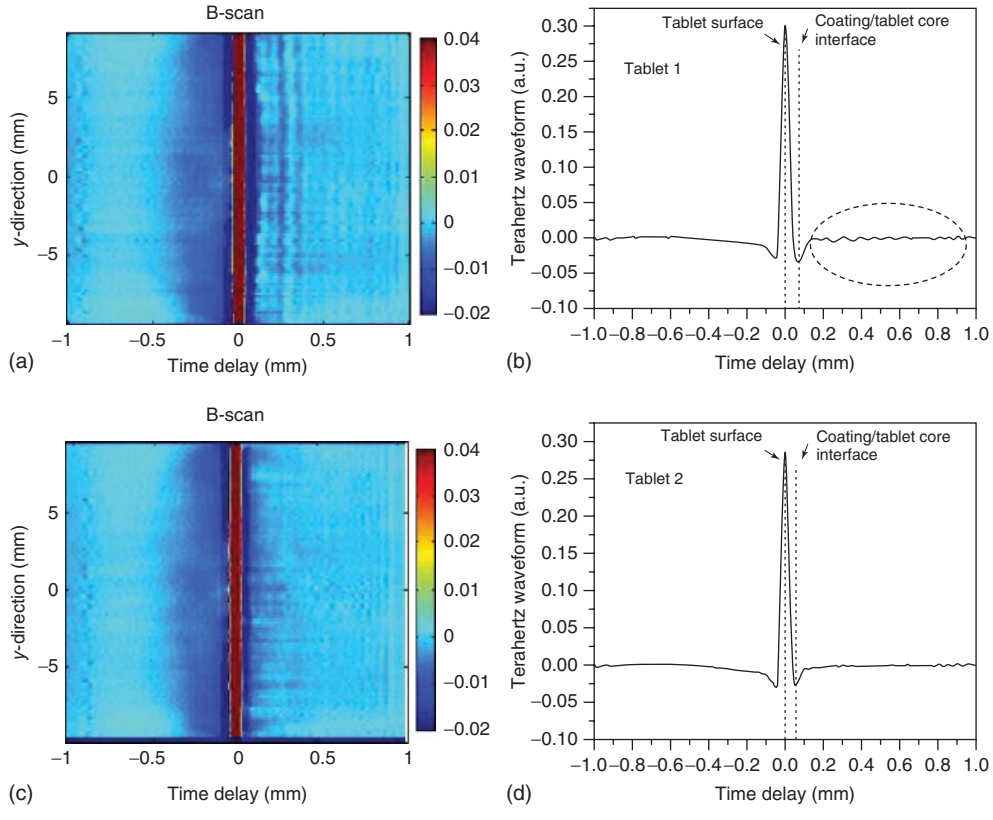

Figure 10.14 (a, c) Cross sections in the *y*-direction of two coated tablets and (b, d) corresponding waveforms. In the cross-section maps, the coat reflections are in red and the coat–core interface appears in blue. (a) The first sample features a succession of additional layers parallel to the coating layer, (b) confirmed by small oscillations in the corresponding waveform, whereas (c, d) the second tablet does not feature these singularities.

1 proved greater in the center band of the sample (Figure 10.15a). The B-scan of the center band of the second tablet is seen in Figure 10.15b for comparison. The substructure appears in yellow and is more or less uniform, constituting a reflection interface that is not observed in sample 2. The additional reflections were attributed to trapped residual moisture, leading to structural and possibly chemical change beneath the coat–core interface, resulting in poor dissolution of the finished drug. THz investigation led to an alternative explanation that did not confirm the first hypothesis.

Functional coatings poorly soluble in acidic media are intended to protect the drug core against degradation from gastric juices in the stomach. Coating thickness and porosity are critical parameters in this case. Release kinetics studies revealed diffusion of API molecules in acidic media for a coating formulation that did not match the expected diffusion barrier performance. Imaging demonstrated

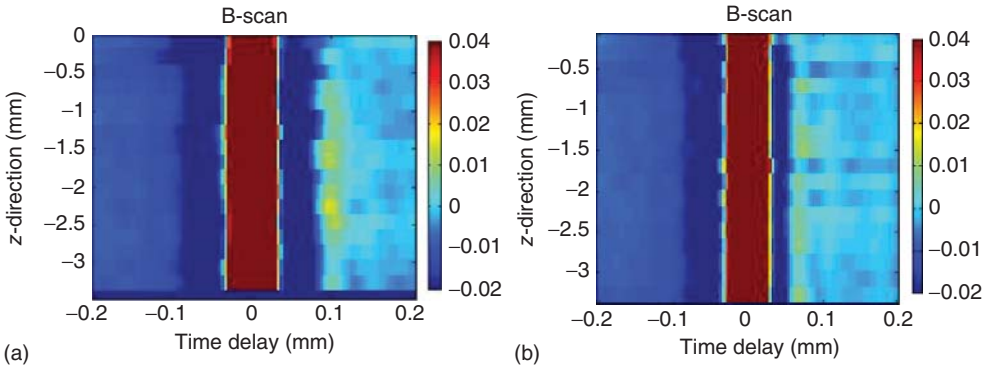

Figure 10.15 Cross-section maps for a center band of (a) tablet 1 and (b) tablet 2. The thick red lines indicate the outer tablet surface, whereas blue lines indicate the reflection from the coat–core interface. The large and irregular yellow lines just below can be attributed to additional, higher reflectance layers.

that nonuniformities affected small portions of the outer coating of a tablet sample and reduced the THz reflection correspondingly. These defective spots appear as round green patches on the surface peak intensity map (Figure 10.16a). The cross section (Figure 10.16b) passes through one defect at about +8 mm distance. The peak intensities from the tablet surface indicate a lower surface refractive index at this position. The corresponding THz waveform reveals strong distortions of the waveform shape when compared to a nondefect point (Figure 10.16c and d) situated on the same cross section. The source of the defect caused pore-type structures in the film coating and was due to undispersed solid particles, that is, pigments, within the coating suspension, resulting in degraded barrier performance.

Two hot melt extruded tablet cores, one with a polyvinyl alcohol (PVA)-based coat and the other with a hydroxypropyl methylcellulose (HPMC)-based coat, differed in their finished product features in particular dissolution profiles. In addition, the HPMC-based film had flaws involving a lack of logo clarity. This was investigated by THz imaging, and the respective surface peak intensity maps were plotted (Figure 10.17a and b). The images indicate a denser coating structure formed by the HPMC-based polymer coat. The peak intensity map of the test sample wall reveals a less reflective structure beneath the coat (Figure 10.18). This indicates altered coat–core interaction in this area of the tablet responsible for the logo-filling defect. Confirmation was provided by X-ray micro-CT imaging (Figure 10.19): the virtual cut shows how the PVA-based coat follows the shaped surface of the logo embossing fairly well, whereas the HPMC-based coat retracts while drying and creates a discernible void between coat and core.

In a parallel study, the HPMC-based coat was applied to wet granulated cores for comparison. The peak intensity map showed lack of homogeneity in the coat affecting the inner core structure (Figure 10.20). Suspected cracking at the

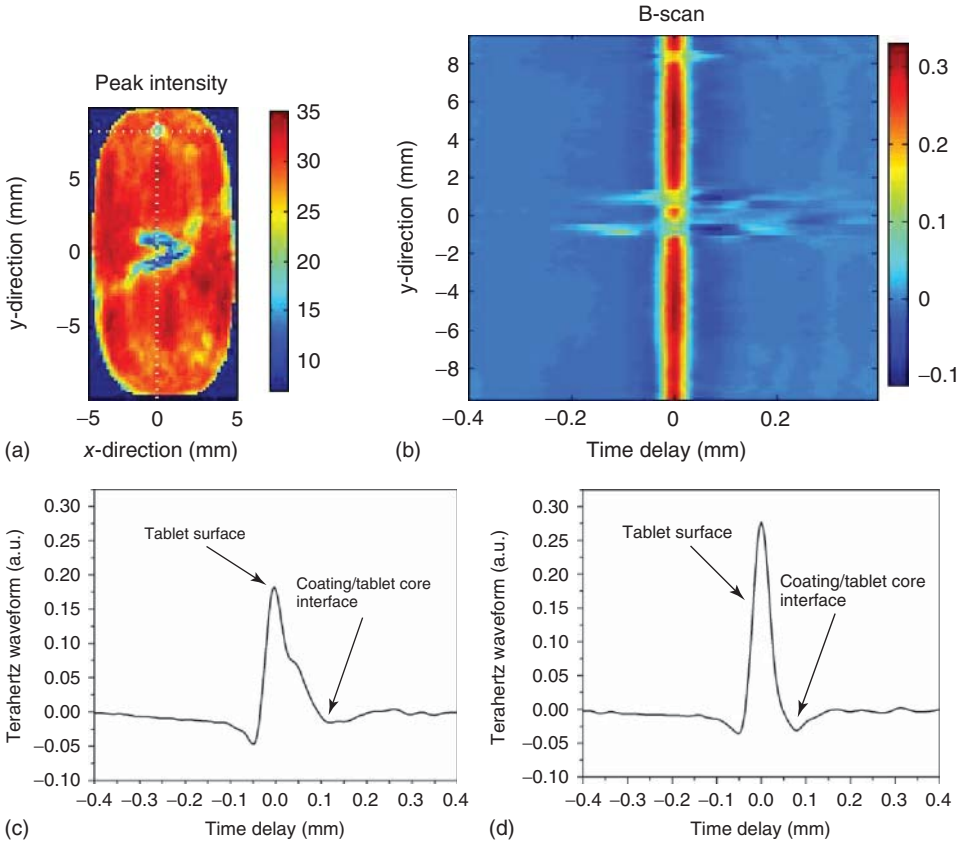

Figure 10.16 (a) Peak intensity map of a tablet showing a surface defect identified as a green circular zone at the center top of the map. In (b), the cross-section map confirms a less intensive reflection at this particular location. (c) Terahertz waveform from the area where the defect occurs that can be compared to (d) a waveform extracted from a nondefect area.

coat–core interface was most present around the tablet wall. It can be predicted that the sample would be unable to withstand further cracking for long. The hypothesis that film coating with HPMC-based coat affected the integrity of the wet granulated cores was challenged. The B-scan (Figure 10.21a) shows a succession of small-scale parallel fluctuations in peak amplitude just below the tablet coat. In addition, the HPMC-coated sample features density variations that begin beyond the parallel ridges and reach deep inside the core. Its PVA counterpart features analog zones with higher density that span more or less homogeneously from beneath the coating deep into the matrix (Figure 10.21b). This observation is critical because the weak reflections can be attributed to small changes in refractive index, originating from irregularities located in the core structure itself. Subsequent imaging demonstrated localized high reflectance

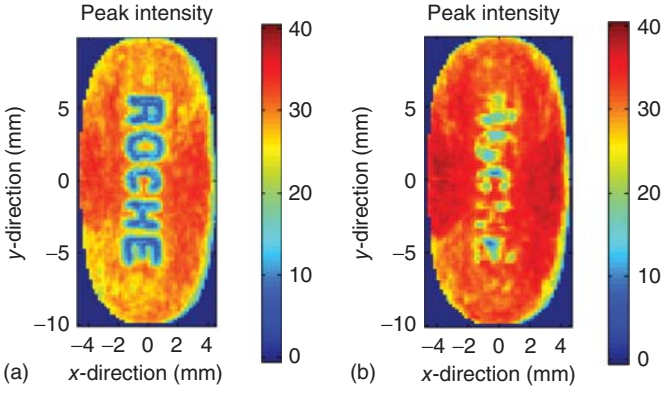

Figure 10.17 Peak intensity maps of an active, hot melt extruded (a) PVA-coated tablet and (b) HPMC-coated tablet demonstrating logo clarity differences.

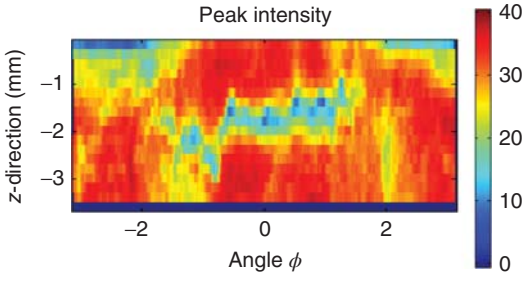

Figure 10.18 Peak intensity map of an HPMC-coated hot melt extruded tablet showing a wall defect beneath the surface.

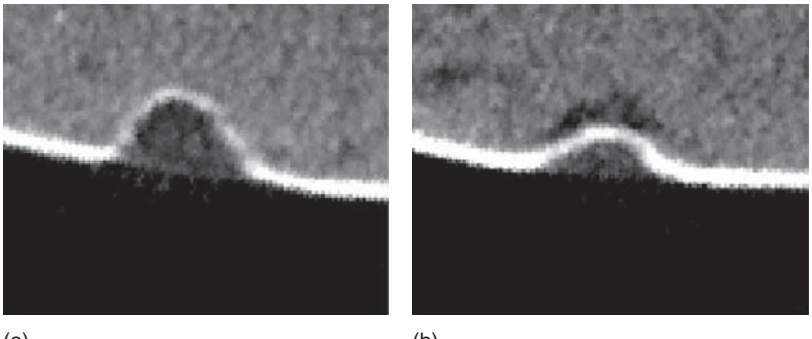

Figure 10.19 X-ray micro-CT images of the logo region showing the PVA coating close to the embossing (a), whereas the HPMC coating builds a gap (b).

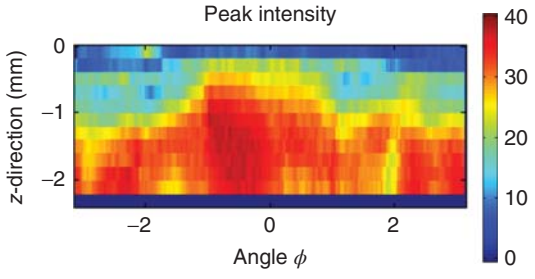

Figure 10.20 Peak intensity map demonstrating a lack of homogeneity at the outer coat that affected the inner core structure in an HPMC-coated wet granulated tablet.

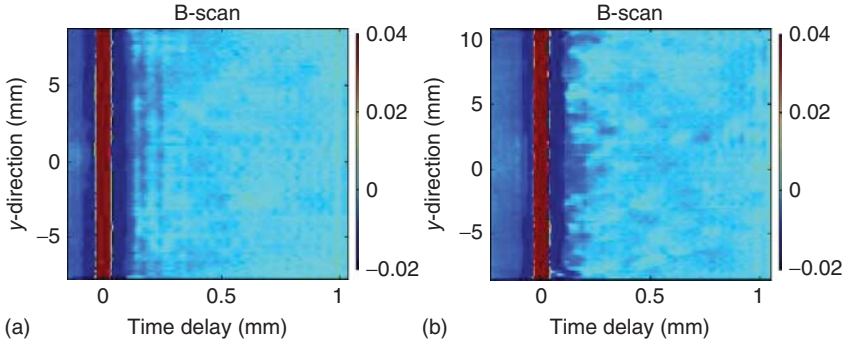

Figure 10.21 Cross sections of a wet granulated (a) HPMC-coated tablet and (b) PVA-coated tablet illustrating flaws in both finished products.

flaws in the core, just below the core–coat interface, consistent with coarse extrudate particles (Figure 10.22). This information led to investigate stress factors originating from the core manufacturing process itself.

During process scale-up relative exposure to spray in an active coating operation was suspected to be nonreproducible. THz-TDI was advantageously used to demonstrate failure due to inappropriate conditions that occurred during that specific layer process. The coating layer thickness of one side of a nonembossed active-coated tablet was 2D mapped (Figure 10.23a). The variation in intensity with increasing distance from the tablet center reflects thinning of the coating layer nearer the tablet edge. Coating thickness in this location was almost 100 μm less than at the surface center. The B-scan showed a series of small-scale fluctuations in peak amplitude at the coat–core interface (Figure 10.23b). These weak reflections are due to small changes in refractive index inside the coating layer itself and to the presence of subsurface structures. These are absent in the tablet core, whereas they are reinforced in the side-band of this particular tablet, as visible in x and y B-scans (Figure 10.24a and b). Owing to this, intratablet differences in coating layer thickness were confirmed in accordance with the 2D mapping.

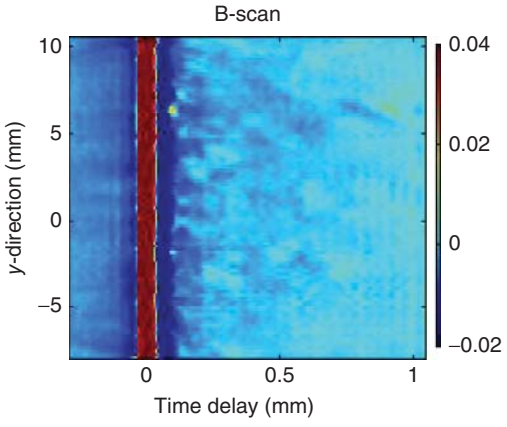

Figure 10.22 Dots of high THz reflection indicating unmilled particles can be seen just below the coat–core interface of a hot melt extruded HPMC-coated sample. Increasing areas of higher reflectance are also present in the core below 0.5 mm.

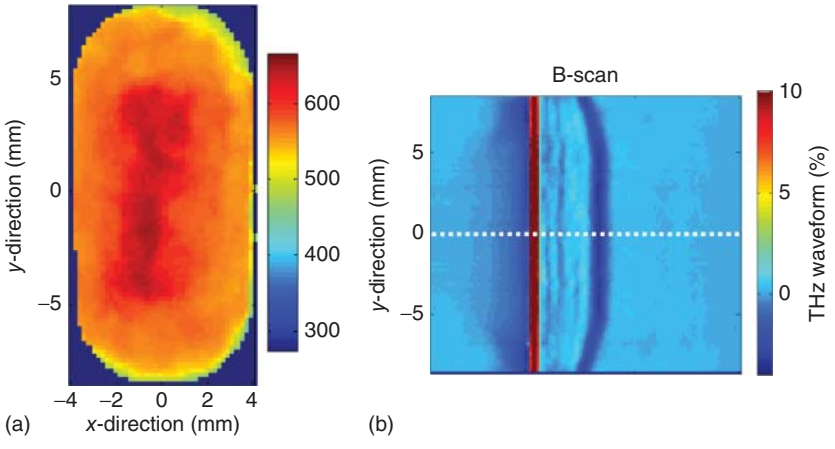

Figure 10.23 (a) Coating thickness of 2D map from a nonembossed side of a tablet showing layer thickness decreasing from the center to the edges. (b) The curved dark blue line in the cross section reflects this thinning of the coat toward the edges.

10.4.6 Discussion

The above examples illustrated many operational characteristics that make THz radiation attractive to evaluate quality within finished drug products. The versatility of THz imaging was demonstrated whenever the coating and core integrity were challenged. Because THz penetrates nondestructively into a wide range of materials, THz measurements reveal a wealth of detail in the internal structure of the probed sample. This allows the *virtual* inspection of singularities and detection of subtle structure variations inside samples with a great variety of visualization

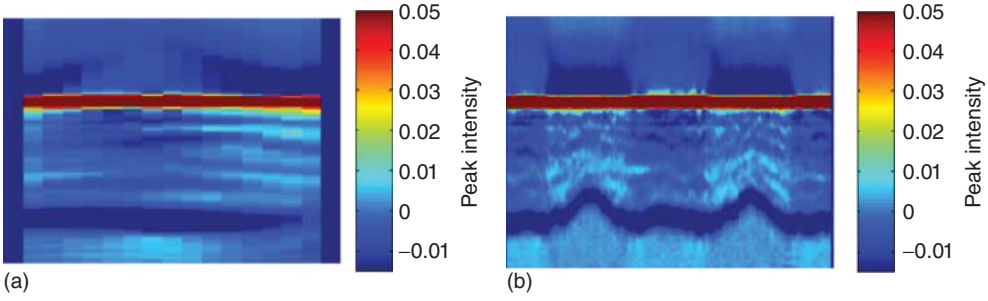

Figure 10.24 (a) *x*-direction and (b) *y*-direction B-scans showing strong irregularities in the refractive index inside the coating layer due to the presence of subsurface structures.

schemes on a computer screen. Because THz-TDI data contain more information per pixel than conventional imaging does, it is not necessary to perform multiple runs to obtain information from different depths within the sample, as is the case for confocal spectroscopic techniques, for example.

Most excipients are amorphous and at the same time almost completely transparent to THz radiation. They therefore do not exhibit particular spectral features. On the contrary, most active molecules are small organic molecular crystals that feature distinct vibrational modes at FIR frequencies. These can be distinguished from the nearly transparent matrix. THz radiation can probe intermolecular vibrations of crystalline solids and characterize solid-state modifications of drug particles [35]. Like Raman spectroscopy, THz spectroscopy produces a fingerprint-like pattern of intermolecular interactions within the sample. This gives THz spectroscopy the potential to quantify polymorphs [36], hydrates, and cocrystals [37]. Similarly, THz can be used to follow the transformation dynamics of dosage forms during degraded storage conditions for stability testing. Water is not recorded in Raman spectroscopy, but it influences THz signals. This can be of help when monitoring water ingression in samples [38].

In other chapters of this book, imaging based on Raman and IR spectroscopic studies has been proposed to assess the physical and chemical characteristics of tablets. Because a full 3D chemical map would require slicing through the tablet, imaging based on optical spectroscopy is destructive, time consuming, and may introduce artifacts into the sample under investigation. Already mentioned X-ray micro-CT is an alternative on the market for nondestructive 3D imaging of tablets and capsules. Micro-CT has a clear advantage in providing a 3D map of the whole microstructure of samples at higher resolutions. A resolution that can reach beyond 20 μm can be achieved, whereas THz imaging is limited at best between 40 and 60 μm, and mostly between 100 and 200 μm. X-rays are readily probing thinner coating layers than THz radiation is capable of. On the other hand, X-ray-based techniques feature little or no chemical specificity. X-ray tomography remains limited by the small differences in electron density observed in a drug formulation, made mostly of organic components. As drug molecules have signal responses similar to those of excipients, micro-CT is unable to visualize

the uniformity of drug molecules in a sample. No correlation or quantification of sample properties can be computed unless inorganic elements are present. Data acquisition and reconstruction are time consuming, and the compound integrity should not be forgotten when using energetic ionizing radiation. Following this, the ability to explore samples down to finest details by nonionizing measurements appears to be a clear advantage of THz. Another fundamental advantage is that sample characteristics can be correlated with the variation of the interface index to predict the behavior of solid dosage forms. For example, a correlation can be computed between the calculated interface index and the dissolution properties of a tablet. For solving coating issues, THz images give information on unexpected interfaces such as voids and cracks, all derived from refractive index variations.

10.5 Going Forward

So far THz imaging has proved to play a significant role in numerous applications. Currently, available systems are mature for implementation in the pharmaceutical industry because penetration depth and resolution obtained ensure users that a large variety of samples are analyzed with sufficient accuracy and reproducibility. However, besides being time consuming, THz imaging instruments still have to overcome some limitations in technology and signal processing to convince a wider community of scientists. In particular, high acquisition cost is subject to criticism, because current systems are designed for specific types of sample; hence, they lack of modularity. More compact, modular, and faster instruments are required for THz imaging to spread out and become a relatively standard analytical tool in a pharmaceutical laboratory. In its favor is the ability previously mentioned to combine imaging with spectroscopic information. The overall system architecture has to be revised to provide a combined device capable of performing both functions simultaneously, as was already achieved in IR and Raman microscopies. It is undeniable that this should help to reduce the purchase cost.

Because spatial resolution of THz-TDI is limited in the FIR domain, increasing lateral and spatial resolutions would be another opportunity to improve overall instrument performance. As already mentioned, current THz imaging systems fall short when spatial resolutions below 60 μm are required. Resolution depends on the width of the incident THz pulse and could be improved using much shorter pulses. The practical wavenumber range should be extended from 100 cm^{-1} to 300 cm^{-1} to better cover both intermolecular and some intramolecular vibration modes. Spectral specificity would then encompass a larger range of materials. A broader spectral range would also help to characterize thinner layer structures because higher spatial resolution can be achieved. Sample presentation to the THz pulse is impractical if the overall geometry or nature of the dosage form fails to comply with the positioning prerequisites. For example, pellets cannot be measured. The prospect of in- or online real-time measurement of coating uniformity and thickness on tablets in motion during processing could open up another

application for THz spectroscopy [39]. Theoretical work to improve conceptualization of the interface index, its amplitude, and shape is progressing and would enhance volumetric data reconstruction [40]. Although THz imaging suffers less from scattering structures in a sample than from optical imaging utilizing IR or visible radiation, scattering effects can become significant when a great number of edges are present on a sample. Better treatment of scattering losses from sharp edges in embossing, breaks, or rough surfaces, for example, would contribute to increase lateral resolution.

Since THz technology is highly promising and delivers valuable information with nondestructive measurements, there is no doubt that higher performance and affordable systems will become available within a few years. Once novel technologies bridging the gap between electronics and optics become mature, it can be predicted that alternative imaging setups will be proposed to industry. The limits in resolution previously mentioned are of the same order as the THz wavelengths and constitute an obstacle for probing samples down to a few micrometers. One promising approach relies on near-field imaging potentially capable of overcoming the current spatial resolution. Different imaging schemes are necessary when THz-TDI cannot provide details of the interior of a sample. Indeed, structural details can be retrieved, provided that interfaces back-reflecting THz pulses are present inside a tablet. Ultimately, then, micro-computed THz tomography could be preferred to construct a 3D model. Last but not least, miniaturization to a compact device comprising battery-operated source and detector of THz radiation could lead to portable systems for probing counterfeits in the field, for example.

10.6 Competition versus Cost: A Challenge for the Future

To maintain market share and introduce new high-quality drugs onto the market, drug companies need to be innovative, cost efficient, and willing not only to improve their existing current technologies but also to adopt radically new methods that break with working traditions. Costs have to be contained, but leaps to more advanced technologies are essential if leadership is to be maintained. A critical consideration is timescale. Technologies delivering fast and pertinent information are more likely to be adopted if they shorten development time while maintaining finished product quality. Targets that can be achieved by implementing 3D imaging include savings in time, more detailed understanding of process issues, fewer analytical tests, and correspondingly reduced costs. Current 3D imaging systems are expensive to buy and maintain; they cannot be considered as a low-cost choice. Analytical costs can be reduced only after the imaging system has entered routine use. During the implementation phase, methods and results will probably have to be confirmed by conventional analytical methods and data modeling. However, once the system is configured and working procedures are mastered, methods and expertise can readily be applied to handle new problems. Easier transfer of expertise will compensate for the higher costs

of the THz system, resulting in cost and time savings in the development of new drug formulations. This is not exactly the case with optical 2D imaging that requires a series of analog samples.

THz imaging offers scientists a new investigative approach to the development and understanding of drugs. It sounds extraordinary to be able to visualize the internal structure of a solid drug preparation without altering it in anyway. At the same time, THz helps to determine the root causes behind coat, core, and coat–core interaction issues. In case this sounds a limited application for THz imaging, 3D imaging is suited to more than just considering coatings and interfaces. The 3D images of finished products recorded during process scale-up can confirm immediately whether the requisite quality standards have been maintained, thereby reducing the risk of product failures during scale-up. Better understanding of a drug's detailed internal structure makes for more rational product design and shortens development time. The option of 3D mapping for finished drug products and the ability to intervene in process events based on details unobtainable by conventional analytical methods are substantial steps toward improved manufacturing control. They enable a sustainable quality level to be achieved throughout the entire production process.

10.7 Conclusion

Over the last years, THz technology has developed rapidly into a new imaging tool for the characterization of solid dosage forms in the pharmaceutical industry. This chapter has shown how THz-TDI can be used for the nondestructive characterization of tablet coatings and cores. It is unlikely ever to be used alone in pharmaceutical laboratories. The combination of multiple imaging techniques for noninvasive pharmaceutical sample analysis will increase our understanding of process issues and reveal hitherto unobserved details in the internal structure of finished products. All these techniques deliver supplementary information at the molecular and structural levels. It is both a technological challenge and a financial challenge to give pharmaceutical companies the opportunity to access multisensory imaging and at the same time invent new ways of assessing drug quality and predicting drug behavior.

Acknowledgments

It would not have been possible for the author to elaborate this chapter without support from Pascal Chalus at the Analytical Development Department of Roche in Basel, who had the opportunity to explore numerous aspects of THz imaging applied to solid dosage forms, and initiated most of the experimental investigations presented here.

References

1. Hollas, J.M. (2004) *Modern Spectroscopy*, 4th edn, John Wiley & Sons, Ltd, Chichester, p. 42.
2. Strachan, C.J., Rades, T., Newnham, D.A., Gordon, K.C., Pepper, M., and Taday, P.F. (2004) Using terahertz pulsed spectroscopy to study cristallinity of pharmaceutical materials. *Chem. Phys. Lett.*, **390** (1-3), 20–24.
3. Walther, M., Fischer, B., and Jepsen, P.U. (2003) Noncovalent intermolecular forces in polycrystalline and amorphous saccharide in the far infrared. *Chem. Phys.*, **288** (2-3), 261–268.
4. Allis, D.G., Fedor, A.M., Korter, T.M., Bjarnason, J.E., and Brown, E.R. (2007) Assignment of the lowest-lying THz absorption signatures in biotin and lactose monohydrate by solid-state density functional theory. *Chem. Phys. Lett.*, **440** (4/6), 203–209.
5. Grichkowsky, D., Chi, C., Duling, I.N., Gallager, W.J., Halbout, J.M., and Ketchen, M.B. (1987) *Proceedings of the Second OSA-IEEE (LEOS) Incline Village, Nevada, Picosecond Electronics and Optoelectronics II*, Springer Series in Electronics and Photonics, vol. 24, Springer, pp. 11–17.
6. Hu, B.B. and Nuss, M.C. (1995) Imaging with THz waves. *Opt. Lett.*, **20** (16), 1716–1718.
7. Fleming, J.W. (1974) High resolution submillimetre wave Fourier-transform spectroscopy of gases. *IEEE Trans. Microwave Theory Tech.*, **22** (12), 1023–1025.
8. Auston, D., Cheung, K., and Smith, P. (1984) Picosecond photoconducting hertzian dipoles. *Appl. Phys. Lett.*, **45** (3), 284–286.
9. Auston, D. (1975) Picosecond optoelectronic switching and gating in silicon. *Appl. Phys. Lett.*, **26** (3), 101–103.
10. Zimdars, D., Valdmanis, J., White, J., Stuk, G., Williamson, S., Winfree, W., and Madaras, E. (2005) in *AIP Conference Proceedings, Review of Progress in Quantitative Non-destructive Evaluation*, vol. 24 (A) (eds D.O. Thompson and D.E. Chimenti), American Institute of Physics, pp. 570–577.
11. Cook, D.J., Decker, B.K., Maislin, G., and Allen, M.G. (2004) Through container THz sensing: applications for explosive screening. *Proc. IEEE Int. Conf. Terahertz Electron.*, **6**, 34–37.
12. Morita, Y., Dobroiu, A., Otani, C., and Kawase, K. (2005) A real-time inspection system using a terahertz technique to detect microleak defects in the seal of flexible plastic packages. *J. Food Prot.*, **68** (4), 833–837.
13. Schmuttenmaer, C.A. (2004) Exploring dynamics in the far-infrared with terahertz spectroscopy. *Chem. Rev.*, **104**, 1759–1779.
14. Barker, D.H., Hedges, D.T., Hartwick, T.S., and Foote, F.B. (1976) Far-infrared imagery. *Appl. Opt.*, **15** (8), 1919–1922.
15. Fitzgerald, A.J., Cole, B.E., and Taday, P.F. (2005) Nondestructive analysis of tablets coating thickness using terahertz pulsed imaging. *J. Pharm. Sci.*, **94** (1), 177–183.
16. Zeitler, J.A., Shen, Y., Baker, C., Taday, P.F., Pepper, M., and Rades, T. (2007) Analysis of coating structures and interfaces in solid oral dosage forms by three dimensional terahertz pulsed imaging. *J. Pharm. Sci.*, **96** (2), 330–340.
17. Shen, Y., Taday, P.F., Newnham, D.A., and Pepper, M. (2005) Chemical mapping using reflection terahertz pulsed imaging. *Semicond. Sci. Technol.*, **20** (7), S254–S257.
18. Shen, Y., Taday, P.F., Newnham, D.A., Kemp, M., Pepper, M., Hwu, R., and Linde, K. (2005) 3D chemical mapping using terahertz pulsed imaging. Proceedings of the SPIE (Terahertz and Gigahertz Electronics and Photonics IV), pp. 24-31.
19. Zeitler, J.A., Taday, P.F., Newnham, D.A., Pepper, M., Gordon, K.C., and Rades, T. (2007) Terahertz pulsed spectroscopy and imaging in the pharmaceutical setting. *J. Pharm. Pharmacol.*, **59** (2), 209–223.
20. May, R.K., Evans, M.J., Zhong, S., Warr, I., Gladden, L.F., Shen, Y., and Zeitler, J.A. (2011) Terahertz in-line sensor for direct coating thickness measurements of individual tablets during film coating

in real-time. *J. Pharm. Sci.*, **100** (4), 1535–1544.
21. Zeitler, J.A. and Gladden, L.F. (2009) In vitro tomography and non-destructive imaging at depth of pharmaceutical solid dosage forms. *Eur. J. Pharm. Biopharm.*, **71** (1), 2–22.
22. Taday, P.F. (2004) Applications of terahertz spectroscopy to pharmaceutical sciences. *Philos. Trans. R. Soc. London, Ser. A*, **362**, 351–364.
23. Palermo, R., Cogdill, R., Short, S., Drennen, J.K. III, and Taday, P.F. (2008) Density mapping and chemical component calibration development of four-component compacts via terahertz pulsed imaging. *J. Pharm. Biomed.*, **46** (1), 36–44.
24. Juuti, M., Tuononen, H., Prykäri, T., Kontturi, V., Kuosmanen, M., Alarousu, E., Ketolainen, J., Myllylä, R., and Peiponen, K.-E. (2009) Optical and terahertz measurement techniques for flat-faced pharmaceutical tablets: a case study of gloss, surface, roughness and bulk properties of starch acetate tablets. *Meas. Sci. Technol.*, **20**, 015301.
25. Tuononen, H., Gornov, E., Zeitler, J.A., Aaltonen, J., and Peiponen, K.-E. (2010) Using modified Kramers–Kronig relations to test transmission spectra of porous media in THz-TDS. *Opt. Lett.*, **35** (5), 631–633.
26. Obradovic, J., Collins, J.H.P., Hirsch, O., Mantle, M.D., Johns, M.L., and Gladden, L.F. (2007) The use of THz time-domain reflection measurements to investigate solvent diffusion in polymers. *Polymer*, **48**, 3494–3503.
27. Ho, L., Mueller, R., Gordon, K.C., Kleinebudde, P., Pepper, M., Rades, T., Shen, Y., Taday, P.F., and Zeitler, J.A. (2009) Terahertz pulsed imaging as an analytical tool for sustained-release tablet film coating. *Eur. J. Pharm. Biopharm.*, **71** (1), 117–123.
28. Zeitler, J.A., Newnham, D.A., Taday, P.F., Threlfall, T.L., Lancaster, R.W., Berg, R.W., Strachan, C.J., Pepper, M., Gordon, K.C., and Rades, T. (2006) Characterization of temperature induced phase transitions in the five polymorphic forms of sulfathiazole by terahertz pulsed spectroscopy and differential scanning calorimetry. *J. Pharm. Sci.*, **95** (11), 2486–2498.
29. Zeitler, J.A., Kogermann, K., Rantanen, J., Rades, T., Taday, P.F., Pepper, M., Aaltonen, J., and Strachan, C.J. (2007) Drug hydrate systems and dehydration processes studied by terahertz pulsed spectroscopy. *Int. J. Pharm.*, **334** (1-2), 78–84.
30. Spencer, J., Gao, Z., Moore, T., Buhse, L., Taday, P.F., Newnham, D.A., Shen, Y., Portieri, A., and Husain, A. (2008) Delayed release tablet dissolution related to coating thickness by terahertz pulsed image mapping. *J. Pharm. Sci.*, **97** (4), 1543–1550.
31. Ho, L., Mueller, R., Gordon, K.C., Kleinebudde, P., Pepper, M., Rades, T., Shen, Y., Taday, P.F., and Zeitler, J.A. (2009) Monitoring the film coating thickness and drug layer uniformity on in-vitro drug release from sustained-release coated pellets: a case study using terahertz pulsed imaging. *J. Pharm. Sci.*, **98** (12), 4866–4876.
32. May, R., Han, L., Alton, J., Zhong, S., Elliott, J., Byers, C., Gladden, L., Evans, M., Shen, Y., and Zeitler, J. (2009) Pharmaceutical tablet hardness measurements with THz pulsed imaging. IEEE 34th International Conference on IRMMW-THz, Busan, South-Korea, pp. 1–2.
33. TeraView Ltd. TPI Imaga 2000, St John's Innovation Park, Cambridge.
34. Davies, A.G., Linfield, E.H., and Johnston, M.B. (2002) The development of terahertz sources and their applications. *Phys. Med. Biol.*, **47**, 3679–3689.
35. Li, R., Zeitler, J.A., Tomerini, D., Parrott, E.P.J., Gladden, L.F., and Day, G.M. (2010) A study into the effect of subtle structural details and disorder on the terahertz spectrum of crystalline benzoic acid. *Phys. Chem.*, **12**, 5329–5340.
36. Taday, P.F., Bradley, I., Arnone, D.A., and Pepper, M. (2003) Using terahertz pulse spectroscopy to study the crystalline structure of a drug: a case study of the polymorphs of ranitidine hydrochloride. *J. Pharm. Sci.*, **92** (4), 831–838.
37. Parrott, E.P.J., Zeitler, J.A., Friscic, T., Pepper, M., Jones, W., Day, G.M., and Gladden, L.F. (2009) Testing the sensitivity of terahertz spectroscopy to

changes in molecular and supramolecular structure: a study of structurally similar cocrystals. *Cryst. Growth Des.*, **9** (3), 1452–1460.

38. Portieri, A., Taday, P.F., and Shen, Y.C. (2007) Terahertz pulsed imaging for non-invasive and non-destructive analysis of the hydration dynamics of HPMC matrix. 58th Pittsburgh Conference on Analytical and Applied Spectroscopy, PITTCON 2007, Chicago, IL.

39. Maurer, L. and Leuenberger, H. (2009) Terahertz pulsed imaging and near-infrared imaging to monitor the coating process of pharmaceutical tablets. *Int. J. Pharm.*, **370**, 8–16.

40. Shen, Y. and Taday, P.F. (2008) Development and application of terahertz pulsed imaging for non-destructive inspection of pharmaceutical tablets. *IEEE J. Sel. Top. Quantum Electron.*, **14** (2), 407–415.

Part V
Imaging Beyond the Diffraction Limit

Infrared and Raman Spectroscopic Imaging, Second Edition. Edited by Reiner Salzer, Heinz W. Siesler.
© 2014 Wiley-VCH Verlag GmbH & Co. KGaA. Published 2014 by Wiley-VCH Verlag GmbH & Co. KGaA.

11
Spectroscopic Imaging of Biological Samples Using Near-Field Methods

Lucas Langelüddecke, Tanja Deckert-Gaudig, and Volker Deckert

11.1
Tip-Enhanced Raman Scattering (TERS)

11.1.1
From SERS to TERS

Almost 40 years ago, the first experiments of Fleischmann *et al.* [1] with pyridine adsorbed to a silver electrode revealed changes in signal intensity and band position compared to normal Raman spectra. Independently, Van Duyne and Creighton [2, 3] showed the appearance of new bands and an increased intensity of the bands up to a factor of five orders of magnitude. Furthermore, they proposed an end-on orientation of the adsorbed pyridine to the silver electrode. This started the area of so-called surface-enhanced Raman scattering (SERS) experiments. In this technique, rough or structured metal surfaces (most commonly silver or gold) or colloidal dispersions of nanoparticles are used to create sites of high enhancement of the electromagnetic field. Consequently, the scattered Raman signal of molecules located in close vicinity to those surfaces will be enhanced. In this way, SERS turned insensitive conventional Raman scattering to a highly sensitive technique [4]. Due to chemical adsorption and potentially gradient-field effects, the spectra can sometimes change significantly with respect to normal Raman spectra – a fact that always has to be taken into account when assigning SERS spectra. Up to now, several studies have claimed and demonstrated the possibility of single-molecule SERS [5–7].

Although SERS could overcome the low sensitivity of conventional Raman spectroscopy, other challenges remain. For instance, the preparation of reproducible SERS substrates is still an issue, and a clear correlation of measured position and recorded spectrum is extremely difficult. This can be overcome by the so-called tip-enhanced Raman scattering (TERS) [8–10]. Instead of using rough substrates or colloids where the sample is adsorbed to, a single structure in the form of a sharp edge or a single nanoparticle is attached to a well-controllable probe similar to an atomic force microscopy (AFM) or scanning tunneling microscopy (STM) tip (see Figure 11.1a–c). In other words, in TERS a SERS substrate has been reduced to a

Infrared and Raman Spectroscopic Imaging, Second Edition. Edited by Reiner Salzer, Heinz W. Siesler.
© 2014 Wiley-VCH Verlag GmbH & Co. KGaA. Published 2014 by Wiley-VCH Verlag GmbH & Co. KGaA.

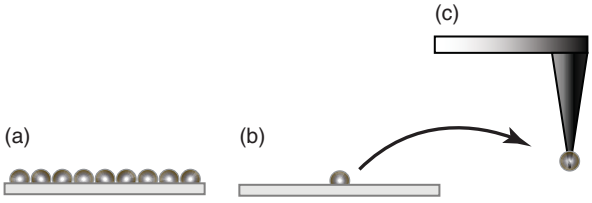

Figure 11.1 Conceptual description of TERS: (a) a rough SERS substrate with many nanoparticle-like structures on the surface – sample will be attached to this surface; (b) just one isolated nanoparticle from an SERS substrate – sample will still be attached to this surface; and (c) one nanoparticle is attached to the end of an AFM or STM tip, which can be positioned deliberately on any sample surface.

single nanoparticle, which is scanned over the sample surface. Consequently, each spectrum can be directly correlated with tip position.

A TERS tip features well-defined and homogeneous enhancement properties and, probably most interesting, the potential to measure with a spatial resolution on the nanometer scale, because the enhanced region directly correlates with the radius of the nanoparticle at the end of the tip (typically around 10–20 nm). Making reproducible tips is still demanding, and producing the optimal tip is a topic in the TERS community. However, several ways exist for TERS tip production that provides usable tips, namely, evaporation of silver or gold to AFM/STM tips or wire etching to name only a few [11]. As this contribution is focusing on current and potential applications of TERS, details of tip manufacturing will not be discussed further.

11.1.2
Investigation of Nonbiological Samples with TERS

In the last one and a half decade, the broad scope of application of TERS was demonstrated on many different samples. In this chapter, selected TERS investigations of nonbiological samples are shown followed by biological specimen. For a quick overview, representative samples and the associated references are listed in Table 11.1.

In particular, carbon nanotubes (CNTs) are frequently investigated by TERS. The enhancement of the characteristic G band (around 1580 cm^{-1}) and D band (around 1330 cm^{-1}) is a major objective of TERS investigations. A nice example for the suitability of TERS in this field is the intensity ratio of G/D. This value can be considered as a quality indicator of CNTs (high quality CNT: G/D $\approx$ 100), which can be nicely visualized with TERS. In case of defects, the D band intensity increases so that the G/D ratio gets smaller allowing conclusions on the CNT quality. The lateral resolution in these experiments was at least around 15 nm [20].

Another very prominent molecule for TERS measurements is malachite green isothiocyanate (MGITC). In a comparative study on CN^- ions and MGITC, it was demonstrated that enhancement factors of around 10^6 could be achieved [16].

Table 11.1 Selected nonbiological samples used in TERS experiments.

Sample	References
Rhodamine 6G (R6G)	[10, 12–14]
Malachite green isothiocyanate (MGITC)	[14–18]
C_{60}	[9, 19]
Carbon nanotubes (CNT)	[20–29]
Brilliant cresyl blue (BCB)	[8, 14, 30, 31]
4,4′-Bipyridine	[32]
Graphene	[33–39]
Inorganic semiconductors	[40–47]

In this context, different refractive indices of underlying substrates were tested in TERS experiments and differences in the enhancement of the Raman signal emerged [14].

11.1.3 Technical Considerations of TERS

TERS would be impossible without STM [48] and/or AFM [49]. It certainly profits from the instrumental developments in scanning probe microscopy and Raman microscopy. In principle, a TERS setup can be built on the basis of well-developed and commercially available techniques. The endeavor is an efficient coupling of both techniques in order to increase the contrast between enhanced and unenhanced/background signal and maintain the setup stability required for a lateral resolution far below the optical diffraction limit. A transmission TERS setup [50] is sketched in Figure 11.2.

11.1.3.1 Application

A TERS setup requires a laser suitable for Raman spectroscopy, an AFM/STM including the respective feedback control of the tip, a focusing unit, and a Raman spectrometer. Different laser wavelengths can be used matching different plasmonic resonances (e.g., Ag, Au, Al). AFMs and STMs can be operated in a variety of modes (tapping, contact, shear force, constant current). The main requirement is a stable feedback to maintain a reliable/constant tip-to-sample distance. Focusing of the laser beam on the TERS tip and matching of the desired resonance conditions of the nanoparticle can be realized in several ways. Mostly the beam is focused by a dry or immersion objective on the tip. A very interesting alternative is the use of parabolic mirrors that allow the highest collection efficiency and the best illumination geometry for dry conditions [51–53]. The addition of special polarization optics to generate radially polarized light instead of commonly used linearly polarized light can further improve the performance of the setup [51, 54, 55]. The enhanced field at the tip apex eventually interacts with the sample, and some fraction of the light is scattered inelastically. This signal can be collected

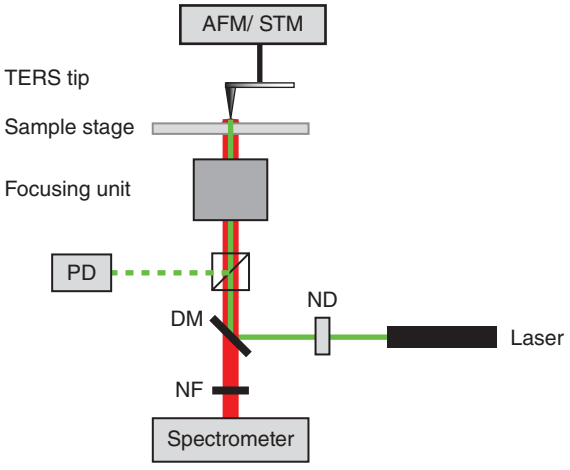

Figure 11.2 Transmission TERS setup. For a detailed explanation, see text. NF, notch filter; DM, dichroic mirror; ND, neutral density filter; and PD, photo diode for setting the tip in the laser focus.

using the same or an additional objective or mirror and is finally detected by a Raman spectrometer.

Different configurations are possible for TERS depending on the specific requirements of the experiment. Mostly this depends on the sample thickness and transparency. Four commonly used geometries are presented in Figure 11.3. One of them is a top-illumination setup where a laser is focused from the top to the tip (see Figure 11.3a) [56]. This requires protruding AFM tips in order to avoid shadowing effects by the cantilever. A big advantage of this setup is that opaque samples can be investigated. The same is true for TERS in side illumination, where the objective is placed not above the tip but illuminates from the side (see Figure 11.3b) [23]. In a back reflection or transmission configuration, sample and substrate must be transparent (see Figure 11.3c) [12, 57]. The advantage of this setup is that a maximum of the scattered light can be collected with high efficiency in particular if immersion lenses are utilized. In Figure 11.3d, a parabolic mirror is used for laser focusing and signal collection. This system features several advantages: first, opaque samples can be investigated with protruding tips at high collection efficiency; second, the system has no chromatic aberrations; third, the longitudinal plasmonic oscillation is more efficiently enhanced; and last but not least, a smaller laser focus can be obtained, leading to a lower background in the spectra [58]. On the other hand, the alignment of the parabolic mirror is more demanding and standard cantilever-based TERS probe cannot be easily implemented.

If biological samples are of interest, experimental conditions should be selected in such a way that the natural state of the sample (pH, osmotic pressure, etc.) is maintained. Many analytical methods require samples in a dry state, that is, cells must be chemically fixed to the substrate, which limit their applications. In order

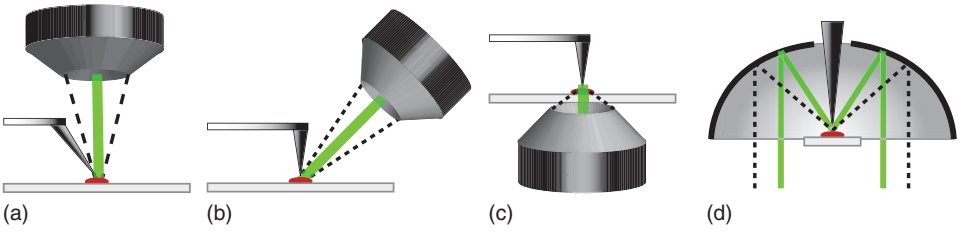

Figure 11.3 Mainly employed TERS configurations: (a) top illumination, (b) side illumination, (c) bottom illumination and (d) illumination through parabolic mirror.

to mimic a native environment, it is often necessary to work in liquids such as buffers or water. AFM measurements in liquids are known for a long time, but in case of TERS experiments the properties of the plasmonic probes can be drastically influenced. The metals can degrade and/or build a thick passivation layer, or dissolved substances can bind to the probes generating unwanted signals. For TERS in liquids, a few approaches have been tested so far. One approach utilizes a self-assembled monolayer of ethanethiolate that covers the TERS tip [59]. This molecule is a rather elegant choice because it is small and hardly attenuates the evanescent field at the probe. The thiolate monolayer produces stable spectra, which can be easily subtracted from the tip-enhanced Raman (TER) spectra of the actual sample. Such a modified tip was successfully used to perform TERS in aqueous solution [59].

Another access to TERS in liquids could be afforded by the diving-bell design, which was successfully applied in near-field scanning optical microscopy (NSOM) experiments on cells [60]. In this approach, an aluminum-coated optical fiber tip attached to a tuning fork was used to excite the molecules. Using tuning forks, the distance between sample and tip can be controlled with a comparable quality as for cantilever-based systems, which are important to achieve a constant and high signal quality. The tuning fork feedback system is also common in dry TERS systems, and hence, this approach should be, in principle, transferable to TERS in liquids by exchanging aluminum by silver.

As shown in the earlier section, a variety of instrumental possibilities are available to achieve optimum TERS results. Depending on the sample, one can choose between back-reflection setup, side illumination, and parabolic mirror setup. On all accounts, signal-to-noise ratio (SNR) and contrast arguments must be balanced with experimental flexibility.

11.2
Detection of Biomolecules

This section focuses on the distinction and identification of only a few and potentially even single biomolecules. The first part provides details about differentiation and identification of molecules such as amino acids and deoxyribonucleic acid/ribonucleic acid (DNA/RNA) bases by their TERS spectrum. In the second

part, it is shown that TERS is capable of tracking structural changes on the molecular level. Such results could give insight into reaction mechanisms of molecules and are important for a basic understanding of, for example, diagnosis and treatment of diseases.

11.2.1 Differentiation/Identification of Single Biomolecules

Amino acids and nucleobases are the building blocks of proteins and DNA/RNA, respectively, and constitute the origin of terrestrial life. One of the major targets of research related to DNA/RNA and proteins is to sequence these macromolecules fastly, cheaply, and with high accuracy. In addition to the sequence (primary structure) in proteins, the secondary and tertiary structures are also important to investigate functionality. Until recently, spectroscopic studies of nucleobases and amino acids were limited to relatively large sample amounts, and a direct approach was hampered by the diffraction limit of conventional optics. Super-resolution fluorescence-based methods such as photo activated localization microscopy (PALM), stochastic optical reconstruction microscopy (STORM), and stimulated emission depletion (STED) achieving nanometer resolution, however, face the problem that labeling is almost always mandatory [61]. At the level of single-molecule investigations of proteins and DNA/RNA, where every segment ultimately has to be labeled, this leads at least to changes in the molecular behavior or, because of steric hindrance, is impossible. TERS can potentially address such a high resolution and, although research on bio-TERS is in an early stage, evidence that only very few molecules can be excited exists [17, 62]. Interestingly, high lateral resolution spectroscopy can result in an uncommon variability of the spectra. The local environment of the detected molecules plays an important role. Thus, averaging effect are less prominent in localized experiments than in bulk experiments. Consequently, the spectra can sometimes resemble those of single crystals where the actual orientation and the polarization of the light play a significant role, leading to strong signal intensity variations as will be shown later.

11.2.1.1 Amino Acids

Main structural molecular characteristics of amino acids are a carboxylic acid and an amino group in one molecule. They can be coupled in a huge variation but only 22 of over 500 known amino acids are proteinogenic, that is, needed for the buildup of polypeptides and proteins. Selected proteinogenic amino acids are discussed in the following with respect to single-molecule detection and the effects of connecting two or more amino acids to a peptide.

TERS experiments on amino acid monolayers have demonstrated that nanocrystalline gold plates provide an excellent substrate [63]. These plates show a surface roughness of 100–200 pm, which is essentially atomically flat. The hexagonal and triangular gold plates have a height of about 20 ± 5 nm and

thus are optically transparent. However, due to the thickness, these gold plates attenuate the laser intensity by ~25–40% if measured in transmission mode. Using such gold plates, the so-called gap mode can be observed. This effect further enhances the field between the sharp metal tip (TERS tip) and the metal surface (gold plate) up to a maximum distance of 30 nm and compensates for the attenuation losses [64].

It is known that adsorbed molecules on flat gold surfaces experience a homogeneous binding environment. In turn, this presence of equal molecular binding sites results in homogeneous TER spectra [18]. For example, the dimer of the amino acid cysteine (cystine) was immobilized for TERS experiments on gold nanoplates by stable covalent Au–S bonds. The TERS results surprisingly revealed two sets of spectra correlating to two distinct species on the gold surface. One set of spectra was assigned to the neutral form of cystine; the second was assigned to the zwitterionic state. As cystine was crystallized from a neutral aqueous solution, mainly the zwitterionic state was present on the gold surface; however, for a decisive distinction, the number of experiments was too low. The neutral form had its carboxyl stretching vibration at 1685 cm^{-1}, whereas the zwitterionic form showed a mode at 1631 cm^{-1}. A shift of the stretching vibration mode of the amine in the two forms was also observed (neutral: 1197 cm^{-1}; zwitterion: 1119 and 1614 cm^{-1}). Another interesting observation in the experiments was Raman bands of the C–S bond: Two bands at 676 and 746 cm^{-1}, respectively, showed the presence of two conformers of the dimer during the measurement. In addition, a weak band matching the S–S bond was observed in the TER spectra at 489 cm^{-1}, which corresponds to a downshift with respect to normal Raman [65]. Variations in intensity can be explained by the small number of molecules probed by the tip, and by the fact that in a TERS experiment also energetically nonfavored nanoparticle–sample interactions can be observed (e.g., the tip can approach sites of a molecule that would usually not be attracted to gold or silver). In SERS experiments, molecules interact chemically with the enhancing particle and a selection of a favored site or a conformation can be even tuned [66].

To differentiate amino acids from proteins with TERS, it is crucial to start under well-defined conditions to attain spectral characteristics at particular sample positions and conformations. In practice, the amino acids tyrosine (Tyr), phenylalanine (Phe), tryptophan (Trp), and a mixture of the latter two on above-mentioned gold nanoplates were investigated with TERS (for structures, see Figure 11.4, top).

For instance, phenylalanine spectra were collected at different evenly spaced positions. The data revealed a homogeneous adsorption of the amino acid. Interestingly, no ring breathing mode was observed around 1000 cm^{-1}, which could be attributed to the fact that the molecules were oriented parallel with respect to the gold surface (see Figure 11.4, modeled structures). According to the orthogonal orientation of the exciting field with respect to the aromatic ring, a ring breathing mode suppression under those conditions could be explained. Supplementary theoretical calculations revealed only a small influence of the tip with the orientation of the amino acids on the gold platelets, which become “flatter” in the

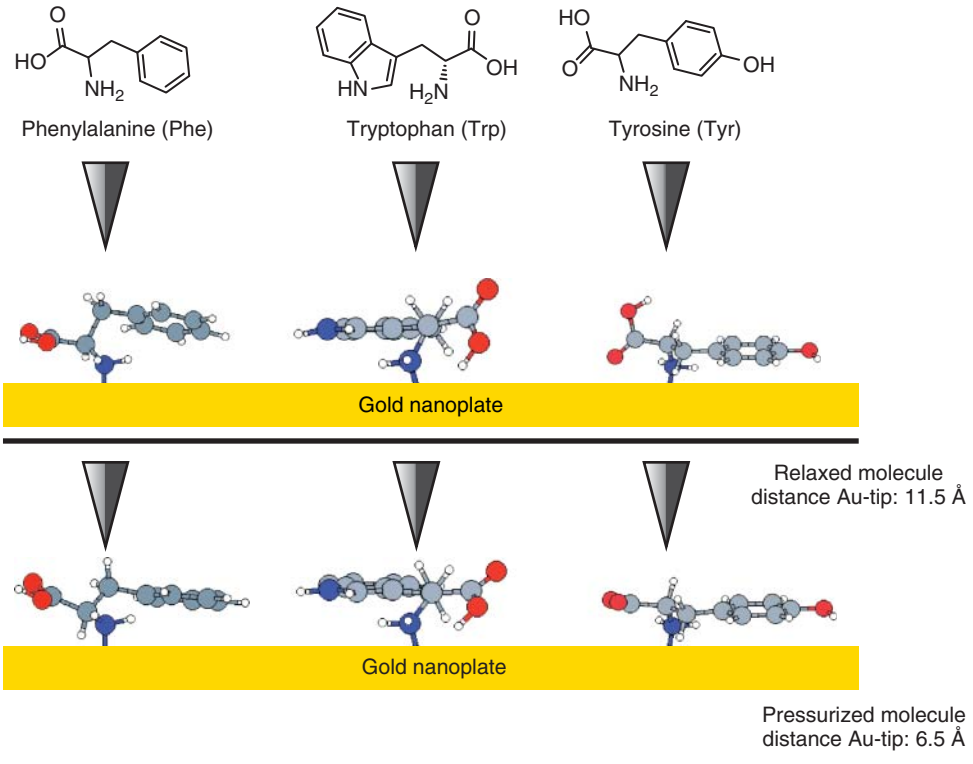

Figure 11.4 Theoretical calculations for the orientation of three different amino acids on Au(111) as a model for the gap between a silver-coated TERS tip and gold nanoplates. (Adapted from Ref. [61], American Chemical Society.)

presence of the tip. This clearly explains the at first glance unexpected appearance of the spectra [67]. Similar results were obtained for tyrosine and tryptophan. It is noteworthy that the quite extreme behavior was a consequence of the orientation under the specific conditions. In proteins, the ring breathing mode of Phe is often observable in TERS. Here, the aromatic ring is integrated to the protein skeletal structure enabling various orientations of the mode. This example neatly shows that a straightforward comparison of TERS spectra with normal Raman and SERS data can be misleading.

The next step toward understanding TER spectra of proteins was the investigation of small peptides. In those experiments, the detection of the peptide bond was of particular interest. In a comparative Raman, SERS, and STM–TERS studies of dipeptides, a tripeptide, and a protein, results were presented by Blum *et al.* in 2012 [65]. Experiments were performed with an STM–TERS setup, which enables a precise sample–tip distance control, which can be applied to either conductive samples or very thin (~1–2 nm) samples on a conductive substrate. In contrast to AFM-based experiments, some additional effects regarding the actual voltage bias between tip and sample must be carefully considered [68]. Using the dipeptides

Phe-Phe and Tyr-Tyr and the tripeptide Tyr-Tyr-Tyr (all immobilized on gold substrates), the authors showed that surface-enhanced Raman (SER) and TER spectra of the substances resembled each other better than the normal Raman spectra resembled the TER spectra. This was explained by molecular interactions of peptide and metal surface, which is present in SERS and TERS but absent in normal Raman spectroscopy. It has to be noted that the spectral patterns of all three methods were the same for the three oligomers. Differences between the different Raman techniques were noticed in band intensities and number of bands. This is only reasonable as standard Raman and SER spectra detect an average of all possible orientations of the investigated molecules. In SERS and TERS, the aforementioned interactions of sample molecule and metal surface can influence the molecular symmetry by bond formation and can change selection rules. Consequently, some additional bands might appear [69, 70]. Last but not least, gradients of the electric field can cause a change of selection rules in the case of SERS and TERS [4, 71]. In TERS, the sharp tip only probes small sample volumes thus only probes few – if not a single – molecules, and so it is possible to monitor different molecular orientations and conformations when moving the tip laterally by just a few nanometers.

The orientation of molecules in gap-mode configuration was addressed in another experiment with a peptide. Oxidized glutathione (Glutathione disulfide, GSSG) was investigated to study the orientation of a peptide structure in a sandwich configuration [72]. GSSG is a sulfide-bridged dimer whose monomer glutathione (GSH) is constructed from the amino acids glutamic acid (Glu), cysteine (Cys), and glycine (Gly).

The homogeneously immobilized molecules on the gold plates were readily identified in the TER spectra. As a result, a preferred orientation of the molecules on the substrate was deduced. Strong bands resulting from COO^- stretching vibrations implied that the molecule was bound to the gold surface via its glutamyl moiety; the absence of a band near 500 cm^{-1} pointed toward the dissociation of the dimer. Furthermore, amide I, II, and III bands (marker bands of the peptide bond) indicated a nondenatured state of the peptide. These results can be considered as an evidence that single amino acids can show not only favored adsorption orientations but also small peptides, which are again important to know whether long peptide chains – namely proteins and polypeptides – are addressed.

In conclusion, TERS allows a clear characterization and distinction of selected amino acids and small peptides. The observed orientation effects could be explained by the small number of molecules contributing to a TERS signal.

11.2.1.2 DNA/RNA Nucleobases and Derivatives

The four nucleobases guanine (G), adenine (A), thymine (T), and cytosine (C) are the essential molecules in the biomacromolecules DNA and RNA.

If they are coupled to a polymeric backbone of sugars (ribose) and phosphates, a single-stranded deoxyribonucleic acid (ssDNA) is generated. In a hybridization step, such strands can combine to a double-stranded deoxyribonucleic acid

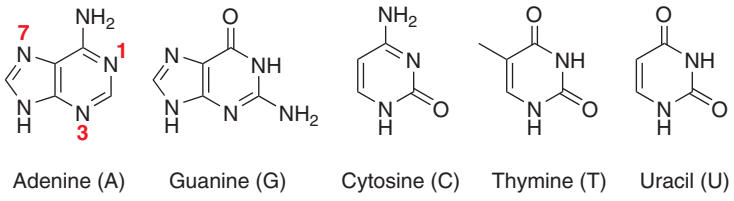

Figure 11.5 Structures of the four DNA bases (A, G, C, and T) and the RNA base (U).

(dsDNA) where the Watson–Crick base pairs A–T and G–C are formed. RNA has an additional OH group at the sugar when compared to that of DNA, and thymine is replaced by uracil (U) (see Figure 11.5).

Although the sequence of DNA/RNA molecules is of huge interest, regarding standard procedures no real need exists for the development of a new direct sequencing method because the established polymerase chain reaction (PCR)-based methods are extremely powerful. This is different if more specific systems such as methylated DNA or ancient DNA need to be analyzed. For those structures, TERS potentially offers an alternative approach because it works at an ultrahigh resolution, which is highly specific and sensitive.

Before TERS was considered, scanning near-field optical microscopy (SNOM) in combination with SERS was used to perform high-resolution structural DNA analysis [73]. In those experiments, brilliant cresyl blue (BCB)-labeled DNA was adsorbed on silver-coated Teflon spheres in order to examine the correlation between topography and near-field Raman spectra.

TERS on DNA bases was demonstrated for the first time in 2004 by Watanabe *et al*. In that work, experiments and density-functional theory (DFT) calculations on adenine molecules in a nanocrystal were presented. From the acquired spectra, which differed from standard Raman spectra, it was concluded that those crystals were mechanically deformed in contact-mode TERS [74]. Consequently, band shifts were observed and attributed to interactions of molecule and metal tip. Comparing SER and TER spectra, a band shift could be observed, too, mainly caused by more specific interactions of adenine and metal. In SERS of adenine on silver island films, molecules were evenly attached to the rough surface by the amino group and its adjacent nitrogen atoms (N1 and N7). In contrast, in contact-mode TERS experiments (i.e., tip always touches the sample), the silver tip was constantly moved over the molecules with a force of $\approx 1-5$ pN per molecule. Based on theoretical calculations, the authors concluded that the TERS probe was selectively pressed to one nitrogen atom (namely N3). Later it was shown that in contact-mode TERS, an adsorption–desorption process of the molecule at the tip could be responsible for the band shift [62].

In addition to mechanical effects, temporal fluctuations were observed in the same experiment. These fluctuations of bands were explained as follows: the tip approached and compressed the adenine molecule and the tip adsorbed adenine. The tip drifts and therefore deformed the molecule; if the tip drifted too far, the dragging force became too big to keep the molecule at the tip resulting

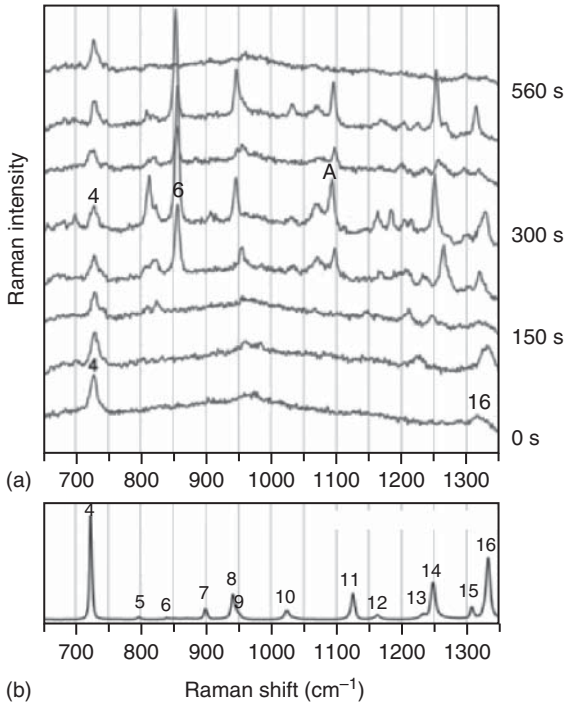

Figure 11.6 (a) Characteristic contact-mode TERS spectra of adenine collected in a time series. (b) Normal Raman spectrum of bulk adenine. (Selected part was adapted from Ref. [62], American Chemical Society.)

in desorption. Simultaneously, a new adenine molecule could adsorb to the tip and the process recurred. Noteworthy here, the silicon signal of the TERS tip remained stable in a range of 0.4 cm^{-1} and was used as a reference. It was found that the band positions of adenine deviated up to 8 cm^{-1} from normal Raman modes. Interestingly, only two bands (band 4 at 728 cm^{-1} and band 16 at 1330 cm^{-1} in Figure 11.6) seemed not to be affected by tip interactions.

This hypothesis was supported by normal Raman and SERS spectra of adenine. Assuming that the electromagnetic field enhancement was constant during the measurements, it is reasonable that chemical and mechanical enhancement mechanisms were responsible for band fluctuations. These mechanisms require a very small distance between the TERS tip and the molecule, as realized in contact-mode TERS.

TERS experiments are strongly dependent on the texture of the nanoparticle at the tip apex (size, roughness, shape). This was demonstrated in a comparative SERS study of the four DNA bases and their corresponding deoxynucleotides (sugar + monophosphate + base), which generally exhibit a smaller Raman cross section and therefore lower band intensities than the pure bases [75]. In addition, TERS experiments of the pure bases thymine and cytosine were included in the study. In contrast to the previous work on adenine, the TER spectra resembled

the normal Raman spectra. This was attributed to the specific position of the silver nanoparticle at the TERS tip. Most likely the signal enhancing silver particle was slightly behind the actual apex. Such geometry would result in an increased sample–tip distance avoiding a direct tip–sample contact. As a result, no chemical interactions (indicated by new bands or band shifts), as shown in the experiments, would be detected.

In addition to the position of the silver particles at the TERS tip, the operation mode of the AFM influences the spectra. In the adenine experiments contact mode was used, whereas for the pyrimidine bases tapping mode (intermittent contact) has been employed. In the latter mode, the tip gently touches the sample at every lowest point of its oscillation (with amplitudes typically 10 nm or smaller). This mode is most suitable for biological samples as there is less possibility of destroying the sample or pushing the specimen compared to contact mode. However, as the tip–sample distance is constantly changing, the overall signal enhancement can be lower.

STM–TERS was also utilized for detecting nonresonant molecules at very low concentrations such as DNA bases at picomoles per square centimeter [76]. Here, the number of molecules in a monolayer coverage in the enhancement region beneath the tip was estimated to be ∼3000. Because of the weak adsorption of DNA bases on Au(111), it was suggested that a submonolayer coverage was present. In spectra of adenine, the enhanced ring breathing mode was detected at 731 cm^{-1} whose intensity was integrated for monolayer and submonolayer coverages. Assuming linearity between band intensity and number of scattering molecules, the authors calculated the smallest detectable number of adenine molecules to be 130, to say 18 $pmol\,cm^{-2}$. These results were compared with a resonant molecule that could be detected at single molecule level [17], concluding that a resonance contribution in TERS is important when it comes to single-molecule detection because the SNR simply gets better.

An important finding was the detection of hydrogen bonds in DNA (which is particularly important for hybridization of DNA) by TERS published by Zhang *et al.* [77]. Adenine (A) and thymine (T) were investigated on Au(111) to utilize the already discussed gap-mode configuration. For a detailed comparison, spectra of the pure bases and of a mixed system (T/A ratio ≈ 55) were discussed.

From the presence and absence of bands, it was possible to gain information about the binding situation of the molecules (e.g., thymine can bind to adenine via a hydrogen bond). The ring vibration mode of bound thymine at 792 cm^{-1} provides evidence for a hydrogen bond because of an orientation change with respect to pure thymine, which is adsorbed flatly to the surface and therefore does not show a ring vibration mode. In addition, the strongly increased in-plane thymine methyl group rocking vibration band at 984 cm^{-1} evidence that (i) thymine was present and (ii) thymine was bound to adenine via a hydrogen bond.

Moreover, a significant shift of the thymine C=O stretching vibration from 1584 to 1600 cm^{-1} (from pure thymine to a mixed sample) was discussed as an indication of a hydrogen bond in the TER spectra. Summarizing all observations, the

base pair was adsorbed such that adenine was closer to the Au(111) surface than thymine. Thymine, on the other hand, was bound to adenine via a hydrogen bond. From these observations, it can be concluded that the base pair must have been oriented in an upright position.

In a further experiment, the influence of a pH < 4.2 to the spectra was examined. At such conditions, no hydrogen bonds between the two bases were found due to complete protonation of the specific nitrogen atoms. Spectral evidence was the presence of thymine-Au and adenine-Au bands at 268 and 220 cm^{-1}, respectively, which confirmed that both molecules were individually bound to the surface. Simultaneously, no thymine ring vibration mode was observable at 792 cm^{-1}.

In summary, it was shown that TERS is applicable for chemically specific and high spatial resolution analyses of biomolecules. In addition, TERS, operating in the so-called gap mode, provides a reliable configuration, for example, heteroatom containing molecules and gives additional enhancements to the Raman signal. It was also demonstrated that the technique is capable to characterize and discern single amino acids and DNA bases and is sensitive enough to identify different molecular orientations.

Reference measurements such as normal Raman and SERS are certainly helpful to rule out coarse artifacts such as picking up sample molecules. However, owing to the high resolution that allows TERS to detect micro ensembles instead of macroscopic amounts of molecules, a direct comparison with bulk spectra is not always sensible.

11.2.2
Detection of Structural/Chemical Changes on a Molecular Level

The importance of the structural distinction of different molecular states can be nicely visualized using hemoglobin (see Figure 11.7b) as an example. This molecule's function is the binding of oxygen (e.g., in the lung) at its heme moiety (see Figure 11.7a) and transporting it to tissues where the oxygen gets released. During the oxygen-binding process, the molecule undergoes conformational changes from a tense state (T-state) to a relaxed state (R-state).

Hemoglobin crystals with an average diameter of 180 nm were investigated to study such changes with high lateral resolution [78]. In the collected TERS data, three types of spectra were evident whose different contributions could mainly be attributed to the vicinity of the tip to different parts of the molecule: (i) heme moiety, (ii) attached protein, and (iii) distinct amino acids such as Phe and His. This aspect is already very remarkable as it demonstrates the high spatial resolution of the measurement, keeping in mind that hemoglobin is approximately spherical and has a diameter of only 5.5 nm. Type (i) spectra showed, among other skeletal vibrational modes of porphyrin, the typical oxidation state marker bands of heme at 1378 cm^{-1}/Fe(III) and 1355 cm^{-1}/Fe(II). Those signals were not observed in the bulk resonance Raman spectra of the crystals, indicating a surface-related

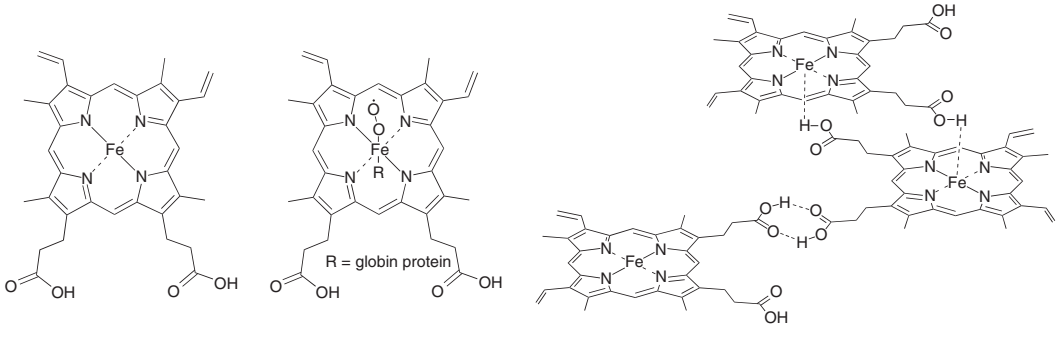

(a) Heme group (b) Heme group in hemoglobin (c) Heme group in hemozoin crystals

Figure 11.7 Heme groups in different binding situations: (a) free heme which is cell toxic; (b) In hemoglobin, the heme is bound to a protein backbone (R). Hemoglobin is ordered in a quaternary structure, meaning that four globular α-helical subunits arrange in a tetrahedral shape. (c) Heme is detoxified in hemozoin crystals, which are insoluble.

oxidation change. Such different oxidation states can occur because of two possible reasons: (i) oxygen atoms were constantly exchanged within different molecules of the crystal and (ii) the silver nanoparticle (TERS tip or SERS substrate) induced an oxidation potentially in combination with the illumination.

In a complementary study, a hemozoin crystal was investigated in the same way [79]. Hemozoin is synthesized when the malarial parasite *Plasmodium falciparum* digests the protein and the free heme, which is toxic for the parasite, is leftover. The crystallization of heme yields hemozoin (see Figure 11.7c), which is insoluble in the cell. In this way, the parasite gets rid of the toxic heme while insoluble crystals of hemozoin with a size of a few hundred nanometers are formed. This happens by dimerization of two heme molecules via one of their carboxyl moieties. The other carboxyl group coordinates with the central iron atom (see Figure 11.7c). For TERS experiments, sectioned and fixed blood cells on glass substrates were used. The crystals appeared to be in the digestive vacuole of the parasite, and TERS spectra could be recorded and distinguished from heme spectra. Similar to the hemoglobin spectra, an enhanced band at 1373 cm^{-1} that could be assigned to the oxidation state marker band (symmetric ring vibration of pyrrole, ν_4) indicated that the iron was in the ferric high spin state (Fe(III)). In principle, there were other bands from 1650 to 1500 cm^{-1} in addition to the Fe(II)/Fe(III) marker bands showing a similar spectral pattern as in resonance Raman experiments. The most important difference between the two methods was the increased intensity of the ν_4 band. Finally, the TER spectra showed good reproducibility as shown in an average of all spectra.

Another molecule containing the heme moiety is cytochrome c (Cc), which can be found, for example, in mitochondria. Yeo *et al*. [80] performed first TERS measurements on isolated Cc molecules [80]. Similar to the studies presented earlier in normal (resonant) Raman spectra, bands resulting from the heme group dominated the spectra. The goal of this study was the distinction of amino acids from heme contributions. From the experiments, three types of spectra were obtained and confirmed a high lateral resolution similar to that of the hemoglobin experiment. Type I spectra showed bands resulting from a low spin Cc^{3+}, whereas type II spectra were dominated by high spin Cc^{3+} with marker bands at 1622 (B_{1g}, $\nu_{10,}$ skeletal stretch vibration) and 1567 cm^{-1} (A_{2g}, $\nu_{19,}$ skeletal stretch vibration). Spectra of type III showed bands that could not be assigned to the heme group, and therefore it was suggested that they originated from amino acids of Cc (histidine, tyrosine, and phenylalanine). These results exactly correlated with the abovementioned data on hemoglobin.

Next, the complexity of the environment of Cc was increased [81]. Whole mitochondria from yeast cells were investigated by TERS. The protein that is located in the inner membrane of a cell showed differences in the oxidation state as tracked along a line on 8 nm distant positions. Virtually all TER spectra show strong contributions of lipids and could be separated in three groups. The first group belonged to a high spin Fe(II) atom in the heme center (oxidation state marker band at 1360 cm^{-1}), and the second group belonged to a low spin

Fe(III) atom in the heme center (oxidation state marker band at 1373 cm^{-1}). At the same time, a mixture of both oxidation states in the spectra was observed and refers to a third group. Consequently, the tip was probably located right between two Cc molecules with different oxidation states. It should be noted that no direct contact of silver particle (at the TERS tip) and Cc was possible because the protein is buried in the lipid layer, whose contributions could also be identified in the spectra and actually is even domination of the spectral features.

In a last example, the detection of isomerization with TERS will be discussed using the imin-enamin tautomerization of histidine. This amino acid was examined using TERS, SERS, and bulk Raman spectroscopy [82]. The main reason for this pH-dependent process is the imidazole ring, which mostly contributes to the basicity of the amino acid. The study demonstrated that histidine adsorbed in two preferred states on a smooth silver nanoplate. TER spectra were collected along two lines every 40 nm. The first line showed an increased presence of a tautomer, which was protonated at its free amino group, having a strongly enhanced NH_3^+ and a negatively charged carboxylic group. For that reason, the iminio nitrogen in the ring could coordinate to the silver substrate, yielding a perpendicular-oriented imidazole ring with respect to the substrate. Although that isomer was bound via the NH_3^+ group to the silver substrate, the carboxyl group formed a charge-transfer complex. This was concluded from a shift toward higher wavenumbers with respect to bulk Raman spectra. Another indication for the perpendicular orientation of the imidazole ring was the generally stronger enhancement of in-plane modes. In the second trace, histidine appears in its neutral form as no NH_3^+ bands were observed. Judging from that, the two isomers could not be distinguished, but considering the band $\nu(NH_2)$, $\nu(C{=}C)$, and $\nu(C{=}N)$ (1592 cm^{-1}) and a weak $\nu(CH\text{-}COO^-)$ (1402 cm^{-1}), it was deduced that histidine was present in a horizontal orientation with the imidazole coordinated toward the substrate. Summarizing, the study showed that two isomers of histidine were identified in these gap-mode TERS experiments. This agreed with the immobilization procedure, which was performed at pH 6–7 where different isomers of histidine indeed could be present. Mostly, the zwitterionic isomer was immobilized as this is the most stable form in aqueous neutral solution.

The preceding section demonstrated that TERS can be applied to obtain high lateral resolution information on structural changes of biomolecules. Spin state, oxidation state changes, and even different tautomers were discriminated by TERS.

11.3 Biopolymers

As mentioned in the earlier section, one goal of TERS is to sequence biomacromolecules such as DNA and proteins. Typically, the distance between DNA bases

in a double strand is about 3.4 Å and therefore far below the diffraction limit. Similarly, proteins exhibit a distance of 3.5 and 1.5 Å between the amino acids in β-sheet and α-helix conformations, respectively. In the following section, it will be shown that TERS is able to differentiate the chemical composition on such a small scale. In particular, for proteins/peptides, it is interesting to investigate conformational changes, which can give important information about the mechanisms of several cellular processes.

11.3.1 DNA/RNA Strands

In an initial experiment, the high sensitivity of TERS was proved measuring along a poly(cytosine) RNA single strand [83]. Spectra were measured at seven different positions along the main axis of a homopolymer strand. All spectra contained the characteristic spectral features of the nucleobase cytosine. Considering the diameter of the tip, it was estimated that the signal corresponded to a maximum of 30–60 molecules beneath the tip with an SNR of about 200. Hence, the SNR for one molecule was about 3–7, and a single base sensitivity for this experiment was deduced. Using more realistic values that in a single strand, the base spacing is more likely around 0.5 nm and the enhanced region of a 20 nm radius tip (according to theoretical modeling) should be between 4 and 10 nm, the number is more likely to be around 10–20 bases with a corresponding SNR of 10–20. From the results, it was concluded that RNA sequencing with TERS is at least in principle possible. Experimentally this could be achieved if the tip is moved in base-to-base size steps along the strand. The spectral changes would then ultimately reveal the primary structure of a RNA or DNA strand by a deconvolution of neighboring spectra.

Another requirement is the capability to discriminate all nucleobases in a DNA/RNA strand with TERS. Thus, poly(A), poly(U), and calf thymus DNA were investigated in the same manner [84]. A profile measurement on a poly(A) strand demonstrated that spectra could only be collected if the tip was positioned exactly on the strand. Interestingly, some ssDNA was adsorbed in a coiled configuration on the mica substrate. In such an arrangement, the phosphate backbone, which usually is attached to mica and therefore is not accessible for the TERS tip, was also detected in the spectra.

In order to take advantage of the gap mode, ultraflat gold substrates were employed for poly(U) strands (see Figure 11.8a,b).

From Figure 11.8c, it is evident that along the strand, reproducible spectra were obtained. The absence of the characteristic ring breathing mode around 800 cm^{-1} led to the conclusion that the uracil bases were oriented parallel to the gold surface (=perpendicular to the tip main axis).

In order to prove that TERS is capable to distinguish all four nucleobases, single-stranded calf thymus DNA was immobilized on mica and spectra were recorded on randomly chosen points on numerous strands. In the recorded spectra, contributions of all four bases could be assigned [84].

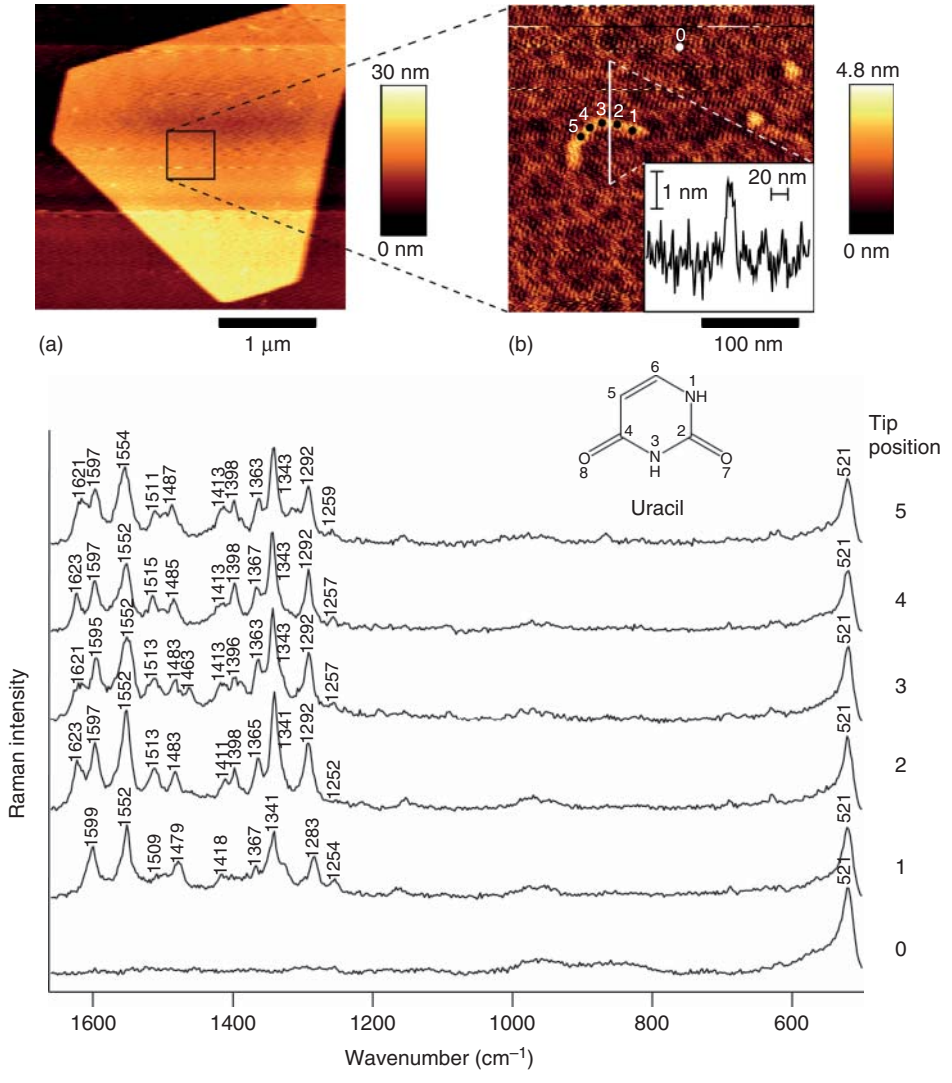

Figure 11.8 Top: (a) AFM topography image of a gold nanoplate with immobilized polyuracil strands, (b) single strand of uracil homopolymer in the magnified area indicated in (a); inset in (b) AFM cross section of the corresponding profile indicated in (b); bottom: TERS spectra of the uracil homopolymer, measured at the positions indicated in (b). (Courtesy of Treffer *et al.* [84], Beilstein Journal of Nanotechnology.)

11.3.2 Proteins and Fibrils

TERS investigations of proteins are closely related to SERS of proteins. Particularly experiments discussing the interaction of protein and metal surface are of

interest [85]. For hemoproteins (cytochrome C, hemoglobin, and myoglobin), it was shown that spectra were mostly dominated by bands of the heme group, the central unit of such ring systems [86, 87]. In different experiments, cytochrome C was investigated using a sandwiched configuration (between silver and gold) to validate that the protein is still in its native conformation [87]. Furthermore, for cytochrome C and hemoglobin, it was established that the very strong enhancement present exactly between nanoparticles (hot spots) allows even single-molecule detection [88, 89]. Although certainly useful for sensitive analytical applications, SERS cannot be used to locally address specific sites as outlined earlier.

At present, fibrils are an attractive research topic because they comprise many unsolved phenomena. Misfolding of proteins to fiber-like structures is related for instance to Alzheimer's and Parkinson's diseases. Starting from the same primary structure (amino acid sequence) of a protein, the secondary structure changes during the fibrillation process in a biologically dramatic manner. As a result, the protein is not active anymore but can even be toxic. An understanding of the misfolding mechanism and how it can be prevented or reversed will shed new light onto the development of those diseases.

TERS provides a technique for the detection of conformational changes (β-sheet vs α-helix) as well as for a direct discrimination of amino acids [90, 91]. The differentiation of different conformations of a peptide chain was performed using amid bands I–III [90]. At the same time, contributions of histidine, phenylalanine, proline, tyrosine, and cystine could be differentiated by their specific marker bands (see Figure 11.9a,b). For that experiment, a step size between the measurement points of 0.5 nm was chosen and a spatial resolution below 1.5 nm was estimated according to the appearance and disappearance of specific marker bands or even whole groups of specific marker bands. This lateral resolution appears to be too high according to standard electromagnetic theory (3–10 nm resolution for 20 nm diameter tips) [92]. Consequently, an additional effect for instance a direct interaction between metal surface and the molecule (chemical enhancement) must also play a role. At present, the origin of this effect is not yet clear.

In a more detailed study, amide I bands at 1640–1659 cm^{-1} indicating unordered/α-helix structures were detected while at different locations clearly a β-sheet conformation of the amide I band at 1664–1678 cm^{-1} was found [91]. The content of pure β-sheet conformation was determined to 34%, whereas the rest was either a mix of unordered/α-helix or α-helix/β-sheet domains. A detailed evaluation of the TERS data revealed that the amino acids Cys and Tyr were mainly present in β-sheet-dominated areas, whereas Pro was typically found in α-helix domains. Since Pro is known to interrupt β-sheet structures by means of its molecular structure, this is consistent with previous results and was found also with nanometer lateral resolution.

In addition, information about the nanoscale hydrophobicity of the fibril surface could be extracted from the data by simply analyzing the number of spectra with

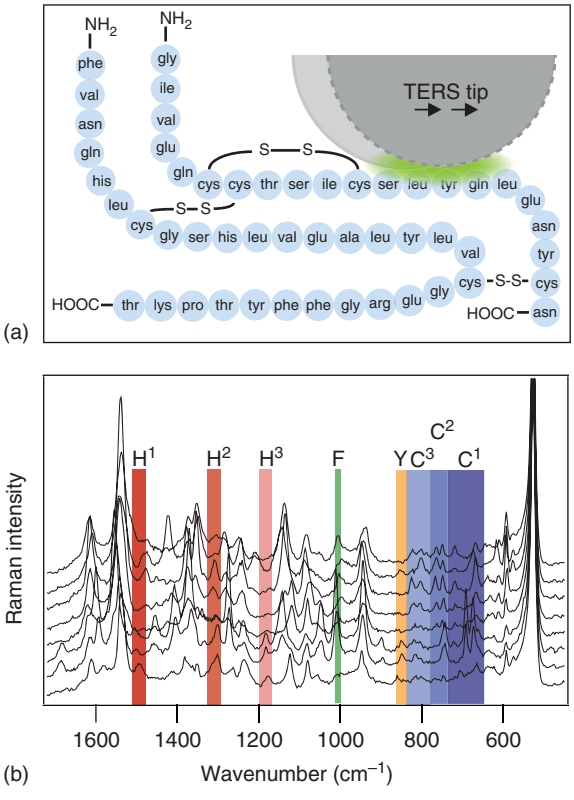

Figure 11.9 (a) Scheme of a single insulin molecule and a TERS probe. The enhanced field is expected to excite only a few amino acids. (b) Selected TER spectra with marker bands of amino acids: green, phenylalanine (F); red, histidine (H); orange, tyrosine (Y); blue, cystine (C). (Modified from Ref. [90], Wiley-VCH.)

bands, indicating hydrophilic groups such as $COOH/COO^-$ (8% of all spectra) and NH_2/NH_3^+ (42% of all spectra) [91]. The value estimated from the TERS data agreed well with the literature.

A question discussing SER and TER spectra of proteins is the frequently observed absence of amid I bands, which was previously shown in SERS studies on biological samples [93]. In the fibril experiment, ~54% of the spectra in a multiple fibril data set revealed suppressed amide I bands. Certainly, it would be most advantageous to detect that band as it provides information about the secondary structure of a protein. The regions of amide II and amide III bands cannot easily be used for such purpose because of an overlap with other bands (mainly CH and C–C).

The suppression phenomenon in TERS/SERS was the focus of two studies [57, 94]. In a study by Blum *et al.* [94], the authors suggested, for example, the dominance of the aromatic modes for the missing amide I band in TER and SER spectra. Besides, they contemplated a too low SNR and an electromagnetic shielding. In

addition, it was proposed that a shielding of the peptide band occurred due to bulky amino acid side chains. But this was considered to be very unlikely since such side chains are still too small to attenuate the complete evanescent field.

In the work of Kurouski *et al.* [57], the suppression was correlated with the spacing of amino acid side chains between metal and peptide backbone. This assumption was supported by SER spectra of short model peptides (penta-Gly; penta-Ala; hexa-Tyr; and Trp-Arg-Trp-Trp-Trp-Trp) on 70 nm gold particles. The first two peptides show an enhanced amide I band in all spectra as they have short side chains and therefore the plasmon enhancement can reach the peptide bond. The latter two showed very heterogeneous spectra with 76% (hexa-Tyr) with amide I bands and 31% for (Trp-Arg-Trp-Trp-Trp-Trp). This supports the aforementioned hypothesis that a bulky side chain affects the interaction of enhancing field and peptide backbone. The same effect was observed in the respective SERS experiments, silver island films. The final answer to this phenomenon is not yet found, but as the amide I band is of crucial importance more experiments will certainly follow to unravel this effect.

For the investigation of any biological sample, it is desirable to have a tool that measures nondestructive, label free, and fast spectral information at every single measurement point – not necessarily with a super-high resolution but with high specificity and sensitivity.

One approach was shown by Paulite *et al.* [95] where self-assembled peptide nanotapes from amyloid fibril β(16–22) fragments ($h \approx 3–5$ nm) on template-stripped gold were imaged by a TERS–STM combination. The notable aspect of this study is the simultaneously collected topographic and spectroscopic information at every point. With that technique, the authors showed that structures invisible in STM can be disclosed by mapping the aromatic ring breathing mode at 1004 cm^{-1} as this band dominated the spectra (see Figure 11.10a,b).

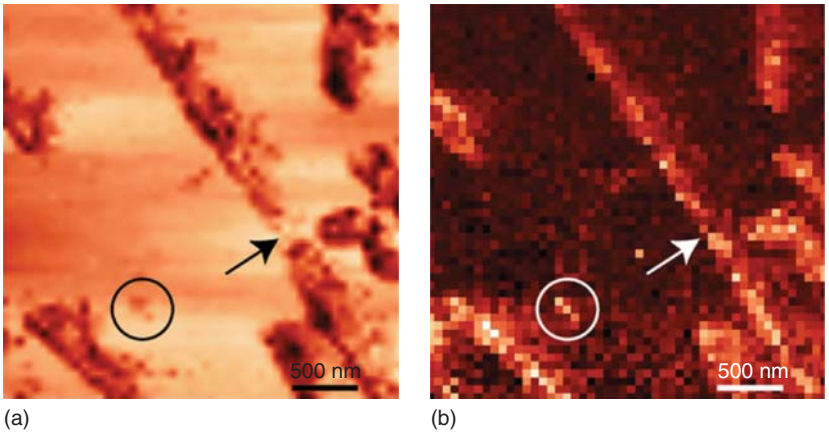

(a) (b)

Figure 11.10 (a) STM topography of amyloid β(16–22) peptide fragments; (b) TERS image of the aromatic ring breathing mode at 1004 cm^{-1} (value of band integral); image size: 50 × 50 px (3 µm × 3 µm); acquisition time per pixel: 1 s. (Adapted from Ref. [95], American Chemical Society.)

In order to investigate membranes and protein receptors located therein, a mapping approach was recently presented that uses functionalized gold nanoparticles (GNPs) [96]. Biotin-labeled GNPs of different sizes were bound to streptavidin-functionalized glass in order to obtain the enhanced Raman signal. A TERS map of the streptavidin marker band at 965 cm^{-1} was superimposed to show the strong correlation between the location of the GNP and the enhancement. Interestingly, the different sizes of GNPs only affected the intensity of a spectrum. Streptavidin was unexpectedly prominent in the spectra as biotin is located in the gap of tip and immobilized particle and therefore should experience the highest enhancement. As explanation, the higher Raman cross section of streptavidin and its migration into the gap was suggested. With an inverted system consisting of biotin-labeled glass and streptavidin-functionalized GNPs, it was demonstrated that TERS is sensitive enough to detect either migration of streptavidin into the gap or biotin bound to streptavidin. Supported by SERS measurements, it was shown that only streptavidin bands were detectable indicating that the protein must have migrated in the first experiment.

In a further mapping study, the high surface sensitivity of TERS was used to get information about the distribution of the adsorbed phosphoprotein osteopontin (OPN) on crystals of calcium oxalate monohydrate (COM) [97]. These crystals, better known as *kidney stones* and *OPN*, can inhibit their growth by adsorbing to the crystals. The distribution of OPN was visualized by Raman maps using the marker bands at 1464 cm^{-1} (OPN and COM) and 1487 cm^{-1} (only COM). To distinguish between COM and OPN, the intensity ratio of the bands was calculated from single point spectra. With increasing 1464/1487 cm^{-1} ratio, the protein concentration also increased. These results demonstrate that the protein preferentially adsorbed to a specific edge of the crystal and to areas with high calcium ion density.

In this chapter, the capabilities of TERS as a label-free and sensitive method for high resolution measurements on large biomolecules such as DNA or protein-related structures were presented. It was demonstrated that it is feasible to detect differences in protein conformations, and mapping experiments revealed that TERS represents an elegant approach to visualize adsorption patterns of proteins.

11.4 Membranes, Viruses, and Bacteria

A major challenge for high spatial resolution technologies is to address complex systems, for example, bacteria and viruses. Here, it is desirable to know the arrangement of subdiffraction limit-sized components on the particle surface. From the arrangement, one can learn about biological processes and interactions on a molecular level (e.g., adhesion). Fluorescence spectroscopy provides an established and proven approach with good specificity and high resolution. One big weakness is the influence of the labels on the behavior of, for example,

self-assembling systems [98]. Another issue is the fact that spatial resolution is limited by the size of the dye labels. Therefore, it can be advantageous to resort to a label-free approach. With SERS experiments, it was shown that immunolabeling of silver nanoparticles provides spatially defined biochemical information with an enhancement factor of ~50 [99]. This modification was adapted to TERS experiments where regions of interest were identified by antibody–antigen interaction by specifically positioning an Au nanoparticle in that place [100]. By scanning the cell surface with a golden TERS tip, it was obvious that even single particles could be distinguished from aggregated particles.

TERS and SERS [101, 102] do not need labels to chemically characterize membranes as shown in a study with an artificial biotin-modified lipid bilayer and biotin-PS [103]. Using the very specific affinity of the covalent bond between streptavidin and biotin, it was possible to attach streptavidin molecules to the membrane. The aim of the study was the differentiation of lipid and protein containing areas. The distinction of the components was accomplished by analyzing specific marker bands in the TERS spectra. Marker bands for lipids are vibrational modes of the phosphate group (830 and 1080 cm^{-1}) and of the polar head group. As this side of the molecule pointed upwards, it directly faced the TERS probe yielding strongly enhanced modes. Another indicator for lipid domains is a band around 1729 cm^{-1}, which generally can be assigned to the C=O stretching mode of the ester moiety. Protein-dominated compartments of the sample could be assigned by the typical protein and amino acid bands (phenylalanine 1005 cm^{-1}, amide II 1565 cm^{-1}, amide I around 1675 cm^{-1}). From the obtained data, it was evident that domains with mixtures of lipids and proteins could also be detected (see Figure 11.11).

The nature of the plasmon resonance of the TERS defines the spectral region, where signal enhancement occurs. For this reason, signals in the C–H stretching mode region (2800–3100 cm^{-1}) where conventional Raman can provide substantial information is not generally useful. Nevertheless, to achieve a better contrast in TER maps, deuteration of the lipid chain or head is possible [104]. This procedure might be considered as a kind of labeling but should not influence the assembly of lipids. In contrast to dye labeling where a new molecule interferes with the sample, an H/D exchange causes a rather small change of the chemical structure. By introducing C–D bonds, one gets a well-pronounced marker band around 2100 cm^{-1} where usually no signal from other biological molecules (except C≡N) appears [105]. The deuterium label approach is a hot topic in pharmaceutical research to track the penetration of drug delivery systems into the uppermost layer of skin (the stratum corneum), which constitutes an important penetration barrier [106, 107].

In further membrane studies, the surface of *Halobacterium salinarum* was investigated in order to visualize the distribution of retinal-free and retinal-containing membrane domains (see Figure 11.12) [108]. Therein, the resonantly enhanced retinal moiety was used as a marker for the light-driven, proton-pump bacteriorhodopsin. In the first step, isolated purple membrane (PM) patches were characterized. In experiments on isolated PM patches, the sites of the retinal

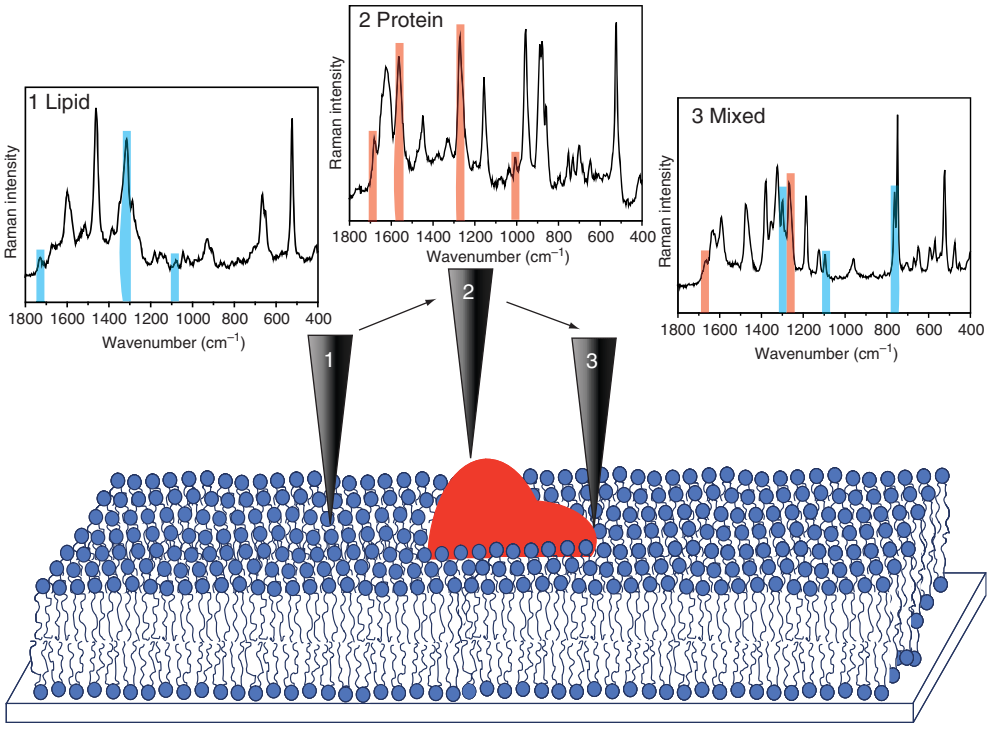

Figure 11.11 TERS probe scans over a modified membrane and spectra are recorded at indicated positions: position 1, lipid domain; position 2, protein domain; position 3, mixed domain. (Modified from Ref. [103], Wiley-VCH.)

were clearly identified in the spectra by using marker bands at 1540 cm^{-1} ν(C=C) and 1635 cm^{-1} ν(C=$NH^{(+)}$). Retinal protein bands were found more often than lipid bands, which agreed well with the estimated protein–lipid ratio of 3 : 1. As expected, the recorded spectra of the bacteria were much more complex: besides PM and lipids, red membrane (dominated by β-carotene) and other proteins were detected. Nevertheless, red membrane and PM domains could be distinguished by their marker bands. According to the spectral information, a map showing the distribution of these membrane constituents could be generated (see Figure 11.12a,b).

Probing bacterial surfaces, it is important to have a high accuracy to differentiate pathogenic species from nonpathogenic species [92]. Accuracies of up to 97% are realistic as demonstrated by an SERS study with 14 different but closely related bacteria strands [109].

The first examined bacterium with TERS was bacterium *Staphylococcus epidermidis* [110–112]. More statistical measurements on *S. epidermidis* were performed by collecting 15 spectra at one point per cell and five cells in total [112]. From these spectra, a single average spectrum for each cell was generated and characteristic bands for teichoic acid (a (1–3)-linked poly(glycerol

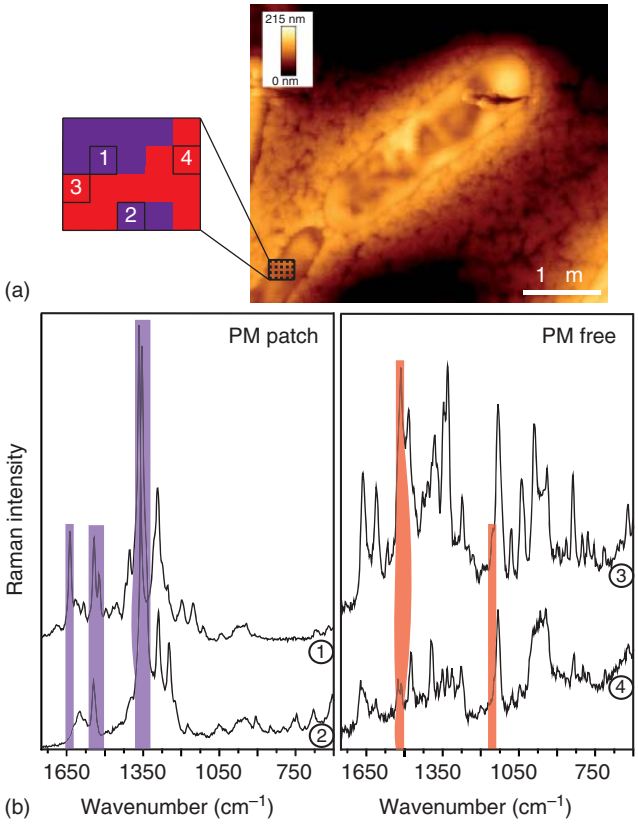

Figure 11.12 (a) AFM image of isolated *Halobacterium salinarum* and the TERS grid with a color map at the left indicating dominating species (red membrane in red, purple membrane in purple); (b) selected TER spectra of retinal-containing and retinal-free membrane. (Modified from Ref. [108], Wiley-VCH.)

phosphate)) and polysaccharide intercellular adhesion (a poly-β-(1–6)-*N*-acetylglucosamine) confirmed the presence of the outer envelope of the gram-positive bacteria.

In subsequent TERS studies of human colon cancer cells (cell line HT29) [113], the intention was an imaging of lipid domains (so-called lipid rafts [114]) and proteins on the cell by using automated multivariate data evaluation on a complex surface. The so-called N-FINDR algorithm works most efficiently for TERS data, but certainly other techniques can be applied in a similar fashion. With that technique, a map of the TERS spectra could be created (see Figure 11.13).

If the data set for TERS measurements becomes large (>100 spectra), such an automated reduction of the data is most useful. However, due to the already discussed intrinsic spectral shifts and intensity variations in TERS (and also SERS), the position of an individual vibrational mode might be shifted depending on its orientation and environment. Hence, it is challenging to build a robust and reliable

Figure 11.13 Distribution of areas with high lipid (green) and protein (red) contents on the cell surface. Scanned area: 90 nm × 90 nm. Blue indicates comparable lipid and protein contents. (Selected part was adapted from Ref. [113], Wiley-VCH.)

algorithm for TER spectra and a topic of current research is to find optimum procedures for this kind of evaluation.

In the earlier section, it was demonstrated that TERS could be specifically used to address biological membranes and surfaces in general. The accuracy of tip-positioning and the signal-enhancing effect at the tip apex facilitates a sensitive and high spatial resolution detection. These attributes enable the characterization of cells, bacteria, and even of viruses on the single particle level. In first TERS experiments, a tobacco mosaic virus (length, 300 nm; diameter, 20 nm) was examined. This virus is built from a protein shell (capsid) and a buried RNA, both of which could be detected in the TERS spectra [115].

A direct discrimination of two virus strains was shown on avipoxvirus (APV) and adeno-associated virus (AAV) particles [116]. The diameter of the viruses was given to be around 350 and ~26 nm, respectively. For every virus type three spectra were recorded, each on a different particle. In the spectra from APV, among others amide I, amide III, and CH_2 stretching bands were assigned and apparent spectral variations (band intensities and band positions) were observed. The spectra recorded on AAV also showed amide I, amide III, and CH_2 stretching bands, but here the spectral variation was smaller. This fact was explained by the different sizes of the investigated particles. The different sizes of the virions made a differentiation by AFM topographies straightforward. However, probing the small particles with a TERS tip, the authors found that the entire virus surface (AAV) contributes to the spectrum whereas on the bigger APV virion different spectra could be collected. This means that TERS can take advantage of its small probing volume when investigating small particles because only few measurements are necessary to fully characterize a single particle.

A differentiation is much more challenging if virions with similar size and shape are examined by TERS. Here, one can take advantage of the high specificity of Raman spectroscopy. A successful discrimination of single viruses is only feasible

by initially building up a TERS virus database. This is the aim of current research and might push TERS forward as a new technique for the characterization of viruses on the single particle level.

11.5 Conclusion

Although still at an early stage, TERS has been applied already to many biological systems and helps to understand of nanoscale phenomena of membrane structures and single proteins. Because of the relevance of biological systems for medical problems, the need for high lateral resolution techniques is raising. In many cases, TERS provides an alternative strategy to established fluorescence-based technologies. If labeling cannot be applied or direct structural information is required, TERS might be the only alternative to perform structural investigations on the nanometer scale.

References

1. Fleischmann, M., Hendra, P.J., and McQuillan, A.J. (1974) Raman spectra of pyridine adsorbed at a silver electrode. *Chem. Phys. Lett.*, **26**, 163–166. doi: 10.1016/0009-2614(74)85388-1
2. Jeanmaire, D.L. and Van Duyne, R.P. (1977) Surface Raman spectroelectrochemistry. 1. Heterocyclic, aromatic, and aliphatic-amines adsorbed on anodized silver electrode. *J. Electroanal. Chem.*, **84**, 1–20. doi: 10.1016/s0022-0728(77)80224-6
3. Albrecht, M.G. and Creighton, J.A. (1977) Anomalously intense raman-spectra of pyridine at a silver electrode. *J. Am. Chem. Soc.*, **99**, 5215–5217. doi: 10.1021/ja00457a071
4. Moskovits, M. (1985) Surface-enhanced spectroscopy. *Rev. Mod. Phys.*, **57**, 783–826.
5. Nie, S. and Emory, S. (1997) Probing single molecules and single nanoparticles by surface-enhanced Raman scattering. *Science*, **275**, 1102.
6. Kneipp, K. *et al* (1997) Single molecule detection using Surface-Enhanced Raman Scattering (SERS). *Phys. Rev. Lett.*, **78**, 1667–1670.
7. Le Ru, E.C., Meyer, M., and Etchegoin, P.G. (2006) Proof of single-molecule sensitivity in Surface Enhanced Raman Scattering (SERS) by means of a two-analyte technique. *J. Phys. Chem. B*, **110**, 1944–1948. doi: 10.1021/jp054732v
8. Stöckle, R.M., Suh, Y.D., Deckert, V., and Zenobi, R. (2000) Nanoscale chemical analysis by tip-enhanced Raman spectroscopy. *Chem. Phys. Lett.*, **318**, 131–136. doi: 10.1016/s0009-2614(99)01451-7
9. Anderson, M.S. (2000) Locally enhanced Raman spectroscopy with an atomic force microscope. *Appl. Phys. Lett.*, **76**, 3130–3132, doi: Pii [S0003-6951(00)00721-X], doi: 10.1063/1.126546.
10. Hayazawa, N., Inouye, Y., Sekkat, Z., and Kawata, S. (2000) Metallized tip amplification of near-field Raman scattering. *Opt. Commun.*, **183**, 333–336. doi: 10.1016/S0030-4018(00)00894-4
11. Yeo, B.-S., Stadler, J., Schmid, T., Zenobi, R., and Zhang, W. (2009) Tip-enhanced Raman spectroscopy – Its status, challenges and future directions. *Chem. Phys. Lett.*, **472**, 1–13. doi: 10.1016/j.cplett.2009.02.023
12. Hayazawa, N., Inouye, Y., Sekkat, Z., and Kawata, S. (2001) Near-field Raman scattering enhanced by a metallized tip.

Chem. Phys. Lett., **335**, 369–374. doi: 10.1016/S0009-2614(01)00065-3

13. Sonntag, M.D. *et al* (2011) Single-molecule tip-enhanced Raman spectroscopy. *J. Phys. Chem. C*, **116**, 478–483. doi: 10.1021/jp209982h
14. Yeo, B.-S., Schmid, T., Zhang, W., and Zenobi, R. (2007) Towards rapid nanoscale chemical analysis using tip-enhanced Raman spectroscopy with Ag-coated dielectric tips. *Anal. Bioanal. Chem.*, **387**, 2655–2662. doi: 10.1007/s00216-007-1165-7
15. Neacsu, C.C., Dreyer, J., Behr, N., and Raschke, M.B. (2006) Scanning-probe Raman spectroscopy with single-molecule sensitivity. *Phys. Rev.*, **B 73**, 193406.
16. Pettinger, B., Ren, B., Picardi, G., Schuster, R., and Ertl, G. (2004) Nanoscale probing of adsorbed species by tip-enhanced raman spectroscopy. *Phys. Rev. Lett.*, **92**, 096101.
17. Domke, K.F., Zhang, D., and Pettinger, B. (2006) Toward Raman fingerprints of single dye molecules at atomically smooth Au(111). *J. Am. Chem. Soc.*, **128**, 14721–14727. doi: 10.1021/ja065820b
18. Domke, K.F., Zhang, D., and Pettinger, B. (2007) Enhanced Raman spectroscopy: single molecules or carbon? *J. Phys. Chem. C*, **111**, 8611–8616. doi: 10.1021/jp071519l
19. Wang, J. *et al* (2003) Apertureless near-field Raman spectroscopy. *J. Microsc. (Oxford)*, **210**, 330–333.
20. Anderson, N., Hartschuh, A., Cronin, S., and Novotny, L. (2005) Nanoscale vibrational analysis of single-walled carbon nanotubes. *J. Am. Chem. Soc.*, **127**, 2533–2537. doi: 10.1021/ja045190i
21. Hartschuh, A., Sánchez, E., Xie, X., and Novotny, L. (2003) High-resolution near-field Raman microscopy of single-walled carbon nanotubes. *Phys. Rev. Lett.*, **90**, 095503.
22. Hartschuh, A., Qian, H., Meixner, A.J., Anderson, N., and Novotny, L. (2006) Tip-enhanced optical spectroscopy for surface analysis in biosciences. *Surf. Interface Anal.*, **38**, 1472–1480. doi: 10.1002/sia.2351
23. Mehtani, D. *et al* (2005) Nano-Raman spectroscopy with side-illumination optics. *J. Raman Spectrosc.*, **36**, 1068–1075. doi: 10.1002/jrs.1409
24. Hayazawa, N., Furusawa, K., and Kawata, S. (2012) Nanometric locking of the tight focus for optical microscopy and tip-enhanced microscopy. *Nanotechnology*, **23**, 465203. doi: 10.1088/0957-4484/23/46/465203
25. Yano, T.-a., Verma, P., Saito, Y., Ichimura, T., and Kawata, S. (2009) Pressure-assisted tip-enhanced Raman imaging at a resolution of a few nanometres. *Nat. Photonics*, **3**, 473–477. doi: http://www.nature.com/nphoton/journal/v3/n8/suppinfo/nphoton.2009.74_S1.html
26. Yu, J., Saito, Y., Ichimura, T., Kawata, S., and Verma, P. (2013) Far-field free tapping-mode tip-enhanced Raman microscopy. *Appl. Phys. Lett.*, **102**, 123110–123114.
27. Peica, N., Thomsen, C., and Maultzsch, J. (2010) Tip-enhanced Raman scattering along a single wall carbon nanotubes bundle. *Phys. Status Solidi B*, **247**, 2818–2822. doi: 10.1002/pssb.201000208
28. Peica, N., Thomsen, C., and Maultzsch, J. (2011) Studying the local character of Raman features of single-walled carbon nanotubes along a bundle using TERS. *Nanoscale Res. Lett.*, **6**, 174. doi: 10.1186/1556-276x-6-174
29. Peica, N. *et al* (2009) Characterization of dye molecules and carbon nanostructures by tip-enhanced Raman spectroscopy. *Phys. Status Solidi B*, **246**, 2708–2712. doi: 10.1002/pssb.200982278
30. Steidtner, J. and Pettinger, B. (2008) Tip-Enhanced Raman spectroscopy and microscopy on single dye molecules with 15 nm resolution. *Phys. Rev. Lett.*, **100**, 236101.
31. Yeo, B.-S., Zhang, W., Vannier, C., and Zenobi, R. (2006) Enhancement of Raman signals with silver-coated tips. *Appl. Spectrosc.*, **60**, 1142–1147. doi: 10.1366/000370206778664662

32. Liu, Z. *et al* (2011) Revealing the molecular structure of single-molecule junctions in different conductance states by fishing-mode tip-enhanced Raman spectroscopy. *Nat. Commun.*, **2**, 305. doi: http://www.nature.com/ncomms/journal/v2/n5/suppinfo/ncomms1310_S1.html
33. Ghislandi, M., Hoffmann, G.G., and Tkalya, E. (2012) Tip-enhanced raman spectroscopy and mapping of graphene sheets. *Appl. Spectrosc.*, **47**, 371–381.
34. Saito, Y., Verma, P., Masui, K., and Inouye, Y. (2009) Nano-scale analysis of graphene layers by tip-enhanced near-field Raman spectroscopy. *J. Raman*, **40**, 1434–1440.
35. Snitka, V., Rodrigues, R.D., and Lendraitis, V. (2011) Novel gold cantilever for nano-Raman spectroscopy of graphene. *Microelectron. Eng.*, **88**, 2759–2762.
36. Stadler, J.J., Schmid, T.T., and Zenobi, R.R. (2011) Nanoscale chemical imaging of single-layer graphene. *ACS Nano*, **5**, 8442–8448. doi: 10.1021/nn2035523
37. Su, W. and Roy, D. (2013) Visualizing graphene edges using tip-enhanced Raman spectroscopy. *J. Vac. Sci. Technol. B: Microelectron. Nanometer Struct.*, **31**, 041808. doi: 10.1116/1.4813848
38. Wang, P. *et al* (2012) Reversible defect in graphene investigated by tip-enhanced Raman spectroscopy. *Plasmonics*, **7**, 555–561.
39. Poliani, E., Nippert, F., and Maultzsch, J. (2012) Effect of gap modes on graphene and multilayer graphene in tip-enhanced Raman spectroscopy. *Phys. Status Solidi B*, **249**, 2511–2514. doi: 10.1002/pssb.201200155
40. Hayazawa, N. *et al* (2007) Visualization of localized strain of a crystalline thin layer at the nanoscale by tip-enhanced Raman spectroscopy and microscopy. *J. Raman Spectrosc.*, **38**, 684–696. doi: 10.1002/jrs.1728
41. Poborchii, V., Tada, T., Kanayama, T., and Geshev, P. (2009) Optimization of tip material and shape for near-UV TERS in Si structures. *J. Raman Spectrosc.*, **40**, 1377–1385. doi: 10.1002/jrs.2417
42. Saito, Y., Motohashi, M., Hayazawa, N., Iyoki, M., and Kawata, S. (2006) Nanoscale characterization of strained silicon by tip-enhanced Raman spectroscope in reflection mode. *Appl. Phys. Lett.*, **88**, 143109. doi: 10.1063/1.2191949
43. Saito, Y., Motohashi, M., Hayazawa, N., and Kawata, S. (2008) Stress imaging of semiconductor surface by tip-enhanced Raman spectroscopy. *J. Microsc. (Oxford)*, **229**, 217–222.
44. Tarun, A., Hayazawa, N., Motohashi, M., and Kawata, S. (2008) Highly efficient tip-enhanced Raman spectroscopy and microscopy of strained silicon. *Rev. Sci. Instrum.*, **79**, 013706. doi: 10.1063/1.2832347
45. Zhu, L. *et al* (2007) Experimental challenges for approaching local strain determination in silicon by nano-Raman spectroscopy. *Mater. Sci.-Poland*, **25**, 19–31.
46. Zhu, L. *et al* (2007) Nano-Raman spectroscopy with metallized atomic force microscopy tips on strained silicon structures. *J. Appl. Phys.*, **101**, 104305. doi: 10.1063/1.2732435
47. Poliani, E. *et al* (2013) Nanoscale imaging of InN segregation and polymorphism in single vertically aligned InGaN/GaN multi quantum well nanorods by tip-enhanced Raman scattering. *Nano Lett.*, **13**, 3205–3212. doi: 10.1021/nl401277y
48. Binnig, G. and Rohrer, H. (1982) Scanning tunneling microscopy. *Helvetica Physica Acta*, **55**, 726–735. doi: 10.5169/seals-115309
49. Binnig, G., Quate, C.F., and Gerber, C. (1986) Atomic force microscope. *Phys. Rev. Lett.*, **56**, 930–933. doi: 10.1103/PhysRevLett.56.930
50. Bailo, E. and Deckert, V. (2008) Tip-enhanced Raman scattering. *Chem. Soc. Rev.*, **37**, 921–930. doi: 10.1039/b705967c
51. Drechsler, A., Lieb, M., Debus, C., Meixner, A., and Tarrach, G. (2001) Confocal microscopy with a high numerical aperture parabolic mirror. *Opt. Express*, **9**, 637–644.

52. Stanciu, C., Sackrow, M., and Meixner, A.J. (2008) High NA particle- and tip-enhanced nanoscale Raman spectroscopy with a parabolic-mirror microscope. *J. Microsc. (Oxford)*, **229**, 247–253.
53. Steidtner, J. and Pettinger, B. (2007) High-resolution microscope for tip-enhanced optical processes in ultrahigh vacuum. *Rev. Sci. Instrum.*, **78**, 103104. doi: 10.1063/1.2794227
54. Hayazawa, N. (2004) Detection and characterization of longitudinal field for tip-enhanced Raman spectroscopy. *Appl. Phys. Lett.*, **85**, 6239–6241.
55. Schultz, Z.D., Stranick, S.J., and Levin, I.W. (2008) Tip-enhanced raman spectroscopy and imaging: an apical illumination geometry. *Appl. Spectrosc.*, **62**, 1173–1179.
56. Chan, K.L. and Kazarian, S.G. (2011) Tip-enhanced Raman mapping with top-illumination AFM. *Nanotechnology*, **22**, 175701. doi: 10.1088/0957-4484/22/17/175701
57. Kurouski, D., Postiglione, T., Deckert-Gaudig, T., Deckert, V., and Lednev, I.K. (2013) Amide I vibrational mode suppression in surface (SERS) and tip (TERS) enhanced Raman spectra of protein specimens. *Analyst*, **138**, 1665–1673. doi: 10.1039/C2AN36478F
58. Zhang, D. *et al* (2009) Parabolic mirror-assisted tip-enhanced spectroscopic imaging for non-transparent materials. *J. Raman Spectrosc.*, **40**, 1371–1376. doi: 10.1002/jrs.2411
59. Schmid, T., Yeo, B.-S., Leong, G., Stadler, J., and Zenobi, R. (2009) Performing tip-enhanced Raman spectroscopy in liquids. *J. Raman Spectrosc.*, **40**, 1392–1399. doi: 10.1002/jrs.2387
60. Koopman, M. *et al* (2004) Near-field scanning optical microscopy in liquid for high resolution single molecule detection on dendritic cells. *FEBS Lett.*, **573**, 6–10. doi: 10.1016/j.febslet.2004.07.035
61. Deckert-Gaudig, T., Rauls, E. and Deckert, V. (2010) Aromatic Amino Acid Monolayers Sandwiched between Gold and Silver: A Combined Tip-Enhanced Raman and Theoretical Approach.. *J. Phys. Chem.*, **114**, 7412–7420. doi: 10.1021/jp9098045
62. Ichimura, T. *et al* (2007) Temporal fluctuation of tip-enhanced Raman spectra of adenine molecules. *J. Phys. Chem. C*, **111**, 9460–9464.
63. Deckert-Gaudig, T. and Deckert, V. (2009) Ultraflat transparent gold nanoplates-ideal substrates for tip-enhanced Raman scattering experiments. *Small*, **5**, 432–436. doi: 10.1002/smll.200801237
64. Zhang, W., Schmid, T., Yeo, B.-S., and Zenobi, R. (2008) Near-Field heating, annealing, and signal loss in tip-enhanced Raman spectroscopy. *J. Phys. Chem. C*, **112**, 2104–2108. doi: 10.1021/jp077457g
65. Blum, C. *et al* (2012) Understanding tip-enhanced Raman spectra of biological molecules: a combined Raman, SERS and TERS study. *J. Raman Spectrosc.*, **43**, 1895–1904. doi: Doi 10.1002/Jrs.4099
66. Papadopoulou, E. and Bell, S.E.J. (2011) Label-free detection of single-base mismatches in DNA by surface-enhanced Raman spectroscopy. *Angew. Chem. Int. Ed.*, **50**, 9058–9061. doi: 10.1002/anie.201102776
67. Singha, A., Dasgupta, S., and Roy, A. (2006) Comparison of metal–amino acid interaction in Phe–Ag and Tyr–Ag complexes by spectroscopic measurements. *Biophys. Chem.*, **120**, 215–224. doi: 10.1016/j.bpc.2005.11.006
68. Sun, M., Zhang, Z., Zheng, H., and Xu, H. (2012) In-situ plasmon-driven chemical reactions revealed by high vacuum tip-enhanced Raman spectroscopy. *Sci. Rep.*, **2**, 647. doi: 10.1038/srep00647
69. Moskovits, M. (1982) Surface selection rules. *J. Chem. Phys.*, **77**, 4408–4416.
70. Erdheim, G.R., Birke, R.L., and Lombardi, J.R. (1980) Surface enhanced raman spectrum of pyrazine. Observation of forbidden lines at the electrode surface. *Chem. Phys. Lett.*, **69**, 495–498. doi: 10.1016/0009-2614(80)85112-8
71. Polubotko, A.M. (1990) SERS phenomenon as a manifestation of quadrupole interaction of light with molecules. *Phys. Lett. A*, **146**, 81–84. doi: 10.1016/0375-9601(90)90034-L

72. Deckert-Gaudig, T., Bailo, E., and Deckert, V. (2009) Tip-enhanced Raman scattering (TERS) of oxidised glutathione on an ultraflat gold nanoplate. *Phys. Chem. Chem. Phys.*, **11**, 7360–7362. doi: 10.1039/B904735B
73. Deckert, V., Zeisel, D., Zenobi, R., and Vo-Dinh, T. (1998) Near-field surface-enhanced Raman Imaging of dye-labeled DNA with 100-nm resolution. *Anal. Chem.*, **70**, 2646–2650. doi: 10.1021/ac971304f
74. Watanabe, H., Ishida, Y., Hayazawa, N., Inouye, Y., and Kawata, S. (2004) Tip-enhanced near-field Raman analysis of tip-pressurized adenine molecule. *Phys. Rev. B*, **69**, 155418.
75. Rasmussen, A. and Deckert, V. (2006) Surface- and tip-enhanced Raman scattering of DNA components. *J. Raman Spectrosc.*, **37**, 311–317. doi: 10.1002/jrs.1480
76. Domke, K.F., Zhang, D., and Pettinger, B. (2007) Tip-enhanced Raman spectra of picomole quantities of DNA nucleobases at Au(111). *J. Am. Chem. Soc.*, **129**, 6708–6709. doi: 10.1021/ja071107q
77. Zhang, D., Domke, K.F., and Pettinger, B. (2010) Tip-enhanced raman spectroscopic studies of the hydrogen bonding between adenine and thymine adsorbed on Au (111). *ChemPhysChem*, **11**, 1662–1665. doi: 10.1002/cphc.200900883
78. Wood, B.R., Asghari-Khiavi, M., Bailo, E., McNaughton, D., and Deckert, V. (2012) Detection of nano-oxidation sites on the surface of hemoglobin crystals using tip-enhanced Raman scattering. *Nano Lett.*, **12**, 1555–1560. doi: 10.1021/nl2044106
79. Wood, B.R. *et al* (2011) Tip-enhanced Raman scattering (TERS) from hemozoin crystals within a sectioned erythrocyte. *Nano Lett.*, **11**, 1868–1873. doi: 10.1021/nl103004n
80. Yeo, B.-S., Madler, S., Schmid, T., Zhang, W., and Zenobi, R. (2008) Tip-enhanced Raman spectroscopy can see more: the case of cytochrome c. *J. Phys. Chem. C*, **112**, 4867–4873. doi: 10.1021/jp709799m
81. Böhme, R. *et al* (2011) Characterizing cytochrome C states – TERS studies of whole mitochondria. *Chem. Commun.*, **47**, 11453–11455. doi: 10.1039/c1cc15246g
82. Deckert-Gaudig, T. and Deckert, V. (2009) Tip-enhanced Raman scattering studies of histidine on novel silver substrates. *J. Raman Spectrosc.*, **40**, 1446–1451. doi: 10.1002/jrs.2359
83. Bailo, E. and Deckert, V. (2008) Tip-enhanced raman spectroscopy of single RNA strands: towards a novel direct-sequencing method. *Angew. Chem. Int. Ed.*, **47**, 1658–1661. doi: 10.1002/anie.200704054
84. Treffer, R., Lin, X., Bailo, E., Deckert-Gaudig, T., and Deckert, V. (2011) Distinction of nucleobases - a tip-enhanced Raman approach. *Beilstein J. Nanotechnol.*, **2**, 628–637. doi: 10.3762/bjnano.2.66
85. Han, X., Zhao, B., and Ozaki, Y. (2009) Surface-enhanced Raman scattering for protein detection. *Anal. Bioanal. Chem.*, **394**, 1719–1727. doi: 10.1007/s00216-009-2702-3
86. Macdonald, I.D.G. and Smith, W.E. (1996) Orientation of cytochrome c adsorbed on a citrate-reduced silver colloid surface. *Langmuir*, **12**, 706–713. doi: 10.1021/la950256w
87. Keating, C.D., Kovaleski, K.M., and Natan, M.J. (1998) Protein: colloid conjugates for surface enhanced Raman scattering: stability and control of protein orientation. *J. Phys. Chem. B*, **102**, 9404–9413. doi: 10.1021/jp982723z
88. Keating, C.D., Kovaleski, K.K., and Natan, M.J. (1998) Heightened electromagnetic fields between metal nanoparticles: surface enhanced raman scattering from metal–cytochrome c-metal sandwiches. *J. Phys. Chem. B*, **102**, 9414–9425. doi: 10.1021/jp982724r
89. Xu, H., Bjerneld, E.J., Käll, M., and Börjesson, L. (1999) Spectroscopy of single hemoglobin molecules by surface enhanced Raman scattering. *Phys. Rev. Lett.*, **83**, 4357–4360.
90. Deckert-Gaudig, T., Kämmer, E., and Deckert, V. (2012) Tracking of nanoscale structural variations on a single amyloid fibril with tip-enhanced

Raman scattering. *J. Biophotonics*, **5**, 215–219. doi: 10.1002/jbio.201100142

91. Kurouski, D., Deckert-Gaudig, T., Deckert, V., and Lednev, I.K. (2012) Structure and composition of insulin fibril surfaces probed by TERS. *J. Am. Chem. Soc.*, **134**, 13323–13329. doi: 10.1021/ja303263y
92. Yang, Z., Aizpurua, J., and Xu, H. (2009) Electromagnetic field enhancement in TERS configurations. *J. Raman Spectrosc.*, **40**, 1343–1348. doi: 10.1002/jrs.2429
93. Podstawka-Proniewicz, E. *et al* (2011) Vibrational characterization of l-leucine phosphonate analogues: FT-IR, FT-Raman, and SERS spectroscopy studies and DFT calculations. *J. Phys. Chem. A*, **115**, 11067–11078. doi: 10.1021/jp207101m
94. Blum, C. *et al* (2012) Missing amide I mode in gap-mode tip-enhanced Raman spectra of proteins. *J. Phys. Chem. C*, **116**, 23061–23066. doi: 10.1021/jp306831p
95. Paulite, M. *et al* (2013) Full spectroscopic tip-enhanced Raman imaging of single nanotapes formed from β-amyloid(1–40) peptide fragments. *ACS Nano*, **7**, 911–920. doi: 10.1021/nn305677k
96. Wang, H. and Schultz, Z.D. (2013) The chemical origin of enhanced signals from tip-enhanced Raman detection of functionalized nanoparticles. *Analyst*, **138**, 3150–3157. doi: 10.1039/C3AN36898J
97. Kazemi-Zanjani, N. *et al* (2012) Label-free mapping of osteopontin adsorption to calcium oxalate monohydrate crystals by tip-enhanced Raman spectroscopy. *J. Am. Chem. Soc.*, **134**, 17076–17082. doi: 10.1021/ja3057562
98. Veatch, S.L., Leung, S.S.W., Hancock, R.E.W., and Thewalt, J.L. (2007) Fluorescent probes alter miscibility phase boundaries in ternary vesicles. *J. Phys. Chem. B*, **111**, 502–504. doi: 10.1021/jp067636i
99. Hodges, M.D. *et al* (2011) Combining immunolabeling and surface-enhanced raman spectroscopy on cell membranes. *ACS Nano*, **5**, 9535–9541. doi: 10.1021/nn202652h
100. Alexander, K.D. and Schultz, Z.D. (2012) Tip-enhanced raman detection of antibody conjugated nanoparticles on cellular membranes. *Anal. Chem.*, **84**, 7408–7414. doi: 10.1021/ac301739k
101. Sweetenham, C.S., Larraona-Puy, M., and Notingher, I. (2011) Simultaneous Surface-Enhanced Raman Spectroscopy (SERS) and Atomic Force Microscopy (AFM) for label-free physicochemical analysis of lipid bilayers. *Appl. Spectrosc.*, **65**, 1387–1392. doi: 10.1366/11-06319
102. Vitol, E.A., Orynbayeva, Z., Friedman, G., and Gogotsi, Y. (2012) Nanoprobes for intracellular and single cell Surface-Enhanced Raman Spectroscopy (SERS). *J. Raman Spectrosc.*, **43**, 817–827. doi: 10.1002/jrs.3100
103. Böhme, R. *et al* (2010) Biochemical imaging below the diffraction limit – probing cellular membrane related structures by Tip-Enhanced Raman Spectroscopy (TERS). *J. Biophotonics*, **3**, 455–461. doi: 10.1002/jbio.201000030
104. Bunow, M.R. and Levin, I.W. (1977) Raman spectra and vibrational assignments for deuterated membrane lipids: 1,2-Dipalmitoyl phosphatidylcholine-d9 and -d62. *Biochim. Biophys. Acta, Lipids Lipid Metab.*, **489**, 191–206. doi: 10.1016/0005-2760(77)90138-2
105. Opilik, L., Bauer, T., Schmid, T., Stadler, J., and Zenobi, R. (2011) Nanoscale chemical imaging of segregated lipid domains using tip-enhanced Raman spectroscopy. *Phys. Chem. Chem. Phys.*, **13**, 9978–9981. doi: 10.1039/c0cp02832k
106. Xiao, C., Moore, D.J., Flach, C.R., and Mendelsohn, R. (2005) Permeation of dimyristoylphosphatidylcholine into skin—structural and spatial information from IR and Raman microscopic imaging. *Vib. Spectrosc.*, **38**, 151–158. doi: 10.1016/j.vibspec.2005.02.017
107. Xiao, C., Moore, D.J., Rerek, M.E., Flach, C.R., and Mendelsohn, R. (2005) Feasibility of tracking phospholipid permeation into skin using infrared and Raman microscopic imaging. *J. Invest. Dermatol.*, **124**, 622–632. doi: 10.1111/j.0022-202X.2004.23608.x

108. Deckert-Gaudig, T. *et al* (2012) Nanoscale distinction of membrane patches – a TERS study of Halobacterium salinarum. *J. Biophotonics*, **5**, 582–591. doi: 10.1002/jbio.201100131

109. Stephen, K.E., Homrighausen, D., DePalma, G., Nakatsu, C.H., and Irudayaraj, J. (2012) Surface enhanced Raman spectroscopy (SERS) for the discrimination of Arthrobacter strains based on variations in cell surface composition. *Analyst*, **137**, 4280–4286. doi: 10.1039/C2AN35578G

110. Budich, C., Neugebauer, U., Popp, J., and Deckert, V. (2008) Cell wall investigations utilizing tip-enhanced Raman scattering. *J. Microsc.*, **229**, 533–539. doi: 10.1111/j.1365-2818.2008.01939.x

111. Neugebauer, U. *et al* (2006) On the way to nanometer-sized information of the bacterial surface by tip-enhanced Raman spectroscopy. *ChemPhysChem*, **7**, 1428–1430. doi: 10.1002/cphc.200600173

112. Neugebauer, U. *et al* (2007) Towards a detailed understanding of bacterial metabolism—spectroscopic characterization of staphylococcus epidermidis. *ChemPhysChem*, **8**, 124–137. doi: 10.1002/cphc.200600507

113. Richter, M., Hedegaard, M., Deckert-Gaudig, T., Lampen, P., and Deckert, V. (2011) Laterally resolved and direct spectroscopic evidence of nanometer-sized lipid and protein domains on a single cell. *Small*, **7**, 209–214. doi: 10.1002/smll.201001503

114. Simons, K. and Ikonen, E. (1997) Functional rafts in cell membranes. *Nature*, **387**, 569–572. doi: 10.1038/42408

115. Cialla, D. *et al* (2009) Raman to the limit: tip-enhanced Raman spectroscopic investigations of a single tobacco mosaic virus. *J. Raman Spectrosc.*, **40**, 240–243. doi: 10.1002/jrs.2123

116. Hermann, P. *et al* (2011) Evaluation of tip-enhanced Raman spectroscopy for characterizing different virus strains. *Analyst*, **136**, 1148–1152. doi: 10.1039/C0AN00531B

12
Infrared Mapping below the Diffraction Limit

Peter R. Griffiths and Ellen V. Miseo

12.1
Introduction and Description of Early Work

In infrared microscopy, the rule of thumb is that you cannot obtain a transmission spectrum of an object smaller than 10 μm in diameter. The 10 μm minimum is based on the diffraction of light around an object at or near the wavelength of light (see Chapter 1). Recently, researchers have developed approaches that can overcome this limit. This chapter explores these new approaches and the theory necessary to understand both the limitations of current techniques and the basis for these novel techniques.

To improve the resolution beyond the diffraction limit, it is necessary to use one of several approaches where the spatial resolution is not limited by diffraction, such techniques are often given the term *nanospectroscopy*. For Raman nanospectroscopy, this has been achieved by tip-enhanced Raman scattering (TERS) (see Chapter 11). However, the huge plasmonic enhancements in the electromagnetic field near sharp silver or gold tips are not found at infrared wavelengths. Instead several other approaches have been investigated that are not limited by diffraction, including near-field microscopy, scattering from a small metallic or semiconductor tip, and photothermal spectroscopy.

12.1.1
Near-Field Microscopy with Small Apertures

Scanning near-field optical microscopy (SNOM) followed the discovery of scanning probe techniques that exploited the tunneling of electrons (in scanning tunneling microscopy, STM) or atomic forces (in atomic force microscopy, AFM) that occur between a sharp scanning tip and a sample. The first SNOM experiments designed to take advantage of this effect employed a minute metallic aperture to confine the electric field of the radiation that is incident on the tip. The aperture that was most commonly employed was a metalized tapered glass fiber. However, in order to achieve submicrometer resolution, the diameter of the aperture had to be so small that its transmission was limited by the waveguide cutoff effect [1]

Infrared and Raman Spectroscopic Imaging, Second Edition. Edited by Reiner Salzer, Heinz W. Siesler.
© 2014 Wiley-VCH Verlag GmbH & Co. KGaA. Published 2014 by Wiley-VCH Verlag GmbH & Co. KGaA.

where light propagation becomes evanescent when the diameter is smaller than the critical cutoff diameter, d_c, which is equal to $0.6\lambda/n$. Provided that the sample is held within the evanescent field (hence the term near-field spectroscopy), it is possible to achieve a spatial resolution that is less than $\lambda/2$.

One of the first attempts to use a small aperture for mid-infrared nanoimaging was reported by Michaels *et al.* [2]. This group described an experiment in which an aperture probe was used as a subwavelength-diameter light source. Infrared radiation from a femtosecond laser that could be tuned from 2.5 to 12 μm was coupled into the fiber. Because of the very short pulses, the full-width at half-height of the beam profile (i.e., the useful spectral range) was about 150 cm^{-1}. Only a very small fraction (<0.01%) of the light was transmitted through a 400 nm aperture but the power of the laser was such that this could be measured. The samples were spin coated onto a glass cover slip and mounted on a metal disk that was supported on three piezoelectric transducers (PZTs) that were used to position the sample relative to the probe. The probe was mounted on a fourth PZT that was used in a shear-force detection circuit to position the tip a few nanometers from the surface. The thickness of the sample was between 300 and 550 nm; it should be noted that the thickness of the sample cannot be greater than the depth of the near field, or else the far-field absorption will dominate the spectrum. The radiation transmitted through the sample was passed through a monochromator to disperse the radiation of interest and then focused on an InSb focal-plane array detector.

The performance of this instrument was demonstrated using a polystyrene/poly(ethyl acrylate) (PS/PEA) blend for which AFM showed the presence of spheroidal inclusions (Figure 12.1a). The image of a different region of the sample

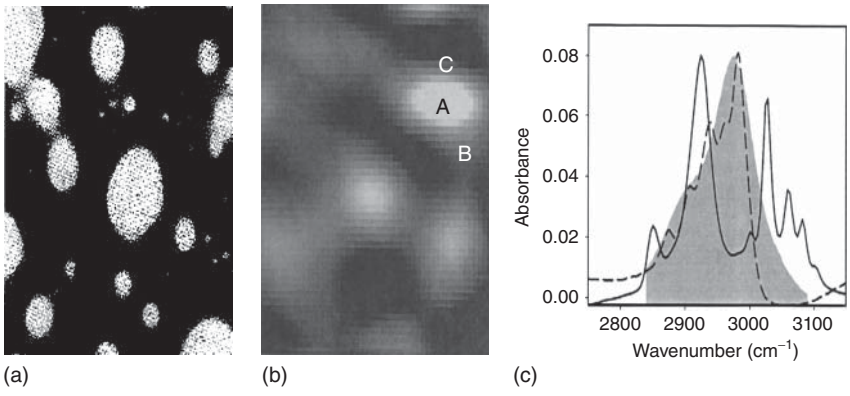

Figure 12.1 (a) 8 × 8 μm tapping mode AFM topographic image of a PS/PEA blend measured with a probe-to-sample separation of about 300 nm; black and white represent the minimum and maximum heights, respectively. (b) Image constructed from the infrared data. (c) Scaled infrared spectra of PS (solid line) and PEA (broken line) with the relative intensity spectrum of the broadband laser used to fabricate the image shown in (b). (Reprinted with permission from Ref. [2]. Copyright 2004, Society for Applied Spectroscopy.)

obtained by SNOM is shown in Figure 12.1b. The spectra of PS (solid line) and PEA (broken line) are shown in Figure 12.1c along with the measured data, which is the single-beam spectrum of the laser with very weak absorption from both components. The relative transmission spectrum in the region where both PS and PEA absorb shows little evidence of absorption by either PS or PEA, but the average transmission differs for the pixels marked A–C in Figure 12.1b, presumably because scattering differences are caused by the topography and height of the samples in regions where the PS-rich spheroidal inclusions protrude above the surface of the matrix. The difference in relative transmittance allowed the image shown in Figure 12.1b to be constructed. The spatial resolution appears to be between 1 and 2 μm, which is better than the diffraction-limited value for mid-infrared radiation, although better resolution than this is required if nanoimaging is to be useful.

The limitations introduced by the minute aperture have meant that few papers have been published on the topic of aperture-based SNOM systems. However, Schnell *et al.* [3] recently reported how mid-infrared radiation could be focused into a very small area through a tapered transmission line. Nanofocusing of 10.7 μm radiation was achieved by propagating a mid-infrared surface wave along a tapered two-wire transmission line. The spot diameter was compressed to 60 nm ($\lambda/150$) at the taper apex. To the best of our knowledge, no nanoimaging results in which this approach has been applied have yet been reported. Most of the major advances in this field have been based on either photothermal (PT) spectroscopy or elastic scattering from a tip. In the remainder of this section, the early work that laid the foundations for some of the remarkable results that have been reported in the past decade will be described.

12.1.2
Scanning Photothermal Microscopy and Microspectroscopy

The first research groups to recognize the feasibility of using photothermal spectroscopy for microscopy with spatial resolution below the diffraction limit were those of Hubert Pollock of Lancaster University in England and Mark Anderson of the Jet Propulsion Laboratory in Pasadena, California. In 1996, Pollack's group [4] described how spatially resolved thermal analysis of samples could be achieved using a miniaturized resistive probe. This type of measurement has been called scanning thermal microscopy [5]. An instrument based on this principle was used to perform surface and subsurface imaging of polymers [6, 7]. Three years later, this group demonstrated the feasibility of using a miniaturized resistive thermometer as a probe to record infrared spectra of polymeric samples by detecting photothermally induced temperature fluctuations at the sample surface [8]. The spatial resolution was no longer determined by the diffraction limit but rather by the size of the contact between the probe and sample, which was a few hundred nanometers. The probe was constructed from a length of "Wollaston wire," which is a 75 μm diameter silver wire with a 5 μm diameter platinum/10% rhodium core. The wire was made into a loop and the silver

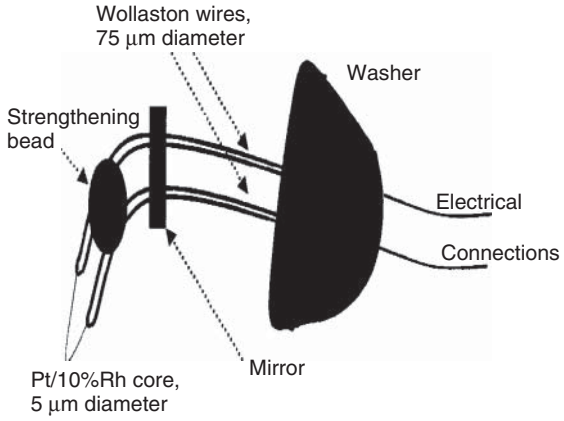

Figure 12.2 Schematic diagram of the thermal probe used by Hammiche *et al*. (Reprinted with permission from Ref. [8]. Copyright 1999, Society for Applied Spectroscopy.)

was etched away to reveal the core over a length of 50 μm, which constitutes the sensing region. A schematic diagram of the thermal probe is shown in Figure 12.2. The mirror indicated in this figure is part of the force feedback system for measuring the deflection of the Wollaston wires when the probe is being used for imaging.

Spectroscopic measurements were then made by mounting this device in the sample compartment of a Fourier transform infrared (FT-IR) spectrometer. The plane of the loop was inclined to the surface to minimize beam blockage. The sample was held at the focus of beam-condensing optics. The interferogram due to the sample absorption was first measured with the probe in contact with the sample. The probe was then lifted away from the sample, and the measured signal was subtracted from the original signal. Because the response time was fairly slow, the interferometer was operated with the He–Ne laser frequency at 2200 Hz, so that the modulation frequencies at 4000 and 400 cm^{-1} were about 550 and 55 Hz, respectively. Measurements were made at low (16 cm^{-1}) resolution, and extensive signal averaging (5000 scans) was needed to obtain an acceptable signal-to-noise ratio (SNR).

The size of the region from which heat reaches the probe is given approximately by the thermal diffusion length, the value of which is determined by the optical velocity of the interferometer [9]. Although the spatial resolution was estimated at "several hundred nanometers," it is probable that it was better at the high wave number region of the spectrum than at longer wavelength because of the increased modulation frequency. When the probe absorbs radiation, its temperature – and hence its resistance – increases. In the report by Hammiche *et al.* [8], the change in resistance was amplified using a Wheatstone bridge. The probe receives heat both by direct absorption of the IR beam by conduction and indirectly by convection from the surrounding air. The part of the temperature rise that is independent of

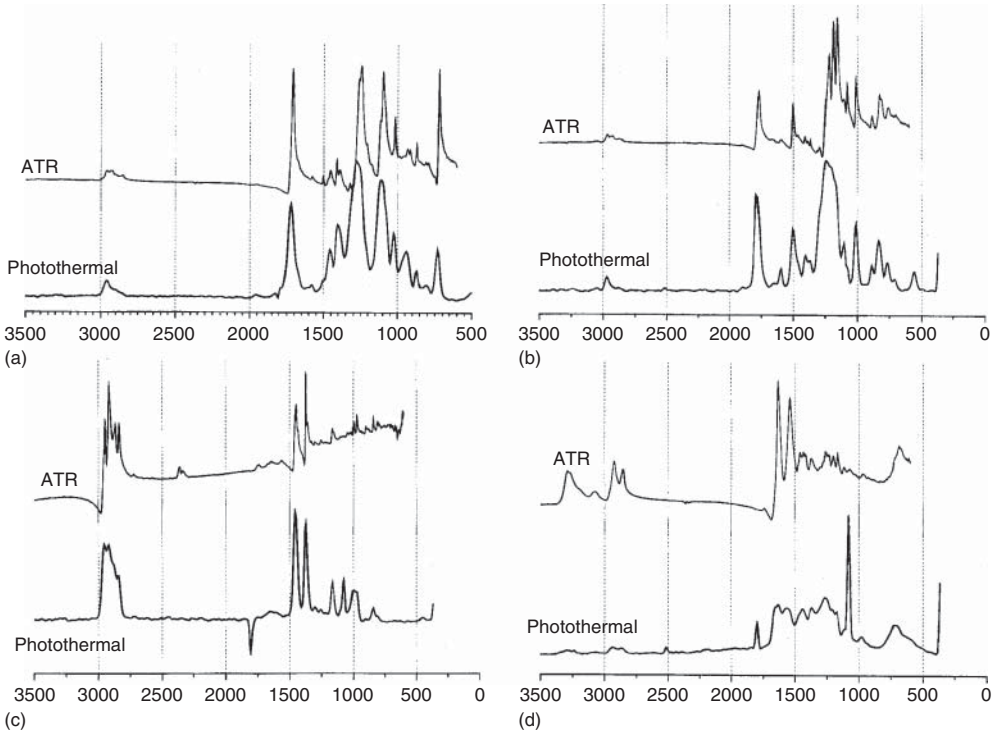

Figure 12.3 Photothermal spectra measured at 16 cm^{-1} resolution (lower trace) and ATR spectra measured at 4 cm^{-1} resolution (upper trace) of (a) poly (butylene terephthalate), (b) polycarbonate, (c) polypropylene, and (d) nylon 6. (Reprinted with permission from Ref. [8]. Copyright 1999, Society for Applied Spectroscopy.)

the sample temperature contains the information on the absorption spectrum of the sample.

Representative results are shown in Figure 12.3, with ATR spectra of the same polymers being shown for comparison [8], although it should be noted that the ATR spectra were measured at higher resolution than the photothermal spectra. The distortion of the stronger bands in the ATR spectra of the more polar polymers is caused by the effect of anomalous dispersion when an internal reflection element (IRE) with a relatively low refractive index, presumably ZnSe, was used. Remarkably the highest quality of photothermal spectrum was measured in the case of polypropylene, which has a relatively weak spectrum, and the lowest quality spectrum was measured in the case of Nylon 6, where the effect of photoacoustic saturation [10] is clearly evident. It is interesting to speculate on whether this spectrum and that of polycarbonate would have been improved had the velocity of the interferometer mirror been increased. Spikes in some of the spectra at 1082 and 1804 cm^{-1} were attributed to supply frequency harmonics.

12.1.3
First Description of AFM/FT-IR

The results obtained by Hammiche *et al.* [4–8] by combining scanning thermal microscopy with an FT-IR spectrometer led to the next logical step, namely combining an atomic force microscope with an FT-IR spectrometer. This was first demonstrated by Anderson in 2000 using a filter spectrometer that consisted of a Globar (incandescent silicon carbide) source, a chopper, and mounting brackets for the filters [11]. A germanium filter was installed to block any visible light that could potentially interfere with the infrared measurement. Polymer films were used as infrared filters for spectral discrimination experiments. The beam was focused onto the cantilever tip of an AFM, as shown schematically in Figure 12.4.

To measure the time-modulated vertical surface deformation, the AFM tip was set at a fixed location on the sample. By setting the height feedback gain at a very low value, the tip could not drift off the sample, which allowed the low-frequency drift to be compensated without damping the chopper frequency. Residue was removed from the surface with the AFM tip cantilever after imaging the sample using conventional AFM scan parameters. For sampling, the tip force on the surface was increased by maximizing the AFM set point; the set point controls the deflection of the cantilever during scanning. The surface was scanned multiple times, after which the normal scan parameters were resumed and the AFM was zoomed out to image a larger region of the sample. The photothermal deformation of the coated tip was measured by adjusting the offset and set point of the AFM to zero, which caused a "false engagement" when there was no contact of the tip with the surface. The AFM could then measure the free-standing cantilever deformation.

Anderson demonstrated the feasibility of the approach shown in Figure 12.4 by showing first that there was no deflection observed for a gold surface (since gold

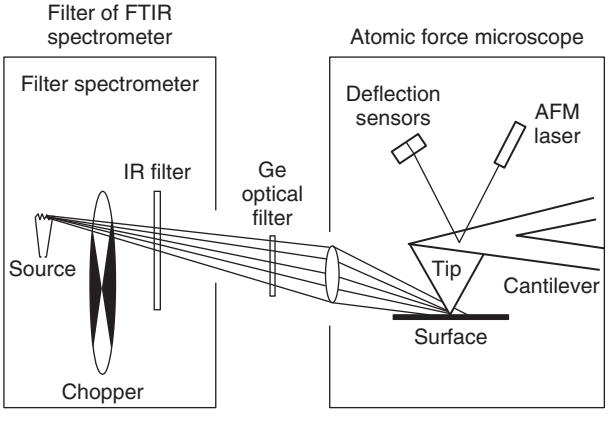

Figure 12.4 Schematic diagram of Anderson's AFM photothermal deflection test. (Reprinted with permission from Ref. [11]. Copyright 2000, Society for Applied Spectroscopy.)

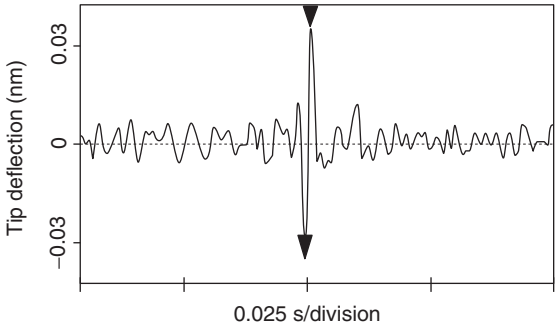

Figure 12.5 AFM cantilever height deflection signal with the tip fixed on a mica substrate and irradiated with the beam modulated by an interferometer. (Reprinted with permission from Ref. [11]. Copyright 2000, Society for Applied Spectroscopy.)

does not absorb infrared radiation). He then replaced the gold with a fluorinated ethylene polymer (FEP) for which he measured a relatively large (4 nm) deflection for each chopper cycle. He then inserted a 50 μm thick film of FEP as a filter, and no signal was measured as the radiation that would have been absorbed by the FEP was blocked by the filter. On replacing the FEP sample with PS (a weaker absorber than FEP), a deflection of 1.5 nm was observed.

When the beam from the Globar was modulated by an interferometer the results were more equivocal, although a signal with the shape of a typical interferogram measured from an incandescent source was measured using a single scan, as shown in Figure 12.5. The sample in this case was mica, the infrared spectrum of which is dominated by the strong Si–O stretch at ~1020 cm^{-1} with the only other strong bands being below 600 cm^{-1}. Thus, we believe that the shape of the interferogram should not have had the appearance seen in Figure 12.5, which is more similar to the signal from a broadband infrared source. The author notes that an improved SNR could be expected if the scan velocity of the interferometer was reduced, if the beam is more precisely focused on the sample, and if software had been written to allow signal averaging. (We note here that Hammiche *et al.* [8] averaged 5000 scans to achieve the results shown in Figure 12.3.)

12.2
Near-Field Microscopy by Elastic Scattering from a Tip

We wrote earlier that the use of an aperture for SNOM was essentially precluded because of the extremely low transmission of narrow metalized glass fibers caused by the waveguide cutoff effect. Several workers recognized the potential of achieving better resolution by using a small scatterer instead of a small aperture [12–16] because an illuminated particle can exhibit enhanced optical fields in its neighborhood that is in turn modified by the presence of a sample. As a result of this near-field interaction, scattered light that is measured in the far field contains

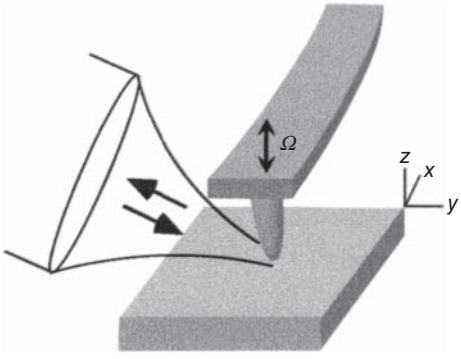

Figure 12.6 Principle of s-SNOM, see text for details. (Reprinted with permission from Ref. [17]. Copyright 2004, Royal Society.)

information on the local optical properties of the sample. This effect has been called *scattering-type scanning near-field optical microscopy* (*s-SNOM*) and is the basis of a commercial instrument that is marketed by Neaspec Gmbh. (Munich, Germany).

The principle of this type of measurement is shown in Figure 12.6 and has been elegantly discussed by Keilmann and Hillenbrand [17]. A focused beam of light illuminates the tip of an AFM, which is first used to produce a topographic image of the sample. The intensity of the scattered light (in this case in the backward direction) is recorded, and an optical image is generated simultaneously. Backscattering is to be preferred so only one focusing lens has to be adjusted. The AFM is used in the tapping mode at the mechanical resonance frequency Ω of the cantilever, so that the near-field optical signal is modulated at harmonics of Ω. Thus, the enormous background scattering from the shaft and cantilever can be discriminated using appropriate lock-in amplification.

The typical radius of curvature of the tip is about 20 nm. The small region between the apex of the tip and the sample (the probing region, which is much smaller than the beam focus) is illuminated by the incident radiation. In the AFM tapping mode, the gap is varied sinusoidally between 0 and ~40 nm so that a strong modulation of the near-field scattering results. Conversely, scattered radiation from the regions of the tip and sample that are outside the probing region is scarcely modulated and can be readily removed from the modulated detector signal.

For highly conductive metal shafts, antenna theory predicts that optical currents can be excited much more strongly in directions parallel to the shaft axis than in the perpendicular direction [1]. This effect was verified by Knoll and Keilmann who showed that the optical image produced using a CO_2 laser loses contrast when the input polarization has no component along the shaft axis, showing that the antenna effect enhances the probing near field in the z-direction [18]. Light scattering at nanoparticles can be dramatically increased at the "hot spots" of optical antennas where the incident radiation is highly concentrated. A detailed

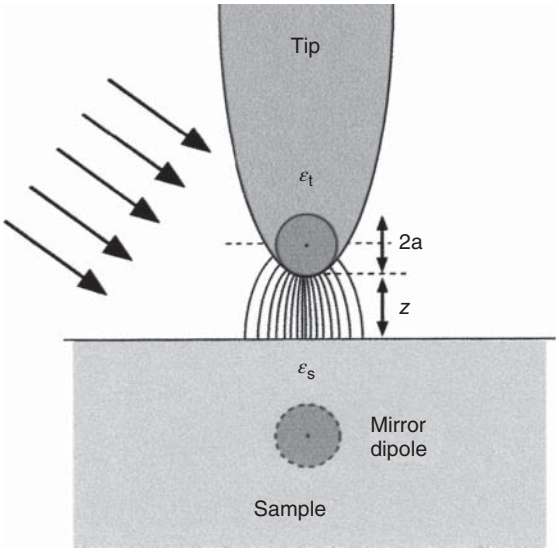

Figure 12.7 Model for the near-field interaction in s-SNOM used by Keilmann and Hillenbrand in which the tip is replaced by a point dipole. (Reprinted with permission from Ref. [17]. Copyright 2004, Royal Society.)

description of the theory of the electromagnetic mechanism of light scattering at single hot spots has been published by Alonso-Gonzalez *et al.* [19].

Using the model shown in Figure 12.7, in which the tip is replaced by a point dipole, Keilmann and Hillenbrand [17] showed that a sample affects the s-SNOM signal only through its complex dielectric value ϵ_s at the wavelength of illumination, which implies that the optical image contrast in an s-SNOM measurement is determined only by the sample's local complex dielectric value ϵ_s (i.e., $\epsilon_s' + i\epsilon_s''$). Furthermore they showed that at very small distances between the sample and the tip, both the scattering amplitude and phase increase sharply so that the spectroscopic information in the region of the tip is dominant (Figure 12.8). As noted earlier, when the AFM is used in the tapping mode at the mechanical resonance frequency, Ω, of the cantilever, the near-field optical signal is modulated at harmonics of Ω, mΩ, and the background scattering from the shaft and cantilever can be discriminated using appropriate lock-in amplification. The harmonics are caused by the nonlinear variation of the near-field scattering amplitude shown in Figure 12.8, whereas the slowly changing background is confined largely to the DC term and lower harmonics. The lowest harmonic for which the large elastic scattering background becomes negligible with respect to the near-field signal, m_0, depends on the wavelength. For $\Delta z = 20$ nm, the value of m_0 for $\lambda = 10$ μm is 2 [20].

This prediction was verified in practice by comparing the s-SNOM amplitude, s, and phase, φ, in the region of the C=O stretching mode of poly(methyl methacrylate) (PMMA) (shown in Figure 12.9c) to the complex dielectric

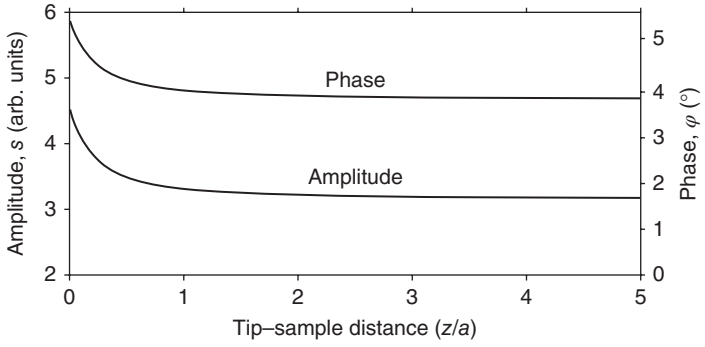

Figure 12.8 Calculated near-field scattering amplitude s and phase φ plotted against the ratio of the distance z between the point dipole (which approximates the spherical end of the tip) and the radius of the point dipole a. (Reprinted with permission from Ref. [17]. Copyright 2004, Royal Society.)

function measured by ellipsometry (Figure 12.9a) and the parameters calculated from the far field absorption, γ, and reflectivity, R (Figure 12.9b) [21]. It can be seen that the agreement is remarkably accurate.

Ocelic *et al.* [22] addressed the problem of suppressing the background signal in s-SNOM and described the application of superheterodyne detection for this purpose. However, the techniques used to demodulate the higher harmonics [23, 24] never completely eliminated the background contribution. Ocelic *et al.* [22] described a more successful approach that eliminated the background interference from the near ultraviolet to the far infrared by simultaneously measuring the near-field signal amplitude and phase by interferometric detection of the scattered light utilizing a phase-modulated reference wave. The system they developed is shown schematically in Figure 12.10. The side bands are seen on the harmonics at Ω, 2Ω, 3Ω, and so on.

In one of the first applications of this type of instrument, a line-tunable CO laser was used to obtain images of a single tobacco mosaic virus (TMV) with a diameter of 18 nm and length of about 300 nm at 1630, 1658, 1679, and 1721 cm^{-1} [25]. The virus particles were cast onto a silicon plate from suspension. The AFM was equipped with a commercially available platinum-covered cantilevered Si tip operated with a tapping frequency of 33 kHz and amplitude of 25 nm. The superheterodyne technique for demodulation described earlier was employed. The images shown in Figure 12.11 demonstrate the success of this approach. The authors remark on the strength of the response exhibited by the virus, which amounts to a $\pm 10\%$ change of scattered signal amplitude and a 10° phase shift when the frequency is tuned through resonance. Typically for transmission spectrometry, the sample should be at least 1 μm (and preferably 10 μm) thick to achieve an optimal spectrum.

The effect of the material from which the AFM tips were constructed was investigated by Haefliger *et al.* [26]. They showed that the low refractive index of the thin oxide layer on the surface of Si tips reduced the antenna effect and therefore

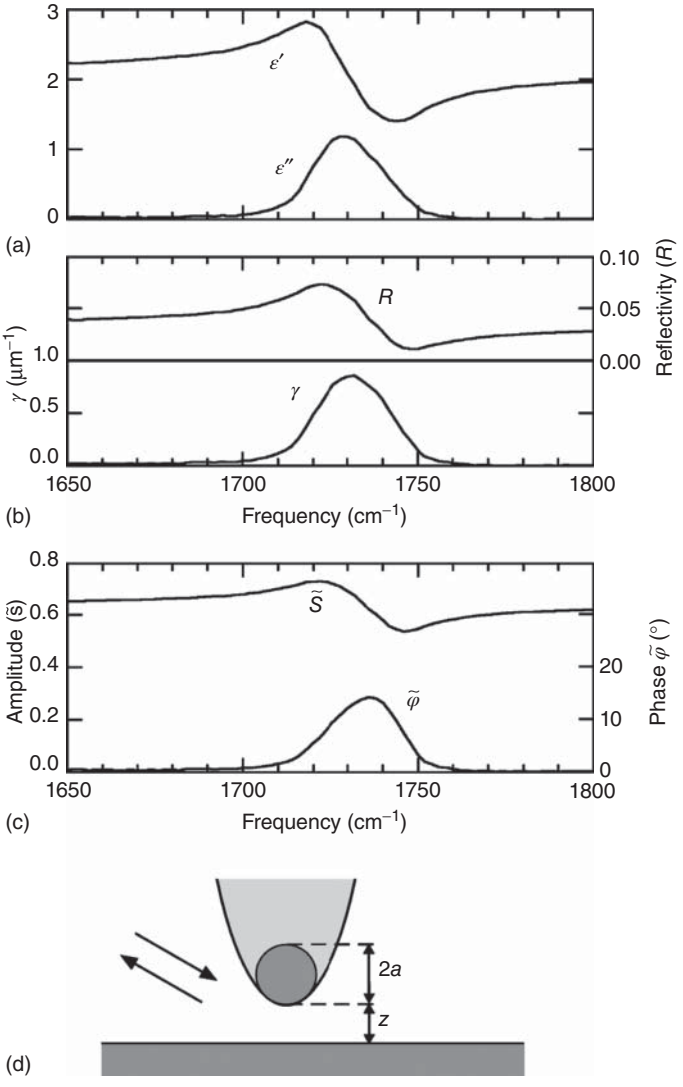

Figure 12.9 (a) Measured dielectric functions ϵ_s' and ϵ_s'', (b) the far-field absorption γ and reflectivity R in the same region, (c) the s-SNOM amplitude s and phase φ in the region between 1650 and 1800 cm^{-1}, and (d) relevant parameters for s-SNOM. (Reprinted with permission from Ref. [21] Copyright 2004 AIP Publishing LLC.)

degraded the sensitivity enhancement of these tips. Etching off the SiO_2 layer in an HF solution buffered with NH_4F significantly improved the performance. Both gold and platinum tips gave rise to near-field images with good contrast but had poorer wear resistance. Dielectric probes fabricated from such materials as Si_3N_4 offer advantages over metal or metal-coated probes as they have a low nonlinear coefficient required for second-harmonic imaging of samples, higher wear

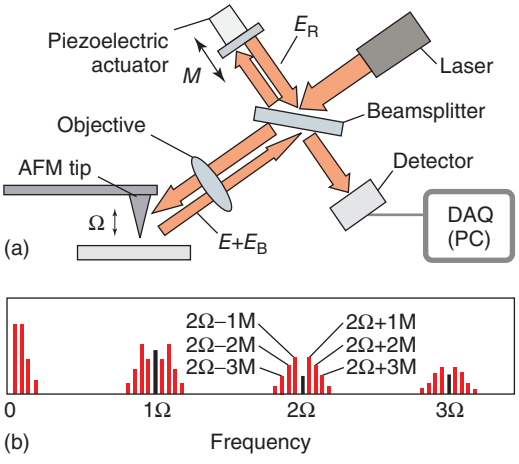

Figure 12.10 (a) Schematic representation of the experimental setup for the interferometric detection of near-field (E) and background (E_B) scattering from an s-SNOM probe employing a phase-modulated reference beam (E_R) of frequency M. (b) Schematic of the detected signal spectrum. (Reprinted with permission from Ref. [22]. Copyright 2006 AIP Publishing LLC.)

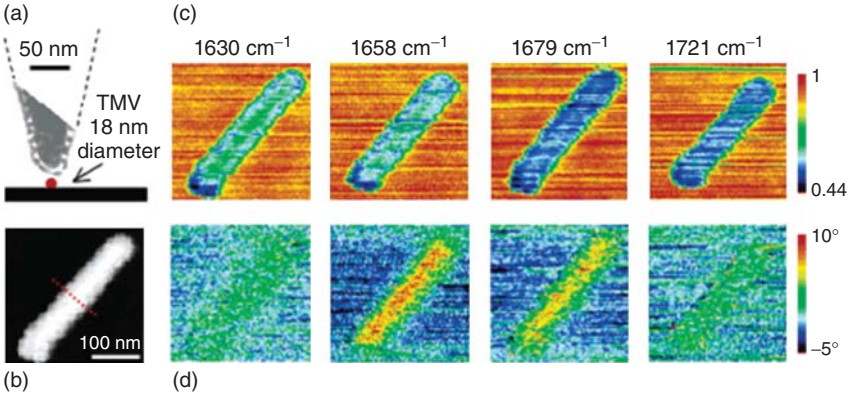

Figure 12.11 Near-field images of a single tobacco mosaic virus (TMV) on a silicon plate. (a) Scale diagram of TMV under the probing tip, (b) transmission electron micrograph of the virus particle, and (c,d) near-field amplitude and phase contrast images recorded at four wavelengths. (Reprinted with permission from Ref. [25]. Copyright 2006, American Chemical Society.)

resistance, higher spatial resolution because of smaller tip diameters, and strong field enhancement by phonon polariton resonance in polar dielectrics.

The early results reported by Hillenbrand's group were achieved by illuminating the AFM tip with a continuous-wave laser, which gave good images but limited the spectral range that can be covered to the output wavelengths of the laser. A related limitation is found when pulses of infrared radiation from a femtosecond laser

that had been down-shifted into the mid infrared by passing the beam through a nonlinear crystal were used to generate the near-field signal [27, 28]. In this case, the wavenumber range is broadened by the limited time of each pulse but is still less than 200 cm^{-1} for most realistic pulse widths. In an attempt to circumvent this limitation by using a thermal source (an incandescent metal coil), Huth *et al.* invoked the use of an asymmetric interferometer with the AFM tip and sample held in one of the arms, as shown in Figure 12.12a [29]. The interferogram was recorded using a demodulation order of $m = 2$. The interferogram and spectrum measured in this way are shown in Figure 12.12b,c, respectively.

This approach was validated by mapping an approximately 1 μm thick p-doped polycrystalline silicon film sandwiched on each side by a 1 μm thick film of silica. The results are shown in Figure 12.13. The authors ascribe the relatively weak signal obtained from silica to the fact that it has a much lower refractive index than silicon. These results show a spatial resolution of about 100 nm and provide evidence that a metal tip can nanofocus blackbody radiation to a near-field spot at the tip apex that is about $\lambda/100$ in diameter.

The SNR of the spectra shown in Figure 12.13 is quite low as a result of the low power of the thermal source that was used. Clearly what is needed is a source with the power of an intense laser and the wavelength coverage of a thermal source. A reasonable compromise was reported by Huth *et al.* who demonstrated the use of a coherent broadband mid-infrared beam that was generated by a difference frequency generator (DFG), where two near-infrared 200 fs pulse trains from an erbium fiber laser system are superimposed in a GaSe crystal [30]. The laser emits two pulse trains, one at 1.55 μm and the other that is broadened and red-shifted. As shown in Figure 12.14a, the output of the nonlinear crystal DFG is focused on an AFM tip that is held in one arm of an asymmetric interferometer in the same manner as shown in Figure 12.12a.

A continuum spectrum can be measured over a range of about 700 cm^{-1}, the center frequency of which can be varied by changing the orientation of the crystal in the DFG. Single-beam spectra measured over two different ranges are shown in Figure 12.14b. (The fainter line above the higher wavenumber spectrum is the result of compensating for absorption by atmospheric water vapor.) Both the spatial resolution and the spectroscopic performance of this system were demonstrated in this paper.

The spatial resolution was shown using a thin film of PMMA on silicon, with the DFG set to give its output between 5 and 9 μm (2000–1100 cm^{-1}; Figure 12.15). When the interferometer was held at the zero path difference (ZPD) point, there was sufficient difference between the spectra of PMMA and Si that the regions of the sample that were covered with PMMA gave rise to a smaller signal than in regions where it was absent. This measurement indicated that the spatial resolution was approximately 20 nm. The spectra of PMMA measured using the s-SNOM system and a transmission spectrum of PMMA measured with a conventional FT-IR spectrometer are shown in Figure 12.16. Even though the relative band intensities in these two spectra are not identical, the doublet of doublets that is characteristic of methacrylates is readily evident in the s-SNOM spectrum. The

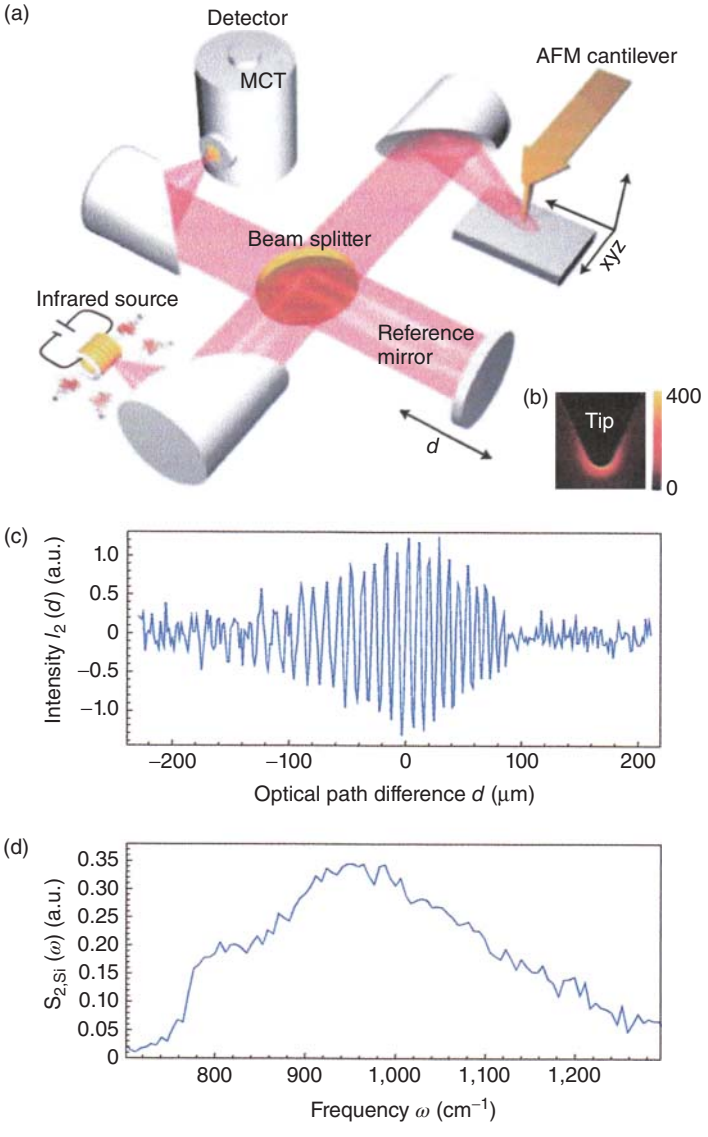

Figure 12.12 (a) Experimental arrangement involving the use of an asymmetric interferometer; (b) distribution of the electric field at the apex of a metal tip of length 10 μm with an apex diameter of 100 nm illuminated by 10.7 μm (935 cm^{-1}) radiation; (c) interferogram recorded from a silicon surface; and (d) near-field spectrum obtained by Fourier transform of this interferogram. (Reprinted by permission from Macmillan Publishers Ltd. from Ref. [29]. Copyright 2011.)

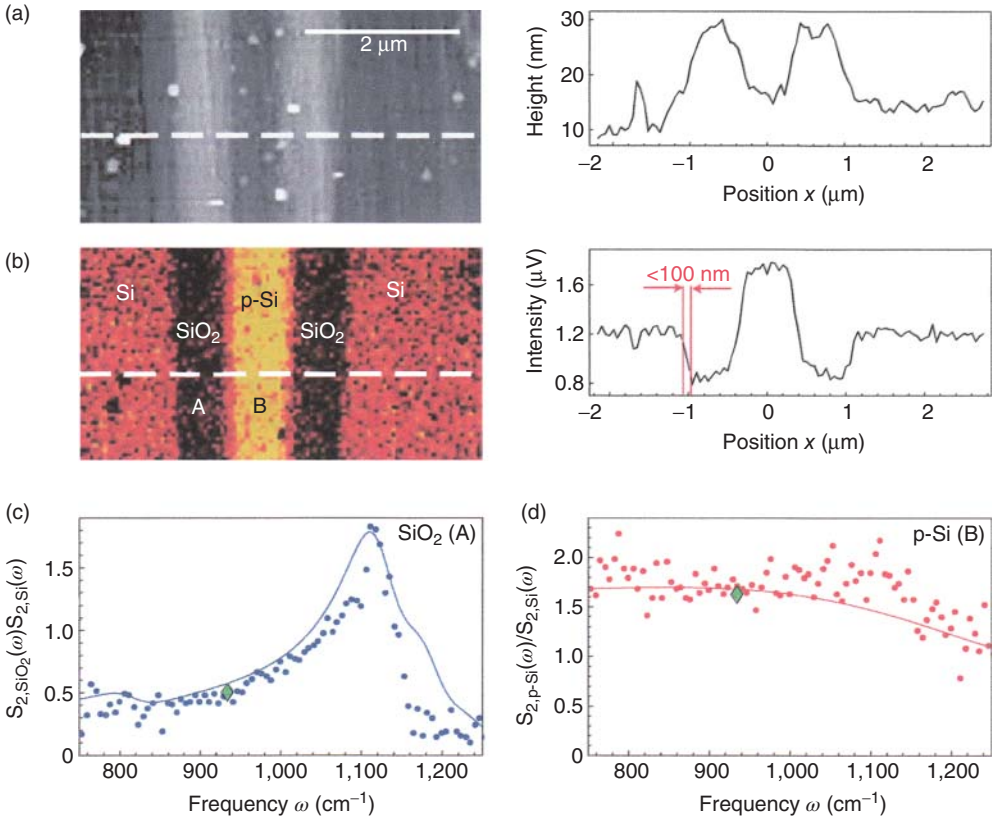

Figure 12.13 (a) Left: Topography image of sample; right: line profile extracted from the dashed white line. (b) Left: Infrared image acquired simultaneously with the topography, right: line profile extracted from the dashed white line. (c) Near-field spectrum taken in the region of the silica, with the solid line showing the result of calculation performed with the finite dipole model of s-SNOM, using a tip radius of 50 nm and a vibration amplitude of 60 nm; the green spot shows the value found using a CO_2 laser. (d) Corresponding data taken in the region of the silicon outer layer. (Reprinted by permission from Macmillan Publishers Ltd. from Ref. [29]. Copyright 2011, Copyright 2011.)

s-SNOM spectrum was measured in the two regions shown in Figure 12.14b. The region between 2000 and 1400 cm^{-1} required an acquisition time of 25 min, and the region between 1400 and 800 cm^{-1} was measured in 16 min. It is presumably because of the very long time required to obtain spectra of individual pixels in an image that the authors chose to use the intensity of the interferogram centerburst to obtain the image shown in Figure 12.15a.

Since the approximate full-width at half-height (FWHH) of each pulse is 100 fs, the distance occupied by each pulse is about 30 μm. The spectra shown in Figure 12.16 are measured at a resolution of 6 cm^{-1}, which means that the maximum optical path difference for the interferometer is 0.17 cm or 1700 μm. The water vapor absorption that is evident in Figure 12.14 indicates that the

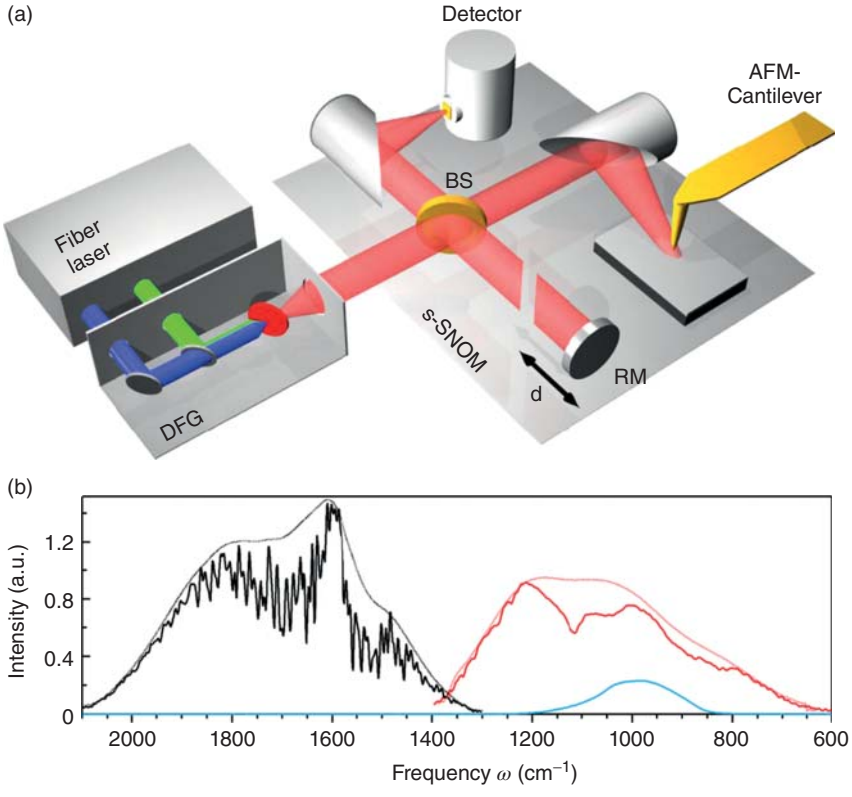

Figure 12.14 (a) Experimental setup using a thermal source and asymmetric interferometer. (b) Single-beam spectra measured at two orientations of the GaSe crystal in the DFG. (Reprinted with permission from Ref. [30]. Copyright 2012, American Chemical Society.)

resolution is a little poorer than 6 cm^{-1} but nowhere near as bad as would be predicted if the beams from the two arms of the interferometer only overlap for 200 fs, which would be about 160 cm^{-1}. To understand the good spectral resolution, the 200 fs pulses should be viewed as a superposition of sinusoidal waves (with very long coherence length) of different frequencies. When the pulse travels through either the sample or atmospheric water vapor, some of the frequencies are absorbed. Superposition of the remaining frequencies now gives a significantly longer "pulse." The sharper the missing spectral line is, the longer the "pulse" will be. Thus, the pulses will overlap over much larger distances, providing the good spectral resolution in case the mirror is translated over long distances (R. Hillenbrand (2013) personal communication to PRG).

Other recent applications of nanospectroscopy using the s-SNOM technique include the chemical mapping of minerals in biological materials [31] and the visualization of methacrylate-embedded human bone sections [32] and undoubtedly many more reports will appear shortly.

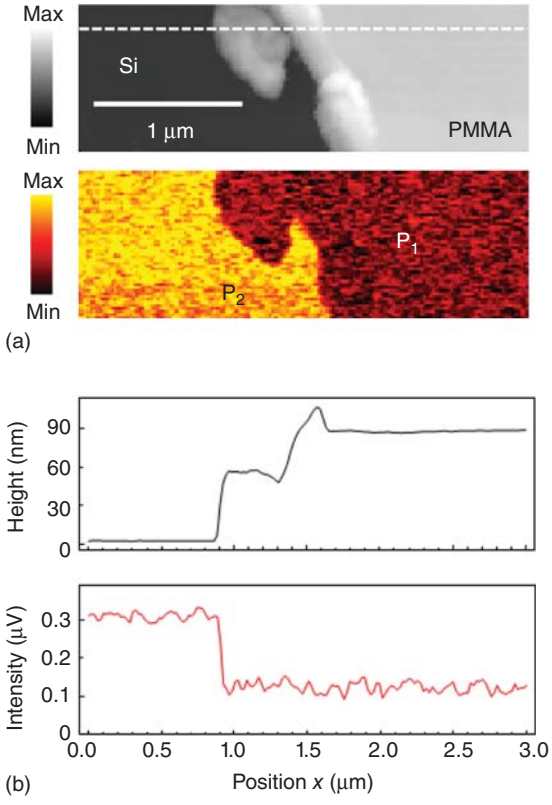

Figure 12.15 (a) Above: AFM topographic image of a 2.5 × 1.0 μm region of the sample of PMMA on Si. Below: Infrared amplitude image obtained by plotting the amplitude of the interferogram at ZPD with the DFG crystal oriented to give the maximum spectral amplitude for $5 < \lambda < 9$ μm. (b) Line profiles of height (above) and infrared signal (below) at the position indicated by the dashed white line. (Reprinted with permission from Ref. [30]. Copyright 2012, American Chemical Society.)

12.3 Combination of AFM and Photothermal FT-IR Spectroscopy

An alternative approach to nanoscale infrared imaging was proposed in 2005 by Dazzi *et al.* [33] and demonstrated in several subsequent papers [34–36]. They developed equipment in which the gold-coated tip of an AFM was located in contact with a thin sample film that had been cast on a triangular prism ZnSe IRE. Light from either a 10 ns CO_2 laser or a 10 μs free electron laser (FEL) was passed into the IRE at an angle such that the beam is internally reflected and the evanescent wave is absorbed at wavelengths where the sample has absorption bands. The sample is heated instantaneously on absorption and the resulting expansion of the sample displaces the AFM tip, so that the cantilever starts to oscillate as a result of sample deformation. Since the AFM

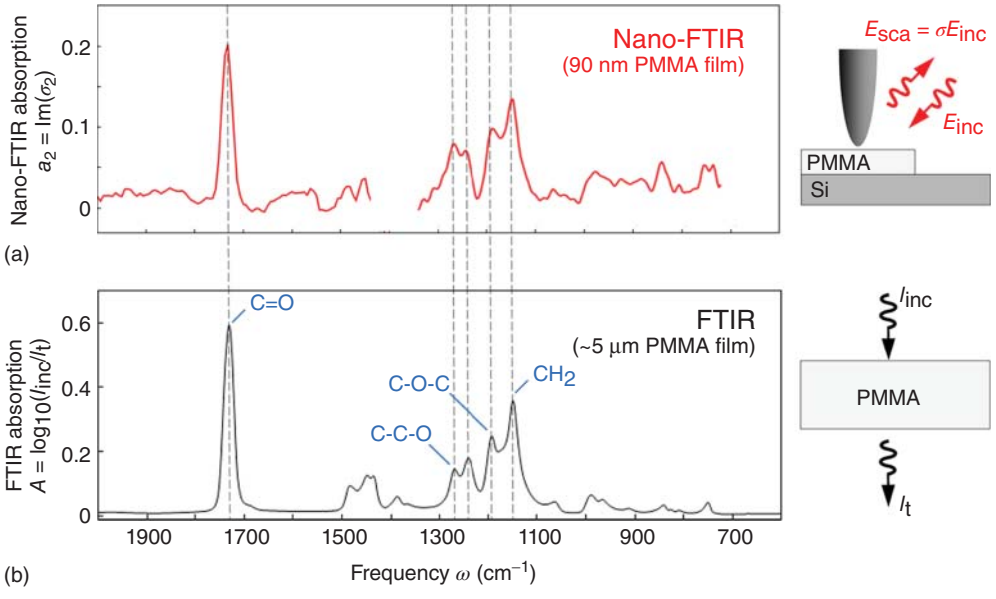

Figure 12.16 Spectra of PMMA measured by (a) s-SNOM at a resolution of 6 cm^{-1} and (b) conventional transmission spectroscopy at a resolution of 4 cm^{-1}. (Reprinted with permission from Ref. [30]. Copyright 2012, American Chemical Society.)

is used in the contact mode, the output signal from the AFM detector is modulated at the resonant frequency of the cantilever (typically between 50 and 70 kHz). The greater the absorption by the sample, the greater is the amplitude of the decaying modulation measured by the AFM detector. A commercial version of this instrument, developed and marketed by Anasys Instruments, Inc. (Santa Barbara, CA), incorporates a small optical parametric oscillator (OPO) rather than the much larger FEL. The OPO converts monochromatic laser pump radiation into a tunable output via a three-wave mixing process with a quantum conversion efficiency that is often greater than 50%. The heart of the OPO is a nonlinear optical crystal in which the pump photon decays into two less energetic photons (signal and idler), so that the sum of their energies is equal to that of the pump photon. The OPO is continuously tunable from 900 to 3600 cm^{-1} and can be tuned to a specific wavelength to create absorption images at a specific wavelength. An optical schematic of this instrument is shown in Figure 12.17a. The deflection signal from the AFM cantilever rings resonates sinusoidally, as shown at the top of Figure 12.17b. The Fourier transform of this signal exhibits several peaks that correspond to contact resonant modes of the cantilever (middle trace of Figure 12.17b). Absorption by the sample causes an increase in the amplitude at the fundamental frequency. The spectrum is obtained by scanning the OPO and plotting the peak amplitude over the desired wavelength range (lower trace of Figure 12.17b).

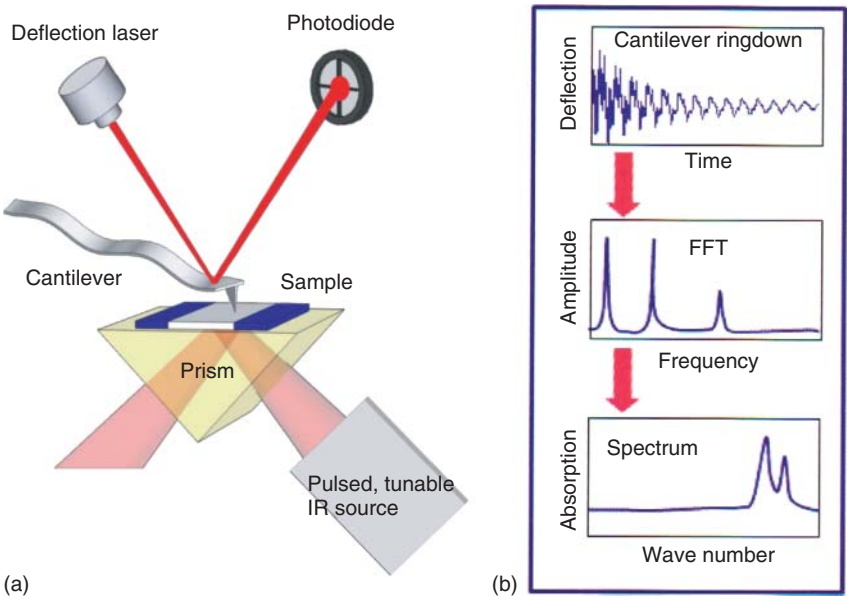

Figure 12.17 (a) Schematic of the AFM-IR experimental setup. (b) The sample is deposited on the upper side of the ZnSe IRE and illuminated by the pulsed infrared pulsed laser. The resulting photothermal expansion generates a brief force under the AFM tip inducing the ringing of the AFM cantilever. The FT of the oscillation signal usually shows several resonances of which the lowest frequency signal is usually analyzed. (Reprinted with permission from Ref. [36]. Copyright 2008, Optical Society of America.)

In the early experiments reported by Dazzi *et al.* [33–36], the amplitude of the oscillation was measured and noise and parasitic signals were rejected through the use of a signal analyzer. The spectrum of the sample was measured by tuning the FEL; the particular FEL used by Dazzi *et al.* could be tuned between 3 and 100 μm (3300 – 100 cm^{-1}). They measured the photothermal infrared spectrum of a single bacterium between 1800 and 1400 cm^{-1} in this way, and a reasonable agreement with the far-field spectrum of a colony of the same bacteria was achieved [36]. Figure 12.18a,b demonstrates the observation of a living fungal cell (*Candida albicans*) obtained by illuminating the sample with 1080 cm^{-1} radiation that corresponds to the absorption of glycogen. The fact that the absorption of the hyphae (the long strand) is approximately constant shows that the glycogen content is constant along the length of the hyphae.

It is noteworthy that these measurements made with an instrument of this type can be made with the sample immersed in water, although the nature of the cantilever response is quite different from when the dried sample was examined since the cantilever frequencies are sensitive to the frictional forces applied to the tip (Figure 12.19a,b) [36]. With the fungus present, the frequency was 31.6 kHz and in the absence of the fungus, when the tip is in contact with the IRE but surrounded

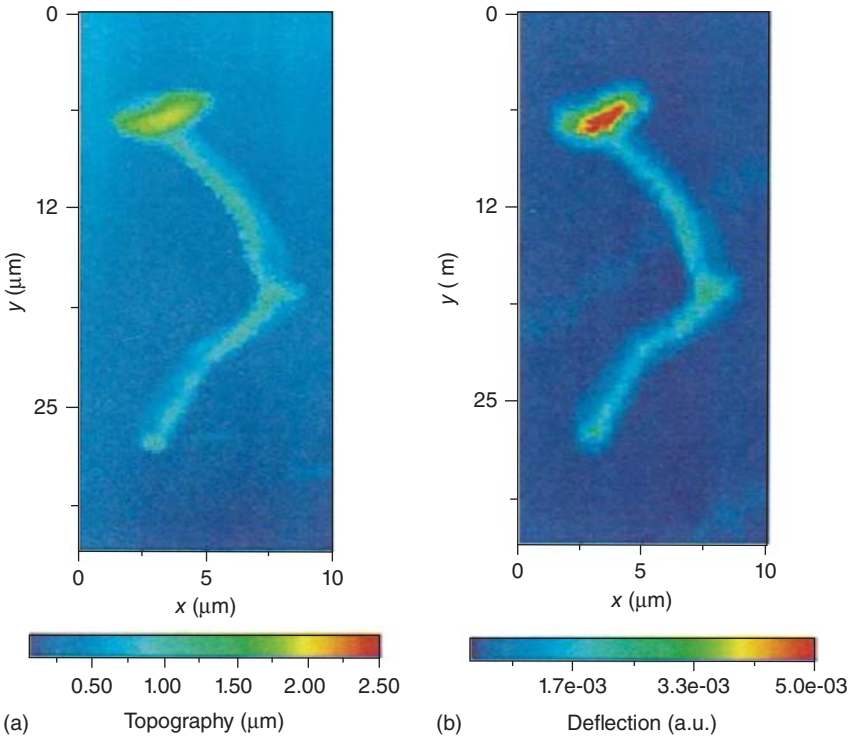

Figure 12.18 (a) AFM topography and (b) AFM-IR mapping of a dried sample of a *Candida albicans* fungus recorded from the cantilever response at 57 kHz. (Reprinted with permission from Ref. [36]. Copyright 2008, Optical Society of America.)

by water, the frequency was 19 kHz. Nonetheless, the spectrum of the blastospores present in the hyphae could be measured (Figure 12.20).

The Anasys instrument has been described in several publications [37–41] of which the review paper by Dazzi *et al.* [41] is the most detailed. The spectra measured with this instrument are essentially identical to those measured on a macrosample of the same material unless, of course, the polymer has microdomains of differing structure either because of immiscibility of two or more copolymers or because of the effect of orientation. The spatial resolution is significantly better than 100 nm, as reported by Dazzi *et al.* who embedded a 3 μm diameter PS bead in epoxy and demonstrated the very rapid change in spectrum on the edge of the PS bead [41].

The sensitivity of these measurements was enhanced by changing the geometry of the cantilever tip [37]. Commercially available rectangular microcantilevers of length 350 μm, width 35 μm, and thickness 2 μm (shown in Figure 12.21a) were used as a point of comparison. The cantilevers were etched with a focused ion beam to create internal paddles that govern the cantilever vibrational characteristics. The first design (Figure 12.21b) improved the vibrational amplitude, and

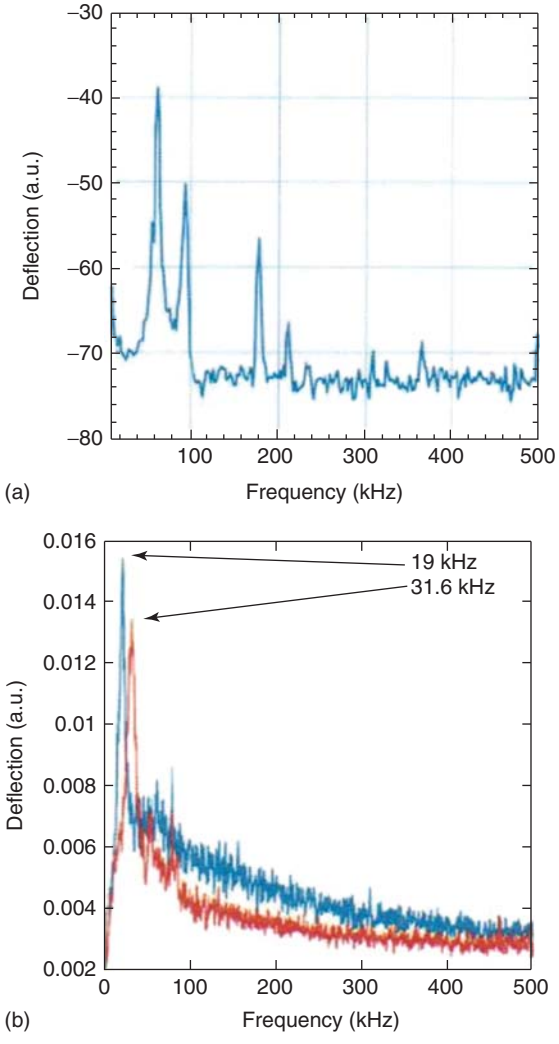

Figure 12.19 Fourier analysis of cantilever response to the IR absorption at 1080 cm^{-1} for (a) dried hyphae on the ZnSe IRE and (b) hyphae in water (blue curve) and for water only (red curve).

hence the sensitivity by a factor of 3 and a further modification (Figure 12.21c) led to a further doubling of the sensitivity.

This type of instrument has been used for a number of applications of polymer characterization, including the spatial differentiation of submicrometer domains in a poly(hydroxyalkanoate) copolymer [42] and multicomponent polymer blends of the type used as organophotovoltaics. An interesting application of AFM-IR was reported by Dazzi *et al.*, in which the chain orientation of the polymers comprising very thin electrospun fibers usually have a diameter (10 nm to 10 μm)

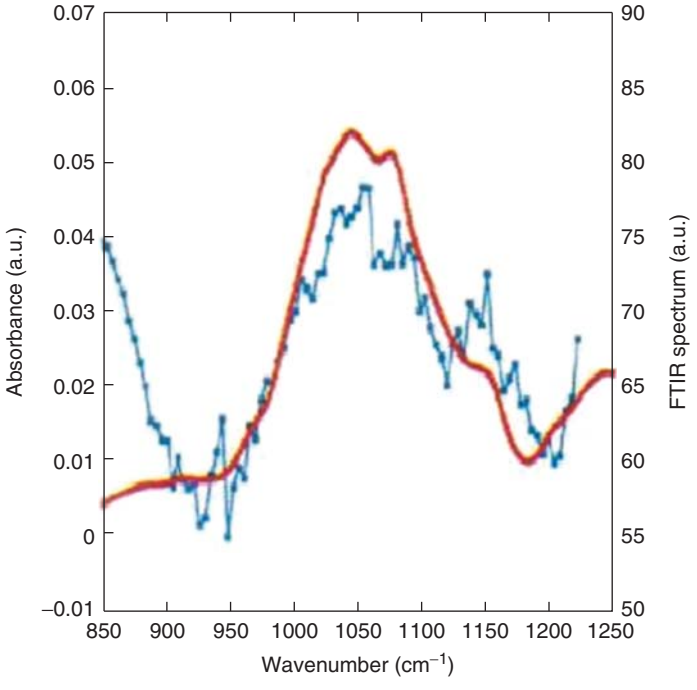

Figure 12.20 FT-IR spectrum of a layer of millions of blastospores (red curve) and PT-IR spectrum of one blastospore in water (blue curve). (Reprinted with permission from Ref. [36]. Copyright 2008, Optical Society of America.)

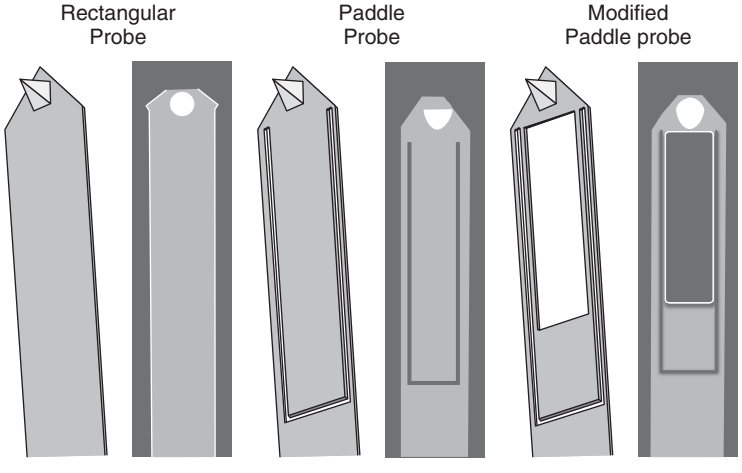

Figure 12.21 3D drawings and SEM images of the AFM cantilevers reported by Kjoller *et al*. [35]. (Reprinted with permission from Ref. [37]. Copyright 2010, IOP Publishing Ltd.)

that is usually below the diffraction limit for mid-infrared wavelengths [42]. Until very recently, the chain orientation of electrospun fibers had to be measured by collecting the fibers on aluminum foil across a 10 μm gap and measuring the polarized spectra using a conventional FT-IR microscope. The average orientation of many fibers was deduced using this technique, but the orientation of an individual fiber could not be characterized. This limitation was alleviated using the Anasys instrument by passing the beam from the OPO through a polarizer before it is transmitted through an individual fiber. Figure 12.22a,b shows the IR images of electrospun poly(vinylidene fluoride) (PVDF) fibers found by tuning the laser source to 1404 cm^{-1} and measuring spectra with light polarized in two perpendicular directions. The spectra are comparable to those measured by collecting a number of fibers oriented in approximately the same direction but several subtle differences can be observed as seen in Figure 12.23. Other exciting recent applications of AFM-IR using the Anasys instrument include an investigation of the structural lipids in human stratum corneum [43] and a study of the morphology of water transport channels and hydrophobic clusters in the ionic polymer, Nafion [44].

The theory of AFM-IR nanospectroscopy has been given by Dazzi *et al.* [34, 45, 46] and Lahiri *et al.* [47]. Lahiri *et al.* examined the various factors that determine the sensitivity of this technique [47]. They reported that in order to record an image with the optimum lateral resolution in the AFM scanning direction, the AFM pixel rate (ξ_{AFM}) is given by

$$\xi_{AFM} = 2n_{pixels}\nu \tag{12.1}$$

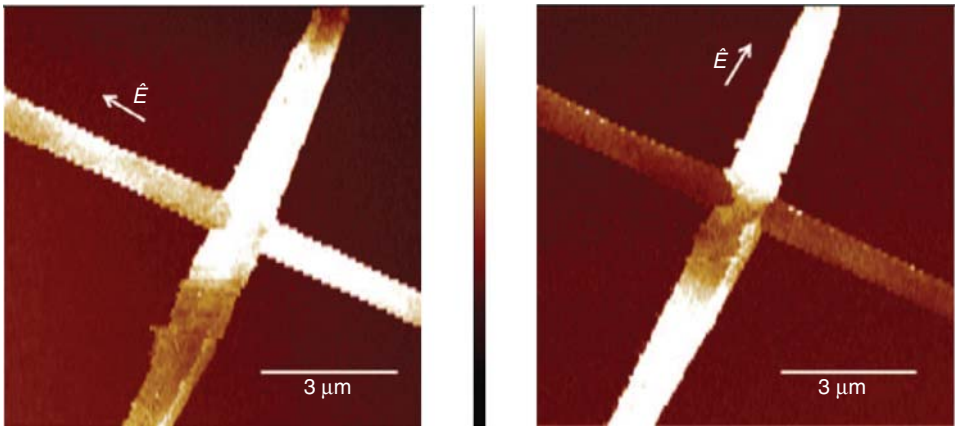

Figure 12.22 IR absorption images of two PDVF fibers collected with the laser tuned to 1404 cm^{-1} by using light polarized in the two perpendicular directions indicated. (Reprinted with permission from Ref. [42]. Copyright 2011, Society for Applied Spectroscopy.)

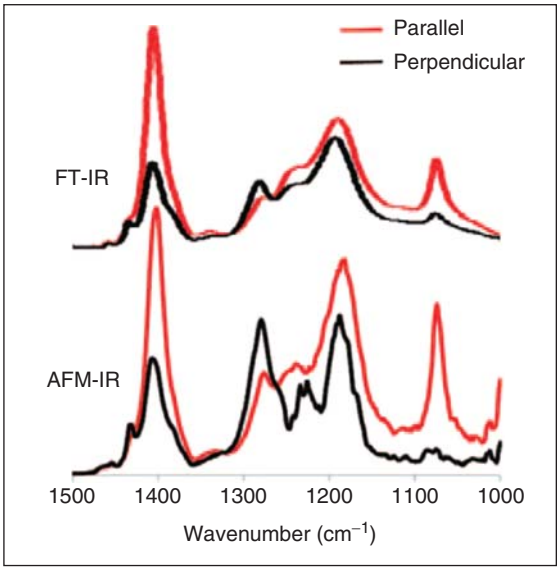

Figure 12.23 (Above) Polarized FT-IR spectra of multiple aligned electrospun fibers collected on aluminum foil across a 10 μm gap. (Below) Polarized AFM-IR spectra collected from the same location on one of the fibers shown in Figure 2.22. (Reprinted with permission from Ref. [42]. Copyright 2011, Society for Applied Spectroscopy.)

which should equal the PT-IR pixel rate (ξ_{IR}) given by

$$\xi_{IR} = \frac{\omega}{n^{\text{ave-pulses}}} \tag{12.2}$$

where n_{pixels} is the number of pixels in the AFM scanning direction (pixels/line), v is the AFM scan rate (lines/s), ω is the laser repetition rate, and $n^{\text{ave-pulses}}$ is the number of pulses per pixel.

The photothermal signal is proportional to the sample's thermal expansion, to the absorbed energy per unit area U_{abs}, and for short laser pulses to the duration of the thermal excitation t_{relax} in the sample. The sample's thermal expansion is proportional to its thickness z while t_{relax} is approximately proportional to z^2. Thus, the photothermal signal S should be proportional to the product of U_{abs} and z^3. The absorption by the sample will depend on the exponentially decaying evanescent electric field intensity. For thicknesses less than the depth of penetration of the evanescent wave d_p, the AFM-IR signal increases with an increase in sample thickness z. For nonabsorbing samples, the value of d_p is given by the well-known equation:

$$d_p = \frac{\lambda}{2\pi} \frac{1}{(n_1^2 \sin^2\theta - n_2^2)^{\frac{1}{2}}} \tag{12.3}$$

When the sample absorbs, d_p is given by the more complex equation [48]:

$$d_p = \frac{\lambda}{2\pi}\left[\frac{\sqrt{\left(n_1^2 \cdot \sin^2\theta - n_2^2 + k_2^2\right)^2 + (2 \cdot n_2 \cdot k_2)^2} + \left(n_1^2 \cdot \sin^2\theta - n_2^2 + k_2^2\right)}{2}\right]^{-\frac{1}{2}} \tag{12.4}$$

Lahiri *et al.* [46] measured the photothermal signal intensity as a function of the thickness of a sample of PMMA at the peak of the C=O stretching band and showed that the curve could be fit to a good approximation by the function $a{\cdot}z^3{\cdot}\exp(-2z/d_p)$, as shown in Figure 12.24. This shows that the sample thickness should be less than 1 μm if the optimum AFM-IR signal is to be obtained. For the peak of the C=O stretching band of PMMA ($\lambda = 5.79$ μm, $k_2 = 0.25$, $n_2 = 1.53$) on ZnSe ($n_1 = 2.4$), the value of d_p calculated using Equation 12.4 is 1.04 μm compared to that of 1.24 μm if $k_2 = 0$.

From the results shown above, it can be seen that the AFM-IR technique employed by Anasys is significantly more sensitive than the s-SNOM technique used by Neaspec but has the disadvantage that the thickness of the sample that is deposited on the IRE should be less than or equal to 1 μm and even less at shorter wavelengths where the C–H, O–H, and N–H stretching bands absorb. Except when an FEL is used, the spectral range of both instruments is limited by the tuning range of the laser. However, recently, Katzenmayer *et al.* [49] reported that the long wavelength limit of the Anasys instrument could be extended by using a laser that employs DFG in a GaSe crystal to emit radiation that is tunable from 1.55 μm (6450 cm^{-1}) to 16 μm (625 cm^{-1}).

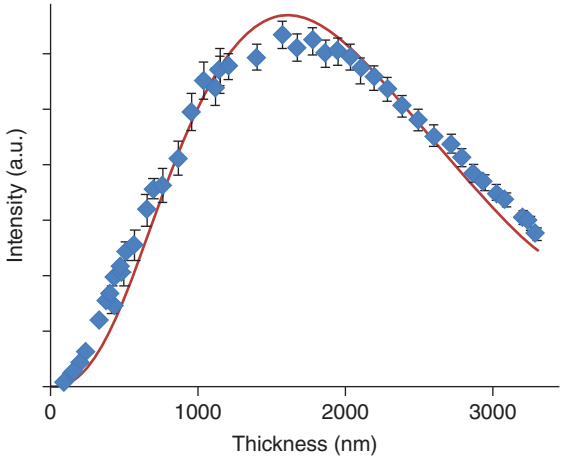

Figure 12.24 (Diamonds) AFM-IR signal at 1720 cm^{-1} as a function of thickness of PMMA. (Red line) Best fit to the function $a{\cdot}z^3{\cdot}\exp(-2z/d_p)$, with d_p equal to 1070 nm. (Reprinted with permission from Ref. [47]. Copyright 2013, American Chemical Society.)

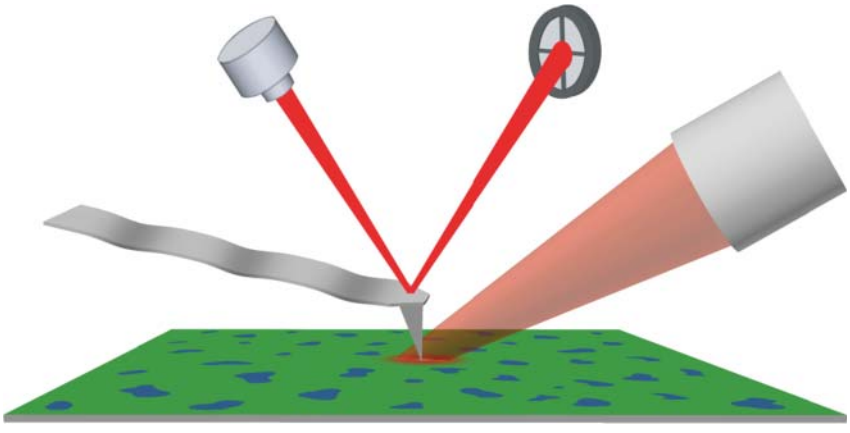

Figure 12.25 Optical configuration of Anasys instrument where the sample is illuminated from above and the need for a thin sample deposited on an IRE is eliminated.

The main disadvantage instruments with the Dazzi design is the need to keep the thickness of the sample significantly less than the depth of penetration of the evanescent wave of the IRE on which the sample is deposited. Very recently, the personnel at Anasys have come up with a way of directing the laser onto the top of the sample in the way shown in Figure 12.25. This configuration has the advantage that it can work on most samples, including those that are impossible to prepare on an IRE. It does have the disadvantage that more light strikes the cantilever, leading to some increased background. Although there is some distortion of the spectrum caused by the increased reflection at strong absorption peaks, the angle at which the sample is illuminated is close to the Brewster angle for many materials, so this effect may be minimized. The sample is illuminated by the pulsed laser for a very short time, and heat is conducted away from the spot so that the sample cools down before the next pulse. We expect that this configuration will be widely accepted in the future.

The measurement of chemical maps using infrared spectroscopy at a spatial resolution below the diffraction limit is clearly a rapidly moving field, and now that powerful instruments are commercially available, we look forward to future developments in the future.

References

1. Jackson, J.D. (1975) *Classical Electrodynamics*, John Wiley & Sons, Inc., New York.
2. Michaels, C.A., Gu, X., Chase, D.B., and Stranick, S.J. (2004) *Appl. Spectrosc.*, **58**, 257.
3. Schnell, M., Alonso-Gonzalez, P., Arzubiaga, L., Hueso, L.E., Chuvilin, A., and Hillenbrand, R. (2011) *Nat. Photonics*, **5**, 283.
4. Hammiche, A., Reading, M., Pollock, H.M., Song, M., and Hourston, D.J. (1996) *Rev. Sci. Instrum.*, **67**, 4268–4274.

5. Price, D.M., Reading, M., Hammiche, A., and Pollock, H.M. (1999) *Int. J. Pharm.*, **192**, 85.
6. Hammiche, A., Pollock, H.M., Song, M., and Hourston, D.J. (1996) *Meas. Sci. Technol.*, **7**, 142.
7. Hammiche, A., Pollock, H.M., Song, M., Hourston, D.J., and Reading, M. (1996) *J. Vac. Sci. Technol*, **B14**, 1486.
8. Hammiche, A., Pollock, H.M., Reading, M., Claybourn, M., Turner, P.H., and Jewkes, K. (1999) *Appl. Spectrosc.*, **53**, 810.
9. Griffiths, P.R. and de Haseth, J.A. (2007) *Fourier Transform Infrared Spectrometry*, 2nd edn, Chapter 16, Wiley Interscience, Hoboken, NJ.
10. Griffiths, P.R. and de Haseth, J.A. (2007) *Fourier Transform Infrared Spectrometry*, 2nd edn, Chapter 16, Wiley Interscience, Hoboken, NJ, pp. 418–419.
11. Anderson, M.S. (2000) *Appl. Spectrosc.*, **54**, 349.
12. O'Keefe, J.L. (1956) *J. Opt. Soc. Am.*, **46**, 359.
13. Wessel, J. (1985) *J. Opt. Soc. Am. B*, **2**, 1538.
14. Wickramasinghe, H.K. and Williams, C.C. (1990) Apertureless near field optical microscope, US Patent 4 947 034.
15. Specht, M., Pedarnig, J.D., Heckl, W.M., and Hänsch, T.W. (1992) *Phys. Rev. Lett.*, **68**, 476.
16. Inouye, Y. and Kawata, S. (1994) *Opt. Lett.*, **19**, 159.
17. Keilmann, F. and Hillenbrand, R. (2004) *Philos. Trans. R. Soc. Lond. A*, **362**, 787.
18. Knoll, B. and Keilmann, F. (1999) *J. Microsc.*, **194**, 512.
19. Alonso-González, P., Abella, P., Schnell, M., Chen, J., Huth, F., García-Extarri, A., Casanova, F., Golmar, F., Arzubiaga, L., Hueso, L.E., Aizpurua, J., and Hillenbrand, R. (2012) *Nat. Commun.*, **3**, 684.
20. Hillenbrand, R., Knoll, B., and Keilmann, F. (2001) *J. Microsc.*, **2002**, 77.
21. Taubner, T., Hillenbrand, R., and Keilmann, F. (2004) *Appl. Phys. Lett.*, **85**, 5064.
22. Ocelic, N., Huber, A., and Hillenbrand, R. (2006) *Appl. Phys. Lett.*, **89**, 101124.
23. Wurtz, G., Bachelot, R., and Royer, P. (2000) *Eur. Phys. J. Appl. Phys.*, **5**, 269.
24. Labardi, M., Patane, S., and Allegrini, M. (2000) *Appl. Phys. Lett.*, **77**, –621.
25. Brehm, M., Taubner, T., Hillenbrand, R., and Keilmann, F. (2006) *Nano Lett.*, **6**, 1307.
26. Haefliger, D., Plizko, J.M., and Hillenbrand, R. (2004) *Appl. Phys. Lett.*, **85**, 4466.
27. Brehm, M., Schliesser, A., and Keilmann, F. (2006) *Opt. Exp.*, **14**, 11122.
28. Amarie, S. and Keilmann, F. (2011) *Phys. Rev. B*, **83**, 045404.
29. Huth, F., Schnell, M., Wittborn, J., Ocelic, N., and Hillenbrand, R. (2011) *Nat. Mater.*, **10**, 352.
30. Huth, F., Govyadinov, A., Amarie, S., Nuansing, W., Keilmann, F., and Hillenbrand, R. (2012) *Nano Lett.*, **12**, 3973.
31. Amarie, S., Zaslansky, P., Kajihara, Y., Greisshaber, E., Schmahl, W.W., and Keilmann, F. (2012) *Beilstein J. Nanotechnol.*, **3**, 312.
32. Gieth, W., Amarie, S., Milz, F., Bamberg, F., and Keilmann, F. (2012) *J. Biophotonics*. doi: 10.1002/jbio.201200172
33. Dazzi, A., Prazeres, R., Glotin, F., and Ortega, J.M. (2005) *Opt. Lett.*, **30**, 2388.
34. Dazzi, A., Prazeres, R., Glotin, F., and Ortega, J.M. (2007) *Ultramicroscopy*, **107**, 1194.
35. Dazzi, A., Prazeres, R., Glotin, F., Ortega, J.M., Al-Sawaftah, M., and de Frutos, M. (2008) *Ultramicroscopy*, **108**, 635.
36. Mayet, C., Dazzi, A., Prazeres, R., Allot, F., Glotin, F., and Ortega, J.M. (2008) *Opt. Lett.*, **33**, 1611.
37. Kjoller, K., Felts, J.R., Cook, D., Prater, C.B., and King, W. (2010) *Nanotechnology*, **21**, 1.
38. Prater, C., Kjoller, K., Shetty, A., and Dazzi, A. (2011) *Laser Focus World*, Vol. 47 (Mar. 2011), pp. 52–54.
39. Marcott, C., Kjoller, K., Lo, M., Prater, C., Shetty, R., and Dazzi, A. (2012) *Spectroscopy*, **27** (2), 60.
40. Marcott, C., Lo, M., Kjoller, K., Prater, C., and Gerrard, D.P (2012) Applications of AFM-IR—Diverse Chemical Composition Analyses at Nanoscale Spatial Resolution. *Microscopy-Today*, Vol. 20 (Nov. 2012), pp. 16–21.

41. Dazzi, A., Prater, C.B., Hui, Q., Chase, D.B., Rabolt, J.F., and Marcott, C. (2012) *Appl. Spectrosc.*, **66**, 1365.
42. Marcott, C., Lo, M., Kjoller, K., Prater, C., and Noda, I. (2011) *Appl. Spectrosc.*, **65**, 1145.
43. Marcott, C., Lo, M., Kjoller, K., Domanov, Y., Balooch, G., and Luengo, G.S. (2013) *Exp. Dermatol.*, **22**, 417.
44. Awatani, T., Midorikawa, H., Kojima, N., Ye, J., and Marcott, C. (2013) *Electrochem. Commun.*, **30**, 5.
45. Dazzi, A. (2009) in *Thermal Nanosystems and Nanomaterials*. (ed. S. Voltz), vol. 118, Springer, Tokyo, p. 469.
46. Dazzi, A., Glotin, F., and Carminati, R. (2010) *J. Appl. Phys.*, **107**, 124519.
47. Lahiri, B., Holland, G., and Centrone, A. (2013) *Small*, **9**, 1876.
48. Hosono, H. (1991) *J. Appl. Phys.*, **69**, 8079.
49. Katzenmayer, A.M., Aksyuk, V., and Centrone, A. (2013) *Anal. Chem.*, **84**, 1972.

Part VI
Developments in Methodology

Infrared and Raman Spectroscopic Imaging, Second Edition. Edited by Reiner Salzer, Heinz W. Siesler.
© 2014 Wiley-VCH Verlag GmbH & Co. KGaA. Published 2014 by Wiley-VCH Verlag GmbH & Co. KGaA.

13
Subsurface Raman Spectroscopy in Turbid Media

Pavel Matousek

13.1
Introduction

In many analytical applications in biomedical and pharmaceutical sciences, it is desirable to noninvasively probe the composition of deep layers of samples with high chemical specificity. Examples may include the diagnosis of bone disease and breast cancer or the noninvasive probing of pharmaceutical products in quality control and drug authentication.

Presently, the main chemically specific optical spectroscopic techniques used in these areas include near-infrared (NIR) absorption spectroscopy, mid-infrared (MIR) spectroscopy, and Raman spectroscopy. Although NIR is widely used in a number of these applications for its simplicity, it suffers from limited chemical specificity [1]. In comparison, both MIR and Raman spectroscopic studies offer a substantially higher degree of chemical specificity, but their use in their traditional form has been so far confined to only shallow layers in turbid media. In the case of MIR, this is because of the requirement for sample thinning or dilution when it comes to bulk probing and incompatibility with aqueous samples as sample matrix and water typically strongly absorb MIR signal. In contrast, Raman spectroscopy does not suffer from these limitations and thus holds a potential to become a mainstream analytical tool in the areas concerned [2]. Although it should be noted that its applicability is limited to samples that do not exhibit strong fluorescence emission in the spectral region coincident with the Raman spectra as this can easily swamp the relatively weak Raman signals. The fluorescence problem can be significantly reduced in many situations using NIR excitation probing away from the electronic absorption bands of most fluorescing species.

Until recently, the Raman method has been used with commercial Raman probes and microscopes predominantly in the backscattering collection mode (Figure 13.1), although in a number of specialist laboratories a 90° collection geometry is also used [1]. The conventional backscattering mode is used mainly for its instrumental simplicity and ease of use; however, this approach permits effective depth discrimination of Raman signals in these media only at very

Infrared and Raman Spectroscopic Imaging, Second Edition. Edited by Reiner Salzer, Heinz W. Siesler.
© 2014 Wiley-VCH Verlag GmbH & Co. KGaA. Published 2014 by Wiley-VCH Verlag GmbH & Co. KGaA.

shallow depths [1]. For example, in living tissue, the accessible depths are typically only several hundred micrometers leaving often many tissue components, such as bones and deep cancerous tissue beyond the reach of this technique.

A substantial extension to the penetration depth of Raman spectroscopy was accomplished utilizing the properties of diffuse light in analogy with NIR absorption tomography [3–5] or fluorescence spectroscopy [6–9]. This chapter reviews recent developments in this area and illustrates the utility of these methods on several practical examples.

13.2 Techniques for Deep Noninvasive Raman Spectroscopy

Several deep noninvasive approaches have been developed from earlier investigations into the photon migration process [3, 10–15]. Here, we constrain our discussion largely to spatial concepts that have emerged and that represent currently the most practical embodiment of deep Raman techniques. Although, it should be noted that time-resolved concepts are also finding their way into this area [16].

13.2.1 Spatially Offset Raman Spectroscopy (SORS)

The basic concept is known as *spatially offset Raman spectroscopy* (*SORS*) [17], and it utilizes the differences in the spatial distribution of Raman photons emerging at the surface from different depths of the probed sample. In this approach, Raman spectra are collected from regions on the sample surface that is spatially offset by different amounts from the point of laser incidence (Figures 13.1 and 13.2). Such spectra contain varying relative Raman contributions from layers located at different depths within the sample. This difference is brought about by the wider lateral diffusion of photons emerging from greater depths and the effect of photon loss at sample-to-air interface [3, 11, 12].

The feasibility of the SORS concept as a tool for obtaining Raman signals from deeply buried layers in turbid media was first demonstrated by Matousek *et al.* [17]. The experiments were performed on a two-layer sample composed of a 1 mm thick PMMA powder layer placed on top of a *trans*-stilbene powder

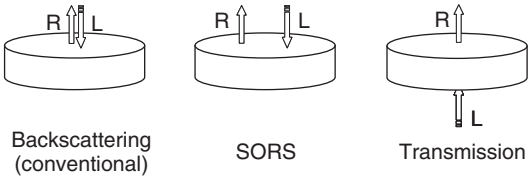

Figure 13.1 Basic types of Raman spectroscopy geometries with respect to the sample: conventional backscattering Raman, SORS, and transmission Raman geometries. Notes: R, Raman light and L, laser beam.

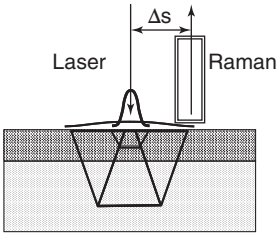

Figure 13.2 Principal of the spatial, SORS, concept for the discrimination of subsurface signals (Δs – spatial offset).

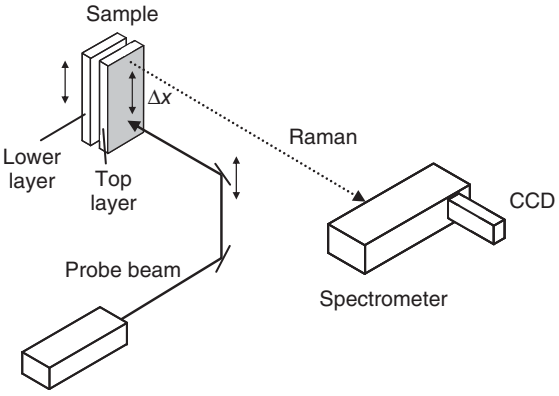

Figure 13.3 Schematic diagram of a basic SORS experimental setup. (Reprinted with permission from [17]. Copyright (2005) The Society for Applied Spectroscopy [17].)

layer using 514 nm as the probe wavelength (Figure 13.3). The results of these measurements are shown in Figure 13.4. The zero-offset spectrum represents a conventional Raman spectrum. By increasing the spatial offset, the surface layer signal (PMMA) diminishes much quicker than that of the sublayer (*trans*-stilbene), and at a spatial offset of >2 mm an order of magnitude improvement in the intensity ratio is achieved. This article also reports on improving the relative ratio between the Raman signals of the two layers by a factor of 19 at a 3.5 mm spatial offset. Interestingly, the quality of the spectra obtained in these measurements was substantially higher than that achieved earlier using more complex picosecond Kerr-gated system [13]. The improvement is ascribed to the higher intensity of Raman signal detected due to the fact that SORS integrates the Raman signal across the entire time domain, unlike that of temporal approach where only a narrow temporal slice is obtained.

If a higher degree of separation of the subsurface signals from the surface contribution is required, then this can be accomplished, for a two-layer system, by a simple scaled subtraction of two spectra obtained at different spatial offsets to cancel the Raman contribution from the surface layer. For a stratified sample with more than two layers, a multivariate data analysis can be applied using a

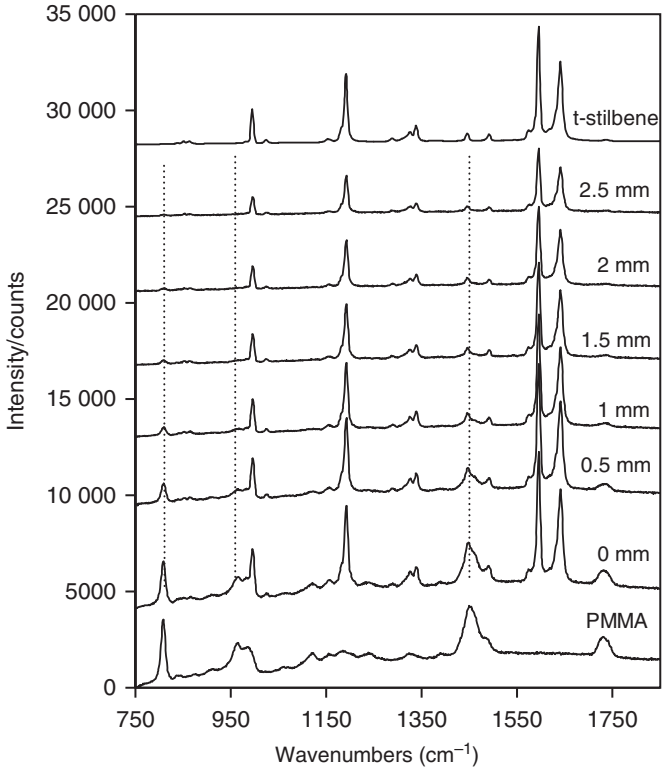

Figure 13.4 A set of SORS spectra collected from a two-layer system consisting of 1 mm thick layer of PMMA made of 20 μm diameter spheres followed by a 2 mm layer of *trans*-stilbene powder measured using 514 nm as the probe wavelength. The spectra are shown for different spatial offsets indicated next to spectra. The top and bottom spectra are those of the individual layers obtained in separate measurements. The spectra are offset for clarity. The acquisition time was 100 s for each spectrum and the average laser power 12 mW. (Reprinted with permission from [17]. Copyright (2005) The Society for Applied Spectroscopy [17].)

more extensive data set. An example of such a procedure is band target entropy minimization (BTEM) [18–22]. A major advantage of these approaches is that a layered system can be decomposed with no *a priori* knowledge of its composition.

The SORS concept can be combined in a relatively straightforward manner, with fiber optic collection scheme developed for conventional Raman spectroscopy earlier by Ma and Ben-Amotz [23] to yield a substantial enhancement of the Raman collection efficiency. In this approach, fibers collecting Raman signal from the sample arranged typically in a ring or disk pattern are reorganized on the spectrograph slit into a linear pattern to match the slit geometry. The use of this concept in SORS was theoretically discussed in work by Matousek *et al.*

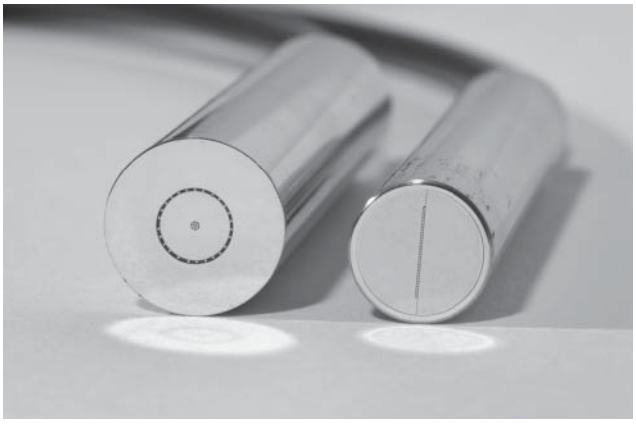

Figure 13.5 A photograph of an SORS ring fiber probe (left – input side, right – output side). (Reprinted with permission from [27]. Copyright (2006) The Society for Applied Spectroscopy [27].)

[17, 24] and experimentally demonstrated by Schulmerich *et al.* [25] who used a commercial fiber probe with fibers arranged at the center of the probe with global illumination configuration [26]. The concept was further developed by Matousek *et al.* [27] who utilized fibers distributed on annuli of different radii (Figure 13.5), with each different radius being presented to a different horizontal section of a 2D CCD detector.

13.2.2 Inverse SORS

Further research in the SORS area led to the development of an effective SORS modality, inverse SORS. This concept removes some inherent artifact limitations to the conventional SORS approach and permits the use of higher laser powers through the provision of a wider illumination zone at the sample. This is beneficial in applications where maximum illumination intensity limits exist such as when probing living tissue *in vivo* or in explosive powder environments.

The concept, which was demonstrated independently by Matousek [28] and Schulmerich *et al.* [29, 30], relies on the collection of Raman light through a group of fibers at the center of a probe and the delivery of the laser beam through a ring-shaped area centered on the collection zone (Figure 13.6). The ring radius defines the SORS spatial offset. In this concept, it is also beneficial that in each readout of the CCD detector, an arbitrary illumination ring radius can be set enabling better tailoring of the experimental conditions to the sample parameters than that possible with conventional SORS probes where rings are built into the fiber probe. The laser beam ring profile can be generated using an axicon (conical lens), and the spatial offsets can be set by adjusting the distance of the axicon from the sample

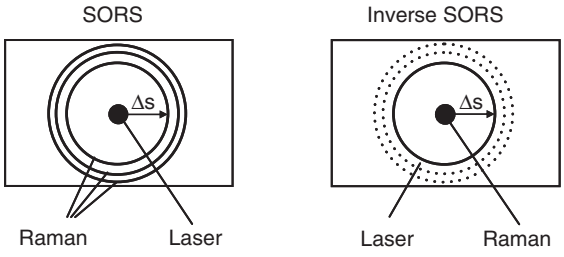

Figure 13.6 Schematic diagram of conventional SORS and inverse SORS concepts showing Raman collection and laser beam delivery geometries. (Reprinted with permission from [28]. Copyright (2006) The Society for Applied Spectroscopy [28].)

[28] or by varying the magnification of a telescope inserted between the sample and axicon [29, 30].

13.2.3 Transmission Raman Spectroscopy

In some analytical applications, the primary goal of the measurement can be the assessment of the overall bulk content of the probed sample instead of the composition of individual layers. This is, for example, the case in the volumetric analysis of pharmaceutical tablets required to establish the overall tablet content. Matousek and Parker [31] demonstrated that a transmission Raman geometry is particularly well suited to such analysis (Figure 13.1). This geometry was introduced in the early days of Raman spectroscopy [32] but was largely unutilized in the area of medical and pharmaceutical analyses. In sharp contrast with the conventional backscattering Raman geometry, the transmission Raman mode dramatically reduces subsampling [33].

This useful feature of the transmission Raman mode was confirmed both experimentally and using Monte Carlo simulations [31]. The numerical results are shown in Figure 13.7 and illustrate that if a thin "impurity" layer is relocated from the surface to a depth of 3 mm within a typical pharmaceutical tablet medium, its conventional backscattering Raman signal is diminished by four orders of magnitude and is typically lost in the dominant signal coming from the surface layers. However, the transmission geometry yields much lower dependence on depth, demonstrating that the transmission concept is much better suited to the probing of the bulk content of turbid media. This work also demonstrates that a good level of Raman signal can be obtained in the transmission geometry with pharmaceutical tablets [31]. Further work has established that signal is weakly biased toward the center of the probed object [34–37]. In many pharmaceutical and biomedical applications such as the noninvasive probing of colored capsules, coated tablets, and subsurface tissue spectroscopy, it is also beneficial that the transmission Raman method effectively diminishes Raman and fluorescence signals originating from the surface layers of the probed sample compared with conventional backscattering Raman geometry [38].

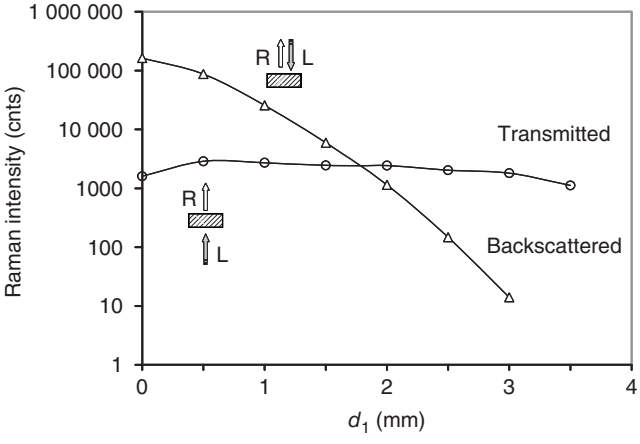

Figure 13.7 Plot of Raman intensities for the backscattering and transmission geometries versus depth (d_1) of an interlayer (impurity) within a pharmaceutical tablet-like medium. The dependencies are the results of Monte Carlo simulations. (Reprinted with permission from [31]. Copyright (2006) The Society for Applied Spectroscopy [31].)

13.2.4
Raman Tomography

Schulmerich *et al.* [26, 39] have demonstrated that SORS concept can also be used as a tomographic tool capable of forming chemically specific images of subsurface structures. The research led to the demonstration of the formation of 3D tomographic images of phantoms and canine hind limb sections to depths of up to 45 mm [40]. Subsequently, Srinivasan *et al.* [41] introduced image-guided Raman spectroscopy combining X-ray computed tomography and Raman tomography to guide the numerical recovery of Raman images [42]. A contrast ratio of 145 : 1 between the cortical bone and background was reached. The concept was further developed by Demers *et al.* [43].

13.2.5
SESORS

Stone *et al.* [44] demonstrated that SORS can be combined with the established surface-enhanced Raman spectroscopy (SERS) to enable the reading of SERS signals from subsurface areas of turbid samples. This opens a prospect for the detection of bioanalytes deep within tissue at very low concentration levels. The method, termed surface enhanced spatially offset Raman spectroscopy *SESORS*, requires the introduction of SERS nanoparticles or an SERS substrate into the sample prior to measurements. Subsequent signal reading is however performed noninvasively. Potential applications include early cancer diagnosis and monitoring of various other medical conditions involving low-concentration level bioanalytes. SESORS multiplex probing capability was demonstrated by

Stone *et al.* [45] who performed the measurements of four different "flavors" of nanoparticles at depths of up to 20 mm in tissue and formed a reconstructed false color image of their subsurface distribution.

13.3 Examples of Application Areas

13.3.1 Probing of Bones through Skin for Disease Diagnosis

There is considerable benefit to be obtained from applying Raman spectroscopy to the analysis of bone matrices (see Chapter 4 of this book). The ability to perform such interrogation noninvasively and safely through soft overlaying tissue opens a host of new potential applications including the diagnosis of brittle bone disease and osteoporosis [14, 46, 47]. For example, currently, dual-energy X-ray absorptiometry (DEXA), which represents the gold standard screening for the diagnosis of osteoporosis, is only 60–70% accurate in the prediction of osteoporotic fracture. This inaccuracy most likely stems from its inability to probe the protein (mainly collagen) components within bones, which constitute about one-third of the bone matrix and also contribute significantly to bone strength. Recently, both temporal and spatial Raman approaches have been applied successfully to this problem building on the pioneering work of Morris *et al.* [14, 48] in this area.

A collaborative team of Draper *et al.* [46] diagnosed successfully *osteogenesis imperfecta* ("brittle bone" disease) in mouse limbs noninvasively through around 1 mm of overlaying soft tissue using a picosecond Kerr-gated Raman approach. The presence of the condition was apparent from a relative intensity change between the collagen and mineral components in the spectra, reflecting a change in their relative concentrations (Figure 13.8). The work demonstrated for the first time the basic feasibility of noninvasive bone disease diagnosis. However, large issues still remained to be resolved. Apart from a high complexity and associated cost of the instrumentation, the experiments necessitated the use of laser intensities two to three orders of magnitude higher than those permissible for safe illumination of human skin [27]. These hurdles were surmounted through the subsequent development of SORS compatible with much safer continuous wave laser beams.

The first use of SORS in the area of noninvasive probing of bones was reported by Schulmerich *et al.* [25]. The team succeeded in the recovery of the Raman spectra of bones transcutaneously from depths of several millimeters in animal and human cadavers. Subsequently, with improved instrumentation based around a ring illumination geometry (equivalent to inverse SORS), Schulmerich *et al.* [29] reached another key milestone demonstrating the feasibility of measuring Raman spectra noninvasively from a depth of 4 mm from chicken tibia with better than 8% accuracy in terms of the relative Raman band intensities between the

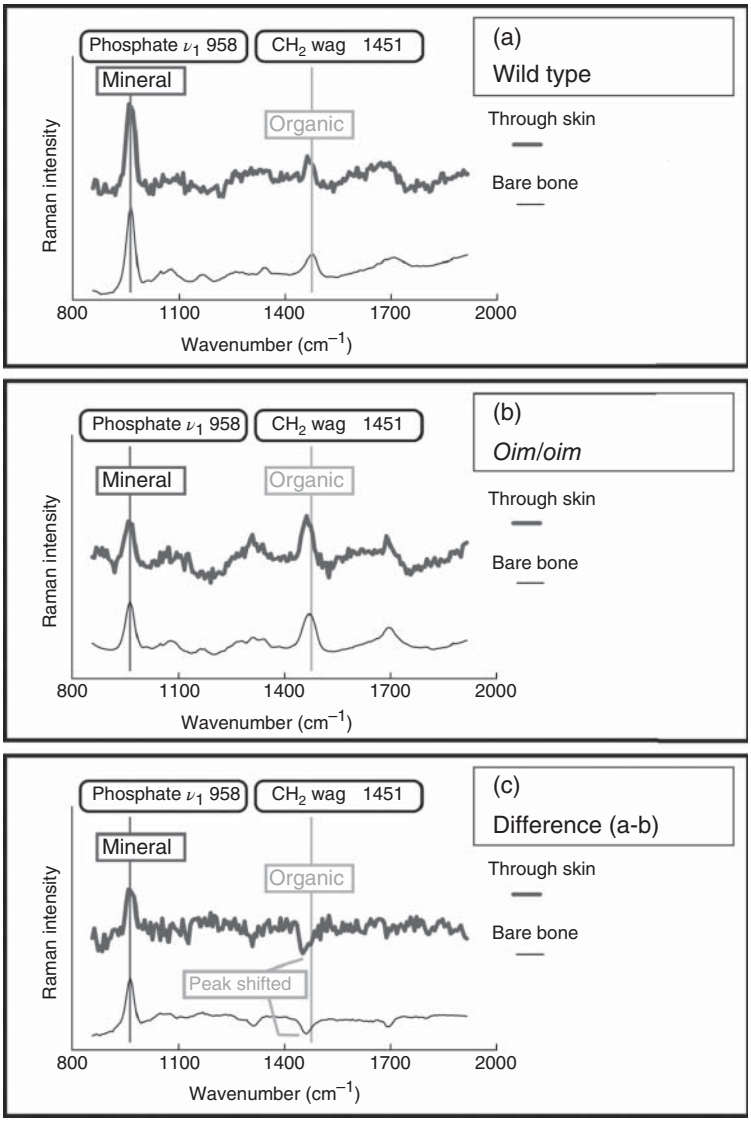

Figure 13.8 Raman spectra of bone measured from two genotypes: wild-type mice and *osteogenesis imperfecta* (*oim/oim*) mice. The spectra were recorded both through the overlying skin and directly on bare bone using the ultrafast Kerr-gated Raman method. (a) Raman spectra of wild-type mice, (b) Raman spectra of *oim/oim* mice, and (c) the different Raman spectra obtained by subtracting the spectra from the two genotypes. The acquisition times were between 7 and 15 min for each spectrum and the laser pulse energy was 340 μJ (average power 340 mW, 1 kHz repetition rate). (Reproduced from [46] with permission of the American Society for Bone and Mineral Research [46].)

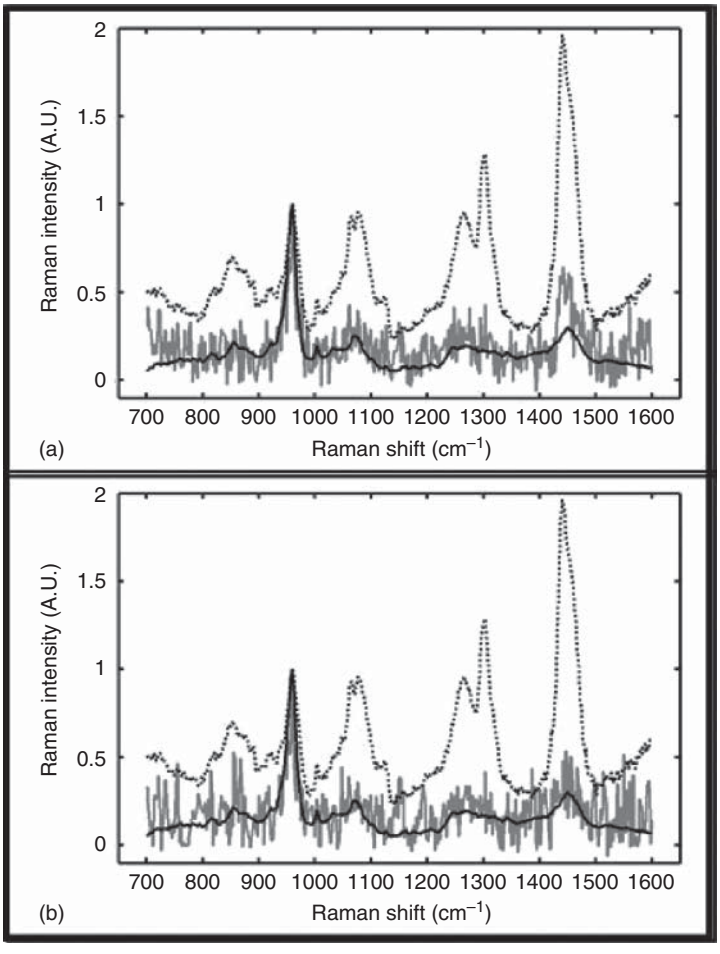

Figure 13.9 Measurements made through 4 mm of overlying tissue on a chicken tibia at the mid-diaphysis using SORS approach. Transcutaneous (dotted), recovered bone factor (gray), and exposed bone (black): (a) recovered bone factor using data from all 50 collection fibers and (b) recovered bone factor using data from the 32 innermost collection fibers. The laser power was 110 mW and the acquisition time 120 s. (Reprinted with permission from [29]. Copyright (2006) The Society of Photo-Optical Instrumentation Engineers [29].)

phosphate (958 cm^{-1}) and carbonate (1070 cm^{-1}) bands. This opened prospects for the potential detection of osteoporosis that is likely to require this level of accuracy as indicated by McCreadie *et al.* on excised bones [47]. The results of these experiments are shown in Figure 13.9. The measurements were performed using 785 nm as the probe wavelength.

Parallel research by Matousek *et al.* [27] demonstrated the feasibility of recovering the Raman spectra of bones from humans *in vivo.* Although the obtained

spectra were of limited quality with some overlaying tissue signals still present, the experiments demonstrated that the key bone features can be measured transcutaneously *in vivo* under totally safe illumination conditions. The measurements were performed with the laser power attenuated to a mere 2 mW, which is well within the maximum permissible exposure limit and approximately equals to the power of a laser pointer. The spectra were collected using a ring fiber probe (Figure 13.5) with zero and 3 mm spatial offsets and then subtracted with a scaling factor to remove the surface layer contributions. The measurements were performed on the thumb distal phalanx bone of volunteers through around 2 mm of overlaying soft tissue. The overall acquisition time was 200 s, and the probe wavelength was 830 nm. Three typical processed Raman spectra are shown in Figure 13.10. The accuracy achieved in this work was limited by the signal-to-noise ratio of the spectra obtained at the very low laser power and did not reach the level required for the diagnosis of conditions such as osteoporosis [47]. However, further improvement of the *in vivo* Raman spectra is possible using the inverse SORS approach [28–30], which permits substantially higher laser powers to be delivered safely into tissue.

In subsequent research, Okagbare *et al.* [49] demonstrated the benefits of using a multifiber laser illuminating multifiber Raman collection system for Raman tomographic imaging of bones transcutaneously and applied it to the monitoring of graft osseointegration used in reconstructions following tumor resection. The principle of the method was demonstrated on a rat tibia. Bone mineral and matrix Raman bands were successfully recovered transcutaneously demonstrating the noninvasive potential of the method.

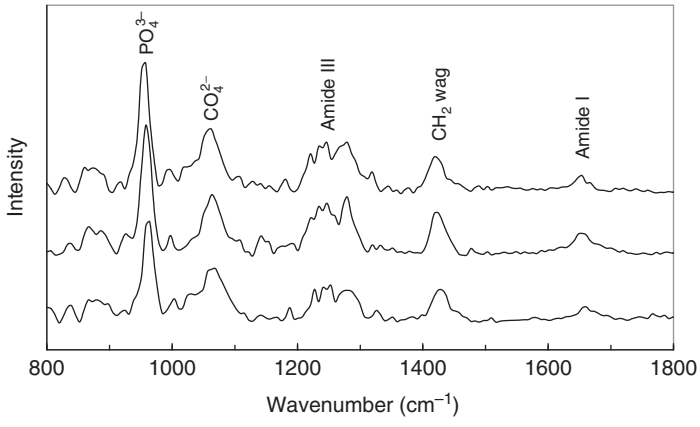

Figure 13.10 The estimates of pure Raman spectra of human bone *in vivo* measured transcutaneously at the distal phalanx of the thumb bones. Three different measurements are shown decomposed from the raw SORS spectra obtained at the zero and 3 mm spatial offsets. The spectra were obtained using a continuous wave laser operating at 827 nm with skin-safe laser power (2 mW). The spectra are offset for clarity. The acquisition time was 200 s for each spectrum. (Reprinted with permission from [27]. Copyright (2006) The Society for Applied Spectroscopy [27].)

13.3.2 Chemical Identification of Calcifications in Breast Cancer Lesions

Another potential application area for deep Raman techniques is the noninvasive detection of calcifications within breast tissue as demonstrated by Baker *et al.* [50], Stone *et al.* [51], and Matousek and Stone [52] using the Kerr-gated Raman, SORS, and transmission Raman methods, respectively, with chicken breast tissue phantoms. The researchers achieved respective penetration depths of 0.9, 8.7, and 16 mm in these experiments. Given the potential for recognizing malignant and benign lesions from the chemical constituency of the calcifications, the techniques hold promise for providing additional diagnostic power to the conventional techniques such as X-ray mammography, which cannot identify the chemical makeup of the calcifications noninvasively nor the type of lesion. Presently, the detection of the presence of suspected calcifications is usually followed by a needle biopsy, which in 70–90% of cases uncovers only benign lesions.

The above research builds on the pioneering work of Haka *et al.* [53], showing that excised calcifications are identifiable by Raman spectroscopy and separable into groups: type I – calcium oxalate dihydrate (cod), and type II – calcium hydroxyapatite (hap). Calcium oxalate crystals are mainly found in benign ductal cysts. Although calcium hydroxyapatite is found both in carcinoma and in benign breast tissue, there is a recognizable spectroscopic difference between those found in benign and malignant lesions.

In this application, the transmission Raman method has to date achieved the highest penetration depth. This method yields the strong suppression of skin fluorescence originating at the NIR wavelengths predominantly from melanin components and has gross insensitivity to the depth of the probed calcifications [52]. The results of the reported feasibility study [52] are shown in Figure 13.11. The experiments were performed at 830 nm with a laser spot diameter of around 4 mm. The Raman light was collected using a fiber bundle consisting of 33 individual optical fibers. The study was performed on a phantom made of a 16 mm slab of chicken tissue with a thin calcified material layer (100–300 μm) placed within the middle of the tissue. With both the calcification types, recognizable chemical signatures were obtained.

Subsequent research utilizing chemometric methods with an improved transmission Raman concept led to the recovery of calcification signals in porcine tissue from depths up to 27 mm [54], about two orders of magnitude deeper than with conventional approaches. As the typical thicknesses of breast in mammographic studies are between 19 and 50 mm, further improvement in the method is still required [52, 55].

13.3.2.1 Cancer Margins

An alternative use of SORS in breast cancer diagnosis is in the determination of cancer margins during surgery when removing lesion from patient. To remove just the right amount of tissue is important, striking balance between leaving no cancerous cells in patient body and making sure not excessive amount of tissue is

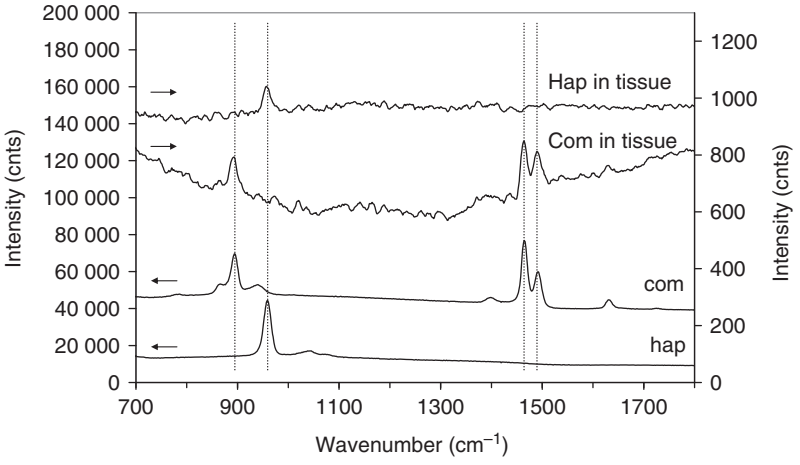

Figure 13.11 Raman spectra of two types of calcified materials (a 100–300 μm thick layer) recovered from a 16 mm thick slab of chicken tissue ("hap in tissue," "com in tissue"). The spectra were obtained by subtracting raw transmission Raman spectra of tissue only from those of tissue containing calcified material. The pure Raman spectra of individual calcified materials are also shown. The acquisition time was 100 s with a laser power of 60 mW. The spectra are offset for clarity. (Reprinted with permission from [52]. Copyright (2007) The Society of Photo-Optical Instrumentation Engineers [52].)

removed. In this area, Keller *et al.* [56] demonstrated the ability of SORS to diagnose soft tissue lesions at depths of several millimeters within healthy soft tissue. Although a number of questions about its efficacy require further investigation, the study laid a major milestone in real-time diagnostics deployable at operating theater.

The concept was further advanced by developing a probe of multiple source–detector offsets developed specifically for intraoperative analysis and permitting sample characterization up to a depth of 2 mm [57]. The performance was tested on 35 frozen–thawed human breast tissue samples *in vitro*. A probabilistic scheme was used to classify the composite spectra as "negative" or "positive" margins. The discrimination was performed with 95% sensitivity and 100% specificity.

13.3.2.2 **Glucose Detection**

A potential to diagnose glucose noninvasively with SESORS [44] was successfully demonstrated by Yuen *et al.* [58]. The concept uses an SERS substrate implanted under the skin consisting of a silver film over nanosphere surfaces functionalized with a mixed self-assembled monolayer. The substrate was implanted subcutaneously into a Sprague Dawley rat. The research demonstrated a viability of monitoring of glucose levels in several rats (6) over a period of 17 days with high glycemic index accuracy [59]. This pioneering experiment shows that SESORS is a viable solution for reliable continuous glucose sensing systems for optimal glycemic control. An alternative approach to glucose sensing utilizing

transmission Raman spectroscopy and employing no SERS substrates was described by Kong *et al.* [60].

13.3.3 Probing of Pharmaceutical Tablets and Capsules in Quality Control

In a number of pharmaceutical process analytical technology (PAT) applications, it is necessary to ascertain the overall bulk content of tablets. Ideally, this should be accomplished quickly and noninvasively with high chemical specificity. A research study by Matousek and Parker [31] outlined the potential of the transmission Raman approach [32] in this area, demonstrating its ability to provide bulk information on the probed object. Further research of Johansson *et al.* [61] demonstrated that transmission Raman spectroscopy can provide adequately accurate quantitative information on the composition of pharmaceutical formulations. In this study, the quantity of the active pharmaceutical ingredient (API) was determined with a relative root mean square error of ±2.2% within 10 s acquisition time per sample outperforming conventional backscattering Raman geometry that yielded a lower relative accuracy (±2.9%) put down to the subsampling. Similar results were obtained by Eliasson *et al.* [62] who reached a relative root mean square error of ±1.2% within 5 s acquisition time.

Recently, Aina *et al.* [63] demonstrated the ability of transmission Raman spectroscopy to also quantify the *polymorphic* content of pharmaceutical formulations. This information is not available from HPLC relying on the dissolution of sample, a step that leads to the loss of polymorphic information. Alternative methods such as X-ray diffraction, NMR, or differential scanning calorimetry suffer from long data acquisition times and/or limited sensitivity. In the concerned study, flufenamic acid was used as a model compound. The challenge of the quantification was heightened by the presence of surface segregation for one polymorphic form on the sample surface. The transmission Raman method was shown to provide a true bulk measurement of the composition in contrast to the conventional backscattering Raman method, which yielded unsatisfactory results because of subsampling.

13.3.4 Forensic and Security Applications

Another important analytical area is the noninvasive detection of counterfeit drugs through plastic or glass bottles and blister packs. Fake drugs can present a serious health risk, and in extreme situations even a serious threat to life as is the case, for example, of antimalarial tablets in eastern Asia [64]. Although NIR absorption spectroscopy is used in this area, its limited chemical specificity restricts its effectiveness. Raman spectroscopy is also used in this application for its high chemical specificity, but its effectiveness varies depending on the color and thickness of the packaging. Generally, the technique can be used

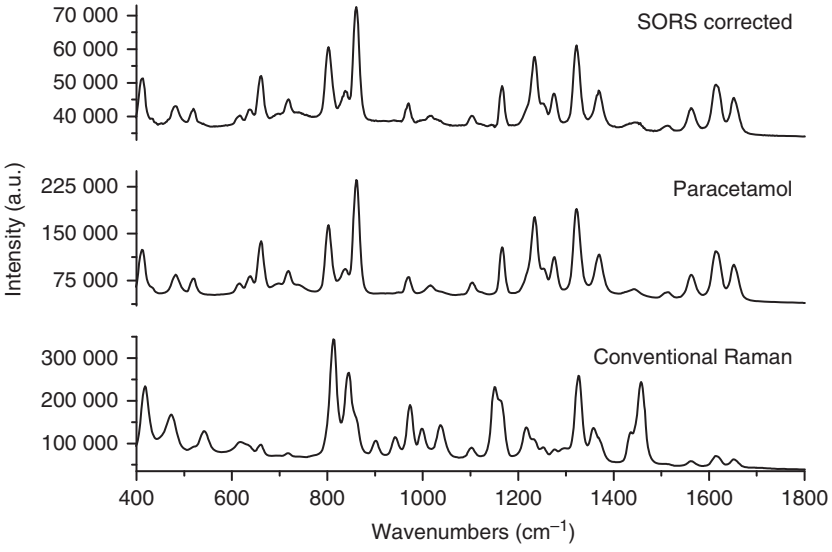

Figure 13.12 Noninvasive Raman spectra of paracetamol tablets measured through a white, diffusely scattering 1.7 mm thick plastic container in drug authentication. Conventional Raman and SORS raw data are shown together with the tablets reference Raman spectrum. The acquisition time was 10 s and the laser beam power 50 mW. (Reprinted in part with permission from [65]. American Chemical Society [65].)

to relatively readily analyze lightly colored capsules and tablets held in blister packs, but darkly colored capsules or thicker packaging such as white plastic bottles can yield an excessive amount of Raman and/or fluorescence emission emanating from the packaging, reducing substantially the sensitivity of the technique.

In this area, Eliasson and Matousek [65] showed that SORS can very effectively suppress the surface Raman and fluorescence signals originating from the capsule, coating, or packaging, thus providing a substantially higher degree of chemical sensitivity than conventional Raman spectroscopy. Figure 13.12 shows the use of SORS and conventional backscattering Raman geometry in the noninvasive probing of white plastic pharmaceutical bottles containing paracetamol tablets. The conventional Raman approach is ineffective in this case, yielding a strong Raman signal originating from the container wall. In contrast, the SORS approach, after the scaled subtraction of two SORS spectra obtained at spatial offsets of 0 and 3 mm, provided a clean Raman spectrum of the tablets held within the bottle. A practical use of this method was subsequently demonstrated on the detection of antimalarial tablets by Ricci *et al.* [66]. As the SORS concept can be potentially incorporated into handheld Raman instruments, it holds a great promise for more accurate and sensitive identification of drugs in the entire supply chain.

In the security sector, a particular topical application is the detection of liquid explosives concealed in bottles without opening them for scanning of passenger

items at airports. In this area, Eliasson *et al.* [67] demonstrated the applicability of SORS to screen a wide range of bottles including the diffusely scattering plastic bottles that are often outside the reach of conventional Raman spectroscopy. In this work, hydrogen peroxide was used as a test precursor for home-made explosives. Further development of this technology was reported by Bloomfield *et al.* [68] who studied a wider range of samples and containers and determined the optimum spatial offset and acquisition time for this application. At present, this technology has acquired an approval for use at EU airports and is expected to be rolled out at airport security checkpoints in near future. Other related areas include the use of SORS in the verification of the content of incoming raw materials through packaging in pharmaceutical manufacturing [69].

13.4 Conclusions

The advent of new noninvasive Raman spectroscopic techniques promises to have a significant impact on many biomedical, security, and industrial analytical applications. Many new exciting practical applications are already emerging including aviation security and pharmaceutical quality control, and others are under intense development. The latter include the diagnosis of diseases such as osteoporosis, brittle bone disease, breast cancer, and monitoring of glucose levels noninvasively.

References

1. Pelletier, M.J. (1999) *Analytical Applications of Raman Spectroscopy*, Blackwell Science, Oxford.
2. Pivonka, D.E., Chalmers, J.M., and Griffiths, P.R. (2007) *Applications of Vibrational Spectroscopy in Pharmaceutical Research and Development*, John Wiley & Sons, Ltd, Chichester.
3. Das, B.B., Liu, F., and Alfano, R.R. (1997) *Rep. Prog. Phys.*, **60**, 227–292.
4. Hebden, J.C., Gibson, A., Yusof, R., Everdell, N., Hillman, E.M.C., Delpy, D.T., Arridge, S.R., Austin, T., Meek, J.H., and Wyatt, J.S. (2002) *Phys. Med. Biol.*, **47**, 4155–4166.
5. Koizumi, H., Yamashita, Y., Maki, A., Yamamoto, T., Ito, Y., Itagaki, H., and Kennan, R. (1999) *J. Biomed. Opt.*, **4**, 403–413.
6. Pfefer, T.J., Schomacker, K.T., Ediger, M.N., and Nishioka, N.S. (2002) *Appl. Opt.*, **41**, 4712–4721.
7. Ghosh, N., Majumder, S.K., Patel, H.S., and Gupta, P.K. (2005) *Opt. Lett.*, **30**, 162–164.
8. Quan, L. and Ramanujam, N. (2002) *Opt. Lett.*, **27**, 104–106.
9. Gebhart, S.C., Majumder, S.K., and Mahadevan-Jansen, A. (2007) *Appl. Opt.*, **46**, 1343–1360.
10. Wu, J., Wang, Y., Perelman, L., Itzkan, I., Dasari, R., and Feld, M.S. (1995) *Appl. Opt.*, **34**, 3425–3430.
11. Everall, N., Hahn, T., Matousek, P., Parker, A.W., and Towrie, M. (2001) *Appl. Spectrosc.*, **55**, 1701–1708.
12. Everall, N., Hahn, T., Matousek, P., Parker, A.W., and Towrie, M. (2004) *Appl. Spectrosc.*, **58**, 591–597.
13. Matousek, P., Everall, N., Towrie, M., and Parker, A.W. (2005) *Appl. Spectrosc.*, **59**, 200–205.
14. Morris, M.D., Matousek, P., Towrie, M., Parker, A.W., Goodship, A.E., and Draper, E.R.C. (2005) *J. Biomed. Opt.*, **10**, 014014.

15. Matousek, P. (2007) *Chem. Soc. Rev.*, **36**, 1292–1304.
16. Buckley, K. and Matousek, P. (2011) *Analyst*, **136**, 3039–3050.
17. Matousek, P., Clark, I.P., Draper, E.R.C., Morris, M.D., Goodship, A.E., Everall, N., Towrie, M., Finney, W.F., and Parker, A.W. (2005) *Appl. Spectrosc.*, **59**, 393–400.
18. Widjaja, E., Li, C.Z., and Garland, M. (2002) *Organometallics*, **21**, 1991–1997.
19. Chew, W., Widjaja, E., and Garland, M. (2002) *Organometallics*, **21**, 1982–1990.
20. Li, C.Z., Widjaja, E., and Garland, M. (2003) *J. Catal.*, **213**, 126–134.
21. Widjaja, E., Li, C.Z., Chew, W., and Garland, M. (2003) *Anal. Chem.*, **75**, 4499–4507.
22. Widjaja, E., Crane, N.J., Chen, T.C., Morris, M.D., Ignelzi, M.A., and McCreadie, B.R. (2003) *Appl. Spectrosc.*, **57**, 1353–1362.
23. Ma, J.Y. and Ben-Amotz, D. (1997) *Appl. Spectrosc.*, **51**, 1845–1848.
24. Matousek, P., Morris, M.D., Everall, N., Clark, I.P., Towrie, M., Draper, E., Goodship, A., and Parker, A.W. (2005) *Appl. Spectrosc.*, **59**, 1485–1492.
25. Schulmerich, M.V., Finney, W.F., Popescu, V., Morris, M.D., Vanasse, T.M., and Goldstein, S.A. (2006) *Proc. SPIE*, **6093**, 60930O.
26. Schulmerich, M.V., Finney, W.F., Fredricks, R.A., and Morris, M.D. (2006) *Appl. Spectrosc.*, **60**, 109–114.
27. Matousek, P., Draper, E.R.C., Goodship, A.E., Clark, I.P., Ronayne, K.L., and Parker, A.W. (2006) *Appl. Spectrosc.*, **60**, 758–763.
28. Matousek, P. (2006) *Appl. Spectrosc.*, **60**, 1341–1347.
29. Schulmerich, M.V., Dooley, K.A., Morris, M.D., Vanasse, T.M., and Goldstein, S.A. (2006) *J. Biomed. Opt.*, **11**, 060502.
30. Schulmerich, M.V., Morris, M.D., Vanasse, T.M., and Goldstein, S.A. (2007) *Proc. SPIE*, **6430**, 643009.
31. Matousek, P. and Parker, A.W. (2006) *Appl. Spectrosc.*, **60**, 1353–1357.
32. Schrader, B. and Bergmann, G. (1967) *Z. Anal. Chem. Fresenius*, **225**, 230–247.
33. Johansson, J., Pettersson, S., and Folestad, S. (2005) *J. Pharm. Biomed. Anal.*, **39**, 510–516.
34. Townshend, N., Littlejohn, D., Nordon, A., Myrick, M.,Andrews, J., and Dallin, P. (2009) PhAT Raman Analysis of Pharmaceutical Tablets.
35. Johansson, J., Svensson, O., Folestad, S., Sparen, A., and Claybourn, M. (2009) Transmission Raman spectroscopy for robust tablet assessment. FACSS Conference Proceedings, Louisville, Kentucky, 2009, Abstract 300, p. 131.
36. Everall, N., Matousek, P., Macleod, N., Ronayne, K.L., and Clark, I.P. (2010) *Appl. Spectrosc.*, **64**, 52–60.
37. Everall, N., Priestnall, I., Dallin, P., Andrews, J., Lewis, I., Davis, K., Owen, H., and George, M.W. (2010) *Appl. Spectrosc.*, **64**, 476–484.
38. Matousek, P. and Parker, A.W. (2007) *J. Raman Spectrosc.*, **38**, 563–567.
39. Schulmerich, M.V., Dooley, K.A., Vanasse, T.M., Goldstein, S.A., and Morris, M.D. (2007) *Appl. Spectrosc.*, **61**, 671–678.
40. Schulmerich, M.V., Cole, J.H., Dooley, K.A., Morris, M.D., Kreider, J.M., Goldstein, S.A., Srinivasan, S., and Pogue, B.W. (2008) *J. Biomed. Opt.*, **13**, 020506.
41. Srinivasan, S., Schulmerich, M., Cole, J.H., Dooley, K.A., Kreider, J.M., Pogue, B.W., Morris, M.D., and Goldstein, S.A. (2008) *Opt. Express*, **16**, 12190–12200.
42. Carpenter, C.M., Pogue, B.W., Jiang, S., Dehghani, H., Wang, X., Paulsen, K.D., Wells, W.A., Forero, J., Kogel, C., Weaver, J.B., Poplack, S.P., and Kaufman, P.A. (2007) *Opt. Lett.*, **32**, 933–935.
43. Demers, J.L., Pogue, B., Leblond, F., Esmonde-White, F., Okagbare, P., and Morris, M. (2011) *Proc. SPIE*, **7892**, 789211.
44. Stone, N., Faulds, K., Graham, D., and Matousek, P. (2010) *Anal. Chem.*, **82**, 3969–3973.
45. Stone, N., Kerssens, M., Lloyd, G.R., Faulds, K., Graham, D., and Matousek, P. (2011) *Chem. Sci.*, **2**, 776–780.
46. Draper, E.R.C., Morris, M.D., Camacho, N.P., Matousek, P., Towrie, M., Parker, A.W., and Goodship, A.E. (2005) *J. Bone Miner. Res.*, **20**, 1968–1972, and references therein.
47. McCreadie, B.R., Morris, M.D., Chen, T., Rao, D.S., Finney, W.F., Widjaja, E.,

and Goldstein, S.A. (2006) *Bone*, **39**, 1190–1195.
48. Carden, A. and Morris, M.D. (2000) *J. Biomed. Opt.*, **5**, 259–268.
49. Okagbare, P.I., Esmonde-White, F.W.L., Goldstein, S.A., and Morris, M.D. (2010) *Analyst*, **135**, 3142–3146.
50. Baker, R., Matousek, P., Ronayne, K.L., Parker, A.W., Rogers, K., and Stone, N. (2007) *Analyst*, **132**, 48–53.
51. Stone, N., Baker, R., Rogers, K., Parker, A.W., and Matousek, P. (2007) *Analyst*, **132**, 899–905.
52. Matousek, P. and Stone, N. (2007) *J. Biomed. Opt.*, **12**, 024008.
53. Haka, A.S., Shafer-Peltier, K.E., Fitzmaurice, M., Crowe, J., Dasari, R.R., and Feld, M.S. (2002) *Cancer Res.*, **62**, 5375–5380.
54. Stone, N. and Matousek, P. (2008) *Cancer Res.*, **68**, 4424–4430.
55. Sardanelli, F., Zandrino, F., Imperiale, A., Bonaldo, E., Quartini, M.G., and Cogorno, N. (2000) *Radiology*, **217**, 576–580.
56. Keller, M.D., Majumder, S.K., and Mahadevan-Jansen, A. (2009) *Opt. Lett.*, **34**, 926–928.
57. Keller, M.D., Vargis, E., de Matos Granja, N., Wilson, R.H., Mycek, M.-A., Kelley, M.C., and Mahadevan-Jansen, A. (2011) *J. Biomed. Opt.*, **16**, 077006.
58. Yuen, J.M., Shah, N.C., Walsh, J.T., Glucksberg, M.R., and Van Duyne, R.P. (2010) *Anal. Chem.*, **82**, 8382–8385.
59. Ma, K., Yuen, J.M., Shah, N.C., Walsh, J.T., Glucksberg, M.R., and Van Duyne, R.P. (2011) *Anal. Chem.*, **83**, 9146–9152.
60. Kong, C.R., Barman, I., Dingari, N.C., Kang, J.W., Galindo, L., Dasari, R.R., and Feld, M.S. (2011) *AIP Adv.*, **1**, 032175.
61. Johansson, J., Sparen, A., Svensson, O., Folestad, S., and Claybourn, M. (2007) *Appl. Spectrosc.*, **61**, 1211–1218.
62. Eliasson, C., Macleod, N.A., Jayes, L.C., Clarke, F.C., Hammond, S.V., Smith, M.R., and Matousek, P. (2008) *J. Pharm. Biomed. Anal.*, **47**, 221–229.
63. Aina, A., Hargreaves, M.D., Matousek, P., and Burley, J.C. (2010) *Analyst*, **135**, 2328–2333.
64. Newton, P.N., Green, M.D., Fernández, F.M., Day, N.P.J., and White, N.J. (2006) *Lancet Infect. Dis.*, **6**, 602–613.
65. Eliasson, C. and Matousek, P. (2007) *Anal. Chem.*, **79**, 1696–1701.
66. Ricci, C., Eliasson, C., Macleod, N.A., Newton, P., Matousek, P., and Kazarian, S.G. (2007) *Anal. Bioanal. Chem.*, **389**, 1525–1532.
67. Eliasson, C., Macleod, N.A., and Matousek, P. (2007) *Anal. Chem.*, **79**, 8185–8189.
68. Bloomfield, M., Loeffen, P.W., and Matousek, P. (2010) *Proc. SPIE*, **7838**, 783808-1–783808-15.
69. Bloomfield, M., Andrews, D., Loeffen, P., Tombling, C., York, T., and Matousek, P. (2013) *J. Pharm. Biomed. Anal.*, **76**, 65–69.

14
Nonlinear Vibrational Spectroscopic Microscopy of Cells and Tissue

Roberta Galli and Gerald Steiner

14.1
Introduction

Advances in optics, light detectors, laser technology, and microscopy techniques have revolutionized the ability to look inside cells, tissue, and organs. Imaging modalities capable of identifying specific molecules have significantly improved our understanding of biological processes on the microscopic scale. The combination of microscopy with use of exogenous labels, for example, immunohistochemistry, achieves high specificity, but the labeling perturbs the system of interest and is difficult to be applied *in vivo*.

Label-free imaging techniques based on endogenous fluorescence or nonlinear optical (NLO) processes, such as absorption or scattering of light, generation of harmonics, combine high resolution and speed, but offer only low specificity, and the number of addressable molecules is limited. However, vibrational microspectroscopy provides the highest intrinsic chemical selectivity, delivering the "fingerprint" of the sample composition. Biomedical applications of infrared and Raman microspectroscopic studies have seen a rapid development in the past years (see Chapter 3 of this book), but both are limited by a number of difficulties, mainly related to lateral resolution and measurement speed, respectively.

This chapter is focused on coherent anti-Stokes Raman scattering (CARS) microscopy as NLO imaging techniques. It reviews design and application of CARS microscopy and its combination with other NLO techniques. Advantages, challenges, and recent developments are discussed in order to demonstrate the potential for clinical applications.

Infrared and Raman Spectroscopic Imaging, Second Edition. Edited by Reiner Salzer, Heinz W. Siesler.
© 2014 Wiley-VCH Verlag GmbH & Co. KGaA. Published 2014 by Wiley-VCH Verlag GmbH & Co. KGaA.

14.2
Principles of Nonlinear Optical Imaging

14.2.1
Important Processes for Nonlinear Optical Imaging

NLO imaging techniques employ processes that involve more than two photons. The most important NLO microscopic techniques for the analysis of cells and tissue are CARS, two photon fluorescence (TPF), second harmonic generation (SHG), and third harmonic generation (THG). Figure 14.1 shows the term schemes of these processes. The CARS process is a third-order NLO process, where two laser pulses interact with a sample via a four-wave mixing process, generating the anti-Stokes field. CARS is often used to highlight the C–H stretching vibration modes of CH_2 groups because they give rise to an intense signal. TPF is a fluorescence excitation process where two photons are coupled to excite electrons from the ground state to the first singlet state. SHG is a second-order coherent process in which two photons are up-converted to exactly twice the wavelength of the exciting laser. In contrast to TPF, the electrons are excited to a virtual state. SHG is sensitive to fiber structures lacking of

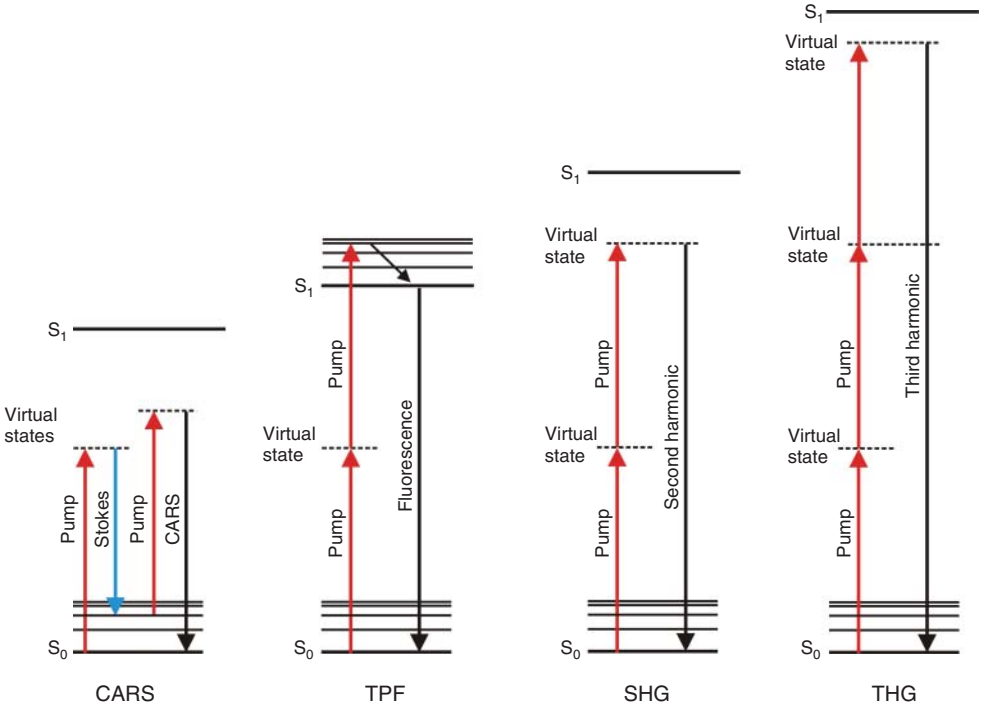

Figure 14.1 Term schemes for the NLO microscopic imaging modalities described in this chapter.

inversion symmetry. THG is similar to SHG. In THG, three photons of the same wavelength excite the electron. THG is also particular sensitive to fiber structures and boundaries. Different NLO modalities can be recorded parallel at the same time by using broadband ultrafast near-infrared laser pulses. Different structures and functional groups in cells and tissue can thus be imaged at once.

14.2.2
Coherent Anti-Stokes Raman Scattering

CARS was first reported in 1965 by Maker and Terhune [1]. The two researchers at Ford Motor Company presented the results of several experiments in which a giant-pulsed ruby laser was used to study NLO effects associated with an induced third-order polarization in the electric field strength. These effects included resonant mixing of waves at three different frequencies that was in fact a coherent anti-Stokes emission. Despite the fact that this first research was conducted at Ford, the name CARS was coined only several years later in 1974 by Begley *et al.* [2] at the Stanford University, which understood the potential of the method and the advantages over spontaneous Raman spectroscopy: a factor 10^5 of improvement in conversion efficiency, spectral and spatial discrimination against fluorescence, low incident average power, and no requirement for a monochromator. They also suggested that CARS could be particularly useful in investigation of biological compounds, where background fluorescence might be a problem for spontaneous Raman studies.

The CARS process can be described as interaction of a pump beam at frequency ω_{pu}, a probe beam at frequency ω_{pr}, and a Stokes beam at frequency ω_s with a sample via a four-wave mixing process, generating an anti-Stokes field at frequency:

$$\omega_{as} = \omega_{pu} + \omega_{pr} - \omega_s \tag{14.1}$$

In standard CARS experiments, pump and probe beams are provided by the same laser source, so that $\omega_{pu} = \omega_{pr} = \omega_p$. When the beat frequency $\omega_p - \omega_s$ (Figure 14.2a) matches the frequency of a Raman-active molecular vibration and phase-matching condition is achieved, the resonant oscillators are coherently driven by the excitation fields, generating a strong anti-Stokes signal at

$$\omega_{as} = 2\omega_p - \omega_s \tag{14.2}$$

In the major part of the experimental set-ups, the pump beam has a fixed frequency, while the Stokes frequency is tuned in order to match the beating frequency. The phase matching is achieved if the laser beams are crossed at angle θ, that is, the phase-matching angle (Figure 14.2b).

The signal arises from the four-wave mixing signal enhancement when the laser frequency difference matches the frequency of the probed vibrational mode. CARS is at the same time a coherent and a resonant process, meaning that it differs in nature from other nonlinear processes such as two-photon excited fluorescence (i.e., only resonant) and SHG (i.e., only coherent). Both aspects determine the peculiar features in a CARS spectroscopic image.

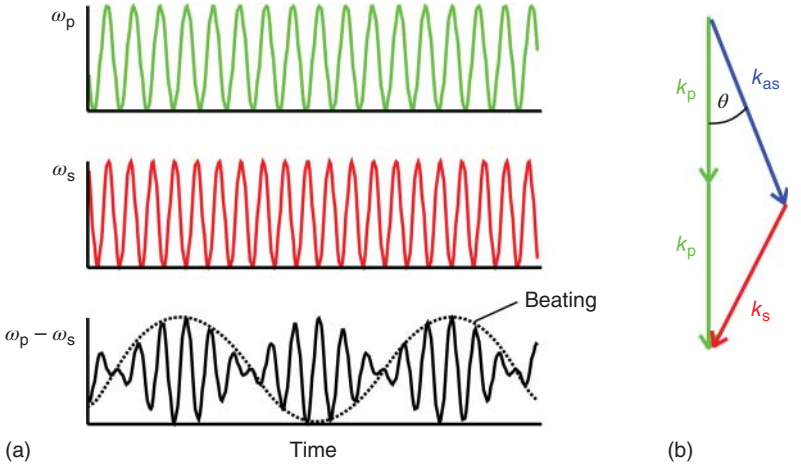

Figure 14.2 (a) Generation of the beating frequency and (b) wave vector diagram for phase-matching condition.

As CARS is a four-wave mixing process [3], the intensity of the CARS signal is proportional to the square modulus of the induced third-order polarization $P^{(3)}$:

$$I_{\mathrm{CARS}} \propto |P^{(3)}|^2 \tag{14.3}$$

The polarization magnitude is determined by the strength E of the electrical fields of pump and Stokes excitation beams and the nonlinear susceptibility $\chi^{(3)}$.

$$P^{(3)} = \chi^{(3)} E_p E_p E_s^* \tag{14.4}$$

In contrast to one-photon electronic resonance, the third-order susceptibility is

$$\chi^{(3)}(\omega_{as}) = \eta_{NR} + \frac{A_t}{\omega_t - 2\omega_p - i\Gamma_t} + \frac{A_t}{\omega_t - (\omega_p + \omega_s) - i\Gamma_t} + \frac{A_t}{\omega_t - 2\omega_s - i\Gamma_t} + \sum_R \frac{A_R}{\omega_R - (\omega_p - \omega_s) - i\Gamma_R} \tag{14.5}$$

where t indicates two-photon transition and R indicates Raman transitions; A, ω, and Γ are strength, frequency, and half-width, respectively. The first term η_{NR} represents nonresonant electronic contributions and is independent of the Raman shift. The second, third, and fourth terms are nonresonant contributions because of two-photon electronic resonance.

The last term is the vibrationally resonant contribution of all Raman transitions excited, and it becomes large when the frequency difference between pump and Stokes matches the frequency of a Raman transition. Its real part has a dispersive lineshape and the imaginary part, which mirrors the spontaneous Raman band, has a Lorentzian shape.

Two-photon resonance is prevented by using near-infrared excitation, so that the first four terms of Equation 14.5 can be combined into a real number denoted

$\chi^{(3)}_{NR}$. E^*_s is the conjugated Stokes field.

$$P^{(3)} = (\chi^{(3)}_R + \chi^{(3)}_{NR})E_p E_p E^*_s \tag{14.6}$$

$$I_{CARS} \propto |\chi^{(3)}_R + \chi^{(3)}_{NR}|^2 = |\chi^{(3)}_R|^2 + |\chi^{(3)}_{NR}|^2 + 2\chi^{(3)}_{NR}\mathrm{Re}\{\chi^{(3)}_R\} \tag{14.7}$$

As a consequence of the complex nature of the susceptibility and the interference between resonant and nonresonant terms, CARS has a dispersive lineshape. With respect to spontaneous Raman band, CARS resonance has therefore a red-frequency shift and differences in band amplitude.

Because CARS has a coherent nature, a strong signal is generated if constructive interference between the beams is maintained in the interaction volume [3]. The necessary phase-matching condition is

$$|\Delta k| l \ll \pi \tag{14.8}$$

where l is the interaction length and

$$\Delta k = k_{as} - (2k_p - k_s) \tag{14.9}$$

Noncollinear beam geometries were used in CARS spectroscopy to minimize the wave vector mismatch and maximize the interaction length. However, the phase-matching condition can be fulfilled with collinear beam geometry in CARS experiments because of the small interaction length of several micrometers and the large cone angle of the wave vectors of the excitation beams under the tight-focusing condition, obtained with high numerical aperture (NA) objectives.

The theoretical model of CARS signal generation from an arbitrary Raman scatterer by tightly focused Gaussian beams in collinear configuration was described by Cheng *et al.* [4]. In the general formulation derived from the NLO wave equation, the coherent radiation field is calculated from a three-dimensional (3D) object. This provides a quantitative description of the contrast mechanisms of CARS.

The numerical model enables to calculate the radiation pattern of the CARS signal from spherical scatterers in the laser focus. When the diameter D of the scatterer is much smaller than the pump wavelength, the phase-matching condition is satisfied in all directions of k_{as}. Therefore, the CARS radiation pattern is symmetric in both the forward and the backward directions. With increasing sample size, the CARS radiation is confined to a small cone angle in the forward direction. The signal from the sample with diameter $3\lambda_p$ already resembles the CARS generation from a bulk medium. These results indicate that the CARS signal from a large scatterer can be efficiently collected with a lens of low NA, whereas collection of the CARS signal from scatterers of subwavelength dimensions needs a high-NA lens.

The analysis of the CARS signal intensity as a function of D of a spherical sample at the laser focus shows that the forward-detected signal first grows rapidly with the increasing diameter D and then becomes saturated when the diameter is larger than $1.0\lambda_p$. The backward-detected (or epi-detected) signal exhibits

the same amplitude as the forward signal when D is much smaller than λ_p. The first maximum is reached when $D = 0.3\lambda_p$. For larger diameters, an oscillating behavior is observed, with results from interference effects associated with the large wave vector mismatch in the backward direction. After the second maximum, the backward signal gradually decreases with an increase in diameter. For $D = 8.0\lambda_p$, the backward signal is 10^5 times smaller than the corresponding forward signal. Therefore, the epi-detection geometry provides a way to image small features embedded in a nonlinear medium. It is worth to note that two further mechanisms provide contrast epi-detected CARS and both are related to the presence of interfaces. The calculations show that while the CARS signal from an interface parallel to the optical axis proceeds forward, the signal generated at an interface perpendicular to the optical axis mainly propagates backward, contributing to the epi-detected CARS signal. Moreover, backward reflection at an index-mismatched interface of the forward-going CARS gives the third contrast mechanism for an epi-detected CARS.

As already mentioned, CARS bands exhibit a dispersive shape. This feature affects also the CARS image contrast as a function of the detuning from the Raman frequency. Because of a blue-shifted dip in the CARS spectrum, the image contrast is lower in case of positive detuning [4]. This is the result of destructive interference between the resonant and the nonresonant signal. The highest image contrast is obtained with a small negative detuning, in accordance with the red shift of the CARS band from the central frequency of the spontaneous Raman band. It is interesting to note that even when the pump and Stokes frequency difference is tuned away from any Raman resonance, the contrast is still present as a result of the different nonresonant susceptibilities of the scatterer and the solvent [5]. As a consequence, the nonresonant signal is dominated by morphological features [6].

The interference between resonant and nonresonant signals is also responsible for another distinguishing feature of CARS images. In real applications, scatterers are normally embedded in a medium. All media have a third-order nonlinear optical response and then both resonant signal and nonresonant background are generated. As CARS is a coherent process, the two signals are not simply additive; they will add and subtract depending on their relative phases. Dark fringes can be observed at the interface between objects such as cells and water. This is explained as a destructive interference mechanism between the object and its surrounding medium [4]. The respective CARS emissions from a composite of resonant and nonresonant objects are out of phase. When the interface between these two media is scanned, their phase difference accounts theoretically for destructive interferences [7]. Moreover, refractive index mismatch between the two media can distort the beams foci and thus change the CARS signal in this special region. The refractive index mismatch is in fact the main reason for the dips appearing at the interface between an object and its surroundings [8, 9].

Interference phenomena also profoundly alter the contrast of objects immersed in a medium by varying the focal position. When the object is translated along the laser propagation axis, the CARS signal intensity is found to be asymmetric

around the focal plane. When the object is located before the focus, it appears as a dark shadow in the bright background, whereas the brightest signal is obtained when the object is behind the focus [10].

The advantages of CARS can be summarized as follows [11, 12]:

- It is fast and nondestructive, so that it can be applied to living cells and tissues.
- It provides contrast based on the intrinsic molecular vibrations of a specimen, avoiding the need for extrinsic labels, so that it is not subjected to photobleaching as immunofluorescence.
- The emission is directional, which permits more effective signal collection.
- The coherent addition results in a quadratic dependence of the signal from the density of molecular oscillators (while spontaneous Raman has a linear dependence).
- The anti-Stokes signal is blue-shifted from the pump and Stokes frequencies, and therefore it is not affected by one-photon fluorescence.
- When using near-infrared excitation wavelengths, CARS can penetrate up to 1 mm inside the tissue.

14.2.3 CARS Microscopy

In CARS spectral microscopy, a CARS spectrum over a wavenumber region is recorded for each pixel. The most common method of spectral CARS microscopy is multiplex CARS microscopy [13–15]. Here, the pump pulse has a narrow bandwidth (e.g., picosecond pulse), whereas the Stokes pulse covers a rather large frequency range (e.g., femtosecond pulse). This is a distinct difference to the earlier described the so-called single-band CARS spectroscopy, where picosecond lasers are used for both pump and Stokes pulses. The advantage of multiplex CARS is the simultaneous excitation of all Raman modes by the large spectral bandwidth of the Stokes pulse, leading to the generation of a broad spectral range of anti-Stokes photons. Thus, by spectral analysis of the CARS signal, the CARS spectrum is obtained. Image acquisition is slower when compared to single-band CARS microscopy, but still faster than in spontaneous Raman microspectroscopy.

Single-band CARS microscopy records the spatial distribution of a single Raman band within the sample and enables video-rate imaging. The quality of single-band CARS images depends on (i) the Raman scattering cross section of the mode to be imaged, (ii) that this mode is spectrally distinct, to avoid spectral interferences with adjacent Raman modes, and (iii) on a high-enough molecular density of oscillators featuring this mode. In biological systems, these conditions are fulfilled for the CH_2 stretching vibration within lipids [16]. Most single-band CARS microscopy studies reported so far were concentrated on lipid imaging.

The first laser scanning CARS microscope, able to image the distribution of specific molecular species inside the sample, was developed almost 10 years later in 1982 at the Naval Research Laboratory by Duncan *et al.* [17], who produced

images of onion-skin cells using the CARS signal produced by the 2450 cm^{-1} band of deuterated water. A noncollinear geometry of the laser beams was used to obtain the phase matching, with the result of a rather unfriendly system with low lateral resolution because of the reduced effective NA.

The breakthrough of CARS microscopy came in 1999. Zumbusch *et al.* [18] used a microscope objective with high NA to focus the beams tightly, relaxing the phase-matching conditions because of the large cone of wave vectors and the short interaction length. Moreover, near-infrared lasers were used, thereby reducing the nonresonant background that strongly affected the previous experiments performed with visible sources. By probing the C–H stretching around 2850 cm^{-1}, living cells were imaged for the first time.

At that time, CARS microscopy was implemented with a sample-scanning scheme [19], so that the data collection speed was principally limited by the slow scanning and by the low photon counting rate that needed to be kept below 5% of the laser repetition rate [18]. The acquisition time for each pixel was several milliseconds, thus a whole image of 512×512 pixels usually required more than 10 min.

High-sensitivity, high-speed CARS microscopy by scanning two collinearly combined laser beams was first reported in 2002 by Cheng *et al.* [8]. By virtue of fast scanning of laser beams at a high repetition rate, the data acquisition time was shortened by two orders of magnitude, enabling to study mitosis and apoptosis of living cells in real time. High 3D resolution was achieved with a water-immersion objective with 1.2 NA.

14.3 Instrumentation for Multimodal Nonlinear Microscopy

A system for single-band CARS microscopy is most commonly composed of three main parts:

- laser sources, providing pump and Stokes beams;
- relay optics, whose main function is to steer the laser beams to the microscope and provide the correct overlap of pump and Stokes laser pulses, necessary to excite the CARS signal inside the specimen;
- scanning microscope, which rasters the laser beams on the sample by use of a scanner and acquires the point-by-point generated signals to build the image.

14.3.1 Laser Sources

Infrared ultrashort laser sources with high pulse energy are most commonly used with pulse length ranging from about 200 fs to some picoseconds and a power up to few hundreds of milliwatts. These types of laser are in safety class 3B. The emitted radiation is potentially dangerous for eyes and skin. Specular reflections

of the laser beams produce permanent damages to the retina. Implementation, use, and maintenance operations complied with the European safety specification IEC 60825.

The choice of the correct laser excitation is of paramount importance to guarantee optimal quality of CARS images. As already described in Equation 14.5, a nonresonant background signal is always superimposed to the resonant signal, and this limits the sensitivity in detecting weak Raman bands. The nonresonant background signal constitutes the major disadvantage of single-band CARS microscopy.

As CARS is a nonlinear process, high-excitation field strengths are necessary for efficient signal generation and therefore short-pulsed lasers are required. However, a compromise between pulse peak power and spectral bandwidth has to be taken into account. If the spectral width of the laser pulses significantly exceeds the width of the Raman bands, the interaction of the laser pulses with the sample causes strong contributions of the nonresonant signal. Considering that Raman bands in condensed matter have bandwidths around $10\,cm^{-1}$, the use of picoseconds pulses, whose bandwidth matches the spectral width of the vibrational transitions, is a common approach to optimize the ratio between resonant signal and nonresonant signal [16]. Mathematical calculations [5] show that the vibrationally nonresonant CARS signal increases quadratically with the pulse spectral width. The vibrationally resonant signal also increases with the spectral width, but is gradually saturated when the spectral width becomes larger than the Raman line width (about $10\,cm^{-1}$ in condensed phase). The use of laser pulses in the femtosecond regime results in a broad CARS band superimposed on a large nonresonant background. With pulses of few picoseconds, the signal-to-background ratio is significantly improved. Further increasing the pulse does not further improve the signal-to-background ratio, but strongly reduces the signal level. As a balance between the absolute signal level and the signal-to-background ratio, the optimal pulse spectral width is 1–2 ps for a typical Raman band [19].

Tunability of the frequency difference of the laser beams is necessary in order to enable matching the frequency of Raman transitions, therefore one of the laser sources, normally the one delivering the Stokes beam, is tunable in wavelength. Up to now, the most common laser sources used for CARS microscopy are based on Ti:sapphire or Nd:YVO_4 lasers with pulse durations from tens of femtoseconds up to 10 ps. Different approaches are possible in order to generate pump and Stokes beams: use of two femtosecond laser sources electronically synchronized [19], pumping of an optical parametric amplifier (OPA) to produce the Stokes beam and use of the residual pump as pump beam [18], pumping of an optical parametric oscillator (OPO) to obtain the pump beam and use the residual pump light as Stokes [20], using signal and idler beams from a synchronously pumped OPO to provide directly the two excitation beams [11, 21].

More recently, fiber laser sources have come to an age in CARS microscopy [22–27]. This new laser sources are small and reliable, particularly suited for a future translation of the technique to the clinical environment.

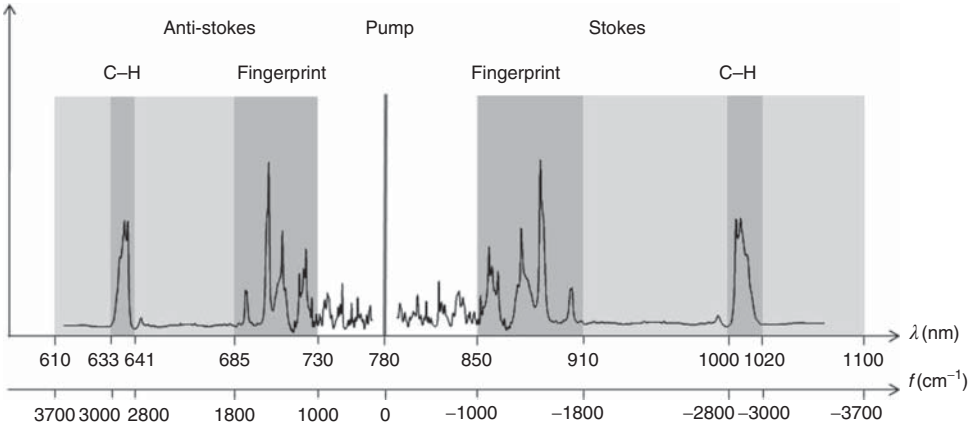

Figure 14.3 The tuning range 850–1100 nm of the Stokes laser source enables to address Raman bands from 800 to 3100 cm^{-1}, which correspond to a CARS signal in the range 610–730 nm. The C–H stretching vibration, between 2800 and 3000 cm^{-1} in the Raman spectrum, requires tuning the Stokes laser source in the range 1000–1020 nm and produces a CARS signal in the range 633–641 nm. The fingerprint region, which in the Raman spectrum covers the range up to 1800 cm^{-1}, requires tuning the Stokes laser source in the range 850–910 nm and produces a CARS signal in the range 685–730 nm.

As an example, Figure 14.3 shows typical wavelength window that is addressed by using two Erbium fiber lasers (Femto Fiber Pro NIR and Femto Fiber Pro TNIR, Toptica Photonics AG, Munich, Germany). The pump beam is provided at 780 nm, while the Stokes beam is tunable in the range 850–1100 nm, enabling to address the C–H stretching vibration of CH_2 groups at high energy and the fingerprint region down to 1000 cm^{-1}.

14.3.2 Optics

The two laser beams exiting the sample have to be correctly directed to the microscope. Therefore, an optical system is necessary that provides overlap in space of the two beams, superposition of the pulses in the time domain, and, depending on the specific configurations, an optical conformation of the beams (such as a modification of divergence, of the polarization). The overlap in space is provided by a beam combiner, for example, a dichroic mirror that selectively reflects one of the laser beams and transmits the other beam. The superposition of the pulse in the time domain is set by use of a delay line, for example, two 45° mirrors mounted on a micrometer stage, folding one of the laser beams and allowing to change the optical path length difference existing between the two laser beams in order to compensate for the existing delay.

14.3.3 Scanning Microscope

The laser scanning microscope integrates a scanning module, which allows to raster the laser beams on the sample in x- and y-direction and a biological microscope (upright or inverted). As CARS requires a tight focalization of the laser beams, objectives with high NA have to be used, leading to a spot dimension well below 1 µm. In case of objectives with NA ≈ 1, the depth of focus is in the order of 1 µm, efficiently enabling Z-sectioning of the samples.

The generated CARS signal can be collected in transmission by a high NA condenser lens or in reflection by the microscope objective itself. The intensity of collected signal, filtered to remove the scattered excitation wavelength and select the spectral range of interest, is measured by a detector that is typically a photomultiplier or an avalanche photodiode. The signal intensities of each pixel finally form the CARS image. The typical acquisition time for each pixel, the so-called dwell time, is in the order of the microsecond.

The ultrashort laser sources used to generate the CARS are also efficient in exciting other multiphoton processes, such as TPF and SHG. As the signals are spectrally separated, it is possible to integrate a multimodal nonlinear microscope, able to acquire simultaneously CARS, TPF, and SHG. Figure 14.4 shows an example of the signals that can be acquired in a multimodal CARS system, where the SHG is produced by the pump beam of an erbium fiber laser emitting at 780 nm.

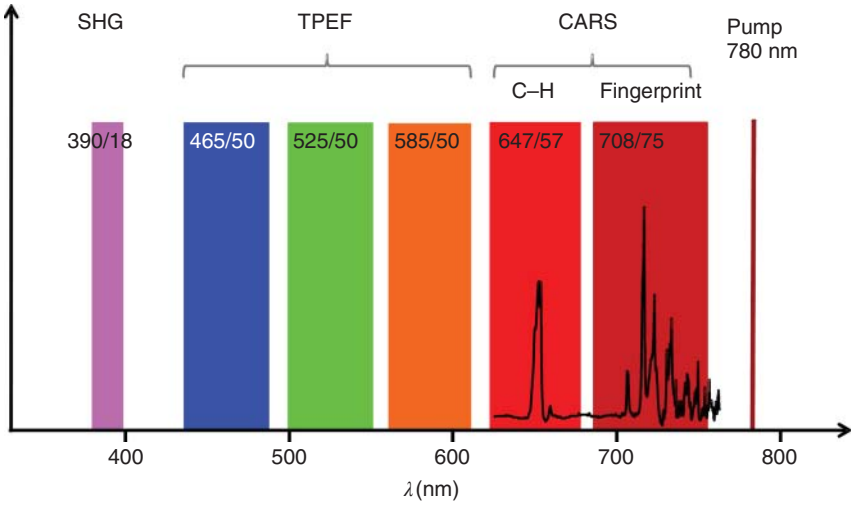

Figure 14.4 Schematic representation of the optical filtering of NLO signals.

14.4 Applications

14.4.1 Identification of Tumor Tissue

Historically, the most addressed topic is cell lipid metabolism. Imaging of neutral lipid droplets in unstained living fibroblast cells was performed by Nan *et al.* already in 2003 [28]. Using laser-scanning CARS system, the accumulation of lipid droplets in the cell cytoplasm during differentiation of fibroblasts to adipocytes was monitored by imaging the frequency for aliphatic C–H vibrations at 2845 cm^{-1}. The same research group demonstrated afterwards the nonperturbative monitoring of intracellular organelle transport in unstained living cells [29]. In further studies, quantitative imaging of the chemistry and physical states of individual lipid droplets was provided by multiplex CARS microscopy, which also showed that different cell types have distinct lipid characteristics [14]. Multiplex CARS was used afterwards to monitor the digestion of lipid droplets in porcine pancreatic lipase to simulate *in vitro* gastrointestinal absorption, and CARS microscopy allowed to map the evolution of the digestion process in the cells [30].

Changes in cell lipid metabolism were also used to address specific diseases of the liver. As the metabolic change produced in hepatic cells by hepatitis C virus (HCV) is characterized by accumulation of lipid droplets, Nan *et al.* [31] used a combination of CARS and two-photon excitation fluorescence (TEPF) microscopies to simultaneously examine the subcellular localization of HCV RNA and changes in lipid phenotype of hepatoma cells. Lyn *et al.* [32] used TPF and CARS microscopies to demonstrate the connection among the dispersion of HCV RNA from replication sites, change in lipid storage, and increase in lipid droplet size.

Cell cycle and cell differentiation is another area of *in vitro* studies. A combination of CARS and TPF microscopies with Raman microspectroscopy was used to study macromolecular organization of the nucleus throughout the cell cycle [33]. For instance, CARS was used to localize the proteins during mitosis by imaging of the Raman band at 2930 cm^{-1}. A few studies also addressed stem cell differentiation by CARS microscopy of Raman bands in the fingerprint region. Identification of differentiated versus undifferentiated states of mouse embryonic stem cells was demonstrated by CARS microscopy with selective observation of DNA- and RNA-specific backbone molecular vibrations [34]. Moreover, differentiation of stem cells in osteoblasts was directly monitored by CARS microscopy using the hydroxyapatite band at 960 cm^{-1} [35].

The study of living organisms exploits the main advantages of CARS microscopy and, of course, is performed in epi-detection. Evans *et al.* [36] in 2005 demonstrated the real-time imaging of dynamic processes *in vivo* on mouse skin. Hellerer *et al.* [37] quantitatively monitored the impact of genetic variations by CARS in metabolic pathways on lipid storage in living *Caenorhabditis elegans*.

The coexistence of neutral and autofluorescent lipid species in living *C. elegans* was demonstrated by Le *et al.* [38], who also analyzed the unsaturation level of lipids in wild-type and mutant *C. elegans* by coupling CARS with fingerprint confocal Raman analyses. The lipid metabolism was also studied by CARS in living Drosophila larvae [39].

Several *ex vivo* studies have been done on animal and human tissues to address specific pathologies that involve a change in lipid quantity and/or distribution inside a variety of tissue types. Using CARS microscopy, Wu *et al.* [40] have demonstrated the specific imaging of fat droplets in intact liver tissues and extracted the hepatic fat content through image analysis over a pathologically significant range.

Alteration in lipid metabolism is associated with several neoplastic diseases. For example, lipid-rich lung carcinomas have been associated with a more aggressive clinical behavior, and CARS microscopy was employed to study cancer cells in excess lipid environments *in vivo* mouse model and *in vitro* [41]. CARS microscopy revealed that intracellular lipid accumulation promoted tissue invasion and showed a lipid accumulation in primary, circulating, and metastasized cancer cells. Also in human patients, circulating cancer cells could be discerned, thanks to the higher CARS signal intensity [42].

Human normal breast tissue, benign proliferative, and invasive carcinomas were imaged *ex vivo* by CARS microscopy [43], distinguishing cancerous lesions from normal tissue and benign proliferative lesion. The geometry and distribution of cancer cell nuclei were extracted and fed to a computerized classification system to further distinguish cancer subtypes. The same methodology was applied to differentiate between normal and cancerous prostatic glands [44], as well as lung cancer from non-neoplastic lung tissues and identify lung cancer subtypes [45, 46], demonstrating that the method has the potential to enable rapid diagnosis of cancer.

Most recent applications involve multimodal CARS microscopy, where CARS microscopy is coupled to other nonlinear imaging modalities on stained or unstained samples. The most diffused multimodal technique involves simultaneous acquisition of CARS, TPF, and SHG. This kind of multimodal NLO microscopy already demonstrated its potential in some applications. Using an all-fiber laser system, multimodal NLO microscopy of both tissue samples and live cells was demonstrated [47]. By using fiber lasers for excitation, multimodal imaging of human oncocytoma and carcinoma provided a detailed insight into cancer morphology and composition, enabling to discern between normal kidney tissue, tumor, and necrosis [27]. As shown in Figure 14.5, a sharp tumor border could be identified in case of oncocytoma. In the normal tissue, the typical morphology of tubules can be recognized, with a single layer of cells that surround an internal lumen and are surrounded by collagen fibers producing an intense SHG signal. Inside the tumor, the epithelial cells still form clusters that superficially resemble renal tubules, but that can be readily distinguished, thanks to the lack of

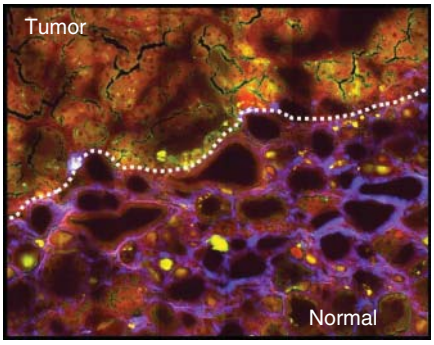

Figure 14.5 Multimodal nonlinear microscopic image of the border (dashed line) between a renal tumor (oncocytoma) and normal kidney tissue. Red: CARS; green: TPF; blue: SGH. (Reproduced with permission from Ref. [27]; © Wiley.)

internal lumen displayed by CARS and to the much SHG lower signal of stroma.

A multimodal NLO imaging system integrating CARS, sum-frequency generation (SFG), and TPF on the same platform was applied to visualize single cells and extracellular matrix (ECM) in fresh carotid arteries [48]. CARS signals arising from CH_2-rich membranes allowed visualization of endothelial cells and smooth muscle cells of the arterial wall; the ECM organization was addressed by TPF from elastin autofluorescence and SFG signals from collagen fibrils. Finally, multimodal CARS microscopy proved very effective in study of morphology and composition of atherosclerotic plaques [49, 50].

The use of the technique in dermatology has already attained a diagnostic level and a hybrid multiphoton CARS tomograph [51, 52] was certified for the clinical use [51].

CARS microscopy is especially suited to image the tissue using the compositional contrast derived from lipid content. The nervous tissue, in both central and peripheral nervous systems, is characterized by a very high content of fats because of the axonal myelin. The different lipid content that characterizes the various nervous tissues generates a compositional contrast in the CARS image that enables to visualize tissue structures. Multimodal CARS microscopy enables to image whole organs, as well as "zoom in" to visualize subcellular details. The tissue structures are fully visualized by the combination of CARS with TPF and SHG. The possibility of label-free imaging of nervous tissue *in vivo* could open a series of important biological and clinical applications for a better understanding and treatment of different pathologic and traumatic states of the nervous system.

14.4.2
Brain Structures and Brain Tumors

The main interest goes to the intraoperative imaging of brain tumors, with the aim to perform *in situ* pathology. Currently, intraoperative neuropathology is

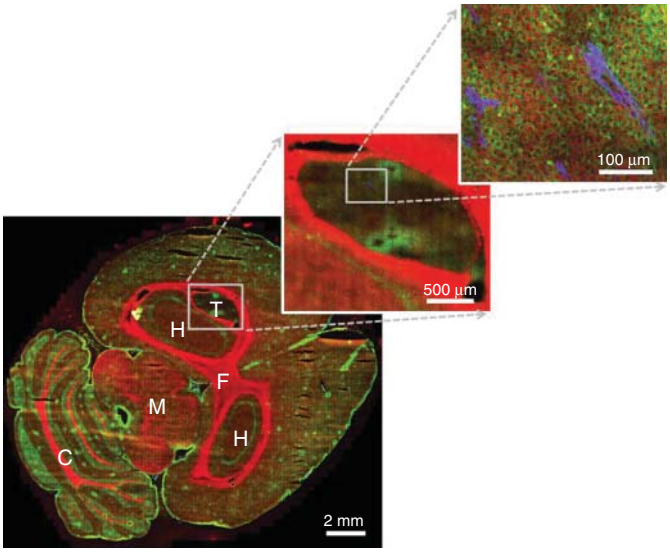

Figure 14.6 Multimodal CARS picture of an unstained mouse brain section with a glioblastoma located in the hippocampus. The CARS signal tuned on the C–H stretching mode of CH_2 groups at 2850 cm^{-1} to image the lipid distribution is shown in red, TPF acquired in the range 500–550 nm is in green, and SHG is in blue. The combination of the three imaging modalities enables to clearly discern the brain structure (C, cerebellum; M, medulla; H, hippocampus; F, axonal fiber tracts). The tumor (T) is grown inside axonal tracts that surround the left hippocampus and is recognizable from the low CARS signal (as brain tumors have lower lipid content with respect the normal tissue). The magnified images of the tumor enable to discern the tumor border with high precision and many details of the neoplastic tissue.

performed on biopsies and this has two drawbacks. First, it slows down the overall operative procedure. Second, normal and neoplastic tissues are distinguished only a posteriori. Providing the surgeon with a fast method to discern *in situ* between normal and neoplastic tissues would greatly improve the possibility of a complete tumor resection by sparing healthy functional tissue. As tumor composition is different from the normal brain tissue, imaging techniques providing chemical contrast – like CARS – can be applied for *in vivo* tumor recognition.

In fact, CARS and multimodal CARS are very sensitive tools to retrieve brain structures down the finest details (Figure 14.6). In the brain, white matter tracts (very rich in myelin) and gray matter regions (poorer in lipids) are visualized by the different CARS contrast. TPF contribute in displaying cellular structures and identify tissue layering, while SHG shows the fibrillar collagen of the ECM of the connective tissue or of the blood vessels. Tumors and tumor margins can be identified by exploiting the lower lipid content that characterize the tumor when compared to normal brain tissue.

The feasibility of CARS microscopy for tissue diagnosis using unstained brain tissue was first demonstrated by Evans *et al.* [53]. CARS microscopy of fresh

unfixed *ex vivo* mouse brain was used to identify normal gray and white matter structures on several scales, to distinguish glioma from normal brain tissue. CARS microscopy was applied to image-myelinated fibers in different regions of a mouse brain by Fu *et al.* as well [54]. The capability of imaging myelinated fibers without exogenous labeling was used to map the whole brain white matter in brain slices and to analyze the microstructural anatomy of brain axons. The combination of CARS with TPF allowed multimodal imaging of myelinated axons and other cells. Furthermore, CARS microscopy of brain on an upright microscope was also demonstrated *in vivo* for the first time. Finally, Pohling *et al.* [15] applied multiplex CARS to the investigation of fresh mouse brain tissue. The combination of imaginary part extraction followed by principal component analysis led to color contrast between gray and white matter as well as layers of granule and Purkinje cells in the cerebellum. In contrast to previous CARS studies of brain tissue, different biological structures were visualized simultaneously and separated from each other.

Unstained samples from the brain of a domestic pig have been investigated by Meyer *et al.* [55] using a multimodal nonlinear imaging approach combining CARS, SHG, and TPF. Furthermore, a human brain specimen with metastasis of lung carcinoma was additionally analyzed. CARS microscopy within the CH-stretching region enabled detection of single cells and nuclei in a brain metastasis, as well as histopathologic grading of tissue [56].

Multimodal NLO microscopy, integrating CARS, TPF and SHG, was used for pathological assessment of human brain tumors on tissue sections [57], to visualize morphological and biochemical information for brain tumor diagnosis and to differentiate between normal and neoplastic tissue according to their morphological features. Figure 14.7 shows the multimodal CARS image of a meningioma as an example. Meningiomas arise from arachnoid cells and tend to be attached to dura. Nevertheless, the profoundly different ECM composition enables to immediately discern between tumor and normal dura.

14.4.3
Normal and Injured Spinal Cord

Axonal tracts in the spinal cord are covered by myelin, an insulating lipid-based substance, which is of paramount importance for the correct signal transmission through the axons and is involved is a series of pathological and traumatic states.

CARS microscopy was used for the study of axonal myelin under physiological conditions in spinal cord, using white matter strips isolated from the spinal cord of guinea pigs and kept alive in oxygen-bubbled Krebs' solution. Both forward- and epi-detected CARS were used to probe the axon bundles and resolve detailed structures such as nodes of Ranvier. In addition, simultaneous CARS microscopy of myelin and TEPF imaging of intra- and extra-axonal calcium was demonstrated [58].

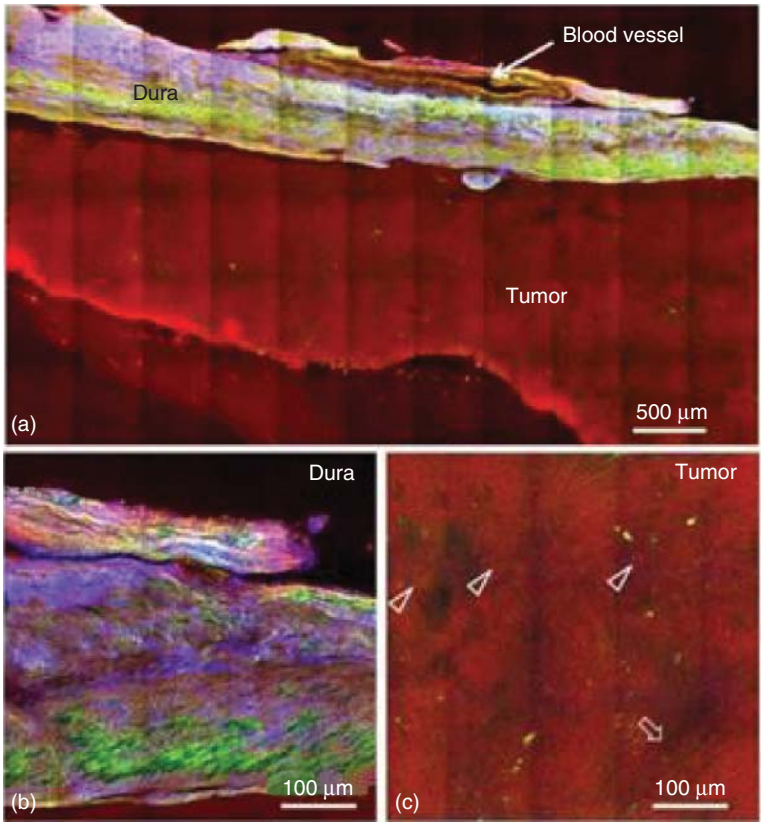

Figure 14.7 Multimodal NLO image of an unstained section of human meningioma; red: CARS; green: TPF; blue: SHG. (a) Overview of the biopsy sample; the tumor is below the dura, a portion of dura is recognizable in the upper part, with a blood vessel, (b) detail of the dura, and (c) detail of the tumor; the arrowheads indicate lobules and small whorls of tumor cells, the arrow indicates a region where the cells are aligned. (Reproduced with permission from Ref. [57]; © SPIE).

Multimodal NLO imaging, for example, simultaneous acquisition of CARS, TPF, and SHG, demonstrated to be able to underline the main three processes triggered by injury in rat spinal cord: demyelination, scarring, and inflammation [26]. As shown in Figure 14.8, reference spectroscopic mapping investigations underlined the different areas and the degree of damage, which could be discerned by a decrease in the intensity of lipid-related bands (accounting for demyelination) as well as by an increase in bands related to ECM components (accounting for fibrotic scarring). NLO microscopy could retrieve the same information in a faster way and in much higher lateral resolution. The distribution of lipids inside the tissue could be obtained from CARS microscopy by tuning the system to excite the symmetric stretching of C–H at 2850 cm^{-1}. Moreover, the fibrotic scar, which is characterized by collagen, could be efficiently addressed by SHG

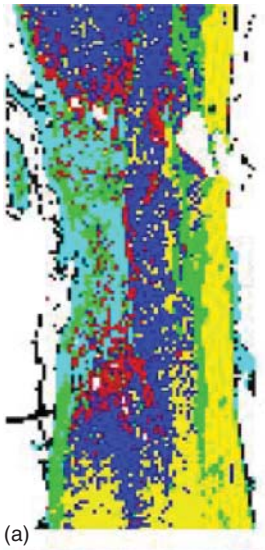
(a)

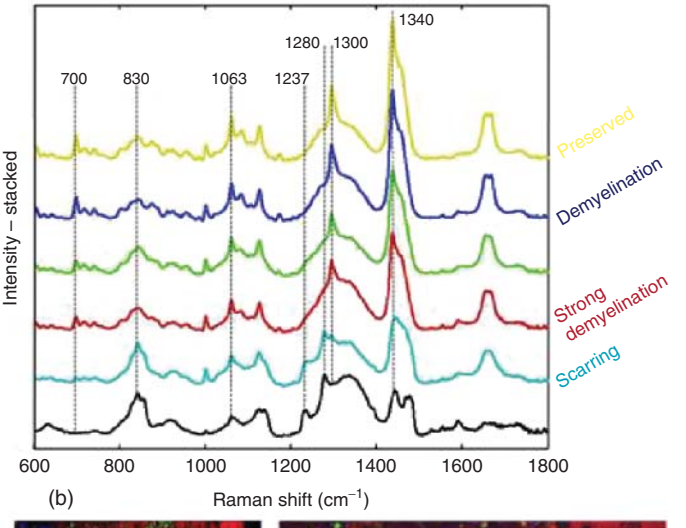
1340
1280
1300
700
830
1063
1237
Preserved
Demyelination
Strong demyelination
Scarring
Intensity – stacked
600
800
1000
1200
1400
1600
1800
(b)
Raman shift (cm−1)

(c)

(d)

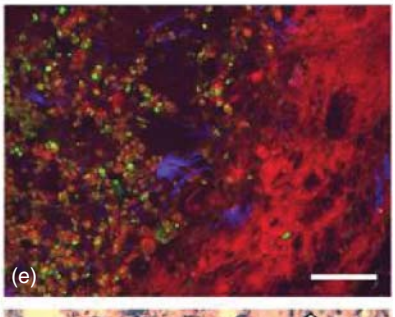
(e)

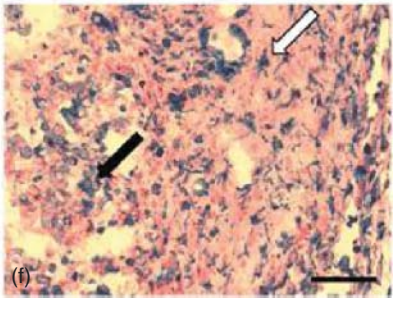
(f)

imaging. Moreover, many morphological details provided by the technology carry significant medical information that cannot be addressed by conventional spectroscopy. The auto-fluorescence green signal arises from round structures that are mainly localized inside the lesion and spread into the surrounding tissue. These structures match cell bodies in size and shape and might be identified as macrophages. In fact, the comparison between Iba1 immunohistochemical staining and multimodal imaging of the unstained consecutive section matched the distribution of activated microglia/macrophages with the distribution pattern of the auto-fluorescent structures. Therefore, TPF enabled to address tissue inflammation.

The ability of CARS microscopy to image the myelin sheath in its natural state was applied to characterize traumatic and pathological states of spinal cord in animal models. Chemically induced myelin degradation and swelling in *ex vivo* spinal tissues and *in vivo* mouse sciatic nerves were monitored by the decrease in CARS intensity and loss of excitation polarization dependence [59]. A combination of immunofluorescence and CARS microscopy was used to visualize myelin retraction at the nodes of Ranvier and at the pathological changes of ion channels in white matter strips from the spinal cord of adult guinea pig [60]. CARS microscopy enabled to image demyelination and remyelination at single-axon level in live rats [61], to study the repair of traumatically injured rat spinal cord by measuring the intra- and extra-axonal space of white matter [62], and to investigate in real-time response of myelin to electrical stimulation [63]. Moreover, CARS microscopy of myelin lipids was also applied to the study of experimental autoimmune encephalomyelitis, which is the animal model for multiple sclerosis. Progressive demyelination with retraction of paranodal

Figure 14.8 Spinal cord injury. (a) spectral image obtained by *k*-means cluster analyses of conventional Raman data acquired on a tissue section. (b) Cluster centroid spectra, ordered from top to bottom by decreasing lipid content. Highlighted bands are significant for tissue degeneration characterization. (c) Immunofluorescence staining on a consecutive section of the sample; red: β-III-tubulin immunoreactivity; green: laminin immunoreactivity; blue: DAPI nuclear staining. The dashed line indicates the resection cavity. Bar: 1 mm. (d) Nonlinear multimodal image of an unstained, nonconsecutive section. Red: CARS; green: endogenous TPF; blue: SHG. The CARS signal shows the distribution of lipid, the TPF signal identifies phagocytic microglia/macrophages, the SHG signal is generated by collagen fibers. The dotted line indicates the area of strongest inflammation, the dashed line indicates the core of fibrotic scarring. Bar: 1 mm. (e) Nonlinear multimodal image of a region at the border of the lesion (box in (d)). Intense CARS signal (red) characterizes the normal nervous tissue on the right side of the picture where almost no macrophages are underlined by endogenous fluorescence (green). Bar: 100 μm. (f) Iba1 immunohistochemical staining of a region similar to (e) (box in (d)); the round, phagocytic cells (black arrow) on the left side of the pictures matches the fluorescent cell pattern displayed by green autofluorescence in (c). In the normal tissue on the right side, the immunohistochemical staining labeled mainly star-shaped microglia (white arrow). Bar: 100 μm. (Modified with permission from Ref. [26]; © ACS.)

myelin at the onset of disease and at the borders of acute demyelinating lesions, as well as partial paranodal myelin restoration during disease remission, was studied [64].

References

1. Maker, P.D. and Terhune, R.W. (1965) Study of optical effects due to an induced polarization third order in electric field strength. *Phys. Rev.*, **137**, A801–A818.
2. Begley, R.F., Harvey, A.B., and Byer, R.L. (1974) Coherent anti-Stokes raman-spectroscopy. *Appl. Phys. Lett.*, **25**, 387–390.
3. Muller, M. and Zumbusch, A. (2007) Coherent anti-Stokes Raman scattering microscopy. *ChemPhysChem*, **8**, 2156–2170.
4. Cheng, J.X., Volkmer, A., and Xie, X.S. (2002) Theoretical and experimental characterization of coherent anti-Stokes Raman scattering microscopy. *J. Opt. Soc. Am. B: Opt. Phys.*, **19**, 1363–1375.
5. Cheng, J.X. and Xie, X.S. (2004) Coherent anti-Stokes Raman scattering microscopy: instrumentation, theory, and applications. *J. Phys. Chem. B*, **108**, 827–840.
6. Akimov, D., Chatzipapadopoulos, S., Meyer, T., Tarcea, N., Dietzek, B., Schmitt, M., and Popp, J. (2009) Different contrast information obtained from CARS and nonresonant FWM images. *J. Raman Spectrosc.*, **40**, 941–947.
7. Gachet, D., Billard, F., Sandeau, N., and Rigneault, H. (2007) Coherent anti-Stokes Raman Scattering (CARS) microscopy imaging at interfaces: evidence of interference effects. *Opt. Express*, **15**, 10408–10420.
8. Cheng, J.X., Jia, Y.K., Zheng, G.F., and Xie, X.S. (2002) Laser-scanning coherent anti-Stokes Raman scattering microscopy and applications to cell biology. *Biophys. J.*, **83**, 502–509.
9. Djaker, N., Gachet, D., Sandeau, N., Lenne, P.F., and Rigneault, H. (2006) Refractive effects in coherent anti-Stokes Raman scattering microscopy. *Appl. Opt.*, **45**, 7005–7011.
10. Popov, K.I., Pegoraro, A.F., Stolow, A., and Ramunno, L. (2011) Image formation in CARS microscopy: effect of the Gouy phase shift. *Opt. Express*, **19**, 5902–5911.
11. Evans, C.L. and Xie, X.S. (2008) Coherent anti-Stokes raman scattering microscopy: chemical imaging for biology and medicine. *Annu. Rev. Anal. Chem.*, **1**, 883–909.
12. Wang, H.W., Fu, Y., Huff, T.B., Le, T.T., Wang, H.F., and Cheng, J.X. (2009) Chasing lipids in health and diseases by coherent anti-Stokes Raman scattering microscopy. *Vib. Spectrosc.*, **50**, 160–167.
13. Chen, J.X., Volkmer, A., Book, L.D., and Xie, X.S. (2002) Multiplex coherent anti-Stokes Raman scattering microspectroscopy and study of lipid vesicles. *J. Phys. Chem. B*, **106**, 8493–8498.
14. Bonn, M., Muller, M., Rinia, H.A., and Burger, K.N.J. (2009) Imaging of chemical and physical state of individual cellular lipid droplets using multiplex CARS microscopy. *J. Raman Spectrosc.*, **40**, 763–769.
15. Pohling, C., Buckup, T., Pagenstecher, A., and Motzkus, M. (2011) Chemoselective imaging of mouse brain tissue via multiplex CARS microscopy. *Biomed. Opt. Express*, **2**, 2110–2116. doi: 10.1364/BOE.2.002110 [doi];147302 [pii]
16. Krafft, C., Dietzek, B., Schmitt, M., and Popp, J. (2012) Raman and coherent anti-Stokes Raman scattering microspectroscopy for biomedical applications. *J. Biomed. Opt.*, **17**, 040801.
17. Duncan, M.D., Reintjes, J., and Manuccia, T.J. (1982) Scanning coherent anti-Stokes Raman microscope. *Opt. Lett.*, **7**, 350–352.
18. Zumbusch, A., Holtom, G.R., and Xie, X.S. (1999) Three-dimensional vibrational imaging by coherent anti-Stokes

Raman scattering. *Phys. Rev. Lett.*, **82**, 4142–4145.
19. Cheng, J.X., Volkmer, A., Book, L.D., and Xie, X.S. (2001) An epi-detected coherent anti-Stokes raman scattering (E-CARS) microscope with high spectral resolution and high sensitivity. *J. Phys. Chem. B*, **105**, 1277–1280.
20. Burkacky, O., Zumbusch, A., Brackmann, C., and Enejder, A. (2006) Dual-pump coherent anti-Stokes-Raman scattering microscopy. *Opt. Lett.*, **31**, 3656–3658.
21. Ganikhanov, F., Carrasco, S., Xie, X.S., Katz, M., Seitz, W., and Kopf, D. (2006) Broadly tunable dual-wavelength light source for coherent anti-Stokes Raman scattering microscopy. *Opt. Lett.*, **31**, 1292–1294.
22. Baumgart, M., Gottschall, T., Abreu-Afonso, J., Diez, A., Meyer, T., Dietzek, B., Rothhardt, M., Popp, J., Limpert, J., and Tunnermann, A. (2012) Alignment-free, all-spliced fiber laser source for CARS microscopy based on four-wave-mixing. *Opt. Express*, **20**, 21010–21018.
23. Krauss, G., Hanke, T., Sell, A., Trautlein, D., Leitenstorfer, A., Selm, R., Winterhalder, M., and Zumbusch, A. (2009) Compact coherent anti-Stokes Raman scattering microscope based on a picosecond two-color Er:fiber laser system. *Opt. Lett.*, **34**, 2847–2849.
24. Selm, R., Winterhalder, M., Zumbusch, A., Krauss, G., Hanke, T., Sell, A., and Leitenstorfer, A. (2010) Ultrabroadband background-free coherent anti-Stokes Raman scattering microscopy based on a compact Er:fiber laser system. *Opt. Lett.*, **35**, 3282–3284.
25. Zumbusch, A., Selm, R., Winterhalder, M., Krauss, G., Hanke, T., Sell, A., Traeutlein, D., and Leitenstorfer, A. (2010) CARS microscopy with a fiber laser. Abstracts of Papers of the American Chemical Society, vol. 239.
26. Galli, R., Uckermann, O., Winterhalder, M.J., Sitoci-Ficici, K.H., Geiger, K.D., Koch, E., Schackert, G., Zumbusch, A., Steiner, G., and Kirsch, M. (2012) Vibrational spectroscopic imaging and multiphoton microscopy of spinal cord injury. *Anal. Chem.*, **84**, 8707–8714.
27. Galli, R., Sablinskas, V., Dasevicius, D., Laurinavicius, A., Jankevicius, F., Koch, E., and Steiner, G. (2013) Nonlinear optical microscopy of kidney tumours. *J. Biophotonics*, **8**, e58332. doi: 10.1002/jbio.201200216
28. Nan, X.L., Cheng, J.X., and Xie, X.S. (2003) Vibrational imaging of lipid droplets in live fibroblast cells with coherent anti-Stokes Raman scattering microscopy. *J. Lipid Res.*, **44**, 2202–2208.
29. Nan, X.L., Potma, E.O., and Xie, X.S. (2006) Nonperturbative chemical imaging of organelle transport in living cells with coherent anti-Stokes Raman scattering microscopy. *Biophys. J.*, **91**, 728–735.
30. Day, J.P.R., Rago, G., Domke, K.F., Velikov, K.P., and Bonn, M. (2010) Label-free imaging of lipophilic bioactive molecules during lipid digestion by multiplex coherent anti-Stokes Raman scattering microspectroscopy. *J. Am. Chem. Soc.*, **132**, 8433–8439.
31. Nan, X.L., Tonary, A.M., Stolow, A., Xie, X.S., and Pezacki, J.P. (2006) Intracellular imaging of HCV RNA and cellular lipids by using simultaneous two-photon fluorescence and coherent anti-Stokes Raman scattering microscopies. *ChemBioChem*, **7**, 1895–1897.
32. Lyn, R.K., Kennedy, D.C., Sagan, S.M., Blais, D.R., Rouleau, Y., Pegoraro, A.F., Xie, X.S., Stolow, A., and Pezacki, J.P. (2009) Direct imaging of the disruption of hepatitis C virus replication complexes by inhibitors of lipid metabolism. *Virology*, **394**, 130–142.
33. Pliss, A., Kuzmin, A.N., Kachynski, A.V., and Prasad, P.N. (2010) Nonlinear optical imaging and Raman microspectrometry of the cell nucleus throughout the cell cycle. *Biophys. J.*, **99**, 3483–3491.
34. Konorov, S.O., Glover, C.H., Piret, J.M., Bryan, J., Schulze, H.G., Blades, M.W., and Turner, R.F.B. (2007) In situ analysis of living embryonic stem cells by coherent anti-Stokes Raman microscopy. *Anal. Chem.*, **79**, 7221–7225.
35. Downes, A., Mouras, R., Bagnaninchi, P., and Elfick, A. (2011) Raman spectroscopy and CARS microscopy of stem cells and their derivatives. *J. Raman Spectrosc.*, **42**, 1864–1870.

36. Evans, C.L., Potma, E.O., Puoris'haag, M., Cote, D., Lin, C.P., and Xie, X.S. (2005) Chemical imaging of tissue in vivo with video-rate coherent anti-Stokes Raman scattering microscopy. *Proc. Natl. Acad. Sci. U.S.A.*, **102**, 16807–16812.
37. Hellerer, T., Axang, C., Brackmann, C., Hillertz, P., Pilon, M., and Enejder, A. (2007) Monitoring of lipid storage in Caenorhabditis elegans using coherent anti-Stokes Raman scattering (CARS) microscopy. *Proc. Natl. Acad. Sci. U.S.A.*, **104**, 14658–14663.
38. Le, T.T., Duren, H.M., Slipchenko, M.N., Hu, C.D., and Cheng, J.X. (2010) Label-free quantitative analysis of lipid metabolism in living Caenorhabditis elegans. *J. Lipid Res.*, **51**, 672–677.
39. Chien, C.H., Chen, W.W., Wu, J.T., and Chang, T.C. (2012) Investigation of lipid homeostasis in living Drosophila by coherent anti-Stokes Raman scattering microscopy. *J. Biomed. Opt.*, **17**, 126001.
40. Wu, Y.M., Chen, H.C., Chang, W.T., Jhan, J.W., Lin, H.L., and Liau, I. (2009) Quantitative assessment of hepatic fat of intact liver tissues with coherent anti-Stokes Raman scattering microscopy. *Anal. Chem.*, **81**, 1496–1504.
41. Le, T.T., Huff, T.B., and Cheng, J.X. (2009) Coherent anti-Stokes Raman scattering imaging of lipids in cancer metastasis. *BMC Cancer*, **9**, 42.
42. Mitra, R., Chao, O., Urasaki, Y., Goodman, O.B., and Le, T.T. (2012) Detection of lipid-rich prostate circulating tumour cells with coherent anti-Stokes Raman scattering microscopy. *BMC Cancer*, **12**, 540.
43. Yang, Y.L., Li, F.H., Gao, L., Wang, Z.Y., Thrall, M.J., Shen, S.S., Wong, K.K., and Wong, S.T.C. (2011) Differential diagnosis of breast cancer using quantitative, label-free and molecular vibrational imaging. *Biomed. Opt. Express*, **2**, 2160–2174.
44. Gao, L., Zhou, H.J., Thrall, M.J., Li, F., Yang, Y.L., Wang, Z.Y., Luo, P.F., Wong, K.K., Palapattu, G.S., and Wong, S.T.C. (2011) Label-free high-resolution imaging of prostate glands and cavernous nerves using coherent anti-Stokes Raman scattering microscopy. *Biomed. Opt. Express*, **2**, 915–926.
45. Gao, L., Li, F.H., Thrall, M.J., Yang, Y.L., Xing, J., Hammoudi, A.A., Zhao, H., Massoud, Y., Cagle, P.T., Fan, Y.B., Wong, K.K., Wang, Z.Y., and Wong, S.T.C. (2011) On-the-spot lung cancer differential diagnosis by label-free, molecular vibrational imaging and knowledge-based classification. *J. Biomed. Opt.*, **16**, 096004.
46. Gao, L., Wang, Z.Y., Li, F.H., Hammoudi, A.A., Thrall, M.J., Cagle, P.T., and Wong, S.T.C. (2012) Differential diagnosis of lung carcinoma with coherent anti-Stokes Raman scattering imaging. *Arch. Pathol. Lab. Med.*, **136**, 1502–1510.
47. Pegoraro, A.F., Ridsdale, A., Moffatt, D.J., Pezacki, J.P., Thomas, B.K., Fu, L.B., Dong, L., Fermann, M.E., and Stolow, A. (2009) All-fiber CARS microscopy of live cells. *Opt. Express*, **17**, 20700–20706.
48. Wang, H.W., Le, T.T., and Cheng, J.X. (2008) Label-free imaging of arterial cells and extracellular matrix using a multimodal CARS microscope. *Opt. Commun.*, **281**, 1813–1822.
49. Lim, R.S., Suhalim, J.L., Miyazaki-Anzai, S., Miyazaki, M., Levi, M., Potma, E.O., and Tromberg, B.J. (2011) Identification of cholesterol crystals in plaques of atherosclerotic mice using hyperspectral CARS imaging. *J. Lipid Res.*, **52**, 2177–2186.
50. Matthaus, C., Dochow, S., Bergner, G., Lattermann, A., Romeike, B.F.M., Marple, E.T., Krafft, C., Dietzek, B., Brehm, B.R., and Popp, J. (2012) In vivo characterization of atherosclerotic plaque depositions by raman-probe spectroscopy and in vitro coherent anti-Stokes Raman scattering microscopic imaging on a rabbit model. *Anal. Chem.*, **84**, 7845–7851.
51. Breunig, H.G., Buckle, R., Kellner-Hofer, M., Weinigel, M., Lademann, J., Sterry, W., and Konig, K. (2012) Combined in vivo multiphoton and CARS imaging of healthy and disease-affected human skin. *Microsc. Res. Tech.*, **75**, 492–498.
52. Breunig, H.G., Weinigel, M., Buckle, R., Kellner-Hofer, M., Lademann, J., Darvin, M.E., Sterry, W., and Konig, K. (2013) Clinical coherent anti-Stokes Raman

scattering and multiphoton tomography of human skin with a femtosecond laser and photonic crystal fiber. *Laser Phys. Lett.*, **10**, 025604.

53. Evans, C.L., Xu, X., Kesari, S., Xie, X.S., Wong, S.T., and Young, G.S. (2007) Chemically-selective imaging of brain structures with CARS microscopy. *Opt. Express*, **15**, 12076–12087. 141231 [pii].
54. Fu, Y., Huff, T.B., Wang, H.W., Wang, H.F., and Cheng, J.X. (2008) Ex vivo and in vivo imaging of myelin fibers in mouse brain by coherent anti-Stokes Raman scattering microscopy. *Opt. Express*, **16**, 19396–19409.
55. Meyer, T., Bergner, N., Bielecki, C., Krafft, C., Akimov, D., Romeike, B.F., Reichart, R., Kalff, R., Dietzek, B., and Popp, J. (2011) Nonlinear microscopy, infrared, and Raman microspectroscopy for brain tumor analysis. *J. Biomed. Opt.*, **16**, 021113. doi: 10.1117/1.3533268
56. Meyer, T., Bergner, N., Medyukhina, A., Dietzek, B., Krafft, C., Romeike, B.F.M., Reichart, R., Kalff, R., and Popp, J. (2012) Interpreting CARS images of tissue within the C-H-stretching region. *J. Biophotonics*, **5**, 729–733.
57. Galli, R., Uckermann, O., Tamosaityte, S., Geiger, K.D., Schackert, G., Steiner, G., Koch, E., and Kirsch, M. (2013) CARS and non-linear microscopy imaging of brain tumors. *Proc. SPIE*, **8797**, 87970E.
58. Wang, H.F., Fu, Y., Zickmund, P., Shi, R.Y., and Cheng, J.X. (2005) Coherent anti-Stokes Raman scattering imaging of axonal myelin in live spinal tissues. *Biophys. J.*, **89**, 581–591. doi: 10.1529/biophysj.105.061911
59. Fu, Y., Wang, H.F., Huff, T.B., Shi, R., and Cheng, J.X. (2007) Coherent anti-Stokes Raman scattering imaging of myelin degradation reveals a calcium-dependent pathway in lyso-PtdCho-induced demyelination. *J. Neurosci. Res.*, **85**, 2870–2881.
60. Ouyang, H., Sun, W.J., Fu, Y., Li, J.M., Cheng, J.X., Nauman, E., and Shi, R.Y. (2010) Compression induces acute demyelination and potassium channel exposure in spinal cord. *J. Neurotrauma*, **27**, 1109–1120. doi: 10.1089/neu.2010.1271
61. Shi, Y.Z., Zhang, D.L., Huff, T.B., Wang, X.F., Shi, R.Y., Xu, X.M., and Cheng, J.X. (2011) Longitudinal in vivo coherent anti-Stokes Raman scattering imaging of demyelination and remyelination in injured spinal cord. *J. Biomed. Opt.*, **16**, 106012.
62. Shi, Y.Z., Kim, S., Huff, T.B., Borgens, R.B., Park, K., Shi, R.Y., and Cheng, J.X. (2010) Effective repair of traumatically injured spinal cord by nanoscale block copolymer micelles. *Nat. Nanotechnol.*, **5**, 80–87.
63. Huff, T.B., Shi, Y.Z., Sun, W.J., Wu, W., Shi, R.Y., and Cheng, J.X. (2011) Real-time CARS imaging reveals a calpain-dependent pathway for paranodal myelin retraction during high-frequency stimulation. *PLoS One*, **6**, e17176.
64. Fu, Y., Frederick, T.J., Huff, T.B., Goings, G.E., Miller, S.D., and Cheng, J.X. (2011) Paranodal myelin retraction in relapsing experimental autoimmune encephalomyelitis visualized by coherent anti-Stokes Raman scattering microscopy. *J. Biomed. Opt.*, **16**, 106006.

15
Widefield FT-IR 2D and 3D Imaging at the Microscale Using Synchrotron Radiation

Eric C. Mattson, Miriam Unger, Julia Sedlmair, Michael Nasse, Ebrahim Aboualizadeh, Zahrasadat Alavi, and Carol J. Hirschmugl

15.1
Introduction

Widefield (WF) spectromicroscopy requires a multipixel detector for measuring thousands of signals in parallel. When combined with an extended high brightness source, such as a large aperture storage ring beamline, and microscope optics, the effective geometric size of a pixel at the sample can be reduced to $0.54 \times 0.54\ \mu m^2$ without sacrificing signal-to-noise quality of spectra [1]. Thus, images are spatially oversampled (similar to megapixel cameras), such that diffraction-limited images can be retrieved at all wavelengths, simultaneously [2, 3]. Collecting high-quality projection images rapidly opens the possibility of measuring samples as a function of time [4] and rotation [5], in the latter case, employing tomographic reconstructions for 3D data recovery at every wavelength. These efforts provide access to 2D and 3D chemical imaging for functional groups that can be detected with mid-IR excitations. In this chapter, the characteristics of synchrotron or storage ring radiation, comparisons between synchrotron-based raster scanning (RS) spectromicroscopy and WF spectromicroscopy, deconvolution, spectromicrotomography, and relevant applications in energy, single-cell imaging, and cultural heritage are discussed.

15.1.1
Synchrotron IR Radiation Sources

High brightness sources of IR radiation are optimal for far-field spectromicroscopy with diffraction-limited spatial resolution. Major developments in sources of IR radiation include radiation emitted from storage rings (SRIR) [6] and lasers [7, 8]. These are high-brightness sources, which means they emit radiation that originates from a point-like spot, and the light is confined to a well-defined small beam (similar to laser beams). This property is desirable to achieve the highest spatially resolved data with spatial resolution comparable to that of the wavelength of the light (<1 μm to 10's μm) concurrent with high

Infrared and Raman Spectroscopic Imaging, Second Edition. Edited by Reiner Salzer, Heinz W. Siesler.
© 2014 Wiley-VCH Verlag GmbH & Co. KGaA. Published 2014 by Wiley-VCH Verlag GmbH & Co. KGaA.

spectral signal-to-noise ratio (SNR). Laser sources are typically monochromatic (providing light at one frequency) or narrowband (providing light across a narrow range of frequencies, for example, quantum cascade lasers [7] or optical parametric amplifier/difference frequency generation (OPA/DFG) [9–13]), while the storage ring sources are inherently broadband. Comparisons between these sources are summarized in Ref. [14].

15.1.2 Synchrotron-Based Infrared Raster-Scanned (IR SR) Spectromicroscopy

Conventional IR RS spectromicroscopy focuses an IR beam to a micrometer-scale spot using a Cassegrain or Schwarzschild optical arrangement [15, 16] and uses a dual-aperture confocal geometry. The aperture illuminates a selected sample area that is raster scanned through the beam to collect data for each pixel, serially, forming the hyperspectral data. The challenge of this approach is to focus enough light through the aperture and onto the sample to achieve sufficient SNR. Conventional thermal sources, with large emittance (area–angle product) and low brightness, provide low photon flux per solid angle. High brightness sources with very low emittance provide higher photon flux focused into a small area [6]. Synchrotron-based RS spectromicroscopy can illuminate sample areas down to 3 × 3 μm^2 [17]. However, to achieve the optimal spatial sampling, one would still need to spatially oversample using step sizes smaller than the pixel size. Since the raster step size is directly proportional to acquisition times and the smaller aperture sizes require longer times to achieve good SNR, this approach is prohibitive for rapid, high-resolution imaging.

15.1.3 Synchrotron-Based Infrared Widefield (IR WF) Spectromicroscopy

The IRENI (InfraRed ENvironmental Imaging) synchrotron beamline was recently developed [1, 18] to address the challenge of the trade-offs between spatial resolution, SNR, and acquisition times. Two unique components of this beamline differentiate it from other beamlines – an extended source to illuminate a large area at the sample plane and a commercial large area focal plane array (FPA) detector. Each element of the detector acts as one pixel in an IR image and contains an entire mid-IR spectrum. IRENI extracts 12 low-emittance synchrotron beams, whose brightness is ≈100 times that of a thermal source, to homogeneously illuminate 4096 pixels of an FPA detector with an effective pixel size of 0.54 × 0.54 μm^2. This is approximately one-hundredth (one-twentieth) the value typically employed for thermal source WF spectromicroscopy (synchrotron-based IR RS spectromicroscopy). A schematic diagram of the IRENI beamline with the individual beam paths and detector illumination is shown in Figure 15.1. It is of note that the FPA employed for imaging with IRENI is actually a 128 × 128 array; but, as stated above, IRENI effectively only uses a 64 × 64 pixel field of view (FOV) of the FPA when using the 74× objective. This

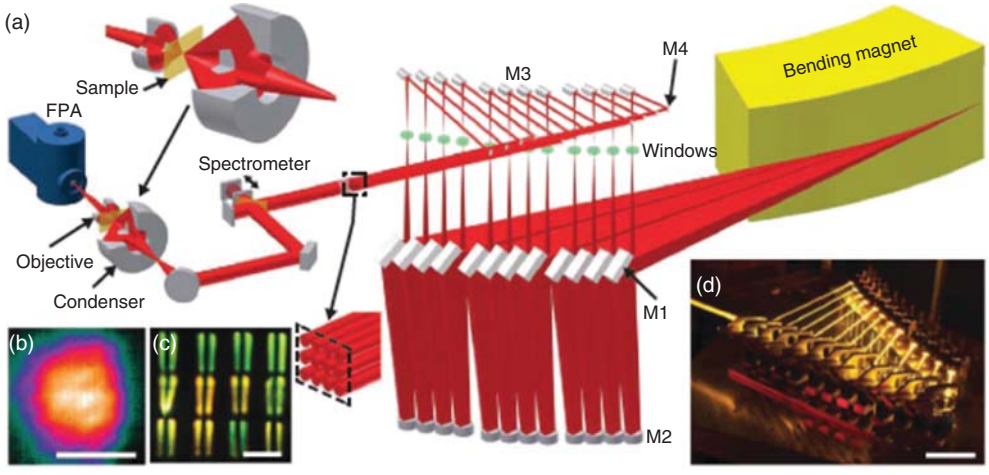

Figure 15.1 IRENI schematic (a) IRENI optical arrangement showing mirrors that direct the beam path from the bending magnet to the spectrometer, through the condensing Schwarzschild, onto the sample, through the objective, and onto the detector. (b) Defocused illumination of the IR beams onto the FPA detector. (c) Conventional image of the visible portion of the focused synchrotron beams. (d) Visualization of the beam path through the M3 and M4 mirrors by a time-lapse photo generated by scattering the visible portion of the beams. (Reproduced with permission from the Nature Publishing Group, Ref. [1] *Nature Methods*.)

limited area was chosen to achieve uniform illumination over the entire FOV, so that mosaicimages comprising many FPA images tiled together have a homogeneous SNR. Simulations reported by Nasse *et al.* [19] predicted that the array of defocused synchrotron beams extends over a maximum area of $80 \times 80\ \mu m^2$; however, the optimally illuminated area at the center of the array only extends over a region of $\approx 40 \times 40\ \mu m^2$. Given the 0.54 μm pixel size, this corresponds to the area effectively subtended by 74×74 pixels. Therefore, although it is possible to achieve some amount of flux over larger arrays (e.g., 96×96 pixels), uniform illumination is best achieved by truncating the effective array size. In practice, this optimally illuminated area is best captured by an array of 64×64 pixels or ≈35 μm.

In IR spectromicrotomagraphy experiments, described further later, the full 128×128 pixel area of the detector is employed. Here, an objective with lower magnification and numerical aperture (NA) is used so as to measure the lowest possible convergence angle and also illuminate as large of an area as possible. Since there is no mosaic-type buildup of FPA tiles in this experiment and the sample is measured from multiple orientations, a lower SNR at the edges of the illuminated areas poses very little problem. The high spatial resolution, good SNR, and low acquisition times provided by the experimental setup at this facility have enabled a broad range of applications from cultural heritage [20–22], materials science [23–25], entomology [26], nanotoxicity [27], tissue [28, 29], and single-cell morphology and biochemistry [30–32].

15.1.4
Synchrotron-Based Infrared Spectromicrotomography

Exploiting the rapid 2D spectral image, acquisition capability of IRENI enables acquisition of a large number of transmission images as a sample is precisely rotated [5]. Thus, collection of projection images as a function of sample angle corresponds to a tomographic data set. For each wavelength, a full 3D representation of the sample can be reconstructed [5], and because we collect a full mid-IR spectrum for each data point, we can produce 4D reconstructions: three spatial dimensions plus a spectral dimension. We have therefore created a novel spectromicrotomography technique that provides not only the rich spectral information and chemical fingerprinting of Fourier Transform Infrared (FT-IR) spectroscopy but also the 3D distribution of those spectral signatures throughout the sample. This spectromicrotomography technique greatly enhances the capabilities of both FT-IR spectroscopy and tomography by creating a "full-color" microtomography where colors can be assigned by specific spectral identification or spectral changes, and each voxel contains a full IR spectrum.

15.2
Optical Evaluation

15.2.1
Microscopy Optics and Diffraction-Limited Resolution

The capabilities afforded by IRENI, namely high SNR, widefield illumination, and spatial oversampling, have lead to significant advances in characterization of IR microscope optics and imaging performance. Here, the spatial resolution and wavelength-dependent point spread functions (PSFs) for a 74× objective (NA = 0.65) are discussed.

As photon-based microscopy approaches increasingly smaller length scales, spatial resolution is limited by the so-called diffraction limit, which arises because of the finite NA of an imaging system, that is, the limited angular region from which an objective can collect the light from the sample being imaged. Consequently, imaging a point source of radiation with a finite objective results in a blurring of the point within the resulting image; the response of the imaging system to a point source is known as the point spread function (PSF). When the distance between the source and observation point of the measurement is much greater than the object being imaged, diffraction effects become relevant, and the blurring of the point source can be considered as physically arising from diffraction of the plane waves radiating from the source and from the aperture of the objective. The physical characteristics of the PSF determine the resolution of the resulting images generated from the optical system since each object being imaged is in essence a superposition of point sources, and the measured image is a convolution of the "true" image with the PSF. The Rayleigh

criterion frames the resolution of the optical system within the characteristics of the PSF and the NA of the objective. The Rayleigh criterion states that the lowest achievable resolution corresponds to the point at which the central maximum of one PSF overlaps with the first zero-crossing of another PSF. Unlike conventional lenses, the resolution criterion for Schwarzschild objectives cannot be cast in closed form. Rather, the contrast difference for conventional lenses is used as the standard for resolution [33]; specifically, for conventional lenses the contrast difference for two PSFs at the Rayleigh criterion is exactly 26.4%. This is the so-called Stelzer or contrast resolution criterion. Thus, for IR objectives, two objects are considered resolved if the contrast difference between them is ≥26.4%. This contrast resolution criterion will be used in the following sections as a marker for spatial resolution.

15.2.2
Experimental and Simulated Point Spread Functions

As measured data are determined by the PSF, understanding IR imaging data critically depends on understanding the PSF of the microscope used. The PSF of the 74× objective used in the Bruker Hyperion 3000 microscope, applied for most of the data presented in this chapter, was determined by measuring the transmission through a 2 μm pinhole at the sample plane, yielding images of the PSF from 1500–4000 cm^{-1}. Figure 15.2 shows the measured PSFs for a 74× objective lens on the Bruker Hyperion 3000 IR microscope, observed at three different locations in the FOV at three different wavelengths. The overall similarity of the PSF across the FOV indicates that the PSF is shift invariant; and as expected a broadening is observed with increasing wavelength. As compared to the conventional Airy function, the Schwarzschild diffraction pattern has amplified intensity of the diffraction maxima in the PSF and a narrower central maximum [3, 15, 34]. The characteristics of the PSF can be understood from Kirchhoff's scalar diffraction theory [35], where the objective is approximated as an annular aperture, described in detail in Ref. [3].

The PSF of a 36× (NA = 0.5) objective was characterized as well [2]; this objective is important for experiments where larger working distance is required. The PSFs as a function of wavelength of the 36× (NA = 0.5) objective are compared to those of the 74× objective in Figure 15.3. In this figure, a–c and g–i show images of the raw PSFs, and the curves in d–f and j–l show profiles extracted from the center of the measured PSFs (black curves). The raw data are compared to fits of the PSF for an analytic annular diffraction pattern, describing the Schwarzschild objective (red curve), and the agreement between the raw data and fit to the model indicate that the annulus is an appropriate approximation to the geometric structure of the objective. As can be seen from these center profiles, the lower magnification and NA of the 36× result in the coarser sampling (1.1 μm geometric pixel size at the sample plane) and the larger spatial extent of the PSF.

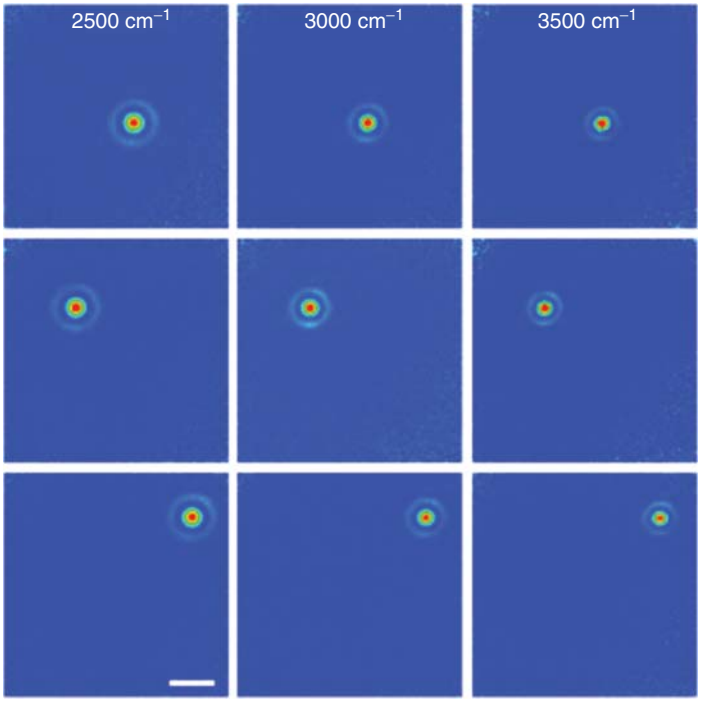

Figure 15.2 Measured PSFs of IRENI. Measured PSFs observed at three different frequencies and three different locations in the field of view. The scale bar is 10 μm. (Reproduced with permission from Copyright 2012 American Chemical Society Publications, Ref. [3] Analytical Chemistry.)

15.3 Mathematical Evaluation of Hyperspectral Cubes

15.3.1 Hyperspectral Deconvolution

Spatial deconvolution of hyperspectral cubes affords the possibility to enhance the spatial resolution that is limited by the diffraction of the imaging wavelength. The problem of deconvolution is substantially more complicated for IR data than for conventional visible microscopy due to the broadband nature of the data. The PSF varies as a function of wavelength, and every image in the hyperspectral cube needs to be reconstructed and normalized such that the resulting spectra at each pixel are reasonable and faithful. In the approach discussed here, a 2D restoration method based on Fourier inversion is applied to an IR image at every wavelength, and the overall image intensity is normalized. Then, these images are reassembled into a hyperspectral cube, from which the reconstructed spectra are extracted. The approach taken for the deconvolution is as follows [2, 3]: the measured image is assumed to be a convolution of the true image and the PSF, and the PSF is a

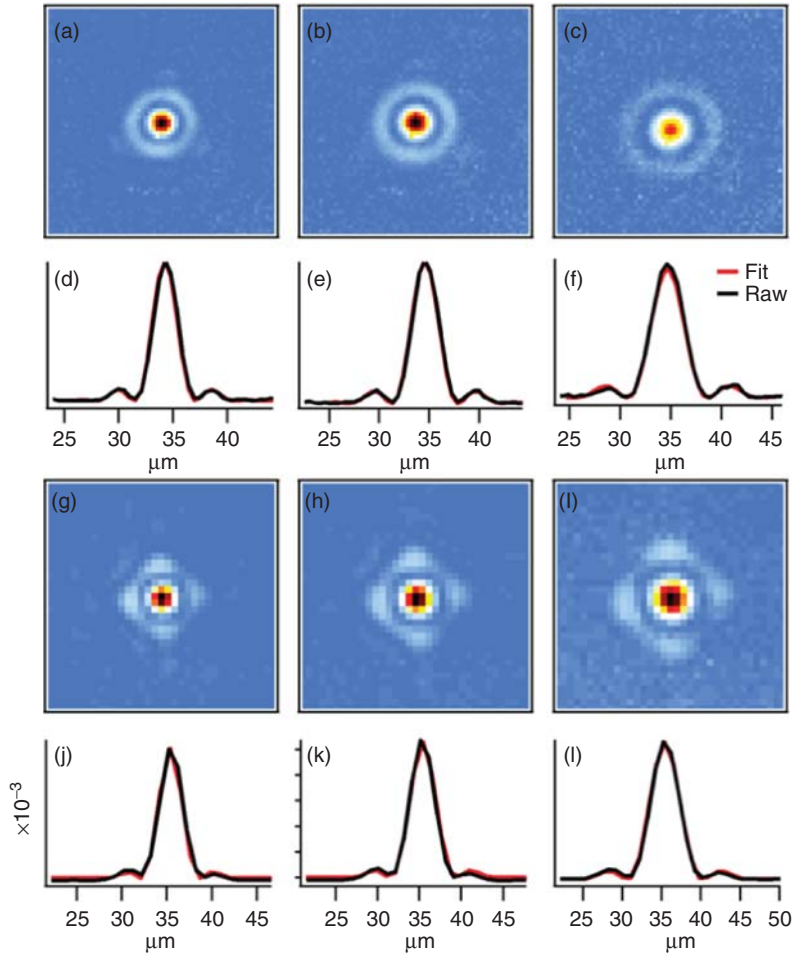

Figure 15.3 Measured and simulated PSFs. Comparison of measured and fitted PSFs for two objectives. (a–f) 74× (NA = 0.65) PSFs, g–l) 36× (NA = 0.5) PSFs at 3500, 3000, and 2500 cm^{-1}. (Reproduced with permission from IOP Publishing Ref. [2] *Journal of Physics: Conference Series*.)

quantity known *a priori*. On the basis of the convolution theorem, the "true" image may be recovered computationally through Fourier inversion:

$$I_{\text{true}} = \text{FT}^{-1}\left[\frac{\text{FT}\left(I_{\text{meas}}\right)}{\text{FT(PSF)}}\right] \tag{15.1}$$

The problem in Equation 15.1 is that the FT(PSF) approaches zero at high frequencies, whereas the measured image does not. In practice, we solve this problem by applying a mathematical filter to allow all spatial frequencies below a certain threshold to contribute to the reconstructed image. The filter has a structure

that is equal to the one below the determined threshold [at which point FT(PSF) becomes zero] and is smoothly and continuously brought to zeroat the threshold. The FT of the deconvoluted image is normalized to the zero-frequency component of the original image. Next, an inverse FT is applied, and the resulting deconvoluted image is scaled such that the amount of light absorbed is the same for the original and deconvoluted images. The process is repeated for all wavelengths in the cube, and the resulting images are reassembled in a new hyperspectral cube.

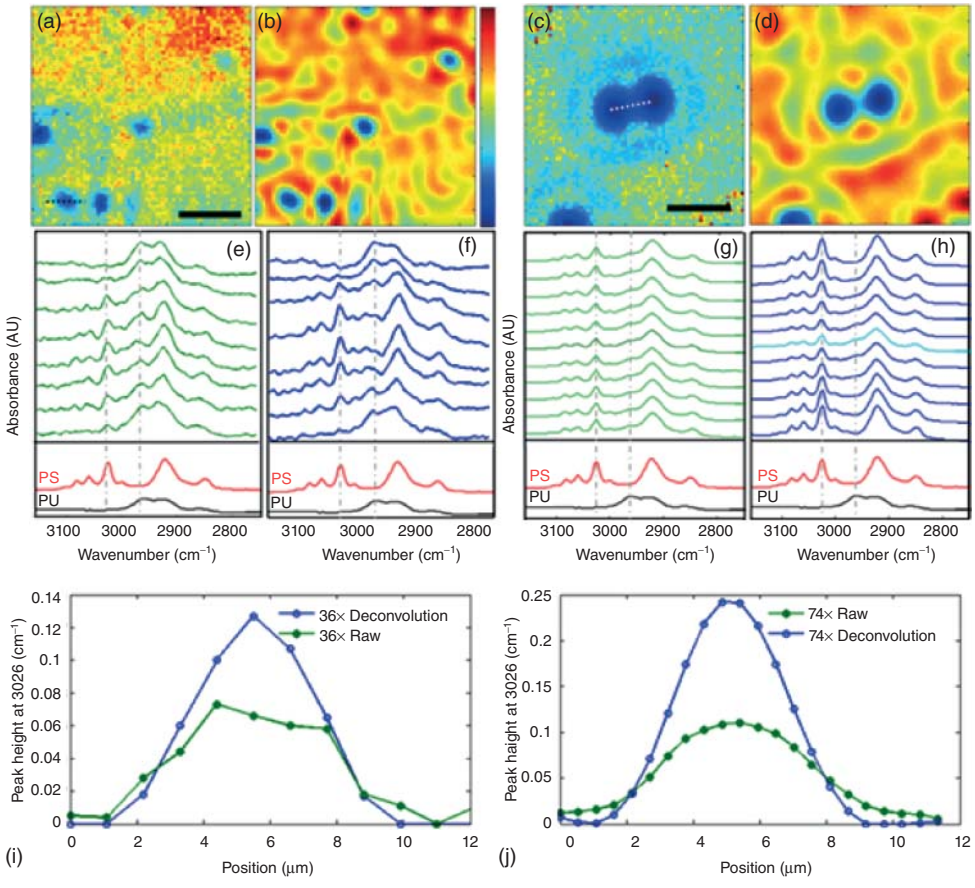

Figure 15.4 Deconvolution of chemical images and spectral reconstructions of a PS/PU sample. (a–d) show original (a,c) and deconvoluted (b,d) chemical images generated by integrating under a PU-specific band (1650–1710 cm^{-1}) for the 36× (a,b) and 74× (c,d) objectives [scale bar = 20 μm in (a), 10 μm in (c)]. In (e–h), we compare spectra taken along lines spanning PS beads from the original and deconvoluted data sets, respectively. (a,c) Spectra from the hyperspectral cubes are extracted along the dashed lines indicated. The bottom two spectra show the PS and PU standard spectra for comparison. We compare the absorbance of the PS band at 3026 cm^{-1} at the positions used for the spectral stacks of both original and deconvoluted data in (i) and from an analogous region in a data set from the 74× objective in (j).

As an example of the method, deconvolution is shown for chemical images of a test sample consisting of 6 μm polystyrene (PS) beads embedded in a matrix of polyurethane (PU). The samples were measured with both 36× and 74× objectives, and deconvolution was applied to both data sets. Figure 15.4a–d shows chemical images generated from integrating over a PU-specific absorption band, with data for 36× (Figure 15.4a,b) and 74× (Figure 15.4c,d) objectives, from both raw (left, Figure 15.4a,c) and deconvoluted (right, Figure 15.4b,d) data. In this color scale, red (blue) corresponds to a high (low) integrated intensity. The integrated images clearly show minima, indicated by the blue circles, at the positions of all of the PS beads. Following deconvolution, the circles become sharper and more well defined. In Figure 15.4e–h, stacks of spectra across individual PS beads (along the lines in Figure 15.4a,c,d) are provided to compare detailed spectral results from the original (Figure 15.4e,g) and deconvoluted (Figure 15.4f,h) data. Moving from off to onto a PS bead, changes in the PS-specific band at 3026 cm^{-1} show much more gradual onsets and decays in the raw data, while in the deconvoluted data, sharper more abrupt transitions are observed. A quantitative analysis of this transition is provided in Figure 15.4, which shows the intensity of this band in the original and deconvoluted 36× data as a function of position along the line in Figure 15.4a. Note that deconvolution causes a shift in spectral weight from the exterior of the bead to the center of the bead, resulting in increased absorption intensity in the center relative to the periphery. This is an indicative of a reduction of the diffraction-induced blurring achieved by the PSF deconvolution. In Figure 15.4j, we show an analogous analysis for data taken with the 74× objective. The results of this line profile analysis are similar to those for the case of the 36× objective. Following deconvolution, there is an increase in the spectral weight localized on the interior of the bead, while the intensity at the periphery decreases more rapidly than in the raw data.

15.3.2
3D Spectromicrotomographic Reconstruction

Computed tomography is a well-established approach [36, 37] used to reconstruct cross-sectional slices through an object from the transmitted projection images taken as a function of angle around a single axis of rotation. These slices can be stacked to produce a 3D image of the object, which can then be visualized by a number of methods, including volume rendering or digitally slicing through the sample along any arbitrary plane. The first demonstration of acquiring wide-ranging spectral images, particularly using the power of FT-IR spectral imaging across the mid-IR fingerprint region, as a function of sample rotation angle to obtain a complete spectral tomographic data set was possible with IRENI [1]. This is feasible since high-quality FT-IR spectral images are collected in about 1 min with WF spectromicroscopy; thus, acquiring a full tomographic data set requiring 100 or more spectral projection images can be obtained in a reasonable amount of time.

Reconstruction for any one wavelength image was accomplished using either filtered backprojection from the ASPIRE package [38–42]. A parallel beam was assumed. Although not strictly correct, the beam waist created by the focus at IR wavelengths of the 12 beams (all wavelengths are 3–10 times longer than the effective pixel resolution) is approximated reasonably well by a parallel beam. Reconstruction of the transmission image of one wavelength is similar to that of the traditional X-ray tomography. By reconstructing all wavelengths, we can reassemble the reconstructed spectrum for every voxel within the 3D space as shown in Figure 15.5. Having a complete spectrum for every voxel [5] can help to interpret chemical/structural variations in different regions of the sample and/or can enable more advanced spectral comparisons and sorting tools such as principal component analysis, cluster analysis, and other statistical analysis techniques.

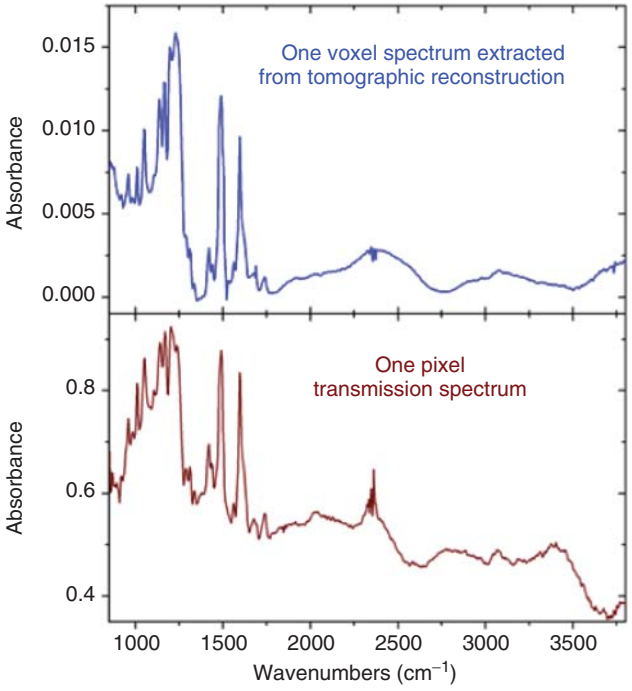

Figure 15.5 Spectra for polyimide target from a 3D voxel and a 2D pixel. Reconstructions of a polyimide microloop were performed at all 816 individual wavelengths. The intensity of one voxel in the stem of the microloop was assembled to extract the spectrum of this one 1.1 × 1.1 × 1.1 μm^3 voxel (upper panel). This extracted spectrum compares well with the conventional transmission spectrum from one 1.1 × 1.1 μm^2 pixel measured through the 25 μm thick stem on this same sample (lower panel). (Reproduced with permission from the Nature Publishing Group, Ref. [5], *Nature Methods*.)

15.4
Widefield versus Raster Scanning Geometries

15.4.1
Effects of Numerical Aperture, Spatial Oversampling, and Deconvolution on Spatial Resolution

Measurement geometry, NA, pixelization, and deconvolution all impact spatial resolution, as will be shown from studies performed with objectives of two different magnifications and NAs (36×, 0.5 NA and 74×, 0.65 NA). The experimental spatial resolution of the 36× and 74× based imaging systems is determined from measured images of United States Air Force (USAF) resolving targets before and after PSF deconvolution, and these data are compared to the optimum resolution obtainable using RS confocal geometries [43]. In Figure 15.6, simulated resolutions based on the parameters determined from the experimental PSFs [3] for

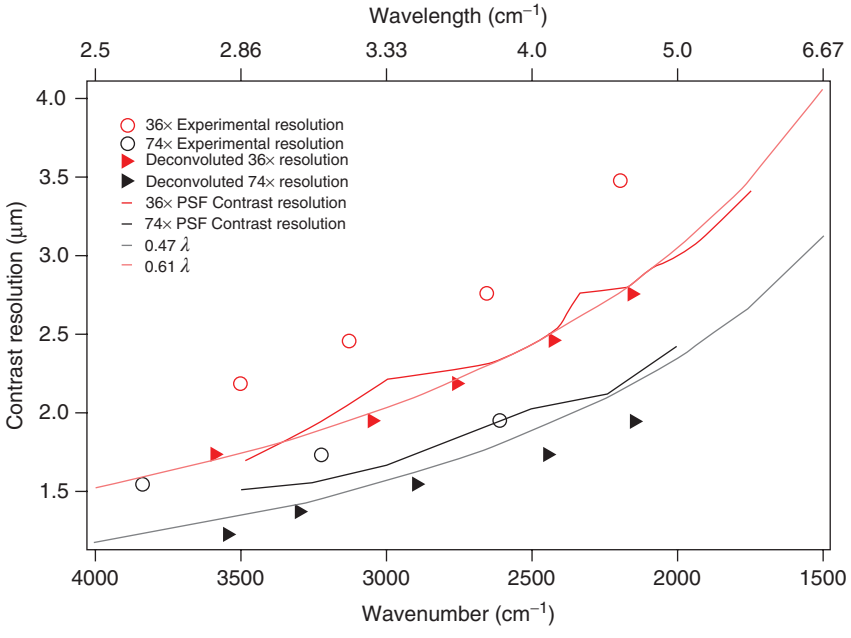

Figure 15.6 Predicted and experimental spatial resolutions of original and deconvoluted data. Contrast resolution PSF (solid lines) determined from simulated PSFs for the 36× (NA 0.5) and 74× (NA 0.6NA) objectives compared to the experimentally determined resolution limit for the 36× (NA 0.5) and 74× (NA 0.6NA) objectives before (open circles) and after (filled triangles) deconvolution determined from USAF target measurements for WF spectromicroscopy. Reported NA-dependent trends for RS spectromicroscopy resolution limits (dotted lines). (Reproduced with permission from the Royal Society of Chemistry, Ref. [43] *Analyst*.)

both objectives are compared with the experimentally determined resolution of both objectives. The point-spread-function contrast resolution (PSFCR) is first considered for two objectives (solid lines and right axis); here full width at 73.6% maximum is calculated because two objects are considered resolved if the contrast difference between them exceeds 26.4% [33]. The PSFCR is substantially smaller for the 74× than for the 36× objective due to the difference in the NA of the objectives. The experimental spatial resolutions of the objectives are shown for original (open circles) and deconvoluted (solid triangles) data. The resolution of the original data for the 74× (black circles) is only slightly above that predicted by the simulated PSFCRs (black line), most likely due to experimental uncertainty in the measurements. In contrast, the 36× (red circles) results show a substantially poorer agreement with the predicted PSFCR (red line) because of the coarser spatial sampling employed with the 36× geometry. The raw data collected with 74× magnification (0.54 × 054 μm^2 projected sample area/pixel) is sufficient to retrieve resolutions similar to the simulated PSFCR, but the original data measured with the 36× magnification (1.1 × 1.1 μm^2 projected sample area/pixel) is unable to achieve the optimal resolution due to the spatial sampling. In order to achieve optimal spatial resolution, the data must be sampled with at least eight pixels spanning the dimension of the PSF for any given wavelength. Using the conventional Rayleigh criterion for the shortest wavelength in the mid-IR (2.5 μm), this corresponds to a pixel size no larger than 0.6 μm for the 74× objective, which is larger than the effective pixel size in the geometry employed here. Conversely, this sampling criterion for the 36× objective requires a pixel spacing no larger than 0.76 μm, which is smaller than the effective pixel size. Thus, the optical setup for the 36× geometry is undersampled for wavelengths below 3.6 μm (2770 cm^{-1}). Following deconvolution, however, both objectives yield resolutions exceeding the predicted PSFCR criterion, yet still retain their expected dependence on NA.

Spatial resolution limits determined in an RS confocal microscope are shown in Figure 15.6; two curves are included that correspond to trends for 0.65 and 0.5 NA objectives (0.47λ describes the confocal Rayleigh criterion resolution for an NA = 0.65 objective, whereas 0.61λ describes the same quantity for an NA = 0.5 objective). The resolution of the original data with the WF geometry and 74× objective (NA = 0.65) shows resolution ranging from comparable (3000–4000 cm^{-1}) to poorer (2000–2500 cm^{-1}) to those described previously [44, 45] for the 0.65 NA RS setup, while the WF 0.5 NA resolution is substantially poorer than the confocal 0.5 NA resolution. Upon PSF deconvolution, however, the resolution of the WF 0.65 NA exceeds the resolution of the RS geometry, while that of the 0.5 NA WF geometry becomes comparable to or slightly better than that of the RS geometry [34, 44, 45]. In sum, with the correct oversampling, one achieves similar spatial resolution for confocal and FPA-based imaging, and application of PSF deconvolution allows for the resolution of WF FPA-based spectromicroscopy to exceed that of RS spectromicroscopy.

15.4.2 Signal-to-Noise Ratio Comparisons

Next, we compare and contrast WF and RS spectromicroscopic studies with results from a study of the surface chemistry of the wings of the Clanger cicada *Psaltoda claripennis.* This sample was studied using a confocal RS spectromicroscopy beamline (AS IRM Beamline) at the Australian Synchrotron and WF spectromicroscopy at IRENI. In brief, we observed a heterogeneous surface distribution of long-chain hydrocarbons, consistent with insect wing structures including hexagonal arrays of spherically capped conical nanoscale pillars [46–49] and epicuticular waxes that are expected to substantially contribute to high contact angles [50–52]. These findings are consistent with this insect wing's previously observed heterogeneous superhydrophobicity [49, 53]. Characteristic bands in the infrared spectra of the wings were assigned primarily to aliphatic hydrocarbon and amide functionalities, which were considered to be an indication of the presence of waxy and proteinaceous components, respectively. In Figure 15.7, chemical distribution maps show that while the protein component is homogeneously distributed, a significant degree of heterogeneity is observed in the distribution of the waxy component, which may contribute to the self-cleaning and aerodynamic properties of the cicada wing.

Comparison of spatial resolution of the Synchrotron Radiation Center (SRC) IRENI beamline with the Australian Synchrotron IRM beamline demonstrates that the former is capable of clearly resolving featuresover a large area at a high-resolution level that is at the theoretical widefield diffraction limit. This is enabled by the optical configuration of the 74× objective combined with the FPA detector, resulting in a significant spatial oversampling across the sample plane, with a projected sample pixel size at the detector of $0.54 \times 0.54\ \mu m^2$. In contrast, the Austrailian Synchrotron - Infrared Microscopy (AS-IRM) beamline is limited in the area it can cover within a reasonable time by the need to acquire data point-by-point. The data presented here were collected with an aperture setting of 5 μm and a spatial step size of 2 μm.

An assessment of spectral noise was made for data collected at both the AS-IRM and the SRC IRENI beamlines. The details of the measurements are provided in Table 15.1. root mean squared (RMS) noise was determined from 2450 to 2550 cm^{-1} for individual spectra, after converting the data from absorbance to percentage transmission. Three spectra were selected in each case. In sum, the two facilities produce similar quality spectral data for $4 \times 4\ \mu m^2$ sample-projected pixels (aperture based on RS spectromicroscopy and binned WF spectromicroscopy) measuring eight co-added scans for the AS-IRM data, and 64 co-added scans for IRENI data, the latter to overcome the noisier characteristics of the FPA detector. When collecting 64 scans at the AS-IRM beamline, the RMS noise level at $4 \times 4\ \mu m^2$ aperture and 6 cm^{-1} resolution was reduced to 0.022% as expected.

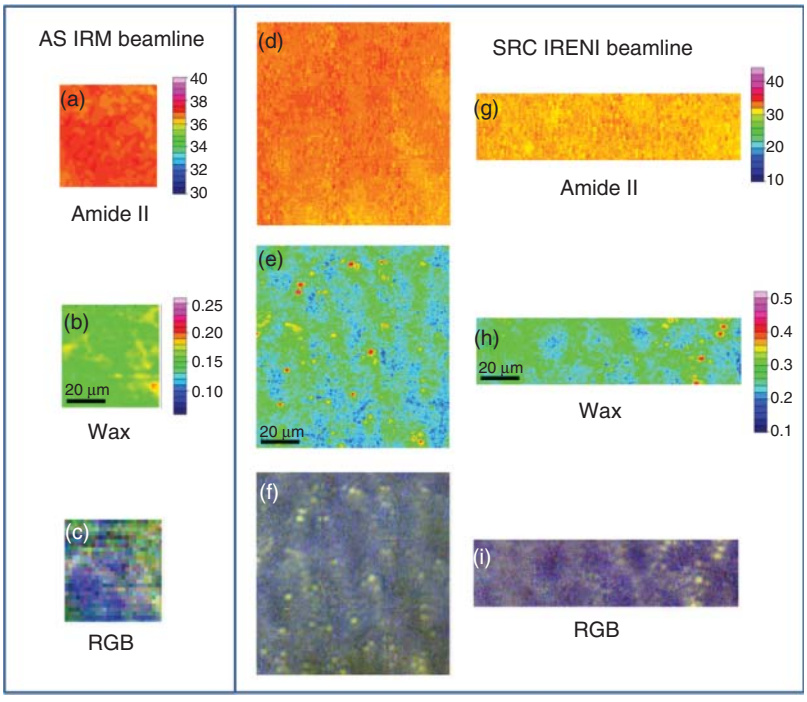

Figure 15.7 Comparison of RS and WF spectromicroscopy for Cicada Wing. Chemical intensity maps of amide II and CH_2 absorbance bands obtained by integration of the respective bands (amide II: 1588–1483 cm^{-1}, ν_{as} CH_2: 2931 2913 cm^{-1}). (a), (b), and (c) represent the images obtained from the IR scans performed at the RS spectromicroscopy beamline at the Australian Synchrotron while (d) to (i) are the respective images obtained from the WF spectromicrscopy IRENI beamline. The intensities of the integrated area of the amide II band (a, d, and g) and CH_2 antisymmetric stretching (b, e, and h) are shown in consistent color scale between beamlines, but with the value range compressed for the amide II maps, to enhance the low level of variation, in particular in image (a). RGB (red, green, and blue) composite images (c, f, and i) show the blended presence of amide II and CH_2 antisymmetric stretching, with R + G representing long-chain hydrocarbon (wax) and B showing amide II (protein). Map dimensions are 50 µm × 50 µm (a–c), 104 µm × 104 µm (d–f), 138 µm × 35 µm (g–i). (Reproduced with permission from John Wiley and Sons, Ref. [26] *Journal of Synchrotron Radiation*.)

15.4.3 Time–Area Trade-Off

Next, we make a comparison of the time required to collect a data set of equivalent signal to noise over a similar spatial area (but with very different spatial resolution). The comparisons are made in Table 15.2. To achieve the spatial IRENI, but using the AS-IRM beamline RS, one would require approximately

Table 15.1 Spectral noise comparison between synchrotron-based raster scanning and widefield spectromicroscopy.

	Aperture/pixel size	No. of co-added spectra	RMS noise (%)[a)]
RS spectromicroscopy (IRM, Australian Synchrotron)	4 μm × 4 μm, aperture defined	8	0.073
	4 μm × 4 μm, aperture defined	64	0.022
WF spectromicroscopy (IRENI, Synchrotron Radiation Center)	0.54 μm × 0.54 μm, effective pixel	64	0.330
	4 μm × 4 μm, binned pixels	64	0.081

a) RMS noise was determined over the spectral region from 2450 to 2550 cm^{-1}, using Bruker OPUS 6.5 software for individual spectra, after conversion from absorbance to percentage transmission. The RMS noise is reported as a percentage noise.

Table 15.2 Time–area trade-off between synchrotron-based raster scanning and widefield spectromicroscopy.

	Aperture/pixel area/step size	Total area	No. of co-added spectra	Time
RS spectromicroscopy (IRM, Australian Synchrotron)	4 μm × 4 μm, 4 μm steps	8 × 8 pixels, 32 μm × 32 μm	8	288 s
	4 μm × 4 μm, 0.5 μm steps	64 × 64 pixels, 32 μm × 32 μm	8	16 380 s 4.55 h
WF spectromicroscopy (IRENI, Synchrotron Radiation Center)	0.54 μm × 0.54 μm, effective pixel size	64 × 64 pixels, 34 μm × 34 μm	64	126 s

130 times longer data collection to cover an equivalent sample area to the IRENI collected data set. This illustrates the advantage gained by FPA instruments through parallel acquisition from multiple detector elements. Improvements in both RS approaches and higher parallelization in electronic readouts of the FPA detectors will reduce both of these times in the future. In sum, synchrotron WF spectromicroscopy is capable of rapidly analyzing large areas at high spatial resolution with high signal to noise, while RS spectromicroscopy with a single-focused beam is able to probe small sample features with the very high spectral signal to noise necessary to observe more subtle spectral differences and weakly absorbing samples.

15.4.4
New Directions: Spectromicrotomography

To take spectral imaging into the third dimension, others have employed confocal depth profiling [54, 55] and serial sample sectioning [56], both of which result in a stack of 2D spectral images. In contrast for IR spectromicrotomography, we achieve 3D chemical imaging with minimal sample preparation. As described earlier, we collect a large number of projection images as a sample is precisely rotated, which corresponds to a tomographic data set. Samples that are typically sliced using a microtome for 2D projection experiments need not be sliced and can be measured in their original state, reducing the impact of embedding and other standard sample preparation techniques. This new capability makes it possible to measure samples that have been challenging up to now.

15.5
Examples

15.5.1
General Applications

15.5.1.1 Nanocellulose

Polyvinyl alcohol (PVOH) has been investigated for use in a wide variety of applications such as drug release or tissue engineering [57, 58]. Often, treatment of PVOH is required to render it more stable in water. The most effective methods for long-term stability involve chemical cross-linking [58]. Nanocellulose is a naturally sourced reinforcement extracted from trees, plants, some marine creatures, or certain bacteria and fungi [59]. Nanocellulose can be relatively easily dispersed in water-soluble polymers such as PVOH and then fabricated into composites. Several researchers have demonstrated mechanical property improvements when nanocellulose is added to PVOH, for example, Refs [60–62]. However, their susceptibility to water and still modest mechanical performance limit the applications in which they can be used. Adding polyacrylic acid (PAA) to PVOH during composite preparation may improve performance by not only cross-linking PVOH but also improving the adhesion between PVOH and nanofibrillated cellulose (NFC) by forming ester linkages with both of them.

The distribution of PAA in model laminates of nanocellulose and PVOH was investigated by FT-IR chemical imaging as can be seen in Figure 15.8. The method was effective spatially in discerning the three components of the composite. However, PAA was found to migrate out of the PVOH matrix and concentrate in the nanocellulose layer of the laminate. This led to a PAA-depleted region in the matrix near the nanocellulose layer, which would likely lead to a weak interphase and limited stress transfer between the fiber and the matrix in the heat-treated composite [24].

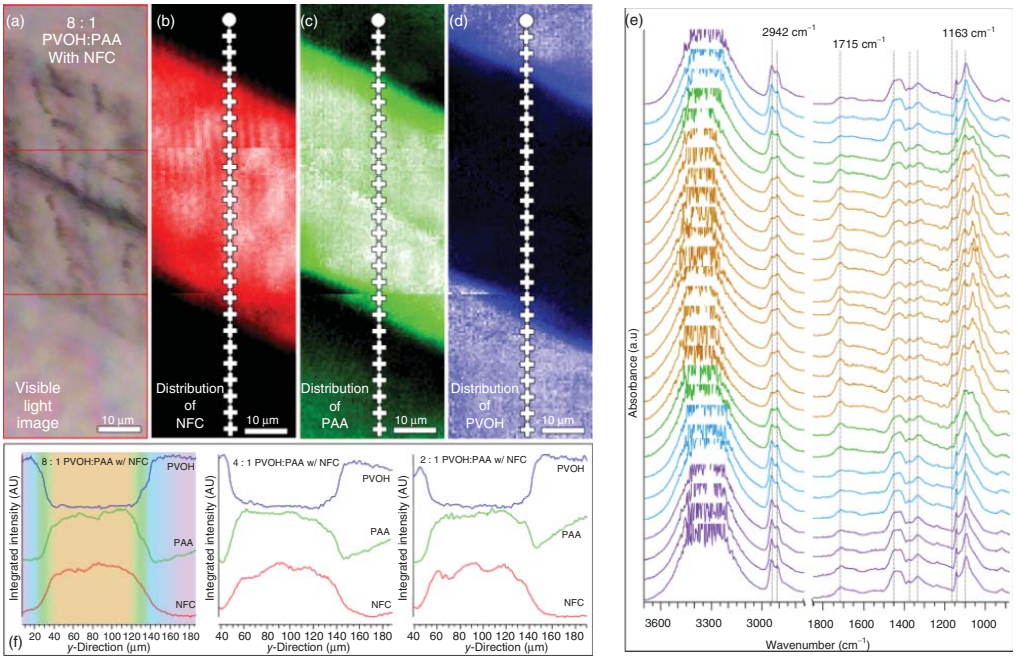

Figure 15.8 Images of a PVOH:NFC laminate containing PAA demonstrating the different chemical compositions in the layers. An 8 : 1 PVOH:PAA weight ratio was used in (a)–(e). (a) Optical micrograph and FT-IR integration images: (b) at 1163 cm^{-1} to show the distribution of nanofibrillated cellulose (NFC), (c) at 1715 cm^{-1} for PAA, and (d) at 2942 cm^{-1} for PVOH. The color scales run from low (dark) to high (bright) concentration. The spectra of the line scans drawn in (b)–(d) are shown in (e). (f) Intensity profiles of the line scans from (b) to (d): the congruence of the layers in the integration images is shown in the left panel. The other two images show the intensity profiles of similar line scans for laminates prepared with 4 : 1 and 2 : 1 PVOH:PAA weight ratios. (Reproduced with permission from Elsevier Ref. [24] *Polymer.*)

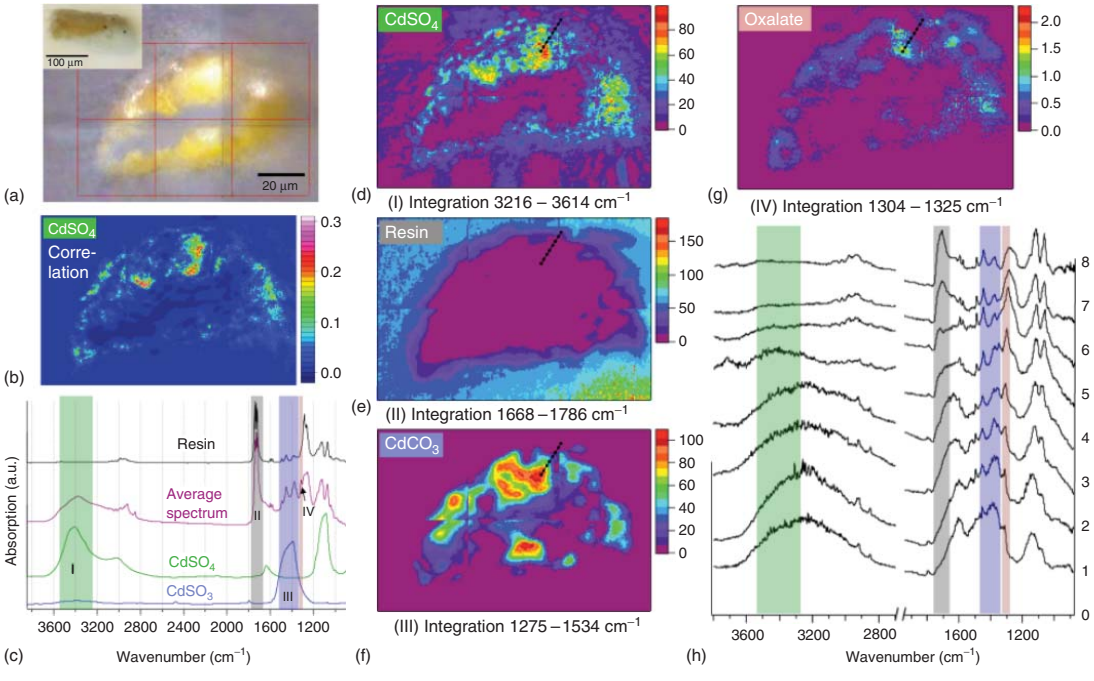
(a)
100 µm
20 µm
(b)
CdSO4
Correlation
0.3
0.2
0.1
0.0
(c)
Resin
Average spectrum
CdSO4
CdSO3
I
II
III
IV
Absorption (a.u.)
3600 3200 2800 2400 2000 1600 1200
Wavenumber (cm−1)
(d)
CdSO4
80
60
40
20
0
(I) Integration 3216 – 3614 cm−1
(e)
Resin
150
100
50
0
(II) Integration 1668 – 1786 cm−1
(f)
CdCO3
100
80
60
40
20
0
(III) Integration 1275 – 1534 cm−1
(g)
Oxalate
2.0
1.5
1.0
0.5
0.0
(IV) Integration 1304 – 1325 cm−1
(h)
8
7
6
5
4
3
2
1
0
3600 3200 2800 1600 1200
Wavenumber (cm−1)

15.5.1.2 Matisse

In the following, the outcome of studying Matisse's *Le Bonheur de vivre* (1905–1906, The Barnes Foundation) with regard to the cadmium containing yellow pigments is shown [22, 63]. The reason for this and other studies [64, 65] is that nanocrystalline cadmium sulfide (CdS) yellow paints used in Impressionist, Post-Impressionist, and early modernist work from the 1880s through the 1920s has been observed to undergo poorly understood chemical and physical changes over time. This results in discoloration accompanying phase transformation.

Cross sections were removed from degraded areas of the painting and embedded in bioplastic resin, which was hardened to a lower hardness than the manufacturer recommended [20], to facilitate slicing the precious sample on a microtome to generate samples that can be measured in transmission. The sample, as is typical for cultural heritage investigations, was friable, and some pigments were lost during the preparation and/or transport.

A paint cross section (113) from the darkened upper left corner of the painting, which is presently brown but has been identified as an intended yellow area [22] from prior oil sketches in which the yellow paint is unaltered, has been investigated with IRENI. Integration over specific spectral regions of cadmium sulfate ($CdSO_4$), cadmium carbonate ($CdCO_3$), and cadmium oxalate, the chemical maps shown in Figure 15.9, was obtained showing the transition between $CdSO_4$ and $CdCO_3$. In the comparison between integrated images and the correlation with reference spectra, it becomes clear that there are significant differences in the distribution of the oxidized Cd phases. It is likely that the original paint and photooxidation of that paint are the sources of these materials within the paint cross section [22].

←

Figure 15.9 Analysis of the paint chip 113 from Matisse's *La Bonheur de vivre*. (a) Micrograph with visible light at 74× magnification; the inset in the upper right shows a high-magnification visible image of the chip. The alteration layer is clearly delineated as is the layer with the dark precipitate causing the discoloration. (b) FT-IR image correlated with the spectrum of $CdSO_4$, shown in (c) in green, with the spectra of the resin (black), the average spectrum (purple), and $CdCO_3$; the characteristic bands used for the integration images (d–g) are marked in roman numbers, relevant spectral areas are marked in corresponding colors for $CdSO_4$ (peak I, green), resin (peak II, gray), $CdCO_3$ (peak III, blue), and oxalate (peak IV, red, d–h). Integration images of the peak areas I–IV as indicated before, showing the necessity of a differentiated integration in comparison with the correlation image. The hotspots of $CdSO_4$ and $CdCO_3$ are very close together but not overlapping. Oxalate and $CdCO_3$ seem to be colocalized. This can be seen in the eight line scan spectra in plot in (h) (marked in d–g). The same spectral areas as in (c) are marked here. For example, an increase in peak III under the bands of the resin can be observed; the rise of the oxalate peak (red, peak IV) seems to be related. (Reproduced with permission from Cambridge University Press Ref. [63] *Microscopy and Microanalysis*.)

15.5.2 Influence of Deconvolution

15.5.2.1 Labeled Cells

A single MDA-MB-231 hormone-independent breast cancer cell labeled with an exogeneous metal carbonyl derivative ($Re(CO)_3N_3$) is analyzed as a demonstration of the impact of oversampling and deconvolution in a biologically relevant sample. IR-specific biomarkers, such as metal carbonyl derivatives, show intense absorptions in the transparent window of biological media between 2000 and 1850 cm^{-1}. Such markers are important in spectromicroscopy applications, as they allow for the unambiguous determination of the localization of cellular organelles in IR microscopic data sets. For example, the $Re(CO)_3N_3$ biomarker shown here [43] is used on single breast cancer cells to specifically label the golgi apparatus (GA) [66, 67]; therefore, chemical images showing its localization within the cell should indicate a spatial distribution displaced from that of the nucleus, which is indicated by the region with the highest amide absorption [66, 68]. Figure 15.10 shows integrated images of the amide I and metal carbonyl functional groups within the cell generated from both raw and deconvoluted data sets taken with the 36× and 74× objectives. The following parameters were used to generate the integrated images: for the amide I band, the integration was performed over 1600–1690 cm^{-1}, with the same baseline. Integration of the biomarker signature was performed over the C=O stretching feature from 2005 to 2040 cm^{-1} with the same baseline. In the raw data taken with both objectives, the distribution of the amide shows a slight displacement from the localization of the biomarker signature, which is discussed further later. Upon comparison of the raw and deconvoluted data from both objectives, it is clear that in all cases the deconvolution produces images showing sharper, more well-definedfeatures with enhanced contrast.

To more qualitatively address the effect of deconvolution on the data from both objectives, intensity profiles through the same position of the cell are shown for both data sets (Figure 15.11). The location of the profile used for the 74× data set is indicated by the white line in Figure 15.10b; all of the 74× profiles in Figure 15.11 from the different functional groups are extracted from the exact same location (dashed line in Figure 15.10b). The location from which the profiles from the 36× data are extracted is shown by the white line in Figure 15.10f. Importantly, these profiles can be used for quantitative comparison between original and deconvoluted data sets. The profiles above allowed for quantification of the change of the dimension of the cell as measured with two objectives, as well as the discrepancy in estimating distances using the two different objectives. The data also showed that deconvolution was much more successful for the data collected with the large NA (oversampled) objective.

15.5.2.2 Layered Polymers – Transmission and Reflection

Synthetic layered polymers are commonly used in art and cultural heritage products. Such materials in art pieces are subject to deterioration such as cracking, deformations, or discolorations [69]. There is an oxygen-barrier film (FR-7750,

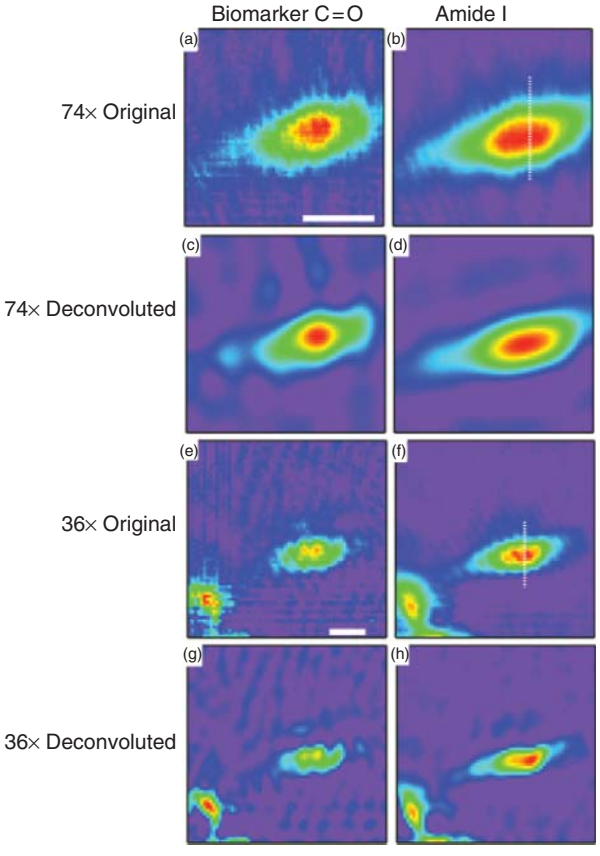

Figure 15.10 Original and deconvoluted images of a breast cancer cell labeled with a metal carbonyl marker taken with both 74× and 36× objectives. (a) and (b) show original chemical images. Note: [color scales: purple (low intensity) – red (high intensity)] of the cell as measured with the 74× objective generated by integrating under C=O stretching of the biomarker (a) and amide 1 (b). Scale bar in (a) is 20 μm. (c) and (d) show the results of deconvolution of the data used to generate (a) and (b). (e) and (f) show the analogous data of (a) and (b) as measured with the 36× objective. Scale bar in (e) is 20 μm. (g,h) show the results of deconvolution of the data used to generate (c,d). (Reproduced with permission from the Royal Society of Chemistry, Ref. [43], *Analyst.*)

Bell Fibre Products) that serves as a surrogate for polymers in cultural heritage objects. Both transmission and reflection chemical images are provided to demonstrate the ability of IRENI in identifying the chemically distinct thin layers [70]. Figure 15.12c includes a visible image of the layered polymer sample with mounting resin, Chlorotrifluoroethylene(CTFE), polyethylene (PE), polyester, polyethylene, and mounting resin layers from top to bottom. The mounting resin is similar to that of the sample mounting medium used for the paint cross section from the Matisse painting. For transmission experiments, the sample was sliced on a microtome. Deconvolution [3] was applied to these results,

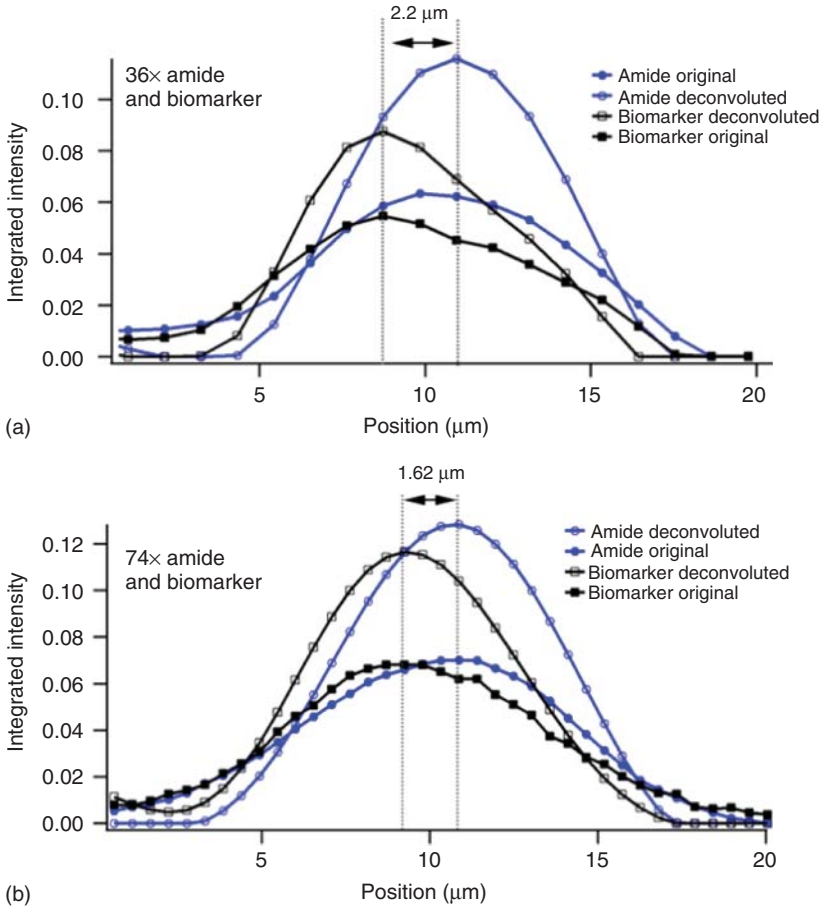

Figure 15.11 Line profiles through chemical images of the labeled cell shown in Figure 15.10. (a) Original and deconvoluted line profiles of the amide and biomarker chemical images shown in Figure 15.10 (e,f and g,h). The profiles all come from the location indicated by the white line in Figure 10H. The displacement between the amide and biomarker signatures is measured to be 2.2 μm. (b) Original and deconvoluted line profiles of the amide and biomarker chemical images shown in Figure 15.11 (a,b and c,d). The profiles all come from the location indicated by the white line in Figure 15.11 b. The displacement between the amide and biomarker signatures is measured to be 1.62 μm. (Reproduced with permission from the Royal Society of Chemistry, Ref. [43], *Analyst*.)

since identifying distinct layers is frequently encountered and therefore critical question. The cultural heritage community prefers to measure samples with a reflection geometry, studying the embedded sample *in situ* in the resin block to enable multimodal imaging on the same sample.

The transmission results highlight the polyethylene layers in Figure 15.12b,d for original and deconvoluted data, respectively. Both contrast and higher SNR are

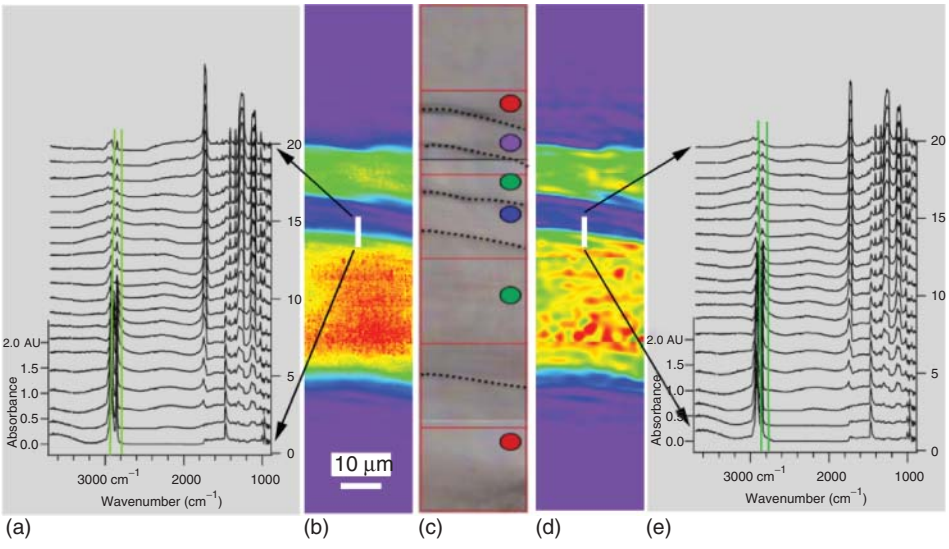

Figure 15.12 Original and deconvoluted transmission from layered polymer sample. Visible image of the layered polymer (c) (layers from top: bioplastic (red dot), CTFE (purple dot), PE (green dot), polyester (blue dot), PE (green dot), bioplastic (red dot)). raw (b), and deconvoluted (d) chemical images of polyethylene layers 2829–2866 cm^{-1} (measured in transmission). Extracted single spectra from the original (a) and deconvoluted (e) data sets taken along the white line in the respective images.

enhanced following PSF deconvolution. The polyethylene chemical image after the deconvolution process shows more details and sharper boundaries at the transitions. Figure 15.12a,e each show a stack of spectra from 20 neighboring single pixels along the white lines from polyethylene to polyester indicated on the original and deconvoluted images, respectively. The polyethylene absorption bands are indicated between green lines. After deconvolution, the decay of CH stretching bands for PE for the above 10 spectra is faster than before the deconvolution, showing the transition between layers more precisely. Thus, deconvolution is an effective tool to clarify and identify boundaries in layered samples [21].

Since it is not always possible to preparetransmission samples for cultural heritage objects and other types of samples, a comparison between transmission and reflection measurements is essential. Reflection measurements using a 20× (0.6 NA) objective were performed for direct comparisons between results from these two geometries [21]. Figure 15.13 shows integrated chemical images corresponding to several different polymers (a, c-f), with a stack of spectra from single pixels across the sample (b) As expected, the reflection results are not well defined spatially because of the larger pixels (2×2 μm^2). The signals are noisier due to a combination of specular and diffuse reflection contributions from the roughened surface that remains after slicing with a diamond knife. Since the derivative-type features mimic the real part of the index of refraction, the Kramers–Kronig (KK) transformation has been applied to the hyperspectral cube

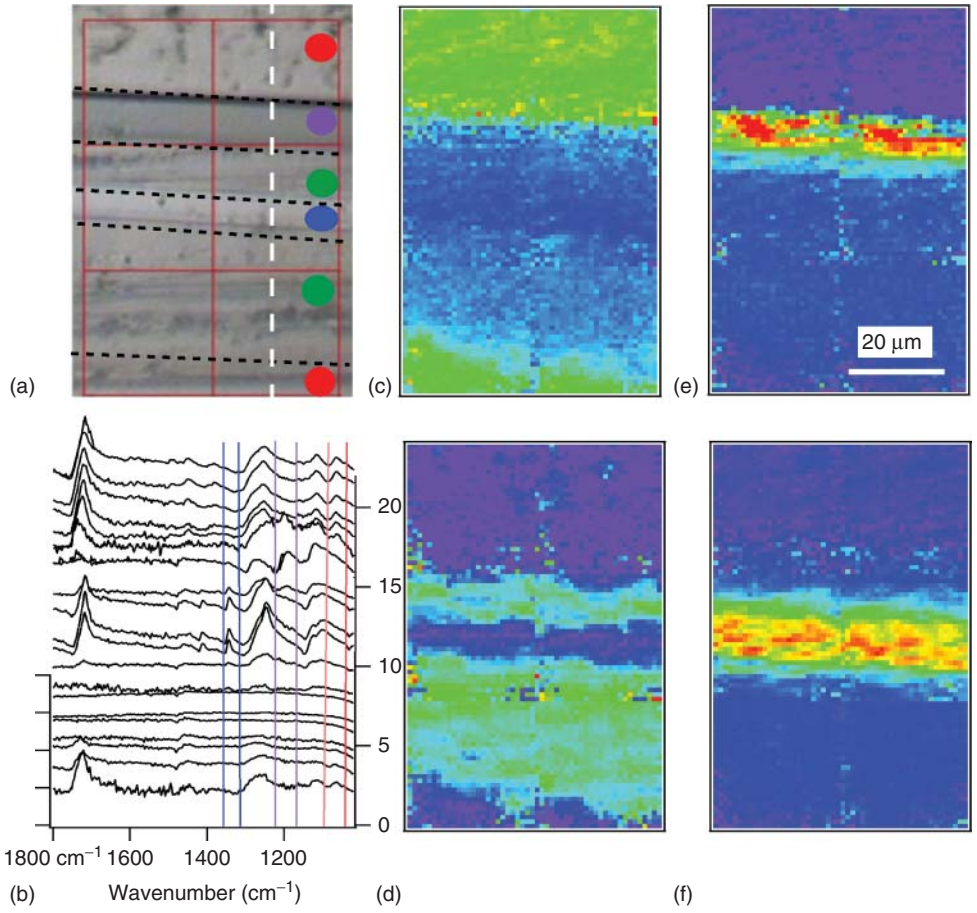

Figure 15.13 Reflectance from layered polymer sample. Visible image (a) of a cross section of the same layered polymer measured in reflection (layers from top: bioplastic (red dot), CTFE (purple dot), PE (green dot), polyester (blue dot), PE (green dot), bioplastic (red dot)). The chemical images (c–e) are generated from KK-corrected data, based on the shown regions in the stack of spectra plot (calculated along the dashed line on visible image) (b) with the following spectral integration windows: (c) polyester-mounting resin 1043–1078 cm^{-1}; (d) PE 2834–2857 cm^{-1}; (e) CTFE 1162–1210 cm^{-1}; and (f) polyester 1325–1352 cm^{-1}.

to extract the imaginary part of the index of refraction, and therefore predominantly absorption spectra, below 2000 cm^{-1}, which are analyzed to create the chemical images. These results suggest that the bright source has the potential to provide an option for employing this desired, but challenging, geometry. A more highly roughened surface would lead to lower signals due to more diffuse scattering and would require Kubelka–Munk corrections that retrieve absorption spectra from scattered radiation. Two observations should be addressed: first, since the Schwarzschild objective both illuminates the sample and the detector

for reflection geometry, the illumination beam structure can be seen in some chemical images and should be ignored. A correction for this would be to include another pair of out-of-focus objectives in the beam path elsewhere, but that would reduce the photon flux further. The second observation is that the typical sample area measured in reflection is significantly smaller because of the reduced signal and illumination areas, requiring significantly longer times for the measurements. Taking into account both sample preparation and measurement issues, the optimum approach can be determined for each experiment.

15.5.3
Time-Dependent Infrared Imaging

Two-dimensional (projection) IR spectromicroscopy of living cells represents a challenging endeavor due to the need for many cells to be suspended in aqueous media, but is desirable to provide full spectral and, therefore, maximal biochemical information simultaneously for an entire cell. Water is strongly absorbing in the mid-IR region, and optical path lengths of water greater than 25 μm result in total absorption over a considerable portion of the mid-IR region. Several groups have developed devices to circumvent this measurement difficulty while preserving the integrity of living cells. These approaches include demountable flow chambers [4, 71] and open [72] closed [71, 73] and aberration free [74] microfluidic devices. In demountable liquid flow chambers, two IR transparent windows form the basis of the chamber and are separated from one another by a thin spacer, often teflon, which serves a dual purpose of providing a fixed distance between the top and bottom window as well as sealing the chamber. Nasse *et al.* [4] designed a custom-demountable flow chamber employing submicrometer diamond films supported by Si wafers as the top and bottom windows of the cell with the small vertical dimensions sue to the small working distance of the 74× objective. The advantage of the use of thin windows is twofold: first, the submicrometer thickness effectively reduces the effect of chromatic aberrations; second, it minimizes the multiple internal reflection in the windows that produces spectral interference fringes. This is the flow cell that has been employed in the following experiments. Other flow cell geometries could also be employed, but for the highest magnification (74×) experiments, there is only 1 mm working distance.

15.5.3.1 Algal Biochemistry: Diatom Response to Changes in Carbon Dixide Supply

The rapid 2D imaging enabled by WF spectromicroscopy at IRENI is an important tool that provides new insight into internal chemical distributions of hydrated living single cells; in particular, changes in concentrations of carbon-containing macromolecules due to environmental stresses can be studied with subcellular spatial resolution. Here, single *Thalassiosira weissflogii* algal cells were imaged while they were maintained in a microfluidic chamber [4] under controlled conditions. These data result in a series of infrared images, enabling chemically specific visualization that is not attainable with visible light imaging, of ongoing chemical processes and morphology in live cells.

The diatoms were harvested from batch cultures where the cells are maintained at 20 °C in a growth chamber with continuous light (100 lmol $(m^2s)^{-1}$ photosynthetically active radiation) and at ambient (390 ppm) CO_2 conditions. During the course of the infrared WF spectromicroscopy measurements, the cells were exposed to high CO_2 medium (5000 ppm CO_2) [75] that was prepared by bubbling fresh media with 5000 ppm CO_2 for at least one night prior to the experiment. Within the microfluidic chamber, the algal cells were maintained at fixed temperature (20°C), in 10 µl of CO_2-controlled medium, with a 15 µm spacer separating the top and bottom of the chamber, and continually illuminated with photosynthetic active light.

Data sets, collected over a span of 8 h, are represented by the images from 0, 3, and 8 h time points. The chemical images, shown in Figure 15.14, are generated by integrating the peak areas of biomolecular functional group absorptions including C–H stretching ($\approx$3000–2800cm^{-1}) of saturated CH_3 and CH_2, the

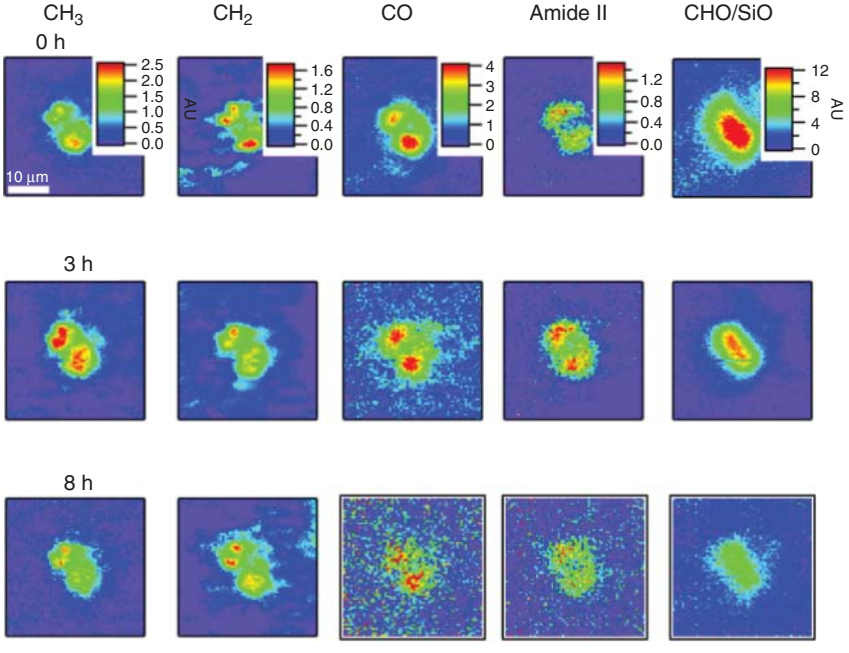

Figure 15.14 Temporally resolved series of infrared images for a *Thalassiosira weissflogii* algal cell. Distributions of biochemically important functional groups and time-dependent changes in the concentrations of several biochemical functional groups maintained in the flow cell. The images are obtained from data sets for one algal cell, collected at 0, 3, and 8 h after exposure to medium containing a high concentration (5000 ppm) of CO_2. The images are displayed using a rainbow scale, with the red/dark (blue) corresponding to the highest (lowest) intensity pixels, and thus corresponding to the highest concentration or quantity of the functional groups for the chemical images. The color scales are preserved for each functional group, thus revealing the variations within the algal cells over time. Scale bar is 10 µm.

N–H in-plane bending of amide groups (≈1570–1500), the C=O stretching of carbonyl functional groups found in fatty acid esters of lipids (≈1760–1710), and the C–O–C and C–C stretching modes of carbohydrates (≈1200–1000). The latter band is superimposed with the Si–O stretching band of the silica shell. Baselines with the same endpoints were used for all integrated areas. Note the clear changes in the CH_3 functional group intensities and distributions with higher concentrations observed in the 3 h chemical image, as compared to the 0 and 8 h time points. This and the other obvious changes demonstrate that real-time detection of variations in organic macromolecular pools is accessible.

15.5.3.2 Surface Chemistry: NH_3 Adsorption on Reduced Graphene Oxide

Time-dependent IR imaging has been used in materials science to probe gas–surface interactions. Mattson *et al.* [25] used *in situ* IR WF spectromicroscopy at the IRENI beamline at SRC [1, 18] to study the adsorption of ammonia on reduced graphene oxide (RGO). The NH_3/RGO system is of great technological relevance because of its significance in molecular sensing and heterogeneous catalysis. In the experiment, micrometer-scale RGO multilayer films were deposited onto a diamond window and examined *in situ* using the custom flow cell [4]. During exposure to NH_3, differential IR absorption spectra were recorded to sample the vibration frequencies of the molecular fragments that adsorbed to the surface. In addition, WF chemical imaging allowed for a visualization of the NH_3/RGO system. Figure 15.15a shows the raw absorbance of the sample at 3300 cm^{-1}. In this case, the absorption contrast comes from the continuum of electronic excitations of graphene spanning the mid-IR region; this allows for a visualization of the sample thickness. Figure 15.15b is a chemical image generated by integrating under the region 3000–3410 cm^{-1}, which accounts for the NH_x and OH stretching vibrations. The integrated image shows that the greatest absorption owing to the adsorbed fragments comes from the central, thicker region of the film, indicating that the adsorbates intercalate in between the individual RGO layers. This was further demonstrated by comparing spectra extracted from thick and thin regions of the film (Figure 15.15c).

15.5.4 Infrared Spectromicrotomography

15.5.4.1 Human Hair

FT-IR spectral images from microtomed cross sections of human hairs have been studied to better understand the differences between hairs from different races ethnicities [76, 77], the effects of various hair products on the microstructure of the hairs [78], and even to compare ancient hairs from Egyptian mummies to modern day hair [79]. Although human hairs typically have a sufficient water content to make IR transmission spectra through their ∼100 μm nominal thicknesses difficult, we wanted to understand if we could obtain useful information about a human hair via tomography without the need for embedding and microsectioning, despite the presence of strongly absorbing water.

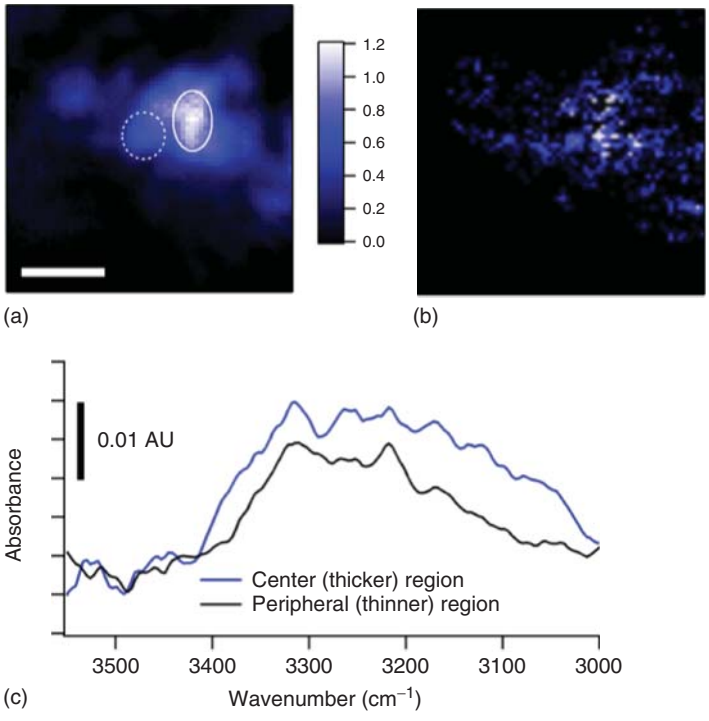

Figure 15.15 Imaging NH_3 adsorbed on reduced graphene oxide. (a) shows the raw absorbance of the sample at one wavelength (3300 cm^{-1}) as a means to visualize the distribution and thickness of the sample. The IR absorbance here is due to a broad electronic background absorption of the RGO. (b) shows an integrated chemical image over the N–H and O–H stretching region, 3000–3410 cm^{-1} to indicate the distribution of the adsorbed fragments; the absorption is greatest in the thickest region of the sample. (c) Averaged spectra from the marked regions in (a) to show the greater absorption of the molecular fragments in the thicker portion of the sample.

A total of 100 hyperspectral data sets as a function of angle were acquired as a hair around its long dimension was rotated. The measured absorption at 1639 cm^{-1} was reconstructed to obtain the 3D images primarily of the protein structure of the hair as shown in Figure 15.16, red color. When looking down the axis of the hair, one sees that the protein intensity is found in the cortex, but not in the medulla, as previously observed with microtomed samples [76]. The medulla, however, is filled with phospholipids (bluish green color), as seen by tomographically reconstructing the 1705 cm^{-1} spectral absorptions. These spectromicrotomography results not only demonstrate that spectrally sensitive reconstructions can be done on larger, fully hydrated biological samples, but they also were obtained without time consuming and potentially damaging and/or modifying effects of embedding and microtoming such samples.

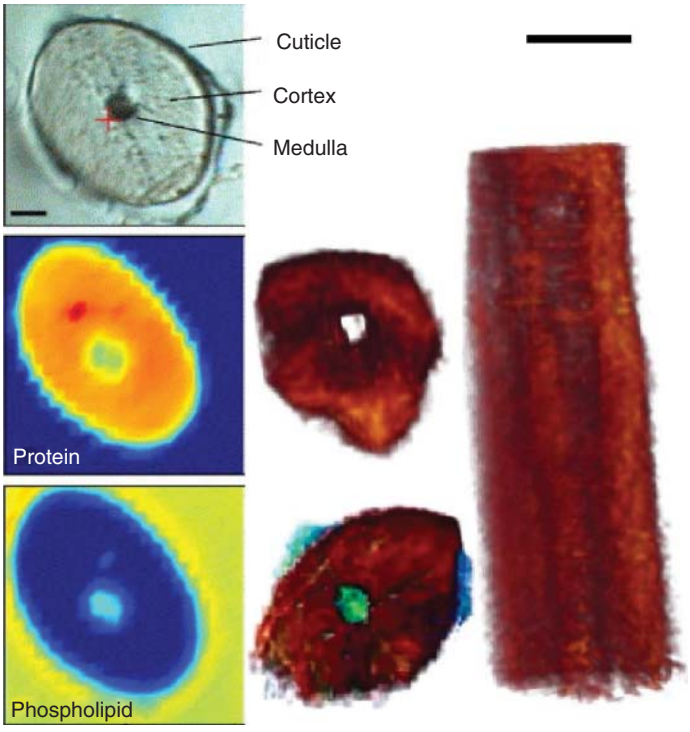

Figure 15.16 2D and 3D chemical imaging of hair. Left panels show a visible micrograph with key substructures labeled, and synchrotron infrared spectral images of the protein and phospholipid concentrations from a cross section of a human hair (from Ref. [76], with permission). On the right are views of the full tomographic reconstructions obtained from an intact human hair showing absorptions of protein (red) and phospholipid (bluish green). The medulla is observed to have little protein as we see the protein reconstruction is indeed hollow (center), but it instead has higher concentrations of phospholipids (center bottom). Scale bars are 25 μm. (Reproduced with permission from the Nature Publishing Group Ref. [5] Nature Methods.)

15.5.4.2 **Populus – Cell Walls of Wood**

Elucidating the 3D molecular architecture of plant cell walls is one of the most challenging problems in plant biology. Although general aspects of how plant cell walls are assembled and synthesized are becoming understood, and an X-ray microtomographic study of pine wood revealed some structural and chemical architecture delineated by density differences [80], the detailed 3D molecular cell wall structure remains poorly understood. A critical step in converting biomass to liquid biofuels and other value-added products is the deconstruction of recalcitrant lignified cell walls. A better understanding of microscale structure and chemical composition will not only enhance basic understanding of plant cell walls but also improve the efficiency of lignocellulose conversion processes.

Populus is a genus of fast-growingdeciduous trees cultivated worldwide for their ecological role in carbon sequestration, nutrient cycling, and remediation, and to provide sustainable wood for lumber, fiber for paper, and renewable lignocellulosic biomass for ethanol, nanocellulose, and bioplastics. *Populus* species are models for tree genetics, molecular biology, cell wall chemistry, and biotechnology. *Populus trichocarpa* was the first tree genome sequenced (2006), creating a resource for genetic modifications that produce trees with desired cell wall properties. A major challenge to genetic improvement is to understand the complex, heterogeneous structure

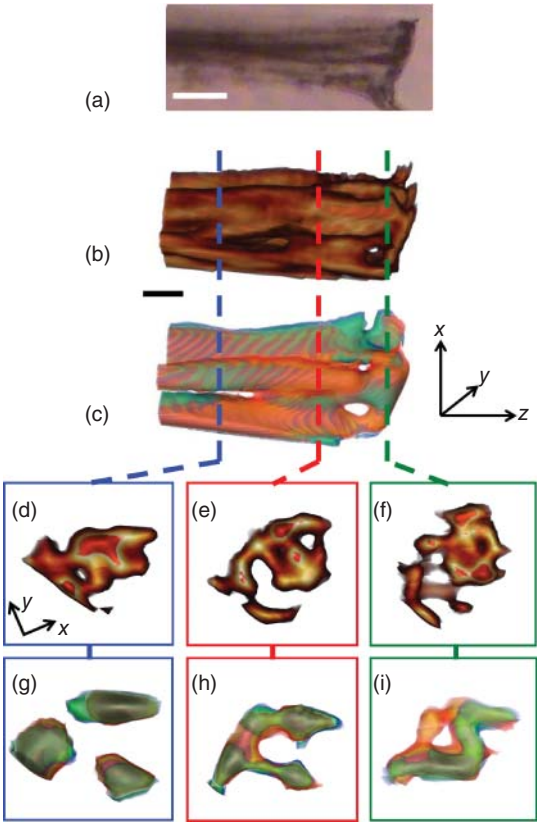

Figure 15.17 Spectromicrotomography of *Populus* wood fiber. A photomicrograph, (a), and 3D reconstructions of populous wood. The brown colors in (b) and (d) through (f) are reconstructed intensities of hydrocarbon-stretching absorption modes between 2804 and 3023 cm^{-1}. The red colors in (c) and (g) through (i) are spectrally associated with lignin (1523–1627 cm^{-1}) superimposed on the bluish green colors associated with holocellulose (1689–1781 cm^{-1}). Panels (d) through (i) are 10 μm thick virtual slices across the vessels at the locations indicated by the dashed lines. (Reproduced with permission from the Nature Publishing Group Ref. [5], Nature Methods.)

of lignocellulose in xylem cell walls. High-resolution 3D images detailing biopolymer interactions in the layers of xylem vessel walls will help meet this challenge.

An infrared spectromicrotomographic data set of a *Populus deltoides* wood sliver (50 μm × 30 μm) was obtained. Reconstructions from specific spectral regions of interest are shown in Figure 15.17. It is observed that the 1523–1627 cm^{-1} and the 1689–1781 cm^{-1} regions corresponding to lignin and holocellulose (hemicellulose and cellulose) spectral absorptions, respectively, show that the specimen has three longitudinal vessels. The CH_2 and CH_3 in 2804–3023 cm^{-1} spectral region also shows intensity in the space between these three vessels. Virtual slices cutting through the three vessel walls in Figure 15.17g–i show that the holocellulose is more prominent in the middle of the wall, whereas lignin is more dominant around the exterior of the wall and middle lamellae between vessels.

15.6 Conclusions

The bright, low-emittance characteristics of the synchrotron light source permit the focusing of IR storage ring radiation down to diffraction-limitedlength scales such that very high SNR is achieved. A realization of the full potential of synchrotron sources has been achieved with the IRENI beamline, which collects all of the radiation from a large angle, bending magnet to illuminate an FPA detector. The high brightness of the source allows the use of high magnification, high NA optics, and small effective pixel sizes that cooperatively yield diffraction-limited spatial resolution throughout the entire mid-IR spectral regions. Furthermore, the use of the FPA detector enables collecting such data on minute timescales. Measurement and deconvolution of the instrumental PSF of the microscope is possible using data acquired with synchrotron sources, and deconvolution techniques enhance spatial resolution and contrast to exceed the conventional diffraction limit.

These approaches have led to advances in 2D projection imaging. Results presented from polymers, biological, and inorganic materials imaging exemplify the power of the synchrotron source for widefield spectromicroscopy applied to a variety of disciplines. In addition to the impressive spatial resolution achieved using the multibeam FPA illumination, the unparalleled SNR provided by the synchrotron enables time-resolved studies of systems ranging from live-cell chemical imaging to reactions at surfaces.

The recent breakthrough of spectromicrotomography has now enabled 3D chemical imaging of samples at micrometer length scales, which is of critical importance in many aspects of biology, medicine, forensics, and materials science. This technique was used to elucidate the 3D architecture of the cell wall components of *Populus* wood as well as human hair.

References

1. Nasse, M.J., Walsh, M.J., Mattson, E.C., Reininger, R., Kajdacsy-Balla, A., Macias, V., Bhargava, R., and Hirschmugl, C.J. (2011) *Nat. Methods*, **8**, 413–U458.
2. Mattson, E.C., Unger, M., Manandhar, B., Alavi, Z., and Hirschmugl, C.J. (2013) *J. Phys. Conf. Ser.*, **425**, 142001.
3. Mattson, E.C., Nasse, M.J., Rak, M., Gough, K.M., and Hirschmugl, C.J. (2012) *Anal. Chem.*, **84**, 6173–6180.
4. Nasse, M.J., Ratti, S., Giordano, M., and Hirschmugl, C.J. (2009) *Appl. Spectrosc.*, **63**, 1181–1186.
5. Martin, M.C., Dabat-Blondeau, C., Unger, M., Sedlmair, J., Parkinson, D.Y., Bechtel, H.A., Illman, B., Castro, J.M., Keiluweit, M., Buschke, D., Ogle, B., Nasse, M.J., and Hirschmugl, C.J. (2013) *Nat. Methods*, **10**, 861–864.
6. Williams, G.P., Hirschmugl, C.J., Kneedler, E.M., Sullivan, E.A., Siddons, D.P., Chabal, Y.J., Hoffman, F., and Moeller, K.D. (1989) *Rev. Sci. Instrum.*, **60**, 2176–2178.
7. Faist, J., Capasso, F., Sivco, D.L., Sirtori, C., Hutchinson, A.L., and Cho, A.Y. (1994) *Science*, **264**, 553–556.
8. Fuji, T. and Suzuki, T. (2007) *Opt. Lett.*, **32**, 3330–3332.
9. Isaienko, O. and Borguet, E. (2012) *Opt. Express*, **20**, 547–561.
10. Lassonde, P., Theberge, F., Payeur, S., Chateauneuf, M., Dubois, J., and Kieffer, J.C. (2011) *Opt. Express*, **19**, 14093–14098.
11. Cheng, M., Reynolds, A., Widgren, H., and Khalil, M. (2012) *Opt. Lett.*, **37**, 1787–1789.
12. Calabrese, C., Stingel, A.M., Shen, L., and Petersen, P.B. (2012) *Opt. Lett.*, **37**, 2265–2267.
13. Petersen, P.B. and Tokmakoff, A. (2010) *Opt. Lett.*, **35**, 1962–1964.
14. Hirschmugl, C.J. and Gough, K.M. (2012) *Appl. Spectrosc.*, **66**, 475–491.
15. Carr, G.L., Chubar, O., and Dumas, P. (2007) *Spectrochemical Analysis Using Infrared Multichannel Detectors*, Blackwell Publishing Ltd, pp. 56–84.
16. Griffiths, P. and De Haseth, J.A. (2007) *Fourier Transform Infrared Spectrometry*, Wiley-Interscience, New York.
17. Dumas, P., Jamin, N., Teillaud, J.L., Miller, L.M., and Beccard, B. (2004) *Faraday Discuss.*, **126**, 289–302.
18. Nasse, M.J., Mattson, E.C., Reininger, R., Kubala, T., Janowski, S., El-Bayyari, Z., and Hirschmugl, C.J. (2011) *Nucl. Instrum. Methods Phys. Res., Sect. A*, **649**, 172–176.
19. Nasse, M.J., Reininger, R., Kubala, T., Janowski, S., and Hirschmugl, C. (2007) *Nucl. Instrum. Methods Phys. Res., Sect. A*, **582**, 107–110.
20. Schmidt-Patterson, C., Carson, D., Phenix, A., Khanjian, H., Trentelman, K., Mass, J., and Hirschmugl, C.J. (2013) *e-Preserv. Sci.*, **10**, 1–9.
21. Unger, M., Mattson, E., Patterson, C.S., Alavi, Z., Carson, D., and Hirschmugl, C.J. (2013) *Appl. Phys. A Mater. Sci. Process.*, **111**, 135–145.
22. Mass, J., Sedlmair, J., Patterson, C.S., Carson, D., Buckley, B., and Hirschmugl, C. (2013) *Analyst*, **138**, 6032–6043.
23. Mattson, E.C., Pu, H.H., Cui, S.M., Schofield, M.A., Rhim, S., Lu, G.H., Nasse, M.J., Ruoff, R.S., Weinert, M., Gajdardziska-Josifovska, M., Chen, J.H., and Hirschmugl, C.J. (2011) *ACS Nano*, **5**, 9710–9717.
24. Clemons, C., Sedlmair, J., Illman, B., Ibach, R., and Hirschmugl, C. (2013) *Polymer*, **54**, 2058–2061.
25. Mattson, E.C., Pande, K., Unger, M., Cui, S.M., Lu, G.H., Gajdardziska-Josifovska, M., Weinert, M., Chen, J.H., and Hirschmugl, C.J. (2013) *J. Phys. Chem. C*, **117**, 10698–10707.
26. Tobin, M.J., Puskar, L., Hasan, J., Webb, H.K., Hirschmugl, C.J., Nasse, M.J., Gervinskas, G., Juodkazis, S., Watson, G.S., Watson, J.A., Crawford, R.J., and Ivanova, E.P. (2013) *J. Synchrotron Radiat.*, **20**, 482–489.
27. Riding, M.J., Trevisan, J., Hirschmugl, C.J., Jones, K.C., Semple, K.T., and Martin, F.L. (2012) *Environ. Int.*, **50**, 56–65.
28. Kastyak-Ibrahim, M.Z., Nasse, M.J., Rak, M., Hirschmugl, C., Del Bigio, M.R.,

Albensi, B.C., and Gough, K.M. (2012) *Neuroimage*, **60**, 376–383.
29. Liao, C.R., Rak, M., Lund, J., Unger, M., Platt, E., Albensi, B.C., Hirschmugl, C.J., and Gough, K.M. (2013) *Analyst*, **138**, 3991–3997.
30. Hackett, M.J., Borondics, F., Brown, D., Hirschmugl, C., Smith, S.E., Paterson, P.G., Nichol, H., Pickering, I.J., and George, G.N. (2013) *ACS Chem. Neurosci.*, **4**, 1071–1080.
31. Fogarty, S.W., Patel, I.I., Trevisan, J., Nakamura, T., Hirschmugl, C.J., Fullwood, N.J., and Martin, F.L. (2013) *Analyst*, **138**, 240–248.
32. Clede, S., Lambert, F., Sandt, C., Kascakova, S., Unger, M., Harte, E., Plamont, M.-A., Saint-Fort, R., Deniset-Besseau, A., Gueroui, Z., Hirschmugl, C., Lecomte, S., Dazzi, A., Vessieres, A., and Policar, C. (2013) *Analyst*, **138**, 5610.
33. Stelzer, E.H.K. (1998) *J. Microsc.*, **189**, 15–24.
34. Carr, G.L. (2001) *Rev. Sci. Instrum.*, **72**, 1613–1619.
35. Hecht, E. (2002) *Optics*, Addison-Wesley, Reading, MA.
36. Herman, G.T. (2010) *Fundamentals of Computerized Tomography: Image Reconstruction from Projection*, 2nd edn, Springer, New York.
37. Hornich, H. (1986) *IEEE Trans. Med. Imaging*, **5**, 169–169.
38. Fessler, J.A., Ficaro, E.P., Clinthorne, N.H., and Lange, K. (1997) *IEEE Trans. Med. Imaging*, **16**, 166–175.
39. Erdogan, H. and Fessler, J.A. (1999) *IEEE Trans. Med. Imaging*, **18**, 801–814.
40. Erdogan, H. and Fessler, J.A. (1999) *Phys. Med. Biol.*, **44**, 2835–2851.
41. Fessler, J.A. and Rogers, W.L. (1996) *IEEE Trans. Image Process.*, **5**, 1346–1358.
42. Stayman, J.W. and Fessler, J.A. (2000) *IEEE Trans. Med. Imaging*, **19**, 601–615.
43. Mattson, E.C., Unger, M., Clede, S., Lambert, F., Policar, C., Imtiaz, A., D'Souza, R., and Hirschmugl, C.J. (2013) *Analyst*, **138**, 5610–5618.
44. Levenson, E., Lerch, P., and Martin, M.C. (2006) *Infrared Phys. Technol.*, **49**, 45–52.
45. Levenson, E., Lerch, P., and Martin, M.C. (2008) *Infrared Phys. Technol.*, **51**, 413–416.
46. Watson, G.S., Myhra, S., Cribb, B.W., and Watson, J.A. (2008) *Biophys. J.*, **94**, 3352–3360.
47. Watson, G.S., Cribb, B.W., and Watson, J.A. (2010) *ACS Nano*, **4**, 129–136.
48. Young, J., Walker, S.M., Bomphrey, R.J., Taylor, G.K., and Thomas, A.L.R. (2009) *Science*, **325**, 1549–1552.
49. Byun, D., Hong, J., Saputra, Ko, J.H., Lee, Y.J., Park, H.C., Byun, B.K., and Lukes, J.R. (2009) *J. Bionic Eng.*, **6**, 63–70.
50. Gorb, S.N., Kesel, A., and Berger, J. (2000) *Arthropod Struct. Dev.*, **29**, 129–135.
51. Kreuz, P., Arnold, W., and Kesel, A.B. (2001) *Ann. Biomed. Eng.*, **29**, 1054–1058.
52. Lockey, K.H. (1960) *J. Exp. Biol.*, **37**, 316–329.
53. Wagner, T., Neinhuis, C., and Barthlott, W. (1996) *Acta Zool.*, **77**, 213–225.
54. Guilhaumou, N., Dumas, P., Carr, G.L., and Williams, G.P. (1998) *Appl. Spectrosc.*, **52**, 1029–1034.
55. Jamme, F., Lagarde, B., Giuliani, A., Garcia, G.A., and Mercury, L. (2013) *J. Phys. Conf. Ser.*, **425**, 142002.
56. McNaughton, D., Wood, B.R., Cox, T.C., Drenkhahn, J.-D., and Bambery, K.R. (2009) in *Infrared and Raman Spectroscopic Imaging* (eds R. Salzer and H.W. Siesler), John Wiley & Sons, Inc., pp. 202–223.
57. Kumeta, K., Nagashima, I., Matsui, S., and Mizoguchi, K. (2003) *J. Appl. Polym. Sci.*, **90**, 2420–2427.
58. Paralikara, S.A., Simonsen, J., and Lombardi, J. (2008) *J. Membr. Sci.*, **320**, 248–258.
59. Moon, R.J., Martini, A., Nairn, J., Simonsen, J., and Youngblood, J. (2011) *Chem. Soc. Rev.*, **40**, 3941–3994.
60. Roohani, M., Habibi, Y., Belgacem, N.M., Ebrahim, G., Karimi, A.N., and Dufresne, A. (2008) *Eur. Polym. J.*, **44**, 2489–2498.
61. Wang, B. and Sain, M. (2007) *Compos. Sci. Technol.*, **67**, 2521–2527.
62. Zimmermann, T., Pohler, E., and Geiger, T. (2004) *Adv. Eng. Mater.*, **6**, 754–761.

63. Sedlmair, J., Mass, J., Schmidt-Patterson, C., and Hirschmugl, C.J. (2013) *Microsc. Microanal.*, **19** (suppl. 2), 1406–1407
64. Mass, J.L., Opila, R., Buckley, B., Cotte, M., Church, J., and Mehta, A. (2013) *Appl. Phys. A Mater. Sci. Process.*, **111**, 59–68.
65. Opila, R.L., Church, J., Fang, F., and Mass, J.L. (2012) *Microsc. Microanal.*, **18**, 896–897.
66. Clede, S., Lambert, F., Sandt, C., Gueroui, Z., Refregiers, M., Plamont, M.A., Dumas, P., Vessieres, A., and Policar, C. (2012) *Chem. Commun.*, **48**, 7729–7731.
67. Clède, S., Lambert, F., Sandt, C., Gueroui, Z., Delsuc, N., Dumas, P., Vessières, A., and Policar, C. (2013) *Biotechnol. Adv.*, **31**, 393–395.
68. Policar, C., Waern, J.B., Plamont, M.A., Clede, S., Mayet, C., Prazeres, R., Ortega, J.M., Vessieres, A., and Dazzi, A. (2011) *Angew. Chem. Int. Ed.*, **50**, 860–864.
69. Bertrand, L., Alban, F., and Graham, M. (2012) *Preservation of Plastic Artefacts in Museum Collections*, Éditions du Comité des Travaux Historiques et Scientifiques, Paris.
70. Maekowa, S. and Elert, K. (2003) *The Use of Oxygen-Free Environments in the Control of Museum Insect Pests*, The Getty Conservation Institute, Los Angeles, CA.
71. Tobin, M.J., Puskar, L., Barber, R.L., Harvey, E.C., Heraud, P., Wood, B.R., Bambery, K.R., Dillon, C.T., and Munro, K.L. (2010) *Vib. Spectrosc.*, **53**, 34–38.
72. Holman, H.Y.N., Miles, R., Hao, Z., Wozei, E., Anderson, L.M., and Yang, H. (2009) *Anal. Chem.*, **81**, 8564–8570.
73. Vaccari, L., Birarda, G., Businaro, L., Pacor, S., and Grenci, G. (2012) *Anal. Chem.*, **84**, 4768–4775.
74. Chan, K.L.A. and Kazarian, S.G. (2013) *Analyst*, **138**, 4040–4047.
75. Palmucci, M., Ratti, S., and Giordano, M. (2011) *J. Phycol.*, **47**, 313–323.
76. Miller, L.M. and Dumas, P. (2006) *Biochim. Biophys. Acta Biomembr.*, **1758**, 846–857.
77. Kreplak, L., Briki, F., Duvault, Y., Doucet, J., Merigoux, C., Leroy, F., Leveque, J.L., Miller, L., Carr, G.L., Williams, G.P., and Dumas, P. (2001) *Int. J. Cosmet. Sci.*, **23**, 369–374.
78. Bantignies, J.L., Fuchs, G., Carr, G.L., Williams, G.P., Lutz, D., and Marull, S. (1998) *Int. J. Cosmet. Sci.*, **20**, 381–394.
79. Bertrand, L., Doucet, J., Dumas, P., Simionovici, A., Tsoucaris, G., and Walter, P. (2003) *J. Synchrotron Radiat.*, **10**, 387–392.
80. Illman, B.L. and Dowd, B.A. (1999) in *Developments in X-ray Tomography II*, vol. 3772 (ed U. Bonse), SPIE, pp. 198–204.

Index

a

acidic phosphate 154
acousto-optic tunable filters (AOTFs) 31–32, 36–37
agricultural crops and mapping and imaging application 244–245
– carbohydrates and endosperm 246, 248–250
– environmental contaminants/crop protection products uptake and fate 253–254
– environmental impact and processing 251–252
– lignin and cellulose 250
– protein secondary structure 250
– tissue-specific functional-group analysis 245
airy disk 5
airy pattern 4
algae and mapping and imaging application 264
– cell wall composition and compound distribution 266
– environmental influences on metabolism 268
– IR techniques 272–273
– Raman techniques 271–272
– taxonomic differentiation and classification 265–266
amino acids and TERS imaging 484–487
anomalous pixels and spectral readings detection and suppression 63
Arabidopsis thaliana mapping and imaging
– IR mapping and imaging 262
– Raman mapping and imaging 262–264
artificial neural networks (ANNs) 190–191, 208, 215
astaxanthin (ATX) 266
asymmetric least squares (AsLSs) 63
Athens HS system 316
atherosclerosis 142
atomic force microscopy (AFM)
– combination with photothermal FT-IR spectroscopy 530–531
– FT-IR 518
attenuated total reflection (ATR) 122, 228, 242, 253, 276, 280, 341, 347–349, 351–358
– ATR FT-IR imaging 398–402
– – biomedical applications 419–421
– – field of view 402–407
– – penetration depth 407–408
– – quantitation 408–410
– – tablet dissolution 415–419
– diamond ATR FT-IR imaging 404–405
– high-throughput studies 430–436
– live cells imaging 427
– micro-ATR FT-IR imaging 403–404
– microspectroscopy 19–20
– new versus old diamond ATR accessory 405–406
attenuated total resolution (ATR) 5, 14, 19, 20, 45–48
Auston switch 49
Australian Synchrotron IRM beamline 597

b

Barrett's esophagus 213
baseline correction 61, 63
Beer–Lambert law 59–60, 68, 81
Bessel functions 18
biological objects classification 323
– ROI in multicompartment products 324–325
– small objects inspection 323–324

Infrared and Raman Spectroscopic Imaging, Second Edition. Edited by Reiner Salzer, Heinz W. Siesler.
© 2014 Wiley-VCH Verlag GmbH & Co. KGaA. Published 2014 by Wiley-VCH Verlag GmbH & Co. KGaA.

biopolymers 494–495
– DNA/RNA strands 495–496
– proteins and fibrils 496–500
bone remodeling 156
brain metastases 134
brain tissue and brain tumors 130
brain tumors 118
bruises 318–319
Bruker FT-IR imaging system (Bruker Optik GmbH, Ettlingen, Germany) 345, 346
Bruker Optics Hyperion 19–20
buccal cells 195, 198–199

c

calibration model 71–73
carbon fiber interface 410–411
carbon nanotubes (CNTs) 253
carbonate content 154
carotenoids 229
Cassegrain objective 7
cellular resolution 137–138
central nervous system (CNS) 117–118
cervical cells 183, 191–193, 198, 203, 209–212, 214–215
cervix uteri and squamous cell carcinoma 139–142
charge-coupled device (CCD) 21–22, 26, 35, 37, 131
– detectors 24–26
chemical mapping 300
– fish 301–303
– fruit 300–301
– HIS pitfalls 306–307
– kernels 305
– laboratory batch cultures 304–305
– meat 303–304
– process monitoring 305–306
– wood 301
chemical movies 435
chemometric tools for image analysis 57–58
– exploratory image analysis 65
– – classical image representations and limitations 65–66
– – multivariate image analysis (MIA) and principal component analysis (PCA) 66–70
– future trends 106
– hyperspectral images 58
– – data set and underlying model 58–60
– image preprocessing 60
– – data pretreatments 63–64
– – image compression 64–65
– – signal preprocessing 61–63
image resolution
– – compound identification 98–100
– – concept 80–81
– – image multiset analysis 91, 93–95
– – quantitative analysis 100–102
– – resolution process 86–91
– – spatial and spectral exploration 81–82
– – superresolution 104–106
– image segmentation 73–74
– – hard and fuzzy segmentation approaches 78–79
– – spatial information in image segmentation 79–80
– – unsupervised and supervised segmentation methods 74–78
– quantitative image information and multivariate image regression 70–73
Christiansen effect 18
ciliated cells 115
coherent anti-Stokes Raman scattering (CARS) 114, 125, 129–130, 136–137, 142–145, 228, 231, 251, 268, 271. *See* also nonlinear vibrational spectroscopic microscopy of cells and tissue
collagen 128, 153, 154, 158–160, 163–165
colon tissue 125–130
columnar cells 115
confocal microscopy 36
connective tissue and extracellular matrix 115–116
cotton seed coat (CSC) 252
cuboidal cells 115
cultured cells 183, 198–200

d

de-noising 61
dentin 153, 154, 159, 163, 164
diagnostic algorithms 190–191
diamond ATR FT-IR imaging 404–405
diffraction-limited microscopy 4–5
diffuse reflection (DR) spectroscopy 8, 34
Digilab UMA-150 7
DNA/RNA nucleobases and derivatives and TERS imaging 487–491
dual aperturing 15–18
dual-energy X-ray absorptiometry (DEXA) 550
dysplasia 139, 213

e

electron multiplying charge-coupled device (EMCCD) 25, 53
epithelium 114
esophageal cells 183, 212–216

essential oils 236–241
Euclidean distance 79
exfoliated cells 183, 195–198
exploratory image analysis 65
– classical image representations and limitations 65–66
– multivariate image analysis (MIA) and principal component analysis (PCA) 66–70
extended multiplicative scatter correction (EMSC) 61
external contamination 312–313
– adulteration and nonconformities 315
– foreign bodies 313–315
– surface contaminations 315–317

f

far-infrared spectroscopy 446–447
FastIR™ accessory 349
feces contamination 315–317
feedback multivariate model selection (FEMOS) 307
field of view (FOV) 402–407, 414–417, 427, 432
– expanded (ZnSe) 406–407
first-generation instruments 39
fixation studies 194–195
– effects of cultured cells 198–200
– of exfoliated cells 195–198
fixed and dried cells comparison 196–198
fixed-size image window-evolving factor analysis (FSIW-EFA) 83–86, 91
flat-field correction 26
flavonoids 234, 236
fluorescence endoscopy 213
focal-plane array (FPA) 13, 15, 39, 41, 43–44, 48, 125, 241, 397
foreign bodies 313–315
– internal 321–322
forensic applications
– counterfeit tablets imaging 424–425
– trace materials and chemical fingerprinting detection 425–427
Fourier transform (FT) Raman mapping 231
Fourier transform infrared (FT-IR) imaging 6–7, 9–11, 13–15, 18, 38–43, 113, 117–119, 121, 124–126, 129–131, 133–136, 139–140, 145, 153–156, 163, 165–166, 185, 193, 219, 228, 241–246, 250–253, 256, 258, 262, 264, 266, 269, 271, 272, 274, 276, 278, 280, 282, 345–346, 397–398
– AFM 518, 529–531
– applications for polymer characterization 361
– – imaging anisotropic materials with polarized radiation 364–370
– – phase separation investigation in biopolymer blends 361–364
– ATR FT-IR imaging 398–402
– – field of view 402–407
– – penetration depth 407–408
– – quantitation 408–410
– examples from published literature 158–160
– macro imaging 347–348
– measurement of imaging 348–349
– micro imaging 346–347
– of inorganic materials 387–388, 393
– – experimental 388
– – mineral phases determination in soils 392–393
– – P-fertilizer–soil reactions determination 388–392
– penetration depth gradient observation in imaging applications 349, 351–354
practical applications
– – forensic applications 424–427
– – high-throughput studies with ATR-FT-IR imaging 430–436
– – live cells imaging 427–429
– – pharmaceuticals 413–424
– – polymer interfaces and blends materials characterization 410–413
– spatial resolution of imaging measurements 354–361
– specimen preparation and typical spectrum 156–158
– transmission imaging 400–401
– – mapping versus FPA 401
Fourier transform near-infrared (FT-NIR) spectrometer 34–35
– applications for diffusion studies 370–372
– – experimental 372–373
– – results and discussion 373–378
free electron laser (FEL) 12–13
front-surface reflection. *See* Kramers–Kronig reflection
fungi 317
fuzzy C-means (FCM) 140

g

glial cells 118
gliosis 118
glycosaminoglycans 116
gold nanoparticles (GNPs) 500

Golden Gate optics 47–49
gray-level co-occurrence matrix (GLCM) 299, 300, 304, 325
grey matter 117

h
hard tissues
– composition and organization 153
– elements detectable by vibrational spectroscopy 153–155
– FT-IR spectroscopy 156–160
– – examples from published literature 158–160
– – specimen preparation and typical spectrum 156–158
– Raman spectroscopy 160–165
– – bone 161–163
– – clinical applications 165–166
– – examples from published literature 163–165
– – instrumental choices, specimen preparation, and typical Raman spectra 160–161
– tissue age versus specimen age
– – biologically important questions 155–156
Harrick FastIR 47
hemozoin crystal 493
hierarchical cluster analysis (HCA) 139
high-throughput studies with ATR-FT-IR imaging 430–432
– imaging and microfluidics 433–436
– transmission mode 432–433
human hair 611–612
hydrogels 412–413
hydroxyapatite 153, 163, 164
hydroxypropyl methylcellulose (HPMC)-based coat 464–465
hyperspectral cube 4
hyperspectral cubes mathematical evaluation
– 3-D spectromicrotomographic reconstruction 593–594
– hyperspectral deconvolution 590–593
hyperspectral images 3, 57, 58
– data set and underlying model 60

i
image multiset analysis 91, 94–95
individual cells infrared spectral imaging medical applications 181–182
– methods 183–191
– – cell collection and culturing methods 183
– – data acquisition 185–187
– – data analysis methods 188–191
– – sample preparation 184
– results and discussion 191–218
– – fixation studies 194–200
– – SCP 191–194, 216–218
– – spectral cytopathology 200–216
– SCP future potential 218–219
infrared and Raman instrumentation for mapping and imaging 3–4
– mapping with pulsed terahertz radiation 48–52
mid-infrared hyperspectral imaging
– – sampling 45–48
– – spectrometers based on 2D array detectors 37–43
– – spectrometers based on hybrid linear array detectors 43–45
mid-infrared microspectroscopy and mapping
– – attenuated total reflection microspectroscopy 19–20
– – detectors 9–11
– – diffraction-limited microscopy 4–5
– – microscopes and sampling techniques 6–8
– – sources 11–14
– – spatial resolution 14–18
– – transmission microspectroscopy 18–19
– near-infrared hyperspectral imaging 30–35
– Raman hyperspectral imaging 35–37
– Raman microspectroscopy and mapping 20–24
– – CCD detectors 24–26
– – spatial resolution 26–29
– – tip-enhanced Raman spectroscopy (TERS) 29–30
infrared and Raman spectroscopic mapping and plant materials imaging 227
– application to agricultural crops 245
– – carbohydrates and endosperm 246, 248–250
– – environmental contaminants/crop protection products uptake and fate 253–254
– – environmental impact and processing 252
– – lignin and cellulose 251
– – protein secondary structure 250
– – tissue-specific functional-group analysis 245
– application to algae 264

– – cell wall composition and compound distribution 266
– – environmental influences on metabolism 268
– – IR techniques 272–273
– – Raman techniques 271
– – taxonomic differentiation and classification 266
– applications to horticultural crops 231
– – carotenoids 229
– – environmental interactions and processing 242–244
– – essential oils 236–241
– – flavonoids 234, 236
– – polyacetylenes 232–234
– – tissue constituents 241
– plant tissue–pathogens interaction 273
– – bacteria and plant pathogens 274–275
– – fungal plant pathogens 275–279
– – nonwoody plants interactions 282
– – plant material fungal degradation 279–281
– wild plants and trees mapping and imaging 254, 256
– – *Arabidopsis thaliana* mapping and imaging 261–262
– – IR mapping and imaging of trees 256–258
– – Raman mapping and imaging of trees 258–261
– – wild plants mapping and imaging 262–264
infrared instrumentation 185
infrared mapping below diffraction limit 513
– AFM and photothermal FT-IR spectroscopy combination 530–535
– near-field microscopy with elastic scattering from tip 519–529
– near-field microscopy with small apertures 513–514
– – AFM/FT-IR 518
– – scanning photothermal microscopy and microspectroscopy 515–518
internal reflection element (IRE) 5, 14–20, 45, 47–48, 517
International Traffic in Arms Regulations (ITAR) 41
IRENI (InfraRed ENvironmental Imaging) 273, 586–588, 593, 597, 599, 605, 609, 611, 615
IRSTEA 311–312
ISL HSI 316
iterative constrained endmembers (ICE) 87

k

Kaiser Optical Systems(Ann Arbor, MI, USA) 131
Kramers–Kronig (KK) transformation 607
Kramers–Kronig reflection 8
Kubelka–Munk corrections 608

l

labeled cells 604
Large Sampling (LS) accessory" (Digilab) 42
layered polymers 604–609
leptomeninges 118
linear discriminant analysis (LDA) algorithm 133, 135, 136
linear logistic regression (LLR) model 319
lipids 155, 163
liquid crystal tunable filter (LCTF) 3, 31–33, 35, 37
live cells imaging
– ATR FT-IR imaging 427
– FT-IR imaging transmission mode in microfluidic devices 427–429
Local Linear Embedding (LLE) algorithm 309
low-e slides 184

m

Malvern Instruments system 33, 34
material and pharmaceutical science applications 341–343
– FT-IR and FT-NIR imaging applications for polymer characterization 361, 378
– – FT-NIR imaging applications for diffusion studies 370–378
– – imaging anisotropic materials with polarized radiation 364–370
– – phase separation investigation in biopolymer blends 361–364
– inorganic materials FT-IR spectroscopic imaging 387–388, 393
– – experimental 388
– – mineral phases determination in soils 392–393
– – P-fertilizer–soil reactions determination 388–392
– NIR and FT-IR imaging instrumentation 343
– – diffuse reflection 343–345
– – FT-IR imaging 345–361
– – NIR imaging in transmission 345
– pharmaceutical drug formulations quality control NIR imaging spectroscopy 378, 386

material and pharmaceutical science applications (*contd.*)
– – active ingredients quantitative determination 379–381
– – active ingredients spatial distribution 381, 383–386
matisse 603
MATLAB 188, 190, 191
MatrixNIR system (Malvern, Olney, MD, USA) 343
meningeomas 118
meninges 118
micro-ATR FT-IR imaging 403–404
mid-infrared hyperspectral imaging
– sampling 45–48
– spectrometers based on 2D array detectors 37–43
– spectrometers based on hybrid linear array detectors 43–45
mid-infrared microspectroscopy and mapping
– – attenuated total reflection microspectroscopy 19–20
– detectors 9–11
– diffraction-limited microscopy 4–5
– microscopes and sampling techniques 6–8
– sources 11–14
– spatial resolution 14–18
– transmission microspectroscopy 18–19
mid-infrared spectroscopy (MIRS) 251–252
Mie theory 18–19
MirrIR slides. *See* low-e slides
MOLE^{TM} 22
mouse brains 130–132
mucin 128
multimodal nonlinear microscopy instrumentation 568
– laser sources 568–570
– optics 570
– scanning microscope 571
multiplicative signal correction (MSC) algorithm 189
multivariate curve resolution-alternating least squares (MCR-ALS) 87–88, 91, 94, 104
multivariate image analysis (MIA) and principal component analysis (PCA) 66–70
muscle tissue 116–117
myelin 117

n

N-FINDR algorithm 503
nanocellulose 600–601
near-field microscopy
– with elastic scattering from tip 519–529
– with small apertures 514
– – AFM/FT-IR 518–519
– – scanning photothermal microscopy and microspectroscopy 515–516
near-field scanning optical microscopy (NSOM) 483
near-infrared (NIR) imaging 3–4, 8, 21, 22, 30–34, 39, 48, 49, 53, 123
– history 295–297
– hyperspectral imaging (HSI) as super analyzer 298
– – chemical mapping 300–307
– – food/agriculture items physical properties analysis 308–310
– – physicochemical or sensory properties of food and agricultural products assessment and quantification 298–300
– hyperspectral imaging (HSI) as super vision system 310, 325
– – biological objects classification 323–325
– – external contamination (foreign bodies and adulteration) 312–317
– – internal defects detection by candling 320–323
– – online NIR imaging emergence 311–312, 326–328
– – RGB system failure in food quality control 310–311
– – surface and subsurface defects 317–320
– reasons for use in food and agricultural products 297–298
near-infrared hyperspectral imaging 30–35
near-infrared spectroscopy (NIRS) 251–252
nervous tissue 117–118
new versus old diamond ATR accessory 405–406
noise equivalent power (NEP) 9
noise-adjusted principal component analysis (NA-PCA) 187
noncollagenous proteins 154
nonlinear vibrational spectroscopic microscopy of cells and tissue 561
applications
– – brain structures and brain tumors 574–576
– – normal and injured spinal cord 576–580
– – tumor disease identification 572–574
– multimodal nonlinear microscopy instrumentation 568
– – laser sources 568–570
– – optics 570
– – scanning microscope 571

nonlinear optical imaging
– – CARS 563–568
– – important processes 562–563
numerical aperture (NA) 5
Nyquist sampling criterion 37

o
oil immersion 14
optical evaluation
– experimental and simulated point spread functions 589–590
– microscopy optics and diffraction-limited resolution 588–589
optical parametric oscillator (OPO) 530
optical property analyzer (OPA) 308
optimal cutting temperature (OCT) 114–118
oral cells 183, 193–195, 200, 202–203, 214
organic matrix content 154

p
PapMap methodology 185–187, 213, 216
partial least squares (PLS) 301
partial least squares discriminant analysis (PLS-DA) 77, 280, 309, 318
partition methods 75–76
peripheral nervous system (PNS) 117
PerkinElmer (Massachusetts, USA) imaging system 345, 346
pharmaceutical industry. *See* under terahertz imaging
pharmaceuticals
– ATR FT-IR imaging
– – biomedical applications 419–421
– – tablet dissolution 415–419
biopharmaceuticals development
– – hanging-drop crystallization 423–424
– – microbatch crystallization 421–422
– – surface modification for protein crystallization 422–423
– compacted tablets imaging 413–415
PHB and PLA blends 364–368
plexus 127
point spread function (PSF) 588–590
– experimental and simulated point spread functions 589–590
– point-spread-function contrast resolution (PSFCR) 596
poly(dimethylsiloxane) (PDMS) films 344–345
polyacetylenes 234
polymer interfaces and blends materials characterization
– carbon fiber interface 410–411
– hydrogels 412–413
– polystyrene 411–412
polymorphonuclear leukocytes (PMNs) 141
polystyrene 411–412
populus and cell walls of wood 613–615
Powell lens 35
preclinical trial 204
primary brain tumors 132–134
principal component analysis (PCA) 61, 66–70, 130, 190, 301, 307, 316, 318, 324
protein crystallization optimizing. *See* biopharmaceuticals development
proteoglycans 153–155, 159, 162–163
pulsed terahertz radiation mapping 48–52
purity index 82

q
Qvision AS (Oslo, Norway) 303

r
Raman endoscopy 213
Raman hyperspectral imaging 35–37
Raman microspectroscopy and mapping 20–24
– CCD detectors 24–26
– spatial resolution 26–29
– tip-enhanced Raman spectroscopy (TERS) 29–30
Raman multilayer emulsion image 95
Raman spectroscopy
– bone 161–163
– clinical applications 165–166
– examples from published literature 163–165
– instrumental choices, specimen preparation, and typical Raman spectra 160–161
Raman tomography 549
Raster scanning versus widefield geometries
– numerical apertures, spatial oversampling, and spatial resolution deconvolution effects 595–596
– signal-to-noise ratio comparisons 597–598
– spectromicrotomography 600
– time–area trade-off 598–599
raw cells 186–187
Rayleigh criterion 588–589
redundant aperturing. *See* dual aperturing
resolution process 86–91
resonance Mie (R-Mie) effect 187
– corrections and data preprocessing 188–190
RMieS-EMSC algorithm 272

S
Savitzky–Golay sliding window algorithm 189
scanning electron microscopy (SEM) 301, 412, 413
scanning near-field optical microscopy (SNOM) 513–515, 519
scattering-type near-field optical microscopy (s-SNOM) 513, 520–522, 525, 527, 537
Schwarzschild objective 7
second harmonic generation (SHG) 562–563
secondary brain tumors 134–137
self-interactive modeling of class analogy (SIMCA) 77, 135–136
SESORS 549–550, 555
short-wavelength infrared (SWIR) HSI system 299, 305, 319, 323
signal-to-noise ratio (SNR) 4, 10, 25–26, 39, 41–44, 53, 127, 400, 403, 404, 425, 427
– comparisons 597–598
SIMPLISMA 81–83, 88, 92
Sintef ICT 303
soft tissues 113–114
– applications 113
– – atherosclerosis 142
– – brain tissue and brain tumors 131–136
– – cervix uteri and squamous cell carcinoma 139–142
– – colon tissue 125–130
– connective tissue and extracellular matrix 116
– epithelium 115
– muscle tissue 117
– nervous tissue 118
– preparation 114
– – FT-IR imaging preparation 121–122
– – general strategies 118–119
– – Raman imaging preparation 123–124
– – reference material vibrational spectra 120–121
spatially offset Raman spectroscopy (SORS) 544–547
– inverse SORS 547–548
spatially resolved spectroscopy (SRS) 308–310
SPECMOD (Centre for Biospectroscopy and DataModelling (Aas, Norway)) 302
spectral cytopathology (SCP) 182
– general aspects 191–194
– of cervical mucosa 210–212
– of esophageal cells 212–216
– of live cells in aqueous environment 216–218
– of oral mucosa cells 202–203
– of urine-borne cells 200–202
Spectrum Spotlight (PerkinElmer) 43
specular reflection. *See* Kramers–Kronig reflection
Spotlight 300 (Perkin Elmer, WalthamMA, USA) 131
squamous cells 115
squamous epithelial tissue 193
step-scan interferometer 39
stimulated Raman scattering (SRS) microscopy 253
Stingray 38, 39, 45
stress-induced phase transformation in poly(vinylidene fluoride) 368–370
subsurface Raman spectroscopy in turbid media 543–544
application areas examples
– – bones probing through skin for disease diagnosis 550–553
– – calcifications chemical identification in breast cancer lesions 554–556
– – forensic and security applications 556–558
– – pharmaceutical tablets and probing in quality control 556
– deep noninvasive Raman spectroscopy 544
– – inverse SORS 547–548
– – Raman tomography 549
– – SESORS 549–550, 555
– – spatially offset Raman spectroscopy (SORS) 544–547
– – transmission Raman spectroscopy 548–549
superresolution 104–106
support vector machines (SVMs) 136, 309
surface and subsurface defects 317–318
– chilling injuries and potential greening area 320
– human-detectable defects 318–320
surface chemistry 611
surface-enhanced resonance Raman spectroscopy (SERRS) 228
surface-enhanced Raman scattering (SERS) 29, 228, 271, 273, 479–480, 549, 555, 556. *See* also tip-enhanced Raman scattering (TERS)
SUSAN (Sustainable and Safe Re-use of Municipal Sewage Sludge for Nutrient Recovery) 387
synchrotron 11–14
synchrotron IR microspectroscopy (SR-IMS) 246, 250

synchrotron IR radiation sources 585–586
synchrotron-based infrared raster-scanned spectromicroscopy 586
synchrotron-based infrared spectromicrotomography 588
synchrotron-based infrared widefield spectromicroscopy 586–587

t
targeted orthogonal partial least squares (T-OPLS) analysis 271
terahertz imaging 445–446, 448
– low wavenumber region in infrared spectrum 463
– – far-infrared spectroscopy 446
– in pharmaceutical industry 452–453
– – competition versus cost 471
– – discussion 468–470
– – experimental setup to measure solid dosage forms 458
– – samples investigation 455, 458
– – solid dosage forms imaging 453–455
– – typical applications to solid dosage forms 460–468
pulse generation and detection
– – concise description 451–452
– – current applications 450–451
– – emission 448–449
– – reception 449–450
– – sampling 450
Thalassiosira weissflogii 609–611
thermal-dependent polymorphic transformation 95
tip-enhanced Raman scattering (TERS) 29–30
– biomolecules detection 483–484
– – single biomolecules differentiation and identification 484–491
– – structural/chemical changes detection on molecular level 491–494
– biopolymers 494–495
– – DNA/RNA strands 495–496
– – proteins and fibrils 496–500
– from SERS 479–480
– membranes, viruses, and bacteria 500–505
– nonbiological samples investigation 480–481
– technical considerations 481–483
tissue constituents 242
tissue defects (internal) 322–323
TOMRA Sorting Solutions Group 314
transflection spectroscopy 7–8
translational cells 115
transmission microspectroscopy 18–19
transmission modes. *See* under Fourier transform infrared (FT-IR)

u
UMA-500 microscope 38
undulator 11–13
unfixed cells time evolution 195–196
urine-borne cells 200–202
urothelial cells 192, 200–202, 214
US Military Critical Technologies List (MCTL) 41

v
vertex component analysis (VCA) 87
vibrational spectroscopy 48
visible and near infrared (VNIR) 319

w
white matter 117
widefield FT-IR 2D and 3D imaging at microscale 585
– examples 600–615
– – infrared spectromicrotomography 611–615
– – labeled cells 604
– – layered polymers 604–609
– – matisse 603
– – nanocellulose 600–601
– – time-dependent infrared imaging 609–611
– hyperspectral cubes mathematical evaluation 590–594
– – 3-D spectromicrotomographic reconstruction 593–594
– – hyperspectral deconvolution 590–593
– optical evaluation 588–589
– – experimental and simulated point spread functions 589–590
– – microscopy optics and diffraction-limited resolution 588–589
– synchrotron-based infrared raster-scanned spectromicroscopy 586
– synchrotron-based infrared spectromicrotomography 588
– synchrotron-based infrared widefield spectromicroscopy 586–587
– synchrotron IR radiation sources 585–586
– widefield versus Raster scanning geometries 595–600
– – numerical apertures, spatial oversampling, and spatial resolution deconvolution effects 595–596

widefield FT-IR 2D and 3D imaging at microscale (*contd*.)
– – signal-to-noise ratio comparisons 597–598
– – spectromicrotomography 600
– – time–area trade-off 598–599
wiggler. *See* undulator
wild plants and trees mapping and imaging 254
– *Arabidopsis thaliana* mapping and imaging 261–262
– IR mapping and imaging of trees 256–258
– Raman mapping and imaging of trees 258–261
– wild plants mapping and imaging 264
WITec alpha300 R confocal Raman microscope 24

X

X-ray absorption near-edge structure (XANES) 389

Z

ZnSe lens 39

WILEY END USER LICENSE AGREEMENT

Go to www.wiley.com/go/eula to access Wiley's ebook EULA.